Fracture and Strength of Solids

Part 2

Behavior of Materials and Structure

DTIC QUALITY INSPECTED 4

20000911 052

Editors:

W. Hwang and K.S. Han

Department of Mechanical Engineering
Pohang University of Science and Technology

DISTRIBUTION STATEMENT
Approved for Public Release
Distribution Unlimited

ttp TRANS TECH PUBLICATIONS

Key Engineering Materials

ISSN 1013-9826

Specializing in the Field of Basic and Applied Aspects of Advanced Ceramic Materials and Composites

Editors:

Erian Armanios
Georgia Institute of Technology
School of Aerospace Engineering
Atlanta, GA 30332, USA
Fax +1 (404) 894 9313
e-mail: erian.armanios@aerospace.gatech.edu

Golam M. Newaz
Wayne State University
Department of Mechanical Engineering
Detroit, Michigan 48202, USA
Fax +1 (313) 577 8789
e-mail: gnewaz@me1.eng.wayne.edu

Yiu-Wing Mai
The University of Sydney
Centre for Advanced Materials Technology
Sydney NSW 2006, Australia
Fax +61 (2) 351 2290
e-mail: mai@tiny.me.su.oz.au

Fred H. Wöhlbier
Trans Tech Publications Ltd
Brandrain 6
CH-8707 Zuerich-Uetikon, Switzerland
Fax +41 (1) 922 10 33
e-mail: f.wohlbier@ttp.net

Editorial Advisory Board:

Australia
C.H.J. Davies (Clayton)
B.H. O'Connor (Perth)
L. Ye (Sydney)

Austria
R. Danzer (Leoben)

Canada
Z. Wang (Toronto)

China P.R.
D.L. Jiang (Shanghai)
J.K. Kim (Kowloon)
Z.G. Wang (Shenyang)
A. Xing (Jinan)

Denmark
B.F. Sorensen (Roskilde)

Egypt
M.A. Taha (Cairo)

France
F. Thevenot (Saint-Etienne)
M. Ignat (Saint Martin d'Hères)

Germany
G. Grathwohl (Bremen)
H. Schmidt (Saarbruecken)
H. Schneider (Köln)
G. Tomandl (Freiberg)
W. Weppner (Kiel)

India
D. Chakravorty (Calcutta)
K. Chattopadhyay (Bangalore)
B.V. Radhakrishna Bhat (Hyderabad)
S. Ray (Roorkee)
B.K. Sarkar (Calcutta)
G.S. Upadhyaya (Kanpur)

Ireland
P. McHugh (Galway)

Israel
R. Fischer (Haifa)

Japan
M. Iwasa (Osaka)
H. Hamada (Kyoto)
M. Mitomo (Ibaraki)
O. Nakamura (Osaka)
H. Sekine (Sendai)
K. Uematsu (Nagaoka)

Korea
S. Baik (Pohang)
C.P. Hong (Seoul)
S.H. Hong (Taejon)

Portugal
R.M. Almeida (Lisboa)

Russia
S.M. Barinov (Moscow)

Singapore
C.Y. Yue (Nanyang)

Slovakia
P. Sajgalik (Bratislava)

Spain
L. Esquivias (Cadiz)
A. Ureña-Fernandez (Madrid)

The Netherlands
R. Fordham (Petten)

UK
A. Hendry (Glasgow)
F.L. Riley (Leeds)
R. Taylor (Manchester)

USA
R. Abbaschian (Gainesville)
D.H. Allen (College Station)
I. Dutta (Monterey)
W.W. Gerberich (Minneapolis)
E.J. Lavernia (Irvine)
S. Mall (Wright-Patterson AFB)
R.O. Ritchie (Berkeley)
J.A. Sekhar (Cincinnati)
J.F. Shackelford (Davis)
J.E. Shelby (Alfred)
A. Shukla (Kingston)
W.O. Soboyejo (Columbus)
R. Solecki (Storrs)
G.J. Weng (New Brunswick)
J.-M. Yang (Los Angeles)

Yugoslavia
D. Uskokovic (Beograd)

Internet:

The table of contents of each volume is freely available on the Internet through Trans Tech Publications' Preview Service (preview@ttp.net) as well as on the World Wide Web at http://www.ttp.net.

Subscription Information:

Key Engineering Materials is published in 18 volumes per year. In 2000, volumes 171-188 are scheduled to be published. The subscription rate is US$ 78.00 per volume or US$ 1404.00 per year.

Trans Tech Publications Ltd
Brandrain 6 • CH-8707 Uetikon-Zuerich • Switzerland
Fax +41 (1) 922 10 33 • e-mail: ttp@ttp.net
http://www.ttp.net

REPORT DOCUMENTATION PAGE

Form Approved

OMB No. 0704-0188

The public reporting burden for this collection of information is estimated to average 1 hour per response, including the time for reviewing instructions, searching existing data sources, gathering and maintaining the data needed, and completing and reviewing the collection of information. Send comments regarding this burden estimate or any other aspect of this collection of information, including suggestions for reducing the burden, to Department of Defense, Washington Headquarters Services, Directorate for Information Operations and Reports (0704-0188), 1215 Jefferson Davis Highway, Suite 1204, Arlington, VA 22202-4302. Respondents should be aware that notwithstanding any other provision of law, no person shall be subject to any penalty for failing to comply with a collection of information if it does not display a currently valid OMB control number.

PLEASE DO NOT RETURN YOUR FORM TO THE ABOVE ADDRESS.

1. REPORT DATE *(DD-MM-YYYY)*	2. REPORT TYPE	3. DATES COVERED *(From - To)*
01-09-2000	Conference Proceedings	16-18 August 2000

4. TITLE AND SUBTITLE

4th International Conference on Fracture & Strength of Solids
Pohang, Korea, 16-18 Aug 00

5a. CONTRACT NUMBER
F6256299M9182

5b. GRANT NUMBER

5c. PROGRAM ELEMENT NUMBER

6. AUTHOR(S)

Conference Committee

5d. PROJECT NUMBER

5e. TASK NUMBER

5f. WORK UNIT NUMBER

7. PERFORMING ORGANIZATION NAME(S) AND ADDRESS(ES)

Pohang Univ. of Science & Technology
Dept of ME, San31 Hyoja-dong
Pohang 790-784
Korea (South)

8. PERFORMING ORGANIZATION REPORT NUMBER

N/A

9. SPONSORING/MONITORING AGENCY NAME(S) AND ADDRESS(ES)

AOARD
UNIT 45002
APO AP 96337-5002

10. SPONSOR/MONITOR'S ACRONYM(S)

AOARD

11. SPONSOR/MONITOR'S REPORT NUMBER(S)

CSP-99-06

12. DISTRIBUTUION/AVAILABILITY STATEMENT

Approved for public release; distribution is unlimited.

13 SUPPLEMENTARY NOTES

14. ABSTRACT

Part 1: Fracture Mechanics of Materials. Includes: Fracture Mechanics; Dynamic Fracture; Computational Mechanics; and Damage Mechanics. (678 Pages)

Part II: Behavior of Materials and Structure: Includes: Fracture Physics; Fatigue and Creep; Polymer and Polymer Composites; Metals, MMCs, Ceramics, and CMCs; and Welding. (672 Pages)

15. SUBJECT TERMS

Fracture Mechanics

16. SECURITY CLASSIFICATION OF:			17. LIMITATION OF ABSTRACT	NUMBER OF PAGES	19a. NAME OF RESPONSIBLE PERSON
a. REPORT	b. ABSTRACT	c. THIS PAGE			Thomas D. Kim
U	U	U	UU	1,350	19b. TELEPHONE NUMBER *(Include area code)* +81-3-5410-4409

Standard Form 298 (Rev. 8/98)
Prescribed by ANSI Std. Z39.18

Fracture and Strength of Solids

Part 2

Fracture and Strength of Solids

Part 2

Behavior of Materials and Structure

Editors:

W. Hwang and K.S. Han
Department of Mechanical Engineering
Pohang University of Science and Technology

TRANS TECH PUBLICATIONS LTD
Switzerland • Germany • UK • USA

Copyright © 2000 Trans Tech Publications Ltd, Switzerland

ISBN 0-87849-861-3 (2-vol. set)

Volumes 183-187 of
Key Engineering Materials
ISSN 1013-9826

***Distributed** in the Americas by*

Trans Tech Publications Inc
PO Box 699, May Street
Enfield, New Hampshire 03748
USA
Phone: (603) 632-7377
Fax: (603) 632-5611
e-mail: ttp@ttp.net
Web: http://www.ttp.net

and worldwide by

Trans Tech Publications Ltd
Brandrain 6
CH-8707 Uetikon-Zuerich
Switzerland
Fax: +41 (1) 922 10 33
e-mail: ttp@ttp.net
Web: http://www.ttp.net

Printed in the United Kingdom
by Hobbs the Printers Ltd,
Totton, Hampshire SO40 3WX

The Proceedings of

Fourth International Conference on Fracture & Strength of Solids

Pohang, Korea, August 16~18, 2000

Organized by

Far East and Oceanic Fracture Society (FEOFS)
The Korean Institute of Metals and Materials
The Korean Society of Mechanical Engineers
The Korean Society of Precision Engineering

Executive Committee

President :	Y.Y. Earmme, Korea Advanced Institute of Sci. &Tech.
Vice-President :	W.H. Chen, National Tsinghua University
	B. Cotterell, National University of Singapore
	K. Kishimoto, Tokyo Institute of Technology
	F. Rose, AMRL-AED
	W. Yang, Tsinghua University
Directors :	M. Kikuchi, Science University of Tokyo
	J.K. Lim, Chonbuk National University
	C.T. Liu, Institute of Mechanics, Academia Sinica
	D. Liu, ASM Assembly Automation Ltd.
	Y.J. Liu, Zhengzhou Research Institute
	Y.W. Mai, University of Sydney
	T. Nishioka, Kobe University of Mercantile Marine
	S.H. Teoh, National University of Singapore
	T.T. Wu, Hong Kong University of Sci. & Tech.
	X.R. Wu, Institute of Aeronautical Materials
	T. Yokobori, Teikyo University
	T.Y. Zhang, Hong Kong University of Sci. & Tech.
Treasurer :	W. Hwang, Pohang University of Sci. & Tech.
Secretary General :	K.S. Han, Pohang University of Sci. & Tech.

Organizing Committee

Chairman :	K.S. Han, Pohang University of Sci. & Tech.
Secretariat :	W. Hwang, Pohang University of Sci. & Tech.
Members :	T.J. Kang, Seoul National University
	B.S. Kim, Korea Institute of Machinery & Materials
	Y.J. Kim, Sungkyunkwan University
	K.Y. Lee, Yonsei University
	S.B. Lee, Korea Advanced Institute of Sci. & Tech.
	O.S. Lee, Inha University
	W.I. Lee, Seoul National University
	J.K. Lim, Chonbuk National University
	H.C. Park, Pohang University of Sci. & Tech.

International Advisory Board

S.N. Atluri	Georgia Institute of Technology
P.T.Y. Chang	Hong Kong University of Sci. & Tech.
W.H. Chen	National Tsinghua University
Y.K. Cheung	Unversity of Hong Kong
C.L. Chow	University of Michigan, Dearborn
B. Cotterell	Nan Yang Technology University
Y.Y. Earmme	Korea Advanced Institute of Sci. & Tech.
J.W. Hutchinson	Harvard University
K.C. Hwang	Tsinghua University
K.S. Kim	Brown University
K.S. Kim	Pohang University of Sci. & Tech.
H. Kobayashi	Tokyo Institute of Technology
Y.W. Mai	University of Sydney
R. McMeeking	University of California, Santa Barbara
C.F. Shih	National University Singapore
P. Tong	Hong Kong University of Sci. & Tech.
J. Xiao	Beijing University of Sci. & Tech.
T. Yokobori	Tekyo University

Sponsors

Far East and Oceanic Fracture Society (FEOFS)
Korea Science and Engineering Foundation
The Korean Federation of Science and Technology Societies
Korea Research Foundation
Air Force Office of Scientific Research
Pohang Iron and Steel Co. (POSCO)
Hyundai Heavy Industry
Safety and Structural Integrity Research Center (SAFE)
Keum Kwang Co.
Pohang University of Science and Technology (POSTECH)

Preface

These proceedings contain papers accepted for presentation at the Fourth International Conference on Fracture and Strength of Solids. The triennial conference is the fourth in the series after the tremendous successes in Singapore (1991), China (1994) and Hong Kong (1997). With the sponsor ship of the Far East and Oceanic Fracture Society (FEOFS), the conference is today the premier one concerned with the mechanics and mechanisms of fracture, fatigue and strength of solids.

The FEOFS was founded for the purpose of presenting the latest findings and exchanging ideas with each other in the fields of fracture and strength of materials and have supported the Conference.

The International Conference on Fracture and Strength of Solids has always maintained a high standard as demonstrated by the number of countries/regions from which papers have been submitted and the high quality papers finally selected for inclusion in this volume. This is also a direct reflection of the continuing growth in the pursuance of research and development in this field. The volume covers broad areas of Fracture Mechanics, Computational Mechanics, Dynamic Fracture, Damage Mechanics, Fracture Physics, Fatigue and Creep, Polymer and Polymer Composites, MMCs and CMCs, Welding etc, that is all the areas of Applied Mechanics Parts.

We wish to thank all authors who contributed papers to the conference and all referees for their efforts to review the papers. Thanks are also due to the members of the Executive Committee, Organizing Committee and the International Advisory Committee for their efforts in making the conference a success. We acknowledge the supports by the local and international sponsors, including Far East and Oceanic Fracture Society (FEOFS), Korea Science and Engineering Foundation, The Korean Federation of Science and Technology Societies, Korea Research Foundation, Air Force Office of Scientific Research, Pohang Iron and Steel Co. (POSCO), Hyundai Heavy Industry, Safety and Structural Integrity Research Center (SAFE), Keum Kwang Co., Pohang University of Science and Technology (POSTECH)

Prof. Kyung Seop Han
Chairman of Conference Organizing Committee

Table of Contents

Part 1: Fracture Mechanics of Materials

Conference Information v

Preface ix

Fracture Mechanics

Length-Scale Effects in Nano- and Micro-Mechanics of Solids
K.-S. Kim and J.A. Hurtado 1

Mechanism-Based Strain Gradient (MSG) Plasticity and the Associated Asymptotic Crack-Tip Fields
K.-C. Hwang and Y. Huang 9

An Analysis of Fatigue Crack Growth Rate Considering Spatial Variation of Fatigue Crack Growth Resistance
S.J. Kim 19

Rectangular Array and Zig-Zag Array of Elliptical Holes in Solids under Uniaxial Tension (Formulae of Maximum Stresses and Tensile Stiffnesses)
H. Igawa 25

Crack Growth in Stainless Steel 304AT 538°C under Fatigue Loading with and without Hold Time
Y.M. Baik and K.S. Kim 31

An Inverse Fracture Problem of a Shear Specimen with Double Cracks
Y. Li, Z. Rui and J. Huang 37

Fracture Mechanics Analysis of Cracked Plate Repaired by Composite Patch
K.H. Chung, W.H. Yang and M.R. Cho 43

Fracture Toughness Test of Small CNS Specimen with an Interface Crack Subjected to Mixed-Mode Loading
K. Machida 49

Theoretical Investigation of Controllable & Regular Fracture Theory
A. Zhou, Y. Wei and F. Lang 55

Crack Identification Using Classical Optimization Technique
M.W. Suh, J.M. Yu and J.H. Lee 61

Study on Strength of Rock Material under Dynamic Triaxial Compressive Loads Based on Sliding Crack Model
H.B. Li, T.J. Li, J. Zhao, J.G. Gao and J.G. Jiang 67

Kinking out of a Mixed Mode Interface Crack
T. Ikeda, Y. Komohara, A. Nakamura and N. Miyazaki 73

Global Crack-Line Displacement Fitting Procedure: Edge Cracks
H.Y. Jiang, Z.L. Li and F.L. Zhan 79

A Stochastic Modeling for Predicting Fatigue Crack Growth under Variable Amplitude Loading
D.S. Shim and J.K. Kim 85

A Highly Accurate BEM in Fracture Mechanics
Z.L. Li, F.L. Zhan and S.H. Du 91

Simulation and Experimental Verification of Axial Multi-Crack Propagation and Crack Kinking in Pressurized Fuselage
A. Shimamoto, T. Oguchi, D.Y. Ju and A.S. Kobayashi 97

Calculation of Stress Intensity Factor Using Weight Function Method for a Patched Crack
J.H. Kim, K.W. Lee, D.C. Seo and S.B. Lee 103

Interaction of a Horizontal Finite Crack with a Center of Dilatation in Elastic Half-Planes
K.T. Chau, R.H.C. Wong and R.C.K. Wong 109

Determinations of Stress Intensity Factor in Isotropic and Anisotropic Body by the Photoelastic and Caustics Methods under Various Load Ratios
A. Shimamoto, J.H. Nam, T. Shimomura and E. Umezaki 115

A Micromechanics Criterion for the Ductile Fracture of a Polycarbonate
T.J. Wang, K. Kishimoto and M. Notomi 121

Effect of Specimen Thickness and Load History on Crack Growth of 7175-T74 Forging Aluminum Alloy
J.Z. Liu, X.R. Wu, C.F. Ding and D.X. You 127

Plastic η Factors Based on Load-CMOD Records for SE(B) Toughness Testing Specimens
Y.-J. Kim 133

Electromagnetic Thermoelastic Solids with an Elliptical Cavity or a Crack under Uniform Heat Flow
X.L. Liu, X.F. Liu, J.X. Liu and J. Zheng 139

Evaluation of Stress Intensity Factor Using White Light Photoelastic Experiment
E. Umezaki, K. Kodama and A. Shimamoto 145

Singularity Intensity Factor Calculation in Plates and Shells Based on the Singular Line Mapping Technique in FEMOL
C. Liu and Y. Xu 151

Collective Evolution Characteristics and Computer Simulation of Voids Near the Crack Tip of Ductile Metal
H. Yu and Y. Hong 157

The Relationship of SIF between Plate and Plane Fracture Problems and the Effect of the Plate Thickness on SIF
Y. Xu and C. Liu 163

Fractographic Approach for Fracture Mode
N. Hattori, S. Nishida and H. Yamamoto 169

Microscopic Deformation at a Crack Tip in a Ferroelectric Material
W. Yang, F. Fang and T. Zhu 175

The Unified Description of the Three-Dimensional Fields at Notches and Cracks
W. Guo, T. Chang and Z. Li 181

Buckling and Fracture of Thin Films under Compression
B. Cotterell and Z. Chen 187

Recent Advances in Three-Dimensional Fracture Mechanics
W. Guo 193

Static Magnetoelastic Coupling in Soft Ferromagnetic Elastic Solids with Collinear Cracks
W. Liang, Y. Shen and M. Zhao 199

A Study on Deformation Energy of P/M Copper and Ingot Material
T. Senthilvelan, A. Venkatraman and K. Raghukandan 205

Fracture Analysis on the Coating Crack Perpendicular to the Interface of Bi-Material
B. Su and C. Li 211

A Combined Model of Short Crack Closure Accounting for Both Plasticity and Roughness Induced Crack Closures
X.P. Zhang, C.H. Wang, J.C. Li, Y.-W. Mai and L. Ye 217

Scattering of Plane Compressional Waves by a Spherical Inhomogeneity with a Linear Spring Type Interface
Z. Zhong and X.B. Yu 223

Dynamic Fracture

From Recent Studies on Impact Fracture of Polymers and Polymer Composites
K. Takahashi 229

Dynamic Stress Intensity Factors of Cylindrical Interface Cracks Subjected to P-Wave
W.J. Feng and Z.Z. Zou 241

Effects of Impact Loading Rate on the Delamination Behavior of Composite Laminates
N.S. Choi 247

Shock Adiabatics of Cement Mortar at Intense Dynamical Loading by Taking into Account the Internal Damage
S. Shih, D. Li and L. Wang 253

A Study on the Impact Failure Mechanism of Aluminum-PMMA Interfacial Crack
D.K. Shin, J.J. Lee and M.Y. Lyu 259

Experimental Analysis of Dynamic Effects in Brittle Fracture of PMMA
K. Arakawa, T. Mada and K. Takahashi 265

Impact Damage Behavior and Evaluation of Residual Strength in Plain-Woven Glass/Epoxy Composites
K.W. Kang and J.K. Kim 271

Measurement of Dynamic Fracture Parameters in the Expansion Process at High Strain Rate
C.Y. Gao, H.J. Shi, C.L. Liu, C.H. Bai and Z.H. Yao 277

A Study on the Development of the Dynamic Photoelastic Experimental Method for Isotropic/Orthotropic Bimaterials
J.S. Hawong, D.C. Shin, O.S. Lee, H.J. Lee and J.K. Ha 283

Evaluation of Large Strain in Ductile Polymers under High Speed Loading
T. Kuboki, T. Mada and K. Takahashi 289

Damages in Woven Polymer Matrix Composites under Impact Loading
T.W. Kim, H. Park, C. Kim and J.H. Lee 295

Applications of the Shadow Spot Method on the Determination of Dynamic Stress Intensity Factors
Z. Li and X. Su 301

High Strain-Rate Deformation of Composite Materials Using a Split Hopkinson Bar Technique
O.S. Lee, J.Y. Lee, G.H. Kim and J.S. Hwang 307

Experimental Studies on Dynamic Fracture Phenomena
T. Nishioka, T. Fujimoto and K. Sakakura 313

The Fracture Problem of Framed Plate under Explosion Loading
Y. Li, Y. Wei and Y. Hou 319

Dynamic Mixed Mode Crack Propagation Behavior of Structural Bonded Joints
O.S. Lee and A.S. Kobayashi 325

Analysis of a Crack in a Functionally Gradient Interface Layer under Static and Dynamic Loading
Y.S. Wang and D. Gross 331

Fundamental Study of Dynamic Stress Wave Using a Dynamic Photoelastic Method
T. Kanemitsu and Y. Sawa 337

Using High-Speed Camera to Investigate Failure Waves in K9 Glass
J. Zhao, C. Sun, Z. Duan, X. Tan, F. Zhao and S. Wen 343

A Study on Dynamic Fracture in Stiffened Cylinder Subjected to a Strong Acoustic Wave
E. Kim, H.L. Yin, K.S. Kim, C.H. Jo, O.S. Lee and C.W. An 349

Computational Mechanics

Static and Mode Analyses of Composite Plates Using Modified 16-Node Solid Elements, and Prediction of Stiffness Errors Resulting from Reduced Integration
Y.D. Kwon, Y.S. Kim, T.H. Yun and M.H. Cho 355

Shape Optimization of General Structures
S.Y. Han and J.S. Maeng 361

Simulation of Crack Growth and Creep Fracture by a Multicrack Growth Model
M. Tanaka 367

Dual-Phase Functionally Graded Composite Materials: Overall and Discrete Analysis Models
J.R. Cho and D.Y. Ha 373

A Study on Efficiency Improvement of Evolutionary Structural Optimization
S.Y. Han, T.H. Lee and J.K. Lim 379

Numerical Simulation of Crack Elongation and Reinforcement Effectiveness of the Isolated Rockmass between Shiplocks of Three Gorges Project
P. Xu and X.-T. Feng 385

Out-Of-Plane ESPI Simulation for the Harmonic Vibration of a Thin Right-Angled Plate
S.S. Jarng, J.H. Lee, H.G. Ahn and J.C. Park 391

Element Modeling for Vibration Analysis of Plate
Y.P. Shi and P. Zeng 397

Hierarchical Models for Laminated Composite Structures Based on p-Extensions
J.R. Cho, S.H. Kim and D.Y. Ha 403

Nonlinear Displacement Field in the Vicinity of Notch-Tip in Rubber Toughened PMMA
M. Todo, K. Arakawa and K. Takahashi 409

Optimum Design for Fatigue Strength Improvement of Spot-Welded T-Type Bus Window Pillar Member
M.H. Kim, D.S. Kim, M.W. Suh and D.H. Bae 415

Dynamic Response Analysis of a Structure under High Over-Load
L. Liu and X. Lin 423

Nonlinear Analysis of Thick Composites with Fiber Waviness under Flexural Loading
H.-J. Chun and S.W. Lee 427

Fuzzy Mathematical Method for Evaluation of Rock Mechanical Indexes
G. Zhang, T. Li and S. Bai 433

Topology Optimization of the Inner Reinforcement for an Automobile Hood Using Modal Design Sensitivity Analysis
T.H. Lee, S.Y. Han and J.K. Lim 439

Computational Studies on Dynamic Fracture Phenomena
T. Nishioka and T. Fujimoto 445

Nonlinear Dynamic Buckling Analysis of a Grid Structure
K.H. Yoon, K.N. Song and Y.S. Lee 451

Dynamic Modeling and Numerical Analysis for Large Scale Chime Group
P. Zeng, L. He and G.H. Tang 457

Plastic Analysis of Square Grillage under A Point Load
S.C. Lee, K.S. Hong and K.S. Kim 463

Finite Element Analyses of Specific Damping Capacity and Undamped/Damped Forced Motion of Composite Plate Using Modified 16-Node Solid Elements
T.H. Yun, Y.D. Kwon, C. Kim and J.G. Park 469

Stress Analysis for New Gasketless Flange and Superseal
N.-A. Noda, K.-I. Takeuchi, Y. Takase and M. Nagawa 475

A Study on Stress Wave Propagation in Stiffened Cylinder Subjected to a Strong Acoustic Wave
J.H. Choi, K.S. Kim, C.H. Jo, O.S. Lee and C.W. An 481

Element-Free Galerkin Methods for Fracture of Functionally-Graded Materials
J. Chen, L. Wu and S. Du 487

A Study on the Shape Design and Contact Characteristic of Wheel-Rail for Rolling Stock
K.D. Sung, W.H. Yang and M.R. Cho 493

Stress Analysis of Toroidal Hole in an Infinite Body
T. Matsuo and N.-A. Noda 499

A Parametric Study on the Fracture Mechanics Analysis of Elbow with Surface Crack
Y.-S. Chang, H.-S. Kim and T.-E. Jin 505

On the Multiple Isoparametric Finite Element Method and Computation of Stress Intensity Factor for Cracks in FGMs
Z.Z. Zou, S.X. Wu and C.Y. Li 511

The Effect of a Longitudinal Stiffener on the Elastic Shear Buckling of Orthotropic Web Plate
S.J. Yoon, J.H. Jung and S.K. Cho 517

Interaction among a Row of N Semi-Elliptical Notches and Edge Cracks
T. Matsuo and N.-A. Noda 523

A Computational Investigation on Metal/Ceramic Joints under Thermal Cyclic Loadings
M.K. Park and S. Bahk 529

Progressive Failure Analysis of Composite Laminates Using 3-D Finite Element Method
S.G. Joo and C.S. Hong 535

The Influence of Plastic Deformation on Interface Fracture Behavior
M. Omiya, K. Kishimoto and T. Shibuya 541

An Analysis of Ironing Limit in Sheet Metal Forming
J.B. Nam and K.S. Han 547

The Versatility of the Method of K_I, K_{II} Analysis by FEM Based on the Stress Value at a Crack Tip
H. Nisitani, T. Teranishi, A. Saimoto and K. Fukuyama 553

Detecting Tool Wear in Face Milling with Different Workpiece Materials
D.W. Cho, W.C. Choi and H.Y. Lee 559

Three Dimensional Finite Element Analysis for Elastic Plastic Crack Propagation in Thin Metallic Plate
H. Okada, Y. Fukui, N. Kumazawa and T. Fujisaki 565

Damage Mechanics

Study on the Bending Fatigue Damage of the Carbon and the Polypropylene Hybrid Fiber Reinforced Concrete
Y. Hua, H.B. Qi, Z.Q. Jiang, S.Z. Huang and S.B. Zhang 571

The Effect of Aging Temperatures and Time on Mechanical Properties of CF8M
J.D. Kwon, J.C. Park, Y.S. Lee, W.H. Lee and Y.W. Park 577

Effect of Temperature on the Damage Behavior of an Adhesively Bonded Butt Joint
A. Fujinami, K. Osaka, T. Fukuda and M. Imanaka 583

Effect of Yield Strength and Crack Depth on COD-Decrease-Parameter m
Q. Li, H. Ni, S. Yang, M. Ma, P. Long and Z. Cui 589

A Study on Intergranular Corrosion of Laser Treated Alloy 600 by DL-EPR Method and Microscopic Examination
Y.S. Lim, H.P. Kim, J.S. Kim and H.S. Kwon 595

Damage of FRP Plates Containing Sharp Notches or Blunt Notches
H. Hyakutake and T. Yamamoto 601

Radiation Damage of Reactor Pressure Vessel Steels Studied by Nondestructive Methods
D.G. Park, T.S. Byun, Y.Y. Song, J.H. Hong and I.S. Kim 607

Reliability Calculation for Piping Containing Circumferential Crack Based on 3-D Elastic-Plastic SFEM
L. Huo, B. He and Y. Zhang 613

Optimum Design of Linear Phased Array Transducer for NDE
J.-H. Lee and S.-W. Choi 619

A Damage Model for Void Configuration and Failure under Different Constrained Deformation Region in Ductile Matrix
M. Kikuchi and M. Geni 625

Modeling of Mechanical Property Degradation by Short-Term Aging at High Temperatures
J. Kim and W.I. Lee 631

On Failure Modes and Strength Characterization of Brittle Disordered Materials under Uniaxial Compression and Tension
C.A. Tang, P. Lin, H.Y. Liu and Z.Z. Liang 637

Influence of Tool Wear on Hole Damage in Small Diameter Drilling of Printed Wiring Boards - Investigation based on Estimation of Cutting Forces and Internal Damage
H. Inoue, T. Hirogaki, E. Aoyama and T. Katayama 643

Damage Tolerance Analysis Software (DATAS) for Crack Growth Life Prediction and Residual Strength Analysis of Aircraft Structures
I.S. Putra 649

Prediction of Piping Failure Behavior using Wide-Plate Test
N.S. Huh, H.J. Cha, J.B. Choi, Y.J. Kim and C.R. Pyo 655

Vibration Sensing and Impact Location Detection Using Optical Fiber Vibration Sensor
Y.C. Yang, W. Hwang, H.C. Park and K.S. Han 661

New Estimates of Effective Moduli of Microcracked Materials
X.Q. Feng 667

Realization of Higher-Mode Deformation of Beams Using Shape Memory Alloy Wires and Piezoceramics
S.M. Pae, H.J. Lee, H.C. Park and W. Hwang 673

Author Index xxv

Keyword Index xxxi

Part 2: Behavior of Materials and Structure

Fracture Physics

Fracture and Strength of Solids Associated with their Textures
D.N. Lee 679

Overview of Fracture of Piezoelectric Ceramics
T.-Y. Zhang, R. Fu, M. Zhao and P. Tong 695

Effect of Heat Treatment and Chemical Composition on Caustic Stress Corrosion Cracking of Alloy 600 and Alloy 690
H.P. Kim, S.S. Hwang, Y.S. Lim, I.H. Kuk and J.S. Kim 707

Nonlinear Evolution Properties of Rock Microfracturing Affected by Environment
X.-T. Feng, T. Li and M. Seto 713

Case Study on Fracture of Motor Whist Wire
H. Sakamoto, T. Yamaguchi and M. Mizumoto 719

The Propagation of a Layer-Confined Love Wave in Layered Piezoelectric Structures
Z.K. Wang, F. Jin, Z. Zong and T.J. Wang 725

Characteristics of Delamination in Graphite/Epoxy Laminates under Static and Impact Loads
J.S. Kook, I.Y. Yang and T. Adachi 731

An Experimental Observation About Dislocation Nucleation Based On Peierls Concept
Y.M. Xing, F.L. Dai and W. Yang 737

Effect of Contact Shape on the Cracking Behaviour
H.-K. Kim and H.-S. Kang 743

Study of Fracture Origin on Low Cycle Fatigue of Spheroidal Graphite Cast Iron Having Various Matrixes
K. Morino, F. Nishimura and H. Nisitani 749

The Propagation Behavior of Love Waves in a Pre-stressed Piezoelectric Layered Structure
F. Jin, Z.K. Wang and T.J. Wang 755

The Effect of Nucleation Time on the Growth of a Microvoid in a Viscoelastic Material
J.K. Chen, Z.P. Huang and S.-L. Bai 761

Effects of Stress Fields around Micro-Surface Defects on the Occurrence of Slip and Micro Cracks
K.R. Lee and J.B. Kim 767

Studies of Fracture of Piezoelectric Ceramics at HKUST
T.-Y. Zhang 773

Tensile and Fracture Behaviors of PC/ABS Polymer Alloy
M. Notomi, K. Kishimoto, T. Wang and T. Shibuya 779

Influence of Stochastic Mesoscopic Structure on Macroscopic Mechanical Behavior of Brittle Material
Y.F. Fu, M.L. Huang and C.A. Tang 785

Fracture and Strength of Notched Thick Composites
B.S. Hwang, S.B. Park, B.H. Kim, I.S. Park, H.S. Song and J.K. Lee 791

A Study on the Integrity Evaluation for PWR Vessel by Pressurized Thermal Shock
S.G. Jung and T.-E. Jin 797

Crack Healing Behavior and Mechanical Property of Mullite/SiC Composite Ceramics
K. Tsuji, K. Ando and S. Sato 803

Multi-Crack Coalesence in Rock-Like Material under Uniaxial and Biaxial Loading
P. Lin, R.H.C. Wong, K.T. Chau and C.A. Tang 809

Effects of Temperature and Stacking Sequence on the Mode I Interlaminar Fracture Behavior of Composite Laminates
H.S. Kim, W.X. Wang and Y. Takao 815

Effect of Remanent Polarization on Electro-mechanical Fields Near an Elliptic Cavity or a Crack in Piezoelectric Ceramics
B. Liu, D.N. Fang and K.C. Hwang 821

Nano-Fractographic Estimation on the Profiles and Dimensions of Fatigue Striation
S.J. Choi, H. Ishii and J.D. Kwon 827

Strength of Crack-Healed Si_3N_4/SiC Composite Ceramics
M.C. Chu, K. Ando, F. Yao and S. Sato 833

Studies on the New Technique of Rapid Solidification and the Mechanical Behaviors of Mocrocrystalline Alloys
Z. Liu, K. Yang and S.-L. Bai 839

The Effects of Texture on K_{IH} in the Radial Direction in Zr-2.5%Nb Pressure Tube Materials
S.S. Kim, S.C, Kwon, K.N. Choo, Y.M. Cheong and Y.S. Kim 845

Influence of Grain Boundary Characteristics on Cavitation Behavior in P/M7475
T. Hirata, S. Tanabe, M. Kohzu and K. Higashi 851

The Effects of Confining Compression on Fracture Coalesence in Rock-like Material
R.H.C. Wong, P. Lin, K.T. Chau and C.A. Tang 857

Fracture Toughness Enhancement Due to Stress/Strain-Induced Martensitic Transformations in Solids
S.V. Gladkovsky and V.A. Gladkovsky 863

Fracture Behavior of a Crack in Gas Pipeline Considering Constraint Effects
D.J. Shim, Y.K. Jang, J.B. Choi and Y.J. Kim 869

Numerical Analysis of Dimple Fracture Process under Different Constraint Conditions
M. Kikuchi and A. Takahashi 875

Microstructure of the Carbon and the Polypropylene Hydrid Fiber Reinforced Concrete Acted by Bending and Tensile Stress
H.B. Qi, Y. Hua, Z.Q. Jiang, S.Z. Huang and S.B. Zhang 881

Acoustic Emission Technique for Pipeline Leak Detection
M.-R. Lee and J.-H. Lee 887

Fracture Behaviors of GFRP Plates Subjected to Impulsive Loading
B. Syam, H. Homma and K. Nakazato 893

Fatigue and Creep

Fatigue Strength Decrease of Structural Materials Caused by Atmosphere Corrosion and Aging
Q.-X. Yang and B.-T. Wang 899

Creep Life and Properties Evaluation by ISM Method and Acoustic Emission for Cr-Mo-V Steels
S.G. Lee 903

Expanding of the Fatigue Life of Thermal Barrier Coating by Mixing $MoSi_2$ to Thermal Sprayed Layer
K. Sonoya and S. Tobe 909

Effects of Pad Material on Fretting Fatigue Behavior in CFRP Laminates
M.-S. Kim and H.-S. Shin 915

Study on Double Shot Peening and Fatigue Limit of Gear
K. Ando, K. Matsui and H. Ishigami 921

A Study on Probabilistic Fatigue and Calendar Fatigue Life
B. Wang and Q. Yang 927

Influence of Microstructures on Fatigue Limit of High Strength Ductile Irons
J.H. Kim and M.G. Kim 933

Fretting Fatigue Behavior of Structural Steels
H. Yamamura, Y. Yamada and R. Ebara 939

Fatigue Failure Model for Composite Laminates under Multi-Axial Cyclic Loading
C.S. Lee, W. Hwang, H.C. Park and K.S. Han 945

A New Method to Deal with the Staircase Fatigue Test
Q.Z. Fang, S.S. Zhang, M.H. Zhao and Y.J. Liu 951

Fatigue Life Prediction of Spot-Welded Joint by Strain Energy Density Factor using Artificial Neural Network
I.S. Sohn and D.H. Bae 957

Fatigue Properties of Tungsten Fiber Reinforced Ti-6Al-4V Alloy
S.Y. Son, S. Nishida, N. Hattori and K. Nakano 963

Failure Analysis of the Fourth Compressor Pans in Aero-Engines
G. Fu and W. Su 969

Thermal Aging and Low Cycle Fatigue Characteristics of CF8M in a Nuclear Reactor Coolant System
J.D. Kwon, S.W. Woo, Y.S. Lee, J.C. Park and Y.W. Park 975

Study of Crack Propagation Behavior on Low Cycle Fatigue in Spheroidal Grahite Cast Iron Based on Observation of Surface and Fracture Section
F. Nishimura, K. Morino and H. Nisitani 981

Cyclic Softening Properties of 30Cr2MoV Steel at Elevated Temperatures
Z.D. Liu, K. Yang, X.P. Mao, S.-L. Bai and J.Y. An 987

A Study on the Corrosion Fatigue Characteristics of 12Cr Alloy Steel
S.Y. Cho, C.H. Kim and D.H. Bae 993

Corrosion Fatigue Crack Initiation Life of a Ship Structural Steel in Dilute Sulfuric Acids
Y. Kobayashi, Y. Tanaka and H. Goto 999

An Analysis of Random Fatigue Strength of K-Type Tubular Joints by Probabilistic Fracture Mechanics Method
G.H. Nie, R. Shi and R.J. Zhang 1005

Fatigue Life Prediction of Bolted Joints Using Fatigue Modulus
C.K. Jung and K.S. Han 1011

Study of Crack Propagation Behavior on Low Cycle Fatigue in Squeeze Cast Aluminium Alloy
K. Morino, F. Nishimura, K. Takahashi, Y.H. Kim and H. Nisitani 1017

Reliability Analysis of Ship Hull Girders Considering the Degradations of Corrosion and Fatigue
H.-H. Sun, G.-H. Liao and Y. Bai 1023

Fatigue Analysis of Vane Components for Gas Turbine Engine
J.H. Kim, K.H. Kim, K.K. Joung, K.C. Ham, J.I. Song and S.I. Bae 1029

Fatigue Crack Growth Simulation and Estimation for Rolling Contact
M. Akama and I. Susuki 1035

The Effect of Tensile Hold Time on the Fatigue Crack Propagation Behavior in STS 3l6L
J.W. Im and B.S. Lim 1041

Fatigue Strength of Crack-Healed Ceramics
K. Ando, M.C. Chu, F. Yao and S. Sato 1047

Polymer and Polymer Composites

Fracture Behaviours of Advanced Polymer Composites under Mixed Mode Loading
K. Kishimoto 1053

Interface Adhesion and Interlaminar Fracture Resistance of Carbon/PEEK Composites influenced by Cooling Rate
J.K. Kim and S.L. Gao 1063

Nondestructive Evaluation of Degree of Fiber Waviness in Thick Composites
H.-J. Chun and P.-S. Jang 1069

The Damage Evaluation of Rigid Particle Filled Polymer
S.-L. Bai, J.K. Chen, Z.P. Huang and Z.D. Liu 1075

Microstructural Morphology of Molded Thin Composites of Thermotropic Liquid Crystalline Polymer and Polyamide 6
N.S. Choi and K. Takahashi 1081

Optimization of Molding Cure Condition on Al 7075/CFRP Sandwich Composite by the Taguchi Method
H.K. Yoon, S.H. Lee and W.K. An 1087

An Application of Localized Flexibility Method to Damage Identification in CFRP Laminated Plate
Y. Aoki and O.I. Byon(Goichi Ben) 1093

Crush Energy Absorbing Characteristics of Graphite/Epoxy Square Tubes
H.C. Park, Y.H. Choi and K.J. Yoon 1099

Surface Modification of Carbon Fibers by Anodic Oxidation and its Effect on Adhesion
J.R. Lee, M.H. Kim and S.J. Park 1105

The Bridging Analysis of Dynamic Crack Propagation in Fiber Reinforced PE Pipelines
Z. Zhuang, S. Qu and Y. Guo 1111

Optimum Stacking Sequence Design of Fiber-Metal Laminates for Using Genetic Algorithm
H.W. Nam, S.W. Jung, W. Hwang and K.S. Han 1117

A Thermomechanical Analysis of MCM-D Substrate of Polymer and Metal Multilayer
J.H. Lim, J.S. Kim, K.W. Paik and Y.Y. Earmme 1123

Failure Behavior and Electrical Property of CFRP and CFGFRP
D.Y. Song, J.B. Park and N. Takeda 1129

Elastic Restraint between the Plate Components of FRP Compression Members
S.J. Yoon, S.K. Jeong and S.H. Chae 1135

Mixed-Mode Ply Cracking in Multidirectional Continuous Fiber Composite Laminates
J. Zhang, K.P. Herrmann and X. Zeng 1141

Axial Crush and Energy Absorption Characteristics of Aluminum/GFRP Hybrid Square Tube
K.H. Kim, K.C. Shin and J.J. Lee 1147

Mechanical Behavior of Carbon/Phenolic Ablative Composites for Nozzle Application
P.W. Kim, S.H. Hong, Y.C. Kim, B.H. Yeh and Y.G. Won 1153

Fracture Pattern and Lamination Configuration on Flexural Fracture of Multiple Layer CFRP
M. Kanemitsu and H. Nakayasu 1159

Strength Prediction of Mechanical Joints in Laminated Composite Plates
K.W. Lee and T.J. Kang 1165

Crystallinity and Mechanical Properties of Glass Fiber Reinforced Thermoplastic Composites by Rapid Press Consolidation Technique
I.J. Shin, D.Y. Kim and D.J. Lee 1171

Fractography of Damaged Carbon Fiber/Epoxy Composites after Low-Velocity Impact
M.S. Sohn, X.Z. Hu and J.K. Kim 1177

Anisotropic Mechanical Behavior of Three Dimensional Glass Fabric Reinforced Composites
H.S. Lee, S.H. Hong, J.R. Lee and Y.K. Kim 1183

Prediction of Compressive Strength of Stiffened Composite Plate after Impact
C.S. Hong, C.W. Kong and C.G. Kim 1189

Void Nucleation Models and their Implications for the Material Behavior of Rubber-Modified Epoxies
H.-Y. Jeong 1195

On-line Frequency Estimation and Adaptive Vibration Control of Composite Structures with Delaminations
K.-H. Rew, J.-H. Han and I. Lee 1201

Metals, MMCs, Ceramics and CMCs

Strength and Fracture of Cu-Based Filamentary Nanocomposites
S.I. Hong, J.H. Chung and H.S. Kim 1207

Modeling of Thermal Shock Spalling Crack in a Ceramic Slabs
P. He and W.J. Clegg 1213

Analytical Study of Prestrain Effects on Elastic Properties in Shape Memory Alloys
H.G. Kim, H.K. Noh, Y.T. Cho, J.Y. Kim, S.K. Park and D.J. Lee 1219

A Study on the Friction and Wear Characteristics of Brake Pads for Al MMC Brake Disc
S.J. Kwon and B.C. Goo 1225

On Targets Strength of Ceramic Materials for Impacting Penetration
Y. Sun, J. Ma, Y. Zhou and T. Li 1231

Effects of Heat Treatment on Bending Strength of Aluminum Alloy Matrix Composites Reinforced Aluminum Borate Whisker
S.C. Huh, H.K. Yoon, K.H. Park and S.P. Lee 1237

Mechanical Properties of Tungsten Fiber Reinforced Ti-6Al-4V Alloy
S. Nishida, K. Hayashi, N. Hattori, K. Nakano, Y. Yanagida and H. Tamasaki 1243

Behavior of Cyclic Fatigue Crack Growth for SiC Ceramics
Y.-H. Huh, K.-J. Yoon, S.-J. Cho and J.H. Song 1249

A Model on the Strengthening and Embrittlement of Devitrified Nanocomposites
H.S. Kim, S.I. Hong and M.-S. Sohn 1255

Contact Damage Analysis of Ceramic/Metal Bilayer Composites with Various Modulus Mismatches
H. Zhao, X. Hu and M.B. Bush 1261

Abrasive Wear Behavior of Hybrid Metal Matrix Composites
J.I. Song, S.I. Bae, K.C. Ham and K.S. Han 1267

Evaluation of Formability Properties of P/M Copper Preforms at Elevated Temperatures
T. Senthilvelan, A. Venkatraman and K. Raghukandan 1273

Effects of Interface and Residual Stress on Mechanical Properties of Ceramic/Metal System
T.W. Kim and S.W. Park 1279

Design and Fabrication of Tooling for P/M Ferrous Gears
A. Venkatraman and T. Senthilvelan 1285

Effects of Sintering Conditions on Mechanical Properties of Mechanically Alloyed Tungsten Heavy Alloys
H.J. Ryu and S.H. Hong 1291

Analysis of Strengthening Mechanism in Hybrid Short Fiber/Particle Reinforced Metal Matrix Composites
S.W. Jung, J.H. Lee, J.B. Nam, H.W. Nam and K.S. Han 1297

Welding

Effects of Welding Process and Crack Orientation on da/dN of Titanium Alloys
Q. Li, H. Ni, S. Yang, Z. Cui, X. Peng and L. Wang 1303

Laser Welding of Ti-Ni Shape Memory Alloy Wire and its Fatigue Properties
Y.S. Kim and J.D. Kim 1309

Investigation on Improving Fatigue Properties of Welded Joints by Ultrasonic Peening Method
L. Huo, D. Wang, Y. Zhang and J. Chen 1315

The Characteristics of Fatigue Strength in Laser Tailored Welded Blanking Sheet Metal
T.Y. Oh, Y.K. Kwon, C.J. Lee and D.S. Kwak 1321

Effect of the Mismatching of J-Integral for Pipe Welded Joint with Circumferential Surface Crack
L.X. Huo, Y.I. Liu, Y.F. Zhang and H.Y. Jing 1327

Validation of Defect Assessment Method for Structures with Weldments
Y.-J. Kim 1333

The Use of Temper Bead Welding for the Repair of Thick Walled Pressure Vessels
R.N. Ibrahim and T. Shehata 1339

Welding Residual Stress Analysis and Fatigue Crack Growth Characteristics of Multi-Pass Welded Pipe Weldment
C.H. Kim, D.H. Bae, S.Y. Cho and B.K. Kim 1345

Author Index 1351

Keyword Index 1357

Key Engineering Materials Vols. 183-187 (2000) pp. 679-694
© 2000 Trans Tech Publications, Switzerland

Fracture and Strength of Solids Associated with their Textures

D. N. Lee

School of Materials Science and Engineering, Seoul National University, Seoul 151-742, Korea

Keywords: Anisotropy, Deformation, Electrodeposition, Fracture, Recrystallization, Strength, Texture, Vapor Deposition

ABSTRACT

It is well known that the plastic deformation, vapor deposition, electrodeposition, casting, and recrystallization and grain growth of materials give rise to the development of characteristic textures, which in turn lead to anisotropic properties. In order to obtain required properties, it is necessary to control the texture of materials. Electromigration, cleavage fracture, and claddings of reactor fuels are known to be texture sensitive. The yield strengths of textured materials are in general anisotropic. The recrystallization texture is related to the deformation history and texture. The recrystallization texture may change during grain growth. These phenomena have been discussed.

1. TEXTURE SENSITIVE FAILURE

1.1. Electromigration

Electromigration is the forced motion of metal ions under the influence of an electric field and is potentially one of the most pernicious failure mechanisms in interconnects of large scale integrated microelectronic devices. The momentum exchange between the electrons and the ions causes the latter at normal operating conditions (under 200°C) to migrate predominantly via grain boundaries leading, eventually, to voids and extrusions near grain boundary triple points and to a failure of entire device. Hummel [1] made an extensive review of electromigration and other related failure mechanisms in thin film metallizations for microelectronic devices. The followings are excerpted from the review.

Holes and Hillocks (Fig. 1) are preferentially formed whenever a gradient in temperature, grain size, geometric features, current density, crystal orientation of the grains, etc., occurs. The growth of these holes leads eventually to the interruption of the continuity of a conducting stripe, a process which is aggravated by elevated temperatures and higher current densities.

The connecting stripes which link the individual parts of very large scale (VLS) integrated circuits (IC) are only about 1 μm thick and about 1-5 μm wide or even narrower. As a consequence, they have sustain current densities near or in excess of 1 MA cm^{-2}. This is several orders of magnitude larger than current densities in domestically used wires. The resulting electron wing induced matter transport from cathode to anode is therefore substantially larger than in bulk materials where only much lower current densities can be maintained before reaching the melting temperature.

Grain boundaries are the preferred nucleation sites for void and hillock formation. In particular,

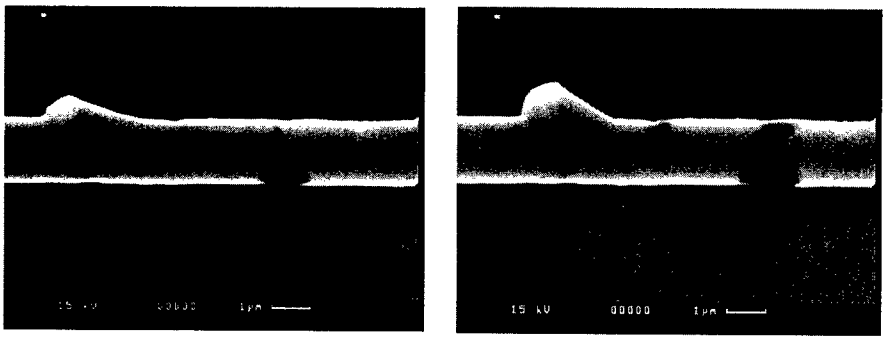


Fig.1. Hillocks and holes developed during electromigration. Width of line was 2 μm and lines were tested at 280°C, 1 MA/cm^2. Direction of electron flow was from right to left.
(Courtesy of Dr. Y. C. Joo)

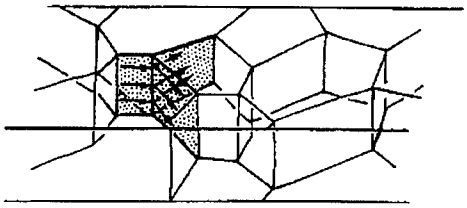


Fig.2. Grain structure emphasizing grain boundary triple point [1].

grain boundary triple points having one path in and two paths out may lead to localized depletion of material (Fig. 2). Texture, that is, the preferred orientation of certain lattice planes with respect to the plane of the IC, has an influence on electromigration resistance [2-4]. Textures also influence the strength in thin films [5]. Grains having the {111} texture are mechanically stronger than those in {110} textured films. Therefore, aluminum films which have a strong {111} texture show an improved electromigration resistance and a decrease in the standard deviation in medial time to failure [2,6,7]. An empirical relationship between the median failure time and the texture of thin films has been given by [4]

$$t_{50} \propto (S/\sigma^2) \log[I_{(111)}/I_{(200)}]^3 \quad (1)$$

where t_{50} is the median time to failure, at which 50% of a large number of identical devices have failed, S the median grain size, σ the standard deviation of the grain size distribution, and $I_{(111)}/I_{(200)}$ the measured X-ray intensity ratio for two crystallographic directions.

It is well known that while voids are characterized by tensile stresses, extrusions occur in regions which display compressive stress [8,9,10]. Experiments suggest that the compressive stress gradients between <110> and <111> oriented grains lead to hillocks by preferred growth of <110> grains out of the plane of the interconnect [11]. The driving force for these growths seems to stem under certain conditions from the elastic strain energy densities between the <110> and <111> grains [11].

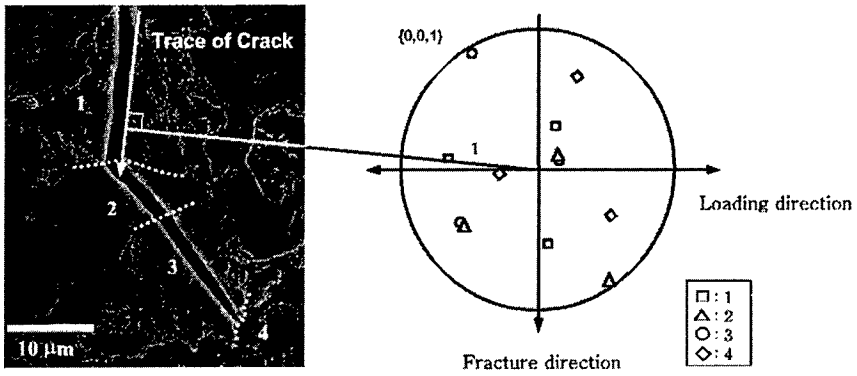


Fig.3. Crack propagation in Mn-Mo-Ni low alloy steel [12].

1.2. The Brittle Crack Propagation in Mn-Mo-Ni Low Alloy Steel

Kim et al. [12] studied the brittle crack propagation in Mn-Mo-Ni low alloy steel (0.17%C, 0.25%Si,1.44%Mn, 0.75%Ni, 0.2% Cr, 0.51% Mo, 0.016% Al, 0.01%Cu, 0.004% V, 0.004% P, and 0.002%S) for reactor pressure vessels.

Figure 3 shows that the crack planes are along the {001} planes. The crack plane normal directions are likely to be aligned with the loading direction and the crack growth is likely to be difficult when the growing crack meets a new grain whose orientation is deviated from that of the growing crack. In order to describe the brittle crack propagation of the steel, they introduced the geometric compatibility factor M defined by

$$M = \cos\alpha \cos\theta \quad (2)$$

where α is the angle between the two crack planes and θ the angle between the loading direction and the crack plane normal. The value of M ranges from zero to one. As the M value decreases, the crack growth is likely to be difficult. The experimental data indicated that the crack propagation took place when $M > 0.55$ whereas cracking was arrested or the crack propagated along grain boundaries when $M < 0.55$. This implies that cracking is influenced by the texture of materials.

1.3. Resistance to PCI Failure

The Pellet Cladding Interaction (PCI) resistance of reactor fuel claddings, Zircaloy-4 or its derivatives, is known to be improved by controlling its texture so that the pole of the (0001) plane can be oriented along the radial direction.

1.4. Local Necking

An annealed strip tension specimen first becomes unstable in the way of a rod, gradually acquiring a neck with a profile radius that drops from infinity as straining continues. This is diffuse necking, so labeled because its initiation is truly diffuse and its development is comparatively diffuse as well. The condition for initiating unstable flow after any amount of prior straining is that somewhere in the material the next increment of strain-induced hardening be canceled out by an accompanying strain-induced softening. Then further straining will tend to concentrate in the place

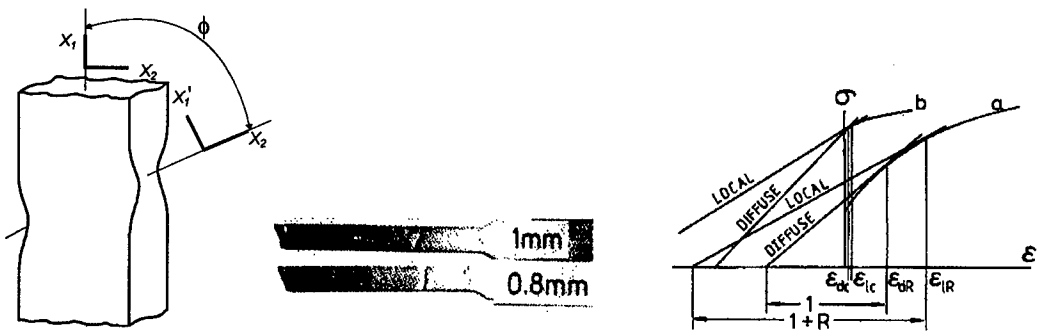


Fig.4. (a) Coordinates in local neck, (b) cold rolled Al strip tension specimen fractured along local neck [13], and (c) strain at unstable flow in ⓐ annealed and ⓑ cold worked specimens.

where resistance to continued flow is first lost. The condition for initiating the instability is given by

$$d\sigma/d\varepsilon_{11} = \sigma \quad (3)$$

There is another possibility of local necking, which is most prominent in sheet material, especially after cold rolling. In local necking the specimen is thinned along a narrow band inclined at angle ϕ to the tension axis (Fig. 4a). The orientation of the band is governed by the need for zero normal strain along its length, or for plane strain in the band. In Fig. 4(a) ε'_{22} must be zero, for only in this way can the material in such a confined region be isolated completely from that attached to it on either side. If ε'_{22} were not zero, adjoining material would have to deform: the band of flow would therefore spread out along X'_1 (or X_1) and the local quality would be lost within the wider bounds of a diffuse neck. The strain ε'_{22} can be calculated as follows:

$$d\varepsilon'_{22} = a_{21}a_{21}\, d\varepsilon_{11} + a_{22}a_{22}\, d\varepsilon_{22} + a_{23}a_{23}\, d\varepsilon_{33} = d\varepsilon_{11}\cos^2\phi + d\varepsilon_{22}\cos^2(\pi/2-\phi) = 0$$

$$d\varepsilon_{11} + d\varepsilon_{22} + d\varepsilon_{33} = 0$$

$$d\varepsilon_{33} / d\varepsilon_{22} = R \quad (4)$$

It follows from the above equations that

$$\phi = (1/2)\cos^{-1}[-1/(1+2R)] \quad (5)$$

In planar anisotropic materials, the plastic strain ratio can vary with angle to the tensile direction. It should be noted that the materials need not be planar isotropic [13]. For isotropic materials, R = 1 and $\phi = 54.7°$. It also follows that $\phi = 90°$ at R = 0, $\phi = 62°$ at R = 0.4, $\phi = 51°$ at R = 2, and $\phi = 49°$ at R = 3. Figure 4(b) shows tensile fractured cold rolled super purity aluminum sheets in which $\phi \cong 55°$.

Local necking also reflects a cancellation of strain-hardening by geometrical softening. The rate of hardening is $d\sigma/d\varepsilon_{11}$, as for diffuse necking, but the rate of softening is different. Now the area is changed only in one dimension, the thickness. Therefore dA = - w dt, with w the fixed width (for

$d\varepsilon'_{22} = 0$), and the rate of geometrical softening (the rate of loss of load-carrying ability per unit of area) is

$$(1/A)(dF/d\varepsilon_{11}) = (1/A)(-\sigma\, w\, dt\, /d\varepsilon_{11}) = -\sigma\, w\, dt\, /\, (w\, t\, d\varepsilon_{11}) = -\,\sigma\, (dt\, /\, t)\, /\, d\varepsilon_{11}$$

$$= -\sigma\, d\varepsilon_{33}\, /d\varepsilon_{11} = \sigma\, /(1+R) \qquad (6)$$

Equating the hardening rate with the softening rate, we obtain [13]

$$d\sigma\, /\, d\varepsilon_{11} = \sigma\, /\, (1+R) \qquad (7)$$

For isotropic materials $d\sigma\, /\, d\varepsilon = \sigma\, /\, 2$. Figure 4(c) shows the criteria for diffuse necking and local necking in pure tension. Since $R > 0$, local necking strain is larger than diffuse necking strain. Once diffuse necking initiates, the uniaxial stress state may not be maintained and the condition of Eq.(7) can not be satisfied. When materials are strain hardened, the both necking strains approach zero and the condition of Eq. (7) can be satisfied, resulting in the local necking. Even annealed specimens can undergo local necking, when the diffuse neck radius is so large that the uniaxial stress state can

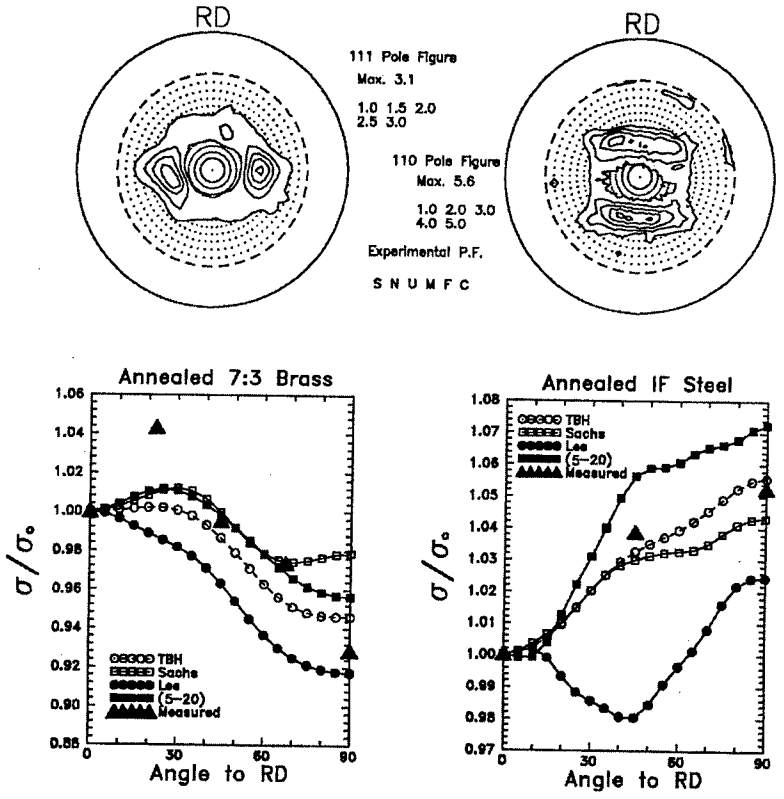


Fig.5. Measured relative yield strengths of (left) 7:3 brass and (right) IF steel sheets as a function of angle between tensile and rolling directions along with values calculated using textures in (left) and (right) based on TBH[14,15], Sachs[16], Lee [17], and Jeong [18] methods.

be approximated before fracturing. As the value of R increases, the difference between both necking strains increases and the possibility of fracture of specimen increases unless its strain rate sensitivity is large, before local necking takes place.

1.5. Anisotropy of Yield Strength

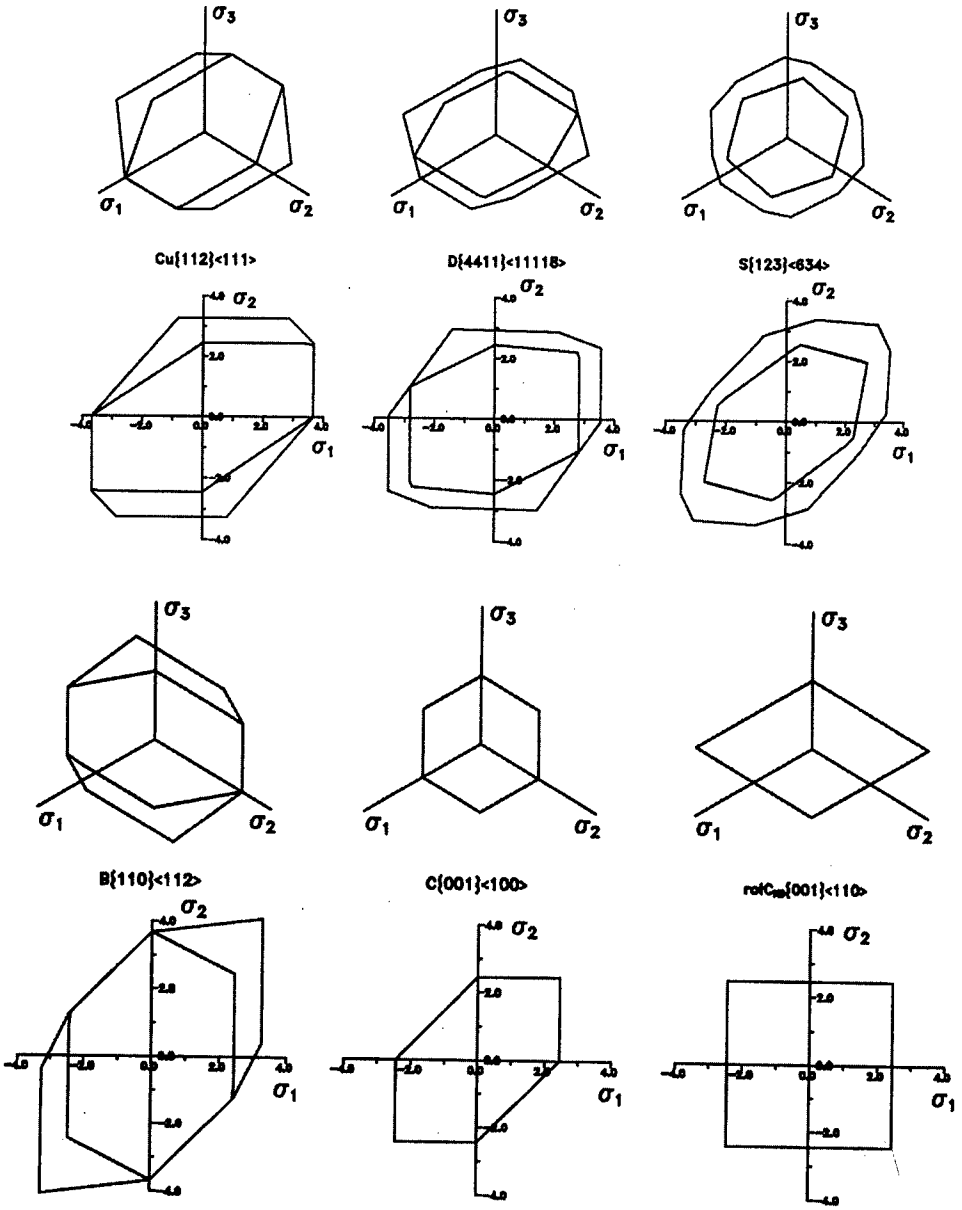


Fig.6. Yield loci of fcc single crystals calculated based on TBH theory [14,15](outer curves) and Sachs [16] theory (inner curves) [18]

The Schmid law indicates that the yield stress depends on the direction of tensile direction. Therefore the yield strength of textured materials must be anisotropic. Figure 5 shows the measured relative yield stresses of annealed 7:3 brass and interstitial free steel as a function of tensile direction along with the values calculated using the measured textures based on various models.

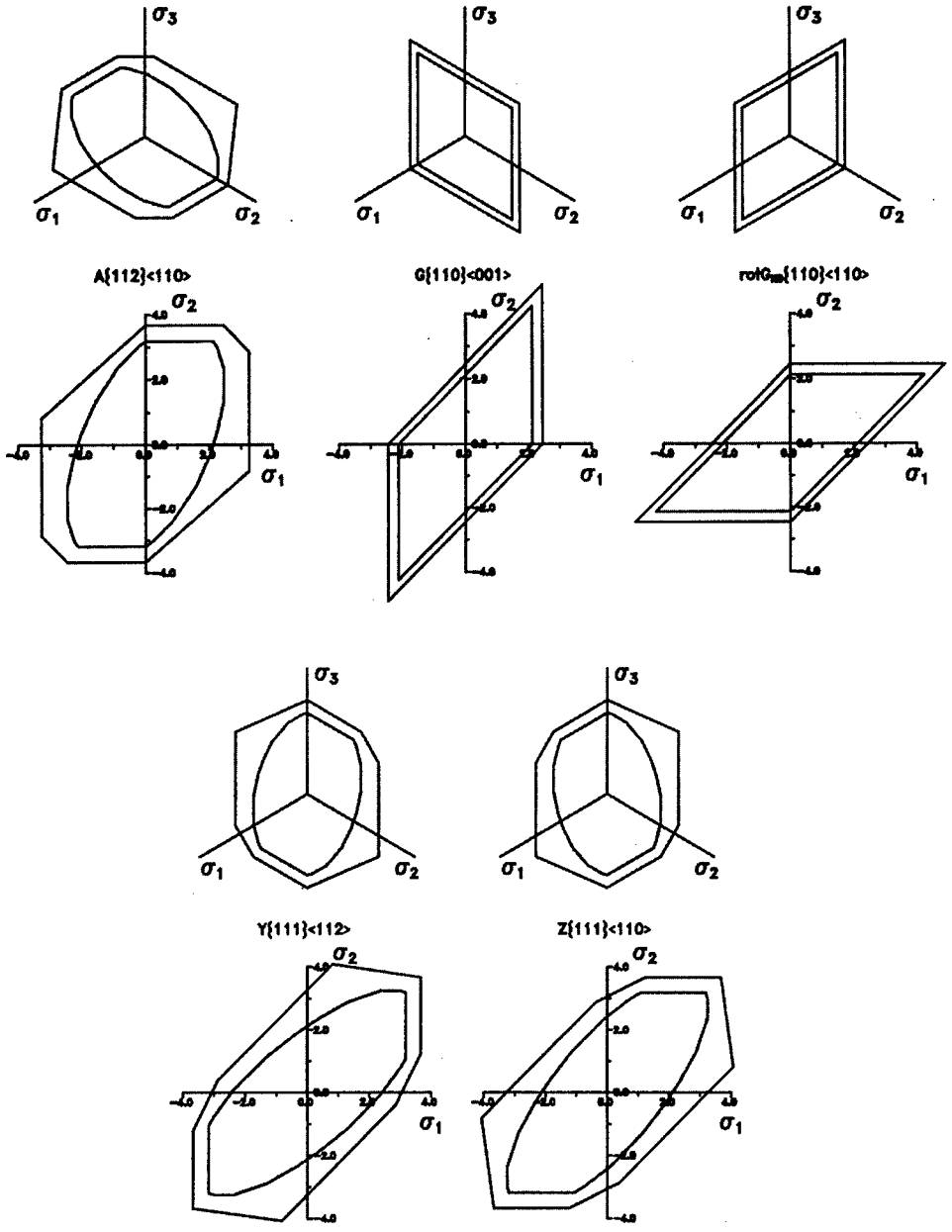


Fig.7. Yield loci of bcc single crystals calculated based on TBH theory [14,15] (outer curves) and Sachs theory [16] (inner curves). Slip systems of {110}, {112}, {123} <111> were assumed to be active [18].

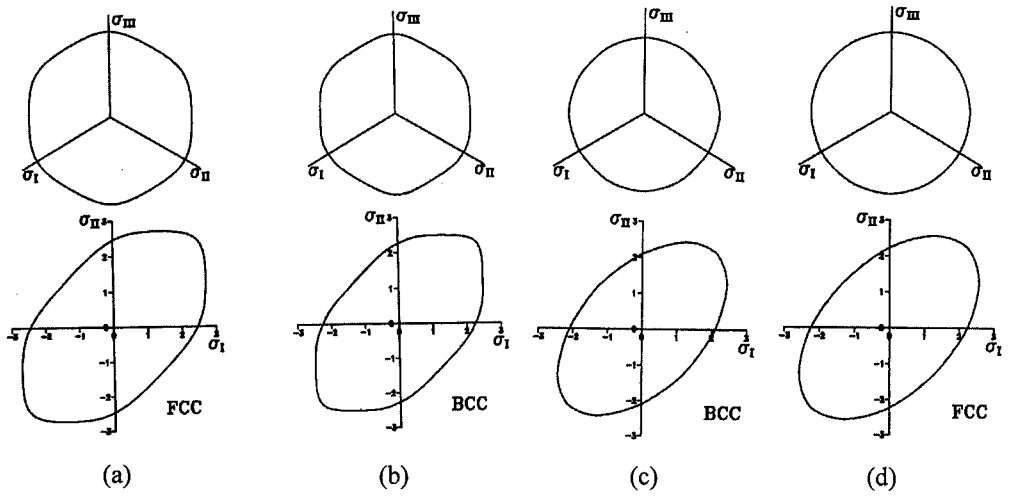


Fig.8. Yield loci of isotropic fcc and bcc polycrystals calculated based on Sachs theory using strain path (a,b) and stress path (c,d) averaging methods [19].

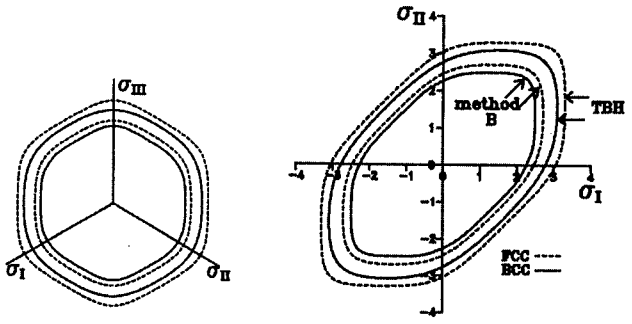


Fig.9. Yield loci of isotropic fcc and bcc polycrystals calculated using strain path averaging method and TBH method [19].

Consequently, the yield locus depends on the textures of materials. Figures 6 and 7 show yield loci of fcc and bcc single crystals calculated based on the Taylor-Bishop-Hill theory [14,15] and Sachs theory [16]. The yield loci of isotropic fcc and bcc materials can be calculated by averaging yield loci of randomly oriented single crystals. Figure 8 shows yield loci of isotropic fcc and bcc polycrystals calculated based on Sachs theory using the strain and stress path averaging methods. The shape of the yield loci in Fig. 8 (a,b) is similar to that calculated using the Taylor-Bishop-Hill method as shown in Fig. 9. However Fig. 8(c,d) is very similar to the Von Mises yield criterion.

2. TEXTURE CONTROL

2.1. Plastic Deformation (Asymmetric Rolling)

Aluminum alloy sheets are considered as one of the high potential substitutes for steel sheets

considering weight reduction of automobiles. However, aluminum alloy sheets have drawbacks such as higher prices and the inferior formability. The inferior formability is mainly due to lower strain rate sensitivities and plastic strain ratios or the Lankford values. The strain rate sensitivity of aluminum may be improved by alloying. But the plastic strain ratios of aluminum alloy sheets are low due to the texture developed in conventional rolling and thermal processes. The texture of aluminum alloy sheets cold rolled by the conventional rolling processes is characterized by the β fiber texture, which changes to the cube texture after annealing. However, the shear texture characterized by the {001}<110>, {111}<110>, and {111}<112> orientations forms in the surface layer of aluminum sheets rolled at high frictions between sheet and rolls and at characteristic deformation geometries.

Recently, the present author and coworkers [20,21] have developed a process called asymmetric rolling which gives rise to more or less uniform shear deformations and so shear deformation textures through the sheet thickness. The {111}<110> and {111}<112> orientation components in the shear deformation texture can enhance the plastic strain ratio. The uniform shear texture through the thickness means a substantial increase in the plastic strain ratio. Indeed, an average plastic strain ratio of 1.5 or higher could be obtained in asymmetrically rolled aluminum and aluminum alloys [22]. This value is almost 2 times higher than that of commercially available aluminum alloy sheets.

Figure 10 shows the measured (111) pole figures of the initial aluminum sheet and the upper surface, the center, and the lower surface layers of aluminum sheet asymmetrically rolled by 50% at a roll radius ratio of 1.5 in which the upper roll radius is 1.5 times larger than the lower roll radius and so the circumferential velocity of the upper roll is 1.5 times higher than that of the lower roll (The best shear deformation texture was obtained at a roll radius ratio of 1.5 with the lower roll radius of 63mm [23]). The deformation was analyzed by the elasto-plastic FEM. Figure 11 shows the deformed meshes obtained by FEM analysis. The deformation history is used to calculate the texture based on the TBH theory. Figure 12 shows the calculated textures. They are similar to the measured textures in Fig. 10, even though calculation was made using an initial specimen of random orientation.

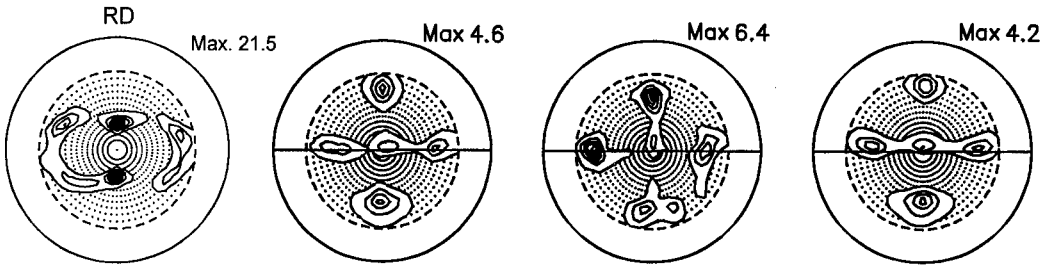


Fig.10. (111) pole figures of initial sheet (1st from left) and upper surface (2nd), center (3rd), and lower surface layers (4th) of 50% asymmetrically rolled aluminum sheets

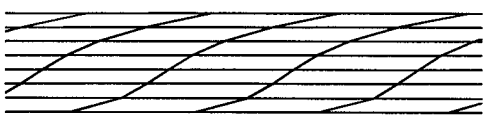


Fig.11. Deformed mesh of 50% asymmetrically rolled aluminum sheet.

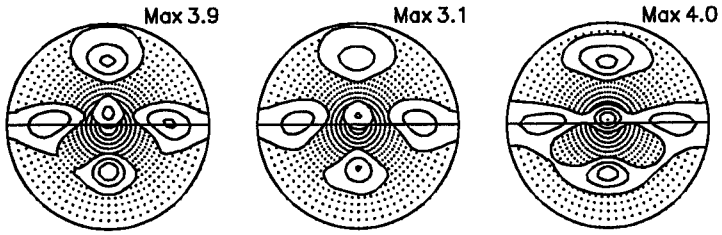


Fig.12. Calculated (111) pole figures of 50% asymmetrically rolled aluminum sheet.

2.2. Recrystallization (Strain Energy Release Maximization Model)

The first theory on the development of the recrystallization texture was suggested by Burgers in 1931. It is often called the oriented nucleation theory in which the preferred activation of a special nucleus determines the final recrystallization texture [24]. The second theory, so called the oriented growth theory, appeared in 1940 [25]. In the theory the preferred growth of grains having a special relationship to the deformed matrix among more randomly distributed nuclei determines the final recrystallization texture.

Since recrystallization is a process of nucleation and growth, it is natural to consider the recrystallization texture from the viewpoint of nucleation and growth. Critical reviews of the theories are available in refs. [26,27]. It is generally agreed that a major driving force for recrystallization is the stored energy due to dislocations generated during deformation and other fabrications. However, they attribute the recrystallization texture mainly to anisotropy of the energy or mobility of boundaries between the fabricated matrix and the recrystallized grains.

The author proposed a model for the evolution of the recrystallization textures, the strain energy release maximization model [28]. In the model, the direction of absolute maximum internal stress due to dislocations generated during fabrication is parallel to the minimum Young's modulus direction in recrystallized grains, whereby the strain energy release during recrystallization can be maximized (Fig.13). The absolute maximum stress direction is shown to be along the Burgers vector.

For multiple slip, the shear strains on active slip systems may not be equal. The dislocation density ρ on a slip system is expected to increase with increasing shear strain γ on the slip system. A few examples of the γ - ρ relation are available [29]. The relation can be approximated to be

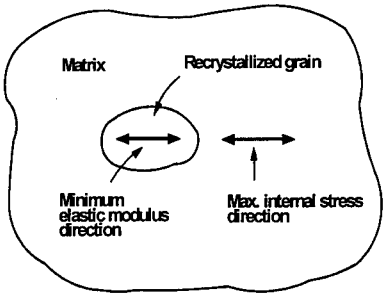


Fig.13. Matrix and recrystallized grains constitute constant volume system, in which energy release can be maximized when absolute maximum internal stress direction becomes parallel to minimum elastic modulus direction of recrystallized grain.

linear. It follows that

$$|\sigma_{max}| \propto \rho \propto \gamma \quad (8)$$

Therefore, the contribution of each active slip system to the absolute maximum stress is approximated to be proportional to the shear strain on it.

When a crystal rotates during deformation, the shear strain increment on slip system $d\gamma$ with respect to strain increment of specimen $d\varepsilon$ can vary with deformation. In this case the contribution of each slip system to the absolute maximum stress will be proportional to

$$\gamma = \int |d\gamma/d\varepsilon| \, d\varepsilon \quad (9)$$

If a deformation texture is stable, the ratio of the strain rates $|d\gamma/d\varepsilon|$ on slip systems is independent of deformation. It is noted that the absolute maximum stress is an internal stress. In order for this method to be used, it is necessary to know active slip systems and shear strains on them. They can be obtained from the deformation texture or from a model which can simulate the deformation texture. For electrodeposits, the maximum internal stress direction can be obtained from their textures.

To obtain the recrystallization texture in general, another orientation relation between the matrix and the recrystallized grain is needed, which can be obtained by physically appropriate reasoning depending situations.

In order to explain this model, two examples are discussed in the following. Axisymmetrically extruded aluminum alloy rod [30], drawn aluminum wire [31] and copper and some copper alloy wires [32] generally have major <111> + minor <001> double fiber textures in the deformed state.

It is well known that the deformation texture changes to <100> when they are recrystallized [31,33,34]. Therefore, the <100> recrystallization texture can be interpreted as originating from the <111> deformation texture.

The change from the <111> deformation texture to the <100> recrystallization texture could be explained by the present model [28]. Figure 14 shows a tetrahedron showing slip planes and slip directions in a fcc metal crystal of the <111> fiber orientation. Since the texture is stable, this orientation determines slip systems. Three m<110> directions are skew to the <111> axis direction and the remaining three s<110> directions are normal to the <111> axis direction where prefix m and s indicate two different kinds of <110> directions. Therefore, slip along the m<110> directions must have been activated to form the <111> texture, while slip along the s<110> directions is inactivated. The vector sum of the three m<110> directions becomes the <111> axis direction. Therefore, the <111> axis direction is the absolute maximum internal stress direction, which will become parallel to the minimum elastic modulus direction of recrystallized crystals according to the present model. The minimum elastic modulus direction of fcc metals is the <100> directions. Therefore, the drawn wire with the <111> fiber texture will have the <100> fiber texture after recrystallization in agreement with the measured results.

Blicharski et al. [35] studied deformation and recrystllization textures of bicrystals of $(123)[41\bar{2}]/(123)[\bar{4}\bar{1}2]$ and $(123)[41\bar{2}]/(\bar{1}\bar{2}\bar{3})[41\bar{2}]$. The experimental textures of the bicrystals were shown to be mixtures of those of component single crystals. Therefore, the discussion will be confined to the crystal of $(123)[41\bar{2}]$. The {111} pole figure determined at the midthickness position of crystal $(123)[41\bar{2}]$ deformed 90% by channel die compression is reproduced in Fig. 15(a). The initial orientation of the component crystals is also indicated in the figure.

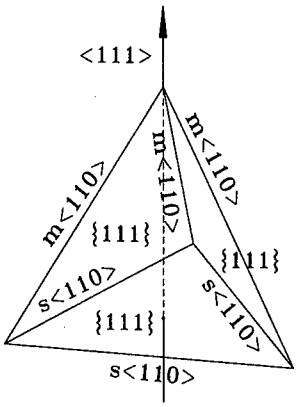


Fig.14. Tetrahedron showing slip systems {111}<110> of fcc metals having <111> fiber texture.

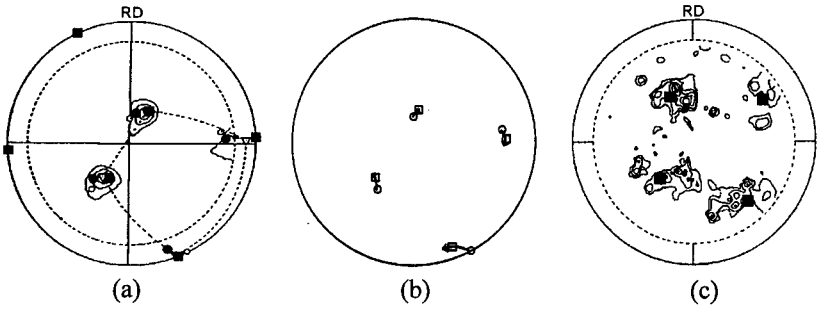


Fig.15. (111) pole figures showing (a) deformation texture [35], (b) change of orientation during deformation, which was calculated using full constraints strain rate sensitivity model with m=0.01 [36], and (c) recrystallization texture of crystal $(123)[41\bar{2}]$ [35]. Open circles indicate initial orientation. Symbol squares in (c) indicate calculated recrystallization texture [36]. Filled circles in (a) and squares in (b) show same orientation.

The recrystallization texture of crystal $(123)[41\bar{2}]$ was determined from specimens annealed at 125°C for 5 min. The {111} pole figure of the fully annealed specimen is reproduced in Fig. 15(c). The slip systems and their shear strains can be obtained in the process of simulation of deformation. Figure 15(b) shows the orientation change of crystal $(123)[41\bar{2}]$ during the plane strain compression calculated using the full constraints strain rate sensitivity models with m=0.01[25,26]. It can be seen that the model simulates the deformation texture reasonably well.

Figure 16 shows the calculated shear strain rate, $d\gamma/d\varepsilon$, on active slip systems of crystal $(123)[41\bar{2}]$ as a function of true thickness strain under the plane strain compression. The changes in shear strain rates on active slip systems are sensitive to strain up to a thickness strain of about 0.5 and not very sensitive afterwards. The measured deformation texture is simulated at the reduction slightly lower than experimental reduction. It may be due to localized deformation like shear band formation occurring in the real deformation. The localized deformation may not be reflected in X-ray measurements. The scattered experimental recrystallization textures may be related to the non-uniform deformation. With the known shear strains on active slip systems, we are in position to

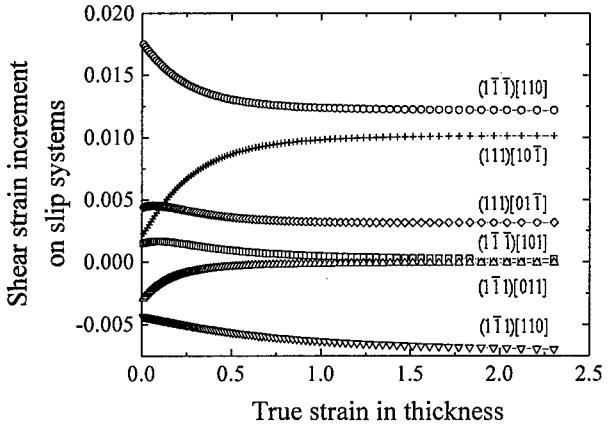


Fig.16. Calculated shear strain at thickness reduction of 0.01 on active slip systems of crystal $(123)[41\bar{2}]$ as a function of strain [36]

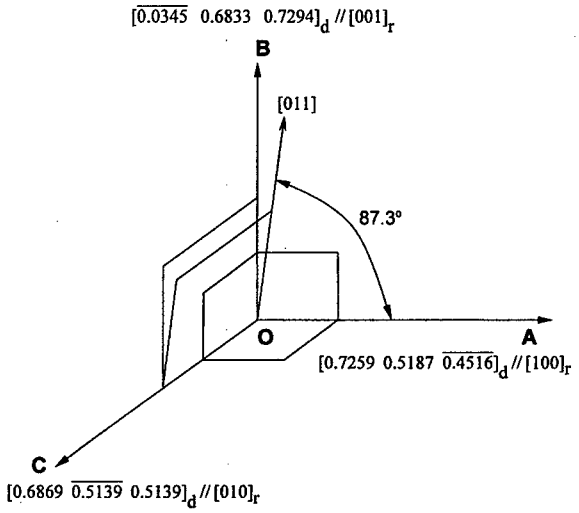


Fig.17. Orientation relations in deformed and recrystallized states. Suffixes d and r indicate deformed and recrystallized states, respectively.

calculate the recrystallization texture.

For a true thickness strain of 2.3 or 90% reduction, the ratios of the γ values in Eq.(9) of the slip systems, $(111)[10\bar{1}]$, $(111)[01\bar{1}]$, $(\bar{1}1\bar{1})[110]$, $(1\bar{1}\bar{1})[110]$, $(\bar{1}1\bar{1})[011]$, and $(1\bar{1}\bar{1})[101]$, are 2091, 776, 1424, 2938, 76, and 139, respectively. The contributions of slip systems, $(\bar{1}1\bar{1})[011]$ and $(1\bar{1}\bar{1})[101]$, are negligible compared with other active slip systems. Therefore, the slip systems, $(111)[10\bar{1}]$, $(111)[01\bar{1}]$, $(\bar{1}1\bar{1})[110]$ and $(1\bar{1}\bar{1})[110]$, are considered in calculating the absolute maximum internal stress direction. It is noted that all the slip directions are designated so that they can be at acute angle one another and the absolute maximum internal stress direction calculated in

Eq.(10) can be at acute angle with the major extension direction or the rolling direction. The absolute maximum stress direction now becomes

$$2091[10\bar{1}] + 776[01\bar{1}] + 1424 \times 0.577[110] + 2938 \times 0.577[110] = [4608\ \ 3293\ \ \overline{2867}] \qquad (10)$$

where the factor 0.577 originated from the fact that the slip systems of $(1\bar{1}1)[110]$ and $(\bar{1}11)[110]$ share the same slip direction [110] [36]. The $[4608\ 3293\ \overline{2867}]$ direction or the $[0.7259\ 0.5187\ \overline{0.4516}]$ direction will become parallel to one of the <100> directions, the minimum Young's modulus direction of aluminum, after recrystallization.

Another orientation relation between the matrix and the recrystallized grain is obtained. If the absolute maximum internal stress direction in the deformed state becomes parallel to one of the <100> directions in the recrystallized state, another one of the <100> directions in the recrystallized state which is normal to the previous <100> will tend to be parallel to a direction which is at the smallest possible angle with another high stress direction in the deformed state. Possible candidates of the high stress direction must be three Burgers vector directions, the [011], [101], and $[1\bar{1}0]$ directions, which have not been used in calculating the maximum internal stress direction among six possible Burgers vector directions. The [011], [101], and $[1\bar{1}0]$ directions are at 87.28°, 78.82°, and 81.57°, respectively, with the absolute maximum internal stress direction, $[0.7259\ 0.5187\ \overline{0.4516}]$. The [011] direction is closest to, but less than 90° with the maximum stress direction. The direction which is at the smallest possible angle with the [011] direction and normal to the maximum internal stress direction (OA in Fig.17) at the same time must be on the plane made of the [011] direction and the direction OA. The direction is shown as OB in Fig.17. The direction OB must be normal to both the plane normal (OC in Fig.17) and the direction OA. The direction OC is obtained by the vector product of the direction OA and the [011] direction. The direction OB is obtained by vector product of the directions OC and OA. The directions OC and OB become the $[0.6869\ \overline{0.5139}\ 0.5139]$ and $[\overline{0.0345}\ 0.6833\ 0.7294]$ directions, respectively. In summary, the $[0.7259\ 0.5187\ \overline{0.4516}]$, $[0.6869\ \overline{0.5139}\ 0.5139]$, and $[\overline{0.0345}\ 0.6833\ 0.7294]$ directions, which are normal to each other, will become parallel to the <100> directions after recrystallization

If the $[0.7259\ 0.5187\ \overline{0.4516}]$, $[0.6869\ \overline{0.5139}\ 0.5139]$, and $[\overline{0.0345}\ 0.6833\ 0.7294]$ unit vectors are set to be parallel to [100], [010], and [001] directions after recrystallization, the rolling plane, (0.1534 0.5101 0.8463), and the rolling direction, $[0.8111\ 0.4242\ \overline{0.4027}]$, in the deformed crystal coordinate system are transformed to the $(\overline{0.0062}\ 0.2781\ 0.9606)$ plane and the $[0.9907\ 0.1322\ \overline{0.0319}]$ direction, respectively, in the recrystallized crystal coordinate system. The result is plotted in Fig.15(c) along with the experimental data. The calculated recrystallization textures are in good agreement with the measured data.

This model could explain the evolution of many otherwise unexplainable recrystallization textures [37-46].

2.3. Grain Growth and Others

During grain growth after recrystallization, the texture of materials may change. The growth texture, often called the secondary recrystallization texture, seems to be controlled by grain boundary energy and mobility, more likely, mobility [45,47]. The texture of vapor deposits and electrodeposits can be controlled by deposition conditions. The deposition parameters are interrelated. The author suggested a model for the evolution of textures of deposits, in which the texture would be controlled by the concentration of vapor or ions adjacent to growing deposits and the lattice surface energy of deposits [48-50]. The texture development in cast materials is related to

the dendritic growth in many cases. The orientation of dendrites is suggested to be controlled by their thermal stress and the lattice surface energy and heat conductivity of materials [51].

CONCLUSION

The plastic deformation, vapor deposition, electrodeposition, casting, and recrystallization and grain growth of materials give rise to the development of characteristic textures, which in turn lead to anisotropy in various properties such as yield strength, cleavage fracture strength, and electromigration characteristics. Therefore, it is necessary to control the texture of materials to obtain required properties. The deformation texture can be reasonably well simulated. The recrystallization texture is related to the deformation history and texture and can be explained by the strain energy release maximization model. The recrystallization texture may change during grain growth. The growth texture seems to be controlled by grain boundary characteristics. The textures of vapor deposits and electrodeposits are controlled by deposition conditions. The texture of cast materials is related in many cases to the dendritic growth.

ACKNOWLEDGEMENT

This work has been supported by National Research Laboratory for Texture Control, Seoul National University.

REFERENCES

1. R.E.Hummel, International Materials Reviews, **39** (1994) no.3, p.97
2. D.B.Knorr, K.P.Rodbell, and D.P.Tracy, MRS Symp. Poc. **225** (1991) p.21
3. J.E.Sanches, Jr., O.Kraft, and E.Arzt, American Inst. of Phys. Conf. Proc., **263** (1992) p.250
4. S.Vaidya and A.S.Sinha, Thin Solid Films, **75** (1981) p.253
5. W.D.Nix, Metall. Trans. **20A** (1989) p.2217
6. R.E.Hummel and D.W.Malone, MRS Sym.Proc., **225** (1991) p.67
7. P.Li, A.S.Yapsir, K.Rajan, and T.-M.Lu, Appl. Phys. Lett., **54** (1989) p.2443
8. W.W.Mullins, Acta Metall., **6** (1959) p.414
9. J.Cho and C.V.Thompson, Appl. Phys. Lett., **54** (1989) p.2577
10. P.A.Beck, J.C.Kremer, L.J.Demer, and Holzworth, Trans. AIME, **175** (1948) p.372
11. J.E.Sanchez,Jr. and E.Arzt, Scripta Metall., **26** (1992) p.1325
12. M.C.Kim, Y.J.Oh, and J.H.Hong, private communication.
13. D.N.Lee and S.H.Park, J. Korean Inst. Met., **25** (1987) p.89
14. G.I.Taylor, J. Inst. Metals, **62** (1938) p.307
15. J.F.W.Bishop and R.Hill, Phil. Mag., **42** (1951) p.414
16. G.Sachs, Z.Verein Deut. Ing., **72** (1928) p.734
17. D.N.Lee and K.H.Oh, J. Mater. Sci., **20** (1985) p.3111
18. H.-T.Jeong, Ph.D. Thesis, Seoul National University, (1997)
19. H.-T.Jeong, D.N.Lee, and K.H.Oh, Mater. Sci. Forum, **157-162** (1994) p.1603
20. C.-H.Choi, K.-H.Kim, and D.N.Lee, Mater. Sci. Forum, **273-275** (1998) p.391
21. C.-H.Choi, K.-H.Kim, S.-Y.Jeong, and D.N.Lee, J. Korean Inst. of Met. & Mater., **35** (1997) p.429
22. C.-H.Choi, K.-H.Kim, and D.N.Lee, Synthesis/Processing of Lightweight Metallic Materials II,

ed. C.M.Ward-Close, F.H.Froes, D.J.Chelleman and S.S.Cho, The Minerals, Metals & Materials Society, Warrendale, PA, USA, (1997) p.37
23. K.-H.Kim and D.N.Lee, unpublished results
24. W.G.Burgers and P.C.Louwerse, Z. Metallkunde, **67** (1931) p.605
25. C.S.Barrett, Trans. AIME, **137** (1940) p.128
26. R.D.Doherty, A.D.Hughes, F.J.Humphreys, J.J.Jonas, D.Juul Jensen, M.E.Kassner, W.E.King, T.R.McNelley, H.J.McQueen, and A.D.Rollett, Mater. Sci. Eng. **A238** (1997) p.219
27. F.J.Humphreys, M.Hatherly, Recrystallization and Related Annealing Phenomena. Pergamon (1995)
28. D.N.Lee, Scripta Metall. Mater. **32** (1995) p.1689
29. M.Zehetbauer, Acta metal. mater. **41** (1993) p.589
30. D.N.Lee, Y.H.Chung, and M.C.Shin, Scripta Metall. **17** (1983) p.339
31. H.Inoue, N.Nakazu N, and H.Yamamoto, in Proc. ICOTOM 6 (ed., S. Nagashima), The Iron and Steel Inst. of Japan, Tokyo (1981) p.591
32. W.R.Hubband, Jr., Trans. AIME **77** (1950) p.581
33. W.A.Backofen, Trans. AIME **191** (1951) p.250
34. G.Bassi, Trans. AIME **191** (1951) p.533
35. M.Blicharski, J.Liu, and H.Hu, Acta mater. **43** (1995) p.3125
36. D.N.Lee and H.-T.Jeong, Mater. Sci. Eng. **A269** (1999) p.49
37. Y.B.Park, D.N.Lee, and G.Gottstein, Acta mater. **46** (1998) p.3371
38. Y.B.Park, D.N.Lee, and G.Gottstein, Mater. Sci. Eng. **A257** (1998) p.178
39. S.H.Lee and D.N.Lee, Mater. Sci. Eng. **A249** (1998) p.84
40. D.N.Lee and H.-T.Jeong, Scripta Mater. **38** (1998) p.1219
41. D.N.Lee, S.Kang, and J.Yang, Plating and Surf. Fin. **82** (Mar. 1995) p.76
42. J.Yang and D.N.Lee, Metals & Materials, **5** (1999) p.465.
43. J.H.Choi, S.Kang, and D.N.Lee, J. Mater. Sci. in press (2000)
44. H.S.Nam and D.N.Lee, J. Electrochem. Soc., **146** (1999) p.3300
45. H.-J.Shin, H.-T.Jeong, and D.N.Lee, Mater. Sci. Eng. **A279** (2000) p.244
46. D.N.Lee, Texture. Microstruct. **26-37** (1996) p.361
47. D.N.Lee and K.-H.Hur, Scripta. Mater. **40** (1999) p.1333
48. D.N.Lee, J. Mater. Sci., **24** (1989) p.4375
49. D.N.Lee, J. Mater. Sci. **34** (1999) p.2575
50. D.N.Lee, J. Korean Inst. Surf. Eng. **32** (1999) p.317
51. D.N.Lee, Y.-G.Lee, K.-H.Kim, and C.-H.Choi, Mater. Chem. Phys. **47** (1997) p.154

Key Engineering Materials Vols. 183-187 (2000) pp. 695-706
© 2000 Trans Tech Publications, Switzerland

Overview of Fracture of Piezoelectric Ceramics

Tong-Yi Zhang, Ran Fu, Minghao Zhao and Pin Tong

Department of Mechanical Engineering, Hong Kong University of Science and Technology, Clear Water Bay, Kowloon Hong Kong, China P.R.

Keywords: Combined Mechanical and Electrical Loading, Energy Release Rate, Fracture, Insulating and Conducting Cracks, Piezoelectric Materials

ABSTRACT

The paper provides an overview for the experimental and theoretical studies on the fracture behavior of piezoelectric ceramics. It first reviews the existing experimental studies and then examines the fracture models and analysis methods. The number of experimental studies has risen greatly in recent years as piezoelectric finds wider applications. In general experimental results show complicated fracture behavior under electrical, mechanical, or combined loading. Fracture data are specially scattered when external electric field is applied. Statistically based fracture criterion is likely required. Data by different researchers sometimes contradict with each other.

The volume of theoretical studies is huge. We discuss various fracture models, fracture criteria and methods of solution for crack problems. At the present time, there is no universally accepted fracture criterion. More studies, especially experimental ones, are needed to provide a better understanding of the fracture behavior of piezoelectric ceramics and to establish more acceptable fracture criteria. The criteria can be statistically based.

1. INTRODUCTION

The mechanical properties of piezoelectric ceramics have been studied extensively for decades. The topic is becoming more important as piezoelectric ceramics finds wider and wider applications in smart structures, microelectronics and microelectromechanical systems. This article presents an overview of the advancements in the understanding of the fracture of piezoelectric ceramics. It summarizes the experimental observations, the fracture mechanics studies and the theoretical modeling of piezoelectric ceramics, and the computational methods for the analysis. Publications in the field are many and, due to page limitations, cannot be all listed. An accompanied paper in this conference summarizes the studies of the topic at the Hong Kong University of Science and Technology [1].

2. EXPERIMENTAL OBSERVATIONS

2.1. Effects of Microstructure and Temperature

Experimental results show that fracture toughness and fracture strength of piezoelectric ceramics are functions of grain size and composition. Pohanka *et al.* [2] found that ferroelastic twinning and microcracking contributed substantially to the fracture toughness in $BaTiO_3$ ceramics with large grains, as shown in Fig. 1. Figure 2 shows that the minimum values of the fracture

toughness of $PbZrO_3$-$PbTiO_3$ ceramics are at the morphotropic boundaries between phases of different crystal structures, whereas the piezoelectric coefficients exhibit the maximums [3].

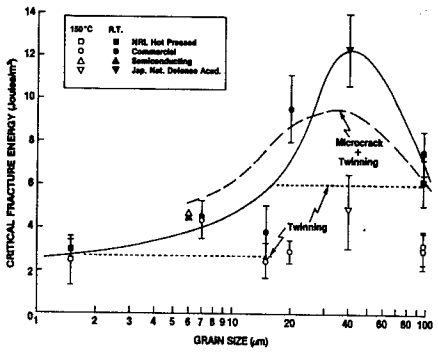


Fig. 1 Fracture energy of $BaTiO_3$ as a function of grain size [2].

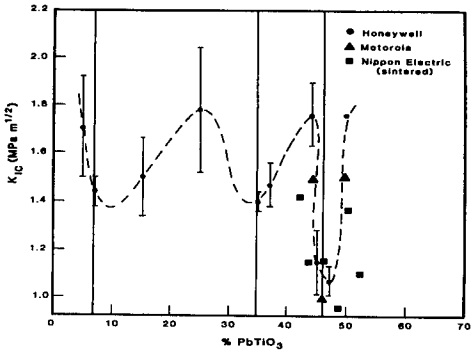


Fig. 2 Fracture toughness as a function of the $PbTiO_3$ ratio in PZT ceramics, vertical lines represent phase boundary [3].

Both the fracture strength and the fracture toughness of piezoelectric ceramics are sensitive to temperature. Cook *et al.* observed that the fracture toughness of $BaTiO_3$ ceramics decreased with increasing temperature between room temperature and the Curie point [4]. Metha and Virkar [5] reported the similar results for unpoled PZT samples. The observed temperature dependence was attributed to the toughening effect of 90°-domain twinning [5]. However, Figs. 3 and 4 show opposite trends for the bending strength and the fracture toughness of poled and unpoled PZT-4 ceramics [6], wherein both properties have their minimums near the Curie point. The similar contradict phenomenon was also observed for PBZT and PZT-NV-1 ceramics [7]. For PZT-841 ceramics, the bending strength exhibits valley-shaped floors at a temperature below the Curie point [8]. Elastic softening accompanies the bending strength reduction and has a peak at the same temperature where the bending strength has its minimum [8].

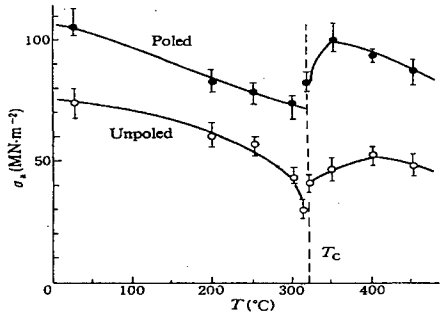


Fig.3 Bending strength of PZT-4 as a function of temperature [7].

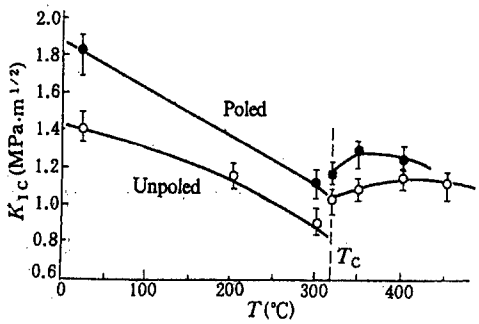


Fig. 4 Fracture toughness of PZT-4 as a function of temperature [7].

2.2. Effects of Electric Field

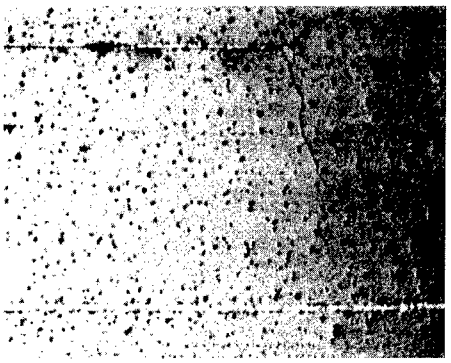


Fig. 5 Crack growth was found in the model of multilayer piezoelectric actuator after 3000 cycles [10].

Effects of electric field on crack initiation and growth have long been the focus of interests in the fracture study of piezoelectric ceramics. McHenry and Koepke [9] observed, in a Navy-III type PZT subjected to double torsion loading, that crack propagation was enhanced by the application of AC or DC electric field perpendicular to pre-existing cracks. Crack initiation and propagation were seen around the tip of internal electrodes in multilayer piezoelectric actuators during cyclic loading, shown in Fig. 5 [10]. Jiang and Cross [11] found that ferroelectric fatigue occurred in low-density (93-97%) lanthanum-doped-PZT (PLZT) ceramics after 10^4 switching cycles, while the high-density (>99%) PLZT specimens of the same composition did not fatigue after 10^9 switching cycles. The ferroelectric fatigue is gauged by the loss of switchable polarization with repeated polarization reversals. The ferroelectric fatigue rate in low-density ceramics was also much higher than that in high-density ceramics. This indicates that the porosity is one of the key factors that affects the ferroelectric fatigue behavior. Jiang *et al.* [12] showed that ferroelectric fatigue of PLZT was accompanied by generation of microcracks near the surfaces of electrodes. White *et al.* [13] and Hill *et al.* [14] also observed microcracks in PZT specimens induced by an AC field at the resonant frequency of the material. With pre-cracks introduced by indentation, steady crack growth was observed perpendicular to the applied field in both PZT and PLZT ceramics under AC electric field that is larger than the coercive field [15, 16] but less than the coercive field [17].

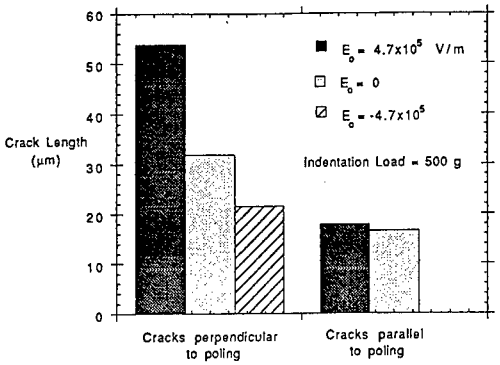


Fig. 6 Linear effect of electric field on the indentation fracture of PZT-8 [18].

The fracture behavior of piezoelectric ceramics under combined static mechanical and electrical loads was studied using indentation induced fracture, three-point bending, and fracture testing on pre-notched compact-tension (CT) specimens. The results of indentation fracture tests on PZT-8 ceramics are shown in Fig. 6. It indicates that a positive electric field promotes crack propagation perpendicular to the poling direction while a negative field retards it [18]. Electric field does not seem to have much effect on cracks parallel to the polling direction. For an indentation load of 4.9 N, a positive electric field of 4.7 kV/cm increases crack length perpendicular to the poling direction by almost 70%, while a negative electric field of -4.7 kV/cm reduces it by 30% as compared to the case of zero applied electric field. An opposite trend, however, was observed in the indentation fracture tests of PZT EC-65 ceramics under an indentation load of 11.76 N. A positive field inhibits crack growth, while a negative field enhances the growth [19]. Other data also show that the indentation fracture behavior is load-dependent but has different trend. Figure 7 plots the indentation results under the indentation loads of 4.45 and 22.24 N [20]. At 4.45 N, the results give the same trend as those in Fig. 6. However, if the indentation load is 22.24 N, both negative and

positive fields facilitate crack propagation. Lynch [21] reported that a positive electric field enhanced the growth of cracks perpendicular to the poling direction in PLZT ceramics, but he did not report the effect of negative field. Park and Sun [22], and Fu and Zhang [23] conducted fracture tests on pre-notched CT samples of PZT-4 and PZT-841 ceramics, respectively. The results of PZT-4 ceramics reveal nearly a linear effect of electric field on the fracture load. The results of PZT-841 ceramics show that the applied electric field increases the scattering of the measured apparent fracture toughness. The applied electric field, either positive or negative, reduces the mean of the apparent fracture toughness [23].

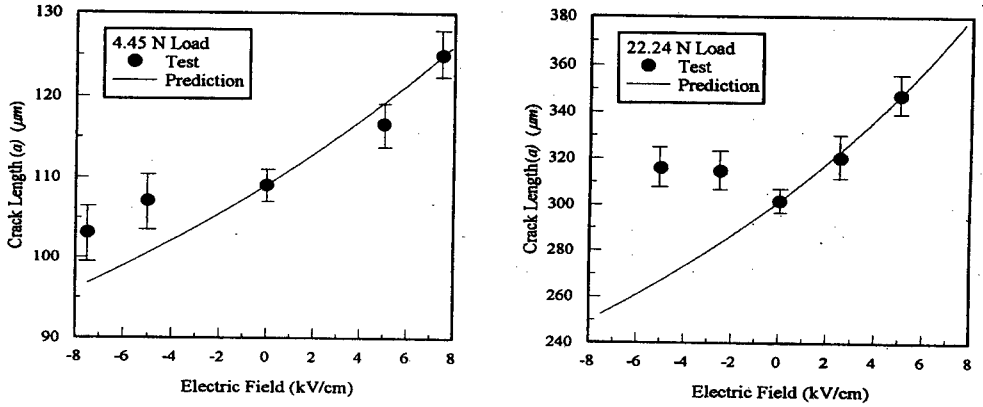


Fig. 7 Load-dependence of indentation fracture of PZT-4 ceramics in the presence of electric field [20].

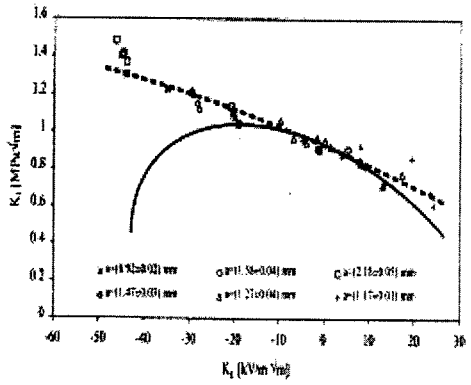


Fig. 8 Apparent critical fracture toughness as a function of electrical intensity factor for conductive cracks [24].

Heyer *et al.* studied the electro-mechanical fracture toughness of conductive cracks in PZT-PIC ceramics [24]. As shown in Fig. 8, when the electrical intensity factor is in the range of -15 kV/m$^{1/2}$ to 15 kV/m$^{1/2}$, the experimental data can be described by linear fracture mechanics. Fu *et al.* [25] found that the fracture toughness of PZT-4 ceramics, expressing in terms of the critical energy release rate, for conductive cracks under a purely electric field, is a material constant about 25 times higher than that under mechanical loading alone.

The bending strength of PZT ceramics also varies with applied electric field. Zhoga and Shpeizman, [26] showed that a positive field of 10 kV/cm enhanced the bending strength of PZT-19 ceramics by 7%, whereas the electric field beyond 10 kV/cm reduced the bending strength (Fig. 9a). A negative field has the similar effect, but the enhancement in the bending strength under lower values of applied electric field is more pronounced as shown in Fig. 9b [26]. Makino and Kamiya [27] conducted three-point bending tests on PZT samples under electric fields in parallel and anti-parallel to the loading direction. Their results show that either a positive or a negative electric field, even at values less than 10 kV/cm, reduces the bending strength

of PZT ceramics. Similar results were reported on the bending strength of PZT-841 [28, 8]. The results show that the electric field induces large scattering in the measured data on the bending strength, and that the bending strength is reduced significantly by positive or negative field larger than 3 kV/cm. For example, the bending strength under a positive field of 20 kV/cm is only half of that without applied electric field.

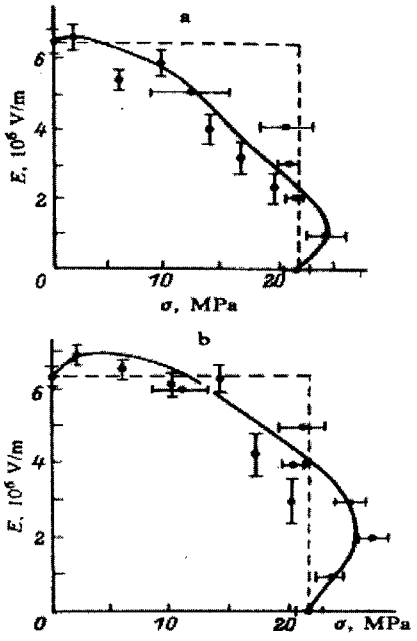


Fig. 9 Fracture or electric breakdown of PZT-19 under combined electrical and mechanical loading [26].

From the discussion above, we see that complicated and diverse failure behaviors associated with piezoelectricity, spontaneous polarization, and intrinsic strain, have been observed. The common features of the experimental observations are as follows: First, applied electric field, particularly if it is comparable to the mechanical field in magnitude, scatters measured data. This implies that more tests are needed to provide reliable data and allow the statistical treatment of the data. Second, an internal stress field is produced when the material goes through the transition from paraelectric phase to ferroelectric phase. The internal stress field is not uniform during poling and changes with applied mechanical and electrical fields. This internal stress field may inhibit or assist the applied loads causing the piezoelectric ceramics to failure. Third, electric charges can be trapped at defects and partial electric discharge can occur locally. This electric discharge behavior may make an insulating crack conduct electrically and thus changes the failure behavior of piezoelectric ceramics.

3. FRACTURE MECHANICS

Mechanical or physical phenomena may be modeled mathematically as boundary value problems. Solving the boundary value problems becomes a key step to quantitatively understand the fracture behavior of piezoelectric ceramics. Landau and Lifschitz [29] laid out the mechanic fundation for piezoelectric materials. Considering Maxwell stresses, Smith and Warren [30] found the 1/r singularity in stresses at crack tip. McMeeking discussed the difference between Maxwell and material stresses and analyzed the mechanical stresses of conductive cracks in dielectric materials [31]. Using finite element simulation, Gong and Suo treated a nonlinear material with quadratic electrostrictive strain in electric displacement [32]. In subsequent discussion, we will focus primarily on linear solutions, which are obtained mostly by methods equivalent to the linear fracture mechanics for anisotropic materials.

3.1 Electric Boundary Condition along Crack Faces

Parton analyzed insulating cracks in piezoelectric medium in 1976 [33]. He used permeable boundary condition, wherein the electric potential and the electric displacement perpendicular to the crack faces were assumed to be continuous across the crack. If one considers a crack as a mathematical slit, the electric field cannot be influenced by the slit. Hence one can expect the boundary condition to be permeable. With permeable boundary condition, Wang and Han [34] obtained the solutions of center crack problems of piezoelectric materials. Impermeable boundary

condition was proposed by Deeg [35] and discussed by Pak [36], McMeeking [37], and Suo et al. [38]. They argued that since the dielectric constant of a piezoelectric medium is several orders of magnitude higher than that of air or vacuum, the electric field inside cracks can be ignored. The utilization of impermeable boundary condition makes the fracture mechanics analysis of piezoelectric materials almost parallel to that for conventional anisotropic media. However, both approximated boundary conditions may lead to large errors in the mechanical and electric fields and in the energy release rate for crack propagation. The exact electric boundary conditions have to be applied along crack faces as well as interfaces between two media [39-59]. A detailed discussion of the boundary conditions is given in the accompanying paper [1]. Zhang, *et al.* [41] pointed out that, under combined mechanical and electric loads, the crack opens and affects the electric field inside the cavity. The change in the electric field in turn affects the crack opening as the crack deformation is very sensitive to the electric field inside the crack.

3.2. Solution Methods

The followings are three widely used methods in the mechanics studies of piezoelectric media:

Complex function method. As in elasticity, the complex function method using the extended Stroh formalism and Lekhnitskii formulation is a very powerful and general method for the analysis of two-dimensional (2D) fracture problems in piezoelectric solids. In 1975, Barnett and Lothe [59] devised the expanded four-dimensional Stroh formalism for piezoelectric materials. This analytical method has been applied extensively and intensively since 1990 [60-65]. For anti-plane deformation and mode III cracks, the four-dimensional Stroh formalism reduces to two complex functions. The Stroh method can also be used to solve inclusion problems [43, 66-71]. Sosa [72] extended the Lekhnitskii method to study defects in piezoelectric media. The method was used later to analyze an elliptical hole in a piezoelectric solid [44, 45, 48]. The solutions for cracks were obtained by setting the minor axis of the ellipse approach to zero. Consequently, the parameters in fracture mechanics, e.g., the stress and electric displacement intensity factors, the energy release rate and so on, were derived analytically.

Potential function method. The potential function method has been used frequently in the study of three-dimensional (3D) fracture of piezoelectric solids [49, 73-82]. For 3D transversely isotropic piezoelectric media, general solutions in terms of potential functions are available [50, 76-78]. Penny-shaped cracks, spheroidal inclusions and elliptical cracks in 3D transversely isotropic piezoelectric media have been analyzed successfully by the potential theory method [76, 77, 79, 80]. Extending the potential theory method for elasticity [83] to piezoelectricity, Chen and Shioya [82] presented a general 3D analysis of a penny-shaped crack subjected to normal mechanical loads. They obtained a closed-form solution for a penny-shaped crack subjected to a pair of concentrated forces acting in opposite directions and a pair of point charges on crack surfaces.

Boundary integral equation method (BIEM), boundary element method (BEM) and finite element method (FEM). The BIEM and BEM are formulated in a form of integral equations based on Green functions [45, 68, 85-90]. The BIEM has unique advantages in fracture mechanics study [84]. Since the BEM needs to discretize boundaries of holes or cracks only, it is high efficient in calculation. Green functions are available for 3D infinite and semi-infinite space problems [49, 54, 75, 92-95] and for two-phase transversely isotropic piezoelectric media [96]. Most of 3D Green solutions are for transversely isotropic media. For materials of lower symmetry, Green functions can be evaluated numerically [35, 97, 98]. Recently, Pan and Tonon [99] derived explicit 3D Green displacements and potentials in anisotropic piezoelectric solids. The Displacement Discontinuity Boundary Integral Equation Method (DBIEM) has been extended also to piezoelectric solids. In this method the displacement and the electric potential discontinuities across the two crack faces are the dependent variables of the integral equation. Fulton and Gao [100] obtained 2D fundamental

solutions for straight dislocations and electric dipole layers in an infinite medium, and studied further the electrical nonlinearity in the fracture of piezoelectric ceramics. Rajapakse and Zhou [101] presented a set of fundamental solutions for generalized edge dislocations. Zhao et al. [102] obtained the fundamental solutions for 3D transversely isotropic piezoelectric media due to displacement and electric potential discontinuities. They then [103] analyzed the planar cracks of arbitrary shape in the isotropic plane subjected to arbitrary mechanical and electric loads that are equal but opposite in direction on the two crack faces. Penny-shaped cracks in a 3D semi-infinite transversely isotropic piezoelectric medium were analyzed and the effect of the free surface was studied [95, 104] by the DDBIEM and an iterative approach. Green functions for dynamic problems were also derived [105,106, 107]. Numerical method or the BEM has been used to solve the boundary integral equations for more complicated problems, such as cracks in a finite body, curved cracks or crack kinking, dynamic fracture, etc [68, 108-111]. Based on the K_{IC} criterion, the numerical results [109] indicate that cracks tend to propagate along a straight line under tensile stress and positive electric field. For a mixed-mode mechanical load superimposed with a positive electric field normal to the crack tends to reduce the crack kink angle. A transverse tensile stress or a positive transverse electric field will enlarge the kink angle from the crack extension direction, while a transverse compressive stress or negative transverse electric field will reduce it.

FEM is the most versatile numerical method. Some commercial software, e.g., ABAQUS, has piezoelectric elements. FEM has been used to calculate stress intensity factors and energy release rates and to study the influence of applied electric field and mechanical boundary conditions on the stress distribution at crack tips [22, 23, 112-116]. Cheng et al. [114] simulated the effects of the applied electric field on the bending behaviors of piezoelectric laminates by incorporating the FEM and the experiment measurements. The bending strength of the PZT core and the interface toughness were obtained.

4. MODELS AND FAILURE CRITERIA

The fracture behavior of piezoelectric ceramics is complex. Since the available experimental data scatter and are limited, there is no single failure or fracture criterion accepted by the community. Models have been proposed to explain the observed complicated failure behavior.

4.1. Total energy release rate

From the point of view of thermodynamics, the total energy release rate of crack propagation may be a good physical property to characterize fracture. For linear piezoelectric ceramics, the total energy release rate equals to the J integral [117]. Fu et al. [25] obtained the J integral for conducting cracks in terms of the applied electric voltage and the sample ligament size. Comparing the experimental data of 30 PZT-4 samples with different ligament sizes, they found that there exists a critical total energy release rate beyond which crack will propagate. This critical total energy release rate is a material property and can used to define the failure criterion for conducting cracks under purely electric loading. For PZT-4, the critical rate under purely electric load is 25 time higher than that under purely mechanical load.

4.2. Mechanical energy release rate

The total energy release rate does not provide a linear relationship between the apparent critical stress intensity factor and the applied electric field as shown by some experimental data (see Fig. 6 as an example) [18, 22]. Arguing that fracture is a mechanical process, Park and Sun [22] suggested to use the mechanical strain energy release rate as the fracture criterion for insulating cracks in piezoelectric materials under combined mechanical and electrical loads. The mechanical energy release rate predicts a linear relationship between the quantities just mentioned. Since the total energy release rate consists of the mechanical and electrical energy release rates, the mechanical

energy release rate model ignores the electric energy release rate. More extensive later tests showed a complex relationship between the apparent critical stress intensity factor and the applied electric field [6, 8, 20, 28, 128].

4.3. Electric Strip Saturation Model

Gao et al. [118] proposed the electric strip saturation model analogy to the classical Dugdale model to explain the linear experimental results between the applied electric field and the fracture load [18, 22]. The electric strip saturation model is based on the hypothesis that piezoelectric ceramics are mechanically brittle and electrically ductile such that electric saturation (yielding) may occur in front of an insulating crack tip. Assuming that the electric saturation zone does not develop during the crack propagation, this model leads to a local energy release rate. The local energy release rate gives the linear relationship almost the same as that predicted by the mechanical energy release rate. In a sense, the electric strip saturation model provides a microscale picture for the mechanical energy release rate. Fulton and Gao [100] and Gao and Barnett [119] resolved the problem using general constitutive equations for piezoelectric ceramics. The effect of the saturation condition on the crack tip field and the stress intensity factors were examined [120-122]. It is interesting that the stress intensity factors can be obtained in some cases without specifying saturation conditions [120]. The Dugdale model solutions for a penny-shaped crack was given by Zhao et al. [123]. They determined the size of the saturation zone and found that the size is independent of the applied stress as in the 2D cases [120-122].

4. 4. Domain Switching Model

Like phase transformation [124], 90°-domain switching produces an internal stress field. If the switching occurs at a crack tip, the internal stress field can shield or anti-shield the crack tip from applied loads. In this case, one may take the local energy release rate or local stress intensity factor as the fracture criterion to calculate the critical applied mechanical and electrical loads. Generally, shielding leads to toughening and anti-shielding assists applied mechanical loads to drive crack propagation. If there is no applied mechanical load, the internal stress field produced by domain switching can also damage piezoelectric samples. The domain switch toughening is equivalent to the twinning toughening [2, 5]. Lynch et al. [16] proposed a domain switch model to explain the cyclic nature of the electric crack propagation. Yang and Zhu further developed the mechanics of domain switching model to predict electric fatigue [109, 125, 126].

4. 5. Domain Wall Motion Model

Domain wall motion results in domain switch. Domain wall motion models were first proposed to understand the contribution of domain wall motion to elastic and dielectric constants and the damping behavior of piezoelectric ceramics [127]. Usually, only a rather simple mathematics treatment is needed in domain wall motion modeling. Fu and Zhang [8] used a domain wall motion model to explain the effects of temperature and electric field on the bending strength of PZT-841 ceramics. The detailed introduction of this model is given in the accompanying paper [1].

4. 6. Wedge Model for Indented Cracks

Jiang and Sun [128] proposed a wedge model for indented cracks to explain the load-dependent behavior, shown in Fig. 7. Without considering applied electric field, they modeled the tensile stress acting on the indentation crack front by a plastic wedge induced by indentation as a central force. Due to the piezoelectric effect, the wedge elongates at a positive electric field and produces a wedge force. In contrast, if a negative field is applied on the wedge, 180° domain switching would take place since the voltage on the crack surface is high and the length of wedge is small. As a result, the wedge effect takes place well under the negative electric field. Jiang and Sun introduced a reduction factor to link the wedge force with the applied electric field. Allowing the

reduction factor to change with applied mechanical load, the wedge model predicts the load-dependent phenomenon well.

5. CONCLUDING REMARKS

The wedge force, the domain switch and the domain wall motion models all account for the internal stress field induced by applied mechanical and/or electrical load. Depending on the nature of the internal stress field, the internal stress field may assist or resist the applied mechanical load to fracture the tested samples. In bending tests of smooth samples, failure may start from points where the resultant of the applied stress and the internal stress has a maximum value and/or the material resistance against fracture is at its minimum. Grain boundaries and defects are the potential locations for crack nucleation [8]. In addition to the internal stress mechanism, partial discharge may be another mechanism for the failure of ferroelectric materials.

Fracture mechanics analysis [18] for linear piezoelectric media under combined electrical and mechanical loads indicates that the electric field inside an insulated crack can be 1000 times higher than the applied electric field. This is due to the fact that the permittivity of the piezoelectric ceramics is 1000 times higher. As a result, local discharge can easily happen between the crack faces, making the crack electrically conducting. The conducting crack will propagate when the external electric field provides sufficient energy. Under combined electrical-mechanical loads, the energy release rate for a conductive crack has its maximum at an angle to the electric loading direction and a reduction in the bending strength can also be anticipated.

In summary, there are voluminous theoretical studies of the fracture of piezoelectric ceramics. There are also a number of fracture models and criteria for the materials. Experimental results show that the fracture behavior is highly complex. No single fracture criterion can explain all the observed failure phenomena. Experimental data on the fracture are still limited and sometimes contradictory. The data scattered greatly especially when electric field is applied. More and careful experimental tests are needed to gain a better understanding of the fracture behaviors. Statistical modeling may be essential for establishing a more uniformly valid failure criterion.

ACKNOWLEDGEMENTS: The work is supported by an RGC grant HKUST6051/97E from the Research Grants Council of the Hong Kong Special Administrative Region, China.

REFERENCES

1. T.-Y. Zhang, The Fourth International Conference on Fracture and Strength of Solids, Pohang, Korea, (2000) (in press)
2. R. C. Pohanka, S. W. Freiman, K. Okazaki, and S. Tashiro, Fracture Mechanics of Ceramics, 5, Eds R. C. Bradt, A. G. Evans, D. P. H. Hasselman and F. F. Lange, Plenum Press, New York, (1983) p353
3. S. W. Freiman, L. Chuck, J. J. Mecholsky, D. L. Shelleman, and L.Storz, Fracture Mechanics of Ceramics, 5, Eds., R. C. Bradt, A. G. Evans, D. P. H. Hasselman and F. F. Lange, Plenum, New York, (1986) p.175
4. R. F. Cook, , S. W. Freiman,, and B. R. Lawn, Ferroelectrics, **50** (1983) p.267
5. K. Mehta, and A. V. Virkar, J. Am. Ceram. Soc. **73** (1990) p.567
6. L. B. Zhang, Q.-C. Zhang, and X-L. Yin, Chinese Science Bulletin, **38** (1993) p.1693
7. S. O. Kramarov, and J. S. Rez, Prog. Crystal Growth and Charact., **22** (1991) p.199
8. R. Fu, and T-Y. Zhang, Acta Mater., (2000) in press.
9. K. D. McHenry, and B. G. Koepke, in *Fracture Mechanics of Ceramics*, 5, eds., R. C. Bradt, A. G. Evans, D. P. H. Hasselman and F. F. Lange, Plenum, New York, (1983) p.337
10. A. Furuta, and K. Uchino, J. Am. Ceram. Soc., **76** (1993) p.1615
11. Q. Y. Jiang and L. E. Cross, J. Mater. Sci., **28** (1993) p.4536

12. Q. Jiang, W. Cao, and L. E. Cross, J. Am. Ceram. Soc., **77** (1994) p.211
13. G. S. White, A. S. Raynes, M. D. Vandin, and S. W. Freiman, J. Am. Ceram. Soc., **77** (1994) p.2603
14. M. D. Hill, G. S. White, C.-S. Hwang, and I. K. Lloyd, J. Am. Ceram. Soc., **79** (1996) p.1915
15. H. Cao, and A. G. Evans, J. Am. Ceram. Soc., **77** (1994) p.1783
16. C. S. Lynch, W. Yang, L. Collier, Z. Suo, and R. M. McMeeking, Ferroelectrics, **166** (1995) p.11
17. T. Zhu, and W. Yang, Acta Mater., **45** (1998) p.4695
18. G. Tobin, Y. E. Pak, Proc. SPIE - Int. Soc. Opt. Eng., **1916** (1993) p.78
19. H. Y. Wang, and R. G. Singh, J. Appl. Phys., **81** (1997) p.7471
20. C.-T. Sun, and S. Park, Proc. SPIE - Int. Soc. Opt. Eng., **2441** (1996) p.213
21. C. S. Lynch, Acta Mater., **46** (1998) p.599
22. S. Park, and C.-T.Sun, J. Am. Ceram. Soc., **78** (1995) p.1475
23. R. Fu, and T.-Y. Zhang, J. Am. Ceram. Soc., (2000) in press
24. V. Heyer, G. A. Schneider, H. Balke, J. Drescher, and H.-A. Bahr, Acta Mater., **46** (1998) p.6615
25. R. Fu, C.-F. Qian, and T.-Y. Zhang, Appl. Phys. Lett., **76** (2000) p.126
26. L. V. Zhoga, and V. V. Shpeizman, Sov. Phys. Solid State, **34** (1992) p.2578
27. H. Makino, and N. Kamiya, Jpn. J. Appl. Phys., **33** (1994) p.5323
28. R. Fu, and T.-Y. Zhang, J. Am. Ceram. Soc., **81** (1998) p.1058
29. L.D. Landau, and E. M. Lifshitz, Electrodynamics of Continuous Media, Pergamon, Oxford, (1960)
30. T. E. Smith and W. E. Warren, J. Math Phys. **45** (1966) p.45
31. R. M. McMeeking, J. Appl. Phys., **62** (1987) p.3116
32. X. Gong and Z. Suo, J. Mech. Phys. Solids, **44** (1996) p.751
33. V. Z. Parton, Acta Astro, **6** (1976) p.671
34. T. C. Wang, and X. L. Han, Acata Mechanica Sinica, **20** (1999) p.95 (in Chinese)
35. W. F. Deeg, Ph D Thesis, Stanford University (1980)
36. Y. E. Pak, J. Appl. Mech., **57** (1990) p.647
37. R. M. McMeeking, J. Appl. Math. Phys., **40** (1989) p.615
38. Z. Suo, C. M. Kuo, D. M. Barnett, and J. R. Willis, J. Mech. Phys. Solids **40** (1992) p.739
39. T.-Y. Zhang, Int. J. Fracture, **66** (1994) R33
40. T.-Y. Zhang and P. Tong, Int. J. Solids Structures, **33** (1996) p.343
41. T.-Y. Zhang, C.-F. Qian and P. Tong, Int. J. Solids Structures, **35** (1998) p.2121
42. Y. Shindo, H. Katsura, and W. Yan, Acta Mech., **117** (1996) p.1
43. M. Y. Chung, and T. C. T. Ting, Int. J Solids Structures, **33** (1996) p.3343
44. H. A. Sosa, and N. Khutoryansky, Int. J Solids Structures, **33**(1996) p.3399
45. C. F. Gao, and W. X. Fan, Appl. Math. Mech., **19** (1998) p.1043
46. C. F. Gao, and W. X. Fan, Appl. Math. Mech., **20** (1999) p.51
47. P. Lu, M. J. Tan, and K. M. Liew, Archive of Applied Mechanics, **68** (1998) p.719-733
48. Q. H. Qin, Acta Mechnica Sinica, **14** (1998) p.157
49. B. Wang, Int. J. Solids Structure, **29**(1992) p.293
50. L. Kogan, C.-Y. Hui, and V. Molkov, Int. J. Solids Structure, **33** (1996) p.2719
51. T.-Y. Zhang and J. E. Hack, J. Appl. Phys., **71** (1992) p.5865
52. S. P. Shen, X. Wang, and Z. B. Kuang, Acta Mechanica Solida Sinica, **16** (1995) p.283 (in Chinese)
53. M. L. Dunn, Engng. Fracture Mech, **48** (1994) p.25
54. M. L. Dunn, and H. A .Wienecki, Int. J. Solids Structures, **33** (1996) p.4571
55. Y. Shindo, F. Natita, and K. Tanaka, Theor. Appl. Fract. Mech., **25** (1996) p.65
56. Y. Shindo, K. Tanaka, and F. Narita, Acta Mechanica, **120** (1997) p.31

57. M. S. Hou, Acta Mechanica Sinica, **29** (1997) p.595 (in Chinese).
58. Y. Shindo, K. Horiguchi, and T. Shindo, Int. J. Engng Sci, **37** (1999) p.687
59. D. M. Barnett, and J. Lothe, Phys Stat Sol (b), **67** (1975) p.105
60. Y. E. Pak, Trans. ASME, J. Appl. Mech., **57** (1990) p.647
61. Y. E. Pak, Trans. ASME, J. Appl. Mech., **57** (1990) p.863
62. Y. E. Pak, Int. J. Solids Structure, **29** (1992) p.2403
63. Y. E. Pak, Int. J. Fracture, **54** (1992) p.79
64. S. B. Park, and C. T. Sun, Int. J. Fracture, **70** (1995) p.203
65. C. F. Gao and W. X. Fan, Mech. Res. Comm., **25** (1998) p.685
66. S. Du, J. Liang, J. Han, and B. Wang, Acta Mech. Sinica, **10** (1994) p.273
67. J. Liang, J. Han, and S. Du, Mech. Res. Comm., **22** (1995), p.43
68. Y. C. Liang, and C. Hwu, Smart Mater. Struct., **5** (1996), p.314
69. Q. H. Qin, and S. W. Yu, Acta Mech. Solid Sinica, **9** (1996) p.151
70. S. W. Yu, and Q. H. Qin, Theor. Appl. Frac. Mech., **25** (1996) p.263
71. S. W. Yu, and Q. H. Qin, Theor. Appl. Frac. Mech., **25** (1996) p.279
72. H. A. Sosa, Int. J. Solids Structures, **28** (1991) p.491
73. H. A. Sosa, and Y. E. Pak, Int. J Solids Structures, **26** (1990), p.1
74. B. Wang, Int. J. Engng. Sci., **30** (1992) p.781
75. M. L. Dunn, Int. J. Engng. Sci., **32** (1994) p.119
76. Z. K. Wang, Acta Mech. Sinica, **10** (1994) p.49
77. Z. K. Wang, and B. L. Zheng, Int. J. Solids Structures, **32** (1995) p.105
78. H. J. Ding, B. Chen, and J. Liang, Int. J. Solids Structure, **33** (1996) p.2283
79. Z. K. Wang and S. H. Huang, Engng. Frac. Mech., **51** (1995) p.447
80. Z. K. Wang and S. H. Huang, Theor. Appl. Fract. Mech., **22** (1995) p.229
81. F. Shang, Z. K. Wang, and Z. Li, Engng. Fract. Mech., **55** (1996) p.737
82. W. Q. Chen, and T. Shioya, J. Mech. Phys. Solids, **47** (1999) p.1459
83. V. I. Fabrikant, Application of Potential Theory in Mechanics: A Selection of New Results. Kluwer Academic, The Nertherland (1989)
84. T. A. Cruse, Computational Mechanics, **18** (1996) p.1
85. J. S. Lee, and L. Z. Jiang, Mech. Res. Comm., **21** (1994) p.47
86. M.Y.Chung, and T.C.T.Ting, ASME, J Appl Mech, **62** (1995) p.423
87. Q. H. Meng, and S. Y. Du, Acta Mechnica Solida Sinica, **16** (1995) p.90 (in Chinese)
88. H. J. Ding, G. Q. Wang, and W. Q. Chen, Science in China, Series E, **27** (1997) p.224
89. J. X. Liu, B. Wang, and S. Y. Du, Appl. Math. Mech., **18** (1997) p.949
90. Q. H. Qin, and Y. W. Mai, Archive of Applied Mechanics, **68** (1998), p.433
91. Y. Benveniste, J. Appl. Physics, **72** (1992) p.1086
92. H. J. Ding, J. Liang, and B. Chen., Science in China, Series A, **26** (1996) p.766
93. M. Akamatsu, and K. Tanuma, Proc. R. Soc. Lond. A, **453** (1997) p.473
94. W. Q. Chen, T. Shioya, and H. J. Ding, Mech. Res. Comm., **26** (1999) p.583
95. M. H. Zhao, Y. P. Shen, G. N. Liu, and Y. J. Liu, Theor. Appl. Fract. Mech., **32** (1999) p.223
96. H. J. Ding, and B. Chen, Int. J. Solids Structures, **34** (1997) p.3041
97. T. Chen, Mech. Res. Comm., **20** (1993) p.271
98. T.Chen, and F.Z.Lin, Mech. Res. Comm, **20** (1993) p.501
99. E. Pan, and F. Tonon, Int. J. Solid Structures, **37** (2000) p.943
100. C. C. Fulton, and H. Gao, Appl. Mech. Rev., **50**(1997)
101. R. K. N. D. Rajapakse, and Y. Zhou, Mechanics of Composite Materials and Structures, **6** (1999) p.97
102. M. H. Zhao, Y. P. Shen, G. N. Liu, and Y. J. Liu, Theor. Appl. Fract. Mech., **26** (1997) p.129
103. M. H. Zhao, Y. P. Shen, G. N. Liu, and Y. J. Liu, Theor. Appl. Fract. Mech., **26** (1997) p.141
104. M. H. Zhao, Y. P. Shen, G. N. Liu, and Y. J. Liu, Theor. Appl. Fract. Mech., **32** (1999) p.233

105.C. H. Daros and H. Antes, Int. J. Solids Structures, **37** (2000) p.1639
106.A. N. Norris, Proc. Roy. Soc. Lond., A **447** (1994) p.175
107.N. Khutoryansky and H. A. Sosa, Int. J. Solids Structures, **32** (1995), p.3307
108.P. Lu, and Mahrenholts. Mech. Res. Comm, **21** (1994) p.605
109.T. Zhu, and W. Yang, Int. J. Solids Structures, **36** (1999) p.5013
110.T. Chen, and F. Z .Lin, Computational Mechanics, **15** (1995) p.485
111.Y. Shindo, E. Ozawa, and J. P. Nowacki, Int. J. Appl. Electromagnetics Mater., **1** (1990) p.77
112.D. Fang, H. Qi, and Z. Yao, Fatigue Fracture Eng. Mate. Struct., **21** (1998) p.1371
113.S. C. Hwang and R. M. McMeeking, Int. J. Solids Structures, **36** (1999) p. 1541.
114.J. Q. Chen, C.-F. Qian, M. H. Zhao, S. W. R. Lee, P. Tong, and T.-Y. Zhang, "Effects of Electric Fields on The Bending Behavior of PZT-5H Piezoelectric Laminates", unpublished work.
115.S. Kumar, and R. N. Singh, Mater. Sci. Engng, A **231** (1997) p.1.
116.R. M. McMeeking, Engng. Fract. Mech., **64** (1999)p.217
117.G. P. Chereponov, Mechanics of Brittle Fracture, McGraw-Hill, New York (1979) p. 317
118.H. Gao, T.-Y. Zhang, and P. Tong, J. Mech. Phys. Solids, **45** (1997) p.491
119.H. Gao, and D. M. Barnett, Int. J. Fracture, **79** (1996) R25
120.C. Q. Ru, Int. J. Solids Structures, **36** (1999), p.869
121.C. Q. Ru, and X. Mao, J. Mech. Phys. Solids, **47** (1999) p.2125
122.Z. Q. Wang, (Wang, T. C.) Acata Mechanica Solida Sinica, **31**(1999), p.311
123.M. H. Zhao, Y. P. Shen, G. N. Liu, and Y. J. Liu, Eng. Analy. Boundary Elements, **23** (1999) p.573
124.R. M. McMeeking and A. G. Evans, J. Am. Ceram. Soc., **65** (1982) p.242
125.W. Yang, and T. Zhu, J. Mech. Phys. Solids, **46** (1998) p.291
126.W. Yang, and T. Zhu, Fatigue Fracture Eng. Mater. Structures, **21** (1998) p.1361
127.G. Arlt, H., Dederichs, and R. Herbiet, *Ferroelectrics.* **74** (1987) p. 37

Key Engineering Materials Vols. 183-187 (2000) pp. 707-712
© 2000 Trans Tech Publications, Switzerland

Effect of Heat Treatment and Chemical Composition on Caustic Stress Corrosion Cracking of Alloy 600 and Alloy 690

H.P. Kim, S.S. Hwang, Y.S. Lim, I.H. Kuk and J.S. Kim

Korea Atomic Energy Research Institute, PO Box 105, Yusong, Taejon 305-600, Korea

Keywords: Alloy 600, Alloy 690, Cr Depletion, Grain Size, Intergranular Carbide, NaOH, Polarization Curve, Stress Corrosion Cracking (SCC)

ABSTRACT

Stress corrosion cracking (SCC) behaviours of Alloy 600, Alloy 690 and Ni-10Cr-10Fe alloy have been studied using C-ring in 40% NaOH solution of 315 °C. Heat treatment of the Ni base Alloys were carefully controlled to systematically study the effect of bulk Cr content in Ni base alloys and the microstructure of Alloy 600 on caustic SCC. Current density on Alloy 690 in polarization curves was higher at a potential of 200mV above corrosion potential than that on Alloy 600. SCC resistance increased with Cr content for the chromium carbide free alloys, probably due to facilitation of SCC crack tip blunting and cross slip with an increase in Cr content. Both thermally treated Alloy 600 and sensitized Alloy 600 have a comparable amount of intergranular carbide. But the former one is more resistant to SCC than the latter one, probably due to slight Cr depletion around the grain boundary in the former one. Sensitized Alloy 600 showed higher SCC resistance than the solution annealed one, probably due to intergranular carbide in sensitized Alloy 600. This implies that the beneficial effect of intergranular carbide overrides the harmful effects of Cr depletion for sensitized Alloy 600. SCC resistance Alloy 600 increased with grain size. These results suggest that SCC resistance of Alloy 600 and Alloy 690 could be optimized by control of grain boundary chromium concentration, intergranular chromium carbide and grain size.

1. INTRODUCTION

Extensive research has been done to improve SCC resistance of steam generator tubings[1,2]. High temperature mill annealed(HTMA) materials with intergranular carbide and large grain size showed better resistance to SCC than low temperature mill annealed(LTMA) materials with intragranuar carbide and small grain size[3]. Thermal treatment producing semicontinuous intergranular carbide was reported to be beneficial[1]. But it has been unclear whether higher resistance to SCC of high temperature mill annealed materials with intergranular carbide is due solely to intergranular carbide, large grain size or a combination of intergranular carbide and large grain size.

Alloy 690 is almost immune to SCC in acidic and neutral environments, yet it still undergoes SCC in caustic environments[4]. To understand the higher SCC resistance of Alloy 690, SCC and polarization behaviour were measured as a function of Cr content in Ni-χCr-10Fe alloys. Alloys with χ=14-17 and χ=27-31 correspond to Alloy 600 and Alloy 690, respectively.

The purpose of this work is to evaluate the effect of bulk Cr content in Ni base alloys, chromium carbide and Cr depletion and grain size on caustic SCC.

2. EXPERMENTAL PROCEDURE

The materials used in this work were two Alloy 600s, an Alloy 690 and a Ni-10Cr-10Fe. Their chemical compositions are shown in Table 1. Heat treatment of the alloys and their designation are shown in Table 2.

Table 1. Chemical composition of materials

Material	C	Cr	Ni	Fe	Si	Mn	P	S	Cu	Ti	Al
Ni-10Cr-10Fe	0.02	10.5	79.7	10.1	0.3	0.3	<0.0	<0.0		0.1	N/A
Alloy 600-1	0.01	15.4	75.1	8.0	0.0	0.3		0.001	0.2		
Alloy 600-2	0.026	16.8	72.3	9.0	0.3	0.8	0.008	0.001	0.01	0.3	0.20
Alloy 690	0.02	29.5	58.9	10.5	0.22	0.32	0.009	0.001	0.01	0.26	0.01

Table 2. Heat treatment of materials and Alloy designation

Designation	Heat treatment
SA Ni-10Cr-10Fe	solution annealed at 1100°C for 30min and then water quenched
SA1 Alloy 600-1	solution annealed at 1000°C for 5min and then water quenched
SA2 Alloy 600-1	solution annealed at 1050°C for 5min and then water quenched
SA3 Alloy 600-1	solution annealed at 1100°C for 60min and then water quenched
SA Alloy 600-2	solution annealed at 1100°C for 30min and then water quenched
SASEN Alloy 600-2	additional heat treatment of SA Alloy 600-2 at 600°C for 24Hrs
SATT Alloy 600-2	additional heat treatment of SA Alloy 600-2 at 715°C for 15Hrs
HTMA Alloy 600-2	commercially high temperature mill annealed
HTMASEN Alloy 600-2	additional heat treatment of HTMA Alloy 600-2 at 600°C for 24Hrs
HTMATT Alloy 600-2	additional heat treatment of HTMA Alloy 600-2 at 715°C for 15Hrs
SA Alloy 690	solution annealed at 1150°C for 30min and then water quenched

Carbide distribution and grain boundary of Alloy 600 was examined by electrolytic etching. Alloy 690 was chemically etched in bromine for 15sec. A modified Huey test was carried out in boiling 25%HNO_3 for 48Hrs.

A Potentiodynamic polarization test was performed at a scan rate of 0.167mV/sec in 40% NaOH with EG&G 273 potentiostat. The 40% NaOH solution was prepared by adding reagent grade NaOH to demineralized water. Reference electrode and counter electrode were an external Ag/AgCl electrode and Pt wire, respectively. All the values of electrode potential were relative to that of external Ag/AgCl electrode unless otherwise indicated.

The SCC test was conducted in 40% NaOH using C-ring specimen at 315°C. The C-ring specimen was held at 200mV above open circuit potential. The SCC fracture surface and cross-sectional area of C-ring specimen were examined with both SEM and optical microscope.

3. RESULTS AND DISCUSSION

3.1 Bulk Cr Content

Potentiodynamic polarization curves were also obtained for SA Ni-10Cr-10Fe alloy, SA Alloy 600-1 and SA Alloy 690 in 40% NaOH at 315°C(Fig.1). The main difference among the three alloys is Cr content. That is, Cr content of the SA Alloy 600 and the SA Alloy690 were about 15 and 30%, respectively. Polarization curves were almost same for SA Ni-10Cr-10Fe alloy and SA Alloy 600 except small differences at potential from passivation potential to 280mV above OCP. Current

density at potential ranging from passivation potential to breakdown potential was higher on SA Alloy 690 than SA Alloy 600-1, suggesting that Cr destabilize passive film in 40% NaOH at 315°C.

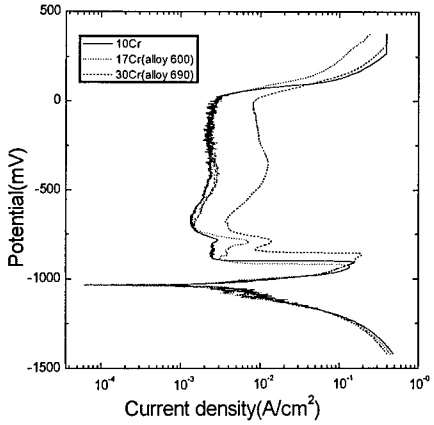


Fig.1 Potentiodynamic polarization curves of SA Ni-10Cr-10Fe, SA Alloy 600-1 and SA Alloy 690 at 315°C in 40% NaOH.

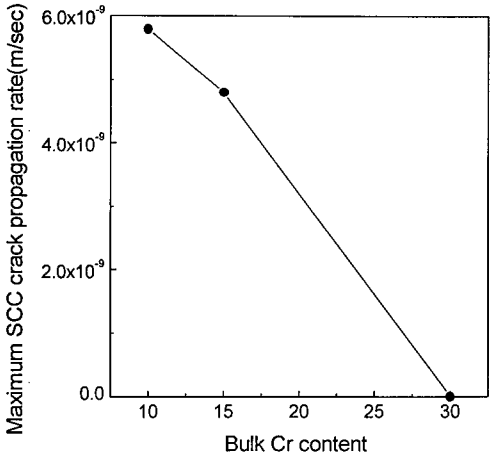


Fig.2 Effect of bulk Cr content in Ni-xCr-10Fe alloy on SCC crack propagation rate.

The effects of bulk Cr content on caustic SCC resistance are shown in Fig.2. SCC resistance of SA Ni-base alloy increased with increase in Cr content of SA Ni-base alloy. Corrosion on stress free regions of SA Alloy 690 was more severe than that on SA Alloy 600. This result is consistent with the potentiodynamic polarization curves(Fig.1), in which current density at 200mV above the corrosion potential is greater on SA Alloy 690 than SA Alloy 600-1. SA Ni-base alloy with 10% Cr showed through wall cracking in stressed regions and no cracking in stress free regions while that with 30% Cr(SA Alloy 690) showed very shallow cracking in both stressed regions and unstressed regions. The shallow crack on the stress free regions of SA Alloy 690 is purely due to intergranular attack. Enhancement of SCC resistance with an increase in Cr content was also reported for Ni base alloys tested by slow strain rate test at 900mVsce in 50% NaOH at 140°C[5] and U-bend specimen in a deaerated 10% NaOH at 325°C[6]. These results suggest that SCC resistance increase with Cr content irrespective of test method and NaOH concentration.

Enhancement of SCC resistance with Cr content might be explained in terms of repassivation kinetics, stacking fault energy and grain boundary character distribution. Stacking fault energy of Ni increased with addition of Cr[7]. For material with high stacking fault energy, screw dislocations are not confined to a particular plane so that stress concentration in the grain boundary is relatively low compared to that with low stacking fault energy.

A fraction of coincidence site lattice boundary (CSLB) ($\Sigma<29$) increases with Cr content in Ni base alloys. A fraction of CSLB ($\Sigma<29$) is about 40% for a conventional Alloy 600 and about 60-70% for a conventional Alloy 690 [8,9]. For Alloy 600, CSLB was more resistant to SCC than the general high angle boundary (GHAB) in pure water[2]. But even GHAB of Alloy 690 are immune to SCC in pure water while CSLB of Alloy 600 was cracked[2]. These facts implied that the CSLB is not the primary controlling factor in SCC of Ni base alloys.

Yamanaka[10] reported that the repassivation rate and Cr enrichment in the inner layer of corrosion oxide increased with Cr content in Ni base alloy in a 4% NaOH solution at 280°C. Higher SCC resistance of Alloy 690 was attributed to a faster repassivation rate and Cr enrichment in the

inner layer. However, the corrosion rate at 200mV above the corrosion potential is accelerated with Cr content in 40% NaOH at 315°C. This implies that the Cr rich inner layer did not reduce dissolution rate, but accelerate dissolution in 40% NaOH at 315°C. So in this work the role of Cr seems to blunt the crack tip by delaying the formation of a stable film at the crack tip and thereby reduce the stress intensity factor.

3.2 Intergranular carbide and Cr depleted region around grain boundary

The grain size number of SA1, SA1SEN and SA1TT were about 4 and the grain size number of HTMA, HTMASEN and HTMATT was about 8. The degree of Cr depletion measured with modified Huey test, the distribution of chromium carbide examined with phospheric acid etching and the maximum SCC crack propagation rate are shown in Table 3. SA1 specimen had no intergranular and intragranular carbide and subsequently no Cr depleted zone near the grain boundary. Both SA1SEN and HTMASEN specimen had heavily Cr depleted zone around the grain boundary and intragranular carbide. Both SA1TT and HTMATT had intergranular carbide and slight chromium depleted zone around the grain boundary because thermal treatment temperature and time are high enough and long enough to heal the Cr depleted zone.

Table 3. Effect of heat treatment on weight loss measured in boiling HNO_3 for 48Hrs (Modified Huey test), distribution of intergranualar carbide and maximum SCC crack propagation rate.

Material	weight loss ($kg/m^2/sec$)	distribution of intergranular carbide	maximum SCC crack propagation rate(m/sec)
SA Alloy 600-2	20×10^{-9}	no intergranular carbide	4.8×10^{-9}
SASEN Alloy 600-2	627×10^{-9}	semicontinous	4.0×10^{-9}
SATT Alloy 600-2	18×10^{-9}	semicontinous	0.7×10^{-9}
HTMA Alloy 600-2	115×10^{-9}	discrete	5.0×10^{-9}
HTMASEN Alloy 600-2	*	semicontinous	2.9×10^{-9}
HTMATT Alloy 600-2	22×10^{-9}	semicontinous	1.4×10^{-9}

*: completely disintergrated

A modified Huey test showed that SASEN is heavily sensitized, SATT is slightly sensitized and SA is free from sensitization. In this work, it was assumed that the Cr concentration at the grain boundary is proportional to weight loss even though the weight loss during modified Huey test is a function of Cr depletion width and concentration of Cr in Cr depleted regions. SCC resistance of heat treated specimens of Alloy 600 should increase in the following order: SASEN, SATT and SA or HTMASEN, HTMA and HTMATT if SCC resistance is solely determined by Cr content in the grain boundaries(Fig.2). In fact, SCC resistance increased with a following order: SA, SASEN and SATT or HTMA, HTMASEN and HTMATT in each group. The amount of intergranuar carbide in SASEN and SATT is almost the same even though SCC resistance of SATT is significantly higher than SASEN. These results suggest that SCC resistance of Alloy 600 is a balance between beneficial effect of intergranular chromium carbide and harmful effect of Cr depleted zone. Fig.3 is schematic diagram showing the effect of intergranular carbide and Cr depletion around the grain boundary. That is, the Cr depleted zone itself is thought to accelerates SCC and intergranular carbide retards SCC.

Intergranular chromium carbide may act as a barrier to SCC by resistance to dissolution or formation of a stable film on cracks by preferential dissolution depending on environment. In addition, it may act as a dislocation source and enhance localized deformation around the grain

boundaries to reduce stress intensity factor. Some of these mechanisms may act individually or concurrently to enhance SCC resistance

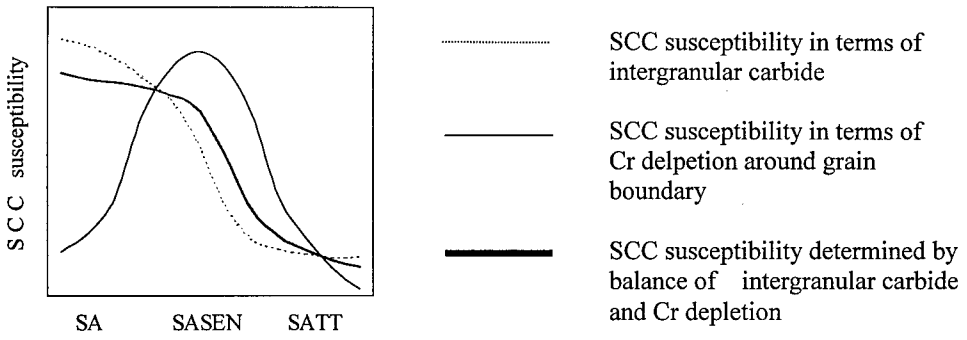


Fig.3 Schematic diagram showing the effect of intergranular carbide and Cr depletion around grain boundary on caustic SCC.



Fig.4 Cross sectional area of C-ring specimen after SCC test. (a): solution annealed at 1000°C for 5min, (b): solution annealed at 1050°C for 5min, (c): solution annealed at 1100°C for 60min

3.3 Grain Size

As grain size increased, 0.2 % yield strength decreased and elongation increased. Yield strength seemed to follow a Hall-Petch relationship, that is, it was inversely proportional to the square root of grain size. HTMA materials with intergranular carbide and large grain size showed better resistance to SCC than LTMA materials with intragranular carbide and small grain size[3]. So it has been unclear whether the higher resistance to SCC of high temperature mill annealed materials with intergranular carbide is due to solely intergranular carbide, large grain size or a combination of intergranular carbide and large grain size. To isolate the effect of grain size on resistance to SCC, mill-annealed material with 0,01% carbon was solution annealed and then water quenched. Solution annealing was carried out at 1000°C for 5min, 1050°C for 5min or 1100°C for 60min to vary grain size. The SA specimen were etched in nital to measure grain size and etched in orthophosperic acid to observe carbide. The MA specimen as well as the SA specimen has neither intergranular nor intragranular carbide. Cooling rate after mill annealing seemed to be fast enough to avoid carbide precipitation. Fig. 4 showed that resistance to SCC increased with an increase in grains size. Using specimen free of carbide, this work showed that the resistance to SCC of materials without both intergranular carbide and intragranular carbide could be improved with an increase in grain size.

4. CONCLUSION

1. As Cr content increased in Ni-χCr-9Fe Alloy, current density in polarization curves increased at potential ranging from then passivation potential to 280mV above the corrosion potential.
2. Increase in Cr content of Ni-χCr-9Fe Alloy results in enhanced SCC resistance at 200mV above the corrosion potential, probably due to blunted crack tip by delaying formation of a stable film and/or stress relaxation at crack tip by facilitated cross slip.
3. Enhanced SCC resistance of Alloy 600 with intergranular chromium carbide seems to be due to mechanochemical action of intergranular chromium carbide.
4. SCC resistance increased with grain size.

ACKNOWEDGEMENT

This work has been done as a part of the Steam Generator Project of the Mid and Long-Term Program financially supported by the MOST in Korea.

REFERENCE

1. G. P. Airey, Optimization of Metallurgical Variables to Improve the Stress Corrosion Resistance of Inconel 600, EPRI NP-1354, March 1980.
2. D. C. Crawford, and G. S. Was, Met. Trans. A Vol. 23A No.4 1992, p. 1195.
3. J. R. Crum and T. Nagashima, Proc. of the 8th Intern. Symp.on Environmental Degradation of Materials in Nuclear Power Systems- Water Reactors, USA, Amelia Island, Fl, 1997, p.127.
4. J. M. Sarver, P. E. Doherty, D. M. Doyle, and G. Palumbo, Proc. of the 7th Intern. Symp.on Environmental Degradation of Materials in Nuclear Power Systems- Water Reactors, USA Breckenridge, Colorado, 1995, p.465.
5. J. K. Sung, J. Koch, T. Angeliu and G. S. Was, Metall. Trans.A Vol. 23A, 1992, p.2887.
6. R. J. Jacko, Corrosion Evaluation of Thermally Treated Alloy 600 Tubing in Primary and Faulted Secondary Water Environments, EPRI NP-16721-SD, 1990.
7. L. E. Murr, , Interfacial Phenomena in a Metals and Alloys, Addison Wesley Publishing Company, 1975, p. 145.
8. P. Lin, G. Palumbo, U. Erb,. and K. T. Aust, Scripta Metallurgical Materialia, Vol.33 No. 9, 1995, p.1387.
9. P. E. Doherty, D. M. Doyle, J. M. Sarver and B. P. Miglin, Proc. of a Conf. on Control of Corrosion on the Secondary Side of Steam Generators, USA, Airlie, Virginia, 1995, p. 401.
10. K. Yamanaka, and J. Murayama, Proc. of the 4th Intern. Symp. on Environmental Degradation of Materials in Nuclear Power Systems-Water Reactors, USA, Georgia, 1989, p. 5-96.

Key Engineering Materials Vols. 183-187 (2000) pp. 713-718
© 2000 Trans Tech Publications, Switzerland

Nonlinear Evolution Properties of Rock Microfracturing Affected by Environment

Xia-Ting Feng[1], Tingjie Li[1] and M. Seto[2]

[1] Institute of Rock and Soil Mechanics, Chinese Academy of Sciences, Wuhan 430071, China P.R.

[2] National Institute for Resources and Environment, Tsukuba 305, Japan

Keywords: Acoustic Emission, Chemical Erosion, Neural Network Modeling, Nonlinear Evolution, Rock Microfracturing Process, Temporal Fractal

ABSTRACT

Microfracturing processes of sandstone and Oshima granites soaked in air, water, chemical solutions DTAB and PEO, have nonlinear evolution properties. Their temporal fractal properties vary as soaking environments. At most of cases it seems to be possible to define two or three fractal subranges (multi fractal structure). Whatever variations are present in fractal properties (from a single fractal structure to multi-fractal structure with $D_1 > D_2$ or $D_1 < D_2$), the lower fractal dimension is generally produced near the failure. The results of predictions for new cases indicate the neural network $NN(n, h, m)$ can be used to describe well acoustic emission event and count evolution in mcirofracturing process of rocks soaked in air. water, chemical solution DTAN and PEO. The number n and h, which vary as conditions of stress environmental erosion, can be adaptive determined by using proposed evolutionary learning algorithm.

1. INTRODUCTION

Identification of microfracturing behaviors of rocks soaked in different environments, particularly chemical solutions, is interesting problem in the field of waste disposal, geothermal development, petroleum engineering, city waste management etc. Some authors discussed influence of water on tensile and compressive strengths, fracture toughness and cracking velocity of rocks [1-4]. Other researchers discussed influence of chemical environment on drilling and hardness of rocks [5-8]. However, it is not clear on the influence mechanism of chemical environment on rock properties. In this paper, the effect of chemical environments (DTAB (Dodecyl Trimethyl Ammonium Bromide), NaCl, or PEO (polyethelene oxide)) on microfracturing of rock were investigated by conducting Brazilian tests, multi-stage triaxial tests, three points bending tests and double torsion tests on sandstone and Oshima granite specimens. Acoustic emission (AE) behaviors monitored during each microfracturing process of rock were conducted by temporal fractal analysis and modeled by neural networks respectively. Predictions for new cases show satisfying results.

2. INFLUENCE OF CHEMCICAL ENVIRONMENT ON ACOUSTIC EMISSION AND FRACTURING BEHAVIORS

Acoustic emission (AE) behaviors evolved as time or stress, effected by chemical solutions are monitored in Brazilian tests, multi-stage triaxial tests, three points bending tests, and double torsion tests on sandstone and Oshima granite specimens by using Mistras 2001 with AE sensors mounted on the surface of the specimen. For granite in double torsion test, erosion of chemical solutions on weak plane was also

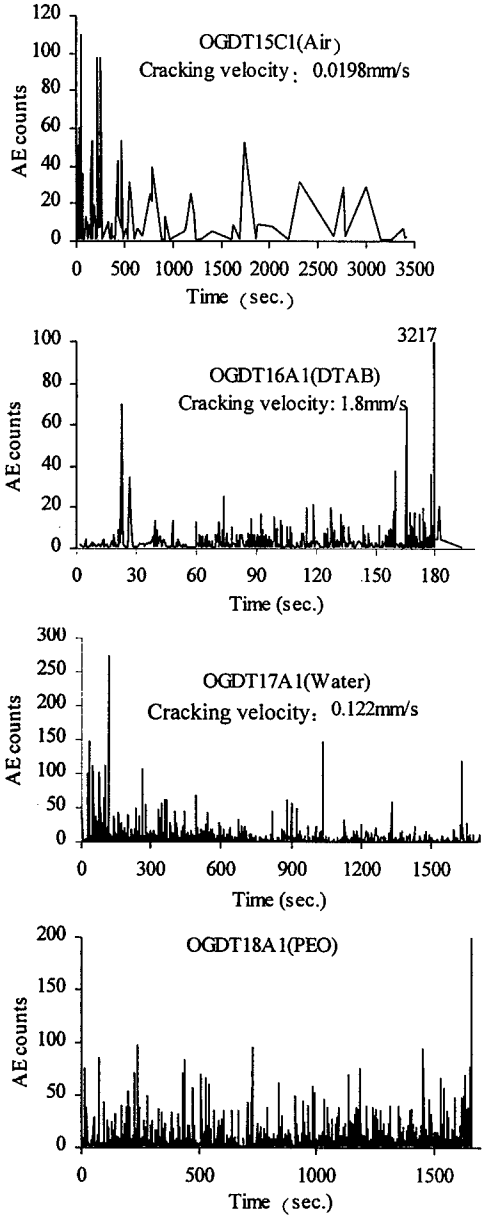


Fig.1. AE behaviors of Oshima granite at creep microfracturing process (Rift plane is parallel to cracking direction)

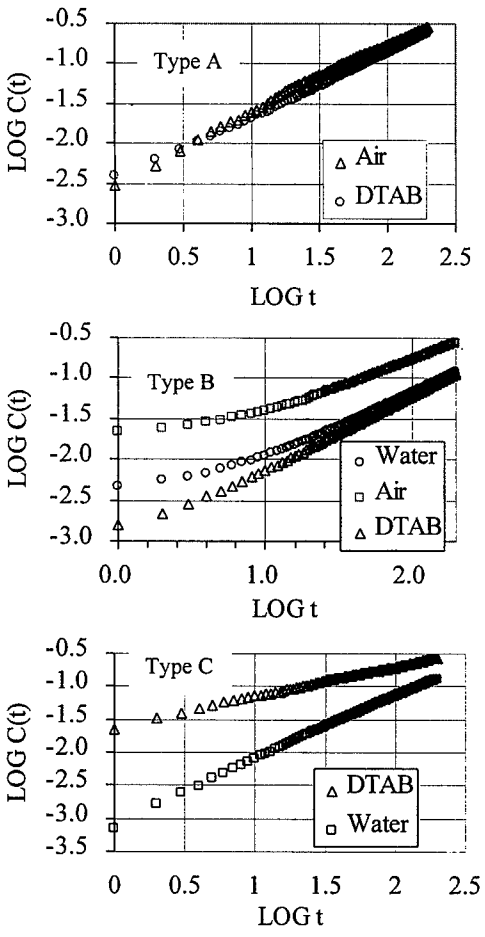


Fig.2. Temporal fractal properties of granite at a creep microfracturing process. Type A: rift plane is parallel to cracking direction, Type B: grain plane is parallel to cracking direction, Type C: hardware plane is parallel to cracking direction.

investigated. There are classes of granite specimen were used. Type A: rift plane is parallel to cracking direction, Type B: grain plane is parallel to cracking direction, Type C: hardware plane is parallel to cracking direction.

Whether soaked in chemical solutions DTAB, PEO, water, or air, initially, when the load was small (e.g. less than 4 kg in double torsion test), no AE occurred. AE became more active as the load increased and the most active while rock get serious fracturing. AE activities are not active during stable relaxation or creep process (as example, see Fig.1).

Stress corrosion cracking in double torsion tests was also significantly affected by the chemical environments and represented the ξ potential dependency. For example, for the same type of Oshima granite specimen with rift plane parallel to cracking direction in double torsion test, the cracking velocities are 0.0198mm/s, 0.122mm/s, and 1.8mm/s for air, water and chemical solution DTAB respectively. If grain plane is parallel to cracking direction, the cracking velocities are then changed to 0.0216mm/s, 0.0336mm/s, and 0.062mm/s for air, water and chemical solution DTAB respectively. Compared to corrosion of air, water or chemical solutions in tip of the crack significantly lowered the fracture toughness of the rock specimen. For example, in a double torsion test of the granite specimen with parallel to hardware plane, the fracture toughness in air condition was 35.353 while the fracture toughness in erosion of water and DTAB decreased to 21.21 and 12.623 respectively. The tensile strength significantly varied with concentration of chemicals and is dependent on ξ potential, while the triaxial strength did not vary significantly with concentration of chemical solutions.

3. TEMPORAL FRACTAL BEHAVIORS

From acoustic emission data in time distribution (shown in Fig.1 as example), A correlation integral $C(t)$ can be calculated for analyzing temporal fractal properties of each rock microfracturing process soaked in different solutions. We can get a series of $C(t_i)$ with various time scale t_i. The plot of LOG $C(t_i)$-LOG t_i (shown in Fig.2 as example) can be used to calculate temporal fractal dimension. The time scales t_i were changed from 1 to 200 s with 1 s interval. For some cases, a single fractal structure can be defined while two or three fractal subranges seem to be possible to be defined for most of cases. D_i refers to fractal dimension of the ith subrange. Temporal fractal properties of microfracturing process of Oshima granites soaked in chemical solutions of DTAB and PEO are summarized in Table 1. The results are compared with that in air and water.

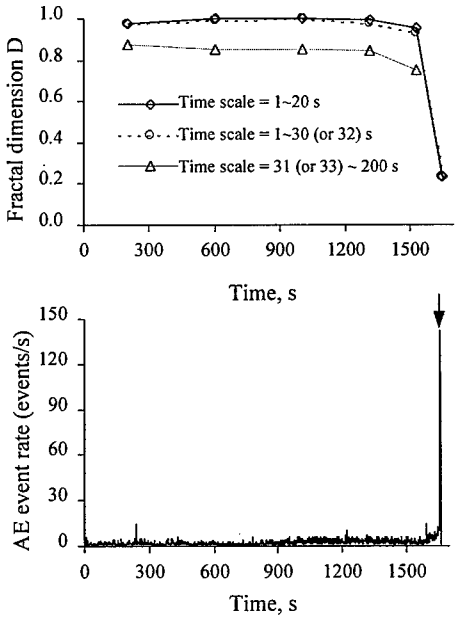


Fig.3. Temporal fractal evolution of type A Oshima granite during creep micro-fracturing process (the arrow indicates failure of specimen)

Whatever variations are present in fractal properties (from a single fractal structure to multi-fractal structure, $D_1 > D_2$ or $D_1 < D_2$), the lower fractal dimension is generally produced near the failure (Fig.3). This result, obtained by

considering the time distribution of rock microfracturing (the number-time relation of micro-fracturing using the time sequences of AE events recorded by the measurement system, rather than AE event rate), is consistent with the conclusion based on the spatial distribution of rockbursts and earthquakes, that the lower fractal dimension (or b value) occurs near the time of a strong earthquake.

Table 1. Temporal fractal properties of chemical erosion on microfracturing process of granite

Stress process	Weak plane	Air	Water	DTAB	PEO
Creep	A	$D_1>D_2$		$D_1<D_2$	$D_1<D_2$
	B	$D_1<D_2$	$D_1<D_2$	$D_1<D_2$	$D_1<D_2$
	C	Single fractal structure	Single fractal structure	$D_1>D_2$	$D_1>D_2$
Stress increase	A	$D_1>D_2$	$D_1>D_2$	$D_1>D_2$	$D_1>D_2$
	B	$D_1>D_2$	$D_1>D_2$	$D_1>D_2$	$D_1>D_2$
	C	$D_1>D_2$	$D_1>D_2$	$D_1>D_2$	$D_1>D_2$
Stress relaxation	A	Single fractal structure or $D_1>D_2$	$D_1>D_2$	$D_1>D_2$	$D_1>D_2$
	B	$D_1>D_2$	$D_1>D_2$	$D_1>D_2$	$D_1>D_2$
	C	$D_1>D_2$	$D_1>D_2$	$D_1>D_2$	$D_1>D_2$

4. NEURAL NETWOR MODELING

Since mircorfracturing process has nonlinear evolution behaviors, neural networks provide strong theoretical tool to model it. Corresponding to each evolutionary process of the system's states, AE behaviors such as the AE event rate, AE count rate in each stress torsion (such as stress increase, relaxation, and creep) process of rock soaked in different solutions were modeled using neural network techniques respectively.

Modeling on creep micro-fracturing behaviors performed on neural networks is to find a neural network $NN(n,h,2)$ to represent the relationship between AE event increments $\Delta CC_j, \Delta CE_j$ with their previous values $(CC_{j-1}, CC_{j-2}, \Lambda, CC_{j-k}, CE_{j-1}, CE_{j-2}, \Lambda, CE_{j-k})$ as follows

$$\begin{aligned} &NN(n,h,2): R^n \to R^m \\ &(\Delta C\hat{C}_j, \Delta C\hat{E}_j) = NN(n,h,2)(CC_{j-1}, CC_{j-2}, \Lambda, CC_{j-k}, CE_{j-1}, CE_{j-2}, \Lambda, CE_{j-k}, u_{j-1}, u_{j-2}, \Lambda, u_{j-k}, \\ &\qquad WP, \Delta u_j) \quad (j = k+1, k+2, \Lambda,) \end{aligned} \tag{3}$$

where $\Delta C\hat{C}_j, \Delta C\hat{E}_j$ are computed values that approximate the measured AE count increment ΔCC_j and AE event increment ΔCE_j at time j respectively. CC_{j-k}, CE_{j-k} are the measured AE counts and AE events at time $j-k$. $u_{j-k}, \Delta u_j$ are the measured displacement at time $j-k$ and displacement increment at time j. WP is type of weak plane. $NN(n,h,2)$ is the model to be determined, which approximates the actual relationship. n and h are the numbers of input nodes, number of nodes at the hidden layer, which are to be learned by using genetic algorithm to train neural network with input of experimental data, $n = 3k+2$.

For modeling of stress increase and relaxation process, neural network model can be written by

$$NN(n,h,2): R^n \rightarrow R^m$$

$$(\Delta C\hat{C}_j, \Delta C\hat{E}_j) = NN(n,h,2)(CC_{j-1}, CC_{j-2}, \Lambda, CC_{j-k}, CE_{j-1}, CE_{j-2}, \Lambda, CE_{j-k}, P_{j-1}, P_{j-2}, \Lambda, P_{j-k}, \Delta P_j) \quad (j=k+1, k+2, \Lambda,)$$

Where, $P_{j-1}, P_{j-2}, \Lambda, P_{j-k}$ is load to produce AE events.

The learned $NN(n,h,2)$ can be used to obtain "true" prediction of the testing cases. It builds the whole predicted curve of cumulative AE counts and cumulative AE events from t = 0 condition. The measured AE events and counts at first k unit times are used as input series to predict their increments $\Delta C\hat{C}_j, \Delta C\hat{E}_j$. These calculated increments are feed back to calculate $C\hat{C}_j, C\hat{E}_j$ (e.g. $C\hat{C}_j = CC_{j-1} + \Delta C\hat{C}_j$, $C\hat{E}_j = CE_{j-1} + \Delta C\hat{E}_j$ (if j = k + 1) or $C\hat{C}_j = C\hat{C}_{j-1} + \Delta C\hat{C}_j$, $C\hat{E}_j = C\hat{E}_{j-1} + \Delta C\hat{E}_j$ (if $j > k+1$). The input series for each next step prediction is then renewed by adding the predicted values $C\hat{C}_j, C\hat{E}_j$ and kept at the same length of k unit time.

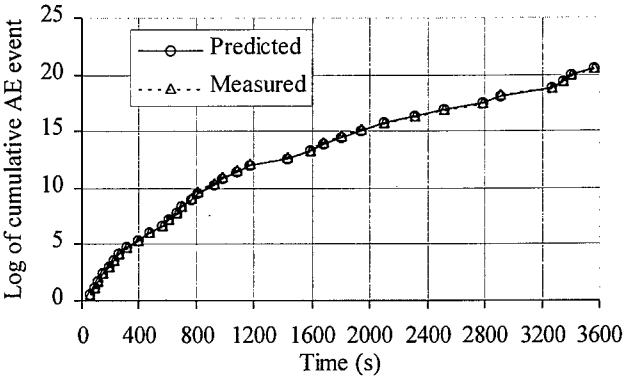


Fig.4. Prediction of the neural network $NN(11,17,2)$ for creep microfracturing of a granite specimen soaked in chemical solution DTAB, which is not used to build model

With application of the modeling method mentioned above, several neural network models $NN(n, h, m)$ have been automatically built to describe AE behaviors in the rock microfracturing process effected by the given chemical solutions, water or air, respectively. For example, at stress increase process, the neural models $NN(10,21,2)$ and $NN(10,20,2)$ were found to describe reasonably well the AE behaviors of micro-fracturing in rock under air and DTAB conditions, and water conditions, respectively. For creep, the model $NN(11,17,2)$ was found to describe reasonably well time behavior of microfracturing in rock under air and chemical solution DTAB conditions, and $NN(10,27,2)$ is suitable for water condition. Fig.4 shows an example of neural network predictions for creep microfracturing of a granite specimen soaked in chemical solution DTAB, which is not used to build model. Good agreement is seen to exist between AE behaviors predicted by the neural models and those measured in experiments for novel cases.

5. CONCLUSIONS

The effect of chemical environments on the strength and crack velocity of rock were investigated by conducting Brazilian tests, multi-stage triaxial tests, three points bending tests and double torsion tests on sandstone and Oshima granite specimens. The specimen was soaked in air, water, chemical solution DTAB, NaCl, or PEO, respectively. Acoustic emission (AE) behaviors were monitored during each microfracturing process of rock. The tensile strength significantly varied with concentration of chemicals and is dependent on ξ potential, while the triaxial strength

did not vary significantly with concentration of chemical solutions. Water or chemical solutions at the crack tip significantly lowered the fracture toughness of the rock specimen when compared to that in air condition. Stress corrosion cracking in double torsion tests was also significantly affected by the chemical environments and represented the ξ potential dependency.

The present study indicates that distributions of acoustic emission (AE) events in the time dimension during microfracturing processes of rock under investigated stress condition have fractal structures that go as $C(t) \propto t^D$, where the fractal dimension D is $0.0 < D < 1.0$. We find that the time distribution of rock microfracturing displays fractal and multiple fractal properties. In some cases, it has a single fractal or multifractal structure. In other cases, it changes from a single fractal structure into a multifractal structure as the evolution of the system dynamic process progresses. We suggest that the heterogeneity of the rock, the distribution of joints or weak planes, the stress level, and the nature of the microfracturing mechanism lead to these multifractal properties. Whatever the fractal structure of the system, the lowest fractal dimension is generally produced at near-failure of the rock. This result concerning the fractal dimension decrease is consistent with the conclusion drawn from the spatial distribution of rock microfracturing. Therefore, from the advantage point of observation of the time distribution of rock microfracturing, the decrease of the fractal dimension has a potential use as a rock failure predictor.

Corresponding to each evolutionary process of the system's states, AE behaviors such as the AE event rate, AE count rate in each stress torsion process were modeled using neural network techniques, respectively. Our result shows that the neural network model *NN* (*n*, *h*, *m*) can effectively describe AE behaviors in rock microfracturing processes. For example, at stress increase process, the neural models *NN*(10,21,2) and *NN*(10,20,2) were found to describe reasonably well the AE behaviors of micro-fracturing in rock under air and DTAB conditions, and water conditions, respectively. For creep, the model *NN*(11,17,2) was found to describe reasonably well time behavior of microfracturing in rock under air and chemical solution DTAB conditions, and *NN*(10,27,2) is suitable for water condition. Good agreement is seen to exist between AE behaviors predicted by the neural models and those measured in experiments for novel cases.

REFERENCES

1. Ishido, T. and Mizutani, H. J. Geophys. Res., (1984) 86 pp. 1763-1775.
2. Lajtai, E. Z., Schmidtke, R. H. and L. P. Bielus. Int. J. Rock Mech. Min. Sci. & Geomech. Abstr., (1987) 24, (4)pp. 247-255.
3. Swolfs, H.S. "Underground Waste Management and Environment Implications", T. D. Cook (ed.) , (1972) pp.224-234.
4. Dunning, J., Douglas, B., Millar, M. and S. McDonald, Pageoph, (1994) 143(1/2/3)pp.151-178.
5. Rebinder, P.A., Schreiner, L.A. and Zhigach, K.F., "Hardness reducers in drilling: a physico-chemical method of facilitating mechanical destruction of rocks during drilling", Akad Naunk, USSR, Moscow, Tansl. By CSIRO, Melboune, Australia,(1944).
6. Westood, A.R.C. and Macmillan, N.H. "The Science of Hardness Testing", ASTM, Celveland, Ohio, (1973)pp. 377-417.
7. Engelmann, W.H., Watson, P.J. Tuzinski, P.A. and Pahlman, J.E. U.S. Bureau of Mines RI9103,(1987).
8. Charles, R. J. Fracture: "Proc. of Int. Conf. on the Atomic Mechanisms of Fracture", MIT Press, Cambridge, Mass, (1959) pp.225-249.

Key Engineering Materials Vols. 183-187 (2000) pp. 719-724
© 2000 Trans Tech Publications, Switzerland

Case Study on Fracture of Motor Whist Wire

H. Sakamoto[1], T. Yamaguchi[2] and M. Mizumoto[2]

[1] Department of Mechanical Engineering & Materials Science,
Kumamoto University, 2-39-1 Kurokami, Kumamoto 860-8555, Japan

[2] Forensic Science Laboratory,Kumamoto Pref. Police H.Q.,
6-18-1, Suizenji, Kumamoto 862-8610, Japan

Keywords: Fatigue, Fractography, Striation-like Marking, Winch, Wire Rope

ABSTRACT

A man dead accident, which a wire rope (diameter : 6 mm , JIS No.3) of a motor winch was torn off and its carrying board connected by the wire rope dropped, was occurred. In this report, we carried out the experiment by using the winch under the same situation at the accident site and checked the defects of components of the winch. The damage carrying board was connected with new wire rope. Free weight and accident weight (about 1860 N) was subjected respectively and the up and down lifting test of carrying board was performed. In the broken wire rope, we examined the fracture causes of the wire rope based on metallography and SEM observation.

1. INTRODUCTION

Wire ropes are widely used as transport members and strength members of machines and structures and many rupture accidents of the wire ropes were reported until now [1]-[5]. But there is a few report in relation to fracture wire rope of light weight's motor winch such as accident one (maximum allowing load : 1320 N) in spite of popular lifting machine. It is very important to make clear the fracture causes of wire rope for safety design, proper use and maintenance. In this study, we examined the fracture causes of the wire rope based on metallography and fractgraphy in this ruptured wire rope. The fracture surfaces of the wire elements were observed by SEM and tensile test was carried out in order to check the strength of the wire element.

2. THE OUTLINE OF THIS ACCIDENT

When a man laid tiles on a roof by using a motor winch, the wire rope (diameter : 6 mm , JIS No.3) was torn off and its carrying board connected by the wire rope dropped and the man was crashed to death under the carrying board. This ruptured wire rope of this motor winch was used for about 1 year, the frequencies in use of the winch were about 6 per a month and the up and down cycles per a work were about 20.

3. THE ACCIDENT'S REPRODUCTION TEST

In order to make clear whether the fracture of the wire rope resulted by the structural defect or not, the accident's reproduction test was carried out under the same situation of the accident. Figure 1 shows the accident site. The working site and the structure of the motor winch was shown in Fig. 2. This winch consists of carrying board, wire rope, pulley, guide ladder and motor. The carrying board lift up along the guide ladder by wire rope through the pulley set the top of the ladder. The angle between lower part of the ladder and the wall is 76° and the angle between upper part of the ladder and wall is 23° .

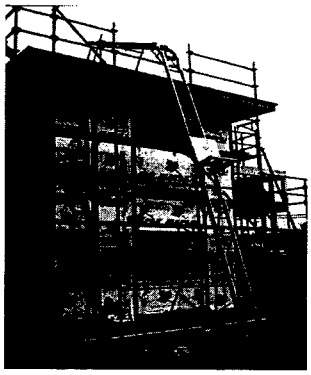


Fig. 1. Accident site.

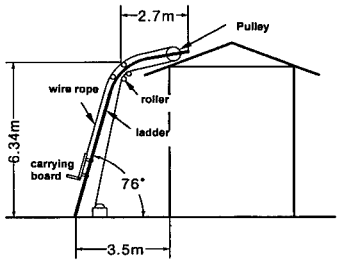


Fig. 2. Working site and the structure of the motor winch.

Before the test, we examine the rolling parts of the pulley and the roller of the accident's one shown in Figs. 3 and 4 and we found that the each movement was normal. Next, using the accident's lifting unit which wire rope was changed for the new one, two kinds of tests were carried out as follows; (1)The going up and down test under load free, (2) The going up test under the weight of 1862N which corresponded to the same one of the accident.

As the results, the winch motor was normal and the movement of the carrying board was smooth under the both loading conditions. No vibration on the ladder and the middle support column was measured and the all behaviors were normal and stable.



Fig. 3. The pulley.

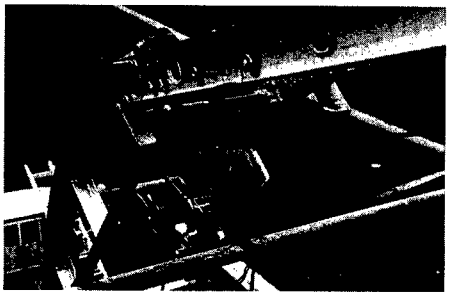


Fig. 4. The roller.

4. EXAMINATION OF THE RUPURE WIRE ROPE

4.1. Appearance inspection and structure of the rope

Figure 5 shows the fracture part of the wire rope. The rupture point was 5.6m length from the connecting point of carrying board. From this rupture length, we can assume that the wire rope broke off when the carrying board reached at middle point of the ladder. The length of surface failure parts of this rope was 1.2m including the fracture parts. The cross section of this wire rope is shown in Fig. 6. The rope diameter is about 5.8mm and consist of 6 strands of 19 steel wire elements (one element diameter: about 0.38mm) and a center string made of artificial fiber.

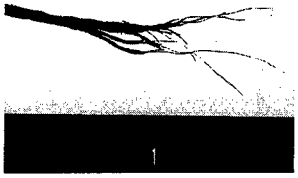


Fig. 5. The fracture part of the wire rope.

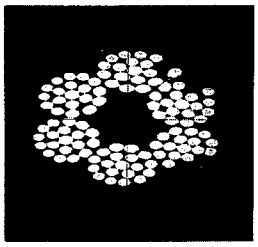


Fig. 6. The cross section of this wire rope.

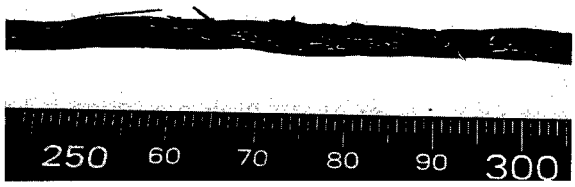


Fig. 7. The appearance of the rope at 0.3m distance from the raptured part.

Figure 7 shows the appearance of the rope at 0.3m distance from the rapture part (carrying board side). On the outside of the rope, many failures were observed such as the snapping of the elements, the abrasion, the corrosion and the plastic deformation, etc. The similar failures were also observed on the another side of the ruptured one. The diameter within 0.3m distance from the rupture part was the average of 5.4mm and the decrease of the cross section area of the neighboring rupture part was recognized.

4.2. Mechanical properties of a element wire

The element wires were pick up at a part away enough from the rupture part and the metallography inspection and the hardness test were examined. The microstructures of the element wire were shown in Figs. 8 and 9. The sorbite texture was observed and Hv460-Hv540 were measured. The tensile strength of elements wire were about 2.28GPa. The Vikers hardnesss and the tensile strength were standard. From these tests of the element wires, it is recognized to be no material defect of the element wires.

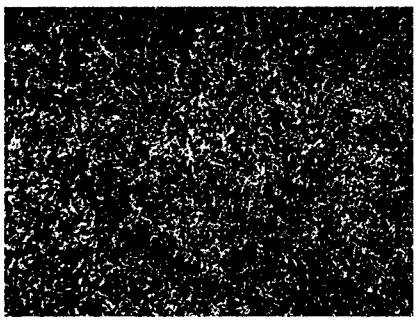


Fig. 8. Micostructure of the element wire. (transverse cross section)



Fig. 9. Microstructure of the element wire. (longitudinal cross section)

4.3. Observation of the fracture surface of the rope

The fracture surface of each element was observed by optical magnifier and classified as 5 types; (1) the cup and cone type fracture, (2) the shear type fracture, (3) the fracture by abrasion, corrosion and cyclic bending, (4) the surface failure by plastic deformation, ware and corrosion etc. after fracture, (5) others. Table 1 shows the appearance of the surfaces of the rupture elements. The photographs by optical magnifier and SEM were shown in Fig. 10~Fig. 13. Figure 10(a) shows the cup and cone type fracture. In this central region, the dimple pattern was observed shown in Fig. 10(b). Figure 11 shows the crack by bending. The example of the fracture after crack propagation is shown in Fig. 12. In Fig. 13, the striation like pattern was observed at the vicinity of external part of the element.

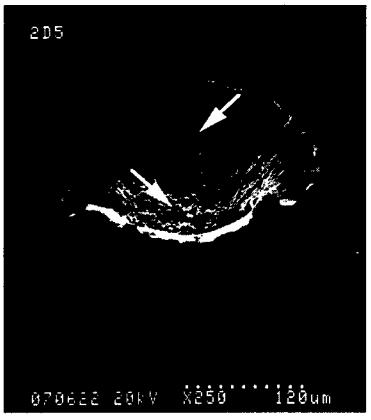


Fig. 10(a). The cup and cone type fracture.

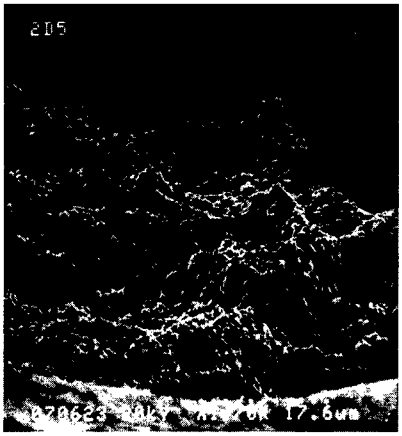


Fig. 10(b). The dimple pattern. (arrow part in Fig.10(a))

Table.1. The appearance of the surfaces of the ruptured elements.

	Fracture type	fracture element wire						total	
		1-A	1-B	1-C	1-D	1-E	1-F		
fracture at accident	cup and cone	2	5	6	5	4	6	28	39
	shear	3	2	1	3	1	1	11	
fracture before accident	fracture by crack occurance	5	5	2	4	2	2	20	74
	surface failure after rupture	9	5	3	2	6	9	34	
	immeasurable	0	2	7	5	5	1	20	
others		0	0	0	0	1	0	1	
total		19	19	19	19	19	19	114	

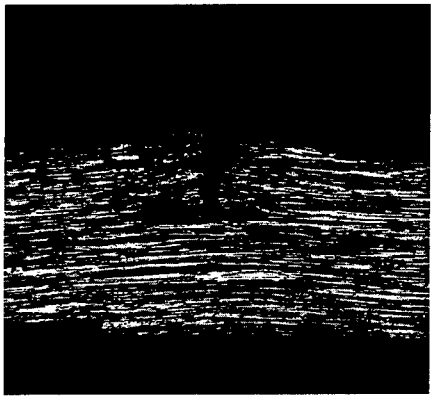


Fig. 11. The crack by bending.

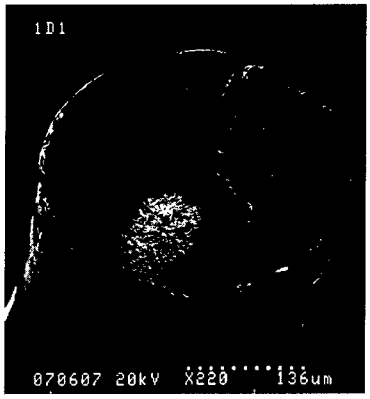


Fig. 12. The fracture after crack propagation.

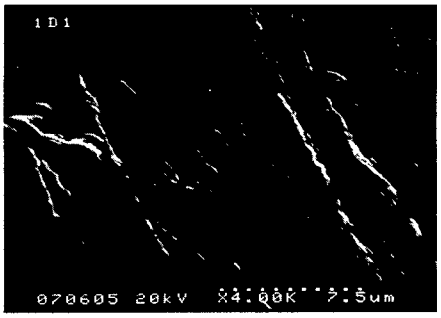


Fig. 13. The striation like pattern.

5. RESULTS AND DISCUSSION

In the accident's wire rope, many snapping and the decrease of cross section of the elements near the fracture part were recognized. Therefore, it is conceivable that the effective cross-section area was considerably decreasing when accident occurred. The wire rope was subjected to the tensile stress by the rolling up, the bending stress by the pulley and the contact and the shearing stress with the pulley and the crack initiation and propagation by the cyclic bending, the abrasion and the plastic deformation of the elements occurred. Once the snapping of a element occurred, the cut of the element proceeded one by one due to the stress increase per one element. From the fracture surfaces of the elements, we can estimate that about 67% of total elements broke off before this rupture accident. The maximum stress 760MPa (tensile stress : 505MPa + bending stress: 252MPa) of the element occurred at the contact part of the pulley and was larger than the sound element by 86%. The fact that this decrease of the effective cross section area made the allowance load of the wire rope lowering largely and the weight in service (1862N) was over the maximum allowance load (1320N) brought about this accident. The occurrences of crack initiation, abrasion and corrosion of the elements were mainly resulted in short lubricant and bad maintenance. This kind of accidents almost all can prevent by daily inspection and keeping the allowance load.

REFERENCE

1.The Japan Society of Mechanical Engineers, JSME data book: Failuer Analysis of Machine and Structure – Case Histories and Techniques – (1984) p.205
2. Wire Rope Handbook Editorial Committee, Wire Rope Handbook, Hakua shobo, (1967)p.376
3. T. Senda, Y. Sogabe, Y.aimitsu and M. Ichiryu, Fracture of Wire Rope Core Ropes under Practical Load, J. Soc. Mat. Sci., 41-461(1992) p.239
4. M. Tanaka, and S. Konosu, Quantitative Evaluation of Damage Behavior of Wire Ropes under S-type Bending Fatigue – For IWRC 6xFi(29)- J.Soc.Mat. Sci., 44-503(1995) p.1086
5. S.Nishida, Failure Analysis in Engineering Applications, Butterworth-Heinemann, (1992) p.39

Key Engineering Materials Vols. 183-187 (2000) pp. 725-730
© 2000 Trans Tech Publications, Switzerland

The Propagation of a Layer-Confined Love Wave in Layered Piezoelectric Structures

Z.K. Wang, F. Jin, Z. Zong and T.J. Wang

Department of Engineering Mechanics, Xi'an Jiaotong University, Xi'an 710049, China P.R.

Keywords: Coupled Electromechanical Field, Love Waves, Phase Velocity, Piezoelectric Layered Structures, Surface Acoustic Wave Devices

ABSTRACT

As to a layered structure consisting of different piezoelectric layer and substrate in intimate contact, it is discovered that when the velocity of the bulk shear wave in the layer is lower than that of in the substrate, Love waves could propagate in the structure. It is further proved in this paper that when the mechanical and electric constants of the two media and the thickness of layer are satisfied with certain relationship, a mechanical perturbation layer-confined Love wave could propagate in such piezoelectric layered structures. The propagation condition of above surface wave and its corresponding velocity equations are obtained by analytical method. Several numerical examples are provided also.

1. INTRODUCTION

In the fields of electronics, ultrasonics, microwave and environmental monitoring, all sorts of surface acoustic wave devices are widely used. Among them, the recently developed Love wave sensors are highly sensitive microacoustic devices [1,2,3]. This paper primarily concerned with the propagation behavior of a peculiar Love wave in the piezoelectric layered structures. As the wave propagates, its mechanical perturbation and electromagnetic perturbation are coupled with each other, but its mechanical perturbation only takes place in the layer and do not penetrate into the substrate. This peculiar motion form is a unique result in piezoelectric structures and does not exist in purely elastic solids. The conclusion of this paper not only further discloses the complex coupled electromechanical behavior of piezoelectric layered structures, but also provides theoretical foundation for the design of high quality electro-acoustic devices in the microwave technology.

2. THEORETICAL ANALYSIS

The piezoelectric layered structure is shown in Fig.1that the layer with uniform thickness h and in intimate contact with the substrate, they are different transversely isotropic piezoelectric media

with their polarization both along z-axis. On condition that the free surface of the layer is mechanical traction-free and provided that the velocity of the bulk shear wave in the layer is lower than that of in the substrate, Love waves could propagate in the structure. Moreover, their first three modes are shown in Fig.2. In order to increase the performance of the Love wave sensors, the mechanical perturbation should be mostly concentrated near the free surface of the devices when wave propagate. Obviously, if the waves with the motion modes that are shown in Fig.3, the mechanical perturbation will only restrict in layer and does not penetrate into substrate. That is to say, a mechanical perturbation layer-confined Love wave can be achieved.

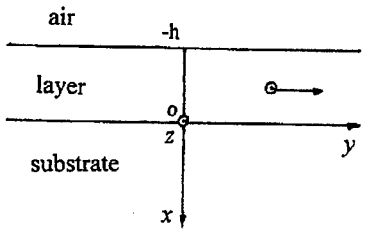


Fig.1 The piezoelectric layered half-space

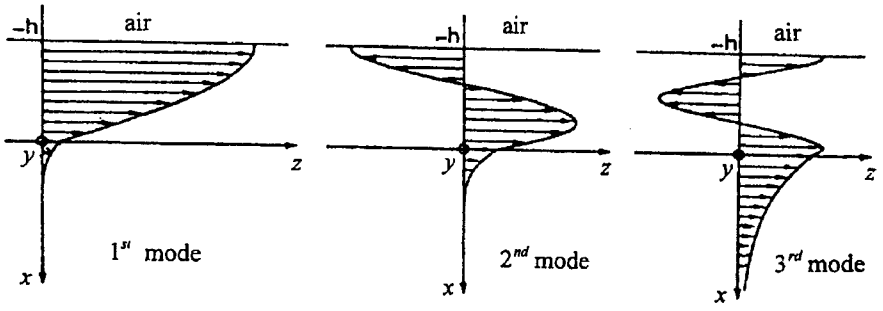


Fig.2 The first three modes of Love waves

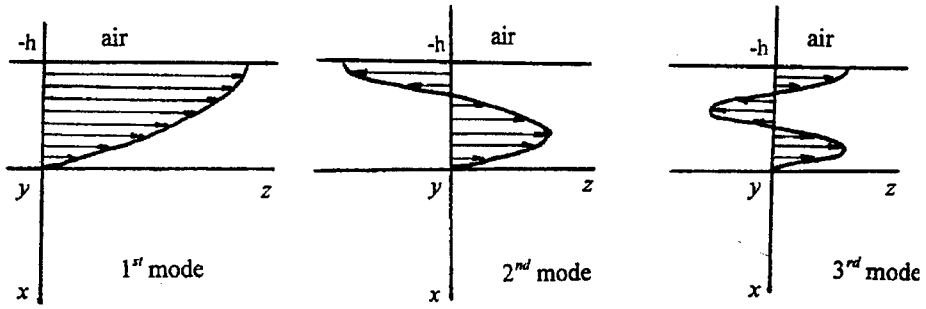


Fig.3 The first three modes of Love waves discussed in this paper

The differential equation of motion for the piezoelectric media can be expressed as the following general form:

$$c_{ijkl}\frac{\partial^2 u_l}{\partial x_j \partial x_k}+e_{kij}\frac{\partial^2 \varphi}{\partial x_j \partial x_k}=\rho\frac{\partial^2 u_i}{\partial t^2} \tag{1a}$$

$$e_{jkl}\frac{\partial^2 u_l}{\partial x_j \partial x_k}-\varepsilon_{jk}\frac{\partial^2 \varphi}{\partial x_j \partial x_k}=0 \tag{1b}$$

where c_{ijkl}, e_{kij} and ε_{jk} are the elastic, piezoelectric and dielectric tensors of a given material. ρ is the mass density of the media, u_l the mechanical displacements, φ the electrical potential function, it related to the electric field intensity with the following form according to the quasi-static approximation:

$$E_i=-\varphi_{,i}\quad (i=1,2,3) \tag{2}$$

As shown in Fig.1, the particles under consideration are making transversely horizontal polarizing movement. The propagation direction of wave can be assumed along the positive direction of y-axis without loss of generality. Thus, we have:

$$u=0,\quad v=0,\quad w=w(x,y,t),\quad \varphi=\varphi(x,y,t) \tag{3}$$

Then the differential equation of motion can be simplified as follows, with respect to layer and substrate, respectively:

$$c_{44}\nabla^2 w_1+e_{15}\nabla^2\varphi_1=\rho\frac{\partial^2 w_1}{\partial t^2} \tag{4a}$$

$$e_{15}\nabla^2 w_1-\varepsilon_{11}\nabla^2\varphi_1=0 \tag{4b}$$

$$c_{44}'\nabla^2 w_2+e_{15}'\nabla^2\varphi_2=\rho'\frac{\partial^2 w_2}{\partial t^2} \tag{5a}$$

$$e_{15}'\nabla^2 w_2-\varepsilon_{11}'\nabla^2\varphi_2=0 \tag{5b}$$

where $\nabla^2=\partial^2/\partial x^2+\partial^2/\partial y^2$ is Laplace operator. As shown in Fig.1, the medium above the layer is air in general, its dielectric constants are very small in comparison with those of the piezoelectric medium and thus the space above the layer can be treated as vacuum. Let $\varphi_0(x,y,t)$ denote the electric potential function of the vacuum, then

$$\nabla^2\varphi_0=0 \tag{6}$$

In addition to Eqs.(4)-(6), the actual motion must satisfy the boundary conditions and the continuity conditions along the interface between two media.

The purpose of this paper is to search for the Love wave of which the mechanical perturbation in substrate is zeroing, so there is an additional condition exists: $w_2(x,y)\equiv 0$. This condition can be assured by satisfying the following equation:

$$w_2(0,y)=0 \tag{7}$$

3. EXISTING CONDITIONS OF THE PECULIAR LOVE WAVE AND NUMERICAL RESULTS

Firstly, the solutions of the wave equation (4) of the layer are assumed to have the following forms:

$$w_1(x,y,t) = W_1(x)\exp[ik(y-ct)] \tag{8a}$$

$$\varphi_1(x,y,t) = \Phi_1(x)\exp[ik(y-ct)] \tag{8b}$$

where $k = 2\pi/\lambda$ is the wave number and λ the wavelength, c denotes the phase velocity of the wave. $W_1(x)$ and $\Phi_1(x)$ are undetermined functions, respectively. The solutions of Eq. (4) are:

$$w_1(x,y,t) = (A_1 \sin\beta x + B_1 \cos\beta x)\exp[ik(y-ct)] \tag{9a}$$

$$\varphi_1(x,y,t) = \left(C_1 e^{-kx} + D_1 e^{kx} + \frac{e_{15}}{\varepsilon_{11}} A_1 \sin\beta x + \frac{e_{15}}{\varepsilon_{11}} \cos\beta x\right)\exp[ik(y-ct)] \tag{9b}$$

The solutions of Eq. (5) can be expressed as the following forms:

$$w_2(x,y,t) = A_2 e^{-bx}\exp[ik(y-ct)] \tag{10a}$$

$$\varphi_2(x,y,t) = \left(C_2 e^{-kx} + \frac{e_{15}'}{\varepsilon_{11}'} A_2 e^{-bx}\right)\exp[ik(y-ct)] \tag{10b}$$

where $b = k\sqrt{1-(c^2/c_{sh}'^2)}$. Notice that φ_0 vanishes for $x \to \infty$, then solution of Eq. (6) is:

$$\varphi_0(x,y,t) = A_0 e^{kx}\exp[ik(y-ct)] \tag{11}$$

By thorough deduction and proof procedure, we can finally arrive at the following expression:

$$\cos(kqh) = \left[sh(kh) + \frac{\varepsilon_{11}'}{\varepsilon_{11}} ch(kh)\right] \Big/ \left(\frac{\varepsilon_{11}'}{\varepsilon_{11}} - \frac{e_{15}'}{e_{15}}\right) \tag{12}$$

where $q = \sqrt{(c^2/c_{sh}^2)-1}$. Let c_{sh} and c_{sh}' denote the velocities of the bulk shear wave in the layer and the substrate, respectively, it can be obtained easily that

$$c_{sh} = \sqrt{(c_{44}\varepsilon_{11} + e_{15}^2)/\rho\varepsilon_{11}} \quad , \quad c_{sh}' = \sqrt{(c_{44}'\varepsilon_{11}' + e_{15}'^2)/\rho'\varepsilon_{11}'}$$

Moreover for the Love waves to propagate in the piezoelectric layered structures, the following expression should be satisfied: $c_{sh} < c < c_{sh}'$

On condition that Eq. (12) is tenable, the phase velocity equations for the electrical open and shorted cases at the free surface of the half-space can be obtained, respectively:

$$\sin(kqh) = \left\{q\left(c_{44}\frac{\varepsilon_{11}}{e_{15}^2} + 1\right)\left[\left(\frac{\varepsilon_{11}}{\varepsilon_0} + \frac{\varepsilon_{11}'}{\varepsilon_{11}}\right)sh(kh) + \left(\frac{\varepsilon_{11}'}{\varepsilon_0} + 1\right)ch(kh)\right]\right\} \Big/ \left(\frac{\varepsilon_{11}'}{\varepsilon_{11}} - \frac{e_{15}'}{e_{15}}\right) \tag{13}$$

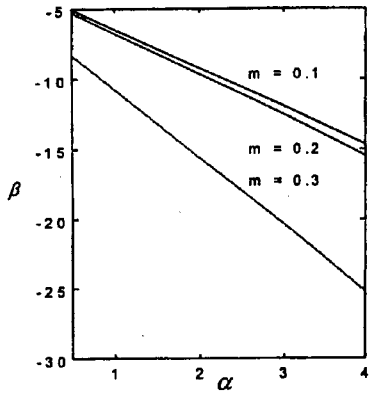


Fig.4 Relationship between α and β with $c = 2500m/s$ (electrically open)

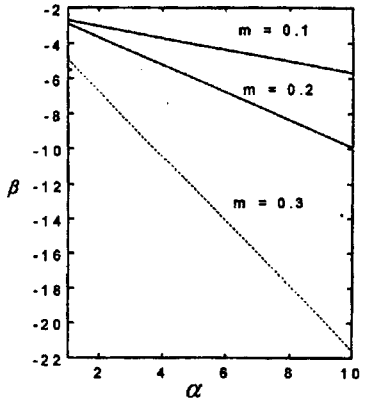


Fig.5 Relationship between α and β with $c = 2500m/s$ (shorted)

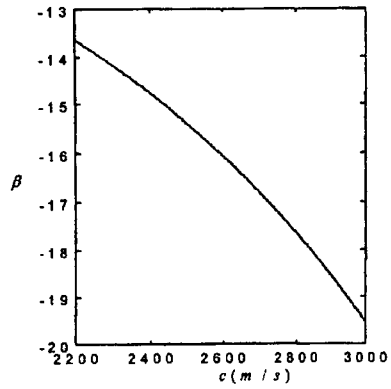


Fig.6 Relationship between c and β with $\alpha = 4$, $m = 0.2$ (electrically open)

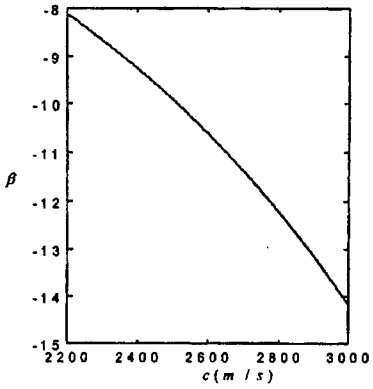


Fig.7 Relationship between c and β with $\alpha = 4$, $m = 0.2$ (shorted)

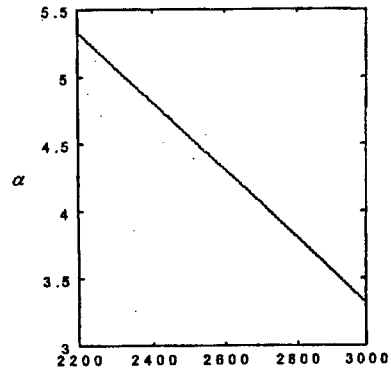


Fig.8 Relationship between c and α with $\beta = -17$, $m = 0.2$ (electrically open)

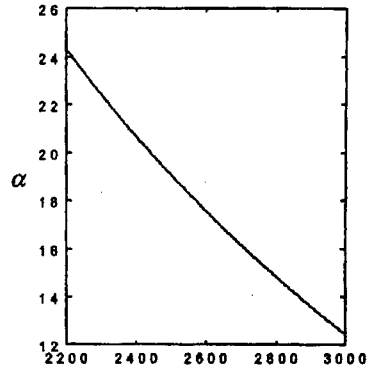


Fig.9 Relationship between c and α with $\beta = -17$, $m = 0.2$ (shorted)

$$\sin(kqh) = \left\{ q\left(c_{44}\frac{\varepsilon_{11}}{e_{15}^{2}} + 1 \right)\left[ch(kh) + \frac{\varepsilon_{11}^{'}}{\varepsilon_{11}} sh(kh) \right] \right\} \Big/ \left(\frac{\varepsilon_{11}^{'}}{\varepsilon_{11}} - \frac{e_{15}^{'}}{e_{15}} \right) \tag{14}$$

The above two equations have already satisfied the propagation conditions of the peculiar Love wave described in above sections. Notice that $k = 2\pi/\lambda$ and in the following analysis we always set variables $\alpha = \varepsilon_{11}^{'}/\varepsilon_1$, $\beta = e_{15}^{'}/e_{15}$ and m=h/λ. It can be seen from Eq. (13) and Eq. (14) that if the phase velocity c and m is pre-determined, then the matching relationship between the electric character parameters of the layer and the substrate can be determined accordingly. On the contrary, if h and α or β is pre-determined, then the variation pattern of the velocity c along with β or α can be obtained also. The above relationships are taken into calculation and the corresponding numerical results are shown in Fig.4 to Fig.9.

It can be found in Fig.4 and Fig.5 that when velocity c and the structural geometrical parameter m is determined, variables α and β take on linear relationship. It is shown in Fig.6 and Fig.7 that when the ratio of dielectric constants of the substrate to those of the layer is pre-determined on condition that m is a certain value, phase velocity c increases when the absolute value of β increase. While Fig.8 and Fig.9 indicate that when the ratio of the piezoelectric constants of substrate/layer media is pre-determined, phase velocity decreases when α increases. It is also shown in above numerical examples that the thickness of the layer can be controlled to have the same order as wavelength, even to be shorted than a wavelength. For $\omega = kc$, and $\lambda = 2\pi/k$, it is easy to see that for a certain value of velocity, the higher the frequency is and the larger the wave number are, the shorter the wavelength is. These results have practical meaning for the application of film/substrate structures in surface acoustic wave technology.

4. CONCLUSIONS

It is verified in this paper that a peculiar Love wave can propagates in the piezoelectric layered medium under certain conditions. The mechanical perturbation of the peculiar Love wave can only occurs in the layer and does not penetrate into the substrate medium; the thickness of the layer can be shorter than a wavelength. These results obtained not only disclose the diversiform electromechanical coupling behavior of the piezoelectric layered structures, but also provide theoretical foundation for designing the electro-acoustic devices in the microwave technology field.

ACKNOWLEDGEMENTS

F. Jin would like to acknowledge the financial support by China Postdoctoral Science Foundation. TJ Wang would like to acknowledge the support by the Science Foundation of China Education Ministry.

REFERENCES

1. J. Du, G. L. Harding, J. A. Ogilvy, P. R. Dencher and M. Lake, Sensors Actuators, **A 56** (1996) p. 211

2. B. Jakoby and M. J. Vellekoop, Smart Materials Structures, **6** (1997) p. 668

3. A. Leidl, I. Oberlack, U. Schaber, B. Mader and Drost, Smart Materials Structures, **6** (1997) p. 680

Key Engineering Materials Vols. 183-187 (2000) pp. 731-736
© 2000 Trans Tech Publications, Switzerland

Characteristics of Delamination in Graphite/Epoxy Laminates under Static and Impact Loads

J.S. Kook[1], I.Y. Yang[2] and T. Adachi[3]

[1] Department of Mechanical Engineering, Daebul University,
72-1 Sanho-ri, Samho-myun, Youngam-kun, Chonnam 526-890, Korea

[2] Department of Mechanical Design Engineering, Chosun University,
375 Seosuk-dong, Dong-gu, Kwangju 501-759, Korea

[3] Department of Mechanical Engineering and Science, Tokyo Institute of Technology,
2-12-1 O-okayama, Meguro-ku, Tokyo 152-8552, Japan

Keywords: Damage Mechanism, Delamination, Fractography, Graphite/Epoxy Laminates, Impact

ABSTRACT

In the present research, the characteristics of delamination in graphite/epoxy laminates subjected to static and impact load are discussed by the method of fractography experimentally. At first, delaminations were developed by double cantilever beam (DCB) test and end-notch flexure (ENF) test for some kinds of laminates. Their fracture surfaces were observed by scanning electron microscope. The propagated orientation of the delamination could be specified from the patterns of fracture surface. Next, each static and impact load was applied to square laminates to generate rip-wise delaminations known as the typical pattern of low velocity impact damage. Based on the pattern specified by DCB and ENF tests, the propagation of delaminations for both loads were identified. Then it is obtained that the delamination in static and impact can be explained by the propagation from the transverse crack and the sequential delamination mechanism respectively.

1. Introduction

Graphite/epoxy laminates have some advantages in aerospace field because of high specific stiffness and strength. The major concern of such a structure in design and maintenance is the reliability of the composites after experiencing various loads through surface contact and impact. It is known that under certain contact and low-energy impact conditions, premature delaminations may be induced in the composites even though there is no sign of damage on the surface. If such premature delaminations exist in composite structure and are not detected, serious accidents can occur because of the substantial reduction in stiffness and strength. It has been known that graphite/epoxy laminates have fractures such as indentation, transverse crack, and delamination

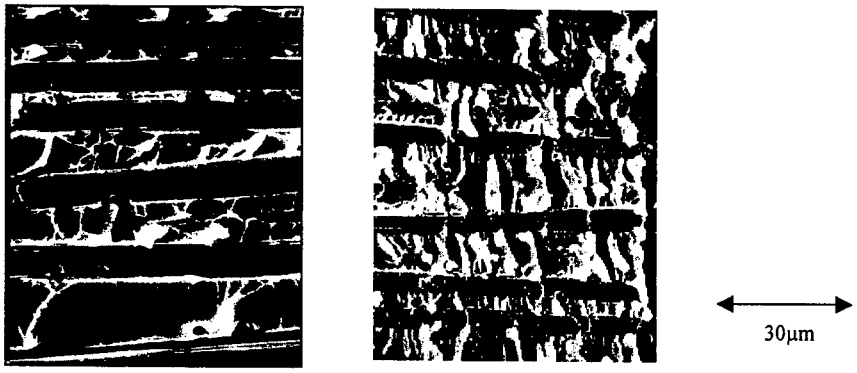
under static and impact load [1]. There are extensive research activities in the field of composite delamination [2-6]. The damage mechanism under static and impact loading should be obtained to design an advanced structure. The Generation of delamination in a composite laminates subjected to low velocity impact is modeled by some researchers. Takeda et al. [7-10] considered that delamination appears by pushing of the generator strip in an impacted layer onto adjacent layer. This is known as sequential delamination mechanism. Joshi et al. [11-13] suggested that delamination develops from transverse crack in an internal layer. Hull and Shi [14] also considered the similar model to Joshi's one.

In the present research, the characteristics of delamination in graphite/epoxy laminates subjected to static and impact load are discussed by method of fractography experimentally. At first, delaminations are developed by double cantilever beam (DCB) test and end-notch flexure (ENF) test for $[0°_2/90°_4/0°_4/90°_4/0°_2]$ laminates. Their delamination surfaces are observed by scanning electron microscopy. It is considered that the features of the delamination surface are correlated to the propagated orientation of the delamination. Next, each static and impact load is applied to square $[0°_6/90°_{12}/0°_6]$ laminates to generate rip-wise delaminations. Based on the relation between the fracture surface patterns and the propagated orientation of the delamination specified by the DCB and ENF tests, the propagation of the delaminations for each load is identified.

2. Delamination of DCB and ENF test

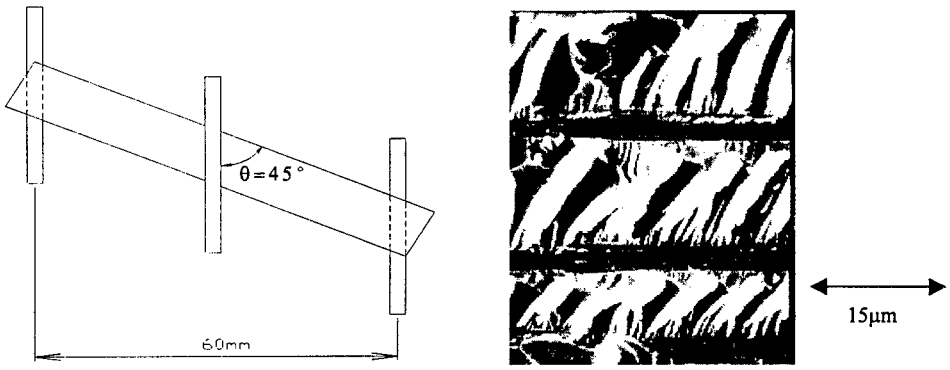
Unidirectional graphite/epoxy material, Torayca T300 fiber with Toray 2500 resin was used. After composite processing, the laminates were cut to 180mm x 40mm in dimension. A pre-existing crack at the middle position of the thickness was introduced by a 10μm thick polymide film in $[0°_2/90°_4/0°_4/90°_4/0°_2]$ laminates.

Testing was performed on an INSTRON servohydraulic load frame under deflection-controlled loading. The observation of their delamination surfaces was examined with a SEM. Fig. 1(a) shows the fractograph of delamination in DCB specimen known as Mode I fracture. Its characteristic has



(a) DCB specimen (b) ENF specimen

Fig. 1 Fracture topography on 90° ply surface (θ=0°)



(a) three-point bending test (b) ENF specimen

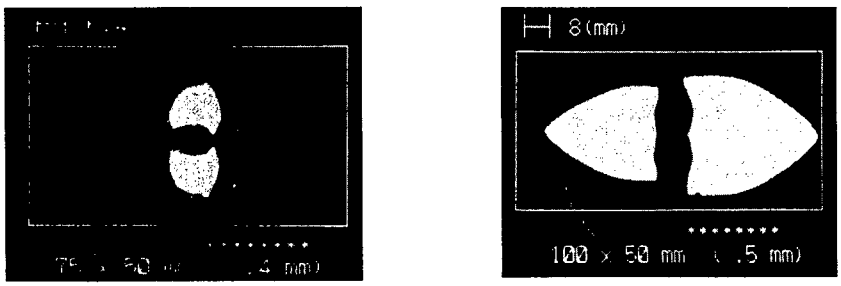
Fig. 2 Fracture topography on 90° ply surface (θ=45°)

the overall flatness on the matrix fracture. Fig. 1(b) shows the fractograph of delamination in ENF specimen known as Mode II. Its characteristic has numerous inclined hackles of the matrix fracture.

Fig. 2(a) shows three-point bending test for the specimen placed in an oblique position. The propagated orientation of delamination doesn't agree to the direction of 0° fiber. From Fig 2(b), it is revealed that the inclined hackles of matrix fracture rotate about 45 degree. Therefore, the orientation of these hackles is found to positively correlate to the direction of induced delamination. From the hackle separation mechanism [15], the orientation of hackles are either coincident with or opposite to the orientation of delamination propagation.

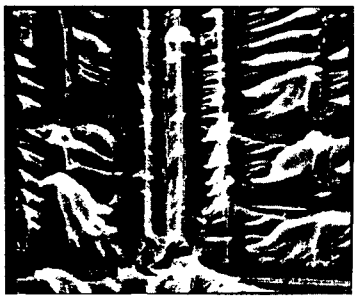
3. Delamination of static and impact test

The laminates had a layup of $[0°_6/90°_{12}/0°_6]$ and specimens were cut to 180mm x180mm in dimension. The specimens were clamped at all edges between two picture-frame plates with a circular opening of ϕ150mm. Static test was performed on an INSTRON servohydraulic load frame

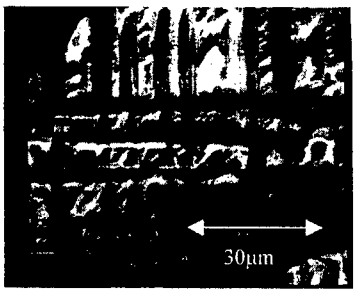


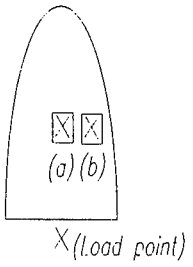
(a) Delamination A (b) Delamination B

Fig. 3 Delamination of laminates subjected to static load



(a) at the center





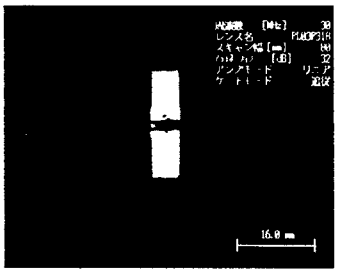
(b) at the right side

Fig.4 Fracture surface on 0° ply side of Delamination A (Static)

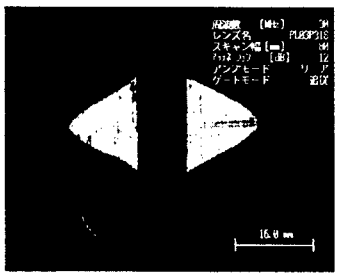
under deflection-controlled loading. The laminated specimen was loaded transversely at the specimen center with the indentor that had a steel ball. Fig. 3 shows the delaminations of each interface observed with an ultrasonic microscope (Hitachi, AT-5000). The term " Delamination A" is defined as the interface near the loading surface and " Delamination B" is defined as the other one.

Fig. 4(a) shows the fracture surface on 0° ply side observed at the center of the Delamination A. At the middle line, there are no hackles but fibers/matrix separations that are exclusively the result of Mode I. The inclined hackles are observed symmetrically on the basis of the middle line in Fig. 4(a). The hackles are mainly result of Mode II. The propagated orientation of delaminations is estimated approximately 60° and 120° from the inclined hackles. Fig. 4(b) shows the fracture surface on 0° ply side observed at the right side of the Delamination A. Inclined hackles are reduced and overall flatness is increased. From the fracture surface, it is result of both mixed Mode I and Mode II. The propagated orientation of the delaminations is changed, and is estimated approximately 75° from the inclined hackles. The fracture surfaces of the Delamination B are similar to those of the Delamination A.

Impact test was performed with an air-gun machine. A specimen was impacted by a ϕ 5mm steel ball with 81.6 m/s. Fig. 5 shows Delamination A and Delamination B observed with the ultrasonic microscope. As shown in Fig. 5, the rip-wise delaminations known as the typical pattern of low

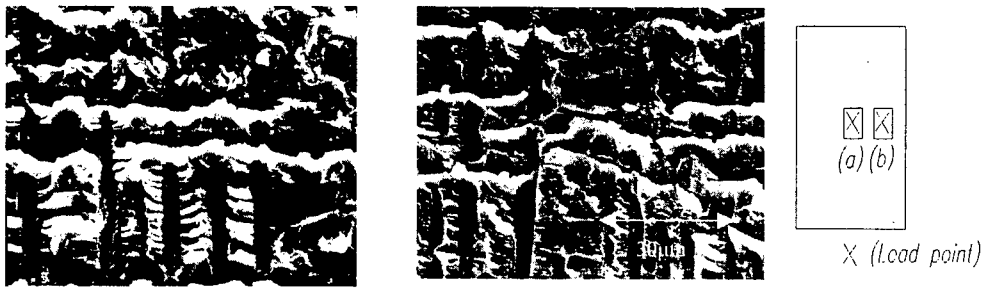


(a) Delamination A



(b) Delamination B

Fig. 5 Delamination of laminates subjected to impact load



(a) at the center (b) at the right side

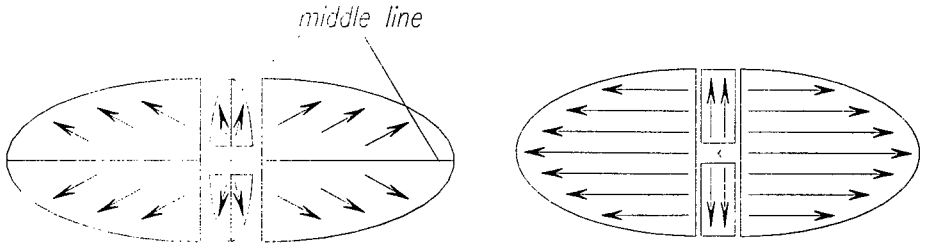
Fig. 6 Fracture surface on 0° ply side of Delamination A (Impact)

velocity damage are similar to static case (Fig.3). Fig. 6(a) shows the fracture surface on 0° ply side observed at the center of the Delamination A. There are hackles but not inclined ones. The propagated orientation of delaminations could be estimated approximately 90° from the hackles. It is shown that mixed mode fracture with waveform is considered as the effect of stress wave propagation. Fig. 6(b) shows the fracture surface on 0° ply side observed at the right side of the Delamination A. The tendency to the fracture surface is similar to that in Fig. 6(a). The fracture surfaces of the Delamination B are also similar to those of the Delamination A.

4. Discussions

From the inclination angles of the hackles, the propagated orientation of the delamination could be estimated. As the summary at the case of static load, the propagated orientation of delamination is shown in Fig. 7(a). The orientation of the delamination is symmetric on the basis of middle line. At the middle line, the fractures are exclusively considered as the result of Mode I. From Fig. 7(a), the fractures near the middle line are mainly considered as the result of Mode II. The other areas are considered as the effect of mixed Mode I and Mode II.

In general, the main transverse crack occurs along the middle line of the delamination. It can be predicted that the delamination propagates from the transverse crack by Fig. 7(a). Then the



(a) Delamination A,B (Static) (b) Delamination A,B (Impact)

Fig. 7 Propagated Orientation of delaminations

mechanism of delamination development during static loading can be explained by Joshi's model [11-13]. As the summary at the case of impact load, the propagated orientation of the delamination is shown in Fig. 7(b). The orientation of the Delamination A is approximately 90° and that of the Delamination B is approximately 0°. The mechanism of delamination development during impact loading can be explained by Takeda's generator strip model [7-10].

So it is obtained that the damage mechanism in static load is different from that in impact load.

5. Conclusions

The characteristics of the delamination in graphite/epoxy laminates subjected to static and impact load were discussed by the method of fractography experimentally. The summaries in the present research are as follows:

The propagated orientation of the delamination can be specified by the features of the fracture surface from the results of the DCB and ENF tests. By the results, the propagated orientation of the delamination in the laminates subjected to static and impact load was identified. It is obtained that the damage mechanism in static load is different from that in impact load. The delamination in static and impact load can be explained by the propagation from the transverse crack and the sequential delamination mechanism respectively.

REFERENCE

1. H. Matsumoto, T. Adachi and S. Ujihashi, Pro. the Oji Int. Seminar on Dynamic Fracture, Japan, Tokyo (1990) p.174
2. J.K. Kim, D.B. Mackay and Y.W. Mai, Composites, **24** (1993) p.485
3. R.A.W. Mines, C.M. Worrall and A.G. Gibson, Composites, **25** (1994) p.95
4. I. Lee, B.N. Kim and K.N. Koo, Composites, **25** (1994) p.281
5. K. Komai, K. Minoshima and H. Yamasaki, Transactions of JSME(Series A), **60** (1994) p.2511
6. M.S. Sohn and X.Z. Hu, Theoretical and Applied Fracture Mechanics, **25** (1996) p.17
7. N. Cristescu, L. E. Malvern and R. L. Sierakowski, ASTM **STP568** (1975) p.159
8. N. Tekeda, R. L. Sierakowski and L.E. Malvern, SAMPE Quarterly (1981) p.9
9. N. Tekeda, R. L. Sierakowski and L.E. Malvern, Composites Technology Review, **4** (1982) p40
10. N. Tekeda, R. L. Sierakowski, C. A. Ross and L. E. Malvern, Experimental Mechanics, **22** (1982) p19
11. S. P. Joshi and C. T. Sun, J. Composite Materials,**19** (1985) p.51
12. H. Y. Choi, R. J. Downs and F. K. Chang, J. Composite Materials, **25** (1991) p.992
13. H. Y. Choi, H. Y. T. Wu and F. K. Chang, J. Composite Materials, **25** (1991) p.1012
14. D. Hull and Y. B. Shi, Composite Structures, **23** (1993) p.99
15. B.W. Smith and R.A. Grove, ASTM **STP 948** (1987) p.154

Key Engineering Materials Vols. 183-187 (2000) pp. 737-742
© 2000 Trans Tech Publications, Switzerland

An Experimental Observation about Dislocation Nucleation Based on Peierls Concept

Y.M. Xing[1,2], F.L. Dai[1] and W. Yang[1]

[1] Department of Engineering Mechanics, Tsinghua University, Beijing 100084, China P.R.

[2] Department of Basic Science, Inner Mongolia Polytechnic University, Hohhot 010062, China P.R.

Keywords: Crack Tip, HREM-Moiré, Nano-Deformation, Quasi-Cleavage Fracture

ABSTRACT

HREM-moiré method[1,2] developed by us is an experimental technique which allows direct measurement to parameters such as displacement, strain and dislocation in nanoscopic range. This technique was used to measure nanoscopic deformation field near the tip of a quasi-cleavage crack in Si. The process of dislocation nucleation was observed. A long dislocation extending about 600 burgers vectors has been found at the crack tip and the slip distribution along it was measured. This distributed dislocation has a similar slip structure to the one based on Peierls concept described by Rice[3], but has much longer slip range. The nanoscopic strain distribution near the crack tip has been obtained. A strain field controlled by linear elastic fracture mechanics at the head of crack tip exists.

1. INTRODUCTION

The mechanism of dislocation nucleation in quasi-cleavage crack has been studied by many researchers. In pioneering work on the model of the competition between cleavage crack growth and dislocation emission from crack tip, Rice and Thomson[4] performed an activation analysis in which the total energy change due to the formation of a dislocation half loop at the crack tip was calculated as a function of loop change radius and dislocation core cut-off radius. This model was very successful in explaining the intrinsic cleavability, i.e. in dividing crystals into those that never cleave (most fcc metals, alkali metals) brittle from intrinsically brittle materials. However, it predicted critical activation energy for the intrinsically brittle materials to initiate plastic deformation were one or more orders of magnitude too high than that achievable by thermal activation. Argon[5] pointed out that the linear elastic solution was no longer valid in the region very close to the crack tip because dislocations were emitted. A Peierls type periodic resistance to the dislocation emission must be used for a more accurate analysis. Ohr[6] used a molecular dynamics approach to determine the non-linear crack tip field, and with this and several other stress field coupling effects, they reduced the critical activation energy for by a factor of 1.5. Since their analysis did not use a Peierls-type core description emission was still about one order of magnitude

too high. The two biggest uncertainties in this model have been the dislocation core cut-off radius and the absence of stress relaxation accompanying dislocation emission. Rice[3] was largely successful in developing a model to explain the effects of dislocation emission, mobility and shielding of a moving tip. Dislocation nucleation from a stressed crack tip was analyzed based on the Peierls concept. A periodic relation between shear stress and atomic displacement was assumed to hold along the most highly stressed slip plane emanating from a crack tip. This allows some small displacement to occur near the crack tip in response to small applied loading and, with increase in loading, the incipient dislocation configuration becomes unstable and leads to a fully formed dislocation which is driven away from the crack tip. The level of applied stress intensity factors required for dislocation nucleation was shown to be proportional to $r_{us,}$ unstable stacking energy which was a solid state parameter defined by Rice. This model avoids the ambiguity of core cut-off radius, and identifies the saddle point instability configuration as a partially nucleated dislocation and calculates its energy barrier per unit length exactly.

Optical techniques have been used extensively in the direct determination of crack tip fields. However, most of them have been in the macroscopic field because of the limited sensitivity and resolution of experimental techniques. HREM-moiré method, an experimental technique with nanometer resolution, was developed by us[1-2]. On this base, this technique is used to analyze experimentally the nano-deformation field of a cleavage crack tip of Si single crystal. Process of dislocation nucleation is observed quantiavely. The nanoscopic strain distribution near the crack tip is measured. The configuration of dislocation is investigated.

2. EXPERIMENTAL PROCEDURE

The material used in this study is Si single crystals, although this experimental technique could have been developed on other crystals as well. Si was chosen to be studied first because it has been studied extensively in the past, and excellent analytical and experimental information exists about its properties; Moreover, it has excellent microscopic periodical structure as a grating so as to obtain high-quality moiré fringes. The samples were cut from a Si sheet in the plane {111}. It is know that {111} plane in Si has larger lattice spacing so that the lattice image can be easily recorded. An atomically sharp pre-crack was generated in the direction of [110] by loading the specimen very slowly in the direction y. The {111} planes in the Si are primary cleavage planes whereas the {110} planes are secondary cleavage planes. Many tests revealed that the surfaces of {110} oriented samples are much smoother than those of {111} orientation. The experimentally measured values of fracture toughness for these two orientations are very close, with the {110} orientation having even a somewhat lower toughness.

The specimens were prepared according to the requirement of HREM. The samples were ground mechanically into sheets with the thickness of 30μm, and further thinned out by ionic bombardment till punching. The dimensions of the specimens are diameter d=2 *mm*, thickness h=30 μm and with the very thin areas around the central holes for TEM analysis. To achieve well controlled cleavage crack growth, constant displacement loading was employed. A small copper ring with diameter of 2 *mm* and thickness of 0.4 *mm* was used for loading the specimen. The ring was pre-compressed radially first, and then glued on one side of the specimen. After glue solidified well, the copper ring was unloaded. The ring could exert tensile force onto the specimen. Since constant-displacement loading was performed crack propagated only very limited distance. Load was still in action here but resultant fracture energy in crack tip was less than critical cleavage energy.

3. EXPERIMENTAL RESULTS

A transparent electronic microscope (JEM-200cx) was used to take the lattice image and the moiré fringes were produced by the method mentioned in reference [1,2]. The magnification employed in the test is 0.2 million so that the lattice lines in [110] direction on the lattice image has a frequency of about 16 lines/mm. A standard grating of 16 lines/mm was used to superpose on to the lattice image and optical filtering technique was employed. Fig. 1 and Fig. 2 show the moiré fringe patterns near a crack-tip with different mismatch fringes due to relative rigid-body rotations between standard

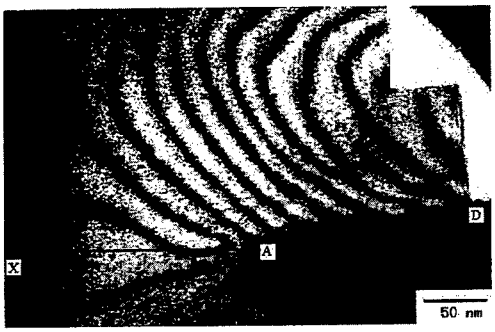


Fig. 1 The fringe pattern without rigid-body rotation mismatch

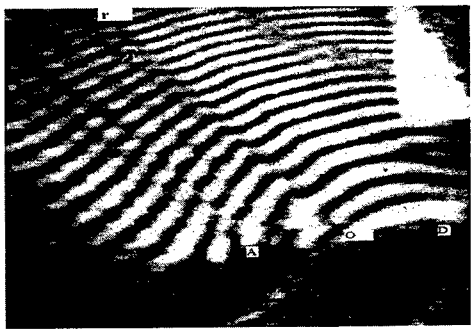


Fig. 2 The fringe pattern with rigid- body rotation(0.011 radian) and constant strain (-0.035) mismatch

grating and lattice image. Fig. 1 is the fringe pattern without rigid-rotation mismatch. The nano-crack was proximately located in the horizontal direction from the point D to the point A. Before loading the crack tip was in the point D. After loading it propagated to the point A. Since the off-plane displacement has a discontinuity along the crack line, which leads to the difficulty of focusing, only fringe pattern upside the crack was obtained. The fringe pattern represents the contour map of the displacement in y-direction, but including initial mismatch fringes due to different initial spacings between lattice image and reference grating.

From the fringe patterns we can observe dislocation emission and distribution along the crack, and obtain the deformation field near the crack tip. There are only a few places where fringe joining or drop happen near the crack line. They correspond to dislocation emissions. Many researchers have observed great amount of dislocation emissions near crack tip in Si. But only a few dislocation emissions were observed here under the propagation of crack under room temperature (T=24.5°C). These dislocations could not move far from the crack but stayed near the crack. The number of dislocation emissions depends on material, temperature, deformation rate and loading method. Before the beginning of unstable propagation of crack, load was exerted very slowly so that a low strain rate in the specimen took place. The low strain rate allowed more dislocations to nucleate and to emit. We can observe more dislocations at the crack start near the point D in the Figure 1. Cleavage fracture occurred after these dislocation emissions. Under the course of unstable propagation of crack, the strain rate became uncontrolled and usually rather high. The dislocation nucleation and emission became much more difficult. Less and less dislocations took place along the crack from the start D to the end A.

Some incomplete dislocations which correspond to some slip traces in about 45°direction with respect to crack, can be observed near the crack end A in Fig. 2. The moiré fringes sheared along these lines. These slip traces are nearly parallel each other. They gives out a fact that crack propagated in step-by-step manner,as illustrated in Fig. 3. Zielinski [7] reported an observation about

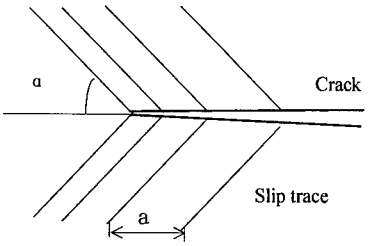


Fig. 3 Schematics of crack growth in step-by-step manner

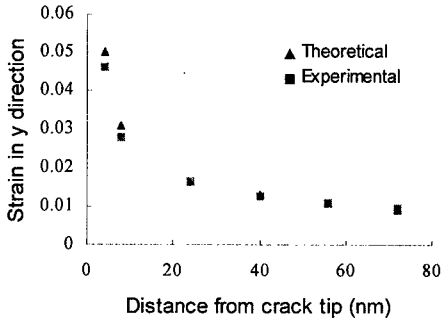


Fig. 4 Strain distribution in y direction ahead of crack tip.

step-by-step crack growth for Fe-2wt%Si and showed that the cleavage crack left 3.5 slip trances of residual dislocations for every 100 nm crack growth, with an average of 18.6 dislocations per trace. Zhu et al [8] defined a a Crack Tip Opening Angle (CTOA) as

$$CTOA = 2\tan^{-1}\frac{nb\sin\alpha}{a} \qquad (1)$$

where b is Burgers vector, n is dislocation number along the slip planes emanating from the current crack tip and then advancing a characteristic distance a by linking a nanocrack formed ahead of it. This expression is based on the assumption of full dislocation emissions along slip plane, omitting the slip deformation caused by incomplete dislocations. When many dislocations emit along the slip plane the slip deformation due to incomplete dislocation is very limited compared with the one due to full dislocations. The omission may be reasonable. In our test, however, only a few dislocations emitted, and no full dislocation took place in some slip planes. The slip due to incomplete dislocation becomes more important and must be considered. We now proceed to establish CTOA expression considering the slip due to both of full dislocations and incomplete dislocation. It can be easily expressed as

$$CTOA = 2\tan^{-1}\frac{nb\sin\alpha + u_i}{a} \qquad (2)$$

Where u_i represents the slip due to incomplete dislocations. It can be determined by numerical analysis and test. The moiré method can be used to determine the parameter CTOA conveniently. From Figure 1, the interval f of fringes nearest crack tip along the crack AD can be measured. Then the CTOA can be calculated as simply

$$CTOA = \frac{b}{f} \qquad (3)$$

Where b is Burgers vector. We obtain that CTOA in this specimen is 0.014 radian.

The strain field near a crack tip plays an important role in affecting failure modes. Thus direct measurement of the strain field distribution ahead of a crack tip would be useful to better understand the microscopic failure mechanism of brittle materials. Up to now all the measurements have been in the macro-mechanics or meso-mechanics range due to the limited resolution of experimental techniques. In this test, the strain distribution in y-direction ahead of the nano-crack tip was obtained from the fringe pattern in Fig. 1, and is shown in square dots in Fig. 4. This strain distribution in y-direction was also calculated by linear elastic fracture mechanics. A comparison between experimental result and theoretical analysis is shown in Fig. 4. The square and triangle dots represent experimental and theoretical values respectively. The experimental strain distribution quite coincides with the strain distribution given by linear elastic fracture mechanics except from the zone very near the crack tip where stress gradient is very steep. It is proved that there exist a zone at the front of crack tip where stresses are controlled by linear elastic fracture mechanics. The failure mechanism of material can be described as cleavage failure after a few dislocation emissions.

The mode of dislocation nucleation is also investigated from the moiré fringe patterns. Two kinds of dislocations can be observed from the fringe pattern. One is located in the right side of Fig. 1. Three dislocations, corresponding to fringe drop and joining, can be observed near the point D. These dislocations belong to common dislocations described by many researchers. The other kind is a special dislocation, a distributed dislocation along the line *or* in Fig. 2. The moiré fringes are sheared along this line. They represent slip between lattice layers. The amount of slip gradually changes along the line *or*. The slip of lattice is zero at the point far from the crack tip and is a Burgers vector at the tip. It is illustrated in Fig. 5. This dislocation has similar structure with the mode based on Peierls' concept described by Rice[3]. This mode was considered largely successful theoretically. However, corresponding experimental results have not been published up to now. This test provides a direct experimental observation.

The range of the slip represents a width of a dislocation, which is of interest by many researchers. In Peierls regime of dislocation nucleation, an analysis of dislocation nucleation from a crack tip was presented based on the Peierls concept as applied to a slip plane emanating from the tip. Shear stress along the slip plane is a periodical function of the amount of slip. Thus Burgers vector produced by

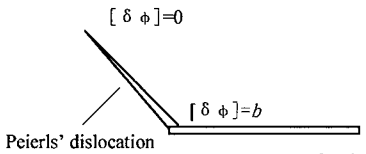


Fig. 5 Schematic of Peierls-mode dislocation

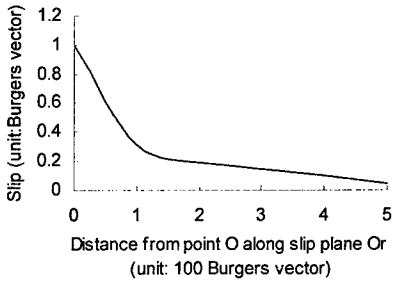


Fig. 6 Slip distribution along a Peierls–mode dislocation

dislocation will distribute on the slip plane rather than concentrate at dislocation core. Rice[3] points out that the width at a crack tip is, at the moment of instability, a moderately broad feature compared to a lattice spacing, thus making more appropriate the use of the Peierls concept. Peierls laments towards that the dislocation core size which he calculated, for an isolated dislocation in an otherwise

perfect lattice, was sufficiently narrow compared to b that the concept of a continuously distributed core displacement, amenable to analysis by continuum elasticity, becomes problematical. The results for nucleation at a crack tip appear to be more favorable.

The core width has also been analyzed by numerical solution. Some such results have been obtained by Beltz and Rice[9] based on a shear stress-slip relation obtained from the Frenkel sinusoid. However, an elementary estimate of the width of the core region can be made in the following inverse manner: since the stress-slip relation rises from u=0 with an initially vertical tangent, matters are simplified by considering model relations $f(u)$ for which u =0 up to a finite value of u_r. In that case the zone of the incipient dislocation, with u >0, will be limited to some finite distance R, to be estimated, ahead of the crack tip. An estimate for value R was given by

$$R = 0.1257\mu b^2 /(1-p)\gamma_{us}$$

Where p is Poison's ratio, r_{us} is unstable stacking energy defined by Rice. For metals r_{us} run from about 0.025 μb to 0.10 μb , this gives (with□=0.3) R□2-7b, a substantial size. For Si, r_{us} =0.42, then, R =4.36b. In our test, the distribution of slip was measured according to moiré fringes in Fig. 2, and shown in Fig. 6. A distribution of u similar to Fig. 5 has been obtained, but the range R is much larger than the value given by Rice. The slip due to a dislocation can extend to about 600 Burgers vectors along the slip plane.

4. CONCLUSION.

HREM Moiré technique used in this study proves to be a very useful tool for measurement of nanoscopic deformation. The results on the crack tip in Si single crystal indicates that a Peierls-mode dislocation nucleation process was observed. A long dislocation extending 600 burgers vectors has been found at the crack tip and the slip distribution along crack tip was measured. This distributed dislocation has similar slip structure to the one based on Peierls concept described by Rice, but has much longer slip range. The nanoscopic strain distribution near the crack tip has been obtained. A strain field controlled by linear elastic fracture mechanics ahead of crack tip exists.

ACKNOWLEDGEMENT

This paper has been supported by National Natural Science Foundation of China (19962001).

REFERENCE

1 Y. M. Xing, F. L. Dai and H. M. Xie, The proceedings of 9th National Conference of Experimental Mechanics, Guangzhou, China(1997).
2 F. L. Dai and Y. M. Xing, ACTA MECHANICA SINICA, **15**(1999), p.283
3 Rice, J.R..,J. Mech. Phys Solids, **40** (1992), p.239.
4 Rice, J. R., Thomson, R., Phil. Mag., **29** (1974), p.:73.
5 Argon, A. S., Acta Metall., **35**(1987), p.185.
6 Ohr, S. M., Mater. Sci. Eng., **1**(1985), p.72
7 W. Zielinski, M. J. Lii and W.W.Gerberich, Acta Metall. Mater. **40**(1992), p.2861
8 T. Zhu, W. Yang and T. Guo, Acta mater., **44**(1996), p.3049
9 G. E. Beltz and J. R. Rice, Acta Metall. Mater., **40**(1992), p.321

Key Engineering Materials Vols. 183-187 (2000) pp. 743-748
© 2000 Trans Tech Publications, Switzerland

Effect of Contact Shape on the Cracking Behaviour

Hyung-Kyu Kim and Heung-Seok Kang

Korea Atomic Energy Research Institute,
150 Dukjin-dong, Yusung, Taejon 305-353, Korea

Keywords: Contact Failure, Crack Closure, Crack Opening Period, Edge Cracks, Fretting, Partial Slip, Punch Shape, Stress Intensity Factor

ABSTRACT

This paper primarily examines the shape of the indenter which can restrain the crack growth in the other body indented. For the shape of the contacting bodies, a punch with rounded apex indenting a half plane is considered as an indenter and the indented body respectively. Partial slip condition is assumed on the contact. Since the contact failure is due to the cyclic shear on the contact, the behaviour of shear traction as well as the boundary of stick and slip regions is examined during the cycle. For analyzing the edge crack, the dislocation density function method is adopted to calculate stress intensity factors (SIFs). The period of crack opening as well as the crack closure during the shear cycle are discussed. Suggestible punch shape for failure-resistance is discussed.

1. INTRODUCTION

In many mechanical components and structures subjected to contact load, it has been widely found that cracks initiate at the vicinity of the contact edges. Press fits, gears, splines and wire popes are usually referred to as the examples, but not limited to them, those can also be extended to some of the nuclear components such as fuel rods, guide thimbles of fuel assembly and U-tubes of steam generators. The velocity of the edge crack is much higher than that of the ordinary fatigue cracking without the contact load, which causes the premature failure of the components and the structures. It is, therefore, important to analyze the edge crack to study and even further to restrain the failure.

The contact loading is usually exerted as a fatigue so that a relative motion of small amplitude is constituted between the contacting bodies. The fatigue phenomenon referred is either the vibratory motion of the contacting body (or bodies) or the far field fatigue loading to it. Fretting fatigue and fretting wear are usually termed as the failure. Due to the contact load, normal and shear tractions are to be formed on the contact surface. To analyze the crack, it is compulsory to evaluate the stresses in the contacting bodies (internal stresses). And, the internal stresses cannot be obtained without knowing the contact tractions. In short, the very first step to investigating the failure phenomena due to contact is obtaining the contact tractions.

In fretting fatigue, the cracking behaviour may well be the first concern [1,2]. In fretting wear,

on the other hand, the cracking behaviour can be used for simulating the wear particle formation. So to speak, the detachment of wear particles may be explained to occur when an edge crack grows and changes direction to the proximate surface. 'The delamination theory of wear' [3] explains that a buried crack parallel to the surface (subsurface crack) grows to form the wear particle. The theory was brought into focus since it was a new approach to explain wear phenomenon by the fracture mechanics. However, it has been often experienced that the edge crack started to grow from the fretted surface in the case of fretting wear as well. So, it is thought here that the analysis of the edge crack subjected to normal and shear tractions can provide an intrinsic approach to the contact failure. This approach has been done, in the case of Hertzian contact, for nuclear fuel fretting problems [4].

In this paper, the approach is extended to further general contact shape. So, a punch with rounded apex is used as the model of contacting body (indenter). As for the contact shear force, partial slip regime is considered not only because it can represent the actual contact condition, but because it can be readily extended mathematically to the gross slip regime. Since the contact load is applied as a fatigue as aforementioned, the behaviour of the edge crack under the cyclic shear is investigated in detail. The final goal of the present subject is to obtain the contact-related parametric values, which can restrain the failure. To this end, this paper concerns the shape of the contacting body (the indenter specifically) primarily, which may be used for the mechanical design of the contacting components in the mechanical industry.

2. ANALYSIS

2.1. Contact Tractions

Fig. 1 shows the geometrical configuration of the present analysis. L is the width, l is the length of the flat region and R is the radius of the apex. Both apexes are assumed to have the same radius and full R's (i.e., $L = l + 2R$). The punch width is fixed constant in the analysis, therefore, the difference of the punch shape is due to that of the radius of the apex only (or the length of the flat region). The length of the punch is regarded as long enough compared with the width to apply the plane strain condition. As for the crack initiated from the contact edge, a is the length, θ is the obliquity of the crack, measured perpendicular to the contact surface. When a contact normal force P is applied by pressing the punch into the half plane, the contact patch will have a certain width due to the deformation of the punch as well as the half plane. The contact width, designated w in Fig. 1, depends on P and the flat region of the punch (or the radius of the apex). When P is fixed constant, the effect of the rounded apex on the normal traction $p(x)$ is given in Fig. 2. $p(x)$ is non-dimensionalized with respect to p_o ($p_o = P/L$). The sharper peak is obtained as the radius decreases, but the traction values increases since the contact width decreases.

In general, the clamping force (i.e., contact normal force) between the contacting bodies is sound at the beginning, so the relative displacement is likely to be very small, as is the shear force. This often constitutes the condition of partial slip. In the case of partial slip, the shear force applied to the contacting bodies is less than that causes a gross slip of the bodies (i.e., $Q < \mu P$, where Q and μ are the shear force and the static friction coefficient respectively). If the clamping loosens or the shear force increases, the contacting bodies slide over each other, which is the gross slip. It is likely that the partial slip begins at the beginning and moves to the gross slip condition later between the contacting bodies. In this paper, the partial slip is dealt with for the contact analysis since it is important to study the early stage of the failure.

To evaluate the contact tractions in a closed form, coupled singular integral equations are used

[5]. However, it is often impossible to evaluate the integral analytically, especially when one of the tractions (usually normal traction) is not defined as a well-formed function. Even though it (normal traction) can be obtained analytically, numerical procedure is much more helpful for the solution if the shear force direction changes sequentially [6]. It can describe the irreversibility of the shear traction easily and provide more flexible choice of the crack initiation location. The essential idea of the numerical method is to use the equally based and overlapped triangular traction elements, which cover the contact width. By applying the displacement as well as the traction boundary conditions, the height of each element is to be evaluated, which is unknown *a prioi*. The details of the method can be consulted in previous issues [6-8]. In the present analysis, the numerical procedure is followed to obtain the shear traction even though the normal traction of the rounded punch with rounded apex is known analytically [9], because it is a rather complicated function to be integrated. The influence of the apex radius on the normal traction is given in Fig. 2. When the normal and the shear tractions are obtained, internal stresses can be readily calculated using the Flamant potential approach [10].

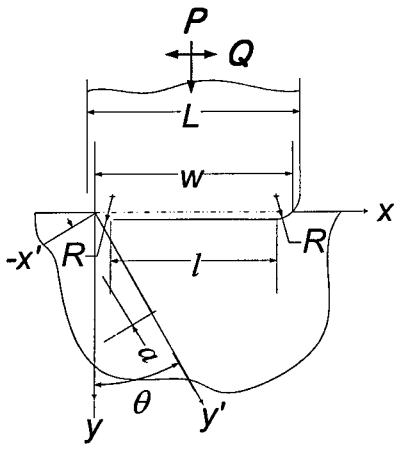


Fig. 1 Geometry of present problem.

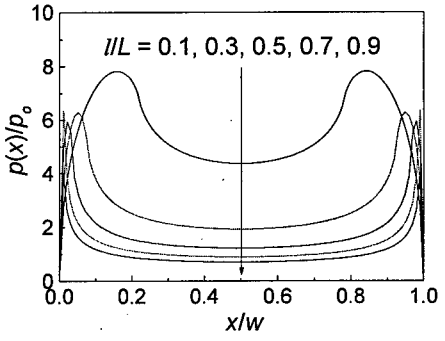


Fig. 2 Contact normal traction profiles.

2.2. Stress Intensity Factors

The dislocation density function method is adopted for evaluating the SIFs, where the crack is assumed as a continuous distribution of edge dislocations (i.e., fictitious dislocations). K_I and K_{II} are to be obtained finally since it is the mixed mode crack problem that consists of opening and in-plane shear. The details of the method can be consulted by some previous issues [2,11], only some key equations are shown here. Fig. 1 can be decomposed into two independent cases: the cracked body without contact tractions and the un-cracked body with tractions. The stresses for each case can be summed linearly, which is the well-known Bueckner theorem [12]. The stresses on the crack should be zero (traction free) , which yield the following simultaneous equations.

$$\sigma_{x'x'}{}^{D} + \sigma_{x'x'}{}^{C} = 0, \quad \tau_{x'y'}{}^{D} + \tau_{x'y'}{}^{C} = 0 \quad \text{(1a,b)}$$

where, the superscripts D and C designate the stresses on the crack line due to the fictitious dislocations and contact tractions respectively. Eq. 1a (the former) is for Mode I (K_I), while Eq. 1b

(the latter) for Mode II (K_{II}) cracking (see the coordinates in Fig. 1).

Eqs. 1a and 1b are the Cauchy type singular integral equations. By mathematical manipulation, those have the form of

$$\frac{1}{\pi}\int_{-1}^{1}\frac{B_i(u)}{u-v}du+\int_{-1}^{1}B_i(u)\overline{K}_i(v,u)du=f_i(v), \qquad (-1\le v\le 1;\quad i=x' \text{ or } y') \quad (2)$$

where, the integral terms are constituted from $\sigma_{x'x'}{}^{D}$ and $\tau_{x'y'}{}^{D}$, and $B_i(u)$ is the dislocation density function to be determined. $\overline{K}_i(v,u)$ is the non singular kernel and $f_i(v)$ are the terms yielded by $\sigma_{x'x'}{}^{C}$ and $\tau_{x'y'}{}^{C}$.

To solve the Eqs. 1a and 1b, a numerical method using the Jacobi polynomial is consulted [13]. By replacing $B_i(u)$ with the multiplication of a weight function ($\sqrt{(1+u)/(1-u)}$ for the edge crack) and a bounded function $\Psi_i(u)$. SIFs are to be evaluated by obtaining $\Psi_i(1)$, the values of $\Psi_i(u)$ at the crack tip, which can be achieved by using a polynomial approach [14]. Consequently,

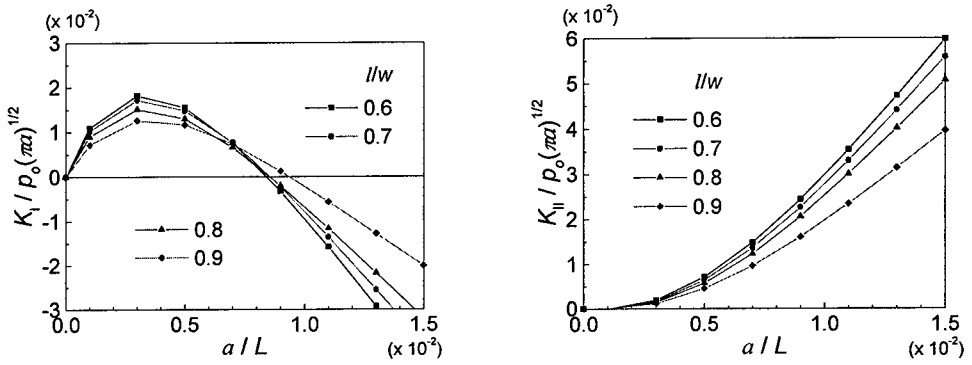
$$K_I=\frac{2\sqrt{2}G}{(1+\kappa)}\sqrt{\pi a}\Psi_{x'}(1) \quad \text{and} \quad K_{II}=\frac{2\sqrt{2}G}{(1+\kappa)}\sqrt{\pi a}\Psi_{y'}(1) \quad (3a,b)$$

where, G is the shear modulus of the half plane, $\kappa=(3-4\nu)$ in plane strain and a is the crack length.

3. RESULTS AND DISCUSSIONS

In Figs. 3a and 3b, the influence of the punch shape (l/w) on the SIFs are shown when $\theta=0°$. The candidate values of l/w is chosen as 0.6 ~ 0.9 since it has been recently found that the punch can possibly restrain the crack growth when l/w is between 0.56 and 0.95 [15]. The evaluated $Q/\mu P$ for the l/w's is 0.61 ~ 0.66. The SIFs is non-dimensionalized with respect to $p_o\sqrt{\pi a}$ and μ is 0.3 in this paper. K_I increases after the crack initiates and reaches a maximum, then it decreases, as the crack grows further. The crack length up to the occurrence of crack closure can be compared with each other punch shape since, if K_I is less than zero, the crack is regarded to be closed. It is shorter as l/w becomes smaller. But the largest maximum of K_I is revealed when l/w = 0.6. However, K_{II} increases continuously as the crack grows. This result is not altered if the crack obliquity (θ) is varied. Only K_{II}/K_I increases as θ increases. The failure by the crack growth may be restrained if the crack closure happens earlier. A crack grows more slowly if the SIFs are smaller when the Paris equation is adopted. Accordingly, the punch shape of restraining the cracking seems to exist when l/w is between 0.8 and 0.9 (l/L = 0.234 and 0.397 respectively) among the results in Fig. 3.

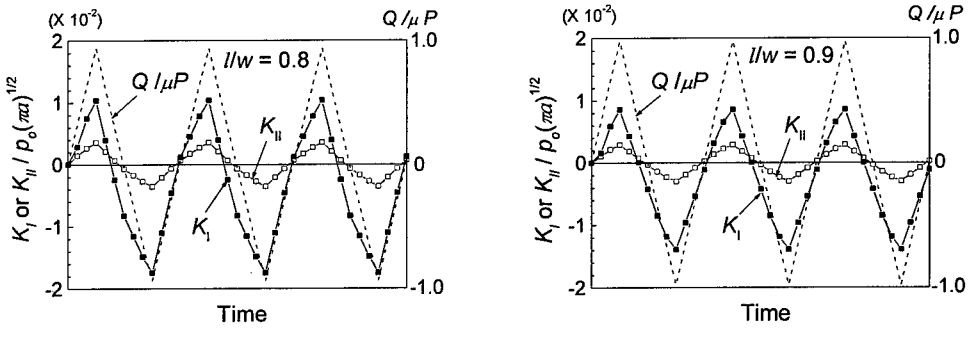
Contact failure happens when the surface shear is applied cyclically in general. The behaviour of the SIFs during the shear cycle is, therefore, worth investigating to pick up the desired punch shape against failure. This is carried out for the above two l/w values, 0.8 and 0.9. It is seen that the SIFs fluctuates following the shear cycle in Figs. 4a and 4b where a/L = 0.001 is used for the crack length and 30° for θ. It seems that the two punch shapes give almost the same behaviour of SIFs. As experienced previously [15], the punch shape does not affect the crack opening period, i.e. the period of positive K_I during the cycle. The only possible parameter for discrimination may be the actual value of SIFs. The punch of l/w = 0.9 is found to have the smaller SIFs, so it is regarded to



(a) (b)

Fig. 3 Effect of apex radius on the stress intensity factors; (a) K_I and (b) K_{II}.

have better resistibility against contact failure than the others in the present analysis, especially in the very early stage of cracking (i.e., when $a/L = 0.001$). A crack grows as the cycle continues. So the results in Figs. 4a and 4b may be regarded as the behaviour during a short period of time since a constant crack length is used. When the crack grows to be longer than $a/L \approx 0.6$ (the cross point of $l/w = 0.8$ and 0.9), the punch of $l/w = 0.8$ is thought to have the better resistibility against the failure. It may be true to pick up the shape, which can restrain the cracking even further, more calculations are needed with finer steps. However, it can be said here that the punch having the flat region of about 23 ~ 40% to the width is suggestible for restraining the cracking failure on the contact.



(a) (b)

Fig. 4 Effect of apex radius on the behaviour of SIFs (a) at $l/w = 0.8$ and (b) at $l/w = 0.9$.

In addition, some interesting features are found during the shear cycle. Firstly, the steady state of the SIFs is reached from the second cycle. It implies that the internal stresses in the half plane during the first cycle are different from those from the second cycle. This is also the feature of the contact tractions [6], which enables the present analysis to be worth. This is because it would be almost impossible to obtain every value of the tractions (internal stresses and SIFs as well) if those vary continuously following the cycle. Secondly, The phase of the shear cycle is not coincident with

that of the SIFs cycle. It is found shifted to the left when *l/w* is smaller, which has already been previously found [15].

4. CONCLUSIONS

An edge crack is analyzed here using the theory of contact mechanics to study the failure induced by contacting. The radius of punch apex (or the length of flat portion) is investigated to find out the desired punch shape to restrain crack growth. From tentative calculations, it can be accomplished when the ratio of the flat portion to the punch width (*l/L*) is in the range of 0.234 ~ 0.397. As *l/L* increases inside the range, the stress intensity factors decrease, but the crack length up to the occurrence of crack closure increases. Calculations with finer steps are required, therefore, to pick up a definite *l/L* desired for restraining the failure. However, for the time being, it is concluded that failure by cracking can be restrained when a punch has the flat region of about 25 ~ 35% to the width.

ACKNOWLEDGEMENT

This project has been carried out under the Nuclear R&D Program by MOST.

REFERENCE

1. P.R. Edwards, The Application of Fracture Mechanics to Predicting Fretting Fatigue, in Fretting Fatigue, R.B. Waterhouse ed., Applied Science Publishers Ltd., London, U.K., (1981) Chapter 3.
2. H.-K. Kim and S.-B. Lee, Theo. Appl. Fract. Mech., **25** (1996) p. 147.
3. N.P. Suh, Wear, 44 (1977) p. 1.
4. H.-K. Kim et al., Korean Nuclear Society Conf. Spring '99, Korea, Pohang (1999) Paper No. 270 in Div. 5E.
5. D.A. Hills, D. Nowell and A. Sackfield, Mechanics of Elastic Contacts, Butterworth-Heinemann Ltd., Oxford, U.K., (1993) p. 49.
6. H.-K. Kim, D.A. Hills and D. Nowell, Int. J. Mech. Sci., **42** (2000) p. 199 (in print).
7. D. Nowell and D.A. Hills, Int. J. Solids Struct., **24** (1988) p. 105.
8. R.H. Bentall and K.L. Johnson, Int. J. Mech. Sci. **10** (1968) p. 637.
9. M. Ciavarella, D.A. Hills and G. Monno, Proc. Instn Mech. Engrs. Part C, **212** (1998) p.319.
10. K.L. Johnson, Contact mechanics, Cambridge University Press, Cambridge, U.K. (1985), p. 19.
11. D. Nowell and D.A. Hills, J. Strain Analysis, **22** (1987) p. 177.
12. H.F. Bueckner, J. Applied Mechanics, 80 (1958) p. 1225.
13. F. Erdogan, G.D. Gupta and T.S. Cook, Numerical solution of singular integral equations, in: Methods of analysis and solutions of crack problems, G.C. Sih ed., Noordhoff International Publishing, Leiden (1973) Chapter 7.
14. S. Krenk, Quart. Appl. Maths., 32 (1975) p. 479.
15. H.-K. Kim and Y.-H. Jung, Engng Fract. Mech., Submitted.

Key Engineering Materials Vols. 183-187 (2000) pp. 749-754
© 2000 Trans Tech Publications, Switzerland

Study of Fracture Origin on Low Cycle Fatigue of Spheroidal Graphite Cast Iron Having Various Matrixes

K. Morino[1], F. Nishimura[1] and H. Nisitani[2]

[1] Department of Mechanical and Electrical Engineering, Tokuyama College of Technology, 3538 Takajo, Kume, Tokuyama, Yamaguchi 745-8585, Japan

[2] Department of Mechanical Engineering, Kyushu Sangyo University, 2-3-1 Matsukadai, Higashi-ku, Fukuoka 813-8503, Japan

Keywords: Blind Hole, Cylindrical Specimen, Fatigue, Fracture Origin, Low Cycle Fatigue, Microshrinkage, SEM, Spheroidal Graphite Cast Iron

ABSTRACT

In this study, in order to specify the kind of defects in fracture origin, low cycle fatigue tests were carried out using cylindrical specimens of three kinds of spheroidal graphite cast iron (ferritic, pearlitic and austempered). The fracture origin was investigated by observing the fracture section. Moreover, in order to clarify the mechanical severity of microshrinkages, the specimen with a small blind hole is used. The main results obtained are as follows: (1) In the materials used in this study, fracture always starts from the microshrinkages that exist on the neighboring surface over the whole plastic strain range. (2) There is no precise relation between the fatigue life and the shape of microshrinkages observed on the fracture section. (3) As to all SGI with a small blind hole, the depth of which equals to the diameter, when the diameter gets more than 0.4mm, SGI always breaks at a hole. However, when a hole with less than 0.2mm diameter, the fracture starts from the microshrinkages.

1. INTRODUCTION

In our previous paper [1], we proposed three factors which control low cycle fatigue life. Among them, the crack initiation length is the most important one, which is the crack length obtained by fitting a straight line to the crack growth curve and extrapolating it to N=0. Since the fracture starts from defects included in the material, crack initiation length of the material with large defects is larger than that of matrix material, and the fatigue life becomes shorter. So, many studies on fracture origin have been carried out [1]. In the case of spheroidal graphite cast iron, it is already known that the fracture on high cycle fatigue starts from microshrinkages [1]. For fracture origin on low cycle fatigue, different results are reported [2] ~ [6]. On the other hand, we have indicated that fracture origin of the material with large defects differ according to the shapes of specimens [1]. In the other experiments, hourglass specimens have been used [2] ~ [6]. To our knowledge, there are no investigation on the details of defects on fracture origin in spheroidal graphite cast iron. So, in this study, in order to know the true fracture origin in spheroidal graphite cast iron, plastic-strain controlled low cycle fatigue tests were carried out using cylindrical specimens. As materials, spheroidal graphite cast iron which had three kinds of matrixes were used. Fracture section is observed by using SEM. Moreover, in order to clarify the mechanical severity of microshrinkages, the specimen with a small blind hole was used.

2. MATERIALS, SPECIMENS AND EXPERIMENTAL PROCEDURES

Spheroidal graphite cast iron (SGI) used in this study are ferritic (FDI), pearlitic (PDI) and austempered (ADI). ADI was austenitized at 1163K for 4 hours and then austempered at 633K for 2 hours. The chemical composition and mechanical properties are shown in Table 1 and 2 respectively. Table 3 shows some characteristics of spheroidal graphite which are measured by the image processing analysis technique. The threshold value of graphite is 12μm.

Figure 1 shows the shape and dimension of the specimen. In this study, cylindrical specimens were used. The diameter d_0 and length l_0 of the central part are 6mm and 9mm respectively. The aspect ratio l_0/d_0 of the central part is decided on 1.5 to obtain the true fatigue behavior [7]. The specimens were finished with diamond paste.

Fatigue tests were carried out using a hydraulic servo testing machine with a capacity of 49kN and frequency ranging from 0.03 to 0.1Hz. Strain was measured by an axial direction extensometer and the machine was set in such a way that the plastic strain range is constant. SEM was used to observe fractured sections.

3. EXPERIMENTAL RESULTS AND DISCUSSION

Figure 2 shows the relation between the plastic strain range $\Delta\varepsilon_p$ and the number of cycles to failure N_f obtained for FDI, PDI and ADI. The plastic strain range $\Delta\varepsilon_p$ was changed from 0.001 to 0.04. These experimental data satisfy the following Manson-Coffin law.

$$\Delta\varepsilon_p \cdot N_f^{0.61} = 0.207 \quad \text{(FDI)} \tag{1}$$
$$\Delta\varepsilon_p \cdot N_f^{0.59} = 0.157 \quad \text{(PDI)} \tag{2}$$
$$\Delta\varepsilon_p \cdot N_f^{0.56} = 0.109 \quad \text{(ADI)} \tag{3}$$

The fatigue life in ADI is a little shorter than that in other cast iron. In this figure, $2\varepsilon_f$ (ε_f : fracture

Table 1 Chemical composition [wt. %]

	C	Si	Mn	P	S	Mg	Cu
FDI	3.83	2.25	0.34	0.023	0.014	0.034	0.05
PDI	3.68	2.07	0.355	0.021	0.007	0.038	0.599
ADI	3.64	2.04	0.33	0.026	0.009	0.034	0.59

Table 2 Mechanical properties [MPa, %]

	$\sigma_{0.2}$	σ_B	ψ	E	H_B
FDI	309	434	19.1	166x10³	144
PDI	463	813	6.6	166x10³	259
ADI	835	1085	9.2	171x10³	336

ψ : Reduction of area

Table 3 Characteristitics of spheroidal graphite

	D_m (μm)	n_g (1/mm²)	f_g (%)	h_g (%)
FDI	24.6	180	8.81	75.4
PDI	28.9	131	8.38	81.2
ADI	22.6	168	7.18	75.0

D_m : Average graphite diameter n_g : Nodule count
f_g : Area fraction of graphite h_g : Nodularity

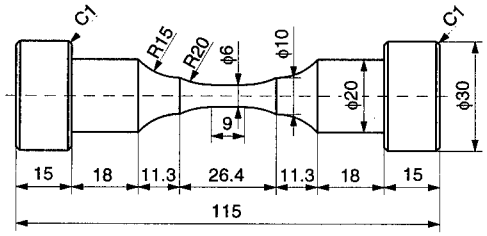


Fig.1 Shape and dimension of specimen

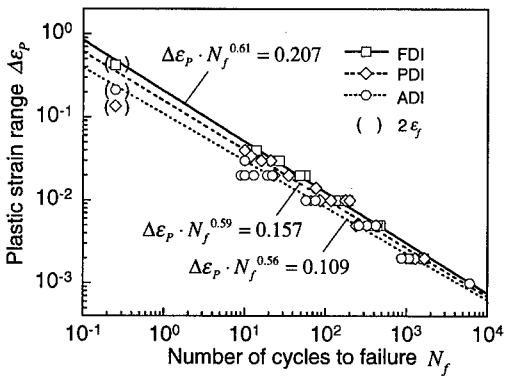


Fig.2 Low cycle fatigue life curves in FDI, PDI and ADI

ductility) is plotted at the number of 1/4 cycle. From Fig. 2, it can be stated that the difference in fatigue life of these spheroidal graphite cast iron is small and that the difference in fracture ductility ε_f does not reflect the fatigue life.

Figure 3 shows a schematic illustration of crack growth curve in the material which following small crack growth law is applicable.

$$\frac{dl}{dN} = C\sigma_a{}^n \cdot l \tag{4}$$

In this case, ln l is almost directly proportional to N from the initiation of crack to the fracture. When the straight line is fitted to crack growth curve and the crack lengths at N=0 and N=N_f are given as l_0^* and l_f^* respectively, the fatigue life N_f is represented as following equation.

$$N_f \cong \ln\frac{l_f^*}{l_0^*} / C\sigma_a{}^n \tag{5}$$

From Eqs. (5) and (4), fatigue life N_f is rewritten as follows:

$$N_f = \ln\frac{l_f^*}{l_0^*}\frac{1}{\left(\frac{dl/dN}{l}\right)} \tag{6}$$

Therefore, for the material in which most of its fatigue life is consumed by the growth of a small crack, except in a special case, the fatigue life is controlled by three factors.

- Crack initiation length : l_0^*
- Crack propagation limit length : l_f^*
- Relative crack growth rate : $(dl/dN)/l$.

Here, these three factors can be considered as three constants [1]. Therefore, various phenomena can be rationally explained by using these three factors.

In general, it is assumed that crack initiation length of the material with defects is larger than that of matrix material because the fracture starts from defects. It has been considered that, on low cycle fatigue in spheroidal graphite cast iron, the fracture origin differs with the material used and the researchers conducting the study [1]. In previous papers [1][8][9], we clarify that the fracture in spheroidal graphite cast iron starts from the microshrinkages. We also clarify that fracture origin differs with a relative size of the microshrinkages and spheroidal graphite [6]. Then, we observed the fracture section by using SEM in order to specify the kind of defects in fracture origin.

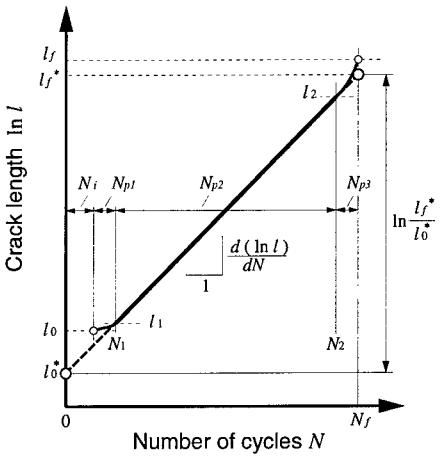


Fig.3 Schematic illustration of crack growth curve

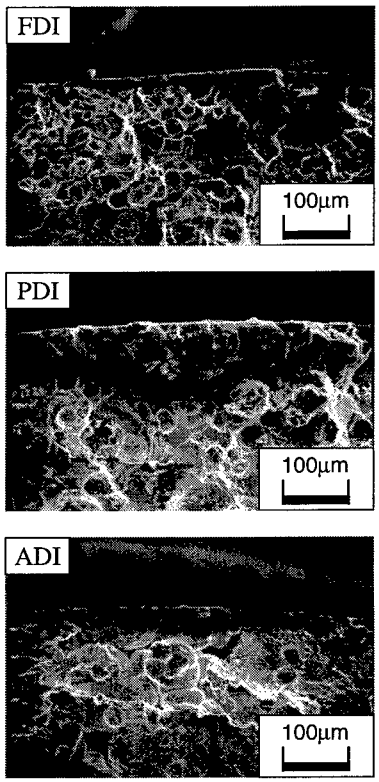


Fig.4 Observation of fracture origin ($\Delta\varepsilon_p$=0.005)

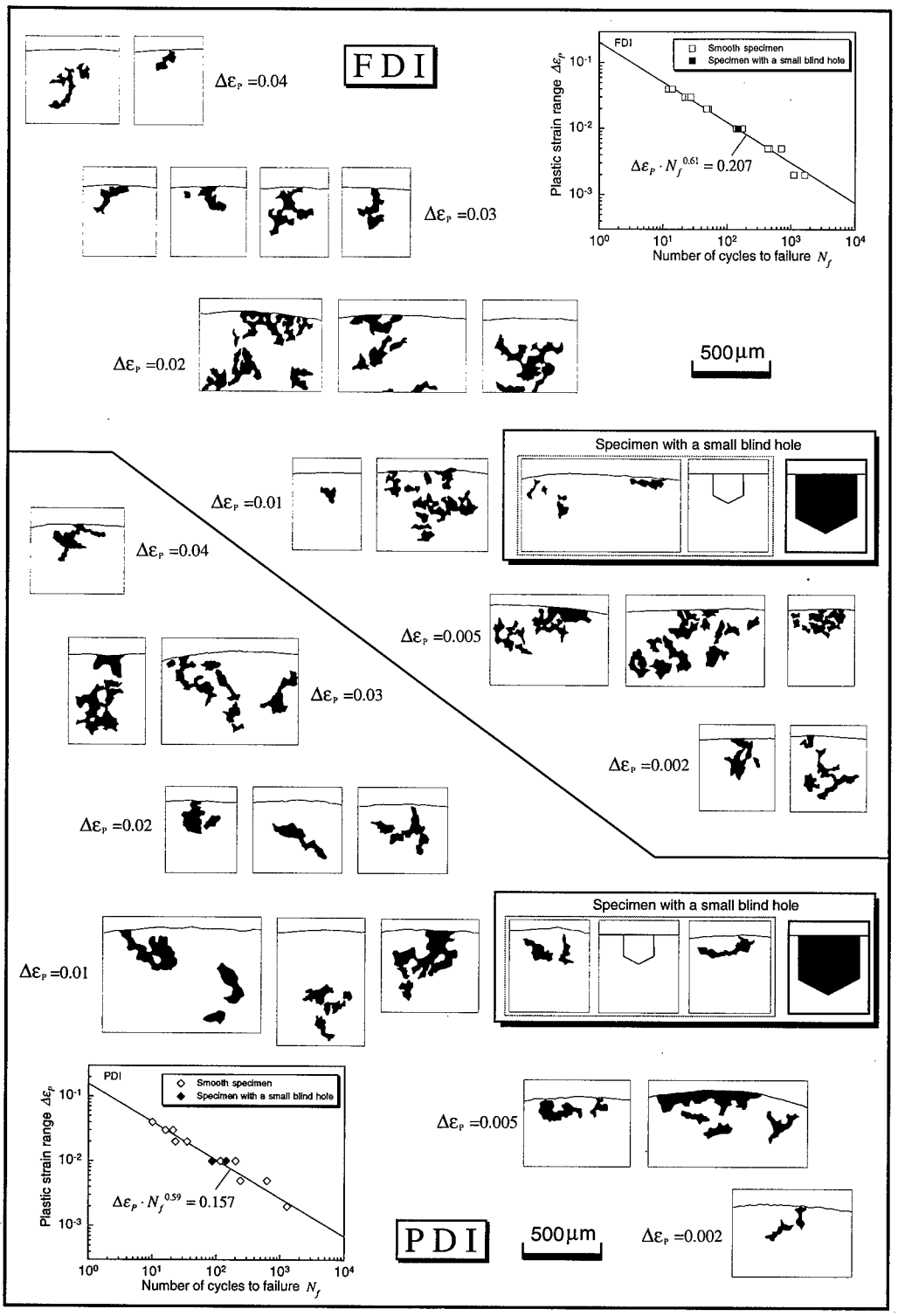


Fig.5-1 Shape of microshrinkages on fracture section observed in the neighborhood of fracture origin

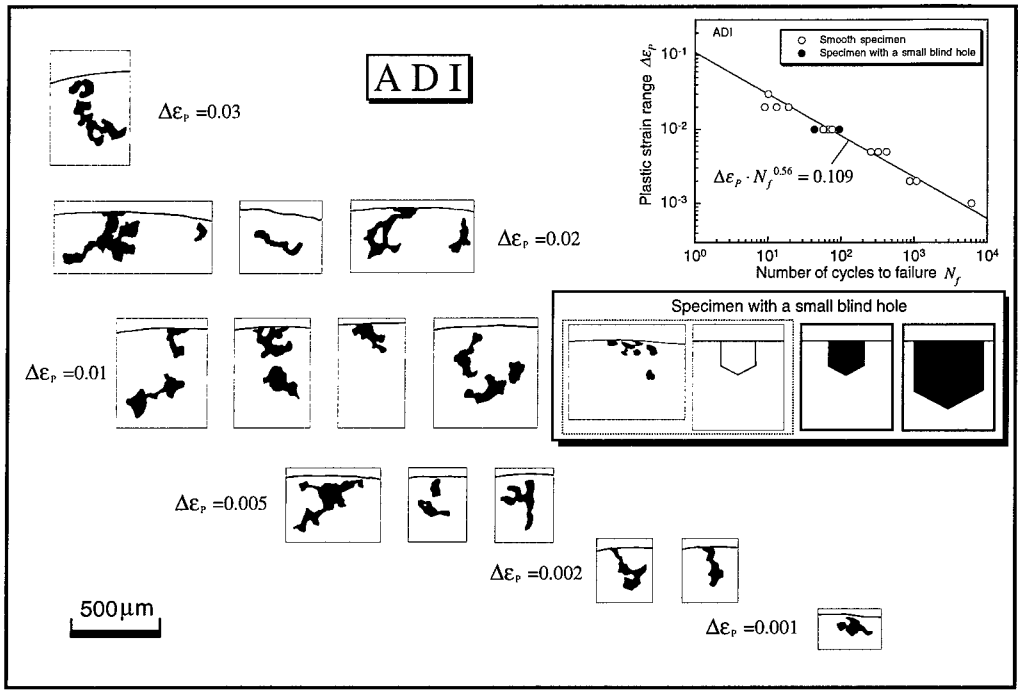


Fig.5-2 Shape of microshrinkages on fracture section observed in the neighborhood of fracture origin

Figure 4 shows SEM micrographs of fracture origin in FDI, PDI and ADI ($\Delta\varepsilon_p$ = 0.005). The main crack initiates from the microshrinkages that exists on the neighboring surface over the whole plastic strain range. In the materials used in this study, fracture did not start from graphite.

Figure 5-1 and 5-2 show the shape of microshrinkages on fracture section observed in the neighborhood of fracture origin. The each shown position of microshrinkages corresponds to the relation of fatigue life in the fatigue life curve. As seen from figures, microshrinkages exist on the neighboring surface over the all specimens. The length of microshrinkages projected on the surface ranges from 100μm to 800μm. Also, there was no precise relation between the plastic strain range and the size of microshrinkages. Moreover, various matrixes did not effect to these results.

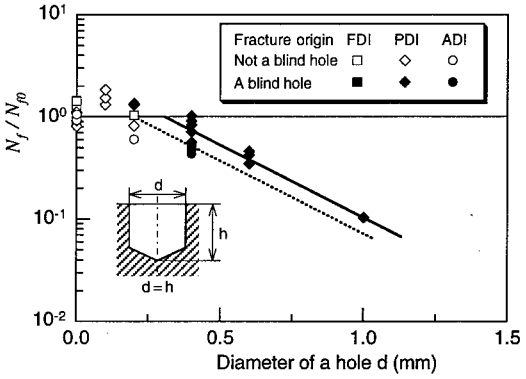


Fig.6 Variation of fatigue life with a small blind hole ($\Delta\varepsilon_p$ = 0.01)

In these figures, the microshrinkages are indicated from left to right in the order of increasing fatigue life. In these materials, the length and the depth of microshrinkages are ample in variation. Then, from two-dimensional point of view, it is concluded that there is no precise relation between the fatigue life and the shape of microshrinkages observed on the fracture section. So, to model the microshrinkages, we drilled a small blind hole (the depth of it equals to the diameter) on the central part of the specimen, and we examined fatigue tests using its specimens in order to clarify the mechanical

severity of microshrinkages. Figure 6 shows the variation of fatigue life in the specimens with a small blind hole ($\Delta\varepsilon_p$=0.01). The diameters of a small blind hole are changed from 0.1mm to 1.0mm. When the diameter gets more than 0.4mm, Spheroidal graphite cast iron always broke at a hole. However, a hole with less than 0.2mm diameter had no effect, the fracture did not start from a small blind hole.

Fig. 5-1 and 5-2 indicate the observed results of fracture origin in the specimens with a hole of 0.2mm diameter. In some of these specimens, fracture starts from the microshrinkages exists on the neighboring surface. The length of microshrinkages projected on the surface was about 300μm. So, it became clear that the mechanical severity of microshrinkage is larger than that of a small blind hole with 0.2mm diameter, and smaller than that of a hole with 0.4mm diameter. This result is consistent with the size of microshrinkages observed in the neighborhood of fracture origin on the fracture section.

Finally, in the materials used in this study, it became clear that the fracture always starts from the microshrinkages that exists on the neighboring surface regardless of the difference of matrix. Also, the mechanical severity of microshrinkages was clarified. However, from two-dimensional point of view, there was no precise relation between the fatigue life and the shape of microshrinkages observed on the fracture section. Then, in order to clarify the relation between the crack initiation length and the microshrinkages, consideration from three-dimensional point of view will be needed.

4. CONCLUSIONS

In order to specify the kind of defects in fracture origin, low cycle fatigue tests were carried out using cylindrical specimens of three kinds of spheroidal graphite cast iron (ferritic, pearlitic and austempered). The fracture origin was investigated by observing the fracture section. The main results obtained are as follows:

(1) In the materials used in this study, fracture always starts from the microshrinkages that exist on the neighboring surface over the whole plastic strain range.
(2) There is no precise relation between the fatigue life and the shape of microshrinkages observed on the fracture section.
(3) As to all SGI with a small blind hole, the depth of which equals to the diameter, when the diameter gets more than 0.4mm, SGI always breaks at a hole. However, when a hole with less than 0.2mm diameter, the fracture starts from the microshrinkages.

REFERENCES

1. K. Morino et al., JSME Int. J., Ser. A, **41**-2, (1998), 243-251.
2. S. Adachi et al., Trans. Jpn. Soc. Mech. Eng., **59**-558, A (1993), 291-296.
3. S. Harada et al., Trans. Jpn. Soc. Mech. Eng., **58**-552, A (1992), 1306-1312.
4. S. Harada et al., Trans. Jpn. Soc. Mech. Eng., **58**-552, A (1992), 1306-1312.
5. S. Harada et al., Trans. Jpn. Soc. Mech. Eng., **60**-572, A (1994), 952-959.
6. Y. Kuroshima et al., Trans. Jpn. Soc. Mech. Eng., **61**-584, A (1995), 705-710.
7. K. Morino et al., Trans. Jpn. Soc. Mech. Eng., **60**-571, A (1994), 682-689.
8. K. Morino et al., Trans. Jpn. Soc. Mech. Eng., **61**-589, A (1995), 2003-2008.
9. K. Morino et al., Trans. Jpn. Soc. Mech. Eng., **64**-625, A (1998), 2320-2325.

Key Engineering Materials Vols. 183-187 (2000) pp. 755-760
© 2000 Trans Tech Publications, Switzerland

The Propagation Behavior of Love Waves in a Pre-stressed Piezoelectric Layered Structure

F. Jin, Z.K. Wang and T.J. Wang

Department of Engineering Mechanics, Xi'an Jiaotong University, Xi'an 710049, China P.R.

Keywords: Initial Stress, Love Waves, Phase Velocity, Piezoelectric Layered Structures, Surface Acoustic Wave Devices

ABSTRACT

It is well known that due to the mismatch of the material properties there exists residual stress during the manufacture process of piezoelectric surface acoustic wave devices. On the other hand, to prevent the piezoelectric material from fragile fracture, the piezoelectric layered structures are usually pre-stressed during the manufacture process. In order to enable the electric excitation of the Love waves, a piezoelectric material can be chosen as substrate of the layered structures. The propagation of Love wave in a layered piezoelectric half-space with initial stress is taken into account in this paper, where a thin elastic film as the guiding layer is in intimate contact with a piezoelectric substrate. The phase velocity equations of Love wave propagation are obtained for electrical open and shorted cases at the free surface, respectively. It is seen that the phase velocity of Love wave decreases and the electromechanical coupling factor increases remarkably as the absolute value of initial stress is greater than 100 MPa. The results obtained in this paper are meaningful for the design of high quality surface acoustic wave (SAW) devices in the microwave technology.

1. INTRODUCTION

Love wave sensors are highly sensitive microacoustic devices, due to the acoustic energy concentration within a few wavelengths near the surface. Such a kind of device is particularly suitable for the measurement of mass density, viscosity and electro-acoustic properties of liquids [1,2]. Jakoby and Vellekoop [3] have presented a review on the properties of Love waves and their applications to sensor devices. The basic configuration supporting the propagation of Love waves consists of a layer that is deposited on a substrate. In the simplest case, guiding layer as well as substrate are isotropic media. To enable the electric excitation of the Love waves, the piezoelectric media is involved in the structures, i.e. the so-called piezoelectric layered structures. Up to now, there are two kind configurations of Love wave sensors that have been put into practical applications for the piezoelectric layered structures: the first configuration is the layer/substrate system with piezoelectric material as the layer and non-piezoelectric material as the substrate; the second is on the contrary. It is well known that due to the mismatch of the material properties, there unavoidably exists residual stress during the manufacture process of piezoelectric surface acoustic

wave devices. On the other hand, to prevent the piezoelectric material from fragile fracture, the piezoelectric layered structures are usually pre-stressed during the manufacture process. To the author's best knowledge, no work has been carried out to discuss the influence of the initial stress on the propagation behavior of Love wave in layered piezoelectric structures. However, this is significant for the design of acoustic wave sensors.

This paper primarily concerned with the effect of the initial pressure on the phase velocity of Love waves in the elastic layer/piezoelectric substrate system. The research results reported in this paper will be useful for the design and application of Love wave sensors.

2. STATEMENT OF THE PROBLEM

As shown in Fig.1, the layered structure consists of a homogeneous elastic layer with uniform thickness h in intimate contact with the transversely isotropic piezoelectric substrate. The polarization direction of the substrate is along z-axis that is perpendicular to the x-y plane. On condition that the free surface of the layer is mechanical traction-free and provided that the velocity of the bulk shear wave in the layer is lower than that of in the substrate, then a Love wave could propagate in the structure. Assume that the propagation direction of Love wave is along positive direction of y-axis without loss of any generality. In this paper, only initial stress component σ_y^0 is considered and the other initial stress components are neglected for the complexity of the problem. For surface acoustic wave devices, the thickness of the substrate is much greater than that of the layer, so the layered structure can be treated as layered half-space and the initial stress in the substrate can be neglected.

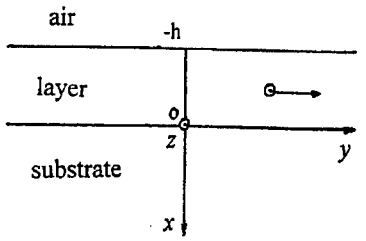


Fig.1 The piezoelectric layered half-space and coordinate system

As shown in Fig.1, the particles under consideration are making transversely horizontal polarizing movement. Thus, we have:

$$u = 0, \quad v = 0, \quad w = w(x, y, t), \quad \varphi = \varphi(x, y, t) \tag{1}$$

For the isotropic elastic layer, the field equations of the pre-stressed non-piezoelectric body can be expressed as:

$$c_{44}' \frac{\partial^2 w_2}{\partial x^2} + (\sigma_y^0 + c_{44}') \frac{\partial^2 w_2}{\partial y^2} = \rho' \frac{\partial^2 w_2}{\partial t^2} \tag{2a}$$

$$\frac{\partial^2 \varphi_2}{\partial x^2} + \frac{\partial^2 \varphi_2}{\partial y^2} = 0 \tag{2b}$$

where ρ', c_{44}', w_2 and φ_2 denote the mass density, elastic constant, mechanical displacement and electrical potential function of the layer, respectively.

Let w_1, φ_1 denote the mechanical displacement and electrical potential in the substrate, then the

coupled electromechanical field equation can be written as follows:

$$c_{44}\left(\frac{\partial^2 w_1}{\partial x^2}+\frac{\partial^2 w_1}{\partial y^2}\right)+e_{15}\left(\frac{\partial^2 \varphi_1}{\partial x^2}+\frac{\partial^2 \varphi_1}{\partial y^2}\right)=\rho\frac{\partial^2 w_1}{\partial t^2} \tag{3a}$$

$$e_{15}\left(\frac{\partial^2 w_1}{\partial x^2}+\frac{\partial^2 w_1}{\partial y^2}\right)-\varepsilon_{11}\left(\frac{\partial^2 \varphi_1}{\partial x^2}+\frac{\partial^2 \varphi_1}{\partial y^2}\right)=0 \tag{3b}$$

where c_{44}, e_{15}, ε_{11} are elastic, piezoelectric, dielectric constant, ρ the mass density of the substrate, respectively. The medium above the layer is air in general, its dielectric constants are very small in comparison with those of the piezoelectric medium and thus the space above the layer can be treated as vacuum. Let $\varphi_0(x,y,t)$ denote the electric potential function of the vacuum, then

$$\nabla^2\varphi_0 = 0 \tag{4}$$

as the Love wave propagate in the layered structure, in addition to the mechanical displacement components and electrical potential satisfy equations (2)-(4), the relevant mechanical and electrical quantities should satisfy the boundary conditions at the surface and the continuity conditions along the interface between two media.

(i) For the electrical open case, the mechanical and electrical conditions at the free surface ($x = -h$) can be read as:

$\tau_{zx}^{(2)}(-h,y)=0$, $\varphi_0(-h,y)=\varphi_2(-h,y)$, and $D_x^{(0)}(-h,y)=D_x^{(2)}(-h,y)$

(ii) The continuity conditions at $x = 0$: the normal components of the stress, mechanical displacement, electrical potential function and electrical displacement are continuous, that is to say

$$w_1(0,y)=w_2(0,y),\quad \tau_{zx}^{(1)}(0,y)=\tau_{zx}^{(2)}(0,y)$$

$$\varphi_1(0,y)=\varphi_2(0,y),\quad D_x^{(1)}(0,y)=D_x^{(2)}(0,y)$$

(iii) For the layered half-space, the following conditions should be satisfied: when $x\to+\infty, w_1\to 0, \varphi_1\to 0$; when $x\to-\infty$, $\varphi_0\to 0$.

3. SOLUTIONS OF THE MECHANICAL DISPLACEMENT AND ELECTRICAL POTENTIAL

The solutions of mechanical displacement and electrical potential in equation (3) can be assumed to have the following forms:

$$w_1(x,y,t)=W_1(x)\exp[ik(y-ct)] \tag{5a}$$

$$\varphi_1(x,y,t)=\Phi_1(x)\exp[ik(y-ct)] \tag{5b}$$

where $k=2\pi/\lambda$ is the wave number, λ the wavelength, c the phase velocity of the wave, $W_1(x)$ and $\Phi_1(x)$ are undetermined functions, respectively.

Let $c_{sh}^{'}$ and c_{sh} denotes the velocity of the bulk shear wave in the layer and the substrate, respectively, then for the Love wave under consideration, the phase velocity c satisfies the following expression: $c_{sh}^{'}<c<c_{sh}$.

Considering the condition (iii), we can obtain the solutions of mechanical displacement and

electrical potential in the substrate as follows corresponding to equation (3):

$$w_1(x,y,t) = A_1 e^{-bx} \exp[ik(y-ct)] \tag{6a}$$

$$\varphi_1(x,y,t) = \left(A_1' e^{-kx} + \frac{e_{15}'}{\varepsilon_{11}'} A_1 e^{-bx} \right) \exp[ik(y-ct)] \tag{6b}$$

where $b = \sqrt{1-[(\rho\varepsilon_{11}c^2)/(c_{44}\varepsilon_{11}+e_{15}^2)]}$

In the same manner, the solutions of the mechanical displacement and electrical potential in the layer corresponding to equation (2) can be read as the following expressions:

$$w_2(x,y,t) = (A_2 e^{-ikb_1 x} + B_2 e^{ikb_1 x}) \exp[ik(y-ct)] \tag{7a}$$

$$\varphi_2(x,y,t) = (A_2' e^{-kx} + B_2' e^{kx}) \exp[ik(y-ct)] \tag{7b}$$

where $b_1 = \sqrt{[(\rho c^2 - \sigma_y^0)/c_{44}'] - 1}$

The solution of equation (4) can be represented as follows according to condition (iii):

$$\varphi_0(x,y,t) = A_0 e^{kx} \exp[ik(y-ct)] \tag{8}$$

4. SOLUTION OF THE PHASE VELOCITY

Substituting Eqs. (6)-(8) and their corresponding stress and electric displacement components into boundary conditions (i)-(ii) in turn, and after some arrangement we can obtain the following homogeneous linear algebraic equations with respect to undetermined constants $A_1, A_2, B_2, B_2', A_1', A_2'$ and A_0 for the electrical open case at the free surface:

$$\begin{aligned}
&-e^{ikb_1 h} A_2 + e^{-ikb_1 h} B_2 = 0 \\
&e^{kh} A_2' + e^{-kh} B_2' - e^{-kh} A_0 = 0 \\
&\varepsilon_{11}' e^{kh} A_2' + e^{-kh} B_2' - e^{-kh} A_0 = 0 \\
&(\frac{c_{44}\varepsilon_{11} + e_{15}^2}{\varepsilon_{11}}) b A_1 + e_{15} A_1' - c_{44}' i b_1 A_2 + c_{44}' i b_1 B_2 = 0 \\
&A_2 + B_2 = A_1 \\
&-\frac{e_{15}}{\varepsilon_{11}} A_1 - A_1' + B_2' + A_2' = 0 \\
&\varepsilon_{11} A_1' - \varepsilon_{11}' B_2' - \varepsilon_{11}' A_2' = 0
\end{aligned} \tag{9}$$

From the existence of the non-trivial solution condition (if and only if by equating the coefficient determinant to be zero), the phase velocity equation for the propagation of Love wave in the piezoelectric layered half-space for the electrical open case at the free surface can be expressed as follows:

$$\begin{aligned}
&[\tan(2\pi m b_1) c_{44}' b_1 - (\frac{c_{44}\varepsilon_{11} + e_{15}^2}{\varepsilon_{11}}) b][(\frac{\varepsilon_{11}'^2 + \varepsilon_0 \varepsilon_{11}}{\varepsilon_0 \varepsilon_{11}}) \tanh(2\pi m) + \frac{\varepsilon_{11}'}{\varepsilon_{11}} + \frac{\varepsilon_{11}'}{\varepsilon_0}] \\
&-\frac{e_{15}^2 \varepsilon_{11}'}{\varepsilon_{11}^2}[1 + \frac{\varepsilon_{11}'}{\varepsilon_0} \tanh(2\pi m)] = 0
\end{aligned} \tag{10}$$

where $m = h/\lambda$ is the ration of the thickness of the layer to the wavelength. The corresponding phase velocity equation for the electrical shorted case at the free surface can be read as:

$$[\tan(2\pi m b_1)c'_{44} - (\frac{c_{44}\varepsilon_{11} + e_{15}^2}{\varepsilon_{11}})b] \cdot [\tanh(2\pi m) + \frac{\varepsilon'_{11}}{\varepsilon_{11}}] - \frac{e_{15}^2 \varepsilon'_{11}}{\varepsilon_{11}^2} = 0 \tag{11}$$

Eqs (10) and (11) are the phase velocity equations of Love wave propagation in the layered piezoelectric structure for the electrical open and shorted cases, respectively. It is seen clearly that the phase velocity is related to the initial stress, the wavelength, layer thickness, elastic, dielectric and piezoelectric constants.

5. NUMERICAL EXAMPLE AND DISCUSSION

To graphically show the effects of initial stress and m (the ratio of layer thickness h to wavelength λ) on the phase velocity and the electromechanical coupling factor k^2, the following material system is considered: Pb glass layer on the Zno substrate. The computational material parameters are taken from [1]. All the material constants used in the computation are summarized in Table1. The dielectric constant of vacuum is $\varepsilon_0 = 8.85 \times 10^{-12}$ F/m.

The phase velocity c can be calculated from Eq. (10) and (11) for electrical open and shorted cases, respectively, for different values of m. Effect of initial stress on the phase velocity c is shown in Fig.2 for Pb glass layer ~ Zno substrate system. It is seen that the effect of initial pressure on phase velocity is negligible as $|\sigma_y^0| < 100$ MPa, while the phase velocity decreases with the increase of initial pressure as $|\sigma_y^0| > 100$ Mpa for electrical open case.

The electromechanical coupling factor k^2 is defined by the formula: $k^2 = 2(c_o - c_s)/c_o$. Where c_o and c_s are the surface wave velocities in electrical open and shorted cases, respectively. This parameter is directly related to the efficiency of a transducer in converting electrical to mechanical energy or vice versa [1,2]. It is an essential parameter for the design of surface acoustic wave sensors, usually the higher values of k^2 are expected in engineering application. Effects of initial pressure on electromechanical coupling factor k^2 for Pb glass layer~Zno substrate system is shown in Fig. 3 for different values of m. It is seen that k^2 increases remarkably with the increase of initial pressure as $|\sigma_y^0| > 100$ Mpa.

6. CONCLUSIONS

The results obtained in this paper show that initial pressure has important effect on the properties of Love wave propagation as $|\sigma_y^0| > 100$ MPa for both electrical open and shorted cases, magnitude of the phase velocity decreases with the increase of $|\sigma_y^0|$. Moreover, it is found that the

Table1 Material constants used in the computation

	$c_{44}(N/m^2)$	$\rho(kg/m^3)$	$e_{15}(C/m^2)$	$\varepsilon_{11}(F/m)$
glass	2.18×10^{10}	3.879×10^3	0	$5.1\varepsilon_0$
Zno	4.23×10^{10}	5.665×10^3	-0.48	$7.57\varepsilon_0$

electromechanical coupling factor increases rapidly with increasing initial stress as $|\sigma_y^0| > 100$ MPa.

In conclusion, the effect of initial pressure in the piezoelectric layered structures on the propagation of Love wave can provide theoretical foundation for the design and practical application of SAW devices.

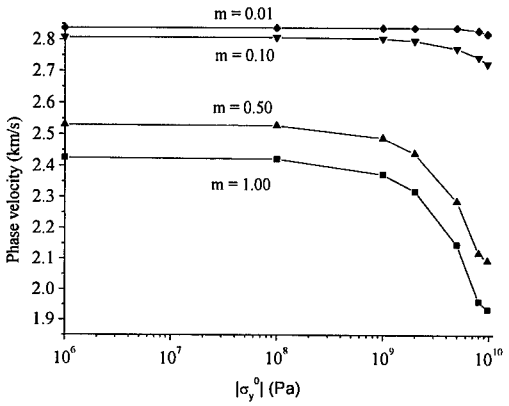


Fig. 2 Phase velocity vs. initial pressure for electrical open case

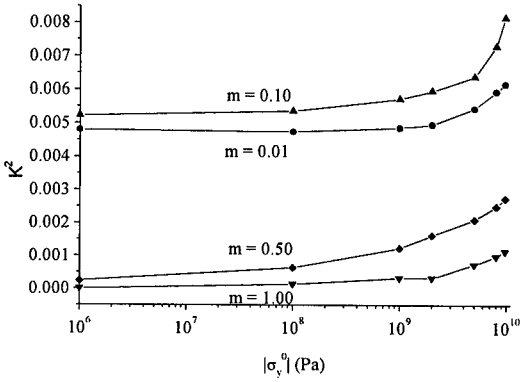


Fig. 3 Values of k^2 vs. initial stress

ACKNOWLEDGEMENTS

F. Jin would like to acknowledge the financial support of China Postdoctoral Science Foundation. TJ Wang would like to acknowledge the support by the Science Foundation of China Education Ministry.

REFERENCES

1. E.Dieulesaint, and D.Royer, Elastic Waves in Solids: Applications to Signal Processing, John Wiley & Sons (1985)
2. G.Kovacs, and A.Venema, Applied Physics Letter, **61** (1992), p. 639
3. B.Jakoby, and M.J.Vellekoop, Smart Material Structure, **6** (1997), p. 668

Key Engineering Materials Vols. 183-187 (2000) pp. 761-766
© 2000 Trans Tech Publications, Switzerland

The Effect of Nucleation Time on the Growth of a Microvoid in a Viscoelastic Material

J.K. Chen[1], Z.P. Huang[1] and S.L. Bai[2]

[1]LNM, Institute of Mechanics, Chinese Academy of Sciences, Beijing 100080, China P.R.

[2]Department of Mechanics and Engineering Sciences, Peking University, Beijing 100871, China P.R.

Keywords: Nucleation Time, Partially Interfacial Debonding, Particulate-Reinforced Composite Materials, Viscoelastic Material, Void Growth

ABSTRACT

In this paper, discussions are focused on the growth of a nucleated void in a viscoelastic material. The in situ tensile tests of specimens made of high-density polyethylene, filled with spherical glass beads (HDPE/GB) are carried out under SEM. The experimental result indicates that the microvoid nucleation is induced by the partially interfacial debonding of particles. By means of the Laplace transform and the Eshelby's equivalent inclusion method, a new analytical expression of the void strain at different nucleation times is derived. It can be seen that the strain of the nucleated void depends not only on the remote strain history, but also on the nucleation time. This expression is also illustrated by numerical examples, and is found to be of great usefulness in the study of damage evolution in viscoelastic materials.

1 INTRODUCTION

It has been found that one of the controlling failure mechanisms in a particulate-reinforced composite material is the nucleation, growth and eventual coalescence of microvoids [1,2]. If the strength of particles is sufficiently high, the microvoids' nucleation may take place at the interface between particles and the matrix [3,4]. In the condition of low stress triaxiality, the microvoids' nucleation occurs due to the partially interfacial debonding of particles [5]. In this paper, discussions are focused on the growth of a nucleated void in a viscoelastic material. Firstly, in situ tensile tests of the specimen made of high-density polyethylene filled with glass beads are performed under SEM. The experiment shows that the microvoid nucleation takes place due to the partially debonding of the interface between particles and the matrix. Then, the growth of a nucleated void embedded in an infinite viscoelastic material is theoretically studied. The expression of the void strain is derived, and it can be seen that the strain of this nucleated void

depends not only on the remote strain history, but also on the nucleation time. Finally, the influences of the remote strain history and the nucleation time on the void strain are discussed by the numerical examples.

2 THE IN SITU TEST OF HDPE/GB UNDER SEM

The test specimen is made of the high-density polyethylene (HDPE) filled with glass beads. In the manufacturing process, the glass beads are treated with coupling agents and then mixed with HDPE powder in a chamber of a high speed mixer and a twin-screw extruder. The pelleted extruder is injection molded into the tensile specimen. The geometry of the specimen is shown in Fig.1.

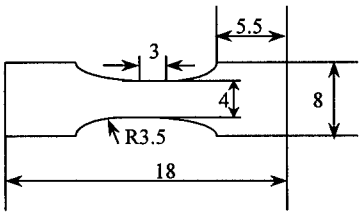


Fig.1. Dimension of in situ test specimens with thickness of 3 mm.

The in situ tensile tests are performed under SEM with the loading rate of about 0.2mm/min. The SEM photographs of the microvoid nucleation and growth are shown in Fig.2.



(a) (b) (c)

Fig.2. SEM photographs of microvoids' nucleation and growth
(a): microvoids' nucleation under the remote stress $\sigma = 5\text{MPa}$;
(b),(c): microvoids' growth under the remote stress $\sigma = 15.8\text{MPa}$

It can be seen that the microvoids' nucleation takes place due to the partially interfacial debonding. Because the glass beads can hardly deform, they will be considered as rigid particles. Hence, it may be assumed from the above experimental observation that under the axial symmetric loading condition, the component of the void stress along the tensile direction and the components of the void strain perpendicular to the tensile direction are equal to zero, i.e.,

$$\sigma_{v11} = 0, \qquad \varepsilon_{v22} = \varepsilon_{v33} = 0 \tag{1}$$

3 THE DEPENDENCE OF THE VOID STRAIN ON THE NUCLEATION TIME

Now consider a spherical rigid inclusion embedded in an infinite viscoelastic matrix. The constitutive relation of the matrix material is given in the form of Stieltjes' convolution as follows:

$$\boldsymbol{\sigma}_0 = \mathbf{L} * \mathrm{d}\, \boldsymbol{\varepsilon}_0, \text{ (or) } \quad \boldsymbol{\varepsilon}_0 = \mathbf{J} * \mathrm{d}\, \boldsymbol{\sigma}_0 \qquad (2a,b)$$

where $\mathbf{L}(t)$ and $\mathbf{J}(t)$ are the fourth order relaxation modulus and creep compliance, respectively.

The Lapalce transform of Eq.(2a) may be written as

$$\overline{\boldsymbol{\sigma}}_0 = s\overline{\mathbf{L}} : \overline{\boldsymbol{\varepsilon}}_0 \qquad (3)$$

where the symbols "—"and "s" denote the Laplace transform and the transform variable respectively.

Suppose a void is nucleated by the partial debonding at the interface between the rigid inclusion and the matrix at time t'. We are interested in calculating the strain of this nucleated void at time t ($\geq$ t'). For simplicity, we assume that the Poisson's ratio of the matrix material can be taken as a constant. Since the rigid inclusion (GB) is spherical, we further assume that the shape of the void is spheroidal.

The void strain is graphically sketched in Fig.3, and may be regarded as the superposition of two sub-problems shown in Fig.4 and Fig.5.

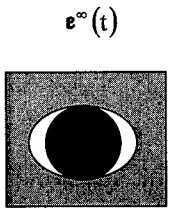


Fig.3. The growth of a nucleated void in an infinite matrix

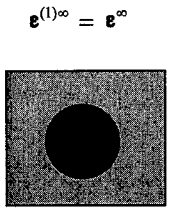


Fig.4. Sub-problem (1) a rigid inclusion in the same matrix material

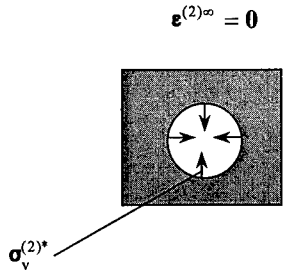


Fig.5. Sub-problem (2) a void with eigen-stress in the same matrix material

In sub-problem (1), a spherical rigid inclusion is embedded in a viscoelastic matrix material subjected to a remote strain history, which is identical with $\boldsymbol{\varepsilon}^{\infty}(t)$ in the original problem. The shape and the size of this rigid inclusion are also the same as those in Fig.3. The interface is supposed to be well bonded during the deformation process, and the stress of the inclusion will be

denoted by $\boldsymbol{\sigma}_p^{(1)}$. According to the Eshelby's equivalent inclusion method, the stress in the inclusion in sub-problem (1) may be obtained and expressed by:

$$\boldsymbol{\sigma}_p^{(1)} = \int_{-\infty}^{t} \mathbf{L}(t-\tau) : \mathbf{S}^{-1} : \frac{d}{d\tau} \boldsymbol{\varepsilon}^{\infty}(\tau) d\tau \tag{4}$$

where **S** is the Eshelby's tensor.

In sub-problem (2), a void is embedded in the same material, but the remote strain is zero. The shape and the size of the void at time t<t' are the same as those of the rigid inclusion shown in Fig.4. However, the void strain at time t (t≥t') in Fig.3 is equal to the one in Fig.5.

The void shown in Fig.5 may also be regarded as an inclusion with the eigenstress $\boldsymbol{\sigma}_v^{*(2)}$. The corresponding stress of this inclusion can be transformed to give

$$\overline{\boldsymbol{\sigma}}_v^{(2)} = s\overline{\mathbf{L}}_v : \overline{\boldsymbol{\varepsilon}}_v + \overline{\boldsymbol{\sigma}}_v^{*(2)} \tag{5}$$

where $\mathbf{L}_v$ denotes the elastic modulus of the void. Now let us introduce $\overline{\boldsymbol{\varepsilon}}^*$ such that $s\overline{\mathbf{L}}_v : \overline{\boldsymbol{\varepsilon}}_v = s\overline{\mathbf{L}} : (\overline{\boldsymbol{\varepsilon}}_v - \overline{\boldsymbol{\varepsilon}}^*)$. Then Eq.(5) may be written in the form:

$$\overline{\boldsymbol{\sigma}}_v^{(2)} = s\overline{\mathbf{L}} : (\overline{\boldsymbol{\varepsilon}}_v - \overline{\boldsymbol{\varepsilon}}^*) + \overline{\sigma}_v^{*(2)} = s\overline{\mathbf{L}} : (\overline{\boldsymbol{\varepsilon}}_v - \overline{\boldsymbol{\varepsilon}}^* - \overline{\boldsymbol{\varepsilon}}_v^{*(2)})$$

where

$$\overline{\boldsymbol{\varepsilon}}_v^{*(2)} = -s\overline{\mathbf{J}} : \overline{\boldsymbol{\sigma}}_v^{*(2)} \tag{6}$$

Noting that the above inclusion in Fig.3 is actually a void, we have

$$\overline{\mathbf{L}}_v = \mathbf{0}, \quad \overline{\boldsymbol{\varepsilon}}_v = \overline{\boldsymbol{\varepsilon}}^* \tag{7}$$

Hence, by virtue of the Eshelby's equivalent inclusion method, the transform of the void strain may be written as

$$\overline{\boldsymbol{\varepsilon}}_v = \mathbf{S} : (\overline{\boldsymbol{\varepsilon}}^* + \overline{\boldsymbol{\varepsilon}}_v^{*(2)}) \tag{8}$$

Substitution of Eq.(6) and Eq.(7) into the above equation yields:

$$\overline{\boldsymbol{\varepsilon}}_v = -(\mathbf{I}-\mathbf{S})^{-1} : \mathbf{S} : s\overline{\mathbf{J}} : \overline{\boldsymbol{\sigma}}_v^{*(2)} \tag{9}$$

Thus, the void strain, as the inverse transform of Eq.(9), may be expressed by

$$\boldsymbol{\varepsilon}_v = -(\mathbf{I}-\mathbf{S})^{-1}:\mathbf{S}:\int_{-\infty}^{t}\mathbf{J}(t-\tau):\frac{d}{d\tau}[\boldsymbol{\sigma}_v^{(2)*}(\tau)]d\tau \qquad (10)$$

In the above equation, $\boldsymbol{\sigma}_v^{(2)*}$ should be determined from the condition of Eq.(1):

$$\sigma_{v11}^{(2)*} = -\sigma_{p11}^{(1)}u(t-t')$$

$$\sigma_{v22}^{(2)*} = \sigma_{v33}^{(2)*} = -A_2\sigma_{p11}^{(1)}u(t-t') \qquad (11)$$

where u(t) is a step function, and A_2 is obtained from Eqs.(1) and (10).The analytical expression of A_2 will not be given here owing to the limitation of space. However, it can be seen that the void strain is a function of the remote strain history and the nucleation time t'.

It should be pointed out that Eq.(10) can also be used to calculate the void strain in the matrix material, which contains a large number of rigid inclusions and nucleated microvoids, if the interaction between these inclusions and microvoids can not be neglected. Several averaging schemes, such as the Mori-Tanaka Scheme and generalized self-consistent Mori-Tanaka scheme(e.g.cf.[7]), may be employed to take into account this interaction if these inclusions and microvoids are randomly distributed. For example, in the Mori-Tanaka Scheme, the remote strain $\boldsymbol{\varepsilon}^{\infty}$ in Eq.(4) should be replaced by the average strain of the matrix material $< \boldsymbol{\varepsilon}_0 >$.

4 NUMERICAL EXAMPLES AND CONCLUSIONS

Now consider an infinitely extended viscoelastic material that contains a rigid spherical inclusion, and is subjected to the applied strain history at infinity. The constitutive relation of the matrix material is assumed to be the Maxwell model with the relaxation modulus:

$$E(t) = E_0\exp(-t/t_m) \qquad (12)$$

where t_m is the relaxation time of the matrix material.

Based on Eq.(10), the void strain under a constant remote strain rate is calculated numerically, and is plotted in Fig.6 and Fig.7, in which $(\varepsilon_{v11})^{elastic}$ denote the components of the void strains in the tensile direction when the relaxation time tends to infinite. It can be seen from these figures that the dependence of the void strain on the nucleation time is quite clear.

The influence of the remote strain history on the void growth is also studied. Two kinds of remote strain histories will be considered: 1) the constant strain rate, $\varepsilon_{11}^{\infty} = a_1 t$ ($a_1 = 1/40(1/s)$), all other components $\varepsilon_{ij}^{\infty} = 0$; 2) the accelerated strain rate, $\varepsilon_{11}^{\infty} = a_2 t^2/2$ ($a_2 = 1/20(1/s^2)$), all other components $\varepsilon_{ij}^{\infty} = 0$.The void strains corresponding to the above two remote strain histories,

(but with the same remote strain at time t=1 s), are compared and shown in Fig.7.

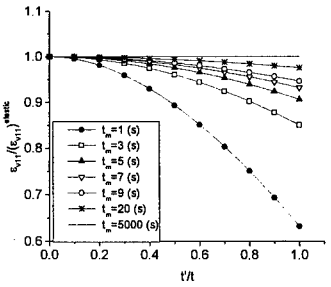


Fig.6. The relations between the component of the void strain ε_{v11} and the nucleation time t' for different relaxation times

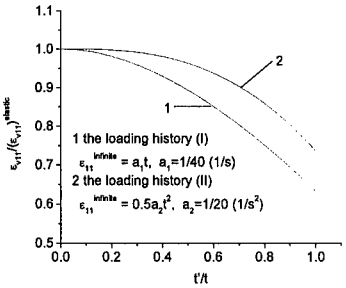


Fig.7. The influence of loading history on the component of void strain ε_{v11}

It may be concluded from the above calculations that:

(1) The void strain, shown in Fig.6, is a function of the nucleation time t'. In the case that t'=0, the void strain calculated from Eq.(10) will be the same as $(\varepsilon_{v11})^{elastic}$, namely, $\varepsilon_{v11}/(\varepsilon_{v11})^{elastic} = 1$. However, for a monotonically increasing remote strain history, the void strain will be a monotonically decreasing function of the nucleation time.

(2) The void strain depends also on the remote strain history. The influence of the remote strain history on the void growth is shown in Fig.7. For the same remote strain at time t, the void strains at time t for different remote strain histories may be different.

(3) The dependence of void strain on the relaxation time is shown in Fig.6. It can be seen that the void strain is a monotonically increasing function of the relaxation time. As the relaxation time tends to infinity, the matrix material becomes an elastic one, and the void strain depends on the remote strain only.

ACKNOLEDGMENT

This work is supported by the National Natural Science Foundation of China under contracts 19632030 and 19872007, and the Natural Science Foundation of Yangzhou University.

+ to whom all correspondences should be addressed

REFERENCES

1. Z.P. Huang, L. M. Yang and K.L. Pan, Advances in Mechanics, 23(1993), p.433-467
2. D.R. Curran, L. Seaman and D.A. Shockey, Physics Reports, 147(5,6)(1987), p.253-388
3. J.K. Chen, Z.P. Huang, S.L. Bai, and Y. Liu, Acta Mechanica Solida Sinica, 12(1999), p.1-8
4. K. Tohgo and T. Chou, JSME Int. J. Series A, 39(1996), p.389-398
5. Y.H. Zhao and G.J.Weng, Inter. J. Plasticity, 12(6)(1996), p.781- 804
6. J.D. Eshelby, Proceedings of the Royal Society of London, A 241(1957), p.376-396
7. L.H. Dai, Z.P. Huang and R. Wang, Polymer Composites, 19(1998), p.506-513

Key Engineering Materials Vols. 183-187 (2000) pp. 767-772
© 2000 Trans Tech Publications, Switzerland

Effects of Stress Fields around Micro-Surface Defects on the Occurrence of Slip and Micro Cracks

K.R. Lee[1] and J.B. Kim[2]

[1] Division of Machinery & Automobiles, Shinsung College,
San 49, Duckma-ri, Jungmi-myun, Dangjin-gun, Chungnam 343-860, Korea

[2] Department of Aeronautical & Mechanical Engineering, Hanseo University,
360 Daegok-ri, Haemi-myun, Seosan, Chungnam 356-820, Korea

Keywords: Finite Element Method, Micro Defects, Slip, Stress Concentration, Stress Interaction Effect

ABSTRACT

The purpose of the study was to identify the effects of stress fields around micro-surface defects that behave as a cause of stress concentration on the occurrence of slip and micro cracks. The shape of defects was cylindrical and the specimen was tested under bending stress. Considering the distribution of defects in materials is various, both experiment and analysis were performed for the specimen with distributed defects. In addition, stress distributions were evaluated by FEA(Finite Element Analysis) for the model with same condition applied to the experimental specimen. The study findings confirmed the range of occurring slip and micro cracks around micro-defects as well as the stress interference effects between various defects. It was noted that the experiment results on the range of stress field to the occurrence of slip and micro cracks were mostly consistent with the results of FEA. Consequently, the distribution and the interaction effects of slip and micro cracks initiated from micro-defects can be identified by FEA.

1. INTRODUCTION

If fatigue cracks initiate from defects, local areas including the defects become stress concentrator [1-3], and accordingly it is expected that the fatigue strength is affected by size and configuration of defects. As it needs lots of time and effort to produce specimen controlled the size and configuration of defects metallurgically, so the characteristic of micro defects is studied using artificial defects instead of natural defects. Size and configuration of defects in material is various and the interval between them is near and far [4]. Specially, if the interval between them is near, there are singular stress fields by stress interaction [5] and fatigue cracks propagate rapidly [6]. Therefore, identifying effects of the defects as stress concentrator on the occurrence of slip and micro cracks would be an important factor in evaluating safety and life-time of machinery structures or elements. The study used experiment and FEA to identify effects of stress fields from micro

defects as well as interaction effects among defects of various sizes on the behaviors of initial micro cracks around defects.

2. EXPERIMENT AND ANALYSIS

2.1. Experiment

Fig.1 shows the shape of specimen used in the experiment with yield strength of 333MPa. The micro defects were made with the diameters of 300μm and 500μm and the depth of 375μm. The experiment used a rotary bending test machine manufactured by SATEC company with maximum capacity of 22.5N-m and 10,000rpm.

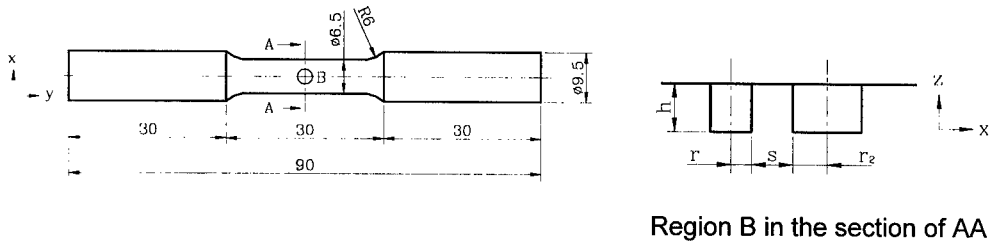


Fig.1. Configuration of rotary bending test specimen

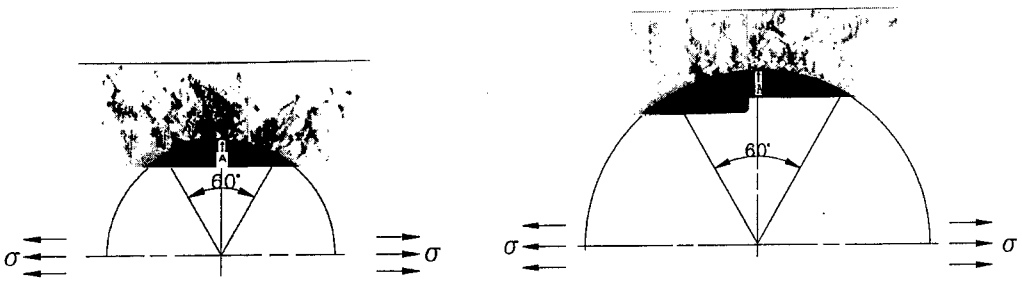
2.2. Analysis Model

For the purpose of analysis, defects are located on the surface of rectangular cross section beam with 7mm x 7mm and 100mm length. The FEA model used 4 point bending beam to produce pure bending state in the center of specimen where micro hole defects exist. 3-dimensional 20-noded iso-parametric element was used in FEA.

3. RESULTS AND DISCUSSION

As shown in Fig.2, slip and micro cracks are distributed with the range of more than ± 30° from the starting point of A to which the maximum normal stress applied. The comparisons of distribution degrees (θ_d) were made on the initiation areas of slip and micro cracks around micro defects. In results, θ_d was 74° at d=300μm while θ_d was 68° at d=500μm, reflecting that θ_d for small defect was larger than that of large defect. Based on the results, the location of slip or micro cracks around defects was expected to occur within the working range of maximum shear stress, including the region of maximum stress concentration.

If defects were located closely, fatigue cracks around defects will be affected by interacting stress among defects. To identify interaction effects of stress on the occurrence of fatigue cracks, the comparison was made between the results of rotary bending test and the results of stress analysis by FEA on different inter-defects intervals with the ET model of same sized defects(d=300μm) and the ED model of different sized defects(d=300μm, d=500μm).

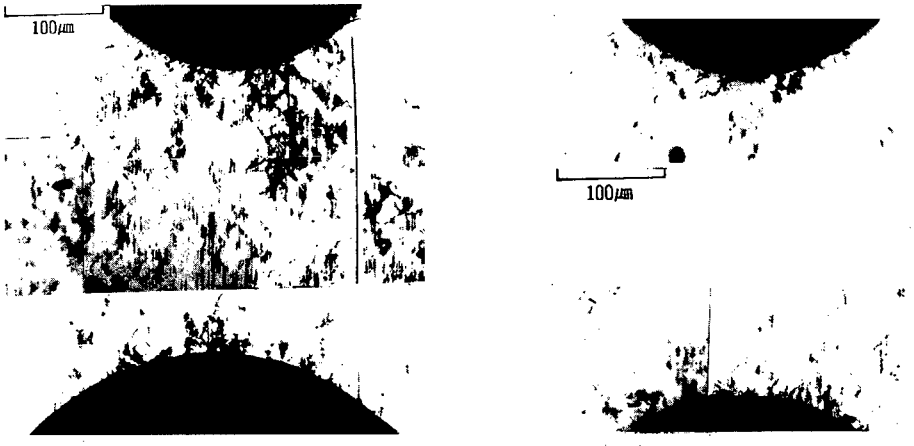


(a) d = 300μm (θ_d = 74°) (b) d = 500μm (θ_d = 68°)

Fig.2. Initiation area of slip and micro cracks around micro defects

Fig.3 shows the distributions of slip and micro cracks in ED model (a) and ET model (b) at inter-defect interval e=2 (e=s/r, s : distance between edges of defects, r : radius of small defect). In Fig.3(a), θ_d of slip and micro cracks at the center of defects was θ_{ds}=76° for d=300μm and θ_{dl}=72° for d=500μm, while θ_{ds}=68° in Fig.3(b). The reason that the distribution degree of ED model was larger than ET model was that interaction effects of stress became larger when the sizes of defects were different than when two defects were same sized. Additionally, the length of crack from small defect was 140μm while the length from large defect was approximately 20μm in (a). This finding suggests that effects of stress increment for small defect by large defect became larger than those for small defect by same-sized small defect, and also interaction effects of stress were relatively larger at small defect than at larger defect.

Fig.4 shows that the results of experiment on various distribution degrees of slip and micro cracks according to the changes of inter-defects interval using ED model. In Fig.4, the values for



(a) d = 300μm, d_2 = 500μm (θ_{ds}=76°, θ_{dl}=72°, N/Nf=20%, Nf=1.3 x 10^5 cycle)

(b) d = 300μm (θ_d=60°, N/Nf=10%, Nf=1.1 x 10^5 cycle)

Fig.3. Initiation of slip and micro cracks around micro defects (interval s=300μm, e=s/r=2)

ED model were represented by (O) for distribution degrees between a-a' and (□) for b-b', while (●) represented distribution degrees of a-a' and b-b' for ET model. The fact that distribution degree(θ_d) of small defect(d=300μm) with larger defect was bigger than with same sized small defect (d=300μm) is due to interaction effects of stress among the defects.

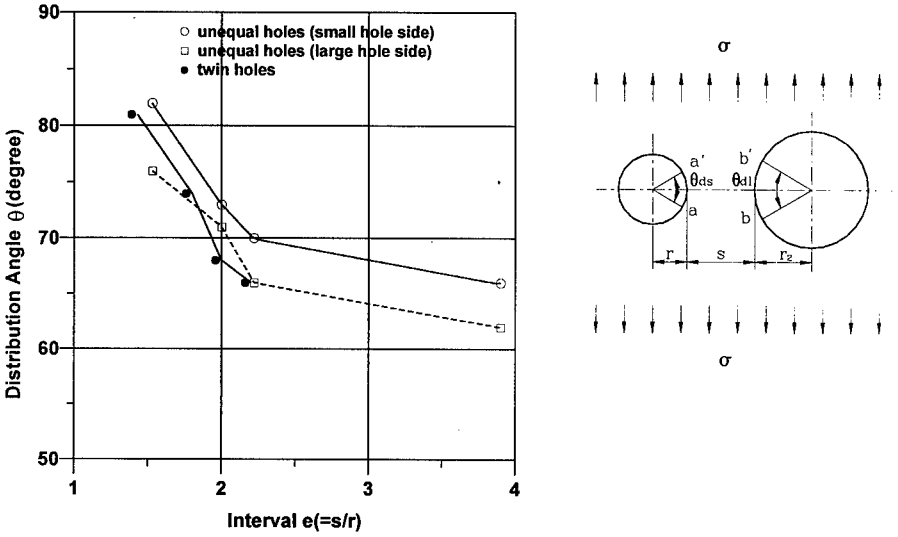


Fig.4. Distribution angle of slip and micro cracks around defects (N/Nf =10～20%)

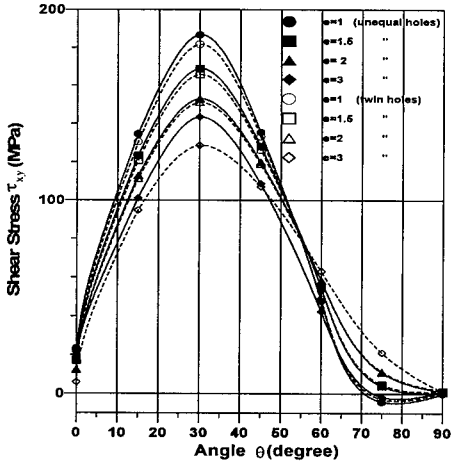


Fig.5. Shear stress around defects (in case of the unequal defects, d=300μm side)

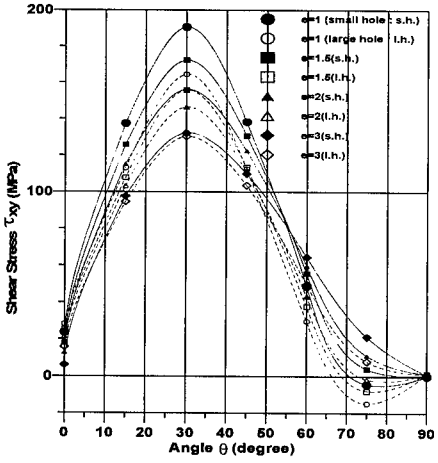


Fig.6. Shear stress around unequal defects

To confirm the results of experiment, FEA was applied to identify interaction effects of stress on the occurrence of slip and micro cracks, and the findings are as follows. The distributions of shear stress around defects at each different inter-defects intervals by FEA are presented in Figs.5 and 6. Fig.5 shows the distributions of shear stress around hole defects for ET model as well as ED model. The analysis results on small defects(d=300μm) were portrayed by solid lines for ED model and broken lines for ET model. The maximum shear stress occurred at θ=30°, and shear stress of ED model was larger than shear stress of ET model at the range(0°≤ θ<55°) that significantly affects slip and micro cracks. Fig.6 represents the analysis result of shear stress distribution around hole defects at different inter-defects intervals for ED model. The solid line represents the analysis result on the defect with d=300μm, while the analysis result on the defect with d=500μm is presented by broken line. The results show that the shear stress of the defect with d=300μm was larger than the shear stress of the defect with d=500μm. The comparison between the experimental results(Fig.4) and the analysis results of shear stress by FEA(Fig.5 and Fig.6) indicates that slip and micro cracks around defects are affected by shear stress, and that the distribution degrees of slip and micro cracks around adjacent defects depend on the interaction effects of stress.

To identify the interaction effects of stress that affect distribution degrees of slip and micro crack, interaction effect factor γ with following definition was used to compare the results from experiments and FEA.

The definition of γ for the experiment :

$$\gamma = \frac{\text{Distribution degree of slip and micro crack around two defects}}{\text{Distribution degree of slip and micro crack around one defect}}$$

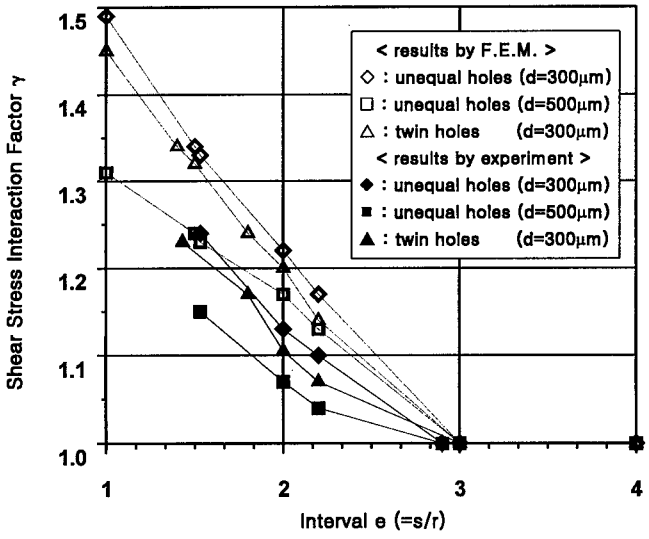


Fig.7. Shear stress interaction factor with variation of interval

The definition of γ for FEA :

$$\gamma = \frac{\text{Maximum shear stress around two defects}}{\text{Maximum shear stress around one defects}}$$

Fig.7 shows the changes of factor γ at different inter-defects intervals. The interaction effect factor of maximum shear stress obtained by FEA was 5~10% bigger than the interaction effect factor of slip and micro cracks obtained by experiment, but the results on defect intervals between experiment and FEA were consistent. Therefore, the occurrence of slip and micro cracks around adjacent defects was closely related to the interaction effects of maximum shear stress.

4. CONCLUSIONS

The purpose of the study was to identify the effects of stress fields around micro defects as a cause of stress concentration on the occurrence of slip and micro cracks, and the results from experiment and FEA are summarized as follows :

(1) The occurrence of slip and micro cracks around micro defects was within the working range of maximum shear stress, including the region of maximum stress concentration.

(2) The interaction effect of stress with two micro defects of different sizes(d=300μm, d=500μm) was larger than the interaction effect of stress with two micro defects of same size(d=300μm), and the interaction effects of stress was larger for small defects than for large defects.

(3) The interaction effect of maximum shear stress between adjacent micro defects by FEA was about 5~10% larger than the interaction effect of slip and micro cracks by experiment, yet the results on defect intervals between experiment and FEA were consistent.

REFERENCE

1. D.Brooksank, K.W.Andrews, Journal Iron & Steel Inst. (1972) p.246
2. G.G.Trantina and M.Barishpolsky, Engineering Fracture Mechanics, **20** (1984) p.1
3. S.H.Song and J.B.Kim, Trans. K.S.M.E, **19** (1995) p.1259
4. S.H. Song and J.B.Kim, Trans. K.S.M.E, **9** (1995) p.351
5. H.Horii and S.Nemat-Nasser, Int. J. Solids Structures, **21** (1985) p.731
6. Y.Murakami and S.Nemat-Nasser, Engineering Fracture Mechanics, **17** (1983) p.193

Key Engineering Materials Vols. 183-187 (2000) pp. 773-778
© 2000 Trans Tech Publications, Switzerland

Studies of Fracture of Piezoelectric Ceramics at HKUST

Tong-Yi Zhang

Department of Mechanical Engineering, Hong Kong University of Science and Technology, Clear Water Bay, Pokfulam Road, Kowloon Hong Kong, China P.R.

Keywords: Combined Mechanical and Electrical Loading, Energy Release Rate, Fracture, Insulating and Conducting Cracks, Piezoelectric Materials

ABSTRACT

The present work reviews our theoretical and experimental studies of the fracture behavior of piezoelectric ceramics. The theoretical results show that for an insulating crack, the energy release rate is independent of the applied electric field either perpendicular or parallel to the crack when the electric field inside the crack is taken into account. For a conducting crack, the applied electric field parallel to the crack drives the crack to propagate. When electric yielding occurs at a crack tip, the global energy release rate is the same as that derived from linear fracture mechanics, while the local energy release rate shows a linear relationship between the fracture toughness and the applied electric field. The experimental results illustrate that for PZT-841 and PZT-4 ceramics, the scattering degree of measured data is considerably enhanced by an applied electric field. Either a positive or a negative electric field reduces the bending strength as well as the fracture toughness. For the PZT-841 ceramics, a two-peak distribution of the bending strength seems to appear under combined mechanical-electrical loading. The experimental results also confirm that there exist mechanical- and electrical-fracture toughness for PZT-4 ceramics and both are material properties. The mechanical and electrical critical energy release rates are respectively 8.7(±1.1) and 223.7(±45.5) N/m. The electrical fracture toughness is 25 times higher than the mechanical one because more energy dissipation such as electric discharging and domain switching accompanies with crack propagation under purely electrical loading.

1. INTRODUCTION

The mechanical reliability of piezoelectric materials becomes increasingly important as they are used in more and more sophisticated areas. Thus, there has been tremendous interest in studying the fracture behavior of those materials [1-30]. One of the most interesting and challenging aspects is about the effect of electric field on the fracture behavior and criterion. Currently, theoretical predictions of the effect of electric field based on linear fracture mechanics do not qualitatively agree with experimental observations. Another of the most interesting and challenging aspects is about the critical energy release rate for a conducting crack loaded under a purely electric field. Is the critical electric energy release rate identical to the critical mechanical energy release rate? We have theoretically and experimentally investigated the fracture behavior of piezoelectric materials for many years. The present work summaries our previous publications to introduce the studies of fracture of piezoelectric materials at the Hong Kong University of Science and Technology

(HKUST) [5-14]. An accompanied paper will present an overview of the relevant work worldwide [31].

2. LINEAR APPROACH [13, 14]

2.1 Electric Boundary Conditions along Insulating Crack Surfaces and Electric Field inside an Insulating Crack

Linear electro-elastic analysis is the first step to understand the fracture behavior of piezoelectric materials under combined mechanical and electrical loading. To simplify the derivation process there are two commonly used electric boundary conditions along insulating crack faces in the literature. The first commonly used boundary condition is the specification that the normal component of electric displacement along the crack faces equals zero and thus ignores the electric field within the crack. The second commonly used boundary condition treats the crack as being electrically permeable, wherein the electric potential and the normal component of electric displacement continuously cross the crack. In order to include the electric field inside an insulating crack, we studied an elliptical cylinder cavity and introduced two dimensionless ratios, α and β. α denotes the ratio of the minor semi-axis to the major semi-axis of the ellipse, while β is the ratio of dielectric constant of the ellipse to the effective dielectric constant of the material. When α approaches zero, there are three limits of the electric displacement inside an insulating crack, depending on the value of α/β. The electric field inside the crack can be ignored if $\alpha/\beta \to \infty$. Since β is at the order of 10^{-3} for most piezoelectric materials, α should be smaller than 10^{-1} to meet $\alpha/\beta \to \infty$. This means that the first commonly used boundary condition may be appropriate only for very short cracks. On the other hand, the second commonly used boundary condition becomes appropriate when $\alpha/\beta \to 0$. The electric field within the elliptic cavity is uniform and its strength depends also on α and β. Letting the crack width approach zero leads to the electric field strength inside the crack three orders higher than the applied because of $\beta \approx 10^{-3}$. As a possible consequence, the insulating crack may breakdown electrically when the electric field inside the crack is higher than a critical value. The electric breakdown will release energy and make the crack conducting, influencing greatly on the fracture behavior of piezoelectric materials.

2.2 Intensity Factors and Energy Release Rates

When the electric field inside an insulating crack is considered, the electric field strength has a finite value at the crack tip, while the stresses and the electric displacement approach infinity at the tip. The mode I, II and III stress intensity factors have the conventional form, whereas the electric displacement intensity factor depends on α and β. The electric displacement intensity factor is consisted of two terms, one term has the conventional form and the other is related to the effective dielectric constant and other materials constants. The other term disappears only when $\beta \to 0$ and $\alpha/\beta \to \infty$, i.e., the electric field inside the crack is ignored. For a slit insulating crack, the applied electric field contributes nothing to the energy release rate when the electric field inside the crack is considered. On the other hand, the electric field impedes crack propagation if the crack opening profile is used as the boundary. The results show that both the geometry and size of the crack have a great influence on fracture behavior of these materials.

When the dielectric constant inside the crack is treated to be infinitely large, the crack becomes conductive. The two dimensionless ratios play also an important role there. If $\alpha\beta \neq 0$, a complex electric displacement intensity factor has to be introduced to describe the mechanical and electric fields near a conducting crack tip. For a conducting crack, an applied electric field parallel to the crack length drives the crack to propagate, which has been experimentally confirmed.

3. ELECTRIC STRIP SATURATION MODEL [9]

An electric strip saturation model was proposed by analogy to the classical Dugdale model to understand the linear experimental results between the applied electric field and the fracture load [23, 28]. The electric strip saturation model is based on the hypothesis that piezoelectric ceramics are mechanically brittle and electrically ductile such that electric saturation (yielding) may occur in front of an insulating crack tip. Assuming the electric saturation zone does not develop during the crack propagation, we derive the local energy release rate. Using the energy release rate as a criterion, the local energy release rate gives a linear prediction between the electric field and the fracture load, which agrees with the experimental results [23, 28]. If the electric saturation zone develops during crack propagation, we obtain the global energy release rate, which is equal to that of a linear piezoelectric crack without electrical yielding. The electric strip saturation model has been further developed to include domain switching.

4. THREE-POINT BENDING TESTS [5, 8]

The material used in this study is poled PZT-841 with an average grain size of 4-5 μm. The composition of PZT-841 is near, but in the tetragonal side of the morphotropic phase boundary.

4.1 Temperature Effect

Three-point bending tests were conducted at 25, 122, 220, or 268 °C, respectively, to measure the temperature dependence of the bending strength, in which the poling direction was parallel with the zigzag surface and 20 samples were tested at each temperature. Fig. 1 shows the plot of bending strengths measured at temperatures 25, 122, 220, and 268 °C, where the curve is plotted from our domain wall motion model which will be discussed later. The bending strength decreases from 97.8 MPa at room temperature to 85.9 MPa at 122 °C, and further decreases to 74.8 MPa at 220 °C, then increases to 90.5 MPa at 268 °C. Our experimental results indicate that a larger strength corresponds to a smaller compliance.

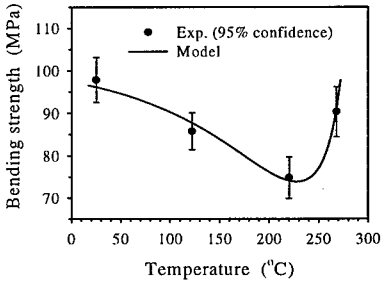


Fig. 1 Temperature dependence of the bending strength.

4.2 Electrical Effect

To study the effect of an electric field on the bending strength, three-point bending tests were carried out at room temperature. The poling direction was perpendicular to the zigzag surface. A DC field up to 20 kV/cm was applied across the sample, either parallel or antiparallel to the poling direction. 50 samples were tested under each electric field. Fig. 2 plots the mean with its error bar of the bending strength versus electric field, where the curve is also plotted from the domain wall motion model. The bending strengths under the electric fields of –3.33, 0, and +3.33 kV/cm are, respectively, 89.9, 88.0, and 89.8 MPa. The statistical u-test analysis at a 95% significance level shows that the

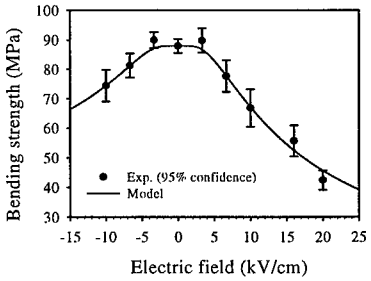


Fig. 2 Effect of an electric field on the bending strength.

electric fields of ± 3.33 kV/cm do not change the bending strength. The bending strengths under the applied fields of –6.7 and +6.7 kV/cm are respectively 81.4 and 77.7 MPa, significantly lower than that without any electric field. The bending strength is further reduced under a higher electric field, either positively or negatively applied, as shown in Fig. 2. The bending strength along the poling direction, i.e., 88.0 MPa, is comparatively smaller than that perpendicular to the poling direction, i.e., 97.8 MPa, due to the anisotropy of the material. Applying an electric field may scatter the data tremendously. As an example, Fig. 3 shows the experimental results under 0 and 10 kV/cm to illustrate the electrically induced data scattering and bimodal distribution.

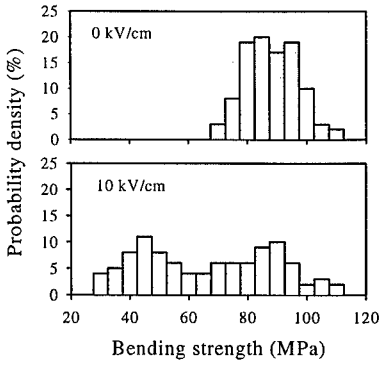


Fig. 3 Probabilistic distribution of the bending strength.

5. DOMAIN WALL MOTION MODEL [8]

A domain wall motion model was proposed to explain the observed phenomena. The model is based on the fact that 90°-domain wall motion generates deformation and internal stresses. Such deformation yields softening in the elastic compliance, while degradation in the bending strength is attributed to the tensile component of the internal stresses. Damping occurs when the motion distance is larger than a critical value. After modeling and measuring the critical stress for triggering damping and the intrinsic strain as functions of temperature, we have the formula for the bending strength and accordingly plot the curve in Fig.1, which fits the experimental data. Using the same model, we assess the electric force acting on a domain wall from the relationship between the motion velocity of domain walls and the applied electric field. This relationship is nonlinear and hence the electric force and the internal stress are nonlinearly related to the applied electric field. As a result, the final formula derived from the model predicts the nonlinear effects of the electric effects on the bending strength, as shown by the curve in Fig. 2.

6. FRACTURE TESTS [6]

Compact Tension (CT) tests and Indentation Fracture (IF) tests were carried out on PZT-841 ceramics under an applied electric field. In the CT tests, the notch on each sample was cut using a diamond saw with a 0.2 mm-thick blade and the notch tip was further sharpened with a wire saw of 0.05 mm in diameter. The poling direction was perpendicular to the notch. About 10 samples were tested at each level of the electric fields, except that 33 samples were tested at the electric field of 15 kV/cm to study the distribution of fracture toughness. We calculated the energy release rate with finite element analysis and then converted the energy release rate into the mode I stress intensity factor. In the IF tests, the load was 49.0 N and the electric field of 4 kV/cm was applied either parallel or antiparallel to the poling direction of the sample. Under each level of

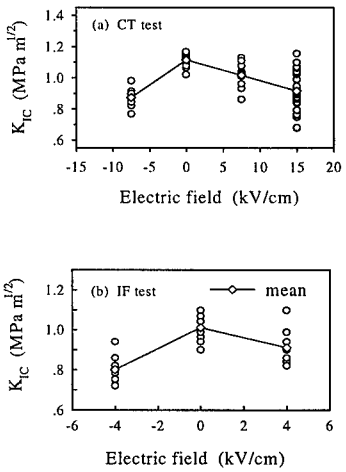


Fig. 4 Effect of an electric field on the fracture toughness.

the electric fields, about 10 indentations were performed. We hare report only the fracture behavior of the cracks perpendicular to the poling direction. Figs. 4(a) and 4(b) show the variation of K_{IC} with the applied electric field obtained from the CT and IF tests, respectively. Under purely mechanical loading, the averaged K_{IC}s are $1.12\pm0.05 MPa\sqrt{m}$ and $1.01\pm0.06 MPa\sqrt{m}$, respectively, from the two methods. The mean value of K_{IC} is reduced by either a positive or a negative applied electric field in both types of testing. In the CT tests, the negative field of 7.5 kV/cm reduces the averaged K_{IC} by $0.25 MPa\sqrt{m}$, while the same strength positive field reduces the averaged K_{IC} by $0.10 MPa\sqrt{m}$. Similarly, in the IF tests, a reduction of $0.21 MPa\sqrt{m}$ or $0.10 MPa\sqrt{m}$ results from the application of a negative or positive field of 4 kV/cm. These facts indicate that a negative field has a stronger influence on the averaged K_{IC} than a positive field does. Applying a positive electric field of 15 kV/cm reduces further the averaged K_{IC} to $0.92\pm0.14 MPa\sqrt{m}$ in the CT tests, resulting in a relative reduction of 18%.

7. CONDUCTING CRACKS [7]

CT samples used in this study were made from poled PZT-4 piezoelectric ceramics and the poling direction was parallel to the notch. A 0.25 mm wide notch in every sample was cut and its tip was sharpened further by a wire saw of radius 0.1 mm. For the conductive crack, silver paint was filled into the notch to make it function as an electrode. In the electric tests, a DC voltage was applied to a sample at the electrodes and increased until the sample was failed. All tests were carried out at room temperature and 30 samples were tested for each loading type. It was observed that electrical breakdown was usually accompanied by fracture. The fracture surfaces are flat for samples fractured under mechanical loads. A critical voltage causes dielectric breakdown tunnel and rough fracture surfaces. We carried out finite element analysis to calculate the energy release rate for the given samples. The critical energy release rate under mechanical loading was calculated from the fracture load and the corresponding ligament, as shown in Fig. 5a. The mean of the mechanical critical energy release rate is G_{IC}^{M}=8.7±0.4 N/m. It is clearly seen that the linear regression of the plot is very close to a horizontal line, indicating that the critical energy release rate is a material constant independent on the sample ligament. Similarly, the critical energy release rate under electric loading was calculated from the critical voltage and the ligament. Fig. 5b presents the electrical critical energy release rate versus sample ligament. The linear regression of the plot is also almost a horizontal line. This fact, in analogy with the mechanical loading situation, means that the electrical critical energy release rate is a material property with the value G_{IC}^{E}=223.7±17.0 N/m for PZT-4 ceramics. The significance of the existence of G_{IC}^{E} is that it enables fracture mechanics concepts to be used in understanding dielectric failure, and it provides a useful material property for designers of electronic and electromechanical devices.

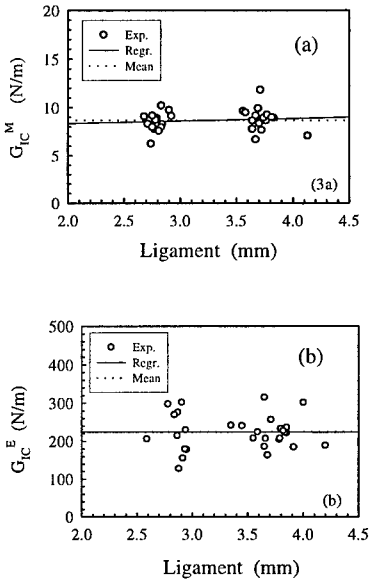


Fig 5 The energy release rate versus the ligament, (a) mechanical loading and (b) electrical loading.

8. CONCLUDING REMARKS

The challenging point in studying the fracture behavior of piezoelectric ceramics lies in the large scattering of experimental data, which demands more experimental work. A statistical theory is also highly demanded for establishing a useful failure criterion.

ACKNOWLEDGEMENTS: The work is fully supported by an RGC grant HKUST6051/97E from the Research Grants Council of the Hong Kong Special Administrative Region, China. Dr. Ran Fu and Professor Pin Tong at HKUST, Professor Cai-Fu Qian from Beijing University of Chemical Technology and Professor Huajian Gao from Stanford University participated in this research.

REFERENCES

1. D.M. Barnett and J. Lothe, *Phys. Stat. Sol. (b),* **67** (1975) p.105.
2. H. Cao and A. G. Evans, *J. Am. Ceram. Soc.*, **76** (1993) p.890.
3. G. P. Cherepanov, *Mechanics of Brittle Fracture*, McGraw-Hill, New York, (1979).
4. W.F.J. Deeg, The analysis of dislocation, crack, and inclusion problems in piezoelectric solids. *PhD Thesis*, Stanford University, (1980).
5. R. Fu and T.-Y. Zhang, *J. Am. Ceram. Soc.*, **81** (1998) p.1058.
6. R. Fu and T.-Y. Zhang, Effect of an Applied Electric Field on the Fracture Toughness of Poled Lead Zirconate Titanate Ceramics, *J. Am. Ceram. Soc.*, in press.
7. R. Fu, C.-F. Qian and T.-Y. Zhang, *Appl. Phys. Letters*, **76** (2000) p.126.
8. R. Fu and T.-Y. Zhang, Influences of Temperature and Electric Field on the Bending Strength of Lead Zirconate Titanate Ceramics, *Acta Mater.*, in press.
9. H. Gao, T.-Y. Zhang and P. Tong, *J. Mech. Phys. Solids,* **45** (1997) p.491.
10. T.-Y. Zhang and J.E. Hack, *J. Appl. Phys.*, **71** (1992) p.5865.
11. T.-Y. Zhang, *Int. J. Fracture,* **66** (1994) R33.
12. T.-Y. Zhang, *Int. J. Fracture,* **68** (1994) R33.
13. T.-Y. Zhang and P. Tong, *Int. J. Solids Structures,* **33** (1996) p.343.
14. T.-Y. Zhang, C.-F. Qian and P. Tong, *Int. J. Solids Structures,* **35** (1998) p.2121.
15. S. Kumar and R. N. Singh, *Acta Mater.*, **44** (1996) p.173.
16. C. S. Lynch, *Acta Mater.*, **44** (1996) p.4137.
17. H. Makino and N. Kmiya, *Jpn. J. Appl. Phys.*, **33** (1994) p.5323.
18. R. M. McMeeking, *J. Appl. Math. Phys.,* **40** (1989) p.615.
19. K. Mehta and A.V. Virkar, *J. Am. Ceram. Soc.*, **73** (1990) p.567.
20. Y.E. Pak, *J. Appl. Mech.,* **57** (1990) p.647.
21. Y. E. Pak, *Int. J. Fracture,* **54** (1992) p.79.
22. Y. E. Pak and A. Tobin, *Mech. Electromagn. Mater. Structures,* **AMD 161/MD 42** (1993) p.51.
23. S. Park and C.-T. Sun, *J. Am. Ceram. Soc.*, **78** (1995) p.1475.
24. H. Sosa and Y. E. Pak, *Int. J. Solids Structures,* **26** (1990) p.1.
25. H. Sosa, *Int. J. Solids Structures,* **29** (1992) p.2613.
26. Z. Suo, C. M. Kuo, D. M. Barnett, and J. R. Willis, *J. Mech. Phys. Solids*, **40** (1992) p.739.
27. Z. Suo, *J. Mech. Phys. Solids,* **41** (1993) p.1155.
28. A. G. Tobin and Y.E. Pak, *Proceedings of the 1993 North American Conference on Smart Structures and Materials: Smart Materials*, ed. V.K. Varadan, **1916**, (1993) p.78.
29. T. Zhu and W. Yang, *J. Mech. Phys. Solids*, **47** (1999) p.81.
30. Q. H. Qin, Y. W. Mai and S. W. Yu, *Int. J. Solids Structures,* **36** (1999) p.427.
31. T.-Y. Zhang, R. Fu, M.-H. Zhao and P. Tong, The Fourth International Conference on Fracture and Strength of Solids, Pohang, Korea, 16-18 August 2000, in press.

Key Engineering Materials Vols. 183-187 (2000) pp. 779-784
© 2000 Trans Tech Publications, Switzerland

Tensile and Fracture Behaviors of PC/ABS Polymer Alloy

Mitsuo Notomi[1], Kikuo Kishimoto[2], Tiejun Wang[3] and Toshikazu Shibuya[2]

[1] Department of Mechanical Engineering, Meiji University,
1-1-1 Higashimita, Tama-ku, Kawasaki-shi, Kanagawa 214-8571, Japan

[2] Department of Mechanical and Intelligent Systems Engineering, Tokyo Institute of Technology,
2-12-1 O-okayama, Meguro-ku, Tokyo 152-8552, Japan

[3] Department of Engineering Mechanics, Xi'an Jiaotong University, Xi'an 710049, China P.R.

Keywords: Crack Extension, Fracture Toughness, Morphology, PC/ABS, Polymer Alloy, SEM Observation, TEM Observation, Tensile Properties

ABSTRACT

The purpose of this study is to investigate the effect of morphology on the tensile properties and fracture properties of Polycarbonate (PC) / acrylonitrile-butadiene-styrene (ABS) polymer alloy. The transmission electron microscope (TEM) observation shows that the co-continuous phase structure is formed at 60/40 compositions of PC/ABS. At 80/20 compositions, PC and ABS form continuous and dispersed phase, respectively. The yield stress, Possion's ratio and tensile strength follow a law of mixture. On the other hand, the Young's modulus appears the maximum value at co-continuous phase structure, i.e., 60/40 compositions. The fracture property in PC/ABS(80/20) is most excellent of all compositions. The microscopic observations suggest that the both effects of the release of triaxial stress by the separation of interface among each phase and the severely damaged deformation of rubber particles during fracture contribute to the toughening of PC/ABS(80/20).

1. INTRODUCTION

Polycarbonate (PC) / acrylonitrile-butadiene-styrene (ABS) alloys are well-known commercial polymer. Their commercial success is due to an appropriate combination of the two components. PC has high thermal stability and good impact behavior. ABS has easy processability and economical benefits. From a scientific point of view, however, it is not well understood why these alloys have such good mechanical and impact properties[1]. As a matter of fact, PC/ABS alloys consist of four polymeric species compounded in complex multiphase systems and their behavior is not yet clearly understood.

Recently, many researchers are interested in the relationship between mechanical properties, especially strength, and meso-structure because it is appeared that this structure strongly affected them[2]. In polymer alloy, the meso-structure corresponds to high-order structure formed by the mixture of each polymeric species, i.e. morphology.

The purpose of this study is to investigate the effect of morphology, which is the structure of blending PC and ABS, on the mechanical properties, i.e. tensile and fracture, of PC/ABS alloys. Because the morphology changes in the contents of each polymer, the six types of specimen based on different ratio of compositions are prepared. The morphology of ABS and PC/ABS alloys is observed by transmission electron microscope (TEM). Material constants of tensile and fracture

Table 1. Mixed ratio of PC to ABS and content of rubber.

PC/ABS (wt%)	100/0	80/20	60/40	50/50	40/60	0/100
Rubber (wt%)	0	3.6	7.2	9	10.8	18

properties are determined by means of mechanical tests. Fractographic analysis by scanning electron microscope (SEM) and TEM observation are performed for the samples after fracture.

2. EXPERIMENTAL

PC, ABS and PC/ABS alloys used in this study were supplied by Japan synthetic rubber Co., Ltd. Mixed ratio of PC to ABS and rubber contents are given in Table 1. Figures 1 to 4 show TEM photomicrographs for four types of PC/ABS alloys. In these photos the rubber of ABS appears black particles, and the region including rubber particles is ABS phase. The gray region corresponds to PC phase. PC forms the continuous phase at compositions with greater than 60wt%. Whereas, ABS forms the continuous phase at compositions with greater than 40wt%. Consequently, an apparent co-continuous phase structure is formed in PC/ABS(60/40). Yan and colleagues[3] showed almost the same variation of morphology due to contents of PC and ABS.

The tensile tests using the dumbbell type specimens were carried out at room temperature with displacement rate of 5mm/min. The Young's modulus, Poisson's ratio, yield stress and tensile strength were determined using the stress-strain curves by these tests. The fracture toughness tests were carried out on compact tension (CT) specimens according to ASTM D5045-93 and E813-89. The K_R curves of stress intensity factor *versus* crack extension length were plotted. From the

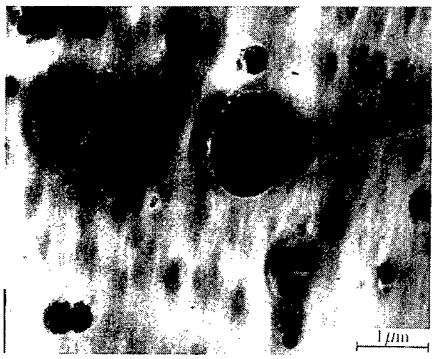


Fig. 1. Morphology of PC/ABS (80/20).

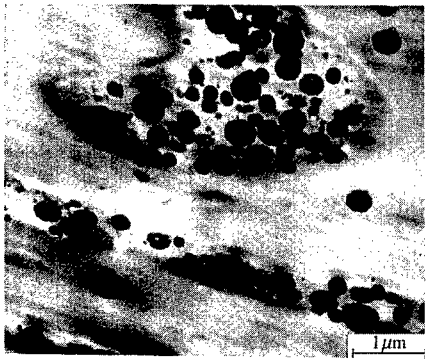


Fig. 2. Morphology of PC/ABS (60/40).

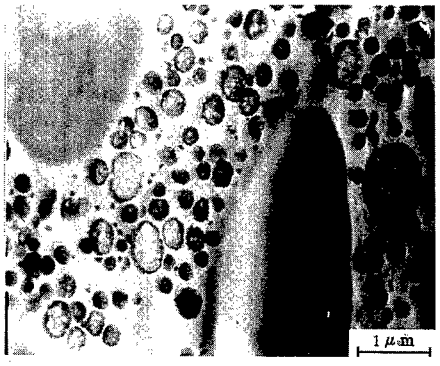


Fig. 3. Morphology of PC/ABS (50/50).

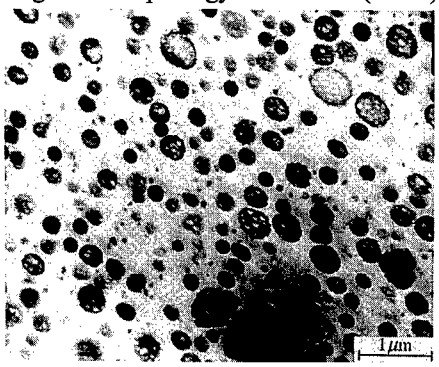


Fig. 4. Morphology of PC/ABS (0/100).

Table 2. Material constants of PC, ABS and PC/ABS.

Specimen (PC/ABS)	100/0	80/20	60/40	50/50	40/60	0/100
Young's modulus [GPa]	2.27	2.32	2.40	2.28	2.26	2.22
Poisson's ratio	0.37	0.36	0.36	0.36	0.35	0.35
Yield stress [MPa]	62.2	58.9	49.1	44.9	42.1	37.8
Tensile strength [MPa]	62.6	61.0	56.1	54.1	50.4	42.2
K_{in} [MPa$\sqrt{m}$]	2.27	2.63	2.87	2.72	2.61	2.43
dK_R/da [MPa/$\sqrt{m}$]	1444	1502	584	418	271	547

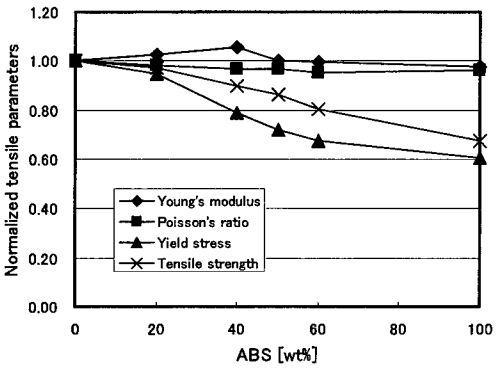


Fig. 5. Normalized tensile properties

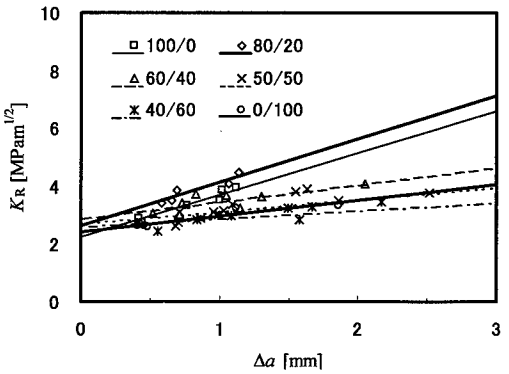


Fig. 6. Crack extension resistance curves.

diagrams, the critical stress intensity factor at crack initiation, i.e. the fracture toughness (K_{in}), and the slope of the crack extension resistance curves (dK_R/da) were determined. After these tests the fracture surfaces of CT specimens were examined by SEM. Furthermore, some samples were cut from the regions underneath fracture surface (almost 5 μm depth) and observed by TEM.

3. RESULTS

3.1. Tensile Properties

Table 2 and Fig. 5 show the material constants related to tensile and the normalized ones divided by the value of PC/ABS(100/0), respectively. All material constants of pure PC are a little lager than those of pure ABS. Although the Possion's ratio, yield stress and tensile strength of PC/ABS alloys follow a law of mixture, Young's modulus increases from 0wt% to 40wt% of ABS compositions and then decreases beyond 40wt% until pure ABS. Greco and colleagues[4] obtained the variation of Young's modulus as a function of PC/ABS blend volumetric composition and that was similar to our result. Although they indicated that the variation near pure PC and ABS followed the Kerner's model for perfect adhesion, they did not explain the variation of thorough compositions. Whereas it is reasonable to suppose that the complex phase mixture of PC and ABS affect the behavior, this will be discussed further.

3.2. Fracture Properties

Figure 6 shows the crack extension resistance curves of PC, ABS and PC/ABS alloys. Table 2 demonstrates the K_{in} and dK_R/da obtained from Fig. 6. The K_{in} of ABS is higher than that of PC and, conversely, the dK_R/da of ABS is lower. Furthermore, the both fracture parameters of PC/ABS alloys do not follow a law of mixture. Although K_{in} has maximum value at PC/ABS(60/40), the dK_R/da has lower value than that of PC/ABS(100/0) and PC/ABS(80/20). In contrast, the K_{in} of PC/ABS(80/20) remains comparable to that of PC/ABS(60/40) and its dK_R/da has the maximum value. Thus, we consider that PC/ABS(80/20) has the most excellent fracture resistance. From Fig.

1, it is clear that the alloy that has the continuous phase of PC and dispersed phase of ABS exhibits superior fracture property.

The authors[5] reported that the impact fracture toughness of PC/ABS(80/20) was the largest value of the alloys. Greco and colleagues[4] also reported the similar result using by Charpy impact tests. Moreover, Lombardo and colleagues[6] demonstrated that the alloys included about 10wt% of ABS compositions had the superior Charpy impact resistance. Accordingly, the PC/ABS(80/20) alloy probably has the best fracture property. Note that the produced companies and the contents of rubber in ABS are different from each other. It is concluded that the K_{in} and dK_R/da are strongly dependent on its contents of PC and ABS, i.e., morphology.

4. DISCUSSIONS

4.1. SEM Observations

The SEM photomicrographs of the fracture surfaces are shown in Figs. 7 to 10. The fracture surface of PC/ABS(100/0) shown in Fig.7 exhibits almost flat except for hemisphere holes with about 10μm diameter. The surface of PC/ABS(0/100) appears to be rougher than PC/ABS(100/0) and some cavities can be seen. These cavities suggest that rubber particles in ABS fell away from the fractured surface. PC/ABS(60/40) (refer to Fig.9) can be seen that the fragments of PC drawn from the surface stand around ABS phase. This behavior likely depends on the ductility of each material; PC is more ductile than ABS. The features of PC/ABS(50/50) and PC/ABS(40/60) are almost similar to that of PC/ABS(60/40).

The surface of PC/ABS(80/20) is rougher than PC/ABS(60/40). In addition, several cavities, including large size can be seen. It is noticed that the dimensions of large cavities applicability are

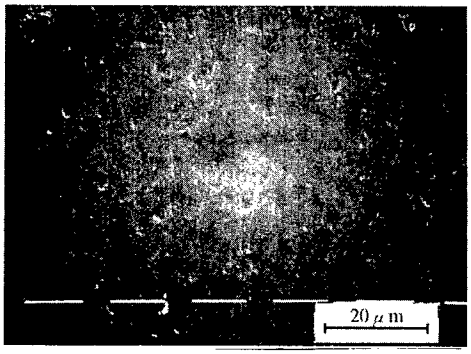


Fig.7. Fracture surface of PC/ABS (100/0) .

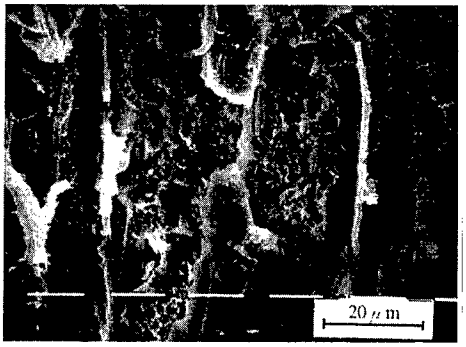


Fig.9. Fracture surface of PC/ABS (60/40).

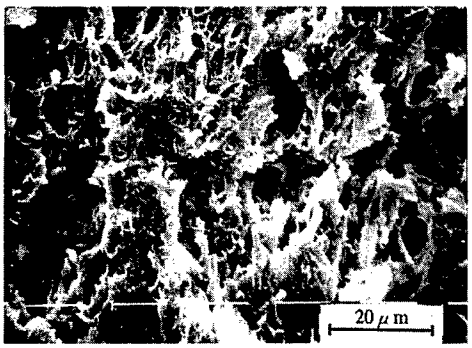


Fig.8. Fracture surface of PC/ABS (80/20).

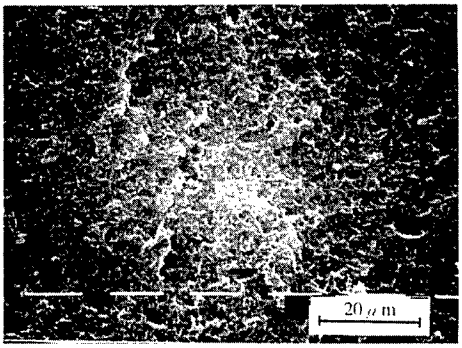


Fig.10. Fracture surface of PC/ABS (0/100).

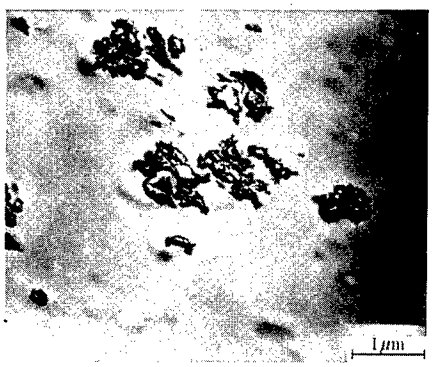


Fig. 11. Morphology of PC/ABS(80/20) after fracture test.

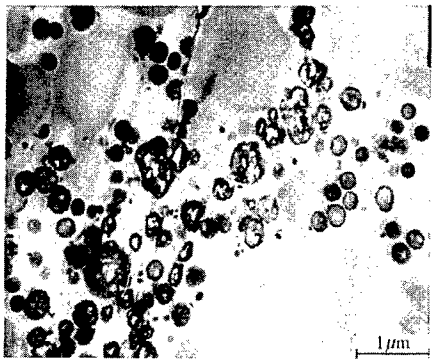


Fig. 13. Morphology of PC/ABS(50/50) after fracture test.

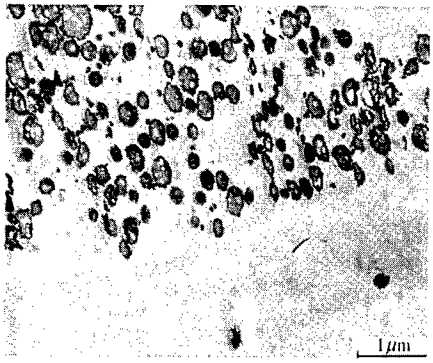


Fig. 12. Morphology of PC/ABS(60/40) after fracture test.

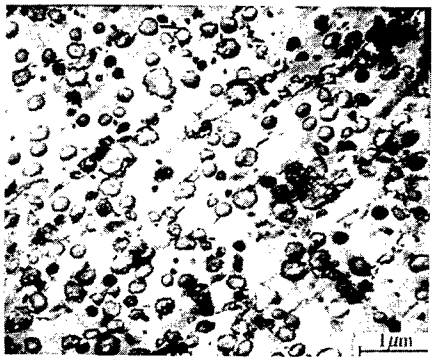


Fig. 14. Morphology of PC/ABS(0/100) after fracture test.

the same as that of ABS dispersed phase.

4.2. TEM Observations

Figures 11 to 14 show the TEM photomicrographs of the samples that are cut from the whitening region underneath the fracture surfaces. On PC/ABS(0/100) (refer to Fig. 14) voids and black lines can be seen in and around rubber particles, respectively, and these lines correspond to crazes. The formation of crazes and voids causes toughening[2]. This toughening mechanism occurs in the alloys that include ABS phase more than 40wt% (refer to Figs. 12 and 13).

In Fig.11, the rubber particles of PC/ABS(80/20) are deformed more than others, and the original shapes disappear (compare with Fig. 1). Furthermore, its interfaces to PC become zigzag shape. Consequently, from both observations we consider that the toughening mechanism of PC/ABS(80/20) that has the superior fracture property is different from the other alloys. We will discuss it next section.

4.3.Toughening Mechanism

The deformation at cross section by fracture surface of PC/ABS(60/40, 50/50, 40/60) and PC/ABS(80/20) are shown in Fig. 15. On the case (a) in Fig. 15, fragments of PC are drawn from the surface because of its ductility. Nevertheless, this hardly contributes to toughening. The evidence can be seen in the fact that the crack extension resistances are the same as that of pure ABS (refer to Fig.6). Because void formation can be seen in Figs. 12 and 13, the toughening of PC/ABS(60/40, 50/50, 40/60) are dominated by the mechanism that is similar to the that of pure ABS in toughening.

As we mentioned before, dK_R/da of PC/ABS(80/20) is higher than that of PC. If a law of

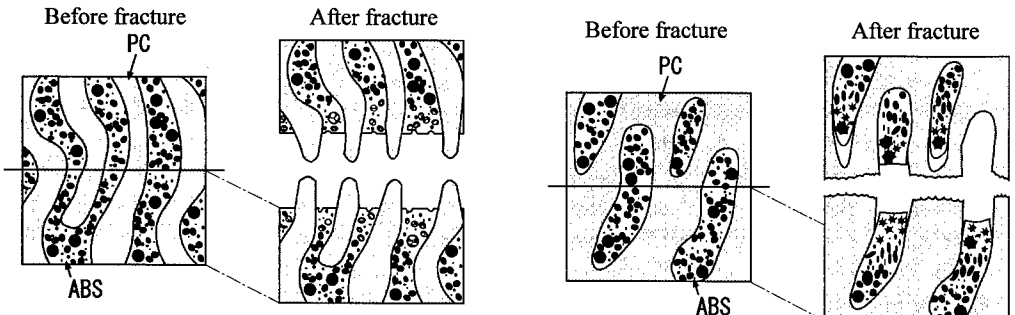


Fig.15. Deformation at cross section by fracture surface of (a) PC/ABS(60/40, 50/50, 40/60) and (b) PC/ABS(80/20) during fracture.

mixture was valid, dK_R/da might be a little less than PC because that of ABS is much small. We consider the reason why the increase of dK_R/da. First, the triaxial stress is released as a result of the separation of ABS dispersed phases from PC phase (refer to Fig. 8). This process promotes the plastic deformation of both materials. Second, from the observation of TEM (refer to Fig. 11) it is clear that the rubber particles in ABS are severely damaged during fracture, and this process consumes the energy of crack extension. Figure 15(b) is drawn the deformation state of cross section near fracture surface. Both effects contribute to improve the fracture property of PC/ABS(80/20) more than the others.

5. CONCLUSIONS

Tensile and fracture tests were performed on PC/ABS alloys, having compositions over the whole range from pure PC to pure ABS. Furthermore, variations of morphology and features of fracture surfaces were observed by SEM and TEM. The morphology of PC/ABS strongly depends on its contents. PC/ABS(60/40) forms co-continuous phase structure, and on PC/ABS(80/20) PC and ABS form continuous and dispersed ones, respectively. The Possion's ratio, yield stress and tensile strength of PC/ABS follow the law of mixture. Young's modulus has the maximum at the morphology as co-continuous phase. However, the fracture property attains maximum when the alloys have the morphology as continuous and dispersed phases of PC and ABS, respectively. From the microscopic observations, it is clear that the toughening mechanisms of PC/ABS(80/20) are the both effects of the triaxial stress release by the separation of interface among each phase and the severely damaged deformation of rubber particles during fracture.

We thank Mr. Tsuneo Chiba who works as a technician at Tokyo Institute of Technology for performing TEM observations, and Mr. Masataka Ishikawa for assistance with experiments.

REFERENCES

1. R.Greco and S.Sorrentino, Advances in Polymer Technology, **13**, 4 (1994) pp.249-258.
2. M. Notomi, K. Kishimoto, T. Shibuya and T. Koizumi, J. Polym. Sci., **72** (1999) pp.435-442.
3. R. J. Yan, W. Li, C. Chen, H. Zhang, B. Jiang and B. Yang, Int. J. Polmeric Mater. 23 (1993) pp.109-113.
4. R. Greco, M. R. Astarita, L. Dong and A. Sorrentino, Adv. Polym. Tech., **13**, 4 (1994) pp.259-274.
5. K. Kishimoto, H. Inohe, M. Notomi and T. Shibuya, J. Soc. Mater. Sci., Japan, **47**,8 (1998) pp.836-840. (in Japanese)
6. B. S. Lombardo, H. Keskkula and D. R. Paul, J. Appl. Polym. Sci., **54** (1994) pp.1697-1720.

Key Engineering Materials Vols. 183-187 (2000) pp. 785-790
© 2000 Trans Tech Publications, Switzerland

Influence of Stochastic Mesoscopic Structure on Macroscopic Mechanical Behavior of Brittle Material

Y.F. Fu[1], M.L. Huang[2] and C.A. Tang[1,3]

[1] CRISR, Resources and Civil Engineering School,
Northeastern University, Shenyang 110006, China P.R.

[2] Resources and Environment School, Liaoning University of Engineering
and Technology, Fuxin 123000, China P.R.

[3] LNM, Institute of Mechanics, Chinese Academy of Science,
Beijing 100080, China P.R.

Keywords: Failure, Heterogeneity, Localization, Mesoscopic, Numerical Simulation

ABSTRACT

A newly developed numerical code, MFPA^{2D} (Material Failure Process Analysis), is applied to study the influence of stochastic mesoscopic structure on macroscopic mechanical behavior of rock-like materials. A set of uniaxial compression tests has been numerically studied with numerical specimens containing pre-existing crack-like flaw. The numerical results reveal the influence of random mesoscopic structure on failure process of brittle material, which indicates that the variation of failure mode is strongly sensitive to the local disorder feature of the specimen. And the patterns of the crack evolution in the specimens are very different from each other due to the random mesoscopic structure in material. The results give a good explanation for various kinds of fracture modes and peak strength variation observed in laboratory studies with specimens made from the same rock block being statistically homogenous in macro scale. In addition, the evolution of crack is more complicated in heterogeneous cases than in homogeneous cases.

1. INTRODUCTION

Essentially, the failure and deformation of rock-like materials is a process of progressive evolution in which the cracks initiate, propagate, interact and coalesce due to external loading. The results from the observations of laboratory and field show that the macroscopic mechanical behavior of highly heterogeneous rock-like material is pronouncedly influenced by the mesoscopic heterogeneity. With regard to failure, many beneficial investigations [1-3] were carried out in the past decades in both experiments and the theory, but most of studies on the mechanism of rock failure are conducted just based on the assumption that rock is homogeneous medium, the influence of the heterogeneity on failure process is seldom considered. However, many rock failure phenomena, such as the activity of induced seismicity, the echelon pattern fracture in crust deformation, the precursor, aftershock of source development of earthquake, etc., are closely related to the heterogeneity of rocks. Hence, the heterogeneity of material must be considered in studying the behavior of rock-like materials. However, there is lacking of mature theory to describe the heterogeneity, the basic character of rock. Nowadays the numerical simulation based on statistical mesoscopic damage

mechanics is regarded as an effective tool to resolve the problem. Of later years, a code of MFPA^{2D} (Material Failure Process Analysis), based on the principles of FEM is developed at Center for Rockburst and Induced Seismicity Research, Northeastern University. And Tang et al [4,5] has studied many problems about failure mechanisms of rock-like materials with MFPA^{2D}. In this paper, by conducting a set of numerical tests on specimens containing pre-existing crack-like flaw under uniaxial compression, MFPA^{2D} is applied to study the influence of stochastic mesoscopic structure on macroscopic mechanical behavior of rock-like materials.

2. OUTLINE OF MFPA^{2D} AND MODEL SETUP

2.1. Brief description of MFPA^{2D}

The MFPA code, developed at the Center for Rockburst and Induced Seismicity Research (CRISR), Northeastern University, China, can be used for modeling the evolution of damage or crack initiation, propagation and coalescence in brittle material. The mesoscopic heterogeneity of material properties can be considered in the code, based on FEM. The mesoscopic heterogeneity represents the variation of the mechanical properties for the elements composed of the material. The consideration of heterogeneity for the elements composed of the material is achieved to assign to the elements random strength and elastic modulus by assuming a Weibull's distribution. The distribution is defined by equation (1) with three parameters, α, α_0 and m.

$$\varphi(\alpha, m) = m \cdot \left(\frac{\alpha}{\alpha_0}\right)^{m-1} \cdot e^{-\left(\frac{\alpha}{\alpha_0}\right)^m} \tag{1}$$

where the α is the element strength or elastic modulus and α_0 is the mean strength or elastic modulus of elements for the material. The parameter m, defined as homogeneity index of the brittle material, controls the shape of the distribution function, which relates to the degree of material heterogeneity. Materials with higher m values represent more homogeneous materials, whereas those with lower m values, more heterogeneous materials.

The more detailed explanation about the MFPA^{2D} can be found in the literature [6].

2.2. Model setup

The specimens with different m value are numerically tested:

1. Four specimens with value $m=2.0$ and same mechanical properties of elements, to study the influence of stochastic mesoscopic structure on the macroscopic behavior,
2. Three specimens with different value $m=1.1,\ 2.0,\ 5.0$, to investigate the effect of heterogeneity.

In all cases, the specimen undergoes plane stress compression. The geometrical and mechanical properties for all the specimens are listed in Table 1. The schematic map (a, b and c) and statistical distribution of strength for elements of specimens (a′, b′ and c′) are in Fig.1.

Table 1. Mechanical and geometrical parameters for the specimens

Parameter	Value
Homogeneity index (m)	1.1, 2.0, 5.0
Mean compressive strength (σ_0)	400 MPa
Mean elastic Modulus (E_0)	60000 MPa
Tension cutoff (λ)	0.1
Frictional angle (ϕ)	30°

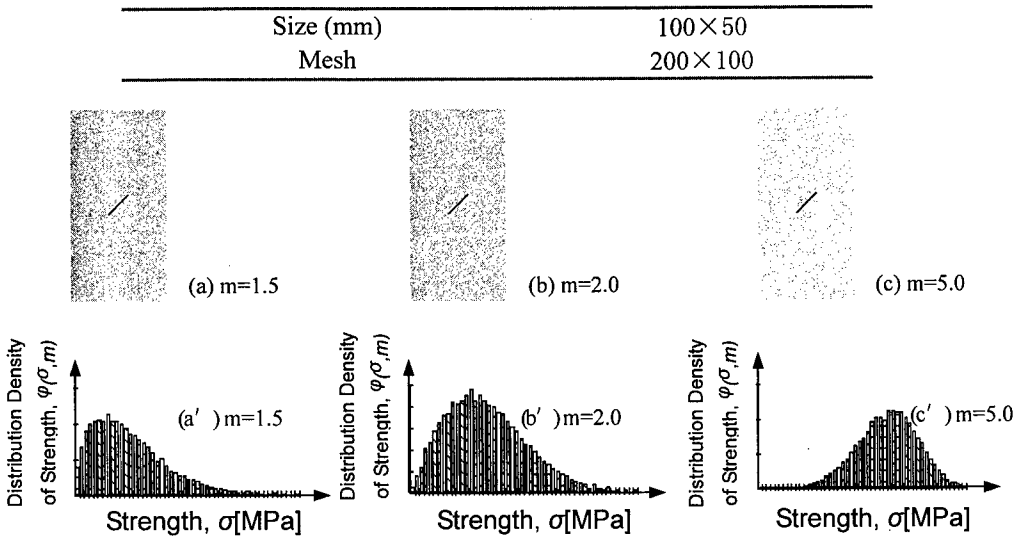


Fig.1. Schematic map of specimens

3. NUMERICAL SIMULATION RESULTS AND DISCUSSION

3.1.Complete stress-strain curve and stress distribution and redistribution

In the case of studying crack propagation in rock specimen, the assumption regarding rock as homogeneous and continuous material can make the mathematical process more convenient, but the

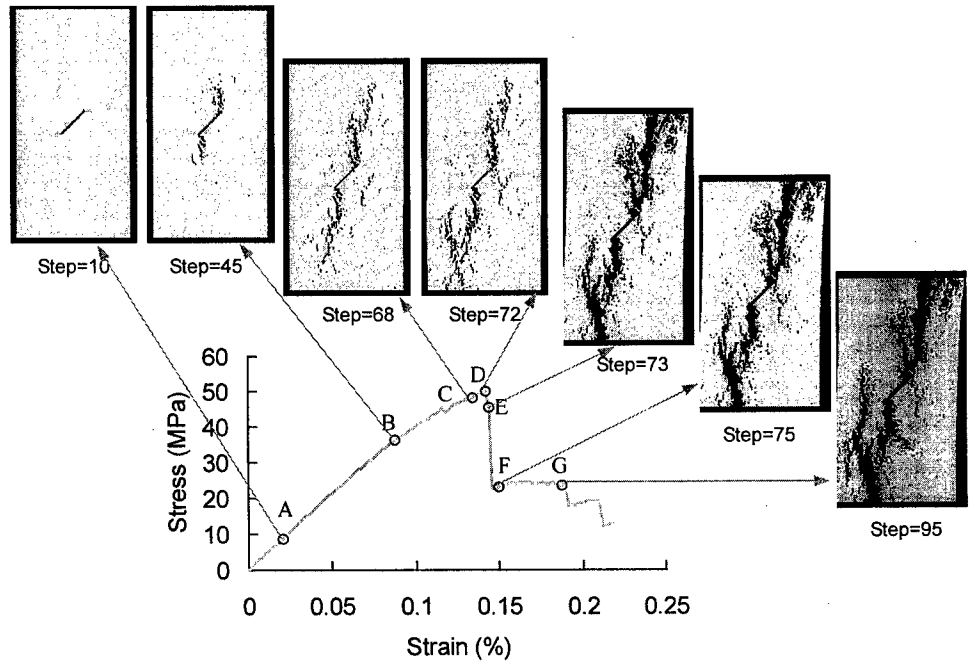


Fig. 2 Failure process of specimen No.1

results caused by the assumption maybe are unaccepted.

Fig.2 shows the failure process of specimen No.1 with homogeneity index m=2.0. Although the pattern of crack propagation is very complicated, it seems closer to the reality of rock failure than the prediction from fracture mechanics based on the assumption of homogeneity continuity. The whole process can be divided into three stages: linear deformation, non-linear deformation and softening, as the following:

1. The stage of linear deformation. During the stage of initial loading the concentrated stress in tips of the pre-existing flaw doesn't reach the critical strength of elements, so the crack propagation doesn't occur. In this time, the macroscopic stress field is still statistically coincided with the analytic solution of fracture mechanics because few elements consisting of the specimen fail during this stage (as shown in step 10). Consequently, the stress-strain curve shows good linearity.

2. The stage of non-linear deformation. With increasing loading, the crack initiates at the tip of the flaw. Although the overall direction of the crack propagation is more or less the same as predicted by fracture mechanics theory, the formation of crack propagation is rather complex and shows discontinuous features. The boundary of crack is very vague and the crack bifurcation occurs frequently (as shown in step 45, 68, and 72). The distribution of stress field gradually changes owning to the increasing number of failure elements and random position of their emergence. The stress-strain curve demonstrates non-linearity.

3. The softening stage. Although the stress decreases 9 percent from the point D to the point E, the climax of number of failure elements occurs (as shown in step 73). After the peak-strength the crack has almost crossed the section of the specimen but still showed a non-zero residual stress (as shown in step 75, 95) and further loading is difficult to drive the cracks for a visible propagation.

3.2.The influence of stochastic mesoscopic structure on macroscopic mechanical behavior

There is a well-known fact that even core specimens obtained from a seemingly homogeneous block of rock show variability both in deformation and strength properties due to the stochastic mesoscopic structure in a specimen. It means that the randomly distributed micro-defects in the specimen result in localization of deformation and failure in different position. In order to study the problem, four specimens with same macroscopic mechanical properties but with different mesoscopic structure are numerically tested subjected to compressive loading. In Fig.3, the numerically obtained stress-strain curves of four specimens are shown. For the whole deformation process of the curves, linear, non-linear, unstable and residual deformation, four stages are suffered for every one of the specimens. All curves are coincided very well during linear and partly non-linear stage before reaching peak strength, and it demonstrates that during the initial stage of low damage the spatial structure of materials is not strongly destroyed, but has weak statistical fluctuation influencing the macroscopic behavior slightly. However, after beyond the point A, the

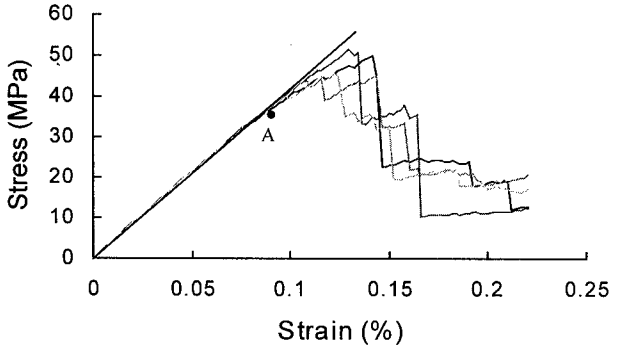


Fig. 3 Stress-strain curves for the four specimens with m=2.0

situation is completely changed. Because of development of micro-fracture in specimen, the original distribution of mechanical properties for elements is changed to larger extent. The macroscopic behaviors of four specimens show pronounced difference in that the curves demonstrate obvious specimen-specific behavior. Although the peak strengths of all specimens vary in a small variation, during the post-peak strength the softening formation of four specimens show larger discretion. On one hand, the softening process is very fast and sudden stress drop occurs for some of them. On the other hand, the weakening process is smooth and progressive failure behavior is observed for other specimens. During the portion of residual strength, the softening for any of the specimens tends to reach a certain value.

In a word, during the stages of initial loading and residual strength portion the macroscopic mechanical behavior is not sensitive to the distribution of mechanical properties for elements, but the situation is completely different during stages of macroscopic fracture of the specimen and softening process. The numerical simulations show that the softening process in the post-peak portion is structurally unstable in which a small difference in mesoscopic structures of the specimens can be strongly enlarged at certain point that leads to big difference in patterns of softening behavior. The results from the simulations agree well with the results obtained by Xia [7].

Fig.4 reveals the fracture patterns of four specimens. The patterns can be divided into two types. The first is the cleavage alone the wing crack of the top and bottom tip of the pre-existing flaw. The second is mixed cleavage including tensile and shear cracks. The first type of fracture demonstrates more strong brittleness than the second type because tensile fracture releases less energy than shear. For the four specimens, the macroscopic mechanical properties, geometry and size of the pre-existing flaw are completely the same, but their fracture patterns show statistical nature and hardly have identical form. In comparison with observations from laboratory, it can be concluded that the distributive character of the heterogeneity plays a crucial role in determining the evolution of fracture, and is a main and rigueur aspect about rock failure. In theory it explains the essential reason of variation and randomicity of failure phenomenon in rock-like materials.

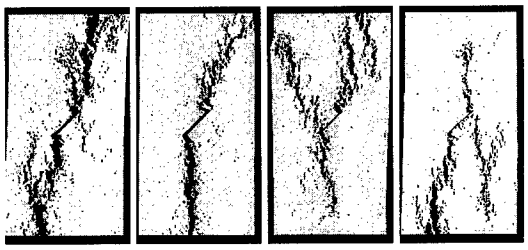


Fig. 4 Fracture pattern of rock specimen with pre-existed flow

3.3.The influence of homogeneity index *m* on macroscopic mechanical behavior

Fig.5 shows fracture pattern of specimens with different homogeneity index 1.5, 2.0 and 5.0. With increasing homogeneity index *m*, the pattern of crack propagation tends to the predicted pattern from fracture mechanics theory, that is, the crack is more smooth and continuous, and the micro-fractures almost concentrate on the advanced tip of the pre-existing flaw or along the path of wing crack propagation. It seems to us that the analytical solution in fracture mechanics is not effective to be used to describe the problems in which the heterogeneity has to be considered. Fig.6 also reveals the same role

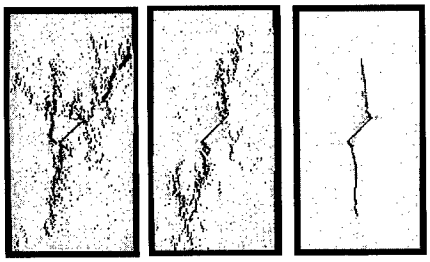


Fig. 5 Fracture mode and of specimens with Different homogeneity index m=1.5, 2.0, 5.0

that the linearity and the brittleness are obviously enhanced with increasing the homogeneity index *m*. Because increasing the heterogeneity of specimen raises the number of low strength element (as shown in Fig.1a', b', c') and the variation magnitude of the local stress concentration that results in macro-fractures in a lower stress level, at last it leads to the strength reduction of specimens.

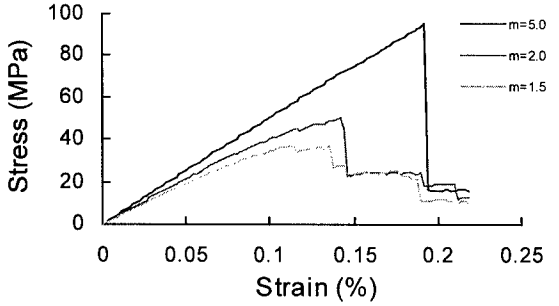


Fig. 6 Stress-strain curve of specimens with different homogeneity index m=1.5, 2.0, 5.0

4. CONCLUSION

The following conclusions are obtained from the numerical simulations:

1. The influence of stochastic mesoscopic structure on fracture mode is much higher than on the peak-strength variation. The macroscopic mechanical behavior is more sensitive to mesoscopic structure after peak strength than before peak-strength, and shows strong specimen-specific behavior. The macroscopic failure of specimens demonstrates catastrophic character and shows different fracture modes.
2. With increasing homogeneity index *m* the macroscopic strength of specimen rises, macroscopic linearity is more obvious, and the macroscopic failure process presents markedly brittle behavior. At the same time, the pattern of crack propagation is closer to the pattern predicated from fracture mechanics, that is, the path of crack propagation is more continuous and smooth.

AKNOWLEDGEMENT: The work presented in this paper was supported by the Chinese National Key Fundamental Research "973 Programme" (No.95-13-07-01) and the National Natural Science Foundation (No.49974009).

REFERENCE

1. N.G.W.Cook, The failure of rock, Int. J. Rock Mech. Min. Sci., **2** (1965) p.389.
2. R. Chen, H. Yan, Deformation precursor of rock failure in Laboratory, ACTA GEOPHYSICA SISICA, **32 Supp.1** (1989) p.246.
3. Tao Zhenyu, Notes on recent development of rock mechanics, ADVANCES IN MECHANICS, **22(2)** (1992) p.161.
4. C.A. Tang, A New Approach to Numerical Method of Modeling Geological Processes and Rock Engineering Problems, Engineering Geology, **49** (1998) p.207.
5. C.A. Tang and P.K. Kaiser, Numerical Simulation of Cumulative Damage and Seismic Energy Release during Brittle Rock Failure–Part I. Fundamentals. Int. J. Rock Mech. & Min. Sci. **35(2)** (1998) p.113.
6. C. A. Tang, Numerical simulation of progressive rock failure and associated seismicity. Int. J. Rock Mech. Min. Sci., **34(2)** (1997) p.249.
7. M. F. Xia, W. S. Han, F. J. Ke and Y. L. Bai, Statistical mesoscopic damage mechanics and damage evolution induced catastrophe (II), ADVANCES IN MECHANICS, **25(1)** (1995) p.1.

Key Engineering Materials Vols. 183-187 (2000) pp. 791-796
© 2000 Trans Tech Publications, Switzerland

Fracture and Strength of Notched Thick Composites

B.S. Hwang[1], S.B. Park[1], B.H. Kim[1], I.S. Park[2], H.S. Song[2] and J.K. Lee[3]

[1] Composite Materials Group, Korea Institute of Machinery and Materials,
66 Sangnam-dong, Changwon, Kyungnam 641-010, Korea

[2] Agency for Defense Development, PO Box 35, Yuseong, Taejon 305-600, Korea

[3] Department of Mechanical Engineering, Dongeui University,
San 24 Gaya-dong, Pusanjin-gu, Pusan 614-042, Korea

Keywords: Fracture Strength of Notch, Molded and Machined Notch, Thick Composites

ABSTRACT

An experimental investigation for the fracture and notch strength of thick laminates has been carried out to develop high quality composite notches for structural use. Thus, the multi-directional laminates are designed and compared to the baseline aluminum. The difference of notch strength caused by manufacturing techniques is also discussed. The notches of selected materials are evaluated by the static test and low-velocity impact test. Failure modes are also observed and assessed. Material design is evaluated by the finite element analysis and confirmed by experiments. The successful results are obtained for thick composite notches, which shows higher strength than aluminum notches.

1. INTRODUCTION

Major applications of composite laminates have been shell structures whose features are large scale, smooth surfaces, and global load carrying capacity. The brittle characteristics and low failure strains of resin matrices and fibers in conjunction with notches, holes, and slits are usually limitations in using composites. Thus, research on this phenomenon has been an important subject [1]. Users are trying to avoid using notches, which cause the degradation of structural performance. Especially, only a few applications containing edge crack type notches and threads such as gears have been introduced [2-4]. However, the lightweight of composites as one of the structural materials is a very important merit for engineers.

In this paper an experimental research was conducted to develop composite notches which have equivalent to or better than aluminum in their strengths. The longitudinal tensile strength of unidirectional carbon composites is much higher than that of aluminum. However, transverse tensile or compressive strength is much lower than aluminum. These are not the realistic laminates for application. Thus, the multi-directional laminates are designed and compared to the baseline material. The difference of notch strength caused by manufacturing techniques is discussed. The molded specimens have resin rich area underneath of the upper mold due to resin entrapment during molding process. The notches of selected materials were evaluated by the static test and low-

velocity impact test. Failure modes were also observed. Material design was evaluated by the finite element analysis and confirmed by experiments. The successful results were obtained for thick composite notches, which shows higher strength than aluminum notches.

2. EXPERIMENTAL

2.1. Design of Materials

Raw materials used in this paper are four kinds such as BMC, UD epoxy prepregs (T300 and T700 grade carbon fibers), and carbon/PEI prepregs. BMC is composed of 0.5-inch short carbon fibers and toughened epoxy. Carbon/PEI is made of unidirectional carbon fibers and polyetherimide thermoplastic resin.

Different kinds of materials are fabricated using the raw materials. Unidirectional prepregs enable to make various materials by laying the plies in multi-directions. In the Fig. 1, (a) is one material but (b), (c), and (d) have different behaviors from even one raw material. In addition, the material (d) may have more different overall properties by changing ply orientations. Throughout this experimental approach the material (d) is more divided into four kinds of laminates, which are [45], [-45], [±45], and [0/+45/90/-45] lay-ups. The details of materials lay-ups are in Table 1 and Fig. 1. T300 and T700 prepregs were used for all above lay-ups but PEI prepreg was used only for [90], [±45], and [0/+45/90/-45] lay-ups.

Table 1. Materials and their lay-ups.

Materials I.D.	Lay-ups	Ply
[0] Lay-up	$[0]_{80}$	80
[90] Lay-up	$[90]_{80}$	80
[45] Lay-up	$[45]_{80}$	80
[-45] Ly-up	$[-45]_{80}$	80
[±45] Lay-up	$[45/-45/45/-45/45/-45/45/-45]_{14}$	98
[0/+45/90/-45] Lay-up	$[0/+45/90/-45]_{14}$	98

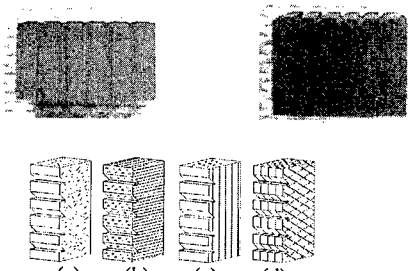


Fig. 1. Samples and specimen configurations, (a) random, (b) [90], (c) [0], (d) multi-angles.

2.3. Fabrication of Specimens

Two sets of steel mold were designed and fabricated. One mold is for the molded notch specimens. Upper mold has multiple screw type male part and lower mold has two cavities. The size of specimen is 15mm wide, 15mm long, and 10mm thick and has six notches at its edge. Another mold is for machined notches from thick composite blocks. For each specimen prepregs were cut and placed in the mold. For machined notch specimens, thick composite blocks, 90 x 90 mm, were fabricated by compression molding method as shown in Fig. 1. Four specimens were cut out from one block. The notches are made in the side edges by in-situ molding or machine grinding. Notch is 1.1 mm deep and 1.0 mm wide. The length of plank is 2.3 mm. The notch angles are 45 and 7 degrees against centerline. All specimens were cured according to the cure cycles of materials vendor and post cured for two hours.

2.3. Static and Dynamic Strength Tests

Static and dynamic notch strengths are measured using the same fixture. Samples are supported from side screws and load is applied through the punch. UTM and Dynatup Drop-Weight System

are used for static and low-velocity impact tests. Notches are multiple in the sample. The evaluation of notch strength is performed in terms of shear strengths. The multiple notches are subjected to the shear type loads. Therefore, the notch strength in this paper is a kind of shear strength of materials to be evaluated. In details, the notch strength is defined by dividing the applied maximum load with the shearing area.

2.4. Stress Analysis of Notches

The finite element analysis is used to model the stress distribution at failure moment for each laminate. A Composite Layer Shell Element of ANSYS® was used to model the constant thick laminate block with a notch.

3. RESULTS AND DISCUSSION

3.1. Static Notch Strength

There are small differences in static mechanical properties of two carbon/epoxy materials such as T300 and T700. When we compare the notch strength of two materials, relatively small differences are found in Fig. 2. However, one can see clear difference in fabrication method of notches from the same figure. The strengths of molded notches are much lower than those of machined notches except [0] lay-up. In [0] lay-up the molded notches are partially supported by continuous fibers in normal direction of load although the resin rich area is dominant in the notches. The machined notches of [0] lay-up are made by grinding the side edges of unidirectional laminated blocks. Thus, the fibers are necessary to be cut to form the notches. The loading direction for the test is 83-degree to loaded surface in these specific specimens, which means that almost pure shear loading is applied at notches. The results of tests are naturally very low because only the fiber and resin matrix interfacial strengths are involved as shown in Fig. 4(a).

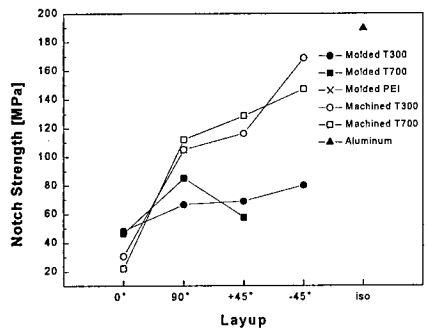


Fig. 2. Machined and molded notch strength of UD laminates block.

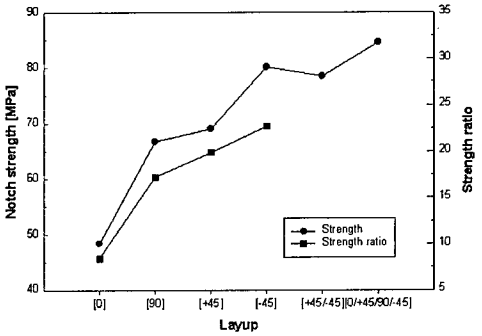
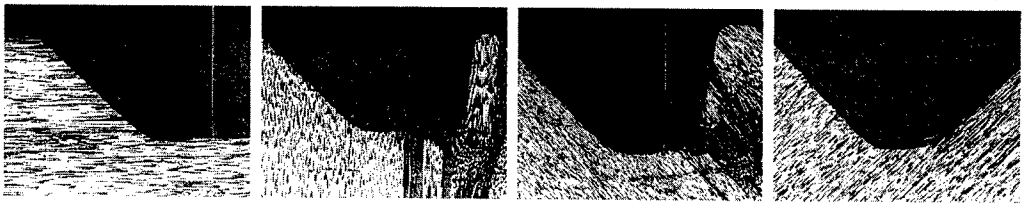


Fig. 3. Molded notch strength in terms of stacking sequence.

In Fig. 2 the notch strength values appear in the order of [-45]>[+45]>[90]>[0] lay-ups. The [90] specimens have less resistance to crack opening mechanism since the notch and fiber directions are the same. The fibers of [+45] specimen, Fig. 4(c), are aligned against the loading direction. The numbers of notches in samples are six and the bottom notch is the sixth one from top.



(a) [0] lay-up (b) [90] lay-up (c) [+45] lay-up (d) [-45] lay-up

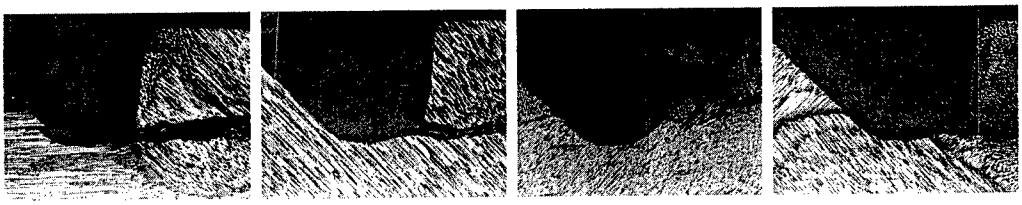
Fig. 4. Failure of UD laminate blocks, T300 material.

The sixth notch cracks and collapses easily at low load because there is no support under the notch. The same interpretation could be made for the [0] machined specimens. On the other hand, [-45] specimens have the opposite fiber directions compared to [+45] specimens. The cracked part is smaller than [+45] specimen and at the same time the crack propagation is hindered by the applied load in associated with the compressive action. In Fig. 2 the molded PEI/carbon specimen (90-deg lay-up, symbol x, 105.05 MPa) shows high performance compared to carbon/epoxy specimens. This is associated with the effect of tough matrix resin.

The composite layer shell element was used to model the thick composite notches. In the finite element analysis the maximum failure load obtained from experiment was applied and the stress distribution for each laminate at failure was calculated. In addition, the equivalent load was applied to each laminate and lamination with maximum shear strength notches was evaluated. Tsai-Wu Failure Criterion was applied to calculate the strength ratios. The higher strength ratio a laminate has, the higher shear strength the notches have in Fig. 3. The calculated strength ratios for unidirectional laminates, [0], [90], [+45], and [-45], were 8.4, 17.2, 19.9, and 22.7. When an equivalent load for [0] lay-up was applied to the other lay-ups, it results in lower strength ratio for the laminate with higher failure strength. The calculated strength ratios were 8.4, 7.8, 8.5, 6.8, 6.14, and 4.04 for [0], [90], [+45], [-45], [±45], and [0/+45/90/-45], respectively. Therefore, one can reduce the magnitude of stresses occurring in the notches by changing the lamination orientations. By FEA we could select proper lay-up angles, which are [±45] and [0/+45/90/-45]. The analysis results appear to be similar trends in strength as shown in Fig. 3.

From Fig. 4 and Fig. 5 we can see the different failure modes. Unidirectional laminates fail along the fiber directions. However, multi-directional laminates start to fail at roots of the notches and cracks propagate to the loading direction. In Fig.4 the failed mode illustrates that the strength of notch is very related to the matrix properties. However, in the multi-directional laminates the notch is packed by the fibers resisting the load in Fig. 5. Thus, the higher load is necessary to cut the fibers in multi-directional laminates.

The real application of composite structures could be possible using multidirectional lay-ups. Two prospective materials lay-ups, [±45] and [0/+45/90/-45], were tested and evaluated. The combination of [+45] and [-45] lay-ups did not give us higher value than [-45] lay-up.



(a) T7Q lay-up (b) T745 lay-up (c) T3Q lay-up (d) T345 lay-up

Fig. 5. Fracture of multi-directional laminate blocks, Materials T300 and T700.

The value of the mixed lay-up remains between [+45] and [-45] lay-ups in the test. [0/+45/90/-45] lay-up shows the better strength values in experiments in Fig. 2 and 3. This laminate represents a combination of strength values in each single direction laminate. However, the multi-directionally laminated notches do not follow the simple mixture rule because [0] and [90] layers have very important roles in this specific load. The fibers in [0] and [90] plies can fully use their own mechanical properties since they are supported by the adjacent [±45] plies. The similar results of experiment could be confirmed in Iosipescu shear test for the same materials.

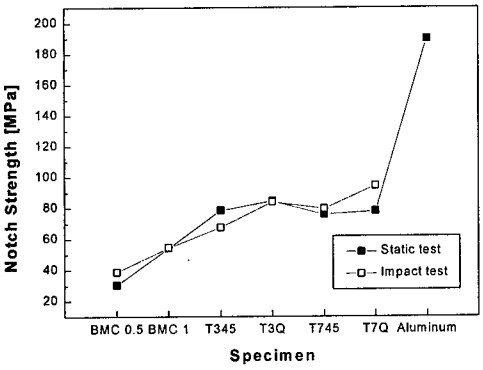
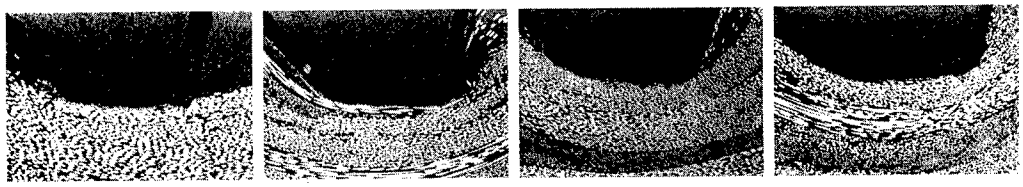


Table 2. Molded and machined notch strength of various materials.

Materials	Type of laminate	Molded Notch Strength [MPa]	Machined Notch Strength [MPa]
T700 / Epoxy	T7Q	77.972	220.839
	T745	75.874	132.557
T300 / Epoxy	T3Q	84.575	206.299
	T345	78.485	158.779
Carbon / PEI	PEIQ	-	239.072
	PEI45	105.05[1)]	168.401
BMC	0.5" random	30.45	-
	0.1" random	54.24	-
Al7075-T651		189.647	-

Note: T7-T700, T3-T300, Q-[0/+45/90/-45] 45-[45/-45], 1) : [90] lay-up for PEI

Fig. 6. Static and impact strength for molded notch materials.



(a) T7Q (b) T345 (c) BMC 0.5inch (d) BMC 1inch

Fig. 7. Fiber distributions of molded specimens.

Fig. 7 explains the compactness of reinforcing fibers in molded notches. Fibers are not evenly distributed and not aligned to resist the applied load. One reason is that the liquid resins flow out and cure at mold surface. In addition, the prepregs were stacked according to the designed angles, but the fibers were bent by compression during the molding process. One can expect the strength

difference of molded and machined notch from observation of Fig. 5 and 7. Even BMC materials have resin rich area under the male molds in Fig. 7 (c) and (d).

3.2. Dynamic Notch Strength

Fig. 6 shows static and dynamic notch strengths for all materials used in this experiment. It does not appear much difference between two types of test such as static and dynamic tests. We can confirm that the low-velocity impact does not have severe effects on the failure of laminates. Thus, the low-velocity impact test are considered as a quasi-static test[5] and substituted as a static test. The maximum tup responses in terms of load were used for failure load of specimens. The impact energy levels were about 60 [J] for laminated specimens and 30 [J] for BMC materials. The failure modes of laminated specimens were the crash of notches. However, BMC had failed at the body beyond the root of notches. Finally, dynamic test showed the same results shown in Fig. 3 and Table 2.

4. SUMMARY AND CONCLUSIONS

An experimental study was conducted to develop composite notches, which have an equivalent to or better strength than aluminum in their shear tests. Some experimental results for thick composite notches were obtained. Four different raw materials were employed and their derivatives were 6 kinds. The multiple notches were made in block. The notches were formed by the molding and machining methods. The notches were subjected to shear type load. Static and dynamic loads were applied and strength was calculated. By the basic experimental approach the materials and process, which result in high notch strength, were determined.

Machined notch specimens brought the better notch strength. Machined notches have the more idealized fiber distributions rather than molded notches by the microscopic observation. The better fiber distribution naturally results in the better strength. BMC materials have the much lower strength values than laminated materials. Unidirectional lay-ups such as [0], [90], [+45], [-45] lay-ups have a gradual increase of strength. Using this results, [±45] and [0/+45/90/-45] lay-ups were selected and tested. Finite element analysis was used to determine these lay-ups as well. Among the tested materials the machined [0/+45/90/-45] lay-ups of carbon/PEI materials had the best result. These quasi-isotropic lay-ups of T300 and T700 materials also had the higher test results than the baseline material, aluminum 7075 for this specific loading condition.

REFERENCE

1. S. C. Tan, Stress Concentrations in Laminated Composites, Technomic Pub., Lancaster, (1994).
2. F. A. Maclaughlin, Proc. of 21st Intel. SAMPE Technical Conference, (1992) p. T699.
3. K. Hamajima and M. Mausuda, Proc. of 4th Japan Intel. SAMPE Sympo., Tokyo (1995), p. 1189.
4. B. S. Hwang, et. al., Proc. of 6th Japan Intel. SAMPE Sympo., Tokyo, Oct. 26 (1999) p. 606.
5. P. O. Sjoblom, J. T. Hartness, and J. T. Cordell, J. Composite Materials, **22** (1988).

Key Engineering Materials Vols. 183-187 (2000) pp. 797-802
© 2000 Trans Tech Publications, Switzerland

A Study on the Integrity Evaluation for PWR Vessel by Pressurized Thermal Shock

S.G. Jung and T.E. Jin

Korea Power Engineering Company
360-9 Mabuk-ri, Kusong-Myon, Yongin-Shi, Kyunggido 449-713, Korea

Keywords: Failure Probability, Pressurized Thermal Shock, Probabilistic Fracture Mechanics, PTS Screening Criteria

ABSTRACT

SECY 82-465[1] and RG 1.154[2] provided guidance to the utilities regarding an acceptable methodology for performing structural integrity evaluation of aging nuclear reactor pressure vessels (RPVs) subjected to pressurized thermal shock (PTS) transients. Probabilistic fracture mechanics (PFM) analysis is a major element of this methodology. RG 1.154 currently specifies that when performing a PFM analysis, all flaws shall be considered as surface flaws that exist in the inner surface of the RPV wall. Recently, PTS analysis was performed for one of the Korean PWR Vessels. As a result of PFM analysis, it was found that current RG. 1.154 methodologies were very conservative. Therefore, to evaluate and quantify the conservatism of RG 1.154, several PFM analyses were performed in this paper, and PFM analysis results were compared with the value from RG 1.154.

1. INTRODUCTION

The PTS events, due to severe overcooling of the RPV followed by repressurization, can occur in PWRs during the PTS transients. Thermal and pressure stresses are both tensile stresses that tend to open existing cracks located near the inner surface of the RPV. Cumulative neutron radiation exposure makes the RPV material more brittle and, therefore, more susceptible to cleavage fracture. For embrittled RPVs, PTS is the major threat to RPV structural integrity. Response to this concern, the NRC established the limit value of fracture toughness (RT_{NDT}) for some PTS events of U.S NPPs and specified screening criteria based on the RT_{NDT} of 270°F for plates, forgings, and axial welds and 300 °F for circumferential welds. RG 1.154 provides guidance regarding an acceptable analysis methodology. PFM analysis is a major element of the RG 1.154 methodology.

Recently, PTS analysis was performed for one of the Korean PWR Vessels. As a result of PFM analysis, it was found that current methodologies were very conservative. Therefore, to evaluate and quantify the conservatism of SECY82-465 and RG 1.154, several PFM analyses were performed in this paper, and PFM analysis results were compared with the value ($5x10^{-6}$/ry) from RG 1.154.

For this study, base case analysis was performed using SECY82-465 methodologies from which the current PTS screening criteria were derived and then evaluated for other 9 cases for identifying impacts on PTS screening criteria.

2. SELECTED PTS TRANSIENTS

Figure 1 illustrate the results of PFM analyses performed in SECY 82-465, from which the current PTS screening criteria were derived. Figure 1 is a plot of the frequency of crack extension as a function of mean surface RT_{NDT} (RT_{NDTs}). The value of RT_{NDTs} corresponding to $5x10^{-6}$ crack extensions per reactor year is approximately 210°F. Adding a residual term of 59°F (2 standard deviation) to account for uncertainty associated with predicting RT_{NDT} yields the PTS screening criteria of approximately 270°F. This PFM analyses that generated the results in Figure 1 were performed for postulated transient sequences obtained from the WOG [1]. The transient groups were derived from the consideration of the various possible sequences following each postulated initiating event such as a steam line break, extended high pressure injection (HPI), steam generator tube rupture, etc.

It can be observed from Figure 1 that the total frequency of crack extension corresponding to $5x10^{-6}$/ry is exclusively due to the extended HPI transient. Therefore, to reconstruct the relevant SECY 82-465 PFM analysis results, it was only necessary to duplicate the results for the extended HPI PTS events for this study. In SECY 82-465, the extended HPI PTS transient was characterized stylistically by T_{final}=125°F, T_{ini}=550°F, β =0.05min^{-1} and constant pressure of 2.25ksi. This transient was determined to have a frequency of occurrence of $1x10^{-4}$ PTS events per reactor year [1]; therefore, the corresponding conditional probability of failure that would produce the maximum acceptable frequency of crack extension is $5x10^{-2}$ failures per PTS events. Therefore, for evaluating the integrity of RPV as a RT_{NDT}, $5x10^{-2}$ value was used as criteria for failure probability. In this analysis, the coolant temperature in contact with the inner surface of the RPV was estimated by stylized the exponential formulation [1].

3. FAILURE PROBABILITY METHODOLOGY

The conditional probability of vessel failure was calculated with the modified VISA II code, which was modified for simulating the various fracture toughness and considering the effects of residual stresses in this paper. The PFM analyses have been performed to evaluate failure risk of the RPV based on crack propagation frequency and failure frequency caused by PTS events. PFM analysis is based on Monte Carlo techniques, i.e., a large number of deterministic analyses are performed on stochastically generated vessels to determine if each vessel, containing a specified number of flaws, will fail when subjected to a specified PTS event at a particular time in the operating life of the vessel. The conditional probability of failure for a specified PTS event is estimated by dividing the number of vessels that fail by the total number of vessels simulated.

Input data used to compare stress intensity factor and material property (K_{IC}, K_{Ia}) for probabilistic fracture analysis are composed of initial crack size distribution, fluence of surface, Cu and Ni contents, and initial RT_{NDT}. All these input data, as well as K_{IC}, K_{Ia}, were statistically simulated.

Comparing stress intensity factor during the transient with K_{IC}, it was determined whether a crack can be initiated or not. Also, comparing with K_{Ia}, it was determined whether a crack can propagate or not. The conditional probability of failure is then evaluated using these processes.

4. ANALYSIS MODEL

This analysis was performed to determine the impact on PTS screening criteria of various modifications to the SECY 82-465 PFM model. PFM model for this analysis is shown in Table 1.

4.1. Model 1 : Base case analysis

SECY 82-465 methodologies, designated as VISA 1 in Table 1, were used as a base case analysis

Table 1. Analysis model for PFM

Case	Flaw shape	Flaw loca.	Flaw dist.	Flaw density	Toughness	Residual stress	Remark
VISA 1	Infinite	Surface	NRC(1)	SECY82-465	NRC	No	SECY82-465(base)
VISA 2	Infinite	Surface	NRC(1)	SECY82-465	NRC	No	HTC(2) correct error
Case 3	AR=6	Surface	NRC(1)	SECY82-465	NRC	No	Modified flaw shape
Case 4	AR=6	Embedded	NRC(1)	SECY82-465	NRC	No	Modified shape/loc.
Case 5	Infinite	Surface	Octavia	SECY82-465	NRC	No	Modified flaw dist.
Case 6	Infinite	Surface	Marshall	RG 1.154	NRC	No	"
Case 7	Infinite	Surface	NRC(1)	SECY82-465	ORNL	No	Modified toughness
Case 8	Infinite	Surface	NRC(1)	SECY82-465	Master	No	"
Case 9	Infinite	Surface	NRC(1)	SECY82-465	NRC	Yes	Inclusion Residual s
Case 10	Infinite	Surface	NRC(1)	SECY82-465	Master	Yes	Residual+Master

(1) OCTAVIA by NRC, (2) Corrected Error of VISA 1 HTC

model; that is all flaws occurring in axial weld regions are axially oriented flaws. Flaw density is 1 flaws/ft^3 for weld regions. The OCTAVIA flaw size distribution function, which was used in the NRC staff, was used for simulating flaw depth. This analysis is very similar to the methodology currently proposed in RG 1.154 except some parameters. The second analysis, designated as VISA 2 in Table 1, is same as base case analysis except that uses corrected heat transfer coefficient of VISA 1, which is derived NRC screening criteria. Table 2 specify the input data and correlation used in the PFM analyses in SECY 82-465. These data and correlation were used in this study to reconstruct the PFM base case results. The major parameters simulated for the base case analysis used herein are crack depth, RT_{NDT}, K_{IC}, K_{Ia} and radiaton-induced ΔRT_{NDT} used Guthrie correlation [3]. Normal distributions were assumed for each of these parameters except the crack depth; mean values, standard deviations and truncation values used in the base analysis are shown in Table 2.

Table 2. Parameters simulated in SECY 82-465

Parameter	Mean value	Standard deviation(σ)	Truncation
Fluence	-	0.3μ	f=0
Cu	0.35	0.025%	-
Ni	0.65	0.0%	-
RT_{NDT0}	20	15°F	±3σ
ΔRT_{NDT}	HEDL	0°F	±3σ
K_{IC}	**NRC**	0.15μ	±σ
K_{Ia}	**NRC**	0.10μ	±σ
Flaw shape/Location	**Infinite surface flaw**		
Flaw depth distribution	**Octavia by NRC**	-	-
Flaw density	**~1/ft^3**	-	-
Beltline region	6 axially oriented weld		
Fluence attenuation Constant	0.33	-	-

4.2. Model 2 : Using Modified Flaw Shape and Location

This analysis model is same as base case analysis except uses modified flaw shape and location. The analysis, designated as Case 3 in Table 1, is identical to the model described in the previous paragraph for base case analysis model (VISA 1) except that surface flaws are semielliptical instead of infinite length flaws. The aspect ratio was determined from a uniform distribution with possibility 6. The analysis, designated as Case 4 in Table 1, is identical to the model described in the previous paragraph for VISA 1 except that flaws are embedded semielliptical instead of infinite surface flaws. The aspect ratio is also uniformly distributed 6. It is assumed that the flaw length before initiation is semielliptical and flaw length after initiation is infinite length in this study. If the inner ligament of buried flaw is less than 0.5a, the flaw is converted to a surface flaws.

4.3. Model 3 : Using Various Flaw Size Distributions

The analysis, designated as Case 5 in Table 1, is identical to the model VISA 1 except that flaw distribution is original OCTAVIA distribution [3] with a flaw density of 1 flaw/ft^3 instead of OCTAVIA code used by NRC staff [3] which is an incorrect interpolation of the original OCTAVIA distribution. The analysis, designated as Case 6 in Table 1, is identical to the model VISA 1 except that flaw distribution is Marshall flaw size distribution (with PSI) [3] with a flaw density of 0.03 flaws/ft^3 instead of OCTAVIA code used by NRC staff.

4.4. Model 4 : Using Various Fracture Toughness

For the PFM analysis, mean values of fracture toughness, K_{IC} and K_{Ia} are required. These values can be estimated as a function of metal temperature and the metal reference nil-ductility transition temperature by employing NRC mean curve [1] and ASME based ORNL curve [4] for RPV ferritic steel respectively. Another fracture toughness curve, Master curve, which is recently developing method [5] yields a key material parameter called reference temperature, T_o, which indicates the location of the transition range fracture toughness curve on the temperature axis. For applying master curve to PFM analysis, reference temperature, T_o, for ferritic steel in the transition range would be required for fluence level. Reference 6 was used to determine the value of T_o. According to this reference, the form of T_o is given equation (1)[6]. To calculate the reference temperature RT_{To} from the following equation (2), value of T_o was used. This reference temperature was used as an alternative indexing reference temperature for the K_{IC}, K_{Ia}, toughness curve, as applicable, in NRC and ORNL curve. Figure 2 shows master curve compared to NRC mean curve and ASME based ORNL curve as a fluence levels $1x10^{19}$ n/cm^2.

$$T_o(^oC)=[1-\exp(-5 \times f)] \times (1.8f+96)-58 \quad (1)$$

$$RT_{To}(^oF) = [T_o + 35](^oF) \quad (2)$$

The analysis, designated as Case 7 in Table 1, is identical to the model VISA 1 except that fracture toughness was applied ASME based ORNL curve instead of NRC mean curve. The analysis, designated as Case 8 in Table 1, is identical to the model VISA 1 except that fracture toughness was applied Master curve instead of NRC mean curve.

4.5. Model 5 : Considering Residual Stresses

This model, designated as Case 9 in Table 1, is identical to the model VISA 1 except that the weld regions include the through wall weld residual stress defined in Reference [7]. The model, designated as Case 10 in Table 1, is identical to the model described in the previous paragraph for Case 8 except that the weld regions include the through wall weld residual stress. Based on reference [7], residual stress distribution in Equation (3) was applied to the original VISA-II code [3] for this study.

$$\text{Residual stress} = \text{surface tensile stress} \times \cos(2\pi \times x/T) \quad (3)$$

5. RESULTS

The results of this study are illustrated in Figure 3 through 6. For VISA 1 analysis (base case analysis), the failure probability of vessel exceeds the value of $5x10^{-2}$ when the limiting beltline RT_{NDTs} is 270°F which is screening criteria of NRC. As illustrated in Figure 3, the failure probability of RPV obtained in the VISA 2 analysis which is corrected heat transfer coefficient error of VISA 1, are somewhat higher than those obtained in the VISA 1 analysis.

5.1. Impacts on Flaw shape and Location

The results of the Case 3 and 4 analysis are illustrated in Figure 3. For Case 3 analysis, the

probability of vessel failure exceeds the value of $5x10^{-2}$ when the limiting beltline RT_{NDT} is 320 °F. For this analysis, the incremental impact of replacing infinite surface flaw with semielliptical flaw is to increase the limiting value of RT_{NDTs} corresponding to $5x10^{-2}$ RPV failure probability from 270°F to 320°F. For Case 4 analysis, the probability of vessel failure didn't exceed the value of $5x10^{-2}$. Impacts on flaw shape, location decrease the failure probability by approximately a factor of 30 and order of 2 respectively.

5.2. Impacts of Flaw size distribution

The result of the Case 5 and 6 analysis are illustrated in Figure 4. For Case 5 analysis, the probability of vessel failure exceeds the value of $5x10^{-2}$ when the limiting beltline RT_{NDTs} is 295°F. For this analysis, the incremental impact of replacing NRC OCTAVIA flaw distribution with original OCTAVIA flaw distribution is to increase the limiting value of RT_{NDTs} corresponding to $5x10^{-2}$ RPV failure probability from 270°F to 295°F. For Case 6 analysis, the probability of vessel failure didn't exceed the value of $5x10^{-2}$. Impacts on flaw size distribution decrease the failure probability by approximately a factor of 2-8.

5.3. Impacts on Fracture toughness Curve

The result of the Case 7 and 8 analysis are illustrated in Figure 5. For Case 7 analysis, the probability of vessel failure exceeds the value of $5x10^{-2}$ when the limiting beltline RT_{NDTs} is 245 °F. For this analysis, the incremental impact of replacing NRC mean curve with ASME base ORNL curve is to decrease the limiting value of RT_{NDTs} corresponding to $5x10^{-2}$ RPV failure probability from 270 °F to 245 °F. For Case 8 analysis, the probability of vessel failure didn't exceed the value of $5x10^{-2}$. Impacts on ORNL curve increase the failure probability by approximately a factor of 4 and impacts on improved fracture toughness as Marshall curve decrease the failure probability by approximately a factor of 2 order.

5.4. Impact on Weld Residual Stress

The result of the Case 9 and 10 analysis are illustrated in Figure 6. For case 9 analysis, the probability of vessel failure exceeds the value of $5x10^{-2}$ when the limiting beltline RT_{NDT} is 235°F. For this analysis, the incremental impact of including the through wall weld residual stress of the weld regions is to decrease the limiting value of RT_{NDTs} corresponding to $5x10^{-2}$ RPV failure probability from 270°F to 235°F. For Case 10 analysis, the probability of vessel failure didn't exceed the value of $5x10^{-2}$. Impacts on residual stress increase the failure probability by approximately a factor of 5.5, whereas application of master curve decrease the failure probability by a factor of 30

6. CONCLUSION

PFM analyses were performed to determine the incremental and cumulative impact of various models. First, an attempt was made to duplicate the results of the SECY 82-465 analysis. Based on this analysis, flaw shape and location, flaw size distribution, and fracture toughness are modified and considered the residual stress. The inclusion of the through wall weld residual stress and application of the ORNL curve as fracture toughness have negative impact on the analysis results; whereas the other model: (1) replacing infinite surface flaw with finite length semielliptical surface flaws (2) replacing surface flaw with embedded flaws (3) using another flaw size distribution (4) using a recently-derived improved fracture toughness as Master curve etc., have positive impact on the analysis results.

From this study, SECY82-465 and RG 1.154 methodologies were identified to be a conservative. Furthermore, the failure probability reduction methodologies were derived to establish the pessimistic PTS screening criteria.

REFERENCE

1. USNRC, NRC Staff Evaluation of Pressurized Thermal Shock, SECY 82-465 (1982)
2. USNRC, Format and content of Plant-Specific PTS Safety Analysis Reports For Pressurized

Water Reactors, Regulatory Guide 1.154 (1987)
3. F. A. Simonen et al. VISA-II, A Computer Code for Predicting the Probability of RPV Failure",Battelle Pacific Northwest Laboratories, USNRC Report NUREG/CR-4486 (1986)
4. R.D. Cheverton and D.G. Ball, "OCA-P : A Deterministic and Probabilistic Fracture Mechanics Code for Application to Pressure Vessels", NUREG/CR-3618 (1984)
5. ASME Sec.XI, "Proposed Code Case for Application of Master Curve Method", Code case N-xxx (1998)
6. K.K. Yoon, "New Development in RPV Integrity Assessment", SAFE9702, Korea (1997)
7. EPRI TR-100251, "White Paper on RPV Integrity Requirements for Level A and B Conditions," (1993)

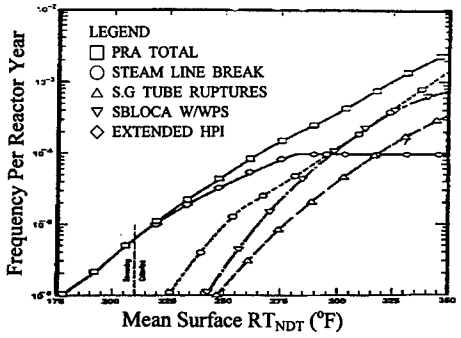


Fig. 1 The results of SECY 82-465

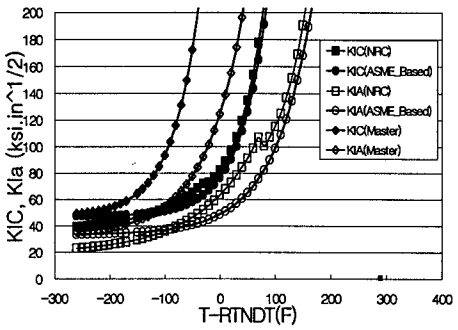


Fig. 2 Comparison of fracture toughness curve

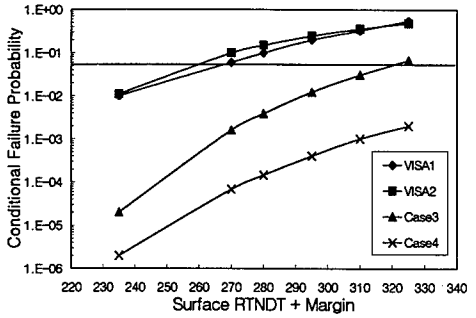


Fig. 3 Failure prob. of RPV as a function of RT_{NDTs} for Case 1,2,3 and 4

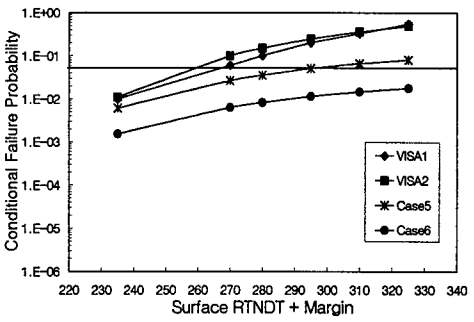


Fig. 4 Failure prob. of RPV as a function of RT_{NDTs} for Case 1,2,5 and 6

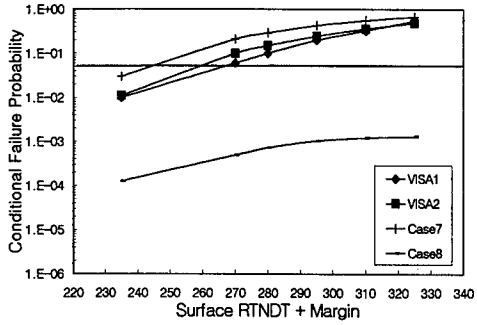


Fig. 5 Failure prob. of RPV as a function of RT_{NDTs} for Case 1,2,7 and 8

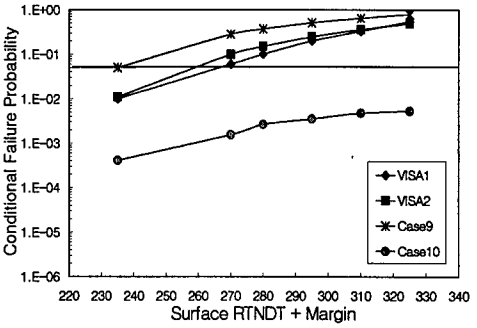


Fig. 6 Failure prob. of RPV as a function of RT_{NDTs} for Case 1,2,9 and 10

Key Engineering Materials Vols. 183-187 (2000) pp. 803-808
© 2000 Trans Tech Publications, Switzerland

Crack Healing Behavior and Mechanical Property of Mullite/SiC Composite Ceramics

Kiichi Tsuji[1], Kotoji Ando[2] and Shigemi Sato[3]

[1] Department of Control & System Engineering, Toin University of Yokohama, Aobaku, Yokohama 240-8502, Japan

[2] Department of Energy & Safety Engineering, Yokohama National University, Hodogaya, Yokohama 240-0067, Japan

[3] R&D Center NHK Spring Incorporated Company, Kanazawaku, Yokohama 236-0004, Japan

Keywords: Bending Strength, Crack Healing, Cyclic Fatigue Strength, Healing Condition, High Temperature Strength, Mullite/SiC Ceramics, Recovery of Strength, Static Fatigue Strength

ABSTRACT

Mechanical properties of sintered Mullite/SiC ceramics related with its significant crack healing behavior are discussed in this paper. This investigation was made on four kinds of specimens such as as-received smooth, heat treated smooth, pre-cracked and pre-crack healed. Pre-crack sizes were 100μ m and 200μ m and they were semi-elliptical in shape. The crack healing was done at 1300℃ for 1 hour in air. The main conclusions were obtained as follows: (a) Mullite/SiC composite ceramic has ability to heal crack (b) Maximum crack size able to be healed is semi-elliptical crack of 200μ m in diameter (c) Crack-healed zone has enough strength up to 1100℃ and most specimens failed outside the crack-healed zone (d) The crack healed specimens recovered their cyclic fatigue and static fatigue strength completely by the healing process (e) The crack healed specimens showed higher cyclic fatigue and static fatigue strength than as-received smooth specimens, and this fact was caused by crack healing.

1. INTRODUCTION

Some engineering ceramics have interesting crack healing behavior[1-4]. If this phenomenon is used in structural materials, it greatly contributes for improvement of the reliability of the ceramic component, reduction of the processing cost, simplification of the maintenance and lifetime of the equipment. However, it is necessary to clarify next various points. (a) The relation between chemical composition and crack-healing ability of the material[5,6]. (b) Heat resistance and oxidation resistance of crack healed zone[5,7]. (c) Crack size which can be healed[7,8,12]. (d) The relation between static strength and crack healing condition of crack healed specimen[1-13]. (e)

Cyclic fatigue and static fatigue strength of crack healed zone. Authors have been carrying out the systematic research on above (a),(b),(c) and (d). They have already confirmed that mullite/SiC system[9,11] (oxide system) and silicon nitride[5-7] (nitride system, yttria to be a sintering additive, and it contains SiC particles of 20vol%) were excellent in four characteristics of (a),(b),(c) and (d). However, the authors are the first to study high temperature strength, cyclic and static fatigue strength properties in the crack healed zone [13]. This paper systematically investigates the high temperature strength, cyclic and static fatigue strength properties of crack healed mullite/SiC composite ceramics.

2. MATERIALS AND TEST METHOD

2.1. Material and sintering method.

The mullite powder is KM101 (average particle size=0.2 μm, Al_2O_3 content =71.8 wt %, KIORITZ Co,. Ltd. Japan) and the SiC powder is Ultrafine (average particle size=0.27 μm, IBIDEN Co,. Ltd. Japan). Manufacturing processes of test specimens are as follows. The mullite powder and SiC powder (15 or 20 vol. % by volume of mullite powder) were wet blended for 24 hours using nylon balls in alcohol. Then powder was dried in a vacuum furnace, until all the solvent had evaporated. The resulting powder was hot pressed (35MPa at 1650℃) for 4 hours in nitrogen gas and it produced a sintered material with the dimensions of 5×90×90mm.

2.2. Specimen and experimental method

The bending strength was evaluated by 3 point bending test on 3×4×40mm specimens in accordance to the JIS Standard[14]. All types of test specimens were surface ground and polished before testing. The cracks were introduced onto the specimens by indentation method using Vickers indenter. Semi-circular crack length (2C) of the surface were about 100 μm or 200 μm, and Vickers load was 9.8N or 29.4N. Some of the as-received smooth specimens and cracked specimens were heat treated at 1300℃ for 1h in order to heal the crack (this heat treated as-received smooth specimen, hereinafter is called the heat treated smooth and cracked specimen is called pre-crack healed). The heating rate was 10℃/min and cooling was done in the furnace. The bending test was carried out at R.T, 800℃, 1000℃, 1100℃, 1200℃ and 1300℃. The crosshead speed of the test was 0.5mm/min. Cyclic fatigue tests were made at a stress ratio R=0.2 and a frequency of 5Hz. Static fatigue tests were made using a dead-load type testing machine. Cyclic and static fatigue tests were carried out at room temperature. Fracture surfaces were examined using SEM in detail. Crystal phases of sintered material and surface oxides were investigated by X-ray diffraction method. The X-ray diffraction analysis condition was CuKα radiation (30kV accelerated voltage and 30 mA electric current) and detector scanning speed of 0.5deg/min. The crack healing at high-temperature was observed in ultrahigh-temperature scanning laser microscope (1LM21H-LK1500 LASER TECH Co., Ltd. Japan)

3. RESULT AND DISCUSSION

3.1. Crack healing behavior of mullite/SiC composite ceramics

Fig.1. shows the experimental data of crack healing behavior of the mullite/SiC composite ceramics. This is a result of the bending test carried out at room temperature. The symbol (○) in the

figure is the result of the as-received smooth specimen which did not conduct the heat treatment and the bending strength was about 400MPa. The symbol (△, ◇) shows the bending strength of the pre-cracked specimens which are introduced the crack of surface length about 100 and 200 μm. The bending strength has decreased up to about 140 and 100MPa. Next, the symbols (●,▲,◆) illustrate the bending strength of heat treated smooth specimens, pre-crack healed (100 μm) specimens and pre-crack healed (200 μm) specimens. After the heat treatment, bending strength of as-received smooth specimens and pre-crack specimens (2C ≒ 100,200 μm) have increased significantly to about 520MPa. All of them show a bending strength higher than that of the original as-received smooth specimens. The fracture of the pre-crack healed specimens occurred outside the crack healed zone and this means fracture was completely healed. The symbol(*) shows the specimens in which fracture occurred outside the pre-crack healed zone. Some specimens were subjected to cyclic and static fatigue tests. They did not break within the designated fatigue limit of 10^6 cycles. Therefore, those specimens were subjected to four point bending test and results were given in the Fig. 1 in the columns named cyclic fatigue and the static fatigue. Fig. 2 (a) and (b) show the fracture surfaces of pre-cracked and pre-crack healed specimens, respectively. As shown in Fig. 2(a), the specimen had been broken through the pre-crack zone. On the other hand, as shown in Fig. 2(b), the fracture of pre-crack healed specimen occurred out side of the pre-crack healed zone.

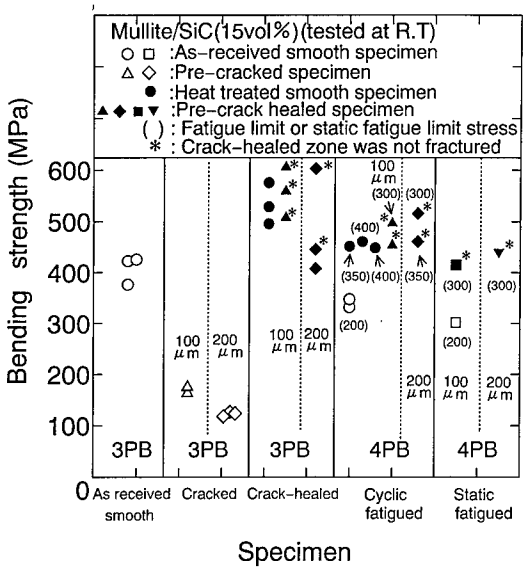


Fig.1. Effects of cracking and healing on bending strength.

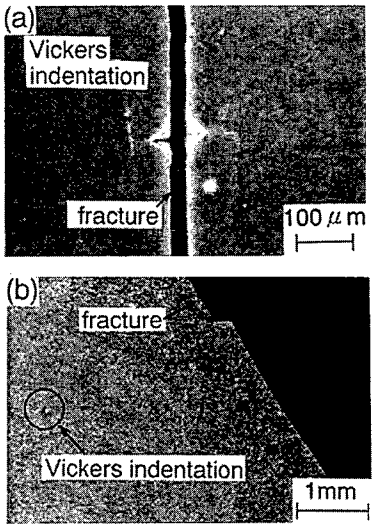


Fig.2. Crack path(a) fracture initiated from indented crack (b)fracture initiated outside pre-cracked zone.

3.2. Effect of pre-crack size on bending strength of heat treated specimen

It is important to determine the maximum crack size to be healed perfectly. This maximum crack size was investigated using specimens with several surface crack lengths. The relation between pre-crack size and bending strength (3 point bending test) at room temperature of 4 types of specimens

is shown in Fig. 3. As-received smooth specimens (○) show bending strength of about 400MPa. However, heat treated smooth specimens (●) show a bending strength of about 580MPa. As a matter of course, pre-cracked specimens (△, ◇) show very low strength and it is depending on crack size. However, pre-crack healed specimens have recovered their strength and show almost the same strength of heat treated smooth specimens (●). This recovery in bending strength was caused by the healing of surface flaws such as cracks and small pores, which were created by grinding and polishing the specimens. From these test results, it can be concluded that this material has ability to heal the semi-circular cracks up to 200 μm in diameter.

3.3. The effect of temperature on the bending strength of pre-crack healed specimen

Fig. 4 shows the temperature dependence of the Mullite/SiC composite. In the experiment range from room temperature to 1300℃, as-received smooth specimens have shown no considerable dependence of bending strength on temperature. The temperature dependence of both types of heat treated smooth specimens and pre-crack healed specimens has shown same tendency within the temperature range investigated. The bending strength decreases with increasing temperature. However, pre-cracked specimens with crack of 100 μm indicate a tendency in which the strength decreases with increasing the temperature up to 800℃, and then abruptly increases in the temperatures beyond 800℃. The strength difference between as-received smooth specimens and both types of heat treated specimens (smooth and pre-cracked) is large up to 1100℃, and then this difference vanishes beyond 1100℃. Therefore, crack healing ability of Mullite/SiC composite is effective up to about 1100℃.

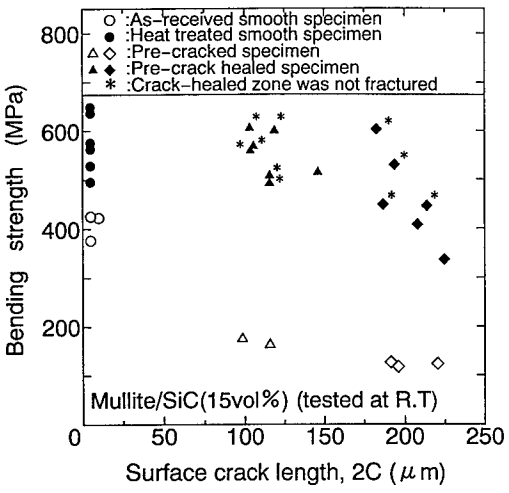


Fig.3.Effect of pre-crack size on bending strengh of heat treated specimen.

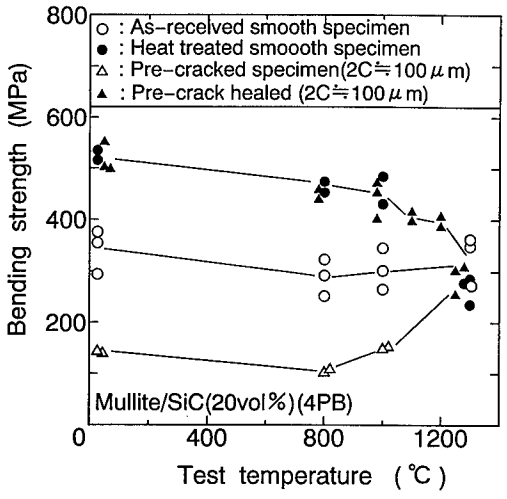


Fig.4.Effect of testing temperature on bending strengh of heat treated specimen.

3.4. Fatigue strength properties of pre-crack healed specimen

Cyclic and static fatigue strength test results of both types of smooth specimens were shown in Fig. 5. The relation between maximum bending strength (σ_{max}) and number of cycles to failure (N_f) or time to failure (t_f) is indicated in the Figure. The monotonic test results have been shown in the left side of the Figure. As shown in Fig. 5, σ_{max}-N_f and σ_{max}-t_f data points have laid on same curve for both types of specimens. Therefore, this curve, hereinafter is called the S-N(t) curve. The specimens which did not break by the test are indicated by arrow (→). σ_{f0} and σ_{t0} were determined by the applied stress on the specimen at $2x10^6$ cycles and 10^6 seconds, respectively. As indicated in the Fig. 5, σ_{f0} and σ_{t0} of as-received smooth specimens have given the same value of 200MPa. On the contrary, heat treated smooth specimens show higher S-N(t) curve than that of as-received smooth specimens. σ_{f0} and σ_{t0} of heat treated smooth specimens are about 350MPa, that is 1.75 times of as-received smooth specimens. Cyclic and static fatigue strength test results of pre-cracked and crack healed specimens were shown in Fig. 6. X and Y axis details of Fig.6 are same with the Fig.5. S-N(t) curves of as-received smooth specimens and heat treated smooth specimens were traced on the Fig. 6 for the clarity of explanation. As shown in Fig. 6, pre-cracked specimens show very low σ_{f0} and σ_{t0}, and they are about 50MPa or less. On the contrary, pre-crack healed specimens show high σ_{f0} and σ_{t0}, and they are about 300MPa, that is 6 times of pre-cracked specimens. However, the pre-crack healed specimens laid under the S-N(t) curve of heat treated smooth specimens. In addition, most pre-crack healed specimens showed a fatigue strength which was higher than the as-received smooth specimens, though fracture occurred in the pre-crack healed zone. For the case of the pre-crack healed specimens with $2C \fallingdotseq 100\,\mu m$, S-N(t) curve was almost same to that of heat treated smooth specimens and most specimens failed outside the crack healed zone. This concludes that the maximum possible size is about $100\,\mu m$, which can be resisted fatigue stresses.

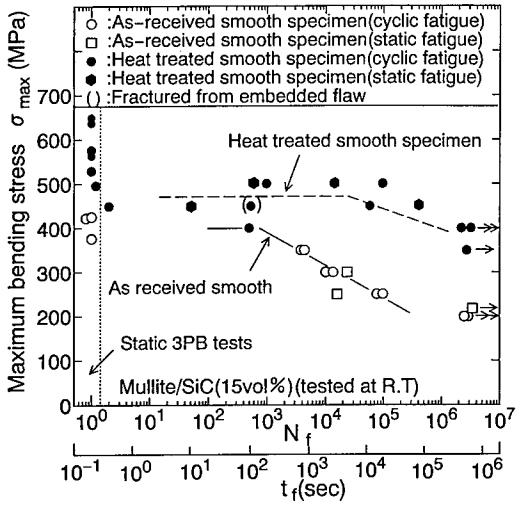


Fig.5. Results of cyclic and static fatigue tests of smooth specimen at R.T.

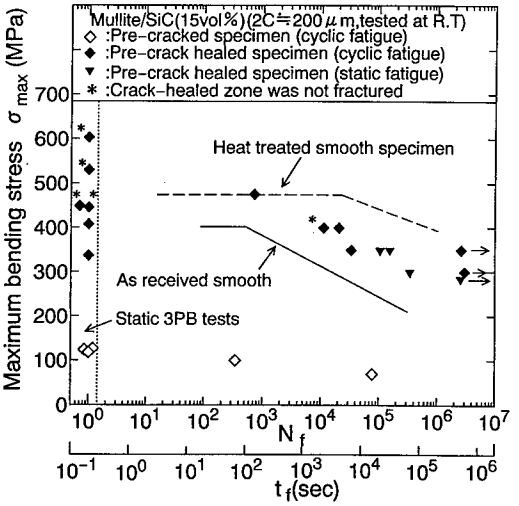


Fig.6.Results of cyclic and static fatigue tests of pre-crack healed specimen at R.T.

4. CONCLUSIONS

Using the sintered mullite/SiC composite ceramics, the crack healing behavior, high temperature strength, cyclic fatigue and static fatigue strength properties were investigated systematically. The main results of this paper are as follows:

(1) Mullite/SiC composite ceramic has ability to heal cracks
(2) The best healing condition was found to be 1300℃, in air for 1h
(3) Maximum crack size able to be healed is semi-elliptical crack of 200 μ m in diameter
(4) Crack healed zone has enough strength up to 1100℃ and most specimen failed outside the pre-cracked zone.
(5) Crack healed specimens showed higher cyclic and static fatigue strength than as-received smooth specimen, and this fact was caused by crack healing
(6) Crack healed zone has enough fatigue strength and most of the fractures occurred outside the pre-cracked zone in pre-crack healed specimen with crack of 100 μ m in diameter.
(7) Fracture of 200 μ m pre-crack healed specimens occurred in pre-cracked zone, but fatigue strength of them were greater than that of the as-received smooth specimens.

REFERENCES

1. J.J.Petrovic and L.A.Jacobson, J. Am. Ceram. Soc., **59** (1976)p.34
2. J.E.Moffatt, W.J.Plumbridge and R.Hermann, British Ceramic Transactions, **95**,(1996)p.23
3. T.K.Gupta, J. Am. Ceram. Soc., **59** (1976)p.259
4. S.R.Choi and V.Tikare, Scripta Metallurgica et Materialia, **26** (1992)p.1263
5. K.Ando, T.Ikeda, S.Sato, F.Yao and Y.Kobayashi. Fatigue Fract. Engng. Mat.Struct. **21** (1998)p.119
6. M.C.Chu,K.Ando,T.Hirasawa,S.Sato and Y.Kobayashi, High Pressure Institute of Japan. **36**-2(1998) p.82 (in Japanese).
7. K.Ando, M.C.Chu, S.Sato, F.Yao and Y.Kobayashi, Jpn. Soc. Mech. Engng. **64**- 623 (1998)p.1936 (in Japanese).
8. K.Ando, S.Sato, Y.Kobayashi and M.C.Chu. Fracture From Defects(ECF-12), (1998)p.497
9. M.C.Chu, S.Sato, Y.Kobayashi and K.Ando, Jpn. Soc. Mech. Engng. **60**-580 (1994)p.2829 (in Japanese).
10. S.Sato,M.C.Chu,Y.Kobayashi andK.Ando, Jpn. Soc. Mech. Engng.A-**61** (1995)p.1023 (in Japanese).
11. M.C.Chu,,S.Sato,,Y.Kobayashiand K.Ando, Fatigue Fract. Engng. Matre. Struct. **18**-9 (1995)p.1019
12. K.Ando,K.Tsuji,T.Hirasawa,Y.Kobayashi,M.C.Chu and Ssato, Jpn. Soc. Mech. Engng . **48** (1999)p.489 (in Japanese).
13. K.Ando,K.Tsuji,M.Ariga and S.Ssato, Jpn. Soc. Mech. Engng .**48** (1999)p.1173 (in Japanese).
14. JIS R1601,Japan Standards Association.(1993)

Key Engineering Materials Vols. 183-187 (2000) pp. 809-814
© 2000 Trans Tech Publications, Switzerland

Multi-crack Coalesence in Rock-like Material under Uniaxial and Biaxial Loading

P. Lin[1], Robina H.C. Wong[1], K.T. Chau[1] and C.A. Tang[2]

[1] Department of Civil and Structural Engineering, The Hong Kong Polytechnic University, Hung Hom, Kowloon Hong Kong, China P.R.

[3] Center for Rockbursts & Induced Seismicity Research, Northeastern University, Shenyang 110006, China P.R.

Keywords: Crack Coalescence, Failure Pattern, Multi-Crack, Peak Strength

ABSTRACT

The influence of the flaw (joint or fracture) distribution, the flaw length and bridge length (the distance between two flaws) on the coalescence and failure mechanism, and the peak strength of rock mass containing multi-cracks are studied under the uniaxial and biaxial loading. Based on the physical experimental testing and numerical simulation (with a newly developed code RFPA^{2D}), it is found that the behavior of multi-crack coalescence, the pattern of failure and peak strength are sensibly affected by the flaw number, the flaw length, bridge length and confining pressure.

1. Introduction

Many brittle materials develop cracks at some stage of their life cycle, for example, concrete, ceramic, and rock. Human always tries to understand the mechanisms behind the initiation, propagation, and coalescence of cracks, through the decades, in particular after the pioneering work of Griffith [1] on the brittle growth of fractures. Much research has been directed towards a better and deeper understanding of the observed phenomena. For example, Wong and Chau [2], Bobet and Einstein [3], Shen et. al [4] have performed some uniaxial or biaxial compression tests on modelling samples containing two opening or closing flaws, but they investigated crack coalescence mode and crack propagating pattern from different point of view. All previous research of the coalescence of two or three cracks can be divided into two groups. The first is to investigate coalescence of multiple edge cracks by considering the crack-spacing/crack depth ratio or to analyze asymmetric kinked crack coalescence of arbitrary size, location and orientation by using theoretical model, such as by Parker [5], Bernard [6], and Jin and Mao[7]. The second group focus on growth of multi-cracks in brittle solids, crack coalescence caused by multi-crack interaction under axial compression [8-10]. Some mathematical models and computer models relevant to the elasticity solution were developed to support the experimental results, such as those by Horii and Nemat-Nasser [9], and Ashby and Hallam [10].

Although most of the studies mentioned above have been done on crack propagation and interaction, they are restricted to samples with a fixed joint configuration, such as fixed flaw length, bridge length and flaw angle. Few studies have been devoted to investigate the influence of the distribution of flaws, the length of flaws and the bridge length on crack coalescence behavior and peak strength under the confining pressure. As we know that natural rock contains many complex joints or fractures distributed with different length and orientation. In general, these joints or fractures interact under confinement condition, which has not been considered fully in previous

studies. Therefore, the main content of this paper will focus on the influence of the flaw number, the length of flaw and bridge and the confining pressure on behavior of multi-crack coalescence, the pattern of failure and peak strength by employing experimental and numerical methods. The experimental device of uniaxial and biaxial compression was designed by Wong [8]. A latest code, RFPA^{2D} (Rock Failure Process Analysis), developed by Tang [11] was applied to simulate the results of experiment.

2. Experiment and Simulation Procedure

2.1 Preparation of Physical Specimen and Test System

In order to compare with our previous work [8], the ingredient and mixture of modelling material used in the present study are the same as those used by Wong [8]. The uniaxial compression strength σ_0, Young's modulus and Poisson ratio of modelling material are 2.32MPa, 0.522GPa and 0.28, respectively. The size of all specimens is 25mm in thickness, 400mm in width and 400mm in length (Fig. 1). The specimens were prepared by using steel moulds. The angle of all pre-existing flaws is fixed at 135°. Three flaw bridges were defined, B1, B2, B3. The angle of B2 is the same as that of the pre-existing flaw. The angles of bridge B1 or B3 were fixed at 75° since it is found from previous study that, when the angle of bridge equals 75°, coalescence is most likely to be observed [2]. Before performing experiments, the specimens were dried in oven at 105° for 5 days, then, were kept in room temperature for one day.

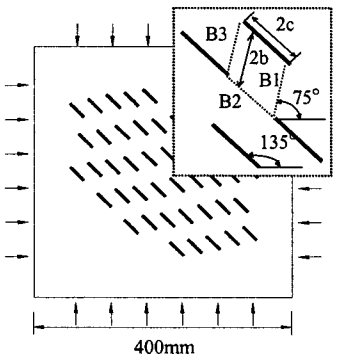


Fig.1 Geometry of specimen

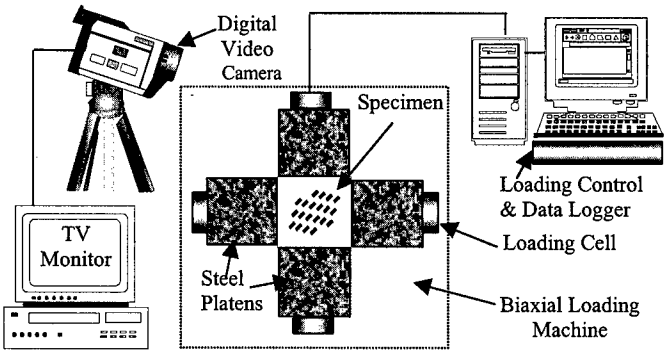


Fig.2 Schematic diagram of the experimental test system

The main components of test system are biaxial loading machine, loading control and data logger system and digital monitor system, shown in Fig.2. The biaxial loading machine provides the loading force and the measurement of displacement through six transducer attaching the loading steel platens. The data of force and displacement were transferred to loading control and data logger system for controlling the axial or lateral loading. The rate of loading was kept at two different velocities during the full loading process. Before the loading reach at 5kN, the rate of loading keeps at 0.2kN/min. For load larger than 5kN, the velocity becomes 0.1kN/min. In this study, the some of the confining pressure equals 1kN. In the digital monitor system, a DCR-TRV900E Digital Video Camera Recorder is used to monitor the process of crack propagation and display the process in real time through a big screen TV.

2.2 Numerical Model

In order to compare the experimental results, and to obtain more insight into the mechanics of multi-crack coalescence inside the rock-like specimen, numerical simulations were carried out by

using a latest code, RFPA^{2D}, which can be used to simulate the deformation, stress distribution, fracture initiation and propagation in heterogeneous materials [11].

Based on the physical parameters, the material parameters and other parameters for simulation were listed in Table 1. Three patterns of numerical models were set up similar to the physical models.

Table 1 Parameters for simulations

General	**Model elements:** 150 × 150 = 22500 elements representing a sample geometry of 400 × 400mm, **The ratio of tension strength to compression strength**=1/6, **friction angle**: 30°, The element property is selected by setting the Weibull's distribution (m, s_0)* as $\mathbf{E_0}$(10, 60000) and σ_0(10, 200). The closed flaw property: $\mathbf{E_0}$ (10, 600) and σ_0(10, 20), **The ratio of Poisson** is 0.25. **Total steps**: 200. **The axial loading** with a displacement control is: 0.002 mm/step. Under the biaxial condition, **the confinement** was fixed at 0.15MPa after the 50th step
Model I	2c=25mm,2b=25mm; Flaw number: 18 & 42; under uniaxial and biaxial loading
Model II	2c=30mm,2b=25mm; Flaw number: 18 & 42; under uniaxial and biaxial loading

* m is a homogeneity index which controls the shape of the distribution function relating to the degree of material heterogeneity. s_0 is the parameter related to the mean value of the material parameters for the elements, such as strength and elastic modulus.

3. Results and Discussion

Over 60 specimens with different number of pre-existing flaw and different flaw and bridge length were tested experimentally and simulated numerically under different confining pressure in this study. Due to the page limitation, the detailed results will be discussed in another paper [12]. Fig. 3 shows some of our results. In Fig. 3, the picture (a), (b), (c),...denotes different physical model and loading conditions. It is found that the crack patterns and failure behavior in the simulations basically coincide with the experimental results. Based on the results of experiment and simulation, discussion is focused on two problems in this paper: coalescence and failure mechanism, and the peak strength.

3.1 Coalescence and Failure Mechanism

By analyzing the results of our experiments and simulations, it is found that the influence of flaw distribution, bridge length and confining pressure on the position of crack initiation, the mode of crack coalescence and the patterns of final failure is significant. Although the failure process of the specimens containing multi-flaws is very complex, the behavior of crack initiation, propagation and coalescence follows some basic principles, most of which are related to the interaction between two or three flaws. The crack nucleates from different positions under different loading conditions, as shown in Fig.4. Under the uniaxial compression, the wing crack initiates from the two tips of flaw and propagates toward the middle (Fig.4 (a)), or initiates from one tip of flaw and propagates to another tip (Fig.4 (b)). However, under the biaxial condition, most of wing cracks nucleate from the centre of the bridge area of overlapping (Fig.4 (c)). With increasing confining pressure, this phenomenon is more apparent. The three modes of crack coalescence are observed: the tension or wing mode, the shear mode and the mixed tension/shear mode, illustrated in Fig.5. The tension or wing mode is mainly occurred at the non-overlap flaws due to the high tensile stress (Fig.5 (b)). This kind of mode is easy to produce with the specimen of evenly distribution flaws (42 flaws) under the uniaxial loading (see in Fig.3 (a), (a')). In shear mode, the crack nucleation at the tips of the pre-existing flaws along the diagonal direction will lead to a shear crack coalescence in the bridge area (Fig.5 (c)). This kind of coalescence is mainly induced by a high shear stress concentration in the bridge area of 18 flaw specimen, see Fig.3 (b), (d),(b'),(d'). The mixed mode made by tension and shear crack is a general mode in the area of over-lap flaws in most physical

and numerical specimens. With decreasing bridge length, the interaction increases and interconnection between overlap flaws becomes easier.

The patterns of final failure depends on the distribution of flaws and the loading condition. For specimens containing 42 flaws under the uniaxial compression, splitting failure induced by tensile cracks is observed see Fig.3 (a) and (a'). However, in specimen containing 18 flaws, the final failure is in a mixed mode including splitting and shear failure (See Fig.3 (b)(b')). The reason may be that: the specimens with 18 flaws are distributed on the diagonal of specimen. Therefore, a strong interaction is generated in the bridge area. Under the compression loading, the maximum shear stress can be induced after the tensile cracks developed at the tips of the pre-existing flaw and the tips of the growing crack. Ultimately, the specimen fails in the form of shear between the flaw tips, or in the form mixed failure mode in between the tips of growth cracks. For those specimens (including 18 flaws and 42 flaws) under the confining pressure, the shear model dominates the final failure (See Fig.3 (c), (d), (c'), (d')).

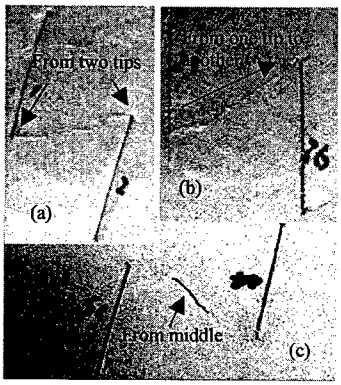


Fig.4 The position of crack initiation between the pre-existing flaws

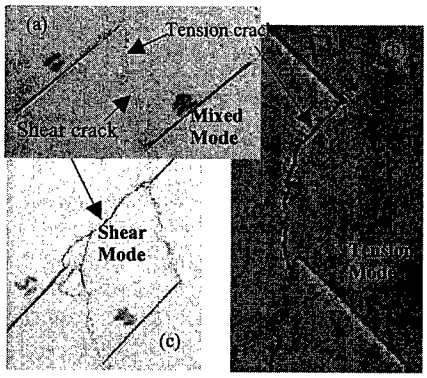


Fig.5 The basic patterns of crack coalescence between the pre-existing flaws

3.2 Peak Strength

The peak strength of physical and numerical specimens with different number of flaws, the length of flaws and the bridge length under the different confining pressure are shown in Table 2. It is clearly show that: the peak strength of specimen is higher under biaxial condition than that under uniaxial condition. Furthermore, with the same number of flaws, the peak strength will decrease with increasing the length of flaws. It is easy to be understood since increasing the length of flaws will increase weak zones.

Table 2. The peak strength of physical and numerical specimens

Specimens			Uniaxial Peak strength (MPa)		Biaxial Peak strength (MPa)	
Flaws number	Flaw length (mm)	Bridge length (mm)	Experimental Value	Numerical Value	Experimental Value	Numerical Value
42	25	25	1.03	0.62	1.09	0.82
42	30	25	0.78	0.61	0.82	0.80
18	25	25	0.85	0.66	1.41	0.85
18	30	25	0.76	0.61	0.88	0.83

In addition, it is interesting to find that peak strength of specimens is independent on the number of flaws. This results in the conclusion that the peak strength of specimens does not strongly depend on the number of pre-existing flaws. The peak strength of specimen with 42 flaws can be either

larger or smaller than that of specimen with 18 flaws. The reason may be related to the flaw distributing pattern (18 flaws concentration along the failure zone) and the number of flaws involved in the formation of shear zone or the number of flaws dominating crack coalescence and the macroscopic failure. Similar conclusion was reported by Wong [8] under uniaxial compression.

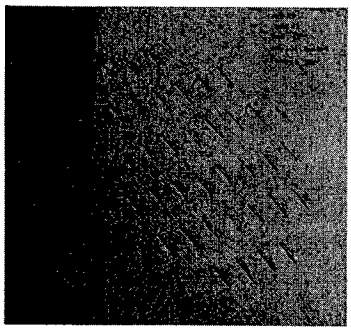
4. Conclusions

(1) For failure mechanisms, under uniaxial and biaxial conditions, the tensile crack is likely to occur between non-overlapping flaws whiles the mixed crack is likely to occur between the overlapping flaws. With the bridge length decrease, the interaction becomes obvious and interconnects become easier between overlap flaws. The confining pressure and the number of flaws have a great influence on the macroscopic eventual failure pattern. When the flaws are concentrated along a shear zone, the macroscopic failure along this direction will be observed under uniaxial or biaxial condition. If the flaws evenly distributed in the specimen, splitting failure will occur under uniaxial compression, and the shear failure will occur under the biaxial compression.
(2) For the peak strength, it will decrease with the increase of flaw length. In addition, peak strength of specimens is independent of the number of flaws, but depends on flaw distribution, and the number of flaws involved in the formation of failure zone. The more flaws distributed along the shear zone, the lower the peak strength will be attained.

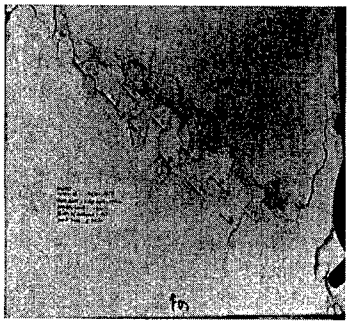
Acknowledgement-The research was supported by the Internal Research Fund of the Hong Kong Polytechnic University to RHCW.

References

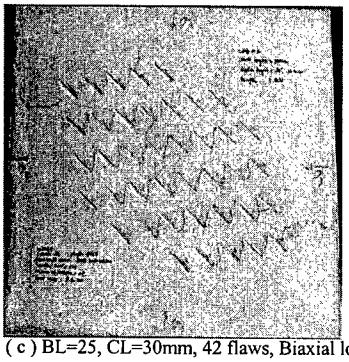
1. Griffith, A.A., The phenomena of rupture and flow in solids, *Phil.Trans.Royal Soc.London*, Series A,**221**(1921) p.163
2. Wong, R.H.C. and Chau, K.T., Crack coalescence in a rock-like material containing two cracks, *Int. J. Rock Mech. min.* Sci., **35**(2)(1998) p.147-164
3. Bobet, A. and Einstein, H.H., Fracture Coalescence in Rock-type Material under Uniaxial and Biaxial Compression, *Int. J. Rock Mech.min.*Sci.,**35**(7)(1998) p.836-888
4. Shen, B., Stephansson, O., Einstein, H.H. and Ghahreman, B., Coalescence of fractures under shear stress experiments. *Journal of Geophysical Research*, **100**(6)(1995) p.5975-5990
5. Parker, A. P., Stability of arrays of multiple edge cracks, *Engineering fracture mechanics*, **62** (1999) p.577-591
6. Bernard, F., A stochastic theroy for the problem of multiple surface crack coalescence, *International journal of fracture*,**91**(1998) p.23-45
7. Jian,N. and Mao, S.W., Analysis of asymmetric kinked cracks of arbitrary size, location and orientation- part I/II: Remote compression/ tension, *Int. J. of fracture* **89**(1998) p.19-84
8. Wong, R.H.C., Failure mechanisms and peak strengths of natural rocks and rock-like solids containing frictional cracks, *Ph.D thesis*, Civil & Structural Eng. Dept., HK Polytechnic Uni.(1997)
9. Horii,H. and Nemat-Nasser,S., Brittle failure in Compression: splitting and brittle-ductile transition *Philosophical Transactions of the Royal Soc. of London*, Series A,**319**(1986) p.337-374
10. Ashby, M.F. and Hallam, S.D., The failure of brittle solids containing small cracks under compressive stress states, Acta Metall, **34**(3)(1986) p.497-510
11. Tang, C.A., Numerical simulation of progressive rock failure and associated seismicity, *Int. J. Rock Mech. Min. Sci.*, **34**(1997) p.249-262
12. Lin,P., Wong, R.H.C., Chau, K.T. and Tang, C.A., The experimental and numerical study on the coalescence mechanisms of multi-jointed solids, *To be submitted*



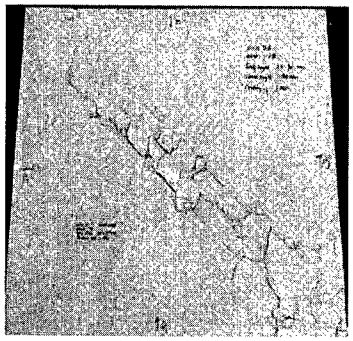
(a) BL=CL=25mm, 42 flaws, Uniaxial loading



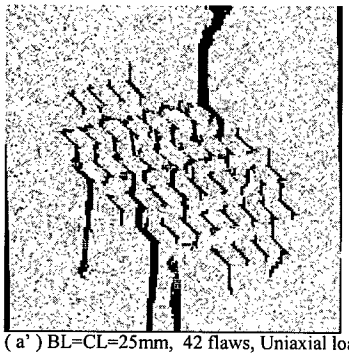
(b) BL=CL=25mm, 18 flaws, Uniaxial loading



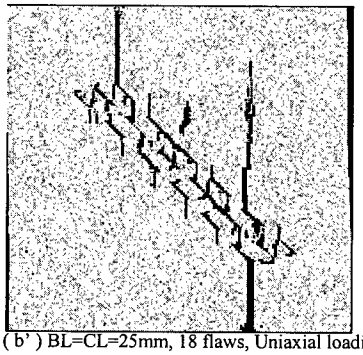
(c) BL=25, CL=30mm, 42 flaws, Biaxial loading



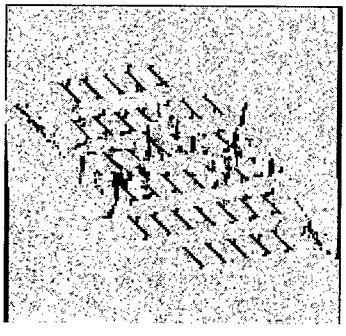
(d) BL=25, CL=30mm, 18 flaws, Biaxial loading



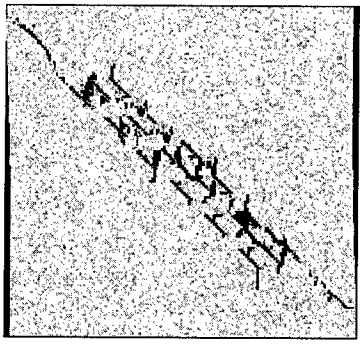
(a') BL=CL=25mm, 42 flaws, Uniaxial loading



(b') BL=CL=25mm, 18 flaws, Uniaxial loading



(c') BL=25, CL=30mm, 42 flaws, Biaxial loading



(d') BL=25, CL=30mm, 18 flaws, Biaxial loading

Fig.3 The experimental (a-d) and numerical (a'-d') results of crack coalescence

Key Engineering Materials Vols. 183-187 (2000) pp. 815-820
© 2000 Trans Tech Publications, Switzerland

Effects of Temperature and Stacking Sequence on the Mode I Interlaminar Fracture Behavior of Composite Laminates

H.S. Kim[1], W.X. Wang[2] and Y. Takao[2]

[1] Department of Aeronautics and Astronautics, Graduate School of Engineering, Kyushu University, 6-10-1, Hakozaki, Higashi-ku, Fukuoka 812-8581, Japan

[2] Research Institute for Applied Mechanics, Kyushu University, 6-1, Kasuga-koen, Kasuga-shi, Fukuoka 816-8580, Japan

Keywords: Fiber Orientation, Interlaminar Fracture Toughness, Mode I, SN-DCB Specimen, Temperature

ABSTRACT

The purpose of the present study was to clarify the effects of temperature and fiber orientation on the Mode I interlaminar fracture toughness, G_I (G_{IC}: G_I at initiation, G_{IR}: G_I at propagation), of carbon/epoxy composite laminates. In our previous study, the conventional double cantilever beam (DCB) tests were performed to investigate the effects of temperature and fiber orientation in CFRP laminates. It was shown that G_I was obviously affected by the temperature and fiber orientation. Especially, in case of the specimen with [45//-45] interface, G_{IR} was considerably affected by both failure mechanisms of crack jumping and fiber bridging. Therefore, in the present study, to suppress the effects of crack jumping and fiber bridging occurred in multidirectional laminates, the side notched double cantilever beam (SN-DCB) specimen is used. DCB tests of [22.5//-22.5] and [45//-45] SN-DCB specimens are conducted at three temperatures, that is, -100°C, 25°C and 150°C. G_{IC} was affected by temperature and fiber orientation, obviously and slightly, respectively. In contrast to G_{IC}, G_{IR} was considerably affected by both temperature and fiber orientation.

1. INTRODUCTION

Fiber reinforced plastics (FRP) have been often used in aerospace and other application fields because of their high specific stiffness and strength, and they are expected to be applied to a wide range of temperature environments. In general, as the FRP laminates are used in a form of multidirectional laminates in order to meet various required material properties, the laminate with different fiber orientations may yield damages such as transverse crack and interlaminar delamination. Especially, the interlaminar delamination significantly decreases structural integrity, such as stiffness and strength. Thus, it is very important to understand and predict the composite's resistance to interlaminar fracture.

Many researchers [1-5] have performed studies on the evaluation of Mode I interlaminar fracture

toughness, G_I, using the DCB specimen of unidirectional laminates at room and various temperatures. However, in practical application FRP laminates are frequently used in a form of multidirectional laminates in order to meet various required material properties, which leads to the interlaminar delamination between layers with different fiber orientations. Therefore, in order to understand the interlaminar fracture behavior in structural composites, it is essential to accurately evaluate the composite's resistance to interlaminar fracture of multidirectional laminates with a delamination between θ and -θ degree layers, that is, θ//-θ. Several researchers [6-11] have studied the G_I for the multidirectional laminates with a delamination between θ and -θ plies. Authors [12] have investigated the effects of temperature and fiber orientation on the G_I of Carbon/Epoxy composites, T800H/#3631, for three types of specimen, [0//0], [22.5//-22.5] and [45//-45], at -100°C, 25°C and 150°C. It was found that G_I (G_{IC}: G_I at initiation, G_{IR}: G_I at propagation) was obviously affected by the temperature and fiber orientation. Especially, in case of the specimen with [45//-45] interface, G_{IR} was considerably affected by both crack jumping and fiber bridging. This G_{IR} can not reflect the interlaminar fracture toughness at propagation along the [45//-45] interface.

In the present study, in order to suppress the effects of crack jumping and fiber bridging occurred in multidirectional laminates, the side notched double cantilever beam (SN-DCB) [6] specimen is used. DCB tests are conducted to clarify the effects of temperature and fiber orientation on the Mode I interlaminar fracture toughness for two types of specimen, [22.5//-22.5] and [45//-45] SN-DCB specimen, at three temperatures of -100°C, 25°C and 150°C. Fracture surface observation is carried out by scanning electron microscope (SEM).

2. EXPERIMENTAL

2.1. Material and specimen fabrication

The laminates used in this study were made of Toray P2212-15 prepregs which consists of carbon fiber (T800H) and epoxy resin (#3631), composed of 24 plies and cured in an autoclave. The fiber volume fraction V_f and final thickness of the laminates were approximately 62% and 3.3mm, respectively. The SN-DCB specimen geometry used is shown in Fig. 1. The stacking sequence of the specimen was selected as shown in Table 1. Type [0//0] SN-DCB specimen was used to compare with the conventional results. A 25μm thick Kapton film with release agent was inserted to make the initial crack and edge delamination. Steel hinges were adhered to transfer the external load into the specimen. The crack length (a_0=37mm) was measured from the center of the hinge pivot pin. The side edge of the specimen was painted with typewriter correction liquid to facilitate the observation and measurement of crack growth during the DCB testing.

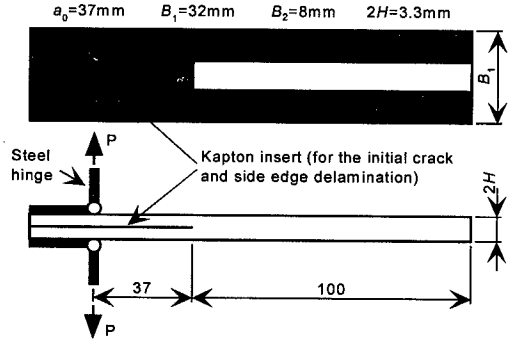


Fig.1. Geometry of SN-DCB specimen.

Table 1. Stacking sequence of SN-DCB specimens

Specimen	Stacking sequence
Type [0/0]	$[0_{12}//0_{12}]$
Type [22.5/-22.5]	[22.5/-22.5/0_8/-22.5/22.5 //-22.5/22.5/0_8/22.5/-22.5]
Type [45/-45]	[45/-45/0_8/-45/45 //-45/45/0_8/45/-45]

2.2. DCB test procedure

The DCB tests were carried out under the displacement control condition using a servo-hydraulic testing machine (MTS 320.34) equipped with a thermostatic chamber which can provide a stable temperature environment from -180°C to 320°C. Both a heater and liquid nitrogen were used to control the temperature. Before loading, the DCB specimen was set in the thermostatic chamber for one hour at the testing temperature. Then, it was loaded in tension perpendicular to their length direction (as shown in Fig. 1) at a constant crosshead speed of 1mm/min. After the crack was extended by a Δa of about 10mm, the specimen was unloaded with a crosshead speed of 1~3mm/min. This procedure was repeated until the crack length became to approximate 70mm.

2.3. Data reduction for SN-DCB specimen

The conventional compliance method [13] was used to evaluate the Mode I interlaminar fracture toughness, G_I, for SN-DCB specimen as follows:

$$\frac{a}{2H} = \alpha_1 (B_1 C)^{\frac{1}{3}} + \alpha_0 \tag{1}$$

$$G_I = \frac{3}{2(2H)} \frac{P^2 (B_1 C)^{\frac{2}{3}}}{B_1 B_2 \alpha_1} \tag{2}$$

where a is the crack length, C is the load line compliance, P is applied load, B_1 is the whole width of the specimen, B_2 is the width of the crack, $2H$ is the thickness of the specimen and α_1 is calculated from Eq. 1 based on the experimental data of crack length a and compliance C. It is noted that the Eq. 2 is equal to the conventional one [13] if B_1=B_2.

3. EXPERIMENTAL RESULTS AND DISCUSSION

3.1. [22.5//-22.5] SN-DCB specimen

The G_I for Type [22.5//-22.5] specimen at three temperatures is shown in Fig. 2. G_{IC} is high in order of -100°C, 25°C and 150°C. And G_{IR} is high in order of 25°C, 150°C and -100°C. Near the initial crack tip (Δa=0mm), a resin rich area exists and the toughness of matrix increases at low temperature. Thus, the G_{IC} becomes large. Moreover, the change of G_{IR} is small and it is nearly the same to G_{IC}.

The G_{IC} at 150°C is the smallest among three temperature cases. In the load-displacement curve, nonlinearity appears much early before the maximum load. Since the point of nonlinearity is related to G_{IC}, the G_{IC} becomes small. However, G_{IR} becomes remarkably large for crack growth, Δa, being

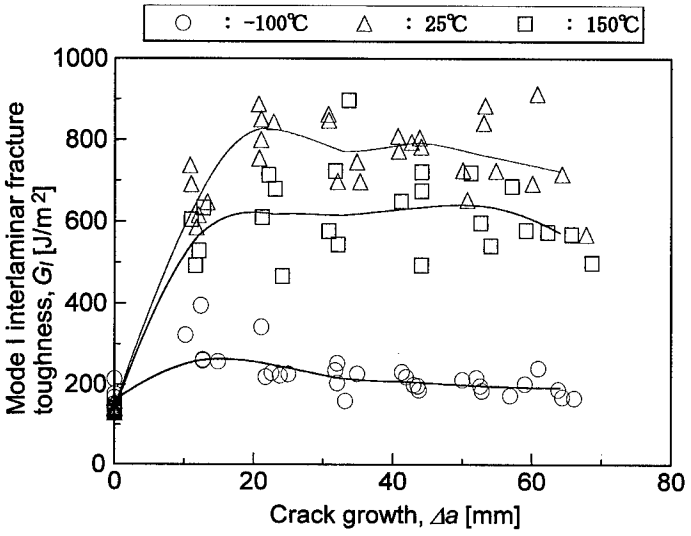


Fig.2. Mode I interlaminar fracture toughness G_I for Type [22.5//-22.5] SN-DCB specimen at three temperatures.

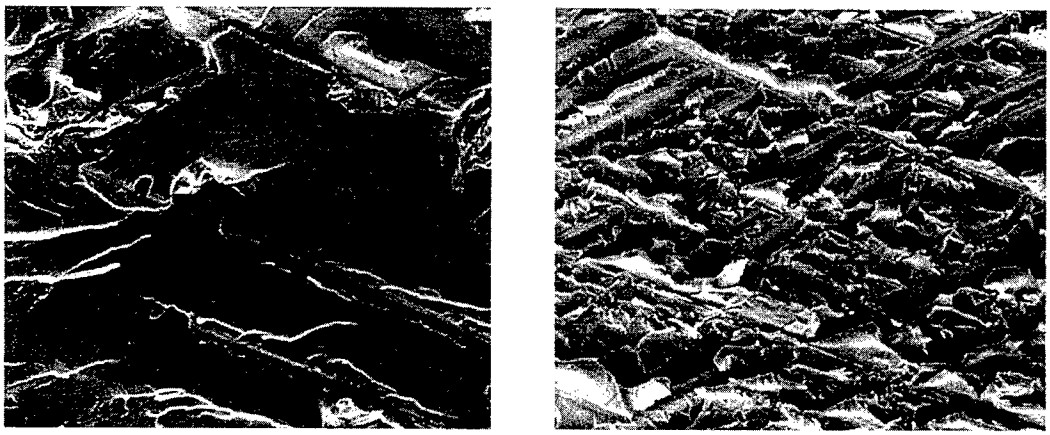


Fig.3. SEM photographs of fracture surface for Type [22.5//-22.5] SN-DCB specimen at -100°C and 150°C.

larger than 10mm. It is also found that G_{IR} at the room temperature remarkably increases with Δa increasing, and that it is lager than the one at 150°C.

Figure 3 shows the SEM photographs of fracture surface for Type [22.5//-22.5] SN-DCB specimen at -100°C and 150°C. At low temperature, a relatively large and flat fracture surface can be seen. This feature suggests a brittle fracture micromechanism. And it also can be seen that the crack propagates mainly within the matrix region. Therefore, it is understand that the decreasing of fracture surface led to a low fracture toughness. At 150°C, it is found that the increasing of temperature led to the increase in area of interfacial debonding and deformation in matrix. Therefore, a higher fracture toughness is expected.

3.2. [45//-45] SN-DCB specimen

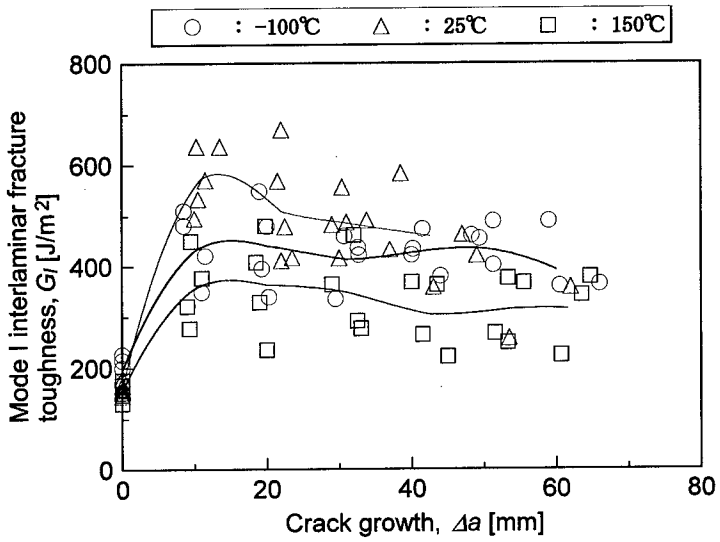


Fig.4. Mode I interlaminar fracture toughness G_I for Type [45//-45] SN-DCB specimen at three temperatures.

The G_I for Type [45//-45] SN-DCB specimen at three temperatures is depicted in Fig. 4. It is found that the G_{IC} is high in order of -100°C, 25°C and 150°C, similar to the case of Type [22.5//-22.5] SN-DCB specimen. The same discussions for G_{IC} of Type [22.5//-22.5] SN-DCB specimen are applicable to the present case. And the behavior of the interlaminar fracture at propagation shows the similar

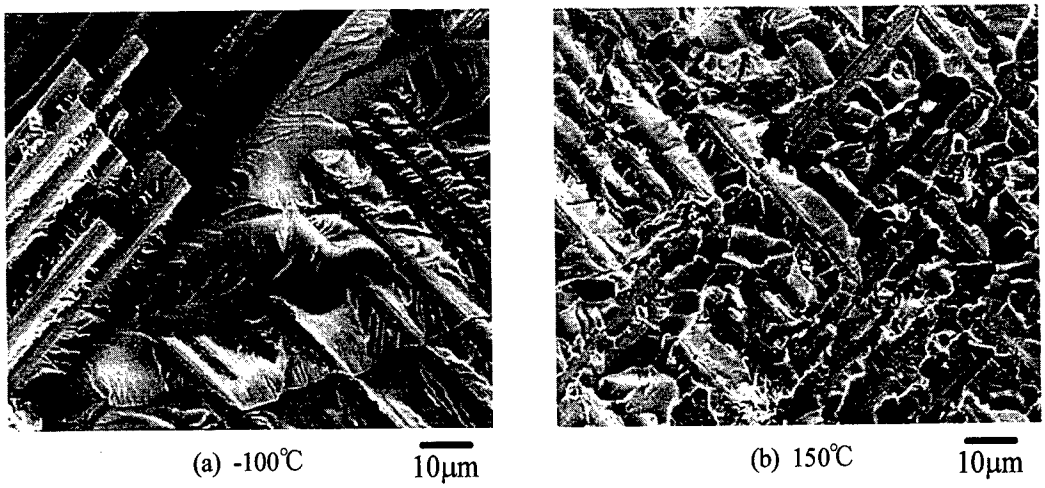


Fig.5. SEM photographs of fracture surface for Type [45//-45] SN-DCB specimen at -100°C and 150°C.

tendency at all temperatures. The G_{IR} is high in order of 25°C, -100°C and 150°C, which is different from that of Type [22.5//-22.5] SN-DCB specimen because of the effects of fiber orientation. In particular, the G_{IR} at 150°C is the smallest among three temperature cases. Figure 5 shows the SEM photographs of fracture surface for Type [45//-45] SN-DCB specimen at -100°C and 150°C. At 150°C, the degradation of the fiber/matrix interface and the matrix can be observed. Therefore, the fracture toughness at 150°C was low. At -100°C, however, since the fracture surface increases, a high fracture toughness is expected.

4. CONCLUSIONS

In the present study, DCB tests using the side notched double cantilever beam (SN-DCB) specimen are conducted to investigate the effects of temperature and fiber orientation on the Mode I interlaminar fracture toughness for two types of specimen, [22.5//-22.5] and [45//-45] SN-DCB specimens, at three temperatures of -100°C, 25°C and 150°C.

G_{IC} was affected by temperature and fiber orientation, obviously and slightly, respectively. In contrast to G_{IC}, G_{IR} was considerably affected by both temperature and fiber orientation.

REFERENCES

1. W.X. Wang, Y. Takao, F.G. Yuan, B.D. Potter, and R.H. Pater, J. Composite Materials, **32** (1998) p. 1508
2. S. Hashemi, A.J. Kinloch, and J.G. Williams, J. Composite Materials, **24** (1990) p. 918
3. A. Garg, and O. Ishai, Engineering Fracture Mechanics, **22** (1985) p. 413
4. H. Kawada, W. Sugiura, K. Miyano, and I. Hayashi, ICCM-10, Canada (1995) p. 93
5. H. Lau, K. Jiang, and R.E. Rowlands, J. Composite Materials, **24** (1990) p. 326
6. P. Robinson, and D.Q. Song, J. Composite Materials, **26** (1992) p. 1554
7. N.S. Choi, A.J. Kinloch, and J.G. Williams, J. Composite Materials, **33** (1999) p. 73
8. D.J. Nicholls, and J.P. Gallagher, J. Reinforced Plastics and Composites, **2** (1983) p. 2
9. H. Chai, Composites, **15** (1984) p. 277
10. C.L. Nailadi, and D.F. Adams, 13th Annual Techn. Conf. Composite Materials, USA, Baltimore (1998)
11. I. Chou, I. Kimpara, K. Kageyama, and I. Ohsawa, J. Materials Science, Japan, **41** (1992) p.1292
12. H.S. Kim, W.X. Wang, and Y. Takao, ICCM-12, France, Paris (1999)
13. Japanese Industrial Standard Group, (in Japanese) JIS K 7086-1993, p. 651

Key Engineering Materials Vols. 183-187 (2000) pp. 821-826
© 2000 Trans Tech Publications, Switzerland

Effect of Remanent Polarization on Electro-mechanical Fields Near an Elliptic Cavity or a Crack in Piezoelectric Ceramics

B. Liu, D.N. Fang and K.C. Hwang

Department of Engineering Mechanics, Tsinghua University, Beijing 100084, China P.R.

Keywords: Cavity, Crack, Piezoelectric Ceramics, Remanent Polarization

ABSTRACT

In this paper the effect of remanent polarization on electric-mechanical fields near an elliptic cavity or a crack in piezoelectric ceramics is studied. The analysis is based on the application of exact electric boundary conditions at the rim of an elliptic cavity and/or a crack. The solutions are derived in a closed form in terms of complex potentials. The result shows that the cavity problem of remanent polarization is similar to the problem of general strain mismatch and the effect of remanent polarization can not be omitted. The same conclusion can also be obtained by adopting the nonlinear boundary conditions for a sharp crack problem. By use of this model we can get calculation results to explain some experimental results.

1. INTRODUCTION

Piezoelectric ceramics are widely used in electromechanical sensors, transducers and actuators. Structural reliability concerns of these devices are calling for a better understanding of the mechanisms of piezoelectric fracture. Theoretical study of fracture mechanics in piezoelectric solids has been made by Parton [1], Deeg [2], McMeeking [3, 4], Pak [5], Sosa [6, 7], Suo *et al.* [8], Duun [9], Park and Sun [10], Zhang and Tong [11], Gao *et al.* [12], and many others. In fact, most used piezoelectric ceramics have ferroelectric crystals. Usually, these piezoelectric ceramics have to be first polarized by applying an electric field in excess of the coercive field before any application in order to get the piezoelectric properties. After unloading, there exists a remanent polarization in the piezoelectric ceramics. In this paper, the main attempts are made to investigate the effect of the remanent polarization, P_r or D_0, on the electromechanical fields near an elliptic void or a crack in an infinite piezoelectric medium (refer to Fig1.). To the best knowledge of the authors, no such kind of effect has been taken into account in the analysis of piezoelectric fracture.

The general process to solve the cavity problem and the crack problem in the anisotropic piezoelectric ceramics is identical to that developed by Sosa and Khutoryansky [13]. And the analysis is based on the application of exact electric boundary conditions at the rim of the elliptic cavity. Expressions for the electromechanical fields near the elliptic cavity are derived in closed forms in terms of complex potentials. The effects of the remanent polarization, D_0 upon the electromechanical fields are analyzed in terms of the solutions.

2. THE DESCRIPTION OF THE PROBLEM AND THE SOLUTION

The material in this modeling is poled or depolarized piezoelectric ceramics with the ferroelectric crystal. There exists remanent polarization in the ceramics. The applied loading is linear and less than the coercive fields so that no domain switching occurs. Thus, linear fracture mechanics will still be able to be employed for such a depolarized ceramic. Because of the existence of the remanent polarization D_0 in ferroelectric ceramics, the accurate constitutive equations under the plane strain conditions ($\varepsilon_{yy} = \varepsilon_{zy} = \varepsilon_{xy} = 0, E_y = 0$) should be

$$\begin{pmatrix} \varepsilon_{xx} \\ \varepsilon_{zz} \\ 2\varepsilon_{xz} \end{pmatrix} = \begin{bmatrix} a_{11} & a_{12} & 0 \\ a_{12} & a_{22} & 0 \\ 0 & 0 & a_{33} \end{bmatrix} \begin{pmatrix} \sigma_{xx} \\ \sigma_{zz} \\ \sigma_{xz} \end{pmatrix} + \begin{bmatrix} 0 & b_{21} \\ 0 & b_{22} \\ b_{13} & 0 \end{bmatrix} \begin{pmatrix} D_x \\ D_z - D_0 \end{pmatrix} \tag{1a}$$

$$\begin{pmatrix} E_x \\ E_z \end{pmatrix} = -\begin{bmatrix} 0 & 0 & b_{13} \\ b_{21} & b_{22} & 0 \end{bmatrix} \begin{pmatrix} \sigma_{xx} \\ \sigma_{zz} \\ \sigma_{xz} \end{pmatrix} + \begin{bmatrix} c_{11} & 0 \\ 0 & c_{22} \end{bmatrix} \begin{pmatrix} D_x \\ D_z - D_0 \end{pmatrix} \tag{1b}$$

where a_{ij}, b_{ij} and c_{ij} are known as the *reduced material constants* refer to Sosa[7], and ε_{ij}, σ_{ij}, E_i and D_i are the components of strain, stress, electric field and electric displacement, respectively. Including D_0 in Equation (1) is the major difference from the constitutive equations adopted others. However, the constitutive equations in the elliptic cavity do not include D_0, shown as follows:

$$\boldsymbol{D}^c = \varepsilon_0 \boldsymbol{E}^c \quad \text{in } \Omega_c \tag{2}$$

where ε_0 is the permittivity of the medium inside the cavity. the superscript "c" refers to the variables in the cavity. If we regard D_0 as a general remanent strain, we note that there exists difference in general remanent strain between inner and outer cavity. But the continuance of normal component of electric displacement at the interface must be satisfied, so that the problem can be looked as the problem of mismatch in general remanent strain.

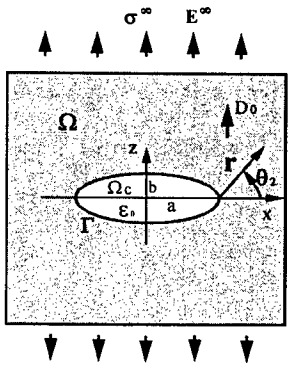


Fig. 1 Schematic of the piezoelectric cavity problem with remanent polarization.

The coordinates are defined as shown in Fig. 1. The positive direction of the z-axis is parallel to the poling direction. The x-y plane is the transversely isotropic plane. Where a, b are minor semi-axis and the major semi-axis of the elliptic cavity, respectively. In the process of solving the problem, we adopt the method proposed by Sosa and Khutoryansky [13]. Because of the restriction

on the paper length, we give the results directly. In order to investigate the influence of D_0, we let loading be zero.

Fig. 2 shows the influence of D_0 on the whole fields, where $|m_{31}|/a$ represents the amplitude of variables in the whole fields. Note that $\alpha = b/a$ is the ratio of minor semi-axis to the major semi-axis of the elliptic cavity. β represents the ratio of the permittivity of the cavity to the permittivity of the ceramic. We find that when $\beta = 0$, that is, the cavity becomes impermeable, the effect of D_0 on the full electromechanical fields does not vary with the change of α. When $\beta = 10^{-4} << 1$, if $\alpha > \beta$, m_{31} is nearly independent of α, but if $\alpha < \beta$, m_{31} will tend to zero as α tends to zero. When β is equal to *1* or larger than *1*, m_{31} will also tend to zero as α tends to zero. In general, with the same α, the effect of D_0 on the electromechanical fields becomes insignificant when β becomes larger. Fig. 3 shows the variation of the tangent stress, $\sigma_{ss}(a,0)$ at the apex of the major semi-axis of the elliptic cavity. When $\beta = 0$, that is, the cavity becomes impermeable, the stress will increase to infinite with α decreasing. However, if $\beta > 0$, $\sigma_{ss}(a,0)$ will tend to be constant as α tends to zero. Moreover, one can note that with the same α, the larger β, the smaller $\sigma_{ss}(a,0)$.

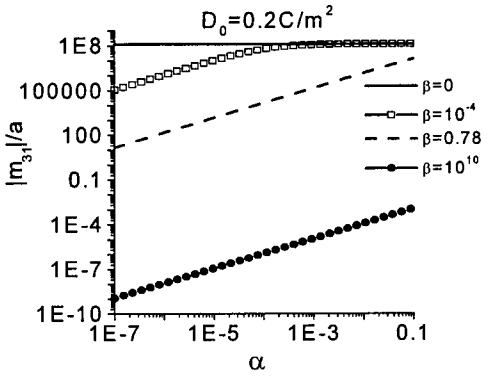


Fig. 2 Variation of $|m_{31}|/a$ as a function of α with the effect of D_0.

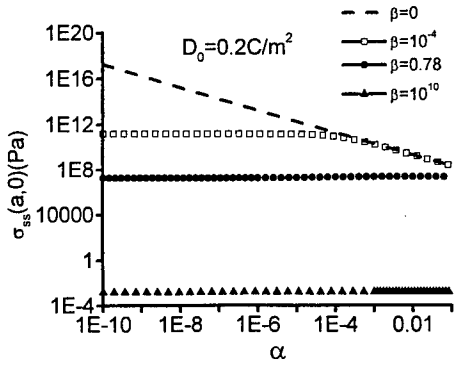


Fig. 3 Variation of the tangent stress at the apex of the major semi-axis of the cavity as a function of

α with the effect of D_0.

In Fig.3, we notice that when β is far smaller than *1*, the tangent stress at the apex of the major semi-axis of the elliptic cavity is tension. Furthermore, it can be founded that the effect of remanent polarization is identical to the effect of a considerable strong positive electric field (parallel to the poling direction), so the tangent stress at the apex of the major semi-axis caused by positive electric field is tension too. Such kind of behavior can be used to explain why a positive electric field promotes the crack growth while a negative electric field (opposite to the poling direction) retards the crack growth. From the same reason, if only a mechanical load is applied, because of the residual stress caused by remanent polarization, the fracture toughness will be anisotropic. That is, the crack grows more easily in the direction perpendicular to polarization than in the direction parallel to polarization.

However, for most values of β, one can find that when α tends to zero, the influence of D_0 tends to zero too. Does the effect of remanent polarization really disappear? Next, we develop a more accurate way to study the sharp crack problem. The problem which is solved is shown as problem(I) in Fig.4. Only the ceramic is regarded as the solving region without considering the crack gap region, and we propose boundary conditions on the crack surfaces. We assume that the electric displacement in the crack is $\tilde{D}$, which can be determined by the following equation.

$$\tilde{D} = \varepsilon_0 \tilde{E} = \varepsilon_0 \frac{-\phi(\tilde{D})}{u_z(\tilde{D})} \tag{3}$$

where $\phi(\tilde{D})$ and $u_z(\tilde{D})$ are the electric potential and the displacement in the *z*-direction of the crack, respectively, and $\tilde{E}$ is the electric field in the crack. The reason why we write ϕ and u_z as functions of $\tilde{D}$ is that $D_n = \tilde{\boldsymbol{D}} \cdot \boldsymbol{n}$ firstly is exposed on crack surface as the boundary condition, then we can obtain ϕ and u_z by solving the problem with this boundary condition. Different values of $\tilde{D}$ will induce different ϕ and u_z. In order to solve problem (I), we divide it into three problems as shown in Fig.4. It is easy to find that the solutions of problem (II) and problem (III) are homogenous fields. Thus, we can mainly focus on solving problem (IV). Since $D_n = 0$ on the crack surfaces, problem (IV) is a impermeable crack problem which has been solved by many researchers already. In this paper, we adopt the method used by Sosa and Khutoryansky [13].

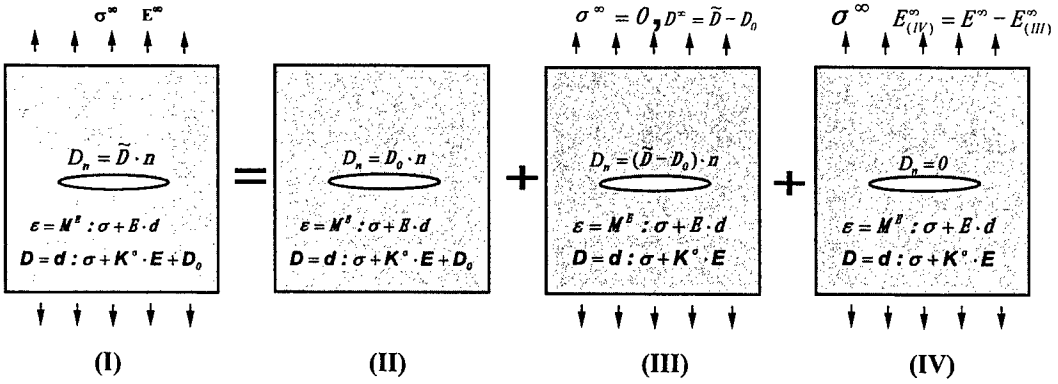


Fig.4 The demonstration of dividing the original problem (I) into three problems as problem(II),(III) and (IV)

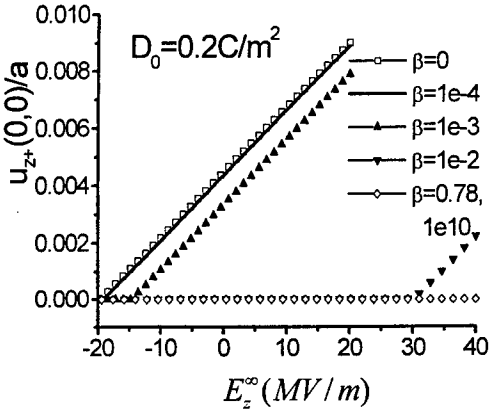


Fig. 5 Variation of the displacement of the upper bank center as a function of E_z^∞ under different β when D_0=0.2C/m^2.

A few samples are calculated. Fig.5 shows that when only an electric load is applied, that is, $E_z^\infty \neq 0$, $E_x^\infty = 0$, $\sigma^\infty = 0$, the displacement at center of the crack upper face varies with the change of E_z^∞ under the different values of β. It can be found that the whole tendency of the crack opening displacement is becoming larger with the increase of the electric field. But in some region the crack is closed, so the crack opening displacement maintains zero. The critical electric field at which the crack starts to open decreases with the decrease of β (in algebraic sense). It is interesting to note that when β is close to or equal to zero, even under the negative electric field, as long as it is not very large, the crack still keeps open. This is greatly different from the situation without considering the non-linear boundary conditions as given in equation (3). Additionally, we note that most curves consist of two segments of smooth curves. The reason is that they correspond to the two solutions of $\tilde{D}$, and we have chosen the physical practicable solution. Therefore, there is a transition point at the boundary of two solutions. When $E_z^\infty = 0$, that is, no loading is applied, the figure indicates that the crack is still open, meanning the effect of D_0. Therefore, the remanent polarization always has an influence on the electromechanical field distribution for the elliptical cavity at any α.

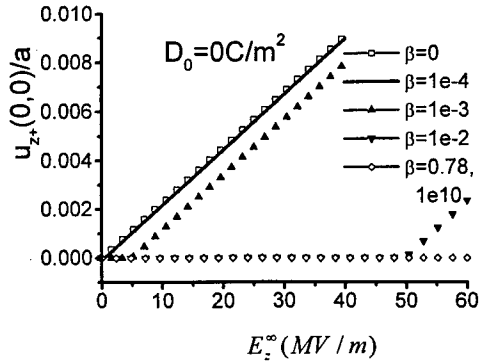


Fig. 6 Variation of the displacement at the center of the crack upper face as a function of E_z^∞ under

different β when D_0=0.0C/m^2.

Fig.6 shows that when D_0=0.0 C/m^2, the displacement at the center of the crack upper face varies with E_2^∞ under the different values of β, corresponding to the case without considering the effect of remanent polarization. Comparing Fig.5 with Fig.6 one can find that both are same except that there is a move of *20MV/m* in the opposite direction of the *x*-axis, indicating that the effect of D_0=*0.2C/m*^{2} is equivalent to the effect of a positive electric field of *20MV/m*, and is coincident with our previous work qualitatively.

3. CONCLUSIONS

1. The effect of remanent polarization D_0 is equivalent to the effect of a positive electric field, and it can not be neglected no matter what value α is.
2. The electric displacements of the crack are not always zero, even when $\beta = 10^{-4}$. From Fig. 5 one can find that the curves are different from those of $\beta = 0$. Hence if one wants to study the crack problem of piezoelectric ceramic accurately, he should adopt non-linear boundary conditions as in equation (3).
3. From the calculated curves, it can be found that the positive electric field always has the tendency to open the crack, while the negative electric field has the tendency to close the crack. And when the crack is closed, the field will degenerate into a homogenous field and lose the singularity at the crack tip, which can be used to explain why the positive electric field promotes the crack growth while the negative electric field retards the crack growth. The same conclusion can be obtained from the elliptical cavity model. Because the tangent stress induced by D_0 is tension, the fracture toughness is anisotropic.

REFERENCE

1. V.Z. Parton, Acta Astronaut. **3** (1976) p. 671
2. W.F. Deeg, The Analysis of Dislocation, Crack, and Inclusion Problem in Piezoelectric Solids: Ph.D Dissertation. Stanford University, U.S.A. (1980)
3. R.M. Mcmeeking, Journal of Applied Mathematics and Physics, **40** (1989) p. 615
4. R.M. Mcmeeking, Int. J. Engng Sci., **28** (1990) p. 605
5. Y.E. Pak, J. of Appl. Mech., **57** (1990) p. 647
6. H. Sosa, Int. J. Solids Structures, **28** (1991) p. 491
7. H. Sosa, Int. J. Solids Structures, **29** (1992) p. 2613
8. Z. Suo, C.M. Kuo, D.M. Barnett and J.R. Willis, J. Mech. Phys. Solids, **40** (1992) p. 739
9. M.L. Dunn, Engineering Fracture Mechanics, , **48** (1994) p. 25
10. S.B. Park and C.T. Sun, Int. J. Fract., **70** (1995) p. 203
11. T.Y. Zhang and P. Tong, Int. J. Solids Structures, **33** (1996) p. 343
12. H.J. Gao, T.Y. Zhang and P. Tong, J. Mech. Phys. Solids, **45** (1997) p. 491
13. H. Sosa and N. Khutoryansky, Int. J. Solids Structures. **33** (1996) p. 3399

Key Engineering Materials Vols. 183-187 (2000) pp. 827-832
© 2000 Trans Tech Publications, Switzerland

Nano-Fractographic Estimation on the Profiles and Dimensions of Fatigue Striation

S.J. Choi[1], H. Ishii[2] and J.D. Kwon[1]

[1] Department of Mechanical Engineering, Yeungnam University,
214-1 Dae-dong, Kyongsan, Kyongbuk 712-749, Korea

[2] Department of Mechanical Engineering, Shizuoka University,
Johoku 3-5-1, Hamamatsu 432-8561, Japan

Keywords: AFM, Nano-Fractography, Stress Ratio, Striation Height, Striation Width

ABSTRACT

Instead of commonly used SEM, AFM (Atomic Force Microscope) was used to study the fatigue fracture surfaces and three-dimensional nano-level information including the height was obtained. Observation was focused on the fatigue striations obtained at various stress ratios in 2017-T351 aluminum alloy. From their three-dimensional AFM images, the widths (SWs) and the heights (SHs) were analyzed. The following results that will be helpful to understand the fatigue crack growth mechanism were obtained. (1) Coincidence of the da/dN and the SW, which is known to hold for da/dN above 10^{-4} mm/cycle, is established down to smaller da/dN of 6×10^{-5} mm/cycle. (2) Between the SH and the SW, a relation of $SH=0.0585(SW)^{1.2}$ was obtained. (3) The ratio of the striation height to its width, SH/SW, was almost constant irrespective of the stress intensity factor range ΔK or the stress ratio R. (4) Not only the SWs but also the SHs were changed linearly with the crack tip opening displacement (CTOD) when plotted on a log-log scale. From these results, the applicability of the AFM to nano-fractography is discussed.

1. INTRODUCTION

Electron micro-fractography is now well established and used as a routine process to analyze the cause of material's failure. Especially, since many failures of the engineering parts or components are by fatigue, not only qualitative but also quantitative analyses in connection with the fracture mechanics have been performed concerning the fatigue fracture surfaces [1].

Striation is a typical pattern observed on the fatigue fracture surface, and it is known that its width (or spacing) corresponds to a crack growth per one loading cycle and the stress intensity factor range can be estimated by measuring the width. Thus, many data are available now for the relationship between macroscopic crack growth rate da/dN and the striation width against the stress intensity factor range. Since opening and blunting process of a crack tip has to be operated for a formation of striation, data of the striation heights in addition to their widths are indispensable to obtain useful information that helps to understand the crack growth mechanism. Besides, it is

reported that the stress ratio can also be known from a ratio of the striation height to its width [2]. However, to get the heights from the conventional SEM fractography is not an easy work.

On the other hand, recently developed SPM (Scanning Probe Microscope), such as STM (Scanning Tunneling Microscope) and AFM (Atomic Force Microscope), is shown to be a powerful tool for nano-scale characterization and measurement of material surfaces, and the height data can also be obtained easily in the atomic level. Thus, application of SPM to the research field on mechanical behavior of materials has started [3, 4], and some studies on the development of fatigue slip bands [5, 6], nucleation and growth of corrosion pits [7], growth of SCC crack [8] and so on have been done using SPM. However, no systematic observations of the fractured surfaces using SPM has been done so far.

In the present study, fatigue fracture surfaces of 2017 aluminum alloy, where striations were dominating were observed by AFM and availability of the AFM fractography is discussed.

2. EXPERIMENTAL PROCEDURE

Fatigue crack growth tests were performed using MTS machine and CT specimens of 2017-T351 Al-alloy. Dimensions of the CT specimen were 50 mm in width, 48 mm in height and 6 mm in thickness, and the yield strength, tensile strength and elongation of the material are 275MPa, 427MPa and 0.22 respectively.

After investigating the fatigue crack growth behavior at various stress ratios (R = 0.1, 0.3, 0.5 and 0.8) in an ambient environment at a frequency of 10Hz, the fracture surfaces were sectioned and observed by AFM. For the observation, AFM-SPA 300 scanner (scanning area of 20 μm x 20 μm) coupled with SPI-3700 probe station manufactured by Seiko Electronics was used under a cyclic contact mode. The silicon tip designed for dynamic force microscope (DFM) was used as a cantilever. Observations were specially focused on the striations and their width and height were analyzed.

3. RESULTS AND DISCUSSION

Fig.1 shows relationship between fatigue crack growth rate, da/dN and stress intensity factor range, ΔK at various stress ratios R. The fatigue crack growth rate, da/dN variation with respect to the effective stress intensity factor range, ΔK_{eff} is included Fig.1. This results is approximately close to those of R=0.5 and 0.8 plotted against ΔK. Hence it is reasonable to assume that no crack closure mechanism is involved when the stress ratios are 0.5 and 0.8 respectively. The effect of crack closure on ΔK at R=0.1 and 0.3 is included in Fig.1.

The typical AFM images of fatigue fracture surface for various crack growth rates under the stress ratio, R=0.1 are shown in Fig.2. The cross sectional profile of the fatigue fracture surface along the line X-Y is shown in the right hand side of (a) in Fig.2. The striations in an area are shown in (a) of Fig.2 when the macroscopic crack growth rate, da/dN=9.1×10^{-5} mm/cycle. The finest striations are observed when minimum width and height are 40 nm and 6 nm respectively. The

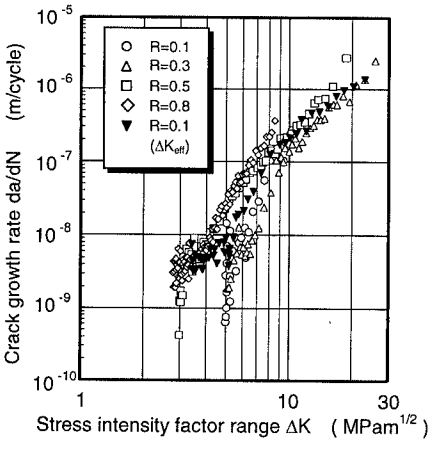


Fig.1. Relationship between stress intensity factor range and crack growth rate.

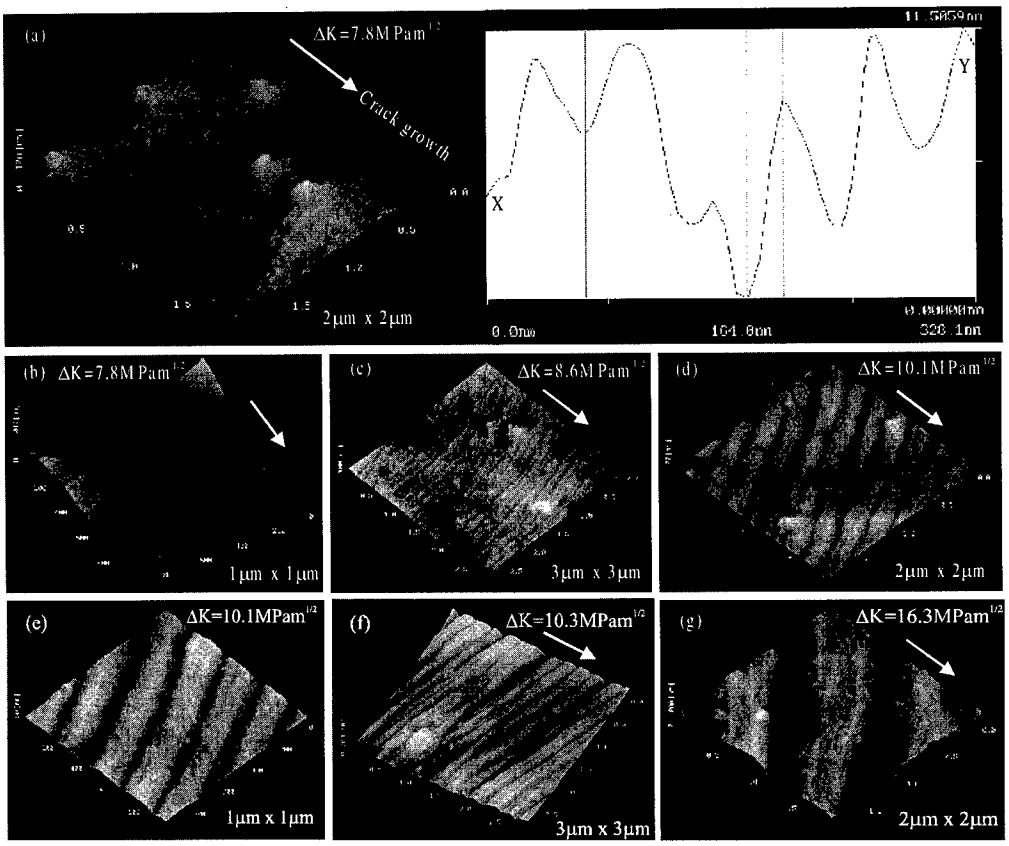


Fig.2. AFM images and cross-sectional profile along the line X-Y of fatigue fracture under stress ratio R=0.1 for 2017-T351 aluminum alloy. White arrow indicates the direction of crack growth.

calculated crack tip opening displacement (CTOD) at these areas was found to be approximately 193 nm using equation (2). Since the striation with a width smaller than 40nm is not observed, this implies that minimum CTOD required to form the striations in the employed aluminum alloy is approximately 190 nm. From this three-dimensional AFM image and cross-sectional profile along the line X-Y shown in (a) of Fig.2, it is clearly seen that all striations are approximately parallel to each other. The configurations of striations are shown in (b) to (g) in Fig.2.

Furthermore, it is shown from this image that the precipitates that were existing ahead of an advancing crack affect the formation of striation. Besides, the fact that in some area, apart a few ten μm from the finest striations, slip bands were prevailing instead of striations seems to suggest that crystallographic orientation play a critical role to the formation of fine striations. A typical AFM image of the slip bands observed in the same area is shown in (b). In this figure, secondary slips are also observed besides the well-developed slip bands with a maximum width of 500 nm and height of 100 nm. These morphologies are similar to the typical ones observed on a surface of deformed single crystals [9].

Figure (c) shows the striations with average width and height of 140 nm and 14 nm, respectively, and they were observed in the area where $da/dN=1.43\times10^{-4}$ mm/cycle.

Striations observed in the area where da/dN=2.43×10^{-4} mm/cycle are shown in figure (d) and (e). Their average width and height were 210nm and 30nm, respectively. These striations are all well aligned, and the cross-sectional profile is a typical groove observed in ductile materials.

Furthermore, the projections as well as the depressions are observed in the figure of (c) and (d). Average width and depth of the depressions are 170 nm and 30 nm and those of the projections are 140 nm and 40 nm respectively, and change in the width and the height of striation occurred at around these depressions and projections. Based on the profile and dimensions of these depressions or projections, they can be regarded as the precipitates. In figure (e), besides the fine precipitates and depressions of the width of 50nm and the height of 15nm, slip bands with the height of a few nm were observed parallel to the grooves.

From the observations mentioned above, it is clear that when the precipitate is larger than a half of the striation width, they hinder the formation of striations. Thus, the width and the height of striation are changed before and after the precipitate. When the precipitates are finer than half the width of striations they only change the cross-sectional profile of the striations locally.

In figure (f) striations observed in the area where da/dN=2.73×10^{-4} mm/cycle are shown. The average width and height were 241 nm and 60 nm, respectively. This figure shows internal cracks with depth of 100 nm along the striations. In figure (g) well-developed striations observed in the area where da/dN=1.4×10^{-3} mm/cycle are shown.

In Fig.3 and Fig.4 striation images at different stress ratios of 0.3 and 0.5 are shown, respectively. By comparing these with previously shown images at R=0.1, no effect of the stress ratio is observed on the image.

Similar AFM observations described above were made for the striations in 250 areas covering various ranges of fatigue crack growth rates and R, and thus obtained striation widths and heights were analyzed.

Fig.5 shows the relationship between the fatigue crack growth rate, da/dN and the striation widths (SW) obtained by AFM. Coincidence of the da/dN and the SW, which is known to hold for

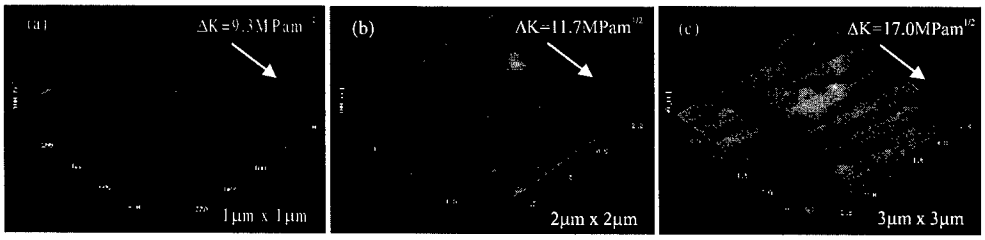


Fig.3. AFM images of fatigue fracture surface under stress ratio R=0.3 for 2017-T351 aluminum alloy. White arrow indicates the direction of crack growth.

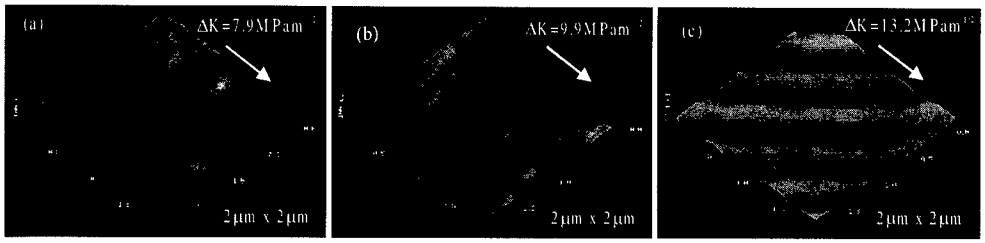


Fig.4. AFM images of fatigue fracture surface under stress ratio R=0.5 for 2017-T351 aluminum alloy. White arrow indicates the direction of crack growth.

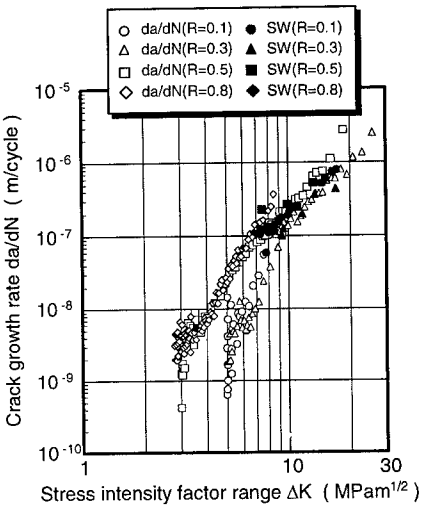


Fig.5. Relationship between stress intensity factor range and crack growth rate, or striation width.

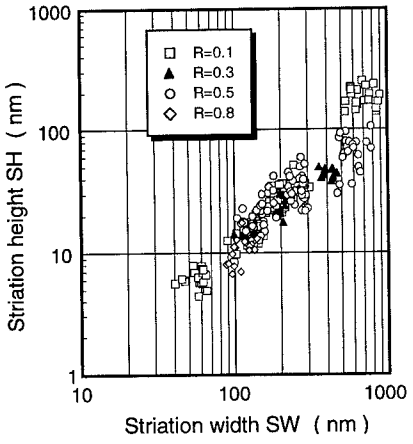


Fig.6. Relationship between striation width and striation height.

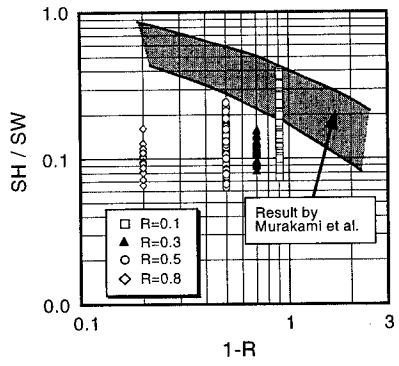


Fig.7. Relationship between stress ratio, (1-R) and ratio of striation height to striation width.

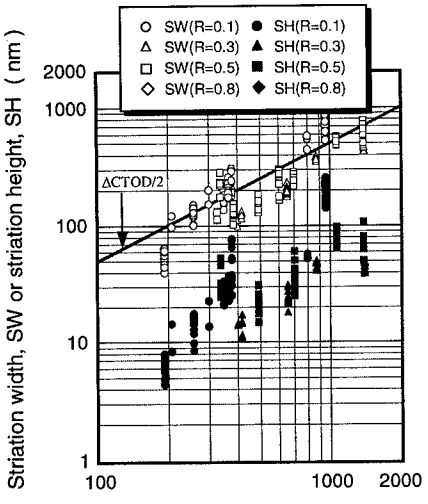


Fig.8. Relationship between crack tip opening displacement and striation width or striation height

da/dN above 10^{-4} mm/cycle, is established down to a smaller da/dN of 6×10^{-5} mm/cycle.

Although no measurement was made above the da/dN range of 10^{-3} mm/cycle, it can be expected from the extrapolation that da/dN becomes larger than the SW as ΔK increases above 18 $MPam^{1/2}$.

Fig.6 shows the relationship between the striation heights (SH) and the SW obtained from the cross-sectional profile. It is clear that in the range of SW from 40 nm to 900 nm, the SH varies linearly with the SW when they are plotted in logarithmic scale. Thus, the following relationship between the height and the width of striation is given in equation (1).

$$SH = 0.0585(SW)^{1.2} \quad (1)$$

Since all results at various stress ratios are included in this figure, the relationship between the stress ratio, (1-R) and SH/SW is re-plotted in Fig.7. Figure 7 shows a confliction against to the results obtained by Murakami et al [2]. According to their results, the ratio of SH/SW in the same material depends only on R and is constant as long as R is fixed, and the stress ratio can be estimated from fractography. Since SH and SW in the present investigation are in a sub-micrometer range while [2] are in a micrometer range, discrepancy of the effect of stress ratio may result from the difference in the measured dimensional scale. However, Further investigation is required to clarify the effect of R on the ratio of SH/SW.

Figure 8 shows the relationship between the SW or the SH and the crack tip opening displacement, CTOD. For calculating the CTOD, following equation based on the plastic blunting mechanism is used [11].

$$CTOD = (1-\nu^2)K_{Ieff}^2/2E\sigma_{ys} \quad (2)$$

Where ν is a Poisson's ratio and K_{Ieff} is an effective stress intensity factor for mode I crack. The result indicats that striation width approximately corresponds to a half of the crack tip opening displacement, which will be an important information when the striation formation mechanism is to be discussed.

3. CONCLUDING REMARKS

For the purpose of applying Atomic Force Microscopy to the fractography, striations appearing on the fatigue fracture surface of 2017 aluminum alloy were observed and the cross-sectional profile, the widths and the heights were analyzed. It is shown that many useful data in discussing the fatigue crack growth mechanism can be obtained by the AFM. Among them are the effect of precipitates on the formation of striation, the relationship between the height and the width of striation, the relationship between a ratio of the striation height to the striation width and the stress intensity factor range and so on.

REFERENCE

1. For example, "Fractography and its application" (in Japanese) Edited by R. Koterazawa (1981), Nikkan Kogyo Shinbunsha.
2. K. Furukawa, Y. Murakami, S. Nishida, Int. J. Fatigue, 20, 509 (1998).
3. D. Sarid, Oxford Series on Optical Science, "Scanning Force Microscopy" (1991) Oxford University Press.
4. S. Chiang and R. J. Wilson, "Images of Materials", Edited by D.B. Wilson, A. R. Pelton and R. Grosky, p.241 (1991) Oxford University Press.
5. T. S. Sriram, M. E. Fine and Y. W. Chung, Acta Metall. Mater., 41, 2515 (1993).
6. Y. Nakai, S. Fukuhara, K. Ohnishi, "Proc. 73rd JSME Annual Meeting', II 418 (1996).
7. H. Masuda, N. Nagashima, S. Matsuoka, Trans. JSME, A-57, 541 (1991).
8. K. Komai, K. Minoshima and T. Miyawaki, Trans. JSME, A-62, 600 (1996).
9. S. Choi, H. Ishii and K. Tohgo, APCFS '96, 683 (1996).
10. Z. S. Basinski and S.J. Basinski, Acta Metall. Mater., 33, 1307 (1985).
11. J.R. Rice, ASTM STP, 415, 247 (1967)

Key Engineering Materials Vols. 183-187 (2000) pp. 833-838
© 2000 Trans Tech Publications, Switzerland

Strength of Crack-Healed Si_3N_4/SiC Composite Ceramics

M.C. Chu[1], K. Ando[1], F. Yao[2] and S. Sato[3]

[1] Department of Energy & Safety Engineering, Yokohama National University, 79-5, Tokiwadai, Hodogaya-ku, Yokohama 240-8501, Japan

[2] Post-graduate Student, Yokohama National University

[3] R & D Center, NHK Spring Inc., 3-10 Hukuura, Kanazawa-ku Yokohama 236-0004, Japan

Keywords: Bending Strength, Ceramic Composite, Crack Healing, Healing Condition, Oxidation, Silicon Nitride, Strength Recovery

ABSTRACT

In the present work, the crack healing behavior of Si_3N_4/SiC composite ceramics with Y_2O_3 8wt% as a sintering additive and its mechanical properties were studied. A semicircular crack(average diameter was about 100μ m) was introduced in the center of specimen using Vickers hardness indenter, and then the specimens were heat treated at elevated temperature in air. The bending strength was measured at temperature ranging from room temperature to 1400 ℃. Bending strength of as-cracked specimen reduced to about 50% of that of as-received specimen. However, bending strength of cracked and healed specimen were recovered completely up to that of as-received specimen. And, most specimens tested failed from outside crack-healed zone. By the systematical investigation, it is concluded that crack healing due to oxidation results in the recovery in bending strength since pre-crack was filled with oxides, such as $Y_2Si_2O_7$, SiO_2 and amorphous oxides. The best healing condition for the specimen is 1200℃ ~ 1300℃, for 1hour in air. The cracked specimen could be healed at the condition of up to at 1400℃ that had enough bending strength

1. INTRODUCTION

Some engineering ceramics have the ability to heal a crack [1]-[7]. If this ability is used on structural components in engineering use a great gain can be anticipated in the following fields [8][9]: (1) to increase in the reliability of structural ceramic members, (2) to decrease in the machining and polishing costs of ceramic members and (3) to decrease in the maintenance costs and prolongation of the life time of ceramic members.

However, there is a large difference in the degree of healing ability of ceramics, which depends on chemical composition and sintering conditions etc. To use this healing ability in structural engineering, there are many problems to be studied. For example, (a) the effect of chemical

composition on the crack-healing ability [10][11], (b) the effect of healing conditions on the strength of the healed zone [12][13], (c) determination of the maximum crack size which can be healed [12][13], (d) knowledge of the high temperature strength of healed-zones [12][13], (e) understanding of the crack healing mechanism [5][10] and (f) assessment of the cyclic fatigue and static fatigue strengths of crack-healed ceramic member [9,14]. With respect to items (a) to (e), authors in this study have already studied systematically the several aspects of these problems.

This paper reports on the mechanical properties of crack-healed Si_3N_4/SiC composites at room and high temperature.

2.EXPERIMENT PROCEDURE

The silicon nitride powder used in this investigation has the following properties: mean particle size is 0.2 μm, the volume ratio of α-Si_3N_4 is about 95% and the rest is β-Si_3N_4. The SiC powder used has a 0.27 μm mean particle size. Si_3N_4/SiC composites were made by hot-pressing method(temperaure:1850℃, time:2h ,pressure:35MPa, atomsphere:N_2) using 8 wt% Y_2O_3 (subsequently called as SNS-Y8) as sintering additives. The materials contained 20wt% of SiC powder, respectively. The sintered material was cut into test pieces measuring 3mm x 4mm x 40mm as shown in Fig.1.

A semi-circular crack was made at the center of the tension surface of the test pieces with a Vickers indenter using a load of 19.6N. By this method, semi-circular cracks of about 100 μm in diameter were made as shown in Fig.2(a). Crack shapes were confirmed on the fracture surfaces of cracked specimen as shown in Fig.2 (b).

In other to determine the optimum healing condition, the pre-cracked specimens were heat treated in air at wide temperature range(800-1400℃) before bending testing.

To evaluate bending strength for rectangular test bar, three and four-point bending test was conducted (outer support span; 30mm, inner load span; 10mm, cross head speed; 0.5mm/min) referring to the JIS1601. Bending strength was measured from at room temperature to 1300℃ in air atmosphere. Three test specimens were used for each data point expect those of five at room temperature.

Scanning electron(Hitachi S-4100) and laser microscopy (Lasertec model 1LM21) was used to observe the morphology of crack and surface of heat-treated specimens. X-ray diffraction machine(Rigaku denki RINT2000) was used to identify the phase present at the surface of a specimen heat-treated at temperature ranging from 800℃ to 1400℃ in air.

3. RESULTS

3.1 Effect of healing condition on bending strength

Fig.3(a) shows the effect of healing condition on bending strength at room temperature of

SNS-Y8. The bending strength of smooth, as-cracked and crack-healed sample were shown in the Fig3(a) as a symbol of ○, △ and ▲ respectively. In the figure,※ symbol shows the sample which was failed outside crack healed zone as shown in Fig.4(b). Bending strength of smooth sample is about 750MPa. And by cracking, the bending strength of the sample was largely reduced to about 350MPa. However, by the crack healing, most samples recovered their bending strength. The most samples which were healed from 900℃,5h to 1400℃,1h, recovered their bending strength completely and most sample failed outside the crack-healed zone. Fig.3(b) shows the effect of healing condition on bending strength at 1300℃. The samples which were healed at 1200℃,1h and 1300℃,1h failed outside crack healed zone. However, the samples that were healed below 1100 ℃ failed from pre-crack zone as shown in Fig.4(a). In both Fig.3(a) and Fig.3(b), the all samples which were healed at 1400℃ failed outside crack healed zone. However, they showed a little lower bending strength. From these facts, it can be concluded that the best healing condition is 1200℃,1h and 1300℃,1h in air.

3.2 Observation of crack-healing behavior

To investigate crack-healing behavior, we observed directly crack-healing process of SNS-Y8 using a laser microscope. The result is shown in Fig.5. Increasing rate of temperature is 10 ℃/min, which is the same condition when a specimen is crack-healed. Fig.5(a) shows a pre-crack at room temperature in air, and the crack size(2C) is about 200 μm. Reached at 1100 ℃(see Fig.5(b)), the crack could be found the crack, which means that it is not healed completely yet. When temperature is increased and reached at 1300 ℃, we could observe only the crack"①" which became shorter than that of room temperature(see Fig5(c)). Finally, after the specimen being exposed in air at 1300 ℃ for 1h, the crack could not be found, and as mentioned section 3.1 and 3.4, the specimen had a sufficient strength both room and elevated temperature. By SEM observation and X-ray diffraction study, it could be found that new materials were produced on surface of the heat- treated specimen. The materials were consisted of crystalline phases of SiO_2, $Y_2Si_2O_7$ and amorphous oxides. From these results, it would be considered that the crack healing due to oxidation results in the recovery in bending strength since pre-crack was filled in oxides, such as SiO_2, $Y_2Si_2O_7$ and amorphous oxides.

3.3 Effect of crack size on bending strength

The dependence of the strength on the crack dimensions is shown in Fig. 6. Crack size was controlled to about 110 μm and 180 μm by controlling Vickers load. In the figure, ※ symbol shows that specimen failed at the outside of the crack-healed zone. The strength of the specimens without any healing decreased rapidly. The strength of specimens with pre-crack of 2C≅110μm reached to about 50% of those for the smooth specimens. In the presence of a 2C≅180μm crack, the bending strength was 40% of smooth specimen strength. By crack-healing treatment, the strength of the specimens including up to 180 μm recovered at room temperature and they showed the same values of the smooth specimens, and all the specimens failed at the outside of the crack-healed

zone.

3.4 High temperature Strength of Crack- Healed Specimen

Temperature dependence of bending strength of crack-healed specimen was tested. Test results are shown in Fig.7. The bending strength of Si_3N_4/SiC composite with Y_2O_3 and Al_2O_3 as sintering additives is almost same up to 1000℃ and the value is about 800MPa. Above 1000℃, the bending strength decreased with increasing the test temperature, dramatically. On the contrary, the bending strength of crack-healed SNS-Y8 material is almost constant up to 1400℃. Moreover, most of the specimens failed outside the crack-healed zone up to 1300℃ similar to the crack path in Fig.4(b).

4.CONCLUSIONS

(1) The sample showed very interesting crack-healing behavior and the best healing condition was found to be in the temperature range from 1200℃ to 1300℃, for 1h, in air.

(2) The crack healing due to oxidation results in the recovery of bending strength since pre-crack was filled in oxides, such as SiO_2, $Y_2Si_2O_7$ and amorphous oxides.

(3) By crack-healing treatment, the strength of the pre-cracked specimens including up to 180 μm crack at room temperature had been recovered and showed the same values as the smooth specimens

(4) The strength of the crack-healed samples were recovered completely by the healing process and most samples failed outside the crack-healed zone when they were subjected to monotonic loading at temperatures up to 1300℃.

REFERENCES

1. J.J.Petrovic and L.A.Jacobson, J. Am. Ceram. Soc., **59**(1-2) (1976) p.34
2. T.K.Gupta, J. Am. Ceram. Soc., **59**(5-6) (1976) p.259
3.S.R.Choi and V.Tikare, Scripta Metallurgica et Materialia, **26**(1992) p.1263
4.J.E.Moffatt, W.J.Plumbridge and R.Hermann, British Ceramic Transactions, **95**-1(1996) p.23
5.M.C.Chu, S.Sato, Y.Kobayashi and K.Ando, Fatigue Fract. Engng. Mater. Struct., **18**-9(1995) p.1019
6. M.C.Chu, S.Sato, Y.Kobayashi and K.Ando, Jpn. Soc. Mech. Engng, **60**-580(1994) p.2829
7. K.Ando, T.Ikeda, S.Sato, F.Yao and Y.Kobayashi, Fatigue Fract. Engng. Mater. Struct., **21**(1998)p.119
8. K.Ando, S.Sato, Y.Kobayashi and M.C.Chu, Fracture From Defects (ECF-12), U.K., Sheffiled, (1998) p.497
9. K.Ando, K.Tsuji, M.Ariga and S.Sato, J. Soc. Mater. Sci., Jpn., **48-10** (1999)p.1173
10. K.Ando, M.C.Chu, S.Sato, F.Yao and Y.Kobayashi, Jpn. Soc. Mech. Engng, **64**-623 (1998) p.1936
11. M.C.Chu, K.Ando, T.Hirasawa, S.Sato and Y.Kobayashi, High Pressure Institute of Japan,

36-2(1998), p.82
12. K.Ando, M.C.Chu, Y.Kobayashi, F.Yao and S.Sato, Jpn. Soc. Mech.Engng, **65**-633(1999)p.1132
13. K.Ando, K.Tsuji, T.Hirasawa, Y.Kobayashi, M.C.Chu and S.Sato, J. Soc. Mater. Sci., Jpn., **48**-5(1999) p.489
14. K.Ando, M.C.Chu, F.Yao and S.Sato, Fatigue Fract. Engng. Mater. Struct., 22(1999)p.897

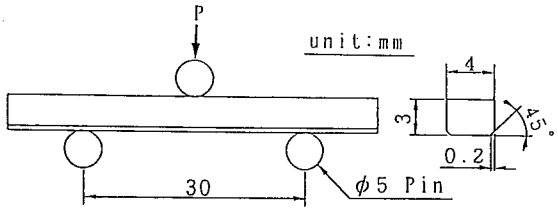
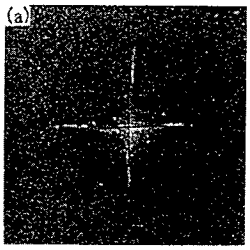


Fig.1 3-point loading system and geometry of test specimen



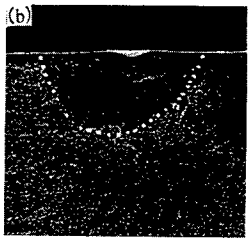
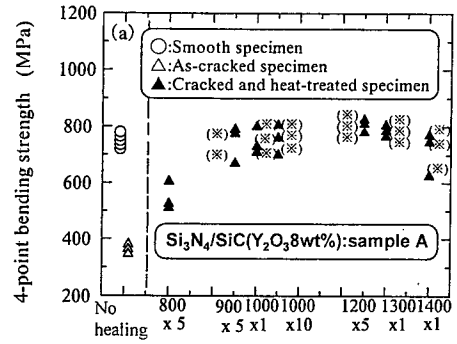


Fig.2 SEM photographs of (a)Vickers indentation and (b) crack shape.



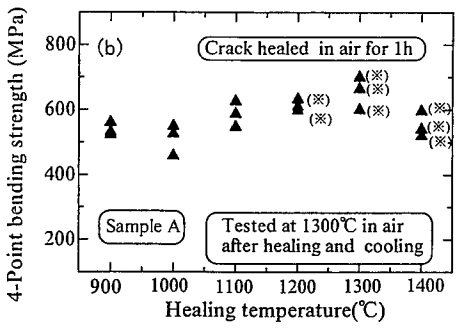
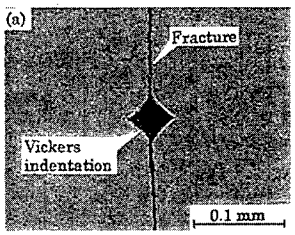


Fig.3 The relationship between crack healing condition and bending strength of $Si_3N_4/SiC(Y_2O_3 8mass\%)$(a)at room temperature and (b)at 1300 ℃.



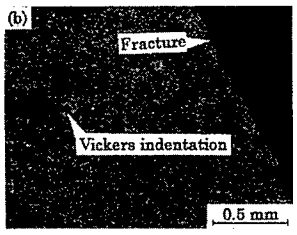


Fig.4 Fracture pattern of specimens. (a)a specimen which failure occurred (a)from the pre-crack and (b)from outside the pre-crack.

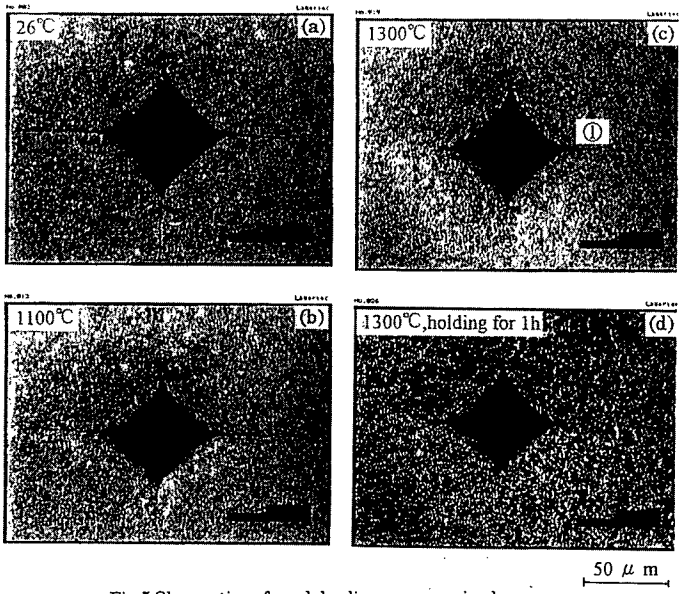


Fig.5 Observation of crack healing process using laser microscope(Si_3N_4/SiC-$Y_2O_3$8wt% composite)

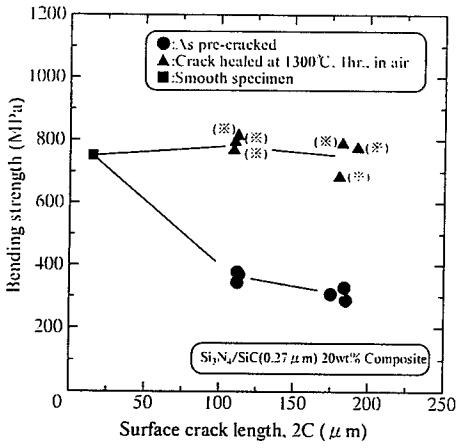


Fig. 6. Effect of heat treatment on bending strength as a function of surface crack length. (※ marked data indicates that fracture occured at outside the crack-healed zone.)

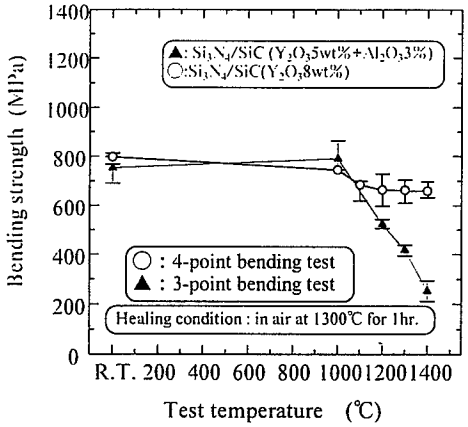


Fig.7 Effect of test temperature on the bending strength of crack healed specimen.

Key Engineering Materials Vols. 183-187 (2000) pp. 839-844
© 2000 Trans Tech Publications, Switzerland

Studies on the New Technique of Rapid Solidification and the Mechanical Behaviors of Mocrocrystalline Alloys

Zongde Liu[1], Kun Yang[1] and Shu-Lin Bai[2]

[1] Department of Power Engineering, North China Electric Power University, Beijing 102206, China P.R.

[2] Department of Mechanics and Engineering Sciences, Peking University, Beijing 100871, China P.R.

Keywords: Coat, Microcrystalline Grain, Rapid Solidification, Spraying, Strength

ABSTRACT

This paper presents a new technique for rapidly spraying coat of metal. A new device is developed and used to spray the gasified metal with a very high speed on the surface of base metal. A metallic foil gasifies in less than 0.1 millisecond while heated quickly by a very large impulse current. The gasified metal sprays and solidifies on the surface of base metal to form a thin layer with the refined grains. The alloys are LY12 aluminum, 1Cr18Ni9Ti stainless steel and H62 copper. A detailed analysis of the RLC circuit is presented. Simplified equations are derived to estimate the currents, the heating rates and the cooling rates. Based on the experimental results, a theoretical model is put forward to estimate the strength of the coat by measuring the grains sizes or the hardness.

1. INTRODUCTION

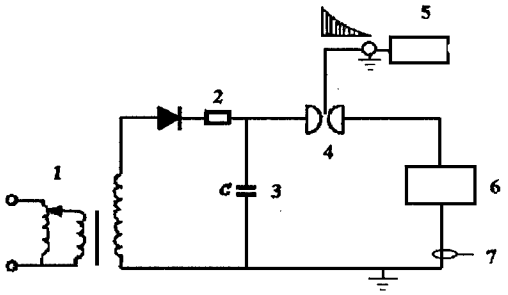
In recent years, some new surface modification technologies have been developed to improve the mechanical properties of materials. Generally, in order to acquire high quality coat with refined grains, the techniques of high energy density, such as laser radiation and electron beam, are used to heat and solidify metals rapidly. The coat also can be acquired by the high speed spraying technique. For the spraying techniques, it is very important to increase the spraying speed in order to obtain a strong bonding strength between the coat and the base material. Unfortunately, the spraying speed by conventional method, e.g. ultrasonic arc spraying method[1], is less than 1500m/s, and the bonding strength is much lower than that of the coat.

This paper presents a new technique for rapidly spraying coat of metal. Based on the calculations, the applicability of the technique to materials is explored. A detailed analysis of the experiment is then presented. The emphasis is put on the understanding of the experiments and its feasibility rather than the mechanical properties of the tested materials.

2. EXPERIMENTAL TECHNIQUE AND RESULTS

2.1 Experimental Descriptions

Newly developed high speed spraying device shown in Fig.1 is employed in the experiment. To heat the metallic foil rapidly, the foil is connected to a RLC circuit in series. A set of capacitors of 1200 μ F can be charged to a high voltage ranging from 2KV to 7KV. When the tri-electrode switch is closed, the capacitors are discharged and produce a large current to heat the metallic foil rapidly. The heating time can be varied from 100 to 600μs, and the average heating rates are 10^5 to10^7 ℃/s. The metal gas sprays on the surface of base metal with high speed and solidifies rapidly because of the heat exchange. The maximal spraying speed could be more than 3000m/s[2]. Rogowski probes looped around the lead wire are used to measure the current of the metallic foil. The tested foils are LY12 aluminum, 1Cr18Ni9Ti stainless steel and H62 copper.



1.Transformer; 2.Resistance; 3.Capacitor; 4.Switch; 5.Ignition system; 6.Spraying device; 7.Rogowski coil

Fig.1. Schematic illustration of the spraying system

2.2 Analysis

Supposing that the total resistance R in the circuit is changeless, we have

$$L\ddot{I} + R\dot{I} + \frac{I}{C} = 0 \qquad (1)$$

$$LC\ddot{V} + RC\dot{V} + V = 0 \qquad (2)$$

where, L is the self-inductance coefficient of the circuit, C is the capacitance, V is the capacitor voltage, I is the metallic foil current, and the identity $dI/dt = \dot{I}$, $dV/dt = \dot{V}$. The initial condition is simply $V(0) = V_0$, $I(0) = 0$.

From differential Eq.1 and 2, we can obtain the solution

$$V(t) = V_0\sqrt{1 + (\frac{\alpha}{\omega})^2}\cos(\omega t)\exp(-\alpha t), \quad I(t) = CV_0\omega[1 + (\frac{\alpha}{\omega})^2]\exp(-\alpha t)\sin(\omega t)$$

where, $\alpha = R/2L$, $\omega = 1/\sqrt{LC}$. The heating duration is only in hundreds microseconds, so the heat loss of the metallic foil can be neglected. Supposing that the heating duration is adiabatic, then the heating rates $\dot{T}$, and the temperature T,

on the metallic foil during joule heating is given by

$$\dot{T} = \frac{I^2 R_f}{c_0 \rho S l} \tag{3}$$

$$T(t) = \int \frac{I^2 R_f}{c_0 \rho S l} dt + T_0 \tag{4}$$

where, R_f and c_0 is the resistance and the specific heat capacity of the metallic foil respectively. ρ, S and l are the density, the cross section and the effective heating length of the metallic foil respectively. T_0 is the initial absolute temperature. The specific heat at the temperature T is given by[2]

$$c_0 = \frac{4.1868}{W}(A + BT) \tag{5}$$

where, W is molecular weight, A and B are material constants.

Supposing that the resistance value R_f is invariable, the heating rates and the temperature can be calculated by Eq. 3 and 4. The copper foil has a square cross section of 0.1 mm^2 (0.1mm×1mm), LY12 and 1Cr18Ni9Ti foils have the same square cross section of 0.2 mm^2 (0.2mm×1mm). All spraying foils have the lengths of 5mm. The currents measured and calculated for 1Cr18Ni9Ti foil at 4.2kV are shown in Fig.2. The agreement is quite good before the metallic foil gasifies. From Fig.2, it is easy to find that the currents decrease to zero rapidly as the metallic foil gasifies.

The heating rates and temperature of the metallic foil during heating are shown in Fig.3 and Fig.4, respectively. According to the curves, the temperature produced by joule heating rises rapidly during the first cycle of currents and becomes almost constant thereafter. It means that the effective heating duration is only about 0.33ms. It is easy to adjust the peak temperature of metallic foil by choosing suitable initial voltage. By measuring the speed of sprayed target[3] and by momentum theorem, the spraying speed is from 1 to 4km/s when the initial voltage is from 2 to 5kV.

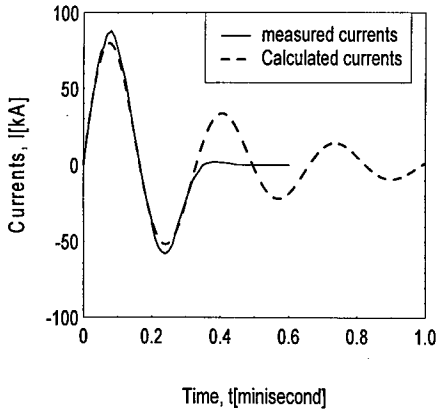


Fig.2. Currents for 1Cr18Ni9Ti foil (initial voltage of V_0=4.2kV)

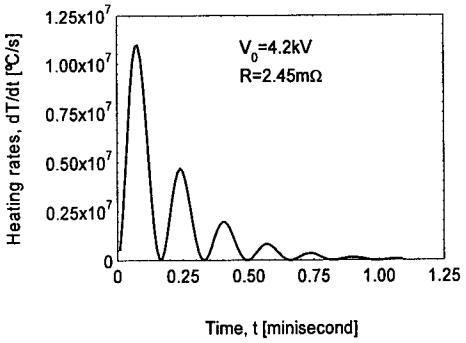


Fig.3. Heating rates of the metallic foil vs. time

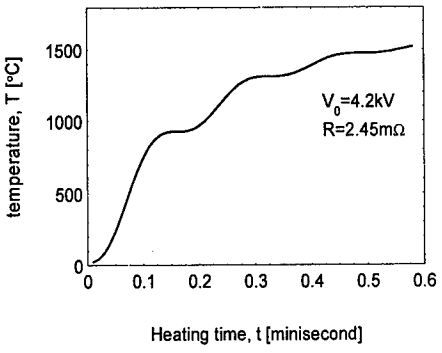


Fig.4. Temperature of the metallic foil vs. time

The thickness of the base material is from 10mm to 30mm, which is much greater than that of coating layer. Therefore, the temperature distribution in the base material can be calculated by using a one-dimensional model. Here, some assumptions are made as follows: (1) The base material is one-dimensional semi-infinite solid. (2) The heat flux rate of metallic gas on the surface of base material is constant. (3) The cooling of the base material is only realized by heat conduction. (4) The heat hidden by the phase change is neglected. (5) Thermal parameters are independent on the temperatures. From the model of Carslaw and Jaeger[3], the differential equation of heat conduction is given by

$$C_p\rho\frac{\partial T(x,t)}{\partial t}=\lambda\frac{\partial^2 T(x,t)}{\partial x^2}+g(x,t) \tag{6}$$

where, ρ is the density of base material, λ is heat conductivity, C_p is the capacity of heat. The equation of heat flow, $g(x, t)$, is written as

$$g(x,t)=q_0\delta(x)H(\tau-t) \tag{7}$$

$$\delta(x)=\begin{cases}1 & x=0\\ 0 & x\neq 0\end{cases} \tag{8}$$

$$H(\tau-t)=\begin{cases}1 & 0<t<\tau\\ 0 & t>\tau\end{cases} \tag{9}$$

where, q_0 is heat power density, τ is the heating time. For pulse heating, the heating time is close to the time of interaction between the metallic gas and the surface of base material. By integration, the solution of Eq.5 is written as follows

$$T_h(x,t)=\frac{q_0}{\lambda}\left[\sqrt{\frac{4\alpha t}{\pi}}\exp\left(-\frac{x^2}{4\alpha t}\right)-x\,erfc\left(\frac{x}{2\sqrt{\alpha t}}\right)\right]+T_0 \tag{10}$$

In the cooling duration, the equation is written as

$$T_c(x,t) = T_h(x,t) - \frac{q_0}{\lambda}\left[\sqrt{\frac{4\alpha\gamma}{\pi}}\exp(-\frac{x^2}{4\alpha\gamma}) - x\,erfc(\frac{x}{2\sqrt{\alpha\gamma}})\right] + T_0 \qquad (11)$$

where, erfc(x) is error function, erf(x)$=\frac{2}{\sqrt{\pi}}\int_0^x e^{-u^2}du$, and erfc$(x)$=1 − erf$(x)$.

Let $q_0\tau$ be constant, the temperature and cooling rate on the surface of base material calculated with Eq.10 and 11 are shown in Fig.5 and Fig.6 respectively. The shorter is the heating time τ, the higher both the peak temperature and the cooling rate. The cooling rate of coat metal is near that of the surface of base material when the thickness of coat is within hundreds μm, which has been proved by the experimental results.

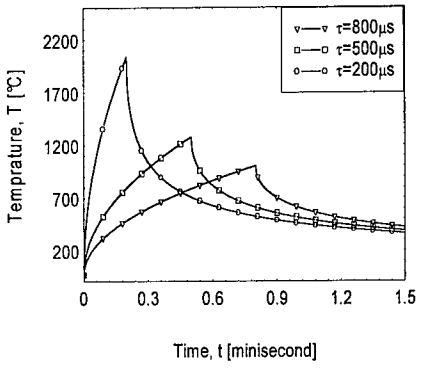


Fig.5. The temperature on the surface of base material vs. time

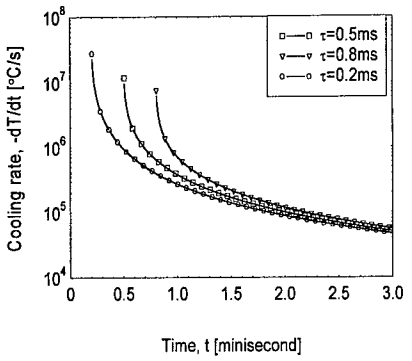


Fig.6. The cooling rate on the surface of base material vs. time

2.3 Results of 1Cr18Ni9Ti Stainless Steel

The hardness of coats is markedly higher than that of the original foils. Furthermore, the hardness of the base metal in the area near the coated surface also increased because of rapid cooling and plastic strain hardening. The thickness of coat depends mainly on the size of the foil, and increases slightly with the increasing initial voltages. The coating thickness of 1Cr18Ni9Ti is 0.2 to 0.36mm. The hardness variation of 1Cr18Ni9Ti coat and base is shown in Fig.7. The higher is the initial voltage, the greater the thickness of high hardness coat.

The grains sizes of the coat refine dramatically because of the high solidifying speed. The average grain size of 1Cr18Ni9Ti coat is about 7.5μm at 4.2kV, whereas the original size is over 26μm. The metallograph of 1Cr18Ni9Ti coat and base close to the coat is shown in Fig.8 and Fig.9. By measuring the hardness, the bonding strength between coat and base material is quite high when the initial voltage is higher than 3kV. When the melting point of coat metal is much higher than that of base metal, the bonding strength is also high.

The relationship between yield strength and grain size can be described by Hall-Petch equation

$$\sigma_s = \sigma_i + k_y D^{-1/2} \tag{12}$$

where, σ_s is the yield stress, σ_i and k_y are the material constants, D is the diameter of grains. The tensile strength of metal increases monotonously with the increasing hardness, so we can simply suppose

$$\sigma_b = f(H) = a + bH + cH^2 \tag{13}$$

where, σ_b and H are the tensile strength and the hardness of the metal respectively, a, b and c are the material constants decided by experimental results.

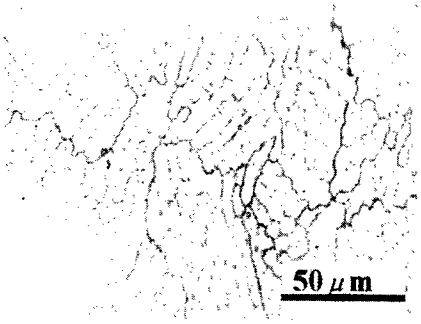


Fig.8. Metallograph of coat

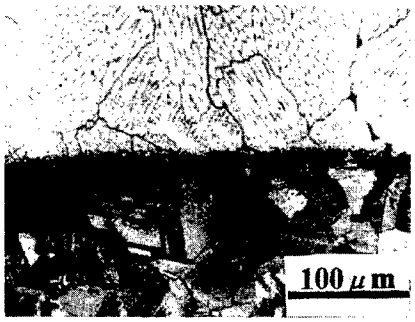


Fig.9. Metallograph of coat and base material

3. CONCLUSIONS

A new high speed spraying method was successfully developed to spray rapid solidifying coat on the surface of metal with ultrasonic speed. The technology is an economical and efficient one by which the coat obtained will have the similar properties with that obtained by laser surface treating technique. Electric explosive methods are an extremely attractive technique for accomplishing these goals. The quality of the coat depends on both the properties of RLC circuit and the shape of spraying device, so the spraying device worths being further studied.

ACKNOLEDGMENT

The Project is supported by National Natural Science Foundation of China (19702003)

REFERENCES

1 D. L. Hale and W. D. Swank, J. Thermal Spray Tech. March, **7** (1998) p.25
2 H. William and Gourdin, J. Appl. Phys., **65** (1989) p.411
3 J. L. Liu, High energy density heat treating, Mech. Indus. Press, Beijing(1997)
4 L. Y. Wang, J. China Surface Engineering (in Chinese), **42** (1999)p.19

Key Engineering Materials Vols. 183-187 (2000) pp. 845-850
© 2000 Trans Tech Publications, Switzerland

The Effects of Texture on K_{IH} in the Radial Direction in Zr-2.5%Nb Pressure Tube Materials

SungSoo Kim*, SangChul Kwon, KeeNam Choo,
YongMoo Cheong and YoungSuk Kim

Korea Atomic Energy Research Institute, PO Box 105, Yousung-Ku, Taejon 305-353, Korea

Keywords: Basal Pole Component (F), Cantilever Beam (CB) Specimen, Delayed Hydride Cracking DHC, Texture, Threshold Stress Intensity Factor (K_{IH}), Zr-2.5%Nb

ABSRACT

The texture dependence of K_{IH} in the radial direction was investigated in Zr-2.5%Nb pressure tube materials for CANDU reactor. The flat cantilever beam specimens were machined and taken at various angles to the longitudinal direction from the flattened pressure tube material and the textures of the cracking planes were varied in the cantilever specimens. The results show that the K_{IH} values decrease linearly at 250°C to the amount of an increase in the basal pole components in the cracking plane. The K_{IH} in the transverse direction specimen has the maximum basal pole component and has the minimum, 9 MPa$\sqrt{m}$. The texture dependence of K_{IH} is explained by the rule of mixture using the basal pole component (F) and a fraction of the ductile matrix (1-F). Rationale for the differences in K_{IH} between the cantilever beam (CB) and the compact tension (CT) specimens is proposed.

1. INTRODUCTION

It has been mentioned that the Zr-2.5%Nb pressure tube has a relatively higher probability of coolant leakage accident in the rolled joint since 1970's, due to the damage mechanism known as delayed hydride cracking (DHC) [1]. It is understood that the DHC crack grows with the repetition of precipitation and fracture of the hydride at the crack tip when the hydride is precipitated and the hydrogen concentration is over the terminal solid solubility at the operating and cool down temperature [2]. The DHC velocity (DHCV) and the K_{IH} in the pressure tube material are very

fundamental properties for the evaluation of pressure tube in CANDU reactor. These properties can be used to estimate whether stable crack growth starts if the size and/or depth of flaw exceed the allowable limit and can be used to predict when the length of the growing crack reaches the critical crack length (CCL).

It is known to the present that the DHCV in the longitudinal direction is about two times faster than that in the radial direction [2] and the K_{IH} values in the radial direction are at least 50% greater than that of the longitudinal [3]. It has been determined that the DHCV increases even higher and the K_{IH} becomes smaller in the sub-sized compact tension (CT) specimen when the basal pole components increase in the direction normal to the cracking plane [3-6]. It has recently been reported that the crack growth rate increases exponentially with the basal pole component in the direction normal to the cracking plane and that K_{IH} decreases linearly with the basal pole component in the Zr-2.5%Nb plate. This behavior was properly explained by the rule of mixture [7].

However, the effects of texture variation on K_{IH} in the radial direction using the cantilever beam (CB) specimen have not yet been systematically investigated in Zr-2.5%Nb pressure tube materials. In this study, the CB specimens were machined in various directions with respect to the transverse direction to vary the texture of the CB specimen in the cracking plane from the flattened pressure tube. The effects of the texture on the K_{IH} were then tested and evaluated systematically.

2. EXPERIMENTAL

The Zr-2.5%Nb pressure tube for the CANDU reactor was flattened by the reverse bend method. Then, the flat CB specimens were machined in various directions, 0, 30, 45, 60, 90° from the longitudinal direction to vary the texture of the CB specimens in the cracking plane, as shown Fig. 1. The cracking directions of all CB specimens were in the radial direction and the dimensions of the specimens were 25.4 m in length, 3.2 mm in width, and 4.2 mm in thickness.

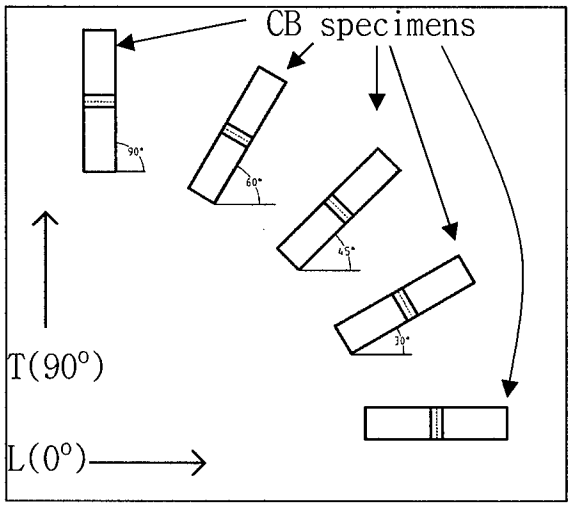


Fig. 1. Machining diagram of tilted CB specimens.

The hydriding processes were described in

Ref. [3] in detail. The stress relieving treatment was conducted at 400°C for 88 hours after hydriding. The inverse pole figures for the various CB specimens were drawn using random and diffracted intensities under the CuKα radiation and the basal pole components were calculated from the inverse pole figures [8]. A fatigue pre-crack was introduced at the crack tip of the cantilever specimen and the final K_I at the crack tip was less than 15 MPa$\sqrt{m}$, since the initial K_I was selected as 17 MPa$\sqrt{m}$, according to the testing procedure. The formula in the calculation of K_{IH} is described in the literature [9].

K_{IH} testing was carried out using a tester which uses the acoustic emission (AE) as a monitor for crack propagation and uses AE counts as a crack length to control the applied load, and the applied load was reduced by 3% at every 3 m crack extension. The criterion for K_{IH} was no AE counts for 24 hours, and the final K_{IH} was calculated using the final crack length and the load after breaking the specimen. The K_{IH} values were measured at 250°C, and all specimens were soak-treated at 307°C for 1 hour prior to loading.

3. RESULTS and DISCUSSION

The direction of hydride in the various specimens showed some differences through the whole thickness, especially at roughly half of the thickness. This phenomenon may be related to the fact that there is a neutral axis in the middle of the thickness and to the residual stress formed by the flattening process using reverse bend fixture.

The textures of the tilted CB specimen in the cracking plane are compared in Fig. 2. The basal pole and the $(10\bar{1}0)$ prism planes are concentrated in the transverse direction (90, T) and longitudinal

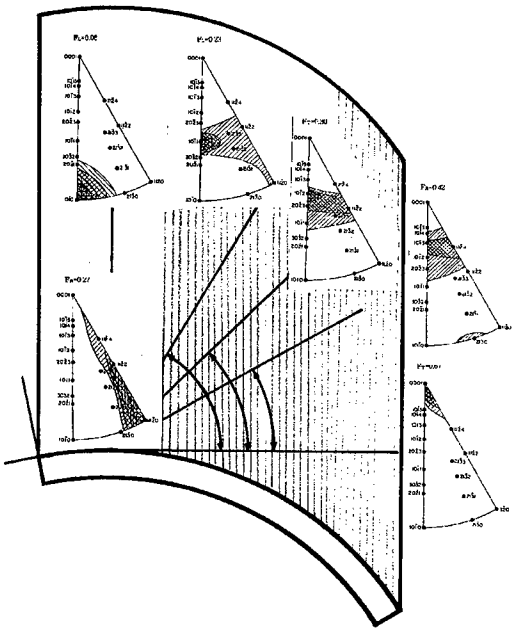


Fig. 2. Inverse pole figures for the variously textured CB specimens.

direction, respectively. The textures of the tilted CB specimens are consistent with the prediction. The basal pole components for each specimen are noted above the inverse pole figure.

The K_{IH} values at 250°C are plotted against the basal pole components in Fig. 3. The K_{IH} values decrease linearly with the increase in the basal pole component. This may be due to the increase in the resolved fraction of the basal planes with an increase in the tilt angle. Therefore, the K_{IH} at 90° showed the minimum values, as the basal pole component in the cracking plane is high and identical to the CT specimen. The longitudinal CB specimens having the basal pole component, F = 0.06, could not be cracked by DHC at all.

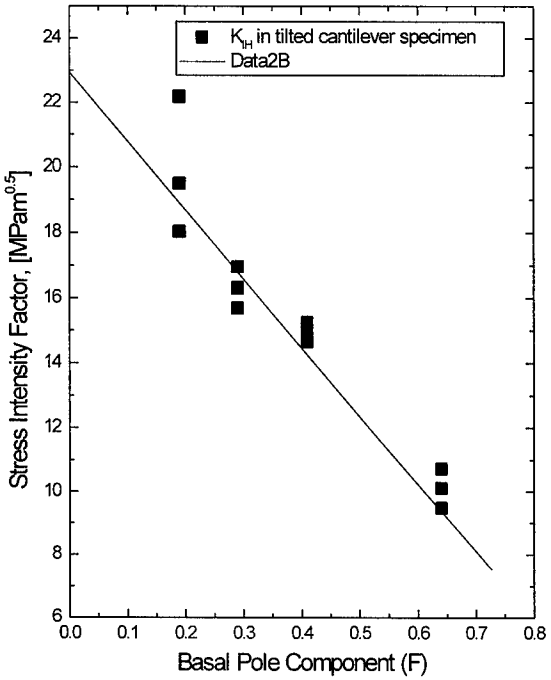


Fig. 3. K_{IH} variation with basal pole components.

The fracture surfaces in the 90° specimens (T) are very smooth since the basal planes in the cracking plane are parallel to the cracking plane, whereas other specimens are very bumpy since the basal planes in the cracking plane are declined to the cracking plane. The stress in the cracking plane becomes smaller due to the resolution of stress similar to the vector in the latter case. It seemed that the angle between the cracking surface and the machine notch increase with the tilt angle.

Because the texture variation was achieved by the rotation of the specimen direction in flattened tube material, it is very useful to compare and to separate the effects of texture on the K_{IH}. Furthermore, it is possible to minimize the microstructural variation during the texture modification. The only possible variation in the tilted CB specimens in this study would be the shape of the grains in the cracking plane.

The K_{IH} values show the linear dependency of the basal pole component in the range of F=0.19-0.64, as shown in Fig. 3. These results are consistent with results reported earlier that the K_{IH} values are lower when the basal pole components are high [5,7]. The results measured from Zircaloy-2 and

Zr-2.5%Nb are plotted together against the basal pole components in Fig. 6 [3-7, 10-11]. This shows that there are no large differences even between the different materials. It is attributed to that the major phase is α-Zr in both materials.

It is understood that the DHC crack grows through the repetition of fracture and the precipitation of hydride. The hydride is very brittle, and the Zr-alloy bearing hydrogen is considered as a composite composed of the brittle hydride and the ductile matrix. The volume fraction of the ductile matrix is described as of (1-F), and that of brittle hydride is as of the basal pole component, F, because the physical meaning of the basal pole component is the fraction of basal plane, as shown in Fig. 4.

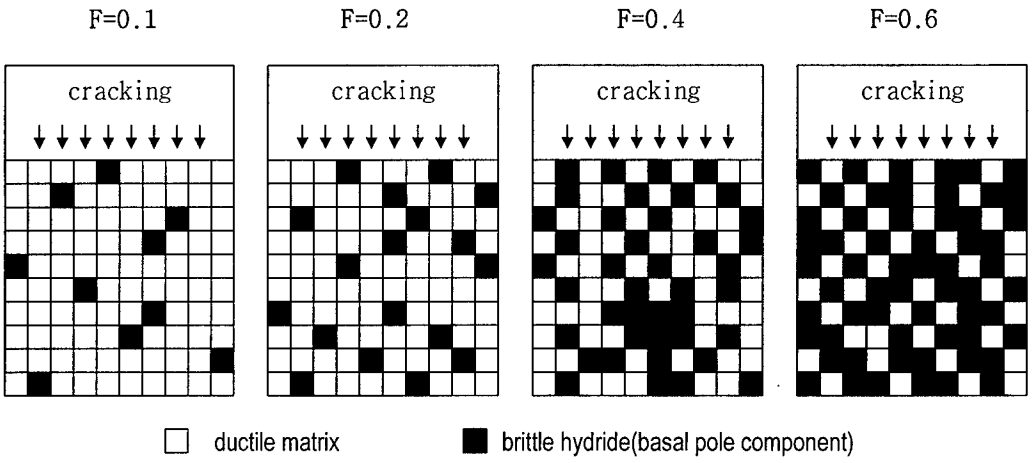


Fig. 4. Schematic illustration of the brittle hydride (F) and ductile matrix (1-F).

Therefore, the basal pole component dependency of K_{IH} can be interpreted by the rule of mixture using the volume fraction and fracture toughness of materials [7]. If the basal pole component is the volume fraction and the remaining volume is the volume fraction of the ductile matrix, the K_{IH} may be expressed by the following equation (1)

$$K_{IH} = F \times K_{IC\ of\ Zr\text{-}hydride} + (1\text{-}F) \times K_{IC\ of\ hydrided\ matrix} \qquad (1)$$

where, $K_{IC\ of\ Zr\text{-}hydride}$ is the fracture toughness which is reported as K_I = 13 MPa$\sqrt{m}$, and $K_{IC\ of\ hydrided\ matrix}$ is the fracture toughness of ductile matrix containing hydrogen. The fracture toughness is not considered as the dynamic, but the static fracture toughness.

The first term in equation (1) describes the quantity of the brittle hydride and the second term describes the quantity of the ductile matrix containing hydride. The dependence of the basal pole

component is evident that the K_{IH} decreases with an increase in the basal pole components. The K_{IH} is the criterion for crack initiation of DHC and there should be a certain bound for K_{IH} dependent on materials. Since the most important application of K_{IH} would be the flaw assessment of the materials of the components in the operating plant, the lower bound values may have a potential for the conservative operation of the plant [7].

4. CONCLUSIONS

The K_{IH} in the radial direction decreases linearly with an increase in the basal pole component in the cracking plane, and this is consistent with the results reported earlier. The texture dependency of K_{IH} in Zr-2.5%Nb CANDU pressure tube material is explained properly by the rule of mixture. This requires using the basal pole component as the volume fraction of brittle matter and the remaining volume, (1-F), as a ductile matrix containing hydrogen. A model is proposed to predict and to interpret K_{IH} behavior to reflect the effect of texture on K_{IH}.

Acknowledgements

This work has been carried out in the CANDU Pressure Tube Materials project as a part of the Nuclear R&D program funded by the Ministry of Science and Technology in Korea. The authors would like to acknowledge those workers in building #375 in AECL-CRL for their help.

REFERENCES

1. C. E. Coleman, and J. F. R. Ambler, Reviews on Coatings and Corrosion III (1979), AECL-6250.
2. S. Sagat, C. E. Coleman, M. Griffiths, and B. J. S. Wilkins, ASTM STP 1245(1994), p. 35.
3. Sung Soo Kim and Young Suk Kim, J. Nuclear Materials, to be published
4. C. E. Coleman, S. Sagat, and K. F. Amouzouvi, AECL Report AECL-9524 (1987).
5. C. E. Coleman, B. A. Cheadle, C. D. Cann, and J. R. Theaker, ASTM STP 1295 (1996), p. 884.
6. C. E. Coleman, Zirconium in the Nuclear Industry, ASTM STP 754 (1982), p. 393.
7. S. S. Kim, S. C. Kwon, and Y. S. Kim, J. Nuclear Materials Vol. 273 (1999), p. 52.
8. J. E. Winegar, Measurement of Crystallographic Texture at Chalk River Nuclear Laboratories, AECL-5626 (1977).
9. S. Sagat, J. F. R. Ambler and C. E. Coleman, Application of Acoustic Emission to Hydride Cracking, AECL report AECL-9254 (1987).
10. H. Huang, and W. J. Mills, Metal. Transactions, 22A (1991), p. 2149.
11. W. J. Mills, and F. H. Huang, Eng. Frac. Mech. 39(1991), p. 241.

Key Engineering Materials Vols. 183-187 (2000) pp. 851-856
© 2000 Trans Tech Publications, Switzerland

Influence of Grain Boundary Characteristics on Cavitation Behavior in P/M7475

T. Hirata, S. Tanabe, M. Kohzu and K. Higashi

Department of Metallurgy and Materials Science, Osaka Prefecture University,
1-1 Gakuen-cho, Sakai 599-8531, Japan

Keywords: Cavitation, Dynamic Recrystallization, Grain Boundary Characteristics, Grain Boundary Triple Junction, High-Strain-Rate-Superplasticity

ABSTRACT

7475 aluminum alloy processed by powder metallurgy (P/M7475) shows high-strain-rate superplasticity (strain rate $>10^{-2}$ s^{-1}). In superplastic deformation the fracture is generally associated with the cavitation and the superplastic elongation strongly depends on the level of internal cavitation during superplastic flow. Cavitation is caused by stress concentration. It is common knowledge that the dominant deformation mechanism during superplastic deformation is grain boundary sliding (GBS). GBS always involves stress concentration at grain boundary triple junction. From the microstructural point of view, grain boundary characteristics may affect the cavitation. However, the influence of grain boundary characteristics on cavitation has not been clarified yet. In this study, cavitation attributed to grain boundary characteristics was investigated.

The materials used for this study were P/M7475 aluminum alloys, quasi-single phase materials. Stress concentrations are often caused at triple junction of boundaries or around the large second particles during grain boundary sliding for quasi-single phase materials. Unless the stress is accommodated during deformation, extensive cavitation must occur and result in early failure. Stress accommodation at triple junctions during superplastic deformation may play an important role in determining superplastic elongation and may be influenced on grain boundary characteristics. Grain boundary characteristics were inspected by orientation imaging microscopy (OIM). In the specimen consisted of low angle boundary, microstructure was evolved by the dynamic recrystallization. The ratio of random boundary increased with strain. This microstructural evolution may influence on stress accommodation and cavitation at triple junction during superplastic deformation.

1. INTRODUCTION

Superplasticity is no longer a subject of academic curiosity, and the process has found applications in forming operations for structural components. Recently, research into superplasticity attained in the relative high strain rates over $10^{-2}s^{-1}$ has developed substantially in the alloys produced by powder metallurgy [1,2]. The strain rates over $10^{-2}s^{-1}$ is close to the commercial hot working rates, so that the superplastic forming is available for the commercial needs. From a commercial point of view, cavities are very important because they are likely to influence on post-forming properties of the alloys and to limit the range of applications of superplastically formed parts. Therefore the studies of cavitation behavior in superplastic flow have been reported a lot [3-5]. It is well established that cavitation can occur in a wide range of materials during superplastic

tensile flow. There is evidence that cavities are most likely to nucleate at grain boundary triple points in quasi-single phase materials because of grain boundary sliding (GBS) during superplastic flow. GBS involves stress concentration at grain boundary triple junction. From the microstructural point of view, grain boundary characteristics may influence on the cavitation. The microstructural evolution caused by the dynamic recrystallization in P/M7475 also effect cavitation behavior. However, the influence of grain boundary characteristics on cavitation in high-strain-rate superplastic materials has not been clarified yet. In this study, cavitation behavior attributed to grain boundary characteristics was investigated in P/M7475.

2. EXPERIMENTS

P/M7475 (Al-5.4Zn-2.1Mg-1.5Cu-0.2Cr-0.7Zr) was processed by rapid solidification processing (RSP) technology. P/M7475 was received in a sheet with a thickness of 1.5 mm with the thermomechanical treatment. The sheet materials were machined into flat tensile samples parallel to the rolling direction with the length of 16 mm and the width of 8 mm.

The tensile tests were performed on an Instron-type testing machine controlled by a computer. This machine can be performed constant strain rate test. The constant strain rate tests were carried out at a strain rate of 10^{-1} s^{-1} where the maximum elongation was obtained (Fig.1) and stopped at any strains.

Microstructural evolution in P/M7475 was investigated to examine the variation in grain boundary characteristics by the orientation imaging microscopy (OIM). OIM is a completely automated system for making spatially specific orientation measurements based on automatic analysis of electron backscatter Kikuchi diffraction patterns [6]. Grain boundary characteristics were investigated for many grains (about 400 grains).

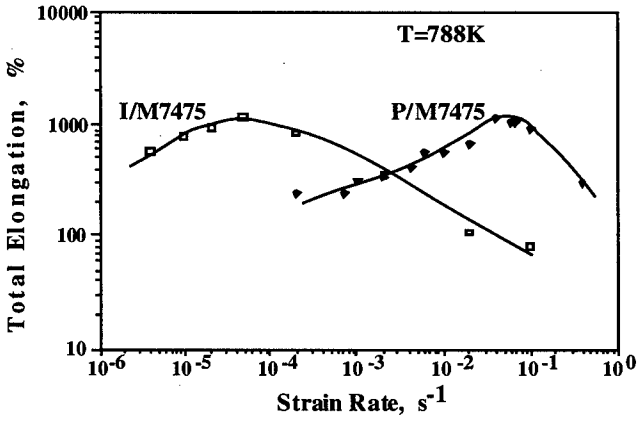


Fig.1 The dependence of strain rate on total elongation.

Deformed specimens at any strains for metallography were polished and then cleaned ultrasonically. Cavitation behavior was observed by the scanning electron microscopy (SEM) and the opticalmicroscope.

3. RESULTS

3.1 Initial Microstructure

The initial microstructure in P/M7475 is shown in Fig.2. P/M7475 is not recrystallized structure in which very small Al_3Zr particles are uniformly distributed and prevented from recrystallization before deformation. In conventional superplastic materials consisted of quasi-single phase, the cavities were observed to have nucleated at the triple junction of the grain boundaries and the intermetallic phase/matrix interfaces. The presence of the particles at the grain boundary was attributed to the limited ability of those phases to contribute to the accommodation of grain boundary sliding. The level of cavitation at a given strain was found to increase, and the corresponding elongation to failure decrease, as the size of the intermetallic particles was increased. In P/M7475, Very small Al_3Zr particles coherent to matrix is distributed. Therefore these particles at the grain boundary may have little influence on cavitation. The size of Al_3Zr particles also may effect microstructure before and during deformation.

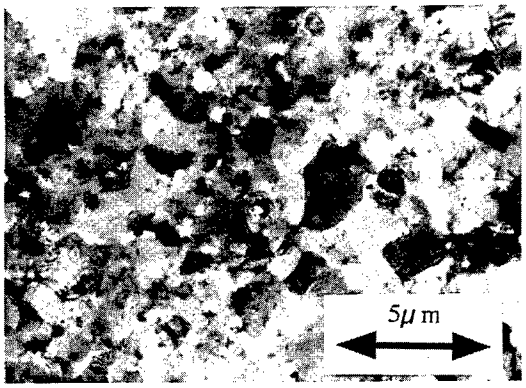


Fig.2 Initial microstructure in P/M7475.

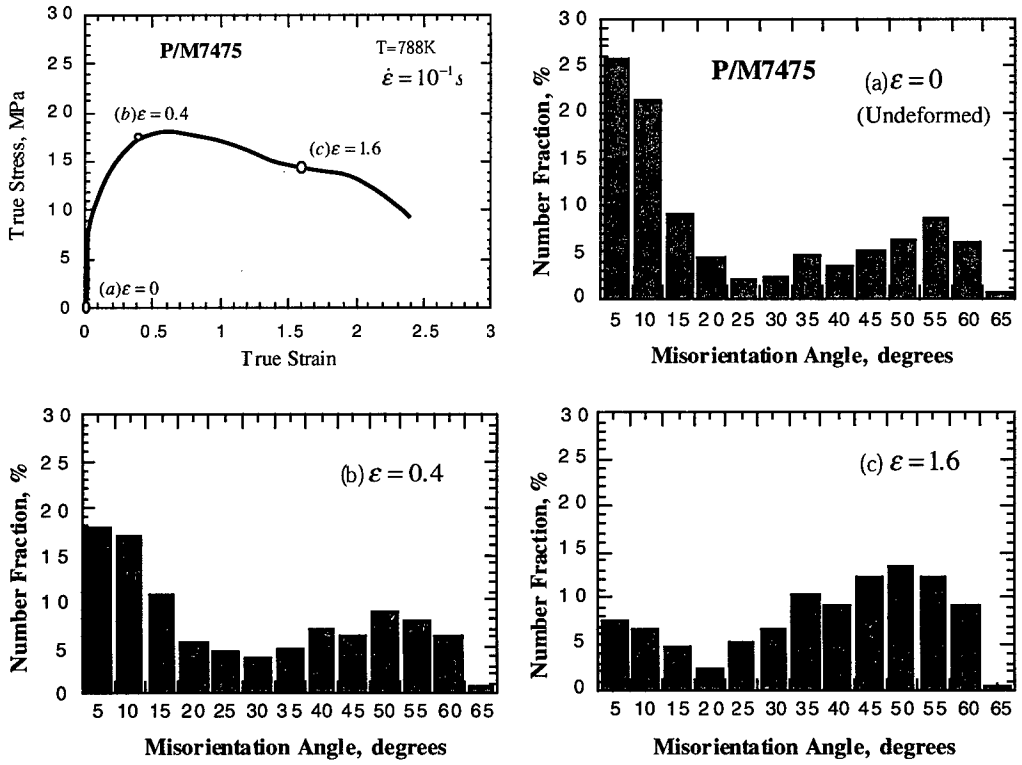


Fig.3 distribution of misorientation angle at grain boundary at various strains shown in the stress strain curve.

2. Microstructural Evolution

The microstructure in P/M7475 is evolved into fine grains by continuous dynamic recrystallization during hot deformation. OIM analysis were performed on the samples deformed to different strains. Microstructural evolution in P/M7475 is shown in Fig.3 and Table 1. The distribution of misorientation angle at various strains (a,b and c) shown in the stress-strain curves is shown in Fig.3 and the variation in the grain boundary characteristics is shown in Table 1. The microstructure is consisted of almost low angle subgrains before hot deformation. However the microstructure is progressively changed into higher angle grains and random grains during deformation. The similar result has been reported in the dynamically recrystallized aluminum alloys [7,8]. This microstructural evolution in P/M7475 may influence on the stress accommodation and cavitation at triple junction during superplastic deformation.

Table 1 The variation of grain boundary characteristics with strain in P/M7475.

True Strain	low angle boundary (%)	coincidence boundary (%)	random boundary (%)
0	56.4	7.2	36.4
0.4	45.5	8.6	45.9
1.6	19.0	10.6	70.4

3.3 Cavitation Behavior

Optical photomicrographs showing cavities in P/M7475 are presented in Fig.4. Cavities can be clearly observed even when the sample was deformed to 49% (true strain of 0.4) elongation, and the shape of cavities is maintained an approximately spherical. Large amounts of cavities are existed at a true strain of 1.6 (Fig.4(c)). Cavities were found to be larger and slightly elongated in the direction of straining. SEM micrograph of cavitation behavior at a true strain of 1.6 in P/M7475 is illustrated in Fig.5.

4. DISCUSSION

It has been reported that there is a strong interrelationship between the occurrence of cavitation, the microstructure of the superplastic material and conditions under which it is deformed [3-5]. Cavitation is caused by the stress concentration. Therefore the high flow stress associated with the large grain size, the low temperature and the high strain rate reduces the critical size of cavity, making the nucleation event easier. In order to obtain the large elongation, the stress concentration must be relaxed.

In P/M7475, the dominant deformation mechanism is dislocation creep at an initial stage of deformation [9]. It is well established that cavitation can occur at the second large particles when the dominant deformation mechanism is dislocation creep. However the second particles are very small, so that cavitation may be not influenced on the second particles in P/M7475. Therefore it is suggested that the amount of cavities be very small.

The dominant deformation mechanism in P/M7475 is changed into grain boundary sliding as misorientation angle at grain boundary is progressively changed into high angle [9]. Grain boundary sliding involves the stress concentration at grain boundary triple junction. Cavitation is also influenced on grain boundary connectivity at triple junctions. It has been reported that cavities preferably nucleate at triple junction where two or more random grain boundaries are connected [5]. It may be considered that the cavity growth is attributed to the result that the ratio of high angle boundary to total boundaries increases gradually in P/M7475.

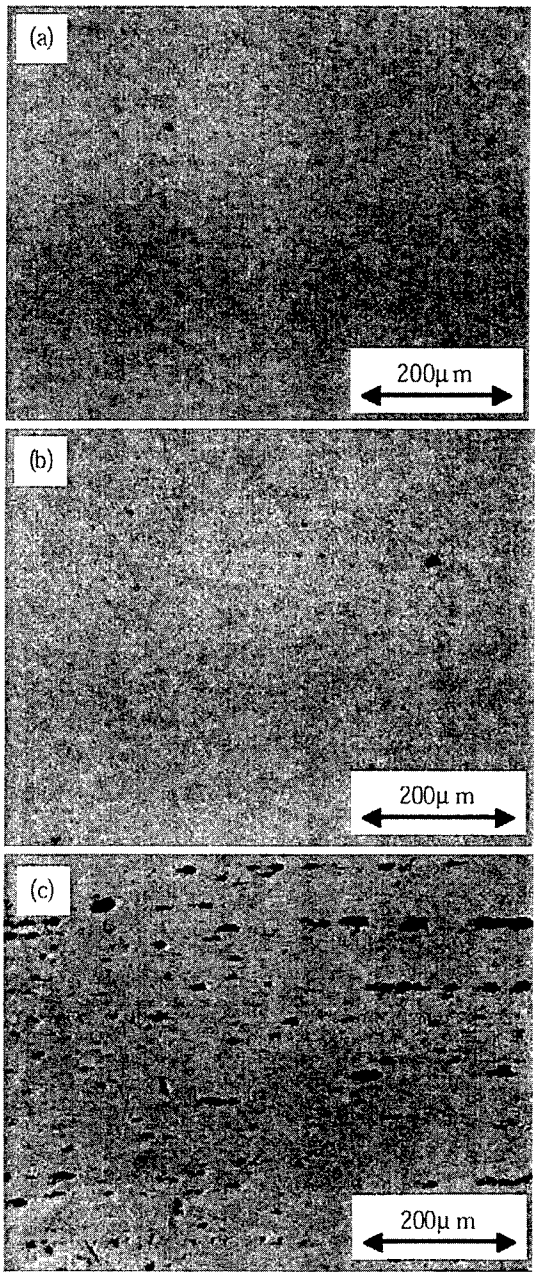


Fig.4 Photomicrographs showing cavitation behavior in P/M7475 at strains of (a)0.4 (b)0.8 and (c)1.6. The stress axis is horizontal.

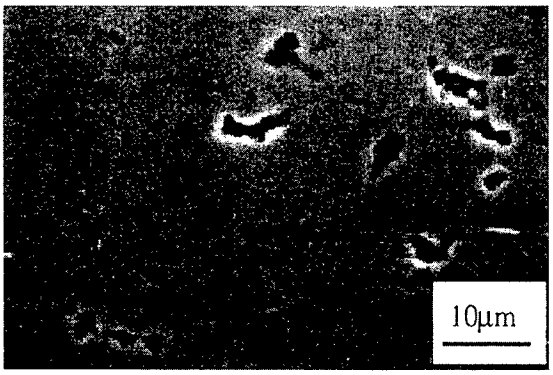


Fig.5 SEM micrograph of P/M7475 at a strain of 1.6. The stress axis is horizontal.

5. CONCLUSIONS

The microstructure in P/M7475 was not recrystallized structure before deformation. However the microstructure was changed during deformation; that is, the misorientation angle at grain boundary was gradually changed into high angle. This result may be considered to influence on the cavitation at triple junction of grain boundaries and the stress accommodation mechanism in P/M7475. The high ratio of high angle boundaries is considered to influence on cavitation in P/M7475.

REFERENCES

1. K. Matsuki, G. Stanick, H. Natagawa and M.Tokizawa, Z. Metal. **79** (1988) p.231

2. K.Higashi, S Tanimura and T. Ito, in M. J. Mayo, M. Kobayashi and J. Wadsworth (Eds.), materials Research Society Symposium Proceedings, **196** (1990) p.385

3. N. Ridley and Z. C. Wang, Materials Science Forum, **233-234** (1997) p.63

4. M. C. Pandey, J. Wadsworth and A. K. Mukherjee, Mat. Sci. Eng. **78** (1986) p.115

5. S. Kobayashi, T. Yoshimura, S. Tsurekawa and T. Watanabe, Materials Science Forum, **304-306** (1999) p.591

6. S. I. Wright, J. Computer-Assisted Microscopy. **5** (1993) p.207

7. K.Matsuki, T. Iwaki, M. Tokizawa and Y. Murakani, Mater. Sci. Tech. **7** (1991) p.513

8. T. R. McNelley, M. E. McMahon and S. J. Hales, Scr. Mater. **36** (1997) p.369

9. T. Hirata, T. Mukai, N. Saito, M. Kohzu, S. Tanabe and K.Higashi, Materials Sci. Forum, **304-306** (1999) p.333

Key Engineering Materials Vols. 183-187 (2000) pp. 857-862
© 2000 Trans Tech Publications, Switzerland

The Effects of Confining Compression on Fracture Coalesence in Rock-like Material

Robina H.C. Wong[1], P. Lin[1], K.T. Chau[1] and C.A. Tang[2]

[1] Department of Civil and Structural Engineering, The Hong Kong Polytechnic University, Hung Hom, Kowloon, Hong Kong, China P.R.

[2] Center for Rockbursts & Induced Seismicity Research, Northeastern University, Shenyang 110006, China P.R.

Keywords: First and Second Crack Coalesence, Peak Strength, Three Flaws

ABSTRACT

This paper primarily studies the effects of confining pressure on the fracture coalescence using modelling rock-like material containing three flaws (cracks). The pre-existing flaw angle α, bridge angle β (angle between two flaws), frictional coefficient μ along flaw surface and the confining pressure were varied. The flaw length and bridge length were fixed. In addition, the failure behavior has been simulated numerically by using the Rock Failure Process Analysis ($RFPA^{2D}$) code to clarify our experimental studies. Based on our experimental observation and numerical simulations, three effects were observed under biaxial compression loading. (1) The growth of tensile crack decreases with the increase of confining pressure. (2) With the increase of confining pressure, mixed mode coalescence (tensile + shear) is dominant, that is shear and tensile crack appear simultaneously within the bridge area. (3) Second coalescence is observed. This second coalescence occurs after the peak strength and after the appearance of the first coalescence. The second coalescence is primarily dominated by the mixed mode coalescence. This phenomenon was not observed under the uniaxial compression test of three-flaw specimens. For effect of confining pressure on peak strength, it is found that peak strength increases with the applied confining pressure. Furthermore, the prediction by the crack model of Ashby and Hallam (1986) agrees with our experimental results only for the case of low confining pressure. For the high confining pressure, Ashby and Hallam's (1986) crack mode should be modified because shear crack was also induced between the bridge area (not just tensile cracks as assumed by Ashby and Hallam, 1986). The numerical simulation using $RFPA^{2D}$ basically coincides with the experimental results for both case of low and high confining pressure.

1. Introduction

Fractures in rocks are normally of finite length, rock failure under compression is believed to be caused by the growth of micro-cracks from the tips of pre-existing fractures through the intact area and by coalescence between the neighboring fractures. This kind of failure is commonly encountered in rock engineering projects during the process of excavation in jointed rock mass. Many extensive researches have been done to investigate crack initiation, propagation , interaction and coalescence under uniaxial compression [1-12]. But in general the failures of in-situ rock occur under multi-axial compressive stresses. For example, underground excavations, high cut slopes and open pit mining are typical examples. The failure pattern, the growth of crack and the strength of rock is expected to be affected by the confining stresses. However, only a few studies investigate

crack coalescence under confining stress [5,6 &13], and these studies focused on the solids containing two or many flaws. None of study investigates the coalescence between three flaws.

This study makes effort to investigate the experimentally and numerically basic modes of coalescence of specimens containing three flaws with different initial flaw arrangement under biaxial compression. In this study, four samples with exactly the same parameters have been created for testing each initial setting. Total 128 specimens with different α, β and μ are made for this study. Fig 1 shows the geometric setting of the specimens. Motivated by our experimental studies, a series of numerical simulation were done by applying the RFPA^{2D} code [14]. For the peak strength study, theoretical model of Ashby and his co-authors [5,6] is employed to compare with our experimental results.

2. Experiment and Simulation Procedure

2.1 Preparation of Specimen and Testing System

The experimental material in this study is the same as adopted by Wong and Chau [10] using barium sulphate, sand, water and plaster with the mixing weight of 2:4:1.15:1. The uniaxial compression stress 'σ_c', the Young's modulus 'E_o', Poisson's ratio ν and fracture toughness 'K_{IC}' of the modeling material are 2.3MPa, 0.5GPa, 0.20 and 0.5MPam$^{1/2}$, respectively. The frictional coefficient of flaw μ is 0.6 and 0.7. The specimens used in this study are 60mm×120mm×25mm. In Fig.1, the symbols ①, ② and ③ represent three pre-existing flaws respectively. The inclination of flaw angle α is 45° and 65°. The rock bridge angle β between flaw ① and ③ varies from 75° to 120° with 15° increments, while the bridge angle between flaw ① and② is fixed at 45°.

The main component of test system is biaxial loading machine as shown in Fig.2. The vertical displacement was measured by using a LVDT transducer attaching the loading platens. The applied forces (lateral and axial loading) were measured by using the load cells (5kN). The loading record was transferred to a data logger system. Two different confining pressures corresponding to applied loads of 0.25kN and 0.75kN were applied. The results and discussion of the experimental study will be presented in section 3.

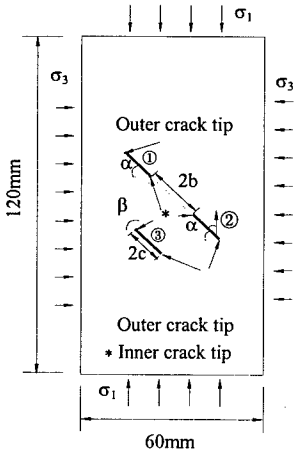


Fig.1 Geometry of three flaw specimen

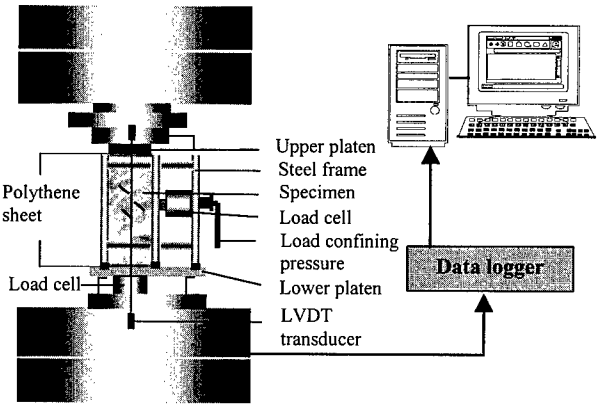


Fig.2 Schematic diagram of the biaxial compression tes

2.2 Numerical Model

In order to interpret the experimental results and obtain more insight into the crack coalescence of the rock-like specimens a series of numerical simulation and analysis were carried out. The simulation was carried out based on Rock Failure Process Analysis (RFPA^{2D}) code [14]. More

details of the numerical analysis are referred to reference [15]. The code RFPA^{2D} can be used to simulate the deformation, stress distribution, fracture initiation and propagation in heterogeneous materials. The consideration of heterogeneity for the elements is achieved to assign to the elements random strength and elastic modulus by assuming a Weibull's distribution φ (m, a_0). m is a homogeneity index which controls the shape of the distribution function relating to the degree of material heterogeneity. a_0 is the parameter related to the mean value of the material parameters for the elements, such as strength and elastic modulus. For the material has higher m values, it is more homogeneous, whereas for the lower m value, the more heterogeneous the material is. The sample used for the simulation was a two-dimensional rectangle block with a mesh of 240×120 = 28800 elements representing 120mm×60 mm sample scale. The material selected for this simulation was brittle with the ratio of σ_c/σ_t =10 (element compressive strength to tensile strength), and the friction angle of ϕ_i =30°. The results and discussion of the numerical simulations are presented in section 3.

3. Results and Discussion

Due to the page limitation, the detailed results will be given and discussed in a separate paper [15]. The discussion in this study focuses on the effect of confining pressure on the coalescence mechanism and the peak strength of three flaw specimen with frictional coefficient μ of 0.6 only. Fig. 3 shows the general failure patterns that we have observed.

3.1 Coalescence and Failure Mechanism under Confining Pressure

Based on the experimental study, two main types of crack were observed: tensile crack and shear crack. In general, it is observed that tensile crack initiates at the inner and outer crack tips (see Fig. 3 cracks A, C an E). Under low confining compression loading (0.25kN), tensile crack always initiates and propagates rapidly in the shape of a slightly-rough-curve-line and towards the other tip of the pre-existing flaw (see Fig. 4a & c). However, under the higher confining compression loading (0.75kN), the propagated crack grows slowly with a rough-curved line to the other tip of flaw (Fig.4 b & d). The surface of the crack is rough and shows some crushed plaster. It is evident that shear crack is induced on the path of the propagation of the crack. (For those crack emanating after the tensile crack is defined as secondary crack). With this observation, the first conclusion can be drawn that the growth rate of tensile crack decreases with the increase confining pressure. It is because the growth of tensile crack being suppressed by the applying confining pressure. Furthermore, the mode of coalescence between two flaws will change from tensile mode to mixed mode (tensile and shear) with the increased confining pressure (see Fig. 4 b & d). It is because when the confining pressure increases, shear stress was also being developed within the bridge. For those specimens with bridge angle 'β' equals 120°, shear crack shows dominance (see Fig, 3 crack F and Fig. 4 e). This shear coalescence does not have any relationship with confining pressure. It is due to the higher stress interaction generated between the bridge area of flaws ① and ② [12]. This shear coalescence can also be observed in specimen with the same joint configuration under the uniaxial compression loading (see Fig. 5 of [11]).

Back to Figure 3 again, the growth of crack C of flaw ① coalesces with flaw ③ when the specimen is at peak load. For his coalescence is call the first coalescence. With the loading decreasing after the peak for one or two minutes, a tensile crack 'D' emanates from the outer tip of flaw ③ and propagates to the flaw ② (see Fig. 3). The propagated crack 'D' ultimately coalesces with flaw ②. For this coalescence is call the second coalescence. The growth rate of the second coalescence crack 'D' is very slow, and its path is rougher than the first coalescence of crack 'C'. Under microscopic observations, the surface of the crack 'D' shows some crushed plaster. It is evident that shear crack is induced. Thus, the second coalescence can be identified as the mixed mode coalescence. The results of the numerical simulations support our experimental results (see Fig. 4 a'-d'). The numerical simulation shows that the tensile 'D' crack emanates and coalesces with

flaw ② after the first coalescence of crack 'C'. This second coalescence crack occurs only under confining pressure. This phenomenon was not observed under the uniaxial compression for specimens of the same joint configurations [9-10].

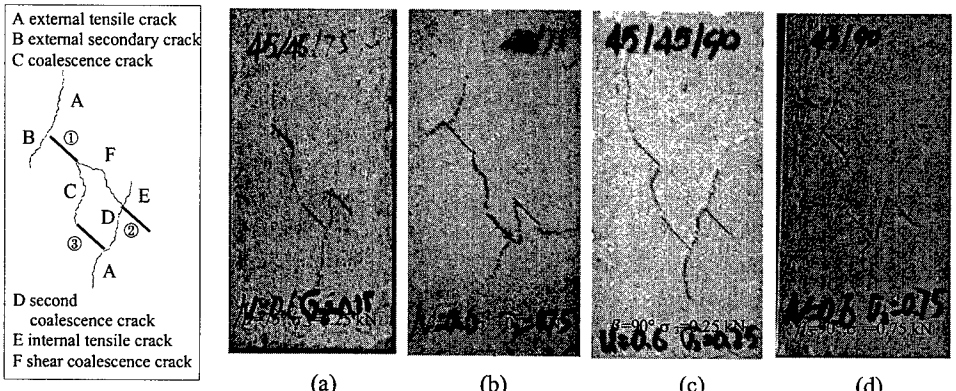


Fig.3 Crack coalescence

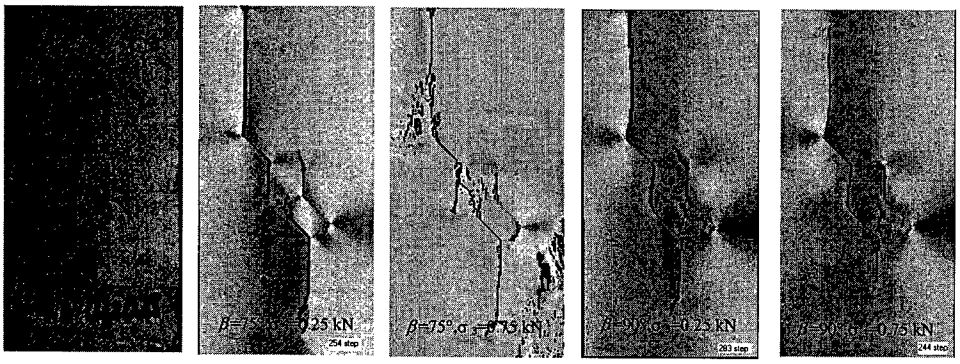


Fig. 4 The experimental and numerical results of crack

3.2 Peak Strength

Wong and Chau [9-10], proposed a crack model modified slightly from Ashby and Hallam [5] model to investigate the peak strength of two flaw and three flaw specimens under the uniaxial compression. The theoretical results agree very well with the experimental study. In this study, we employed Ashby and Hallam's [5] model again with slightly modification to predict the peak strength of three flaw specimens under confining pressure. The following expression is derived from Ashby and Hallam's [5] model in terms of fracture toughness K_{IC}, the flaw length 2c, the flaw angle (ψ measured from the σ_1 direction), frictional coefficient on flaw surface μ and flaw density ε [ε=Nc/A where N is the number of crack (with length c) per area A].

$$K_I = \frac{\sqrt{\pi c}}{(1+L)^{3/2}}\{(\sigma_1-\sigma_3)\sin 2\psi - \mu[(\sigma_1+\sigma_3)+(\sigma_3-\sigma_1)\cos 2\psi]-4.3\sigma_3 L\}\left[0.23L+1/\sqrt{3(1+L)}\right]+$$
$$\left\{\sqrt{2\varepsilon c(L+\cos\psi)}\left[\sigma_1-8\varepsilon\sigma_3(L+\cos\psi)^3\right]\left[\sigma_1-2\varepsilon\sigma_3(L+\cos\psi)^3\right]\right\} \quad (1)$$

If

$$A = \frac{\sqrt{\pi c}}{(1+L)^{3/2}} \quad B = 0.23L + 1/\sqrt{3(1+L)} \quad D = L + \cos\psi \quad \psi = 90-\alpha \quad L = l_{max}\sin\beta/c$$

$$E = 2FABH - 20c\sigma_3\varepsilon^2 D^4 \quad F = K_I + ABG\,\sigma_3 + 4.3LAB\,\sigma_3 \quad G = \sin 2\psi + \mu\cos 2\psi + \mu$$

$$H = \sin 2\psi + \mu \cos 2\psi - \mu \qquad I = A^2 B^2 H^2 - 2\varepsilon cD \qquad J = F^2 - 32\varepsilon^3 cD^7 \sigma_3^2$$

Then: $$\sigma_1 = \frac{E - \sqrt{E^2 - 4IJ}}{2I} \tag{2}$$

The theoretical peak strength of specimen can be calculated by using (2) with the different crack angle, bridge angle, and under different confining pressures. The theoretical predictions and the experimental observations are listed in Table 1. From this Table, there are two observations being drawn. First, both experimental and theoretical results indicate that the higher confining pressure applied, the higher peak strength of solids will be obtained. Second, the theoretical peak strength agrees very well with the experimental results at the lower confining pressure (σ_3= 0.082MPa). However, for a higher confining pressure (σ_3= 0.25MPa), the value of theoretical peak strength is over estimated by about 70%. It seems that Ashby and Hallam's [5] crack model cannot be applied to specimens under high confining pressure. After a careful study, the following reasons are proposed to explain why Ashby and Hallam's model [5] does not agree with our experimental result when the confining pressure is high.

(1) **Different experimental approach:** According to the experimental setting of Sammis and Ashby (see Fig. 2 of [6]), the applied confining stress is $\lambda\sigma_1$. That is the confining pressure increase with the applied axial stress with a fixed ratio of λ ($\lambda=\sigma_3/\sigma_1$). But in our study, the applied confining pressure 'σ_3' is a constant value after a certain stress level. Thus, it may cause the difference between the results of prediction and the experiments. But if λ is fixed in our study during the testing, we do believe that the peak strength of the experiment will be higher. However, more testing should be carried out to confirm our speculation. (2) **Different modes of coalescence:** The basic assumption in the model of Ashby and his co-authors [5, 6] is tensile crack. They assumed that the whole coalescence process including crack initiation, propagation and interaction are all of tensile nature. However, under high confining pressure, shear crack becomes more dominant. Therefore, the crack model of Ashby and his co-authors [5, 6] may not be applicable. A modification of the crack model to incorporate shear crack initiation and propagation is required.

Table 1 The compare of experimental and theoretical peak strengths

μ	α(°)	β_1(°)	Peak Strength σ_3=0.082MPa		Peak Strength σ_3=0.25MPa	
			Experimental	Theoretical	Experimental	Theoretical
0.6	45	75	2.16	2.23	2.53	4.18
	45	90	1.97	2.25	2.45	4.28
	45	105	1.87	2.23	1.90	4.18
	45	120	2.21	2.17	2.68	3.93
	65	75	2.08	2.09	2.46	4.01
	65	90	2.18	2.12	2.39	4.12
	65	105	2.07	2.09	2.32	4.01
	65	120	2.07	2.01	2.25	3.71

4. Conclusion

In this study, three flaw models are considered numerically and experimentally to investigate the effect of confining pressure on the coalescence mechanisms of rock-like material. Total 128 specimens containing three pre-existing flaws were tested. A series of numerical simulations were carried out by using RFPA^{2D} [14] code for comparing with the experimental results. Based on the

experimental observations and the numerical simulations, three phenomena were observed under biaxial compression loading. (1) Tensile crack initiation and its growth decrease with the increase of confining pressure. (2) Mixed mode coalescence (tensile + shear) is dominant with the increase of confining pressure, that is shear and tensile crack appears simultaneously within the bridge area. (3) The second coalescence crack can only be observed under the confining pressure. This coalescence occurs after the peak strength and after the appearance of the first coalescence. The second coalescence is of mixed type mode. For peak strength study, it is found that peak strength increases with the applied confining pressure. The predicted value using the crack model of Ashby and Hallam [5] agrees well with our experimental results when the confining pressure is low. But for high confining pressure, Ashby and Hallam's crack model [5] can not be applied in this study due to the difference of experimental setting and mode of crack coalescence. A modification should be done on the model of Ashby and Hallam's [5] before it can be applied satisfactorily. The numerical simulation using $RFPA^{2D}$ basically coincides with the experimental results in both low and high confining pressure. However, more testing should be carried out to confirm our observation.

Acknowledgement-The research was supported by the Internal Research Fund of the Hong Kong Polytechnic University to RHCW.

References

1. Griffith, A.A., The phenomena of rupture and flow in solids, *Phil.Trans.Royal Soc.London*, Series A, **221** (1921) p.163
2. Hoek,E. and Bieniawski, Z.T., Brittle fracture propagation in under compression, *International Journal of Fracture Mechanics*,**1** (1965) p.137-155
3. Horii,H. and Nemat-Nasser,S., Compression-induced microcrack growth in brittle solids: axial splitting and shear failure, *Journal of Geophysical Research*, **90**(B4) (1985) p. 3105-3125
4. Horii,H. and Nemat-Nasser,S., Brittle failure in Compression: splitting and brittle-ductile transition, *Philosophical Transactions of the Royal Society of London*, Series A,**319** (1986) P.337-374
5. Ashby, M.F. and S.D. Hallam, The failure of brittle solids containing small cracks under compressive stress states, *Acta Metall.*, **34 (3)** (1986) p. 497-510
6. Sammis,C.G., and Ashby,M.F., The failure of brittle porous solids under compressive stress states,*Acta,metall*,**34**(3) (1986) p.511-526
7. Reyes, O. and Einstein, H.H., Fracture mechanism of fractured rock – a fracture coalescence model, *Proc. 7th Int. Conf. On Rock Mech.*, **1** (1991) p.333-340
8. Shen, B., Stephansson, O., Einstein, H.H. and Ghahreman, B., Coalescence of fractures under shear stress experiments. *Journal of Geophysical Research*, **100**(6) (1995) p. 5975-5990
9. Wong R.H.C. and Chau K.T., The coalescence of frictional cracks and the shear zone formation in brittle solids under compressive stresses, *Int. J. of Rock Mech. & Min. Sci.,* Vol.34, No.3/4, (1997) p.366, paper no. 335
10. Wong, R.H.C. and Chau, K.T., Crack coalescence in a rock-like material containing two cracks, *Int. J. Rock Mech. min.* Sci., **35**(2) (1998) p.147-164
11. Wong R. H. C., Chau K.T., Lin P. and Tang C.A., Analysis of crack coalescence in rock-like materials containing three flaws - Part I: Experimental approach, submitted to *Journal of Geophysical Research*, 1999
12. Tang C.A , Wong R. H. C., Chau K.T. and Lin P., Analysis of crack coalescence in rock-like materials containing three flaws - Part II: Numerical approach, submitted to *Journal of Geophysical Research*, 1999
13. Bobet, A. and Einstein, H.H., Fracture Coalescence in Rock-type Material under Uniaxial and Biaxial Compression, *Int. J. Rock Mech.min.*Sci.,**35**(7) (1998) p. 836-888
14. Tang, C.A., Numerical simulation of progressive rock failure and associated seismicity, *Int. J. Rock Mech. Min. Sci.*, **34**, 249-262,1997
15. Wong, R.H.C., Lin,P., Chau, K.T. & Tang, C.A., Numerical and Experimental study on the effects of confining compression on fracture coalescence in rock-like material, To be submitted.

Key Engineering Materials Vols. 183-187 (2000) pp. 863-868
© 2000 Trans Tech Publications, Switzerland

Fracture Toughness Enhancement Due to Stress/Strain-Induced Martensitic Transformations in Solids

S.V. Gladkovsky[1] and V.A. Gladkovsky[2]

[1] Urals State Technical University-UPI, 19, Mira Street, 620002 Yekaterinburg, Russia

[2] Perm State Technical University, 29a Komsomolskiy Ave., 614600 Perm, Russia

Keywords: Austenite, Fracture Toughness, Martensitic Transformation, Mechanical Loading, Metastable Phases, Microstructure

ABSTRACT

The role of stress/train-induced phase transformations in metastable solids with different chemical composition, level of mechanical properties and type of microstructure is discussed. The presented results highlight the universal role of martensitic transformations at the crack tip as a factor of fracture resistance enhancement of metastable materials. The peculiarities of crack propagation and phase composition changes in metastable Fe-Mn steels while cyclic loading are studied.

1.INTRODUCTION

Since early 30-s it has been shown that deformation-induced austenite-to martensite transformation at the test temperature below M_d gives an abnormal relative elongation rise in metastable austenitic steels [1]. In the middle 60-s S.Antolovich and B.Singh [2] give evidence of abnormal K_{1c} Vs test temperature relationship due to $\gamma \rightarrow \alpha'$ transformation in TRIP (Transformation Induced Plasticity)-steels. For the past years a number of metastable materials having mechanical properties and fracture resistance parameters enhancement effect significantly increased. But the role of stress/strain-induced phase transformation in mechanical behaviour and microstructural mechanism of crack propagation in solids with different type of matrix and retained metastable phases is not clear. The presented study is aimed at the evaluation of common features of fracture behaviour of different metastable solids in order to present mechanically-activated martensitic transformations as a universal microstructural mechanism of fracture toughness enhancement.

2. EXPERIMENTAL PROCEDURE

A combination of chemical composition, industrial technology and heat treatment regimes make it possible to vary stability of metastable phases of researched materials under plastic deformation conditions. Instron-1185, 1273 and EUS-20 test machines were used for evaluation of yield and tensile strength as well as fracture toughness and fatigue resistance parameters. K_{1c} critical values were estimated according to Russian standard (GOST 25.506-85) similar to ASTM E 399-74 standard. Fractographical observation were performed by means of JSM-U3 electron microscope. Fractal dimension parameter (D) was calculated using equation

$$D = 1 - \log_{\alpha}(L_1/L_2) \qquad (1)$$

where $-\alpha = \eta_2/\eta_1$ – the relation of magnifications of fracture surface profiles $(1 < \eta_1 < 2)$,

-L_1 и L_2-lenth of fracture surface profiles at the given magnifications –x80 and x500- of optical microscope ($L_1 < L_2$).
A special SIAMS-600 program for quantitative metallography analyses was used for preliminary picture adjustment and precise crack profile measurement.

3. RESULTS AND DISCUSSION

Experimental results, presented in table 1, indicate that stress/strain-induced martensitic transformation in solids of different chemical, microstructural composition and strength level may significantly enhance fracture resistance parameters.

Table 1. Comparative mechanical and fracture resistance parameters of solids containing mechanically-metastable phases

Material	Phase stability	Transformation type	σ_u MPa	K_{1c} MPa·$\sqrt{M}$	$T \cdot 10^2$ MPa^2·$\sqrt{M}$
0,01%C-18%Ni-9%Co-5%Mo	Stable	$\gamma \rightarrow \alpha'$	2080	72,4	1440
	Metastable		2140	84,0	1750
0,3%C-11%Mn	Metastable	$\gamma \rightarrow \alpha'$	1220*	24,2*	248*
0,05%C-20%Mn-2%Si	Semi-stable	$\gamma \rightarrow \varepsilon$, $\gamma \rightarrow \alpha'$	1020*	38,8*	175*
	Metastable		1150*	48,0*	264*
1,5%C-12%Cr-0,6%Mo	Stable	$\gamma \rightarrow \alpha'$	1670	44,0	736
	Metastable		675	31,3	210
Ti-6%Al-4%V-4%Mo	Stable	$\beta \rightarrow \alpha'' \rightarrow \alpha$	1620*	22*	319*
	Metastable		1575*	27*	391*
ZrO_2-Y_2O_3-Al_2O_3**	Stable	t→m	370	4,5	-
	Metastable		570	8,2	-

* Tested at -196°C; **Ceramic 5x5x55 mm specimen subjected to 3-point bending;

The austenite phase stability of the researched Fe-Mn-based industrial steels was regulated by chemical composition. For rising austenite stability in 0,05%C-20%Mn-2%Si a special treatment including hot rolling at 500°C with 30% reduction per area was imposed. Besides, after such treatment the quantity of as-quenched ε-martensite decreased from 55 to 0%. In 1,5%C-12%Cr-0,6%Mo tool steel a great amount of metastable austenite (up to 85-90%) was produced by rising the temperature of quenching from 1020 to 1200°C. Dwelling on experimental results on Fe-Mn and Fe-Cr steels (Table 1) it becomes clear that in containing more than 0,25% C metastable steels the embrittlement role of stress/strain- induced α′-martensite overwhelms the favourable influence of martensitic transformations on fracture toughness. From this point of view one can understand the deterioration of K_{1c} values of 1,5%C-12%Cr-0,6%Mo after austenite-forming heat-treatment though the volume fraction of $\gamma \rightarrow \alpha'$ transformation was very close to 50%. The very specific low-temperature fracture resistance of Fe-Mn austenitic steels and alloys [3] may also result low values of K_{1c}.

It was shown that along side with static fracture toughness the structural strength of number of industrial steels and alloys may be substantially improved by providing controlled contents of metastable phases. For evaluation of the structural strength V.S.Ivanova's et al.[4] engineering fracture T-criterion ($T = K_{1c} \cdot \sigma_{0,2}$) was used.

Consequent cycle of $\beta \rightarrow \tau \rightarrow$''$\alpha \rightarrow \alpha$ strain-induced martensitic transformations in dual-phase Ti- 6%Al-4%V-4%Mo alloy, discovered by M.A. Djakova et el. [5], markedly affect tensile mechanical properties temperature dependence. But K_{1c} dependence Vs testing temperature was not studied. For this reason the favourable influence of metastable β-phase on fracture toughness of Ti-alloy was evaluated by changing the temperature of preliminary quenching from 800 to 860°C.

The positive role of martensitic type t→m transformation on fracture resistance of metastable ceramics, discovered by A.H.Heuer [6], was once again confirmed on partially stabilised ZrO_2-Y_2O_3-Al_2O_3 composition (table 1). A combined way of ceramics phase stability regulating was implemented (powder grain size and chemical composition changes). It must be mentioned that stress-induced t→m transformation in ZrO_2-based ceramics develops under elastic/pseudo-elastic loading conditions and lead to formation of some dimple zones on dominating cleavage fracture surface.

As for high-strength 18%Ni-9%Co-5%Mo, 10Cr-8Ni-9Co-2Mo-Ti and 11Cr-10Ni-2Mo-1Cu-1Ti maraging steels from 5 to 46% of metastable austenite volume fraction in accordance with [7] was produced by rapid heating to 820°C in melted NaCl-KCl salts mixture prior to final ageing. Presented in Table 1 and 2 data indicate the favourable role of limited amount of metastable austenite phase (up to 15-20%). in mechanical properties and fracture resistance enhancement. The further γ-phase contents increase in maraging steels causes drastic strength degradation. On the other hand the formation of 13% more stable austenite in 11Cr-10Ni-2Mo-1Cu-1Ti maraging steel do not improve impact and fracture toughness values (KCU and K_{1c}) significantly. Due to complicated microstructure of researched maraging steels fractographical observation make it unable to select specific fracture surface parameters correlating with fracture resistance. So a fractal geometry approach [4] was used for more detailed characterisation of maraging steels fracture behaviour. The values of calculated fractal D-parameter (table 2) clear up, that the formation of metastable austenite phase lead to increase both K_{1c} and fractal dimension (D) along side with some dimple areas appearance on fracture surface.

Table 2. The influence of austenite contents and volume of $\gamma \rightarrow \alpha'$ transformation on mechanical properties and fracture parameters of maraging steels

Austenite contents, %	Volume of $\gamma \rightarrow \alpha'$ transformation, %	$\sigma_{0.2}$ MPa	KCU. MJ/m^2	K_{1c} MPa·m$^{1/2}$	D	Fracture mode
10Cr-8Ni-9Co-2Mo-Ti maraging steel						
15	10	1700	0,6	49*	1,1	QCF
46	30	1540	1,0	55*	1,22	QCF+D
11Cr-10Ni-2Mo-1Cu-1Ti maraging steel						
0	0	1800	0,05	37	1,08	CF
13	3	1730	0,1	40	1,09	QCF+CF

QCF- quasi-cleavage facets; CF- cleavage facets; D-dimples;
*K_{1c} values obtained at -196°C, all others – at 20°C;

The character of austenite–to martensite transformations influence on fracture resistance have specific peculiarities while changing test conditions from static to cyclic loading. The results of performed on metastable 0,05%C-20%Mn-2%Si-1%Ti non-ferromagnetic steel low cyclic fatigue

tests ($N<10^5$ cycles) and surface phase composition X-ray analyses give evidence that severe deformation conditions in the cyclic plastic zone at the crack tip sufficiently activate the formation of α′-martensite. It may be noted from Table 3, that the volume fraction of produced α′-phase on cyclic fracture surface depending on ΔK exceeds 45%. It is clear from the presented on fig.1 results that fatigue crack propagation at high amplitudes (ΔK =45-55 MPa·$m^{1/2}$) lead to more active α′-formation which may be the most evident reason of fatigue process acceleration.

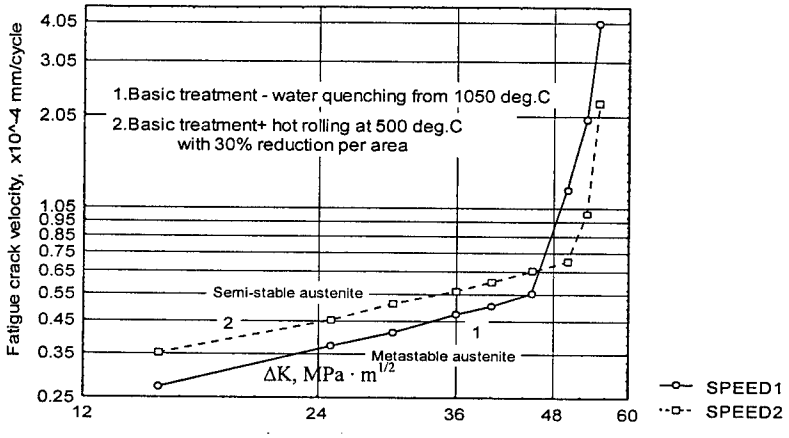


Fig.1 The influence of ΔK span on fatigue crack velocity of Fe-20%Mn-2%Si steel

Preliminary hot rolling at 500°C of 0,05%C-20%Mn-2%Si steel making γ-phase more stable towards plastic deformation deteriorates cyclic fracture resistance at low ΔK values, but enhances fatigue strength at high loading amplitudes (ΔK =45-55 MPa·$m^{1/2}$).

Table 3 Average phase composition of metastable 0,05%C-20%Mn-2%Si steel on cyclic crack surface depending on ΔK values

Treatment	ΔK values, MPa·$m^{1/2}$	Phase composition, %		
		γ	ε	α′
Standard type (water quenching from (1050°C), ε =55%; γ=45%;	15-20	11	65	24
	45-55	3	50	47
Standard + hot rolling at 500°C, with 30% reduction per area, γ=100%;	15-20	92	5	3
	45-55	39	36	25

It may be concluded from X-rays analyses data that α′-martensite contents (3-47%) and the level of microstresses ($\Delta a/a$=1,6-1,8 x 10^{-3}) in cyclic plastic zone is in 1,5 times higher as compared to the surface of static crack propagation. One can see that γ→ε, γ→α′ martensitic transformation decrease crack growth in the range of ΔK =15-40 MPa x $m^{1/2}$ values, but markedly accelerates crack growth in high amplitude area. So, while cyclic loading at ΔK> 40 MPa x $m^{1/2}$/

Fe-20%Mn steels with metastable γ-phase have no advantage in comparison with more stable austenitic steels.

Based on the whole experimental data it is considered that possible fracture toughness enhancement of metastable solids my be attributed to the following reasons:

1.Relaxation of normal tension stresses at the crack tip due to volume changes during $\gamma \rightarrow \alpha'$ martensitic transformation according to E.Hornbogen [8];
2.Micro-TRIP effect at the crack tip;
3.Microstructural inhomogeneity growth in transformed zone which favours crack deviation and branching;
4.Additional energy dissipation at the crack tip due to martensitic transformations according to W.Gerberich et.al. [9];

The role of the named factors is of a synergetic type and it greatly depends on strength, plasticity, fracture mechanism of matrix phase and products of stress/strain-induced martensitic transformations. For high-strength and low-plastic materials tested at plain-strain conditions such as Ti-alloys and ceramics the role of relaxation factor seems to be more significant. As for maraging steels all factors are valid, but the role of stress relaxation decreases along side with strength degradation. For ductile metals having fracture process under plain–stress conditions the role of stress relaxation seems to be negligible. In this case according to crack tip stress distribution analyses [10] tensile stress is found to be constant and do not exceed yield stress. So the contribution of micro-TRIP effect and microstructural inhomogeneity in metastable solids fracture toughness enhancement is considered to be increasing.

REFERENCE

1. Z.Nishiyama, Sci. Rep. Tohoku Univ., **23** (1934) p.637
2.S.Antolovich, B.Singh, Met.Trans., **2** (1971) p.2135
3.I.N.Bogachev,V.F. Egolaev, Microstructure and properties of ferro-manganese alloys. Moscow: Metallurgia, 1973, 295 p. (in Russian)
4.V.S. Ivanova et.al., Synergetics and fractals in material science. Moscow: Nauka, 1994, 383 p. (in Russian)
5.M.A. Djakova et al., Heat and Chemical-Heat Treatment of Steels and Alloys, Perm, (1987) p.73 (in Russian)
6.A.H.Heuer, J. Of the American Ceramic Society, **70**, N 10, (1987) p.689
7.S.V.Gladkovskii et al., The Physics of Metals and Metallography, **87**, N 3, (1999) p.
8.E. Hornbogen, Acta Metallurgica, **26**, N 1, (1978) p.147
9. W.W. Gerberich et.al., Met.Trans., **2** (1971) p.2343
10. J.F. Knott, Fundamentals of Fracture Mechanics. Moscow: Metallurgia, 1978, 256p.

Key Engineering Materials Vols. 183-187 (2000) pp. 869-874
© 2000 Trans Tech Publications, Switzerland

Fracture Behavior of a Crack in Gas Pipeline Considering Constraint Effects

D.J. Shim, Y.K. Jang, J.B. Choi and Y.J. Kim

School of Mechanical Engineering, SungKyunKwan University,
300 Ch'onch'on-dong, Changan-Ku, Suwon 440-746, Korea

Keywords: Constraint Effects, Finite Element Analysis, *J*-Integral, *J*-*Q* Analysis, SENB Specimen, SENT Specimen

ABSTRACT

The assessment of defects in underground pipeline is required to prevent serious accidents. FFP(Fitness For Purpose) type defect assessment methodologies based on ECA (Engineering Critical Analysis) have been established and are in use for the structural integrity evaluation of gas pipelines. ECA usually includes the fracture mechanics analysis, and it assumes that *J*-integral uniquely characterizes crack-tip stress-strain fields. It has been, however, revealed that it is not sufficient to characterize the crack-tip field under low levels of constraint with a single parameter. Since pipeline structures are made of ductile material, locally loaded in tension, cracks may experience low level of constraint, and therefore, *J*-dominance will be lost. For this reason, the level of constraint must be quantified to establish a precise assessment procedure for pipeline defects. The objective of this paper is to investigate the fracture behavior of a crack in gas pipelines by quantifying the level of constraint. For this purpose, SENB(Single Edge Notched Bending) and SENT(Single Edge Notched Tension) specimen tests were performed, and subsequently *J*-*Q* analyses were performed for both specimens based on 2-D finite element analyses. *Q* values have been tabulated for various crack depths in SENB and SENT specimens.

1. INTRODUCTION

Pipelines are one of the most convenient and cost effective ways of transporting natural energy resources, such as gases and oils, over long distance. As the number of pipelines increase, the failure of pipelines are increasing as well. Fitness-for-purpose defect assessments based on ECA(Engineering Critical Analysis) have been established to prevent failure of pipelines. Major design codes, such as PD 6493[1], R6[2], are also used for the assessment of the integrity of pipelines. These codes are based on the assumption that the *J*-integral uniquely characterizes the crack-tip stress-strain field. However, it has been suggested that a single parameter might not be sufficient to characterize the crack-tip field under low levels of constraint[3-5].

While a pipeline is mainly subjected to a global bending, the local loading on a defect can be considered as a uniaxial tension, as shown in Fig. 1(a). In this case, if the defect depth is shallow, the defect experiences low levels of constraint, and *J*-dominance will be lost. Since the fracture toughness, J_{IC} or δ_c, is obtained from a bending loaded test specimen geometry which shows high levels of constraint, the application of J_{IC} as a fracture criterion for the geometries having low levels of constraint is known to be unduly conservative[6,7]. Therefore, it is necessary to quantitatively correlate the fracture behavior of test specimens to that of real pipelines considering constraint effects.

In order to investigate the fracture behavior and to quantify the in-plane constraint of a test specimen, material tests and *J*-*Q* analyses based on 2-D finite element analyses were performed for SENB specimens(Fig. 1(b)). The same procedure was repeated for SENT specimens(Fig. 1(c)) to simulate the fracture behavior of a crack in a real gas pipeline.

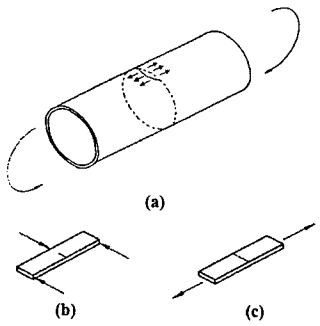


Fig. 1. Specimen and model configuration.

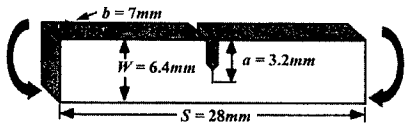


Fig. 2. Geometry of the SENB specimen.

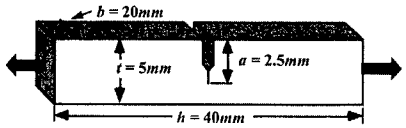


Fig. 3. Geometry of the SENT specimen.

2. THE *J-Q* APPROACH

Hutchinson[8], Rice and Rosengren[9] showed that the *J*-integral characterizes crack-tip conditions with the following equation in a nonlinear material satisfying the Ramberg-Osgood uniaxial stress-strain relationship:

$$\frac{\varepsilon}{\varepsilon_o} = \frac{\sigma}{\sigma_o} + \alpha\left(\frac{\sigma}{\sigma_o}\right)^n \tag{1}$$

where σ_o is an effective yield strength, ε_o is the yield strain, α is a dimensionless constant and n is the strain hardening exponent.

The stresses and strains in the vicinity of the crack-tip under yielding conditions can be described in terms of *J*-integral by:

$$\sigma_{ij} = \sigma_o\left(\frac{J}{\alpha\sigma_o\varepsilon_o I_n r}\right)^{\frac{1}{n+1}} \tilde{\sigma}_{ij}(\theta, n) \tag{2}$$

$$\varepsilon_{ij} = \alpha\varepsilon_o\left(\frac{J}{\alpha\sigma_o\varepsilon_o I_n r}\right)^{\frac{n}{n+1}} \tilde{\varepsilon}_{ij}(\theta, n) \tag{3}$$

where I_n is a constant which is a function of n, and $\tilde{\sigma}_{ij}, \tilde{\varepsilon}_{ij}$ are known dimensionless functions of the circumferential position, θ, and the hardening exponent, n. In Eq. (2) and Eq. (3) the *J*-integral is the amplitude of the stress or strain singularity; these equations are often referred to as the HRR field equations.

O'Dowd and Shih[4,5] suggested the *J-Q* theory by observing the difference between the actual crack-tip stress field and the HRR stress field. They noted that the difference corresponds approximately to a uniform shift of the hydrostatic stress field in front of the crack-tip. O'Dowd and Shih designated the amplitude of this approximate difference field by the Q parameter, which represents the state of triaxiality, for the quantification of in-plane constraint. Eq. (2) then becomes

$$\sigma_{ij} \approx (\sigma_{ij})_{HRR} + Q\sigma_o\delta_{ij} \quad \left(|\theta| < \frac{\pi}{2}\right) \tag{4}$$

where δ_{ij} is the Kronecker delta. From Eq. (4), Q is defined as

$$Q \equiv \frac{\sigma_{\theta\theta} - (\sigma_{\theta\theta})_{HRR}}{\sigma_o} \quad \text{at} \quad \theta = 0, \ \frac{r\sigma_o}{J} = 2 \tag{5}$$

where $\sigma_{\theta\theta}$ is the actual perpendicular stress acting near the crack-tip , and $(\sigma_{\theta\theta})_{HRR}$ is the stress calculated by HRR solution. The distance $r/(J/\sigma_o) = 2$ is chosen so that Q is evaluated outside the finite strain region but still within the J-Q analysis.

3. EXPERIMENTAL

3.1. Specimen Tests

The pipe used in this study was KS D 3507 with the diameter and the thickness of 300*mm* and 6.4*mm*, respectively. Tensile tests were performed for the base metal at room temperature(24℃) in accordance with the ASTM E8 standards[10].

Geometries of the SENB and SENT specimens used for tests are shown in Figs. 2 and 3, respectively. Both specimens were pre-cracked under three point bending loads. Tests were performed for SENB specimens with a/W=0.5 and SENT specimens with a/t=0.5. A 10*mm* clip gauge was used to measure the crack mouth opening displacements(CMOD) of SENB specimens and a 10*mm* extensometer was used to measure the displacements of the SENT specimens.

3.2. Experimental Results

Results of the tensile tests are summarized in Table 1. The stress-strain curves were curve fitted using the Ramberg-Osgood equation, and resulting α and n were 6 and 8, respectively. The measured stress-strain curves with Ramberg-Osgood curve fit are shown in Fig. 4.

Test results of SENB and SENT specimens are shown in Figs. 5 and 6, respectively. For SENB specimens, there was no evidence of brittle crack extension associated with pop-in behavior prior to the attainment of maximum load. There was no evidence of ductile tearing for SENT specimens as well, which means that the dominant failure mode for all the specimens can be considered as plastic collapse.

Table 1. Tensile properties of the KS D 3507 (Base metal)

Yield strength	Tensile strength	Young's modulus	Elongation
303 *Mpa*	378 *MPa*	196 *GPa*	36.6%

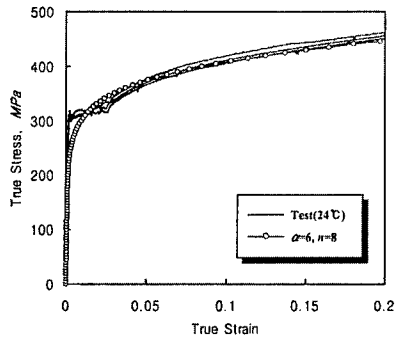


Fig. 4. True stress-true strain curves for KS D 3507 with Ramberg-Osgood curve fit.

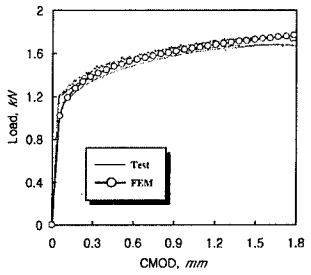


Fig. 5. Comparison between test and FEM simulation results for SENB specimens.

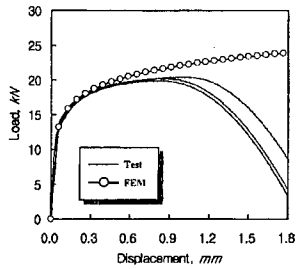


Fig. 6. Comparison between test and FEM simulation results for SENT specimens.

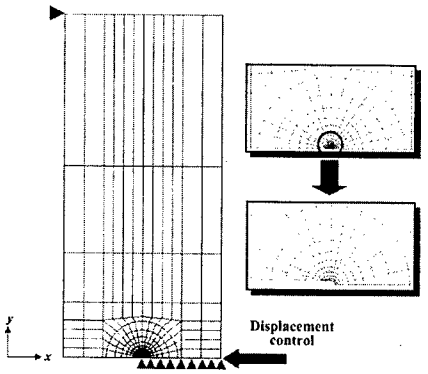


Fig. 7. Two-dimensional mesh and boundary conditions for SENB specimen, a/W=0.5.

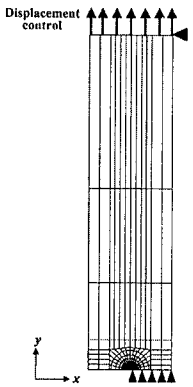


Fig. 8. Two-dimensional mesh and boundary conditions for SENT specimen, a/t=0.5.

4. FINITE ELEMENT ANALYSES

4.1. Finite Element Models

In order to investigate the in-plane constraint effects of SENB and SENT specimens, two-dimensional plane strain finite element analyses were performed. Crack depths of a/W = 0.25, 0.5, 0.75 and a/t = 0.25, 0.5, 0.75 were considered for SENB and SENT, respectively. Meshes used for the analysis are shown in Figs. 7 and 8. Due to the symmetry, only the upper-half plane was modeled for both specimens. Loading and boundary conditions were applied in accordance with the actual test conditions. Eight node iso-parametric quadrilateral hybrid elements with reduced integration were used for all analyses. When the purpose of the analysis is to analyze crack-tip stress and strains, a very high level of mesh refinement is required. The focused crack-tip mesh was composed of 20 contours and 16 layers as shown in Fig. 7.

Since the small strain analysis provides more stable results over the full range of loading, all cases in this paper were analyzed with the small strain analysis. In order to verify the designed model, SENB and SENT test simulations were performed using small strain analysis, and results were compared with those for the actual test.

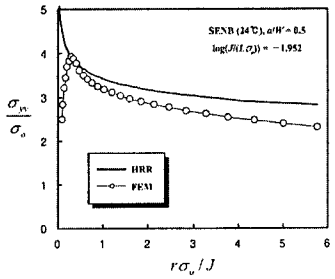
4.2. *J-Q* Analyses

The J-integral was calculated for twenty contours surrounding the crack-tip, with the first contour at the crack-tip. Contours for J-integral calculation were carefully selected to avoid the finite strain zone at the crack-tip. HRR stress fields were obtained from Eq. (2) using the calculated J-integral values. Actual stress fields were obtained by calculating the stress values at nodes along the crack ligament. Q values were calculated for three different crack depths of SENB and SENT specimens, respectively.

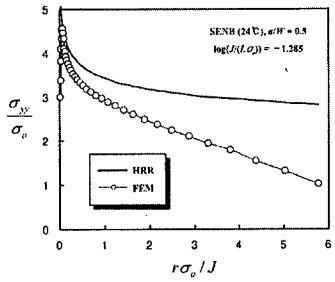
4.3. Results and Discussions

Results of SENB and SENT test simulations are shown in Figs. 5 and 6, respectively. For SENB specimens, the agreement between simulation results and test results is excellent before the attainment of maximum load. SENT test simulation results also agree well with the test results until the displacement reaches about 0.4*mm*. The difference beyond this point is due to the localized necking of the test specimens. On the basis of simulation results, J-Q analyses were performed in the region where simulation and test results agree.

The difference between the HRR field and the actual stress field for an SENB specimen(a/W=0.5) are shown in Figs. 9(a) and 9(b) for low and high levels of loading, respectively. While Q values at low levels of loadings were successfully calculated, Q values were not attainable at high levels of loading due to the deviation of stress field between HRR and actual state with increasing distance from the crack-tip as shown in Fig. 9(b). Fig. 10 shows the evaluation of Q for

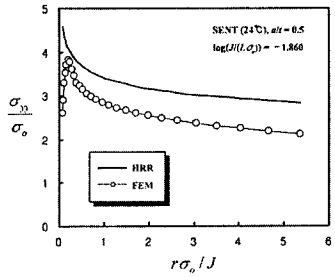


(a)

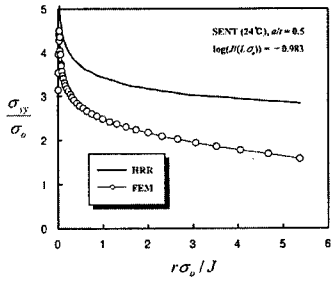


(b)

Fig. 9. *J-Q* stress fields for an SENB specimen, a/W=0.5.



(a)



(b)

Fig. 11. *J-Q* stress fields for an SENT specimen, a/t=0.5.

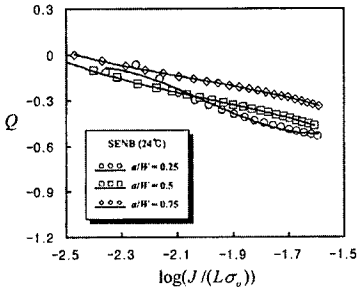


Fig. 10. Q values for SENB specimens.

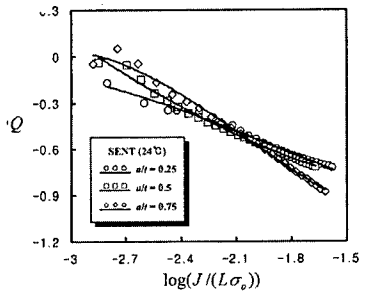


Fig. 12. Q values for SENT specimens.

Table 2. Q results for SENB specimens

a/W	a_0	a_1	a_2	a_3
0.25	11.726	19.615	10.183	1.692
0.5	-3.899	-4.631	-2.120	-0.354
0.75	-3.354	-4.011	-1.787	-0.289

$Q = a_0 + a_1 X + a_2 X^2 + a_3 X^3 \qquad X = \log(J/(L\sigma_o))$

Table 3. Q results for SENT specimens

a/t	a_0	a_1	a_2	a_3
0.25	-1.032	0.255	0.390	0.069
0.5	-0.585	0.639	0.397	0.036
0.75	-0.035	2.428	1.609	0.264

$Q = a_0 + a_1 X + a_2 X^2 + a_3 X^3 \qquad X = \log(J/(L\sigma_o))$

three different SENB specimens (a/W=0.25, 0.5, 0.75) with increasing J-integral. It is shown that the high triaxiality is maintained for very low levels of loading. However, as the load increases, the triaxiality decreases gradually due to plastic deformations. Deeply cracked specimens showed high constraints at the crack-tip than shallow crack specimens. However, the difference was not considerable. The final Q values for SENB specimens are tabulated using polynomial curve fitting in Table 2.

The difference between the HRR field and the actual stress field for an SENT specimen(a/t=0.5) is shown in Figs. 11(a) and 11(b) for low and high levels of loading, respectively. Evaluation of Q was applicable for both low and high levels of loading. Fig. 12 shows Q values for three different SENT specimens (a/t=0.25, 0.5, 0.75) with increasing J-integral. It is observed that the loss of triaxiality accelerates with increasing load, which implies that HRR fields at high levels of loading overestimate actual stress fields. Under low levels of loading, shallow cracks produce high triaxiality compared with deeper cracks. This trend was maintained before the load level reaches $\log(J/(L\sigma_o))$=-2.1, as shown in Fig. 12. Beyond this point, the trend was reversed. This behavior seems to be caused by high plastic deformations at the ligament, and failure mode in this region is expected to be dominated by plastic collapse rather than fracture. The final Q values for SENT specimens are tabulated using polynomial curve fitting in Table 3.

5. CONCLUSIONS

The investigation of in-plane constraint effects was achieved by performing J-Q analyses, based on two-dimensional plane strain finite element analyses, for SENB and SENT specimens. For SENB specimens, high triaxiality was maintained at low levels of loading, but J-Q analysis was not applicable at high levels of loading. J-Q analysis of SENT specimens was applicable over the full range of loading, and rapid loss of triaxiality was observed with increasing load. SENT specimens showed plastic collapse characteristics at loads higher than $\log(J/(L\sigma_o))$=-2.1.

Future areas for extension of this research include J-Q analysis of three-dimensional surface crack in wide-plate specimen and real pipeline structures. Also, the constraint effect should be considered in evaluating these surface cracks in real pipeline structures.

AKNOWLEDGEMENTS

The authors are grateful for the support provided by a grant from the Safety and Structural Integrity Research Center at the Sungkyunkwan University.

REFERENCES

1. BSI PD 6493, Guidance on Method for Assessing the Acceptability of Flaws in the Fusion Welded Structures, British Standards Institution, London (1991)
2. R/H/R6-Revision 3, Assessment of the Integrity of Structures Containing Defects, British Energy (1998)
3. Betegon, C. and Hancock, J., Journal of Applied Mechanics, Vol. **58** (1991) pp.104-110
4. O'Dowd, N.P., and Shih, C.F., Journal of Mechanics and Physics of Solids, Vol. **39**, No. **8** (1991) pp.989-1015
5. O'Dowd, N.P., and Shih, C.F., Journal of Mechanics and Physics of Solids, Vol. **40**, No. **5** (1992) pp.939-963
6. Choi, J.B., MASc thesis, University of Waterloo, Canada (1993)
7. Choi, J.B., Proceedings of the KSME 1997 Spring Annual Meeting A (1997) pp.173-178
8. Hutchinson, J.W., Journal of the Mechanics and Physics of Solids, Vol. **16** (1968) pp.13-31
9. Rice, J.R. and Rosengren, G.F., Journal of the Mechanics and Physics of Solids, Vol. **16** (1968) pp.1-12
10. ASTM E8, Standard Test Method for Tension Testing of Metallic Materials, 1995 Annual Book of ASTM Standards, Vol. 3.01 (1995) pp.56-76

Key Engineering Materials Vols. 183-187 (2000) pp. 875-880
© 2000 Trans Tech Publications, Switzerland

Numerical Analysis of Dimple Fracture Process under Different Constraint Conditions

Masanori Kikuchi[1] and Akiyuki Takahashi[2]

[1] Department of Mechanical Engineering, Science University of Tokyo, Noda-shi, Chiba-ken 278-8500, Japan

[2] Graduation School, Science University of Tokyo, Japan

Keywords: Constraint Effects, Dimple Fracture, FEM Analysis, Gurson' s Constitutive Function, Stress Triaxiality, Void

ABSTRACT

Three kinds of fracture specimens are tested under different constraint conditions. One is 3PB(3 Point Bending) specimen, another is CCT(Center Cracked Tension) specimen, and the third one is called CCB(Center Cracked Bending) specimen. By the SEM (Scanning Electron Microscope) observation, it is shown that the roughness of fracture surface is different from each other largely. The number of large voids and the average diameter of them are also different from each other. They are the effect of constraint condition. The dimple fracture process is simulated by the finite element method. By the finite element analyses, the crack tip stress fields are obtained. The distribution pattern of the high stress triaxiality area agrees with the fracture surface roughness qualitatively. The distribution of the void volume fraction also agrees with the experimental data. The macroscopic parameter, J integral, is also evaluated and the constraint effect on the critical value of J is discussed.

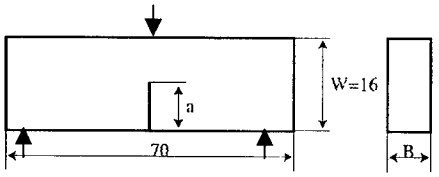
1. INTRODUCTION

It has been pointed out that the fracture toughness is largely affected by the condition of constraint at the crack tip. It is called constraint effect and has been studied by many authors [1-3]. From the practical viewpoint, this effect is evaluated by the local approach. The change of the apparent fracture toughness is well estimated by this approach [4-6]. But the effect of the constraint on the microscopic fracture process has not been studied yet. In this study, the microscopic fracture process under different constraint conditions is studied experimentally. The change of the apparent J_{IC} value is evaluated. Then, the fracture surface is observed using SEM, and the effect of constraint condition is evaluated quantitatively. The three-dimensional FEM analysis is conducted using Gurson's constitutive equation and the dimple fracture is simulated. The effect of the change of the constraint condition at the crack tip on the dimple fracture process is studied and discussed.

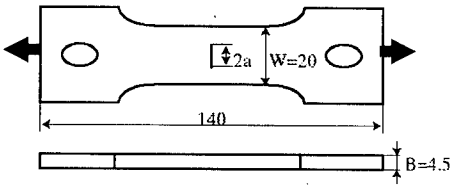
2. EXPERIMENTS

Figure 1 shows the shape and size of three kinds of fracture specimen used in this study. The crack length and the width of 3PB specimen are changed as shown in this figure. The crack

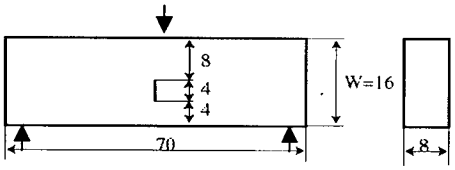
length of CCT specimen is also changed in two cases. Figure 2 is the stress pattern at the crack tip of these specimens neglecting the stress concentration by the crack tip. For 3PB specimen, the stress is the largest at the crack tip and decreases gradually as the distance from the crack tip increases. In the CCT specimen, the stress keeps constant value, and in CCB specimen, stress increases as the distance from the crack tip increases. The material of the specimen is A533B steel, which is used for the reactor pressure vessel.



B=3 a/W= 0.1, 0.3, 0.55
B=8 a/W= 0.1, 0.3, 0.55
B=16 a/W= 0.1, 0.3, 0.55
(Crack length : a= 1.6, 4.8, 8.0)
(a) Three point-bend(3PB) specimen

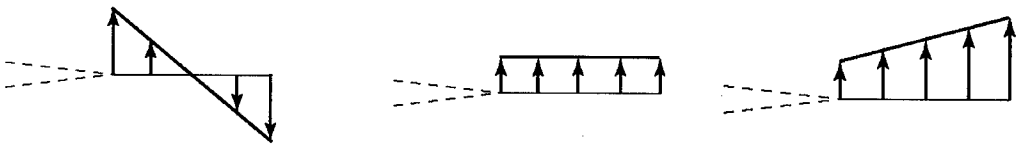


2a/W= 0.4, 0.6
(Crack length : 2a= 8.0 12.0)
(b) CCT specimen



(c) CCB specimen

Fig.1 Configuration of three kinds of specimen



(a) 3PB specimen (b) CCT specimen (c) CCB specimen

Fig.2 Stress pattern at the crack tip (Neglecting stress concentration by the crack)

Table 1 J_{IC} value (kN/m)

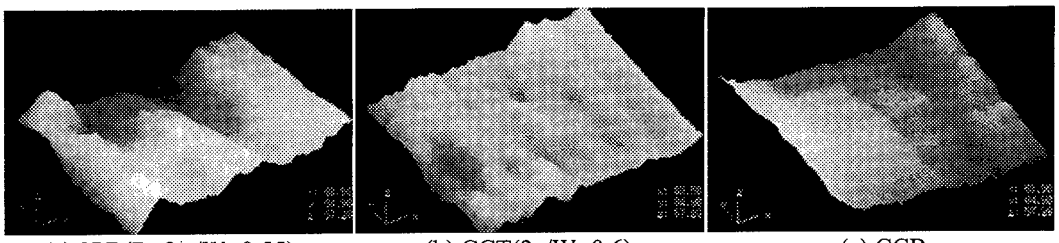
(3PB)

a/W	0.1	0.3	0.55
B=3	306	175	151
B=8	339	239	135
B=16	413	173	165

(CCT)

2a/W	0.4	0.6
B=4.5	185	186

The fracture toughness is evaluated using 3PB and CCT specimens based on the testing standard[7] and using the conventional equations. The results are shown in Table 1. Not all of them are valid J_{IC} values, they are called apparent J_{IC} value. The apparent J_{IC} values are strongly affected by the initial crack length and the specimen thickness in 3PB specimen. Generally speaking, it decreases gradually as the specimen thickness increases and the initial crack length increases. In CCT specimen, the initial crack length has not large effect on the apparent J_{IC} values. As the result of the specimen of B=8mm and a/W=0.55 satisfies the size condition of the fracture toughness testing standard, the valid J_{IC} value of this material is 135kN/m. All other apparent values are larger than this valid one. It is the effect of the constraint condition at the crack tip.



(a) 3PB(B=8,a/W=0.55) (b) CCT(2a/W=0.6) (c) CCB

Fig.3 Fracture surface

Table 2 Average dimple diameter

	a/W(2a/W)	Number of dimples	Average diameter(μm)	Measured area(μm^2)
3PB(B=3)	0.1			400 x 500
	0.3	44	14.6	
	0.55	41	15.3	
3PB(B=8)	0.1	171	19.1	400 x 1500(x2)
	0.3	161	18.6	
	0.55	190	17.8	
3PB(B=16)	0.1	85	17.3	400 x 2600
	0.3	107	17.1	
	0.55	175	18.6	
CCT	0.4	61	14.2	400 x 500(x2)
	0.6	60	16.9	

Figure 3 shows the SEM photos of three specimens. They are the photos taken near the mid-plane of the specimen and near the initial crack tip. It is obvious that the surface roughness of each specimen is largely different from each other. In 3PB specimen, large dimples are observed and the roughness of the surface is the largest. In CCT specimen, the roughness becomes smaller than that of 3PB specimen. In CCB specimen, the fracture surface is smooth and large dimples disappear. The diameter of dimples is measured using these photos. The diameter changes from 1 micrometer to over 100 micrometer. In this study, only larger dimples over 10 micrometers diameter are measured in each specimen. Table 2 shows the results. The number of dimples over 10 micrometers and the average of them of 3PB and CCT specimens are shown in this table. The diameter of 3PB specimen is a little larger than that of CCT specimen. In CCB specimen, dimples over 10 micrometers are not observed at all. These results are qualitatively corresponding to the experimental observation on the roughness of fracture surface of three specimens. The results show that the change of the constraint condition at the crack tip affects largely on the microscopic fracture process such as nucleation, growth and the coalescence of voids.

3. FEM ANALYSIS BY GURSON'S CONSTITUTIVE EQUATION

The simulation of the nucleation, growth and coalescence of voids is performed. For this purpose, three-dimensional FEM analysis using the constitutive equation proposed by Gurson and later modified by Tvergaard[8] is conducted. For the use of Gurson's model, the finite deformation analysis is needed, and it is known that very fine mesh pattern should be used for the accurate numerical simulation. Figure 4 is one example of mesh pattern of 3PB specimen. The crack length is a/W=0.55 and the specimen thickness is B=8mm. The total number of element is 15495 and the number of joint is 80470. As it is impossible to solve this problem by a single CPU, parallel computing is conducted where 10 CPUs are used. Figure 5 shows decomposed domain of the numerical model for the parallel computing. The model is decomposed into large number of

small domains and they are shared to each CPU. The convergence is obtained by the iteration process.

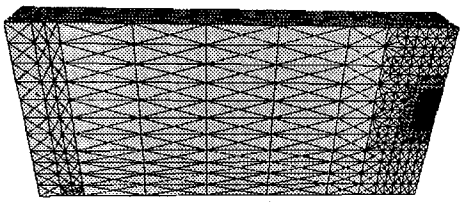


Fig.4 Mesh pattern of 3PB specimen

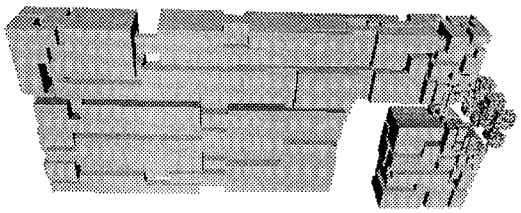
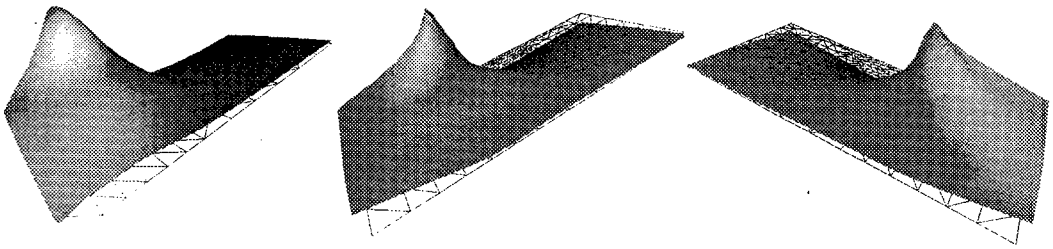
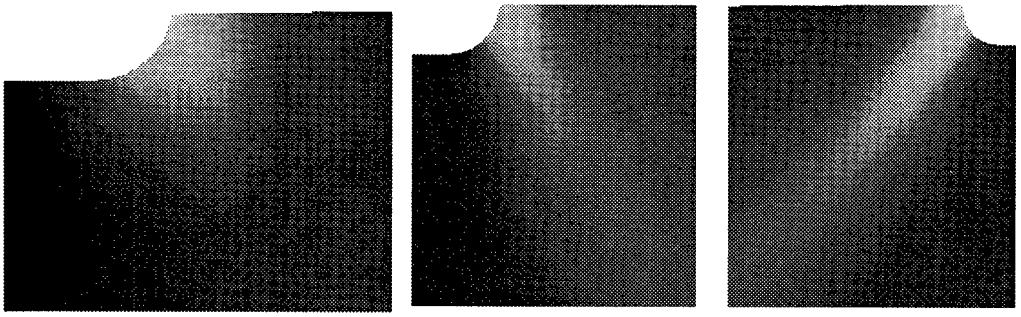


Fig.5 Hierarchical domain decomposition of 3PB mesh



(a) 3PB (b) CCT (c) CCB

Fig.6 Distribution of dilatational stress near the crack tip

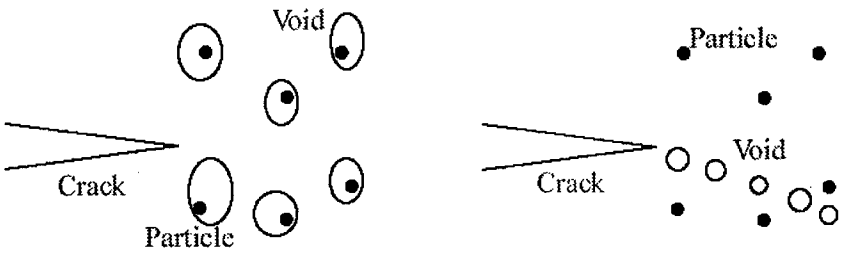


(a) 3PB (b) CCT (c) CCB

Fig.7 Distribution of equivalent plastic strain near the crack tip

Figures 6(a)-(c) show the distributions of the dilatational stress near the crack tip for three specimens after large amount of deformation. They are the results at the mid-plane of three specimens. In every case, the maximum dilatational stress occurs at the crack tip. In 3PB specimen, the high dilatational stress region exists around the crack tip. But in CCT and CCB specimens, the sharp peak of the dilatational stress is observed at the crack tip, and the stress decreases sharply from the crack tip. The slope of CCB specimen is steeper than that of CCT specimen. The summit of the distribution of CCB specimen is along 45 degree from the crack line. Figures 7(a)-(c) show the distributions of void volume fraction in three specimens. The distribution patterns are similar to those of dilatational stress. The high void volume fraction area spreads around the crack tip in wide area in 3PB specimen, and it becomes restricted in CCT and CCB specimens. It means that the void nucleation and growth occurs in 3PB specimen in wide area around the crack tip, and in CCT and CCB specimens, the void growth occurs in some restricted area at the crack tip. It is shown that in CCB specimen, high void volume fraction area exists along 45 degree line from the crack tip and in very narrow area. These results are related

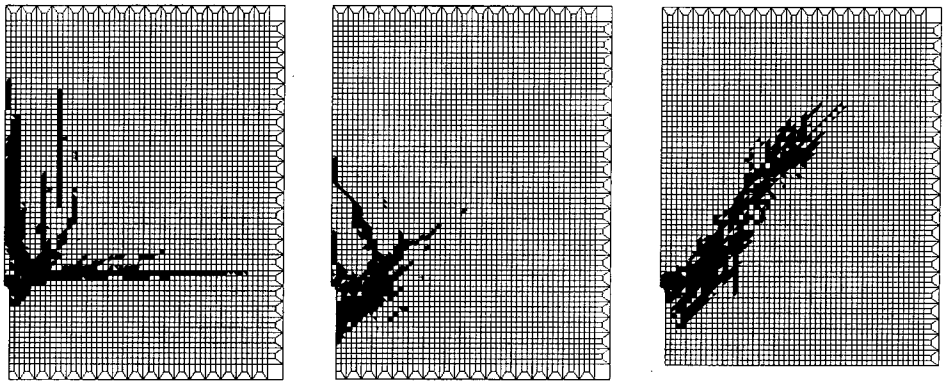
with the experimental observation of the dimple fracture surfaces as shown in Fig.3.



(a) Large voids (b) Small voids

Fig.8 Nucleation of large and small voids

In general, large voids are nucleated from large impurities or segregated particles. They are distributed in a random manner in the material. In 3PB specimen, high dilatational area spreads around the crack tip. Then large voids may be nucleated in many locations with different levels around the crack tip (Figure 8(a)). As a result, the dimple fracture surface becomes rough and many large voids are observed on the dimple fracture surface. In CCB specimen, the high dilatational stress area is restricted in a narrow area. Then large voids are not nucleated so many, and small voids are nucleated in this narrow area. It is the reason that the dimple fracture surface of CCB specimen is smooth and no large voids are observed on the fracture surface(Figure 8(b)). Comparing Figure 6(b) with (c), and Figure 7(b) with (c), One estimates that the fracture behavior of CCT specimen is between the process of 3PB and CCB specimens.



(a) 3PB (b) CCT (c) CCB

Fig.9 Fracture pattern(Two dimensional analysis)

Figure 9 shows the results of the fracture analysis using two dimensional models. In 3PB specimen, the fracture area spreads in wide area around the crack tip, and it is very sharp and smooth in CCB specimen. These figures agree very well with the experimental ones qualitatively.

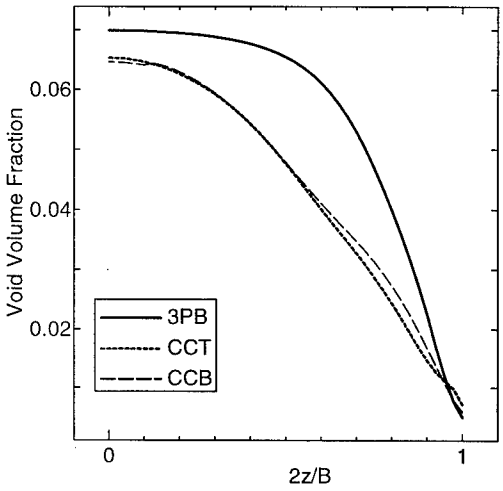


Fig.10 Distribution of void volume fraction along the crack tip

The distributions of void volume fraction at the crack tip along the crack front are shown in Figure 10. The abscissa of this figure is the location along the thickness direction. 2z/B=0.0 means the mid-plane of the specimen, and 1.0 is the surface of the specimen. The void volume fraction of 3PB specimen is nearly constant inside of the specimen, and decreases near the free surface. The results of CCT and CCB specimens are similar to each other. They keep to decrease from the mid-plane to the free surface. It is estimated that the dimple fracture area is wide in 3PB specimen and narrow in other specimens. It is the reason that the 3PB specimen is used as the standard specimen for the fracture toughness evaluation in the testing standard.

4. CONCLUDING REMARKS

By changing the loading condition at the crack tip, fracture tests were conducted using three kinds of specimens. Macroscopically, the change of the constraint condition at the crack tip results in the difference of the apparent J_{IC} values. Microscopically, it appears the difference of the dimple fracture process, such as void nucleation and growth. It is shown that such effect can be simulated qualitatively by the three-dimensional FEM analysis using Gurson's constitutive equation. By changing the thickness of the specimen, the thickness effect on the constraint condition may be evaluated by this method. It is our further target.

REFERENCES

1. T. L. Anderson, Int. J. Fracture, 41 (1989) pp.79-104
2. W. A. Sorem, R. H. Dodds, S. T. Rolfe, Int. J. Fracture, 47 (1991) pp.105-126
3. O'Dowd N. P, and Shih C. F., J. Mech. Phys. Solids, 39 (1991) p.989
4. Xia L. and Shih C. F., J. Mech. Phys. 44 (1996) p.603
5. Ruggieri C. and Dodds Jr., Int. J. Fracture, 79 (1996) p.309
6. Koers R. W. J., Kroom A. H. M., and Bakker A., Prediction of Cleavage Fracture in the Bittle to Ductile Transition Region of a Ferric Steel, Constraint Effects in Fracture Theory and Applications: 2nd Volume, ASTM STP 1244, (1995)
7. JSME Standard S-0001, Japan Society of Mechanical Engineers, Tokyo(1981)
8. V. Tvergaard, Int. J. Fracture 18 (1982) pp.237-252

Key Engineering Materials Vols. 183-187 (2000) pp. 881-886
© 2000 Trans Tech Publications, Switzerland

Microstructure of the Carbon and the Polypropylene Hydrid Fiber Reinforced Concrete Acted by Bending and Tensile Stress

H.B. Qi, Y. Hua, Z.Q. Jiang, S.Z. Huang and S.B. Zhang

Research Institute of Materials Science and Engineering, Shijiazhuang Railway Institute,
15 Beihuan east road, Shijiazhuang, Hebei 050043, China P.R.

Keywords: Carbon Fiber, Hybrid Fiber Reinforced Concrete, Microstructure, Polypropylene Fiber

ABSTRACT

Specimens of carbon and polypropylene hybrid fiber reinforced concrete (C-P HFRC), which acted by the bending and tensile stresses, were tested in a Scanning Electron Microscopy (SEM). Fibers pull-out, fiber debonding from matrix and fiber fracture were dynamically observed. The C-P HFRC's failure morphology and processes were described in detail. Results indicate that, in the tensile district, debonding between the matrix and the fiber occurred at approximately 45° to the tensile direction, and a great number of carbon fibers were pulled out, a small number of polypropylene fibers were greatly deformed and fractured. As the C-P HFRC enduring the bending stress, both the carbon and the polypropylene fibers were debonding from the matrix along the fiber latitude, and some of the fibers were fractured. When the stress state was on relatively high level, the stress was always first transferred from the matrix to the carbon fibers. If the carbon fibers could not bear the stress, the polypropylene fibers would undertake most of them and lead to a large amount of deformation induced failure. In the section, where the carbon and the polypropylene fibers were orthogonal distributed, the fibers perpendiculars to the principal stress were fractured by tensile stress, but the fibers parallel to the principal stress had no damage. As a whole, some hybrid effects on the C-P HFRC's macroscopic properties were examined.

1. INTRODUCTION

Research on the properties of the carbon and the polypropylene hybrid fiber reinforced concrete (C-P HFRC) is not fully carried out until recent years [1, 2]. When the C-P HFRC acted by the bending and tensile stress, respectively, the damage characteristics such as fiber deform, fiber fracture and fiber pull-out from the matrix, were received relatively little attention. But these characteristics were the fundamental conditions for applying the C-P HFRC as a structure material. Meanwhile, research on fiber pullout, deform and fracture can help us to understand the strengthening mechanism and the effects of carbon fiber and the polypropylene fiber on the concrete.

The purpose of this paper is to reveal the damage and failure Characteristic of the C-P HFRC, which acted by the tensile stress and the bending stress respectively, in a SEM environment. This could lead the C-P HFRC to actual applications.

2. EXPERIMENTAL PROCEDURES

2.1. Raw Materials

Basic properties of fibers are outlined in Table 1.

Table 1. Fiber properties

	Diameter (μm)	Density (g/cm)	UTS (MPa)	Modulus (GPa)	Poisson's Ratio	Elongation (%)
Ⅰ-type carbon fiber	6. 0	1. 60	2555	235	0. 35	1. 2
Polypropylene fiber	10. 0	0. 90	400	8. 0	0. 29	8. 0

The matrix of the C-P HFRC is the Ⅱ - type Portland cement and it's flexural strength at temperature 20±3℃ and relative humidity ≥90% and after 28d is 7.8MPa.

2.2. Compact Sample

The W/C ratio of the compact samples was 0.50, C:S:W=1:3. 0: 0. 50, the volume fraction of the carbon fiber and the polypropylene fiber were 1.0, 1.5 and 0.5, 0.7, respectively. The size of the compact sample was 10×5×50mm. The laying of hybrid fiber had two types: one was along the length direction, the another was two dimensional orthogonal distributed.

2.3. Experimental Methods

Three-point bend testing method was applied in this paper. When the specimens were applied by the tensile stress, both ends of the specimen were stuck by load heads with epoxy resin. All of the tests were tested inside a SEM, which enable to observe and take photos for fibers debonding, fibers cracking and fibers fracturing. The loads were gradually applied.

3. RESULTS AND DISCUSSION

As the C-P HFRC specimen failure took place under the bending and tensile load, respectively, the failure morphology of the carbon fibers and the polypropylene fibers could be approximately distinguished as the following six forms:

(1) when the C-P HFRC acted by the tensile loads, the interface bonding failure between the fiber and the matrix took place at 45° to the tensile direction, accompanying with a small amount of fibers fractured. (See Fig. 1 and Fig. 2)



Fig.1. Images of the C-P HFRC debonding interface at 45° to the tensile direction(SEM)



Fig. 2. Images of the C-P HFRC tensile failure(SEM)

This indicates that the bonding strength between the fiber and the matrix was higher than the tensile stress, and a number of fibers fractured because it's tensile strength were lower than the tensile stress.

(2) When the C-P HFRC applied by the bending loads, a greater degree of the carbon fiber was pulled-out, and a small number of the polypropylene fiber had a deformation induced fracture (See Fig. 3 and Fig. 4) in the tensile regime. This indicates that when the loads transfer from the matrix to fiber, the carbon fiber first beard absolutely loads which led itself to being pulled out at the weaken bonding strength between the carbon fiber and the matrix. Subsequently, the loads transfer to the polypropylene fiber, some of the polypropylene fibers were fractured as the bonding strength between the polypropylene fibers and the matrix was higher than it's tensile strength, and a small amount of the polypropylene fibers had a large deformation. As a result, the C-P HFRC was subjected to a large deformation too.



Fig.3. Track of the carbon fiber pull-out from the matrix



Fig.4. Images of the polypropylene fiber deformed and fractured (SEM)

(3) When the volume fraction of the carbon fiber was higher than that of the polypropylene fiber and the C-P HFRC acted by tensile loads, it could be found that both the carbon fiber and the polypropylene fiber were uniformly fractured at the fracture surface before deformed. (See Fig. 5 and Fig. 6)

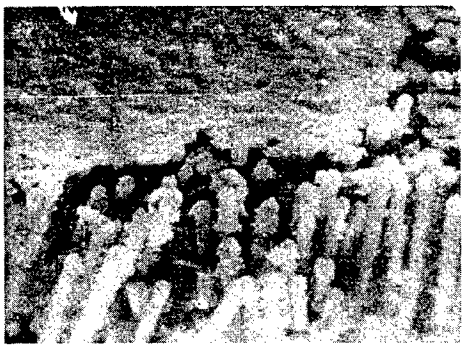


Fig.5. Images of fiber were debonding from the matrix and the polypropylene fiber produced ductile deformation

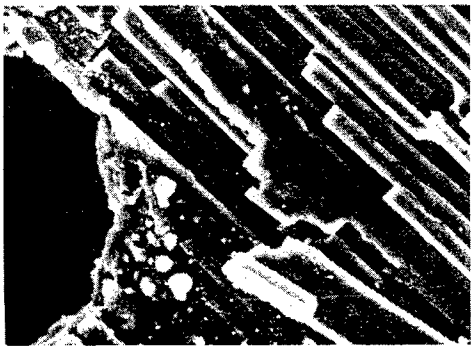


Fig.6. Images of the uniformly fracture surface(SEM)

(4) When the C-P HFRC specimen acted by the bending loads, the debonding took place along the carbon and the polypropylene fibers length direction and some of fibers crazed. (See Fig. 7, Fig. 8 and Fig. 9)

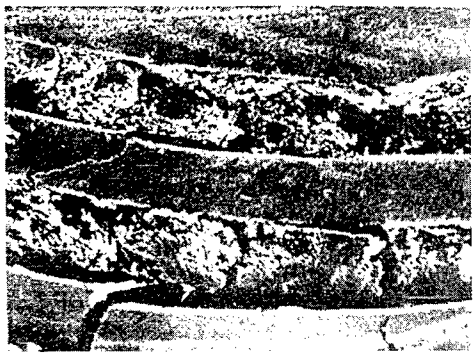


Fig.7. Fibers debonding along the length length direction and crazing



Fig.8. Fibers peel off from the matrix at the fracture surface, but still "bridge" the matrix



Fig.9 Morphology of the C-P HFRC bending failure

(5) At the lower stress states (σ / σ max=0.4～0.6), the propagation of internal crack could be hindered by the carbon fibers and the polypropylene fibers are shown in Fig. 10. The cracks can continue to propagate when stress increase to cause the fibers being pulled out or fractured.

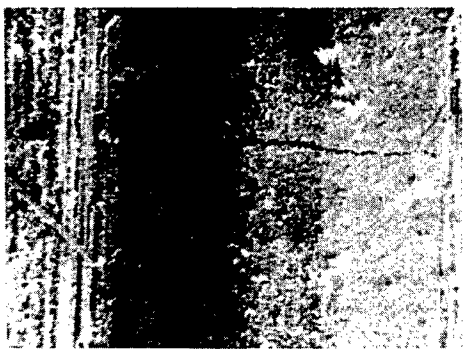


Fig.10. Images of the internal crack tip which hinder by fibers (SEM)

(6) In the specimen, where the carbon and the polypropylene fibers were orthogonal distributed, the fibers perpendicular to the principal stress failure in a tensile fracture, but the fibers parallel to the principal stress had almost no damage. (See Fig. 11 and Fig. 3)

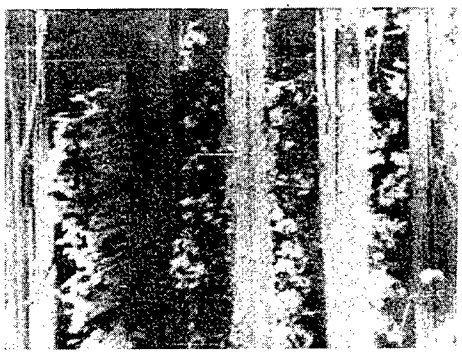


Fig.11. Images of surface which fibers were orthogonal distributed (SEM)

From the two figures, we could find out that this section was highly stress-insensitive, and the bonding strength between the fibers and the matrix was very high and most of the fractured fibers fractured along the fiber length direction.

4. CONCLUSIONS

The following conclusions can be drawn from the present study.

(1) The microstructure of the C-P HFRC acted by the bending and the tensile load produced obviously changed, transferring from the early continuos development to the later noncontinous development.

(2) With the increasing of the stress level, the carbon fibers and the polypropylene fibers could effect at different structural levels. When the stress level was relatively low the hybrid fibers would hinder the crack propagate. When the stress level was relatively high, the carbon fibers were debonded from the matrix and eventually fractured. Most of the polypropylene fibers were fractured and produced a large deformation.

(3) The hybrid fiber failure in the C- P HFRC exhibits six basic types which could be determined by the stress level, the interface bonding strength and the fiber volume fraction and so on.

(4) The strengthening and toughening of the C-P HFRC were due to the hybrid fiber which could eliminate the crack sources and hinder the crack propagate.

REFERENCE

1. S. Diamond. Proceeding of a Conference Held at Tapton Hall, England, Sheffield(1976) p.2
2. S. Diamond and S.Mindess. Cement Conference Res., **22**(1992) p.67

Key Engineering Materials Vols. 183-187 (2000) pp. 887-892
© 2000 Trans Tech Publications, Switzerland

Acoustic Emission Technique for Pipeline Leak Detection

Min-Rae Lee[1] and Joon-Hyun Lee[2]

[1] Graduate School of Mechanical Design Engineering,
Pusan National University, Pusan 609-735, Korea

[2] School of Mechanical Engineering,
Pusan National University, Pusan 609-735, Korea

Keywords: Acoustic Emission, Attenuation-Based Method, Leak Detection, Nondestructive Evaluation, On-Line Monitoring, Source Location, Time-of-Flight Base of Method

ABSTRACT

In this study, acoustic emission(AE) technique has been applied to detect pipeline leaks. There have been analyzed using two different methods for determining source location; 1) reduction in signal amplitude with increasing distance form the source(attenuation-based methods), and 2) increase in signal transit time with increasing distance from the source(time-of-flight based methods). The results on the characteristics of wave propagation and the effect of attenuation in pipeline are presented. It was confirmed that the characteristics of the signal generated by the turbulence of gas in the pipeline is wide band signal having less than 600KHz.

1. INTRODUCTION

Acoustic Emission(AE) technique[1] is one of the nondestructive testing with demonstrated capabilities for monitoring structural integrity, detecting leaks and incipient failure in mechanical equipment, and for characterizing materials behavior[2,3]. Especially AE method is very useful to prevent catastrophic failure of large scale structures with unknown discontinuities. There have been many efforts on studies of acoustic emission because of an advantage of on-line monitoring during an in-service inspection. But the leak study on a pipeline is relatively rare[4-6] and has not yet been fully explored.

Frequently, the gas or oil is most transported by a network of pipelines. Long , high volume transmission pipeline are monitored for evidence of leaks using available techniques, but in the most cases the leak is detected only after significant volume of fluid was lost from the pipeline. Since the failure of piping systems generally appears to start with a small inaudible leak, it is necessary to detect a starting leak, just before failure. The leak in a pipeline generated acoustic waves, these waves propagate in the pipeline wall. Especially, the turbulent flow through a breakage generates waves propagating alone the pipeline wall. In this study, AE technique has been applied to detect pipeline leaks and there have been analyzed using two different methods for determining source location; 1) reduction in signal amplitude with increasing distance from the

source(attenuation based methods), and 2) increase in signal transit time with increasing distance from the source(time-of-flight based methods).

2. ATTENUATION BASED METHODS

Typically, there exist two types of acoustic emission signals; burst and continuous signals. The leaky signal is continuous signal and it become overlapped to the extent that differentiation between the individual events is sometimes impossible. For this reason, it should concern with parameters such as r.m.s. voltage when dealing with AE leak monitoring. Also, noise signal will cause error in calculating source location. Such an error does in face occasionally occur in practice. Therefore in this case, the r.m.s.(root mean square) value is used to evaluate leak source location.

The effective of r.m.s. value E of the high frequency sound transducer signals E_i is used as a measuring variable according to the formula ;

$$E = \sqrt{\frac{1}{T}\int E_i^2 \cdot dt} = \left(\frac{1}{T}\int E_i^2 \cdot dt\right)^2 \quad (1)$$

Assume that the r.m.s.(E_{eff}) value of measured signal is the sum of the noise r.m.s.(E_0) and the true signal r.m.s.(E_L), so that ;

$$E_{eff} = \sqrt{E_L^2 + E_0^2} \quad (2)$$

Then if the noise is known, the true signal can be calculated. Also, in order to more accurate leak location, the effective measuring position X is compensated by means of special calibration by calculation, in accordance with the following formula ;

$$X = \alpha_1 \cdot x \quad (3)$$

$$X = X_1 + \alpha_2 (x - x_1) \quad (4)$$

$$X = X_{II} + \alpha_3 (x - x_{II}) \quad (5)$$

The effective measuring position X_1, X_2, X_3 and X_4 for the four AE sensors are plotted in Fig. 1. These effective measuring position $X_1 \ldots X_4$ are obtained from the location coordination x_1,x_2,x_3 and x_4 of the measuring position by taking the various damping coefficients $\alpha_1, \alpha_2, \alpha_3$. In the segment I, it is thus generally true that $X = \alpha_1 \cdot x$. In the segment II, it is true that $X = X_1 + \alpha_2 (x - x_1)$. In the segment III, it is true that $X = X_{II} + \alpha_3 (x - x_{II})$. Fig. 1 shows bar diagram in which the aforementioned r.m.s. values are shown through effective measuring position X.

Two compensating straight lines S_1 and S_2 that are inclined opposite one another can then be drawn through the end points of the bars. The intersection of these two straight line S_1 and S_2 is ascertained, therefore it is identified the actual leak point.

2.1 TIME OF FLIGHT BASED METHODS

The linear source location method has been applied to detect leak in the pipelines by using the transit time difference between two test detector(sensor). Assume that an AE signal occurs

somewhere on the pipe and that resulting elastic waves propagate in the both directions at the same constant velocity (Fig. 2). However, if the time difference between the signals is measured, source location can be performed. If the difference between signals at sensor 1 and sensor 2 was zero, it would indicate a precisely midway between the two sensors.

The time difference between signals is equal to the time taken to cross the entire pair separation, or ;

$$\Delta T = \frac{L}{C} \tag{6}$$

where L is the distance between sensors and C is the constant wave velocity ; and ΔT is the time difference. The source location would then be location at sensor 2. In general, the source location d is given by ;

$$d = \frac{1}{2}(L - \Delta T \cdot C) \tag{7}$$

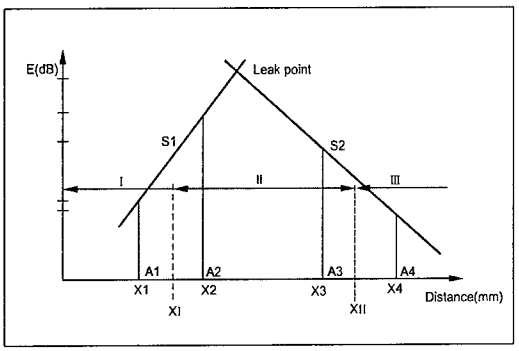


Fig.1 The bar diagram of effective measuring Position by r.m.s. values.

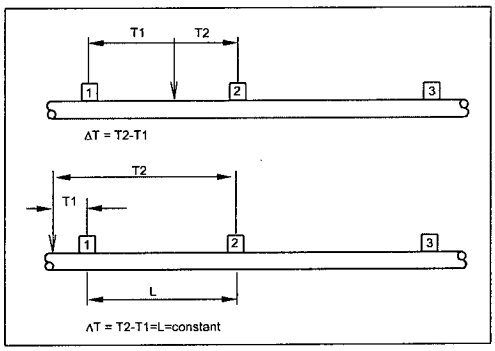


Fig. 2 The transmission time difference between sensors for linear source location.

3. MATERIAL AND EXPERIMENTAL PROCEDURE

Experimental measurements were made on a 6m long, 19mm outside diameter and 1mm in wall thickness. The material of pipeline was copper. The test was performed on nitrogen gas as flow media and run at pipeline pressure 5 and 10 kg_f/cm^2. The leak sources with hole sized ranging from 0.3 to 1.0mm were drilled in the pipe. Fig. 3 illustrates a schematic diagram of experimental apparatus for AE leak testing.

An experimental set-up is consisted of AE equipment of MISTRAS system to record r.m.s. signal level and a digital oscilloscope to record waveforms and spectral information. Four AE sensors were used ; three resonant types with 150kHz, 225kHz and 500kHz(PAC Model R15, MICRO 30, PICO), and one broadband type(PAC Model WD). The sensors were positioned along the pipeline, as shown in Fig. 3. AE signals detected by sensors are amplified at the preamplifier having a fixed gain of 40dB. After passing the band pass filter of 100~300kHz to remove background noise signal, the signals were further magnified by the main amplifier(40dB), and then transferred to the AE system. The detected signals are recorded and the r.m.s. values of each

detector signal are compared in the system with the corresponding background signal stored in the computer memory. Leak is detected on the basis of the significant difference in the leak signal and background signal.

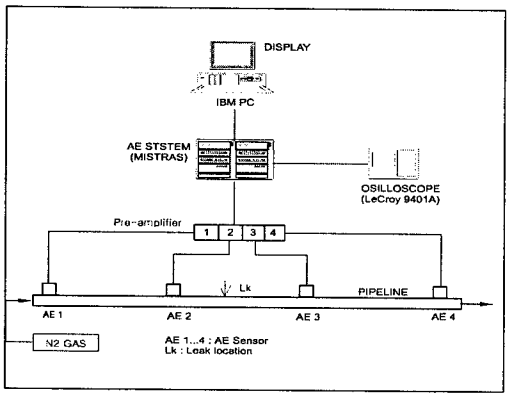


Fig. 3. The schematic diagram of experiment set-up for leak detection.

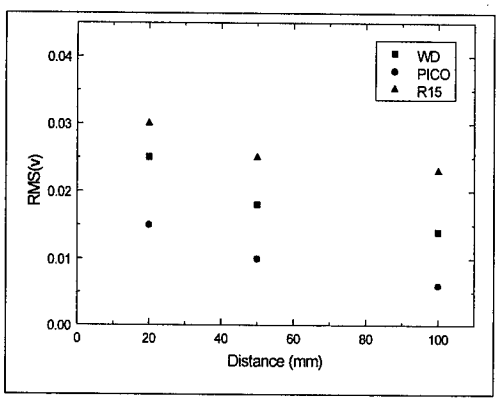


Fig. 4. The comparison of measuring sensitivity of sensor for leak.

4. EXPERIMENTAL RESULTS

Fig. 4 shows representative data obtained from the 1.0mm diameter holes at a pressure of 10 kg_f/cm^2. As shown in this Figure, the sensitivity of the system was decreased by increasing the spacing between the sensors. However, in this case, the lowest frequency sensor(150kHz) was the best for detection a small leak. The broadband sensor was the worst, hardly detecting anything less than the 0.3mm source.

Fig. 5 shows typical AE waveform and its corresponding frequency spectrum which were taken for the largest(1.0mm) leak source at 10 kg_f/cm^2. In addition, AE waveform and the correspond frequency spectrum for the same leak source at 5 kg_f/cm^2 are also shown in Fig. 6. It was found that both spectrum are concentrated in the range of 140~160kHz. However, the signal level normally increased with the pressure and hole size.

Fig. 7(a) shows the bar diagram taken from r.m.s. values of various sensors in which does not compensated for damping coefficient at various locations along a measurement segment. From the result of the Fig. 7(a), the leak location was indicated about 2,030mm for actual leak point(about 1,800mm) and the measuring error was more than 7 percent. Such an error does in fact occasionally occur in practice. As shown in Fig. 1, the source location method to eliminate the error was performed. The method has proven itself especially in the case where two sound-damping components are located in the region between two sensors, especially if such sound-damping components are also located in the vicinity of the leak.

Fig. 7(b) is a bar diagram in which the aforementioned r.m.s. value are shown through effective measuring position X. It could be obtained more accurate leak location within 5 percent of the error comparing with Fig. 7(a). This is because local differences are compensated by means of special calibration for calculation from Eq.(3-5).

Fig. 8 shows the result of leak location obtained from linear source location method based on the time-of-flight. As shown in Fig. 8, the measuring error of leak location was more than 8 percent. In practice, the determination of ΔT between the each sensor is difficult because of complex

physical phenomenon such as wave propagation path as well as mode conversion.

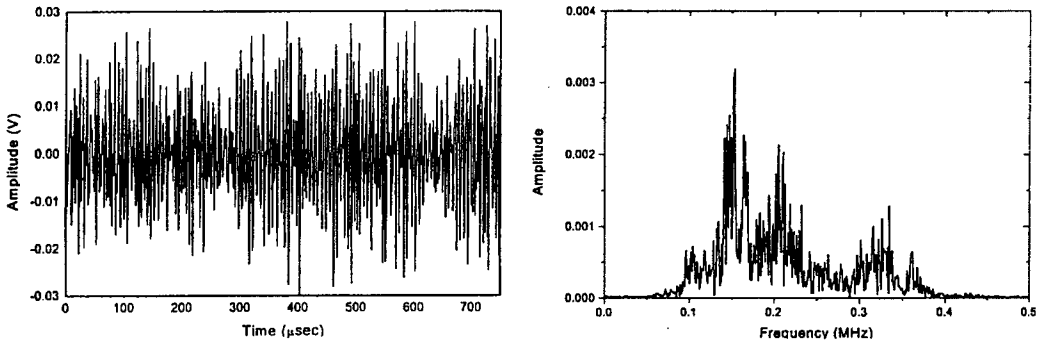


Fig. 5. The waveform and spectrum at $10Kg_f/cm^2$

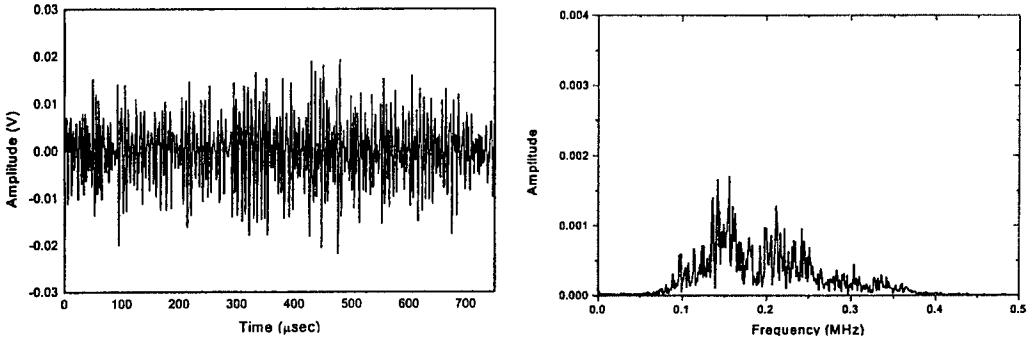
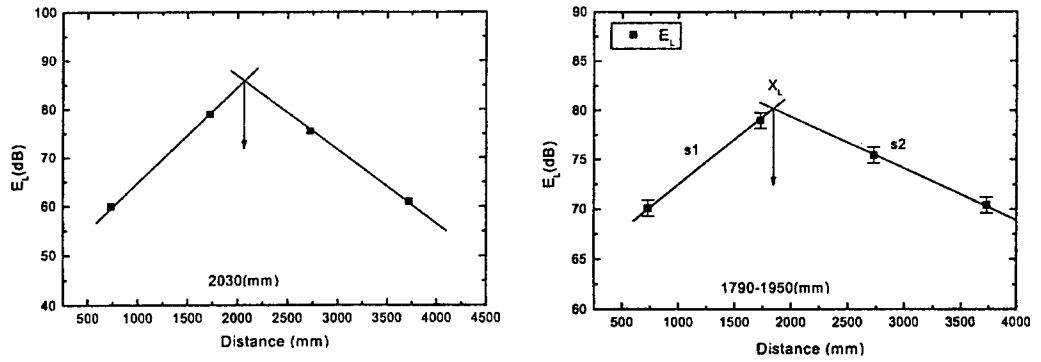


Fig. 6. The waveform and spectrum at $5Kg_f/cm^2$



(a) The r.m.s. value vs. each sensor distance without effective location coordination x.

(b) The r.m.s. value vs. each sensor distance through effective location coordinates x.

Fig. 7 The bar diagram at various location along a measurement segment.

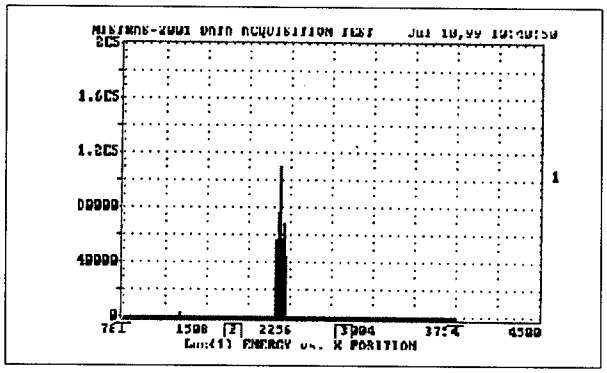


Fig. 8. The source location of leak based on time-of-flight

From the above the results, it was significant decrease in the measuring error of leak source location by attenuation based method. However, the precision of leak source location might be improved by considering more accurate value of the attenuation coefficient. The attenuation base method for source location may be employed in the primary loop of a nuclear power plant.

4. CONCLUSION

In this study, acoustic emission technique has been applied to detecting leak of the pipeline. The results obtained in the present study are as follows ;

1. The attenuation based method which included a bar diagram at various locations along a measurement segments was more effective to detect leaks. The precision of leak source location may be improved by considering more accurate values of the attenuation coefficients.

2. The sensitivity to leak detect was increased more at low-frequency sensor than at high-frequency sensor and resonant sensor having 150kHz was the best for detecting leak in the study. Most of spectra of leak signals were concentrated in the frequency band between approximately 140 and 160kHz

ACKNOWLEDGEMENT

This work was performed by the financial support of the Safety and Structural Integrity Research Center under Sungkyunkwan university

REFERENCE

1. Nondestructive Testing Handbook 5, American Society for Nondestructive Testing, Inc.,(1987)
2. J. H. Lee and M. R. Lee, ICCE 5, U.S.A. (1998) p. 533-534
3. J. H. Lee and W. J. Sung, Review of Progress in Quantitative Nondestructive Evaluation 17, Plenum Press, New York, U.S.A. (1998) p. 549-556
4. J. Reason, Acoustic Leak Detection Provides Early Warning of Piping Failure, in Power (1987) p. 372-373
5. A. E. Lord, Jr., J. N. Densher, and R. M. Koerner, J. Materials Evaluation (1976) p. 49-60
6. A. A. Pollock and S. Y. Hsu, J. Acoustic Emission 1 (1982) p. 237-240

Key Engineering Materials Vols. 183-187 (2000) pp. 893-898
© 2000 Trans Tech Publications, Switzerland

Fracture Behaviors of GFRP Plates Subjected to Impulsive Loading

Bustami Syam[1], Hiroomi Homma[2] and Kohji Nakazato[2]

[1] Department of Mechanical Engineering, University of Sumatera Utara,
Jl. Almamater, Kampus USU Medan 20155, Indonesia

[2] Department of Mechanical Engineering, Toyohashi University of Technology,
1-1 Tempaku-cho, Toyohashi 441-8580, Japan

Keywords: Damage Zone, Dynamic Fracture Toughness, Viscoelastic

ABSTRACT

The dynamic fracture tests to obtain the fracture toughness property using an air-gun apparatus were carried for a glass fiber reinforced plastic specimen. The dynamic fracture toughness was evaluated by examination of cracking at an initial slit root of the specimens. After impact, before the crack initiation at the slit root, a whitened damage zone was created near the slit tip. The damage zone consisted of micro cracking in the matrix, de-bonding between a fiber and the matrix, and the fracture of the fibers. The comparison of the dynamic fracture toughness and static fracture toughness showed that the former is around 12 Mpa$\sqrt{m}$ and apparently higher than the later, 7 MPa$\sqrt{m}$.

1. INTRODUCTION

Structural elements made of composite, e.g. fiber reinforced plastics (FRP) composites, are now used in a variety of components for automotive, aerospace, marine, and architectural structures in addition to consumer products such as skis, tennis racket, and golf clubs for they possess high specific strength, high specific stiffness, and high resistance against environmental attack.

Fracture toughness of FRP is one important property to be evaluated when the application of FRP to aircrafts, ships and other structures is considered. Yanada and Homma [1] evaluated the static fracture toughness of glass fiber reinforced plastic materials taking into account the stable crack growth process. The stable crack growth resulted from a damage zone formed at a crack tip. The detail observation of the damage zone revealed micro-cracking in the matrix, de-bonding of fibers and the matrix, and fiber breaking [2~4]. The matrix of the FRP is plastics that possess more or less viscoelastic. So, a loading rate effect on the fracture toughness was investigated to maintain the FRP structure integrity [5].

In this work, the dynamic fracture toughness is evaluated under impact loading and compared with the static fracture toughness, as a continuation of work that has been done before [6]. Because a damage zone ahead of the crack tip is considered as a controlling factor of the crack initiation, much attention is paid onto the damage zone shape and the mechanisms. To clarify the viscoelastic property of the used glass fiber reinforced plastics, Young′s modulus is also measured in a wide range of the loading rate.

2. EXPERIMENTAL PROCEDURES

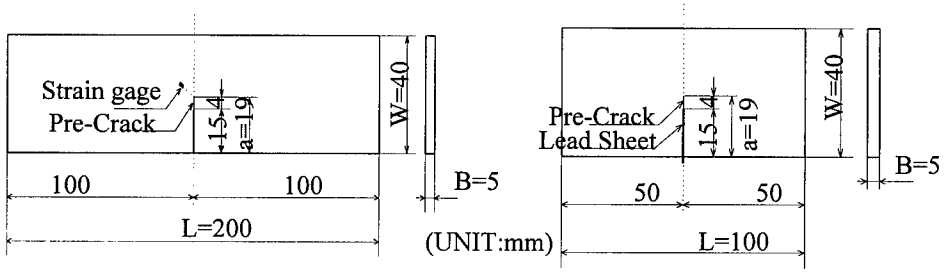
2.1. Material and specimens

A glass fiber reinforced plastic sheet of five layers was fabricated by hand lay up in the laboratory. The sheet is cured for four hours at 120 ^{0}C. The components of GFRP are E-glass chopped strand mat and unsaturated polyester of which physical properties are shown in Table 1 including the physical properties of GFRP laminate. In this work, several kinds of tests were carried out: Young's modulus test, a static and a dynamic fracture toughness test. Dimensions and geometries of specimens used for fracture toughness tests are shown in Fig. 1.

The specimens for the Young's modulus tests are of bars with 100mm in length for four-point bend test and 300mm in length for impact tests. Both specimens have the same cross section: 10mm wide and 5mm thick. Four-point bend specimens are used to measure the Young's modulus under the quasi-static loading rate regime in accordance with the ASTM-D790M standard test method. The Young's modulus at high loading rates was measured by use of the air gun compressor. The static and the dynamic fracture toughness were measured by the three-point bend specimen and the one-point bend specimen shown in Figs. 1(a) and (b), respectively. The initial crack is introduced with a narrow slit of 0.6 mm width and a fine slit of 0.1 mm width is further introduced from the slit edge.

Table 1. Mechanical properties of GFRP

GFRP Laminated	Young's Modulus	11.7 (GPa)
	Poisson ratio	0.32
	Density	1440 (kg/m^3)
	Glass Fiber Contents	33(wt%0
	Glass Fiber Orientation	Random
	Glass Mat	Chopped
	Ply	5
	Matrix	Unsaturated Polyester
Unsaturated Polyester	Young's Modulus	5.4 (GPa)
	Density	1165 (kg/m^3)
Glass Fiber	Young's Modulus	11.7 (GPa)
	Density	2450 (kg/m^3)
	Fiber Type	E Glass



(a) Specimen for the static fracture toughness test

(b) Specimen for the dynamic fracture toughness test

Fig. 1. Specimens for static and impact fracture toghness tests

2.2. Measuring methods of the mechanical properties

Young's modulus

Young's moduli of the unsaturated polyester and the GFRP were measured in accordance with the ASTM-D790M standard for a strain rate of 0.0001 to 1.0 1/s. An air-gun compressor was used for the strain rate beyond 1.0 1/s; the theory of stress wave propagation in one-dimensional bar was adopted [7]. The air-gun test setup is shown in Fig. 2. The same setup is also used for the dynamic fracture toughness test. Only a specimen is replaced with the specimens shown in Fig. 1(a) and (b) for the dynamic fracture toughness.

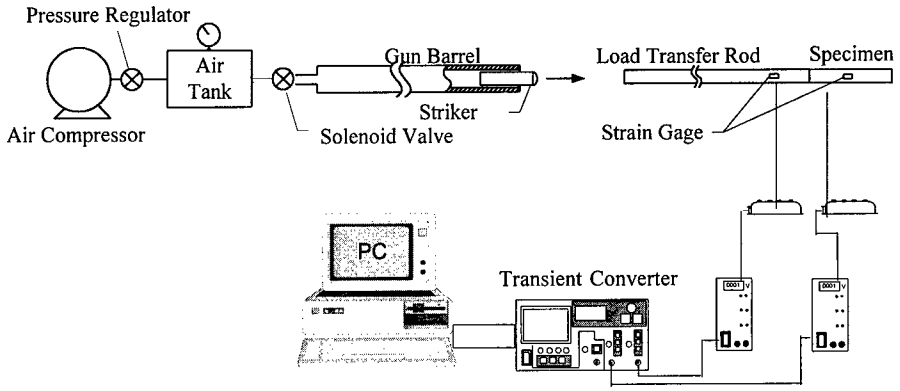


Fig. 2. Air-Gun Apparatus

Fracture toughness

A static fracture toughness test was carried out in accordance with the ASTM-E399 standard for the plain strain fracture toughness test for metallic materials. However, the 5% offline method to define the crack initiation cannot be applied to the GFRP specimen, because the nonlinear property in the load-deflection curve resulted not from the plastic deformation at the crack tip, but from a damage zone consisting of micro-cracking of the matrix, de-bonding of fibers and the matrix, and fiber breaking. The crack initiation is defined as cracking more than 90% of through the thickness at the slit root. The observation method is illustrated in Fig.3. The dynamic fracture toughness test was carried out by use of the test setup as shown in Fig. 2. The detail test method is not described here, because it is described somewhere [2,6].

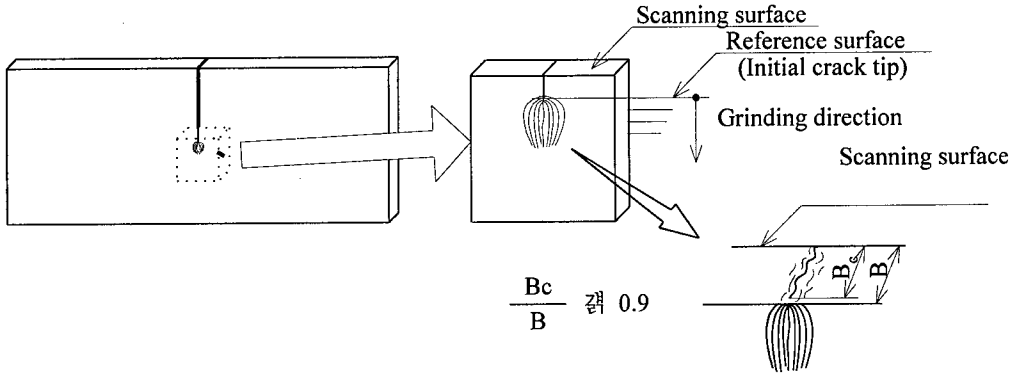


Fig. 3. Measurement of Crack Growth

The crack initiation was defined by the same method described above for the static fracture toughness test. The stress intensity sustained by the specimen was measured by a strain gage mounted near the crack tip. This method was developed by Dally and Sanford [3] for linear elastic materials such as metals. Applicability of this method to viscoelastic materials such as GFRP will be discussed later.

3. EXPERIMENTAL RESULTS

3.1. Strain rate effect on Young's modulus

Young′ s moduli of the unsaturated polyester and the GFRP are plotted as the function of the strain rate in Figs. 4(a) and (b). In the figures, the red marks indicate the results measured by the ASTM standard and the blue marks indicate the results measured by the air-gun impact loading system. The Young′ s modulus of the unsaturated polyester increases by 20% as the strain rate increases from 10^{-5} to 10^{3} 1/s whereas the GFRP Young′ s modulus increases by 30% with the same order of an increase in the strain rate. The sensitivity of the Young′ s modulus against the strain rate is more intensive in the GFRP than in the unsaturated polyester alone.

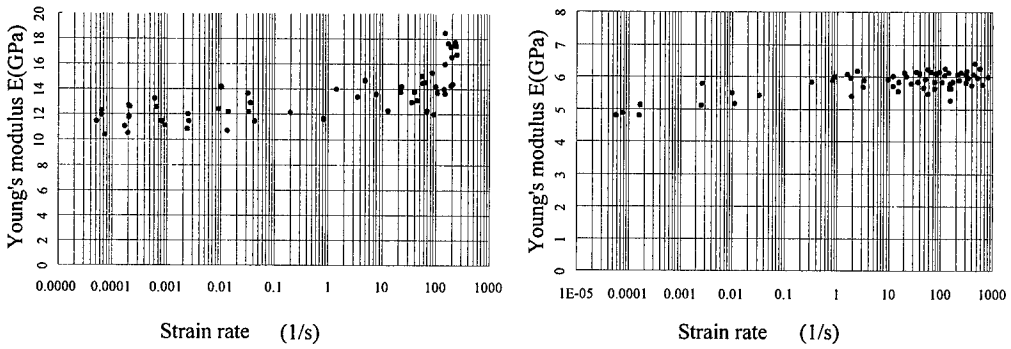
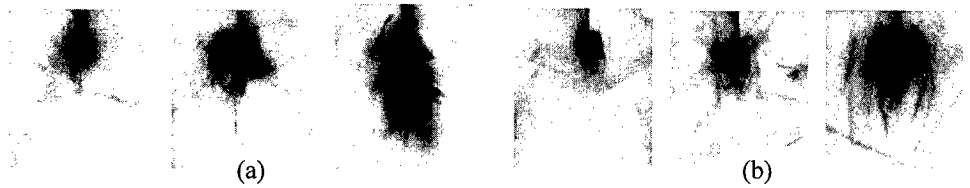


Fig. 4. Young's modulus vs. Strain rate

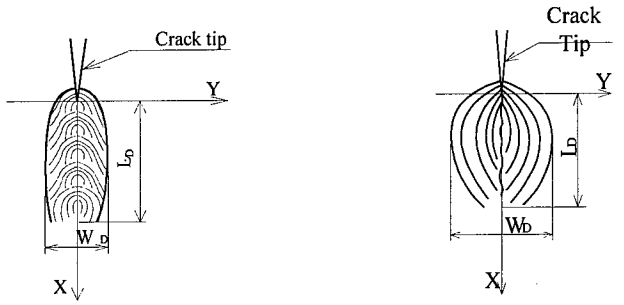
3.2 Damage zone and fracture toughness

A damage zone is formed ahead of the crack tip prior to the crack initiation. The close observation of the damage zone clarified that the damage results from micro-cracking in the matrix, de-bonding of interfaces between fibers and the matrix, and fiber breaking. The damage zone can be identified as a whitened pattern. It is visible by naked eyes. Observation results of the damage zone are shown in Figs. 5(a) and (b). The photographs were taken by use of the transmitted light through the specimen thickness.



(Unit: MPa $\sqrt{m}$)

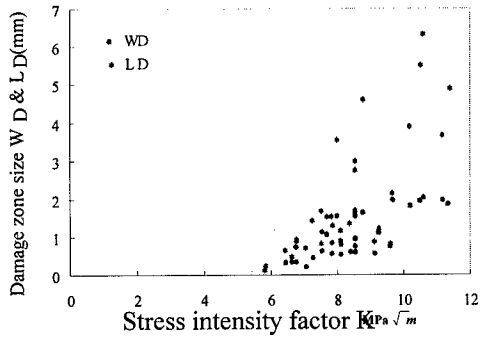
Fig. 5. Damage zone ahead of the crack tip
(a) Damage zone under static loading; (b) Damage zone under dynamic loading



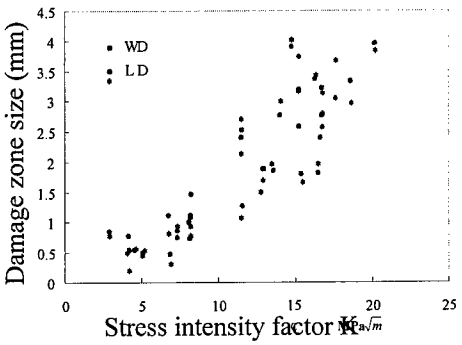
(a) (b)

Fig. 6. Schematic diagram of damage zone developed ahead of the crack tip
(a) under static loading; (b) under dynamic loading

The schematic views of the damage zones formed under the static and the dynamic loading are shown in Fig. 6. Under the dynamic loading, the damage zone is approximately circular and increases in the diameter with the applied stress intensity. On the other hand, the damage zone under the static loading is elliptical and increases in the major axis while the minor axis is kept constant. The sizes of the damage zone, W_D and L_D are plotted as a function of the applied stress intensity in Fig. 7(a) and (b). Under the dynamic loading, the damage zone is formed by the low stress intensity level of around 3 MPa$\sqrt{m}$ and increases in both the length and the width linearly with the stress intensity up to 4 mm. Under the static loading, the damage zone is formed by around 6 MPa$\sqrt{m}$ and increases in both the length and the width up to 2 mm. A crack growth amount measured by the method described above is plotted as a function of the applied stress intensity in Fig. 8. Fracture toughness value for the crack initiation is defined as 7 MPa$\sqrt{m}$ for the static loading and 13 MPa$\sqrt{m}$ for the dynamic loading.



(a) static loading



(b) dynamic loading

Fig. 7 Damage zone size as a function of applied stress intensity

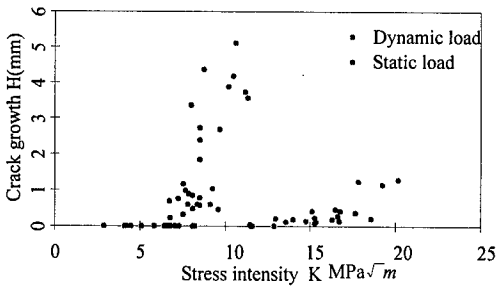


Fig. 8. Crack growth amount as function of applied stress intensity

4. DISCUSSION

4.1. Effect of viscoelastic properties on the crack tip stress

It should be noticed that the GFRP is a viscoelastic material as shown in Fig. 4. In the first calculation, Young's modulus is uniform over all the specimens and takes the value of 12 GPa. The strain rate is the highest at the crack tip and in the range of 5×10^{-3} to 1 1/S. As seen in Fig.4(b), Young's modulus does not change in the strain rate range mentioned above. The strain rate at the crack tip is the highest and 10^3 1/S. The strain rate decreases to 1 1/S as the position is 1 mm far from the crack tip. As seen in Fig. 4(b), Young's modulus increases to 16 GPa at the crack tip.

5. CONCLUSIONS

The conclusions of the present study are obtained as follows: (1) Dynamic fracture toughness of GFRP is much higher than the static one; the dynamic one is around 13 MPa$\sqrt{m}$ whereas the static one is around 7 MPa$\sqrt{m}$, (2) Attributes of the damage zone ahead of the crack tip are distinguishable between the static and the dynamic loading. For the same applied stress intensity, the impulsive loading built a smaller damage zone than the static loading. This may result from the viscosity of the matrix, and (3) Appearance of the damage zone was also different in both the loading types. In the damage zone produced by the static loading, all the mechanisms, the micro cracking, debonding of the fibers and the matrix and fiber breaking took place uniformly over the zone. On the other hand, the debonding characterized the damage zone by the dynamic loading. It means that the heterogeneous damage takes place under the dynamic loading.

REFERENCES

1. H. Yanada and H. Homma, J. of Material Science, **31** (1983)
2. H. Homma and K. Mitsubayashi, Int. J. of Materials and Product Technology, **4** No.2 (1989)
3. H. Homma, K. Mitsubayashi, and Y. Kanto, Computational Mechanics' 91, edited by Atluri, Beskos and Yagawa, (1991)
4. Y. Kanto and H. Homma, Trans. of the 11th Int. Conf. on Structural Mechanics in Reactor Technology, Tokyo **G1** (1991)
5. C.T. Liu and M.D. Le, Proc. of 7th International Congress on Experimental Mechanics (1992)

Key Engineering Materials Vols. 183-187 (2000) pp. 899-902
© 2000 Trans Tech Publications, Switzerland

Fatigue Strength Decrease of Structural Materials Caused by Atmosphere Corrosion and Aging

Qing-Xiong Yang and Bin-Tuan Wang

Northwestern Polytechnical University (NPU), Xi'an 710072, China P.R.

Keywords: Atmosphere Corrosion, Fatigue Calendar Life, Fatigue Strength

ABSTRACT

A description of the purpose and procedure of such a long-term atmosphere exposure experiment, the details about the specimen, exposure experiment site, and fatigue strength testing are presented. Some typical testing results are introduced. From these results some interesting conclusions are deduced.

1. FOREWORD

1.1. Purpose of Experiment

Besides the traditional two fatigue criteria of aircraft (flight hours and number of flights), a third criterion is recently demanded: the aircraft service "calendar life".

During service time, the fatigue strength of structural material is continuously decreasing. When predicting an aircraft fatigue calendar life, this decrement should be taken into account. To find out the decrement against calendar year, a long-term experiment is conducted.

For the military aircraft, a very large percentage of hours in its service time is staying on the ground. So the decreasing of the fatigue strength under the ground condition is examined.

1.2. Procedure of Experiment

A lot of specimens have been exposing in an atmosphere environment test station. The specimens are divided into seven parts and planned being tested after exposed in the environment 0, 1, 2, 4, 7, 10 and 15 years to obtain the fatigue strength at such separated duration.

At present, the 0, 1, 2, and 4 year's experiment results have been obtained and will be discussed in this paper.

2. SPECIMEN [1]

The specimens are made of two kind of material: high strength aluminum alloy Lc4-cs and high strength steel 30CrMnSiNi2A. Each material was manufactured to three types of specimen. Type I-- plain plate without hole; Type II-- central holed plate and Type III-- central holed plate with hole cold expanded. The specimen configuration is as Fig.1, dimensions are listed in Table 1. [2] All the specimens are heat treated and surface protected as same as the corresponding structural parts, i.e. aluminum specimens are anodized and painted, and the high strength steel specimens are phosphorated and painted. All holes are filled with no load bolt.

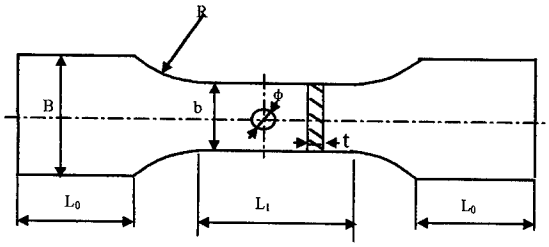


Fig.1. Configuration of specimens [2]

Table 1. Dimensions in Fig.1. [2]

Material	L_1 mm	b mm	B mm	L_0 mm	R mm	ϕ mm	t mm
Lc4-cs	84.6	22	50	60	50	6	4
30CrMnSiNi2A	84.6	22	50	60	50	6	7

3. ATMOSPHERE CORROSION AND AGING TEST SITE [1]

All the specimens have been putting in a testing site located at a worst environment place, The Hainan Island.

That site is 350m by the sea and 12.3m above the sea level. The typical yearly average value of water deposit is 198mm and the pH value of the rainwater is 5.1. The specimens were put in a shed to simulate the structural detail is assembled in the inner portion of an aircraft or the aircraft is put in a hangar.

4. FATIGUE TEST [1]

To test the specimen, a constant load spectrum was applied to the following groups listed in Table 2. For the plain specimens of two materials a various stress level are applied, but all stress ratio (= S_{min} / S_{max}) are taken as 0.06

Table 2. [1]

Specimen Type	P_{max} (MPa)	P_{min} (MPa)	Frequency (HZ)
Lc4-cs Type II and III	300.0	18.0	6
30CrMnSiNi2A Type II and III	800.0	48.0	1

The test purpose is to get the fracture life under the loading spectrum. If the break did not occur over four times of the expected fatigue life, then the test will be ceased.

The reported fatigue life is in cycles by taking logarithm average of the results of five specimens.

5. ANALYSIS AND CONCLUSION

To investigate the decreasing of fatigue strength, a parameter "life increase ratio" R is introduced. The ratio R means: at the same testing load condition, the fatigue life of certain specimen compares with the fatigue life of plain specimen of same material tested at 0 year.

$$R = \frac{\text{fatigue life of certain specimen at certain year}}{\text{fatigue life of plain specimen of same material tested at 0 year}}$$

Some typical curves of R against calendar year are laid out in following figures (Fig.2 and Fig.3).

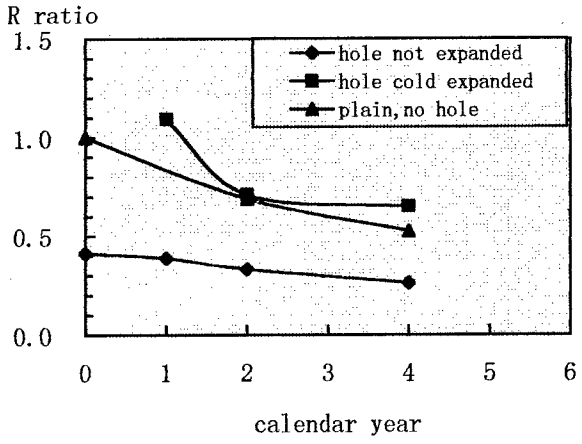


Fig.2. Fatigue life decreasing against calendar year, high strength aluminum Lc4-cs specimen.[2]

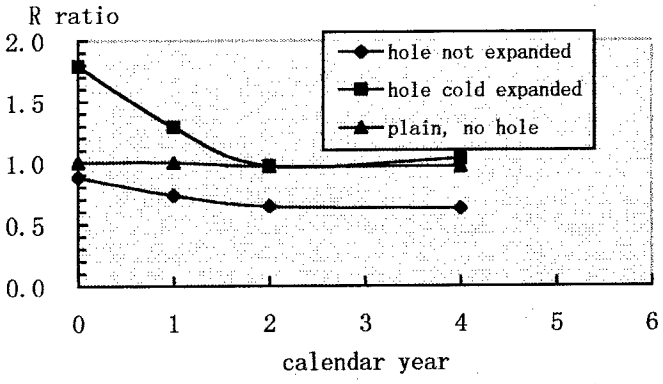


Fig.3. Fatigue strength decreasing against calendar year, high strength steel 30CrMnSiNi2A specimen.[2]

From these figures, some conclusion is deduced as following:

(1) All the holed specimens will decrease their fatigue strength against calendar year. Even the Lc4-cs plain specimen, which is the original material but coated by industrial surface protecting layer, is also decreasing. Only the 30CrMnSiNi2A plain specimen almost did not decrease its fatigue strength.

(2) Hole being cold expanded could significantly increase its fatigue life, the R ratio at 0 year could even rise up to 2~3. But during the first two calendar years, the R ratio is dropping down rapidly. Then afterwards, the R ratio maintains almost the same.

(3) Applying a cold expand process to a hole is superior. It could increase its fatigue strength obviously at any time, compared with a hole not expanded. Furthermore, it makes a cold expanded hole has a fatigue strength not less than that of a plain specimen at any time. In other words: a holed specimen if the hole being cold expanded, it may be treated as a plain specimen in prediction of fatigue life.

(4) When predict the fatigue life of a structure, this decrement of fatigue strength should be taken into account. In present, this account usually did not being noticed. In engineering practice, only let the predicted (by testing or by calculation) fatigue life being divided by a safety coefficient 3~4 to obtain a much smaller value as its service life. Such a coefficient could only be empirical. It should cover much engineering errors and deviations. As for want it also covering the corrosion and aging effect, is it good enough? It has no sound basis.

(5) For a long-term prediction of calendar fatigue life of a structure, approximately using the fatigue strength at 2~4 year of all kind of specimen as a constant value in the calculation, it may be acceptable in engineering practice.

(6) At present time, perhaps only such a long-term exposure experiment could obtain the decrement of material fatigue strength against calendar years. Some times an accelerating test may be conducted in laboratory to obtain the fatigue strength decrement. Which is applying a corrosion environment accompany with the fatigue testing. But the corrosion environment could hardly simulate the real atmosphere environment properly and could not give out the equivalent calendar time as the specimen exposed in real atmosphere environment. Besides it could not involve the aging effect.

REFERENCE

1. Wang Bin-Tuan, Yang Qing-Xiong, et al., Report of Environment Exposure and Aging Experiment on Lc4-cs and 30CrMnSiNi2A Specimens About Fatigue Characteristics (in Chinese), Restricted Report, Nov.1998
2. Same as [1], Sept. 1999, Revised in Mar. 2000

Key Engineering Materials Vols. 183-187 (2000) pp. 903-908
© 2000 Trans Tech Publications, Switzerland

Creep Life and Properties Evaluation by ISM Method and Acoustic Emission for Cr-Mo-V Steels

S.G. Lee

Korea Electric Power Research Institute, Korea Electric Power Corporation,
103-16 Munji-dong, Yusung-gu, Taejon 305-380, Korea

Keywords: Acoustic Emission (AE), AE Count, AE Energy, AE Hit, Creep Life, Creep Rupture Strength, ISM Method, LMP Method, TTP Method

ABSTRACT

In this paper, a study on the prediction of long time creep rupture strength and safety life for Cr-Mo-V steels were performed by using round-bar type specimens under static load at 500～700℃ by the initial strain method(ISM) as a new approach, comparing with the results by time-temperature parameter(TTP) predicting method such as Larson-Miller parameter(LMP), Orr-Sherby-Dorn parameter(OSDP) and Manson-Succop Parameter(MSP), etc. As an important result, the empirical equations for creep life and strength prediction of Cr-Mo-V steels were derived by using the ISM. And also, it was considered that the various creep properties such as initial strain, transition creep, steady state creep, accelerated creep, crack and fracture in creep curve could be qualitatively related to acoustic emission(AE) properties such as counts vs. time, event vs. time, etc.

1. INTRODUCTION

It is one of the fundamental necessities in designing, manufacturing operating and maintaining the rotors to understand correctly the long time creep properties of steam turbine rotors used for power electric generation under high temperature and high pressure. However it is actually inevitable to predict the long time (10^5 hours) strength of practical necessity by extrapolation from the data of somewhat short time creep rupture test[1-2]. For this purpose, TTP method based on chemical reaction speed theory used for extrapolation, such as LMP, OSDP, etc., has been considered and used so far[2-3]. But these TTP,s have some difficulties that the peculiar material constants must be determined for application and also the high degree functions must be used. Otherwise, the minimum commitment method(MCM) developed by the program based on TTP, is also very difficult to understand for actual application. So, in this paper, as more simple method, ISM[4-5] applied to a study on the prediction of long term creep rupture strength and safety life for 1.2%Cr-Mo-V steam turbine rotor steels under static load at 500~700℃, comparing with the results by TTP and MCM.

Analyzing the relationships of AE signal properties such as AE cumulative counts versus time, AE cumulative hits versus time, other AE parameters and creep properties of each creep stages, it was confirmed that AE evaluation for monitoring high temperature creep properties in real time could be possible qualitatively at present.

2. SPECIMENS AND EXPERIMENTAL PROCEDURES

Specimens were used 1.2%Cr-Mo-V steels, which have been used for steam turbine rotor steel under high temperature and high pressure for the power electric generation. Fig. 1 represents the profile of the specimens and applied specification used for creep test.

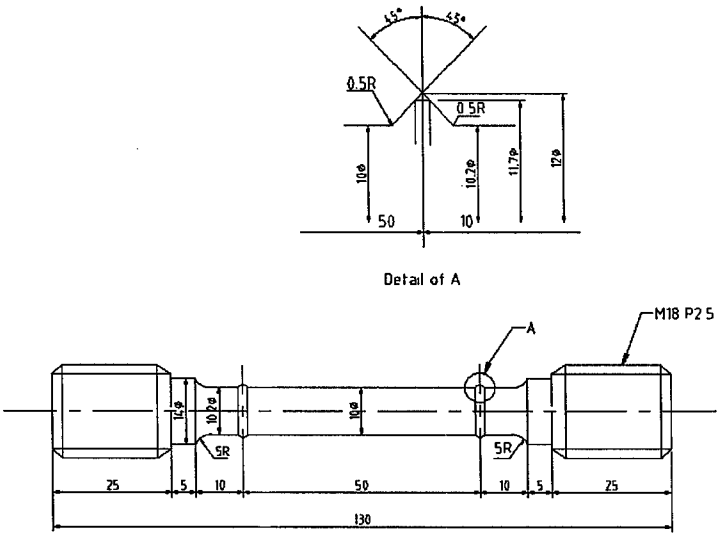


Fig.1. Profile of specimens and applied specifications
(Uniaxial Creep: ASTM E139-83)

3. BACKGROUND OF ISM

The creep initial strain (ε_0) can be quantitatively related to prediction of creep properties (fracture time t_r, creep rupture stress σ, etc.) in short term creep test of heat resisting steels (SUS303, SUH3) and the friction weld under static load at 700℃ and are suggested the following models[4]:

$$t_r = a(\varepsilon_0)^{-b}, \quad \varepsilon_0 = c(\sigma)^d \tag{1}$$

Where a. b. c and d are constants concerning materials. It was also noted afterward by Oh et al.[5-6] that the creep property prediction by ISM is more reliable than by other TTP methods. It was also known by Mitra et al.[7] that the initial strain in high temperature creep test for Al and Ni is similar to the strain under the same stress of the monotonic tensile-strain curve, the initial strain and stress have the linear relationship in high temperature creep test for 9Cr-Mo-V-Nb steel, and the initial strain affects on the transition creep rate in creep test for Cu under cyclic creep, respectively.

4. RESULTS AND DISCUSSIONS

4.1. Creep Life Prediction by ISM

By creep test results for 1.2%Cr-Mo-V steel under various creep stresses (13~806 MPa) at the high temperatures of 500, 600 and 700℃, we could acquired empirical and calculated data by ISM and the relationship of creep rupture time(tr, hr) versus steady state creep rate (ε_0 hr^{-1}) (Monkman-Grant relation). The empirical equation was calculated by a regression analysis using the least squares method and can be modeled as the following :

$$t_r = 1.92 / 10^{-1} \quad \varepsilon s^{-0.71} \; (R^2 = 0.97), \quad t_r(\varepsilon_0)^m = K \tag{2}$$

Where m and K are constants concerning materials. This equation model is very coincident with Monkman and Grant's[8]. From the empirical results of initial strain (ε_0 %) versus the normalized creep stress (σ /E), the empirical equation was calculated and can be modeled as follows, which is very coincident with Mitra et al.,s [7].

$$\varepsilon_0 = 2.71 \times 10^{3(\sigma/E)\,1.50} \; (R^2 = 0.99, S = 0.06), \quad \varepsilon_0 = d(\sigma / E)^e \tag{3}$$

Where E is elastic modulus according to temperatures, d and e are constants concerning materials. Meanwhile, ε s - σ and ε s-(σ /E) equations are expressed as the following :

$$\varepsilon_s = A \sigma^n \quad \text{(by Norton' s[9])} \tag{4}$$

$$\varepsilon_s = C (\sigma / E)^n \tag{5}$$

Where A. C and n are constants concerning materials at experimental temperatures, and E is elastic modulus according to temperatures. Form Eq.3 and 5, $\varepsilon_0 \sim \varepsilon$ s equation can be derived as follows :

$$\varepsilon_0 = d (\varepsilon_s / C)^{e/n} \tag{6}$$

Where d. e. n and C are constants concerning materials. From Eq.2 and 6, the following $\varepsilon_0 \sim$ tr equation can be derived as follows :

$$\varepsilon_0 = d (K / C^m t_r)^{e/mn} \tag{7}$$

And from $\varepsilon_0 \sim t_r$ and $\varepsilon_0 \sim \sigma$ equations according to each temperature variance of 500, 600 and 700℃ for 1.2%Cr-Mo-V, σ -T-ε_0 – t_r equation can be derived as follows :

$$t_r / \sigma = \alpha (\varepsilon_0)^{\beta} \tag{8}$$

4.2. Reliablility of Creep Prediction by ISM

Fig. 2 shows the comparison of creep rupture strength versus temperature relationship according to rupture time by ISM with TTP and MCM for 1.2%Cr-Mo-V steels, respectively. It is clarified in Fig. 2 that not only the 10^3~10^4 hours creep rupture strengths obtained by ISM are maximum 5% lower than those by TTP but also 10^5 hours creep rupture strengths by ISM are similar to those of the lower band by TTP, while 10^2 hours creep rupture strengths by ISM are very similar to those by TTP and MCM. So that, it is confirmed that the long-time creep life prediction of steam turbine rotor steel(1.2%Cr-Mo-V) by ISM could be accomplished at initial real-time in process by

measuring the initial strain only, and utilized more reliably for creep design, operation and maintenance of turbine rotors than by TTP or MCM.

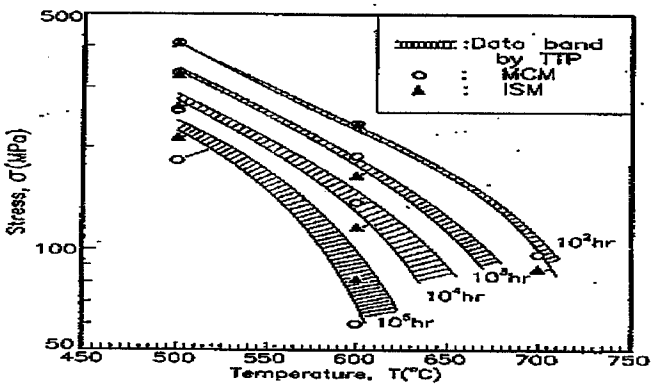


Fig.2. Comparison of creep rupture strength-temperature relationship according to rupture time by ISM with by TTP and MCM for 1.2%Cr-Mo-V steels.

4.3. Evaluation of High Temperature Creep by AE

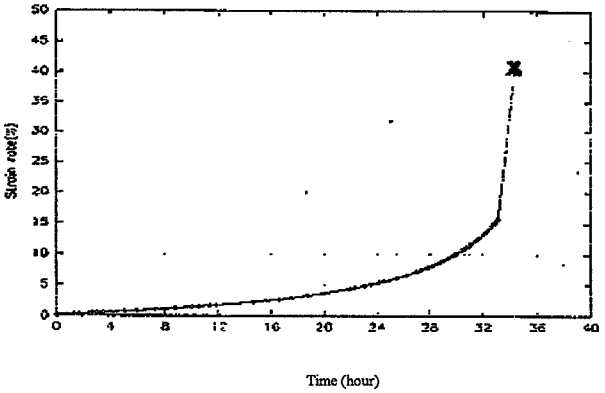
Fig. 3 shows the typical relationship between creep behavior and AE properties during creep test of 1.2%Cr-Mo-V steel under stress of 35~42 kg/mm^2 and 22~25 kg/mm^2 (t_r=4~309 hrs) at 700℃. It is considered that the various creep properties such as initial strain, transition creep(1st creep stage), steady state creep(2nd creep stage), accelerated creep(3rd creep stage), and fracture in creep curve could be qualitatively related to AE properties such as counts vs. time, hit and energy vs. time, etc. Analyzing the relationships of AE signal properties such as AE cumulative counts versus time, AE cumulative hits versus time, other AE parameters and creep properties of each creep stages, it was confirmed that AE evaluation for monitoring high temperature creep properties in real time could be possible qualitatively at present.

Fig. 3(b) shows the relationship between AE cumulative counts and creep test time during creep test. AE cumulative counts mean the total number of signal counts in excess of certain thresold level among AE burst signals acquired during creep test. Because time axis of creep curve in Fig. 3(a) is same as time axis in Fig. 3(b), amounts of AE cumulative counts according to creep stages and creep time can be measured from Fig. 3(b). In Fig. 3(b), it is confirmed that AE cumulative counts indicate about 2,000 counts until 1st creep stage, about 6,000 counts until 2nd creep stage and about 15,800 counts until 3rd creep stage, respectively. Fig. 3(c) shows the relationship between AE cumulative hits and creep test time during creep test. AE cumulative hit means a parameter showing the total numbers of AE burst signals acquired during creep test. Using analyzing method same as AE cumulative counts, creep properties versus creep stage can be evaluated. And also, AE parameters versus creep stage can be analyzed by the same method as Fig. 3(b). From Fig. 3(c), it is confirmed that AE cumulative hits indicate about 22 hits in 1st creep stage, about 60 hits in 2nd creep stage, and about 150 hits in 3rd creep stage, respectively.

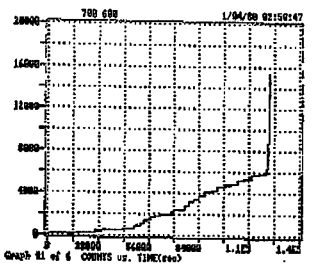
Fig. 3(d) and Fig. 3(e) show numbers of AE count and hit versus creep test time, numbers of AE count and hit in real time can be measured from these Figures. Fig. 3(f) shows amplitude distribution of AE signals during creep test, it has range of about 55~80dB and also about 72dB peak amplitude. Because these range of amplitude distribution and magnitude of peak amplitude are

different in various material, high temperature creep properties can be classfied from measuring of AE signal amplitude. Fig. 3(g) shows the relationship between AE energy and creep test time during creep test. AE energy means a parameter showing intergrating value of AE signal voltage. Using AE energy, creep properties versus creep stage can be evaluated by the same method as AE cumulative counts and hits.

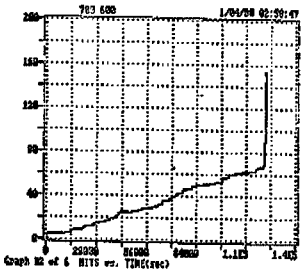
Temperature(°C)	Load(kgf)	Stress(kgf/mm2)	Initial strain(%)	Fractical time(hr)
700	600	7.64	0.025	34.25



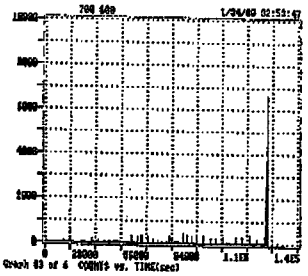
(a) creep curve for 1.2%Cr-Mo-V steel



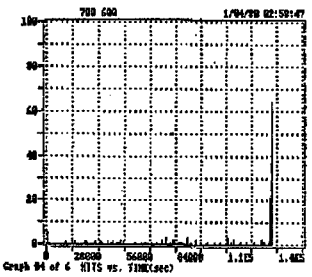
(b) cumulative counts vs. time



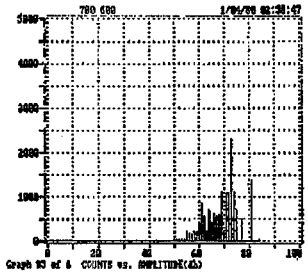
(c) cumulative hits vs. time



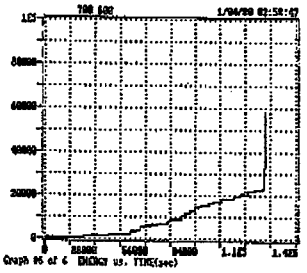
(d) AE count rate vs. time



(e) AE hits vs. time



(f) AE counts vs. amplitude



(g) AE energy vs. time

Fig.3.Relationship between creep behavior and AE properties during creep test

CONCLUSION

1. The empirical equation for long-time creep life and creep rupture strength prediction of steam turbine rotor steel was derived by using the ISM., And it was well clarified that the result by the ISM was safer than by the TTP for predicting creep strength, because not only $10^3 \sim 10^4$ hours ceep strengths obtained by the ISM were maximum 5% lower than those by TTP but also 10^5 hours strengths by the ISM were similar to those of the lower band by TTP, while 10^2 hours creep strengths by the ISM were very similar to those by TTP and MCM.
3. It was confirmed that AE evaluation for monitoring high temperature creep properties in real time could be possible qualitatively at present.

REFERENCES

1. Araki, Toru, NRIM Creep Date Sheet, No. 9A(1979) p.1-14
2. Manson. S.S. and Ensign, C.R, Interpolation and Extrapolation of Creep Rupture Data by the Minimum Commitment Method-part I Focal-point Convergence (1971) p.299-398
3. Hizel L.C. and Sherby, O.D., Time-Temperature Parameters for Creep-Rupture Analysis, ASM Pub. No. D8-100(1968) p.115
4. Oh, S.K., Study on Strength Analysis of Friction Welded Joints and In-Process Monitoring of the Welding Using Acoustic Emission Techniques, Ph.D. Thesis, Keio University, Japan, 85-46(1982) p.302
5. Oh, S.K, and Kunio, A, Effect of Initial Strain on Evaluation of High Temperature Creep Properties of Friction Welded Joints, Proc. of Asian-Pacific Congress on Materials Strength Evaluation 86(1986) p.549-554
6. Oh, Sae-Kyoo and Seon-jin Kim, Development of Long-Time Creep Safety Life Prediction of Steam Turbine Rotor Steel and AE Evaluation(Ist report)-Possiblility of Creep Prediction by Initial Strain Method, Proceedings of 6th International Offshore and Polar Engineering Conference, ISOPE Los Angels(1996) p.275-279
7. Mitra, S.K. and McLean, D., Work Hardening and Recovery in Creep, Proc. R. Society, A295(19 66) p.288-299
8. Monkman, F.C. and Grant, N.J., Proc. ASTM, Vol. 56(1956) p.600-602.
9. Norton, F.H., The Creep of Steel at High Temperature, Mcgraw-Hill, New York(1929) p.67

Key Engineering Materials Vols. 183-187 (2000) pp. 909-914
© 2000 Trans Tech Publications, Switzerland

Expanding of the Fatigue Life of Thermal Barrier Coating by Mixing $MoSi_2$ to Thermal Sprayed Layer

Keiji Sonoya[1] and Shogo Tobe[2]

[1] Ishikawajima-Harima Heavy Industries Co., Ltd., Yokohama 235-8501, Japan

[2] Ashikaga Institute of Technology, Ashikaga-shi, Tochigi-ken 326, Japan

Keywords: APS, Fatigue Life, $MoSi_2$, SiO_2, Thermal Barrier Coating, VPS

ABSTRACT

Recent trends of turbine blades of advanced aircraft gas turbine engines are to increase output power of the engines, to increase engine efficiency and to reduce environmental emission, and thus, higher operating temperatures of the engines are required. One of the technologies for increasing the operating temperature is a thermal barrier splayed coating [1.2]. The coating usually consists of a bonding coating layer of an alloy of NiCrAlY on the turbine blade and a top layer of ZrO_2-Y_2O_3, namely, partially stabilized zirconia (PSZ).

However, conventional coating systems deteriorate during turbine operation due to thermal and mechanical stresses imposed and corrosion actions by combustion gas coming from combustion chambers. Thus, the main issue is to develop measures against high oxidation rate and low fatigue life of the bonding coating layer. An idea for enhancing oxidation resistance and fatigue life as well of thermal barrier coatings consisting of a zirconia-based coating is to provide with a self-healing capability to the coating by diffusing a suitable substance to fatigue crack surfaces formed in the coating. Excessive oxidation of the NiCrAlY layer beneath is prevented for extending fatigue life of the splayed barrier coating. Several investigations have been conducted on the matter, and a research paper [3] claims that $MoSi_2$ in a splayed coating has a self-healing capability for cracks formed in the coating by embedding the cracks with SiO_2 formed from $MoSi_2$ at high temperatures.

Thus, a new coating system containing NiCrAlY, $MoSi_2$, and PSZ is expected to be developed instead of a two-layer coating system of NiCrAlY and PSZ. The coating system developed could be a three-layer system, or a two-layer system, one with a NiCrAlY layer and the other layer is either a gradient composition of $MoSi_2$ and PSZ, a mixed layer of $MoSi_2$ and PSZ, or a mixed layer of PSZ and SiO_2. The other possibility is a three-layer coating with an intermediate layer of mixed powder of $MoSi_2$ and NiCrAlY between the bonding layer and the top layer.

Furthermore, a monitoring method for detecting cracking conditions in heating and cooling cycles by signals of acoustic emission is discussed. A possibility of estimating fatigue life by utilizing an X-ray method for measuring residual stress is considered as well.

1. EXPERIMENTAL METHODS

1.1 Specimens

Two splay coating methods, an atmospheric pressure plasma splaying (APS) method, and a reduced pressure plasma splaying (VPS) method, are used for preparing five kinds of coatings using splaying materials listed below. The splaying conditions are summarized in Table 1.

substrate material: SUS316 (dimension: 92 x 15 x 3 mm)
bonding coating : NiCrAlY
intermediate coating : mainly $MoSi_2$ if employed
top coating : mainly ZrO_2

Table 1 Splaying conditions

An atmospheric plasma coating method (APS)

plasma gas	output (kW)	splay distance (mm)
$Ar+H_2$	45	120

A reduced pressure splay coating method (VPS)

plasma gas	output (kW)	splay distance (mm)	Pressure (Torr.)
$Ar+H_2$	43	275	65

Table 2 Numbers of cycles at a crack detected

Specimen Film	Numbers of cycles at a crack detected
A	1
B	1
C	20
D	60 (no cracking)
E	1

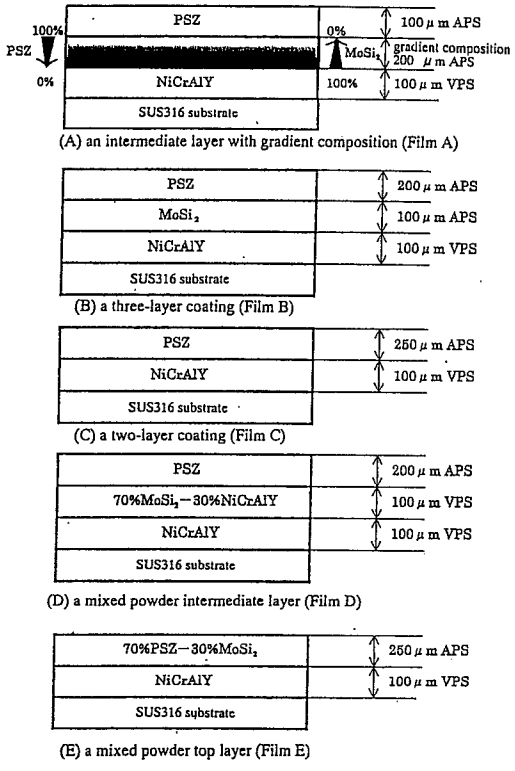


Fig. 1 Schematic structure of the films tested

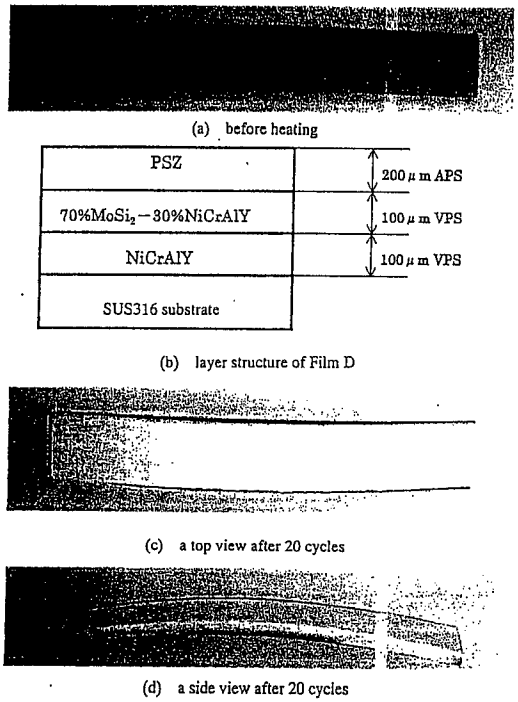


Fig. 2 Sample profiles before and after 20 cycles of Film D

1.2 Splay coating methods

A coating surface of a substrate plate of SUS316 is sand-blasted with #100 alumina grit, and then, is coated with the bonding coating by one of the plasma splay coating methods. After the bonding coating is made, a two-layer coating specimen is prepared by splaying the top coating on the bonding coating. A three-layer coating specimen is prepared by splaying an intermediate layer and a top layer on the bonding coating successively.

Layer structures of the specimens employed are shown in Fig. 1 schematically, and are explained.

(1) Film A:
This film is termed a specimen of a gradient compositional intermediate layer. A bonding coating is splayed by the VPS method on a substrate plate, and an intermediate layer is splayed by the APS method while gradient composition by 10% each with respect to PSZ and $MoSi_2$ is formed, and, finally, the top layer is formed by APS with PSZ.
(2) Film B:
This film is termed a distinctive three-layer coating. A bonding coating is splayed by the VPS method on a substrate plate, an intermediate layer is splayed by the APS method on the bonding layer with $MoSi_2$, and the top layer is splayed by the APS method with PSZ.
(3) Film C:
This film is termed a distinctive two-layer coating. A bonding coating is splayed by the VPS method on a substrate plate, and a top layer is splayed by the APS with PSZ. The film is a current industrial coating.
(4) Film D:
This film is termed a cermet type intermediate layer coating. A bonding coating is splayed by the VPS on a substrate plate, an intermediate layer is splayed by the APS with mixed cermet of $MoSi_2$ + 30% NiCrAlY, and the top layer is splayed by the APS with PSZ.
(5) Film E:
This film is termed a mixed powder top layer two-layer coating. A bonding coating is splayed by the VPS on a substrate plate, and the top layer is splayed by the APS with mixed powder of PSZ + 30% $MoSi_2$.

1.3 Cyclic heating and cooling tests

Cyclic heating and cooling tests are conducted on various specimens prior to implementation of the following evaluation. One cycle of the cyclic test consists of heating a specimen in a test furnace at 900 °C for two hours and cooling in ambient atmosphere for 10 min.
(1) Observation of peeling
Quality of the films is evaluated by observing peeling tendencies of the films.
(2) Measurement of residual stress
After each cycle of the cyclic test, each specimen is measured by an X-ray diffraction method for evaluating residual stress on the surface of the substrate plate.
(3) Identification of phases present
Crystalline phases in the samples are measured by the X-ray diffraction method for the presence of a SiO_2 phase in the films presumably acting for sealing cracks formed in top layers after films containing a $MoSi_2$ layer are heated for maximum 72 hours at 1000 °C.
(4) SEM observation
The surfaces and cross sections of the specimens are observed by SEM after every heating and cooling cycle.
(5) Monitoring acoustic emission (AE)
AE monitoring is performed during the cyclic tests for detecting initiation of a crack.

2. EXPERIMENTAL RESULTS AND DISCUSSION

2.1 Cyclic heating and cooling tests

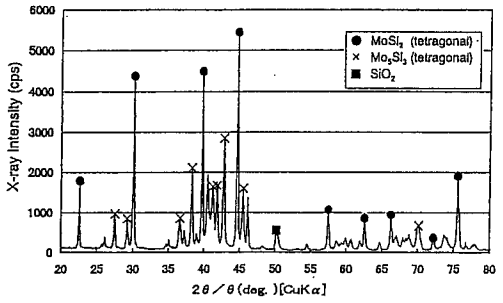
Table 2 shows the number of cycles of the cyclic tests before any peeling of the films is detected. Films A, B, D and E contain $MoSi_2$ in the films, and Films A, B, and E survived only one cycle of the tests with initiating cracks around the boundary regions of the bonding coatings and the top coatings. The reason for the premature cracking is believed to be the presence of the phase transformation point of $MoSi_2$ about 700 °C from the β-phase to α-phase in the cooling cycle with sudden increase of the volume being enough for causing cracking.

Film D shows no crack after 60 cycles of the tests. The film has an intermediate layer of $MoSi_2$ + 30% NiCrAlY, suggesting very strong adhesiveness to the bonding layer even with the phase transformation of the $MoSi_2$ to occur. This situation is clearly shown in Fig. 2 for the profiles of a specimen before and after the cyclic test. The addition of NiCrAlY to a $MoSi_2$ layer clearly improves adhesion between the intermediate and bonding layers.

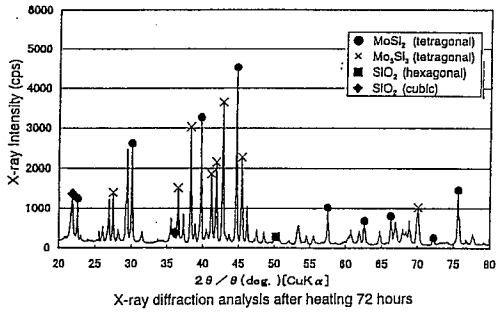
2.2 Self-healing property of cracks of $MoSi_2$

For investigating formation of SiO_2 that is assumed to be capable in sealing cracks, films

containing $MoSi_2$ are heated at 1000 °C for 72 hours, and are subjected to X-ray diffraction analyses at room temperature for phases present. Figs. 3-A and 3-B show various phases in the films before and after the heating tests of Film A and Film D prepared by the APS and by the VPS respectively.

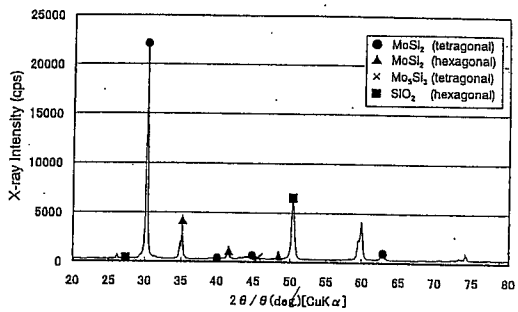


X-ray diffraction analysis before heating

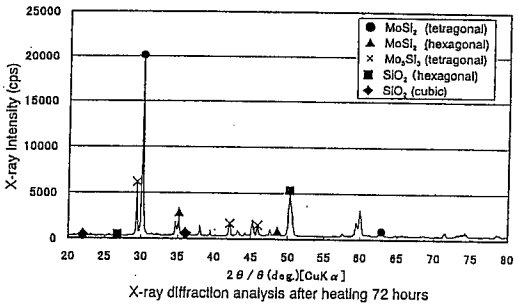


X-ray diffraction analysis after heating 72 hours

Fig. 3-A Phases identified in APS $MoSi_2$ film of Film A



X-ray diffraction analysis before heating



X-ray diffraction analysis after heating 72 hours

Fig. 3-B Phases identified in VPS $MoSi_2$ film of Film D

Film A before the heating test shows presence of the Mo_5Si_3 phase in addition to the $MoSi_2$ phase. The oxidizing atmosphere for the APS is believed to cause removal of Si in some extents from $MoSi_2$ during the APS. This subsilicide has been found to have no self-healing property based on formation of SiO_2 films [4].

Film A after the heating test shows formation of some extent of SiO_2 that is assumed to promote sealing cracks formed.

Film D has improved adhesiveness as shown in Table 2. Film D before the heating test is found to show no trace of Mo_5Si_3 because the film is prepared by the VPS in an environment with a very small partial pressure of oxygen. Heated specimen of Film D shows formation of SiO_2.

Thus, the crack self-healing property of $MoSi_2$ is believed to be high in Film D. A mechanism for the assumed self-healing property of $MoSi_2$ in a film is schematically shown in Fig. 4. A crack in a $MoSi_2$ layer promotes the following reaction to occur.
Namely,

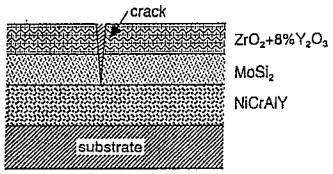
$$MoSi_2 + 3O_2 \rightarrow MoO_2 + 2SiO_2$$

MoO_2 sublimates, and SiO_2 precipitates in the crack. Thus, the crack is assumed to be sealed.

2.3 Measurement of residual stress after the cyclic heating tests

Fig. 5 shows X-ray measurement results of residual stresses on the substrate surfaces of Film C and D after each heating cycle. The substrates of both films show increased residual stresses with respect to the number of the test cycles. With further increases of the cycles, the residual stress is

reduced for a while, and then, it tends to start to increase again. With repeating the sequence, films are supposed to be cracked finally. The situation suggests possibility of assessing life expectancy of a film by a cyclic test.



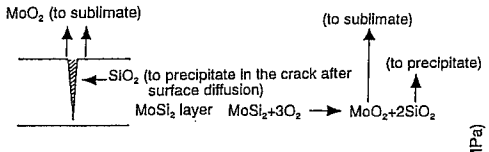


Fig. 4 A proposed self-healing mechanism

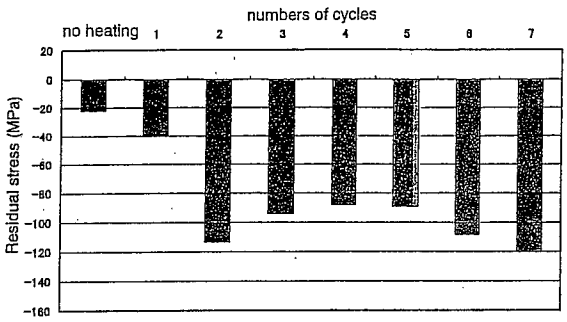


Fig. 5-A mean residual stress and numbers of cycles for Film C

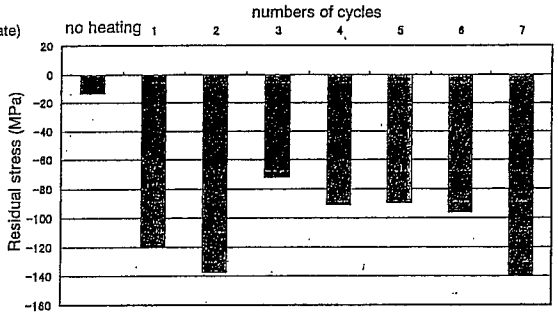


Fig. 5-B mean residual stress and numbers of cycles for Film D

Fig. 5 Mean residual stress against numbers of heat cycles for Film C and Film D

2.4 AE monitoring during the cyclic tests

AE signals are monitored for anticipating detection of cracking events during the cyclic heating and cooling tests. The results show that films consisting of $MoSi_2$ layers have AE signals as three times frequently at cooling stages than films without $MoSi_2$ layers. Furthermore, many AE events with higher amplitude are found to occur at the first halves of the cooling stages. This behavior is believed to be caused by the phase transformation of the $MoSi_2$ phase.

3. CONCLUSION

A layer of $MoSi_2$ is added to a conventional two-layer thermal barrier splayed coating for extending life of splayed thermal barrier coatings. Furthermore, a method for adding a $MoSi_2$ layer with a gradient compositional layer, or with a cermet layer is developed. The obtained results are listed below.

(1) An introducing method of an intermediate layer between a bonding layer and a top layer, namely, of a layer consisting of cermet of $MoSi_2$ + 30% NiCrAlY, is developed. The three-layer splayed coating is found to increase adhesion strength between these layers regardless of a large thermal expansion to be induced by the phase transformation of $MoSi_2$. The enhanced adhesion strength is found to increase life of the coating compared to conventional thermal barrier splayed coatings.

(2) Phase identification analyses of heating test specimens clearly show formation of SiO_2 in the specimens containing $MoSi_2$. This result suggests the presence of self-healing capability for cracks formed in the films containing $MoSi_2$.

(3) Residual stress on substrate surface increased with respect to the number of the test cycles. With further increase of the cycles, the residual stress is reduced for a while, and then, it tends to start to increase again.

REFERENCES

1. Keiji Sonoya, and Shigeru Kitahara: Characteristics of thermal stress induced cracking of plasma splayed ZrO_2-NiCrAlY coatings (JA), Hyomen Gijutu (Surface Technology), 49, No.10, (1998), pp 72-76.
2. Ryuji Okamoto, and Nobumasa Ueda: Development of heat and corrosion resistant coatings for gas turbine engines (JA), Kawasaki Heavy Ind Technical Review, No.112, Jan. 1992.
3. Masahiro Fukumoto, and Toshiro Ueda: Oxidation resistant characteristics of splayed $MoSi_2$ coatings (JA), Yosha (Splayed coatings), 30. No.4 (1993),pp.163-168.
4. N. Zacchetti: High-Temperature Oxidation-Resistant Properties of Low Pressure Plasma Splayed $MoSi_2$ coating on Niobium Alloys, Proceeding of ITSC, Orlando, Fl., USA, 28 May 5 June 1992.

Key Engineering Materials Vols. 183-187 (2000) pp. 915-920
© 2000 Trans Tech Publications, Switzerland

Effects of Pad Material on Fretting Fatigue Behavior in CFRP Laminates

Moon-Saeng Kim[1] and Hyung-Seop Shin[2]

[1] Department of Mechanical Design Engineering, Pusan National University,
30 Changjeon-dong, Kumjeong-ku, Pusan 609-735, Korea

[2] Department of Mechanical Engineering, Andong National University,
388 Songchun-dong, Andong, Kyungbuk 760-749, Korea

Keywords: CFRP Laminates, Fatigue Strength, Fretting Fatigue, Fretting Pad Material, Friction Coefficient, Surface Roughness

ABSTRACT

Effects of pad materials and surface roughness on the fatigue strength in CFRP laminates under fretting condition were studied. A fixture was designed to give a normal contact force to the specimen and monitor a friction force caused at the fretted area during fatigue testing. As a result, the influence of pad materials and surface roughness on fatigue strength existed in A-type laminates, but not in B-type ones. Some difference at high fatigue stress levels appeared differently according to stacking sequence of laminates. The normal and friction forces at fretted area showed a similar behavior regardless of the applied stress level, although there existed some difference according to pad materials. The variation of friction coefficient along the fatigue life ratio showed a similar behavior regardless of pad materials. The friction coefficient had a value larger than 1 at an early stage less than 20% of fatigue life, after then it reduced to 0.5-0.6.

1. INTRODUCTION

Carbon fiber reinforced plastics (CFRP), which represent superior properties such as light weight, high strength, remarkable fatigue endurance and good vibration reduction, have been used in the fields of air and ground transportation vehicles. In the application of these materials to structural components, it is inevitable to have connecting parts. When the connected structure is subjected to repeated load or vibrations, damage has occurred due to fretting at contact area of connected parts, which is called a fretting fatigue. Fretting fatigue is one of important phenomena inducing a dramatic reduction of fatigue strength in CFRP laminates [1,2]. Consequently, it an unexpected failure of CFRP structures due to fretting damage could be expected.

However, when compared with metallic materials [1,2], few studies have been made on fretting fatigue or fretting wear of polymer composites [3,4]. In order to clarify the fretting fatigue behavior in this kind of materials, more efforts are still necessary. From previous researches [3,4], it has been known that the fretting damage caused in the 0° layers that carries most of applied load produced the reduction of the fatigue strength in CFRP laminates. And the effect of contact stress on fatigue strength appeared significantly in laminates having 0° layer on both surfaces [4]. Considering fretting conditions have always contacting area, the pad material and the initial roughness of pad

surface will also be important parameters to influence on the fretting damage.

In this study, the influences of pad material and surface roughness on the fatigue strength of CFRP laminates were examined using laminates having different stacking sequences.

2. EXPERIMENTAL

2.1. Specimens

Specimens used were laminated with 16 plies of Carbon/Epoxy HT series unidirectional prepregs. They were supplied with the square plate of 250mmx250mm and cut down to a shape of coupon with dimensions of 10mmx200mmx'2mm for fatigue testing. Two type of laminates having different stacking sequences were prepared as follows;

A-type laminate : $[0^\circ_2/90^\circ_2/0^\circ_2/90^\circ_2]_{sym}$
B-type laminate : $[\pm 45^\circ/0^\circ_2/\pm 45^\circ/0^\circ_2]_{sym}$

where, 0° layer coincides with the direction of the fatigue loading applied to specimens. Aluminum end tabs are located to make easy load transfer and protect the specimen surface from gripping. Table 1 shows mechanical properties in each type laminate obtained from static tensile tests.

Table 1 Mechanical properties in each type laminate.

Laminate type	Young's modulus (GPa)	Tensile strength (MPa)	Strain at failure (%)
A	41	844	2.07
B	57	1,022	1.83

2.2. Fretting fatigue test

In order to obtain S-N curves for CFRP laminate specimens under fretting condition, a specially designed fixture is attached to the specimen to give a contact stress to the specimen. Fatigue tests were carried out with a frequency of 10Hz at a stress ratio of R=0.05. The contact stress of p=25MPa was applied initially to the specimen. The assembled schematic view was shown in Fig. 1. Basically, the fixture has included a retainer ring, a pair of bolts, arms and fretting pad pins. Adjusting a pair of bolts can generate a sustained static load to give a contact stress to the specimen through fretting pad pins. Eventually, cylindrical pad pins with flat surfaces serving as fretting pads were pressed against two opposite

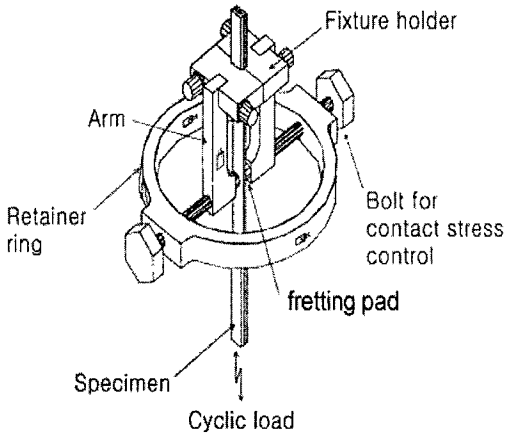


Fig. 1 Assembled view of fixture for fretting fatigue test.

sides of the specimen, serving as fretting pads.

In order to investigate the effect of pad material on the fatigue strength under fretting condition, three kinds of materials were adopted: a mild steel (S45C), brass and Al alloy (A2024). Their hardness values were shown in Table 2. The pad pins had different surface roughness of 0.1μm Ra (smooth surface) and 3μm Ra (rough surface). The pin is 8mm in diameter. Using strain gages attached to the retainer ring and arms, the static normal force loaded to the specimen and the friction force caused at fretted areas was measured, respectively. And the friction coefficient μ at the fretted area was calculated from the Coulomb's law, $\mu = F/N$, where F is the friction force and N is the normal force measured.

Table 2 Hardness of pad pins materials (at the load of 9.8N).

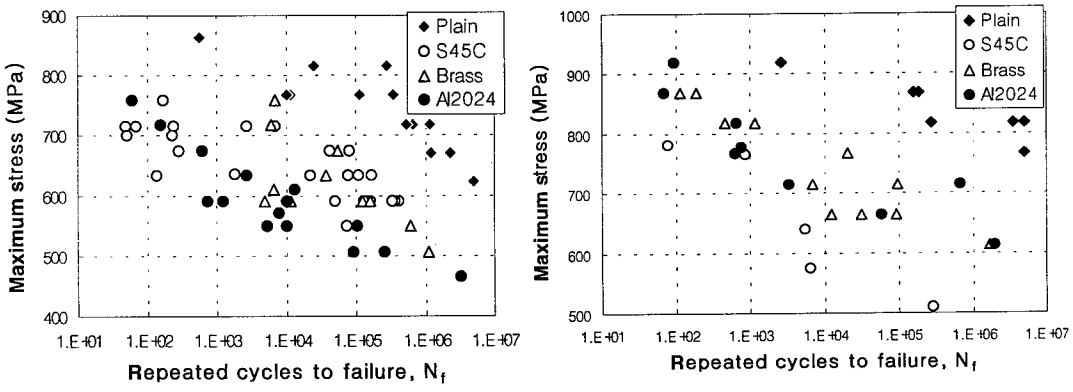
Material	Mild steel (S45C)	Brass	Al alloy (A2024)
Hv	259	135	167

3. RESULTS AND DISCUSSION

3.1. Effect of pad material on fatigue strength

The S-N curves obtained from fretting fatigue tests using pad pins with smooth surface are shown in Figs 2 (a) and (b). Results of the plain fatigue test are also plotted in the same figures. Considering non-uniform stress state within a specimen under fretting condition, relatively good S-N curves were obtained. When compared with the cases of plain fatigue, it could be found that the fretting influenced on the fatigue strength in both type of laminate specimens, so it led to a shorter repeated cycles to failure. The dependence of pad material on the S-N curve existed significantly in A-type laminate, but seldom in B-type one.

In the A-type laminate specimen of Fig. 2 (a), a wide data spreading existed in the case of S45C pad, but a relatively good S-N curve obtained in the case of A2024 pad. In the case of brass pad, excepting some data that represented early failure at 600MPa, it showed most superior S-N curve



(a) A-type laminate (b) B-type laminate

Fig. 2 S-N curves obtained under fretting condition using smooth surface pad pins.

out of tested pad materials. Therefore, there was a sequence of Brass, S45C and A2024 in fatigue strength according to pad material at the same stress level. At low stress amplitude region, however, the dependence of the pad material on the fatigue strength became less.

On the other hand, in the B-type laminate of Fig. 2 (b), there was little influence of pad material on the fatigue strength than in the A-type laminate, and all of them laid relatively narrow band. The reason is related to the fact that in B-type specimens the failure site was located at other places away from the fretted area [4] so that the effect of fretting conditions including contact stress, pad materials didn't appear on the fatigue strength behavior.

3.2 Effect of pad surface roughness on fatigue strength

As mentioned in the previous section, the effect of pad material on the fatigue strength existed only in A-type laminate, but not in B-type one. Therefore, the effect of surface roughness on the fatigue strength is expected only in A-type laminate specimens. Fig. 3 shows S-N curves obtained using pad pins with rough surface (R_a=3) in A-type laminate. Comparing them with the results of smooth surface shown in Fig 2 (a), the dependence of pad material on fatigue strength and the data scattering became less as compared with cases of smooth surface. But, the rough surface led to lower fatigue strength in the cases of S45C and brass pad materials. At low stress amplitude regions, amplitude region, the surface roughness dependence on the fatigue strength became less and it approached to the case of smooth surface.

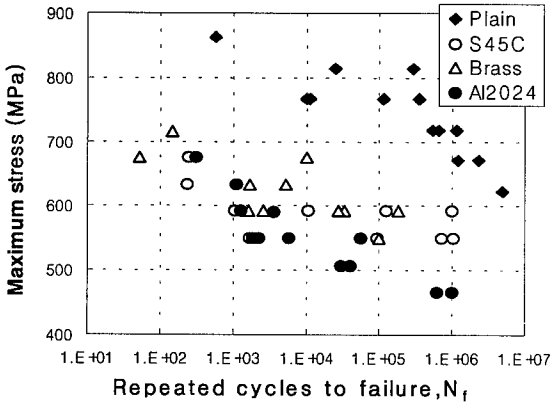


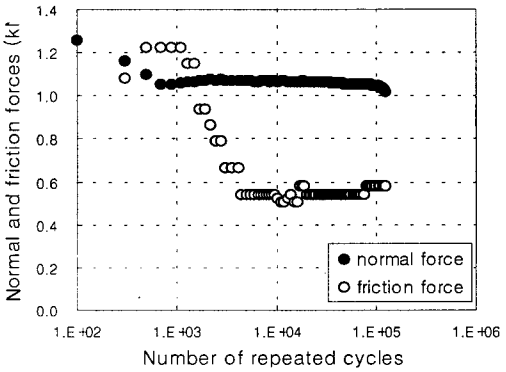
Fig. 3 S-N curves obtained using rough surface pads in A-type laminate.

3.3 Variation of friction coefficient during fretting fatigue

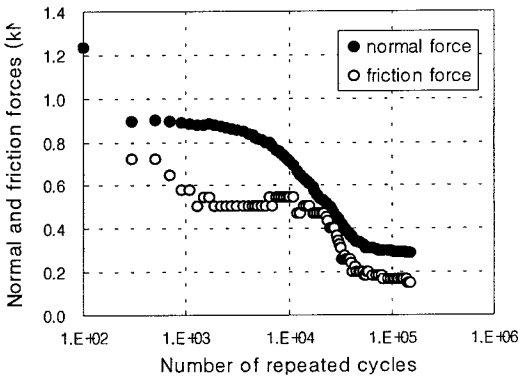
In order to investigate the wear behavior at contact area which is closely related to the damage due to fretting fatigue, the measurement of normal and friction forces caused at fretted area were carried out using pad pins with smooth surface.

Figures 4 (a), (b) and (c) show the variation of both forces with increase of repeated cycles. Firstly, in the S45C pad of Fig. 4 (a), the normal force dropped slightly at early stage of fatigue, but over 10^3 cycles it had a nearly constant value of 1.05kN until failure of specimen. The friction force, however, increased to 1.2kN at an early stage of failure representing higher value than the normal force. When repeated cycles exceeded over 10^3 cycles, it dropped rapidly and held a contact value of 0.55kN. This behavior in friction force is related to the large difference in hardness between pad material and CFRP specimen. Even at the early stage of fatigue, the wear occurred significantly at the surface of CFRP laminate, but little at the surface of S45C pad and it resulted in a drop of normal force. Through the examination of pad surface after fretting fatigue test, a relatively small wear in the cases of S45C pad as compared with the ones of Brass and A2024 pads could be found.

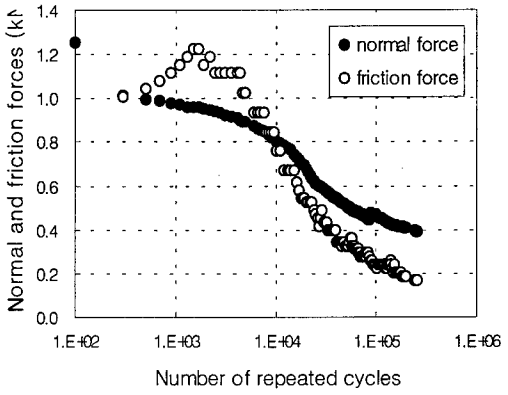
In the case of Brass pad having the lowest hardness, it can be seen from Fig. 4 (b) that the normal force dropped to 0.9kN even at 300cycles. At that time, the friction force was quite a low value of 0.7kN when compared with the case of S45C pad. The hardness of brass pad is so low that



(a) S45C pad (N_f=1.2x10^5)



(b) Brass pad (N_f=1.6x10^5)



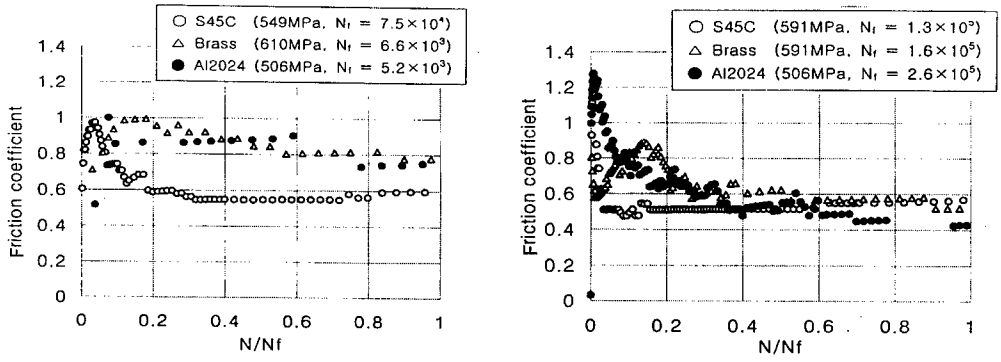
(c) A2024 pad (N_f=2.6x10^5)

Fig. 4 Variations of normal and friction forces with repeated cycles for each pad material.

a significant wear occurred at both surfaces of laminates specimen and brass pad even at early stage of fatigue. The friction force in the case of A2024 pad, as shown in Fig. 4 (c), showed a similar behavior to the case of S45C pad of (a). It decreased gradually with the normal force when the repeated cycles exceeded 3x10^3 representing as an intermediate degree in behavior.

In order to investigate the friction characteristics at contact surfaces that will influence on the fretting damage, the variation of friction coefficient during the fatigue lives was shown in Fig. 5 (a) and (b). They correspond to different fatigue life regions where the fatigue lives are below and above 10^5 cycles, respectively.

At first, in the case having fatigue lives below 10^{5}cycles, the friction coefficient increased up to the value of 1.0, at an early stage of fatigue, but when exceeded 10% of fatigue life, it showed a stable value for each pad material; μ =0.8-0.9 for A2024 and Brass pads and μ=0.6 for S45C pad, respectively. The low friction coefficient for S45C pad was related to its longer fatigue life, as compared with other two pad materials. On the other hand, in the case having fatigue lives over 10^5 cycles of Fig. 7(b), there was a large fluctuation of friction coefficient at an early stage until 20% of fatigue life showing a value higher than 1 or close to 1 according to pad materials. After then, it



(a) At regions $N_f<10^5$ (b) At regions $N_f>10^5$

Fig. 5 Variation of friction coeffcient against N/N_f in each case.

showed a stable behavior having a constant value in the range of 0.5 to 0.6. The friction coefficient obtained during the fretting fatigue test was larger than the one(μ =0.2) obtained through a standard wear test in CFRP laminates [5]. This suggests that CFRP laminates subjected to fretting fatigue are located at more severe conditions in a viewpoint of tribology.

SUMMARY

The influences of pad materials and surface roughness on the fatigue strength under fretting condition were different according to stacking sequence of laminates. Their influences on fatigue strength existed only in A-type laminates at high stress amplitude levels, but not in B-type ones. The influence of the pad surface roughness on the fatigue strength existed only at high fatigue stress levels over 600MPa. In the cases of mild steel and brass material pad, eventually, the rough surface pad produced less repeated cycles to failure as compared with the smooth one. During fretting fatigue tests, normal and friction forces at fretted area were measured simultaneously. With increase of repeated cycles, both forces were degraded in a similar type regardless of applied stress amplitude levels, although there existed some difference in the behavior according to pad materials. The variation of friction coefficient with repeated cycles was also similar regardless of fretting pad materials. In the cases having $N_f>10^5$, the friction coefficient showed a high value larger than 1 at an early stage less than 20% of fatigue life, after then it reduced to a stable value in the range of 0.5 to 0.6.

ACKNOWLEDGEMENT

This study was supported by the Academic Research Fund (ME-96-C06) of the Ministry of Education, Republic of Korea. The authors would like to express their appreciation to Prof. Y. Mutoh of Nagaoka Univ. of Tech., also to Mr. J. H. Kim of a graduate student of PNU for his help.

REFERENCES

1. Y. Mutoh, Mechanisms of Fretting Fatigue, JSME Int. Journal, **A-38**, (1995) p. 405.
2. R. B. Waterhouse, (Ed.) Fretting Fatigue, Applied Science, London, (1981).
3. O. Jacobs, K. Schulte and K. Friedrich, ASTM STP 1159 (1992) p. 243.
4. M. S. Kim, H. S. Shin and H. Y. Kong, Trans. KSME, **22** (1998) p. 1833. (in Korean)
5. I. H. Sung, I. W. Yeo and D. E. Kim, J. KLSE, **12** (1996) p. 6. (in Korean)

Key Engineering Materials Vols. 183-187 (2000) pp. 921-926
© 2000 Trans Tech Publications, Switzerland

Study on Double Shot Peening and Fatigue Limit of Gear

K. Ando[1], K. Matsui[2] and H. Ishigami[2]

[1] Department of Energy & Safety Engineering, Yokohama National University, 79-5, Tokiwadai, Hodogaya, Yokohama 240-0067, Japan

[2] Post-graduate Student, Yokohama National University, Japan

Keywords: Compressive Residual Stress, Contour Induction Heating, Double Shot Peening, Fatigue Limit, Gear, Stress Double Shot Peening, Stress Shot Peening

ABSTRACT

The authors proposed stress double shot peening and it was applied to gear. The followings are main results obtained: (a)By double shot peening, residual stress distribution near the sample surface was improved considerably. (b)By stress double shot peening, maximum compressive residual stress(σ_{max}) and surface compressive residual stress(σ_S) were markedly improved. (c)By applying these technique to gear, fatigue limit of gear was increased markedly.

1. INTRODUCTION

Due to environmental factors and fuel economy, most vehicles are now required to undergo weight reduction. For this purpose, it is useful to increase the fatigue limit of vehicle components. There are two popular ways to increase fatigue limit: (a) To increase the Vickers hardness (HV) of the material. (b) To introduce a higher compressive residual stress in the component. If the HV of the component is now about 700, it is very difficult to increase the HV to the higher level. On the contrary, technique (b) is a very appropriate method for the component. Shot peening is a very popular technique for method (b), and it is used widely.

Typical residual stress distribution by normal shot peening is shown in Fig.1, schematically. There are two problems with normal shot peening: (1)The σ_S is about 40-60% of σ_{max}. However, it is shown that σ_S is a very important value to increase fatigue limit of the component by analyzing stress intensity factor and by experiment on coil spring[1]. Thus the technique is important to increase σ_S to the almost same value of σ_{max} as shown in Fig.1 by dotted line. (2)It is very difficult to introduce higher compressive residual stress to hard material. However, it can be assumed that higher compressive residual stress is desirable to increase fatigue limit [1,2,4].

Then, the authors studied on double shot peening (DSP) and stress double shot peening (SDSP) to improve residual stress distribution[3], and these technique are applied to gear to increase fatigue limit[2,4].

2. MATERIALS, SAMPLES AND TEST METHOD

The two kinds of material were used for test. Their chemical composition were listed in Table 1.The material(a) is induction heated and tempered(IH,HV≒700) for shot peening test. The sample size is 3mmX30mmX100mm. The two kinds of gear were tested. The materials for gear were quenched and tempered to HV≒200. Then they were machined to the gear [module: 3.0, pressure angle: $14^0 30'$, number of tooth: 36, helix angle and hand:17^0 right hand, over ball dia.:123.584mm].

The gear A was made of material (a). The gear A was firstly contour induction heated and tempered(CIH, HV≒750), then it was double shot peened. The gear B was made of the material (b), and was vacuum carbarized to C≒0.8wt%. Subsequently it was contour induction heated and tempered(HV≒850), then it was double shot peened. Shot peening conditions were listed in Table 2. To measure residual stress, the micro X-ray stress measuring apparatus was used. The surface of test piece was masked with window of Φ5mm, and polished to the specified depth using electrolytic polishing method. The X-ray stress measuring conditions are: X-ray spectrum=Cr-K_a beam and X-ray beam injection diameter=Φ2mm. A residual stress was calculated by 2θ -$\sin^2\phi$ method (ϕ :0,10,20,30 and 40deg). The fatigue testing system of gear was shown in Fig.2, schematically. The test has been made using electro-hydraulic testing machine in air at stress ratio (R=0.1).

3. TEST RESULTS

3.1. Residual Stress Distribution by Shot Peening

Fig.3 shows the residual stress distribution by various shot peening. The symbol △ shows the residual stress distribution by single shot peening(SP) with Φ=0.6mm shot particle. The σ_{max} and σ_S are about 1050MPa and 500MPa, respectively. The symbol ▲ shows the residual stress distribution by double shot peening(DSP.) with Φ=0.6mm and 0.08mm shot particle. By double shot peening, σ_{max} is changed a little, however, σ_S is increased by about 100%. The symbol □ shows the residual stress distribution by stress single shot peening(SSP) at applied stress=1000MPa. The σ_{max} and σ_S are about 1600MPa and 1100MPa, respectively. The symbol ■ shows the residual stress distribution by stress double shot peening(SDSP.). By stress double shot peening, σ_{max} is changed a little, however, σ_S is increased by about 46%. The symbol ○ shows the residual stress distribution by stress shot peening(SSP) at applied stress=1400MPa. The σ_{max} and σ_S are about 1800MPa and 1450MPa, respectively. The both stresses are increased remarkably compared with SSP at applied stress 1000MPa. Moreover, the symbol ● shows the residual stress distribution by stress double shot peening(SDSP) at applied stress=1400MPa. The σ_{max} and σ_S are increased considerably, and they reached up to about 2000MPa and 1800MPa, respectively. From these test results, it can be concluded following three facts: (a)Double shot peening(DSP) is a very useful technique to improve σ_S. (b)Stress shot peening(SSP) is a very useful technique to improve both σ_{max} and σ_S. (c) Stress double shot peening (SDSP) is a excellent technique to distribute the residual stress ideally.

3.2. Fatigue Strength of Gear

Fig.4 shows residual stress distribution in gear A. The symbol ▲ shows residual stress distribution at tooth root after contour induction heating. The σ_{max} and σ_S are about 800MPa and 700MPa, respectively and they are not high enough. The symbol ● shows the residual stress distribution after double shot peening. The σ_{max} and σ_S are 1450MPa and 1190MPa, respectively and showed very higher value. These gears were fatigue tested and S-N curves were shown in Fig.5. As CIH gear shows the range of fatigue limit(R=0.1) of 1256MPa, however, double shot peened CIH gear showed the range of fatigue limit($\Delta \sigma_w$) of 1710MPa. The range of fatigue limit increased by 36% by double shot peening. Fig.6 shows residual stress distribution in gear B. The symbol ■ shows residual stress distribution at tooth root after contour induction heating. The σ_{max} and σ_S are about 1030MPa and 800MPa, respectively and they are not enough high compared with their yield stress. The symbol ● shows the residual stress distribution after double shot peening. The σ_{max} and σ_S are same and 1860MPa and showed very higher value. These gears were also fatigue tested and S-N curves were shown in Fig.7. As vacuum carburized(VC) gear shows the range of fatigue limit(R=0.1) of 883MPa, however, double shot peened CIH gear showed the range of fatigue limit($\Delta \sigma_w$) of 2207MPa. The range of fatigue limit increased by 150% by contour induction heating and double shot peening. In the both gears, most cracks were initiated from surface. Only in two gears, crack initiated from inside as shown in Fig.5 with suffix f.

4. CONCLUSION

The residual stress distribution by shot peening has been studied systematically. Double shot peening was applied to gears and their fatigue limit was examined. The main results are as follows:

(1) Double shot peening(DSP) is a very useful technique to improve σ_S.
(2) Stress shot peening(SSP) is a very useful technique to improve both σ_{max} and σ_S.
(3) Stress double shot peening(SDSP) is a excellent technique to increase σ_{max}, σ_S and d_0. By using this technique, very high compressive residual stress($\sigma_{max} \fallingdotseq 2000$MPa) can be introduced in very hard material(HV$\fallingdotseq$700) .
(4) By applying double shot peening, range of fatigue limit(R=0.1) is increased up to 1170MPa(Gear A) and up to 2207MPa(Gear B), respectively.

REFERENCE

1. A.Tange and K.Ando: Proceedings of Sympo. on Fract. & Fract. Mech. 10th,P.6,Kyoto,Japan.
2. K.Matsui, H.Eto, K.Kawasaki, Y.Misaka and K.Ando: Transactions Japan Society Mechanical Engineers. **637-65**(1999) P.1942
3. H.Ishigami, K.Matsui, Y.Jin and K.Ando: Fatigue Fact. Engng. Mat. Struct. (Submitted)
4. K.Matsui, H.Eto, K.Yukitake, Y.Misaka and K.Ando: Transactions Japan Society Mechanical Engineers (Submitted)

Table 1 Chemical compositions of materials used(wt.%).

Material	C	Si	Mn	P	S	Ni	Cr	Mo
Steel (a)	0.51	0.20	0.74	0.02	0.02	0.04	0.11	-
Steel (b)	0.19	0.06	0.84	0.010	0.019	0.09	0.107	0.40

Table 2 Shot peening conditions.

	SP,SSP	SDSP		RSP,SRSP	RDSP,SRDSP	
Peening machine	Impeller type	Primary Impeller type	Secondary Air Nozzle type	Air Nozzle type	Primary Air Nozzle type	Secondary Air Nozzle type
Shot diameter	ϕ0.60mm	ϕ0.60mm	ϕ0.08mm	ϕ0.60mm	ϕ0.60mm	ϕ0.08mm
Shot hardness	560HV	560HV	700HV	700HV	700HV	700HV
Shot velocity	73m/s	73m/s	Gauge pressure 0.3MPa	Gauge pressure 0.4MPa	Gauge pressure 0.4MPa	Gauge pressure 0.3MPa
Shot distance	350mm	350mm	40mm	32mm	32mm	32mm
Coverage	300%	300%	300%	300%	300%	300%
Arc height	0.48mmA	0.48mmA	0.30mmN	0.55mmA	0.55mmA	0.28mmN

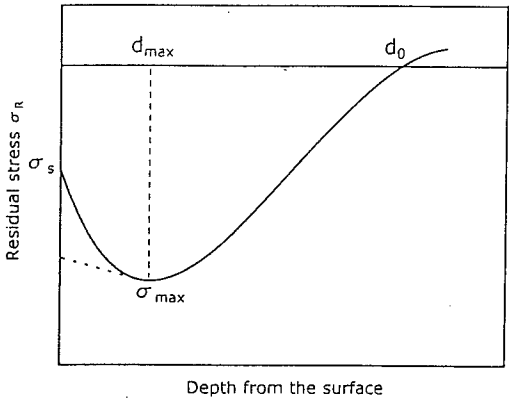


Fig. 1 Schematic illustration of residual stress distribution by normal shot peening.

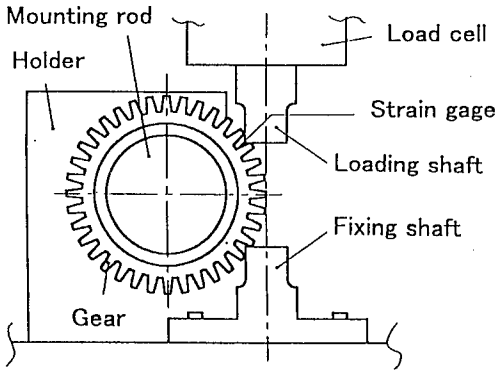
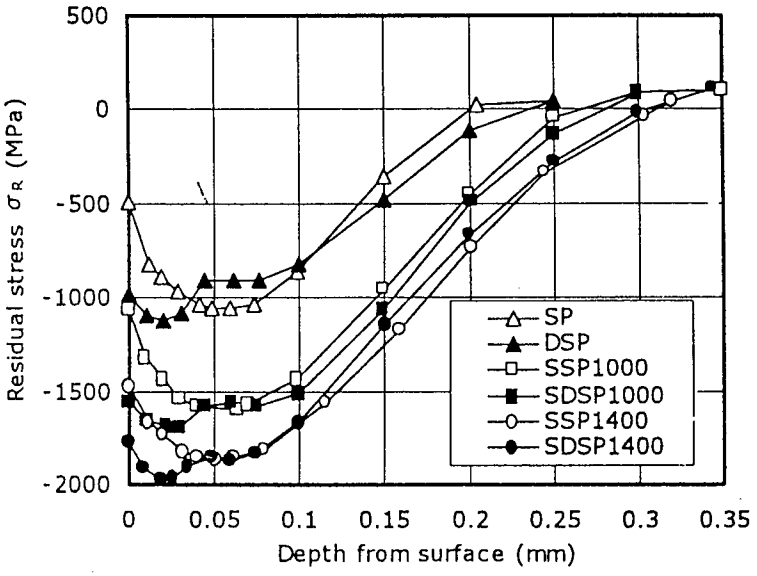
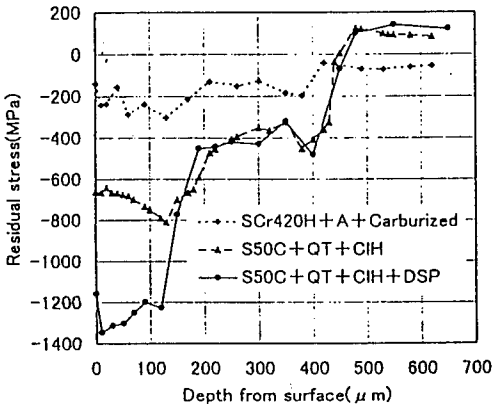


Fig. 2 Schematic illustration of fatigue test method of gear.

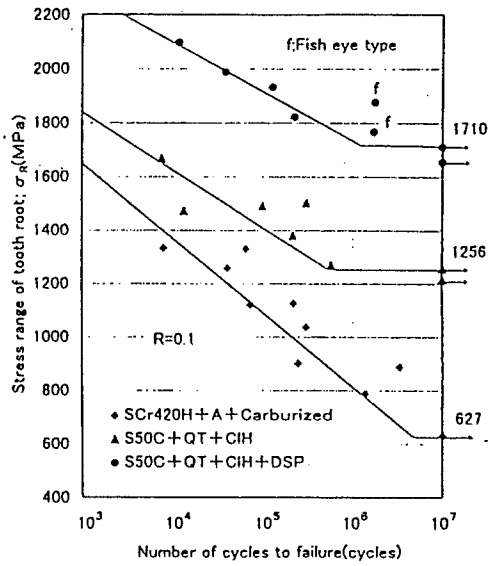


↑ Fig. 3 Residual stress distribution by shot peening.



↑ Fig. 4 Residual stress distribution in Gear A.

↓ Fig. 5 S-N curve of Gear A.



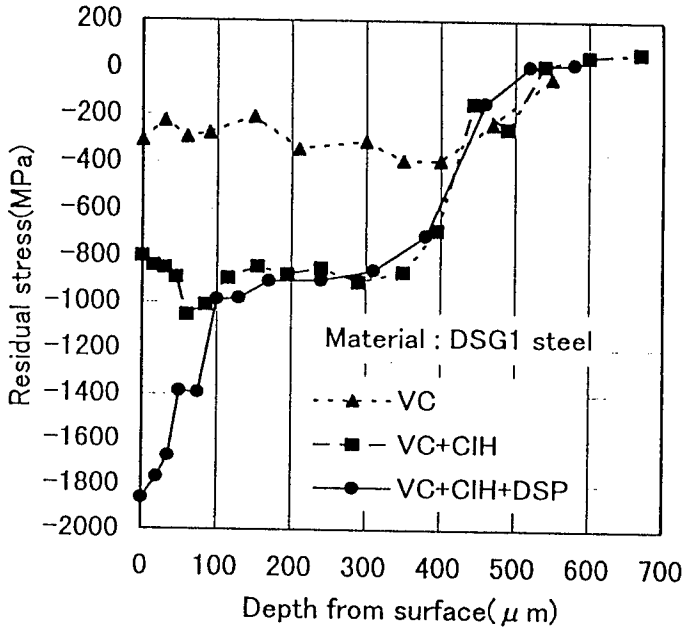


Fig. 6 Residual stress distribution in Gear B.

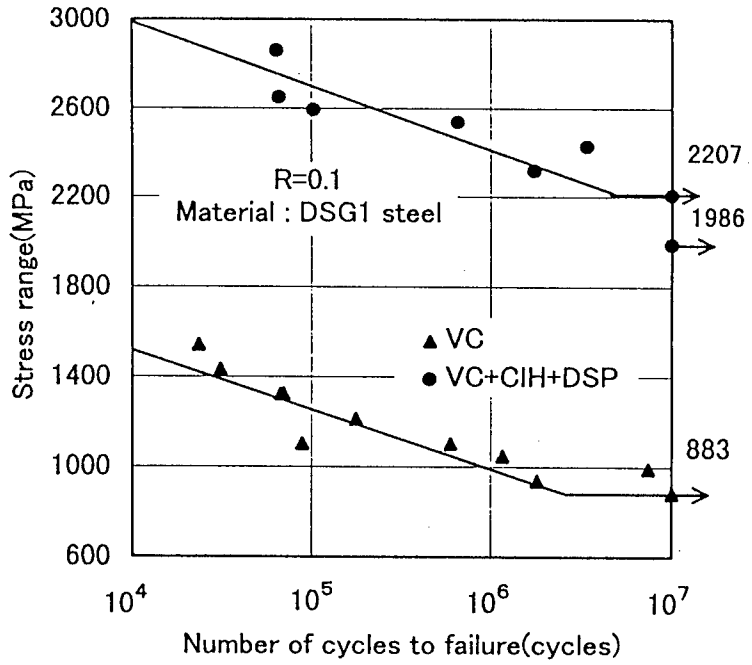


Fig. 7 S-N curve of Gear B.

Key Engineering Materials Vols. 183-187 (2000) pp. 927-932
© 2000 Trans Tech Publications, Switzerland

A Study on Probabilistic Fatigue and Calendar Fatigue Life

Bintuan Wang and Qingxiong Yang

Department of Aircraft Engineering, Northwestern Polytechnical University,
Xi'an 710072, China P.R.

Keywords: Atmosphere Corrosion, Calendar Fatigue Life, Cumulative Damage, Fatigue Reliability, Probabilistic Fatigue

ABSTRACT

Based on the effect of an atmosphere corrosion environment on the fatigue property of metals, a new dynamic probabilistic fatigue model has been presented. It describes the statistical distribution parameters of the fatigue property as a function of both loading cycles and the pre-corrosion calendar time of the material. To verify this model, it is applied to calculate the fatigue life reliability of specimens exposed in an atmosphere environment for 0,1,2 and 4 calendar years. Also it is used in predicting the calendar fatigue life of airframe structure elements. It is shown that this model is very reasonable and effective to predict fatigue reliability and calendar fatigue life.

1. PREFACE

There are many complex factors concerning the corrosion of airframe material, and thus so far there is no effective methods for predicting the calendar fatigue life of a structure. Two major methods have been used to predict the service life of material in a corrosion environment. One of them is the corrosion damage severity evaluating model [1], which can only be applied to structures subjected to steady loading or no loading. It does not consider the effect of the corrosion environment on the fatigue property of material. The other one is similar to the traditional fatigue life predicting method only by taking the corrosion environment as a loading condition [2]. None of them can solve the problem of the fatigue property decrease of material in an atmosphere corrosion environment. So, they can not be applied practically in predicting the calendar fatigue life of a structure. To overcome these shortcomings, this paper develops a new dynamic probabilistic fatigue model.

2. FATIGUE DAMAGE DYNAMIC STATISTICAL MODEL (FDDS)

2.1. Test Basis

For specimens of LC4CS aluminum alloy and 30CrMnSiNi2A high strength steel exposed to an atmosphere environment for 1,2 and 4 years, fatigue test result shows that [3,4]:

(1) The fatigue life of materials follows log-normal distributions or two-parameter-weibull distributions.

(2) The mean of fatigue life decreases with the elapse of calendar time, and the deviation

increases with the elapse of calendar time. The coefficient of variation of fatigue life then increases with the elapse of calendar time.
(3) Fatigue stress-life curves (S-N_f curves) change with pre-corrosion calendar time

2.2. FDDS-Model

Based on the above test result and the quasi-dynamic fatigue damage statistical model[5,7],the main points of the FDDS-model are as follow:
(1) The definition of damage.

The damage introduced by each cycle is defined as

$$D_i(T_i) = 1/[N_{fi}(T_i)] \tag{1}$$

where all the D_i and the life cycle N_{fi} at a stress level i are random variables, which depend on the loading and material property at calendar time T_i, further, we have

$$\ln D_i = -\ln N_{fi} \tag{2}$$

That is, for materials subjected to a corrosion environment with the same calendar time, the distribution of D_i is the same as that of N_{fi} for the corresponding stress cycle. Since N_{fi} follows a log-normal distribution then

$$\mu_{LD_i} = -\mu_{LN_{fi}} = -\ln(\mu_{N_{fi}} / \sqrt{1+\eta_{N_{fi}}^2}) \tag{3}$$

$$\sigma_{LD_i}^2 = \sigma_{LN_{fi}}^2 = \ln(1+\eta_{N_{fi}}^2) \tag{4}$$

where $\mu_{LN_{fi}} = \mu_{LN_{fi}}(T_i), \sigma_{LN_{fi}} = \sigma_{LN_{fi}}(T_i)$ and $\eta_{N_{fi}} = \eta_{N_{fi}}(T_i)$

That is, all these statistical parameters are variable with T.
(2)The cumulative damage principle

When a specimen is subjected to an n cycle loading at time T_n

$$D(n,T_n) = \sum_{i=1}^{n} D_i(T_i) = D_1(T_1) + D_2(T_2)\big|_{D_1} + \cdots + D_n(T_n)\big|_{D_{n-1}} \tag{5}$$

$$D_i(T_i) = f_i(\Delta\sigma_i, \Delta\varepsilon_i, R_i, T_i)\big|_{D_{i-1}(T_{i-1}) = f_{i-1}(\Delta\sigma_{i-1}, \Delta\varepsilon_{i-1}, R_{i-1}, T_{i-1})} \tag{6}$$

where $f_i(\cdot)$ represents a complex function, and $\Delta\varepsilon_i$, $\Delta\sigma_i$ and R_i are stress range, strain range and strain ratio, respectively. Here, a modified local stress-strain method [8] is applied, which considers cyclic hardening/softening of material and adopts a transient cyclic stress-strain curve to calculate the local stress and strain. Thus, the damage is obtained by iteration from formula (6).

According to the central limit theorem, $D(n,T_n) = \sum_{i=1}^{n} D_i(T_i)$ can be considered to follow a normal distribution if n is large enough (this is easily satisfied for the fatigue problem). Since the loading sequence effect is already considered, $D_1, D_2, \cdots D_n$ are independent from each other, then

$$\mu_D = \sum_{i=1}^{n} \mu_{D_i} = \sum_{i=1}^{n} \exp(\mu_{LD_i} + \frac{1}{2}\sigma_{LD_i}^2) = \sum_{i=1}^{n} \frac{1+\eta_{N_{fi}}^2}{\mu_{N_{fi}}} \tag{7}$$

$$\sigma_D = \sqrt{\sum_{i=1}^{n} \sigma_{D_i}^2} = \sqrt{\sum_{i=1}^{n} \frac{(1+\eta_{N_{fi}}^2)\eta_{N_{fi}}^2}{\mu_{N_{fi}}^2}} \tag{8}$$

Here it is necessary to point out that, for all types of loading spectrum, at different calendar times T_i (i=1,2,$\cdots n$), usually there are $\mu_{D_1} \neq \mu_{D_2} \neq \cdots \neq \mu_{D_n}$ and $\sigma_{D_1} \neq \sigma_{D_2} \neq \cdots \neq \sigma_{D_n}$. However, for specimens subjected to a constant-amplitude loading spectrum and without being corroded, $\mu_{D_1} = \mu_{D_2} = \cdots = \mu_{D_n}$ and $\sigma_{D_1} = \sigma_{D_2} = \cdots = \sigma_{D_n}$.

(3)The critical cumulative damage D_c

D_c is also a random variable affected by the material, loading and working environment. It is shown that D_c can be assumed to follow the log-normal distribution for most metals under steady loading, and $\mu_{D_c} \approx 1$, $\eta_{D_c} \approx \eta_{N_f}$ [5-7]. Considering the effect of atmospheric corrosion and aging on material, the coefficient of variation η_{N_f} increases with calendar time. So η_{D_c} also increases with calendar time. The distribution of D_c will then certainly change and can be assumed as: $\mu_{D_c} \approx 1$, $\eta_{D_c} = \eta_{D_c}(T) \approx \eta_{N_f}(T)$. From the above points, the FDDS model can be established, and the life reliability function is

$$R(T) = P(D < D_c) = \int_{-\infty}^{+\infty} f_{D_c}(t) F_D(t) dt = \int_{0}^{\infty} \frac{1}{\sigma_{LD_c}\sqrt{2\pi}} \exp[-\frac{(\ln t - \mu_{LD_c})^2}{2\sigma_{LD_c}^2}] \phi(\frac{t-\mu_D}{\sigma_D}) dt \tag{9}$$

The integral Eq.9 can not be solved directly, here a normal distribution to approximate the distribution of $R(T)$ is used:

$$R(T) = P(D < D_c) = 1 - P[(D_c - D) < 0] = 1 - \phi(-\frac{\mu_Z}{\sigma_Z}) \tag{10}$$

$$\mu_Z = \mu_{D_c} - \mu_D; \quad \sigma_Z = \sqrt{\sigma_{D_c}^2 + \sigma_D^2} \tag{11}$$

where $\phi(\cdot)$ is the standard normal distribution function.

3. APPLICATION EXAMPLES

3.1. Predicting Life Reliability

Fig.1 shows a comparison between Eq.10 and test data for LC4CS aluminum alloy central-hole plates [3] (dog-bone shaped specimens, K_t=2.4, constant-amplitude loading: σ_{max}=300MPa, σ_{min}=18MPa, the specimens had been pre-corroded in an atmospheric corrosion environment for

1,2,and 4 years). At R(T)=50% , the errors between the predicted life and test results are 3.5%, 4.0%, 1.85%, 6.4% for specimens of 0,1,2 and 4 years, respectively.

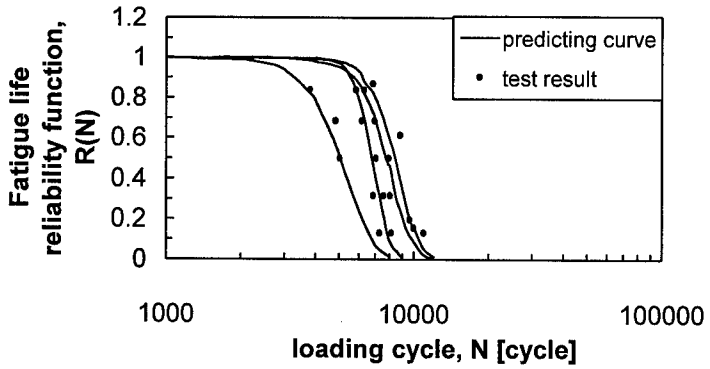


Fig.1. LC4CS central-hole-plate reliability curves(from right to left in sequence-0,1,2,4 year)

3.2 Predicting Calendar Fatigue Life

The LC4CS ear-shaped joint of an aircraft wing beam, with a stress concentration factor K_t=3.17, is subjected to the nominal stress spectrum of a loading 'block' (200 flight hours) in Table 2 [9]. On the basis of test results of our research, the parameter of $\varepsilon_{eq} \sim N_f$ relation (Eq.12) is listed in Table 1, the other fatigue properties are taken to be the same as that for 0 years.

Table 1. The parameters in Eq.12

E MPa	m	ε_u %	ε_e %	a_1	a_0				
					0 year	1 year	2 year	3 year	≥4 year
72572	0.82	8.905	0.092	3.12837	3.64163	3.61476	3.5501	3.49896	3.44097

$$\varepsilon_{eq} = (2\varepsilon_a)^m (\sigma_{\max}/E)^{1-m}$$

$$\log N_f = a_0 + a_1 \tanh^{-1}\{[\log(\varepsilon_u \varepsilon_e) - \log(\varepsilon_{eq}^2)]/[\log \varepsilon_u - \log \varepsilon_e]\} \quad (12)$$

Table 2. Nominal stress spectrum of a loading 'block'(200 flight hours)

Loading sequence	1	2	3	4	5	6	7	8
S_{max}(MPa)	92.1	196.0	33.4	423.7	383.5	274.6	191.2	161.8
S_{min}(MPa)	41.2	49.0	41.2	41.2	41.2	41.2	47.8	41.2
Cycles	145	146	59	1	13	234	137	40

The predicted life result is 39.3 blocks. If the ordinary fatigue property of the material is used, the predicted life is 59 blocks (the test life is 65 blocks). Usually a training aircraft could accomplish 'a block'(200 flight hours) of training within a calendar year. The smallest life scatter factor for the aircraft structure is 4, so the safe service life is only 39.3/4≈10 years.(In fact, the corrosion fatigue life scatter factor could be larger than that without corrosion.)

4. CONCLUSION

(1) When airframe material is subjected to atmospheric environment corrosion for several years, the statistical distribution parameters of fatigue life will change with calendar time.

(2) The FDDS model presented in this paper, based on an in-depth mechanism study of the fatigue damage stochastic process, considers the loading sequence effects, cyclic hardening/softening effects and especially the atmospheric corrosion effects, so it is more suitable for predicting fatigue reliability.

(3) Two application examples indicate that fatigue life reliability decreases with calendar time(Fig1),and the predicted calendar fatigue life is shorter than the life without considering the atmospheric environment corrosion effect. So it is practical to use the FDDS model to predict calendar fatigue life.

REFERENCE

1. Lu G.Z, Tong X.Y: Fatigue and Fracture, Aviation Industry Press, Beijing(1998)p.1
2. Jiang Z.G, Corrosion Fatigue of Aircraft structure, Aviation Industry Press, Beijing(1992)p. 43
3. Wang Bintuan, Fan Jianhua and Yang Qingxiong, ACTA METALLURGICA SINICA, **35** (1999) p.1163
4. Wang Bintuan, Fan Jianhua, Sun Qin et al, J. Aircraft Engineering, **3** (1999) p.42
5. Liao Min, Xu Xiaofei and Yang Qingxiong, Int. J. Fatigue, **17** (1995) p.559
6. Tanaka S.,Ichkawa M. and Alikata S., Int. J. Fatigue, **2** (1980) p.159
7. Liao Min, Ph.d Thesis, Northwestern Polytechnical University, China, Xi'an(1993)
8. Wang Bintuan and Yang Qingxiong, ACTA AERONAUTICA ET ASTRONAUTICA SINICA, **3**(2000)
9. The science and technology committee of aviation industry ministry: Analytical Handbook for Strain Fatigue, Science Press, Beijing(1987) p.166

Key Engineering Materials Vols. 183-187 (2000) pp. 933-938
© 2000 Trans Tech Publications, Switzerland

Influence of Microstructures on Fatigue Limit of High Strength Ductile Irons

J.H. Kim and M.G. Kim

Division of Mechanical and Mechatronics Engineering, Kangwon National University,
192-1, Hyoja-dong, Chunchon, Kangwon 200-701, Korea

Keywords: 2-Phase, Ductile Iron, Fatigue, Fatigue Limit, Heat Treatment, Microstructure

ABSTRACT

Rotary bending fatigue tests were performed to investigate the effects of 2-phase microstructure on fatigue limit with prepared specimens in high strength ductile irons. The used specimens have different matrix structures. Series A has sorbite and series B has bainite. Fatigue limits of both specimens are improved compared with as cast specimen, and in case of series B the fatigue limit is higher than any others. The reason why the fatigue limit of series A shows inferiority to that of series B is that transition of micro fatigue cracks to meso crack occurs very rapidly, so increased stress intensity factor drives the fatigue crack growth. In case of series B, bainite, the γ layer contained in bainitic structure interferes with the rapid growth of micro fatigue crack to meso crack, and also α layer around graphite has the higher capacity for the absorption of plastic deformation energy than sorbite.

1. INTRODUCTION

Ductile iron has several engineering and manufacturing advantages compared with cast steels. These include an excellent damping capacity, better wear resistance, 20-40% lower manufacturing cost and lower volume shrinkage during solidification [1]. In particular, austempered ductile iron(ADI) is an alloyed and heat treated ductile or nodular cast iron. It has emerged as an important engineering material in recent years because of its excellent mechanical properties. ADI has been used as structural components in wide diverse fields such as gears, crankshafts, locomotive wheels, agricultural equipments and etc. The combination of high strength with good ductility, good wear resistance, good fatigue properties and fracture toughness achieved by ADI suggests that the engineering applications of this material will continue to expand in the coming years [2].

It is subjected to an isothermal heat treatment process called austempering. Austempering process involves austenitizing the alloy in the temperature range of 870 to 980℃ for 1 to 2 hr and then quenching it to an intermediate temperature range of 260 to 500℃ and holding there for sufficient time, usually 2 to 4 hr. This results in an unique microstructure in which the matrix consists of a mixture of ferrite and high carbon austenite. This unique structure is often referred to as bainite or ausferrite [3]. Besides this, the microstructure also consists of graphite nodules dispersed in it. The microstructure of ADI is different from austempered steels in which the microstructure primarily consists of ferrite and carbide.

Most of studies on ADI have been carried out on ductile iron with a predominantly pearlitic microstructure. Therefore, very little information is currently available in literature on the mechanical properties of ADI with ferritic microstructure.

The microstructures of ductile cast irons could be easily transformed to different one which has superior characteristics by means of heat treatments. So it is one of the important assignments to establish the systematization about the variances for fatigue characteristics in ductile irons.

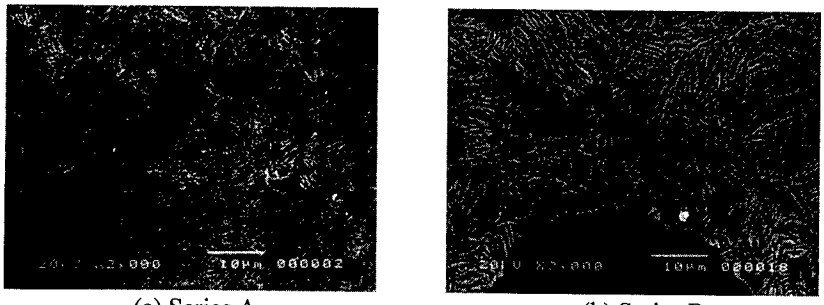
On the other hand, ductile irons for essential structural parts often require higher fatigue reliabilities even though they have heavy weight. However, ductile irons have the distinctive features that the coarse structures are followed by the slower solidification rates. So, it is inevitably required the proper heat treatment which transforms the coarse structure to fine one in order to obtain high fatigue reliability.

The present study was therefore undertaken to investigate the effects of microstructure on fatigue limit of the high strength ductile irons which have sorbite and bainite based on the fractography.

2. EXPERIMENTAL PROCEDURE

The material used for this study is a commercial grade products, GCD45 as per KS [4]. Chemical composition is given in Table 1. Round cylindrical samples with minimum diameter for rotary bending fatigue tester were prepared .

After fabrication the specimens were heat treated. Table 2 shows the detailed heat treatment processes. Fig. 1 shows the microstructures of specimen series. Mechanical property is measured for the two ductile irons and the data are given in Table 3. Five samples were tested and the average values from these samples were taken as the representative of the test data. Ultimate tensile strength, 0.2% proof yield strength and % elongation were obtained from the load versus displacement plot. Micro vicker's hardness was taken as average values from 30 points with the indentation loads of 50 g on the samples. Also, Table 4 shows the characteristics of graphite nodule obtained by KS [4]. Three test samples were measured and the average values from these samples were taken as the representative of the measurement data. Mean diameter, nodularity, area fraction and nodule count were obtained from the measurement.



(a) Series A (b) Series B

Fig.1. Microstructures of specimen series.

Table 1. Chemical compositions of experimental material (wt.%, Balanced Fe)

C	Si	Mn	P	S	Mg
3.75	3.0	0.15	0.03	0.015	0.04

Table 2. Details of heat treatment and microstructures of specimen series.

	Process of heat treatment	Structure
Series A	900 °C , 1hr → W.C → 600 °C , 1hr → F.C	Sorbite
Series B	900 °C , 1hr → S.C → 380 °C , 2hr → A.C	Bainite

F.C : Furnace cooling
W.C : Water cooling
S. C : Salt bath cooling
A. C : Air cooling

Table 3. Mechanical properties of specimen series.

	σ_B	σ_Y	δ	Hv
Series A	869	507	7	480
Series B	1065	799	9	512

σ_B : Ultimate tensile strength(MPa)
σ_Y : Yield strength(MPa), 0.2% proof stress
δ : Elongation(%)
Hv : Vickers hardness

Table 4. Characteristics of surface graphite.

	D_{sg}	H_{sg}	A_{sg}	N_{sg}
Series A	23	70	27	146
Series B	29	86	12	74

D_{sg} : Average diameter of graphite(μm)
H_{sg} : Nodularity of graphite(μm)
A_{sg} : Area fraction of graphite(μm)
N_{sg} : Nodule count of graphite($1/mm^2$)

After heat treatment the cylindrical specimens were grounded and then polished with emery paper(grit level : from 80 to 2000) and allumina powder with 0.3 μm grit level to mirror surface. Tests were performed using rotary bending fatigue tester(R = -1.0) at room temperature, and the test frequency was 60 Hz with constant speed of 3500 rpm.

3. RESULTS AND DISCUSSION

3.1. S-N curve and crack origin

Fig. 2 shows the S-N curves of specimen series. The data of as cast specimen which has bull's eye type microstructure are put together for reference [5]. From Fig. 2, the fatigue limits of series A and series B are improved compared with as cast specimen, and the rate of climb of series A which has sorbite microstructure is merely 13% but that of series B which has bainite microstructure is as

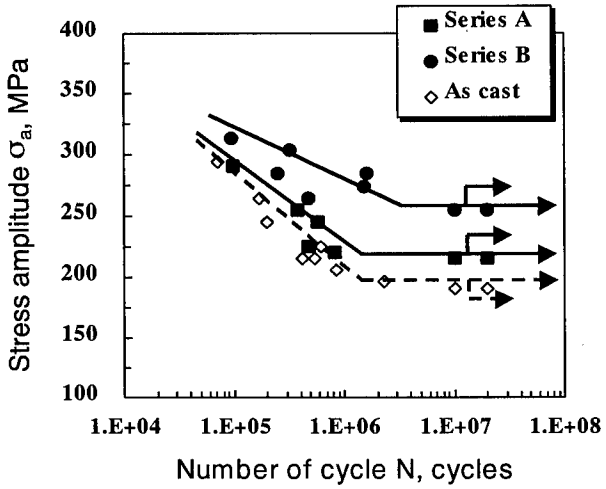
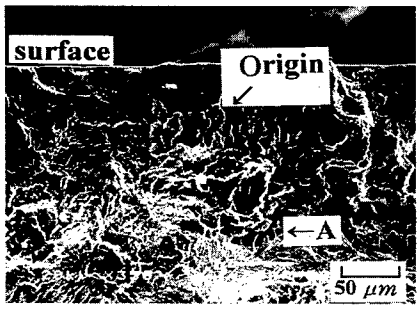
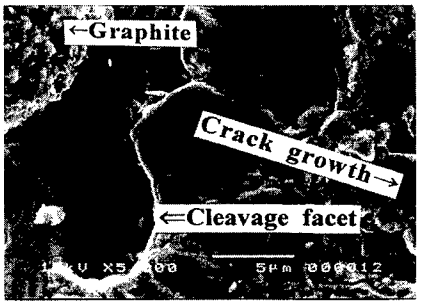


Fig. 2. The S-N curves of specimen series.

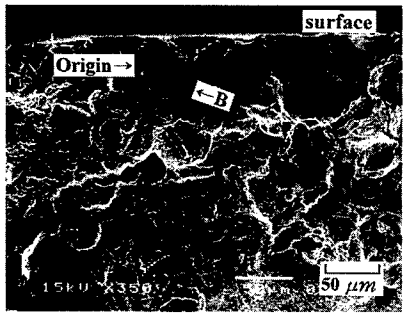


(a) Macroscopic observation

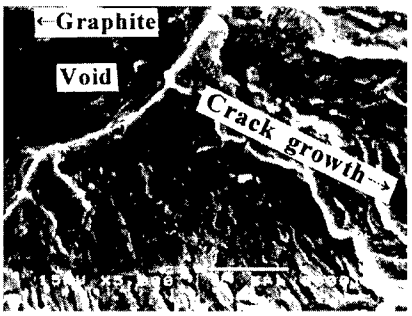


(b) Enlarged phography of A in (a)

Fig.3. Example of cleavage facet observed at fatigue crack origin and the adjacent graphite in series A, σ_a=255MPa, N_f =3.8×10^5.



(a) Macroscopic observation



(b) Enlarged phography of B in (a)

Fig.4. Example of cleavage facet observed at fatigue crack origin and the adjacent graphite in series B, σ_a=265MPa, N_f =4.7×10^5.

high as 35%. From the above facts, it can be estimated that the fatigue life of high strength ductile irons is governed by the fatigue crack initiation behavior [6] and the growth behavior of micro fatigue crack commenced at internal defect to meso crack.

Fig. 3 and Fig. 4 show the SEM photographs of fatigue crack origin of fractured specimen in series A and series B under cyclic loading. From Fig, 3(a) and Fig. 4(a), in all specimens, graphite was observed in fatigue crack origin in both specimen series, and it is known that the fatigue crack originates at the graphite ruggedness caused by heat treatment [7]. Therefore, in this study the detailed examination on the mechanisms of micro fatigue crack initiation and meso crack growth was carried out based on fractography.

3.2. Fractography on meso crack range

As a result of the SEM observation on the fatigue crack origin of series A, the cleavage facet showed in Fig. 3 was observed around the graphite being fatigue crack origin and adjacent graphite in almost of the fractured specimens. Fig. 3(b) is the enlarged SEM photograph of marked A in Fig. 3(a), and it is confirmed that the meso crack range formed along with the cleavage facet at crack origin was transited to typical fatigue fracture surface.

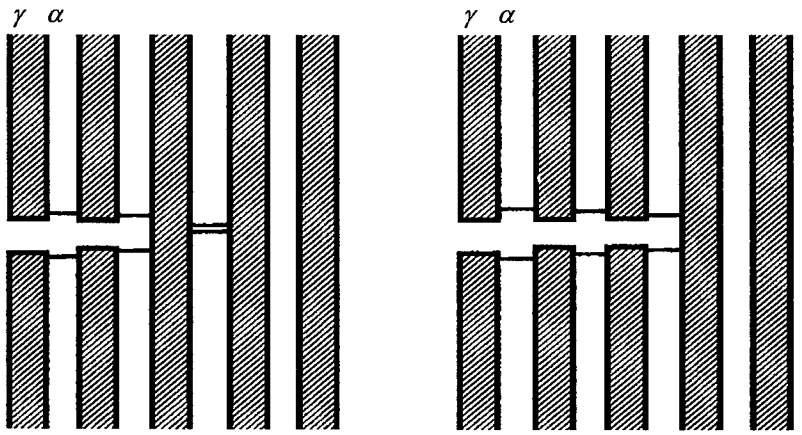
In spite of the relatively low stress amplitude, the reason of cleavage facet occurrence at crack origin is that the microstructure around the graphite is embrittled during the heat treatment process.

On the other hand, from the size of meso crack range and stress intensity factor being followed by the equation (1) below [8], it is known that the rapid growth of micro fatigue crack commenced at stress concentration place to meso crack increases the stress intensity factor at crack tip which drives the crack propagation. Therefore, it can be concluded that due to the local embrittlement of microstructure and easy meso crack range formation at crack origin, the fatigue limit of series A is low compared with series B.

$$K_a = \sigma_a \sqrt{\pi \sqrt{A}} \tag{1}$$

where, σ_a is stress amplitude(MPa) and $\sqrt{A}$ means size of meso crack range(m). Fig. 4 shows the SEM photographs of fatigue crack origin in series B. From Fig. 4, the fatigue origin is graphite nodule which exists just below the surface. The cleavage facet are not observed around fatigue crack origin and adjacent graphite. Instead, it is confirmed that the void around the graphite are observed. The void formed by the fact that the separation of graphite nodule from micro structure which has superior absorption capability of deformation energy occurs prior to fatigue crack commencement at graphite. Therefore, it is known that the resistance of series B, which has the superior absorption capability of deformation energy to fatigue crack initiation is greater than that of series A. And also in Fig. 4(b), the marked ridge and valley which is the typical fatigue crack are observed on the fracture surface. This unique characteristics of fracture surface means that the fatigue crack growth behavior is very sensitive to the micro structure composed of α layer and γ layer. So, it is postulated that the process of fatigue crack growth comply with the schematic illustration in Fig. 5. That is, the α layer which deforms without difficulty compared with γ layer makes a ridge, and vice versa, γ layer does valley. Also, it is one of the reasons for unique fracture surface characteristics that the adjacent α layer deforms before the crack propagates to the next γ layer. So, it is deducted that the γ layer existing in bainite micro structure interferes with the fatigue crack growth, and eventually the rapid enhancement of meso crack range are repressed.

Therefore, it can be known that the higher fatigue limit of series B is mainly caused by the effects of γ layer existing in micro structure.



(a) Fatigue crack confronting γ layer (b) Fatigue crack going through γ layer

Fig. 5. Schematic illustration for the processes of fatigue crack growth in series B.

4. CONCLUSIONS

Rotary bending fatigue tests were performed to investigate the effects of microstructures on fatigue limit with prepared specimens of high strength ductile irons. The used specimens have different microstructures each other. Series A has sorbite and series B has bainite. Obtained main results are as follows.

Fatigue limits of both specimens are improved compared with as cast specimen, and in case of series B the fatigue limit is higher than any other. The reason why the fatigue limit of series A shows inferiority to that of series B is that transition of micro fatigue cracks to meso crack occurs very rapidly, so increased stress intensity factor drives the fatigue crack growth.

In case of series B, bainite, the γ layer contained in bainitic structure interfere with the rapid growth of micro fatigue crack to meso crack, and also α layer around graphite has the higher capacity for the absorption of plastic deformation energy than sorbite

REFERENCE

1. S.R. Lampman : ASM Handbook, **19**(1996)
2. D.C Choi, J. Korea Foundary Soc., **10-4**(1990) p.294
3. M.N. James and L. Wenfong, J. Mater. Sci. Eng. **A265**(1999) p. 129
4. KS D 4302, Korea Standard, ROK UDC 669(1984) p. 1
5. M.G. Kim and J.H. Kim, Trans. KSAE, **7-5**(1999) p. 1404
6. M.G. Kim and J.H. Kim, Trans. KSME, **23-2**(1999) p. 287
7. T. Nakamura, et al, Trans. JSME, **61-582**(1995) p. 231
8. M.G. Kim and J.H. Kim, Proc. '99 Spring Meeting of KSME, **A**(1999) p. 725

Key Engineering Materials Vols. 183-187 (2000) pp. 939-944
© 2000 Trans Tech Publications, Switzerland

Fretting Fatigue Behavior of Structural Steels

H. Yamamura[1], Y. Yamada[2] and R. Ebara[3]

[1] Environmental Affairs Department, Mitsubishi Motors Corporation,
5-33-8, Shiba, Minato-ku, Tokyo 108-8410, Japan

[2] Hiroshima R & D Center, Mitsubishi Heavy Industries Ltd.,
4-6-22, Kan-On-Shin-Machi, Hiroshima 733-8553, Japan

[3] Department of Advanced Materials Science, Kagawa University,
1-1, Saiwai-cho, Takamatsu-city, Kagawa 760-8526, Japan

Keywords: Contact Area, Defric Coating, Fretting Fatigue, Pit, Structural Steels

ABSTRACT

Fretting fatigue tests were conducted on structural steels such as SCM415H,SCM440 and SAPH45 and Cast iron, FC25. Consequently, It was clarified that the stress over the contact area where fretting fatigue failure initiate was depend on the Vickers hardness number of the steel surface. It was also clarified that the repeated bending stress at the contact area where fretting fatigue failure initiate linearly decreased as stress over the contact area increased. The stress over the contact area where fretting fatigue initiate was increased by eighty percent in application of Defric coating to SCM440. Striation, fretting debris and pit were predominantly observed on the surface of the contact area. Crack initiation mode was transcrystalline on SCM440 and SAPH45、and was intergranular on SCM415H. It can be concluded that the fretting fatigue crack initiate from a pit formed at the contact area due to the slip movement.

1 INTRODUCTION

Failure and functional difficulty due to fretting fatigue are frequently observed on the bolted machine components. However the available countermeasure cannot be applied because of the poor understanding of fretting fatigue behavior. It is important to find out the adequate combination of materials, effective surface treatment and optimum lubricating method in order to prevent fretting

fatigue failure of machine components. The main purpose of this paper is to present the fretting fatigue behavior of structural steel such as SCM415H,SCM440 and SAPH45 and cast iron , FC25. The availability of Defric coating to prevent fretting fatigue is also exemplified.

2 EXPERIMENTAL PROCEDURE

The chemical compositions and mechanical properties of tested materials are shown in Table1. The fretting fatigue specimen is shown in Fig.1 The fretting shoe and the bolt are shown in Fig.2. Table 2 shows the materials combination of the fretting fatigue specimen and the shoe. The Defric coating of which MoS_2 was dried and burned at 443K for five minutes after phosphate treatment was used for the fretting fatigue specimen surface of SCM440.

Table1 Chemical compositions and mechanical properties of tested materials

Materials	Chemical compositions(%)							Mechanical properties				
	C	Si	Mn	P	S	Cr	Mo	σ_{02} MPa	σ_B MPa	ε %	ψ %	Hv
SCM415H[1)]	0.16	0.28	0.73	0.021	0.018	0.98	0.15	716.4	995.4	21.9	66.6	289
SCM440[2)]	0.39	0.27	0.75	0.024	0.006	0.98	0.15	905.1	1050.6	19.2	57	373
SAPH45	0.16	0.24	1.16	0.014	0.008	—	—	337.3	504.0	38.4	70.2	146
FC25	3.47	2.05	0.79	0.023	0.029	—	—	—	195.1	0.63	0.63	255

Note:1) carbonized depth;0.71mm, surface hardness; Hv 689
2)Quench & Tempered

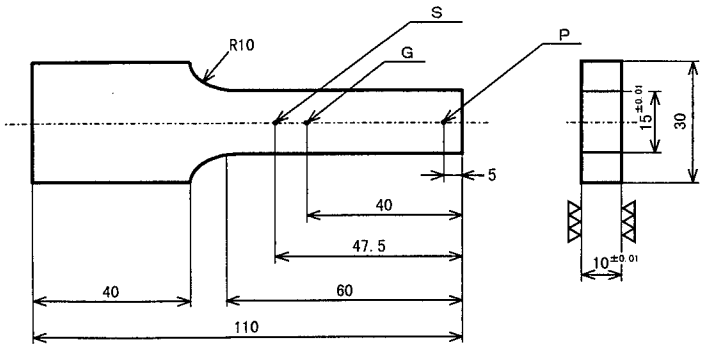


Fig.1 Fretting fatigue specimen
P: loaded point, G: strain measured point, S: contact point with shoe

The fretting fatigue tests were conducted by use of the fretting fatigue specimen with bolt-tightened

shoe on both side as shown in Fig. 2 1. The bolt was made in maraging steel. The contact pressure was applied to the point S in Fig.1. The contact load was gained from the strain measured by the strain gauge fixed at the center of the bolt. The contact between fretting fatigue specimen and shoe is so called the contact between a plate and a disc. The contact width is too small as compared with the plate width. Therefore the contact stress can be calculated by use of the Hertzian Equation as shown in eq.(1) and eq.(2).

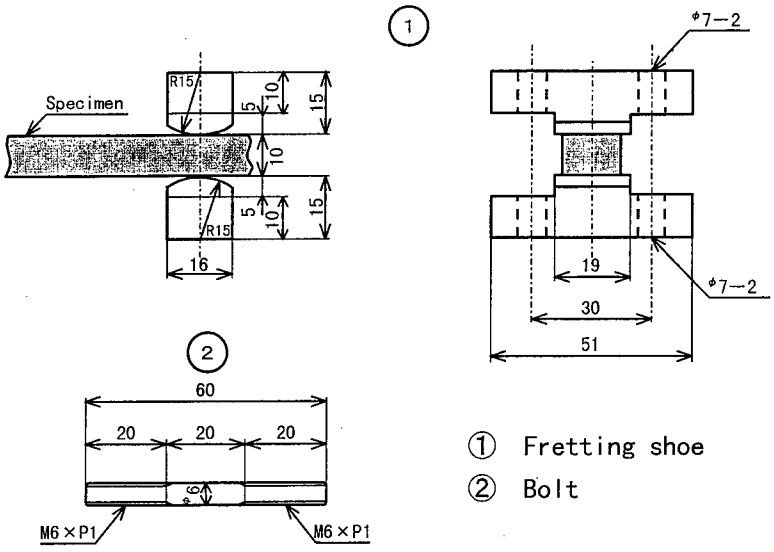


Fig.2 Fretting shoe and bolt

Table2 Materials combination of specimen and shoe

	Specimen	Shoe
1	SCM415H	SCM415H
2	SAPH45	SS41
3	SCM440	SCM440
4	SCM440 (Defric coat)	SCM440
5	FC25	SCM440

For the combination of 1 to 4 in Table 2

$$Pmax=0.418(PE_1/lR_1)^{1/2} \quad (1)$$

For the combination of 5 in Table 2

$$Pmax=0.591\{ P/l\ (E_1E_2/E_1+E_2)(1/R_1)\}^{1/2} \qquad (2)$$

where Pmax= the maximum contact stress (MPa)

P= contact load per unit width(MPa)

R_1= radius of the shoe

E_1= Young's modulus of the shoe (MPa)

E_2= Young's modulus of the fretting fatigue specimen (MPa)

l = the contact length

The plane bending stress was the corrected stress on the S spot calculated by the strain from the strain gained by the strain gauge fixed on the G point.

The plane bending fatigue testing machine(4.9kN) was used. The testing frequency was 13.3 Hz. The surface and the fracture surface were observed by SEM.

3 EXPERIMENTAL RESULTS AND DISCUSSION

Fig.3 shows the fretting fatigue testing results of SCM440. Although some scatter can be seen on the data , it is apparent from this Figure that the contact stress where fretting fatigue crack initiate is about 1300MPa. The larger the contact stress the fretting fatigue crack easily initiate at the same bending stress.

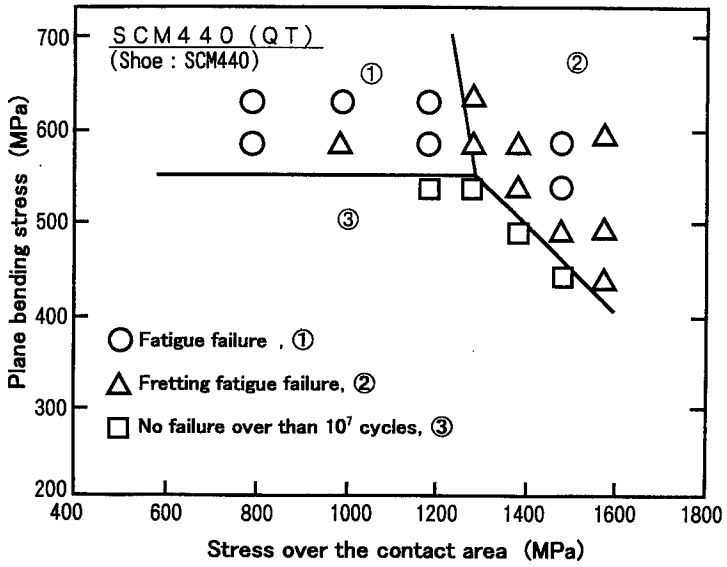


Fig.3 Relation between plane bending stress and stress over the contact area

The similar testing results were observed on SAPH45 and SCM415H . However no fretting fatigue crack initiated on FC25. It is also apparent that the relation between plane bending stress and stress

over the contact area can be classified into the three area such as the area where fatigue failure occurs , the area where fretting fatigue failure occurs and the area where no failure occurs over than 10^7 cycles. This similar findings can be seen on S38C steel [1] and Ti-6Al-4V alloy [2] .

Application of Defric coating to SCM440 increased the contact stress where fretting fatigue crack initiate up to 2350MPa. The surface hardness of Defric coated SCM440 was Hv 538. Fig.4 shows the relationship between stress over the contact area and surface hardness of tested materials. The larger the surface hardness, the larger the stress over the contact area is. It can be mentioned that this relation seems to be useful when we select the material against fretting fatigue failure. However, these data were taken from fretting fatigue tests without relative slip. For wider practical application fretting fatigue behavior with relative slip and impact stress should be clarified in future.

Fig.5 shows the surface observation results of SCM440. The striation (Flg.5 b)), fretted debris (Fig.5 c)) and pit(Fig.5d)) were predominantly observed on contact area. It can be observed from Fig.5d) that the crack initiated from the depth of the pit. The pit initiate when fretting debris was removed from the striation formed due to the contact slip movement. These phenomena were also observed on Ti-6Al-4V alloy. Therefore, it can be concluded from above mentioned fact that the fretting fatigue crack initiate from the pit where stress concentrate. The crack initiation mode were transgranular of SCM440 and SAPH45 and that for SCM415H was intergranular. While the crack propagation mode of SCM440 and SAPH45 was striation and that for SAPH45 was mixed mode of intergranular and transgranular.The intergranular fracture is frequently observed on carbonized steel.

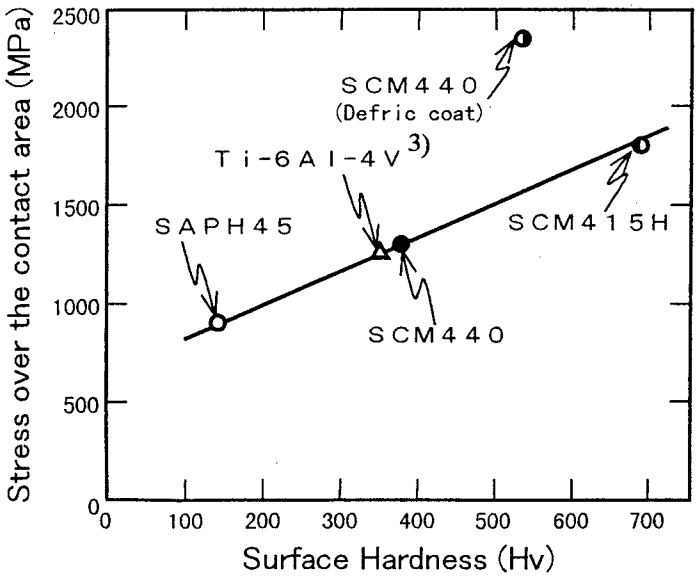


Fig.4 Relation between surface hardness and stress over the contact area

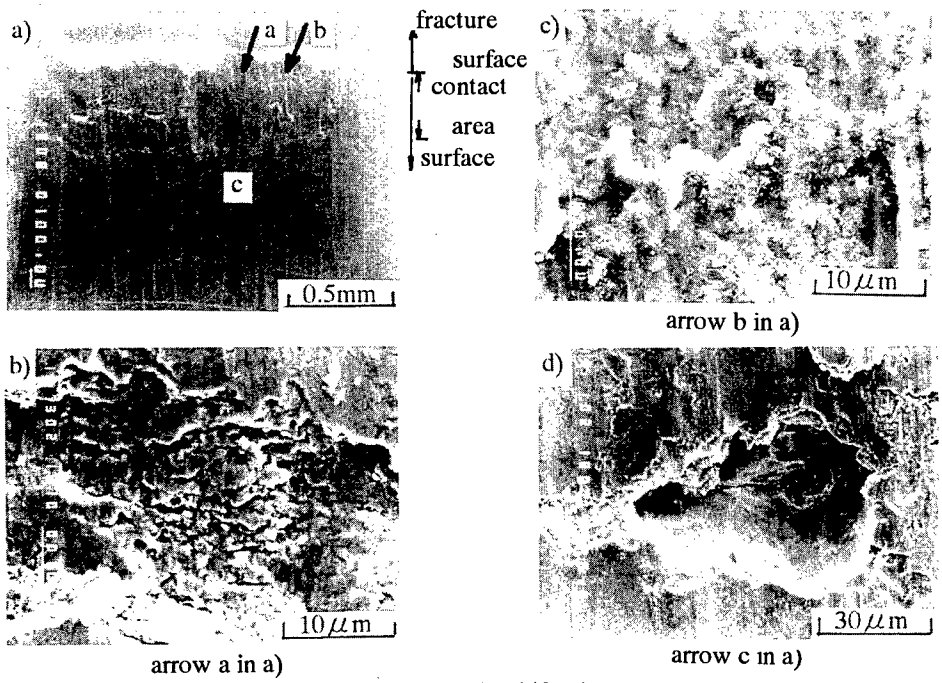


Fig.5 Surface observations results of SCM440 ,plane bending stress;490 MPa stress over the contact area;1372MPa ,1.3 x10^6 cycles

4.CONCLUSION

1 The stress over the contact area where fretting fatigue crack initiate is 1800,1300 and 900 MPa for SCM415H, SCM440 and SAPH45 , respectively and is depend on the surface hardness of the tested material. The larger the stress over the contact area the plane bending stress which fretting fatigue crack initiate decreases.

2. The stress over the contact area of SCM440 where fretting fatigue crack initiate increases from 1300MPa to 2350 MPa by Defric coating. It can be mentioned that the Defric coating is useful surface treatment against fretting fatigue.

3. The fretting fatigue crack did not initiate on FC25 up to 2000MPa of the stress over the contact area.

4 Fretting fatigue crack initiate from the pit where stress concentrate. The pit initiate when fretting debris was removed from the striation formed due to the contact slip movement.

5. The crack initiation mode were transgranular of SCM440 and SAPH45 and that for SCM415H was intergranular. While the crack propagation mode of SCM440 and SAPH45 was striation and that for SAPH45 was mixed mode of intergranular and transgranular.

REFERENCE

1. R.B.Waterhouse: Fretting Corrosion , Pergamon Press (1972) p.8

2. K.Nishioka and K.Hirakawa, Trans.JSME ,37(1971) p.1051

3. R.Ebara and M.Fujimura, Proc. of the thirty second annual meeting of JSMS (1983) p.238

Key Engineering Materials Vols. 183-187 (2000) pp. 945-950
© 2000 Trans Tech Publications, Switzerland

Fatigue Failure Model for Composite Laminates under Multi-Axial Cyclic Loading

C.S. Lee, W. Hwang, H.C. Park and K.S. Han

Department of Mechanical Engineering, Pohang University of Science and Technology
San 31 Hyoja-dong, Nam-gu, Pohang 790-784, Korea

Keywords: Carbon/Epoxy Laminates, Cumulative Damage, Fatigue Life Prediction, Fatigue Modulus, Multi-Axial Loading

ABSTRACT

Fatigue life prediction equation is proposed based on fatigue modulus concept. Fatigue modulus degradation rate at any fatigue cycle was assumed as a power function of number of fatigue cycles. New stress function describing the relation of initial fatigue modulus and elastic modulus was used to describe material non-linearity at the first cycle. Fatigue modulus at failure is assumed to be proportional to applied stress level. Material constants in the equation can be determined from static and uniaxial cyclic loading. Using cumulative damage model, fatigue life prediction on composite laminates under multi-axial stress conditions was derived as functions of applied stress level and number of fatigue cycles. The fatigue failure model was verified by fatigue tests using bi-directional (cross-ply) carbon fiber-epoxy composite tubes under combined axial and torsional loading. It was shown that the proposed equations have wide applicability and the presented prediction agreed well with experimental data.

1. INTRODUCTION

The majority of components and structures in service are subjected to multi-axial loading conditions, resulting in biaxial and triaxial states of stress. Pressure vessels, turbine blades, crank shafts and aircraft structures are all common examples. Failure mechanisms of FRP are more complex under multi-axial loading than under uniaxial loading. Evaluation of FRP under multi-axial loading, thus, is important for designing composite structures. Moreover, fatigue analysis has been required as one of the essential procedures to determine a service life for reliable design of the structures. Development of analytical method for the prediction of fatigue life in terms of fatigue load and fatigue cycles is needed for general laminates under multi-axial loading.

Under uniaxial loading, some theories for fatigue life prediction of FRP have been proposed at constant amplitude stress condition [1-5] and at two-stress level [6-8]. A damage variable using a modulus degradation rate has been successfully applied [5-7]. Fawaz and Ellyin [9] proposed a new model, which predicts the fatigue failure of FRP under multi-axial stresses, varying minimum to

maximum cyclic stress ratios and different fiber orientations with respect to the loading directions by introducing the concept of elementary blocks. However, it may be difficult to apply his model to multi-directional composite laminates. Recently Fawaz [10] presents a phenomenological model for predicting the multi-axial fatigue failure of FRP using a tensor polynomial formulation. Until now, there is no theory considering material non-linearty for fatigue life prediction of composite materials subjected to biaxial loads.

In this study, fatigue modulus was used for stiffness parameter. When the material degradation with fatigue cycles progresses without the change of stiffness, the fatigue modulus decreases, while conventional modulus such as elastic modulus and secant modulus is constant. Therefore, fatigue modulus describes fatigue behavior of materials more effectively. Fatigue life prediction on composite laminates has been made for multi-axial stress condition as well as uniaxial stress condition.

2. THEORETICAL ANALYSIS

2.1. Fatigue Modulus Concept

The stress-strain curve of composite materials under cyclic loading changes due to degradation as shown in Fig. 1. Fatigue modulus F is a slope of a line on', while E and S denote elastic modulus and secant modulus, respectively. Therefore,

$$F(n,q) = \frac{\sigma_a}{\varepsilon(n)} = \sigma_u \frac{q}{\varepsilon(n)} \tag{1}$$

where $F(n,q)$ is the fatigue modulus at the nth loading cycle, $\varepsilon(n)$ is the resultant strain at the nth loading cycle, and q denotes the ratio of applied stress σ_a to ultimate strength σ_u.

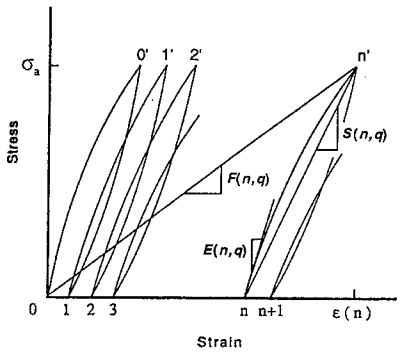


Fig. 1. Fatigue modulus concept

The fatigue modulus F of a material is a function of n and q. For the fiber-dominated composite laminates the stress/strain relation is almost linear up to failure. Hence, the fatigue modulus at the zeroth cycle F_0 is assumed to be the same as the elastic modulus E_0, and the fatigue modulus at fracture is defined as F_f at the number of cycles to failure, N. Here, F_0 should be constant, whereas F_f depends on applied stress. However, matrix dominated laminates such as cross-ply CFRP, under torsional loading, show a material non-linearity. The fatigue modulus at initial and final state depends on

the applied stress level and has the relation of

$$F_0 = G(q)E_0 \tag{2}$$

$$F_f = qE_0/p \tag{3}$$

where $G(q) = -Zq/\ln(1-Zq)$ and $Z = \sigma_u/\xi$. Dimensionless number Z can be determined from the static stress/strain relation of $\sigma = \xi[1-\exp(-r\varepsilon)]$ [11]. Z indicates whether the material shows linear or nonlinear behavior. Z approaches zero for the fiber dominated composites, while Z gets near unity for the matrix dominated composites. And material constant p is relatied to a fatigue failure criterion of $\varepsilon_f = \phi\varepsilon_u$, where $\phi = pG(1)$. It implies that the failure of composite laminates under fatigue loading occurs when the fatigue resultant strain reaches ϕ times the static ultimate strain. This point makes the proposed equation to be used for more general purpose, including fiber dominant (linear) and matrix dominant (nonlinear) composite materials.

2.2. Fatigue Modulus Degradation Model and Uniaxial Fatigue Life Prediction

The fatigue modulus degradation rate at any fatigue cycle can be assumed as a power function of number of fatigue cycles,

$$\mathrm{d}F(n,q)/\mathrm{d}n = -F_0 ACn^{C-1} \tag{4}$$

where A and C are material constants.

Integration of Eq.4 with Eqs. 2 and 3 gives the lifetime prediction equation for single stress level fatigue loading,

$$N = \left[\left\{1 + (pZ)^{-1}\ln(1-Zq)\right\}/A\right]^{1/C} \tag{5}$$

Proposed equation underestimates the lifetime at low- and high-lifetime range, which is good for structural design. Eq.5 is more useful for the materials showing highly non-linearity in applied stress-lifetime plot. In that case, the correlation coefficient for the simple linear equation, such as conventional S-N curve, must be very low.

2.3. Damage Model and Multi-Axial Fatigue Life Prediction

Fatigue damage of a material depends on number of fatigue cycles n, applied stress level q, frequency f, temperature T, moisture content M, geometric shape of the specimen, *etc.* As a first approach, constant environmental conditions are assumed. In addition, the effect of frequency and temperature rise during a fatigue test is ignored because it was controlled in small range during the test. There are many indicators to describe the degree of internal damage state of composite materials. For example, number of cracks, crack length, delaminated area, residual stiffness,

residual strength and residual strain can be used such indicators. Among them, modulus is often chosen as an indicator for the damage variable D, which is defined, in this study, using fatigue modulus and resultant strain as follows.

$$D = \frac{\varepsilon(n,\sigma_a) - \varepsilon_0}{\varepsilon_f - \varepsilon_0} = \frac{F_f}{F(n,\sigma_a)} \frac{F_0 - F(n,\sigma_a)}{F_0 - F_f} \tag{6}$$

where D is the damage variable under corresponding stress σ_a.

The cumulative damage models can be derived as functions of applied stress level q, number of fatigue cycles n, and material constants:

$$D = g(n)h(q) \tag{7.a}$$

$$\text{where, } g(n) = An^C/(1 - An^C) \tag{7.b}$$

$$h(q) = -\ln(1 - Zq)/[pZ + \ln(1 - Zq)] \tag{7.c}$$

where $g(n)$ describes the effect of fatigue cycles on fatigue damage, while $h(q)$ is function of applied stress level including static properties.

Using Eq.7, we can calculate the degree of fatigue damage for the each loading direction under multi-axial loading. Problem remained is how much does each loading contribute to material damage. In this study, one possible model can be made as

$$D = 0 \qquad \text{at initial state} \tag{8.a}$$

$$D = \sum_{i=1}^{w} D_i = 1 \qquad \text{at failure} \tag{8.b}$$

where w is the number of loading direction, D_2 and D_6 are damage by σ_2 and σ_6, respectively.

3. EXPERIMENTAL

The cross-ply composite tubes were made using the lapped molding technique. Details are in Ref. 12. The fiber was T300 grade carbon fiber, and epoxy resin was used as matrix. The specimens have an inner diameter of 20 mm, a wall thickness of ~ 0.7 mm and a gage length of 50 mm. The volume fraction of fibers was ~ 58 %. The grips and the end reinforcements were designed to minimize stress concentrations in the test section.

An MTS 809 Axial-Torsional Test Systems device was used for static and fatigue tests. Tension-tension fatigue tests were carried out at five biaxial ratios (R_b = ∞, 10, 5, 2, 0) under load and torque controlled mode. The ratios of index stress to ultimate strength (applied stress level q) used were 0.9-0.6. The stress ratio R was 0.05 and the loads were proportionally applied to the specimens using sinusoidal wave form. The frequency was 0.25-1 Hz, which should cause

negligible temperature rise during test. All tests were conducted at room temperature under laboratory conditions.

4. RESULTS AND DISCUSSION

In the static test, highly nonlinear stress/strain response was shown in the torsional loading, while linear relation in tension. The constant Z are estimated using the stress/strain responses and the results are presented in Table 1. In the fatigue test some extreme scattering cases were observed. The life distribution was investigated using a Weibull distribution [13]. The slope of S-N curve decrease with increasing biaxial ratio. Uniaxial fatigue life predictions and experimental data are compared in Fig. 2(a). In the figure, further prediction made by S-N relation is also shown. Conventional S-N curve can be written as follows:

$$q = k\log(N) + d \tag{9}$$

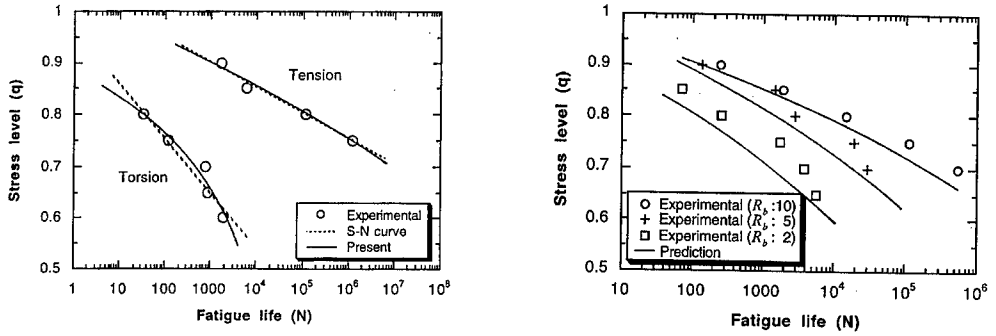
where k and d are material constants.

Table 1. Estimation of material constants

Equations	Constants	Values	
		Tension	Torsion
Proposed	Z	0.2639	0.9374
(Eq. 5)	p	2.2243	1.9869
	A	0.4378	1.8812
	C	0.0219	0.1870
	E_{rms}	0.0934	0.0543
S-N curve	k	-0.0497	-0.1046
(Eq. 9)	d	1.0503	0.9656
	E_{rms}	0.0818	0.0841

To compare the accuracy of prediction equations, the RMS (root mean square) error could be defined as $E_{rms} = \left[\sum^{m}\left(\log N_{\exp} - \log N_{cal}\right)^2\right]^{1/2} \Big/ m$ where $N_{\exp}$ is the experimental data, N_{cal} is the fatigue life predicted by life equations, and m is the number of data. In this study the constants in Eqs. 5 and 9 are estimated by the least square methods using the SAS program [14]. The results are presented in Table 1. The results show that the proposed equation predict fatigue life very well for this material system under single stress level cyclic loading.

The prediction of multi-axial fatigue life using the damage model is compared with experimental data in Fig. 2(b). The comparison shows reasonable correlation with the experimental data, though there exist some errors at low biaxial ratio.



(a) at uniaxial fatigue loading (b) at multi-axial fatigue loading

Fig. 2. Comparison of predictions with experimental data

5. CONCLUSIONS

The equation developed based on the fatigue modulus concept could predict fatigue life of composite materials, involving matrix dominant as well as fiber dominated behavior, as a function of applied stress level. To predict fatigue life at multi-axial loading, cumulative damage model was derived as functions of applied stress level and number of fatigue cycle. It was shown that the proposed equation are more practical in fatigue life prediction of composite materials due to flexibility of curve and the prediction agrees well with experimental data.

REFERENCES

1. J. N.Yang and M. D.Liu, J. Composite Materials, **11** (1977) p.176
2. H.T.Hahn and R.Y.Kim, J. Composite Materials, **10** (1976) p.156
3. A.Poursartip and P.W.R.Beaumont, Composites Science and Technology, **25** (1986) p.283
4. J.N. Yang, L.J.Lee, and D.Y.Sheu, Composite Structures, **21** (1992) p.91
5. L.Ye, Composites Science and Technology, **36** (1989) p.339
6. W.Hwang and K.S.Han, Compo. Mater.: Fatigue and Fracture, ASTM STP **1012**, (1989) p.87
7. W.Hwang, C.S.Lee, H.C.Park, and K.S.Han, J. Advanced Materials., **26** (1995) p.3
8. J.R.Schaff and B.D.Davidson, J. Composite Materials, **31** (1997) p.128
9. Z.Fawaz and F.Ellyin, J. Composite Materials, **28** (1994) p.1432
10. Z.Fawaz, 5th International Conf. Composites Engineering, USA, Las Vegas, (1998) p.283
11. C.S.Lee and W.Hwang, Polymer Composites, **21** (2000) (to appear)
12. C.S.Lee, W.Hwang, H.C.Park, and K.S.Han, Compo. Sci. and Technol., **59** (1999) p.1779
13. C.S.Lee and W.Hwang, Materials Science Engineering A (to appear)
14. N.C.Cary, SAS user's guide: statics, Version 6 ed., SAS Institute (1987)

Key Engineering Materials Vols. 183-187 (2000) pp. 951-956
© 2000 Trans Tech Publications, Switzerland

A New Method to Deal with the Staircase Fatigue Test

Q.Z. Fang, S.S. Zhang, M.H. Zhao and Y.J. Liu

Zhengzhou Research Institute of Mechanical Engineering, Zhengzhou 450052, China P.R.

Keywords: Fatigue, Fatigue Test, P-S-N Curve, Staircase, Statistics

ABSTRACT

A new method to deal with the staircase fatigue test statistical distributions was presented. Numerical imitation and experimental test results to demonstrate this method were illustrated. The conventional staircase method was effective only when the attention was paid to the mean strength at a selected fatigue life N, but the standard deviation s calculated with conventional staircase method is a function of the stress increment d used in staircase fatigue test and the theoretical standard deviation σ of the fatigue strength. This can be described with the following formula.

$$s^2/\sigma^2 = 0.87478\left(d/\sigma\right)^{1.58885}$$

Therefore, s is unreliable to represent the dispersion of the fatigue strengths. Fatigue experiments for several steels were conducted in ambient and under water environment. There were three types of specimens. These were smooth specimens that had no stress raiser and two kinds of circular cut specimens with stress concentration factors of 2.5 and 1.95 respectively. The results were presented in the article. The standard deviation σ_1 of the fatigue strengths for the selected fixed fatigue life N in the staircase method for each kind of experiment was calculated with the new method and the result was compared with the corresponding s calculated with the conventional method. It was demonstrated that s^2/σ_1^2 was a reasonable approximation of s^2/σ^2. Therefore σ_1 was a reasonable approximation of σ. A group test strategy that can be used to deal with the unbroken test points instead of the staircase test strategy was also presented.

1. INTRODUCTION

It is often the case that some specimen cannot be fractured when fatigue experiment is conducted. Some one introduced staircase method to deal with this problem [1~3]. Many of these problems are solved this way. The staircase method is such that most specimens are tested near the median fatigue strength for N cycles. So it is a good method when the attention is paid only to the mean strength for a selected fixed fatigue life N. But when more attention is paid to the distributions of the fatigue lives or the fatigue strengths, the staircase method could not be an effective one any more. Because this method provides limited information regarding the dispersion of the conceptual fatigue strength distribution, and some wrong statistics could be given out [1,4]. The reference gave out an intensive discussion on this problem with numerical imitation methods on computer. The standard deviation (S.D.) calculated with staircase method depended on the stress increment used in the staircase method experiment, not converging to the true standard deviation. In the present article, more discussion would be conducted with some experimental

results.

2. METHOD

In general, fatigue life distribution for a selected experimental stress can be expressed with a log normal distribution function. With this supposal, the problem can be dealt with easily. Generally a P-S-N curve can be expressed with the following formula (1).

$$\log N_p = c + m\log(S - S_0) + u_p\sigma_N$$
$$\sigma_N = a + b\log(S - S_0) \qquad (1)$$

Note: c, m, a, b, S_0—the coefficients associated with the material and the structure.
σ_N— the S.D. of log N for the corresponding stress level.
u_p— a value decided by standard normal distribution N(0,1) for a survival probability P.
N_p — the survival life with a probability P for each given stress amplitude.

For each specimen, if it has a survival probability P at one stress level S_1, it will most probably also have a survival probability P at another stress level S_2 because the survival probabilities reflect the quality of the specimen. For each batch of specimen, if there is some specimen failed before the mean fatigue life for a given stress amplitude, there will most likely be the same number of specimens whose fatigue lives are longer then the mean at the same stress amplitude. This is because the fatigue lives conform to a symmetry distribution (log normal distribution). With these properties of the fatigue life distribution, one can easily convert the fatigue lives at different stress amplitude to the fatigue lives at the mean strength for the selected fatigue life witch can be deducted by the staircase method. One can deduct the following formula with the formula (2).

$$\log N_{p1} - \log N_{P2} = m(\log(S_1 - S_0) - \log(S_2 - S_0)) \qquad (2)$$

Note: N_{p1} — the survival life with a probability P for stress S_1.
N_{p2} — the survival life with a probability P for stress S_2.
S_0, m — the parameters deducted by best fitting S-N curve.

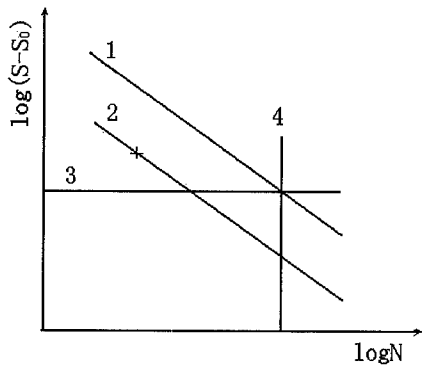


Fig.1 The depiction of the converting method

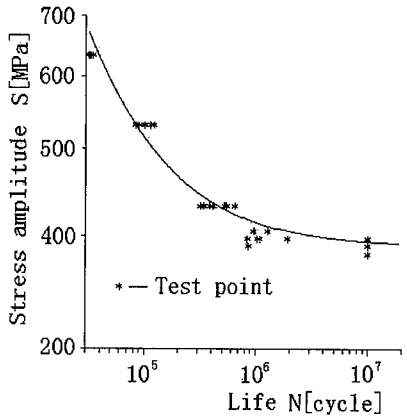


Fig. 2 The test results for 42CrV

Here we omit the influence of the coefficient b in the formula (1), because the influence is generally small. Fig.

1 gives out a diagram illustration of this procedure. Here the line 1 is the median S-N curve, the line 3 and 4 represent the mean fatigue strength and the selected fixed fatigue life of the staircase test respectively. The point "+" represents one of the test points in the staircase test. The line 2 passes through the "+" test point. The cross points between line 3 and 4 can give out the converted fatigue life and fatigue strength respectively.

Then one can calculate the S.D. of the log fatigue lives to the log fixed life at the mean strength. So one can also calculate the S.D. of the fatigue strength to the mean strength calculated with conventional staircase method for the fixed life.

3. EXPERIMENT RESULTS

Fatigue experiments are conducted for 42CrV and 40Cr. Three kinds of specimens are used. These are smooth specimens that have no stress raiser and two kinds of circular cut specimens with stress concentration factors of 2.5 and 1.95 respectively. Most of these experiments are performed in the ambient environment. One is conducted under water environment. All these experiments are conducted with several groups of tests for some selected stress amplitudes and one group of test in which the staircase method is used. So we can use the above methods to produce a best fitting S-N curve, Table 1. The test results of 42CrNiMo are also included here.

Table 1. The best fitting results of the fatigue experiments

Specimen	Best fitting S-N curve	R	n	K_t
40Cr smooth under water	$\log N = 8.2424 - 1.5064\log(S - 326.3346)$ $\sigma_N = 0.3400 - 0.1242\log(S - 326.3346)$	-0.9999 -0.9421	54	1
40Cr smooth ambient	$\log N = 8.2141 - 1.6472\log(S - 367.8750)$ $\sigma_N = 5.4397 - 2.9909\log(S - 367.8750)$	-0.9912 -0.9572	44	1
40Cr r1 ambient	$\log N = 9.1450 - 2.2173\log(S - 223.1750)$ $\sigma_N = 6.0829 - 3.3447\log(S - 223.1750)$	-0.9860 -0.8708	32	1.95
40Cr r0.45 ambient	$\log N = 8.2639 - 1.8548\log(S - 201.1050)$ $\sigma_N = 5.7067 - 3.4539\log(S - 201.1050)$	-0.9905 -0.9385	36	2.5
42CrV smooth ambient	$\log N = 7.9111 - 1.3705\log(S - 389.7450)$ $\sigma_N = 3.2399 - 1.6644\log(S - 389.7450)$	-0.9994 -0.9560	36	1
42CrV r1 ambient	$\log N = 8.3651 - 1.7473\log(S - 242.3050)$ $\sigma_N = 4.0926 - 2.3234\log(S - 242.3050)$	-0.9938 -0.9167	36	1.95
42CrV r0.45 ambient	$\log N = 7.4986 - 1.2332\log(S - 199.1350)$ $\sigma_N = 2.6730 - 1.5147\log(S - 1.991350)$	-0.9990 -0.9687	36	2.5
42CrNiMo r0.5 ambient	$\log N = 7.6978 - 1.3760\log(S - 220.6450)$ $\sigma_N = 2.4426 - 1.2043\log(S - 220.6450)$	-0.9946 -0.9335	60	
42CrNiMo r.25 ambient	$\log N = 8.4331 - 1.6828\log(S - 196.125)$ $\sigma_N = 3.4325 - 1.6072\log(S - 196.125)$	-0.9992 -0.9325	62	

Where: n — total test number.

K_t — stress concentration factor.

N — mean fatigue life for stress amplitude S.

Fig. 2 presents one of these experiment results.

With these best fitting parameters, we can give out the standard deviations (S.D.) of the fatigue strengths for the fatigue lives that the staircase methods selected. Table 2 gives out the results. Table 2 also gives out the standard deviations calculated with the conventional staircase method.

Table 2. S.D. calculated with two methods

Specimen	s	σ_1	Increment d	s^2/σ_1^2	d/σ_1
40Cr smooth under water	5.0472	1.4339	9.81	12.390	6.8415
40Cr smooth ambient	7.7303	4.2937	7.36	3.2414	1.7141
40Cr r1 ambient	8.4650	5.3735	7.36	2.4816	1.3697
40Cr r0.45 ambient	6.2951	3.1512	7.36	3.9907	2.3356
42CrV smooth ambient	6.1865	3.2514	7.79	3.6203	2.3959
42CrV r1 ambient	6.2950	3.8231	6.87	2.7112	1.7970
42CrV r0.45 ambient	5.5365	1.7135	6.87	10.440	4.0093
42CrNiMo r0.5 ambient	4.1278	2.3366	4.9	3.1208	2.0971
42CrNiMo r0.25 ambient	8.3994	5.4325	9.81	2.3905	1.8058

Note: s — standard deviation of the fatigue strength calculated with conventional staircase method for the selected fatigue life.

σ_1 — standard deviation of the fatigue strength calculated with the new method for the selected fatigue life.

d — stress increment selected in the staircase method.

4. DISCUSSION

As we learned from reference [1,4], the s in table 2 is unreliable. It is a function of d and the theoretical standard deviation σ of the fatigue strength.

Here a brief description of the relevant results in reference [4] is given out. Several groups of P-S-N curves of different materials and structures as the theoretical distributions are selected from [5]. Numerical tests were conducted for these theoretical distributions with group test method and staircase method. It is shown that unrelated with the theoretical distributions, s^2/σ^2 is a function of (d/σ).

Recalculate the numerical imitation results with the method given in reference [4], so that (d/ σ) can cover a larger range. Similar results are given out. Formula (3) is the best fitting results.

$$s^2/\sigma^2 = 0.87478\left(d/\sigma\right)^{1.58885} \tag{3}$$

Fig. 3 represents the imitation results. The symbol "□" represents the imitation points. The regression line represents the formula (3). The symbol "+" represents the test points described by $(s^2/\sigma_1^2,\ d/\sigma_1)$. It can be learned from Fig. 3 that $(s^2/\sigma_1^2,\ d/\sigma_1)$ is a reasonable approximate of $(s^2/\sigma^2,\ d/\sigma)$. Therefore it can be concluded that σ_1 was a reasonable representative of σ.

Numerical imitation of the new method is also conducted here. Fig. 4 gives out the imitation results for the comparison of the σ_1 and σ. Here n_s is the total number of specimens used in the staircase method. With these results, it can be concluded that unrelated with the value of the selected stress increments in the staircase numerical imitation tests $(d/\sigma=0.3—3)$, the σ_1^2/σ^2 will converge to 1 with the increase of n_s. In other words, σ_1 will converge to σ with the increase of the number of test specimens.

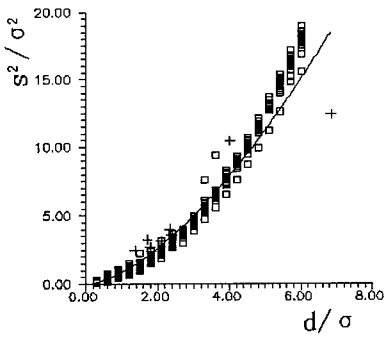


Fig. 3 The imitation and test results

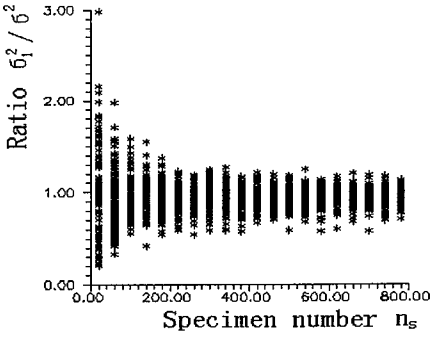


Fig. 4 The relationship between σ_1^2/σ^2 and n_s

5. GROUP TEST STRATEGY

It can be concluded here that the above statistics method can give out a reasonable result for staircase test. But it is not convenient to deal with if the parameter m could not be got easily. It can mislead the results if the parameter m cannot be selected properly. Therefore another method was presented.

With this method, a group of specimens can be tested at a suitable stress level and terminated at a selected fatigue life. n_s represents total number of the specimens tested. n_l denotes the number of the unbroken specimens (or the number of the specimens whose lives are longer than the selected fatigue life). Reorder the test points from small to large lives. Remove the first n_l test points and the unbroken specimens and calculate the log mean with the remaining test points $n_r = n_s - 2n_l$. Here n_r must be larger than 0. The log mean value given above is supposed to be the log mean of the sample. Two times of the log mean value minus the n_l log lives of the smaller fatigue life test points respectively, then n_l new test points are gotten. For log normal distribution, the n_l new test points have same probability density as the n_l unbroken test points. Therefore replace the unbroken test points with the new n_l test points. Till now the distribution parameters of the sample can be calculated with the conventional statistical method.

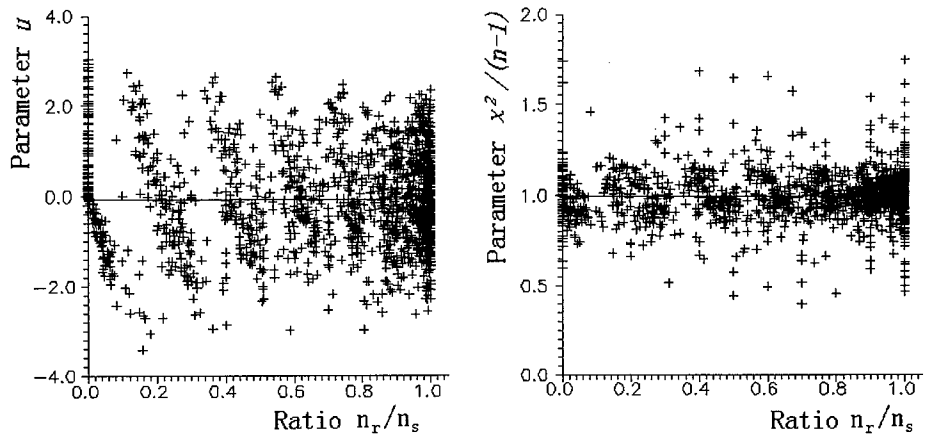


Fig. 5 The effects of the selected terminating position on the sample mean and variance screening parameters

With the theoretical distribution selected in reference [4], numerical imitation was conducted with the n_s from 20 to 600 and different selected fatigue life at which the test stopped. Fig. 5 gives out the imitation results. Where

$$u = \left(\overline{X} - \mu_0\right) / \left(\sigma / \sqrt{n}\right) \tag{4}$$

$$\chi^2 = (n-1)s^2/\sigma^2 \tag{5}$$

Here, μ_0 denotes the true mean value, σ denotes the true standard deviation, $\overline{X}$ denotes the mean of the sample, s denotes the standard deviation calculated with the above method, $n=n_s$ denotes the number of the specimens tested.

When $n_r/n_s=0$, use the median value denotes the mean of the sample. When the $n_r/n_s=1$, it is same as the conventional group test method. It is proved with numerical imitation method that the mean and the standard deviation calculated with the above method can converge to the true value respectively with the increasing of the n_s. It can also be learned from Fig. 5 that the above method could give out similar results as the conventional group test method when $n_r/n_s>0.2\sim0.3$. In other words, the above group test strategy could give out reasonable results when over 60% of the specimen tested failed before the selected fatigue life.

6. CONCLUSION

With the numerical imitation test and experimental test results, the following conclusions can be produced.

1) The conventional staircase method can only give out a good mean value of the fatigue strengths for a fixed fatigue life.

2) The standard deviation s calculated with the conventional staircase method is unreliable. It is a function of d and the theoretical standard deviation σ of the fatigue strength.

3) The standard deviation calculated with the new method is a reasonable approximation of the true value.

4) The group test strategy can be used to deal with the unbroken specimens in the fatigue test for generating P-S-N curve.

REFRENCE

1. R.E.Little, E.H.Jebe: Statistical Design of Fatigue Experiments, Applied Science Publishers Ltd. London, England (1975) p. 168~197
2. N. E. Frost, K. J .Marsh, L. P.Pook: Metal Fatigue, Clarendon Press, Oxford, England (1974) p. 424~427
3. Methods of Fatigue Testing, Guide to the Application of Statistics, B.S. 3518: Part 5, British Standards Institution(1966) p. 33~~36
4. Q.Z. Fang, S.B. Zhao, S.L.Han: Several Useful Statistical Methods Used for Dealing with P-S-N Curve, J. of Mechanical Strength, V. 21, No. 1 (1999) p. 63~65
5. S.B. Zhao, Z.B.Wang: Fatigue Protection Design-Method & Data, Mechanical Industry Press, Beijing, China (1997) p. 226, 325~343

Key Engineering Materials Vols. 183-187 (2000) pp. 957-962
© 2000 Trans Tech Publications, Switzerland

Fatigue Life Prediction of Spot-Welded Joint by Strain Energy Density Factor using Artificial Neural Network

Ilseon Sohn[1] and Dongho Bae[2]

[1] Lab. Test Team, R&D Center, Ssangyong Motors,
150-3, Chilkoi-Dong, Pyungtaek-Si, Kyunggi-Do 459-050, Korea

[2] Department of Mechanical Engineering, Sungkyunkwan University,
300 Chunchun-Dong, Changan-Gu, Suwon-Si 440-746, Korea

Keywords: Artificial Neural Network, Fatigue Design Criterion, Fatigue Life Prediction, Reliability, Spot-Welded Joint, Strain Energy Density Factor

ABSTRACT

In establishing the long-life fatigue design criterion of the spot-welded thin sheet structures such as the automobile and the train, it is necessary to estimate the fatigue strength of spot-welded joints systematically and reasonably. But, those data cannot apply to the design of slightly modified shape spot-welded joints directly. For the prediction of fatigue life of spot-welded joint with slightly modified shape, additional fatigue tests are generally required. To avoid that effort, the fatigue life prediction method using artificial neural network is proposed. The reliability of the proposed method was then estimated using the theory of Weibull probability distribution function.

Form the results, the reliability of the proposed fatigue life prediction method by the strain energy density factor is 85%. The fatigue life predicted by the strain energy density factor equation is in good agreement with that obtained from the actual fatigue test result. Therefore, it is possible to predict the fatigue life of in-plane bending (IB) type spot-welded joint having a slightly modified shape without any additional fatigue tests.

1. INTRODUCTION

Accurate stress analysis and systematic fatigue strength assessment are very important to determine the long-life fatigue design criterion. However, it is very difficult to determine the fatigue design criterion in the actual structure. Thus, after the estimation of the fatigue strength of simulated specimen the same structural and mechanical characteristics, which has as the actual structure, the fatigue design criterion is generally determined and applied to the fatigue design of the actual spot-welded structure.

In general, the most typical and traditional method for fatigue strength evaluation has been known as the ΔP - N_f relation. However, it is difficult to estimate systematically since the fatigue strength by taking the effects of various geometrical factors into account, due to that the relationship between fatigue load range (ΔP) and fatigue life (N_f) is different with material properties, geometry and the loading condition [1]. This indicates that a lot of cost and time for it have to be taken. But, if the fatigue life of spot-welded joint can be predicted by the reliable systematic fatigue strength

evaluation method from the already accumulated fatigue data, then the fatigue design criterion can be determined without any additional fatigue tests. Therefore, in order to develop a method satisfying such requirement, the strain energy density factor [2] was adopted to predict fatigue life without fatigue test when applied to slightly modified structure.

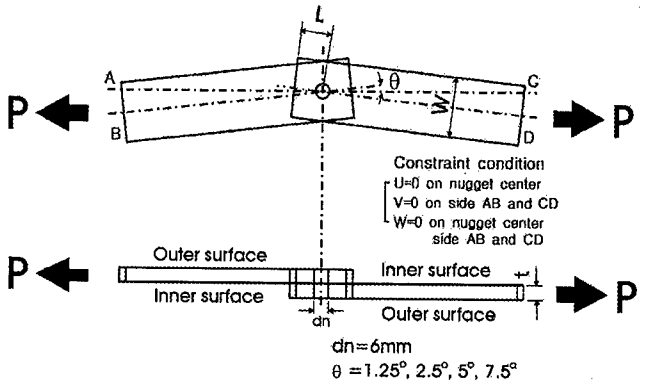


Fig. 1. Configuration of in-plane bending type spot-welded joint.

By estimating the strain energy density factor and loading effect, the ΔP - N_f relations obtained from fatigue test results for IB-type spot-welded joint (Fig.1) can be systematically rearranged to the ΔS - N_f relation. Its reliability and performance were then verified by using the theory of Weibull probability distribution [3]. The reliability of the proposed fatigue life prediction method is 85%. The fatigue life predicted by the equation show a good agreement with the actual fatigue test result. It is expected that newly developed method for fatigue life prediction will be able to offer the design flexibility to designer as will as to reduce the cost and time for additional fatigue tests.

2. THEORY OF STRAIN ENERGY DENSITY FACTOR

For an elastic material, the stored strain energy in a element $dV = dxdydz$ under a general three dimensional stress system is given by:

$$dW = \left[\frac{1}{2E}(\sigma_x^2+\sigma_y^2+\sigma_z^2)-\frac{\nu}{E}(\sigma_x\sigma_y+\sigma_y\sigma_z+\sigma_z\sigma_x)+\frac{1}{2\mu}(\tau_{xy}^2+\tau_{xz}^2+\tau_{yz}^2)\right]dV \tag{1}$$

From the equation (1), the strain energy density factor (S) expressed as:

$$S = a_{11}K_1^2 + 2a_{12}K_1K_2 + a_{22}K_2^2 + a_{33}K_3^2 \tag{2}$$

Represents the amplitude or the intensity of the strain energy density field and it varies with the polar angle θ. The values of coefficients a_{ij} $(i, j=1,2,3)$ are given by:

$$\begin{aligned} a_{11} &= \frac{1}{16\mu}[(3-4\nu-\cos\theta)(1+\cos\theta)] \\ a_{12} &= \frac{1}{16\mu}2\sin\theta[\cos\theta-(1-2\nu)] \\ a_{22} &= \frac{1}{16\mu}[4(1-\nu)(1-\cos\theta)+(1+\cos\theta)(3\cos\theta-1)] \end{aligned} \tag{3}$$

$$a_{33} = \frac{1}{4\mu}$$

3. FATIGUE TEST

The configuration of fatigue test specimen is the same as that in numerical analysis model (Fig.1). Material used for fatigue test is used the Korean automobile mild steel called SPCC. The resistance spot welding was processed under the welding condition recommended from RWMA class-C [4]. The diameter of the electrode used for spot-welding was 6mm, which is general size of electrode applying in actual field. Fatigue tests are generally conducted under the condition in which the load ratio is zero and the frequency is 30Hz at room temperature.

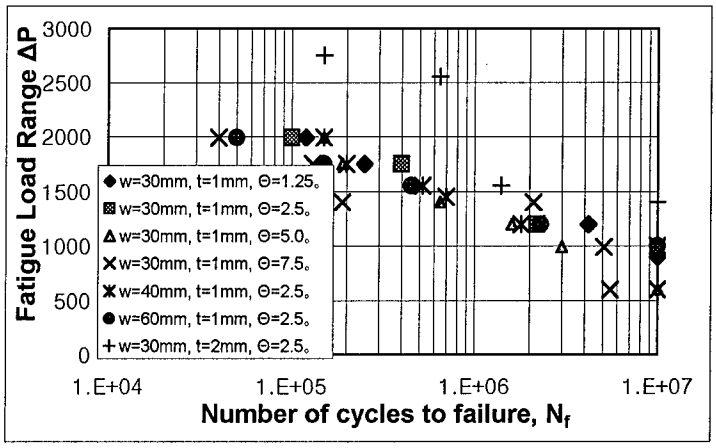


Fig. 2 $\Delta P - N_f$ relation of various IB type spot-welded joint

Fatigue test were carried out on a servo-hydraulic power system (MTS, ±10 ton). In fatigue tests of spot-welded joints in the case of IB (in-plane bending) type subjected to tensile shear load, the simple grip cannot be used due to in-plane bending deformation generating in the vicinity of the spot weld. Thus, in this test, in order to take account of the effects of in-plane deformation and force by tension-shear load, the special designed pin joint grip was used to control the in-plane bending effect [5]. From the fatigue test, the ΔP - N_f relation is obtained as shown in Fig. 2.

4. FATIGUE LIFE PREDICTION BY STRAIN ENERGY DENSITY FACTOR

4.1. The strain energy density factor equation

To calculate the strain energy density factor, it is necessary to obtain the true strain at the nugget edge of the spot weld. It was known that the maximum principal strain at the nugget edge of the spot weld was influenced by the geometrical factor of the joint. Its sensitivity on the thickness and width of the plate and on the joint angle was particularly found to be large [5]. This indicates that the strain energy density factor at the nugget edge can be defined as a function of the applied

that the strain energy density factor at the nugget edge can be defined as a function of the applied load and the geometrical factors.

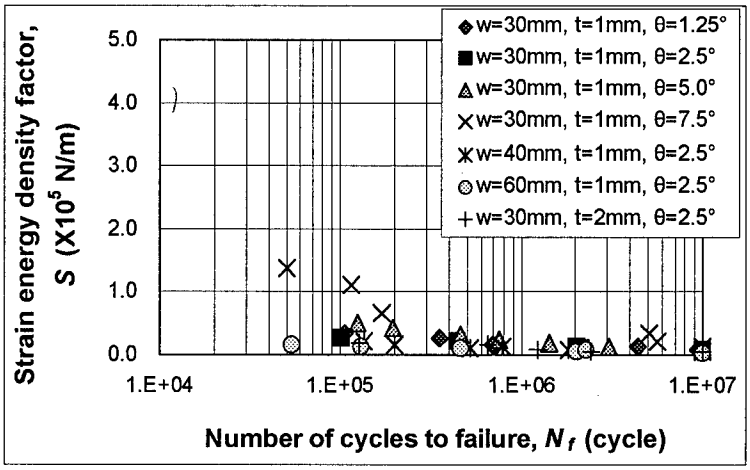


Fig. 3 $\Delta S - N_f$ relation of various IB type spot-welded joint.

In this study, the parameter was previously defined as the following shape coefficient that was presented in the normalized geometrical factors. The shape function is given by:

$$F_s = f(\frac{t}{t_0}, \frac{W}{W_0}, \frac{\theta}{\theta_0}) \tag{4}$$

t_0 : thickness of specimen for normalizing (mm)

W_0 : width of specimen for normalizing (mm)

θ_0 : joint angle of specimen for normalizing (degree)

Form the relationship between the stain energy density factor and the load applied to the joint, the strain energy density factor equation is expressed as:

$$S = F_s S_n \frac{P}{P_0} \tag{5}$$

where, S_n is the normal strain energy density factor (N/m) and P_0 is the standard load (=981N). From the equation (5), the ΔP - N_f relation is rearranged to the ΔS - N_f relation in Fig. 3.

4.2. Calculation using artificial neural network

To apply the newly developed fatigue life prediction method, two kinds of data set were required. One data set was fatigue life from the test and other data set was true strain energy density data from finite element analysis. Using this two data set, fatigue life of untested specimen was predicted using artificial neural network method.

The sigmoid function of artificial neural network [6] was applied to define the shape coefficient (F_s) of the equation (4). The momentum and adaptive control were applied to improve back propagation algorithm. Fig. 4 shows the mean square error of artificial neural network. Its

error range is very small.

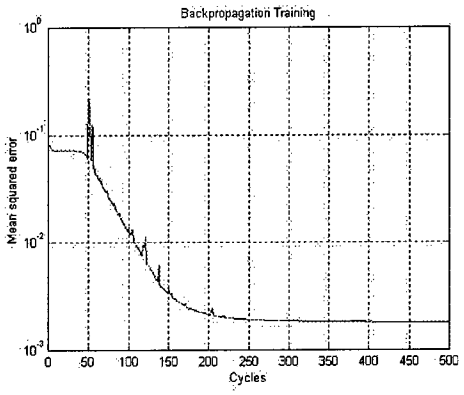


Fig. 4 The mean square error of the strain energy density factor equation using artificial neural network.

4.3. Reliability verification of the fatigue design method

Applicability of Weibull probability distribution function to fatigue life prediction of spot-welded lap joint was previously investigated. Form the investigated results, reliability estimation of the proposed fatigue life prediction methods by the strain energy density factor had good results was verified using 3-parameters Weibull distribution function [7].

Form the result, reliability of the proposed fatigue life prediction method by the strain energy density factor was estimated by 85%. Therefore, it was found that the proposed fatigue life prediction method by the strain energy density factor had high reliability, and was applicable to fatigue life prediction of spot-welded joint having specific dimension not yet tested.

4.4. Fatigue life prediction

In this study, by the strain energy density factor equation using artificial neural network, it was tried to predict fatigue life of IB type spot-welded joint having specific dimension and loading condition without additional fatigue tests.

Table 1 Comparison of fatigue life.

Specimen and load condition	Fatigue life by test (cycle)	Fatigue life by prediction (cycle)
$W=30mm, t=1mm, \theta=2.5, \Delta P=981N$	1.0×10^7	1.0×10^7
$W=60mm, t=1mm, \theta=2.5, \Delta P=1570N$	4.6×10^5	4.8×10^5
$W=30mm, t=2mm, \theta=2.5, \Delta P=1374N$	9.6×10^6	1.0×10^7
$W=30mm, t=1mm, \theta=7.5, \Delta P=785N$	5.6×10^6	5.3×10^6
$W=30mm, t=1mm, \theta=6.0, \Delta P=1100N$	N/A	1.5×10^6
$W=40mm, t=1.5mm, \theta=2.5, \Delta P=1400N$	N/A	5.1×10^6

Table 1 illustrates comparison of the fatigue life calculated by the strain energy density factor equation and by fatigue test, respectively. It can be found to be in good agreement with both of the results.

5. CONCLUSION

For the prediction of fatigue life of spot-welded joint with slightly modified shape, additional fatigue tests are generally required. To avoid that effort, fatigue life prediction method using artificial neural network about slightly modify shape structure will was proposed. And reliability of the proposed method was estimated using the theory of Weibull probability distribution function.

1. The reliability of the proposed fatigue life prediction method by the strain energy density factor is 85%.
2. Fatigue life predicted by the strain energy density factor equation using artificial neural network was found to be in good agreement with the fatigue life obtained from the actual fatigue test results.
3. It is expected that the proposed fatigue life prediction method will be able to offer the design flexibility to designer as well as to make reduce the cost and time for additional fatigue tests.

REFERENCE

1. D.H.Bae, J.E.Niisawa and N.Tomioka, Theoretical Analysis of Distribution of Single Spot-Welded lap Joint under Tension-shear Load, Transaction of JSAE, 39 (1988) p.627
2. G.C.Sih, Mechanics o fracture; Method of Analysis and Solution of Crack Problem, 1, Noordhoff International Publishing (1973) p.xxii
3. J.Schijve, A Normal Distribution and a Weibull Distribution for Fatigue Lives, Fatigue Fracture Engineering material Structure, 1-8 (1993) p.851
4. RWMA Committee, RWMA, Residual Spot Welding Manual Vol. 1 (1981) p. 119
5. I.S.Sohn, Ph.D thesis; a Study of Fatigue Design Methods and Expert System Development for Thin Steel Sheet Spot welded Lap Joint, SungKyunKwan University, Seoul, (1998)
6. R.H.Nielsen, Neurocomputing, Addison-Wesley publishing Co., (1989)
7. T.Sakai, Estimation of 3 Parameter of Weibull distribution in Relation to Parameter Estimation of Fatigue Distribution, Japanese Material, 29-316 (1979) p.17

Key Engineering Materials Vols. 183-187 (2000) pp. 963-968
© 2000 Trans Tech Publications, Switzerland

Fatigue Properties of Tungsten Fiber Reinforced Ti-6Al-4V Alloy

S.Y. Son[1], S. Nishida[1], N. Hattori[1] and K. Nakano[2]

[1] Faculty of Science and Engineering, Saga University,
Honjo-machi 1, Saga-shi 840-8502, Japan

[2] Takatda Engineering Ltd. Co., Kitakyushu 808-0143, Japan

Keywords: Fatigue Limit, Porosity, Tungsten Fiber Content Ratio, Tungsten Fiber Reinforced Ti-6Al-4V (W/Ti-6Al-4V) Alloy

ABSTRACT

Fatigue properties of tungsten fiber reinforced Ti-6Al-4V (W/Ti-6Al-4V) alloy have been investigated. Materials used in this study were three kinds of W/Ti-6Al-4V produced by HIP (Hot Isostatic Pressing) with fiber content ratio of 6, 9, 12vol.%, respectively. Increase of hardness and a slight improvement of tensile strength were obtained with the increase of fiber content ratio in W/Ti-6Al-4V comparing to the conventional Ti-6Al-4V alloy but their fatigue limits were unexpectedly deteriorated. The observation of crack on the surface of specimen showed that multi-cracks initiated and coalesced due to cycles of load. Fracture surface observed with scanning electron microscope (SEM) displayed many small porosties in these W/Ti-6Al-4V. It is considerably concluded that unexpected performance of Ti-matrix would be due to the porosities and microstructure defects in this work's circumstance that takes a major role in deteriorating their fatigue limit was resulted from an inadequate fabricating process.

1. INTRODUCTION

Titanium has an exceptionally high strength to weight ratio and applications of its alloys have been developed continuously for specified purposes in severe environment such as spaceships, turbine blades, nuclear reactors, submarines and food industries, etc. Ti-6Al-4V alloy is a typical titanium alloy, which broadly employed in several engineering applications and the MMCs (metal matrix composites) using this alloy for the matrix with various reinforcements such as particles, whiskers, fibers, etc. have been studying and being expected as one of most currently advanced materials[1,2,3].

Tungsten (W) possesses show high melting point and excellent mechanical properties. It can be produced in form of fibers therefore tungsten fibers have been attempted to use for the reinforcement in a Ti-6Al-4V matrix for developing a new type of MMC.

The aim of this study is to investigate the fatigue properties of the tungsten fiber reinforced Ti-6Al-4V (W/ Ti-6Al-4V) relating to the weight ratio of reinforcement.

This paper relates to failure story in view point of fatigue properties, though it relates to success story instatic tensile ones.

2. EXPERIMENTAL PROCEDURE

2.1 Materials and specimen

The W/Ti-6Al-4V MMCs used in this work were cast by HIP (Hot Isostatic Pressing) [4,5]. Fiber contents were varied in a range of 6, 9 and 12vol.% (20, 30 and 40wt%). Table.1 shows the chemical composition of Ti-6Al-4V.

Ti powder produced by atomizing method at 100μm average size was mixed to tungsten fibers (diameter d=20 μm, length l=1mm, average aspect ratio l/d=48.2 and tensile strength σ_B = 3430 MPa) in specified ratios under the conditions of 60 rpm for 0.5hr then HIP processed at 950℃/100 MPa for 1hr in Argon gas. Rotary swaging (RS), free forging (FF) and shape forging (SF) were next applied in order to improve the distribution of reinforcing fibers in the matrix.

Configuration of fatigue test specimen is shown in Fig. 1. Partial shallow notch (R=0.3mm) was machined at the central portion for taking it easy to observe the fatigue crack initiation process.

Table.1 Chemical compositions of Ti-6Al-4V alloy mass%

Al	V	Fe	O	C	N	H
6.14	3.93	0.17	0.19	0.011	0.014	0.009

Table.2 Tensile strength of W / Ti-6Al-4V MMCs

Volume fraction of W fiber vol.%	Tensile strength Mpa
0	1088
6	1144
9	1520
12	1288

2.2 Test procedure

All of specimens were annealed at 600℃ for 0.5hr in a vacuum furnace. After annealing, in order to investigate the effect of residual stress or stress concentration effects due to machining process, one group of specimens was mechanically polished with emery paper (#400~3000) then with polishing powder (Al_2O_3/0.1 μm) then being with etching in a solution of 10%HF + 20%HNO_3. Another group of specimens was electro-polished (0.5Am/2min).

Ono type rotating bending fatigue-testing machine (3000rpm) was used for fatigue tests. Specimen's surface was monitored by replica method and the successive-taken replicas of surface state were analyzed with an optical microscope. Fracture surface was investigated using scanning electron microscope (SEM). Vickers Hardness was measured at the load of 1.96N and 0.245N, respectively.

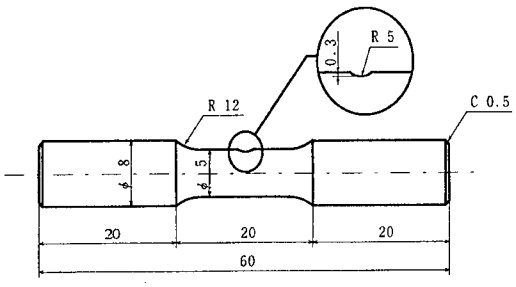


Fig. 1. Shape and dimensions of specimen.

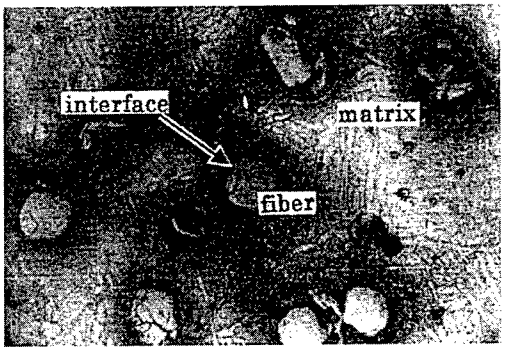


Fig. 2. Optical microstructure of W/Ti-6Al-4V.
25 μm

3. RESULTS

Table. 3. Results of Vickers hardness test.

Volume fraction of W fiber vol.%	Average	Surface	Core	Matrix	Interface
0	-	340.0	415.0	-	-
6	381.0	373.0	410.0	359.5	424.6
9	405.5	379.9	421.3	382.2	453.5
12	418.2	396.0	431.3	406.0	437.5

Fig. 2 representatively shows the microstructure of W/Ti-6Al-4V. Ti-6Al-4V matrix and W-fibers make the interface which appears as a gray layer between matrix and fibers as shown in this figure. Fig. 3 shows surface observation of three kinds of MMCs used in this experiment, respectively. This figure shows that the clusters of fibers do not exist apparently in the three MMCs and comparatively good distribution of fibers has been achieved.

Table. 2 lists the result of tensile test and density ratio at W/Ti-6Al-4V MMCs which made by HIP. It shows higher tensile strength than conventional Ti-6Al-4V.

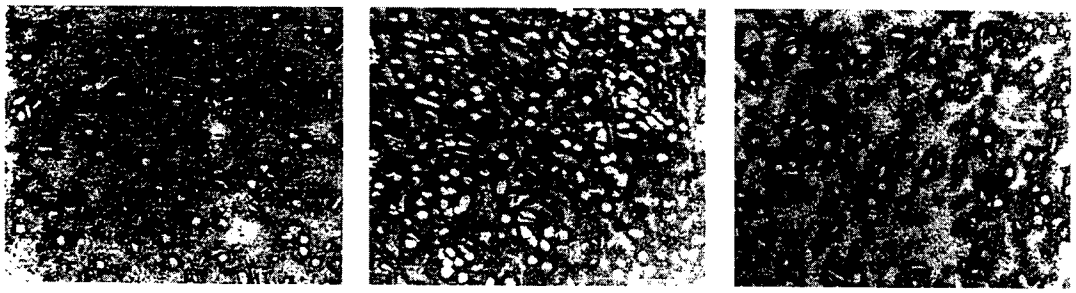
Fig. 4 illustrates S-N curves of mechanically polished specimens (Fig. 4 (a)) and electro-polished specimens (Fig. 4 (b)) respectively. The fatigue limits of MMCs were approximately 40% lower than that of Ti-6Al-4V. Corresponding to the fiber content ratio, fatigue limit value decreases in the order of 12 - 9 - 6wt% for the electro-polished specimens, but decreases in the order of 9 - 6 - 12wt% for the mechanically polished specimens. The overall fatigue limit value of the latter group is higher.

Table 3 reports the hardness of MMCs and Ti-6Al-4V. The hardness of MMCs was superior to that of the alloy and the hardness of the surface is normally higher than that of the core. In addition, that of the interface layer of matrix/fiber exhibits slightly higher value than the matrix.

Fig. 5 shows SEM fractographs of a MMC's specimen and Fig. 6 shows the successive observation of surface crack in the 9 vol.% electro-polished MMC specimen.

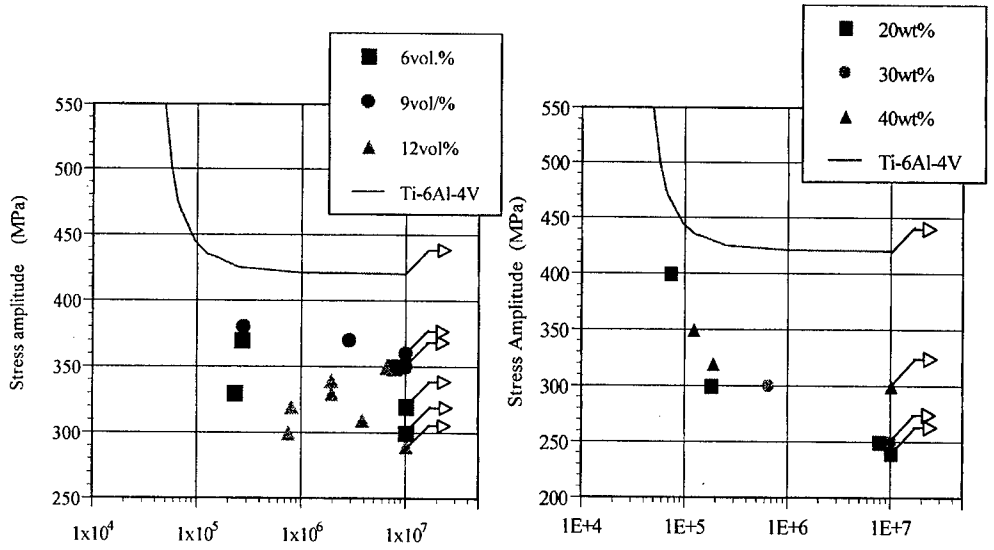
4. DISCUSSION

Relating to the effect of polishing method, mechanically polished specimens show a higher fatigue



(a) 6 vol.% (b) 9 vol.% (c) 40vol.% ——100 μm

Fig. 3. SEM observation of the surface (Electro-polished materials).

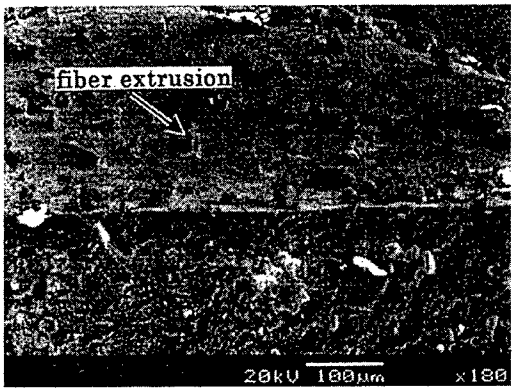


(a) Mechanically polished materials (b) Electro-polished materials

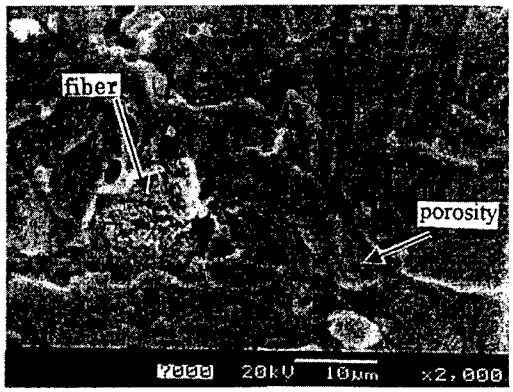
Fig. 4. S-N curves of various fiber content ratio.

limit than the electro-polished ones. The electro-polished specimens surface contain the W-fibers extrusion [Fig.5 (a)] resulted from the fact that W-fibers were relatively cathodic with respect to the Ti-6Al-4V matrix during electro-polishing process. Since the extrusion of W-fibers may cause stress concentration at their interfaces with the matrix, it is attributed as one of the reasons that this extrusion by W-fibers deteriorate the fatigue limit in this circumstance. In the other hand, the residual stress due to the mechanical process applied for the mechanically polished specimens may play a crucial role in preventing crack initiation and hence the rather fatigue limit was obtained for this group.

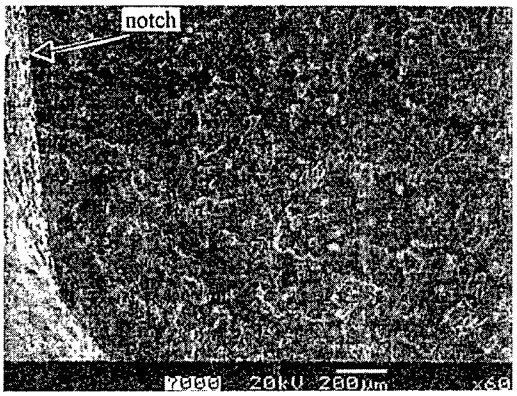
Typical fracture surface of MMC specimens is shown in Fig. 5. Generally speaking, fracture surface of W/Ti-6Al-4V MMCs presents numerous broken W-fibers in a brittle (cleavage) fractured Ti-matrix. In Fig. 5 (b), the interface of W-fiber/Ti-matrix apparently contains some defects but however the overall fracture surface shown in Fig. 5 (c) shows a vast majority of broken W-fibers rather than pull-out W-fibers. Therefore the W-fiber/Ti-matrix interface was relatively strong. Fig. 5



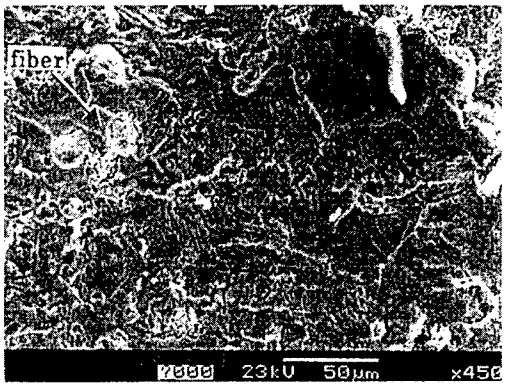
(a) Fibers extrusion (12 vol.%, E.P)



(b) matrix bonding situation (6 vol.%, M.P)



(c) Multi initiation crack (12 vol.%, E.P)



(d) Porosity in the fracture surface (6 vol.%, M.P)

Fig. 5. SEM of fracture surface.

(d) shows evidences of uncompletedly bonding of Ti particulates due to probably insufficient HIP and a large number of porosities were observed here and there on the fatigue fracture surface. The deterioration of fatigue limit in MMC is considered relating to a low ductility matrix, porosity defects and micro-voids during HIP fabricating process.

Quantitative analysis of porosity density indicated by percentage of area exposing on a specified fatigue fracture surface area shows a result of 3.94% for 12 vol.% specimen, 3.55% for 9 vol.% specimen and 3.26% for 6 vol.% specimen respectively. These results indicate the porosity presenting in the W/Ti-6Al-4V MMCs may take an important role in decreasing their fatigue limit. In addition, W/Ti-6Al-4V MMCs showed a tendency of multi-cracks initiation [Fig. 5 (c)]. Several cracks were observed initiating from the surface of fatigue specimen then coalescing in propagation.

Based on the results of successive observation of replicas, crack initiation in MMCs occurs in less than 30% of the fatigue life. Multi-cracks initiate from micro-voids or porosities and cracks coalescence were speculated for fatigue crack process according to the obtained surface observation and SEM fractographs but so far it unfortunately has been a lack of strongly evident experimental results for this current discussion due to the limitation of surface observation method. Successive micrographs in Fig. 6 illustrate representatively this discussion.

The overall results obtained in this work assumed that an inadequate process in fabricating W/Ti-6Al-4V MMCs resulted in a relatively brittle and high porosity Ti-matrix, which took its

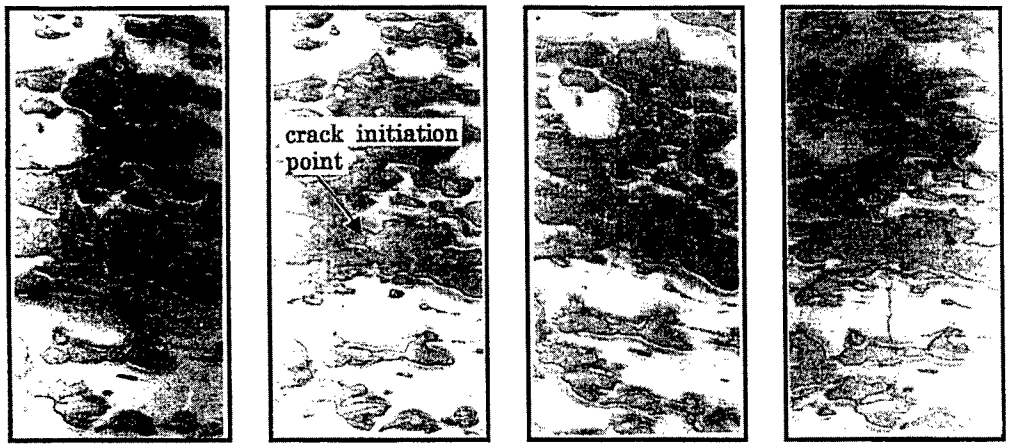


Fig. 6. Successive observation of crack propagation (9 vol.% electro-polishing).

major role in the deterioration of fatigue strength. Further works in order to improve the quality of Ti-matrix in these MMCs are crucially required.

5. CONCLUSIONS

The following concluding remarks are summarize beside on the preceding experimental results and discussions:

1. Though the static tensile properties of MMCs are superior to those of conventional Ti-6Al-4V alloy, the fatigue limit of MMCs becomes deteriorated in spite of containing the W-fiber reinforcement.
2. Porosity existence of the W/Ti-6Al-4V MMCs was not observed at the tensile tested fracture surface, but many porosities were observed in the fatigue tested specimen.
3. The improvement of fatigue property of this MMC could be expected through a more adequate fabricating process (especially, HIP condition), which possibly improves the ductility and prevents porosity problem in the Ti-matrix.

ACKNOWLEDGEMENT

The authors would like to express for the cooperation by Mr. Y. Yanagida and T. Tamasaki, in addition the authors would like to appreciate Dr. K. Hayashi for his kind helpfulness.

REFERENCES

1. W.F.Smith., Structure and Properties of Engineering Alloys, McGraw-Hill Book Co., (1994).
2. R.O.Ritchie, R.H.Dauskardt and B.N.Cox., Fatigue of Advanced Materials, MEPE Ltd, (1991).
3. T.Kimura et al., Journal of the Japan Society of Machanical Engineers,28(11),(1998), pp.897-901
4. Titanium material researchers, Present aspect of Titanium material research in Japan,(1989),pp.81
5. M.A.Iman and C.A.Gilmore., Metal Trans., vol.14(A), (1983), pp.233-238.
6. B.N. Cox and C.S. LO., Acta metal, mater., 40(7), (1992), pp.1487-1496.

Key Engineering Materials Vols. 183-187 (2000) pp. 969-974
© 2000 Trans Tech Publications, Switzerland

Failure Analysis of the Fourth Compressor Pans in Aero-Engines

Guoru Fu and Wei Su

Beijing Aeronautical Technology Research Center, POB 9203-16, Beijing 100076, China P.R.

Keywords: Aero-Engine, Failure, Fatigue, Fracture, Resonances, Stress, Stress Concentration, The Fourth Compressor Pan

ABSTRACT

Three incidents of wheel flange bursting-incidents of the fourth compressor pan had happened in succession in one year for one type of aero-engine. Through fracture and stress analysis in this paper, the conclusion as follows is drawn: it is high-low cycle complex fatigue resulting in the wheel flange bursting; the internal reasons are the rather great finish residual tensile stress in the fatigue source and the stress concentration caused by the non-smooth surface of transition; the external reason is the abnormal vibration--resonance while the fourth pan working.

1. FRACTURE ANALYSIS

Three incidents of wheel flange bursting-incidents of the fourth compressor pan had happened in succession in one year for one type of aero-engine, which has been used for about thirty years and whose production quantity was over one thousand. This kind of faults did not happen before.

The fracture features caused by the three incidents are similar to each other, so it could be explained in detail through analyzing the fracture of the first incident (Fig.1).

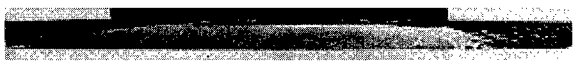


Fig.1.Fracture face

The fracture including fatigue region and instant disconnection region can be found through macro-examination. The crack originates from the front head face. The fatigue curve can be found obviously in the smooth fracture of arc region (L: 60mm, W: 4mm) near the head face, which is the fatigue region. The instant disconnection region is situated on the double sides and the rear (the angle between the board and the rear is about 45°). The fatigue cracking extends unsymmetrical 14mm in the pan rotating direction and 46mm in the opposition. The macroscopic nature shows that the fatigue area is relative big and the fatigue cracking extends fully.

It can be found the fatigue cracking originated from the transition face between the head face and the wheel flange "R3" through micro-examination (Fig.2), and the fatigue cracking originated from the transition line between the head face and the wheel flange "R3" through observation of the enlarged source region (Fig.3). The source region is rougher than the other, lots of cracks and machining or squeezing deformation vestige could be seen in the flank (Fig.4).

Similar machining vestige also is found in other transition region. The width of fatigue striations near the source is less than 1 μ m(Fig.5). No material defects and corrosion marks were found in source region after analyzing with X-energy spectrometer . The natures of the fatigue extension region are typical fatigue characteristics (Fig.6).

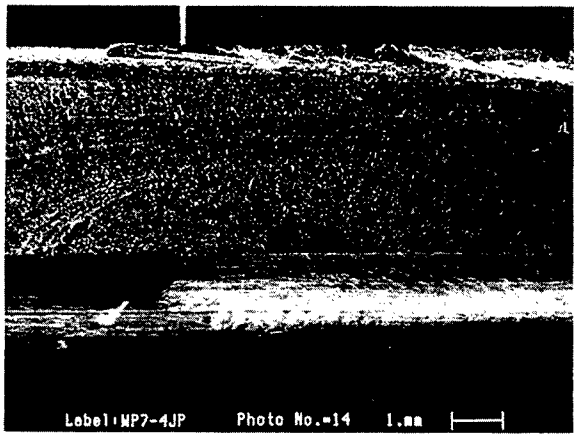


Fig.2.The crack source region

The above fracture natures show that it is high-low cycle complex fatigue.

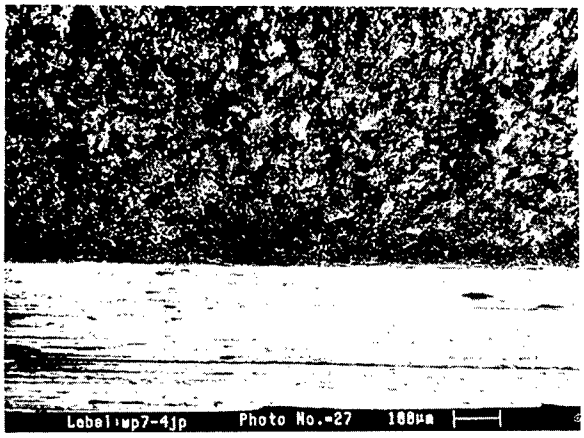


Fig.3.The prime position of crack

2.ANALYSIS AND MEASUREMENT

(1). Measurement of the "R" and observation of the transition face: Through sampling near crack region and observing the section corresponding to the source region, the number of "R" (3.0mm) meets the drawing requirement. It could be found with naked eye that the transition face between the board and the circle-arc "R" is not slick and there are obvious transition lines in it. In the section , the surface of the board is not tangent but transverse with circle-arc "R" , the angle is 156.6 ° (Fig.7).

(2). Measurement of hardness: Through measuring the sample from the board near fracture with Brine' s machine, the number of hardness (d=3.23~3.27) meets the drawing requirement (d=3.15~3.45).

(3). Measurement of the board thickness: The thickness of the board that near the fracture and under the transition line between the "R" and the board 1mm is 4.38 mm, it meets the drawing requirement.

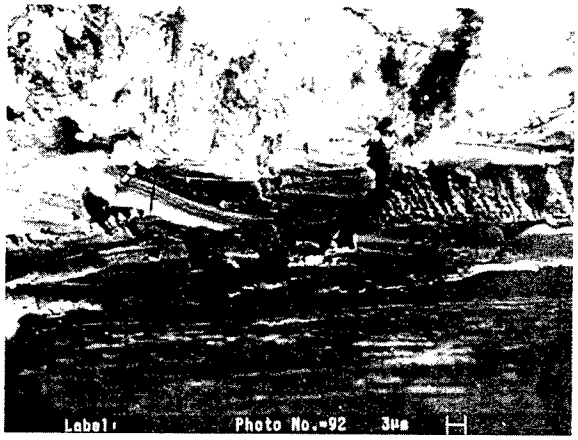


Fig.4.The flank of the source

(4). No crack is found in other position through detection of defects with ultrasonic wave on the head face of the compressor pan.

3.STRESS ANALYSIS

Fig.8 shows the structure and the stress bearing of the fourth pan[1]. In normal working condition, the transition region between the wheel flange and the board bears several stress as follows: the centrifugal force caused by impeller and wheel flange(σ_r); the thermal stress caused by

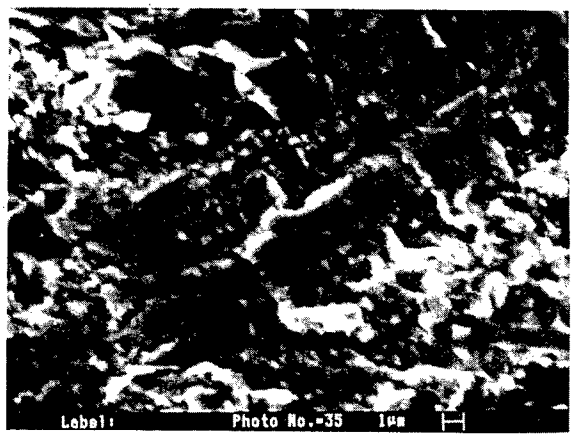


Fig.5.Fatigue striation near the source

heated inequable along the thickness of the compressor pan(M_t); the moment of torsion caused by circle aerodynamic force that the working impeller bearing(M_n); the bending moment caused by the

axial aerodynamic force that the working impeller bearing and the differential static pressure between two sides of the compressor pan(M_w); the pretightening force existing the connection between the fourth pan and the journal of the fifth(σ_p); the dynamic load caused by vibration of the impeller and the pan(σ_v), and the finish residual stress(σ_d).

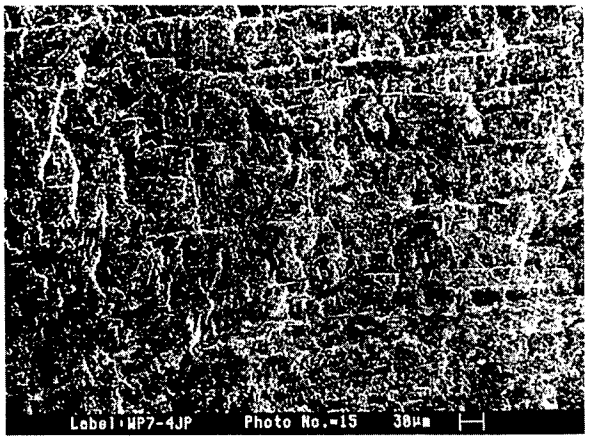


Fig.6.Fatigue nature in the developed region

The fracture analysis shows that the fracture nature of the fourth pan was high-low cycle

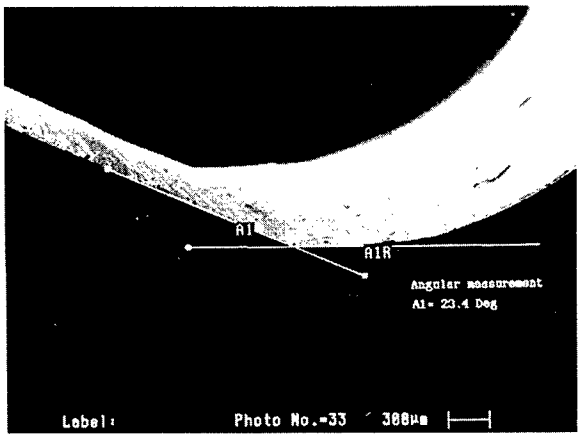


Fig.7: transverse line between the board and the wheel flange "R"

complex fatigue caused by the centrifugal force and the addition of vibrating stress. The fourth compressor pan is the cantilever structure whose mode damping is rather small, so very small stimulate stress can result in resonance when the outside stimulating frequency is close to nature frequency, and hence rather big vibrating stress should be created in the "R3" transition face. The result by test bed shows there is a resonance point when n_2=97~98% rotation speed, so the existence of the abnormal vibration relating to engine assembling is possible and is random while the fourth pan working. Although the resonance stress tested in the ground is only about 100MPa, it may be rather great if in the air. So the abnormal vibration is the important external cause resulting in failure.

The temperature in the rear of the fourth pan is higher than that in the front, so the thermal stress makes the front pressed. As compressor' s pressure boosting function, the compressive stress in the rear is bigger than that in the front. The bending moment caused by differential pressure also make the crack region pressed. As the head face of the fourth pan being free and the assemblage between the back face and the journal of the fifth pan being thermal fit, the pretightening force also made the crack region pressed. All above analysis show that the stress that the head face of the transition between the wheel flange of the fourth pan and the board bearing is smaller than the back bearing. The finite element calculation also proves this, the stress in the head face is 374 MPa and 1.2 times in the back. The analysis on vibration nature of the fourth pan shows that the vibration stress in transition region is relatively high compared with other region while vibrating, but they are equal to each other between the front and the rear.

4.REASON ANALYSIS

Based on the failure appearance and the fracture natures, it can be concluded that three wheel flange-busting incidents have common characteristics as follows:

(1). The survival life of the failure –engine is shorter than the rated value;
(2). The failures happened all in the engineer rotational speed being highest.
(3). All the crack region are situated on the transition between the front face of the fourth pan and the board;
(4). All the failure nature are high -low cycle complex fatigue;
(5). All the fatigue cracks originate from the front face , and it extends fully;
(6). No material and metallurgical defects are found in the source region or near, the mechanical performance and board thickness all coincided with the design desire;
(7). No crack is found in other region.

The above common features show that the three failures have the same mode and reason.

The material of the fourth pan is 1Cr11Ni2W2MoV, its limit of yielding is 878MPa and limit of fatigue is 665MPa(mid-value, room-temperature, $N=10^7$),475MPa(-3 σ , 300℃, $N=10^7$). The stress in the transition surface is smaller than that in the back, and is smaller than the limit of fatigue no matter in normal working or in vibrating condition, this shows there are abnormal factors in the head face of the failure pan.

The crack origination region is relatively rough, but the crack extension region is relatively smooth. Lots of smaller cracks could be seen in the flank of the source region by micro-examination. No obvious material defects and corrosion marks are found in it, so it can conclude that the eruptive stress of fatigue is relatively big and it exists mainly in the surface of the source region. Only visual check on the transition was done during application and repair, so the abnormal factor bringing about crack is simply the work dimensional error and the residual stress resulted from the processing. A calculation show that the stress-concentration coefficient resulted from non-smooth transition in the head only is 1.12, and it is not enough to result in the crack. As no method to measure the original residual stress in the crack region, samples from other good condition region were tested for the measurement of residual stress. Results are as follows: the residual stress in the board is –487MPa, that in the "R3" circle-arc between the wheel flange and the board is –262MPa, that in the transition between "R3" corresponding to the crack source and the board is –21MPa(all above are compressive stress). Because the residual stress in the transition between "R3" and the board is rather smaller than that in other region, the transition is vulnerable region. Through above analysis, the conclusion can be drawn that the bigger work-residual tensile stress exists possibly in

the crack eruption region and that the stress itself is the internal reason resulting in crack.

Although the residual stress disappeared after crack produced, the vibration while the pan working would make the crack extend continually in the high-low cycle complex fatigue mode.

Because the circles aerodynamic force that the working impeller bearing make the pan rotate, it produces the moment of torsion in the pan. This made the end of crack close in the rotation direction but open on the opposite, so the crack extends unsymmetrical bigger in the rotation direction than on the opposite.

5.CONCLUSIONS

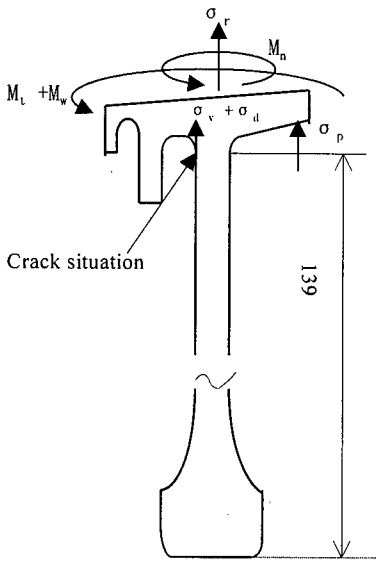


Fig.8.The fourth pan structure graph

(1). The failure nature of the fourth pan is high-low cycle complex fatigue, the fatigue crack originates from the transition surface between the wheel flange "R" and the head face of the board.

(2). Rather great machining residual tensile stress in the fatigue source and the stress concentration caused by the non smooth surface of the transition are the internal reason resulting in the fatigue crack.

(3). The abnormal vibration — resonance while the fourth pan working is the important external reason resulting in failure.

(4). No metallurgical and material defects corresponding to the extension of the crack are found.

6.REFERENCES

1. P. Zhong, H. Yan, Cracks analysis of the fourth compressor pans in aero-engines, Failure analysis of representative cases in aerial equipment, National defence industry publishing company, 1998.2, Beijing.

Key Engineering Materials Vols. 183-187 (2000) pp. 975-980
© 2000 Trans Tech Publications, Switzerland

Thermal Aging and Low Cycle Fatigue Characteristics of CF8M in a Nuclear Reactor Coolant System

J.D. Kwon[1], S.W. Woo[1], Y.S. Lee[1], J.C. Park[1] and Y.W. Park[2]

[1] Department of Mechanical Engineering, Yeungnam University, 214-1 Dae-dong, Kyongsan, Kyongbuk 712-749, Korea

[2] Korea Institute of Nuclear Safety, Taejon 305-338, Korea

Keywords: CF8M, Cyclic Hardening, Cyclic Stress-Strain Curve, Low Cycle Fatigue, Strain Control, Thermal Aging

ABSTRACT

Thermal aging occurs when a primary reactor cooling system is exposed for long period of time to a reactor operating temperature between 290～330℃. The purpose of the present investigation is to find the effect of thermal aging of CF8M on a low cycle fatigue life. The specimen of CF8M is prepared by an artificially accelerated aging technique maintained for 300 and 1800hrs. at 430℃, respectively. The low cycle fatigue tests using virgin and two aged specimens are performed at room temperature for various total strain amplitudes of 0.3, 0.5, 0.8, 1.0, 1.2 and 1.5%. Through the experiment, it is found that the fatigue life is rapidly reduced the increase of aging time. The experimental fatigue life estimation formulas between the virgin and two aged specimens are obtained.

1. INTROUCTION

Structural degradations exposed to high temperatures and pressures for a long period of time are often experienced in the components of a primary reactor coolant system(RCS) and this experience requires an evaluation of the safeguards related to structural integrity[1,2]. Austenitic-ferritic duplex cast stainless steel(CF8M) is used in a primary reactor coolant system. It is noted that CF8M is degraded at a temperature of 475℃ and the operating temperature range of the pressurized water reactor, 290～330℃[3,4].

When elbow and T-shape components connected in a RCS are exposed to high pressure fluids, these components are exposed to impingement corrosion[5]. It is quite natural that stress concentrations arise in a portion of impingement corrosion and the corrosion causes higher stress values than the design. The level of stress values, for example, can be varied due to heating-cooling transient through the normal inspection period. If this transient is considered as one cycle, the structure can experience low cycle fatigue, respectively.

Chtara et al.[6] performed low cycle fatigue experiments of duplex stainless steel. They found that the nitrogen atom in austenite stainless steel plays an important role in cyclic plastic deformation in both the austenite and ferrite phases even though major plastic deformation is caused by deformation that occurs in the ferrite phase. They estimated low cycle fatigue cumulative damage takes place. Xia et al.[7] investigated the cyclic and dislocation behavior of Fe-Cr-Mn-N

dual phase stainless steel.

In the present paper, the artificially accelerated degraded method of CF8M is developed at 430℃ and various classes of degraded specimens are prepared. The relationship between strain amplitude and low cycle fatigue life, and the relationship between stress amplitude and low cycle fatigue life are found through low cycle fatigue experiments using degraded and virgin specimens.

2. SPECIMEN PREPARATION AND THE TESTING METHOD

The tested specimen in the present investigation is ASTM A351 Grade CF8M cast stainless steel used in a primary reactor cooling system. The chemical compositions are shown in Table 1.

The artificially accelerated aging method has an advantage in that the material can be degraded in a short period of time. The aging temperature is 430℃. The thermal embrittlement varies linearly when the aging temperatures between 300℃ and 400℃[3]. However, a more severe embrittlement is observed at 475℃ particularly when it exceeds the linear range. Materials degradation can also be observed in the operating temperature range of the pressurized water reactor when it is between 290~330℃[3,4]. In order to reduce the aging time, a degradation of 430℃ is selected. The 430℃ degraded specimens are held for 300 and 1800hrs, respectively, and then are water quenched[8].

The tested specimen adheres to the specifications of ASTM E 606[9] and these characteristics are shown in Fig. 1. The parallel portion(ϕ7) and the curved portion(R28) are created by high precision lapping in order to minimize the effect of surface roughness on the overall measurements. The experiments are performed at room temperature. The center of the parallel portion is measured and a knife-edge, that is 12.5mm with the center in the parallel portion is installed. Cyclic stress-strain curves are obtained using a companion specimen with various strain amplitudes.

Raske and Morrow[10] suggested that a low cycle fatigue experiment be performed under a total strain amplitude between ±0.2 and ±2.0%. The present experiments are performed under a 0.2Hz condition with continuous triangle waveforms. Total strain amplitudes(ε_{ta}) of 0.3, 0.5, 0.8, 1.0, 1.2 and 1.5% are applied to the virgin specimens, the degraded specimens for 300hrs and for 1800hrs, respectively, at 430℃. Rao et al.[11] suggested that fatigue life can be determined by the cycle number corresponding to a 20% stress reduction in order to protect the fracture surface of the specimens. However, the fatigue life in the present experiments is determined by the cycle number when the load is reduced to less than 10kg. This is so because CF8M exhibits large elongation.

3. RESULTS AND DISCUSSION OF THE LOW CYCLE FATIGUE EXPERIMENTS

3.1 Cyclic stress-strain curves

Typical results of the hysteresis loops obtained under total strain amplitude of 0.8% are shown in Fig. 2. Fig. 2 includes virgin and degraded specimens for 300hrs and 1800hrs, respectively, at 430℃.

Table 1. Chemical composition of CF8M.

Composition, wt. %				
C	Mn	P	S	Ferrite Content 9.6 %
0.074	1.21	0.0318	0.0126	
Si	Ni	Cr	Mo	
1.14	9.59	18.67	2.73	

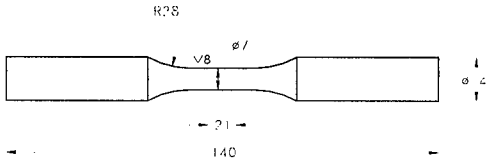


Fig. 1. Configuration of uniform-gage specimens For low cycle fatigue tests.

The results of the hysteresis loops under various ε_{ta} are shown to have similar curves to that shown Fig. 2. All hysteresis loops shown in Fig. 2 show an inflection curve in the low cycles before the specimen fails. This is consistent with the results of [9]. The inflection point is shown because the elongation of CF8M is large.

The cyclic stress-strain curve for each strain amplitude is obtained as N/N_f=0.5, where N_f is the cycles to failure. The extreme points of the various cyclic stress-strain curves are connected and are shown in Fig. 3. The stress values are increased with ε_{ta} for identically aged specimens in Fig. 3. Therefore, it can be concluded that the stress ranges increase with the degradation of the specimens.

3.2 Stress amplitude variations with respect to the cycle ratio

The stress amplitudes(σ_a) with respect to the cycle ratio(N/N_f) for various applied strain amplitudes are shown in a), b) and c) of Fig. 4. Figures a), b) and c) are stress amplitudes of virgin and degraded specimen for 300hrs and 1800hrs, respectively, at 430℃. Significant degradation is observed in the initial stage of the fatigue experiment, especially, for large strain amplitude applications. The variations are not significant with the progress of the fatigue except within the vicinity of failure. The stress amplitude variations for small strain amplitude applications can not recognize the significant variations with respect to N/N_f. The stress amplitudes with respect to N/N_f increase with degradation as seen in a), b) and c) of Fig. 4.

The ratios of the tensile strength to 0.2% offset yielding stress(σ_u/σ_y) for the virgin and the two classes of degraded specimens are σ_u/σ_y =531/314=1.69 for the virgin, 620/327=1.90 for the 300hrs aged specimen and 624/335=1.87 for the 1800hrs aged specimen, respectively, at 430℃. Manson and Smith[12] show that if a material is $\sigma_u/\sigma_y \geq 1.4$, then the material exhibits cyclic hardening. If a material shows $\sigma_u/\sigma_y \leq 1.2$, then the material exhibits cyclic softening. When the results obtained by

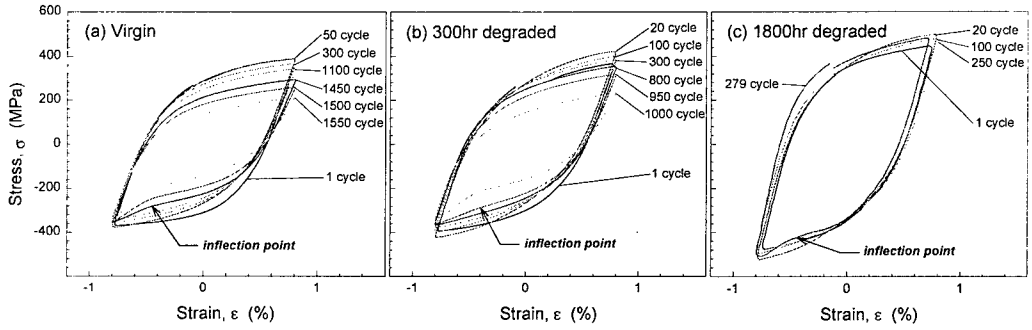


Fig. 2. Hysteresis loop for virgin and degraded materials at ε_{ta} =0.8%.

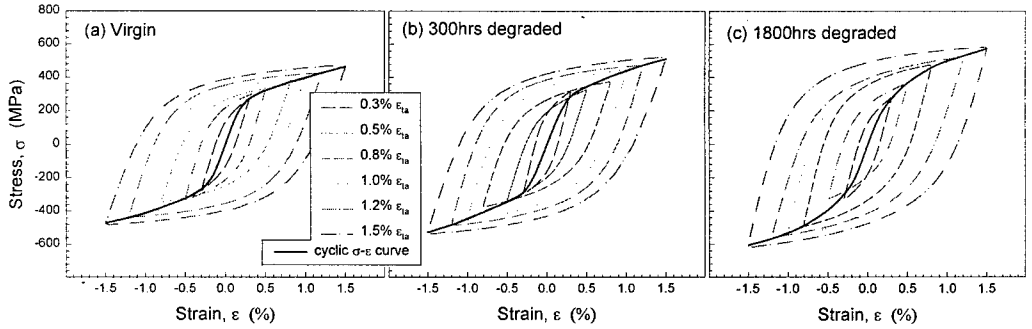


Fig. 3. Cyclic stress-strain curves for virgin and degraded materials.

Manson and Smith are compared with those obtained in the present investigation, CF8M of both virgin and degraded specimens exhibit cyclic hardening and these results are consistent with the results found by Manson and Smith.

Rapid stress reductions that occur at $N/N_f \sim 0.9$ are observed for all specimens, as seen in Fig. 4. These results may be caused by the significant elongation of CF8M. The rapid reductions of stresses result into an inflection point as noted in Fig. 3.

3.3 Characteristics of low cycle fatigue life and strength

The low cycle fatigue-life relationship can be expressed in ASTM[9] as,

$$\Delta\varepsilon_t / 2 = \left[\sigma_f' / E\right](N_f)^b + \varepsilon_f'(N_f)^c \qquad (1)$$

where σ_f': fatigue strength coefficient, E: Young's modulus, b: fatigue strength exponent(or Basquin's exponent), ε_f': fatigue ductility coefficient, c: fatigue ductility exponent, and N_f: cycles to failure.

The characteristic curves related to low cycle fatigue tests are shown in Fig. 5. Figures a), b) and c) are elastic, plastic and total strain amplitude variations with respect to fatigue life(N_f). The elastic strain amplitude, ε_{ea}, and the plastic strain amplitude, ε_{pa}, have a linear relationship with respect to N_f in log-log plots. These relationships are postulated in Basquin's method[13]. The values of b and c in eq.(1) can be found from the slopes shown in a) and b) in Fig. 5, respectively. The parameters in eq.(1) are found using the least square method and the experimental data of CF8M. Those values are given in Table 2.

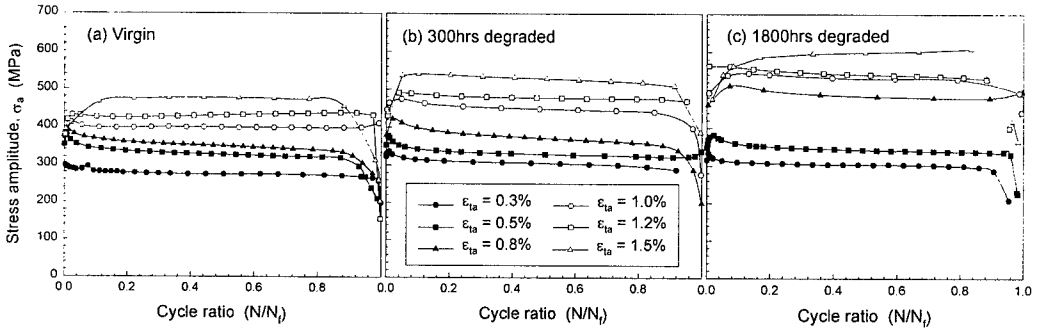


Fig. 4. Cyclic stress response curves for virgin and degraded materials.

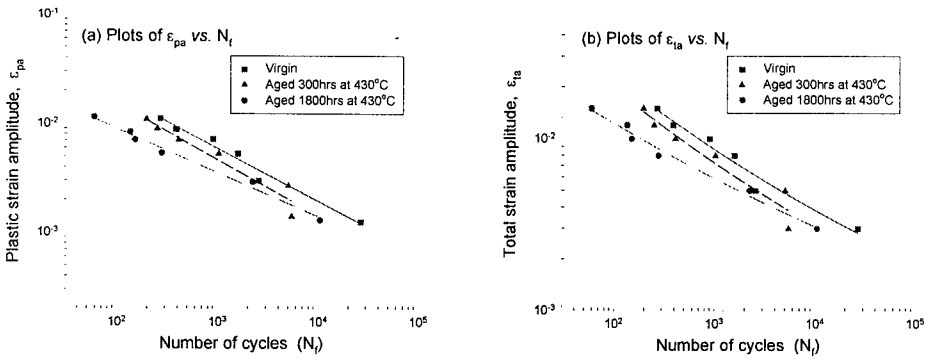


Fig. 5. Relationships between plastic, total strain amplitudes and fatigue life in CF8M.

Low cycle fatigue life decreases significantly with the increase of degradation under the identical strain amplitude, as shown in Fig. 5. The significant difference in the fatigue life between virgin and the degraded specimens as shown in Fig. 5 can not be observed.

Plastic strain amplitude is larger than elastic strain amplitude in the low cycle fatigue tests in Fig. 5 and ε_{pa} affects on low cycle fatigue life. The relationship between the total strain amplitude and the cycles to failure shows a shape similar to that between ε_{pa} and N_f.

The log-log relationship between stress amplitude(σ_a) and N_f are shown in Fig. 6 and this relationship shows that the linear relationship and the results are consistent with Basquin's results[13]. The relationship between σ_a and N_f is expressed in eq.(2) as,

$$\sigma_a = \sigma_f' (N_f)^b \qquad (2)$$

The values of b and σ_f' are obtained by the least square method and those values are shown in Fig. 6 for both virgin and degraded materials. Stress amplitude corresponding to σ_a at one cycle, σ_f' is increased with degradation. The decreasing rate of fatigue strength with respect to the cycle to failure(N_f), namely $|b|$ values shows that the virgin specimen is found to be at a minimum value. However, the fatigue life(N_f) under the same, identical stress amplitude does not show any significant difference between the virgin and degraded specimens.

4. SUMMARY AND CONCLUSIONS

Low cycle tests are performed using the virgin and degraded specimens for both 300hrs and 1800hrs, respectively, at 430℃. The CF8M specimens are degraded using an artificially accelerated aging technique. The low cycle fatigue tests are performed using the above three classes of specimens applying total strain amplitudes of 0.3, 0.5, 0.8, 1.0, 1.2 and 1.5%, respectively, at room temperature. Through low cycle fatigue tests using virgin, and two kinds of degraded CF8M specimens, the following conclusions are made:

1) The effects of degradation on fatigue life are able to distinguish and identify fatigue through the relationship that exists between constant strain amplitude and fatigue life. The low cycle fatigue life of the CF8M degraded specimen is decreased significantly from that of the virgin specimen. This is caused by an increase of the ferritic phase activity as the specimen degrades.

Table 2. Values of σ_f'/E, b, ε_f', c obtained low cycle fatigue tests.

Variable / Kind	σ_f'/E	b	ε_f'	c
Virgin	0.0089	-0.1669	0.1689	-0.4845
300hrs degraded	0.0097	-0.1897	0.1644	-0.5152
1800hr degraded	0.0064	-0.1460	0.0575	-0.4032

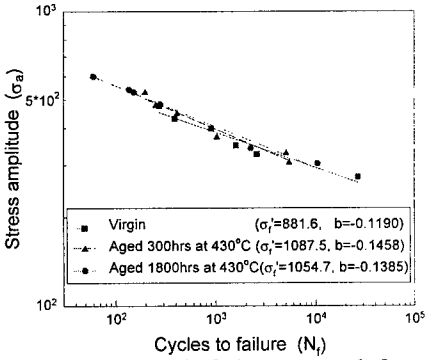


Fig. 6. Low cycle fatigue strength for virgin and degraded materials.

2) Stress amplitudes increase rapidly in the early stages of cyclic strain applications(the initial stages of fatigue). Stress amplitudes level off in the progress towards fatigue until the specimens the fail. The rapid increase of σ_a in the initial fatigue test stage is more pronounced with increase of degradation.
3) The parameters of CF8M involved in the relationship between ε_{ia} and N_f(eq.(1)) and between σ_a and N_f(eq.(2)) are found. These results can be used to predict the low cycle fatigue life estimation of CF8M as the degradation occurs.

ACKNOWLEDGEMENTS

The authors are grateful for the support provided by a grant from the Korea Institute of Nuclear Safety. This manuscript is prepared and the experiments are performed under grant No. KINS/HR-252.

REFERENCE

1. G. K. Robert and G. R. Andre, "A Component Wear-out Analysis on Control Rod Drive Mechanisms," Westinghouse, Pittsburgh (1985)
2. A. G. Ware, ASTM STP 756 (1982) p.165-189
4. O. K Chopra and H. M. Chung, "Aging Degradation of Cast Stainless Steels: Effect on Mechanical Properties", Environmental Degradation of Materials in Nuclear Power Systems-Water Reactor, The Metallurgical Society, Warrendale, PA (1988) p.737-748.
5. Metals Handbook Ninth Edition, ASM International, Vol.13, Corrosion (1987) p.338-343.
6. S. Degallaix, H. Chtara and J. C. Gagnepain, "Low-Cycle Fatigue Cumulative Damage in Duplex Stainless Steel," Fatigue '96 (1996) p.602-606.
7. Y. B. Xia and Z. G. Wang, "Low Cycle Fatigue Behaviour of a New Type of Stainless Steel," Mat. Sci. and Eng., A151 (1992) p.29-35.
8. J. D. Kwon, J. C. Park, Y. S. Lee, W. H. Lee and Y. W. Park, "An Investigation of the Degradation Characteristics for Casting Stainless Steel, CF8M, Under High Temperature," Nuclear Engineering and Design (accepted to Dec. 1999)
9. ASTM E 606-77T (1977) p.654-671.
10. D. T. Raske and J. D. Morrow, ASTM STP 465 (1969) p.1-25.
11. K. B. S. Rao. R. Sandhya, S. K. Ray, S. L. Manson and Rodriguez, Int. J. Fatigue, Vol.7 (1985) p.141-147.
12. R. W. Smith, M. H. Hirschberg and S. S. Manson, "Fatigue Behavior of Materials Under Strain Cycling in Low and Intermediate Life Range," NASA TND-1574 (1963)
13. O. H. Basquin, "The Exponential Law of Endurance Tests," ASTEA, Vol.10 (1910) p.625-630.

Key Engineering Materials Vols. 183-187 (2000) pp. 981-986
© 2000 Trans Tech Publications, Switzerland

Study of Crack Propagation Behavior on Low Cycle Fatigue in Spheroidal Grahite Cast Iron Based on Observation of Surface and Fracture Section

F. Nishimura[1], K. Morino[1] and H. Nisitani[2]

[1] Department of Mechanical and Electrical Engineering, Tokuyama College of Technology, 3538 Takajo, Kume, Tokuyama, Yamaguchi 745-8585, Japan

[2] Department of Mechanical Engineering, Kyushu Sangyo University, 2-3-1 Matsukadai, Higashi-ku, Fukuoka 813-8503, Japan

Keywords: Crack Coalescence, Crack Propagation, Fatigue, Low Cycle Fatigue, Microshrinkage, SEM, Spheroidal Graphite Cast Iron

ABSTRACT

In this paper, in order to clarify the effect of the crack coalescence for the crack growth rate, low cycle fatigue tests were carried out using two kinds of spheroidal graphite cast iron (SGI). The crack propagation behavior from the crack initiation to the fracture was investigated by observing the surface of specimens and their fracture section. The main results obtained are as follows: (1) The variation range of the crack growth curves in SGI is larger than that in its matrix material. This tendency is caused by the occurrence of the crack coalescence and the difference of crack initiation length. (2) In most cases that the crack growth rate is accelerated, the microshrinkage exists on the neighboring surface. (3) The crack coalescence is not the main factor for accelerating the crack growth rate.

1. INTRODUCTION

Spheroidal graphite cast iron (SGI) is used for various machine parts which need high strength and toughness. Recently, strength against low cycle fatigue has been required. In our previous papers [1]-[6], we have been carried out several investigations on low cycle fatigue in SGI. We clarified that low cycle fatigue life in pearlitic spheroidal graphite cast iron (PDI) is about one tenth shorter than that in matrix material, and acceleration of the crack growth rate in PDI is one of the causes for decrease of fatigue life [3]. Moreover, we proposed three factors controlling low cycle fatigue life (crack initiation length, crack propagation limit length and relative crack growth rate) [3].

On the other hand, it is known that a main crack in SGI initiates from the microshrinkage that exists on the neighboring surface, and many preexisting cracks initiate from other microshrinkages and spheroidal graphite. According to the observation of crack propagation behavior in SGI, a main crack was repeatedly connected with preexisting cracks, and crack propagation behavior in SGI was very complicated [1]-[5] [7]-[9]. However, there is no detailed investigation on the effect of the crack coalescence for the crack growth rate. In this paper, plastic-strain-controlled low cycle fatigue tests were carried out using two kinds of SGI. Also, the effect of the crack coalescence for the crack growth rate was examined by a microscopic perspective.

2. MATERIALS, SPECIMENS AND EXPERIMENTAL PROCEDURES

The materials used in this study were ferritic (JIS FCD400; FDI) and pearlitic (JIS FCD700; PDI) spheroidal graphite cast iron. The chemical composition and mechanical properties are shown in Table 1. Table 2 shows some characteristics of spheroidal graphite which are measured by the image processing analysis technique. The threshold value of graphite is 12μm.

Figure 1 shows the shape and dimension of specimen. In this study, cylindrical specimens are used. The diameter d_0 and length l_0 of the central part are 6mm and 9mm respectively. The aspect ratio l_0/d_0 of the central part is made into 1.5 to obtain true fatigue behavior [10]. The specimens were finished with diamond paste. Before testing, the central part of the specimens was etched lightly in 3% nital.

Fatigue tests were carried out using a hydraulic servo testing machine with a capacity of 49kN and frequency ranging from 0.03 to 0.1Hz. Strain was measured by an axial direction extensometer and the machine was set in such a way that the plastic strain range is constant. Plastic replicas were used to measure the crack length and to observe the successive fatigue damage on the specimen surface. Also, SEM was used to observe the fracture sections.

Table 1 Chemical composition and mechanical properties

	Chemical composition [wt. %]							Mechanical properties [MPa, %]				
	C	Si	Mn	P	S	Mg	Cu	$\sigma_{0.2}$	σ_B	ψ	E	H_B
FDI	3.83	2.25	0.34	0.023	0.014	0.034	0.05	309	434	19.2	166x10³	144
PDI	3.68	2.07	0.355	0.021	0.007	0.038	0.599	463	813	6.6	166x10³	259

Table 2 Characteristics of spheroidal graphite

	D_m (μm)	n_g (1/mm²)	f_g (%)	h_g (%)
FDI	24.6	180	8.81	75.4
PDI	28.9	131	8.38	81.2

D_m : Average graphite diameter n_g : Nodule count
f_g : Area fraction of graphite h_g : Nodularity

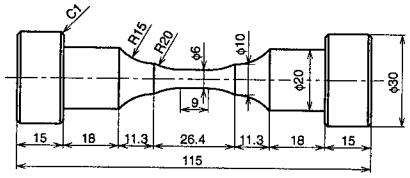


Fig.1 Shape and dimension of specimen

3. EXPERIMENTAL RESULTS AND DISCUSSION

3.1 Comparison of Fatigue Life and Crack Growth Behavior

Figure 2 shows the relation between the plastic strain range $\Delta\varepsilon_p$ and the number of cycles to failure N_f obtained for FDI and PDI. These experimental data satisfy the following Manson-Coffin law.

$$\Delta\varepsilon_p \cdot N_f^{0.61} = 0.207 \quad \text{(FDI)} \quad (1)$$

$$\Delta\varepsilon_p \cdot N_f^{0.59} = 0.157 \quad \text{(PDI)} \quad (2)$$

From Fig. 2, the difference in fatigue life of these spheroidal graphite cast iron is small , and the difference in fracture ductility ε_f does not reflect the fatigue life. In this figure, $2\varepsilon_f$ is plotted at number of 1/4 cycle. The fatigue life of PDI is longer than the life estimated from

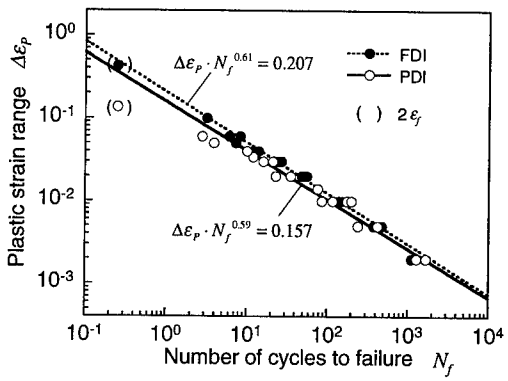


Fig.2 Low cycle fatigue life curves in FDI and PDI

fracture ductility. This result corresponds to that obtained by using aluminium alloys [11].

Figure 3 shows the relation between the logarithm of crack length ln$l$ and the relative number of cycles N/N_f obtained for FDI and PDI. Both of a main crack in these materials initiate from the microshrinkage that exist on the neighboring surface in the early stage of total fatigue life (N/N_f<0.03), and most of the fatigue life are both consumed by the growth of a small crack. Additionally, both of the variation range of the crack growth curves in these materials are larger than that in annealed carbon steel. On the other hand, we know that many preexisting cracks initiate from other microshrinkages and spheroidal graphite, and a main crack is repeatedly connected with preexisting cracks. However, it has never been make clear whether the crack coalescence causes the acceleration of the crack growth rate. Then, the crack propagation behavior from the crack initiation to the fracture was investigated on the surface of specimens and in their fracture section.

3.2 Crack Propagation Behavior in Spheroidal Graphite Cast Iron

Figure 4 shows the crack growth curve, continuous photographs of crack propagating on the surface and the shape of cracks on fracture section in FDI. In the figure of fracture section, the shape of cracks at the fracture observed by metallurgical microscope and the microshrinkage observed by using SEM are illustrated. In this case, the shape of cracks on fracture section correspond to photographs of crack propagating. Figure 5 shows the shape of cracks on vertical sections in FDI and PDI, which was observed by using the heatbaking method immediately before fracture. In FDI, only one crack is seen. The length of the crack on the surface is about 1.5mm. In PDI, two cracks are seen. The lengths are about 0.6mm and 0.4mm respectively. However, the shape of cracks is ellipsoidal regardless of number of cracks and its length. Therefore, the shape of cracks is indicated with ellipsoidal one.

Figure 4 shows a typical example that some microshrinkages exist on the neighboring surface. In this case, three cracks initiate from microshrinkages. These cracks grow individually in the early stage of total fatigue life. After that, the crack Ⓐ is connected with other cracks (Ⓑ and Ⓒ). At that time, the crack growth rate is accelerated every time (① ~ ④). However, after connection, the crack growth rate is always suppressed. Consequently, the crack growth curves in this case are discontinuous and showed the state of steps. As a whole, the crack growth rate in the plural crack propagation period (before ④) was the same as average rate in this material. Additionally, during the propagation period

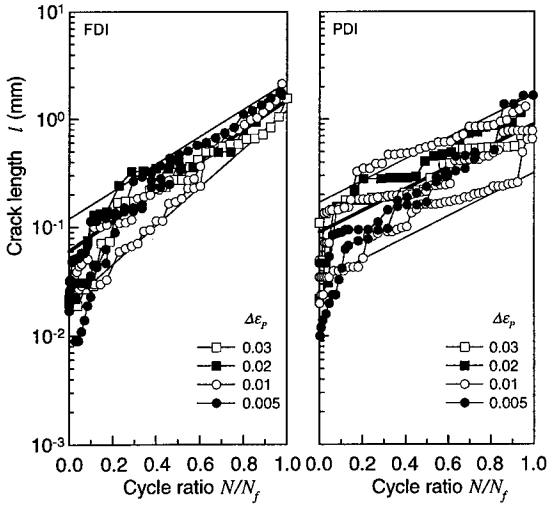


Fig.3 Crack growth curves in FDI and PDI

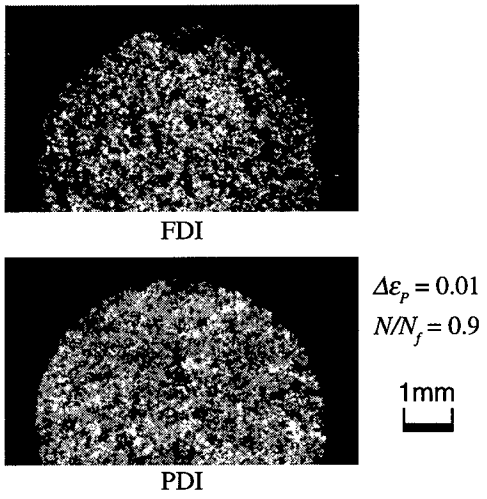
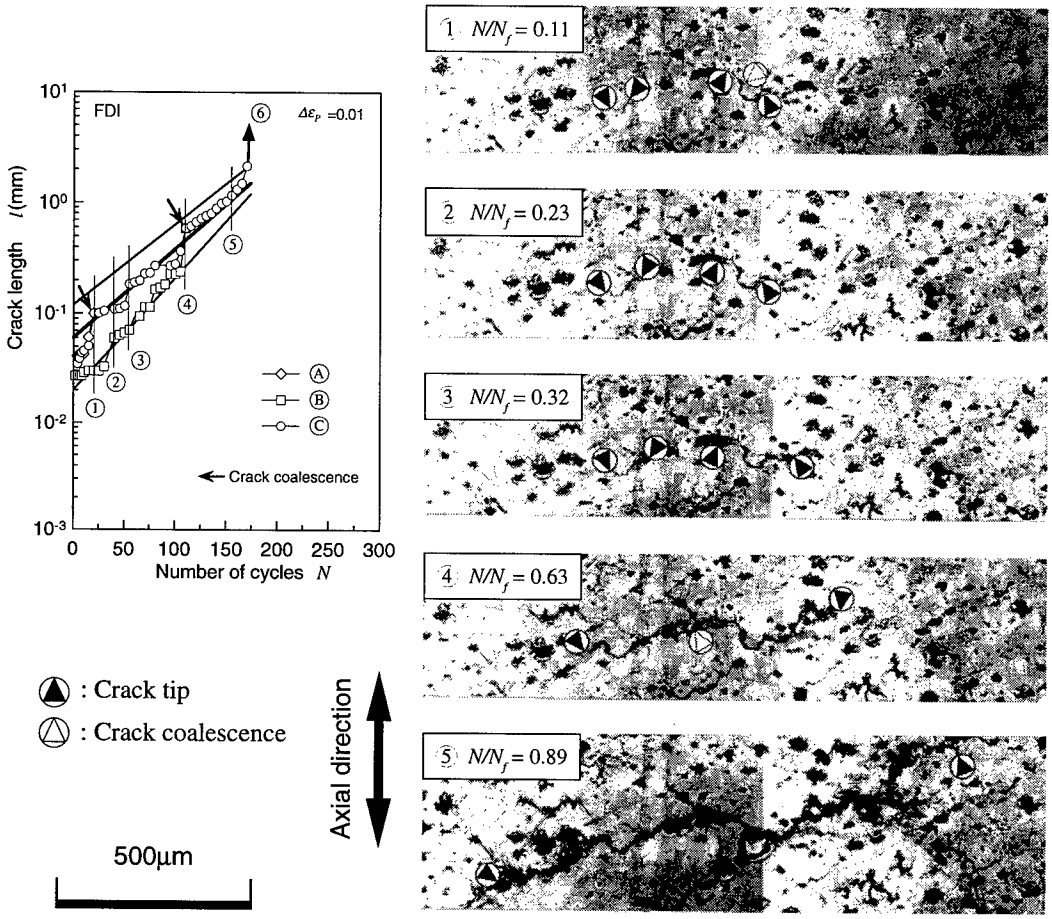


Fig.5 Shape of cracks in FDI and PDI



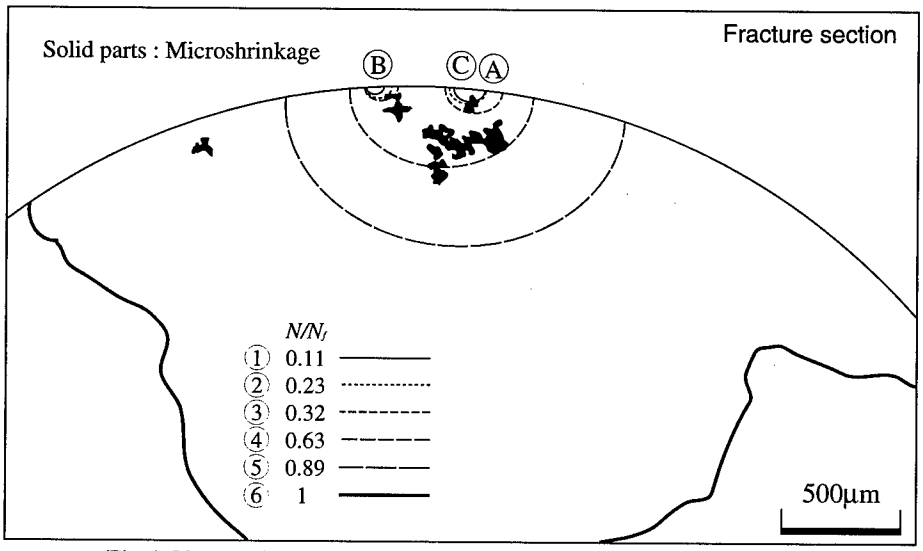
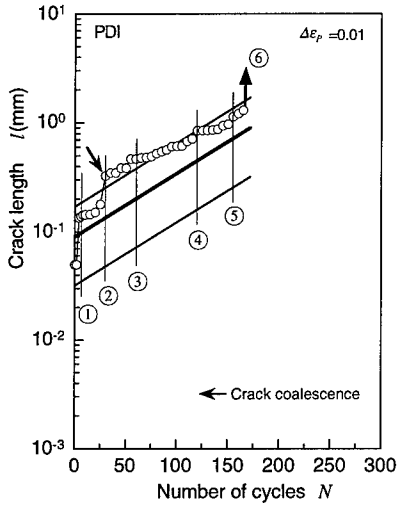
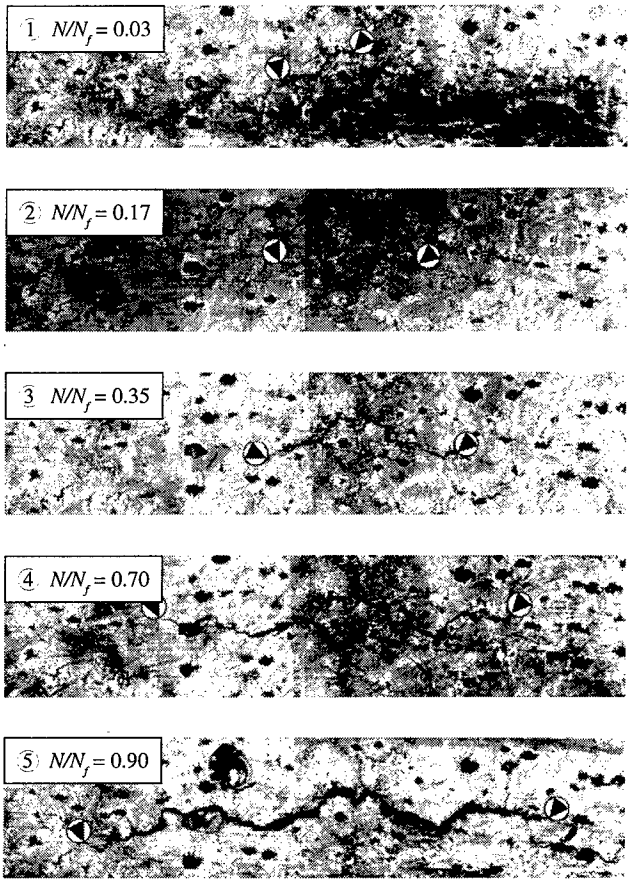


Fig.4 Observation of crack propagation behavior in FDI ($\Delta\varepsilon_p$ = 0.01)





: Crack tip
: Crack coalescence

500μm

Axial direction

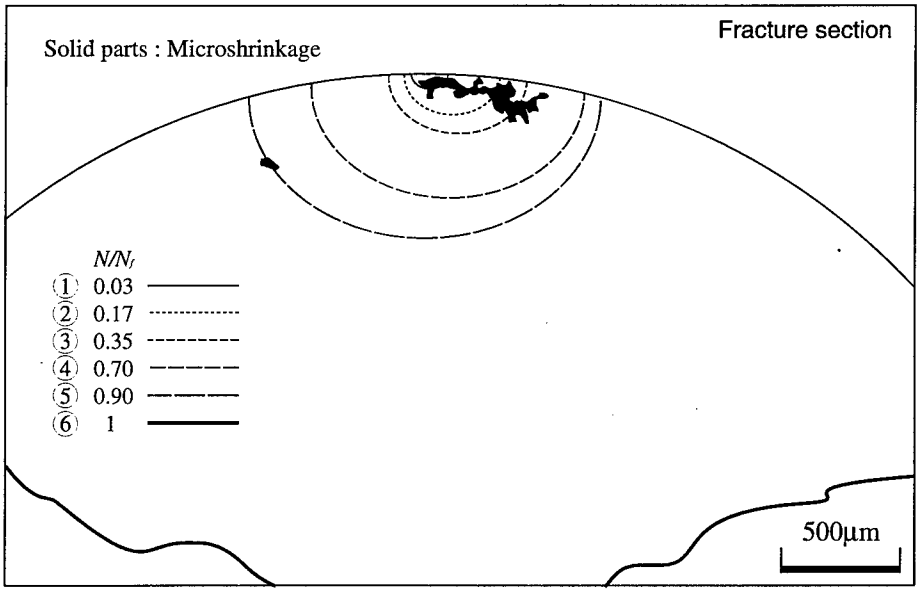


Fig.6 Observation of crack propagation behavior in PDI ($\Delta\varepsilon_P$ = 0.01)

of only one crack (after ④), the crack growth rate was the same as average one.

Figure 6 is an example of PDI ($\Delta\varepsilon_p = 0.01$) that is observed in the same way as in Fig. 4. This shows an example that the projected length on the surface of a microshrinkage is large. As seen from the figure of fracture section, in this material, only one crack initiates from a microshrinkage. The length of microshrinkage projected on the surface is about 500μm. This crack initiation length is about 100μm, which is larger than average one. When a main crack is spread into the microshrinkage, the crack growth rate is also accelerated (②). After spread, the crack growth rate is suppressed. After that, when the length of crack is larger than that of the microshrinkage (after ③), the crack growth rate is also the same as average one in this material. In consequence, the crack length after ② became larger than the average length.

It is already known that the variation range of the crack growth curve in SGI is larger than that of its matrix material [2][4][5]. As has been noted, in both SGI used in this study, behavior of the crack coalescence and suppression were similar regardless of the matrix used. Also, it became clear that the microshrinkage exists on the neighboring surface related to the acceleration of the crack growth rate. That is, this tendency can be explained by the occurrence of the crack coalescence and the difference of crack initiation length.

Finally, when a main crack is connected with preexisting cracks, the crack growth rate is accelerated. After connection, the crack growth rate is suppressed. Consequently, the crack growth curve in SGI is discontinuous and showed the state of steps. As a whole, the crack growth rate was the same as average rate in SGI. That is, it is considered that the crack coalescence is not the main factor for accelerating crack growth rate. Moreover, the crack acceleration is not related with the plastic strain ranges.

4. CONCLUSIONS

Plastic-strain-controlled low cycle fatigue tests were carried out in ferritic and pearlitic spheroidal graphite cast iron. The effect of the crack coalescence for the crack growth rate was investigated from a microscopic perspective. The main results obtained are as follows:

(1) The variation range of the crack growth curves in SGI is larger than that of its matrix material. This tendency is caused by the occurrence of the crack coalescence and the difference of crack initiation length.

(2) In most cases that the crack growth rate is accelerated, the microshrinkage exists on the neighboring surface.

(3) The crack coalescence is not the main factor for accelerating the crack growth rate.

REFERENCES

1. K. Morino, et al., Strength of DCI'93, (1993), 27-32, JSME-MMD.
2. K. Morino, et al., Trans. Jpn. Soc. Mech. Eng., **61**-589, A (1995), 2003-2008.
3. K. Morino, et al., JSME Int. J., Ser. A, **41**-2, (1998), 243-251.
4. F. Nishimura, et al., ICM & M '97, (1997), 27-32.
5. K. Morino, et al., Trans. Jpn. Soc. Mech. Eng., **64**-625, A (1998), 2320-2325.
6. F. Nishimura, et al., Trans. Jpn. Soc. Mech. Eng., **65**-630, A (1999), 358-363.
7. S. Harada, et al., Trans. Jpn. Soc. Mech. Eng., **58**-552, A (1992), 1306-1312.
8. S. Harada, et al., Trans. Jpn. Soc. Mech. Eng., **60**-572, A (1994), 952-959.
9. Y. Kuroshima, et al., Trans. Jpn. Soc. Mech. Eng., **61**-584, A (1995), 705-710.
10. K. Morino, et al., Trans. Jpn. Soc. Mech. Eng., **60**-571, A (1994), 682-689.
11. K. Morino, et al., Trans. Jpn. Soc. Mech. Eng., **64**-622, A (1998), 1443-1448.

Key Engineering Materials Vols. 183-187 (2000) pp. 987-992
© 2000 Trans Tech Publications, Switzerland

Cyclic Softening Properties of 30Cr2MoV Steel at Elevated Temperatures

Z.D. Liu[1], K. Yang[1], X.P. Mao[1], Shu-Lin Bai[2] and J.Y. An[1]

[1] Department of Power Engineering, North China Electric Power University, Beijing 102206, China P.R.

[2] Department of Mechanics and Engineering Sciences, Peking University, Beijing 100871, China P.R.

Keywords: 30Cr2MoV Steel, Hardness, Low Cycle Fatigue, Remaining Life, Softening

ABSTRACT

The low cycle fatigue tests for 30Cr2MoV steel are performed at both room temperature and elevated temperature. The softening properties are investigated. Based on the experimental results, the quantitative relationship between the hardness and remaining life is established. An equation to predict the remaining life of metals with the hardness values is proposed. A modified Mason-Coffin equation including the aging effect is also derived. Both experimental and theoretical results show that it is valuable to predict the remaining life of steam turbine rotor by the measurement of hardness.

1. INTRODUCTION

The damage may accumulate in critical regions in the high temperature components of steam power plants in service due to applied stress, low-cycle fatigue, creep and aging at elevated temperature. For these components there is a need to improve the accuracy of remaining life prediction as a means of providing the basis for planned optimum replacement schedules and where possible to allow the extension of operating live beyond the original design[1]. The difficulty arises from the uncertainties in the input data required for remaining life calculations. The uncertainties include the variation in the operational stresses and temperatures, material properties and actual equipment conditions. Therefore, new methods for post-service condition assessment should be developed for the high temperature components. The hardness measurement is a non-destructive technique to detect the damage caused by fatigue or creep, and it has successfully been used in the assessment of remaining life of critical components in steam power plants[2, 3]. Unfortunately, in conventional low-cycle fatigue tests, the hardness of the tested materials is poorly studied. In this presentation, the low cycle fatigue tests of 30Cr2MoV steel at both room temperature and elevated temperature are performed. The softening properties of studied steel are also investigated. Based on the experimental results, the quantitative relationship between the hardness and fatigue damage is established, and the softening properties can be estimated by measuring the changes in hardness.

2. EXPERIMENTAL DESCRIPTIONS

The specimens are sectioned from the rim region of high pressure stage of a new 300MW turbine rotor. Firstly, they are normalized at 970~990°C and 930~950°C, respectively, and cooled in the air. Secondly, they are tempered at 680~700°C, followed by a cooling in a stove. The microstructure of the metals treated is composed of tempered sorbite and a small amount of ferrite. The specimens used in LCF and tensile tests are taken from the rotors along the axis direction of the rotors. The chemical composition of 30Cr2MoV steel is given in table 1. The LCF tests at room temperatures and elevated temperature are performed with a CSS-MTS-280-100KN servo-hydraulic test system. A triangular loading waveform is used for all constant-amplitude tests that are undertaken under fully reversed axial strain control conditions. The strain rates range from 0.003 to $0.005s^{-1}$. The axial strain amplitudes range from 0.002 to 0.01.

Table 1. Chemical composition of 30Cr2MoV steel (wt.%)

C	Si	Mn	P	S	Cr	Mo	V	Ni
0.24	0.39	0.50	0.020	0.0053	1.59	0.63	0.25	0.02

3. RESULTS BY LCF TESTS AND DISCUSSIONS

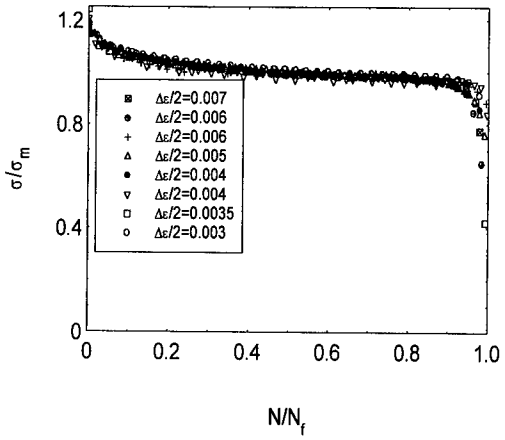


Fig.1. Dimensionless stress amplitude (peak value) vs. cyclic numbers at 20℃

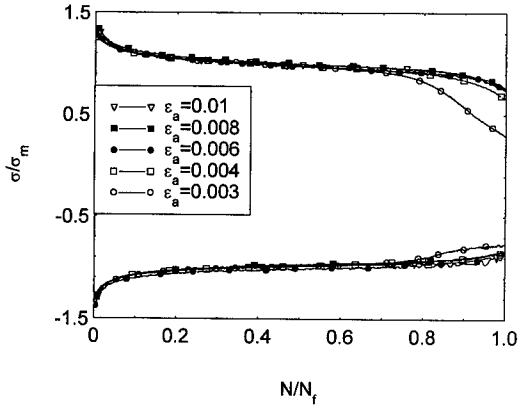


Fig.2. Dimensionless stress amplitude (peak and valley) vs. cyclic numbers at 550℃

The relationship between dimensionless stress amplitudes and dimensionless cyclic numbers at room temperature and 550℃ is shown in Fig.1 and Fig.2, respectively. From Fig.1 and Fig.2, we can find an interesting result, i.e. all experimental data of dimensionless stress are only related to the dimensionless cyclic numbers. Suppose that the results are correct at all strain amplitudes, by introducing a remaining life fraction

$$\psi = 1 - N / N_f \qquad (1)$$

we have for 30Cr2MoV steel studied,

$$\frac{\sigma}{\sigma_m} = a + b\exp(c\psi) \qquad (2)$$

where, σ_m is the stable stress amplitude corresponding to $N = 0.5N_f$. From Eq.2, the rupture cyclic number, N_f, and the stable cyclic stress amplitude, σ_m, can be predicted from the cyclic number N ($N << N_f$) at any strain amplitude. The value, σ_m, should be predicted much more accurately than N_f because the experimental data of N_f are possibly quite disperse.

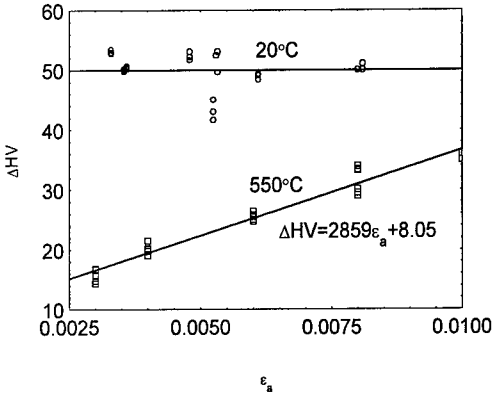


Fig.3. Stress-strain curve by cyclic and monotonic tension

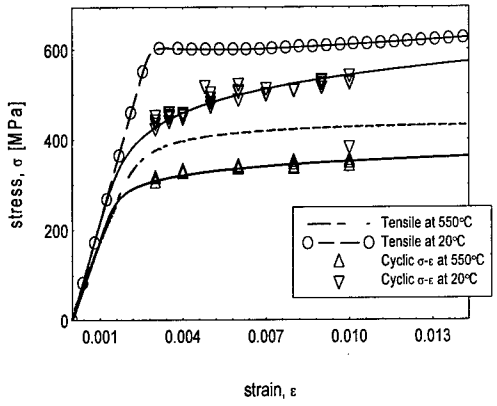


Fig.4. The hardness variation vs the strain amplitude

Fig.3 shows the comparison between the tensile stress-strain curve and the stable cyclic stress-strain curve at room temperatures and at 550℃. The cyclic stress-strain equation is given by

$$\varepsilon_a = \begin{cases} \dfrac{\sigma_a}{21700} + \left(\dfrac{\sigma_a}{756.8}\right)^{\frac{1}{0.07671}} & 20\,^\circ C \\ \dfrac{\sigma_a}{17500} + \left(\dfrac{\sigma_a}{406.72}\right)^{\frac{1}{0.037504}} & 550\,^\circ C \end{cases} \qquad (3)$$

The relationship between the strain amplitude and the life of LCF can be described by Mason-Coffin equation as follows

$$\begin{aligned} \Delta\varepsilon_t/2 &= \Delta\varepsilon_e/2 + \Delta\varepsilon_p/2 \\ &= (\sigma_f'/E)(2N_f)^b + \varepsilon_f'(2N_f)^c \end{aligned} \qquad (4)$$

Table 2. Constants of 30Cr2MoV steel at different temperatures at the reliability of 50%

Test temperature	σ_f/E	b	ε_f'	c
20℃	0.00357	-0.056476	0.28074	-0.5599
550°C	0.003193	-0.06308	1.91734	-0.908078

where σ_f' is fatigue strength coefficient, ε_f' is fatigue ductility coefficient, b and c are fatigue strength exponent and fatigue plastic exponent respectively. Table 2 gives all the values at room temperature and 550℃.

Fig.4 shows the hardness variation of the specimens ruptured by LCF tests at room temperature and at 550℃. It is found that the hardness is independent on the strain amplitude, ε_a, at room temperature. However, the hardness is strongly affected by the strain amplitude, ε_a, at 550℃. According to the results and by making the extrapolation of the results, a linear equation of hardness variation as a function of strain amplitude at given temperature can be written as

$$\Delta H = \Delta H_0 + c_0 \varepsilon_a \tag{5}$$

where, ΔH_0 and c_0 are the material constants at given temperature. When the strain amplitude, ε_a, is constant, the hardness equation is written as

$$H=G(\psi) \tag{6}$$

Suppose that the softening properties of hardness are approximately the same as that of stress softening process, then from Eq. 2, we have

$$H = d_1[1 + d_2 \exp(d_3 \psi)] \tag{7}$$

where, d_1, d_2, d_3, are the fitting constants by experiment. It is easy to get the initial hardness and the residual hardness of the specimens ruptured by LCF tests. Let

$$H = \begin{cases} H_0 & \psi = 1 \\ H_f & \psi = 0 \end{cases} \tag{8}$$

Using Eq.7 and Eq.8, we obtain

$$d_1 = \frac{H_f \exp(d_3) - H_0}{\exp(d_3) - 1}, \quad d_2 = \frac{H_0 - H_f}{H_f \exp(d_3) - H_0}$$

The constant, d_3, is the cyclic softening coefficient of the material, and it can be easily acquired by the experimental results. From Eq.7, the remaining life fraction, ψ, is given by

$$\psi = \frac{1}{d_3} \ln\left[\frac{1 + \exp(d_3)(H/H_0 - H_f/H_0)}{1 - H_f/H_0}\right] \tag{9}$$

Eq. 6 can be used to predict the remaining fatigue life of a turbine rotor by detecting the changes in hardness. From Fig.5, it is easy to find that the nonlinear softening properties at different remaining life fraction are decided by k_3, e.g. when the remaining life fraction, ψ, is smaller than 0.6, the hardness values corresponding to $k_3 = 10$ are changeless.

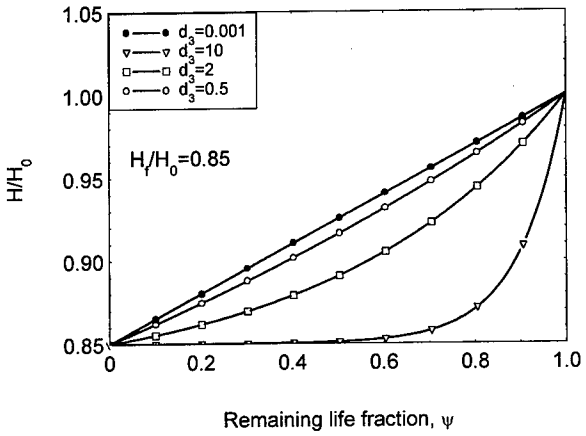


Fig.5. The hardness decreasing after fatigue rupture at different strain amplitudes

The reduction in hardness is caused by the damage during the LCF tests, the aging effect at elevated temperatures and the creep damage. In the area near the surface of the rotor, the softening is mainly caused by fatigue and aging, so the equation to describe the changes in hardness is given by

$$\Delta H = H_0 - H = f_1[T(c+\log t)] + f_2(\psi) \tag{10}$$

In the area near centric hole of a rotor, the softening properties are mainly controlled by creep and aging, then we have

$$\Delta H = H_0 - H = f_1[T(c+\log t)] + f_3(\sigma, T, t) \tag{11}$$

where, H is the hardness under the tempering time t, at room temperature, and the constant c can be derived by[4]

$$c = \frac{T_1 \log t_1 - T_2 \log t_2}{T_2 - T_1} \tag{12}$$

where t_1, t_2 are the tempering times needed to obtain the hardness value at different temperatures T_1 and T_2, respectively. The modified Mason-Coffin Eq. including the aging effect is written by

$$\Delta\varepsilon_t = \Delta\varepsilon_e + \Delta\varepsilon_p = C_1 N_f^{\alpha_1} + C_2 N_f^{\alpha_2} \tag{13}$$

where, $C_1 = 10^{\beta_1 \Delta HV_a + \beta_2}$, $C_2 = \beta_3 \Delta HV_a + \beta_4$, and $\Delta HV_a = f_1[T(c+\log t)]$. β_1, β_2, β_3 and β_4 are the constants decided by experimental results. The components in power plants operating at elevated temperature regime are subjected to both complicated loading conditions (such as fatigue, steady state creep or cyclic creep) and aging. In the conventional linear damage accumulation rules, the interaction between the different loading situations and aging is not taken into account. Because the effects of aging are included, Eq.13 should be more accurate than the conventional fatigue equation at elevated temperatures.

4. CONCLUSIONS

The dimensionless stress amplitude is only related to the remaining life fraction, which may be very valuable for reducing the amount of LCF experimental work. The components of power plants operating at elevated temperature regime are subjected to both complicated loading conditions (fatigue, steady state creep or cyclic creep) and aging. These conditions can not be taken into account for the conventional linear damage accumulation rules. A modified Mason-Coffin equation is proposed and should be more accurate because the aging effect is included. Both experimental and theoretical results show that it is valuable to predict the remaining life of steam turbine rotor by measuring the hardness variation. The hardness values measured can also be used as a means of identifying the critical regions in the component, e.g. overheated regions, overstress region,etc. In these regions, the hardness is markedly different from the original hardness value.

ACKNOWLEDGMENT

The project is supported by National Electric Corporation and National Natural Science Foundation of China (19702003)

REFERENCES

1. Y. Li and J. Wang, Int. J. Fatigue, **14** (1992) p.169
2. R. Viswanathan and R. I. Jaffee, J. Engng. Mater. Tech. **105** (1983) p.286
3. J. H. Hollomon and L. D. Jaffee, Trans. AIME **162** (1945) p.223
4. L. R. Larson and J. Miller, Trans. ASME, **74** (1952) p.765
5. A. Liu, J. Turbine Tech. (in Chinese), **40** (1998) p.184
6. C. Peng, Turbine Tech. (in Chinese), **37** (1995) p.144
7. Y. Zhu, China Electric Power (in Chinese), **22** (1989) p.65

Key Engineering Materials Vols. 183-187 (2000) pp. 993-998
© 2000 Trans Tech Publications, Switzerland

A Study on the Corrosion Fatigue Characteristics of 12Cr Alloy Steel

S.Y. Cho, C.H. Kim and D.H. Bae

Department of Mechanical Engineering, Sungkyunkwan University,
300 Chunchun-dong, Jangan-ku, Suwon, 440-746, Korea

Keywords: Compliance Method, Corrosion Cell, Corrosion Fatigue Characteristic, Crack Growth Rate, Horizontal Fatigue Tester, Stress Intensity Factor

ABSTRACT

In order to estimate reliability of the 12Cr alloy steel using as the material of turbine blade in the steam power plant, its corrosion fatigue characteristics was investigated under the various corrosive environments such as distilled water, 3.5% NaCl solution and 12.7% (1M) Na_2SO_4 solution, respectively. The parameter additionally considered was solution temperature: 25, 60, 90, and 150℃. The horizontal fatigue tester and the corrosion cell which were developed by the material joining and reliability evaluation laboratory of SungKyunKwan University, were used. Corrosion fatigue crack length was measured by the compliance method recommended in ASTM E-647-95. For analysis of crack growth behavior, fracture surfaces were fracto-graphically observed by using SEM. From the results, the corrosion fatigue characteristics in 12.7 wt% (1M) Na_2SO_4 solution and distilled water was similar to that of in air at 25℃. But the crack growth rate in 3.5wt.% NaCl solution was faster than that of in air under the same ΔK range. And, in the same environment, the crack growth rate was increased with the temperature of solution increased. The reasons showing these results are due to the difference of the crack growth mechanism according to the electro-chemical activity of the corrosion factors. The fracture surfaces of 12Cr alloy steel showed striation and trans-granular fracture type in low temperature and the beginning of crack growth. But, according as the temperature and ΔK increased, crack growth behaviors were transferred to inter-granular fracture type.

1. INTRODUCTION

The turbine blades of the steam power plant are put in corrosive environments at the lower pressure stage, and also, periodical fatigue during its operating occurs the breakdown accident [1]. Thus, in order to secure reliability of them, it is necessary to estimate the corrosion sensitivities and corrosion fatigue characteristics of turbine blade material under real environments, systematically and scientifically. But, to date, the design data or information considering environments on the material is so lake. The material of turbine blade, which is 12~13%Cr alloy steel, is reliable in case

of high purity vapor. However, as various impurities actually flow into the steam turbine from the other facilities such as the steam generator, over-heater and so on, its reliability is reduced. In particular, when sulfide and chloride, even though its amount will be a little, are included in the steam, those fatally affect to corrosion damage of the blade. That is, if they are absorbed and concentrated on the surface of the blades, corrosion pits are generated on the surface of turbine blade from the electro-chemical reactions between them and the material. These pits generated become the cracking points by the service load [2]. Therefore, in this study, in order to estimate the corrosion fatigue characteristics of 12Cr alloy steel, corrosion fatigue tests were estimated under some condition determined from the results of electro-chemical polarization tests, and compared with the results of in air. For analysis the mechanism of crack growth behavior in each environment, the fracture surface of the specimen was fracto-graphically observed by using scanning electron microscope.

2. EXPERIMENTAL ESTIMATION OF CORROSION FATIGUE CHARACTERISTICS ON THE 12Cr ALLOY STEEL

2.1. Specimen

Test specimen is 12Cr alloy steel, which is one of the martensitic stainless steels using as the material of turbine blade in the steam power plant. Chemical composition and mechanical properties of the material is illustrated in Table 1. And compact tension (CT) type specimen was prepared according to ASTM E-647-95 as shown in Fig.1.

Table 1. Chemical composition and mechanical properties

Element	C	Si	Mn	P	S	Ni	Cr	Mo	Al	Cu
Content(%)	0.16	0.34	0.46	0.016	0.003	0.18	11.9	0.09	0.006	0.06

Ultimate tensile strength (Mpa)	0.2% offset yield strength (Mpa)	Elongation (%)	Hardness (Rc)
1205	989.4	13	38

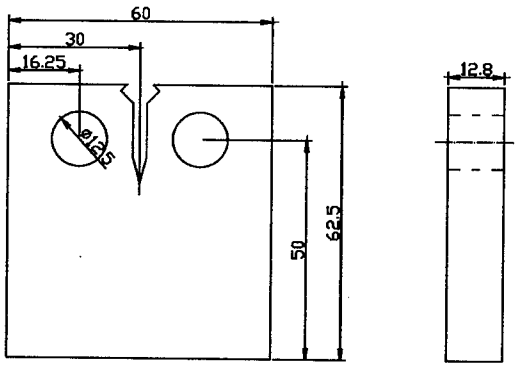


Fig.1 Configuration of specimen

2.2. Corrosion fatigue testing system

In this study, corrosion fatigue testing system (capacity: 2 tons), which was developed by the material joining and reliability evaluation laboratory of SungKyunKwan University, was used. Configuration of testing system is as shown in Fig.2. Corrosive environment in the corrosion cell is

necessary to maintain the chemical equilibrium during the test. In order to satisfy such condition, corrosion cell was prepared in two types; one is by acrylic plate for 25, 60 and 90℃, another is by steel tube of which its inner side is coated by epoxy bond to prevent the galvanic corrosion in high temperature (150℃) and pressure (6 bar) environment[3]. The other components such as specimen grips, heater, and thermo- couple setting up within the corrosion cell were also prevented from the contact with solution. Corrosive solution of the corrosion cell during the test was constantly maintained by automatic thermo-controller and thermo–couple.

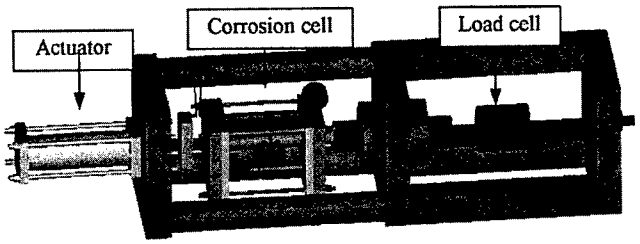


Fig.2. Horizontal fatigue tester

2.3. Test conditions and method

In this study, in order to estimate the corrosion fatigue characteristics of 12Cr alloy steel in the sulfide and chloride environments considering temperature, environmental conditions for corrosion fatigue tests were decided as the most susceptible environments among the electro-chemical polarization test results that were previously conducted to estimate corrosion susceptibility on the various corrosive environments. Environmental and mechanical conditions are as follows: 3.5wt.% NaCl solution, 12.7wt.% Na_2SO_4 solution and distilled water, and 25, 60, 90, 150℃ for each solution. And mechanical conditions determined by ASTM E 647-95 are as follows: load ratio(R)= 0.1, maximum load = 7848N, frequency (f)= 0.5Hz.

The crack length propagating by fatigue load is generally measured by using the traveling microscope and the other measuring systems. But, in case of corrosion fatigue test, it is difficult to measure the crack length due to corrosion products on the surface of the specimen. Moreover, in case of high temperature and pressure conditions, inside of the corrosion cell is difficult to monitor. Thus, in order to measure the corrosion fatigue crack length, the indirect compliance method was applied. Calibration curve for the compliance method applied the equation recommended by ASTM E 647-95[4]

3. RESULTS AND DISCUSSION

Fig.3 is the crack growth characteristic curves of 12Cr alloy steel in 3.5wt.% NaCl solution, 12.7wt.% Na_2SO_4 solution and distilled water, and compared with that of in air. Crack growth characteristics in Na_2SO_4 12.7wt.% solution and distilled water under 25℃ are similar to that of in air. But, the crack growth rate in NaCl 3.5wt.% solution is faster than in air under the same ΔK. these results mean that, when the temperature is 25℃, 12Cr alloy steel is more sensitive to 3.5wt.% NaCl solution than the other environments. However, the crack growth rates in every solutions are faster than in air under 60, 90, 150℃. This also means that the temperature of solution is an important factor affecting to the corrosion fatigue characteristic of the 12Cr alloy steel. The reason why the crack growth rate is generally faster in the corrosive environment than in air can be

assumed by owing to electro-chemical activities of the various corrosion factors. In particular, the temperature among the various factors accelerates electro-chemical reaction between the metal and solution [5]. Therefore, according as the temperature is increased, electro-chemical activities of corrosion factors such as Cl^- ion in NaCl solution and SO_4^{2-} ion in Na_2SO_4 solution, the dissolved oxygen and so on increase and affect to corrosion reaction on the surface of specimen as well as around of the crack tip. Thus, by these mechanisms mentioned above, the crack growth behaviors are also different according to the corrosive environments and the dominant fracture mechanism.

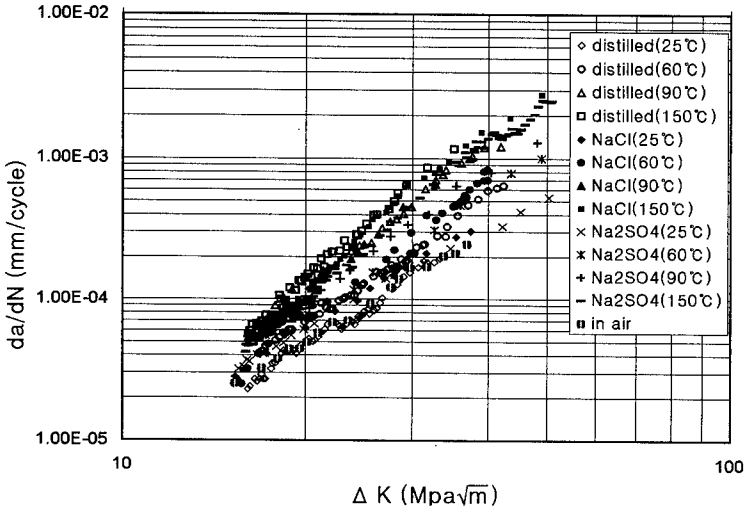


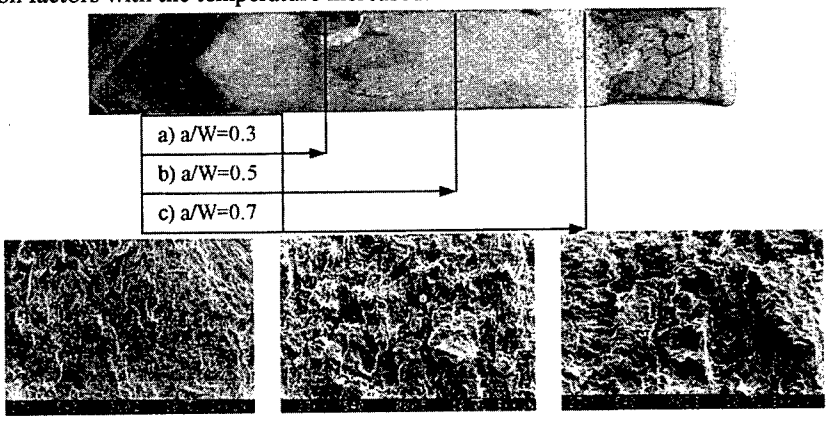
Fig.3. The characteristic curves of 12Cr alloy steel in various environments

It has been known that fatigue crack growth behaviors generally show different characteristic according to following micro-structural types of the fracture surface [6].

da/dN (intergranular fracture)>dadN (cleavage fracture)
>da/dN (dimple fracture)> da/dN (striation) (1)

In this study, in order to analysis the corrosion fatigue mechanism of 12Cr alloy steel in various environments, the facture surface of each specimen was observed by SEM (scanning electron microscope, ×540) after corrosion fatigue tests. As the examples, Figs.3-6 show the fractographs of the specimens tested in various environments of 90℃ such as 3.5wt.% NaCl solution, 12.7wt.% Na_2SO_4 solution, distilled water, and in air. In case of in-air, as shown in Fig.3, it can find that fatigue crack growth behavior is transgranular fracture type in low ΔK range (which means the range of slow crack growth rate). But, according as the fatigue crack is propagated, its behavior is transferred to intergranular+transgranular+dimple dominated by intergranular fracture in high ΔK range (which means the range of high crack growth rate). In distilled water of room temperature, behavior of corrosion fatigue crack was similar to that of in air. However, it was also transferred from intergranular+transgranular+dimple to intergranular fracture with the temperature of distilled water and ΔK increase. And, in cases of 3.5wt.% and NaCl solution and 12.7wt.% Na_2SO_4 solution, as shown in Figs. 5 and 6, it is difficult to find out the particular difference of corrosion fatigue crack behaviors between them in the beginning of crack growth. But it was transferred from intergranular+dimple to intergranular fracture with their temperatures and ΔK increase. As mentioned above, under the corrosive environments applied in this study, the effects of the corrosion factors (Cl^-, SO_4^{-2}) were not distinguished in the beginning of corrosion fatigue crack

growth. But, according as the temperature of the solutions and ΔK increased, crack growth behavior in each solution showed different characteristic due to electro-chemical activities increase of corrosion factors with the temperature increased.



a) a/W=0.3 b) a/W=0.5 c) a/W=0.7

Fig.3. Fractographs of fracture surface in air



a) a/W=0.3 b) a/W=0.5 c) a/W=0.7

Fig.4. Fractographs of fracture surface in 3.5wt.% NaCl solution of 90℃



a) a/W=0.3 b) a/W=0.5 c) a/W=0.7

Fig.5. Fractographs of fracture surface in Na_2SO_4 12.7wt.% solution of 90℃



a) a/W=0.3 b) a/W=0.5 c) a/W=0.7

Fig.6. Fractographs of fracture surface in distilled water of 90℃

4. CONCLUSIONS

The corrosion fatigue characteristics of the 12Cr alloy steel using as material of the turbine blade in the steam power plant was investigated under the various corrosive environments such as distilled water, 3.5wt% NaCl solution and 12.7wt%(1M) Na_2SO_4 solution. And their results were compared with in air. The parameter considered additionally was the solution temperatures which are room temperature (25℃), 60℃, 90℃ under the atmospheric pressure, and 150℃ under 4.5bar. Obtained results are as follows;

1) The crack growth characteristics of 12Cr alloy steel in 12.7wt%(1M) Na_2SO_4 solution and distilled water under 25℃ and the atmospheric pressure are similar to that of in air. But the crack growth rate in NaCl 3.5wt.% solution is faster than that of in air at the same ΔK.
2) However, when the temperature of each solution is increased, the crack growth rate of 12Cr alloy steel is faster than in-air due to increasing of electro-chemical activities of corrosion factors such as Cl^- ion in NaCl solution and SO_4^{2-} ion in Na_2SO_4 solution, the dissolved oxygen and so on, and affecting to corrosion reaction on the surface of specimen as well as around of the crack tip. This means that the temperature of solution is an important factor affecting to the corrosion fatigue characteristic of the 12Cr alloy steel.
3) At the low temperature and in the beginning of the corrosion fatigue crack growth, the effects of the corrosion factors (Cl^-, SO_4^{-2}) on the fatigue crack growth behavior of 12Cr alloy steel was not distinguished, and the fatigue crack growth behavior was also dominated by striation and trans-granular fracture type. But, according as the solution temperature and ΔK were increased, its tendency was transferred to inter-granular fracture type due to increasing of electro-chemical activities of the corrosion factors with the temperature increased.

ACKNOLEDGEMENTS

The authors are grateful for the support provided by a grant from the Korea Science and Engineering Foundation(KOSEF) and Safety and Structural Integrity Research Center at the Sungkyunkwan University

REFERENCE

1.JSME, Corrosion and Fracture, Japan Engineering Pub. (1984) pp.71-74
2. ASM HANDBOOK vol. 19, Fatigue and Fracture, ASM international (1996) p.195
3. Denny A.Jones, Principles and Prevention of Corrosion, Prentice Hall (1991) pp.11-12
4. Standard Test Method for Measurement of Fatigue Crack Growth Rates, ASTM E647-95 (1995) pp.578-614
5. ASM HANDBOOK vol. 19, Fatigue and Fracture, ASM international (1996) p.185
6. J. Y. Otera, Fractograph and its application, Daily Engineering News Paper Co., pp.31-76

Key Engineering Materials Vols. 183-187 (2000) pp. 999-1004
© 2000 Trans Tech Publications, Switzerland

Corrosion Fatigue Crack Initiation Life of a Ship Structural Steel in Dilute Sulfuric Acids

Y. Kobayashi, Y. Tanaka and H. Goto

Ship Research Institute, Structure Mechanics Division, Ministry of Transport,
6-38-1, Shinkawa, Mitaka, Tokyo 181-0004, Japan

Keywords: Corrosion Fatigue, Crack Initiation, Dilute Sulfuric Acid, Equivalent Stress, Fatigue Life, Notch, Stress Concentration Factor, Stress Intensity Factor Range, Threshold

ABSTRACT

This paper describes corrosion fatigue for notched specimens in dilute sulfuric acids. The acids are typical corrosion environments of condensate from coal vapor in a coal cargo hold. Fatigue data were consolidated as the relationships between an equivalent stress at a notch root and a fatigue crack initiation life. The life in the dilute sulfuric acids was shorter than that in seawater because of a severe dissolution of iron. The long term corrosion fatigue was also estimated from the relationship between a stress intensity factor range to the fatigue crack initiation and the life. The corrosion wastage was considered to the estimate of the fatigue crack initiation life.

1. INTRODUCTION

Aged bulk carriers sometimes caused sinking accidents because of the corrosion wastage in cargo holds. A main cause is reported as the following [1]; coal vapor condenses at side plates in contact with seawater, and the condensate turns into a dilute sulfuric acid. In fact, authors confirmed that an exudation solution from coal was changed into dilute sulfuric acids (pH2.5 to 3) by a sulfuric ion[2].

The purpose of this study is to obtain the corrosion fatigue life on a typical corrosion environment (dilute sulfuric acids at pH4 or pH2) in the coal cargo holds. The corrosion fatigue was expressed by using an equivalent stress, Seq, and a fatigue crack initiation life, Nc. The Seq on the procedure of MIL-HDBK-5[3] was applied to the stress at a notch root[4, 5]. The Seq-Nc relations were consolidated as one line every test environment irrespective of the difference of stress concentration factors. For the long term corrosion fatigue, the relationships between a stress intensity factor range, ΔK, and Nc were expressed in consideration of the corrosion wastage. The index of Paris's equation was applied to the slope of the ΔK-Nc relation. The lowest fatigue strength was estimated from a shape of a corrosion pit.

2. TESTING PROCEDURE

2.1 Material and Specimen

A material used in this study was TMCP steel, K32A of 10mm thick. The plate was shot blasted and coated with a primer. The lower yield point, ultimate tensile strength, and elongation at failure were 364MPa, 473MPa, and 35% in tensile tests, respectively. Shapes and dimensions of notched specimens are shown in Fig.1. The loading direction was corresponding to the rolling direction. Mechanical notches were machined on both sides. The notches were polished by emery papers of #400 to #800. The stress concentration factors of the notches, Kt, were 1.2, 2.0, 2.93, and 3.77.

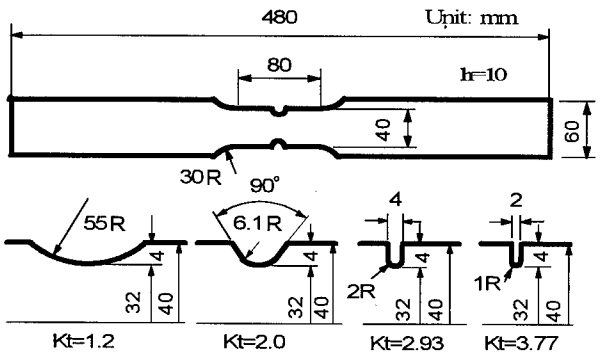


Fig.1 Shapes and dimensions of notched specimens

2.2 Test Method

Full digital controlled servo machines with a loading range of 100-300kN were used in fatigue tests. The specimens were clamped by hydraulic chucks. A sinusoidal load was applied to the specimens, and the stress ratio, R, was 0.1. The cycling rate was 0.17Hz.

Corrosion fatigue tests were carried out under a natural corrosion condition in the dilute sulfuric acids at pH4 and pH2. The testing solution was maintained under the conditions of 25 °C in temperature and an air saturated by bubbling in dissolved oxygen. The solution was circulated from a stored tank(60 *l*'s) to a test tank(0.6 *l*'s) with a specimen. A quantity of flow was 1.2 to 1.8 *l*/min. The solution was changed two or three times per minute in the test tank. The specimens were in an independent corrosive system, because it was isolated electrically from chucks of the testing machines.

Number of cycles to the crack initiation (crack initiation life, Nc) were detected by a DC potential difference to the cracked area of $10mm^2$, that is, the depth of the through-thickness crack was 1mm.

3. RESULTS AND DISCUSSION

3.1 Relationships between Seq and Nc

For the stress at the notch root on the notched specimens, the equivalent stress, Seq, on the MIL-HDBK-5 were applied by authors[4]. The Seq-Nc relation has a merit that the data are collected every test environment irrespective of the difference of Kt. The Seq is defined as Eq.1.

$$Seq = \Delta S^{n} * Smax^{1-n} \qquad (1)$$

Where ΔS is a stress range(*Smax-*Smin), n is a material constant(n=0.6487) for steels obtained from the welded joint specimens[6].

The Seq-Nc relations in dilute sulfuric acids are plotted in Fig.2. Fig.2 also shows the Seq-Nc relations of the notched specimens, butt welded joint specimen and transverse welded joint specimens in air and in seawater. The equivalent stress levels, Luy(440MPa) and Lly(340MPa), are shown by dotted lines, and they have physical meanings as following. When the notch root is under R=0.1 and an elastic condition, the Luy denotes that *Smax reaches the plastic starting stress on the peak values of true stress-strain relations in cyclic tensile-compressive tests of hourglass specimens. The Lly denotes that *Smax reaches the lower yield point of a plate specimen.

The Seq-Nc relations are shown in Fig.2. All curves were expressed by Eq.2, but they broke at the level Lly. We can understand crack initiation mechanisms from these curves as follows.

$$Seq = CeNc^{k} \qquad (2)$$

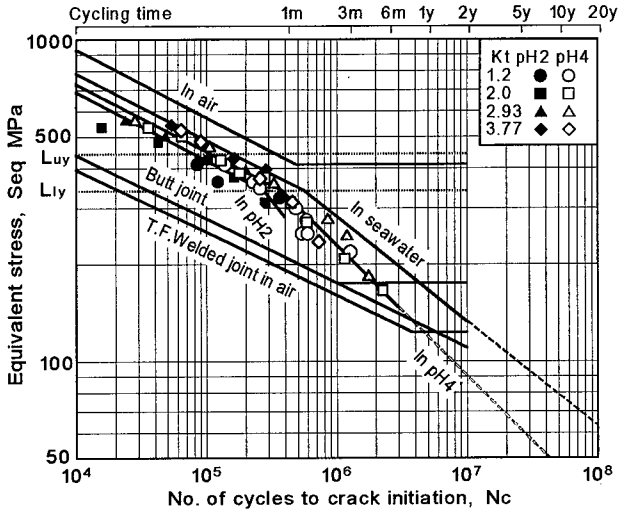


Fig.2 Relationships between Seq and Nc in H_2SO_4 at pH4 and at pH2

a) Crack initiation for Seq>Lly

The slopes of the notched specimens in the dilute sulfuric acids were nearly equal to that in air and in seawater, and welded joint specimens in air. The crack initiation lives were shorter than that in seawater. The scatter of the life was small in pH4, but was large in pH2. The fatigue life of pH2 trended to increase with an increase of Kt.

For the above mentioned, the equal slope means that the corrosion fatigue crack initiation mechanism does not change with that in air. The corrosive dissolution is added to surface defects, and then the fatigue crack initiates from corrosion pits. The life deceases with decrease of pH. This reason is considered the difference of a growth rate of a fatigue crack or a corrosion pit in different pH. The scattering life in pH2 may be caused by an effect of a corrosive dissolution on an applied stress. Because the shape of a notch for Kt=3.77 is regarded as a long crack in comparison with that for Kt=1.2, and then a crack tip becomes insensitive in a severe corrosion environment. Therefore, most such corrosion pits cannot grow up to a propagating fatigue crack.

In range of Luy>Seq>Lly, the fatigue lives scattered in seawater, but the scattering did not see in dilute sulfuric acids. This is caused by the difference of corrosive dissolution, and the small range of scattering means that a non-propagating crack does not form in a severe environment.

b) Crack initiation for Seq<Lly

The Seq-Nc curves had different slopes as the boundary at the level Lly. This trend was the same in seawater. The slope of pH4 was steeper than that of seawater, because the growth rate of corrosion pits was fast. The crack initiation lives of pH2 were shorter than those of pH4. The slope of pH2 became more steep in the range less than Lly because of the severe corrosive dissolution. From these results, the difference of dissolution clearly has a great influence in the growth of corrosion pits on the first step of a crack initiation.

3.2 Relationships between ΔK and Nc

Long term corrosion fatigue tests are necessary for findings of the lowest corrosion fatigue limit from the Seq-Nc relations. The tests are very difficult with one thing or another. Authors expressed the long term corrosion fatigue as a ΔK-Nc relation [7]. ΔK is the stress intensity factor range at crack initiation, and is calculated from Nisitani's method [8].

The ΔK-Nc relation is useful to the expression of fatigue data, and has the following significance.

In crack growth tests of a long crack under Paris Eq.3, the indexes, m, of pH4 and pH3 were nearly equal to that of seawater. Therefore, the environments clearly had not a great influence in the m.

$$da/dN = C\,\Delta K^{m} \qquad (3)$$

Moreover, if Eq.3 is keeping on the crack depth of 1mm at a notch root, the slope of the ΔK-Nc relations ought to become -1/m despite the environment condition. In an equal crack depth on same notch shapes, the ΔK-Nc relations can be dealt with as the nominal S-N curves based on a crack initiation, because the ΔK is proportional to the nominal stress range.

Eq.3 is applicable to a propagation of an enough long crack. If Eq.3 can apply to a crack length of a=1mm, ΔK is translated from Eq.3 into Eq.4. The constant, C, and index, m, were almost the same in pH4 and pH3. Therefore, the m can apply to the slope of pH2.

$$\Delta K = 313N^{-1/m} \qquad (4)$$

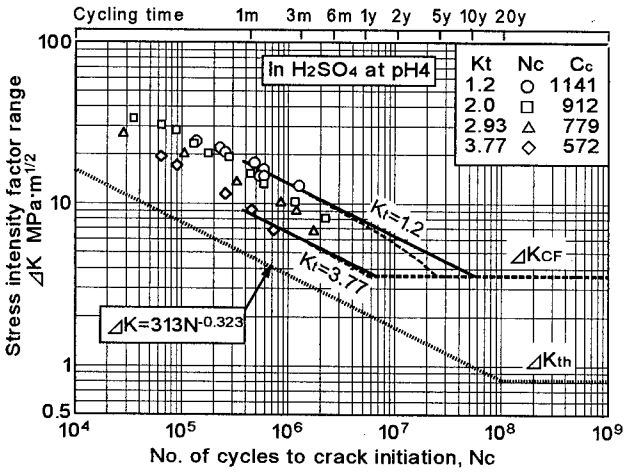


Fig.3 Relationships between ΔK and Nc in H_2SO_4 at pH4

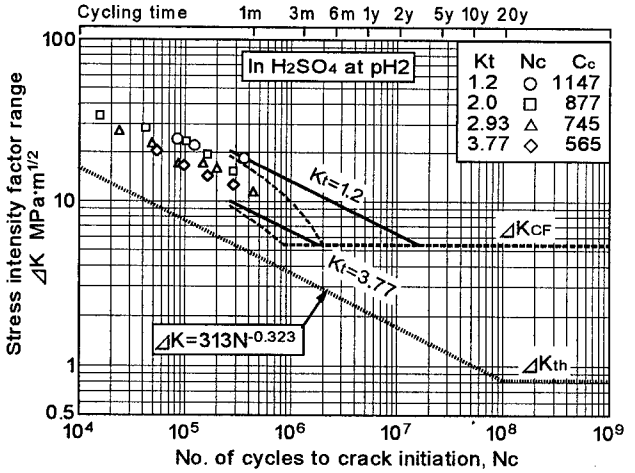


Fig.4 Relationships between ΔK and Nc in H_2SO_4 at pH2

In Fig.3 and in Fig.4, the dotted lines show the ΔK-Nc relation of the slope for Eq.4. ΔKth is a threshold stress intensity factor range. The fatigue data for pH4 and pH2 are also plotted in Fig.3 and in Fig.4, respectively. The solid lines are correspondent to the data of the Kt=1.2 and 3.77, respectively. These slopes are equal to the dotted line. However a fatigue life for reaching until 1mm is not given. Therefore, the fatigue life was decided from experimental crack initiation cycles. The cycles were the mean value of the data within an elastic range for the maximum stress at the notch root. Those data are below the Lly in Fig .2. The ΔK-Nc relations are expressed by Eq.5. A Cc is a constant.

$$\Delta K = CcNc^{-1/m} \qquad (5)$$

The ΔK_{CF} is a threshold stress intensity factor range in the corrosion environment, and was calculated from the shape of the corrosion pit to crack initiation by using Murakami's equation[9]. It is considered that the ΔKth raises up to ΔK_{CF} in the corrosion environment because of the blunting of a crack tip. The ΔK_{CF} is correspondent to the fatigue limit of the S-N curve for nominal stress. The ΔK_{CF} is also a boundary level whether corrosion pits grow into a fatigue crack or progress as the corrosion wastage.

As shown in Fig.3 and in Fig.4, the solid lines are seemingly as if they can extend up to the short life range. In this range, the maximum stress at the notch root was over the yield point. This trend was not seen in seawater at all [7]. Though there is no actual proof, there is no special reason except the severe dissolution at crack tips. Therefore, the crack initiation life seems to be controlled by the blunting of surface defects and crack tips.

In the next place, we discuss the ΔK-Nc relations in consideration of the corrosion wastage. The corrosion wastage, f(Rc,y), is expressed as a function of a corrosion rate, Rc, and a year, y. The f(Rc,y) is also dependent to the dimension of the specimen. We assume that the decrease of the cross section area at the notches causes directly the increase of the applied stress. Then, the ΔK-Nc relation including corrosion wastage becomes Eq.6.

$$\Delta K = f(Rc,y)CcNc^{-1/m} \qquad (6)$$

These lines are shown as the broken lines in Fig.3 and Fig.4. These lines are correspondent to the Rc=0.2mm/year for pH4, and Rc=5.5mm/year for pH2, respectively.

3.3 Effects of Kt on ΔK-Nc relations in corrosion fatigue

The relationships between Cc and Kt are plotted in Fig.5. The Cc-Kt relations are given by the linear line of Eq.7.

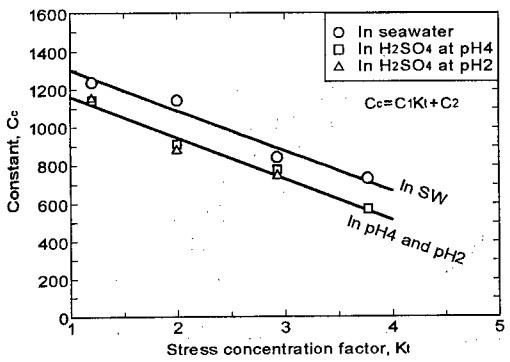


Fig.5 Relationships between Cc and Kt

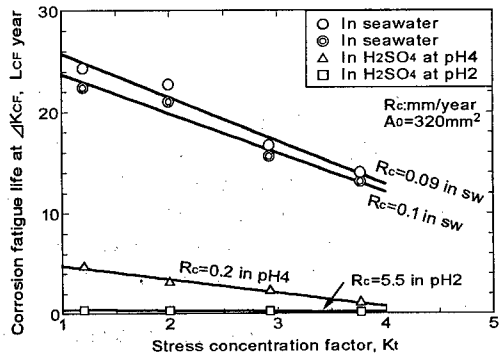


Fig.6 Relationships between L_{CF} and Kt

$$Cc = C_1 Kt + C_2 \qquad (7)$$

The environmental difference of pH4 and pH2 did not influence the Cc. The slope constant, C_1, was almost the same in the environment of the seawater and the dilute sulfuric acids, because both of the slope of the ΔK-Nc relations, -1/m, were nearly equal each other. Therefore, those had parallel lines. The constant C_2 means the level of ΔK, and the C_2 of the dilute sulfuric acids was lower than that of the seawater (pH8.2). The C_2 depends on the environment, and decides the fatigue life. As the results of the above mentioned, the basic ΔK-Nc relation can be estimated from the Cc-Kt relation.

In the next place, the relationships between the crack initiation life, L_{CF}, for ΔK_{CF} and Kt are clarified in Fig.6. The unit of L_{CF} is a year in the cycling rate of 0.17Hz. The L_{CF} is dependent on Kt and Rc. This reason can be explained as follows. The ΔK-Nc relation and Kt are in proportion to each other as Eq.7; therefore, the L_{CF} decreases linearly with an increase of Kt. The difference of the slope in Fig.6 is caused by the quadratic form of f(Rc,y) and effect of the Rc for f(Rc,y). The L_{CF} was not influence to the Kt under the fast Rc. This links to controlling for initiation of fatigue cracks.

4. CONCLUSION

The corrosion fatigue tests of notched specimens were carried out in the dilute sulfuric acids substituted for the corrosion environment of coal cargo holds. The conclusions based on the fatigue crack initiation life are as follows;

1) The fatigue crack initiation life can be expressed by the Seq-Nc relation irrespective of Kt every corrosion environment. The Seq-Nc line is broken at the equivalent stress Lly, where Lly denotes that the maximum stress reaches the lower yield point. For Seq>Lly the slopes are almost the same in air, seawater, and dilute sulfuric acids, but for Seq<Lly they increase with decrease of pH. The mechanism of fatigue crack initiation does not change with the dilute sulfuric acid and the seawater. The difference of the corrosion rate, however, is influence to the growth of corrosion pits and the fatigue crack initiation.

2) The corrosion fatigue strength can estimate from the $\Delta K=CcNc^{-1/m}$ by using the index of Paris's equation, m. It becomes $\Delta K=f(Rc,y)CcNc^{-1/m}$ in consideration of the corrosion wastage for the long term corrosion fatigue. The constant, Cc, is proportional to Kt, and those slopes are almost the same in the seawater and in the dilute sulfuric acid.

3) The ΔK_{CF} is the lowest corrosion fatigue strength, and a boundary level whether corrosion pits grow into a fatigue crack or progress as the corrosion wastage. The fatigue life, L_{CF}, to the ΔK_{CF} depends on a specimen size. The L_{CF} depends on Kt for a slow corrosion rate, but does not for a fast corrosion rate because of severe corrosion dissolution.

REFERENCE

1. Transactions of Nippon Kaiji Kyoukai, No.219 (1992), pp.79~117.
2. Y. Kobayashi et al., J. of the Soc. Naval Architects of Japan, Vol.185 (1999), pp.221~232.
3. Military Standard Hand Book-5G, Defense Printing Service Detachment Office, (1994).
4. Y. Kobayashi et al., J. of the Soc. Naval Architects of Japan, Vol.182 (1997), pp.751~761.
5. Y. Kobayashi et al., Key Engineering Materials, Vol.145~149 (1998), pp.1037~1042.
6. K. Matsuoka and E. Fujii, J. of the Soc. Naval Architects of Japan, Vol.178 (1995), pp.513~522.
7. Y. Kobayashi et al., J. of the Soc. Naval Architects of Japan, Vol.183 (1998), pp.383~390.
8. H. Nisitani et al., Program on Versatile 2D Stress Analysis Based upon Body Force Method, Baifukan (1994).
9. Y. Murakami et al., J. of the Soc. of Materials Science, Japan, Vol.35, No.396 (1985), pp.998~1003.

Key Engineering Materials Vols. 183-187 (2000) pp. 1005-1010
© 2000 Trans Tech Publications, Switzerland

An Analysis of Random Fatigue Strength of K-Type Tubular Joints by Probabilistic Fracture Mechanics Method

G.H. Nie, R. Shi and R.J. Zhang

Key Laboratory of Solid Mechanics of MOE, Department of Engineering Mechanics, Tongji University, Shanghai 200092, China P.R.

Keywords: Fracture Mechanics, K-Type Tubular Joints, Life of Propagation, Random Fatigue, Surface Crack

ABSTRACT

This paper deals with random fatigue of welded K-type tubular joints subjected to axial or out-of-plane bending load. By regarding the sizes of initial surface cracks and material constants as random variables with some probabilistic distributions, incorporating the effect of the weld, five hundred random samples are generated, statistical computational results of life of crack propagation and effect of change of crack shape are finally obtained and compared with experimental data available based on a regression analysis. Meanwhile, crack propagation behaviors are also investigated and the computational results show that the shapes of propagating cracks finally tend to stable shapes when the crack propagates through the wall-thickness.

1. INTRODUCTION

As a special form of structures, tubular joints (multi-duct pipes) welded by circular cylindrical shells (circular tubes) have been widely used in engineering. One of the primary factors that are responsible for many serious accidents is the insufficient fatigue strength of the joints and connected pipe ends. Much attention should therefore be paid to fatigue analysis of such structures.

The appearance and development of crack in a tubular joint is a very complex and complicated process. Experimental results for simple joints have shown that cracks normally are initiated at the weld toe of the connection. In the first place, several initiation sites may appear, and then small cracks join up to produce large cracks, and eventually one predominate crack will reach a maximum tolerable size. For through-the-thickness cracks, Paris and Erdogan[1] proposed a power law relation between the crack growth and the stress intensity range, which is so called the Paris law (or equation) and is fitted well to the experimental data. Further, owing to the Paris equation, a pair of coupled equations have been introduced for surface cracks[2,3]. These fatigue crack growth damage models have been used to analyze the fatigue strength and predict the fatigue life of the welded joints[4]. In fatigue analysis based on most present design code, all parameters are taken at their expected values except for a conservative choice of the fatigue strength, i.e. S-N curve. The fatigue strength or life is a single value quantity usually arrived at in a deterministic manner.

However, some factors including distribution pattern of cracks, material properties and dynamic loading response behavior, are random in nature and should thus be treated probabilistically for a realistic analysis. In this connection, some models have been proposed to analyze random fatigue strength of T-type tubular joints (the chord and brace are welded along two orthogonal directions) under axial, in-plane or out-of-plane bending load[5-7]. The models incorporate the effects of several above-mentioned factors on fatigue life of the structures.

Based on the mentioned above, a random fatigue analysis is done in this paper for K-type tubular joints whose one brace intersected the chord at 90^0 and the second at 45^0. By considering sizes of the surface crack situated at the weld toe and chord, i.e. the crack depth and length a_o, c_o, and material constant C as random variables which are Weibull distributed and log-normal distributed, respectively, incorporating the effect of the weld, five hundred random samples are generated, and analyses are given in a deterministic manner for each sample, statistical computational results of life of crack propagation and effect of change of crack shape are finally obtained. A comparison between the computed crack propagation life and the experimental data available is made based on a regression analysis.

2. PARIS LAWS FOR CRACK PROPAGATION AND CYCLIC STRESS INTENSITY FACTORS

In general, the fatigue life of structures includes three portions: the first is the life of inspected visible crack, the second is the life of crack propagation, the third is the life till the failure of the structures (or until fatigue experiment stops). For the welded structures, the fatigue life is mainly is the portion of crack propagation. As experimental results have shown, cracks of welded tubular joints are the surface cracks situated at the weld toe and chord, and they propagate through the thickness and along the surface under cyclic loads. The propagation process can be described by using the coupled Paris equations in the following

$$\frac{da}{dN} = C_d(\Delta K_d)^{m_d} \tag{1a}$$

$$\frac{dc}{dN} = C_s(\Delta K_s)^{m_s} \tag{1b}$$

in which C_d, m_d and C_s, m_s are the material constants in the directions of the crack depth and length, respectively. ΔK_d and ΔK_s are the corresponding stress intensity factor ranges expressed by

$$\Delta K_d = \left[M_{km(d)}Y_{m(d)}\Delta\sigma_m + M_{kb(d)}Y_{b(d)}\Delta\sigma_b\right]\sqrt{\pi a} \tag{2a}$$

$$\Delta K_s = \left[M_{km(s)}Y_{m(s)}\Delta\sigma_m + M_{kb(s)}Y_{b(s)}\Delta\sigma_b\right]\sqrt{\pi a} \tag{2b}$$

where $\Delta\sigma_m, \Delta\sigma_b$ are membrane and bending stress ranges, respectively. M_{km}, M_{kb} are the corresponding magnification factors due to the present of weld. To describe the stress distribution in the tubular joint, especially the largest stress level at the weld toe, $\Delta\sigma_m, \Delta\sigma_b$ are characterized by

hot-spot stress range which includes the effect of overall geometry of the structures. The hot-spot stress range $\Delta\sigma = E\Delta\varepsilon$ can be determined by the real strains measured with micro-strain gauge. Further, adopting the mathematical expressions fitted from numerical results of a three-dimensional finite element analysis, the stress intensity factor ranges can be written by

$$\Delta K_d = \left[M_{km(d)}\Delta\sigma_m + M_{kb(d)}H\left(\frac{\pi}{2}\right)\Delta\sigma_b \right]\sqrt{\pi a/Q}\quad F\left(\frac{a}{t},\frac{a}{c},\frac{\pi}{2}\right) \tag{3a}$$

$$\Delta K_s = \left[M_{km(s)}\Delta\sigma_m + M_{kb(s)}H(0)\Delta\sigma_b \right]\sqrt{\pi a/Q}\quad F\left(\frac{a}{t},\frac{a}{c},0\right) \tag{3b}$$

where a, $2c$ are the sizes of surface crack in the directions of the depth and length respectively, and t is the wall-thickness through the chord. The formulae for $H(...), F(...)$ are listed in Ref.[2], and M_{km}, M_{kb} are chosen as follows[8,9]

$$M_{km(d)} = 1+(K_{tm}-1)\exp\left[-35(K_{tm}-1)\frac{a}{t}\right],\quad M_{kb(d)} = 1+(K_{tb}-1)\exp\left[-35(K_{tb}-1)\frac{a}{t}\right]$$

$$M_{km(s)} = K_{tm},\quad M_{kb(s)} = K_{tb} \tag{4a,b,c,d}$$

The above equation shows that, if a/t is smaller, $M_{km(d)} \to K_{tm}$, $M_{kb(d)} \to K_{tb}$ while $M_{km(d)} \to 1, M_{kb(d)} \to 1$ if a/t gets larger(e.g. $\frac{a}{t} = 0.4$). The latter indicates the effect of the weld can be neglected for a deeper surface crack.

3. RANDOM VARIABLES AND GENERATION OF RANDOM NUMBERS

For random variables which have Weibull probability distribution characterized by shape parameter α, scale parameter β and shift parameter δ, e.g. initial crack sizes a_o, c_o, a random number denoted by y , can be determined by

$$y = \delta + (-\beta\ln x)^{1/\alpha} \tag{5}$$

where x is a random number corresponding to a uniform distribution between 0 and 1.

For a random variable which has normal probability distribution with mean value μ and variance σ^2, e.g. $\ln C$ (ln is natural logarithm to the base e), its random number denoted by z, can be generated by

$$z = \mu + \sigma\frac{\sum_{i=1}^{n} x_i - \frac{n}{2}}{\sqrt{\frac{n}{12}}} \tag{6a}$$

in which n is large enough, and usually it can be taken as n=12. The above equation is thus simplified to

$$z = \mu + \sigma\left(\sum_{i=1}^{12} x_i - 6\right) \tag{6b}$$

where x_i has the same meaning as that for x.

4. NUMERICAL COMPUTATION ON SURFACE CRACKS PROPAGATION LIFE

For each random sample of initial crack sizes a_0, c_0 and material constant C, a iterative computation can be done by using Eq.(1), and fatigue crack propagation life, N, is finally derived based on the failure criteria that the crack propagates through the wall-thickness. In computation the propagation increment at the deepest point of crack, Δa, is chosen as iterative step-length. The specific iterative process consists of three steps[6][7]: (1)giving an initial value of Δa_1 for initial crack sizes a_0, c_0, the use of Eq.(1a) leads to propagation life $N_1 = \Delta N_1$, and the increment at the length, Δc_1, is also obtained. The crack sizes due to the propagation become $a_1 = a_0 + \Delta a_1$, $c_1 = c_0 + \Delta c_1$; (2)giving iterative value Δa_2, taking step (1), the crack sizes and corresponding propagation life are derived as $a_2 = a_1 + \Delta a_2 = a_0 + \Delta a_1 + \Delta a_2$, $c_2 = c_1 + \Delta c_2 = c_0 + \Delta c_1 + \Delta c_2$, and $N_2 = N_1 + \Delta N_2 = \Delta N_1 + \Delta N_2$; (3) taking repeatedly the above steps until the crack propagates through the wall-thickness of the chord, i.e. $a_M = a_0 + \sum_{i=1}^{M} \Delta a_i = t$. So, the crack size in the direction of the length is $c_M = c_0 + \sum_{i=1}^{M} \Delta c_i$ and the total propagation life is $N = \sum_{i=1}^{M} \Delta N_i$.

For the purpose of giving accuracy of computation, an iterative value of Δa_i is chosen during the iterative process to satisfy that the error for every two stress intensity ranges around each iteration does not exceed 1%.

5. EXAMPLES AND ANALYSIS

In computation the geometry sizes of the structures are chosen from the experimental models used in British Welded Institute, as listed in Table1 [10][11]. The loading mode is axial (AX) or out-of-plane bending (OPB). Elastic modulus $E = 0.21\times10^6\ N/mm^2$, material constant for fatigue propagation $m = 3.1$, $\ln C$ is normal distributed, i.e. $\ln C \sim N(\mu, \sigma^2)$ where $\mu = -29.84$,

$\sigma^2 = 0.55$. a_0 has a Weibull distribution denoted by $a_0 \sim Weibull(\alpha, \beta, \delta)$ with $\alpha = 2.101$, $\beta = 0.0024$, $\delta = 0.00002$, and $a_0/c_0 = 0.15$ [6]. The initial iterative value $\Delta a_1 = 0.0005(mm)$. All the computation is carried out on HP-UX Workstation.

Table1 Some related data of k-type tubular joints

Specimen No.	diameter of the chord (mm)	thickness of the chord (mm)	hot-spot strain range ($\times 10^{-6}$)	Loading mode	remarks
1	457	16	600	AX	two braces separated by a small distance
2	457	16	780	AX	two braces separated by a small distance
3	168	6.3	930	OPB	two braces separated by a small distance
4	168	6.3	1110	OPB	two braces not separated
5	168	6.3	1190	OPB	two braces not separated
6	168	6.3	1300	OPB	two braces not separated

Table 2 Values of fatigue life

Specimen No.	test value for entire fatigue process N	test value for the propagation portion $N_P = 66\%N$	sample mean value $\overline{N}_r$
1	4.9×10^6	3.2340×10^6	3.18998×10^6
2	1.2×10^6	0.7920×10^6	1.41438×10^6
3	1.2×10^7	0.7920×10^7	0.115014×10^7
4	2.3×10^6	0.1518×10^7	0.664583×10^6
5	1.6×10^6	0.1056×10^7	0.535617×10^6
6	1.3×10^6	0.8580×10^6	0.407215×10^6

Table 3 Sample mean values for various shapes of initial cracks

a_0/c_0	0.15	0.20	0.30	0.50	0.60	0.80	1.00
$\overline{N}_r(\times10^6)$	3.1898	3.23921	3.30718	3.38948	3.41781	3.46152	3.49472

The experimental and computation results are shown in Table 2. The data indicate that the values of computation are close to the ones of experiment, and the former is smaller. For the same structures denoted by specimen No. 4-6, a regression analysis on the experimental and computational values of propagation life is performed respectively, and the regression results are written in the following

$$\lg N_p = 14.5802 - 3.55513 \lg \Delta\sigma \quad \text{or} \quad \lg N_p = -4.34097 - 3.55513 \lg \Delta\varepsilon \qquad (7a,b)$$

$$\lg \overline{N_r} = 13.162 - 3.10003 \lg \Delta\sigma \quad \text{or} \quad \lg \overline{N_r} = -3.33705 - 3.10003 \lg \Delta\varepsilon \qquad (8a,b)$$

The above results show that the experiment values agree well with computational ones.

Further, to investigate the effect of initial crack shape on fatigue crack propagation life, specimen no.1 is chosen as a computation model, and mean values of samples for various values of a_0/c_0 are arranged in Table 3. It is observed that the maximum error is lower than 10%, it implies that a change in initial crack shape will not have a remarkable effect on the change of crack propagation life. Meanwhile, the computational results for the propagation behaviors of surface cracks indicate that the shapes of propagating cracks finally tend to stable shapes when the crack propagates through the wall-thickness. For the axial load, $a/c \to 0.0751$ while $a/c \to 0.0740$ for the out-of-plane bending load.

6. CONCLUSIONS

(1) By considering initial crack sizes and material constant as random variables, choosing the proper probabilistic distributions and generating the corresponding random sample, applying the coupled Paris equations, random fatigue problem is solved effectively. The method described in this paper can be adopted to analyze random fatigue strength (life prediction) of various types of welded tubular joints.
(2) The change of initial shape of surface crack has not a great effect on the life of fatigue crack propagation.
(3) The final shape of surface crack which propagates through the wall-thickness of the chord is stable, and is not correlative with its initial state.

ACKNOWLEDGEMENT: The work is partially supported by Foundation for the Key Speciality of the Shanghai Education Commission, China.

REFERENCES

1. P. Paris and F. Erdogan, ASME J. of Basic Engineering, **85** (1963) p.528
2. J.C. Newman, and I.S. Raju, Engineering Fracture Mechanics, **15** (1981) p.185
3. W. Shang-Xian, Engineering Fracture Mechanics, **22** (1985) p. 897
4. D.R.V. Delft, O.D. Dijkstra and H.H. Snijder, Proc. OTC, paper 5352, Houston, Taxas, U.S.A. (1986)
5. Y.H. Zhang *et al.*, Ocean Engineering, **8** (1990) p.15
6. G.H. Nie *et al.*, Proc. of Int. Conf. on Comp. Meth. in Struct. and Geotech. Engng, Hong Kong (1994) p.1226
7. G.H. Nie, et al., Appl. Math. Mech., **15** (1994) p.1017
8. F.V. Lawrence, N.J. Ho and P.K. Mazumdar, Ann. Rev. Mater. Sci., **11** (1981) p. 401
9. O.D. Dijkstra , H.H. Snijder, J.L. Overbeeke and H.Wildschut, Steel in Marine Structures , Amsterdam , The Netherlands (1987) p.885
10. J.G. Wylde, and A. McDonald, Proceedings of the Second International Conference on the Behavior of Off-Shore Structures, London, England (1997) p.535
11. A. McDonald, and J.G. Wylde, Fatigue Off-Shore Structural Steels, Thomas Telford Ltd., London, England (1981) p. 89

Key Engineering Materials Vols. 183-187 (2000) pp. 1011-1016
© 2000 Trans Tech Publications, Switzerland

Fatigue Life Prediction of Bolted Joints Using Fatigue Modulus

C.K. Jung and K.S. Han

Department of Mechanical Engineering, Pohang University of Science and Technology San 31 Hyoja-dong, Nam-gu, Pohang 790-784, Korea

Keywords: Fatigue Life Prediction, Fatigue Modulus, Mechanically Fastened Joints, Stress Concentration, SUS304

ABSTRACT

The fatigue life prediction of SUS304 stainless steel with bolted joints has been investigated using fatigue modulus concept proposed by Hwang & Han. In this paper, modified fatigue life prediction equation (MFLPE) is derived by fatigue modulus degradation model, which is a exponential function of fatigue modulus, fatigue cycle and load transfer level in order to consider the relaxation of stress concentration due to fasteners. Tests have been performed using various load transfer levels to verify the derived prediction equation. The experimental results show that fatigue modulus can be used as a parameter to represent fatigue damage and the geometry parameters affect the constants in the fatigue life prediction equation.

1. INTRODUCTION

The fatigue characteristics of notches, aimed at uses of joints with fasteners, have been studied for various types of geometry. Most of previous studies used mainly the fracture mechanics approach that investigates crack propagation of notch specimens under fatigue loading[1]. As this system of veins, Lee[2] studied characteristics of fatigue behavior of mechanically fastened joints and load transfer effects with tests of specimens of aluminum. Landy and Armen[3] announced enhanced stop-drill repair procedures for cracked structures. And Huth[4] introduced primary joint parameters and studied the influence of fastener flexibility on the load transfer and the fatigue life. Although these studies identify the effect of fasteners, it is not suitable to understand the only effect of fasteners on fatigue strength.

Meanwhile, Hwang and Han[5,6] introduced a new concept called "fatigue modulus", which is defined as a slope of applied stress and resultant strain at a specific cycle, and derived theoretical equation for predicting fatigue life using the fatigue modulus and its degradation rate under constant and variable amplitude loading. Also, Lee[7] and Ahn[8] noted that the fatigue modulus concept can be used to predict the fatigue life of SS304 and formulated predicting equations under some assumptions.

This study is aimed at characterizing the fatigue behavior of mechanically fastened joints, identifying the relaxation of stress concentration and clarifying the effect of clamping force on

Table 1. Chemical composition of SS304

C	Si	Mn	P	S	Ni	Cr
0.052	0.64	1.21	0.023	0.011	9.16	1.13

fatigue strength. Fatigue tests were conducted for plate-type specimens with bolted holes and the stress concentration near notch was shown using finite element method. Also, defining the load transfer factor and adopting fatigue modulus concept, fatigue life prediction equation was derived considering the effect of fasteners.

2. EXPERIMENTAL PRECEDURE

2.1. Material and Specimen Preparation

As the specimen material, a 2mm-thick plate of SS304 stainless steel was selected. This material have many uses such as heat exchangers, tubes of superheater and chemical plants, because of its good corrosion-resisting and heat resisting property. The chemical composition and mechanical properties are presented in Table 1.

From the plate, dogbone specimens with 6-mm diameter hole were prepared for tension test as shown in Fig.1. The longitudinal axis of the specimen was in the original plate rolling direction. The specimens for fatigue test had the same geometry and material as tension test specimens and a steel fastener was installed in the hole.

2.2. Test

The tension test was performed in room temperature and in displacement controlled mode, employing MTS(100kN USA) machine. The fatigue test was performed in room temperature, employing the same machine. In all tests, fatigue life measured under tension-to-tension haversine waveform loading with a stress ratio of 0.1 and frequency of 10 Hz. At the stress ratios of 0.8, 0.7, 0.6, 0.5, 0.45 and 0.4 to the ultimate strength, tests were performed on three specimens at each case. And 6Nm and 8Nm torque were taken as the clamping force of fasteners.

3. LIFE PREDICTION EQUATION

3.1. Fatigue Modulus Concept

Fatigue modulus is represented by a line between applied stress and resultant strain at a specific loading cycle, n. The fatigue modulus is a slope of a line o-n' in Fig. 2. Therefore,

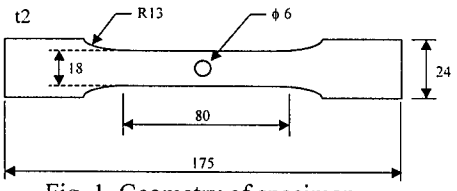


Fig. 1. Geometry of specimen

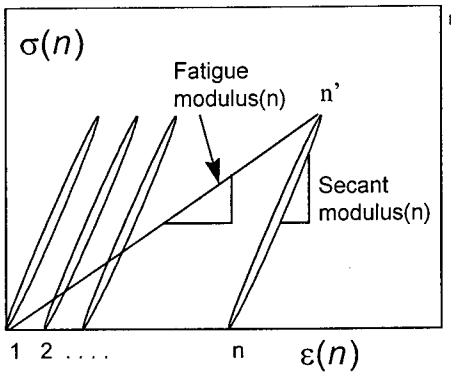


Fig. 2. Fatigue modulus concept

$$F(n,q)=\frac{\sigma_a}{\varepsilon(n)}=\sigma_u\frac{q}{\varepsilon(n)} \tag{1}$$

where,

$F(n,q)$: fatigue modulus at nth loading cycle
$\varepsilon(n)$: resultant strain at nth loading cycle
q : stress ratio applied σ_a stress , to ultimate strength σ_u

Fatigue modulus, F, of a material is a function of loading cycle, n and applied stress, q. But it can be expressed as a function of loading cycle only under constant loading condition.

3.2. Life Prediction Equation

Assume that fatigue modulus degradation rate, *dF/dn*, is followed by a power function of fatigue cycle, n and load transfer factor, L, affects the constants of fatigue modulus degradation rate, i.e.,

$$\frac{dF}{dn}=-A\frac{CKn^{CK-1}}{BLF^{BL-1}} \tag{2}$$

where, *A, B, C* are material constants and *K, L* are constants of load transfer,
Integration of Eq. 2 from n_1 to n_2 gives;

$$F^{BL}(n_2)-F^{BL}(n_1)=-A(n_2^{CK}-n_1^{CK}) \tag{3}$$

Substitution of $n_2=n$ and $n_1=0$ into the above equation follows;

$$F^{BL}(n)-F^{BL}(0)=-An^{CK} \tag{4}$$

At failure, where $n=N$, Eq. 4 becomes,

$$F_f^{BL}-F_0^{BL}=-AN^{CK} \tag{5}$$

Table 2. Results of tension test

Yield Strength	Tensile Strength	Young's Modulus
400 MPa	680 MPa	155 GPa

In Eq. 5, F_0, being the fatigue modulus at the first cycle, is the elastic modulus and Ff is the fatigue modulus at failure. Further manipulation can be made by adopting reference modulus, F_R.

$$F_0 / F_R = p \tag{6-1}$$

$$F_f / F_R = f(q) = q \tag{6-2}$$

where p and q are material constant and stress level, respectively.
From Eq. 5 and Eq. 6, fatigue life equation can be written as,

$$N = [M(p^{BL} - Q^{BL})]^{1/CK} \tag{7}$$

where, $M = F_R^{BL} / A$ and B, C, K, L are constants obtained from experiment data.

4. RESULTS AND DISCUSSIONS

4.1. Tension and Fatigue test

Results of tension test are presented in Table 2. The S-N graph is represented in Fig. 3. In the case of 0N-M, with no fasteners, has fatigue life of 10^6 cycles at 0.2~0.25 stress ratio level. The life of 6N-M and 8N-M specimens is more than 10^6 cycles at 0.3 and 0.35 stress level, respectively. Though the fatigue life is approximately the same among three cases at the high stress level, it tends to be longer according to the magnitude of clamping force as the stress level decreases. And the case of 8N-M specimen shows 10% longer life than that of 6N-M. It can be thought that the clamping force can not affect significantly at the high stress level because of the relatively large difference of applied force and clamping forces. And the effects of clamping force may become

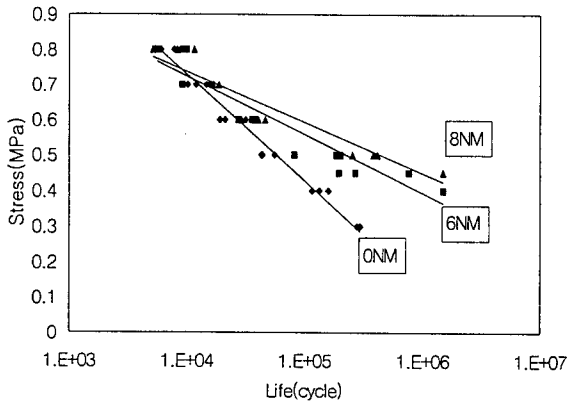


Fig. 3. S-N graph for three types of specimen

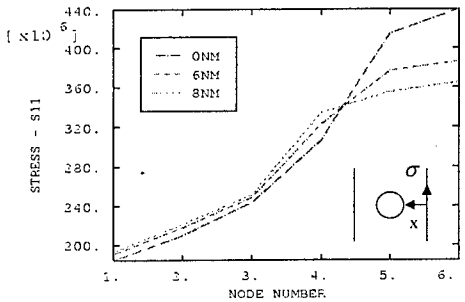


Fig 4. σ_{xx} along the center line(270MPa)

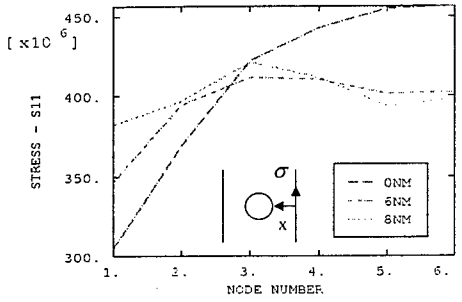


Fig. 5. σ_{xx} along the center line(400MPa)

larger because of the small difference of two sorts of forces. This phenomenon may be related to the difference of applied force and clamping forces. And the effects of clamping force may become larger because of the small difference of two sorts of forces. This phenomenon may be related to the load transfer effects through the bolt-nut joints and the friction effects between fastener and material.

4.2. FEM analysis

Finite element analysis shows the stress concentration of the circumference of notch for two cases (Fig.4, Fig. 5). As shown in Fig.4 and Fig. 5, the stress concentration at the notch tip decreases as the clamping force increases. Comparing the stress at the tip with the stress at the boundary, decreasing tip stress and increasing boundary stress results in lower gradient of stress through the specimen as the clamping stress increases. Accordingly, the relaxation of stress concentration due to fasteners may cause the extension of fatigue life. And the gradient of the stress distribution is affected nonlinearly by the clamping forces. Then it is supposed that the effect of clamping forces on the extension of fatigue life has this non-linearity also.

4.3. Application of Prediction Equation

From the data of fatigue tests on the 0N-M and the 8N-M specimen, the constants of the equation derived above can be calculated. And with an assumption of power law relation of these constants according to the clamping force, the fatigue life equation of the 8N-M case can be evaluated as follows;

$$N = [(-0.1646)(0.4776 - q^{\frac{1}{1.265}})]^{\frac{1}{-0.3207}} \tag{8}$$

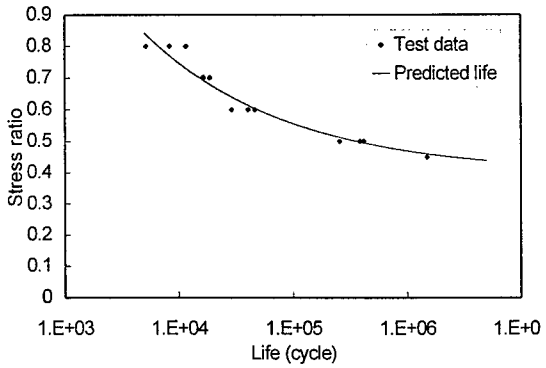


Fig. 6. Comparison of predicted life with experiment data

The calculated fatigue life and experiment data are plotted in Fig. 6. As shown in Fig.6 , predicted life is close to the experimental data.

5. CONCLUSIONS

In this study, fatigue test performed for circular notched SS304 plate with preinstalled fasteners in the hole. Fatigue life prediction equation is derived from the fatigue modulus concept and compared with the test data.

1. By assuming that fatigue degradation rate is a function of fatigue modulus and fatigue cycle, and by adopting load transfer factor of fastener, life prediction equation derived is valid and applicable to notched specimens.

2. The fact that the predicted life is close to the test data shows that the constants of fatigue modulus degradation model contain geometry data representing notch effects.

Acknowledgements

The authors wish to thank to Safety and Structural Integrity Research Center for financial assistance.

REFERENCE

1. Kremple E., ASTM STP 549, ASTM (1974) pp. 165-178.
2. Eun U. Lee, ASTM STP 927, ASTM (1985) pp. 95-115.
3. Michael A. Landy, Harry Armen, Jr., and Harvey L. Eidinoff, ASTM STP 927, ASTM (1985) pp.190-220.
4. Heimo Huth, ASTM STP 927, ASTM (1985) pp221-250.
5. W. Hwang and K. S. Han, J. of Composite Materials, **20**(1986) pp.125-153.
6. W. Hwang and K.S. Han, Composite Materials : Fatigue and Fracture (2nd Volume), ASTM STP1012 (1989) pp.87-102.
7. J.H. Lee, H.W. Nam, K.S. Han, Proceedings of the KSME (1998) pp.236-240.
8. I.H. Ahn, J.H. Lee, K.S. Han, Proceedings of the KSME (1999) pp.993-998.

Key Engineering Materials Vols. 183-187 (2000) pp. 1017-1022
© 2000 Trans Tech Publications, Switzerland

Study of Crack Propagation Behavior on Low Cycle Fatigue in Squeeze Cast Aluminium Alloy

K. Morino[1], F. Nishimura[1], K. Takahashi[1], Y.H. Kim[2] and H. Nisitani[3]

[1] Department of Mechanical and Electrical Engineering, Tokuyama College of Technology, 3538 Takajo, Kume, Tokuyama, Yamaguchi 745-8585, Japan

[2] Department of Mechanical and Materials Engineering, Korea Maritime University, #1 Dongsam-dong, Youngdo-ku, Pusan 606-791, Korea

[3] Department of Mechanical Engineering, Kyushu Sangyo University, 2-3-1 Matsukadai, Higashi-ku, Fukuoka 813-8503, Japan

Keywords: Crack Propagation, Eutectic Silicon Particle, Low Cycle Fatigue, Squeeze Cast Aluminium Alloy

ABSTRACT

In order to clarify the effect of eutectic silicon particles on low cycle fatigue, low cycle fatigue tests were carried out using squeeze cast aluminium alloy (JIS AC4CH) and anti-corrosion aluminium alloy (JIS A6061-T6). AC4CH and A6061-T6 are both aluminium alloys that mainly contain silicon and magnesium. The crack propagation behavior from the crack initiation to the fracture was investigated in detail by observing the surface of specimens and their fracture section. Our experiments have clarified that AC4CH has two kinds of crack growth rate depending on two different crack propagation routes. That is, AC4CH has the same crack growth rate as A6061-T6 if the crack is propagated on the matrix region. The crack growth rate in AC4CH is faster than that in A6061-T6 if the crack is propagated through the high density region of eutectic silicon particles.

1. INTRODUCTION

In our previous paper [1], we clarified that low cycle fatigue life in AC4CH is approximately 1/3 of that in A6061-T6 at same plastic strain range. Also we showed the following three facts as the cause of the decrease in fatigue life : (1) Crack initiation length in AC4CH is larger than that in A6061-T6. (2) Crack propagation limit length in AC4CH is smaller than that in A6061-T6. (3) Relative crack growth rate in AC4CH is faster than that in A6061-T6. Additionally, we clarified that eutectic silicon particles are related to these phenomenon. However, no detailed investigation of crack propagation behavior has been carried out.

On the other hand, as to high cycle fatigue in squeeze cast aluminium alloy, detailed investigations that were aimed at crack initiation and crack propagation behavior have been carried out [2]-[7]. Besides, the effect of eutectic silicon particles on crack propagation behavior has been clarified [2][6][7]. However, few investigations have been done on low cycle fatigue. Low cycle fatigue tests were difficult, because specimens were easily buckled during the experiment.

In this study, low cycle fatigue tests were carried out using AC4CH and A6061-T6. The crack

propagation behavior from the crack initiation to the fracture was investigated in detail by observing the surface of specimens and their fracture sections.

2. MATERIALS, SPECIMENS AND EXPERIMENTAL PROCEDURES

Al-Si-Mg aluminium alloy (JIS AC4CH) was used in this study. AC4CH was performed by solution heat treatment at 803K for 3 hours and age hardening treatment at 433K for 3 hours. Anti-corrosion aluminium alloy (JIS A6061-T6) was used as compared material. The microstructures, chemical composition and mechanical properties of AC4CH and A6061-T6 are shown in Fig. 1, Table 1 and Table 2, respectively.

Figure 2 shows the shape and dimension of specimen. In this study, cylindrical specimens were used. The diameter d_0 and length l_0 of the central part are 6 mm and 9 mm, respectively ($l_0/d_0 = 1.5$). Its aspect ratio is decided to obtain the true fatigue behavior [8]. The central parts of the specimens were finished with emery paper and diamond paste. Furthermore, the specimens were polished about 50 μm by electropolishing to remove the work layer.

Fatigue tests were carried out using an electro-hydraulic servo testing machine with a capacity of 29kN and frequency ranging from 0.03 to 0.1 Hz. The strain was measured by axial extensometer and the machine was controlled to make the plastic strain range constant.

Plastic replicas were used to measure the crack length and to observe successive fatigue damage on the specimen surface. Also, SEM was used to observe fracture sections.

3. EXPERIMENTAL RESULTS AND DISCUSSION

Figure 3 shows the relation between plastic strain range $\Delta\varepsilon_p$ and number of cycles to failure N_f obtained for AC4CH and A6061-T6. In this figure, $2\varepsilon_f$ (ε_f: fracture ductility) is plotted at number of 1/4 cycle. Experimental data of both materials satisfy the following Manson-Coffin law.

Table 1 Chemical composition [wt.%]

	Si	Mg	Fe	Cu	Mn	Cr	Zn	Ti	Al
AC4CH	7.0	0.3	0.2	-	-	-	-	-	Bal.
A6061-T6	0.58	0.98	0.18	0.20	0.01	0.07	0.01	0.02	Bal.

Table 2 Mechanical properties

	$\sigma_{0.2}$	σ_B	σ_T	ψ	ε_f	E
AC4CH	218	300	370	22.7	0.257	69.2x10³
A6061-T6	290	313	536	60.9	0.939	69.6x10³

$\sigma_{0.2}$: 0.2% proof stress MPa
σ_B : Tensile strength MPa
σ_T : True fracture stress MPa
ψ : Reduction of area %
ε_f : Fracture ductility
E : Young's Modulus MPa

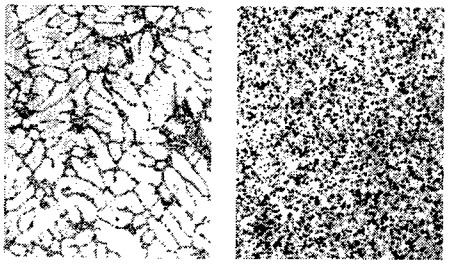


Fig.1 Microstructures

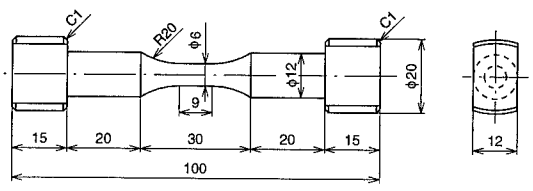


Fig.2 Shape and dimension of specimen

$$\Delta\varepsilon_P \cdot N_f^{0.65} = 0.21 \quad \text{(AC4CH)} \tag{1}$$

$$\Delta\varepsilon_P \cdot N_f^{0.74} = 0.69 \quad \text{(A6061-T6)} \tag{2}$$

The fatigue life in AC4CH is approximately 1/3 of that in A6061-T6 at same plastic strain range. Additionally, many tests were carried out at same plastic strain range ($\Delta\varepsilon_P = 0.01$) to investigate the amount of scatter in fatigue life of AC4CH. The experiments showed that the amount of scatter was from 1/3 to 3 times as much as average fatigue life in the case of $\Delta\varepsilon_P = 0.01$.

On low cycle fatigue tests using AC4CH, in most cases, cracks started from a high density region of eutectic silicon particles that exists on the surface [1]. First of all, we observed in detail the fracture section by using SEM in order to grasp the aspect of the fracture origin. Figure 4 shows an SEM micrograph of fracture origin in AC4CH ($\Delta\varepsilon_P = 0.02$). As a result, it was clarified that the shorter the fatigue life, the larger the size of high density region of eutectic silicon particles on the fracture origin. That is, there was a correlation between the size of high density region of eutectic silicon particles and the fatigue life.

Figure 5 shows a comparison of the crack growth curves between AC4CH and A6061-T6 in the case of $\Delta\varepsilon_P = 0.01$. In AC4CH, Type A is a specimen that shows fatigue life close to the average. Type B is a specimen that shows the fatigue life 2 times as long as the average one. It shows that the crack initiation length of both specimens in AC4CH are larger than that in A6061-T6. It is caused by the cracks started from the high density region of eutectic silicon particles in AC4CH [1]. As to the crack growth rate, the logarithm of crack length ln$l$ in Type A of AC4CH is almost proportional to the number of cycles N from the crack initiation to the fracture. And its crack growth rate is faster than that in A6061-T6. The other hand, Type B has the same crack growth rate as Type A until the crack length is about 200 μm. After that, however, the crack growth rate slows down and it becomes almost the same value as A6061-T6.

According to our continuous observation, it was clarified that the crack is propagated through the high density region of eutectic silicon particles in some cases. In other cases, it was propagated along the chain of eutectic silicon particles. In the case of Type A and Type B, the cracks were propagated almost along the chain of eutectic silicon particles. However, there was no distinct difference between Type A and Type B in the observation on the surface. The above results led us to detailed investigation on the crack propagation

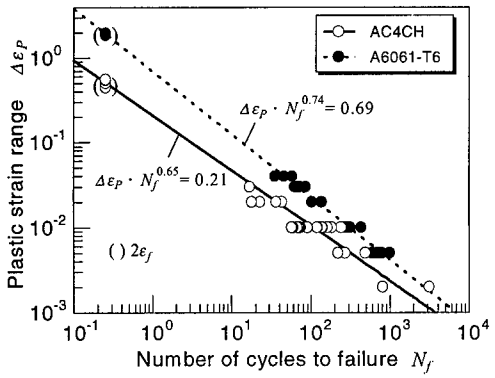


Fig.3 Low cycle fatigue life curves in AC4CH and A6061-T6

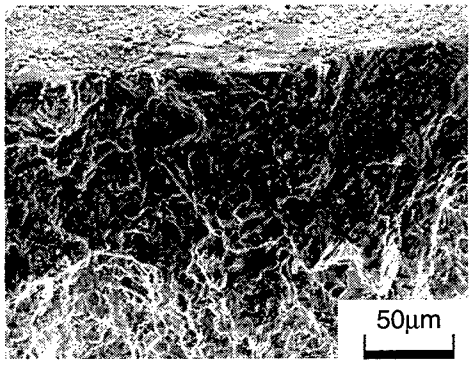


Fig.4 Fracture origin observed in AC4CH ($\Delta\varepsilon_P = 0.02$)

behavior.

Figure 6 shows the shape of cracks on vertical section in the case of cycle ratio $N/N_f = 0.98$ in AC4CH. It was observed by liquid penetrant test. The shape of crack in AC4CH was ellipsoidal and similar to that of the general metal materials. Consequently, in Fig. 7 and Fig. 8, the shape of cracks on fracture sections were approximately illustrated by ellipsoid based on the position of crack tips observed on surface.

Figure 7 shows the crack growth curve, continuous micrographs of crack propagating on the surface and the shape of cracks on fracture section in Type A. In Fig. 7, a darkly shaded part of the fracture section represents high density region of eutectic silicon particles, whose part is related to the crack initiation. Two lightly shaded parts represent another high density region of eutectic silicon particles, whose parts are directly unrelated to the crack initiation. As seen from the figure, high density region of eutectic silicon particles exists on the neighboring surface. In the early stage of fatigue life, three cracks started from high density region of eutectic silicon particles. After that, the cracks were connected each other, and then fracture was followed. In Fig. 7, the cracks are propagated through the high density region of the eutectic silicon particles from the crack initiation to the fracture not only on the surface but in the inside of the specimen in Type A. At this time, the logarithm of crack length $\ln l$ is proportional to number of cycles N.

Figure 8 shows the same observed example in Type B as that in Fig. 7. In this case, high density region of eutectic silicon particles that exists on the neighboring surface is relatively small. Its projected length on surface is about 200 μm. In the early stage of fatigue life, like Type A, two cracks started from high density region of eutectic silicon particles. After that, the cracks were connected and then fracture was followed. However, Type B shows quite different crack propagation behavior from that in Type A. That is, the crack is propagated through the high density region of the eutectic silicon particles in the inside of specimen, and

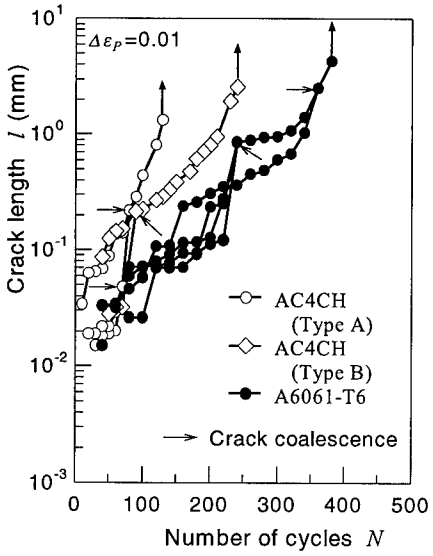


Fig.5 Comparison of crack growth curves between AC4CH and A6061-T6

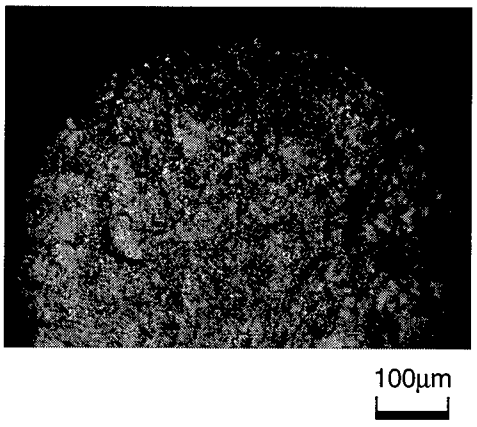


Fig.6 Shape of cracks on vertical section in AC4CH observed by liquid penetrant test ($\Delta\varepsilon_p = 0.01$, $N/N_f = 0.98$)

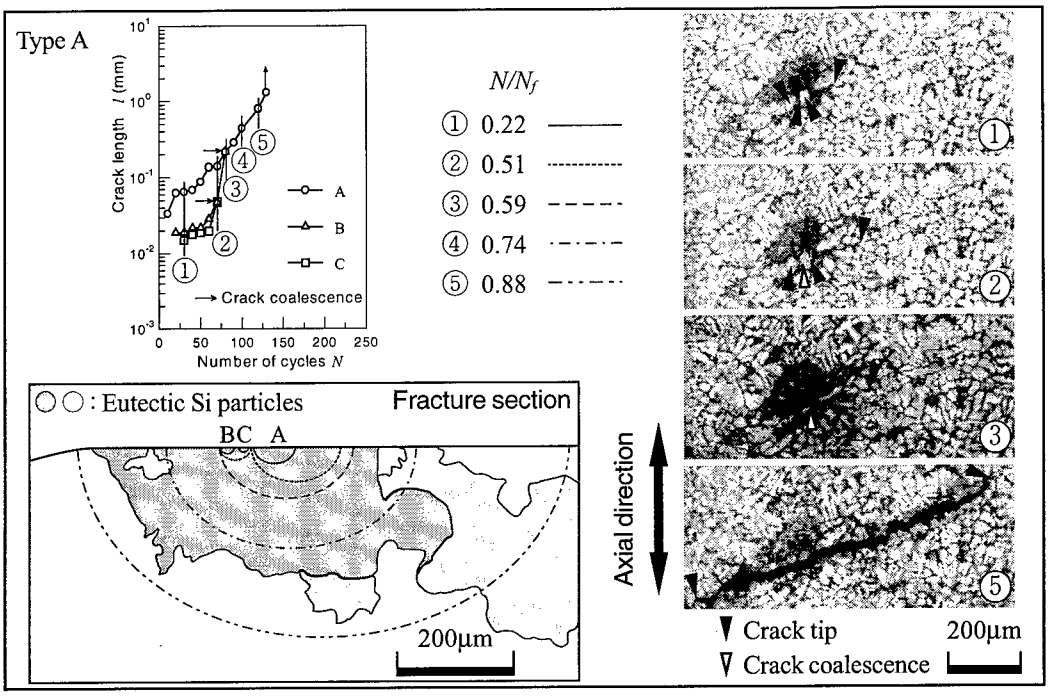


Fig.7 Observation of crack propagation behavior in Type A of AC4CH ($\Delta\varepsilon_p = 0.01$)

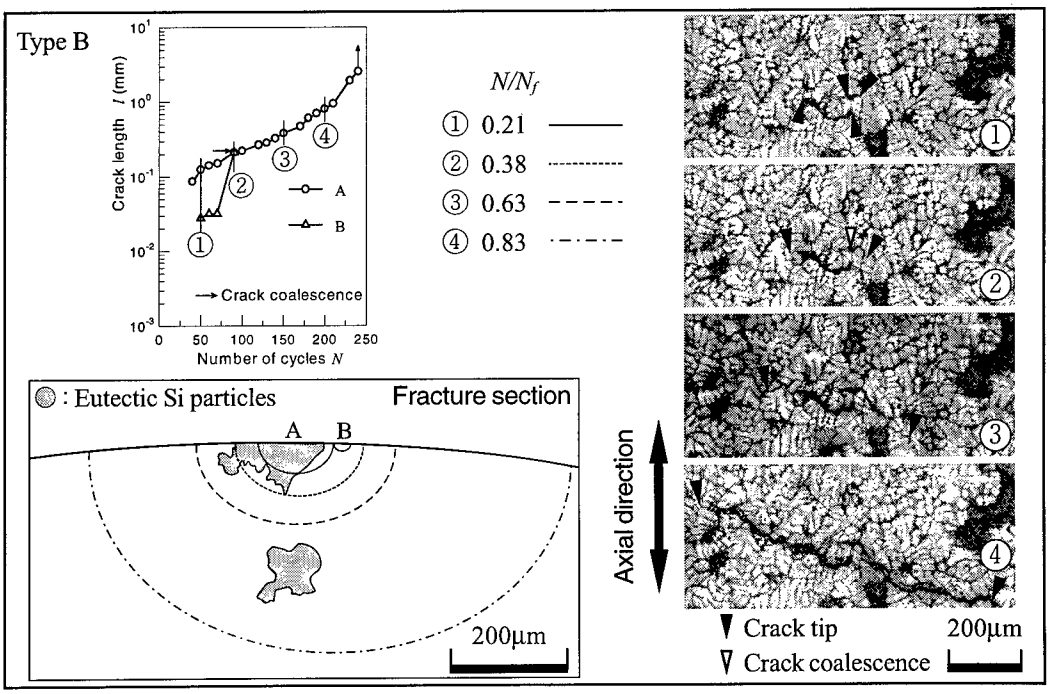


Fig.8 Observation of crack propagation behavior in Type B of AC4CH ($\Delta\varepsilon_p = 0.01$)

shows the same crack growth rate as that in Type A until the crack length become to be about 200 μm (②). However, after that, in the inside of specimen, the crack is propagated in the matrix region and the crack growth rate slows down. At this time, the number of cycles corresponds to the changed point (②) of the crack growth curve.

Thus, it is considered that AC4CH on low cycle fatigue has two kinds of crack growth rate depending on two different crack propagation routes in the inside of specimen. That is, AC4CH has the same crack growth rate as A6061-T6 if the crack is propagated on the matrix part. The crack growth rate in AC4CH is faster than that in A6061-T6 if the crack is propagated through the high density region of eutectic silicon particles. This is because the crack is propagated on the interface between eutectic silicon particles and grain boundary. In AC4CH, interface easily separates off on low cycle fatigue tests accompanied by repeated plastic deformation.

In high cycle fatigue, eutectic silicon particles became the fracture origin and they acted as resisting factors for crack propagation [6]. However, on low cycle fatigue, eutectic silicon particles became not only the fracture origin but also the accelerated factor of the crack growth rate. That is, eutectic silicon particles shorten the fatigue life and they act as the cause of scatter.

4. CONCLUSIONS

We carried out low cycle fatigue tests and investigated crack propagation behavior in detail by observing surface and fracture section using AC4CH and A6061-T6. The main results obtained are as follows :

(1) On low cycle fatigue, AC4CH has two kinds of crack growth rate depending on two different crack propagation routes. That is, AC4CH has the same crack growth rate as A6061-T6 if the crack is propagated on the matrix region. The crack growth rate in AC4CH is faster than that in A6061-T6 if the crack is propagated through the high density region of eutectic silicon particles.

(2) On low cycle fatigue, the shape of crack in AC4CH is ellipsoidal, which is similar to those in the general metal materials.

(3) On low cycle fatigue, eutectic silicon particles shorten the fatigue life and they act as the cause of scatter.

REFERENCES

1. K. Morino, et al., Trans. Jpn. Soc. Mech. Eng., **65**-640, A(1999), 2524-2529.
2. H. Egashira, et al., J. JILM. **39**, (1989), 886-892.
3. N. Kawagoishi, et al., Trans. Jpn. Soc. Mech. Eng., **55**-516, A(1989), 1733-1739.
4. K. Shiozawa, et al., Trans. Jpn. Soc. Mech. Eng., **57**-538, A(1991), 1279-1286.
5. K. Shiozawa, et al., Trans. Jpn. Soc. Mech. Eng., **58**-547, A(1992), 341-347.
6. N. Kawagoishi, et al., Trans. Jpn. Soc. Mech. Eng., **60**-570, A(1994), 358-363.
7. K. Shiozawa, et al.,Trans. Jpn. Soc. Mech. Eng., **60**-571, A(1994), 663-670.
8. K. Morino, et al.,Trans. Jpn. Soc. Mech. Eng., **60**-571, A(1994), 682-689.

Key Engineering Materials Vols. 183-187 (2000) pp. 1023-1028
© 2000 Trans Tech Publications, Switzerland

Reliability Analysis of Ship Hull Girders Considering the Degradations of Corrosion and Fatigue

Hai-Hong Sun[1], Guo-Hong Liao[1] and Yong Bai[2]

[1] School of Naval Architecture and Civil Engineering, Wuhan Transportation University, Wuhan 430063, China P.R.

[2] School of Science and Technology, Stavanger College, P.O. Box 2557 Ullandhaug, N-4004 Stavanger, Norway

Keywords: Corrosion and Fatigue, Progressive Collapse, Response Surface Method, Sensitivity Analysis, Ship Hull Girders, Time-Variation Reliability Assessment

ABSTRACT

The reliability analysis based on ultimate strength of midsection for ship hull girders subjected to degradations due to corrosion and fatigue is presented in this paper. The corrosion is considered a random process with a constant mean value and the crack propagation is predicted based on *Paris-Erdogen* equation. 'Failure' occurs when the combined value of stillwater and wave-induced bending moments exceeds the ultimate strength of hull girders. The time-variation reliability for a bulk carrier ship hull girder is quantified. The purpose of this analysis is to discover the information, which can be used for risk assessment relative to decisions on corrosion and fatigue margins during the ship's life by ship owners and rule societies.

1. INTRODUCTION

Structural failure of ship hull girders due to extreme bending moments is the most catastrophic event. The rules given by the classification societies have to assure that the probability of this event is sufficiently low. In order to estimate the probability of failure it is necessary to address not only the random nature of the maximum bending moment the ship undergoes, but also the random nature of the ultimate strength of ship hull girders [1].

The ultimate strength of ship hull girders usually degrades due to corrosion and fatigue. Both the bending moment the ship undergoes and the hull ultimate strength need to be described with stochastic processes. The time-variation reliability assessment should be concentrated in [2-5].

The time-variation reliability assessment relative to the ultimate strength of the midsection for ship hull girders subjected to the degradations of corrosion and fatigue is presented in this paper. The corrosion effect is considered a random process with a constant mean value and the crack propagation is predicted based on *Paris-Erdogen* equation. 'Failure' occurs when the maximum combined value of stillwater and wave-induced bending moments exceeds the ultimate strength of hull girder. The *Ferry-Borges* method is applied to combine the two stochastic processes of stillwater and wave-induced bending moments. A simplified method of computing the ultimate value of the longitudinal bending moment of the midsections from the progressive collapse analysis of the hull girder is introduced. Since the limit state function is expressed implicitly and has a nonlinear form, an effective response surface approach is used to evaluate the failure function at checking points based on the method from Bucher and Bourgund[6] and a modified Monte Carlo simulation to evaluate the failure probability[7]. As a demonstration, the results of time-variation

reliability assessment are provided for a bulk carrier hull girder.

2. TIME-VARIATION RELIABILITY METHOD

In the present study, ship hull collapse due to vertical bending moment is only take into account. The limit state function at any time t is given by

$$g(\mathbf{x}|t) = C_u M_u(t) - C_p[\phi_s M_s(t) + M_w(t)] \tag{1}$$

where $M_u(t)$ is the ultimate strength, $M_s(t)$ and $M_w(t)$ are the stillwater and wave-induced bending moments respectively; C_u and C_p represent the model errors in predicting the hull's ultimate strength and combined total bending moment the ship experiences; φ_s is the load combination factor of still water bending moment.

The failure probability at the service time T is expressed by

$$P_f(T) = \int_0^T \left[\int_{g(\mathbf{x}|t)<0} \cdots \int f_X(\mathbf{x}|t) d\mathbf{x} \right] f_T(t) dt \tag{2}$$

where $f_X(\mathbf{x}|t)$ is the joint probability density function; $f_T(t)$ is the probability density function of occurrence time T, which is assumed as a uniform distribution, $f_T(t) = 1/T$. Therefore, Eq.(2) can be rewritten by

$$P_f(T) = \frac{1}{T} \int_0^T P_f(t) dt \tag{3}$$

where $P_f(t)$ is the conditional failure probability at time t, defined by

$$P_f(t) = \int_{g(\mathbf{x}|t)<0} \cdots \int f_X(\mathbf{x}|t) d\mathbf{x} \tag{4}$$

The corresponding conditional reliability index is obtained by

$$\beta(t) = \Phi^{-1}[P_f(t)] \tag{5}$$

3. LOAD EFFECTS AND COMBINATION

Ships are generally subjected to combined actions of stillwater and wave-induced bending moments. Stillwater bending moment (SWBM) is likely to change at each departure and smaller changes may occur during a voyage. However, it varies from one condition to another due to loading patterns and human action and needs to be considered as stochastic process in long term. Wave-induced moment (VWBM) is the result from the wave action. Due to the random nature of ocean, it is stochastic process both in short-term and long-term.

Statistical analysis of SWBM has been addressed since 1970s. Many authors reported that maximum SWBM was approximately fitted as normal distribution[8-9]. These analyses were centered on the mean and COV of SWBM in the critical midsection of a ship.

At present, a Poisson rectangular pulse process in time domain may model the SWBM. Its cumulative distribution at any time is fitted by a normal distribution and is given by

$$\Phi_{M_s}(M_s) = \frac{1}{\sqrt{2\pi}\sigma_{M_s}} \int_0^{M_s} \exp\left[-\frac{1}{2} \left(\frac{M_s - \mu_{M_s}}{\sigma_{M_s}} \right)^2 \right] dM_s \tag{6}$$

where μ_{M_s} and σ_{M_s} are the mean and standard variance. When the COV of SWBM, $\xi_{M_s} = \sigma_{M_s}/\mu_{M_s}$, is determined, μ_{M_s} can be given at $1/\nu_s T_0$ exceedance level

$$\mu_{M_s} = \frac{M_{s,0}}{1+\xi_{M_s}\Phi^{-1}(1-\frac{1}{\nu_s T_0})} \tag{7}$$

where ν_s is the mean arrival rate of one load condition and $M_{s,0}$ is the specified maximum SWBM in a design lifetime of T_0=20 years which can be determined by DnV rule[10].

The CDF for the largest of the individual SWBM can be found for a total of the $\nu_s T$ repetitions using the extreme theory,

$$F_{M_{s,T}} = \left[F_{M_s}(M_s)\right]^{\nu_s T} \tag{8}$$

Many research efforts have been made on the prediction of VWBM experienced on the ship hulls using linear and nonlinear methods. VWBM is naturally stochastic process and may be described by either short-term or long-term statistics. The long-term VWBM is based on the weighted short-term statistics. It is generally accepted that the long-term VWBM can be modeled as a Poisson process and the peak of each individual VWBM, M_w, can be well approximated by a Weibull distribution.

$$F_{M_w}(M_w) = 1-\exp\left[-\ln(\nu_w T_0)\left(\frac{M_w}{M_{w,0}}\right)^{h_w}\right] \tag{9}$$

where ν_w is the mean arrival rate of one wave cycle; h_w is the shape parameter varying from 0.9 to 1.1 and reasonably taking 1.0 as a representative value; $M_{w,0}$ is the maximum VWBM in the reference design period T_0=20 years. Similar to that of SWBM, the CDF for the largest of the individual VWBM can be found for a total of the $\nu_w T$ repetitions,

$$F_{M_{w,T}}(M_w) = [F_{M_w}(M_w)]^{\nu_w T} \tag{10}$$

In the existing ship rules, the maximum SWBM and VWBM occur at the same time, but actually they are not necessary. Based on *Ferry-Borges* method, the CDF of the combined bending moment is expressed as following

$$F_{M_t}(M_t) = \int_0^{M_t} \frac{\phi_{M_s}(M_t - u)du}{1+\nu_w/\nu_s[1-F_{M_w}(u)]} \tag{11}$$

The maximum combined bending moment at a given period T is obtained by

$$F(M_t) = 1-1/\nu_s T$$

The load combination factor for SWBM , φ_s is given by

$$M_{t,T} = M_{w,T} + \varphi_s M_{s,T} \tag{12}$$

4. A SIMPLIFIED METHOD FOR ULTIMATE STRENGTH

A simplified method to compute the ultimate value of the longitudinal bending moment at the midsection of ship hull girders is introduced, which is similar to Ref.[11], but the formulas of the effective width of plating from Guedes Soares [12] and the beam-columns in the large post-collapse

region are adopted. It can take account of all the manufacturing residual imperfections including deflection and stress of plating and column. The detailed description was given in Ref.[5].

To predict the crack propagation and fatigue life, the *Paris-Erdogan* equation is used. Crack size is determined by the integration of *Paris-Erdogan* equation

$$a(t)=[a_0^{(1-m/2)}+(1-\frac{m}{2})C(\Delta\sigma Y\sqrt{\pi})^m \nu_0 t]^{\frac{1}{1-m/2}} \tag{13}$$

where a is the crack size; ν_0 is the mean zero upcrossing rate; $\Delta\sigma$ is the stress range; Y is the geometry function; C and m are material parameters.

The complete fatigue life T_f is equal to the sum of the time to crack propagation T_p with the time to crack initiation T_i[13],

$$T_i = kT_p \tag{14}$$

where k can vary between 0.1 to 0.15. The crack size is assumed to have a normal distribution.

Corrosion is another degradation effect for steel ships. Corrosion does not occur as long as the anti-corrosive paint coating remains effective. Usually the paint coating life T_o is assumed to be fitted by a Weibull distribution

$$f(T_o)=\frac{\alpha}{\beta}\left(\frac{T_o}{\beta}\right)^{\alpha-1}\exp\left[-\left(\frac{T_o}{\beta}\right)^{\alpha}\right] \tag{15}$$

The corrosion effect is considered a random process with a constant annual corrosion rate after the paint coating life. For the present calculation, the distribution parameters are $\alpha=2$ and $\beta=4.2$.

5. A RESPONSE SURFACE METHOD

Since the limit state function $g(\mathbf{x}|t)$ is expressed implicitly and has a nonlinear form, the evaluation of the failure probability requires expensive computational effort integrating Eq.(4) and the response surface method is applied.

At present, a response surface with a polynomial type function including squared terms but not cross terms is adopted,

$$G(\mathbf{x})=a+\sum_{i=1}^{r}b_i x_i+\sum_{i=1}^{r}c_i {x_i}^2 \tag{16}$$

where r is the number of basic random variables; $\mathbf{x}=(x_1,x_2,\cdots,x_r)$ is the basic random vector; a,b_i,and c_i are the unknown coefficients that can be determined using $2r$+1 sampling points. The sampling points are selected to be located at the design point $(\bar{x}_1,\bar{x}_2,\cdots,\bar{x}_r)$ and other $2r$ points $(\bar{x}_1,\cdots,\bar{x}_i\pm f\sigma_i,\cdots,\bar{x}_r)$, where f is a parameter determining the upper and lower bounds of selection range. This process should be iterative to guarantee that the sampling points chosen from the new design point include the information from the original failure surface sufficiently. Once the response surface is defined, the failure probability is computed using modified Monte Carlo simulation technique [7].

6. TIME-VARIATION RELIABILITY ASSESSMENT

The time-variation reliability estimation for a bulk carrier hull girder subjected to the degradations of corrosion and fatigue is demonstrated. The relevant principal particulars of the bulk carrier are listed in table 1. The midship hull girder is shown in Fig.1.

Table 1: The principal particulars

Description	Value
Length, between perpendiculars	218.0m
Breadth, molded	32.2m
Depth, molded	18.7m
Block coefficient	0.816
Transverse web frame spacing	4.25m

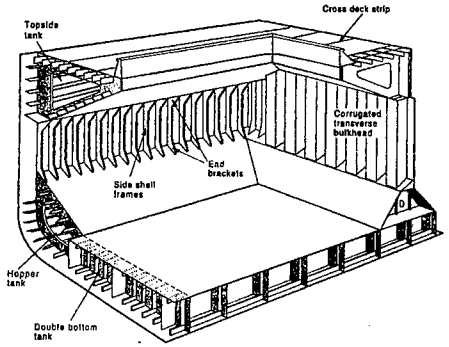


Fig.1 Midship hull girder

Because the sagging failure mode is more critical, the results of the bulk carrier in sagging condition are only emphasized on.

The COV of SWBM is assumed 0.4 and the mean value is $0.47M_{s,0}$ from Eq.(7). The combination factor of still water bending moment, φ_s, with the one-year reference period is 0.80.

The mean moment-curvature response for this ship at the 15th service year is shown in Fig.2. The maximum moment value is 3,104.37 MNm.

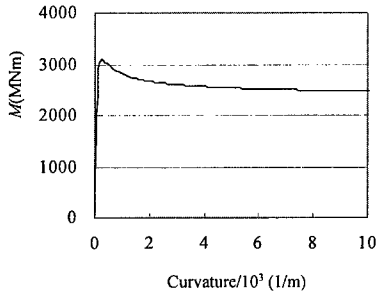


Fig.2 Mean moment-curvature

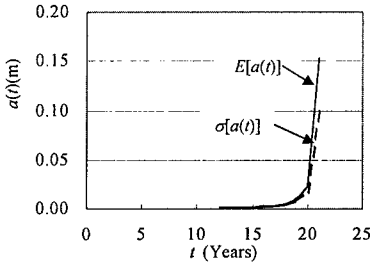


Fig. 3 Crack size

The crack size of a stiffened panel in the deck with time is shown in Fig.3. The mean ultimate strength with time is shown in Fig.4. The ultimate strength has a smooth decrease before the 20th service year. But at the 20th service year, the mean ultimate strength has a sudden drop-off since the crack size has a sharp increase.

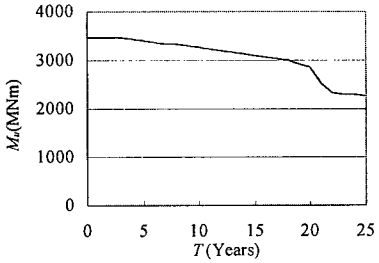


Fig.4 Mean ultimate strength

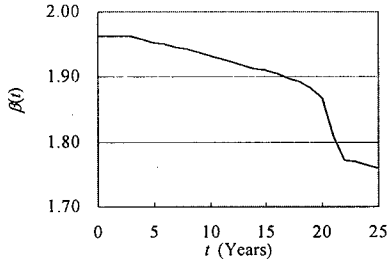


Fig.5 Conditional reliability index

Fig. 5 shows the conditional reliability index. The reliability index ranges between 1.96 and 1.87 during 20 service years and the corresponding failure probability ranges between 2.49×10^{-2} and 3.08×10^{-2}. A sudden drop-off of reliability index exists at the 20th service year similar to the ultimate strength. Therefore very detailed inspection should be carried out for the fatigue damage when the service years of the bulk carrier is over 20.

7. CONCLUSIONS

Time-variation structural reliability assessment of ship hull girders relative to the ultimate strength requires the consideration of the following three aspects: (1) load effects and their combination, (2) the hull ultimate strength, and (3) methods of reliability analysis.

In this paper, the *Ferry-Borges* method is applied to combine the two stochastic processes of stillwater and wave-induced bending moments. A simplified method to compute the ultimate value of the longitudinal bending moment at the hull midsection is introduced, which can take account of all manufacturing imperfections. The corrosion is considered a random process with a constant mean value and the crack propagation is predicted based on *Paris-Erdogen* equation. An effective response surface approach is used to evaluate the failure function at sampling points and a modified Monte Carlo simulation technique to evaluate the failure probability. The time-variation reliability is quantified for a bulk carrier hull girder. It is found that the ultimate strength and reliability index have a smooth decrease before the 20th service year. But at the 20th service year, they have a sudden drop-off since the crack size has a sharp increase. The analytical results can be used for risk assessment relative to decisions on corrosion and fatigue margins during the ship's life by ship owners and rule societies.

REFERENCES

1. A E.Mansour, Assessment of reliability of ship structures, Ship Structure Committee, SSC-398(1997)
2. C.Guedes Soares and Y.Garbatov, Journal of Ship Research, **43**(1999) p.65-78
3. P.H.Wirsching, et al, Marine Structures, **10**(1997) p.501-518
4. G.Casella and E.Rizzuto, Marine Structures, **11**(1998) p.373-399
5. H.H.Sun, T.Y.Xiao and S.K.Zhang, 18th OMAE, St. Johns, Canada(1999) OMAE-99-6007
6. C.G.Bucher and U.A.Bourgound, Structural Safety, **7**(1990) p.57-66
7. H.H.Sun and T.Y.Chen, ISOPE-97, Montreal, Canada , **4**(1997) p.361-366
8. C.Guedes Soares, Structural Safety, **8**(1990) p.353-368
9. A E.Mansour, Probability based ship design procedures: loads and load combination, Ship Structure Committee, SSC-373(1994)
10. X.Wang, G.Jiao and T.Moan, SNAME Transaction, **104** (1996) p.3-30
11. M.K.Rahman and M.Chowdhury, Journal of Ship Research, **40**(1996) p.244-257
12. C.Guedes Soares, Journal of Construction Steel Research, **9**(1988) p.287-310
13. Bureau Veritas, Cyclic fatigue of steel ship weld joints(1984)

Key Engineering Materials Vols. 183-187 (2000) pp. 1029-1034
© 2000 Trans Tech Publications, Switzerland

Fatigue Analysis of Vane Components for Gas Turbine Engine

J.H. Kim[1], K.H. Kim[1], K.K. Joung[1], K.C. Ham[2], J.I. Song[3] and S.I. Bae[3]

[1] Engine Engineering Center, Samsung Aerospace,
28 Sungju-dong, Changwon, Kyongnam 641-716, Korea

[2] Department of Machine Design, Inha Technical Junior College,
4 Yonghyun-dong, Nam-gu, Inchon 402-752, Korea

[3] Department of Mechanical Engineering, Changwon National University,
9 Sarim-dong, Changwon, Kyongnam 641-773, Korea

Keywords: Fatigue Test, Gas Turbine, Inconel 718, Life Prediction, Notch Sensitivity Factor, S-N Curve, Vane Components

ABSTRACT

Causes of vibration of gas turbines include the path of flow media, the unbalance of rotor, and miscellaneous effects of other components and the vibration may lead the vane components to fatigue failure. In this case the fatigue phenomena is high frequency and it is a major cause of failure of the vane components at relatively low stress level. In this paper, dynamic characteristics of vane components such as natural frequency and mode shape are measured and used for the fatigue test. Material of the vane is Ni based Inconel 718 and fatigue limit and 95% reliability fatigue limit are obtained. These values are used for prediction of the life of the vane. Comparison of the results of the fatigue test of the vane components with S-N curve of the bulk material reveals that the notch sensitivity factor is lower than 1.

1. INTRODUCTION

For the design of blade or vane components of a gas turbine, the possibility of fatigue failure is occurred by the media in flow path and the resonance phenomena is the most important point to consider a material failure. The vane is exited periodically during the operation of the gas turbine by the interference of flow fields and the evaluations of structural stability and dynamic characteristics of the vane are necessary[1,2]. Especially, the failure of only one vane may occur the failure of the total system of gas turbine engine which has hundreds of blade and vane[3]. The evaluation and certification of the strength of vanes and blades are necessary but they are expensive and time-consuming processes.

The dynamic characteristics of vane components such as natural frequency and mode shape are measured[4], and the fatigue test is executed by using these characteristics. The vane is fixed in a fixture and excited with resonance of 1st natural frequency. The stress distribution of vane components is analyzed by finite element program and the calibration test of vane components are

executed. The results of fatigue test are plotted in S-N curve behavior using finite element analysis results and compared with the S-N curve of the material.

2. EXPERIMENTAL PROCEDURE

2.1 Dynamic Characteristics of Vane Components

Block diagram of experimental device for dynamic characteristics of vane components in gas turbine, such as natural frequency and mode shape, is represented in Fig.1. A non-contact laser sensor is used as the displacement sensor for vibration measurements. It is connected to FFT analyzer and A/D converter through the signal conditioner. The signal from impact hammer is also connected as the same manner with the displacement sensor. The modal parameter and mode shape are obtained from the frequency response function[4].

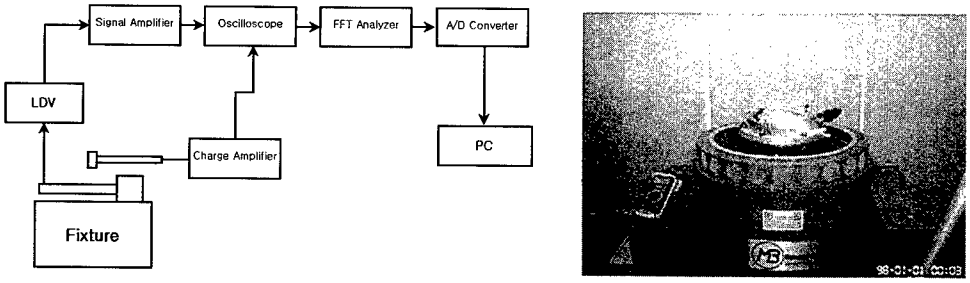


Fig. 1. Block diagram of the compressive vane component for dynamic characteristics

Experimental procedure in this study is as follows. (1) The experimental apparatus is represented in Fig.1. (2) Points for impact and measuring are selected to measure the natural frequency and mode shape. (3) After fixing a vane to the fixture, the velocity of vane is measured from the signal of impact hammer through the frequency range of interest. (4) Then the natural frequency and mode shape are obtained by impacting the selected positions as shown in Fig.2.

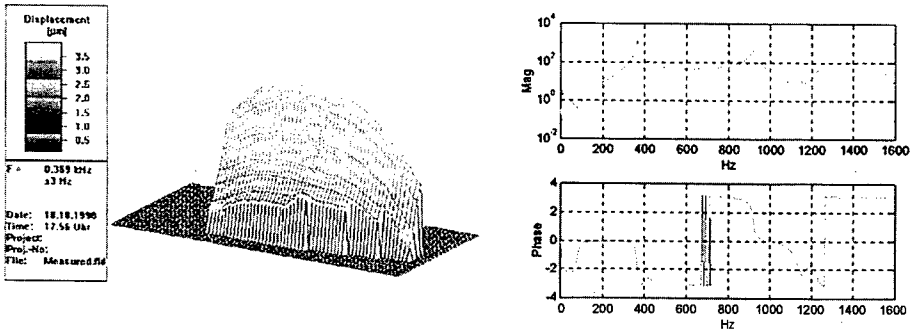


Fig. 2. Mode shape and natural frequency of vane components

2.2 Material Properties of Vane Components

Inconel 718 is used as the material of vane of gas turbine. The compositions of Inconel 718(AMS5663) material are represented in Table 1 and mechanical properties of the material are represented in Table 2.

Table 1. Compositions of Inconel 718(AMS5663) material

Composition	Ni	Cr	Mo	Cb	Ti	Al	Fe	C	Ta	Others	Remark
Ratio(%)	52.5	19.0	3.0	5.1	0.90	0.50	18.0	0.05	0.10	0.85	solution & precipitation heat treated

Table 2. Mechanical properties of Inconel 718(AMS5663) material at room temperature

Specimen Orientation	Tensile Strength (ksi)	(MPa)	0.2% Yield Strength (ksi)	(MPa)	Elongation in 4D(%)	Reduction of Area(%)	Remark
L	185	1276	150	1034	12	15	Determined in accordance with ASTM E 8 L:longitudinal T: transverse
L-T (Forgings)	180	1241	150	1034	10	12	
T (Bars)	180	1241	150	1034	6	8	

2.3 Stress Analysis of Vane Components

ABAQUS which is a commercial finite element analysis program is used to analyze stress distribution of vane components. The HEXA8 element is used for precise analysis. The numbers of node and elements are 14834 and 10818 respectively. The equivalent stress of vane at the moment of resonance state is represented in Fig. 3. And the position of maximum stress and the position of strain gauge attachment are also represented in Fig. 3. It is revealed that the maximum von-Mises stress at the maximum stress position is 2.57 times greater than that of the position of strain gauge from this figure.

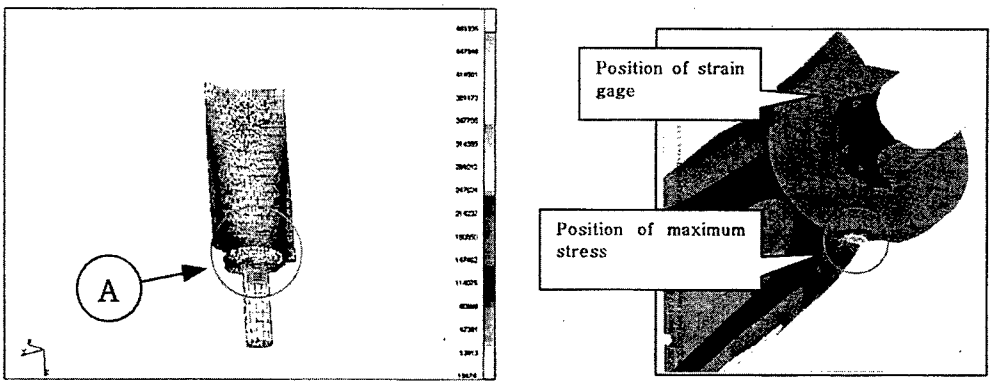
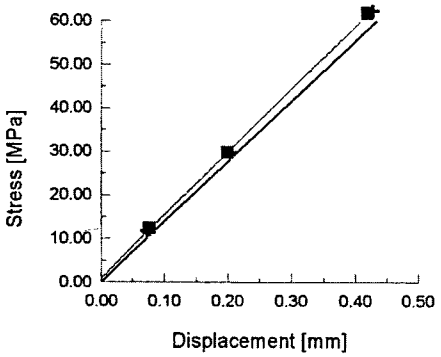


Fig. 3. Von Mises stress of vane components. (Analized by ABAQUS)

2.4 Calibration tests of vane components

Because of the early failure of strain gauge, the displacement or speed of tip of the vane must be used to measure the fatigue stress[6]. So the calibration test is executed to obtain the relation of fatigue stress at the position of strain gauge and the displacement of tip of the vane. The strain gauge is attached at the position where it could be attached to, that is at the maximum root thickness position as represented in Fig.3 and Fig.4. The strain gauge of the model number CEA-06-032UW-120 is used. The length of strain gauge is 0.3mm, the gauge factor is 2.08, and the repeatability is 10^5 cycle at the strain control condition of $\pm$ 1,500μ ε . The results of calibration test are represented in Fig. 4. The reason of the variation of the data is that the thickness of vane was different for each other according to the length, so the displacement was different each other. We used each curve for the calculation of fatigue stress.



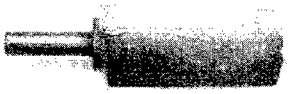
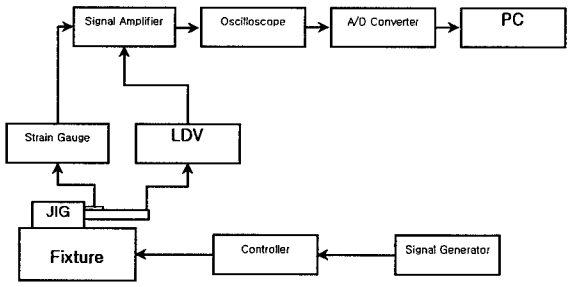


Fig. 4. Stress and displacement relation of vane components.

2.5 Fatigue Test of Vane Component

The results of the calibration test of vane components are compared with the results of finite element analysis. The maximum stress is occurred at the surface position where the gas pressure is applied and is 2.57 times greater than that of the position in which the strain gauge is attached. The 1st natural frequency in analysis is 388.7Hz and shows good agreement with experimental data. And the direction of crack extension is 45 degrees with the principal direction at the maximum stress site. In this research, we had defined that the fracture is occurred at the instance when the 1st natural frequency is 2 % less than that of starting instance.



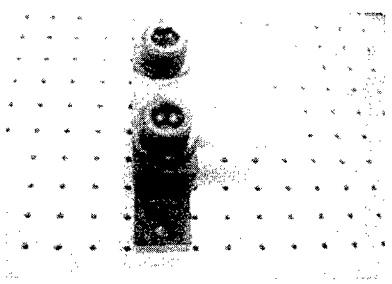


Fig. 5. Block diagram of fatigue test and calibration.

The vane component fatigue tests are performed as follows. (1) The specimen is fixed to the fixture. (2) The value of displacements corresponding to the expected fatigue stress is calculated with referencing the calibration value. (3) The stress and vibration frequency are measured from experiment that is executed by exciting the specimen to 1st natural frequency. (4) If the specimen is failed less than the 10^7 cycles, the level of stress in next experiment is lower than that level. And if the specimen is not failed until the 10^7 cycles, the level of stress in next experiment is higher than that level.

3. RESULT AND DISCUSSION

The test results of 10 specimens are represented in Table 3. The fatigue cracks are initiated at the maximum stress position. Some cracks are produced in leading and trailing edges. The test is executed in 6 stress levels, and the S-N curves are represented in Fig. 6. The fatigue limit in 1×10^7 cycles is 284 MPa, and 223 MPa is calculated as 95% reliability fatigue limit at strain gauge position. The stress ratio at the maximum stress site with strain gauge position is 2.57. So the fatigue limit in maximum stress position is calculated and represented in Table 4. and Fig. 6. The fatigue limit at maximum stress position in 1×10^7 cycles is 732 MPa, and 575 MPa is calculated as 95% reliability fatigue limit[7].

The S-N curve from component fatigue test is a little higher than that of material. The maximum stress was calculated from the stress concentration, but the real fatigue strength at the notch position is less than that of stress concentration. From the results above, it is confirmed that the notch sensitivity factor, i.e., the ratio of notch fatigue factor with stress concentration factor, is lower than 1.

Table 3. Results of vane components fatigue test

Levels	Stress at strain gauge(MPa)	Maximum Stress(MPa)	No. of cycles (10^5)	Frequency (Hz)	Position of crack	No. of specimen
1	414	1032	3.00	361.2	maximum stress	#080
			5.00	380.7	maximum stress	#200
2	379	948	2.50	379.2	maximum stress	#120
			3.50	363.7	maximum stress	#030
3	345	862	3.00	371.1	Trailing Edge	#230
			3.30	366.4	maximum stress	#090
4	328	818	6.57	365.1	maximum stress	#220
5	310	775	1.30	376.4	maximum stress	#150
			7.60	383.8	Leading Edge	#070
6	276	690	1.00	362.0	Did not Fail	#050

Table 4. Fatigue strength analysis

Positions	mean value of fatigue strength (ksi)	(MPa)	95% reliability fatigue strength (ksi)	(MPa)
Strain gage attachment	41.2	284	32.3	223
Maximum stress	106.1	732	83.3	575

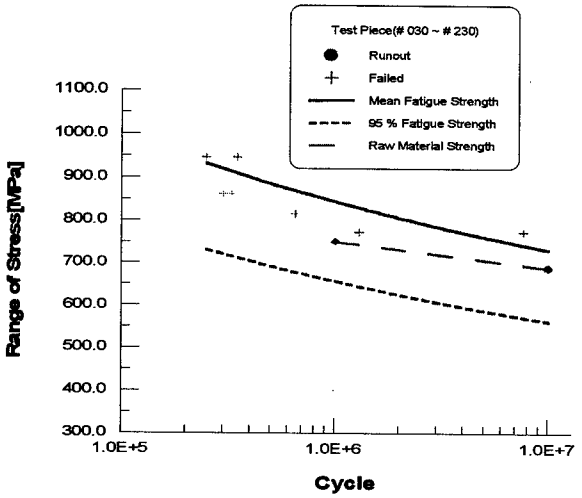


Fig. 6. S-N curve of vane components.

4. CONCLUSIONS

In this paper, the fatigue test of vane components in gas turbine is executed using dynamic characteristics such as resonance and natural frequency. The results in this study are as follows.

(1) The components fatigue tests using resonance phenomena are executed successfully and the fatigue life prediction in a design state could be possible.

(2) Fatigue limit and 95% reliability fatigue limit are obtained and those values will be used for the life prediction of the vane components.

(3) From the comparison the vane component fatigue test with the S-N curve of bulk material, it is confirmed that the notch sensitivity factor is lower than 1.

REFERENCE

1. U. Wahlen, I. Sjunnesson, and P. Groth, AIAA, (1997)
2. Jeffrey S. Turcotte, AIAA, **98-1850**
3. A.L.Berne, T.V.Dementieva, "Determination of Dynamic Force in Blades with Ring Lock"
4. Ewins, D. J., "Modal Testing : Theory and Practice. ", Research Studies Press Ltd. (1986)
5. Inman, Daniel J., "Engineering Vibration.", Prentice-Hall (1994)
6. H.E.Frankel, M.N.Torrey and C.A.Moyer, ASTM Special Technical Publication **91-A** (second Edition)
7. Kurt L. Nichol, "Numerical strain gage Representation", AIAA, **98-1720**

Key Engineering Materials Vols. 183-187 (2000) pp. 1035-1040
© 2000 Trans Tech Publications, Switzerland

Fatigue Crack Growth Simulation and Estimation for Rolling Contact

M. Akama[1] and I. Susuki[2]

[1] Materials Technology Development Div., Railway Technical Research Institute,
2-8-38, Hikari-cho, Kokubunji-shi, Tokyo 185-8540, Japan

[2] Structures and Materials Research Center, National Aerospace Laboratory,
7-44-1, Jindaiji Higashi-machi, Chofu-shi, Tokyo 182-8522, Japan

Keywords: Crack Propagation, Mixed Mode Loading, Rolling Contact Fatigue

ABSTRACT

Rolling contact fatigue is still an important problem in various mechanical applications. So a method was developed and prepared to observe the fatigue crack propagation under mixed mode of I and II which can simulate rolling contact conditions by an in-plane biaxial fatigue machine. In the experiments, simplified cycles were applied to the analysis of rolling contact fatigue cracks including the effect of water trapped inside the cracks. Growth rate law was obtained by means of least square regression analysis in terms of the effective stress intensity factor range. The criterion for the branching of these cracks under the mixed mode loading was presented. The effects of heat treatment of steel were also investigated.

1. INTRODUCTION

Wheel shelling and squats of rail are the loss of large pieces of metal from wheel treads and rail head as a result of wheel-rail rolling contact fatigue. This kind of crack develops easily inside them when water exists. The subject is related to both safety and costly problems for the railway industry. If the rate of growth of these cracks can be calculated accurately, appropriate action will be taken to maintain the integrity of wheel and rail, and save considerable amounts of cost. So the fatigue tests are performed to obtain the fatigue crack growth rate and the criterion for the branching under the mixed mode I and II loading cycles which can simulate rolling contact conditions by an in-plane biaxial fatigue machine using wheel and rail steels. In these tests, simplified cycles are applied to the analysis of rolling contact fatigue cracks including the effect of water trapped inside the cracks. The effects of heat treatment of steel are also investigated.

2. EXPERIMENTAL PROCEDURE

2.1. Biaxial Fatigue Machine

An in-plain biaxial testing system was prepared for the investigation of crack propagation under mixed mode conditions. This biaxial testing machine consists of four hydraulic actuators of

200kN(tension/compression) capacity each for static and fatigue loads. These four actuator assemblies make two pairs, and are rigidly mounted in an octagonal box-shaped frame diagonally (Fig.1). The frame is of heavy duty welded construction, and placed horizontally. A load cell and a linear variable differential transformers are installed in each actuator assembly. The components include four hydraulic actuator assemblies, manifolds, a control console and a hydraulic pump unit. To obtain and keep the designated stress ratios during fatigue tests, an improved control system was developed and introduced into this work. Two pairs of actuators were controlled by feed-back signals of not only load signals but also by the positioning ones.

2.2. Specimen and Applied Loading

Specimen and applied loading were referred to in the study by Wong et al. [1]. A cruciform specimen with a 45° inclined center crack was used. It has a uniformly stressed square working section,

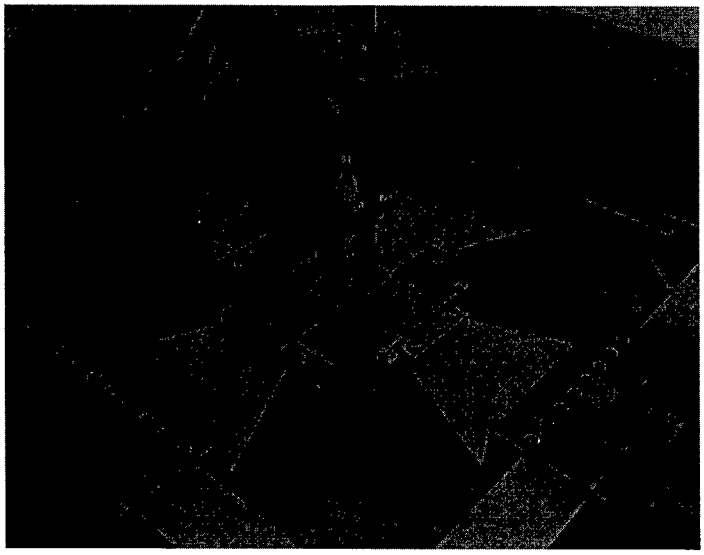


Fig.1 Biaxial testing machine

Table 1. Chemical composition and heat treatments of specimens

C	Si	Mn	P	S
0.65	0.26	0.73	0.016	0.01

(both wheel and rail steel)

Austenitize	Isothermal transformation
860℃×2hour	490℃×7hour

(wheel steel only)

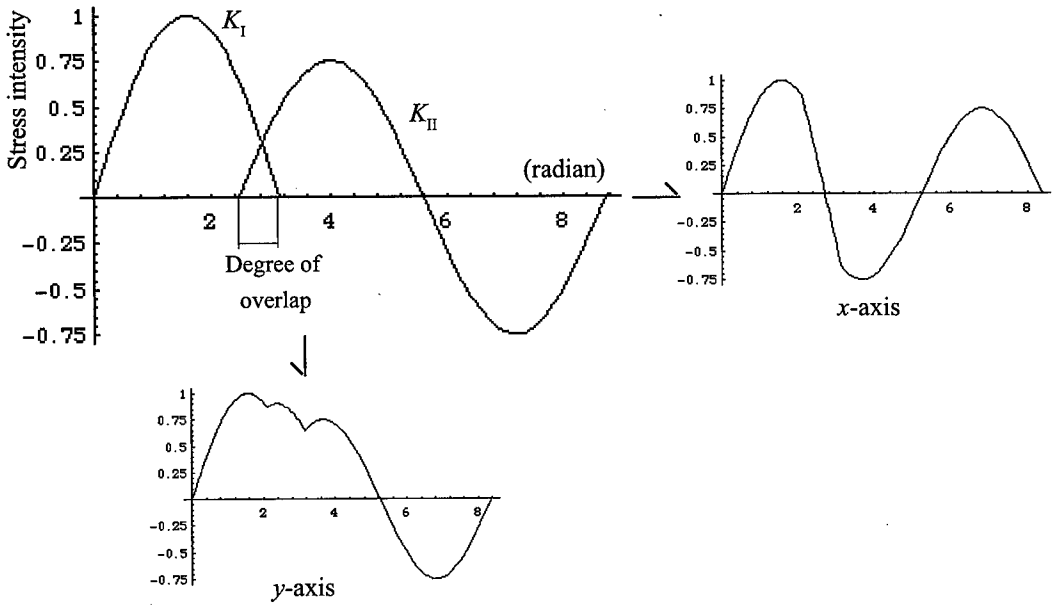


Fig.2 Applied sequential loading cycle
($\Delta K_{IInom} / \Delta K_{Inom}$=1.5, overlap = 60 °)

Table 2. Experimental conditions

	Rail	Wheel
$\Delta K_{IInom} / \Delta K_{Inom}$	1.0, 1.5, 1.6, 1.7, 1.8, 2.0	1.0
Degree of overlap (degree)	0, 10, 20, 30, 40, 50, 60, 70, 80, 90, 120, 150	10, 20, 30, 40, 50, 60, 70, 80, 90, 120, 150

72mm by 72mm, 4mm thickness, to observe propagation behaviors. Two kinds of steel were used as the specimen, wheel steel and rail steel. Their chemical compositions and heat treatment are shown in Table 1.

The loading history was similar to that experienced by rolling contact fatigue crack obtained from the theoretical models developed by various researchers [2 - 4]. It was simulated by actuating both axes of the biaxial machine to apply the required mode I and II load sequence to the crack. The tests were performed in dry conditions with a testing frequency of less than 1.0Hz. The loading history is shown in Fig.2. The ratios of nominal mode II stress intensity factor (ΔK_{IInom}) to nominal mode I stress intensity factor (ΔK_{Inom}), the degree of overlap between the mode I and the mode II loading cycles examined are shown in Table 2.

The effective stress intensity ranges experienced by the crack tip (ΔK_{Ieff} and ΔK_{IIeff}) were measured in each experiment. They are defined as follows:

$$\Delta K_{Ieff} = U_I \Delta K_{Inom} = U_I Y \Delta\sigma\sqrt{\pi a} \quad (1)$$

$$\Delta K_{IIeff} = U_{II} \Delta K_{IInom} = U_{II} Y \Delta\tau\sqrt{\pi a} \quad (2)$$

where $Y = \sqrt{\sec(\pi a/2W)}$; a is a half length of the crack; W is a half diagonal of the working section of specimen, and U_I and U_{II} are the closure ratio and locking ratio, respectively.

3. EXPERIMENTAL RESULTS

3.1. Crack Closure and Locking Ratio

The surface replica method was used to measure the mode I opening and mode II sliding displacements near the crack tip. Figure 3 shows the examples of crack closure and locking ratios of rail steel derived from the experiments. These were multiplied by the nominal values to obtain the effective values.

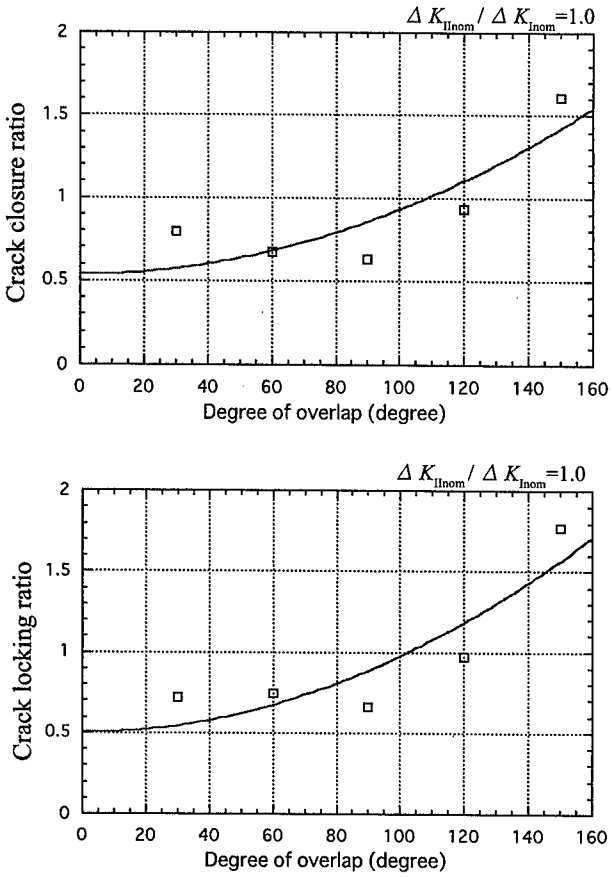


Fig.3 Crack closure ratio and locking ratio

3.2. Fatigue Crack Growth Rate under Mixed Mode Loading

Figure 4 shows the co-planar crack growth rate derived from the cruciform specimen tests for both wheel and rail steel in terms of the nominal stress intensity factor ΔK_{Inom}. The fatigue crack growth rate under mixed mode loading was assumed to be controlled by both the mode I and the mode II mechanism. Figure 5 shows the co-planar crack growth rate for rail steel in terms of both the effective stress intensity factor ΔK_{Ieff} and ΔK_{IIeff}. Wong et al. [1] proposed a model of growth rate expressed as:

$$da/dN = C\left[\Delta K_{IIeff} \times \left\{1 + \left(\Delta K_{Ieff}/\Delta K_{IIeff}\right)^m\right\}\right]^n \quad (3)$$

where C, m and n are material constants. By means of least square regression analysis, the constants

for rail steel were obtained as follows.

$$C = 4.25 \times 10^{-11}$$
$$m = 0.95$$
$$n = 2.23$$

The rate for wheel steel is higher than that for rail steel when the stress intensities are small but approximately the same when they become greater.

3.3. Crack Branching Conditions

It was understood that the co-planar crack growth can be obtained from this type of loading cycle under a suitable combination of K_{Inom} and K_{IInom}, or it branches otherwise. It can be anticipated that the ratio of $\Delta K_{\mathrm{IInom}} / \Delta K_{\mathrm{Inom}}$ and degree of overlap may be the controlling parameters for branching conditions. Figure 6 shows the boundary between co-planer crack growth and branch crack growth on the graph of $\Delta K_{\mathrm{IInom}} / \Delta K_{\mathrm{Inom}}$ against the degree of overlap for rail steel.

4. DISCUSSION

It was found that a delayed retardation behavior of crack growth occurred under some conditions. In this case, there exists a large extent of crack growth retardation even to the effective stress intensity range. In the retardation region, the fatigue crack grew in a

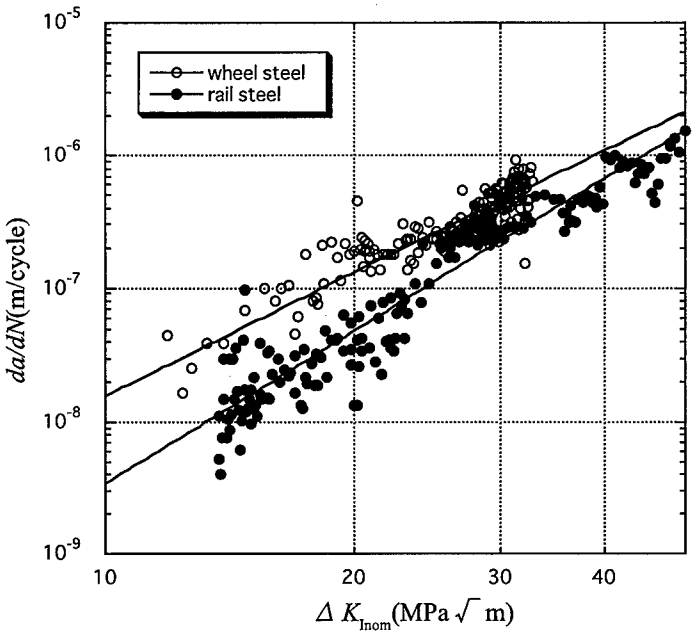


Fig. 4 Co-planar crack growth rate against nominal mode I stress intensity factor range

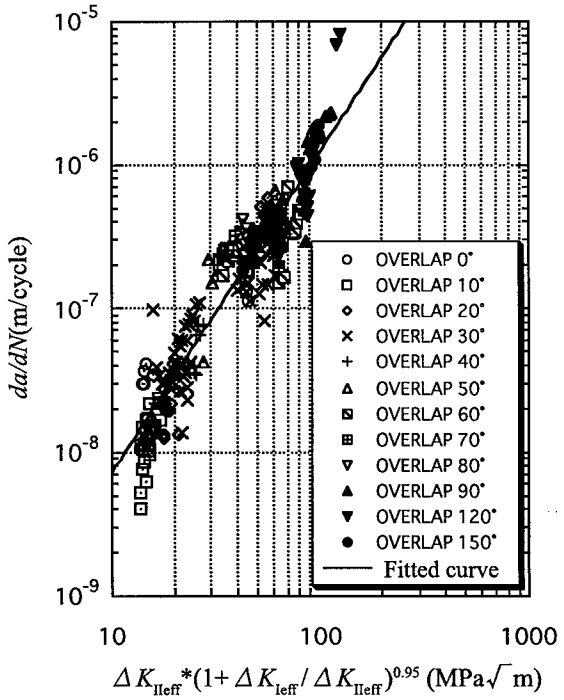


Fig. 5 Co-planar crack growth rate against effective mode I stress intensity factor range

zigzag manner in the preferential slip directions of the material. Frequent crack branching was found at small intervals of crack advance, and microscopic crack deflection was also observed. Instantaneous crack tip opening displacement (CTOD) of crack that propagated later seemed to decrease. It was thought that this instantaneous decrease of CTOD was resulted from the decentralization of crack driving force and caused the retardation of crack growth rate.

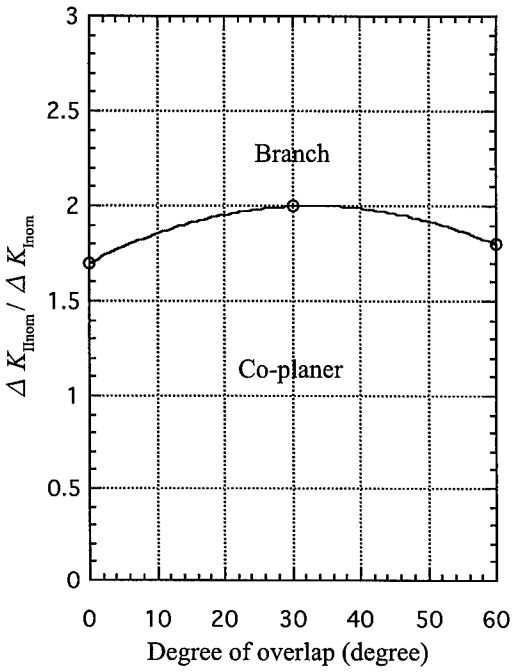


Fig.6 $\Delta K_{IInom} / \Delta K_{Inom}$ against degree of overlap

5. CONCLUSIONS

Fatigue tests were performed to obtain the fatigue crack growth rate and criterion for branching under mixed mode I and II loading cycles which can simulate rolling contact conditions by an in-plane biaxial fatigue machine using wheel and rail steels. The effects of heat treatment of steel were also investigated.

6. ACKNOWLEDGEMENTS

Authors gratefully acknowledge Mr. T. Nakata and Mr. T. Sato, students of Tokyo Denki University, who helped this study in experimental programs.

REFERENCE

1. S.L.Wong et al., Wear, **191**(1996) pp.45-53
2. L.M.Keer and M.D.Bryant, J. Lubr. Technol., Trans. ASME, **105** (1983) pp.198-205
3. A.F.Bower, J. Tribol., Trans. ASME, **110** (1988) pp.704-711
4. M.Kaneta and Y.Murakami, J. Tribol., Trans. ASME, **113** (1991) pp.270-275

Key Engineering Materials Vols. 183-187 (2000) pp. 1041-1046
© 2000 Trans Tech Publications, Switzerland

The Effect of Tensile Hold Time on the Fatigue Crack Propagation Behavior in STS 316L

J.W. Im[1] and B.S. Lim[2]

[1] Graduate School, SungKyunKwan University,
300 Chunchun-Dong, Jangan-Ku, Suwon 440-746, Korea

[2] School of Mechanical Engineering, SungKyunKwan University,
300 Chunchun-Dong, Jangan-Ku, Suwon 440-746, Korea

Keywords: Creep-Fatigue, High Temperature Fatigue Crack Growth, Hold Time, STS 316L

ABSTRACT

The heat resistant material may experience static loading, cyclic loading or both during operation. An experimental study of crack growth behavior of STS 316L austenitic stainless steel under fatigue and creep-fatigue loading conditions was carried out on compact tension specimens at various tensile hold times using trapezoidal waveform. In the crack growth experiments under hold time loading conditions, tensile hold times were ranged from 5 seconds to 100 seconds and its behavior was characterized using the ΔK parameter.

The fatigue crack growth rates generally increase with hold times. In this material, however, the crack growth rates decrease when the hold times are relatively short. This is attributed to a decline in the cyclic crack growth rate as a result of blunting at the crack tip by creep deformation.

1. INTRODUCTION

Stainless steel has good high temperature strength and corrosion resistivity and it is used for exhaust system, mold, and muffler in automobile. Especially, austenitic stainless steel has outstanding machinability, weldability, and high temperature strength. Therefore, it is widely used for high temperature equipment such as pipe and tube in power plants besides automobile [1].

Many structures or components are exposed to both static and cyclic loads. At high temperature, material damage due to creep deformation and nucleation and propagation of crack due to fatigue causes an early fracture of components. Especially, high temperature equipment such as pressure vessel, boiler, and reactor of nuclear power plants are subjected to both static loading and cyclic loading and therefore, damage occurs by creep along with fatigue [2,3].

Most materials show decrease in fatigue life as tensile hold time increases. In some other materials, however, fatigue life tends to increase when tensile hold time is relatively short.

Parida and Nicholas[4] tested Ti-24Al-11Nb, by applying 2 *sec.*, 10 *sec.*, and 100 *sec.* tensile

hold times at 649 ℃ with frequency of 1 *Hz* at the maximum load and at the minimum load. As the result, it was found that when tensile hold time was applied at the minimum load, the crack growth rate was faster than the one in pure fatigue. The reason is degradation due to increased exposure time to high temperature environment. However, when the tensile hold time was applied at the maximum load, the crack growth rate was slower than that in pure fatigue. It was concluded that this is due to the blunting at the crack tip due to increased ductility and large plastic region at the crack tip. Adefris et al. [5] tested 1Cr-1Mo-0.25V steel by applying 100 *sec.*, 15 *min.*, and 8 *hr.* tensile hold times at 538 ℃ with frequency of 1 *Hz*. The result of 100 *sec.* tensile hold time test showed much lower crack growth rate compared to pure fatigue one at relatively low ΔK. The authors explained that this is also due to the blunting at the crack tip due to creep effect of tensile hold time. For the crack to propagate again resharpening time is required and therefore overall crack growth rate decreases. Similar research results by Jata et al. [6] were reported using an aluminum alloy 8009.

In this study, the high temperature fatigue crack behavior of STS 316L for various tensile hold times was examined and an effect of tensile hold time on high temperature fatigue was analyzed by using fracture mechanics parameter ΔK. To find out the creep behavior, the creep crack growth was characterized using C_t parameter.

2. EXPERIMENTAL PROCEDURE

2.1 Specimen Preparation

Specimen was made out of STS 316L, an austenitic stainless steel, and its chemical composition was shown in Table 1.

Table 1 Chemical composition of STS 316L (wt.%)

C	Si	Mn	P	S	Cr	Ni	Mo	Fe
0.02	0.62	0.69	0.021	0.002	17.37	12.23	2.16	Bal.

The heat treatment included solution treatment at 1130 ℃ for 20 *min.* to get rid of precipitates. Fatigue test specimens were in CT specimen shape as shown in Fig. 1.

2.2 Tensile and Fatigue Test

To evaluate the effect of tensile hold time on high temperature fatigue crack of STS 316L, room temperature and high temperature tensile tests and tensile hold time applied fatigue tests were carried out using solution treated specimens. Tensile test specimens were prepared according to KS B 0801. Tests were performed according to ASTM E 8 and E 21.

Fatigue tests were carried out using a 10 *ton* capacity Shimadzu Dynamic Testing System

which is hydraulic-powered servo at 600 ℃ according to ASTM E 647. Trapezoidal waveform was used for loading. The tensile hold times were applied at the maximum load. The test conditions are shown in Table 2. Crack length was measured using Electric Potential Drop Method (EPDM).

Table 2 Conditions of the fatigue tests

Hold time	Loading waveform	Rise(decay) time	Load ratio	Initial ΔK ($MPa\sqrt{m}$)	Final ΔK ($MPa\sqrt{m}$)
0 *sec.*	Triangular	0.05 *sec.*	0.1	15.4	23.6
5 *sec.*	Trapezoidal	0.05 *sec.*	0.1	15.1	25.3
10 *sec.*	Trapezoidal	0.05 *sec.*	0.1	14.6	25.3
50 *sec.*	Trapezoidal	0.05 *sec.*	0.1	20.6	26.6
100 *sec.*	Trapezoidal	0.05 *sec.*	0.1	20.4	26.4

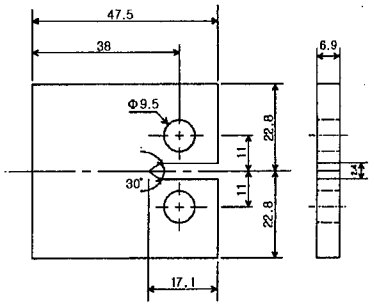


Fig. 1. Geometry of fatigue crack growth test specimen.

2.3 Creep Crack Growth Test

Creep crack growth tests were carried out with a dead weight type creep tester at 600 ℃ under 3.4 *kN*. The specimen was same as the fatigue test specimen except notch length, a, which was machined to the $0.4W$ and then 2 *mm* of fatigue pre-crack was made. The magnitude of C_t was estimated according to ASTM E 1457.

2.4 Fatigue Fracture Surface Observation

To study the change of crack growth rate by fractography, aspects of the fracture surface due to tensile hold time were examined with Scanning Electron Microscope (SEM).

3. RESULTS AND DISCUSSIONS

3.1 Tensile Test

The result of tensile test at the room temperature and 600 ℃ are shown in Table 3. It can be seen that the yield strength and the tensile strength decrease significantly at 600 ℃ and that both elongation and area reduction decrease also. The high temperature plasticity constant, D, and the plasticity exponent, m, were calculated from the tensile test curves using equation (1) and the results are shown in Table 3.

Table 3 Tensile Properties of STS 316L

Temp.	Y.S.	U.T.S.	Elong.	R.A.	Plasticity constant, D	Plasticity exponent, m
R.T.	239.8 *MPa*	589.0 *MPa*	46.7%	77.2%	-	-
600 ℃	132.1 *MPa*	422.3 *MPa*	26.5%	67.3%	2.81E-12 MPa^{-m}	3.94

$$\varepsilon_p = D\sigma^m \tag{1}$$

Where, ε_p is the plastic strain.

3.2 Creep Crack Growth Test

The C_t parameter is used to indicate crack growth rate that includes the transition creep region. By plotting *da/dt* vs. C_t obtained from the test results, the crack growth rate, *da/dt*, was found in the form of

$$da/dt=0.08C_t^{0.72} \tag{2}$$

3.3 Fatigue Test with Tensile Hold Time

Fig. 3 shows the fatigue test results of 0 *sec.*, 5 *sec.*, 10 *sec.*, 50 *sec.*, and 100 *sec.* tensile hold times with *da/dN* and ΔK curve. The results of fatigue test with 0 *sec.* and 5 *sec.* tensile hold time were similar to each other as can be observed in the figure but mainly the 5 *sec.* tensile hold time one showed decrease in crack growth rate compared to the pure fatigue one. Also, the crack growth rate of tensile hold time of 10 *sec.* decreased compared to the 0 *sec.* and 5 *sec.* ones. When crack growth rates were compared within the ΔK range of 20.4 $MPa\sqrt{m}$ to 26.6 $MPa\sqrt{m}$, it can be seen that as the hold time increases from 0 to 10 *sec.*, the rate decreased but as hold times are further increased to 50 and 100 *sec.* the rate ceased to decrease, but began to increase. When the pure fatigue crack growth rate and the tensile hold time applied fatigue crack growth rates were compared at where ΔK is 23 $MPa\sqrt{m}$, the percent decrease was 10.5% for 5 *sec.*, 40.5% for 10 *sec.*, 42.0% for 50 *sec.*, and 22.8% for 100 *sec.*.

From the above result, it can be seen that STS 316L steel tends to decrease in crack growth rate compared to the pure fatigue one in the relatively short tensile hold time within the ΔK range of this study.

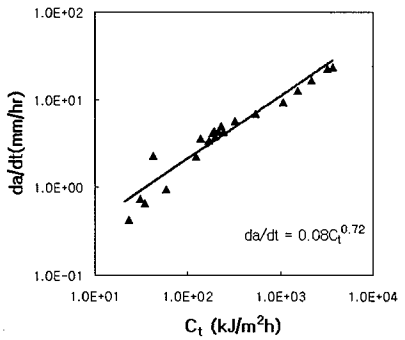


Fig. 2. Creep crack growth rate vs. C_t at 600 ℃.

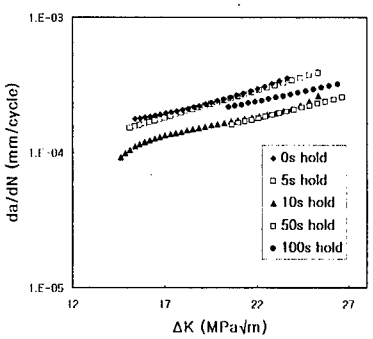


Fig. 3. *da/dN* vs. ΔK curve at various tensile hold times (0, 5, 10, 50, and 100 *sec.*).

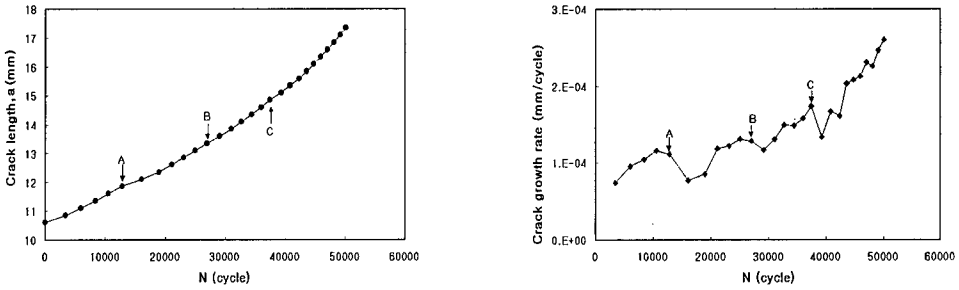


Fig. 4. Results of *a-N* curve (left) and the fatigue crack growth rate(right) with hold times of 80 *min.* applied at the maximum load at different crack length at 600 ℃

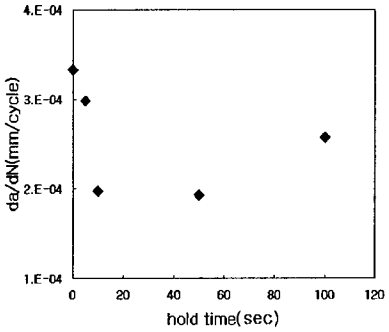


Fig. 5. Crack growth rate as a function of hold time. At ΔK is 23 $MPa\sqrt{m}$

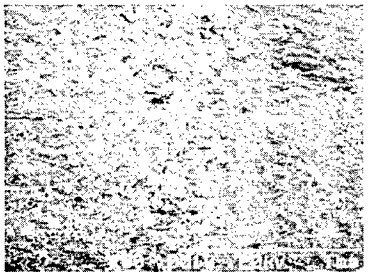


Fig. 6. Fractured surface of fatigue crack growth test with 80 *min.* hold time applied at the maximum load in Fig. 4

Another test was carried out to observe the effect of creep load on fatigue crack growth fracture mechanism. Intermittent tensile hold times, which were longer than those of fatigue crack growth test with trapezoidal waveform, were applied to pure fatigue crack growth test. The result showed decrease of crack growth rates after applying tensile hold times compared to the crack growth rates before applying tensile hold times. This behavior was caused by blunting at crack tip due to creep deformation as shown in the fractography. It is considered that the blunting at crack tip was one of the reasons for decrease of crack growth rates in trapezoidal waveform fatigue test.

Fig. 5 shows the crack growth rates where ΔK is 23 $MPa\sqrt{m}$ for each hold time. This result is similar to the study of Adefris et al.[5], which tested 1Cr-1Mo-0.25V steel. In trapezoidal waveform, the crack growth rate at the increasing and decreasing load parts which are the crack growth rate of fatigue, decreases gradually with increasing hold time due to creep deformation. On the other hand, in the part where tensile hold time was applied, the crack growth rate due to creep increases as the tensile hold time increases. As a result, in relatively short tensile hold time, overall crack growth rate decreases due to blunting at the crack tip and cycle-dependent crack growth behavior is dominating. As the tensile hold time increases, crack growth rate by creep increases causing overall crack growth rate to increase and time-dependent crack growth behavior is

dominating.

Fig. 6 is the picture of fracture surface of fatigue test specimen with applied tensile hold time of 80 *min.* at the maximum load during pure fatigue test taken by SEM. As can be seen in the picture, dimples caused by creep deformation were observed on the fracture surface which indicates the occurrence of blunting at the crack tip that would lead to the decrease in crack growth rate.

4. CONCLUSIONS

In this study, STS 316L steel was tested for fatigue crack propagation test by applying tensile hold time in trapezoidal waveform and creep crack growth test at 600 ℃ and the following results were obtained.

(1) STS 316L showed decrease of crack growth rates in relatively short tensile hold times compared to that of the fatigue test with no tensile hold time. As the tensile hold times increased, however, the crack growth rates increased.
(2) The crack growth rates after intermittent tensile hold times decreased compared to the rates before the intermittent tensile hold times in pure fatigue test. It was due to blunting at crack tip by creep deformation.
(3) Using C_t parameter, the creep crack growth rate at 600 ℃ was found to $da/dt=0.08C_t^{0.72}$.

ACKNOWLEDGEMENTS

The authors are grateful for the support provided by a grant from the Korea Science & Engineering Foundation (KOSEF) and Safety and Structural Integrity Research Center at the Sungkyunkwan University.

REFERENCE

1. U.S.Kim, et al., Automobile Technical Handbook, KSAE, **4** (1996) pp. 8~12
2. J.H.Lee,: A Study on New Creep Fracture Parameter Considering Load Increasing Conditions, Ph.D. Thesis, Sungkyunkwan Univ.,(1997)
3. S.W.Nam, J.W.Hong, J. KSME, **24** (1984) 4 pp. 225~261
4. Basant K. Parida and Theodore Nicholas, Materials Science and Engineering, **A153** (1992) pp.493~498
5. N. Adefris, A. Saxena and D. L. McDowell, Fatigue Fract. Engng. Mater. Struct. **19** (1996) 4 pp.401~411
6. K. V. Jata, D. Maxwell and T. Nicholas, J. Engng. Maters. and Tech., **116** (1994) pp.45~53

Key Engineering Materials Vols. 183-187 (2000) pp. 1047-1052
© 2000 Trans Tech Publications, Switzerland

Fatigue Strength of Crack-healed Ceramics

K. Ando[1], M.C. Chu[1], F. Yao[2] and S. Sato[3]

[1] Department of Energy & Safety Engineering, Yokohama National University, 79-5, Hodogaya, Yokohama 240-0067, Japan

[2] Post-graduate Student, Yokohama National University, Japan

[3] NHK Spring Co. Ltd., 3-10 Fukuura, Kanazawaku, Yokohama 236-0004, Japan

Keywords: Crack Healing, Crack-Healed Zone, Cyclic Fatigue Strength, High Temperature Strength, Recovery of Strength, Si_3N_4/SiC Ceramics, Static Fatigue Strength

ABSTRACT

Si_3N_4/SiC composite ceramics were sintered and three-point bending specimens were made. A semi-circular surface crack of 110μ m in diameter was made on each specimen. By using three kinds of specimen(smooth, cracked and crack-healed) crack-healing behavior, cyclic and static fatigue strengths were determined systematically at room temperature and at 1000^0C. The main conclusions are as follows (1)Si_3N_4/SiC composite ceramics have the ability to heal crack (2)Crack-healed specimens showed similar cyclic and static fatigue strengths as smooth specimens, this being caused by crack-healing. (3)Crack-healed zones had a sufficient fatigue strength and most fractures occurred outside the pre-cracked zone in those crack-healed specimens.

1. INTRODUCTION

Some engineering ceramics have the ability to heal a crack[1]-[8]. However, there is a large difference in the degree of healing ability of ceramics which depends on chemical composition and sintering conditions etc. To use this healing ability in structural engineering, there are many problems to be overcome. For example, (a)The effect of chemical composition on the crack-healing ability[11][12], (b)The effect of healing conditions on the strength of the healed-zone[13][14], (c)Determination of the maximum crack size which can be healed [13][14], (d)Knowledge of the high temperature strength of healed-zones[9][11][13][14], (e)Understanding of the crack-healing mechanism[5][11] and (f)Assessment of the cyclic fatigue and static fatigue strengths of crack-healed ceramic member[10]. With respect to items (a) to (f), the present authors have already studied systematically the several aspects of these problems[5]-[7][9]-[15].

This paper reports on the cyclic and static fatigue strengths of crack-healed silicon nitride

structural members at room temperature and 1000^0C[15].

2. MATERIALS, SPECIMEN AND TEST METHOD

The silicon nitride powder used in this investigation has the following properties: mean particle size = 0.2 μm, the volume ratio of α-Si_3N_4 is about 95% and the rest is β-Si_3N_4.The SiC powder used has a 0.27 μm mean particle size. The samples were made with a mixture of silicon nitride, 20 vol% SiC powder and 8 wt% Y_2O_3 as an additive powder. To this mixture, alcohol was added and blended completely for 48h. The mixture was subsequently hot-pressed at 1850^0 C and 35 MPa for 1 h in nitrogen gas. The sintered material has the following microstructure: average grain size of the matrix Si_3N_4 =0.43 μm, average aspect ratio=6.0, volume ratio of α-Si_3N_4 is 22.5% and the rest is β-Si_3N_4, grain boundary crystals are $Y_{20}N_4Si_{12}O_{18}$, $Y_2Si_3N_4O_3$ and $YNSiO_2$. The sintered material was then cut into test pieces measuring 3x4x40mm as shown in Fig.1. The reasons that this silicon nitride was picked as a test material within our large number of investigations are as follows: (a)Grain boundary of material crystallized well and has high strength even at high temperature.[7][13],(b)This material has the highest crack-healing ability[9]-[15], (c)Crack-healed zones of this material has the highest bending strength at 1400^0C(600MPa to 700MPa)[9][13].

A semi-circular crack was made at the center of the tension surface of the test pieces with a Vickers indenter using a load of 19.6N. By this method, semi-circular cracks of 110 μm in diameter were made as shown in Fig.2.

The crack-healing condition has a large effect on fracture behavior[11]. It is found that the best healing condition for these materials is at a temperature of 1300^0C, a healing time of 1 h in an environment of air as shown in Fig.3[11][13]. Thus, all cracked samples were healed under these conditions.

All fracture tests were made on a three point loading system. The cross-head speed in the monotonic tests is 0.5mm/min. At 1300^0C and 1400^0C, the effect of cross-head speed on fracture mode and fracture stress were studied. For these tests, three cross-head speeds were used:0.5mm/min, 0.01mm/min and 0.001mm/min. These tests were to evaluate the sensitivity to static fatigue at very high temperatures. Cyclic fatigue tests were made at room temperature at a stress ratio R=0.2 and a frequency=8Hz. Static fatigue tests were made at 1000^0C by using a dead-load type of testing machine.

3. TEST RESULTS

3.1. Crack-Healing Behavior and Strength at High Temperature

Fig.3 shows the effect of healing conditions on bending strength. These tests were made on samples from batch A using a four point loading system. Fig.3(a) shows the effect of healing condition on bending strength at room temperature. The bending strength of smooth samples are about 750MPa. By cracking, the bending strength was largely reduced to about 350MPa. However, by crack-healing, the samples recovered their bending strength. Most of the samples which were healed in the temperature range from 900^0C to 1400^0C, recovered their bending strength completely and they failed outside the crack-healed zone as shown in Fig.5(a). Fig.3(b)

shows the effect of healing condition on bending strength at 1300^{0}C. Most of the samples failed outside the crack-healed zone when they were healed at 1200^{0}C and 1300^{0}C. However, all samples which were healed below 1100^{0}C failed from the pre-crack. From these facts, it can be concluded that the best healing condition is in the temperature range 1200^{0}C to 1300^{0}C,for 1h in air.

The effect of cross-head speed on bending strength at 1300^{0}C and 1400^{0}C were tested using samples from batch B. All the samples were pre-cracked and healed at 1300^{0}C for 1h in air. The results were shown in Fig.4. At 1300^{0}C, bending strength increased with increase in cross-head speed. And at the cross-head speed of 0.5mm/min, all the samples failed outside the crack-healed zone as shown in Fig.5(a). However, at cross-head speeds lower than 0.01mm/min, all the samples failed from the pre-crack. On the contrary, at 1400^{0}C, bending strength is almost independent of cross-head speed. However, all the samples failed from the pre-cracked zones as shown in Fig 5(b).

3.2. Cyclic Fatigue Strength at Room Temperature

Three kinds of sample from batch B were used for cyclic fatigue tests: a smooth sample, a cracked sample and a crack-healed sample. The test results of the cyclic fatigue tests were shown in Fig.6 as a correlation with maximum bending stress(σ_{max}) and number of cycles to failure(N_f). On the left side of Fig.6, monotonic test results are also shown. Symbols X,△ and ● show the bending strength of the smooth, cracked and crack-healed samples, respectively. For this batch, the bending strength of the smooth samples(X) scattered to a certain extent giving a mean fracture stress of 830MPa. Due to cracking, the bending strength decreased to about 380MPa. However, by healing, the bending strength was recovered to a level similar to the smooth samples. The cyclic fatigue tests were stopped at N=2x10^6 cycles. The samples which did not fracture in a test are marked by an arrow symbol(→). The maximum stress at which a sample did not fracture up to N=2x10^6 cycles is denoted as σ_{fo}. The σ_{fo} for the smooth sample is about 600MPa, and the σ_{fo} for cracked samples is about 200MPa. After a fatigue test, the crack tips of the samples were investigated using an SEM. It was found that the crack grew in the both directions by about 0.3mm. On the contrary, the σ_{fo} for the crack-healed sample is about 730MPa. This value is about 3.5 times as large as the σ_{fo} value for the cracked specimens and is a little higher than that for the smooth specimens. Of course, this recovery of σ_{fo} was caused by mainly crack-healing. Nevertheless the crack-healed sample has an indentation which works as a stress concentrator, and it showed a little higher σ_{fo} than that of a smooth specimen. To investigate this reason, the residual stress on the surface of crack-healed specimens were measured by the X ray technique. It was found that there was a compressive stress of (206±60)MPa, and it was assumed that this compressive residual stress increased the σ_{fo} of the crack-healed sample to a certain extent.

Crack paths of cracked and crack-healed specimens are shown in Fig.7(a) and (b), respectively. In the crack-healed specimen, the fatigue crack initiated outside the crack- healed zone indicating that it has an adequate fatigue strength. Fig.8 shows a fatigue crack initiation site on a crack-healed sample. The fatigue crack was initiated from a small embedded flaw(pore). The diameter of the flaw is about 15 μm as shown in Fig.8(b).

3.3.Static Fatigue Strength at 1000^{0}C

Static fatigue properties of the smooth and the crack-healed samples from batch B were tested at 1000^{0}C. The test results are shown in Fig.9. Monotonic test results at room temperature are shown on the left side of the figure. All the samples did not fracture in the static fatigue test at 1000^{0}C. The applied stress at which a sample did not fracture up to 10^6 second is denoted as σ_{to}. From Fig.9, σ_{to} of smooth and crack-healed samples are assumed to be over 700MPa. These facts indicate that parent material and crack-healed zones are not sensitive to static fatigue at 1000^{0}C. Also, σ_{to} of the cracked sample is defined to be over 300MPa. As can be seen from Fig.3(a), crack-healing can occur within 1h at 1000^{0}C. There is of course a possibility that the crack was healed during the static fatigue test. In fact, a similar phenomenon is observed in mullite/SiC ceramics during slow strain rate tests at 1200^{0}Cand 1300^{0}C[14].

Anyway, from those test results, it can be concluded that the crack-healed zone has a sufficient strength for cyclic fatigue and static fatigue at room temperature and 1000^{0}C, respectively.

4. CONCLUSIONS

Si_3N_4/SiC composite ceramics have been sintered and tested under three point bending. A semi-circular crack was made on each specimen surface. By using these specimens crack-healing behavior, cyclic and static fatigue properties were investigated systematically.

The main results are as follows:

(1) The samples showed very interesting crack-healing behavior, and the best healing condition was found to be in the temperature range from 1200^{0}C to 1300^{0}C, for 1h, in air.

(2) The strength of the crack-healed samples were recovered completely by the healing process and most samples failed outside the crack-healed zone when subjected to monotonic loading at temperatures up to 1300^{0}C.

(3) The cyclic fatigue strength of crack-healed samples at room temperature was recovered completely by the healing process and most samples failed outside the crack-healed zone.

(4) The static fatigue strength of crack-healed samples at 1000^{0}C was similar to parent material and hence the crack-healed zone is concluded to be non-sensitive to static fatigue.

REFERENCES

1. J.J.Petrovic and L.A.Jacobson, J. Am. Ceram. Soc.,**59**(1-2) (1976) p.34
2. T.K.Gupta, J. Am. Ceram. Soc.,**59**(5-6) (1976)p.259-262.
3.S.R.Choi and V.Tikare, Scripta Metallurgica et Materialia.,**26**(1992)p.1263
4.J.E.Moffatt, W.J.Plumbridge and R.Hermann, British Ceramic Transactions,**95-1** (1996)p.23
5.M.C.Chu, S.Sato, Y.Kobayashi and K.Ando, Fatigue Fract. Engng. Mater. Struct., **18-9** (1995)p.1019
6. M.C.Chu, S.Sato, Y.Kobayashi and K.Ando, Jpn. Soc. Mech. Engng **60-580**(1994)p.2829
7. K.Ando, T.Ikeda, S.Sato, F.Yao and Y.Kobayashi, Fatigue Fract. Engng. Mater. Struct.,**21** (1998)p.119
8. Y.Z.Zhang, L.Edwards and W.J.Plumbridge, J. Am. Ceram. Soc. **81**(1998)p.1861
9. K.Ando, S.Sato, Y.Kobayashi and M.C.Chu, Fracture From Defects(ECF-12, Edited by M.W.Brown, E.R.de los Rios and K.J.Miller), U.K., Sheffiled (1998) p.497

10. K.Ando, K.Tsuji, M.Ariga and S.Sato, J. Soc. Mater. Sci., Jpn, **48-10** (1999)p.1173
11. K.Ando, M.C.Chu, S.Sato, F.Yao and Y.Kobayashi, Jpn. Soc. Mech. Engng, **64-623** (1998) p.1936
12. M.C.Chu, K.Ando, T.Hirasawa, S.Sato and Y.Kobayashi, High Pressure Institute of Japan, **36-2** (1998)p.82
13. K.Ando, M.C.Chu, Y.Kobayashi, F.Yao and S.Sato, Jpn. Soc. Mech. Engng, **65-633** (1999)p.1132
14. K.Ando, K.Tsuji, T.Hirasawa,Y.Kobayashi and S.Sato, J. Soc. Mater. Sci., Jpn, **48-5**(1999)p.489
15. K.Ando, M.C.Chu, F.Yao and S.Sato, Fatigue Fract. Engng. Mater. Struct., **22**(1999)p.897

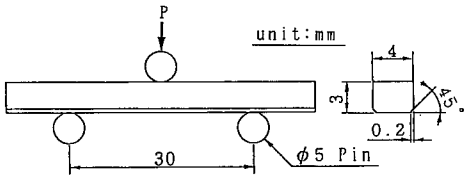


Fig.1 3-point loading system and geometry of test specimen

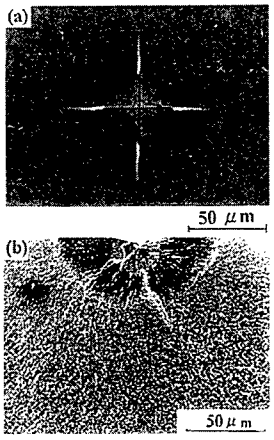


Fig. 2. SEM photographs of (a) indented crack and (b) crack surface.

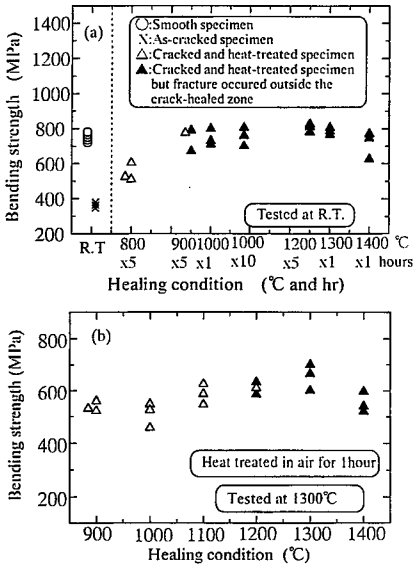


Fig.3 Relationship between healing condition and bending strength at (a)room temperature and at (b)1300℃

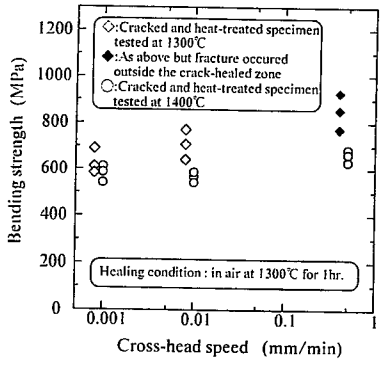


Fig.4. Relationship between cross-head speed and bending strength

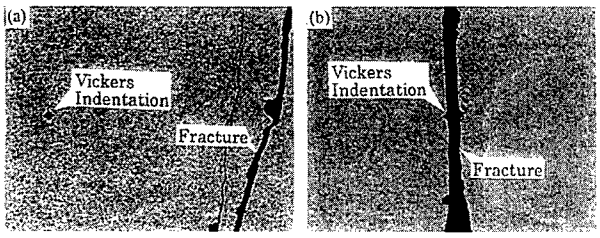


Fig.5 Fracture pattern of crack and fracture surface of crack-healed specimens.
(a) Cross-head speed:0.5mm/min, tested at 1300℃(σ_f=851MPa)
(b) Cross-head speed:0.01mm/min, tested at 1300℃(σ_F=714MPa)

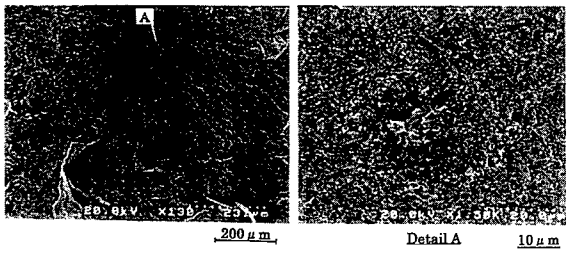


Fig.8 SEM photographs of fracture initiation site of a crack healed specimen (σ_{max}=760MPa, N_f=2.0×10^5 cycles).

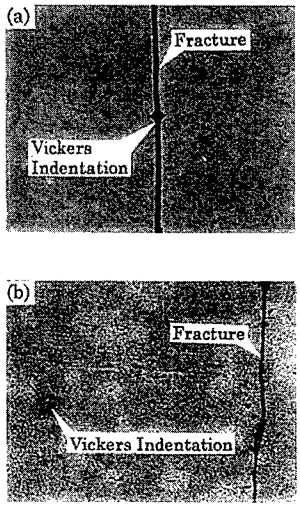


Fig.7 Fracture pattern of cyclic fatigue test
(a) as-cracked specimen(σ_{max}=300MPa, N_f=5320 cycles) and (b)crack healed specimen (σ_{max}=700MPa,N_f=2.35×10^5 cycles)

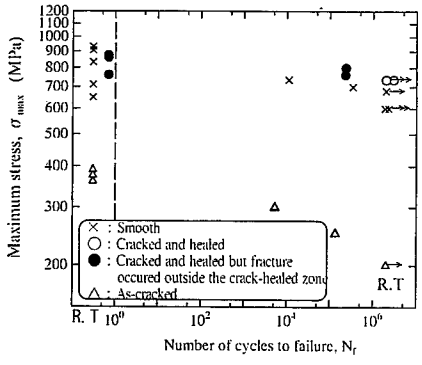


Fig.6 Relationship between maximum stress and number of cycles to failure

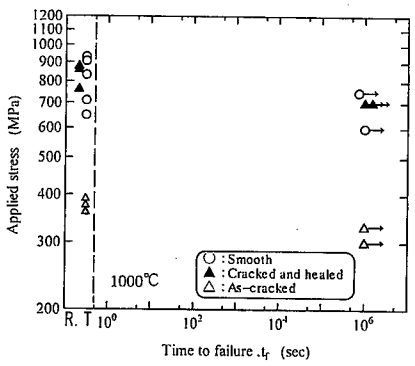


Fig.9 Results of static fatigue test at 1000℃ in air.

Key Engineering Materials Vols. 183-187 (2000) pp. 1053-1062
© 2000 Trans Tech Publications, Switzerland

Fracture Behaviours of Advanced Polymer Composites under Mixed Mode Loading

Kikuo Kishimoto

Department of Mechanical Sciences and Engineering, Tokyo Institute of Technology,
2-12-1 O-okayama, Meguro-ku, Tokyo 152-8552, Japan

Keywords: Fracture Boundary Curve, Local Fracture Criterion, Maximum Hoop Stress Criterion, Mixed Mode Fracture, PC/ABS, Polymer Alloy, Shear Fracture, Silica Particulate Filled Epoxide Resin

ABSTRACT

Fracture behaviours under mixed mode loading conditions for two types of advanced polymer composites were addressed. In the first part of the paper, mixed-mode fracture behaviours of PC/ABS resins were discussed. At a certain value of mixed mode loading ratio with high mode II components, crack due to shear type fracture initiates at the initial crack tip. Fracture toughness increases under mixed mode loading with lower in mode II component, while it reduces with the appearance of shear type fracture. Fracture toughness and the appearance of shear type fracture depend on blending ratio of PC and ABS. In the later part of the paper, the epoxide resin, containing 70wt% silica particles, have been examined. The specimen fractured in a brittle manner under room temperature conditions and the results obeyed the maximum hoop stress criterion. On the other hand, the results at high temperature showed a relatively low dependency on mode II stress intensity factors. In order to clarify the differences of the fracture behaviour, finite element analysis has been conducted.

1. INTRODUCTION

Usages of polymer composites in engineering component spread broadly in recent years. The importance of the knowledge of the way they respond to mechanical loading is increasing. Structural members are usually subjected to complex loading and the tip of the existing crack is deformed under mixed-mode loading. Therefore, the mixed mode fracture problems are important issue for safety assessment of engineering structures [1]. In this paper fracture behaviours under mixed mode loading conditions will be addressed for two types of advanced polymer materials.

Polymer alloys or polymer blends have become one of the most widely used materials in engineering application recently [2-4]. To improve the reliability of the materials, extensive studies are required on their fracture behaviours. Polycarbonate (PC)/ acrylonitryle-butadiene-styrene (ABS) blends is one of the most widely used as engineering plastics [5,6]. In the first part of the paper, PC/ABS resin is selected to examine the fracture behaviours of polymer alloy under mixed mode loading.

The latter half of the paper is concerned with the fracture behaviour of the silica filled epoxy resin. This type of resin is frequently used as encapsulant material in semiconductor packaging. Silica particles are employed to reduce the thermal-expansion mismatch between resin and chip. However, plastic encapsulated devices are not hermetically closed and moisture-induced mechanisms sometimes cause the degradation of the plastic package [7]. In order to improve the reliability of the integrated circuit (IC) chips, extensive studies have been conducted on the fracture behaviour of the encapsulant materials and more accurate strength evaluation procedures [8-10].

2. PC/ABS RESINS

2.1 Material and Experimental Procedures

Polymer alloys examined in this study are given in Table 1 [11,12]. The blending ratios of PC/ABS are 100/0, 80/20, 60/40, 50/50, 40/60 and 0/100 in wt%. PC forms the continuous phase at compositions with greater than 60wt% while ABS forms the continuous phase at compositions with smaller than that.

A compact-tension-shear (CTS) specimen of dimensions 40.1 x 74 x 3.25 mm as shown in Fig. 1 was used for mixed-mode fracture tests. Fracture process and the whitening zone at the crack tip were observed by means of a video microscope. Finite element analyses were conducted to obtain the stress intensity factors of compact-tension-shear specimen [13].

Table 1 Materials used in this study (PC/ABS resin)

PC/ ABS (wt%)	Rubber (wt%)	Mass Density g/cm^3	Young's Modulus GPa	K_{Iin} MPam$^{1/2}$
100/0	0.0	1.17	2.51	2.27
80/20	3.6	1.15	2.63	2.63
60/40	7.2	1.12	2.75	2.88
50/50	9.0	1.11	2.66	2.72
40/60	10.8	1.09	2.62	2.61
0/100	18.0	1.03	2.49	2.43

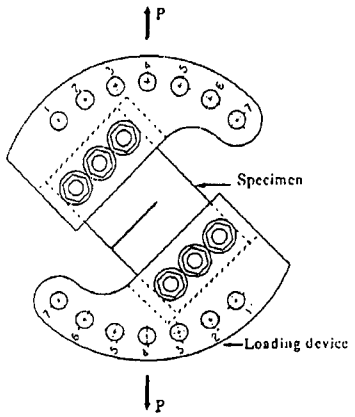


Fig .1 Configuration of compact-tension-shear specimen and device for mixed mode loading.

2.2 Crack Propagation Behaviours

The crack propagation of PC, PC/ABS blends and ABS resins occurs in a stable manner. There exist the stress-whitening zone around the crack tip is due to cavitations of the rubber particle generating by hydrostatic stress. Figure 2 shows stress-whitening zone and crack extension for each type of PC/ABS blends under mixed mode loading. Whitening zone expands more widely in PC/ABS blends (from frame 1 to 4) than in ABS resin (frame 5).

Figure 3 shows the sequence of deformation and fracture process of PC/ABS (80/20) under mode I (a), mixed mode with the lower (b) and higher in mode II component (c). Appearances of the crack-tip region before crack initiation are shown in frame 1. Then frame 2 of (a) and (b) is just after crack initiation. For higher mode II component (c), there are two stages of fracture process occurred at the crack tip. First, crack initiation (frame 2) occurred in shear type with the direction parallel to the initial crack tip denoted by an arrow in the flame. Then, opening type of crack appears on the surface of shear type fracture as shown in frame 3. Finally, this crack propagates in the direction at a certain angle to the initial crack until final failure.

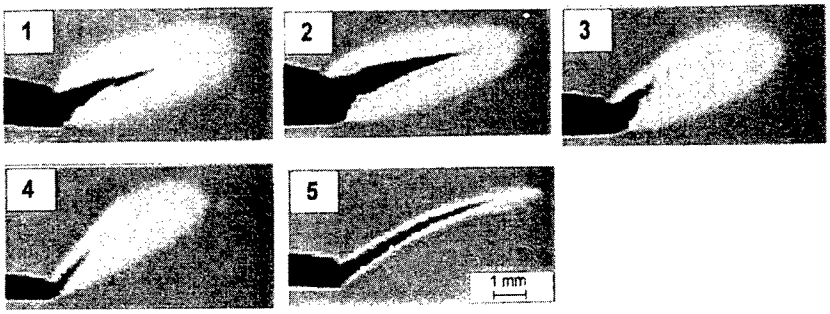
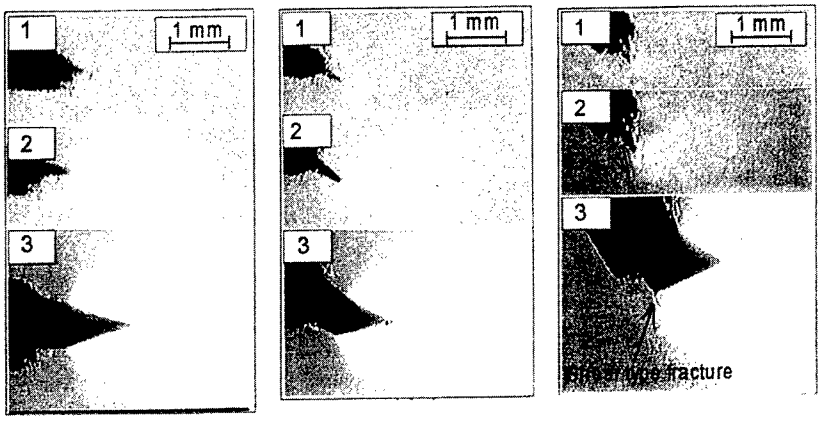
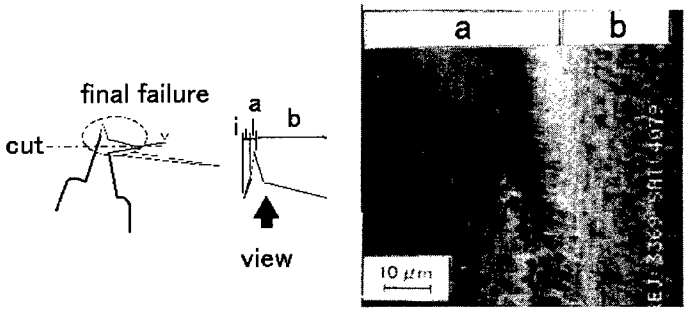


Fig. 2 Stress whitening zone and crack extension of PC/ABS blends under mixed mode loading; K_{II}/K_I = 0.34. (1) (80/20), (2) (60/40), (3) (50/50), (4) (40/60), (5) (0/100).



(a) (b) (c)

Fig. 3 Sequence of deformation and fracture process at the crack tip for PC/ABS (80/20). (a) K_{II}/K_I = 0.0. (b) K_{II}/K_I = 0.34. (c) K_{II}/K_I = 0.62.



(1) (2)

Fig. 4 SEM observation of fracture surface around the crack tip of PC/ABS (80/20) (K_{II}/K_I = 0.62). (1) Schematic figure of SEM specimen preparation. (2) SEM image of fracture surface.

Figure 4 shows SEM images of the fracture surface of PC/ABS (80/20) under mixed mode with higher mode II component. There are two stages of fracture process: (a) smooth region corresponding to shear type fracture and (b) rougher fracture surface corresponding to opening type fracture. Final failure occurred by opening type.

Appearances of the shear type fracture depending on the loading angle ϕ are plotted in Fig. 5 where ϕ is the angle between loading direction and initial crack. Solid line in the figure indicates the critical loading angle at which shear type fracture occurred firstly then are followed by opening type fracture. Shear type fracture occurs in lager loading angle (lower mode II components) for PC/ABS (80/20) and PC/ABS (60/40) than other tested materials. These results suggest that shear type fracture tens to occur for lower mode II component for the materials with higher fracture toughness (see Table 1).

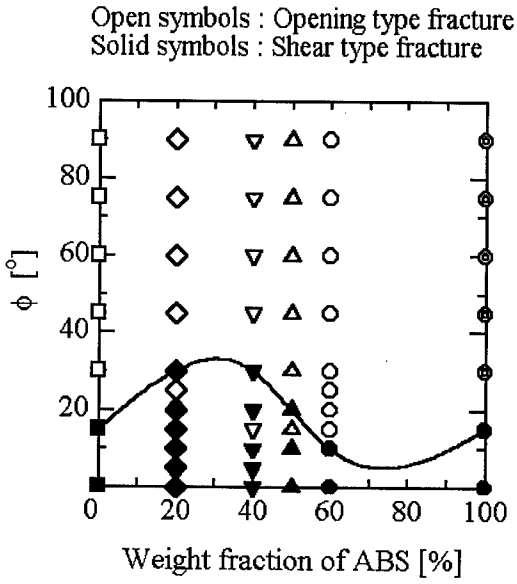


Fig. 5 Critical loading angle at which shear type fracture occur.

2.3 Fracture Boundary Curve

The critical stress intensity factors K_I / K_{II} at initiation of opening type of fracture are plotted in Fig. 6 where both axes are normalized by the critical stress intensity factor K_{Iin} under mode I loading. The open symbols denote the pure opening type of fracture process, and the closed symbols denote the appearance of shear type fracture. The solid line indicates the fracture boundary curve corresponding to the maximum hoop criterion (tangential stress criterion) [14]. This criterion is considered to be applicable to brittle materials. In this criterion, the relationship between K_I and K_{II} given by

$$\left(\frac{K_I}{K_{Ic}}\cos^2\theta_0 - \frac{3}{2}\frac{K_{II}}{K_{Ic}}\sin^2\theta_0\right)\cos\frac{\theta_0}{2} = 1, \tag{1}$$

where θ_o denotes the direction at which hoop stress takes its maximum value, and given by

$$\theta_0 = \sin^{-1}\left(\frac{\kappa}{\sqrt{1+9\kappa^2}}\right) - \tan^{-1}3\kappa \tag{2}$$

with the mixed mode ratio, $\kappa = K_{II} / K_I$.

Critical values of K_I and K_{II} for all type of tested materials are larger than that of maximum hoop stress criterion. At a relatively low in mode II component says $K_{II}/K_{Iin} < 0.40$, the fracture resistance is higher in mixed mode loading case than pure mode I case. When mode II component exceeds some critical value, the fracture resistance of all tested materials decreases. The decrease in the fracture resistance corresponds to the appearance of the sear type fracture. Figure 7 illustrates these tendencies of the fracture boundary curves mentioned. The present experimental results suggest that the transition of the fracture resistance occurred in lower mode II component for the material type with the high fracture toughness.

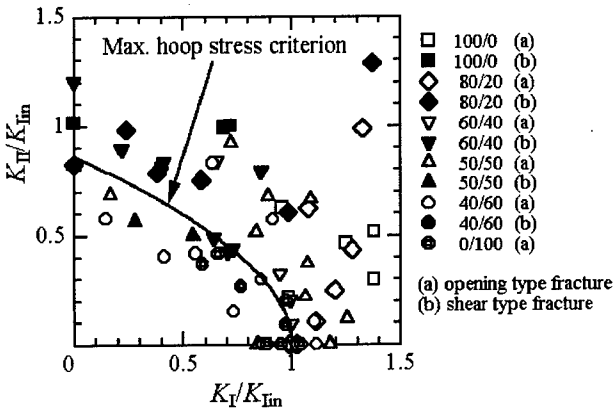


Fig. 6 Critical stress intensity factor under mixed mode loading

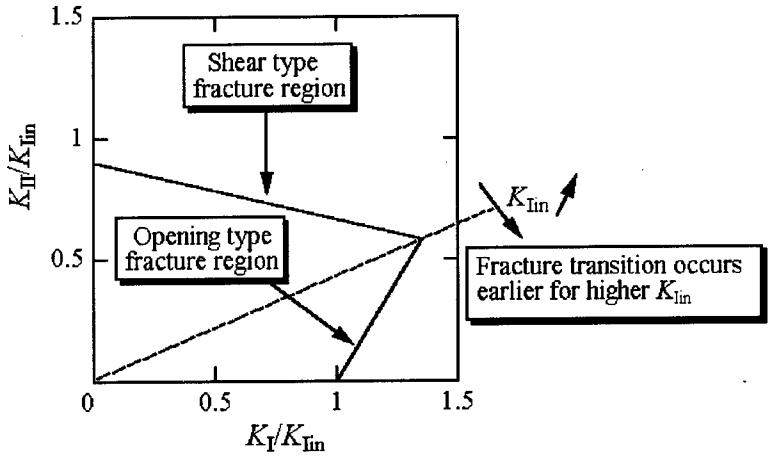


Fig. 7 Schematic illustration of fracture boundary curve under mixed mode loading.

3. SILICA FILLED EPOXIED RESINS

3.1 Material and Experimental Procedures

The material tested was epoxy resin filled with 70wt% angular shaped silica particles. The silica filled epoxide resins are used as encapsulant materials in semiconductor packaging. The dimension of the

specimens is 80 mm × 10 mm × 4 mm. Specimens were made by an injection molding, and were stored in a low humidity chamber at room temperature after they had been received. A small notch with 0.1 mm in width was machined to the specimens by the diamond-compounded blade. For pre-cracking, the bridge indentation (BI) method was employed [15]. As compared to fatigue pre-cracking, the present method is more reliable and there is a less possibility to be unsuccessful in introducing a crack [10] . In order to eliminate moisture content in the specimens and to maintain reproducibility of the experimental conditions, the specimens were dried out at 125°C for 24 hours. The fracture tests were conducted at room temperature and 250°C. Three-point and four-point bending were employed for mode I and mixed mode testing, respectively. Figure 8 illustrates the loading configurations. For four-point bending test, various mixed mode ratios can be obtained by changing the crack position x. The critical value of the mode I stress intensity factor K_{IC} are calculated for the three-point bend specimen from the crack length a and the maximum load P at failure [16]. For four-point specimen, the stress intensity factors, K_I and K_{II} were determined by the finite element method with the path-independent $\hat{J}$-integral [1].

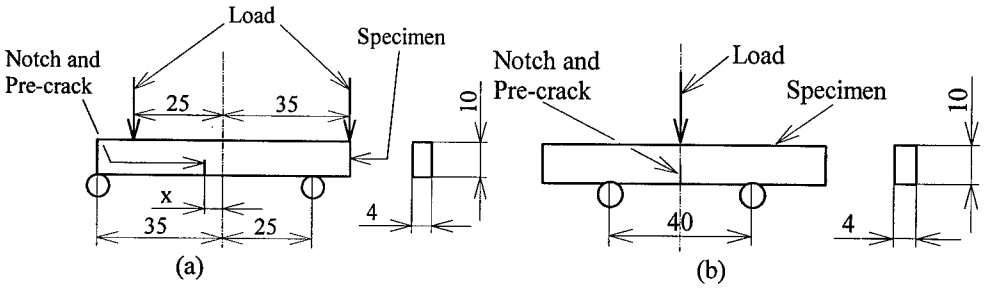


Figure 8 Specimen geometry and loading configuration: (a) three-point bending for Mode I loading and (b) four-point bending for mixed mode loading; all dimensions in mm.

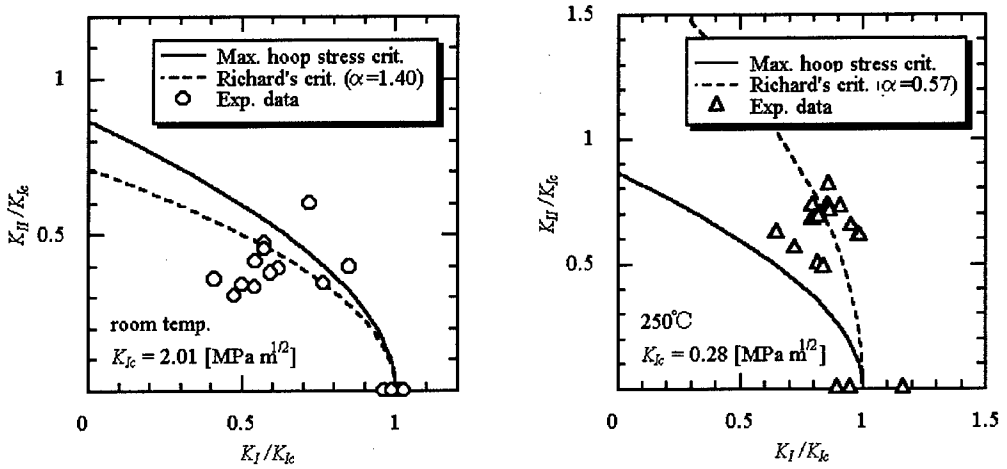
3.2 Experimental Results

Critical stress intensity factors at crack initiation for room temperature are shown in Fig.9(a) where the both axes are normalized by the plane strain fracture toughness K_{IC}=2.01MPam$^{1/2}$. The solid line indicates the fracture boundary curve corresponding to the maximum hoop criterion. The fracture boundary curve proposed by Richard [17] is also shown in the figure by dashed line, and is given by

$$\frac{K_I}{K_{Ic}} + \alpha_1^2 \left(\frac{K_{II}}{K_{Ic}} \right)^2 = 1 \tag{3}$$

where α_1 is the ratio of the critical stress intensity factors at mode I and mode II loading and is a material constant, $\alpha_1 = K_{IIc} / K_{Ic}$. Equation (3) is considered as a generalized fracture criterion for previously proposed other criterion. For example, if α_1 takes 1.155, Eq.(3) reduces to the maximum hoop stress criterion. For the present material at room temperature, α_1=1.40 has been obtained for the experimental results.

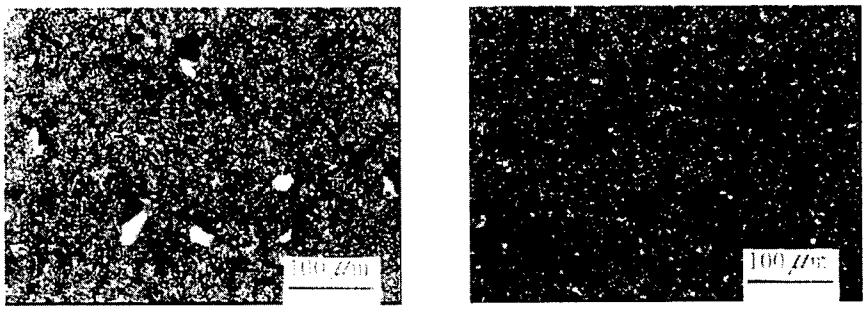
The results at 250°C are shown in Fig.9(b). The value of K_{IC}=0.28MPam$^{1/2}$ has been obtained. Fracture resistant significantly reduces at high temperature. The results show relatively low dependency on mode II stress intensity factors. The value of α_1=0.57 has been obtained. This results indicate that the encapsulant resin dose not follow the maximum hoop stress criterion at high temperature.



(a) room temperature (b) 250°C

Figure 9 Critical values of stress intensity factor of silica particulate epoxide resin temperature, and fracture boundary curves of the maximum hoop stress criterion and Richard's criterion.

Figures 10 show the SLM micrograph of fracture surface of the encapsulant resin under mixed mode loading. The many cracked silica particles are observed on the surfaces of the specimens fractured at room temperatures. This indicates that the cracking of the silica particles triggers the macroscopic crack initiation at room temperature. At the crack-tip, the hydrostatic component of the stress is large. This restricts the plastic deformation and the debonding of the interface is restrained. Therefore, fracture would occur by the cracking of silica particles that have smaller failure strain. Once silica particles brake, three-axis stress component is released and then epoxy resin may be deformed plastically. On the other hand, the surfaces of the specimen fractured at 250 °C are rough and mostly occupied by epoxide resin. This fact indicates that the crack propagates in epoxide region that becomes weak at high temperature. There are no significant differences of fracture surfaces between mode I and mixed mode fracture. This suggests that the local fracture process be not depending on the mixed mode ratio.



(a) (b)

Figure 10 Scanning laser micrographs of the fracture surface of silica particulate epoxide resin under mixed mode loading: (a) at room temperature (K_{II}/K_I =0.47) and (b) at 250 °C (K_{II}/K_I =0.58).

3.3 Finite Element Analysis

To investigate the effects of the temperature on the mixed mode fracture behaviour of silica particulate filled epoxide resin, finite element analysis has been conducted on the deformation fields near the crack-tip. The vicinity of the crack-tip is modelled as composite of epoxy resin and silica-particles. On the other hand, outer region is modelled as homogeneous material whose material constants have been obtained by analysing the composite model. In the analysis, both materials are approximated as liner elastic solid. Epoxy resin would exhibit the rate dependent nonlinear behaviour, especially at high temperate. Thus the elastic constant employed is considered as an equivalent rigidity of the material.

Figures 11(a) and (b) show the whole configuration of the finite element mesh in which the eight node quadrilateral iso-parametric element. A slit, which simulates a crack, is introduced and the initial radius of the slit is assumed to be 5 μ m. Minute subdivision of the near-tip region is shown in Fig.6(c) where the white parts correspond to silica particles and dark regions are epoxy resins. This mesh pattern is generated based on the SLM observation of the cross section of the specimen as shown in Fig.1. Perfect bonding of the interface of the two materials is assumed.

Young's modulus E of the homogenized region are obtained by analysing a similar a mesh pattern as shown in Fig.5(c) under uniform tensile loading: a crack is removed in this computation. The values of Young's modulus E and Poisons ratio ν used for silica particle are 78GPa and 0.25, respectively which are independent of temperature. For epoxy resin, E=2.9GPa and $\nu = 0.35$ at room temperature, and E=0.15GPa and $\nu = 0.45$ at 250 °C are employed. As a results, E=5.8GPa and E=0.33GPa have been obtained at room temperature and 250 °C, respectively. In the following computation, Poison ratio is assumed to be 0.3 at both temperatures.

In the present analysis, we consider the local fracture criteria for each material. The materials constants appeared in the criteria are determined by using the experimental results of bending strength and the critical value of mode I stress intensity factor K_{IC}. And then, we consider the fracture behavior under mixed mode loading.

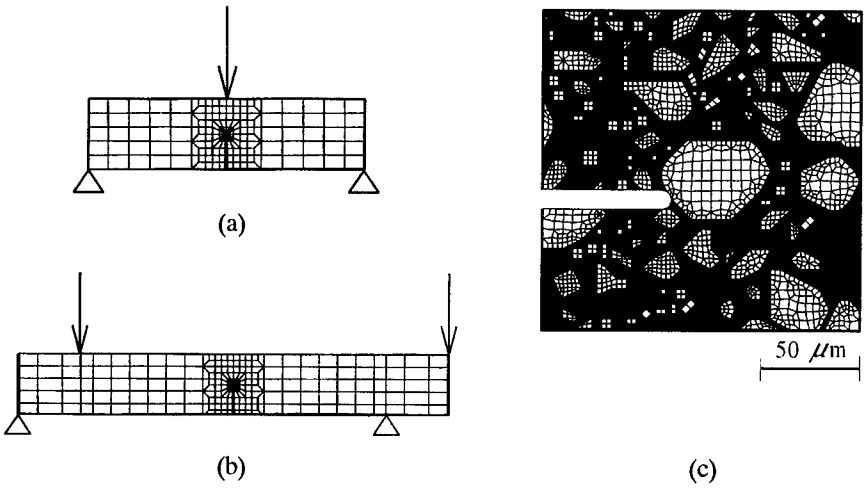


Figure 11 Finite element meshes: (a) three-point bend specimen, (b) four-point bend specimen, and (c) enlargement of the crack-tip region.

Since silica is brittle material, we assume that silica particle is cracked when the principal stress σ_1 reaches a critical value σ_c:

$$\sigma_1 > \sigma_c . \tag{4}$$

In the analysis the average value of σ_1 for each particle is used for the above criterion. From the analysis of three-point bend specimen subjected to mode I loading with K_{IC} =2.01MPam$^{1/2}$ at room temperature, σ_c =260MPa has been obtained and is assumed to be constant for the temperature range considered.

As described above, the crack propagates in the epoxide resin at 250°C. The following strain based fracture criterion is employed for epoxy resin [18]:

$$\varepsilon_{eq} > \varepsilon_f \tag{5}$$

where

$$\varepsilon_f = \varepsilon_n + \alpha \exp\left(-\frac{2}{3}\frac{\sigma_m}{\sigma_{eq}}\right) \tag{6}$$

In the above equation, σ_m and σ_{eq} are the mean stress and the equivalent Misses stress, respectively, and ε_n and α are material constants. From the bending stress σ_B=39MPa and the fracture toughness K_{IC}=0.28MPam$^{1/2}$ at 250°C, the finite element analyses on three-point bend specimen with crack and without crack yield ε_n=0.31 and α=0.62. In the analyses, Eq.(10) has been applied to each element to obtain candidate sets for ε_n and α, and the final results have been determined to fit to two kinds of analyses.

Finite element analyses have been conducted on mixed mode loading cases. The critical values of the stress intensity factors were determined by using the local fracture criterion. Numerical results on the fracture boundary curves are shown in Fig.7 with the experimental results. The fracture boundary curves based on the cracking of silica and failure of epoxide resin coincide well with the experimental results at room temperature and at 250°C, respectively. This agreement between numerical and experimental results accord with the fracture surface observation in which the cracking of the silica particles and failure of epoxide resin predominate at each temperature.

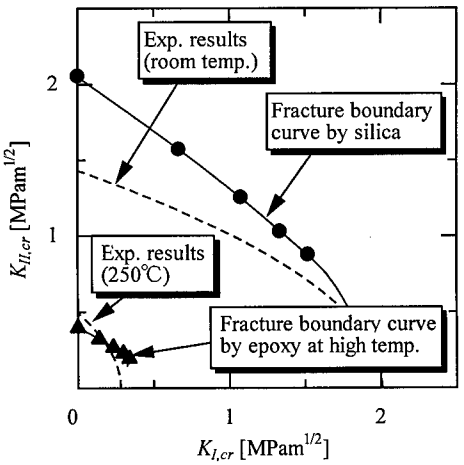


Figure 7 Comparison of the finite element analysis with experimental results.

4. CONCULUSIONS

Fracture behaviours of PC/ABS and silica filled epoxide resins under mixed mode loading were discussed. PC/ABS is ductile polymer alloy while silica filled epoxide resin is relatively brittle composites. In PC/ABS, at a certain value of mixed mode loading ratio with high mode II components, crack due to shear type fracture initiates at the initial crack tip. Fracture toughness increases under mixed mode loading with lower in mode II component, while it reduces with the appearance of shear type fracture. The shear type fracture appears lower mode II component for PC/ABS with higher fracture toughness. In silica filled epoxide resin, the specimen fractured in a brittle manner under room temperature conditions and the results obeyed the maximum hoop stress criterion. On the other hand, the results at high temperature showed a relatively low dependency on mode II stress intensity factors. The fracture boundary curves, obtained by a finite element analysis that was based on the local failure criteria for the silica particles and the epoxide resin, well describes the temperature dependence of the mixed mode fracture behaviour of this material.

5. REFERENCES

1. K.Kishimoto and S. Aoki, "Finite Element Analysis on Mixed-Mode Fracture," Mixed-Mode Fatigue and Fracture, ESIS 14 (1993) 267.
2. L. A. Utracki, Polymer Alloys and Blends: Thermodynamics and Rheology, Hanser, Munich, (1989).
3. A. A. Collyer Ed., Rubber Toughened Engineering Plastics, Chapman & Hall, (1994).
4. R. Greco, and A. Sorrentino, Advances in Polymer Technology, **3** (1994) 249.
5. M. L. Lu, and F. C. Chang, Polymer, **36** (1995) 2541.
6. M. L. Lu, K. C. Chiou, and F. C. Chang, Polymer, **37** (1996) 4289.
7. M. Kitano, S. Kawai, M. Nishimura and K. Nishi, Proc. 26th Int. Reliability Physics Sympo. (1988) 90.
8. A. Nishimura, A. Yaguchi, and S. Kawai, Transaction of Japan Soc. Mat. Sci. Japan (in Japanese), **38** (1989) 1322.
9. N. Kawamura, T. Kawakami, K. Matsumoto, K. Sawada, and H. Taguchi, Advances in Electronic Packaging, ASME, EEP **4**-1 (1993) 91.
10. K. Kishimoto, M. Motomi, T. Koizumi, N. Kawamura and T. Kawakami, Mechanics and Materials for Electronic Packaging, Vol.2, Thermal and Mechanical Behavior and Modeling, ASME AMD 187 (1994) 11.
11. K. Kishimoto, H. Inoue, M. Notomi, and T. Shibuya, Journal of The Society of Materials Science, Japan (in Japanese), **47**-8 (1998) 836.
12. M. Notomi, M. Ishikawa, K. Kishimoto, H. Inoue, and T. Shibuya, Proc. of 14th Int. Conf. on Polymer Processing Society, (1998) 541.
13. Husaini, M. Notomi, K. Kishimoto, and T. Shibuya, Materials Science Research Internatinaol, **3** (1997) 158.
14. F. Erdogan. and G.C. Sih, Journal of Basic Engng, **85** (1963) 519.
15. T. Nose and T. Fujii, Journal of Am. Ceram. Soc., **71** (1988) 328.
16. Standard Test Method for Plane-Strain Fracture Toughness and Strain Energy Release Rate of Plastic Materials, American Society of Testing and Materials D5045-93, (1994).
17. H. A. Richard, Int. Conf. on Role of Fracture Mechanics in Modern Technology, G.C. Sih, H. Nisitani and T. Ishihara Eds, Elsevier Science Publishers (1987) 577.
18. J. W. Hancock and A. C. Mackenzie, Journal of Mech. Phys. Solids, **24** (1976) 147

Key Engineering Materials Vols. 183-187 (2000) pp. 1063-1068
© 2000 Trans Tech Publications, Switzerland

Interface Adhesion and Interlaminar Fracture Resistance of Carbon/PEEK Composites influenced by Cooling Rate

J.K. Kim and S.L. Gao

Department of Mechanical Engineering, Hong Kong University of Science and Technology, Clear Water Bay, Pokfulam Road, Kowloon, Hong Kong, China P.R.

Keywords: Carbon/PEEK Composite, Cooling Rate, Crystallinity, Interface Adhesion, Interlaminar Fracture Toughness, Matrix Ductility

ABSTRACT

A study has been made of the cooling rate influence on interlaminar fracture toughness of unidirectional carbon/PEEK composites. It is shown that the propagation values of both mode I and II propagation interlaminar fracture toughness increased with increasing cooling rate toward a saturation level. The cooling rate dependency of the composite interlaminar fracture toughness is the result of complex interactions between two important properties; matrix ductility and fibre-matrix interface bond strength. These two properties varied in totally an opposite manner against cooling rate through its effect on crystallinity. The plastic deformation of PEEK matrix played a predominant role for composite toughness, while an adequate interface bond is required to allow matrix deformation to take place fully.

1. INTRODUCTION

An important method to enhance the interlaminar fracture toughness of composites is to control the interphase properties [1,2]. Although there are no simple and quantitative relationships available for interface/interlaminar optimisation, various physio-chemical and thermo-mechanical principles can be used to qualitatively design the interface. It is well known that the translation of matrix resin fracture toughness to mode I interlaminar toughness of unidirectional fibre composites is highly dependent on the fibre-matrix adhesion [3]. Based on the above, much research has been made to study the processing conditions of thermoplastic matrix composites. In particular, the effects of cooling rate on crystallinity, interface adhesion and mechanical properties of carbon fibre PEEK matrix composites have received much attention. The fibre-matrix interface bond strength and matrix modulus and strength decreased, while the matrix ductility increased with increasing cooling rate, due to its dominant role in determining the degree of crystallinity [4].

However, the previous interlaminar fracture toughness results showed little consensus with respect to cooling rate. It is noted that the G_{IC} varied between 1.2 and 2.5 kJ/m^2 at a cooling rate of 1°/min for apparently the same fibre and matrix materials, and the G_{IIC} values displayed more scattering at a low range of cooling rate. While the G_{IC} values increased somehow [5-10], a slight drop [6] was also reported between 0.5 and 80°C/min. Large increases in G_{IC} and G_{IIC} were noted at cooling rates below 2°C/min [5,8,9], whereas they became roughly constant above 80°/min. It is uncertain as to whether the above inconsistency was due to genuine material characteristics or

experimental artifacts. In addition, the cooling rate studied so far has been limited to narrow ranges. In this paper, a specific study is made of the relationship between the fibre-matrix adhesion, matrix ductility and composite interlaminar fracture toughness over a wide range of cooling rates. The ultimate aim is thus to establish an optimal processing cooling rate window that can produce balanced mechanical and fracture characteristics of the composite.

2. EXPERIMENTS

All composite specimens were prepared using APC-2 prepregs that contained continuous AS4 carbon fibres of 64% by volume and a PEEK matrix (ICI Fiberite). The details of processing conditions and control of cooling rate are essentially the same as those reported previously [4]. Laminates of nominal thickness 3mm were formed by hand lay-up of 24 unidirectional plies of prepreg. Compressed air or water was supplied through the channels of hot press to obtain the cooling rates between 1°C/min to 180°C/min. Double cantilever beam (DCB) and end notched flexure (ENF) specimens employed for the mode I and mode II interlaminar fracture tests, and the mode I and II interlaminar fracture toughness values were calculated based on the compliance method [11]. Both the initiation and propagation values corresponding to crack initiation and plateau fracture toughness, respectively, are reported here.

3. RESULTS

Fig. 1 illustrates the crack growth resistance curves (R-curves) for specimens processed at different cooling rates, and the corresponding initiation and propagation values are summarised in Fig. 2. As expected, the R curves showed an increase in G_{IC} value for the initial few mm of crack growth and then leveled off at almost a constant value, $G_{IC,Prop}$ with further increasing the crack length. The initial increase in fracture resistance is known to be due mainly to the evolution of fibre bridging across the fracture surfaces, and to a less extent interface debonding and fibre pullout. Both the initiation and propagation values, $G_{IC,Init}$ and $G_{IC,Prop}$, increased with increasing cooling rate, as a direct consequence of improved matrix ductility and thus the ability to deform plastically. It was estimated that matrix deformation contributes more than 75% of composite interlaminar fracture toughness while the other failure mechanisms, such as interface debonding, fibre bridging and pullout, contribute the remaining 25% for carbon fibre thermoplastic matrix composites [12]. However, it is not clear why the $G_{IC,Init}$ value slightly dropped when the cooling rate was increased from 80 to 180C°/min. The initial and propagation values, $G_{IIC,Init}$ and $G_{IIC,Prop}$, of mode II interlaminar fracture toughness are plotted as a function of cooling rate in Fig. 3. The trends with respect to cooling rate were basically similar to those observed for the mode I interlaminar fracture toughness. The magnitudes were generally higher by about 0.5kJ/m^2. The differences between the initiation and propagation values were also much larger than the mode I result, suggesting that these fracture energies showed different responses to cooling rate.

The fracture surface was examined using a SEM, and typical microphotographs are shown in Figs. 4 and 5. For all specimens tested, there was evidence of interfacial debonding, matrix plastic deformation, fibre breaks, and fibre pull out as well as fibre bridging during the propagation. In the slow cooled specimens that showed a high interface bond strength and brittle matrix [4], the fracture surface was characterized by crystal markings in the matrix (Fig. 4(a)), along with limited interfacial debonding, fibre breaks, and fibre pull out. The distinctive fracture markings are reminiscent of spherullitic structure of crystallised PEEK [13]. In mode II loading, the stiff crystallites were shown stretched along the loading direction (Fig. 5(a)). The majority of fibres were

coated with the matrix material in both mode I and mode II test specimens, indicating a strong fibre-matrix interface bond which was even greater than the matrix strength. The clean matrix fracture without hackle markings suggests brittle fracture of matrix crystallites and the crack propagation occurred primarily in the main plane. In contrast to the brittle interlaminar fracture observed in the slow cooled specimens, the fracture surfaces for fast cooled specimens were dominated by the extensive plastic deformation of the matrix (Fig. 4(b) and 5(b)) along with fibre-matrix interfacial debonding. The distinct morphology arising from matrix deformation reflects the loading mode. In the DCB test, the matrix material was stretched perpendicular to the fibre surface, whereas in the ENF test, plastic shear occurred at an angle 20~30° to the fibre axis, reflecting the thickness of matrix layer between the reinforcing fibres.

4. DISCUSSION AND CONCLUDING REMARKS

It was noted that the fast cooled specimens exhibited extensive multi-layer delaminations in the wake of crack tip. To establish quantitative correlation with the mode I interlaminar fracture toughness, crude estimates were made of the fracture process zone or damage zone size in front of crack tip, $2R_p$, on the basis of the linear elastic fracture mechanics equation: $R \approx (K_{IC} / \sigma_y)^2 / 3\pi$, where K_{IC} and σ_y are the stress intensity factor and yield strength of matrix material. The damage zone sizes estimated thereby are approximately 74μm and 286μm for the slow cooled and fast cooled specimens, as presented in Table 1. These values are well compared with the predictions based on the mechanical properties measured previously [14]. The damage zone size was mainly responsible for the increasing crack growth resistance behavior observed in Fig. 1.

The PEEK resin displayed a remarkable 230 % improvement in fracture toughness from G_{IC}^m = 1.78kJ/m^2 to 5.83 kJ/m^2 when the cooling rate was changed from 1 to 80°C/min. Meanwhile, the corresponding increase in G_{IC} was less than 50 % for the same range of cooling rate, resulting in only partial transfer of matrix toughness to composite fracture toughness. This observation is summarized in Fig. 6 along with relevant data compiled previously [11]. Of note is that the results obtained in the present study fell just near the upper bound of experimental data scatter reported previously. However, the general trend was congruent with the well-established explanations as follows. For brittle resins, including the PEEK matrix processed at a cooling rate 1°C/min, the composite toughness G_{IC} is similar to or even higher than the matrix toughness, G_{IC}^m. As the resin toughness increases, the increase in composite G_{IC}^c would be a small fraction of the increase in resin, G_{IC}^m. Therefore, for ductile resins, such as the PEEK resin obtained at cooling rates at or above 80°C/min, the composite G_{IC}^c becomes much smaller than the G_{IC}^m. Amongst established explanation is the suppression of the toughening effect in a thin matrix film between the stiff, reinforcing fibres that act as rigid fillers and constrain plastic deformation and microcracking at the crack tip [3]. Another reason is that the premature interface debonding does not allow extensive matrix deformation to occur. Unless the interfacial adhesion is improved, the ductile PEEK rein resulting from high cooling rates is not fully translated to the composite fracture toughness. In the slow cooled composites, however, the interlaminar fracture toughness was low mainly because of the brittle matrix material arising from the high degree of crystallinity although the interface bond was strong. The strong interface adhesion did not much contribute to the toughness because of the predominant role of matrix ductility in forming the fracture process zone around the crack tip. Thus, it is not surprising to have a similar value for G_{IC}^m and G_{IC}.

It was shown in the preceding section that cooling rate influences the interlaminar fracture resistance through its effects on matrix ductility and interface bond strength. It appears that the

matrix ductility and interface bond strength counterbalance each other rather than being synergistic. It is of particular interest to look into the correlation amongst all these parameters, as illustrated in Fig. 7. It is worth noting that matrix ductility is roughly proportional to cooling rate, while the converse is true for interface bond strength. Both the initiation and propagation values, $G_{IC,Init}$ and $G_{IC,Prop}$, increased in a similar manner to matrix ductility between 1°C/min and 80°C/min. A further increase above 80°C/min did not to the same extent. It seems that the weak interface bond strength obtained at high cooling rates led to premature debonding, which in turn played a significant role to impair the toughness contributed by the high matrix ductility.

REFERENCES

1 J.K. Kim, Key Eng Mater. 141-143 (1998) 149.
2 J.K. Kim and Y.W. Mai, Comp. Sci. Technol. 41 (1991) 333.
3 W.L. Bradley, Key Eng. Mater. 37 (1989) p161.
4 S.L. Gao and J.K. Kim, Composites Part A, in press 2000.
5 P.T. Curtis, P. Davies, I.K. Partridge and J.P. Sainty, In: Proc. ICCM 6/ECCM 2. Elsevier, London. 1987, Vol. 4, p401.
6 P. Davies. W.J. Cantwell, C. Moulin and H.H. Kausch, Comp. Sci. Technol. 36 (1989) 153.
7 A. Lustiger, F.S. Uralil and G.M. Newaz, Polym. Compos. 11(1990) p65.
8 P. Vautey, SAMPE Quart. 21 (1990) p23.
9 P. Davies, W.J. Cantwell, P.Y. Jar, H. Richard, D.J. Neville and H.H. Kausch, T.K. O'Brien ed. In: Composite Materials: Fatigue and Fracture. ASTM STP 1110, Philadelphia, PA. 1991, p70.
10 T. Vu-Khanh and S. Frikha, J Thermoplas. Compos. Mater. 12 (1999) p84.
11 J.K. Kim, C. Baillie, J. Poh and Y.W. Mai, Comp. Sci. Technol. 43 (1992) p283.
12 P.J. Hine, B. Brew, R.A. Duckett and I.M. Ward, Comp. Sci. Technol. 35 (1989) p31.
13 R.A. Crick, D.C. Leach, P.J. Meakin and D.R. Moore, J. Mater. Sci. 22 (1987) p2094.
14 M.F. Talbott, G.S. Springer and L.A. Berglund, J. Compos. Mater. 21 (1987) p1056.

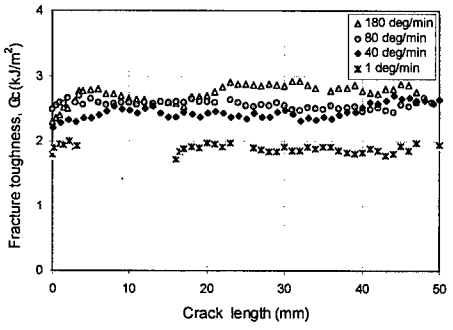


Fig. 1 Plots of mode I interlaminar fracture toughness versus crack length for specimens with cooling rates: (✳) 1 °C/min, (◆) 40 °C/min, (●) 80 °C/min and (Δ) 180 °C/min

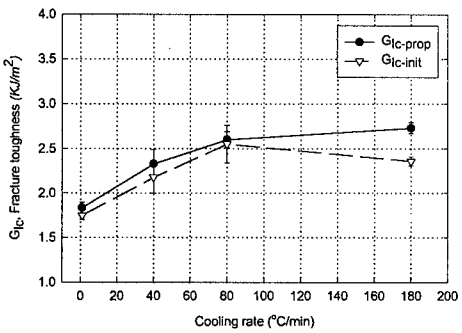


Fig. 2 Initiation $G_{IC\text{-}init}$ (∇) and propagation $G_{IC\text{-}prop}$ (●) values of mode I interlaminar fracture toughness as a function of cooling rate.

Table 1 Fracture toughness of PEEK resin and damage zone size in carbon fibre-PEEK matrix composite. Values in parentheses are taken or estimated from Talbott et al. [14].

Cooling Rate (°C/min)	Modulus E (GPa)	Yield Strength σ_y (MPa)	Stress Intensity Factor, K_{IC} (MPa $m^{1/2}$)	Fracture Toughness of PEEK resin, $G_{IC}{}^{m} \cong K^2_{IC}/E$ (kJ/m^2)	Damage Zone Size $R_p \cong K^2_{IC}/(3\pi\sigma^2_y)$ (μm)
1	4.6 (4.6)	108 (100)	(2.86)	1.78 (1.78)	73.7 (86.7)
80	4.0 (3.6)	93 (92)	(4.83)	5.83 (6.48)	286.2 (292.4)

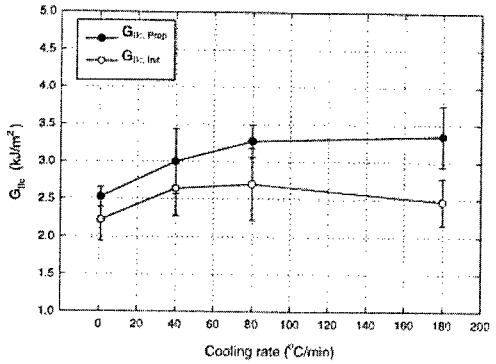
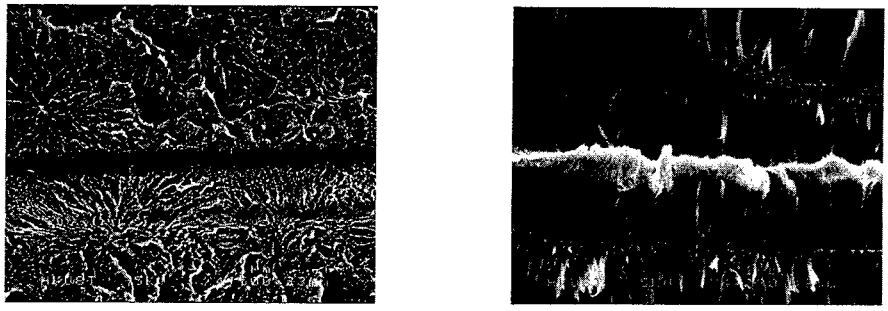
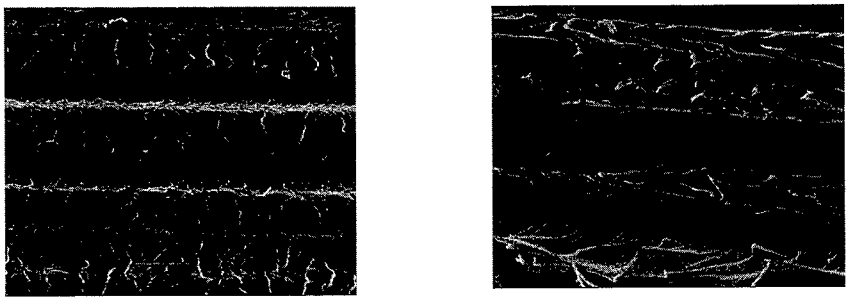


Fig. 3 Initiation $G_{IC\text{-}init}$ (o) and propagation $G_{IC\text{-}prop}$ (•) values of mode II interlaminar fracture toughness as a function of cooling rate.



(a) (b)

Fig. 4 SEM micrographs of Mode I interlaminar fracture surfaces of specimens cooled at (a) 1°C/min (b) 180 °C/min.



(a) (b)

Fig. 5 SEM micrographs of Mode II fracture surfaces: (a) 1°C/min and (b) 180°C/min.

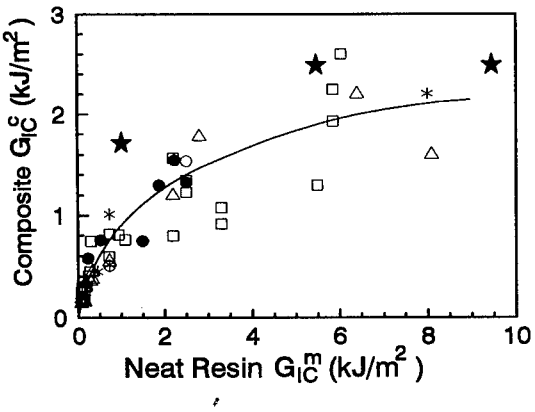


Fig. 6 Composite Mode I interlaminar fracture toughness (G_{IC}) as a function of resin toughness (G_{IC}^{m}). After Kim et al. [11], (★) present work.

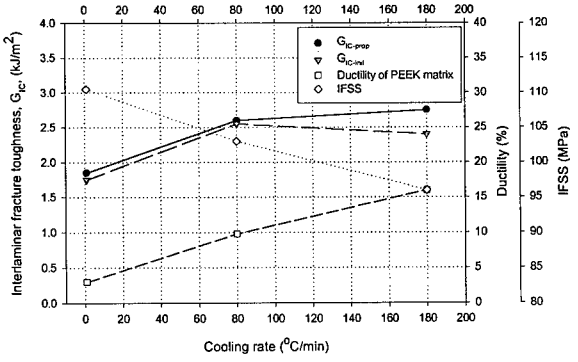


Fig. 7 Variations of composite mode I interlaminar fracture toughness, matrix ductility and interface shear bond strength (IFSS) as a function of cooling rate.

Key Engineering Materials Vols. 183-187 (2000) pp. 1069-1074
© 2000 Trans Tech Publications, Switzerland

Nondestructive Evaluation of Degree of Fiber Waviness in Thick Composites

H.-J. Chun[1] and P.-S. Jang[2]

[1] School of Electrical & Mechanical Engineering, Yonsei University, 134, Shinchon-dong, Seodaemun-gu, Seoul 120-749, Korea

[2] Department of Mechanical Engineering, Yonsei University, 134 Shinchon-dong, Seodaemun-gu, Seoul 120-749, Korea

Keywords: Fiber Waviness, Nondestructive Evaluation, Thick Composites, Ultrasonics

ABSTRACT

An experimental investigation was conducted nondestructively to evaluate the degree of fiber waviness in thick composite materials using ultrasonics. An analytical model, based on the ray and plane wave theories, was proposed to understand the ultrasonic wave propagation in composites with uniform fiber waviness. In the model, the composites were assumed to have continuous fibers with sinusoidal waviness in a matrix. The experiments were conducted on the specially fabricated thick composite specimens with various degrees of uniform fiber waviness using the conventional through-transmission method. For the given positions of transmitter, the locations of receiver with the maximum energy of received wave were measured along with the traveling time of the wave. From these and conjugated results from the analytical model, the paths of ultrasonic wave, wavelength of fiber waviness, concave and convex regions of fiber waviness and amplitude of fiber waviness were determined. Then, the nondestructively determined values were compared with the actual measurements obtained from the test specimens. Good agreements were observed among them.

1. INTRODUCTION

Fiber waviness is one of the manufacturing defects frequently encountered in thick composite structures. It results from local buckling of prepreg or wet hoop-wound filament strands under pressure exerted by the overwrapped layers during the filament winding process or from lamination residual stress built up during curing. Its characteristic can be represented by the through thickness undulation of fibers within thick composite laminates.

According to a number of studies on the behavior of thick composites with fiber waviness, fiber waviness causes degradation of strength and stiffness significantly[1-2]. Therefore, nondestructive evaluation technique that can detect fiber waviness of thick composite is needed for integrity of structures. For this purpose, there have been the investigations that attempt to explain how wave propagates in thick composites with fiber waviness[2-3].

In this paper, both theoretical and experimental investigations were conducted to evaluate uniform fiber waviness in thick composites nondestructively. The ray paths were predicted for waves insonified at various positions in the model. The experiments were conducted on specially fabricated thick composite specimens with various degrees of uniform fiber waviness using the conventional through-transmission method.

2. ANALYSIS

Figure 1 shows the geometry of model with sinusoidal fiber waviness. It is assumed that all the fibers are parallel to each other and have sinusoidal curvature along one spatial coordinate direction (x axis). The angle between the tangent to fiber and the x axis is a function of x, and it is given by,

$$\theta_f = \tan^{-1}\left(\frac{2\pi a}{\lambda}\cos\left(\frac{2\pi x}{\lambda}+\frac{\pi}{2}\right)\right) \tag{1}$$

where a and λ are the amplitude and wavelength of fiber waviness, respectively. θ_f is defined as the angle between the tangent to fiber and the x axis.

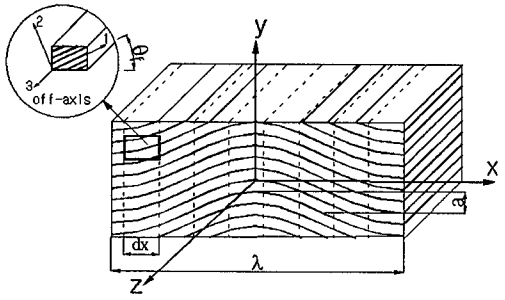


Fig. 1 Schematic drawing of a representative volume of composite materials with fiber waviness.

For waves propagating in the x-y plane, waves have quasi-modes and actually propagate along the direction of group waves with group velocity due to effects of anisotropy on waves[4-6]. The group velocity of quasi-longitudinal or quasi-transverse wave can be determined by known phase velocity and polarization vector[6].

$$(v_g)_i = \frac{1}{\rho} C_{ijkl} m_j p_k p_l \tag{2}$$

where m_i, p_i, ρ and C_{ijkl} are slowness vector, polarization vector, density and stiffness, respectively.

Because the elastic properties of thick composites with fiber waviness change continuously as wave propagates, analytical model is proposed to consider refraction of wave as shown below. For

incident wave with elastic properties of the i^{th} ray point, two refracted waves and two reflected waves at the i+1th ray point are considered to calculate the wave propagation direction. Based on Snell's law, the wave normal of refracted and reflected waves are obtained from Christoffel's equation in terms of slowness[7].

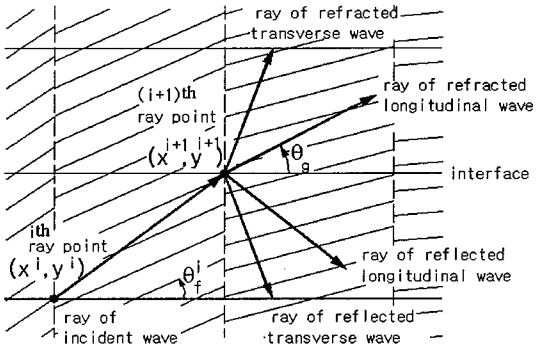


Fig. 2 Schematic drawing showing infinitesimally short length elements for analysis.

The group waves for all waves are also obtained using Eq. 3 at the i+1th ray point with each phase velocity and its polarization vector. Finally, the ray path is given by

$$x^{i+1} = x^i + \Delta\cos\theta_g \ , \qquad y^{i+1} = y^i + \Delta\sin\theta_g \tag{4}$$

where superscript i and Δ are step number and discrete ray increment, respectively. θ_g is the angle of group velocity determined by fiber orientation angle.

3. EXPERIMENTAL PROCEDURES

The materials investigated in this study were DMS 2224 graphite/epoxy composites (Hexcel, Inc.). Ultrasonic inspections were conducted on specially fabricated thick composite specimens with uniform fiber waviness. The fiber waviness ratios (a/λ) were 0.011, 0.034 and 0.059. The standard composite specimens without fiber waviness were fabricated for comparing experimental results with those with fiber waviness and also used for the characterization by conventional wave velocity measurement method. The elastic constants of standard specimen listed in Table 1 were used for input data for the numerical ray tracing model as on-axis stiffnesses.

Table 1 Stiffnesses of DMS 2224 graphite/epoxy unidirectional composites

Stiffnesses	C_{11}	C_{22}	C_{12}	C_{44}	C_{55}
Value	129.74 GPa	14.04 GPa	6.38 GPa	3.45 GPa	6.12 GPa

Pulser/reciver (5072PR, Panametrics Inc.) and longitudinal transducers (10MHz central frequency, Panametrics Inc.) were operated in through-transmission mode as shown in Fig. 3. The captured

ultrasonic signals in oscilloscope (ScopeStation 140, LeCroy Inc.) were stored into the personal computer via GPIB bus.

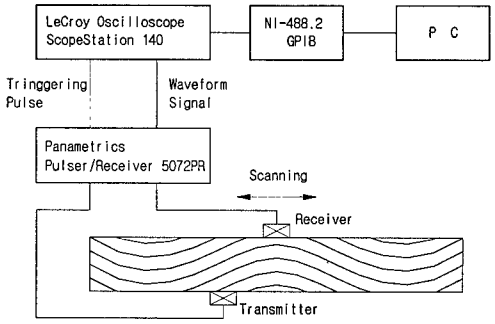


Fig. 3 Schematic drawing of experimental setup.

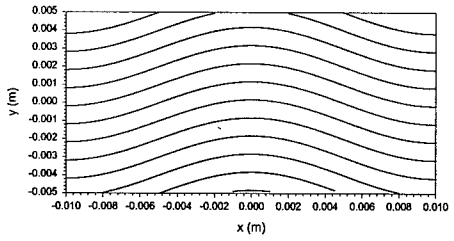
For a given position of transmitting transducer, waveforms were recorded as receiving transducer moved along x axis at 1mm interval. The energy P of received wave was obtained by integrating the magnitude of signal $s(t)$ as below.

$$P = \int |s(t)|\, dt$$

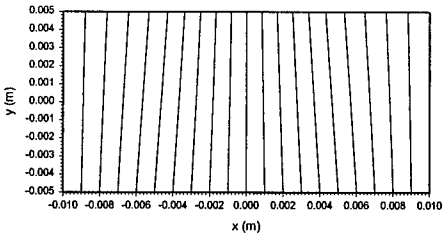
For a particular position of transmitting transducer, received energy of wave at various positions were represented as relative values to the maximum value of P.

4. RESULTS AND DISCUSSION

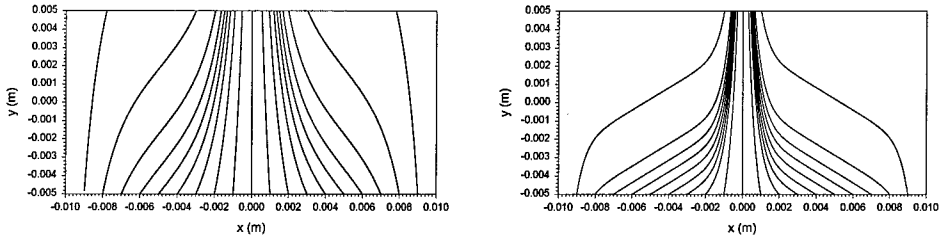
The numerical simulations were conducted for the waviness model with various fiber waviness ratios. Incident wave was normal to the surface of model and wave source was considered as a point-like source. The ray paths are shown in Fig. 4. As the results of simulation, insonified waves at different locations propagate toward adjacent concave region of fiber waviness.



(a) Schematic drawing of thick composite specimen showing fiber waviness (a/λ) of 0.059



(b) Ray paths with fiber waviness (a/λ) of 0.011

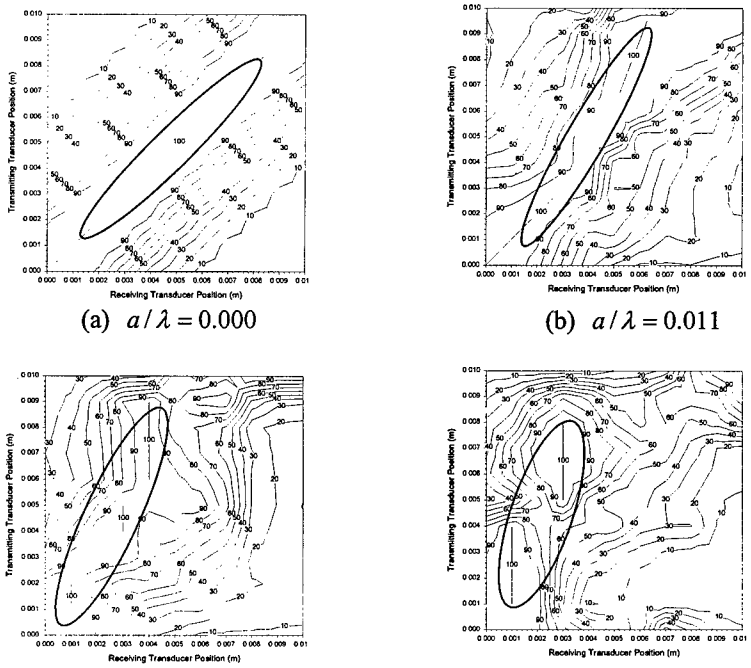


(c) Ray paths with fiber waviness (a/λ) of 0.034

(d) Ray paths with fiber waviness (a/λ) of 0.059

Fig. 4 Ray paths of quasi-longitudinal wave in composites with the various degrees of uniform fiber waviness.

Waves insonified at various bottom positions were detected at the opposite side of the specimen. It was observed that the energy of wave converged to the adjacent peak of fiber waviness. For the standard specimen without fiber waviness, waves with the maximum energy were detected at the same location in the x-axis as that of transmitting transducer, and energy distribution of received energy was symmetric to it. The location where maximum energy of wave was detected moved to the convex region of fiber waviness as the degree of fiber waviness increased. That is expected from the predicted results. This tendency is obviously shown in the contour plots of energy distribution of received wave. The regions checked by ellipse in Fig. 5 are the locations where maximum energy of wave is detected for various positions of transmitting transducer.



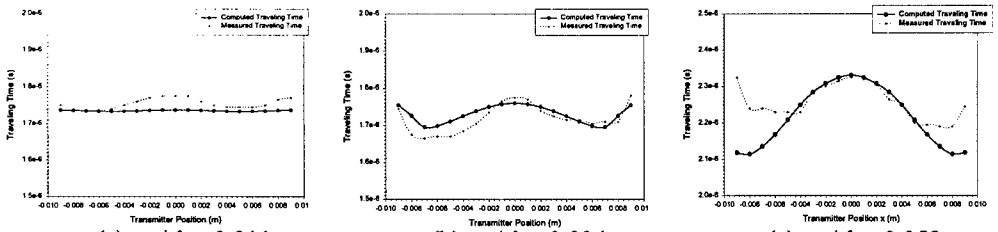
(a) $a/\lambda = 0.000$

(b) $a/\lambda = 0.011$

(c) $a/\lambda = 0.034$

(d) $a/\lambda = 0.059$

Fig. 5 Contour plots of energy distribution of received wave for the various degrees of fiber waviness.



(a) $a/\lambda = 0.011$ (b) $a/\lambda = 0.034$ (c) $a/\lambda = 0.059$

Fig. 6 Plots of computed traveling time and measured traveling time versus position of transmitting transducer for the various degrees of fiber waviness (Thickness : (a) and (b) 5.3mm, (c) 7mm).

The predicted traveling time and measured traveling time of wave are shown in Fig. 6. The traveling time of wave was measured at the location where maximum energy was detected. As the degree of fiber waviness increased, variation of traveling time was also increased. Some discrepancies were found, but tendency of traveling time obtained by the experiments was similar to those of predicted results. This discrepancies might be caused by assumption that wave-source is point-like source.

5. CONCLUSIONS

Based on the results from the numerical simulations and experiments, the following conclusions are obtained for the nondestructive evaluation of fiber waviness in thick composites.

1. If the maximum energy of received wave is detected at the same locations in the x-axis for both transmitting and receiving transducers, it indicates convex or concave peak of fiber waviness. The wavelength of fiber waviness is determined quantitatively by the relative distance between the peaks.
2. The degree of fiber waviness is qualitatively determined by considering energy converging region and the relative distance between two transducers.
3. By considering the energy distribution of received waves for a position of transmitting transducers, concave or convex region of fiber waviness is distinguished.

ACKNOWLEDGEMENT

The authors are grateful for the support provided by Brain Korea 21 from Korea Research Foundation (KRF).

REFERENCES

1. H.-J. Chun, I. M. Daniel, J.-Y. Shin, AIAA/ASME/ASCE/AHS/ASC Structures, Structural Dynamics, and Materials Conf. and Exhibit. Vol. 1, ST. LOUIS, MO, (1999) p.467
2. Shi-Chang Wooh, Isaac M. Daniel, Ultrasonics, **33** (1995) p. 3
3. Kwang Yul Kim, Wei Zou, Wolfgang Sachse, J. Acoustical Society of America, **103** (1998), p. 2296
4. Edmund G. Henneke II, J. Acoustical Society of America, **51** (1972) p. 210
5. S. I. Rokhlin, T. K. Bolland, Laszlo Adler, J. Acoustical Society of America, **79** (1986), p. 906
6. Adan H. Nayfeh, Wave propagation in layered anisotropic media with application to composite, North-Holland (1995)
7. Fedor I. Fedorov, Theory of elastic waves in crystals, Plenum press. New York (1968)

Key Engineering Materials Vols. 183-187 (2000) pp. 1075-1080
© 2000 Trans Tech Publications, Switzerland

The Damage Evaluation of Rigid Particle Filled Polymer

S.L. Bai[1,2], J.K. Chen[3], Z.P. Huang[1] and Z.D. Liu[4]

[1] Department of Mechanics and Engineering Science,
Peking University, Beijing 100871, China P.R.

[2] State Key Laboratory of Nonlinear Mechanics, Institute of Mechanics,
Chinese Academy of Sciences, Beijing 100080, China P.R.

[3] Yangzhou University, Yangzhou 225009, China P.R.

[4] Department of Power Engineering, North China Electric Power University,
Beijing 102206, China P.R.

Keywords: Cyclic Loading, Damage, Experimental Study, Polymer, Rigid Particle

ABSTRACT

In this paper, the rigid particle filled polymer is studied in the hope to understand the real damage mechanisms. Two damage parameters were introduced and measured. One is the macro-damage of the materials calculated from the modulus measured, another is micro-damage describing the interfacial debonding or the percentage of the particle debonded from the matrix. The damage rate of the macro damage decreases, while the micro damage increases with the applied stress.

1. INTRODUCTION

The rigid particle filled polymer has received much attention since the first study was made in 1984[1]. Much work was focused on the brittle-ductile transition of such materials [2-4]. The rigid particle can greatly improve the strength and modulus of polymers, and also in some cases the toughness if suitable parameters such as the size, volume fraction of particles and the adhesive strength of the interface etc. are well designed [5,6]. The reinforcing and toughening mechanisms are related to the damage evolution process in the materials. The voids induced by the interfacial debonding for particle filled polymers contribute to a great extent to the damage. If the interfacial adhesion is weak, the interfacial crack will be created early and then developed into void with the continuous application of the load. In this case, the void growth and coalescence will play an important role in the damage evolution of the materials. However, if the interface adhesion is too strong to be debonded, the matrix crazing will take place and predominate in the damage evolution process, the toughening effect can not be achieved. The growth and coalescence of the voids induced by interfacial debonding was studied theoretically [7,8]. For particle filled polymer, the interfacial debonding represents one of the main factors controlling the damage. Much often, the

modulus change is chosen as a parameter to describe the damage level. By theoretical analysis, the modulus change due to the void formation and growth could be predicted [9]. Also by experiments, the modulus variation can be measured as a function of applied stress or strain.

In this paper, a experimental study was carried out on the damage evolution in a particle filled polymer. Both macro cyclic tensile tests and in situ tensile tests are carried out. The percentage of particles debonded is measured as a function of applied strain. The variation of Young's modulus is also measured.

2. MATERIALS AND EXPERIMENTAL STUDY

Both pure high density polythylene(HDPE) and glass bead(GB) filled HDPE are used as the studied materials. In the manufacture process of GB/HDPE composites, the glass beads are pretreated with 10% of γ-aminopropyltriethoxysilane. The mixture of HDPE, HDPE-g-MA and glass beads with weight ratio of 984.54:71.82:143.64 grams is put into the chamber of a high speed mixer, and then blended in a twin-screw extruder. The pelleted extrudate is injection molded into tensile samples. A strong chemical bonding at the interface is formed according to the chemical analysis. The volume fraction of the glass beads is 5%. The micrograph in Fig.1 shows the particle distribution in the matrix. The size distribution of the particles is shown in Fig.2 with the maximum concentration at about 22μm in diameter.

Both monotonic and cyclic tensile tests are carried out on a MTS810. The geometry of tensile samples refers to the standards ASTM D638, type M. The gage length is 50mm and the strain rate is 3×10^{-5}/s. *In situ* tensile tests are undertaken under a scanning electronic microscope (SEM) with the effective sample section of $4\times3\times1mm^3$. During the *in situ* tensile tests, a continuous observation of the damage evolution process is made.

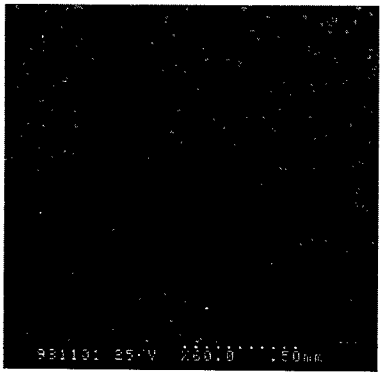


Fig.1. The particle distribution

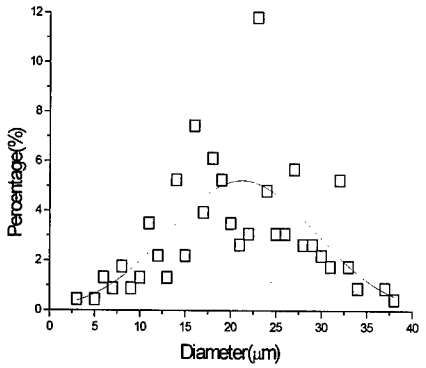


Fig.2. Size distribution of the particles

3. RESULTS AND DISCUSSION

3.1 Macro-behavior under tension

Fig.3 gives the monotonic tensile σ–ε curves of GB/HDPE and HDPE. It can be seen that GB/HDPE composite has better mechanical properties than pure HDPE, reflected by 7.4% of

increase in maximum tensile stress and 15.2% in Young's modulus. This result proves the fact that rigid particles can improve the mechanical properties of polymers. Here, the studied materials are too ductile to be ruptured. So the final strain is chosen to be 25 %.

The curves in Fig.4 represent the cyclic process of HDPE and GB/HDPE until 20% of final applied strain. After each load-unload cycle, the slope of unloading σ–ε curves is measured. In Fig.5 the modulus change is given as a function of applied maximum stress at each cycle. The GB/HDPE has the same type of modulus variation with HDPE. From the fact that GB volume fraction is low, the mechanical properties of GB/HDPE are mainly controlled by the matrix. Therefore, the mechanical behavior of two materials are similar.

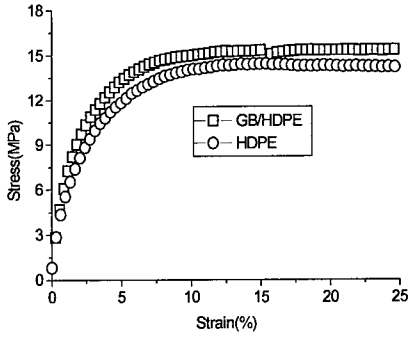


Fig.3. Monotonic tensile curves

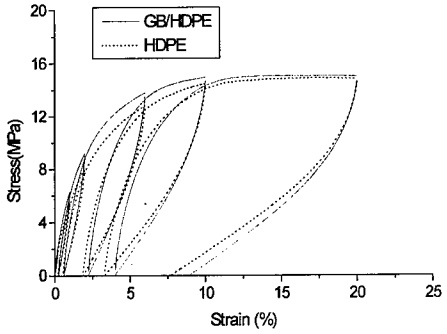


Fig.4. Cyclic tensile curves

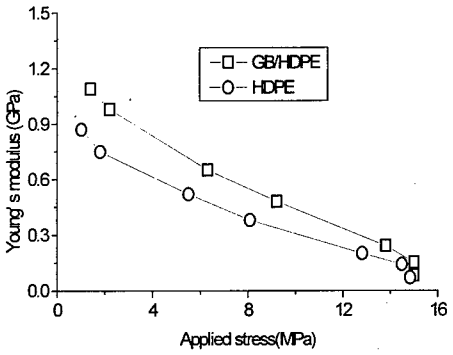


Fig.5. Young's modulus versus σ

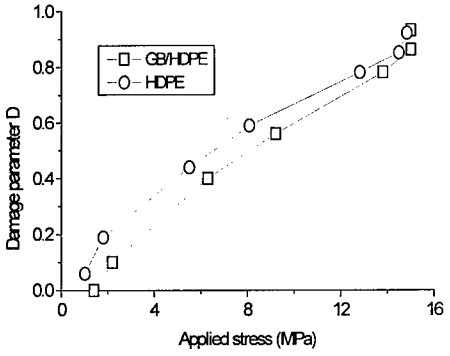


Fig.6. Damage parameter D versus σ

It is noted that with the increasing of applied stress, the difference of Young's modulus between two materials becomes less and less. Owing to the low volume fraction of GB, the voids induced by the interfacial debonding contribute in a limited extent to the modulus. So, the damage in the materials is caused mainly by the matrix microcracking. The interfacial debonding occurred under high external stress. The GBs can still resist the matrix contraction after the interfacial debonding, but the damage in the matrix predominates.

If we use the damage concept, the damage degree of the materials can be expressed by the variation of Young's modulus: $D = 1-E/E_0$, here, D called damage parameter, E_0 and E are the Young's modulus of intact and damaged materials respectively. The damage degree D as a function of the applied stress is shown in Fig.6. According to D values, under a given stress, HDPE is more damaged than GB/HDPE. At high stress, the damage of two materials is almost same.

3.2-*In situ* tensile tests

In order to observe the damage evolution process for GB/HDPE, the *in situ* tensile tests are carried out under SEM. During the test, the interfacial debonding is observed as shown in Fig.7. The interfacial debonding is initiated at two poles of the GB and the interfacial crack growths into void with the continuous loading. The interface at the top and bottom of GB seems to be in contact. The interfacial debonding represents one of the main damage mechanisms for GB/HDPE. $D^* = V_f n/N$ is defined as the damage parameter related to the interface debonding. n and N are the number of the GBs debonded and the total number of the GB in the materials respectively. It is supposed that a GBs debonded can be considered as a void which has the same volume as the GB. In reality, the GB debonded can still resist the transverse constraction of the matrix, so D* should be considered as the upper limite of the damage induced by the interfacial debonding.

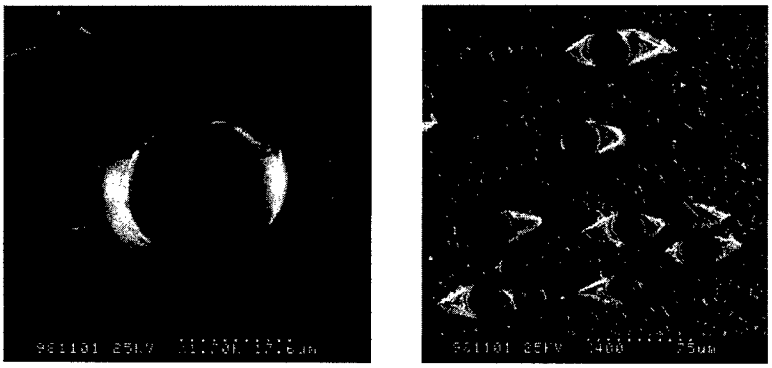


Fig.7. Micrographs showing the interfacial debonding and void formation

The variation of D* as a function of applied stress is shown in Fig.8. The tendance of this D^*-σ curve is different from that of D-σ curves. According to D^*-σ curve, the damage rate $dD^*/d\sigma$ is more and more great. D* value is much smaller than D value. In fact, D* is included in D which is composed of two parts : matrix damage and the interfacial debonding. The matrix damage is mainly the microcrazes created under the stress. With the increasing of GB volume fraction, D* value will be closer to D value. From D^*-σ and D-σ curves, it is found that the damage rate $dD^*/d\sigma$ increases with the applied strain, while $dD/d\sigma$ decreases. This difference is owing to the different damage mechanisms which are brittle for the interfacial debonding and ductile for the microcrazing of matrix.

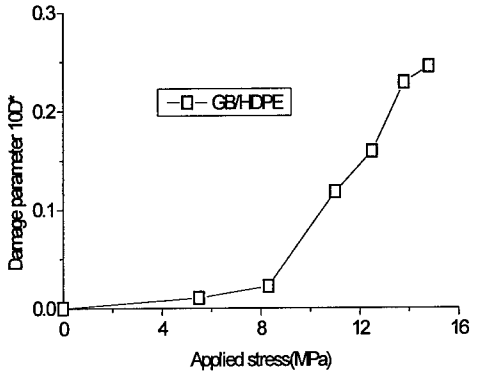


Fig.8. Damage parameters D* as a function of applied stress

4. CONCLUSIONS

The damage of rigid particle filled polymer materials is studied quantitatively. Two damage parameters are measured. First one D describes the macro-damage evolution of the materials. Second one D* represents the micro-damage evolution characterized by the interfacial debonding. The damage rate $dD/d\sigma$ decreases, while $dD^*/d\sigma$ inceases with the applied stress. This result reflects the different damage mechanisms induced by the interfacial debonding and by the matrix microcrazing.

ACKNOWLEDGMENT

This work is supported by the National Natural Science Foundation of China (19872007 and 19632030)

REFERENCES

1. T. Kurauchi and T. Ohta, J. Mater. Sci., **19**(1984), P.1699
2. S. Wu, Polymer, **26** (1985). P.1855
3. S. Wu and A. Margolina, Polymer, **31**(1990), P.971
4. Q. Fu and G. H. Wang, J. Appl. Polym. Sci. **49** (1993), P.673
5. K-K. Koo, T. Inoue and K. Miyasaka, Polymer Engin. Sci. **25** (1985), P.741
6. J.C. Angola, Y. Fujita, T. Sakai and T.Inoue, J. Polym. Sci., Polym. Phys. **26** (1988), P.807
7. Z. P. Huang, J. K. Chen, H. L. Li and Y. Liu, Proc. IUTAM. Sym. On Rheology of Bodies with Defects, (Wang R. ed.), Kluwer Academic Publishers, 1998, P.133
8. J. G. Ning and Z. P. Huang, Progress in Natural Science, **8**(6)(1998), P.726
9. G. K. Hu , Int. J. Plasticity, **12** (1996), P.439

Key Engineering Materials Vols. 183-187 (2000) pp. 1081-1086
© 2000 Trans Tech Publications, Switzerland

Microstructural Morphology of Molded Thin Composites of Thermotropic Liquid Crystalline Polymer and Polyamide 6

N.S. Choi[1] and K. Takahashi[2]

[1] Department of Mechanical Engineering, Hanyang University, Ansan-si, Kyunggi-do 425-791, Korea

[2] Research Institute for Applied Mechanics, Kyushu University, Kasuga, Fukuoka 816-8580, Japan

Keywords: Bend Strength, Epoxy Fraction, Injection Moulding, Multi-Layered Structure, Polyamide 6, Thermotropic Liquid Crystalline Polymers

ABSTRACT

Microstructural morphology of moulded composites of thermotropic liquid crystalline polymer(LCP) and polyamide 6 (PA6) was studied as a function of epoxy fraction. Injection-moulding of a thin composite plaque from extruded LCP/PA6 pellets at a temperature below the melting point of the LCP fibrils generated a multi-layered structure; while the surface skin layer with a thickness of 65-120μm indicated a transverse orientation, the sub-skin layer was oriented in the flow direction and arc-curved flow traces featured in the core layer. The plaques containing 4.8vol% epoxy exhibited superior bending strength and large fracture strain.

1. INTRODUCTION

In recent years improvements in the mechanical properties of isotropic thermoplastic polymers have been achieved by blending the polymers with a thermotropic liquid crystalline polymer (LCP) [1-7]. During melt blending with a thermoplastic polymer, fibrous LCP domains representing rigid-rod molecular order at a liquid mesophase state are formed under the influence of elongational and/or shearing flow. Since the LCP experiences a state of liquid mesophase with low viscosity, the polymer blend is more easily processed than the base polymer; also, wear on the processing equipment is much reduced.

When the blends are extruded and drawn, in-situ formed LCP fibrils are mostly aligned in the blends, thus improving the mechanical properties substantially. When moulding temperature is raised beyond the melting point of LCP, injection moulding of the blends can bring about not only in-situ LCP fibrillation but also formation of very complex anisotropic morphology patterns.

A few researchers [4,5] have proposed a method of moulding composite structures without melting the LCP fibrils; they used the extruded fibers containing in-situ-formed dispersed fibrils of LCP in a thermoplastic matrix. In the present study, extruded pellets containing in-situ formed LCP fibrils and polyamide 6 (PA6) matrix were employed for injection-moulding at a temperature below the melting point of the LCP fibrils. We performed a study on various morphological characteristics of the skin and core layers of moulded plaques and on the relationship with their bending strength.

2. EXPERIMENTAL

2.1. Materials manufacturing

Three kinds of resin were used for this study: Liquid crystalline thermotropic polymer (LCP) in the form of extruded pellets (Vectra A950, Hoechst Celanese Co.); thermoplastic polyamide 6 (PA6) with molecular weight Mw=30,000 in the form of pellets (nylon 1030B, Ube Industries Ltd.); two-functional epoxy resin in the form of flakes (Epiclon 7050, Dainippon Ink & Chemicals Inc.).

LCP pellets, PA6 pellets and epoxy flakes were dried in a vacuum oven for 24 hours at 80°C, and were weighed. We then prepared four kinds of mixtures: LCP/PA6/epoxy in volume fractions (%) = 30/70/0, 30/67.6/2.4, 30/65.2/4.8, 30/60.9/9.1. The mixture was extruded with an Ikegai PCM30 extruder, equipped with a set of twin screw (screw diameter=30mm, length to diameter ratio =17) and a straight die-head (hole diameter=3mm, hole length to diameter ratio=10). Cylinder temperature of the extruder was kept at 270°C, since a previous flow testing had revealed that melt viscosity of the LCP polymer at the temperature was equivalent to that of PA6 and so finely dispersed LCP droplets could form in PA6 matrix. The shear rate at the die region was about 200/s. Extruded strands which passed over the die-head were quenched in a water bath and then drawn at a take-up speed of 55m/min. The cold strands were cut into pellets using a pelletizer.

The blended pellets were dried in a vacuum oven at 90°C for 24 hours. Moulding was carried out with a preplasticizing injection moulding machine (Nissei PS60E, Nissei Plastic Industrial Co.). The pellets were melted in a heated cylinder at 220°C so that only PA6 matrix was in the molten state, and were injected into end-gated

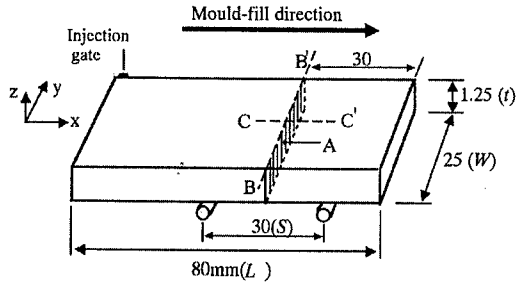


Fig. 1 Specimen geometry and mould fill direction

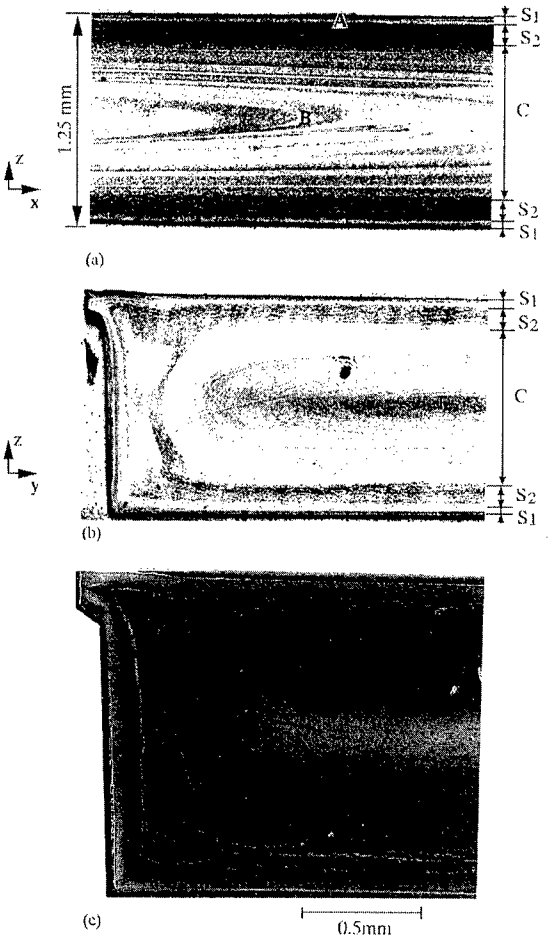


Fig. 2 Micrographs of the cross-sections revealing the skin-core structure and injection-flow patterns: optically-observed (a) x-z and (b) y-z section in Fig.1. (c) SEM observation of the same section as (b).

plaque-shaped moulds which were kept at 70°C. It should be mentioned that the LCP fibrils were not completely melted during the injection moulding. The moulded plaque geometry and mould fill direction are shown in Fig. 1. Plaques 80mm long, 12mm wide, 1.2mm thick were employed as bending test specimens.

2.2. Microstructural morphology observation and flexural test

The plaques were sectioned and polished along the lines B-B' (y direction) and C-C' (x direction) as illustrated in Fig. 1. Microstructural morphology on the surface was examined under a reflection optical microscope and then with a field-emission type scanning electron microscope (SEM). Specimen surface was sputter-coated with gold prior to SEM observation.

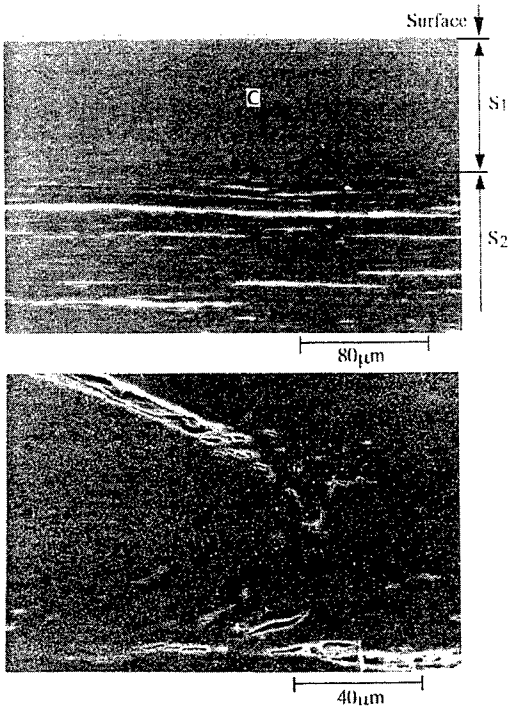


Fig. 3 Scanning electron micrographs (a) and (b) taken from areas A and B in Fig.2(a), respectively.

As illustrated in Fig.1, each specimen was placed on two fixed roller supports separated at a distance (*S*) of 30mm. A bending load was applied to the specimen by another roller at the position B-B' at a crosshead speed of 50mm/min.

3. RESULTS AND DISCUSSION

3.1.Microstructural characteristics of the skin and core layers

Figs. 2a and 2b show typical optically-observed microstructures of the polished x-z and y-z cross-sections of a LCP30vol%/(PA6+epoxy4.8vol%) plaque, respectively. Similar flow patterns were observed throughout the whole cross section except the part of 1.5mm in depth near the side edge (Fig.2b). Regarding the figures, first, morphological anisotropy was obvious; the macroscopic structure pattern formed in the mould-fill direction (Fig.2a) was completely different from that in the transverse direction (Fig.2b). Second, three distinct layers were seen stacked from the plaque surface to the interior; a bright surface layer (surface skin layer, S1), a dark layer (sub-skin layer, S2) under S1 and a core layer (C) in which flow traces were observed as arc-like parabolic patterns. The thickness of the S1 and the S2 layer was about 65μm and 120μm, respectively.

On the other hand, one can see in the S2 layer in Fig.3a that the LCP domains were oriented in the mould-fill direction and a considerable number of cleavage did appear between the domains and PA6 matrix. The cleavages formed in any part of the S2 layer as shown in Fig.2c. This seems to imply that tensile stresses were raised transverse to the S2 layer during the molding process and that there had been LCP/PA6 interfaces weak enough to be failed by the stresses. Cleavages were also

seen along the arc-curved flow lines in the central region of the C layer (Figs. 2a and 3b). This indicates that the C layer having curved weak regions should have been affected by biaxial tensile stresses.

We consider that during the cooling process following the injection moulding tensile thermal stresses were somehow caused in the S2 and C layers because of different LCP orientations at each layer, i.e. of different thermal expansion coefficients and elastic moduli. Using a finite element program (Ansys version 5.3), stress distribution due to different thermal contraction at each layer can be analyzed. Based on a two-dimensional finite element model thermally loaded by a temperature drop (Δ T=-200°C), a calculated distribution of the normal stresses σ_y and σ_z is shown in Fig. 4. In the S2 layer both the tensile stress σ_z and the compressive stress σ_y are generated. Although the value of σ_z (about 1.0MPa) is not so high, it may be enough to induce the interfacial delamination if there are weakly bonded parts being distributed over the LCP/PA6 interfaces. In the C layer σ_y and σ_z are both tensile. It seems these biaxial tensile stresses that have caused the curved cleavage (Fig.3b) along the poor adhesion region between some of the neighboring curved flows.

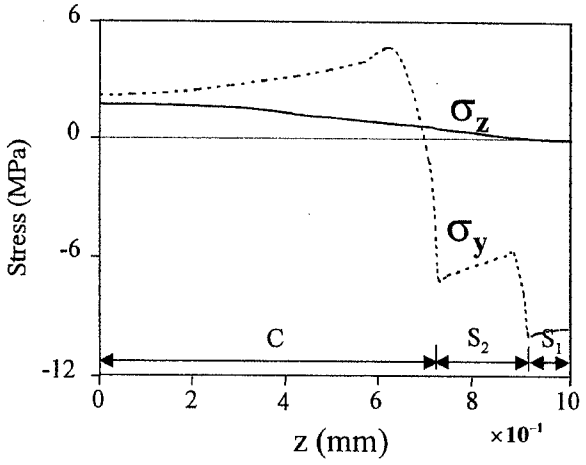


Fig. 4 Normal stress (σ_z, σ_x) distribution along the thickness (z) direction in the respective layers.

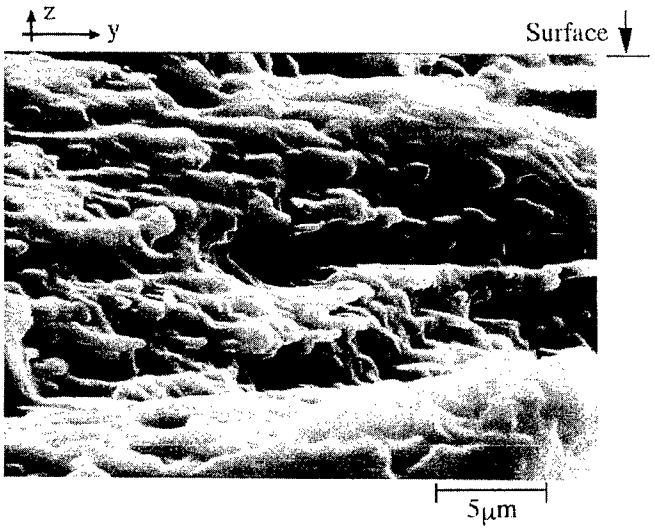


Fig. 5 Scanning electron micrograghs of the fracture surface (y-z plane) taken from the surface skin layer in a molded LCP30vol%/(PA6+epoxy4.8vol%) specimen.

To make a further morphological study, a notched LCP30vol% /(PA6+epoxy4.8vol%) plaque immersed in liquid nitrogen was broken by impact loading in such a direction that could cause a transverse sectioning. The fracture surface of the S1 layer (Fig.5) revealed fibrillar LCP domains. The fibrils 0.3 - 2 μm in diameter were oriented perpendicularly to the flow direction, i.e. in the y-direction. Figures 5b and 3a show that LCP

Table 1 Bending properites of moulded LCP30vol.%/(PA6+ epoxy) composites as a function of epoxy volume fraction

Epoxy fraction (vol%)	Flexural modulus E_{flex} (GPa)	Flexural strength σ_{max} (MPa)	Strain energy at fracture U_{total} ($x10^{-2}J/m^2$)
0	$5.6^{+0.2}_{-0.3}$	$157.3^{+5.6}_{-6.0}$	$2.7^{+0.1}_{-0.1}$
2.4	$5.4^{+0.2}_{-0.2}$	$143.4^{+3.3}_{-3.0}$	$3.1^{+0.1}_{-0.2}$
4.8	$5.6^{+0.4}_{-0.3}$	$154.5^{+5.2}_{-5.6}$	$3.3^{+0.1}_{-0.2}$
9.1	$4.1^{+0.1}_{-0.1}$	$119.1^{+5.6}_{-5.3}$	$1.1^{+0.3}_{-0.2}$

domains in the S2 layer featured in a mixture of lamellar and fibrillar structures. On the basis of the above observations, orientation and distribution of LCP fibrils or lamellae in the moulded plaque are schematically presented in Fig. 6.

For an injection-moulded LCP bar, Ophir and Ide [6] reported seven distinct layer structures: The surface skin layer with high orientation in the flow direction, a layer which might originate from the 'fountain flow'(elongational flow) at the melt front; the sub-skin layer which is almost unoriented and probably caused by the 'spreading radial flow'; the core layer which tends to be rather transversely oriented because of the shearing flow; the center layer produced by converging and 'plug flow'. After experiments using thin-wall large-area plaques 3.2mm in thickness, Kenig et al.[7] suggested that the skin layer thickness might be determined by the heat transfer process during the mould filling. In the case of the present study, the S1 layer about 65 μm in thickness had a very distinctive orientation: most of the LCP fibrils were oriented in the transverse direction. The transverse orientation must have been caused by the rotational and shearing flow field, which can be generated in a region very close to the fixed surface of the mould wall, as presumed from the Newtonian hydrodynamic principle of viscosity [8]. These peculiar microstructures were observed even when the fractions of epoxy component contained in the moulded LCP/PA6 plaques were different.

3.2. Epoxy fraction effects on bending properties

The data obtained from our flexural experiments are listed in Table 1. the composite containing epoxy 4.8vol% is a material considerably improved in bending properties.

4. CONCLUSIONS

Microstructural morphology of injection-moulded composite plaques of thermotropic liquid crystalline polymer(LCP) and polyamide 6 (PA6) have been investigated as a function of epoxy

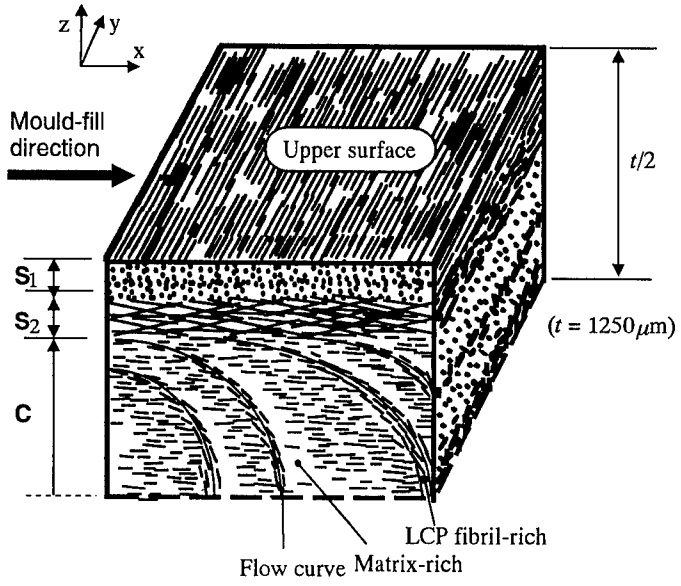


Fig. 6 Schematic orientation and distribution of LCP fibril or lamelae in the moulded specimen of Fig.1.

fraction. (1) Injection-moulding of LCP/PA6 plaques at a temperature below the melting point of the LCP fibrils generated the multi-layered structure: the surface skin layer 65-120 μm thick and transversely oriented, the sub-skin layer oriented in the flow direction, and the core layer presenting arc-curved flow patterns. Similar microstructural orientations in the respective layers were observed in the moulded LCP/PA6 plaques containing various fractions of epoxy. (2) Cleavages were observed in the sub-skin layer when the tensile stress was induced in the transverse direction during the moulding process. (3) The composite plaques containing epoxy4.8vol% were superior to the other specimens in strength and strain under the bend test.

ACKNOWLEDGEMENTS: This work was supported by grant No. 981-1003-019-2 from the Basic Research Program of the Korea Science and Engineering Foundation. The authors would express their appreciation to Mr. M.Kurokawa in Starlite Co. who kindly provided specimens.

REFERENCES

1. G. KISS, *Polym. Eng. Sci.*, **27** (1987)p.410.
2. S. S. BAFNA, et al. *Polym. Eng. Sci.*, **33** (1993)p.808.
3. A. I. ISAYEV and M. MODIC, *Polym. Comp.*, **8** (1987)p.158.
4. B. R. BASSETT and A. F. YEE, *Polym. Comp.*, **11** (1990)p.10.
5. M. KUROKAWA and S. NAGAI, *Polym. Eng. Sci.*, **39** (1999)p.872.
6. Z.OHIR and Y.IDE, Polym.Eng.Sci., **23** (1983)p.792.
7. S. KENIG, et al., *Polym.Comp.*, **9** (1988)p.20.
8. Y.C.FUNG: A 1st Cource in Cont. Mechanics, (Prentice Hall, NJ 1994)p.183.

Key Engineering Materials Vols. 183-187 (2000) pp. 1087-1092
© 2000 Trans Tech Publications, Switzerland

Optimization of Molding Cure Condition on Al 7075/CFRP Sandwich Composite by the Taguchi Method

H.K. Yoon[1], S.H. Lee[2] and W.K. An[3]

[1] Department of Mechanical Engineering, Graduate School of Dong-eui University, 24 Gaya dong, Pusan jin-ku, Pusan 614-714, Korea

[2] Department of Industrial Engineering, Graduate School of Dong-eui University, 24 Gaya dong, Pusan jin-ku, Pusan 614-714, Korea

[3] Korean Science and Engineering Foundation (KOSEF), 180-1, Kajung-dong, Yousung-ku, Taejon 305-350, Korea

Keywords: Co-Curing Method, Curing Method, Secondary Curing Method, Taguchi Method, Unidirectional Carbon Prepreg

ABSTRACT

The optimization of a molding cure cycle on the carbon fiber reinforced aluminum layer laminate (CARALL) was investigated by the Taguchi Method in experimental design. CARALL specimens were fabricated with CFRP prepreg and Al 7075 by using an autoclave. Design methods were systematically performed using an $L_8(4^1\times 2^4)$ orthogonal array table of the experimental design. In the experimental design, three molding cure cycle parameters (molding pressure, curing method and dwell time at curing temperature) were considered and the effects of the parameters on the peel strength were investigated. The analysis of variance for the experimental results indicated that curing method and dwell time at curing temperature are the most significant parameters in the peel strength.

1. INTRODUCTION

CARALL Laminates are a new family of structural materials developed for fatigue critical applications requiring light sheet. [1-3] These materials are bonded arrangements of thin aluminum alloy sheets and alternating plies of epoxy resin, impregnated with unidirectional carbon fibers. The principal benefit of the resulting hybrid composite is ability to retard and self-arrest fatigue cracking by transfer of loads from the metal to the stronger unbroken fibers in the crack wake. [4] Generally, there are 3 curing processes in CARALL laminate composites ; one is to apply a curing cycle, recommended by the manufacturing company, as it is; another is an experimental method of trial and error, and the other is to use a curing cycle-through-analysis model. In the case of experimental method of trial and error, it takes too much time to get the curing cycle. On the other hand, curing process-through-analysis model has both a merit to be able to get the optimal curing cycle, and two demerits to be necessary for lots of data, which is difficult for measurement, and to have a difficulty in controlling manufacturing process in production process. Recently, Taguchi

Method of logical experimental plan method, which is under discussion and concern at various branches, is a very useful way to determine the optimal condition for a product or process by analyzing experimental result, by mean of experimental plan which is named orthogonal array table, through analysis of variance. Taguchi Method is an engineering methodology for improving productivity during research and development so that high-quality products can be produced quickly and at low cost.[7-8] In this study, We should have a decision to optimal peel-strength of autoclave cure for Al 7075/CFRP sandwich composite by Taguchi method.

2. Experimental Method

2.1. Experimental Material

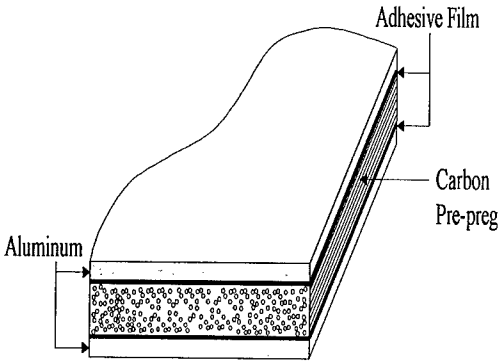


Fig. 1 Schematic illustration of CARALL laminates

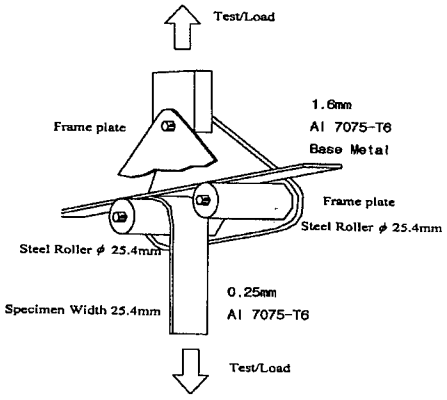


Fig. 2 Schematic illustration of floating roller peel strength test

Carbon prepreg of CARALL was unidirectional carbon/epoxy prepreg supplied F584-4 of HEXEL Co. Ltd, American. Carbon prepreg was a thin sheet that was impregnated with epoxy resin matrix with unidirectional carbon/epoxy of 0.13 mm thickness. Figure 1 is a schematic illustration of CARALL laminates. As seen in the figure, the laminate was cured with an Al 7075-73 alloy and unidirectional carbon prepreg using adhesive film.

2.2. Factor Selection

Control factors of autoclave cure were curing method, heat velocity, pressure of autoclave, curing temperature, sustain time of curing temperature and cooling velocity, factors were selected sustain temperature of curing method, pressure of autoclave and curing temperature Title

2.3. Level Selection

The Curing methods of CARALL material production are a co-curing method and a secondary curing method. Co-curing method was cured at the same time, after before treated Al plate and carbon/epoxy prepreg were laid up using adhesive film. Secondary curing method was cured, after cured carbon/epoxy laminate and Al plate were laid up using adhesive film. In this study, two method applied to optimal curing method. Also, pressure conditions of autoclave curing time were two kinds of 0.35 MPa and 0.59 MPa , and sustain times of curing time were 60 minute, 90 minute and 120 minute. Table 1 is control factor and level of autoclave by experimental plan method.

Table 1 Control factor and levels

Label	Factor	Levels		
		1	2	3
T	Time	60 min.	90 min.	120 min.
P	Pressure	0.35MPa	0.59MPa	
M	method	co-curing	se-curing	

2.4. Measurement of Characteristic Value

The Characteristic value of experimental plan method was a selected floating roller peel strength. Floating roller peel test is the same figure 2. As seen in the figure, a tensile test was performed on specimen of width 25.4 mm × length 254 mm. The velocity of a cross head is adjusted as 152 mm/min. Stress is the mean load divided by specimen width, and specimens are five specimen of equal curing condition.

2.5. Curing Method

The CARALL laminates composite was cured in a autoclave by the process as shown in figure 3, to an optimal curing cycle of composites. Figure 3 is a schematic illustration of lay-up system. Curing conditions were cured to 177℃ with heat velocity of 2.5℃/min in a fixed state of autoclave pressure. After the cure finished, it cool to room temperature with a cooling velocity of 3℃/min.

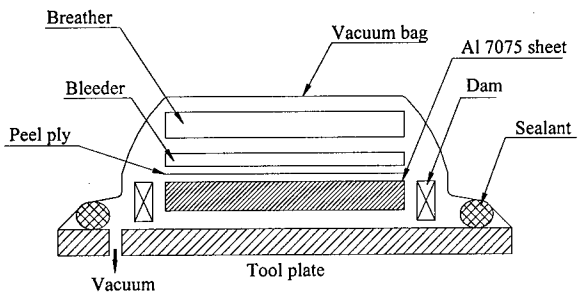


Fig.3 Schematic illustration of lay-up system

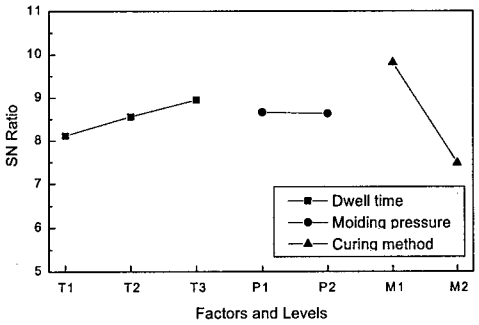


Fig. 4 Plot factor effects for SNratio

3. Experimental Results and Investigation

3.1. Effect of Control Factor

We selected the control factors and their levels as shown in Table 1, and assigned them to an L_8 ($4^1\times 2^4$) orthogonal array. The an L_8 ($4^1\times 2^4$) orthogonal array, after columns 1, 2, and 3 in the $L_8(2^7)$ standard orthogonal array are merged, is shown in Table 2. Then, dummy level technique can be applied to use a three-level factor(T). The dummy level technique is a modification to an orthogonal array's column having three or more levels in order to allow the use of a factor having fewer levels. A signal-to-noise analysis was performed using the standard large-the-better signal-to-noise transformation.

$$SNi = -10\log\left\{\frac{1}{5}\left(\frac{1}{y_{t1}^2}+\frac{1}{y_{t2}^2}+\frac{1}{y_{t3}^2}+\frac{1}{y_{t4}^2}+\frac{1}{y_{t5}^2}\right)\right\}$$

Table 2 L8 orthogonal array and factor assignment

Expt. No	T	P	E	M	E	Data					Mean	SN Ratio
	1	2	3	4	5							
1	1	1	1	1	1	2.89	3.53	2.81	2.51	2.96	2.94	9.21
2	1	2	2	2	2	2.04	2.27	2.20	2.27	2.53	2.26	7.03
3	2	1	1	2	2	2.60	2.86	1.97	2.88	2.15	2.49	7.62
4	2	2	2	1	1	3.03	3.17	2.86	2.72	3.22	3.00	9.49
5	3	1	2	1	2	2.89	3.88	2.84	3.20	3.36	3.25	10.03
6	3	2	1	2	1	2.46	2.08	2.51	2.51	2.37	2.39	7.49
7	3	1	2	2	1	2.13	3.17	2.17	2.51	2.63	2.52	7.77
8	3	2	1	1	2	3.24	3.53	3.15	3.74	3.19	3.37	10.50

The factor effects are displayed graphically in Fig. 4. Table 3 shows results of analysis of variance on SN ratio. In Table 3 we see that the molding pressure (P) is not significant. So a new ANOVA table, Table 4, was formed by pooling the sum of squares of the factor P with the error sum of squares. The factor T and M stood out as being significant at 10%. The factor M had the largest effect (89%) on the SN ratio. The next step in analyzing the experimental data was to determine the optimum condition. This is done simply by selecting the level that yielded the highest S/N ratio for each significant control factor.

Table 3 ANOVA table for SN ratio

Source	Sum of squares	d.f	Mean squares	F	P-Value	Percent contribution
T	0.93	2	0.46	3.92	0.15	5.70
P	0.00	1	0.00	0.02	0.90	-0.96
M	10.87	1	10.87	91.66	0.00	88.43
E	0.36	3	0.12			6.83
Total	12.16	7				

Table 4 Pooled ANOVA table for SN ratio

Source	Sum of squares	d.f	Mean squares	F	P-Value	Percent contribution
T	0.93	2	0.46	5.20	0.08	6.18
M	10.87	1	10.87	121.44	0.00	88.67
E	0.36	4	0.09			5.15
total	12.16	7				

The Optimum condition was found to be M1 and T3. The predicted signal-to-noise at the optimum condition is given by the following equations.

$$\hat{SN}(M_1T_3) = \overline{M}_1 + \overline{T}_3 - \overline{T}$$

$$= 9.81 + 8.95 - 8.64 = 10.12\,(dB)$$

where

$\overline{T}$ = Overall signal - to - noise ratio average

$\overline{M}_1$ = Signal - to - noise ratio of the curing method at level 1.

$\overline{T}_3$ = Signal - to - noise ratio of the dwell time at level 3.

3.2 Effect of Curing Method

Figure 5 is the shape of co-curing and secondary curing specimen. As seen in the figure, the specimen of lower part and middle part are co-curing specimen, and the upper part was secondary curing specimen. Co-curing specimen, lower and middle part, was inappropriate to apply, for it is measure deformation.On the other hand, secondary curing specimen was sustained very stable measure in general process. So that, curing method was selected secondary curing method

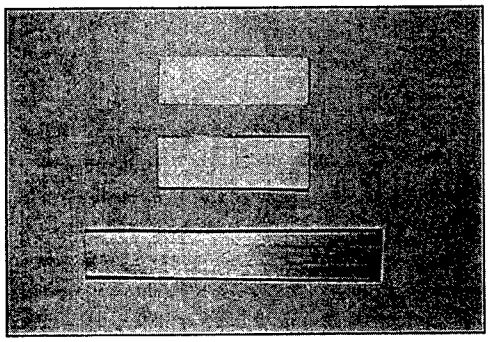


Fig.5 Shape of co-curing and secondary curing specimen
upper) secondary curing : short size
medium) co-curing : short size
lower) co-curing : long size

3.3 Optimum Curing Condition

To optimize the peel strength for the secondary-curing method, an additional experiment (experimental runs 1 and 5 in Table 5) was conducted, and thus the problem can be treated as a two-factor factorial design experiment. A summary of factor effects is tabulated in Table 6, and the factor effects are displayed graphically in figure 6.

Table 5 Two factor factorial design and data

Expt. No	P	T	Data					Mean	SN Ratio
1	1	1	2.36	3.08	2.32	2.06	2.42	2.45	7.56
2	1	2	2.60	2.86	1.97	2.88	2.15	2.49	7.62
3	1	3	2.13	3.17	2.17	2.51	2.63	2.52	7.77
4	2	1	2.04	2.27	2.20	2.27	2.53	2.26	7.03
5	2	2	2.06	2.10	2.72	2.04	2.77	2.34	7.13
6	2	3	2.46	2.08	2.51	2.51	2.37	2.39	7.49

Table 6 Factor level average for raw data and SN Ratio

Source	Sum of squares	d.f.	Mean squares	F	P-Value	Percent contribution
P	0.28	1	0.28	32.05	0.03	64.95
T	0.12	2	0.06	6.88	0.13	24.59
E	0.02	2	0.01			10.46
Total	0.42	5				

It is clear that the molding pressure (P) and dwell time (T) have a significant effect on the S/N ratio. From Table 6 and Figure 6, the optimum level of significant factors is determined as P1 and T3. We can estimate the SN ratio and mean peel strength for this optimum condition as:

$$\hat{SN}(P_1T_3) = \overline{P}_1 + \overline{T}_3 - \overline{T}$$
$$= 7.65 + 7.63 - 7.43 = 7.85(dB)$$
$$\overline{y}(P_1T_3) = 2.49 + 2.45 - 2.41 = 2.52(N/mm)$$

Figure 7 shows the results of curing cycle of an Al 7075/CFRP sandwich composite decided by the Taguchi method in an experimental design.

As seen in the figure, heat temperature and cooling velocity are 2.5 ℃/min and 3℃/min, curing temperature is 177℃, curing method is secondary curing method, pressure of autoclave is 0.35 MPa, and the sustain time of curing temperature is 120 min.

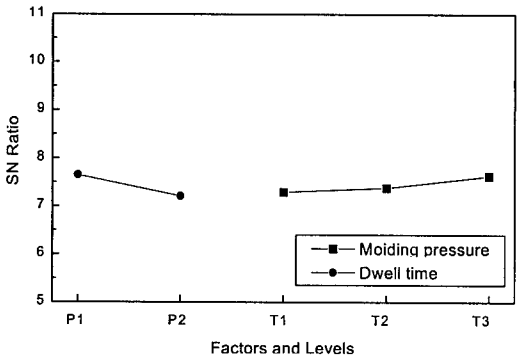


Fig. 6 Plot of factor effects for SN ratio

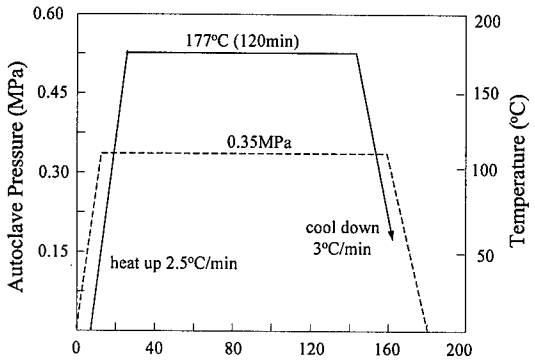


Fig. 7 The resultsof optimum curing cycle

4. Conclusion

We decided to select optimum curing cycle of autoclave cure for Al 7075/CFRP sandwich composite by Taguchi method. The results were as follows;

1) The decisive time of curing cycle decreased by experimental plan method
2) Peel strength of co-curing method is higher than that of secondary curing method, but we discovered an inequality of carbon/epoxy thickness in the quality of manufactured goods.
3) Optimum curing cycle of CARALL composite was decided ; heat temperature and cooling velocity are 2.5℃/min, curing temperature is 177℃, curing method is secondary curing method, pressure of autoclave is 0.35 MPa, sustain time of curing temperature is 120 min.

ACKNOWLEDGEMENTS

The authors wish to acknowledge the financial support of the Dong-EUI University Research Foundation made in the program year of 1999 (DEURF - 1999AB027)

REFERENCE

1. A. K. Dhingra and T.P. Doherty. "Future Trends in Advanced Fibers and Composites", '93 International Conference on Composite Materials (1993) pp.29-34
2. D. H. Middleton, "Composite Materials in Aircraft structures- The Involvement of the united States Aircraft Industry in the Development of Advanced Composite Materials", Longman Scientific & Technical, John Weily Inc., New York (1990) pp.273-288
3. C. T. Lin, P. W. Kao and F.S. Lang, "Fatigue Behavior of Carbon Fiber-Reinforced Aluminum Laminates", Composites, Vol. 22. No. 2 (1991) pp.135-141
4. R. Marissen, L. B. Vogelesang, "Fatigue Mechanisms in ARALL, a Fatigue Resistant Hybrid Aluminum Aramid Composite Material" In Fatigue 87, 1987, pp.1271-1279.
5. David Jackson, "Reaction Injection Molding", 7th Symposium on Taguchi Methods (1989) pp.19-26
6. Brett R.M. Kyle, "Investigation of a Plastics Reprocessing Process", 7th Symposium on Taguchi Methods (1989) pp.389-400

Key Engineering Materials Vols. 183-187 (2000) pp. 1093-1098
© 2000 Trans Tech Publications, Switzerland

An Application of Localized Flexibility Method to Damage Identification in CFRP Laminated Plate

Yoshio Aoki[1] and O-IL Byon(Goichi Ben)[2]

[1] College of Sciences and Technology, Department of Precision Machinery Engineering, Nihon University, 7-24-1 Narashino-dai, Funabashi, Chiba 274-8501, Japan

[2] College of Industrial Technology, Department of Mechanical Engineering, Nihon University, 1-2-1 Izumi-cho, Narashino, Chiba 275-8575, Japan

Keywords: CFRP, Damage Detection, FEM, Inverse Problem, Localized Flexibility

ABSTRACT

This paper presents modal-based structural damage detection. Specifically, we focus on localized flexibility properties that can be deduced from the experimentally determined global flexibility matrix. We describe the underlying damage detection theory that can be viewed a generalized flexibility formulation in three different generalized coordinates, viz., localized or substructural displacement, elemental deformation-basis and element strain-basis. The three localized flexibilities are applied to a CFRP plate having interior damage. The results show that the elemental strain-basis flexibility is most accurate in detecting the damage of the CFRP laminates.

1. INTRODUCTION

CFRP laminated composites have very favorable strength and stiffness-to-weight ratio among engineering materials, which make their aerospace applications highly desirable and weight savings translate directly into higher performance. A major concern in using these composites is their vulnerability to impulsive loading by space debris, pebbles and dusts. This is because crack or damage caused by inter-laminar delaminations or fiber-matrix debonding in the laminated composites, although not visible on the surface, significantly reduces their strength and/or stiffness. A rational method for the detection of damage location and damage modes or mechanisms in composites can therefore facilitate a wider acceptance of composites by the practicing engineers.

To this end, several damage detection methods have been proposed, which include ultrasonic crack detection, wave propagation and scattering, modal testing, among other [1],[2]. We applied the localized flexibility method to damage identification in CFRP laminated beam and showed a good agreement of analytical results with the experimental ones [3]. The objective of the present paper is to offer a model-based damage detection technique by relying on vibrations test data. It should be mentioned that on-site vibration test is becoming economical and mobile as new miniaturized sensors of both contact and non-contact high-fidelity types which are readily available.

The present paper is organized as follows. First, a brief review of the variational formulation of the partitioned equations of motion for a vibrating structures is described. Second, by solving for the partitioned or substructural displacement, the relation between the partitioned flexibility and the global flexibility is established. The relation of the global frequency response function (FRF) to the partitioned FRF is then established by using the input/output invariance requirement. Third, by decomposing the elemental output displacement vector in terms of the strain amplitudes, a theory for strain output-based damage detection is derived by treating the strain gauge records. The damage location is estimated by the present three localized flexibility changes for CFRP laminated plate.

2. REVIEW OF LOCALIZED FLEXIBILITY FORMULATION

2.1 Global Flexibility Matrix

The discrete energy functional Π for a linear damped structure can be expressed as

$$\Pi(u_g) = u_g^T(\tfrac{1}{2}K_g u_g - f_g^D), \quad K_g = L^T K L, \quad K = \begin{bmatrix} K^1 & & \\ & K^2 & \\ & & K^{n_s} \end{bmatrix}, \quad f_g^D = f_g - M_g\ddot{u}_g - C_g\dot{u}_g \qquad (1)$$

where u_g is the displacement vector of the assembled structure; f_g^D is D`Alambert`s force vector that consists of the applied force vector f_g, the resisting inertia force $M_g\ddot{u}_g$, and the dissipating force $C_g\dot{u}_g$, K_g is the assembled stiffness matrix; C_g is the assembled damping matrix; M_g is the mass matrix of the assembled structure; K is the block diagonal collection of unassembled substructural stiffness matrices; L is the Boolean assembly matrix that relates the global and substructural displacements; the superscript (˙) designates time differentiation, and the subscript (g) designates 'an assembled global structure' to distinguish from 'partitioned substructures'.

The discrete damped, time-invariant linear equations of motion for vibrating structures can be obtained from the stationary value of the preceding discrete energy functional, viz., $\delta\Pi = 0$:

$$M_g\ddot{u}_g + C_g\dot{u}_g + K_g u_g = f_g \qquad (2)$$

The input-output relation, referred to as the *frequency response function* (FRF), is obtained by substituting a harmonic form of the input-output vectors as

$$\begin{bmatrix} u_g \\ f_g \end{bmatrix} = e^{j\omega t}\begin{bmatrix} \bar{u}_g \\ \bar{f}_g \end{bmatrix} \qquad (3)$$

and solving for the frequency-domain output $\bar{u}_g$:

$$\bar{u}_g = H_g(\omega)\bar{f}_g, \qquad H_g(\omega) = (K_g + j\omega C_g - \omega^2 M_g)^{-1} \qquad (4)$$

where $H_g(\omega)$ will be called the 'global' flexibility matrix and becomes to K_g^{-1} ($=F_g$) in the quasi-static limit ($\omega \to 0$). This matrix can be obtained in terms of the eigen modes Φ and eigen values Λ as

$$F_g = \Phi\Lambda^{-1}\Phi^T, \quad \Phi^T M_g \Phi = I, \quad \Phi^T K_g \Phi = \Lambda \qquad (5)$$

In practice, the size of the experimentally identified global flexibility matrix is given by

$$F_g = \Phi_m \Lambda_m^{-1} \Phi_m^T \qquad (6)$$

where the subscript (m) denotes the measured modes and mode shapes which are substantially smaller than the analytical mode size.

2.2 Substructural Flexibility Equation

Since our objective is to identify the damage location and the global flexibility-based damage indicators are known to mask localized damage attributes, we employ a general partitioned flexibility method presented by Park and Felippa [4] to relate the experimentally measured global flexibility matrix in Eq.(6) in term of the corresponding localized flexibility matrices. This is accomplished as follows. First, a structure that is in equilibrium under applied forces is partitioned into substructures or elements. Hence, each of the partitioned substructures would be subject to the corresponding applied forces plus the Lagrange multipliers acting along the substructural partition interfaces. In order to maintain the kinematical compatibility along the partitioned boundaries, the displacement vector of the partitioned substructures u must satisfy the following relation:

$$u - Lu_g = 0 \qquad (7)$$

where u are the collections of all the substructural displacements. The element-by-element force vector f that is conjugate with the substrutural displacement is given by

$$L^T f = f_g \qquad (8)$$

so that the desired FRF must assume the following form:

$$\bar{u} = H(\omega)\bar{f} \tag{9}$$

Observe that Eq.(9) relates the input $\bar{f}$ that is acting on each substructure defined in Eq.(8) to the output of individual substructural displacements $\bar{u}$ introduced in Eq.(7). Therefore, by introducing a Lagrange multiplier vector λ_f to enforce the kinematic compatibility condition Eq.(7), the system energy functional expressed in terms of the global nodal variables given in Eq.(1) is transformed into the three-variable functional:

$$\Pi(u,\lambda_f,u_g) = u^T(\tfrac{1}{2}Ku - f + M\ddot{u} + C\dot{u}) - \lambda_f^T B^T(u - Lu_g) \tag{10}$$

where and M and C are the substructural mass and damping matrices, and B is a constraint projection matrix that extracts the partition boundary substructural nodes. The stationary value of the above functional leads to the following equations of motion for partitioned structures:

$$\begin{bmatrix} M\ddot{} + C\dot{} + K & -B & 0 \\ -B^T & 0 & L_b \\ 0 & L_b^T & 0 \end{bmatrix} \begin{Bmatrix} u \\ \lambda_f \\ u_g \end{Bmatrix} = \begin{Bmatrix} f \\ 0 \\ 0 \end{Bmatrix}, \quad L_b = B^T L \tag{11}$$

The substructure-by-substructure FRF that is sought after can now be obtained from Eq.(11) as

$$H(\omega) = H_e(\omega)\{I - BK_B(\omega)[I - L_b H_L(\omega)L_b{}^T K_B(\omega)]B^T H_e(\omega)\} \tag{12}$$

$$H_e(\omega) = (K + j\omega C - \omega^2 M)^{-1}, \quad K_B(\omega) = (B^T H_e(\omega) B)^{-1}, \quad H_L(\omega) = (L_b{}^T K_B(\omega) L_b)^{-1}$$

It can be shown that the substructural FRF $H(\omega)$ can also be obtained in terms of the global FRF $H_g(\omega)$, viz.,

$$H(\omega) = LH_g(\omega)L^T = L(K_g + j\omega C_g - \omega^2 M_g)^{-1} L^T \tag{13}$$

Observe that the substructural FRF given by Eq.(12) reveals the substructural compositions consisting of the substructural mass, damping and stiffness matrices. On the other hand, the same FRF obtained by the input/output invariance property given by Eq.(13) masks the substructural compositions, showing only the global quantities. Their combined use leads to an important application in detecting damages as shown below. For the quasistatic limit, i.e., ($\omega \to 0$), the two expressions provide the following Ricatti-like equation:

$$\begin{aligned} LF_g L^T &= F\{I - BF_B^{-1}[I - L_b F_L L_b^T F_B^{-1}]B^T F\} \\ F = K^{-1}, F_B &= (B^T F B), F_L = (L_b^T F_B^{-1} L_b)^{-1} \end{aligned} \tag{14}$$

where F is called the substructural flexibility matrix of block diagonal form.

2.3 Deformation-Basis Flexibilities

The substructural flexibility matrix $F=K^{-1}$ given in Eq.(14) consists of both free-free deformation modes plus the rigid body modes. This poses no difficulty when the experimentally identified global flexibility Fg in Eq.(6) is a full basis matrix, viz., the eigenvector Φ_m is a square matrix. In practice the measured modes are often a fraction of the sensor output numbers, namely, for Φ_m (s > m) where s is the number of the sensors and m is the measured mode numbers. This observation motivated us to transform the free-free substructural flexibility matrix F into a constrained deformation flexibility which can lead to a sharper indication of damage. Let us decompose the substructural displacements u further into deformational and rigid parts:

$$u = d + R\alpha \tag{15}$$

where d is the deformational part, R describe the substructural rigid-mode shapes, and α are the rigid-mode amplitudes. In order to eliminate the rigid-body motions from the substructural displacements, we partition Eq.(15) according to:

$$\begin{Bmatrix} u_c \\ u_f \end{Bmatrix} = \begin{Bmatrix} d_c \\ d_f \end{Bmatrix} + \begin{Bmatrix} R_c \\ R_f \end{Bmatrix}\alpha, \quad R = \begin{bmatrix} R^1 & & & \\ & R^2 & & \\ & & \ddots & \\ & & & R^{n_s} \end{bmatrix} \tag{16}$$

where R_c is a square invertible submatrix corresponding to 'temporarily constrained nodes' and R_f refers to unconstrained nodes. Hence, R_c would be a (3 x 3) matrix. Similarly, the constrained-node rigid-body amplitudes R_c for other substructural cases can be chosen. Solving for α from the first row of Eq.(16), we obtain

$$\alpha = R_c^{-1}(u_c - d_c) \tag{17}$$

We now introduce a deformation measure that represents deformations at nodes *f* with respect to nodes *c*:

$$v = d_f - R_f R_c^{-1} d_c = Tu = TLu_g, \quad T = [-\bar{R}\ I], \quad \bar{R} = R_f R_c^{-1} \tag{18}$$

Using this relation, its conjugate force vectors are given by

$$T^T f_v = f \Rightarrow L^T T^T f_v = L^T f = f_g \tag{19}$$

The variational functional Eq.(10) expressed in terms of the substructural displacement u is transformed into that of the deformation variable v, which in the quasi-static limit becomes:

$$\Pi(v, \lambda_v, u_g) = v^T(\tfrac{1}{2}K_v v - f_v) - \lambda_v^T B_v^T(v - TLu_g), \quad K = T^T K_v T \tag{20}$$

A simple expression is obtained if the constraint operator B_v is chosen as a nullspace of TL, viz.,

$$B_v^T(TL) = 0 \tag{21}$$

So that the stationary condition $\delta\Pi = 0$ of Eq.(20) yields

$$\begin{bmatrix} K_v & -B_v \\ -B_v^T & 0 \end{bmatrix} \begin{Bmatrix} v \\ \lambda_v \end{Bmatrix} = \begin{Bmatrix} f_v \\ 0 \end{Bmatrix} \tag{22}$$

which will be called the deformational quasi-static equations of motion for partitioned structures. A Riccati-like equation which relates the global flexibility to the deformation-basis substructural flexibility can be obtained in a similar manner as for the substructural displacement case Eq.(14):

$$TLF_g L^T T^T = P_v^T F_v P_v, \quad F_v = K_v^{-1}, \quad P_v = I - B_v[B_v^T F_v B_v]^{-1} B_v^T F_v \tag{23}$$

2.4 Strain-Basis Flexibilities

We have experienced that the use of the deformational flexibilities F_v yields an adequate identification of damage locations. In many applications not only identifying damage locations but also damage mechanisms are equally important. For only through understanding damage mechanisms one can develop damage prevention measures. An effective approach to detect damage mechanisms is to utilize strain-basis substructural flexibilities. As an example, a typical substructure consists of membrane, transverse shear and bending strains. By identifying which of the three strains underwent a major strain change, one may deduce the damage mechanisms. The necessary transformation to obtain a strain-basis flexibilities is shown below. Let us assume that the strain output s can be related to the substructural displacement u according to

$$s = Du = DLu_g \tag{24}$$

where D is the discrete strain-displacement relation matrix that can be derived in a variety of ways, e.g., by relying on the finite element shape functions. With this change of basis, one arrives at the following strain-basis functional and the corresponding equations of motion in quasi-static form:

$$\Pi(s, \lambda_s) = s^T(\tfrac{1}{2}K_s s - f_s) - \lambda_s^T B_s^T(s - DLu_g), \qquad K = D^T K_s D, \quad B_s^T(DL) = 0 \tag{25}$$

$$L^T D^T f_s = f_g \Rightarrow \begin{bmatrix} K_s & -B_s \\ -B_s^T & 0 \end{bmatrix} \begin{Bmatrix} s \\ \lambda_s \end{Bmatrix} = \begin{Bmatrix} f_s \\ 0 \end{Bmatrix}$$

The global flexibility F_g is then related to the strain-basis substructural flexibility F_s according to:

$$DLF_g L^T D^T = P_s^T F_s P_s, \quad F_s = K_s^{-1}, \quad P_s = I - B_s[B_s^T F_s B_s]^{-1} B_s^T F_s \tag{26}$$

which can be used not only for localized damage detection but more importantly for identifying damage mechanisms.

3. APPLICATIONS TO DAMAGE DETECTION IN CONTINUUM CFRP COMPOSITES

For illustrating the applicability of the localized damage detection techniques reviewed in the preceding section to continuum composites, we evaluate the methods to analytical problems.

3.1 Analytical Demonstration

In order to demonstrate the validity of the damage detection methods outlined in the preceding section, a CFRP $[0/45/90/-45]_{2S}$ quasi-isotropic laminated plate having width and length of 200mm both and 2mm thickness and fixed at vertical edges is chosen as an example (see Fig.1). The laminated plate is divided into 25 same-size plate elements in the FEM analysis and the bending rigidity of the center (13^{th}) element is assumed to 85% value of other elements due to the damage. For offering the relative performance of three methods, the global flexibility F_g is adopted as an inverse of the global stiffness matrix that is obtained from the corresponding FEM analysis. For damage detection we have employed the following damage indicator δ:

$$\delta^{ns} = \mathrm{diag}(F^{ns}_{damage} - F^{ns}_{healthy}) / F^{ns}_{healthy} \qquad (27)$$

where the superscript (ns) designates the substructural component or degree of freedom.

In Figs.2 - 4, the dashed line indicates the damage indicator by using the 108 eigen values and eigen vectors in the global flexibility matrix F_g and the solid line is the damage indicator by using only the first ten eigen values and modes in the F_g. When the free-free substructural flexibility method is used, the damage is detected at the degree of freedom from 115 to 126 corresponding to 13^{th} element as shown in Fig.2. The resulting damage indicator as dashed line provides the location of damage correctly and the rigidity ratio of the corresponding element shows the assumed value of 0.85. Since the only the first ten eigenvalues and modes are used for calculating the global flexibility F_g in Eq.(6), the damage indicator as solid line cannot be accurately computed. Nevertheless, the locations of damaged elements are correctly determined. As for the deformation-based flexibility method, the damage should occur at the degree of freedoms from 94 to 102 is shown in Fig.3. Both of damage indicators correctly trace those nine degrees of freedom, but the dashed ones is overestimated for the assumed reduced bending rigidity. Finally, Fig.4 shows the damage indication based on the strain-basis flexibilities not only correctly detects the damaged 13^{th} element (25^{th} and 26^{th} degrees of freedom) but also computes almost same the

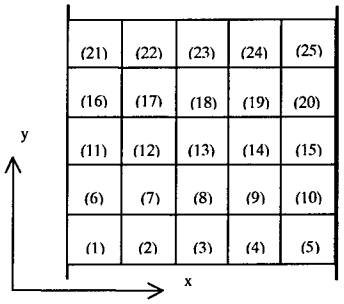


Fig.1 Partitioned Elements

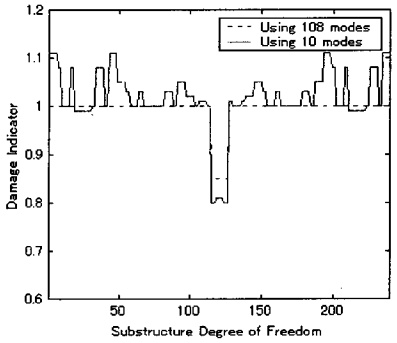


Fig.2 Damage Detection based on Substructural Flexibility

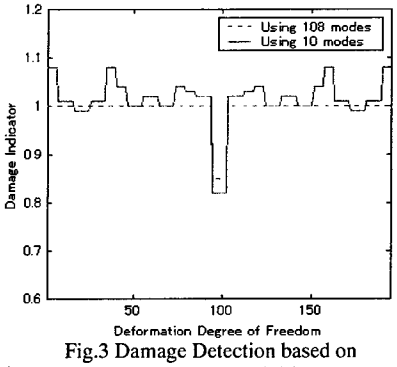


Fig.3 Damage Detection based on Deformation Flexibility

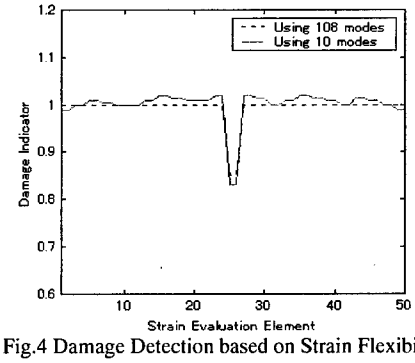


Fig.4 Damage Detection based on Strain Flexibility

damage indicator of 0.85. So far as the identification in CFRP laminates is concerned, the strain-basis damage indication can predict it well within acceptable accuracy ranges.

Next, the effects of the additional damage locations for the same CFRP laminated plate are investigated by varying the rigidity in the 2nd, 10th and 13th elements via the strain based flexibility method. For these example problems, the bending rigidity EI is reduced by 85% for those elements by modifying the first ten eigenvalues and eigenvectors in the global flexibility matrix F_g accordingly. Fig.5 shows that the reductions of bending rigidity for the respective elements are larger somewhat in all three cases but their locations are correctly determined.

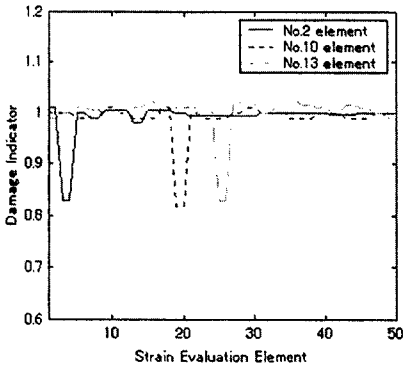


Fig.5 Analytical Damage Detection based on Strain Flexibility for Various Damage Locations

4. CONCLUSION

The damage indicator that utilizes the three localized flexibilities has been applied to the damage detection of CFRP laminated composite plate. The free-free localized flexibility and the deformation-basis flexibilities can make use of conventional output data such as acceleration or displacement. The strain-basis localized flexibility can utilize a combination of the conventional modal testy output as well as the strain output. The main features of the present study are summarized as follows.

1) The relative accuracy fidelities of the three localized flexibilities are evaluated as applied to the damage detection of CFRP quasi-isotropic laminated plates analytically. All three flexibility methods accurately captured the locations of rigidity changes. Among the three, the strain-basis flexibility method is most accurate.

2) In using analytically determined ten-mode global flexibility matrices of the three composite laminated plates, damage detections are carried out by the strain-basis flexibility method. The results demonstrate that damage locations are identified with high confidence as well as reasonably accurate change in the bending rigidities.

It should be noted that the present damage location and damage mechanisms identification procedure based on the localized strain-basis flexibilities can process each substructural input/output independently for spatially localized damage assessment, thus making the present procedure attractive for online health monitoring. This and related aspects are under active investigation.

REFERENCES

1. Doebling, S. W. et al, "Damage Identification and Health Monitoring of Structural and Mechanical System form Changes in Their Vibration characteristics: A Literature Survey", Los Alamos National Laboratory, Report No.LA-12767-MS, 1996, Los Alamos, NM.

2. Park, K.C., Reich, G.W. and Alvin, K.F., "Damage Detection Using Localized Flexibilities", Structural Health Monitoring, Current Status and Perspectives, Chang, F.K., Ed., Technomic Pub., 1997, p.125-139

3. Byon, O.I., Aoki, Y., Yamaguchi, T., Park, K.C. and G. W. Reigh, "Damage Detection of CFRP Laminates Composites by Localized Flexibility Method", Proceedings of 12th International Conference on Composite Materials, July, 1999, p.375

4. Park, K.C. and Felippa, C.A., "A Variational Framework for Solution Method Developments in Structural Mechanics", Journal of Applied Mechanics, March, 65/1(1998), p.242-249

Key Engineering Materials Vols. 183-187 (2000) pp. 1099-1104
© 2000 Trans Tech Publications, Switzerland

Crush Energy Absorbing Characteristics of Graphite/Epoxy Square Tubes

Hoon Cheol Park, Younho Choi and Kwang Joon Yoon

Department of Aerospace Engineering, Konkuk University,
93-1 Mojin-dong, Kwangjin-gu, Seoul 143-701, Korea

Keywords: Crush Energy Absorption, Failure Analysis, Finite Element Analysis, Graphite/Epoxy Square Tubes

ABSTRACT

In the present study, effect of stacking sequence on the peak load and the average sustained load of graphite/epoxy square tubes is investigated using the crush test. In the crush test, compressive load is applied on the top of composite square tubes under the stroke control with cross-head speed of 0.3mm/sec. The experimental data shows that the square tube with $[(+45/-45)_4]_T$ has the highest peak load. Whereas tubes with $[(0)_8]_T$ and $[(90)_8]_T$ showed poor crush energy absorbing characteristics, tubes with $[(0/90)_4]_T$ had the improved peak load and the average sustained load. In addition to the experimental survey, the finite element analysis is used to estimate the peak load of the graphite/epoxy square tubes with $[(0/90)_4]_T$ and $[(0/\pm 45/90)_2]_T$. The first buckling mode of the tube is superimposed to the perfect geometry and the distributed compressive load is applied on the top of the tubes for failure analysis. The lowest applied compressive load that makes failure criteria equal to one is regarded as the peak load of each tube. The estimated peak loads of the composite tubes with $[(0/90)_4]_T$ and $[(0/\pm 45/90)_2]_T$ agreed well with the measured peak loads using the failure analysis.

1. INTRODUCTION

Aircraft structures must be designed such that they can absorb crush energy during emergency landing. Crush energy absorbing characteristic of a structure depends on the material used for the structure, construction method and shape of elementary substructures, and the assembly method of each substructure[1]. Fiber reinforced composite material can be a candidate material for the construction of crush energy absorbing structures due to its superior specific stiffness and specific strength. Therefore, intensive researches have been conducted to figure out the failure mechanism of composite structure[2-5]. Comparatively, crush energy characteristics of composite square tubes are not deeply studied, even though several papers can be found in the literature[3]. Most of the existing works are focused on the experimental survey of the failure mechanism and energy absorbing characteristics of composite structural elements, such as plates and circular tubes. Recently, efforts to estimate the energy absorbing characteristics of composite circular tubes have been made[6-7].

In the present study, effect of stacking sequence of graphite/epoxy square tubes on the energy absorbing characteristics was experimentally investigated. In addition to the experimental survey, a finite element modeling technique is proposed to estimate the peak loads of the tubes with $[(0/90)_4]_T$

and $[(0/\pm45/90)_2]_T$.

2. CRUSH TEST OF COMPOSITE SQUARE TUBES

In the present work, a manufacturing method to construct composite square tubes has been developed. In the following sections, the manufacturing method, the crush test method, and the test result are explained.

2.1. Manufacturing of Graphite/epoxy Square Tubes

Firstly, graphite/epoxy prepregs were laminated as desired. The laminated graphite/epoxy prepregs were wrapped around the square silicon rubber extrude as shown in Fig. 1. Release film and other films are placed between the prepreg and the silicon rubber extrude.

Because one of the main purpose was to investigate effect of the stacking sequence on the peak load and the average sustained load, the prepreg was laminated as $[+\theta/-\theta]$, and then the prepreg was wrapped four times around the silicon rubber, so that the resulting square tube had $[(+\theta/-\theta)_4]_T$ lay-up. In the present study, ply angles θ were selected as 0, 30, 45, 60, and 90 degrees. In the similar way, graphite/epoxy square tubes with $[(0/90)_4]_T$ and $[(0/\pm45/90)_2]_T$ were manufactured.

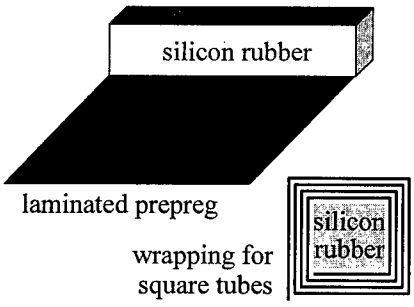


Fig. 1. Prepreg wrapping for square tubes

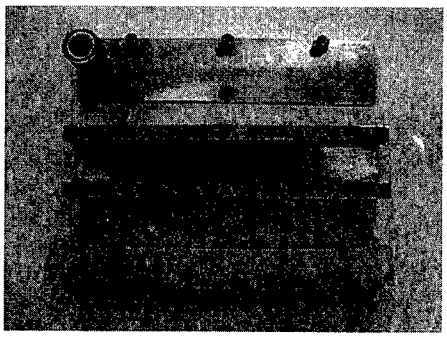


Fig. 2. Mold and silicon rubber

The wrapped tube and silicon rubber extrude were plugged in the aluminum mold shown in Fig. 2 and the mold is placed in the autoclave. To cure the composite tube, only temperature was raised according to pre-determined cure cycle. In the present process, the inner pressure from the thermal expansion of silicon rubber took the role to compact the laminated prepreg.

For the crush test, the cured square tubes with 40×40×80mm(length) were prepared. On the loading side of the tube, 45° initiator was set-up for the progressive collapse of the tubes.

2.2. Crush Test

The graphite/epoxy tubes were crushed using the material test equipment(MTS 810) with the cross-head speed of 0.3mm/sec. Fig. 3 shows the hydraulic grip(MTS 647) and the installed crush jigs. The tubes are placed between the upper and lower jigs.

During the crush test, the load-stroke curve was recorded using the data acquisition system. More than three times of the same crush tests were conducted for tubes with the same stacking sequence. Each crush test was stopped when the stroke reached to 20 mm because the load-stroke curve did not change very much after 20mm of stroke.

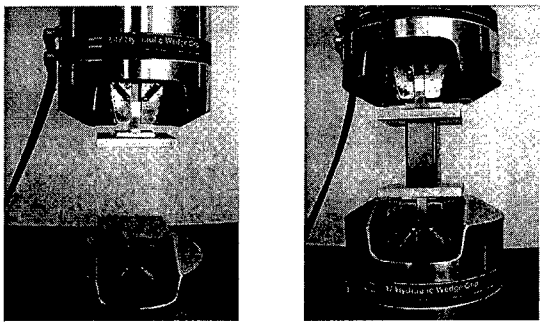


Fig. 3. Installed crush jigs and the composite square tube

2.3. Test Result

(1) Failure Modes

Most composite square tubes failed after buckling, but the failure modes were quite different depending on the stacking sequence of the tubes. Tubes with $[(0)_8]_T$ collapsed in global mode as shown in Fig. 4(a). Initial failure of $[(+30/-30)_4]_T$ and $[(+45/-45)_4]_T$ tubes started from the four corners of the loaded edge and long cracks were formed in the fiber direction as shown in Fig. 4(b) and (c). Failure of $[(+60/-60)_4]_T$ and $[(90)_8]_T$ tubes also started from the loaded corners and they progressively collapsed in a wavy shape as shown in Fig. 4(d) and (e). However, tubes with $[(90)_8]_T$ failed without buckling.



(a) $[(0)_8]_T$ (b) $[(+30/-30)_4]_T$ (c) $[(+45/-45)_4]_T$ (d) $[(+60/-60)_4]_T$ (e) $[(90)_8]_T$

Fig. 4. Failure modes of graphite/epoxy tubes

(2) Peak Load and Average Load

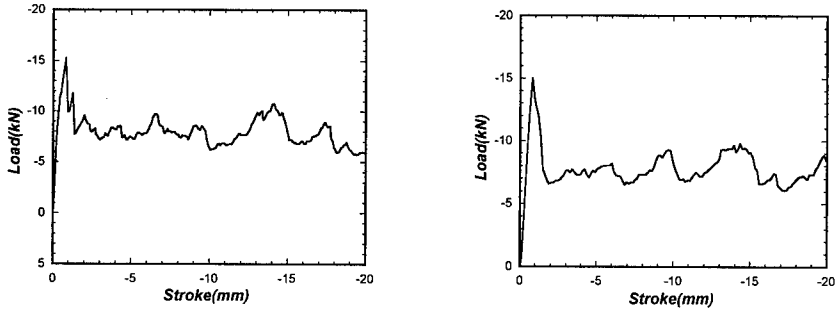
Table 1 and 2 summarize the peak loads and average sustained loads of various tubes. From the tables, it can be noticed that the $[(+45/-45)_4]_T$ tube has the highest peak load and the $[(+60/-60)_4]_T$ tube has the highest average sustained load. Tubes with $[(0)_8]_T$ or $[(90)_8]_T$ have the lowest peak load and average sustained load. The peak load and the average sustained load of the $[(0/90)_4]_T$ tube were quite high, even though composite tubes with $[(0)_8]_T$ or $[(90)_8]_T$ showed poor energy absorbing characteristics. The peak load of the $[(0/\pm45/90)_2]_T$ tube is very close to that of the $[(0/90)_4]_T$ tube, but the average sustained load is slightly higher than that of the $[(0/90)_4]_T$ tube. Fig. 5(a) and (b) are the representative load-stroke curves for the tubes with $[(0/90)_4]_T$ and $[(0/\pm45/90)_2]_T$, respectively.

Table 1. Peak loads(*kN*) of graphite/epoxy square tubes

Ply lay-up	Tube #1	Tube #2	Tube #3	Average
$[(0)_8]_T$	-9.070	-10.907	-8.728	-9.568
$[(+30/-30)_4]_T$	-15.939	-17.599	-17.123	-16.887
$[(+45/-45)_4]_T$	-19.467	-19.464	-17.358	-18.763
$[(+60/-60)_4]_T$	-16.197	-16.095	-16.025	-16.106
$[(90)_8]_T$	-8.032	-7.224	-7.469	-7.575
$[(0/90)_4]_T$	-14.294	-15.271	-15.335	-14.967
$[(0/\pm45/90)_2]_T$	-14.795	-15.018	-15.091	-14.968

Table 2. Average sustained loads(*kN*) of graphite/epoxy square tubes

Ply lay-up	Tube #1	Tube #2	Tube #3	Average
$[(0)_8]_T$	-2.100	-2.245	-2.271	-2.205
$[(+30/-30)_4]_T$	-5.479	-5.927	-5.389	-5.688
$[(+45/-45)_4]_T$	-6.600	-6.592	-5.164	-6.119
$[(+60/-60)_4]_T$	-7.709	-8.233	-7.975	-7.872
$[(90)_8]_T$	-3.754	-3.275	-5.134	-4.054
$[(0/90)_4]_T$	-8.787	-7.957	-10.307	-9.017
$[(0/\pm45/90)_2]_T$	-7.795	-7.735	-8.739	-8.089



(a) $[(0/90)_4]_T$ tube (b) $[(0/\pm45/90)_2]_T$ tube

Fig. 5. Load-stroke curves: crush speed = 0.3mm/sec

3. ESTIMATION OF PEAK LOAD USING THE FINITE ELEMENT ANALYSIS

3.1. Finite Element Modeling

Computational prediction of full crush process of a structure requires large computing time. Moreover, it is more difficult to obtain good estimation of crush characteristics for composite structures than for the conventional isotropic structures. In the present paper, we propose a reasonable method to estimate the peak load of the $[(0/90)_4]_T$ and $[(0/\pm45/90)_2]_T$ square tubes using the finite element analysis.

From the observation during the crush tests, these composite tubes started to fail after buckling. In the present method, therefore, the buckling mode is superimposed to the original perfect square tube geometry and crush load is applied until the tube experiences the first failure.

MSC/NASTRAN is used for the buckling analysis. The tube is modeled using 512 QUAD4 shell elements. Along the loading edge, uniform distributed load is applied to obtain the buckling load and mode. The normal translation in z-direction at all of the grid points lying on the other side(marked as ● in Fig. 6) and three translations at the center grid point of the each side(marked as ■ in Fig. 6) are constrained as the boundary condition. The buckling mode is shown in Fig. 7.

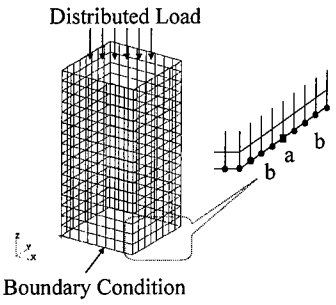


Fig. 6. Load and boundary condition

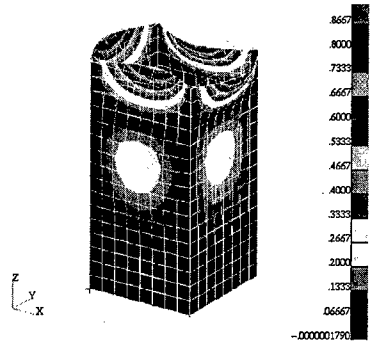


Fig. 7. Buckling mode

3.2. Estimation of Peak Load

The buckling mode is superimposed to the original tube geometry for the linear failure analysis. Since the absolute displacement cannot be determined at the instability, the maximum displacement is assumed as the thickness of the tube. Because failure of the tubes started to fail at the four corners of the loading edge during the crush test, the load is assumed to be slightly concentrated at the corners of the loading edge. The lowest total compressive load that makes the failure criteria equal to one at the elements located at around the corners is regarded as the peak load.

Table 3. Estimated failure loads and the peak load from the crush test (kN)

Failure Criteria	$[(0/90)_4]_T$ tubes		$[(0/\pm45/90)_2]_T$ tubes	
	Estimation	Experiment	Estimation	Experiment
Max. Strain	-18.5 (1.05)	-14.967	-19.5 (1.02)	14.968
Hoffman	-17.0 (1.02)		-18.0 (1.06)	
Tsai-Hill	-18.5 (1.00)		-19.5 (1.01)	
Tsai-Wu	-17.0 (1.05)		-18.0 (1.05)	

The estimated peak loads and the peak load obtained from the crush test are compared in Table 3. The relative error between the estimated peak loads using Tsai-Wu(or Hoffman) failure criterion[8] and the crush test results are within 20%. The table represents that the present method can approximately estimated the peak load of the $[(0/90)_4]_T$ and $[(0/\pm45/90)_2]_T$ square tubes.

4. CONCLCUSION

In the present paper, effect of stacking sequence on the crush energy absorbing characteristics of

graphite/epoxy square tubes has been experimentally investigated. Composite tubes with $[(0)_8]_T$ or $[(90)_8]_T$ showed poor energy absorbing characteristics. The $[(+45/-45)_4]_T$ tube had the highest peak load and the $[(+60/-60)_4]_T$ tube had the highest average sustained load. Therefore, the [+45/-45] and [+60/-60] layers seems to contribute to improving the energy absorbing characteristics of the composite square tube.

However, it was found that the peak load and the average sustained load of the $[(0/90)_4]_T$ tube were quite high. The peak load of the $[(0/\pm45/90)_2]_T$ tube was close to that of the $[(0/90)_4]_T$ tube, and the average sustained load of the $[(0/\pm45/90)_2]_T$ tube was slightly lower than that of the $[(0/90)_4]_T$ tube. Therefore, we can conclude that the 0 and 90 degree layers may contribute to improvement of the crush energy absorbing characteristics when they are laminated together.

Numerical calculation has shown that the proposed finite element modeling technique can estimate the peak load of the graphite/epoxy tubes within the 20% relative error to the experimental peak load.

ACKNOWLEDGEMENT

This paper was supported by Konkuk University in 1999.

REFERENCE

1. J.K. Sen, "Designing for Crushworthy All-Composite Helicopter Fuselage," *AHS Journal*, Vol. 32, No. 2 (1987) pp. 56-66
2. G.L. Farley, Relationship Between Mechanical-Property and Energy-Absorbing Trends for Composite Tube, **NASA TP-3284** (1992)
3. G.L. Farley, "Crushing Characteristics of Continuous Fiber-Reinforced Composite Tube," *Journal of Composite Materials*, Vol. 26, No. 1 (1992) pp. 37-50
4. G.L. Farley, "The Effects of Crushing Speed on the Energy-Absorption Capability of Composite Tubes," *Journal of Composite Materials*, Vol. 25, October (1991) pp. 1314-1329
5. P.H. Thornton, "The Crush Behavior of Pultruded Tubes at High Strain Rates," *Journal of Composite Materials*, Vol. 24, June (1997) pp. 594-615
6. N.K. Gupta, R.Velmuruan and S.K. Gupta, "An Analysis of Axial Crushing of Composite Tubes," *Jouranl of Composite Materials*, Vol. 24, No. 13 (1997) pp. 1262-1286
7. H. Hamada and S. Ramakrishna, "A FEM Method for Prediction of Energy Absorption Capability of Crashworthy Polymer Composite Materials," *Journal of Reinforced Plastics and Composites*, Vol. 16, No. 3 (1997) pp. 226-242
8. **Practical Finite Element Modeling Techniques Using MSC/NASTRAN**, The MSC Institute of Education (1994)

Key Engineering Materials Vols. 183-187 (2000) pp. 1105-1110
© 2000 Trans Tech Publications, Switzerland

Surface Modification of Carbon Fibers by Anodic Oxidation and its Effect on Adhesion

J.R. Lee, M.H. Kim and S.J. Park

Advanced Materials Division, Korea Research Institute of Chemical Technology,
PO Box 107, Yusong, Taejon 305-600, Korea

Keywords: Anodic Oxidation, Carbon Fiber, FT-IR, Interlaminar Shear Strength (ILSS), Phenol Resin, XPS

ABSTRACT

PAN-based high strength carbon fibers were electrochemically treated in an ammonium hydroxide electrolyte for the increasing of surface functional groups on fiber surfaces, resulting in enhancing fiber-matrix adhesion of the composites. According to the FT-IR and XPS measurements, it revealed that the surface functional groups on fibers induced by electrochemical treatment were largely dominated in the mechanical interfacial properties of composites, i.e., the interlaminar shear strength (ILSS). Also, a good correlation between $(O_{1s}+N_{1s})/C_{1s}$ and ILSS was established and found that the 5 $A.m^{-2}$ current density was the optimum condition for this system.

1. INTRODUCTION

Carbon fibers have become one of the most important reinforcing materials in recent years, being characterized by extremely high strength and modulus together with lightweight. In real carbon fiber-reinforced plastic matrix composites, it is well known that the interfacial adhesion between fiber and matrix is poor to ensure a good mechanical performance [1].

The degree of interfacial adhesion at interfaces in a composite system is of considerable importance, since load stress transfers from one matrix to the fiber. It is also well known that the interfacial adhesion between fiber and matrix depends, to a large extent, on the surface area, wettability, and functionality of carbon fiber surfaces. In this respect, surface treatment of carbon fibers is industrially essential for their real applications [2, 3].

Meanwhile, although various methods used to modify the surface properties of the fibers are largely introduced in terms of gaseous oxidation, liquid phase oxidation, whiskerization and polymer coating, the electrochemical surface treatment (i.e., anodic oxidation) is one of the most widely used industrial method with uniform and continuous processes [1, 4].

The aim of the present work is to study the effect of anodic surface treatment on the fiber surfaces and to investigate the relationship between surface properties of the fibers and mechanical interfacial properties of the resulting composites.

2. EXPERIMENTAL

2.1 Materials and sample preparation

The fibers used in this study were untreated and unsized polyacrylonitrile (PAN)-based carbon fibers, TZ-307, manufactured by Taekwang of Korea. The anodic surface treatment of carbon fibers was carried out with a constant rate (1 $mm.min^{-1}$) in a laboratory pilot system, and the electrolyte used was 10 wt% ammonium hydroxide solution. The electric current densities used in this work were 0, 1.5, 5, 10, 15 $A.m^{-2}$. The phenol resin used in a matrix was resole type, CB-8057, supplied from Kangnam Co. of Korea.

Unidirectional carbon fibers-phenol composites were prepared by continuous impregnation of the fibers using a drum winding technique. Specimens were prepared from laminates composed of 22 plies and fabricated in a hot-press with following steps in Fig. 1.

2.1 Spectroscopic analyses and mechanical properties

The surface functional groups on anodized fibers determined by FT-IR (Model Perkin Elmer 175). Also, the X-ray photoelectron spectroscopy (XPS, or ESCA) experiment was performed on an ESCA LAB MK-II (VG Scientific Co.) equipped with a magnesium x-ray source. The base pressure in the sample chamber was controlled in the range of 10^{-8} to 10^{-9} torr.

Interlaminar shear strength (ILSS) of the composites was determined by Instron 1121 according to the ASTM D-2344. A span-to-depth ratio of 6:1 and cross-head speed of 2 $mm.min^{-1}$ were used.

3. RESULTS AND DISCUSSION

3.1 Surface functionality

Fig. 2 shows the FT-IR spectra of anodized carbon fibers in ammonium hydroxide solution as a function of current density. As seen in Fig. 2, the bands occurred at 3450, 1635, and 1200-1050 cm^{-1} are, respectively, attributed to the O-H stretching mode of hydroxyl group, the C=O of carboxyl/ester groups, and C-O of hydroxyl/ether groups increases with increasing the current densities of the treatments up to 1.5 - 5 $A.m^{-2}$, then a marginal decrease in surface functionality is observed for the strong current densities used in this work.

Meanwhile, it is well known that XPS is a very useful apparatus in the determination of chemical compositions of the carbon fiber surfaces [5]. As shown in Table 1, the amounts of surface oxygen groups increase with increasing the current densities of the treatments up to 5 $A.m^{-2}$, and

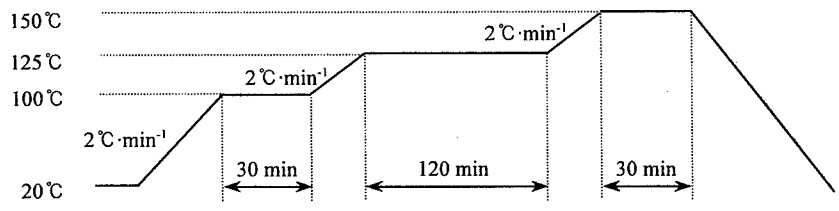


Fig. 1 Curing process of the composites

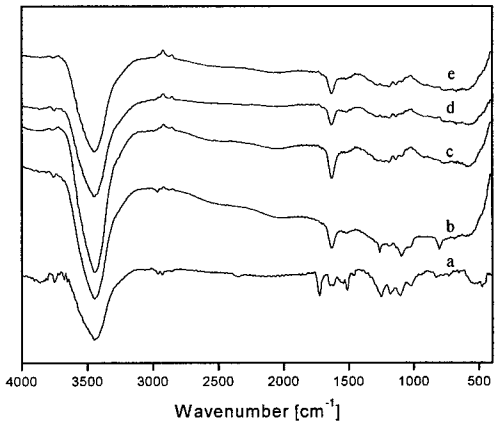


Fig. 2 FT-IR spectra of anodized carbon fibers studied.
(a: as-received, b: 1.5, c: 5, d: 10, e: 15 $A.m^{-2}$)

nitrogen groups continually increase with the current evolutions in ammonium hydroxide electrolytic solution. The large variation of the oxygen group is due to the varying surface acidity or hydroxyl and carboxyl groups on the fibers, as mentioned above FT-IR data. The increase of nitrogen groups may arise from amine, amide, and pyridine-type structures, resulting in the basic surface functional groups [6]. The $(O_{1s}+N_{1s})/C_{1s}$ atomic ratio as the current densities is also indicated in Table 1, and this ratio increase with an increase in the electric current density up to about 5 $A.m^{-2}$.

Therefore, it is noted that the anodic treatment in ammonium hydroxide solution makes an important role in increasing the surface functional groups of carbon fibers, including oxygen and nitrogen. Moreover, it is clearly expected that the increasing of surface functional groups on the fibers improves the surface energy of the fibers as well as the degree of adhesion by establishing secondary or van der Waals forces at the interfaces between fiber and phenolic resin matrix [7, 8].

Table. 1 Surface chemical compositions of the carbon fibers from XPS analysis

Current density [$A.m^{-2}$]	Element			
	C_{1s}	O_{1s}	N_{1s}	$(O_{1s}+N_{1s})/C_{1s}$ [%]
as-received	79.4	19.6	1.0	25.9
1.5	68.6	30.8	0.6	45.8
5	64.4	33.8	1.8	55.3
10	68.9	29.1	2.0	45.1
15	74.2	23.3	2.5	34.8

3.2 Mechanical properties

It is generally accepted that the mechanical properties of composites depend strongly on the degree of adhesion at interfaces between fiber and matrix. ILSS of the composites was calculated by the following Eq. (1).

$$ILSS = \frac{3}{4}\frac{P}{bd} \tag{1}$$

where, P is the force at moment of break [N], b and d the specimen width and thickness [m], respectively.

Fig. 3 shows the evolution of ILSS of the composites versus the electric current density. As a result, it is found that a maximum strength value is found about 32 MPa at the anodic treatment of 5 $A.m^{-2}$. It is considered that additional energy to extend the interfacial crack at this condition is attributed to enhancing the interfacial adhesion of the composites.

When the surface functionality of the fibers is plotted as a function of the ILSS, a direct relationship can also be seen in Fig. 4. It is obvious that the changes in the surface properties of the fibers strongly affect the measured ILSS for this system. As mentioned above, this is a consequence of the improving of surface functional groups on fibers, resulting in growing fiber-matrix physical adhesion of the composites.

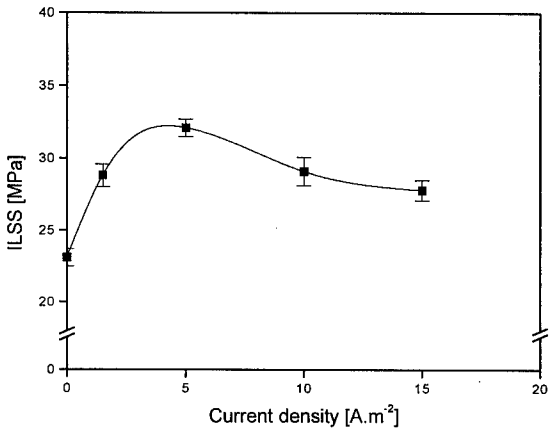


Fig. 3 Evolution of ILSS as a function of the electric current density studied.

4. CONCLUSIONS

In this study on electrochemical surface treatment of carbon fibers, it is concluded that the surface functionality induced by electrochemical oxidation is directly correlated with improvement

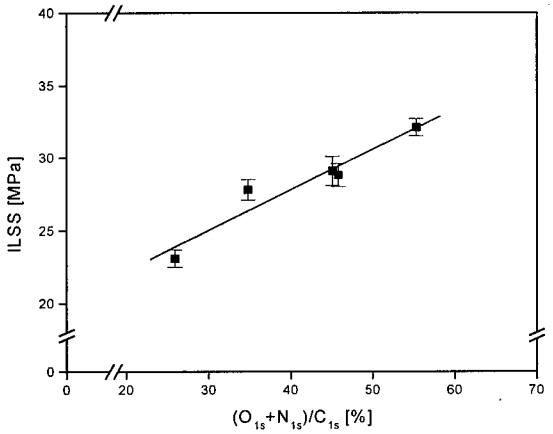


Fig. 4 Dependence of the ILSS of composites on the $(O_{1s}+N_{1s})/C_{1s}$ as atomic ratio of the fibers studied.

of the fiber-matrix adhesion on composite mechanical interfacial properties. But no significant improvement in either surface functionality or ILSS is realized in the case of strong anodic treatment. This is to be a consequence of the degradation for physical and geometrical bonding properties between fiber and phenolic resin matrix, resulting in decreasing long-range force (largely van der Waals force and hydrogen bonding).

5. REFERENCES

1. J.B. Donnet and R.C. Bansal, Carbon Fibers, 2nd ed. Marcel Dekker, New York (1990)
2. F.M. Fowkes, J. Adhesion Sci. Technol., **1** (1987) p. 7
3. J.D.H. Hughes, Compo. Sci. Technol., **41** (1991) p. 13
4. C. Jones, Compo. Sci. Technol., **42** (1991) p. 275
5. T. Wang and P.M.A. Sherwood, Chem. Mater., **7** (1995) p. 1020
6. C. Kozlowski and P.M.A. Sherwood, Carbon, **24** (1986) p. 357
7. J.N. Israelachvili, Intermolecular and Surface Forces, 2nd. ed. Academic Press, San Diego (1991)
8. S.J. Park, Interfacial Forces and Fields: Theory and Applications, ed. by J.P. Hsu, Marcel Dekker, New York (1999) p. 385

Key Engineering Materials Vols. 183-187 (2000) pp. 1111-1116
© 2000 Trans Tech Publications, Switzerland

The Bridging Analysis of Dynamic Crack Propagation in Fiber Reinforced PE Pipelines

Zhuo Zhuang, Shaoxing Qu and Yongjin Guo

Department of Mechanical Engineering, Tsinghua University, Beijing 100084, China P.R.

Keywords: Composite Material, Dynamic Fracture Mechanics, Fiber Bridge, Finite Element

ABSTRACT

A theoretical model of dynamic damage bridging is developed in this paper for fiber composite materials. The dynamic equations are deduced for fiber/matrix bonded, debonding, friction sliding and pull out. Through analysis of the energy equation during the debonding process, the dynamic criteria under constant friction and Coulomb friction are obtained. This model has been incorporated into the finite element code to analyze and evaluate the dynamic fracture in the fiber polyethylene composite pipelines.

1. INTRODUCTION

Since new fiber polyethylene (PE) composite pipes are contemplated for use by gas industry, a major challenge is to perform a computational analysis for the cracked and uncracked pipes. During crack propagation in fibers reinforced PE pipelines, fibers behind crack do not break and pull out immediately. These uncracked fibers provide bridging restraint across the crack opening, absorb part of energy and reduce crack driving force, as shown in Fig. 1. Static bridging models have been developed in the references [1-3]. However, dynamic problems occur more often in the field of fracture mechanics and result in the problem more complicate than the static ones. This is one of the most challenge issues in the dynamic fracture mechanics and composite materials.

Through studying of damage mechanism for fiber reinforced composite in single direction, dynamic equations of debonding, friction sliding and pull out have been deduced. Fiber debonding is reviewed as mode II interface fracture. The behavior of energy released and debonding velocity, as well as the debonding length is obtained under the conditions of constant friction and Coulomb friction. The fiber debonding and pulling out in the bridging model has been implemented in the finite element analysis to evaluate the dynamic fracture toughness in PE gas pipelines. The limited length of fiber pulling out is a very important parameter, which is consistent with crack tip opening displacement (CTOD) behind the crack. It is also incorporated into the numerical code to evaluate the fracture criterion.

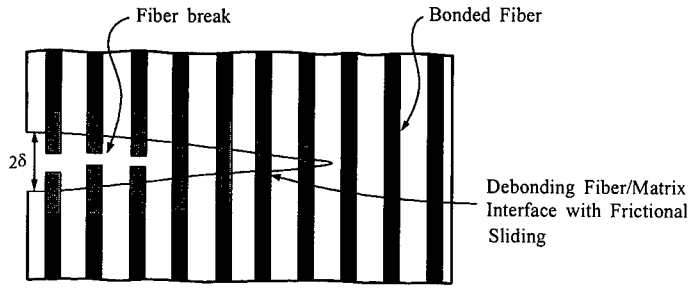


Fig.1 The dynamic bridging model behind the crack

2. DYNAMIC DEBONDING MODEL

In order to study dynamic debonding problem, we assure the debonding as a mode II crack and also consider inertial forces of fiber and matrix. A cylindrical debonding model is given in Fig. 2.

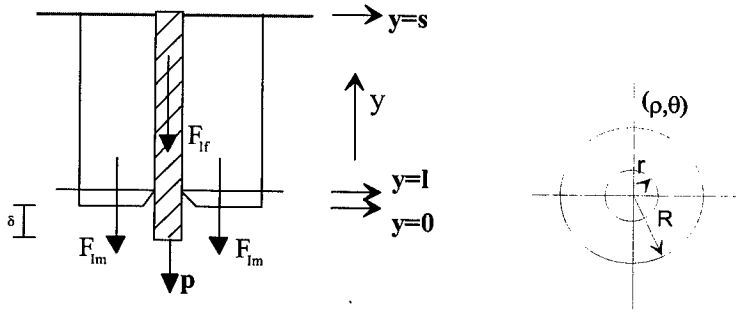


Fig. 2 Fiber dynamic debonding model

At one end of this model, fiber and matrix are fixed. At the other end, the fiber is subjected to a force P. F_{Im} and F_{If} are inertia forces of matrix and fiber, respectively. δ is a pull-out length of the fiber, and l is the debonding depth. R and r are radius of the matrix and fiber, respectively. In the following analysis, all properties of fiber are identified by subscript f, and those of matrix m.

For an infinitesimal length dy in the debonding zone of $0 \le y \le l$ in Fig. 2, the governing equations is given as follows:

$$\begin{cases} \dfrac{\partial^2 u_f}{\partial y^2} = A\tau + B\ddot{u}_f + C\ddot{u}_m \\ \dfrac{\partial^2 u_m}{\partial y^2} = D\tau + E\ddot{u}_f + F\ddot{u}_m \end{cases} \tag{1}$$

Where A, B, C, D are defined as in the reference [4], τ is unknown force and can be determined by

the frictional conditions between fiber and matrix, and u_f and u_m are displacements of fiber and matrix, respectively. Two kinds of frictional conditions are considered: constant friction and Coulomb friction.

3. DEBONDING WITH CONSTANT FRICTION

Under the condition of debonding with constant friction, Equation (1) can be rewritten as

$$\begin{cases} \dfrac{\partial^2 u_f}{\partial y^2} - B\ddot{u}_f - C\ddot{u}_m = A\tau_0 \\ \dfrac{\partial^2 u_m}{\partial y^2} - E\ddot{u}_f - F\ddot{u}_m = D\tau_0 \end{cases} \tag{2}$$

From the equilibrium equation, the following expression of debonding velocity $\dot{l}$ can be obtained,

$$\left[2\pi r\tau + \rho_f \pi r^2 \ddot{u}_f(l,t)\right]\frac{dl}{dt} = \frac{dP(t)}{dt} - \frac{dP_f(l,t)}{dt} - \int_0^l \rho_f \pi r^2 \frac{\partial \ddot{u}_f}{\partial t} dy \tag{3}$$

It is difficult to determine $\dot{l}$ only through equation (3), thus, numerical method is suggested. If debonding velocity $\dot{l}(t)$ at time t is known, then the velocity at $t+\Delta t$ is given by

$$\dot{l}(t+\Delta t) = \frac{dl(t+\Delta t)}{dt} = \frac{\dot{P}(t+\Delta t) - \dot{P}_f(l(t),t) - \int_0^{l(t)} \rho_f \pi r^2 \dfrac{\partial \ddot{u}_f(y,t)}{\partial t} dy}{2\pi r\tau + \rho_f \pi r^2 \ddot{u}_f(l(t),t)} \tag{4}$$

Through analysis of energy equation during debonding dl process, dynamic debonding criteria under both constant friction and Coulomb friction are obtained as following as:

$$dE_W - dE_D = dG + dE_E + dE_K \tag{5}$$

Where, E_W represents external works, E_D is dissipation energy by friction, G is crack driving force, E_E is strain energy and E_K is kinetic energy.

$$\begin{aligned} &\frac{1}{2}P(t)\frac{\partial u_f(0,t)}{\partial t} + \frac{1}{2}2\pi r\tau\frac{dl}{dt}[u_f(l,t) - u_m(l,t)] + \frac{1}{2}\int_0^l 2\pi r\tau \frac{\partial[u_f(y,t) - u_m(y,t)]}{\partial t} dy \\ &= 2\pi r\frac{dl}{dt}2\xi(t) - \frac{\partial}{\partial t}\int_\Omega \frac{1}{2}\rho\frac{\partial^2 u}{\partial t^2} u d\Omega dt + \frac{\partial}{\partial t}\int_\Omega \frac{1}{2}\rho\left(\frac{\partial u}{\partial t}\right)^2 d\Omega dt \end{aligned} \tag{6}$$

For the model in Fig. 1, equation (5) can be expressed as above.

Here, $\xi(t)$ is the special work of fracture. It can be determined from the single-fiber pull-out test. It is also treated as debonding toughness.

4. DEBONDING WITH COULOMB FRICTION

We define $\tau = -\mu q^*$. Where the interface stress q^* has been defined in reference [4] and μ is the frictional coefficient between fiber and matrix. The governing equation is given by:

$$\frac{\partial^2}{\partial y^2}\mathbf{U} = \mathbf{G}\bullet\frac{\partial}{\partial y}\mathbf{U} + \mathbf{H}\bullet\ddot{} \tag{7}$$

Where

$$\mathbf{G} = \xi\begin{bmatrix}(\alpha_{11}-\alpha_{12})(\alpha\nu_f\alpha_{22}+\gamma\nu_m\alpha_{21}) & (\alpha_{11}-\alpha_{12})(-\alpha\nu_f\alpha_{12}-\gamma\nu_m\alpha_{11})\\ (\alpha_{21}-\alpha_{22})(\alpha\nu_f\alpha_{22}+\gamma\nu_m\alpha_{21}) & (\alpha_{21}-\alpha_{22})(-\alpha\nu_f\alpha_{12}-\gamma\nu_m\alpha_{11})\end{bmatrix}$$

$$\mathbf{H} = \begin{bmatrix}\eta\alpha_{11} & \zeta\alpha_{12}\\ \eta\alpha_{21} & \zeta\alpha_{22}\end{bmatrix}, \qquad \mathbf{U} = \begin{bmatrix}u_f\\ u_m\end{bmatrix}, \qquad \eta = \pi r^2\rho_f$$

$$\xi = \frac{2\mu}{r(\alpha_{11}\alpha_{22}-\alpha_{12}\alpha_{21})}\frac{1}{\alpha(1-\nu_f)+1+\nu_m+2\gamma}, \qquad \zeta = \pi(R^2-r^2)\rho_m$$

Where α_{11}, α_{12}, α_{21} and α_{22} are defined in reference [4]. The debonding velocity under this condition is expressed as below.

$$\begin{aligned}\left[-2\pi r\mu q^*(l,t)+\rho_f\pi r^2\ddot{u}_f(l,t)\right]\frac{dl}{dt} &= \frac{dP(t)}{dt}-\frac{dP_f(l,t)}{dt}-\int_0^l 2\pi r\mu\frac{\partial q^*(y,t)}{\partial t}dy\\ &\quad -\int_0^l\rho_f\pi r^2\frac{\partial\ddot{u}_f}{\partial t}dy\end{aligned} \tag{8}$$

The debonding criterion equation is obtained:

$$\begin{aligned}&\frac{1}{2}P(t)\frac{\partial u_f(0,t)}{\partial t}+\frac{1}{2}2\pi r\mu q^*(l,t)\frac{dl}{dt}[-u_f(l,t)+u_m(l,t)]\\ &+\frac{1}{2}\int_0^l 2\pi r\mu q^*(y,t)\frac{\partial[-u_f(y,t)+u_m(y,t)]}{\partial t}dy\\ &=2\pi r\frac{dl}{dt}2\xi(t)-\frac{\partial}{\partial t}\int_\Omega\frac{1}{2}\rho\frac{\partial^2 u}{\partial t^2}ud\Omega dt+\frac{\partial}{\partial t}\int_\Omega\frac{1}{2}\rho\left(\frac{\partial u}{\partial t}\right)^2 d\Omega dt\end{aligned} \tag{9}$$

The equation (6) and (9) are called debonding criteria equations when the frictions are considered.

5. NUMERICAL ANALYSIS

The dynamic damage mechanism of fiber reinforced materials has been carried out analytically. This dynamic bridging model [4] has been implemented in the numerical analysis to evaluate the dynamic fracture toughness in fiber composite PE pipelines. This is accomplished using a finite element code PFRAC (Pipeline FRacture Analysis Code) which has been developed to analyze the complete fluid/structure/fracture interaction events that take place in the fractured gas pipelines [5-6]. The PFRAC code was developed initially for isotropic pipe materials. The modifications carried out here consider the anisotropic pipe material, to simulate fiber-PE composite gas pipelines. The criterion of dynamic crack initiation and propagation in the pipe is governed by the following equation:

$$G(a, p, SDR, h) = G_d(T, v, h) \tag{10}$$

where, G is the dynamically calculated value of crack driving force, G_d is the experimentally determined dynamic fracture toughness, a is crack length, p is pressure on the pipe, SDR is standard dimension ratio (diameter/thickness), v is crack velocity, T is temperature and h is thickness.

In addition, the fiber broken condition behind the crack is also studied. Because of the complexity of bridging mode, it is no easy to determine the configuration of bridging surface. A criterion of the fiber pull out length is posed in the analysis.

$$\delta = l_c(D, r, V_f) \tag{11}$$

Where δ is the calculated fiber length being pulled out, l_c is the limited tension length determined experimentally for the broken fiber, D is diameter of pipe and r represents the radium of fiber and V_f is volume fraction of the fibers. The average fiber length can be calculated from the crack tip opening displacement (CTOD) in the program. Thus, this criterion can be evaluated numerically.

Crack driving force G can be calculated out through nodal force released method. Figure 3 shows the difference between G of fiber reinforced PE pipe and that of pure PE pipe.

Comparing the results from the figure above, the crack driving forces decrease significantly in the fiber reinforced PE pipelines.

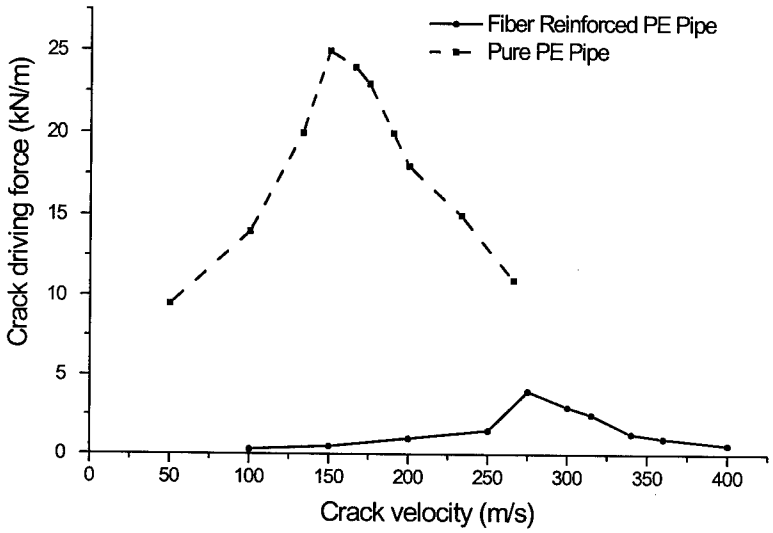


Figure 3 Crack driving force of fiber reinforced PE pipe and pure PE pipe under different crack velocity (p =0.4MPa, D=250mm, SDR=11, L/D=1.5, $V_f = 50\%$)

ACKNOWLEDGMENT

The project is supported by the National Natural Science Foundation of China (19672027)

REFERENCES

1. Y.C. Gao, Y.W. Mai, B. Cotterell, Fracture of fiber-reinforced material, J. Appl. Math. Phys. **39**(1988) p.550
2. J.W. Hutchinson, H.M. Jensen, Models of fiber debonding and pull-out in brittle composites with friction, Mech. Mate. **9**(1990) p.139
3. Y.C. Gao, Damage theory of fiber-reinforced material, Chinese Science (A), 2, 1989 (in Chinese) p.151
4. Z. Zhuang, SX. Qu, Bridging models of dynamic crack in fiber reinforced material and numerical analysis, In: Proceedings of European Conference on Computational Mechanics, Munich, Germany, 1999, p.196
5. Z. Zhuang, P.E. O'Donoghue, Material fracture toughness determination for polyethylene pipe materials using small scale test results, Acta Mechanica Sinica, 1997, **13**(1), p.63
6. Z. Zhuang, Y.J. Guo, The Analysis for Dynamic Fracture Mechanism in Pipelines, Engineering Fracture Mechanics, 1999, **64**(3), p.271
7. Z. Zhuang, YJ. Guo, SX. Qu, YM. Dong, The Study of Toughness for Fiber Composite PE Pipes, Engineering Mechanics (in Chinese), 2000, **17**(4) (in press)

Key Engineering Materials Vols. 183-187 (2000) pp. 1117-1122
© 2000 Trans Tech Publications, Switzerland

Optimum Stacking Sequence Design of Fiber-Metal Laminates for Using Genetic Algorithm

H.W. Nam, S.W. Jung, W. Hwang and K.S. Han

Department of Mechanical Engineering, Pohang University of Science and Technology
San 31 Hyoja-dong, Nam-gu, Pohang 790-784, Korea

Keywords: Failure Index, Fiber-Metal Laminates, Genetic Algorithm, Optimum Design

ABSTRACT

This research uses genetic algorithms to study the optimal design of FML subject to various loading conditions. To analyze the FML, the finite element method based on shear deformation theory is used. Tasi-Hill failure criterion and Miser yield criterion are used as the fitness functions of the fiber prepreg and the metal laminate, and the ply orientation angles are design variables. In the genetic algorithm, tournament selection and the uniform crossover method are used. The elitist model is also used for an effective evolution strategy and the creeping random search method is adopted in order to approach the solution with high accuracy. Optimization results are given for various loading conditions and compared with CFRP(Carbon Fiber Reinforced Plastic). The results show that the FML is more excellent than the CFRP in most of the loading conditions. Especially the FML shows good mechanical performances in point loading conditions and it is more stable to unexpected loading.

1. INTRODUCTION

The FML(Fiber-Metal Laminate) is a new type of composite materials recently emerged. It consists of thin metal laminate bonded with fiber (aramid, carbon, glass, etc) prepreg, and it nearly includes all the advantages of metallic and composite materials, for example: good plasticity, impact resistance, processibility, light weight and excellent fatigue properties [1].

This paper uses a genetic algorithm to find the optimal stacking sequence of FML under various loading conditions optimized for maximum strength. The optimum stacking sequence of FML are sought considering the properties of metal laminate and the number of fiber prepreg and compared with the CFRP from the viewpoint of the FI (failure index).

2. GENERAL THEORY

2.1. FEM Analysis

The variable finite element method based on first order shear deformation theory and the

penalty plate-bending element, proposed by Reddy [2], are used for the analysis of Fiber-Metal laminates. A Lagrange plate element with a second order nodes is used, in which there are 5 degrees of freedom (u, v, w, θ_x, θ_y).

The strain energy (u) is obtained by integrating over the area of the element :

$$u = \frac{1}{2}\int_A [\mathbf{N}]^T \boldsymbol{\varepsilon}_0 \, dA + \frac{1}{2}\int_A [\mathbf{M}]^T \boldsymbol{\kappa} \, dA + \frac{1}{2}\int_A [\mathbf{Q}]^T \overline{\gamma} \, dA \tag{1}$$

Equation (1) can be written as:

$$u = \sum_e \frac{1}{2}\mathbf{d}_e^T \mathbf{K}_e^T \mathbf{d}_e \tag{2}$$

where $\mathbf{K}_e$ is the stiffness matrix of element:

$$\begin{aligned}\mathbf{K}_{ij} &= \int_A \mathbf{B}_i^T \mathbf{D}\mathbf{B}_j \, dA \\ &= \int_A \left\{\mathbf{B}_{ei}^T [\mathbf{A}]\mathbf{B}_{ej} + \mathbf{B}_{bi}^T [\mathbf{B}]B_{ej}\right\}dA \\ &+ \int_A \left\{\mathbf{B}_{ei}^T [\mathbf{B}]\mathbf{B}_{bj} + \mathbf{B}_{bi}^T [\mathbf{D}]\mathbf{B}_{bj}\right\}dA \\ &+ \int_A \mathbf{B}_{si}^T [\mathbf{DS}]\mathbf{B}_{sj} \, dA\end{aligned} \tag{3}$$

and

$$\mathbf{B}_i = \begin{pmatrix} \mathbf{B}_{ei} \\ \mathbf{B}_{bi} \\ \mathbf{B}_{si} \end{pmatrix} \tag{4}$$

$$\mathbf{D} = \begin{bmatrix} [\mathbf{A}] & [\mathbf{B}] & 0 \\ [\mathbf{B}] & [\mathbf{D}] & 0 \\ 0 & 0 & [\mathbf{DS}] \end{bmatrix} \tag{5}$$

The total potential energy of plate, π is

$$\pi = U + V \tag{6}$$

where U is strain energy and V is the potential energy due to external loads. By minimizing π with respect to the displacement $\mathbf{d}_i$, we can obtain the final matrix equation:

$$\mathbf{Kd} = \mathbf{f} \tag{7}$$

The strains are obtained from the strains and curvatures on the mid-plane. The stresses are calculated at the integration point per each laminate by putting the strains into the constitutive equation. Finally, σ_1, σ_2, τ_{12} can be obtained by transforming the calculated stresses into the fiber orientation. FI can therefore be obtained by using Tsai-Hill failure criterion and Miser-yield criterion.

2.3. Optimization

The aim of this study is to maximize the strength of FML by altering the ply orientation. The ply orientation angles of FML are taken as design variables, and Tsai-Hill failure criterion [3] and Miser yield criterion are used as the fitness functions. Genetic algorithm is used to find the maximum or minimum value. The ply angle is coded as a binary number and is mapped to a

decimal number linearly in the range of design variables. The optimization problem can be expressed in mathematical form:

Minimize

$$\textit{fiber prepreg}: f_{TH}(\theta)=\frac{\sigma^2_1}{X^2}-\frac{\sigma_1\sigma_2}{X^2}+\frac{\sigma^2_2}{Y^2}+\frac{\tau^2_{12}}{S^2} \qquad (8)$$

$$\textit{metal laminate}: f_{MY}(\theta)=\frac{\sigma^2_x}{Y_i^2}-\frac{\sigma_x\sigma_y}{Y_i^2}+\frac{\sigma^2_y}{Y_i^2}+\frac{3\tau^2_{xy}}{Y_i^2}$$

subject to $-90^\circ \le \theta \le 90^\circ$

where $f_{TH}(\theta), f_{MY}(\theta)$ are respectively Tsai-Hill quadratic failure criterion and Miser yield criterion, taken as the FI. The fitness function is calculated by the finite element method under various loading conditions. The total number of elements is denoted as p, the number of integration points within one element is q, and the number of piles is r. The fitness function is calculated at each point of $\{p, q, r\}$. Among these calculated fitness functions, the maximum fitness function is sought and minimized. This procedure can be written:

Minimize

$$Max\begin{bmatrix} f^1{}_{TH}(\theta_1), & f^1{}_{TH}(\theta_2), & \Lambda & f^1{}_{TH}(\theta_r) \\ f^1{}_{MY}(\theta_1), & f^1{}_{MY}(\theta_2), & \Lambda & f^1{}_{MY}(\theta_r) \\ & \text{M} & & \\ f^2{}_{TH}(\theta_1), & f^2{}_{TH}(\theta_2), & \Lambda & f^2{}_{TH}(\theta_r) \\ f^2{}_{MY}(\theta_1), & f^2{}_{MY}(\theta_2), & \Lambda & f^2{}_{MY}(\theta_r) \\ & \text{M} & & \\ f^{p\times q}{}_{TH}(\theta_1), & f^{p\times q}{}_{TH}(\theta_2), & \Lambda & f^{p\times q}{}_{TH}(\theta_r) \\ f^{p\times q}{}_{MY}(\theta_1), & f^{p\times q}{}_{MY}(\theta_2), & \Lambda & f^{p\times q}{}_{MY}(\theta_r) \end{bmatrix} \qquad (9)$$

subject to $-90^\circ \le \theta \le 90^\circ$

2.4. Operation of the Genetic Algorithm

The roulette wheel method is widely used. But this method cannot occupy the population of next generation dominantly, although individuals have high fitness. By contrast, the tournament selection chooses a random set of individuals and picks out the best among them. The tournament selection also has the characteristic of controlling the next generation according to reproduction of dominant individuals by varying the tournament size. Therefore, in this research, tournament selection with tournament size of 2 (binary tournaments) is used. Elitist selection ensures that the best chromosome is passed into the new generation if it is not selected through another process of selection. The elitist model is also used in this study.

Crossover is the main genetic operator. It operates on two chromosomes and generates offspring by combining features of both chromosomes. In this study, uniform crossover that has a strong crossover effect is used; the crossover rate is 0.5 [4].

Mutation expands the search space by random changes of string bits in the chromosome that

alter the chromosome overall. Consequently, the existing population from seeking local minima using mutation can be prevented. In this study, the search space is expanded by restarting the genetic algorithm with the new population if there is little difference between elite fitness and the average fitness of the population.

3. RESULTS AND DISCUSSION

Optimum designs of the 3/2 and 3/4 FML subject to various loading conditions were sought using the genetic algorithm. The designations 3/2 and 3/4 correspond to [Metal/Fiber/Metal /Fiber/Metal] and [Metal/Fiber/Fiber/Metal/Fiber/Fiber/Metal], respectively. The fiber prepreg is graphite/epoxy and the metal laminates are Al2024-T3 and Al7075-T6.

Throughout the calculations, plates have thickness h = 4mm, b/a=1, and a/h=25, except for the plate under cylindrical bending (h = 4mm, b/a=2, and a/h=25). The population number is 100 and chromosomes have 15 bitstrings per variable. Optimum solutions are obtained by iteration of the design variables. The interval is :

$$\Delta\theta_i = \frac{90-(-90)}{2^{15}-1} = 0.005493\text{K} \qquad (10)$$

Optimum designs of FML have been performed under uniaxial, cylindrical bending, biaxial, point, uniform and combined loading conditions. The boundaries are simply supported (Fig. 1 (a)) except for a case of uniaxial tensile loading (Fig. 1 (b)) and cylindrical bending (Fig. 1 (c)).

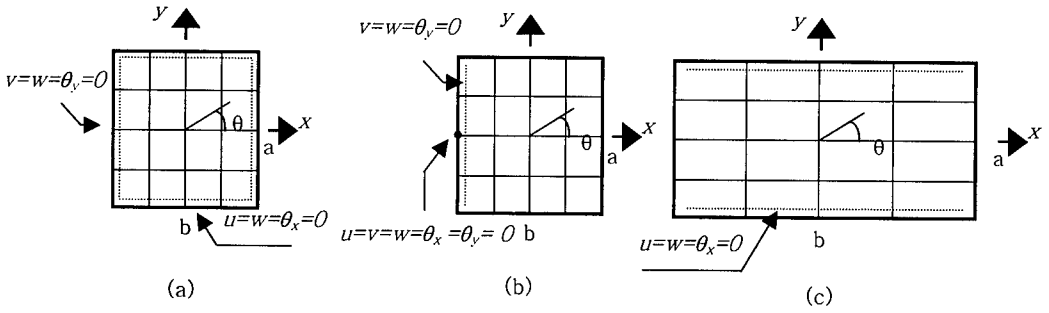


Fig.1. Boundary conditions

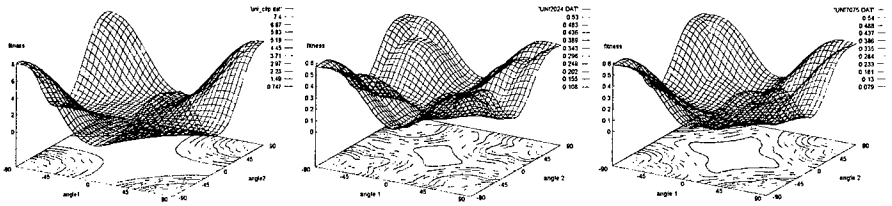
-Uniaxial Loading and Cylindrical bending

To verify the present method, optimum solution of CFRP and FML subjected to uniaxial loading(N_x=0.5MN/m) and cylindrical bending(q=1MN/m^2) are sought. Table 1 represents the optimum stacking sequence of CFRP and FML under uniaxial loading and cylindrical bending. The indication in the Table ((f):fiber prepreg, (m):metal laminate) is the material which the maximum FI is found in. It is obvious that the maximum strength of CFRP and FML occurs when all layer angles are 0^o under a uniaxial loading and 90^o under a cylindrical bending. The same results are obtained in this study.

Fig. 2 shows the fitness functions of all possible ply angle under uniaxial loading in 4 plies CFRP, the 3/4 FML-Al2024 and 3/4 FML-Al7075. It can be seen that minimum failure index is found for a $[0^o]_{2s}$ CFRP and [M/0/0/M/0/0/M] FML. Fig. 3 shows the fitness functions of all possible ply angle under cylindrical bending. As it can be seen from Figure, the minimum failure index is found for a $[90^o]_{2s}$ CFRP and [M/90/90/M/90/90/M] FML.

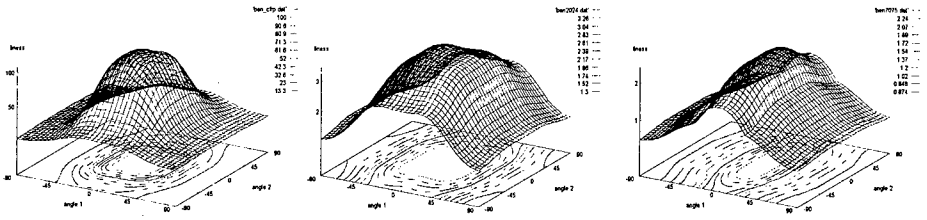
Table 1. Optimum design for uniaxial loading and cylindrical bending

Material	Ply	Optimum angle (uniaxial loading)	Optimum FI	Optimum angle (cylindrical bending)	Optimum FI
FRP	4	[0.002/0.01]s	0.0068	[89.96/-89.79]s	0.139
FRP	6	[0.03/0.019/-0.04]s	0.0068	[89.81/-89.99/90]s	0.139
FRP	8	[2.81/-1.05/-0.53/-1.41]s	0.0068	[90/-90/90/-90]s	0.139
FMLC (2024)	3/2	[M/0/M/0/M]	0.0744 (m)	[M/89.99/M/89.99/M]	1.291 (m)
FMLC (2024)	3/4	[M/0.012/0.008 /M/0.008/0.012/M]	0.0608 (m)	[M/89.91/89.82/M /89.82/89.91/M]	1.085 (m)
FMLC (7075)	3/2	[M/0.008/M/0.008/M]	0.0342 (m)	[M/89.99/M/89.99/M]	0.598 (m)
FMLC (7075)	3/4	[M/0.002/0.008 /M/0.008/0.002/M]	0.0278 (m)	[M/89.84/89.91/M /89.91/89.84/M]	0.500 (m)



(a) (b) (c)

Fig. 2 Fitness function of (a) 4-ply FRP (b) 3/4 FMLC-Al2024 and (c) 3/4 FMLC-Al7075 for uniaxial loading



(a) (b) (c)

Fig. 3 Fitness function of (a) 4-ply FRP (b) 3/4 FMLC-Al2024 and (c) 3/4 FMLC-Al7075 for cylindrical bending

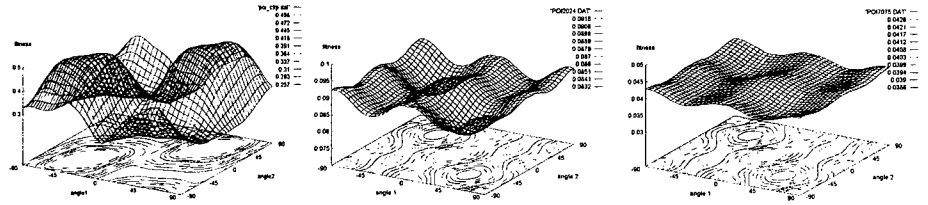
Compared with the CFRP, the FI of FML in optimum ply angle is higher, but in general, the FI of FML is much lower than the FI of CFRP. The results show that the FML is more stable to unexpected loading compared with the CFRP.

As increased the number of fiber prepreg, the FI of FML in optimum ply angle is decreased. This is caused by the increment of longitudinal loading capability of FML as increase the number of fiber prepreg. Mechanical preformances of FML are influence by metal laminate. In this study, two kinds of metal laminate, Al2024 and Al7075, are used to analyze the FML. In optimum designed FML, the FI of FML-Al7075 is lower than the FI of FML-Al2024 because the yield strength of Al7075 is higher than that of Al2024.

- Point Loading

Optimum designs, when a point load (P=1kN) is applied to the center of the plate, were sought. In all the analyzed FML, the 3/2 FML-Al7075 has the lowest FI and the 3/4 FML-Al2024 has the highest FI. The optimum plies angles are near the 45 degree, the worst plies angles are near the 85 degree.

Under the point loading conditions, the FI of FML are lower than that of CFRP regardless of the number of fiber prepreg or the kinds of metal laminate. This means that the FML is more excellent than the CFRP in this loading condition. Fig. 4 shows the fitness functions of all possible ply angle under point loading. It shows that the FI deviation of FML is smaller than that of CFRP. From this result, it is possible to conclude that the FML is well endure to unexpected loading than the CFRP.



(a) (b) (c)

Fig. 4 Fitness function of (a) 4-ply FRP (b) 3/4 FMLC-Al2024 and (c) 3/4 FMLC-Al7075 for point loading

4. CONCLUSION

1. The optimum stacking sequence of FML subject to various loading conditions are obtained using genetic algorithms without auxiliary information such as derivatives of objective function and initial guessing point
2. The FML are more excellent than the CFRP in most of the loading conditions, especially it shows good mechanical performances in point loading conditions.
3. The FML are more stable to unexpected loading compared with the CFRP.

ACKNOWLEDGEMENT

The authors wish to acknowledge the financial supports of the Korea Research Foundation made in the program year of 1998 (No:1998-017-E00002).

REFERENCE

1. Vogelesang, L. B. and Gunnick, J. W. Mater. Design, **7** (2) (1984).
2. Reddy, J. M. AIAA Journal, **9** (5) (1971) p. 912-917
3. Rowlands, R. E. Handbook of Composites: Failure Mechanics of Composites, G.C. Sih and A.M. Skudra. Eds. North-Amsterdam. New-York. Oxford: Elsevier Science Publishers. **3** (1985) p. 91-92.
4. Lawrence Davis. Handbook of Genetic Algorithms, Van Nostrand Reinhold. (1991) p. 46-50.

Key Engineering Materials Vols. 183-187 (2000) pp. 1123-1128
© 2000 Trans Tech Publications, Switzerland

A Thermomechanical Analysis of MCM-D Substrate of Polymer and Metal Multilayer

J.H. Lim[1], J.S. Kim[2], K.W. Paik[3] and Y.Y. Earmme[1]

[1] Department of Mechanical Engineering, Korea Advanced Institute of Science and Technology, 373-1 Kusong-dong, Yusung-gu, Taejon 305-701, Korea

[2] Consulting Division, LG-EDS Systems Inc., Yoido-dong, Youngdungpo-gu, Seoul 150-721, Korea

[3] Department of Materials Science and Engineering, Korea Advanced Institute of Science and Engineering, 373-1 Kusong-dong, Yusung-gu, Taejon 305-701, Korea

Keywords: CBA, Lamination, Laser Profilometry, MCM-D, Multilayer, Stoney's Formula, Stress Relaxation, Thermomechanical Bow

ABSTRACT

A multichip module (MCM) substrate is an example of multilayer structure under thermal loading. In MCM-D substrate, various thin film technologies are used and the number of layers increases to meet the demands of electronic industry. This multilayer substrate has the properties which are not well taken care of in the usual thermal stress analysis: that is, (i) each layer experiences the different thermal history because the multilayers are made by the sequential build-up of the alternating layers of polymer dielectric and metal conductor films, (ii) a single film thickness cannot be assumed to be infinitesimal any more compared to the others, (iii) the polymer films seem to undergo the relaxation of stress

In this study, the thermomechanical bowing was experimentally measured layer-by-layer during the sequential build-up of the alternating layers, and it is compared with the result of the thermomechanical stress analysis of the multilayer MCM-D substrate based on a model which takes into account the different thermal history of each layer and the effect of the film thickness.

1. INTRODUCTION

The thermomechanical behavior of multilayer structures is a subject of interest for many years(see, for instance, Flinn[1] and the references thereof). A few useful closed-form expressions were developed under certain assumptions, using different approximations. Nevertheless, most of

them are rarely supported by the experimental investigation. In this study, the thermomechanical behavior(especially the bow) of the multilayer structure was experimentally observed layer-by-layer during the sequential build-up of the alternating layers of polymer dielectric and metal conductor films. The similar multilayer polymer/metal structure is being used in microelectronics industry for the multichip module (MCM) substrate fabrication.

Some of the key thermomechanical issues during the MCM-D substrate fabrication are the amount of substrate bowing, and the thermal stress caused by the mismatch of the coefficients of thermal expansion (CTE). While the thermal stress causes the mechanical failure of films, such as the adhesion reduction, contact peel-off, or variations in electrical properties[2,3], the substrate bowing directly affects the basic fabrication processes, such as the vacuum mounting for handling and the substrate sawing after fabrication[3].

It is the internal stress that causes the substrate to bow. Since the magnitude of the internal stress is related to the amount of the substrate bowing, most of the stress measurement equipment is based on the substrate curvature or bow measurement, and afterwards the internal stress is inferred employing the relation such as the Stoney's formula[4]. In this study, multilayer bowing is quantitatively measured during the sequential build-up of the alternating layers of the polymer and metal films, of which each layer is processed by lamination(polymer films) and sputtering(metal films). The analysis presented here focuses on the thermomechanical bowing rather than the stresses and the measured bow values are compared with the calculated.

2. EXPERIMENT

The multilayer structure of this study was made by the sequential bulid-up of the alternating layers. First, the Coverlay(CL) polymer film was fabricated by a lamination process(to be further explained later) on a Si substrate and the structure composed of the Si and CL film was thermally cycled to measure the thermomechanical bowing as a function of temperature. The aluminum thin film was then deposited onto the first CL film(which was on Si) and thermally cycled again for the measurement of bowing, followed by a 2nd lamination of CL on the layer of aluminum, and so on. Totally six layers were fabricated by that sequence and the maximum bow values of each structure, denoted by Si/CL, Si/CL/Al, Si/CL/Al/CL, Si/CL/Al/CL/Al, Si/CL/Al/CL/Al/CL, and Si/CL/Al/CL/Al/CL/Al, respectively, were measured every time each layer is added using a laser profilometry[1]. At each measurement the thermal cycling was performed between 25 °C and 150°C, and the bow values obtained at the 2nd cooling cycle were used to compare with the calculated value as explained in section 4.

For the CL film fabrication, a lamination process was used. The lamination fixture used the heat and pressure at T = 150°C and p = 40psi to bond an overlay film onto a base-substrate using a polymeric adhesive. The substrate was 525μm thick (100) single crystal silicon (Si) wafer with a diameter of 10cm. The CL film, a composite of 25.4μm Kapton film and 25.4μm epoxy adhesive, was applied to the silicon substrate. The physical constants of the Si substrate, the dielectric film

CL, and the aluminum metal film are summarized in Table 1. The aluminum thin film of 0.9μm thickness was deposited by DC magnetron sputtering. The target used for depositing the aluminum film was 99.999% pure and the base pressure was 2×10^{-6} torr. There was no external heating of the substrate except the sputter-heating due to the aluminum ion bombardment. The DC power was set at 200W and the thickness of the metal film was controlled by adjusting the deposition time. The aluminum thin film of 0.9μm thickness was obtained by sputtering for 2000 seconds.

Table 1. Physical constants for the lamination-based MCM-D substrate materials (25°C)

Materials	E (GPa)	ν	α (10^{-6}/°C)	t (μm)
Silicon	141	0.22	2.6	525
Coverlay	0.5	0.37	60	50.8
Aluminum	67.3	0.33	23.4	0.9

3. THERMOMECHANICAL ANALYSIS

In a recently published paper[5], we have developed an analytic model called composite beam analysis(CBA) that provides a better method to describe the thermomechanical behavior of the lamination-based MCM-D substrate. The CBA is extended in this work in order to include the effect of different thermal history of each layer as well as the film thickness on thermomechanical bowing of the multilayer.

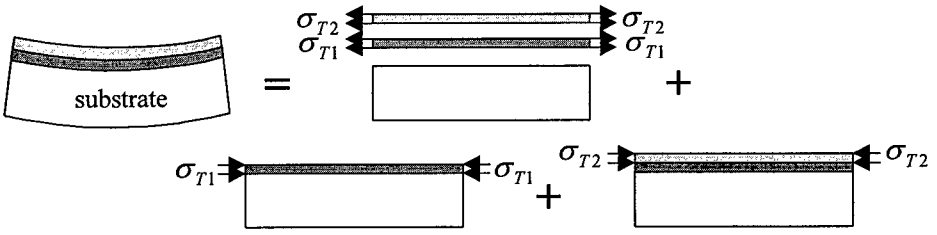


Fig. 1. "Cut and paste" procedure for the solution of thermal residual stresses and bowing of the structure of 2-layeres on a substrate.

Figure 1 shows the basic concept of CBA applied to the structure of 2-layers on a substrate. By a so-called "cut and paste" technique, a curvature induced by thermal stress can be simulated by a combination of edge loads. The multilayer in Fig. 1, which is assumed to be a beam, exhibits a beam bending and the amount of curvature is calculated based on the composite beam theory[5]. In the case of the structure of 2-layers on a substrate, the maximum bow value B is

$$B=\frac{3L_s^{\,2}}{2\hat{E}_s t_s^{\,2}}\left[\hat{E}_1 t_1(t_s+t_1/2-\delta_1)\cdot\Delta\alpha_1\Delta T_1+\hat{E}_2 t_2(t_s+t_1+t_2/2-\delta_2)\cdot\Delta\alpha_2\Delta T_2\right] \tag{1}$$

$$\delta_1=\frac{(\hat{E}_s t_s^{\,2}+2\hat{E}_1 t_1 t_s+\hat{E}_1 t_1^{\,2})}{2(\hat{E}_s t_s+\hat{E}_1 t_1)},\quad \delta_2=\frac{\left\{\hat{E}_s t_s^{\,2}+\hat{E}_1 t_1(2t_s+t_1)+\hat{E}_2 t_2(2t_s+2t_1+t_2)\right\}}{2(\hat{E}_s t_s+\hat{E}_1 t_1+\hat{E}_2 t_2)} \tag{2}$$

where $\hat{E}\left(=E/_{1-\nu}\right)$ is the biaxial modulus, α is the coefficient of thermal expansion, T is the temperature, T_i is the film process temperature, $\Delta\alpha_i=\alpha_i-\alpha_s$, $\Delta T_i=T_i-T$, t is the thickness of layer, δ is the distance of a neutral axis from the lowest surface of the specimen, and the subscript i(i = 1,2) and s denote the film and substrate, respectively. In a similar way, the thermomechanical analysis of a general n-layered structure can be extended easily. The complete equation of B for a general n-layered structure is not presented here for brevity, however, it can be written in an abbreviated form as

$$B=\frac{3L_s^{\,2}}{2\hat{E}_s t_s^{\,2}}\left[f_1\cdot\Delta\alpha_1\Delta T_1+f_2\cdot\Delta\alpha_2\Delta T_2+\cdots+f_n\cdot\Delta\alpha_n\Delta T_n\right] \tag{3}$$

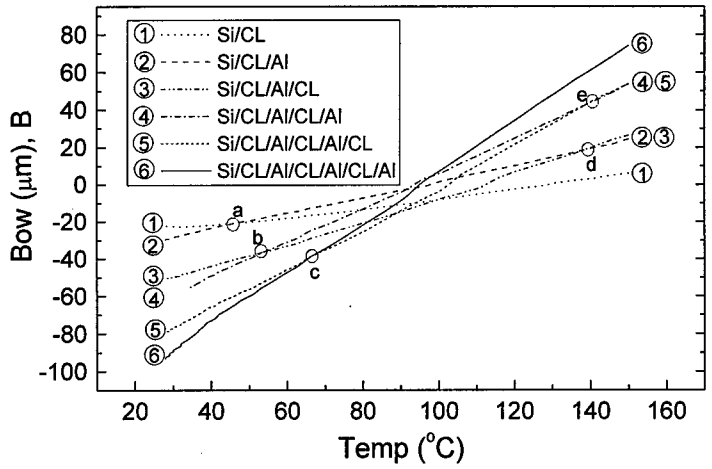
where f_i is the function of E_s, E_i, t_s, t_i.

4. RESULT AND DISCUSSION

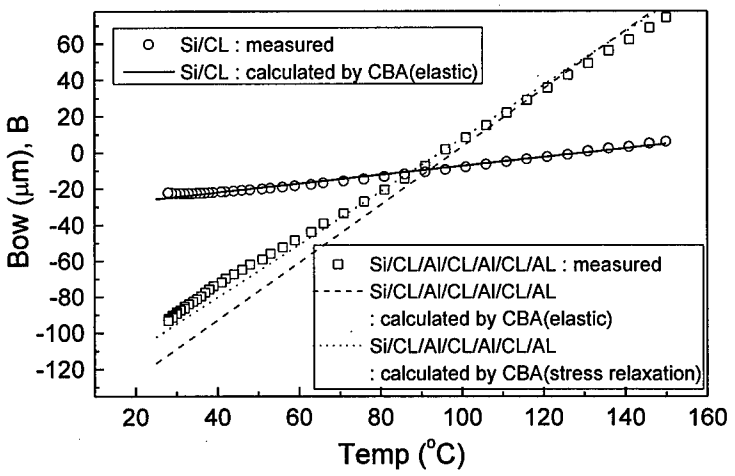
Eight wafers of each multilayered structure were measured with less than 5% deviation. When the CL films are thermally cycled, the intrinsic stress as well as the thermal stress influences B, which manifests itself as a nonlinear slope dB/dT. This intrinsic stress at the first heating cycle(from T = 25 °C to T = 150°C) is presumably due to the moisture absorption[6], since the polymer dielectric materials absorb some amount of moisture during the storage period in a humid environment. A reproducible hysteresis is obtained for the next cycles. Therefore, the cooling curve(from T = 150 °C to T = 25°C) from the 2nd cycle is used to measure B in order to minimize the nonlinear intrinsic stress effect[7], and to compare the result with the calculated value.

Figure 2(a) shows the result of the bow for the polymer/metal multilayer structures of up to six layers. The cooling curves form the 2nd cycle of Si/CL, Si/CL/Al, Si/CL/Al/CL, Si/CL/Al/CL/Al, Si/CL/Al/CL/Al/CL, and Si/CL/Al/CL/Al/CL/Al are denoted by ①, ②, ③, ④, ⑤, and ⑥ in the figure, respectively. The points a(the intersection of ① and ②), b(the intersection of ③ and ④), and c(the intersection of ⑤ and ⑥) seem to be related with the process temperature of the sputtering in which the additional aluminum layer is deposited on the CL surface. On the other hand, d(the intersection of ② and ③) and e(the intersection of ④ and ⑤) seem to be related with the process

temperature of the lamination in which the additional CL layer is laminated on the aluminum surface The process temperature of sputtering is known[8] to be about $T \cong 46°C$, however, as seen at the points a, b, and c in Fig. 2(a), it varies depending on the total thickness of the already existing polymer layers, which have the low heat conductivity.



(a)



(b)

Fig. 2. (a) The cooling curves from the 2nd cooling cycle for the Si/CL, Si/CL/Al, Si/CL/Al/CL, Si/CL/Al/CL, Si/CL/Al/CL/Al/CL, and Si/CL/Al/CL/Al/CL/Al multilayer structures are presented, where CL denotes the Coverlay film, (b) Comparison of the measured bow with the calculated values taken by CBA.

In Fig. 2(b) the experimental values of bowing, B are compared with the calculated values using the extended CBA, selecting the two cases ① and ⑥ for clear presentation. In the calculation, we choose T_1(the process temperature of the CL) = 150°C and T_2(the process temperature of the aluminum) = 46°C. In Case ①, the calculated values of the bow by CBA(solid line in the figure), in which the linear elastic behavior is assumed and the physical property values in Table 1 are used, provide a good estimation of the measured values(open circles in the figure). However, as the more layers are fabricated(see Case ⑥), the calculated values(dashed line in the figure) show a slight deviation from the measured values(open squares in the figure). This difference between the measured and calculated values seems to be due to the stress relaxation effect of the CL film. When the CL film is fabricated at 150°C, the pre-existing layers of CL are thermally stressed due to the CTE mismatch with the aluminum. Because of the viscoelastic properties of epoxy polymers, the thermal stress in the CL film is relaxed. The dotted line shows the calculated values of the bowing of Case ⑥ by simply reducing σ_{Ti} (i = 1,2) in Fig. 1 by 25%. It gives fairly good results. The more detailed study of the stress relaxation seems to be needed.

5. CONCLUSION

The thermomechanical behavior of the multilayer structure(especially the bow) was experimentally measured layer-by-layer during the sequential build-up of the alternating layers of the polymer dielectric and metal conductor films. A thermomechanical stress analysis of the multilayer MCM-D substrate is also performed. It is found that the characteristics of each fabrication process and the materials involved in the processes must be well understood to precisely describe the multilayer behavior. The analytical solutions presented here provides the good estimation of B as a function of T. The proposed model accounts for the different thermal history of each layer and the effect of the film thickness.

REFERENCE

1. P. Flinn, Mater. Res. Soc. Proc., **130** (1990) p. 41
2. H. Liu and S. Murarka, J. Appl. Phys., **72** (1992) p.3458
3. C. Chao, K. Scholz, J. Leibovitz, M. Cobarruviaz, and C. Chang, IEEE Transactions on Components, Hybrids, and Manufacturing Technology, **12** (1989) p. 180
4. G. Stoney, Proc. R. Soc. London, Ser. A **82** (1909) p. 172
5. J.S. Kim, J.H. Lim, K.W. Paik, and Y.Y. Earmme, Applied Physics Letters, **74** (1999) p.3507
6. A. Voloshin, P. Tsao, and R. Pearson, Journal of Electronic Packaging, **120** (1998) p.314
7. S. Bruck, and D. Knorr, Mater. Res. Soc. Proc., **264** (1992) p.251
8. W. Nix, Metall. Trans. A **20A** (1989) p. 2217

Key Engineering Materials Vols. 183-187 (2000) pp. 1129-1134
© 2000 Trans Tech Publications, Switzerland

Failure Behavior and Electrical Property of CFRP and CFGFRP

D.Y. Song, J.B. Park and N. Takeda

Komaba Open Laboratory, University of Tokyo,
4-6-1 Komaba, Meguro-ku, Tokyo 153-8904, Japan

Keywords: Carbon Fiber, CFGFRP, CFRP, Electrical Resistance, Failure Behavior, Monte Carlo Simulation

ABSTRACT

This paper studies the correlation between the mechanical damage and the change of electrical resistance for unidirectional CFRP and CFGFRP (Carbon Fiber/Glass Fiber Reinforced Plastics) composites. This study is performed using experimental and numerical methods, and the results of two methods are compared. The change of electrical resistance is measured under the condition of simple tension and loading-unloading, and the failure process of two types of CFRP is investigated using an optical microscope. A Monte Carlo simulation is performed to predict the change in electrical resistance due to strain and damage (fracture) of carbon fibers. Through these works, it is revealed that the change of electrical resistance had a close relation with the damage process and there is a good agreement between experimental and predicted results.

1. INTRODUCTION

The electrical resistance of conductive wires changes proportionally according to the change of cross-sectional area and length. This means that the change in electrical resistance of conductive wire is affected by its mechanical deformation and damage. So, to understand the main reason of the change of electrical resistance in CFRP, which consists of conductive carbon fibers and non-conductive epoxy matrix, the damage accumulation mechanism should be considered seriously. According to the existing fracture theory of composite, the stress distribution of composites is significantly affected by fracture modes such as matrix-fiber interface debonding, fiber breakage, and matrix crack. In this study, two types of carbon fibers with different electromechanical properties were selected. And simple tension and loading-unloading tests and failure progress observation using an optical microscope were carried out for CFRP and CFGFRP hybrid composites. Moreover, using the shear-lag theory and Weibull distribution of fiber strength, a Monte Carlo simulation is performed for prediction of the change in electrical resistance due to strain and fiber fracture. The predicted results were compared with the experimental results in order to check the validity of the numerical model.

2. EXPERIMENT AND ANALYSIS

2.1. Test Materials and Experimental Procedure

Two types of carbon fiber (PAN based Torayca T700S and M46J of diameter 7 and 5μm, tensile strength 4.9 and 4.21GPa, Young's modulus 230.3 and 436.1GPa, ultimate elongation 2.1 and 1%, respectively) and E-glass fiber (diameter 13μm, tensile strength 1.47GPa, Young's modulus 76GPa) were used as raw materials for CFRP and CFGFRP composites. The electrical resistivity of T700S and M46J carbon fibers was 16.2 and 9.7μΩm, respectively. Composite laminates were fabricated by carbon and glass fibers and epoxy matrix (the curing conducted at 130°C and 3.92MPa for 2hrs). The electrodes for measuring electrical resistance of CFGFRP were prepared by inserting thin conductive wires between CFRP and GFRP prepreg sheets during layup process. The electrodes of CFRP were attached at the surface of the specimen. The dimensions of specimens were 160mm in length, 30mm in width (where, the thickness of CFGFRP and CFRP were 0.6~0.95mm and 0.1mm, respectively). The volume fractions of carbon fibers in the CFGFRP and CFRP were about 9~15 and 60%, respectively. Tensile tests were conducted at the crosshead speed of 0.5mm/min. The electrical resistance was measured using two-probe DC method. A constant current of 1mA was applied on the composites, and the change in electrical resistance due to loading was plotted simultaneously with stress and strain.

2.2. Numerical Analysis

Monte Carlo simulation approach was used to evaluate quantitatively the correlation between mechanical damage and electrical resistance change in composites. For this analysis, the shear lag analysis method was used to calculate the stress distribution of composites. The simulation was carried out according to the following procedure: at first, the tensile strength of each fiber element was assigned using two-parameter Weibull distribution. Then, the nodal displacement of proposed model is calculated by finite difference method based on successive over relaxation algorithm for unit displacement, u_o (Fig. 1). From this displacement, the tensile stress of fiber element and the shear stress of matrix element are obtained using the following Eq. 1:

$$\sigma_{i,j} = E\frac{u_{i,j} - u_{i,j-1}}{\Delta x}, \quad \tau_{i,j} = G\frac{u_{i+1,j}(or, u_{i,j+1} - u_{i,j})}{\Delta x} \tag{1}$$

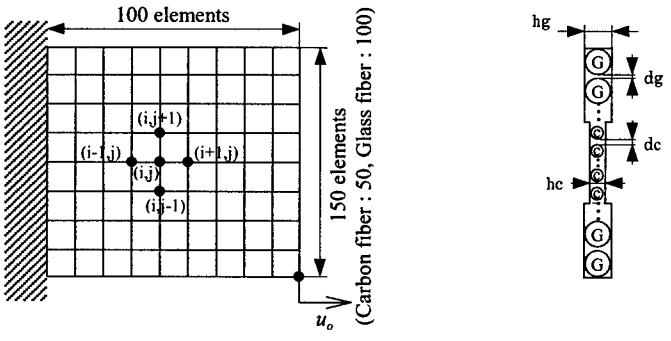


Fig. 1 2-D analysis model for CFRP and CFGFRP composites.

Whether the fiber elements will break or not is determined by comparing their tensile stresses to the assigned fiber strengths, and the debonding behavior of matrix elements is reviewed by comparing their shear stresses to interfacial shear strengths. If debonding occurs between fiber and matrix, the fiber is assumed to slide on the matrix with a constant frictional stress [1]. Also, if there is the breakage in fiber and/or matrix elements, the nodal displacement is calculated again considering the change of the surrounding element and applying the state function (C_1, C_2, and C_3) in Eq.2.

$$U_{i,j}=\frac{1}{C_1+C_2C_3\Delta X^2}\left[U_{i,j-1}+U_{i,j+1}+C_2\Delta X^2(U_{i+1,j}+U_{i-1,j})\right] \tag{2}$$

where, $U_{i,j}$ is the dimensionless displacement ($U_{i,j}=u_{i,j}/\xi$, $\xi=\sqrt{(EAd/Gh)}$ [1]), and C_1, C_2, and C_3 are the state functions which represent the fracture state of fiber and matrix elements. d is the distance between fibers, E and A are the modulus and cross-sectional area of the fibers. h is the thickness of the composite. G is the shear modulus of the matrix. $\Delta X=\Delta x/\xi$ is the dimensionless length (Δx: the length of a fiber element). These procedures are repeated until no new breakage occurs. If no new break occurs, the composite apparent stress and strain were determined. The relative change of the electrical resistance in the composite can be determined using Eq. 3.

$$\frac{\Delta R}{R_0}=\frac{R-R_0}{R_0}=\frac{(1+\varepsilon)}{(1-\nu\,\varepsilon)^2}\frac{N}{(N-N_f)}-1 \tag{3}$$

where, R is the electrical resistance of the fiber bundle with fractured fibers of N_f, N is the number of fibers, R_0 is the initial resistance of the fiber bundle, ε and ν are the strain and Poisson's ratio of fibers, respectively. These procedures were repeated until the stress drops, i.e. the fracture of composites.

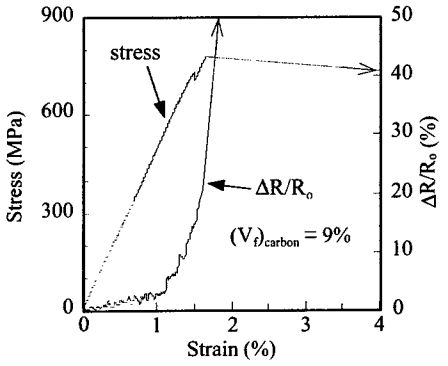


Fig. 2 Stress vs. strain, resistance vs. strain curve of CFGFRP-T700S.

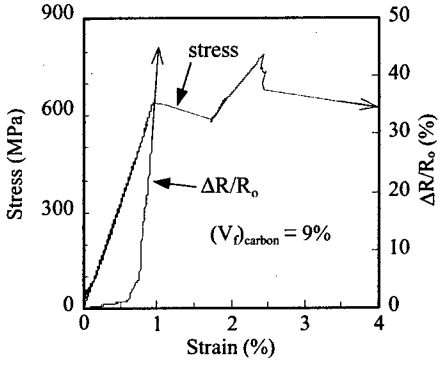


Fig. 3 Stress vs. strain, resistance vs. strain curve of CFGFRP-M46J.

3. RESULTS AND DISCUSSION

3.1. Relations of Stress/Strain and Change in Electrical Resistance/Strain

Figs. 2 and 3 show the stress/strain and electrical resistance change/strain curves obtained from tensile tests of CFGFRP. For T700S, the stress increases linearly up to 1.5% strain, and then shows a sudden drop due to the failure at the interlayer between carbon and glass layers. After 1.7% strain when carbon fibers were fractured, the specimen supported stress up to about 4% strain owing to the presence of glass fibers. In the case of M46J, the stress decreases temporarily after the failure of carbon fiber layer but increases again until about 2.5% strain. At this time, the interfacial debonding and/or matrix cracks in glass fiber layers were hardly observed unlike as T700S. This seems to be due to the difference of the stress/strain behavior of M46J and T700S. On the other hand, the change in electrical resistance of T700S increases almost linearly up to about 1% strain. But after 1% strain the electrical resistance increases more steeply in non-linear shape, and increases extensively near 1.8% strain. This is attributed to the deformation, cracking, and breakage of carbon fiber, respectively [2-4]. For M46J, the entire tendency of electrical resistance is similar to T700S, but after linear increase of resistance, its change is more rapid than that of T700S. This difference of electrical resistance change seems to be related to the different failure mechanisms of T700S and M46J.

Fig. 4 shows the electrical resistance/strain curves of CFRP lamina under repeated loading and unloading test. When the strain was removed, electrical resistance decreased, but did not return along the initial line and left some permanent change in electrical resistance. Fig. 5 shows the increase of residual electrical resistance with the applied maximum strain. The residual electrical resistance of CFRP depended upon the maximum strain applied (this behavior was also identified for CFGFRP composites). This means that the change in the internal structure and the fractured number of carbon fibers owing to the applied loads affect the residual resistance of CFRP. These facts suggest that the CFRP and CFGFRP have the ability to memorize the maximum strain applied in the form of residual electrical resistance.

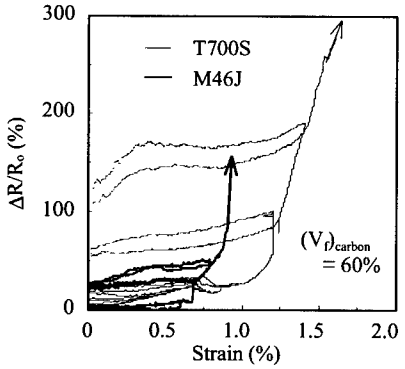


Fig. 4 The change in electrical resistance/strain under repeated loading and unloading : CFRP

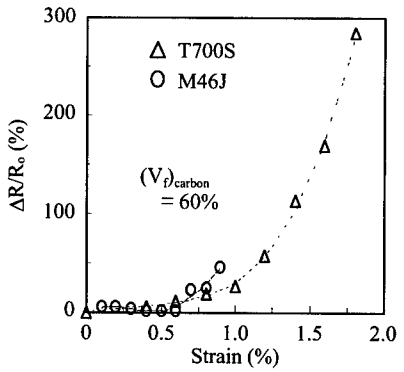
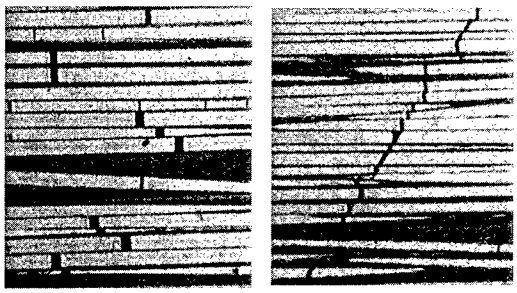


Fig. 5 The comparison of residual resistance change : CFRP.

3.2. Optical Observation of Failure Process

Fig. 6 shows the photos of fracture appearances observed on the surfaces of CFRP specimens just before failure. For CF-T700S, fiber breakage occurred randomly on the whole surface and fiber/matrix debondings were easily observed at the broken fiber ends. This is due to the shear stress concentrations generated by the fiber breakage. Pull-out fibers were significantly observed on the fractured section of the specimen and their lengths are relatively large. For CF-M46J, the initial crack occurred at the stress level nearly equal to that of CF-T700S, but this crack rapidly propagated across the specimen in connection with the breakage of neighboring fibers by subsequent loading. Furthermore, fiber/matrix debonding was hardly observed. The overall crack propagation path is almost straight and perpendicular to the load direction. This is probably due to the relatively strong adhesion of the fiber/matrix interface. Considering these results and the difference in the behavior of resistance change, there should be a close relation with failure process and electric resistance change.



(a) CF-T700S (b) CF-M46J

Fig. 6 Fracture appearances just before fracture.

3.2.3 Comparison between Simulation and Experimental Results

The input data and material constants used in the simulation are shown in Table 1. Fig. 7 shows the comparison between the experiment and simulation for CFRP. There is reasonable agreement with the simulation and experimental results. Fig. 8 shows the simulation examples of stress/strain, fracture

Table 1. Input data used in the simulation

Materials	Carbon fiber		Glass Fiber	Epoxy
	T700S	M46J		
Young's modulus of fiber, E(GPa)	230	436	76	3.5
Cross-sectional area of fiber, A(μm^2)	38.5	19.6	200.9	
Shear modulus of matrix, G(GPa)				1.3
Distance between fibers, d(μm)	2.16	1.55	7.50	
* Weibull scale parameter, σ_0(GPa)	4.9	4.2	1.2	
* Weibull shape parameter, m	5.5	5.5	10	
* Interfacial shear strength, τ_i(MPa)				30
* Friction stress at interface, τ_f(MPa)				15
* Fiber element length, Δx(μm)	7	5	13	
Thickness of composite, h (μm)	23	23	23	

* These were assumed by considering Refs. [6-8]

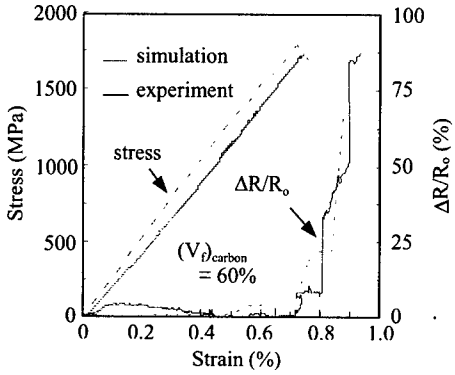


Fig. 7 Comparison of simulation and experimental result : CFRP –M46J.

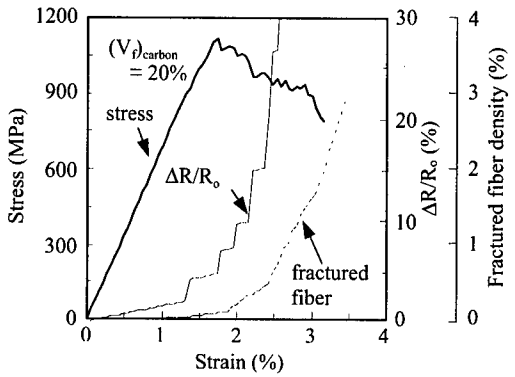


Fig. 8 A simulation example : CFGFRP – T700S.

density of carbon fiber, and relative resistance change for CFGFRP. The electrical resistance in this example shows the same tendency to the experiment. It has the linear increase up to about 1.3% strain, more steep non-linear increase up to 1.8%, and drastic increase near fracture strain (see Fig. 1). Considering these results, it is possible to evaluate the damage state in the structure by comparing simulation results with the measured results during and after loading.

4. CONCLUSIONS

The relationship between the mechanical damage and the change in electrical resistance in CFRP and CFGFRP hybrid composites was experimentally investigated and numerically simulated. Test results revealed that the change in the electrical resistance was closely related with the failure mechanisms. The predicted results by a Monte Carlo simulation showed reasonable agreement with the experimental results. Therefore, by comparing the simulation results with the measured results of electrical resistance, it is possible to evaluate the damage state quantitatively during and after loading.

REFERENCES

1. J.Yuan et al, Composite Science and Technology, **52** (1994) p.197
2. N. Muto et al., J. Japanese Society of Composite Materials, **18**, No.3 (1992) p.144
3. K.Schulte and H. Wittich, Proc. ICCM-10, Whistler (1995) p.349
4. X. Wang and D. D. L. Chung, 5th SPIE Conference, San Diego (1998) p.242
5. H. Hukuda, J. Composite Materials, **16** (1982) p.371
6. J.Aveston and J. M. Sillwood, J. Materials Science, **11** (1976) p.1877
7. M. Shioya and A. Takaku, Composite Science and Technology, **55** (1995) p.33
8. M. R'Mill et al, Composite Science of Technology, **56** (1996) p.831

Key Engineering Materials Vols. 183-187 (2000) pp. 1135-1140
© 2000 Trans Tech Publications, Switzerland

Elastic Restraint between the Plate Components of FRP Compression Members

S.J. Yoon, S.K. Jeong and S.H. Chae

Department of Civil Engineering, Hongik University, 72-1 Sangsu-dong, Mapo-gu, Seoul 121-791, Korea

Keywords: Elastic Restraint, FRP, Local Buckling Strength, Orthotropic Structural Shapes

ABSTRACT

Due to the attractive material properties, fiber reinforced plastic (FRP) materials are considered as an alternative of conventional construction materials. However, due to the absence of reliable design criteria and guidelines, most of engineers are hesitant to design with these materials. To develop such design guidelines, comprehensive research on the structural behavior under various loading conditions must be conducted not only experimentally but also analytically. In this paper, we presented the design chart for the local buckling strength of orthotropic compression members considering the elastic restraining effect between the adjacent plate components. In addition, the dominant plate component initiating the local buckling is identified and simplified design equation for the local buckling of FRP structural shapes is proposed.

1. INTRODUCTION

Due to the rapid developments and advances in the field of manufacturing composites, fiber reinforced polymeric plastic composite structural shapes are produced using the pultrusion process which is known to be one of the most cost effective manufacturing techniques [1]. This material is frequently assumed to be orthotropic or more specifically transversely isotropic and readily available in the field of civil engineering. Such a trend is expected to continue because this material is recognized as an alternative to overcome the deficiency arising in the use of conventional construction materials such as steel and/or concrete. In spite of their superior mechanical and physical properties, most of engineers are reluctant to design with fiber reinforced plastic structural members because of the absence of reliable design criteria.

In general, structural shapes are made of several plate components and boundary conditions of those plate elements must be determined by considering the elastic restraining effect of adjacent

plates. In the local buckling mode, one plate element buckles first and the other plates buckle after that plate based on the dimension of the cross-sectional configuration in which the plate is elastically restrained at the junction by the adjacent plate elements. Thus, the distinction of plate component which leading local buckling of member is very important for the determination of section dimension in the manufacturing of structural shapes.

In this research, we presented the graphical form of results, which can identify the plate leading local buckling of orthotropic compression member. Moreover, using the presented graphical form of results, we also derived the simplified equation for computing the buckling loads, which could be used in the preliminary design of fiber-reinforced polymeric structural members.

2. BUCKLING OF ORTHOTROPIC PLATE

Using the dimensionless parameters $\xi = x/a$ and $\eta = y/b$, the differential equation of orthotropic plate under uniform compression, as shown in Fig. 1, takes the form [2, 3]:

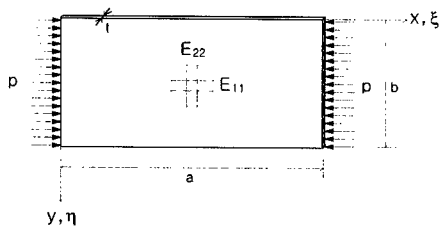


Fig. 1 Orthotropic plate under uniform compression

$$s^4\lambda_1^4\frac{\partial^4 w}{\partial\xi^4}+2s^2\lambda_2^2\frac{\partial^4 w}{\partial\xi^2\partial\eta^2}+\frac{\partial^4 w}{\partial\eta^4}+\pi^2 s^2\lambda_1^2 k\frac{\partial^2 w}{\partial\xi^2}=0 \tag{1}$$

where

$$s=\frac{b}{a},\quad \lambda_1=\left(\frac{D_{11}}{D_{22}}\right)^{\frac{1}{4}},\quad \lambda_2=\left(\frac{D_{12}+2D_{66}}{D_{22}}\right)^{\frac{1}{2}},\quad k=\frac{pb^2}{\pi^2\sqrt{D_{11}D_{22}}} \tag{2-1,2,3,4}$$

In the above equations D_{11} and D_{22} are the flexural rigidities of plate with respect to the material property directions 1 and 2, and D_{66} is the twisting rigidity of plate. The letter k indicates the buckling coefficient of plate for calculating buckling strength following Timoshenko (1963)[4].

The solution of equation (1) can be taken in the form:

$$w=(A_1\cosh\alpha\eta+A_2\sinh\alpha\eta+A_3\cos\beta\eta+A_4\sin\beta\eta)\sin m\pi\xi \tag{3}$$

where A_1, A_2, A_3, and A_4 are arbitrary unknown constants associated with plate deflection and must be determined from the boundary conditions along the unloaded edges. The letter m denotes the number of half-sine waves in the longitudinal direction of plate. The parameters α and β can be shown to have the forms, respectively:

$$\alpha = m\pi s\lambda_2 \sqrt{1+\sqrt{1-\left(\frac{\lambda_1}{\lambda_2}\right)^4\left(1-\frac{k}{m^2 s^2 \lambda_1^{\,2}}\right)}} \tag{4-1}$$

$$\beta = m\pi s\lambda_2 \sqrt{-1+\sqrt{1-\left(\frac{\lambda_1}{\lambda_2}\right)^4\left(1-\frac{k}{m^2 s^2 \lambda_1^{\,2}}\right)}} \tag{4-2}$$

3. LOCAL BUCKLING OF ORTHOTROPIC COMPRESSION MEMBERS

Local buckling equation presented herein is quoted from the references by authors [2, 3], so, for brevity, only the appropriate result is repeated. This result is used for the examination of restraint effect of orthotropic plate components.

Consider a short structural I-shape member of length L, which is composed of five rectangular orthotropic plates as shown in Fig. 2. This member has two common junctions meeting three plate components. Some assumptions are adopted following Bulson (1969)[5], in addition to the basic assumptions of thin plates (Szilard, 1974)[6]:

- The junction of the plate components remains straight when buckling occurs,
- Original angles between plate components are unchanged during buckling,
- Plate thickness does not differ significantly so that the wavelengths of the buckles occurring in all plates can be assumed to be the same and occur simultaneously.

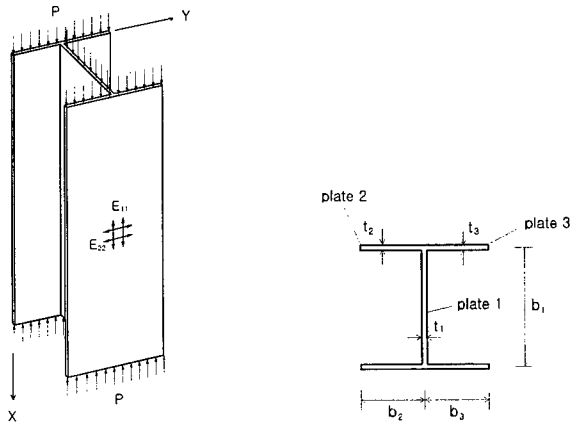


Fig. 2 Orthotropic I-shape section member under uniform compression

Considering above assumptions, we can find the local buckling equation of I-shape orthotropic compression member as follows [2, 3]:

$$\left(\frac{SSY}{FSY}\right)_1 + \frac{1}{\delta_2 \omega_2^{\,3}} \cdot \left(\frac{SFR}{FFR}\right)_2 + \frac{1}{\delta_3 \omega_3^{\,3}} \cdot \left(\frac{SFR}{FFR}\right)_3 = 0 \tag{5}$$

where, SSY, FSY, SFR, and FFR are the transcendental form of buckling equation of plate (see Fig. 1) with the following boundary conditions in unloaded edges, respectively:

SSY: Simply supported at $\eta = 0$, a plane of symmetry at $\eta = 1/2$
FSY: Fixedly supported at $\eta = 0$, a plane of symmetry at $\eta = 1/2$
SFR: Simply supported at $\eta = 0$, free at $\eta = 1$
FFR: Fixedly supported at $\eta = 0$, free at $\eta = 1$

In equation (5), subscripts 1, 2, and 3 after parenthesis denote each plate component, δ_2, δ_3 are the width ratio of plate 2 and plate 1, plate 3 and plate 1, respectively, and ω_2, ω_3 are the thickness ratio of plate 1 and plate 2, plate 1 and plate 3, respectively. The minimum buckling coefficient k_1 for concentrically loaded orthotropic column is shown in Fig. 3 graphically. To verify the solution, the graphical form of results of minimum buckling coefficient k_1 of concentrically loaded isotropic I-shape columns is also presented as shown in Fig. 4. Identical results given by Bulson (1969)[5] and Galambos (1988)[7] are obtained.

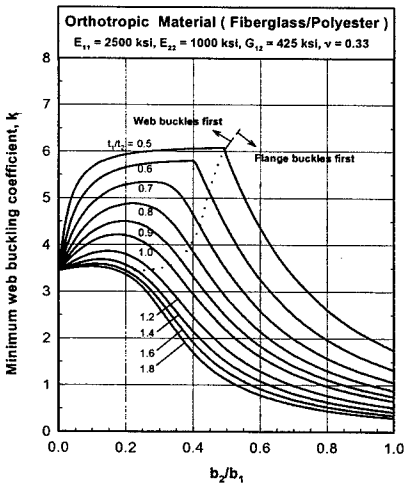


Fig. 3 Minimum web local buckling coefficient of orthotropic I-shape column

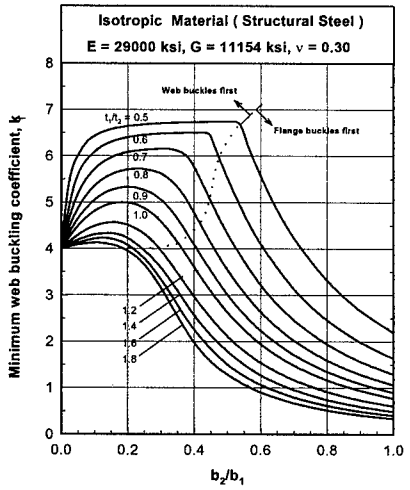


Fig.4 Minimum web local buckling coefficient of isotropic I-shape column

In Fig. 3 for the orthotropic structural I-shapes and in Fig. 4 for the structural steel, dotted line indicates the point where the flange and web buckle simultaneously.

4. DERIVATION OF APPROXIMATE EQUATION

By examining the web local buckling curves of I-shape column, the local buckling coefficient k_1 for the specific values of t_1/t_2 which is similar to that in reference [8], is approximated by the following simplified equations:

For $0.1 \le \dfrac{b_2}{b_1} \le u$, buckling of web restrained by the flange

$$k_1 = p_1\left(\frac{b_2}{b_1}\right)^2 + q_1\left(\frac{b_2}{b_1}\right) + r_1$$

For $u \le \frac{b_2}{b_1} \le 1.0$, buckling of flange restrained by the web

$$k_1 = p_2\left(\frac{b_1}{b_2}\right)^2 + q_2\left(\frac{b_1}{b_2}\right) + r_2$$

in which the coefficients u, p_1, q_1, r_1, p_2, q_2, and r_2 are obtained from curve-fitting for the practical range of flange and web width ratio (0.1 to 1.0) as shown in Fig. 5. Also the simplified equation is examined for the thickness ratio between web and flange plate of 0.5, 0.7, and 1.0. Coefficients of simplified equations, equation (6) and equation (7), are listed in Table 1.

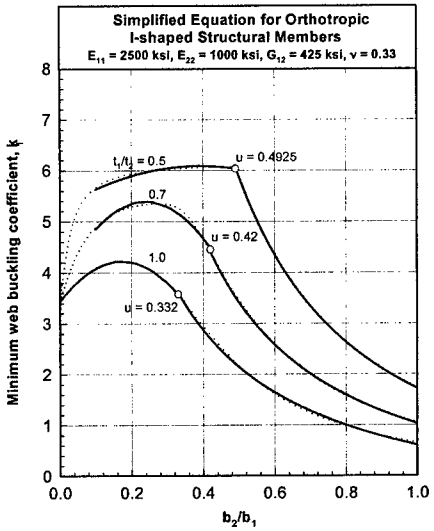


Fig. 5 Simplified equations for I-shaped orthotropic column

Table 1. Coefficients for simplified equations of I-shaped columns under uniform compression

t_1/t_2	0.5	0.7	1.0
u	0.4925	0.4200	0.3320
p_1	-5.39	-27.64	-26.02
q_1	4.21	13.24	9.00
r_1	5.26	3.80	3.44
p_2	0.69	0.17	-0.06
q_2	2.12	1.89	1.71
r_2	-1.09	-1.03	-1.03

5. CONCLUSION

In this paper, we discussed the local buckling analysis of pultruded fiber reinforced I-shape structural member. Pultruded fiber reinforced plastic (FRP) composite is assumed as an orthotropic material. Since the FRP structural shapes are composed of flat plate elements, local buckling of the member could be a major design consideration. In addition, in the determination of cross-sectional dimension at the manufacturing stage, it is an essential to distinguish which plate component governs the local buckling behavior of the member. Based on the classical orthotropic plate theory we presented the graphical form of results that can estimate the local buckling strength. To overcome the complexities and difficulties in the theoretical analysis we proposed simplified equation for estimating local buckling strength of FRP columns. The simplified equations are divided into two portions by points which indicate that there is no elastic restraint, that is, at those points flange and web buckle simultaneously. The results are plotted into graphical form so that the engineer can easily estimate the local buckling strength of FRP structural members.

REFERENCES

1. Strongwell, Extern Fiberglass Structural Shapes Design Manual, Morrison Molded Fiberglass Company, Bristol, Virginia (1988)
2. S.J.Yoon, and S.H.Chae, Journal of Structural Division, KSCE, Mar, **1**. (1999) pp. 75
3. S.J.Yoon, Ph.D.Thesis, Georgia Institute of Technology, Atlanta, Georgia (1993)
4. S.P.Timoshenko and J.M.Gere, Theory of Elastic Stability, 2nd ed., McGraw-Hill Book Co., Inc., New York (1961)
5. P.S. Bulson, The Stability of Flat Plates, American Elsevier Publishing Company Inc., New York (1969)
6. R.Szilard, Theory and Analysis of Plates, Prentice-Hall, Inc., Englewood Cliffs, New Jersey (1974)
7. T.V.Galambos, Guide to Stability Design Criteria for Metal Structures, 4th ed., John Wiley & Sons, Inc., New York (1988)
8. B.S.Shih, Ph.D.Thesis, Georgia Institute of Technology, Atlanta, Georgia (1994)

Key Engineering Materials Vols. 183-187 (2000) pp. 1141-1146
© 2000 Trans Tech Publications, Switzerland

Mixed-Mode Ply Cracking in Multidirectional Continuous Fiber Composite Laminates

Junqian Zhang[1], K.P. Herrmann[2] and Xiangguo Zeng[1]

[1] Department of Engineering Mechanics, Chongqing University, Chongqing 400044, China P.R.

[2] Laboratory for Technical Mechanics, University of Paderborn, Pohlweg 47-49, D-33098 Paderborn, Germany

Keywords: Laminate, Matrix Cracking, Mixed-Mode, Stacking Sequence

ABSTRACT

In this contribution the transverse cracking in general multidirectional composite laminates other than the cross-ply lay-ups is studied under a combined in-plane extension and shear loading. The formation of a new full-width ply crack is modeled by analyzing such a problem that the through-thickness-crack in the considered lamina initiating from the laminate edge propagates into the interior of the laminate, quickly reaching a steady state. In particular, included in the study is the evaluation of the energy release rate (ERR) that is considered as a driving force for the ply cracking. The total ERR and the mode-I and mode-II components are computed by utilizing the solutions for the ply stresses and displacements. The effect of the lay-up parameters on the ERR is examined, suggesting that the closest neighbor layer imposes a primary constraint on the lamina to prevent it from cracking, whereas the constraining influence of remote plies could be ignored.

1. INTRODUCTION

When a multidirectional composite laminate is subjected to a static or fatigue tensile loading, the ply cracks (matrix cracks) develop parallel to the fibers in the 90-deg plies as well as in the off-axis laminae long before the catastrophic laminate fracture. The ply cracking in the 90-deg lamina within the cross-ply laminates has been investigated extensively based on the strain energy release rate version in fracture mechanics where the steady-state cracking was used explicitly or implicitly. The stress analyses for the cracked laminates were carried by using the methods based on shear-lag arguments [1-5], laminate plate theories [6,7] and variational methods [8,9]. None of the references cited above, except for the stress analysis methods developed recently in refs. [10,11], can apply to a general lay-up configuration other than the cross-ply laminates.

For the general lay-up laminates the ply cracking in the 90-deg layers experiences the mixed-mode conditions under a combined in-plane extension and shear loading, while the ply cracking in the off-axis laminae takes place always in the mixed-mode involving mode-I and mode-II because of the extension-shear coupling, even the laminate load is applied in uni-axial tension. The importance of the steady-state growth of the through-thickness-crack in the considered lamina is addressed in order to analyze the rate of energy required for the formation of a new full-width ply crack. The total ERR for the ply crack formation and the mode-I and mode-II components are computed by utilizing the solutions for the ply stresses and displacements that were ready in ref. [10]. The constraining effects on the ply cracking are examined.

2. STEADY-STATE CRACK PROPAGATION

Consider a general symmetric multidirectional continuous fiber composite laminate containing a 90-deg lamina that may locate at either the center or the off-center of the laminate, Fig.1. A ply coordinate system, x_1-x_2-x_3, is introduced for the 90-deg layer of interest such that the x_1 and x_2-axes are parallel and perpendicular to the fibers in the 90-deg layer, respectively, and the x_3-axis starts from the mid-plane of the lamina. The laminate is subjected to general in-plane loading involving combined extensional and shear loading. What we concern is to model the ply cracking in the 90-deg lamina, Fig.1. For the problem concerning the ply cracking in an off-axial lamina, such a lamina may be viewed as 'a local 90-deg layer' with respect to the ply coordinate system and the applied loads should be transformed appropriately from the laminate coordinate system to the ply coordinate system.

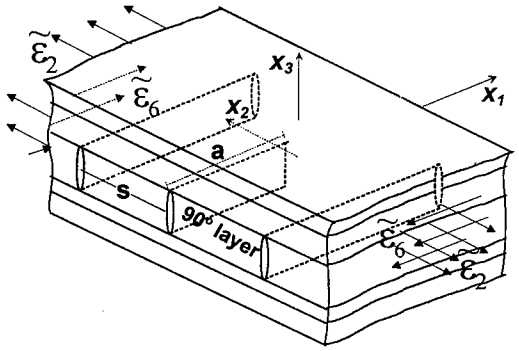


Fig. 1. A through-thickness-crack in the 90-deg

The matrix crack nuclei initiate in some regions at the edge of specimen, generally believed to be where fibers are closely spaced or even in contact [1]. Because the thickness is small with respect to the width for laminates, the matrix crack, after initiation, grows rapidly across the thickness of the lamina, and then propagates along the fiber direction (width) slowly or unstably, depending on the constraint from the neighbor plies [1,12]. Therefore, it seems reasonable to assume that a ply through-thickness-crack initiating from the edge of the laminate extends towards the width of the specimen (Fig.1). Let $\overline{G}$ be the average of the strain energy release rate G through the lamina thickness, i.e.

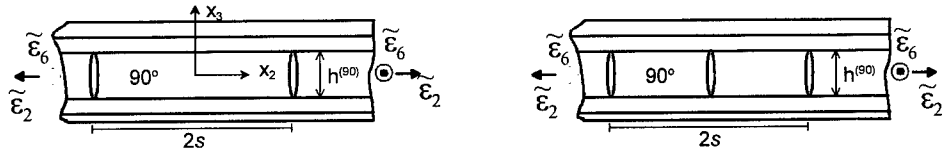
$$\overline{G}(2s,a)=\frac{1}{h^{(90)}}\int_{-\frac{h^{(90)}}{2}}^{\frac{h^{(90)}}{2}}G(2s,a,x_3)dx_3\,, \tag{1}$$

where $h^{(90)}$ is the thickness of the 90-deg layer; the $\overline{G}$ values for the growing crack may vary as a function of the crack length for a given crack spacing. As the through-thickness-crack grows beyond the characteristic length and may reaches a steady-state propagation, $\overline{G}$ becomes independent of crack length, a. It was shown in [9,13] that the ERR for a through-thickness-crack advancing in a steady-state condition, $\overline{G}_{ss}$, was consistent with the rate of energy (the right-hand side of Eq.2) required for a full-width ply crack forming spontaneously, i.e.

$$\overline{G}_{ss}(2s)=\frac{1}{h^{(90)}}[SE(2s)-SE(s)], \tag{2}$$

where $SE(2s)$ and $SE(s)$ stand for the strain energy per unit width of the crack interval, $2s$, before and after the newly cracking under generalized plane strain condition, respectively, Fig.2. Therefore, the full-width crack model can be used rigorously if the steady-state crack propagation takes place. The questions that arise are: will the steady state take place?, how do such parameters as the lamina thickness, material properties mismatches and crack spacing influence the occurrence of the steady-

state crack propagation besides the free-edge effect? In order to accurately answer the questions experimental tests and 3D finite element analyses, which involve a large number of lay-up configurations, need to be conducted for determination of the ERR as a function of the length of a growing ply crack. Such kind of results, however, are very limited. Nevertheless, the available experimental evidences [12] for the cross-ply laminates indicate qualitatively that the ply cracks grow across the width slowly for a thin 90-deg lamina and unstably for a thick lamina. This



(a) Before the newly cracking (b) After the newly cracking

Fig. 2. The full-width ply crack model

suggests that the steady state may take place beyond the characteristic length for the thin lamina, and never happen before the unstable growth for the thick lamina at least at the stage of large crack spacing. This argument is further supported by the 3D finite element analysis (FEA) results in [13] that the ERR for the growing crack increases with the ply crack length for the thick 90-deg lamina at the stage of large crack spacing, and the steady state gets to happen as the crack spacing gets as small as the lamina thickness. Thus, the steady-state crack propagation seems valid for a constrained thin lamina and for a constrained thick lamina at the stage of small crack spacing. However, at the stage of low crack density the through-thickness-crack starts to propagate unstably after reaching a critical length, a_0. From the FEA results just mentioned it can be inferred that the ERR for onset of the unstable growth of a through-thickness-crack is smaller than the rate of energy associated with a full-width crack. Thus, the full-width crack model overestimates the ERR for a thick lamina at the initial stage of ply cracking (or underestimates the strain to the first ply failure).

3 EVALUATION OF THE ERR FOR CRACKING

The through-thickness-crack advancing from the edge into the interior of the laminate may experience mixed-mode (mode-I plus mode-II) conditions. The strain energy difference in Eq.2 must be equal to the work done by tractions in the generalized plane strain problem shown in Fig. 2 such that

$$\overline{G}_{ss}(2s) = \overline{G}_I(2s) + \overline{G}_{II}(2s) = \frac{1}{2h^{(90)}}(N_2^{(90)}\overline{\delta}_2 + N_6^{(90)}\overline{\delta}_6), \tag{3}$$

where $N_2^{(90)}$ and $N_6^{(90)}$ are extension and shear forces per unit width of the 90-deg lamina at the midway between the pre-existing two cracks, Fig. 2a; $\overline{\delta}_2$ and $\overline{\delta}_6$ are opening and shear discontinuity displacements of the new crack, Fig. 2b. Consequently, the mode I and mode II components of the ERR are defined by

$$\overline{G}_I = \frac{1}{2h^{(90)}} N_2^{(90)} \overline{\delta}_2, \tag{4}$$

$$\overline{G}_{II} = \frac{1}{2h^{(90)}} N_6^{(90)} \overline{\delta}_6. \tag{5}$$

The solutions for the ply forces and displacements within the cracked laminate in Fig.2a were readily obtained in [10]. By substituting x_2=0 into the solutions one can obtain the ply forces at the midway between the two pre-existing cracks where the new cracking may take place,

$$N_2^{(90)}(2s) = h^{(90)}(1-\zeta_{22}(s)(Q_{22}^0 \widetilde{\varepsilon}_2 + Q_{12}^0 \widetilde{\varepsilon}_1), \tag{6}$$

$$N_6^{(90)}(2s) = h^{(90)}(1-\zeta_{66}(s))Q_{66}^0 \widetilde{\varepsilon}_6, \tag{7}$$

where Q_{ij}^0 are the in-plane stiffnesses of an intact lamina, and

$$\zeta_{22}(s) = \sum_j [\gamma_{j2}^{(I)} - \frac{1}{2}(\gamma_{j2}^{(II)} + \gamma_{j2}^{(III)}) \frac{\lambda_j s}{\sinh(\lambda_j s)}] \Phi_{j1}(s), \tag{8}$$

$$\zeta_{66}(s) = \sum_j [\gamma_{j6}^{(I)} - \frac{1}{2}(\gamma_{j6}^{(II)} + \gamma_{j6}^{(III)}) \frac{\lambda_j s}{\sinh(\lambda_j s)}] \Phi_{j2}(s), \tag{9}$$

for the cracked lamina that locates at the off-center of the laminate, and

$$\zeta_{22}(s) = \sum_j [\gamma_{j2}^{(I)} - \gamma_{j2}^{(II)} \frac{\lambda_j s}{\sinh(\lambda_j s)}] \Phi_{j1}(s), \tag{10}$$

$$\zeta_{66}(s) = \sum_j [\gamma_{j6}^{(I)} - \gamma_{j6}^{(II)} \frac{\lambda_j s}{\sinh(\lambda_j s)}] \Phi_{j2}(s), \tag{11}$$

for the cracked lamina that locates at the center of the laminate. All the parameters appearing in the Eqs.6-11, are given in ref. [10]. Since the crack spacing is reduced from $2s$ before the cracking (Fig. 2a) to s after the midway cracking (Fig. 2b), the displacement jumps across the new crack of the midway can be evaluated by using the displacement solutions, which were derived in [10] for a crack spacing of $2s$, along with a substitution of $2s$ by the crack spacing of s. The average displacement jumps at the crack surface are

$$\overline{\delta}_2(s) = s\Lambda_{22}(s)(\widetilde{\varepsilon}_2 + \frac{Q_{12}^0}{Q_{22}^0} \widetilde{\varepsilon}_1), \tag{12}$$

$$\overline{\delta}_6(s) = s\Lambda_{66}(s)\widetilde{\varepsilon}_6, \tag{13}$$

where the parameters, Λ_{22} and Λ_{66}, are called the *in-situ* damage effective functions (IDEFs) characterizing the degradation in the stiffness of the cracked lamina within the laminate, which

were derived as functions of the crack spacing and the constraining parameters in ref. [10]. Substitution of Eqs.6,7,12,13 into Eqs.4,5 gives

$$\overline{G}_I(2s) = g_I(2s)(\tilde{\varepsilon}_2 + \frac{Q_{12}^0}{Q_{22}^0}\tilde{\varepsilon}_1)^2, \tag{14}$$

$$\overline{G}_{II}(2s) = g_{II}(2s)\tilde{\varepsilon}_6^{\,2}, \tag{15}$$

where

$$g_I(2s) = \frac{1}{2}s\Lambda_{22}(s)(1-\zeta_{22}(s))Q_{22}^0, \tag{16}$$

$$g_{II}(2s) = \frac{1}{2}s\Lambda_{66}(s)(1-\zeta_{66}(s))Q_{66}^0, \tag{17}$$

where g_I and g_{II} are the mode-I and mode-II energy release rates normalized by the laminate strains, and depend on the laminate properties and the crack spacing. They are good measures for quantifying the influences of the constraint on the ply cracking because for a constant laminate strain the overall strain of the cracked lamina (equal to the laminate strain) does not change with changing lay-ups of the constraining sublaminates.

4. RESULTS

For a purpose of illustration the normalized mode-I and mode-II ERRs for the 90-deg ply cracking, g_I and g_{II}, are plotted as a function of the crack density. Figs. 3-4 demonstrate the influence of the

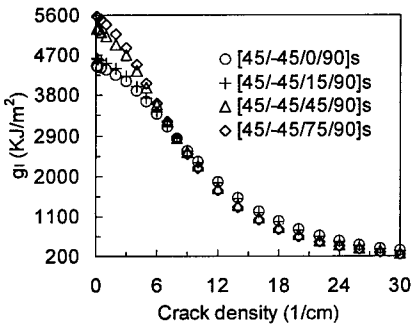


Fig.3. Influence of the nearest layer on the mode-I 90-deg ply cracking.

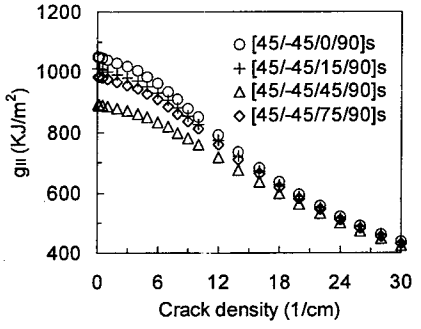


Fig.4. Influence of the nearest layer on the mode-II 90-deg ply cracking.

primary constraining layer on the 90-deg ply cracking by allowing the fiber orientation of the nearest neighbor layer to vary from laminate to laminate and by keeping the other plies unchanged. The notable discrepancy between the laminates at the stage of low crack density implies that the closest neighbor layer of the cracked lamina influences the cracking behavior significantly. Moreover, Fig.3 shows that the curve of mode-I ERR versus crack density for a smaller fiber angle lies below the curve for a bigger fiber angle, suggesting that the constraining effect gets stronger as the fiber orientation angle of the constraining layer gets smaller. From Fig.4 it can be seen that the 90-deg lamina constrained by the 45-deg layer over by the other orientation layers has a lower driving force for the mode-II cracking. The reason seems that the 45-deg lamina has maximum in-

plane shear modulus. Figs. 5-6 illustrate the influence of the secondary constraining plies on the

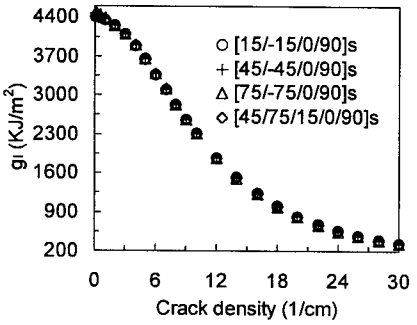


Fig.5. Influence of the remote plies on the mode-I 90-deg ply cracking.

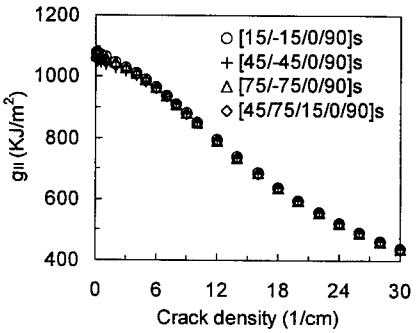


Fig.6. Influence of the remote plies on the mode-II 90-deg ply cracking.

cracking. Invisible differences in the mode-I and mode-II ERR between the laminates, which have different plies except for the common 90-deg lamina and primary constraining ply, suggest that the stacking sequence and lay-ups of the plies away from the cracked lamina has no significant influence on the cracking. It is seen from Figs.4 through 6 that the ERR components decrease as the crack density increases. Therefore, an additional applied load is required for a new crack formation, suggesting that the multiplication of the ply cracks takes place in a stable manner.

ACKNOWLEDGMENT

One of the authors (JZ) gratefully acknowledges the financial supports by the National Science Foundation of China under grant number 19972076 and the Alexander von Humboldt-Foundation of Germany.

REFERENCE

1. A. Parvizi and J. E. Bailey, J. Materials Science, **13** (1978) p. 2131.
2. Y. M. Han and H. T. Hahn, Composites Science and Technology, **31** (1989) p. 165.
3. L. R. Dharani and H. Tang, Int. J. Fracture, **46** (1990) p. 123.
4. J. Zhang, J. Fan and C. Soutis, Composites, **23** (1992) p. 291.
5. J. Zhang, J. Fan and C. Soutis, Composites, **23** (1992) p. 299.
6. G. N. Praveen and J. N. Reddy, IUTAM Symp. on Microstructure-Property Interaction in Composite Materials, R. Pyrz (ed.), (1994) p. 301.
7. J. Zhang, J. Fan and K. P. Herrmann, Int. J. Solids & Struct., **36** (1999) p. 813.
8. J. A. Nairn, J. Composite Materials, **23** (1989) p. 1106.
9. N. J. Pagano, G. A. Schoeppner, R. Kim and F. L. Abrams, Composites Science and Technology, **58** (1998) p. 1811.
10. J. Zhang and K. P. Herrmann, Composites Part A, **30** (1999) p. 683.
11. L. N. McCartney, NPL Report CMMT (A) 50, National Physical Laboratory, UK (1996).
12. L. Boniface, P. A. Smith, M. G. Bader and A. H. Rezaifard, J. Composite Materials, **31** (1997) p.1080.
13. J. W. Hutchinson and Z. Suo, Advances in Applied Mechanics **29**, Academic Press, New York (1992) p. 63.
14. F. J. Guild, S. L. Ogin and P. A. Smith, J. Composite Materials, **27** (1993) p.646.

Key Engineering Materials Vols. 183-187 (2000) pp. 1147-1152
© 2000 Trans Tech Publications, Switzerland

Axial Crush and Energy Absorption Characteristics of Aluminum/GFRP Hybrid Square Tube

K.H. Kim, K.C. Shin and J.J. Lee

Department of Mechanical Engineering, Korea Advanced Institute of Science and Technology, 373-1 Kusong-dong, Yusung-gu, Taejon 305-701, Korea

Keywords: Aluminum/GFRP Hybrid Tube, Axial Crush, Energy Absorption Characteristics, Trigger Mechanism

ABSTRACT

In this study, static axial crush tests were performed with the aluminum/GFRP hybrid tubes. Glass/Epoxy prepregs were wrapped around aluminum tube and then co-cured. The failure of hybrid tube was stable and progressive without trigger mechanism, and specific energy absorption was increased to maximum 33% in comparison with aluminum tube. The best energy absorption performance was obtained for the 90° plies hybrid tube. Aluminum/GFRP hybrid tube showed effective energy absorption capability because wrapped composite tube constrains the deflection of aluminum tube. The failure of hybrid tube was stable without trigger mechanism because inner aluminum tube could play the role of crack initiator and controller. Mean crushing load could be calculated by modified plastic hinge collapse model for hybrid material. The calculated results by this model showed a good agreement with the experimental results. Aluminum/GFRP hybrid tube showed good energy absorption and easy production capability.

1. Introduction

Light weight structure of vehicle is very important issue for modern vehicles which mainly use internal-combustion engines because this light weight structure of vehicle can reduce exhaust gas and improve fuel consumption ratio. One of the light weight materials for the vehicle is aluminum. Aluminum alloy is used to produce vehicle components like pistons, engine blocks, chassis, hoods, fenders, doors, etc. But press manufacturing is difficult due to strain concentration and low ductility. Also it needs much electrical energy and large size of facilities because of bad spot welding characteristic. Another light weight material is composite material. Composites have high specific stiffness and strength, good fatigue property and damping characteristic. But it is difficult to design because composite materials show anisotropic characteristics. They have also problem with high cost and difficult recycling.

Upper and lower side rails of vehicle front structure is main impact energy absorber when vehicle crashes. The front structure which supports engine mount and suspension is composed of each side rail and apron. Generally, the cross section shape of side rails is square, rectangular, or hourglass tube. And these 4 side rails absorb 70% of impact energy by progressive plastic deformation. The contribution to crash energy absorption of the apron is small in comparison with side rails.[1]

Many research works have been performed on the side rail made of composites. Thornton investigated the axial collapse of circular tubes made of carbon, Kevlar, and glass fiber composites. He also suggested the trigger mechanism to prevent catastropic failure of brittle composites and to induce stable and progressive failure. Fig. 2 shows two kinds of the trigger mechanism; bevel and tulip trigger. But they have the bad efficiency to manufacture.

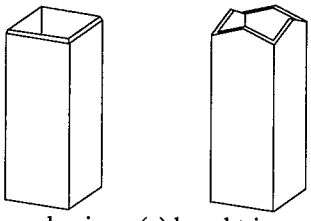


Fig. 1.1 Trigger mechanisms (a) bevel trigger (b) tulip trigger

In this study, Aluminum/GFRP hybrid square tube is suggested to compensate the defects of aluminum and composite tubes. It is presented that this hybrid tube can absorb energy in stable manner without trigger mechanisms.

2. Axial crush experiments of Aluminum/GFRP hybrid tube

2.1 Experimental details

The size of aluminum tubes of 6063T5, used in this study, was 45×45×1.2 (mm) and the length was 200mm. Glass/Epoxy prepregs were wrapped around the aluminum tube. Then this Aluminum/GFRP hybrid tube was co-cured. Pure GFRP tubes were also made for the purpose of comparison with hybrid tubes. Table 1 shows properties of these materials.

Table 1. Properties of aluminum and GFRP

	Density (kg/m^3)	E (GPa)	σ_u (MPa)
Aluminum (6063T5)	2700	68.9	209
Glass/Epoxy	1980	43.5	1000 (0°) 50 (90°)

Experimental parameters of each tube are as follows.

- ply orientation : 0°, 90°, 0°/90°, ±45° where the 0° direction coincides with the axis of the tube.
- thickness : 8plies(1mm), 16plies(2mm), 24plies(3mm)
- trigger mechanism : hybrid tube(non-triggered) , GFRP tube(triggered)

The specimens were clamped at the lower end and free at the top. They were compressed with a speed of 5mm/min and total compression stroke was 90mm. Two identical specimens were tested for each case.

2.2 Experimental data

(1) Aluminum tube

The area of load-deflection cruve means the energy absorption capacity. Specific energy absorption can be defined as follows.

$$S.E.A = E_s = \frac{E_{absorbed}}{m_{crushed}} = \frac{\int_0^{\delta} Pdx}{\rho A \delta}$$

where P and δ denote load and deflection, respectively.

The mean crushing load of aluminum tube was 9.21kN, The absorbed energy was 832.29J, Specific energy absorption was 16.94kJ/kg.

(2) GFRP composite tube

The 0° direction tube showed catastropic failure. The splits are located at the four corners of the rectangular tube and the absorbed energy was very poor in spite of the trigger mechanism. On the other hands, the failure of 90° direction tube was stable and progressive. No splits existed but the crack propagated along the fiber direction. For the 0°/90° and ±45° tubes, local failure of material occurred and interlaminar cracks are formed. As the deformation proceeded further, the externally formed fronds curl downward. Overall energy absorption mechanism during collapse is listed as follows: inter/intralaminar crack propagation; fronds bending; axial splitting; flexural damage; friction between laminates, platen and fronds.[2]

Table 2. Experimental results of G/E tube

		Peak load(kN)	Mean crushing load(kN)	E_s(kJ/kg)
8 ply	0°	3.24	1.12	0.35
	90°	5.92	9.57	3.05
	0°/90°	8.98	12.34	3.84
	±45°	8.24	11.74	3.74
16 ply	0°	13.31	2.49	1.59
	90°	22.03	20.58	13.13
	0°/90°	26.61	18.91	11.61
	±45°	32.05	20.03	12.76
24 ply	0°	38.27	4.76	4.66
	90°	35.04	26.61	25.97
	0°/90°	46.39	29.83	28.96
	±45°	51.34	25.68	25.25

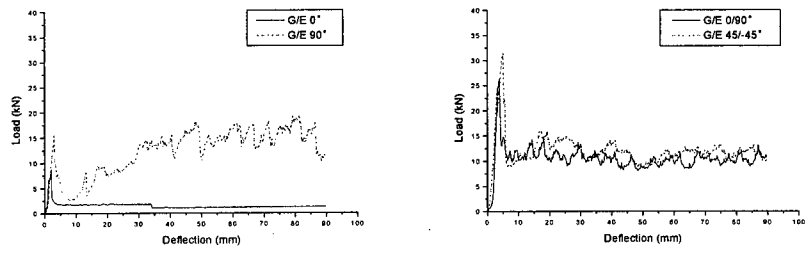


Fig. 2.1 Load-displacement graph of 16ply G/E composite tube

(3) Aluminum/GFRP hybrid tube

Table 3 summarizes the data from the tests carried out, and Fig. 2.2 shows load-deflection curves of hybrid tubes. The best energy absorption performance was obtained for the 90° plies hybrid tube due to the stable local buckling with two different materials. The wrapped composite tube

constrains the deflection of aluminum tube. The failure of hybrid composite tube was stable and progressive without trigger mechanism because inner aluminum tube could play the role of crack initiator and controller. The 0°/90° and ±45° direction tubes shows the mixed crushing mode. The inner aluminum tubes absorb energy by plastic deformation, while the outer composite tubes absorbs energy by crack propagation and fronds bending. The 0° direction tube cannot absorb much energy because debonding of each material was occurred.

Table 3. Experimental results of Al-G/E hybrid tube

		Peak load(kN)	Mean crushing load(kN)	E_s (kJ/kg)
8 ply	0°	61.22	13.36	11.21
	90°	52.62	20.22	17.05
	0°/90°	58.04	19.09	16.27
	±45°	60.79	18.24	15.70
16 ply	0°	86.18	11.13	12.69
	90°	79.71	26.33	31.33
	0°/90°	104.24	20.20	23.66
	±45°	77.03	21.44	25.75
24 ply	0°	233.22	8.73	13.17
	90°	90.94	32.52	48.03
	0°/90°	192.05	24.92	36.70
	±45°	129.76	30.71	46.57

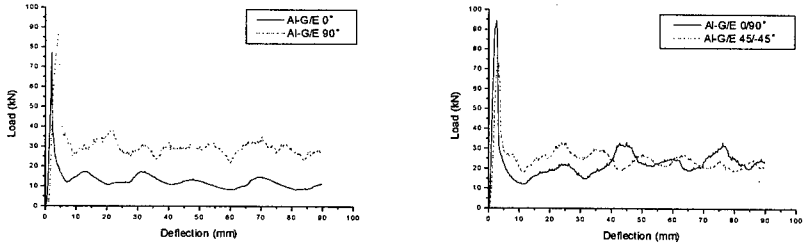


Fig. 2.2 Load-Deflection graph of 16ply Al-G/E hybrid

2.3 Discussion

(1) The energy absorption capacity according to the ply orientation

Fig. 2.3 shows the energy absorption according to the ply orientation. The composite tubes except 0° direction show similar energy absorption capability. Generally, 0°/90° direction tube absorbed more energy than others. For the hybrid tubes, 90° direction tube was the most efficient tube. However, 0°/90° direction tube was less efficient than pure composite tube.

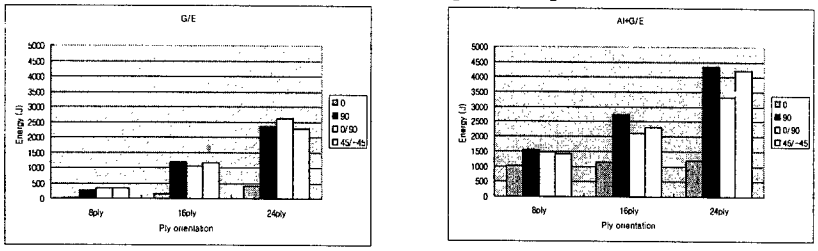


Fig. 2.3 Energy absorption of (a) G/E (b) Al/GFRP hybrid

(2) Comparison of specific energy absorption capacity of hybrid tube

Based on the 90° plies hybrid tube, the energy absorption capacity of Aluminum, composite, and hybrid tubes with same width and mass of hybrid tube was shown on Fig. 2.4. The result of aluminum tube was calculated theoretically by equation Wierzbicki and Abramowicz proposed. The result of composite tube was calculated using interpolation of data from thickness/width curve[5]. The thicker hybrid tubes are, the more efficient the energy absorption can be. Mean crushing load of 24 plies hybrid tube is improved by 32.9% in comparison with the aluminum tube, and 9% with composite tube.

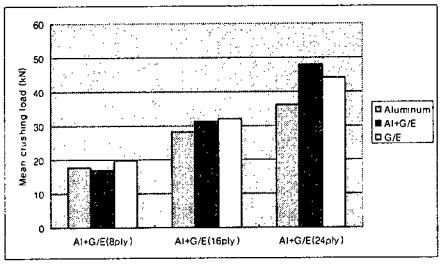


Fig. 2.4 Mean crushing load with respect to same hybrid tube mass

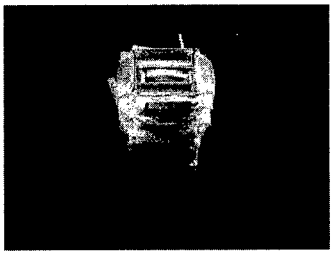


Fig. 2.5 Deformation of 90° hybrid tubes (8plies)

3. Theoretical analysis

The modified energy absorption model by Wierzbick and Abramowicz[3] was used to analyze the energy absorption capacity of the hybrid tube. Fig. 3.1 shows 1/4 of the basic folding mechanism of symmetric rectangular tube. The energy was absorbed mainly at (1) toroidal surface (2) horizontal cylindrical surface and (3) inclined conical surface. The following assumptions was provided:

Firstly, the structure consists initially of planar surfaces. secondly, the Aluminum and The composite are regarded as rigid-perfectly plastic with a constant value of the flow stress. thirdly, the local wave buckling length 2H remains constant.

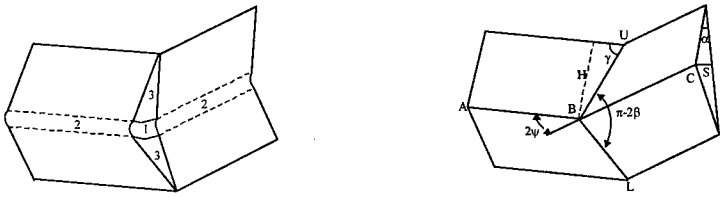


Fig. 3.1 (a) basic folding mechanism (b) geometry of basic folding mechanism

The energy dissipated through axial crush process can be expressed as follows.

$$\dot{E}_{\text{int}} = \int_S (M^{\alpha\beta}\dot{\kappa}_{\alpha\beta} + N^{\alpha\beta}\dot{\lambda}_{\alpha\beta})dS + \int_L M_0\dot{\theta}\,dl \qquad (3.1)$$

The first integral term is a energy dissipation rate of toroidal surface and the next integral term is a energy dissipation rate at each hinge line.

The energy dissipated by toroidal surface is

$$E_1 = 4HbN_0I_1(\psi_0) \quad \text{where} \quad I_1(\psi_0) = \frac{\pi}{(\pi - 2\psi_0)\tan\psi_0}\int_0^{\pi/2}\cos\alpha\left\{\sin\psi_0\sin\left(\frac{\pi - 2\psi_0}{\pi}\right)\beta\right\}d\alpha \qquad (3.2)$$

The energy dissipated by each hinge line is

$$E_2 = 2\int_0^{\pi/2} M_0 C d\alpha = \pi M_0 C \qquad (3.3)$$

$$E_3 = 4M_0^H \frac{H^2}{b} I_3(\psi_0) \quad \text{where} \quad I_3(\psi_0) = \frac{1}{\tan\psi_0}\int_0^{\pi/2} \frac{\cos\alpha}{\sin\gamma} d\alpha \tag{3.4}$$

where 2H is the height of element, C is total width, $2\psi_0=90°$, $N_0 = \sigma_0 t_m + \sigma_c t_c$,

$M_0 = \frac{1}{4}\sigma_0 t_m^2 \left\{1 + 2\left(\frac{\sigma_c}{\sigma_0}\right)\left(\frac{t_c}{t_m}\right) + 2\left(\frac{\sigma_c}{\sigma_0}\right)\left(\frac{t_c}{t_m}\right)^2 - \left(\frac{\sigma_c}{\sigma_0}\right)^2\left(\frac{t_c}{t_m}\right)^2\right\}$ and $M_0^H = \frac{1}{4}\sigma_c^H t_c^2 \left\{1 + 2\left(\frac{\sigma_0}{\sigma_c^H}\right)\left(\frac{t_m}{t_c}\right) + 2\left(\frac{\sigma_0}{\sigma_c^H}\right)\left(\frac{t_m}{t_c}\right)^2 - \left(\frac{\sigma_0}{\sigma_c^H}\right)^2\left(\frac{t_m}{t_c}\right)^2\right\}$

To determine the mean crushing load, the external work is equated to internal work and minimized with respect to b and H.[5]

$$P_m = 3\sqrt[3]{D_1 D_2 D_3}\sqrt[3]{\frac{C}{t}} \quad \text{where} \quad D_1 = 8N_0 t I_1 \;,\; D_2 = 2\pi M_0 \;,\; D_3 = 8M_0^H I_3 \tag{3.5}$$

The values of the integrals are for I_1=0.8195, I_3=1.1478. Assume that the flow stresses are 92% of the tensile strength. For 90° hybrid tubes, mean crushing load-composite thickness curve is shown in Fig. 3.2. In this figure, the predicted energy absorption capacity shows relatively good agreement with experimental results.

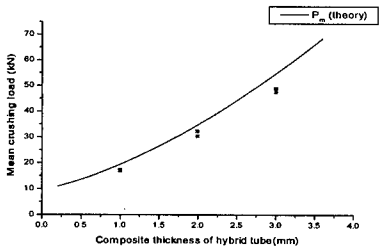


Fig. 3.2 Mean crushing load with respect to composite thickness of hybrid tube

4. Conclusions

In this study, the aluminum/GFRP co-cured hybrid tubes are suggested to improve energy absorption efficiency of vehicle chassis. The hybrid tubes show stable failure without trigger mechanism and also showed good energy absorption capacity. Especially, 90° direction hybrid tube shows best efficiency. The suggested analytical model for the calculation of energy absorption capacity of hybrid tubes, based on the plastic hinge model of metal, shows a good agreement with experimental results.

5. Reference

1. G. L. Farley, J. Compos. Mater., **26** (1992) p. 37
2. A. G. Mamalis and D. E. Manolakos, Compos. Struct., **37** (1997) p. 109
3. T. Wierzbicki and W. Abramowicz, J. Appl. Mech., **50** (1983) p. 727
4. A. G. Mamalis, Int. J. Impact Eng., **11** (1991) p. 185
5. K. H. Kim and J. J. Lee, Axial crush and energy absorption characteristics of aluminum/GFRP hybrid square tube, M. S. Thesis in KAIST (2000)

Key Engineering Materials Vols. 183-187 (2000) pp. 1153-1158
© 2000 Trans Tech Publications, Switzerland

Mechanical Behavior of Carbon/Phenolic Ablative Composites for Nozzle Application

P.W. Kim[1], S.H. Hong[1], Y.C. Kim[2], B.H. Yeh[2] and Y.G. Won[2]

[1] Department of Materials Science and Technology, Korea Advanced Institute of Science and Engineering, 373-1 Kusong-dong, Yusung-gu, Taejon 305-701, Korea

[2] Agency for Defence Development, PO Box 35, Yusung-gu, Taejon 305-701, Korea

Keywords: 8 Harness Woven Fabric, Ablative Composites, Across-Laminar, Delamination, Fiber Pull-Out, Undulation, With-Laminar

ABSTRACT

Carbon/phenolic composites were fabricated by an infiltration of phenolic resin into 8 harness satin woven fabric of PAN-based carbon fibers. The tensile and compressive behaviors of carbon/phenolic composites were observed in with-laminar/0° warp, with-laminar/45° warp, with-laminar/90° warp and across-laminar directions. The tensile and compressive tests were performed at 200~700℃ under N_2 atmosphere to reduce the oxidation of phenolic resin. The tensile strengths of carbon/phenolic composites in with-laminar/0° warp and with-laminar/90° warp directions were about 7-10 times higher than those in with-laminar/45° warp direction, which was analyzed due to a change of fracture mode from fiber pull-out to tensile failure of fibers. The compressive strengths of carbon/phenolic in across-laminar direction were about 10 times higher than those in with-laminar/45° warp direction. The compressive failure was occurred by tensile fracture of fibers in across-laminar direction, while was changed into delamination fracture by buckling of fibers in with-laminar/45° warp direction. Tensile and compressive strengths of carbon/phenolic composites decreased to about 50% at 400℃, and to about 10% at 700℃ compared to those at room temperature. The main reasons for the decrease of tensile and compressive strengths with increasing the temperature were analyzed due to both the thermal residual stress induced by anisotropic thermal expansion of carbon fibers and the reduction of bond strength between fibers and matrix resulting from thermal degradation of phenolic resin.

1. INTRODUCTION

Ablative materials have been often applied to protect the nozzle cases of rockets or missiles at high temperature during the erosion of the materials by absorbing the high input of incident thermal energy[1-3]. The fiber reinforced polymer matrix composites are the most useful ablative materials due to their low density, high strength and low thermal conductivity. Because carbon fiber has high strength and good stability at high temperature and phenolic resin has high char yield after thermal decomposition, carbon/phenolic composite is one of the good candidate for ablative materials. In addition, the 2-D woven carbon fiber reinforced phenolic matrix composite has better in-plane uniformity and stability than unidirectional fiber reinforced phenolic matrix composites[4-6].

Nozzles for rockets or missiles are placed under severe conditions of temperature ranged 2000~3000℃ and pressure ranged 10~14MPa during combustion of fuel. Ablative composites are failed by erosion due to thermal degradation at high temperature and due to high pressure of combustion gases. Therefore, the analyses of mechanical and thermal properties of the ablative composites are required for the design, performance, and durability of nozzle components[7]. In this study, the tensile and compressive strengths were measured and the failure mechanisms were analyzed with varying the temperature and orientation of carbon/phenolic ablative composites.

2. EXPERIMENTAL PROCEDURES

The ablative composites were fabricated using phenolic resin matrix(KC-98) reinforced by 8 harness satin woven fabric of PAN-based carbon(TZ-307). The structure of 8 harness satin woven fabric is shown in Fig.1. Carbon/phenolic composites were stacked-up with the same orientation and cured by hot pressing with 40MPa at 80℃ for 90 minutes, 120℃ for 90 minutes and 155℃ for 180 minutes.

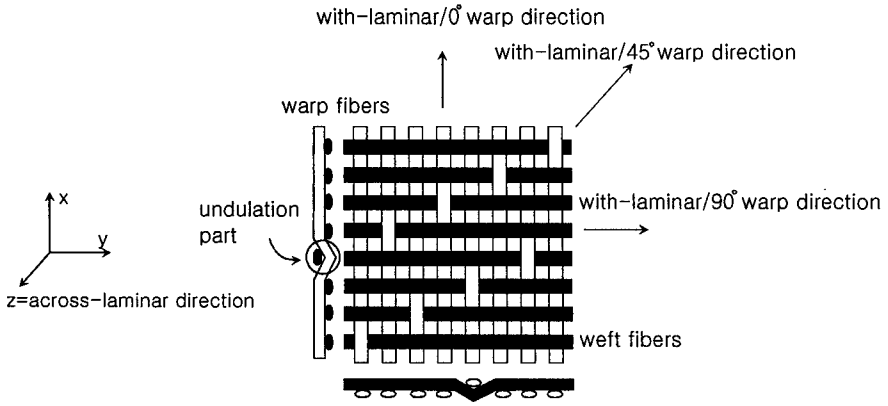


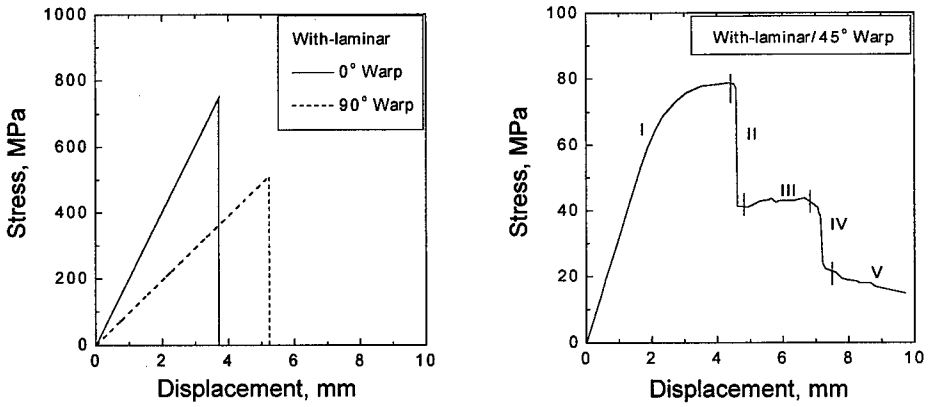
Fig. 1. Structure and orientation of 8 harness satin woven carbon fabric.

Tensile and compressive tests were performed at temperature ranged 25~700℃ under N_2 atmosphere. Designation on the test directions represented also in the above Fig. 1. Specimens for tensile tests were machined following ASTM D3039 for room temperature tests, and following ASTM D638 for high temperature tests. Specimens for compressive tests were machined following ASTM D695. Tensile and compressive tests were performed with a constant strain rate of 0.006/min. The specimens were heated up to a test temperature with heating rate of 10℃/min and were held 20 minutes at the test temperature for thermal equilibrium, and followed by the tensile or compressive tests.

3. RESULTS AND DISCUSSION

3-1. Tensile behavior of Carbon/Phenolic Composites

Tensile tests were performed in with-laminar/0° warp, with-laminar/45° warp and with-laminar/90° warp directions. Tensile strengths of carbon/phenolic composites at 25°C. were measured as 747.3 MPa, 73.6 MPa and 509.9 MPa in with-laminar/0° warp, with-laminar/45° warp and with-laminar/90° warp directions, respectively.



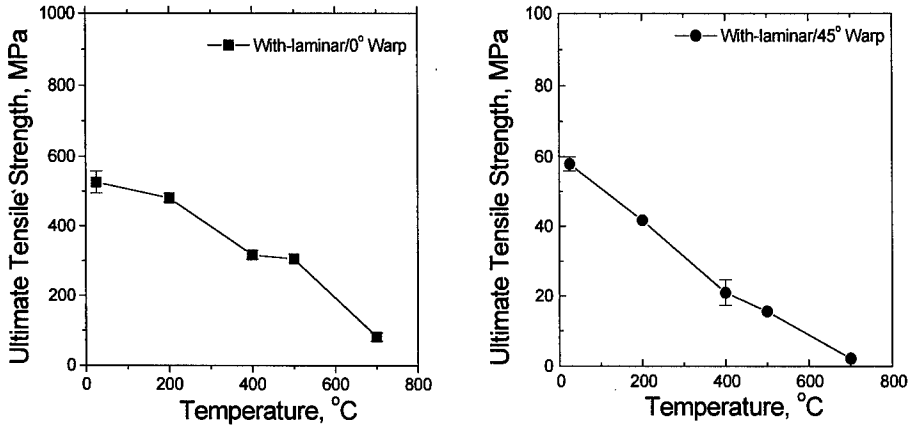
(a) (b)

Fig. 2. Stress-displacement curves of carbon/phenolic composites at 25°C obtained by tensile tests, (a) with-laminar/0° warp and with-laminar/90° warp directions, (b) with-laminar/45° warp direction.

Fig. 2 shows the stress-displacement curves of carbon/phenolic composites at 25°C. The stress-displacement curves in with-laminar/0° warp and with-laminar/90° warp directions show elastic deformation, and followed by a failure by fracturing of longitudinal fibers. While the stress-displacement curve in with-laminar/45° warp direction shows 2-step fracture behavior by the pull-out of fibers. Carbon/phenolic composites in with-laminar/0° warp and with-laminar/90° warp direction were failed by the preferential fiber fracture at the undulation parts. The fiber fracture occurred with an angle of 18.4° inclined to the tensile axis. The undulation parts in 8 harness woven fabric are inclined with an angle of 18.4° from the warp direction of fibers. It is regarded that fiber fracture occurred at the undulation parts due to the stress concentration. In tension of carbon/phenolic in with-laminar/45° warp direction, 2-step failure occurred as shown in Fig. 2 (b). In tension of with-laminar/45°warp direction, tensile load was transferred to the fiber/matrix interface in shear stress, while tensile load was transferred to the fibers parallel to the tensile axis in tension of with-laminar/0° warp or with-laminar/90° warp directions. Fibers in with-laminar/45° warp direction were rearranged more parallel to the tensile axis by interfacial shear stress. The rearrangement of fibers brought about fiber/matrix interfacial debonding, and finally failure of carbon/phenolic composite occurred by the fiber pull-out out of woven fabric structure.

Tensile tests of carbon/phenolic composites at high temperature were performed in with-laminar/0° warp and with-laminar/45° warp directions. Tensile strengths of carbon/phenolic composites decreased with increasing temperature as shown in Fig. 3. Tensile strength in with-laminar/0° warp direction decreased more slowly than in with-laminar/45° warp direction, which was analyzed due to a difference of the fracture mode with varying tensile loading direction. When

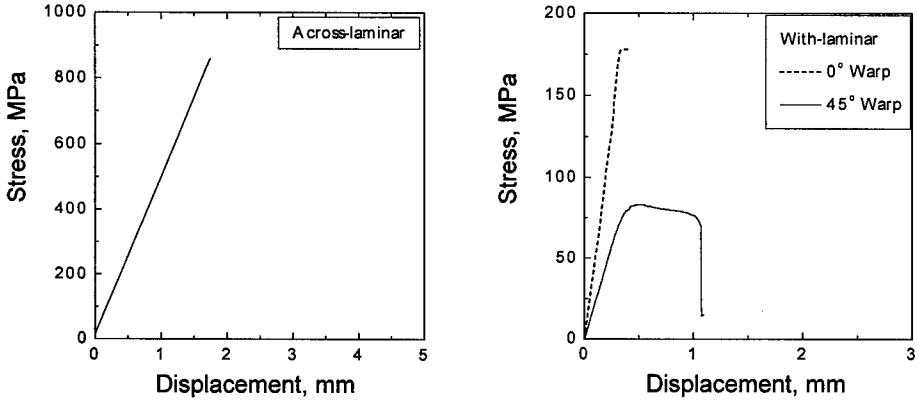
fracture mode is dominated by the fiber fracture, the reason for the decrease of tensile strength of carbon/phenolic composites with increasing temperature had not been reported clearly, One possible explanation is that the decrease of tensile strength was analyzed due to thermal stress induced on woven fabric by anisotropy of CTE between longitudinal and transverse directions of carbon fiber[8]. When fracture mode is dominated by the fiber pull-out, the decrease of tensile strengths of carbon/phenolic composites was analyzed due to the degradation of fiber/matrix interface by the thermal decomposition of the phenolic resin.



(a) (b)

Fig. 3. Variation of ultimate tensile strengths of carbon/phenolic composites with varying the temperature, (a) with-laminar/0° warp direction, (b) with-laminar/45° warp direction.

3-2. Compressive behavior of Carbon/Phenolic Composites

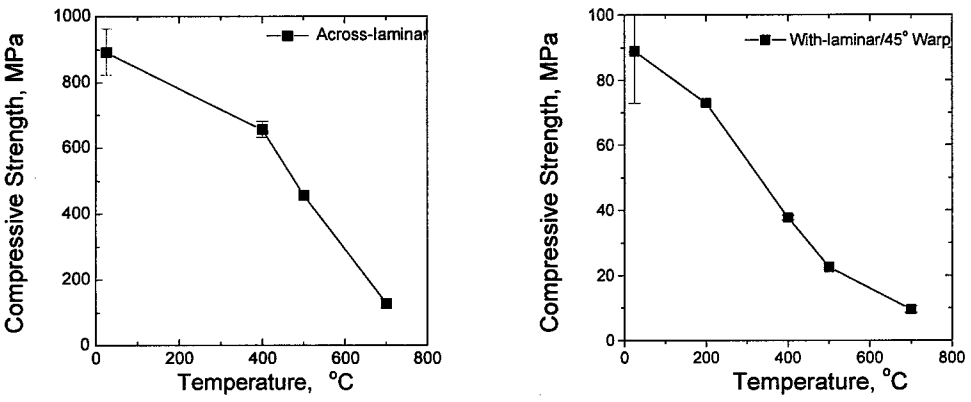


(a) (b)

Fig. 4. Stress-displacement curves of carbon/phenolic composites at 25°C obtained by compressive tests, (a) across-laminar direction, (b) with-laminar/0° warp and with-laminar/45° warp directions.

Compressive test of carbon/phenolic composites were performed in with-laminar/0° warp, with-laminar/45° warp and across-laminar directions. Compressive strengths of carbon/phenolic were measured as 175.0 MPa, 89.0 MPa and 859.2 MPa in with-laminar/0° warp, with-laminar/45° warp and across-laminar directions, respectively, at 25°C. Compressive deformation behaviors of carbon/phenolic composites in with-laminar/0° warp and across-laminar directions showed a brittle fracture contrary to those in with-laminar/45° warp direction as shown Fig. 4. Compressive loading in with-laminar/0° warp direction caused the shear fracture of warp fibers at undulation parts after elastic deformation. Cracks were formed due to the fiber fracture by compressive load and were propagated by the delamination or connected with other cracks in other laminae. Compressive loading in with-laminar/45° warp direction caused the buckling of a laminae, then the buckling of a laminae was transmitted to the whole specimen by shear and followed by a delamination of carbon/phenolic composites. Compressive loading in across-laminar direction caused a trans-laminar shear stress on carbon fibers after the rupture of matrix. Tensile stress was induced by the trans-laminar shear stress on carbon fibers in fiber direction, and finally lead to tensile fracture of fibers.

Compression tests were performed in with-laminar/45° warp and across-laminar directions. Fig. 5 shows that the compressive strength of carbon/phenolic composites decreased with increasing temperature. Compressive strength of carbon/phenolic composites decreased more slowly with increasing temperature in across-laminar direction than in with-laminar/45° warp direction, which was analyzed due to a change of the fracture mode with varying the loading direction.



(a) (b)

Fig. 5. The variation of compressive strengths of carbon/phenolic composites with varying the temperature, (a) across-laminar direction, (b) with-laminar/45° warp direction.

4. CONCLUSIONS

The tensile fracture mode of carbon/phenolic composites changed from fiber fracture to fiber pull-out with varying the loading direction from with-laminar/0° or 90° warp directions to with-laminar/45° warp direction. The tensile failure of carbon/phenolic composite occurred by the fracture of longitudinal fibers at the undulation parts in woven fabric structure when loaded in with-laminar/0° or 90° warp directions. The tensile failure of carbon/phenolic composite occurred by the

pull-out of fibers when loaded in with-laminar/45° warp direction. The compressive fracture of carbon/phenolic composites occurred by shear fracture of fiber in with-laminar/0° warp, while occurred by buckling, shear and delamination in with-laminar/45° warp direction. The compressive fracture of carbon/phenolic composite occurred by the tensile fracture of fibers, which was induced by the trans-laminar shear stress, in across-laminar direction. Tensile and compressive strength of carbon/phenolic composites decreased more slowly in fiber fracture mode than in fiber pull-out or buckling mode with increasing the temperature. The reasons for the decrease in strength of carbon/phenolic composites was analyzed due to both the thermal stress induced by anisotropy of CTE of carbon fibers and thermal decomposition of phenolic resin.

REFERENCES

1. A.M. Morisson, J. Space. Rockettes, **12** (1975) p. 633
2. H. Wesshaus and I. Engleberg, J. Advanced Materials, **Jan** (1997) p. 16
3. C.G. Goetzel, High Temp. High Press., **12** (1980) p. 131
4. N.K. Naik, Woven Fabric Composites, Technomic Pub. Com., Inc., Penn. (1994)
5. E.H. Stokes, J. Thermophysics and Heat Transfer, **9** (1995) p. 352
6. J.H. Byun, Trans. the Korean Society of Mechanical Engi. A, **12** (1997) p. 1757
7. W.M. Rohsenow and J.P. Hartnett, Handbook of Heat Transfer, McGraw-Hill, New York (1973)
8. R.E. Ely, Journal of American Ceramics Society, **48** (1965) p. 358

Key Engineering Materials Vols. 183-187 (2000) pp. 1159-1164
© 2000 Trans Tech Publications, Switzerland

Fracture Pattern and Lamination Configuration on Flexural Fracture of Multiple Layer CFRP

M. Kanemitsu[1] and H. Nakayasu[2]

[1] Department of Mechanical Engineering, Kanazawa Technical College,
2-270 Hisayasu, Kanazawa 921-8601, Japan

[2] High Technology Research Center (HRC), Konan University,
8-9-1 Okamoto, Higashinada-ku, Kobe 659-8501, Japan

Keywords: Configuration of Lamina, Equivalent Engineering Modulus, Flexural Strength, Lamination Theory, Multiple Layers CFRP, Orientation Angle

ABSTRACT

This paper provides a design tool that may enable the designers to estimate the flexural strength for the target combination of lamina, which they wish to establish the mechanical properties for the material members of system. In line with these objectives, this paper shows the experimental results and theoretical consideration. Experimental analysis was performed for 4 kinds of orientation angle and 16 kinds of combination of 26 layers. The relation between flexural fracture strength and equivalent engineering modulus was investigated from the viewpoints of lamination theory.

1. INTRODUCTION

It is well known as a common feature of composite materials that the prominent anisotropy in mechanical properties is observed in unidirectional CFRP, which has higher specific strength and stiffness along the carbon fiber reinforced components[1,2]. On the other hands, when the direction of loading can not be specified, the material design tends to suppress this anisotropy in order to perform the robust design of composite laminate[5]. Though some failure criteria for these kinds of anisotropy materials[3,4] have been proposed, it is difficult to estimate the strength and mechanical features of various kinds of multiple layer laminate for flexural fracture because of the complexities of combination of lamination effects.

In this paper, we propose the practical estimation method of the flexural strength of multiple layers CFRP laminates with any kinds of orientation angle, where evaluation of equivalent engineering flexural modulus was examined from lamination theory[5-7]. For the verification of the validity of proposed method, the comparative study of experimental and theoretical approaches is also performed to evaluate the equivalent engineering flexural modulus and to estimate the flexural strength for multiple layers CFRP laminates.

2. FLEXURAL BENDING TEST FOR MULTIPLE LAYERS CFRP

2.1. Experimental Conditions

Various kinds of CFRP specimens with multiple layers were subjected to 3 points bending test whose aspect is illustrated in Fig. 1. 16 kinds of plate CFRP specimen (10mm × 100mm × 3mm) were molded by prepreg sheet with curing and pressure condition shown in Table1. The compositions of CFRP specimen is also given in Table 1. These CFRP specimens have 26 layers with symmetric orientation angles to neutral axis(z=0) in Fig. 3, whose configurations corresponding to specimen type from A to P are represented in Table 3. The mechanical properties of unidirectional CFRP specimen (Type A) are given in Table 2 which shows remarkable anisotropy.

Table 1. Composition and curing condition of CFRP

Prepreg sheet	IM-600 (TOHO RAYON Co.LTD)
Matrix	EPOXY RESIN
Volume fraction of fiber	60 %
Curing condition	30MPa pressure stress was subjected during 0.5 hours at temperature 130°C

Table 2. Mechanical properties of unidirectional CFRP

Tensile Strength	2695 (MPa)
Longitudinal modulus E_L	136.8 (GPa)
Transverse modulus E_T	10.0 (GPa)
Shearing modulus G_{LT}	5.55 (GPa)
ILSS(Inter Lamina Shear Strength)	93.1 (MPa)
Specific Gravity	1.23
Longitudinal Poisson's ratio ν_L	0.28
Transverse Poisson's ratio ν_T	0.02

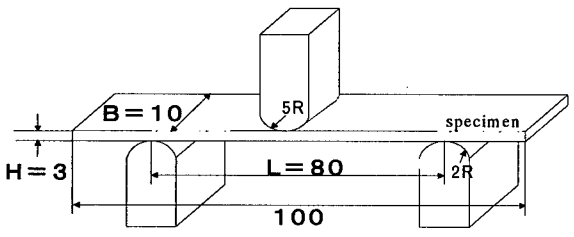


Fig.1. Aspect of three points bending test and geometry of specimens.

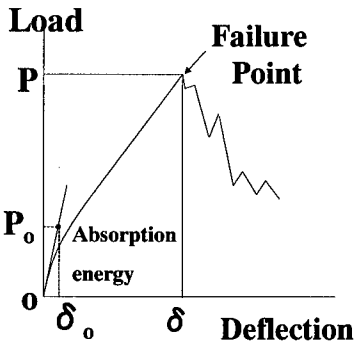


Fig.2. Mechanical behavior of CFRP f or flexural load

2.2. Experimental Results

The flexural strength was calculated by the equation

Table 3. Summary of experimental results

Type of specimen	Configuration $[\theta_n, \theta_{n-1}, \ldots, \theta_2, \theta_1]_s$	Flexural strength σ (MPa)	Ultimate strain ε (%)	Absorption energy J_A (J)	Flexural modulus E^* (GPa)
A	$[0°]_s$	1227	0.91	1.38	136.8
B	$[90°]_s$	64.34	0.69	0.08	9.6
C	[0°,90°,0°,90°,0°,90°,0°, 90°,0°,90°,0°,90°,0°]$_s$	1010	1.23	1.73	85.3
D	[90°,0°,90°,0°,90°,0°,90°, 0°,90°,0°,90°,0°,90°]$_s$	961.3	1.45	1.88	67.4
E	[0°,90°]$_s$	968.1	0.85	1.10	115.9
F	[90°,0°]$_s$	631.5	2.65	2.29	24.3
G	[0°,90°,0°,90° ,0°,90°,0°]$_s$	927.2	1.06	1.30	88.9
H	[90° ,0°,90°,0°,90° ,0°,90°]$_s$	868.7	1.45	1.52	61.1
I	[45°,-45°,45°,-45°,45°,-45°,45°, -45°,45°,-45°,45°,-45°,45°]$_s$	204.6	2.60	0.85	16.8
J	[45°,-45°,45°,-45°,45°,-45°,45°]$_s$	195.7	2.94	0.93	17.4
K	[0°,-45°,45°,0°,-45°,45°,0°,-45°, 45°,0°,-45°,45°]$_s$	909.6	1.12	1.27	81.3
L	[0°,-45°,45°,0°,90°, -45°,45° ,0°, 90°,-45°,45°,90°,]$_s$	854.9	1.27	1.20	67.7
M	[45°,0°,-45°,0°,45°,0°,-45°,0°, 45°,0°,-45°,0°,45°]$_s$	1011	1.48	1.85	68.4
N	[0°,-45°,45°,90°,0°,-45°,45°,90°, 0°,-45°,45°,90°,0°]$_s$	813.3	1.27	1.21	64.2
O	[45°,-45°,90°,0°]$_s$	535.2	3.18	2.42	29.6
P	[90°,-45°,45°,0°,90°,-45°,45°,0°, 90°,-45°,45°,0°,90°]$_s$	796.3	2.10	2.10	35.0

$$\sigma = \frac{M}{Z} = \frac{3}{2}\frac{PL}{BH^2}, \quad Z = \frac{BH^2}{6}, \quad M = \frac{PL}{4} \tag{1}$$

where P is the maximum load obtained by experiments which is illustrated in Fig. 2, and Z and M are the modulus of section and flexural moment M respectively. Using σ, the ultimate strain is obtained by

$$\varepsilon = \frac{\sigma H}{L^2} \times \delta \times 100 \qquad (\%) \tag{2}$$

where δ is the deflection defined in Fig.2. The flexural modulus E* in experiment is also obtained as a tangent at the region of initial loading in the figure, i.e.,

$$E^* = \frac{P_0 L^3}{4BH^3 \delta_0} \tag{3}$$

which is corresponding to the longitudinal flexural modulus, and the absorption energy is obtained from the area in triangle in Fig.2.

The results of three points bending test were summarized in Table 3, where flexural strength σ, ultimate strain ε, absorption energy J_A and flexural modulus

E* were listed. The values in the table are mean values of experimental results from 3 ~ 5 sample specimens.

3. DISCUSSIONS

If the coordinates system for the multiple layer laminates with various lamination angle θ_m and distance from neutral axis(z=0) h_m (m=1,2,...,n) are defined as Fig.3(a) and (b), the relationship between moment and deflection for symmetric laminates is represented by the forms[5]:

$$\begin{Bmatrix} M_x \\ M_y \\ M_s \end{Bmatrix} = \begin{bmatrix} D_{xx} & D_{xy} & D_{xs} \\ D_{xx} & D_{yy} & D_{ys} \\ D_{xs} & D_{ys} & D_{ss} \end{bmatrix} \begin{Bmatrix} K_x \\ K_y \\ K_s \end{Bmatrix} \qquad (M_x, M_y, M_{xy}) = \sum_{m=1}^{n} \int_{h_{m-1}}^{h_m} (\sigma_x^{(m)}, \sigma_y^{(m)}, \tau_{xy}^{(m)}) z dz \tag{4}$$

where $\sigma_x^{(m)}$, $\sigma_x^{(m)}$ and $\tau_x^{(m)}$ are the stress in m-th layer with the strain based on

$$\varepsilon_x = \varepsilon_x^0 + zK_x, \varepsilon_y = \varepsilon_y^0 + zK_y, \gamma_{xy} = \gamma_{xy}^0 + zK_{xy} \tag{5}$$

The bending stiffness matrix Dij (i,j=x,y,s) is calculated by

$$D_{ij} = 2\sum_{m=1}^{n} \int_{h_{m-1}}^{h_m} z^2 E_{ij}^{(m)} dz \qquad (i, j = x, y, s) \tag{6}$$

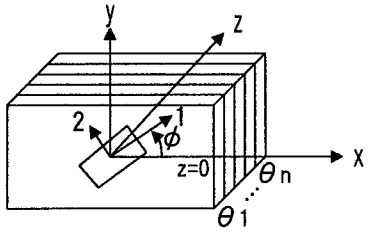
where s means shear direction.
Since h_m (m=1,2,...,n) means the distance from neutral axis to top surface of m-th ply, the thickness of m-th ply is h_m-h_{m-1}, and the specimen is molded by 26 prepreg sheets, the thickness of minimum layer Δh is approximately estimated by Δh=3.0/26 (mm).

Thus the equation (4) is rewritten for the case of 1-direction loading which has ϕ angle from x-axis in Fig. 3(a)

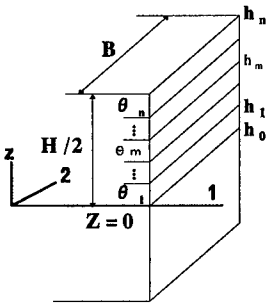
$$\begin{Bmatrix} M_1 \\ 0 \\ 0 \end{Bmatrix} = \begin{bmatrix} D_{11}(\phi) & D_{12}(\phi) & D_{1s}(\phi) \\ D_{12}(\phi) & D_{22}(\phi) & D_{2s}(\phi) \\ D_{1s}(\phi) & D_{2s}(\phi) & D_{ss}(\phi) \end{bmatrix} \begin{Bmatrix} K_x \\ K_y \\ K_s \end{Bmatrix} \tag{7}$$

The elements of stiffness matrix $D_{ij}(\phi)$ in Eq.(7) are obtained by

$$D_{ij}(\phi) = 2\sum_{m=1}^{n} \int_{h_{m-1}}^{h_m} z^2 E_{ij}^{(m)}(\theta^{(m)}) dz \qquad (i, j = 1,2,s), \quad \theta^{(m)} = \theta_m - \phi \tag{8}$$



(a) x-y-s and 1-2-s coordinate system



(b) lamination angle of layer

Fig.3. Coordinate system of composite laminate

where

$$E_{11}(\theta^{(m)}) = \frac{E_T}{1-\nu_L\nu_T}\sin^4\theta^{(m)} + 2\left(\frac{\nu_L E_T}{1-\nu_L\nu_T} + 2G_{LT}\right)\sin^2\theta^{(m)}\cos^2\theta^{(m)} + \frac{E_L}{1-\nu_L\nu_T}\cos^4\theta^{(m)}$$

$$E_{12}(\theta^{(m)}) = \frac{\nu_L E_T}{1-\nu_L\nu_T}(\sin^4\theta^{(m)} + \cos^4\theta^{(m)}) + \left(\frac{E_L + E_T}{1-\nu_L\nu_T} - 4G_{LT}\right)\sin^2\theta^{(m)}\cos^2\theta^{(m)}$$

$$E_{1s}(\theta^{(m)}) = \frac{1}{2}\left[\frac{E_T}{1-\nu_L\nu_T}\sin^2\theta^{(m)}\cos 2\theta^{(m)} - \frac{E_L}{1-\nu_L\nu_T}\cos^2\theta^{(m)}\sin 2\theta^{(m)} + \left(\frac{\nu_L E_T}{1-\nu_L\nu_T} + 2G_{LT}\right)\sin 2\theta^{(m)}\cos 2\theta^{(m)}\right]$$

$$E_{22}(\theta^{(m)}) = \frac{E_L}{1-\nu_L\nu_T}\sin^4\theta^{(m)} + 2\left(\frac{\nu_L E_T}{1-\nu_L\nu_T} + 2G_{LT}\right)\sin^2\theta^{(m)}\cos^2\theta^{(m)} + \frac{E_T}{1-\nu_L\nu_T}\cos^4\theta^{(m)}$$

$$E_{2s}(\theta^{(m)}) = \frac{1}{2}\left[\frac{E_T}{1-\nu_L\nu_T}\cos^2\theta^{(m)}\sin 2\theta^{(m)} - \frac{E_L}{1-\nu_L\nu_T}\sin^2\theta^{(m)}\sin 2\theta^{(m)} - \left(\frac{\nu_L E_T}{1-\nu_L\nu_T} + 2G_{LT}\right)\sin 2\theta^{(m)}\cos 2\theta^{(m)}\right]$$

$$E_{ss}(\theta^{(m)}) = \frac{1}{4}\left[\frac{E_L + E_T - 2\nu_L E_T}{1-\nu_L\nu_T}\sin^2 2\theta^{(m)} + 4G_{LT}\cos^2 2\theta^{(m)}\right] \tag{9}$$

Using $D_{ij}(\phi)$ the 1-direction flexural stiffness $D_1(\phi)$ will be derived by the equation[5]

$$D_1(\phi) = \frac{D_{11}(\phi)D_{22}(\phi)D_{ss}(\phi) + 2D_{12}(\phi)D_{1s}(\phi)D_{2s}(\phi) - D_{11}(\phi)D_{2s}(\phi)^2 - D_{22}(\phi)D_{1s}(\phi)^2 - D_{ss}(\phi)D_{12}(\phi)^2}{D_{11}(\phi)D_{22}(\phi) - D_{12}(\phi)^2} \tag{10}$$

which is called the equivalent engineering stiffness. Thus the 1-direction equivalent engineering flexural modulus of laminates $E_1(\phi)$ will be transformed from $D_1(\phi)$ as follows

$$E_1(\phi) = \frac{3D_1(\phi)}{2H^3} \tag{11}$$

which is corresponding to E* in Eq.(4).

Fig. 4 shows the behavior of $E_1(\phi)$, where the value of $E_1(\phi)/E_L$ (theoretical) and E^*/E_L are plotted for the value of ϕ. It is found that the experimental results coincide to those of theoretical values for the various configurations of lamina and ϕ.

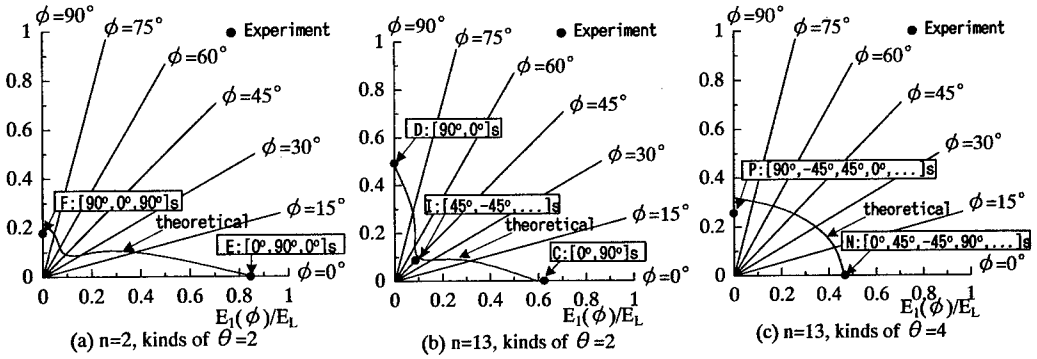


Fig.4. $E_1(\phi)/E_L$ (theoretical) and E^*/E_L(experimental)

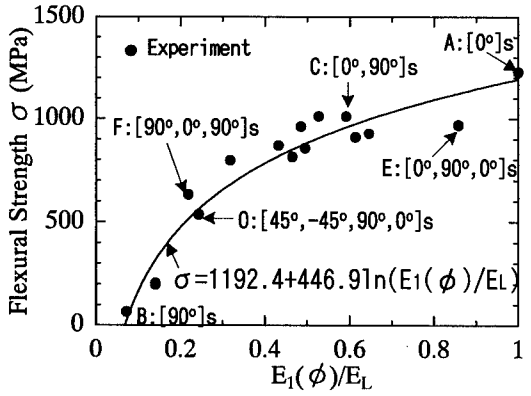


Fig.5. Flexural strength and $E_1(\phi)/E_L$

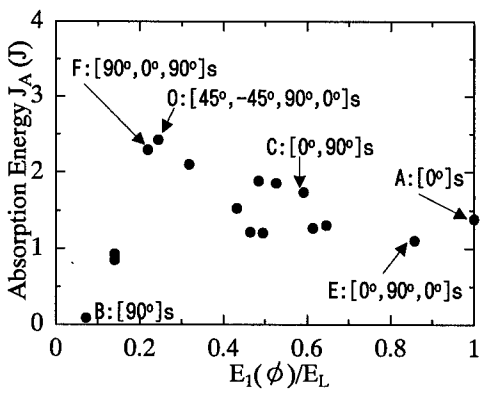


Fig.6. $E_1(\phi)/E_L$ and absorption energy

Secondly, the relationship between flexural strength and $E_1(\phi)/E_L$ is plotted in Fig. 5. By the use of least square analysis, the flexural strength σ can be estimated from the 1-direction equivalent engineering flexural modulus $E_1(\phi)$.

$$\sigma = 1192.4 + 446.9 \ln [E_1(\phi)/E_L] \quad \text{(MPa)} \qquad (12)$$

where $E_1(\phi)$ is obtained by Eqs.(10) and (11). From Fig. 5, when the value of $E_1(\phi)/E_L$ is large, the flexural strength increases logarithmically.

Another consideration are paid for the relation between absorption energy J_A and $E_1(\phi)/E_L$ illustrated in Fig.6. The Fig.6 and Figs.4,5 enable the designer to select the appropriate combination of configuration of layers for design objectives such as flexural strength, modulus, absorption energy and ultimate strain.

4. CONCLUDING REMARKS

It was verified that the agreement between the resultant equivalent engineering flexural modulus and the flexural modulus E* in experiment is well. The flexural strength σ can be estimated from Eq.(12). Advanced approach such as the determination of optimum configuration of lamina to the design objects, which are connected to the strength and other mechanical features, must be a future work.

ACKNOWLEDGEMENT

The authors express great thanks to the Grant-in-Aid for Scientific Research Fund of the Ministry of Education, Science, sports and Culture of Japan (Grant No. 11650109).

REFERENCES

1. Y.Miyano and M.Kanemitsu, Fiber Science and Technology, **18** (1983) p.65
2. Y.Miyano, M.kanemitsu, T.Kunio, H.A.Kuhn, SAMPE Journal, **21** (1985) p.33
3. R.Hill: The Mathematical Theory of Plasticity, Clarendon, Oxford (1950) p.317
4. S.W.Tsai, E.M.Wu: J. Composite Materials, **5** (1971) p.58
5. S.W.Tsai, Composites Design, THINK COMPOSITES, (1988) p.8-1
6. S.W.Tsai, H.T.Hahn: Introduction to Composite Materials, TECHNOMIC Publishing Co., Inc.,(1980)
7. T.Hayashi(Ed.): Handbook of Composite Materials Engineering, JUSE(Japanese Union of Scientists and Engineers) (1971) p.521 (in Japanese)

Key Engineering Materials Vols. 183-187 (2000) pp. 1165-1170
© 2000 Trans Tech Publications, Switzerland

Strength Prediction of Mechanical Joints in Laminated Composite Plates

Kyung Woo Lee[1] and Tae Jin Kang[2]

[1] Division of Fashion & Textile, Dong-A University,
840 Hadan-dong, Saha-gu, Pusan 604-714, Korea

[2] Department of Fiber and Polymer Science, Seoul National University,
San 56-1, Shinlim-dong, Kwanak-gu, Seoul 151-742, Korea

Keywords: Failure Criterion, Joint Strength, Laminated Composites, Pinned Joint, Progressive Failure Analysis

ABSTRACT

An investigation into the pinned joint strength of laminated composite plates was performed. Numerical prediction of joint strength using only composite's lamina properties and ply orientation has been made by using commercially available, general purpose finite element code. The results showed that friction have a significant influence on the distribution and the maximum value of stress around the hole. The technique of progressive failure analysis was used to obtain first–ply failure load, residual strength, and ultimate strength. It has been shown that the predicted strengths were reasonably consistent with experimental data.

1. INTRODUCTION

Advanced composites have been applied extensively for aircrafts and space vehicles. Due to the high strength-to-weight ratio, the application of modern composites is also being expanded into other areas of engineering including ground transportation vehicles, sports goods and medical equipment. Mechanically fastened joints have certain advantages such as easy inspection, no need for special surface treatment and high tolerance to the effects of environment. However, special attention must be given to the design of the joint, because the load bearing capacity can be considerably reduced by stress concentrations around holes. Numerous pin joint stress analyses have been reported using numerical finite element approach. Chang and Chang developed a progressive damage model for bolted joints in laminated composites [1]. The model is capable of assessing damage accumulated in laminates during mechanical loading and of predicting the ultimate strength of the joint. Lessard and Shokrieh performed linear and non-linear two-dimensional progressive damage analysis for pinned joint failure in laminated composites [2]. In their model, the pin was considered as a perfectly rigid pin and zero radial displacement boundary condition was used. Hung and Chang investigated the bearing failure of a mechanically fastened laminated composite joint and developed a cumulative damage model [3]. In their model, it was assumed that pin is rigid and friction between pin and hole is negligible.

2.PROBLEM DESCRIPTION AND TERMINOLOGY

A laminated composite plate containing a pin-loaded hole is subjected to a uniform displacement at one end as shown in Fig.1. All load is transferred from the laminate to the pin. The geometric terms defined in the figure are the width, W, the edge distance, E, the hole diameter, D, and the laminate thickness, T.

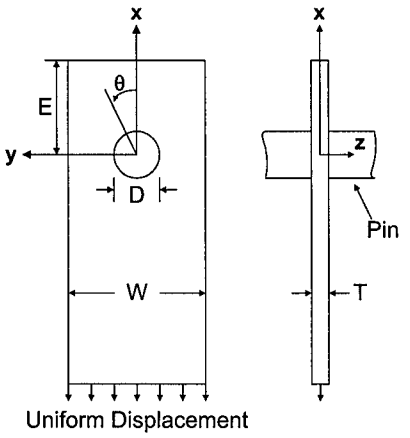


Fig.1. Geometry of the laminated composite containing a pin loaded hole

3. MODELING OF MECHANICALLY FASTENED JOINTS IN LAMINATED STRUCTURES

The progressive failure analysis as well as the prediction of joint strength is strongly dependent upon the accuracy of the stress analysis, which is important for the prediction of failure modes. Much research is dedicated to finding ways to model the action of pin properly. Fig.2 shows three ways to model the interface between the pin and the hole.

The first approach is to impose a cosine radial load distribution around the hole boundary to simulated the effect of the pin as shown in Fig. 2a. This approach is easy to apply, however as De Jong demonstrated, the stress obtained this method would be invalid especially when the degree of orthotropy increases or friction between the pin and the hole is considered [4]. Furthermore, this method is highly inaccurate in post-failure domain, when hole edge stresses may be changed because of damage.

A better model is to use displacement boundary constraints shown in Fig. 2b. Normally, the pin is modeled by preventing radial displacement on the loaded section of the boundary [2]. The pin in this case is assumed to be rigid and forces nodes along the hole to be fixed radially but free tangentially. The stresses obtained around the hole by this method are more reliable. But the user must decide upon the total angle of contact between the pin and the hole and this method cannot account for friction between the pin and the hole.

These problems can be relieved by using surface element, available in many commercial finite element codes, to model the contact mechanism between the pin and the hole as shown in Fig.2c. This element is particularly advantageous in that the friction between the pin and the hole and the pin clearance can be easily considered .

In this study, the pin was modeled as a rigid body and the surface of the rigid-body was described using the "RIGID SURFACE" option in ABAQUS/Standard code [5]. Here, no assumptions were made in advance for pin load distribution. Two-dimensional plane stress elements

having 4 node points, 4 integration points were used to model plies in laminated composites.

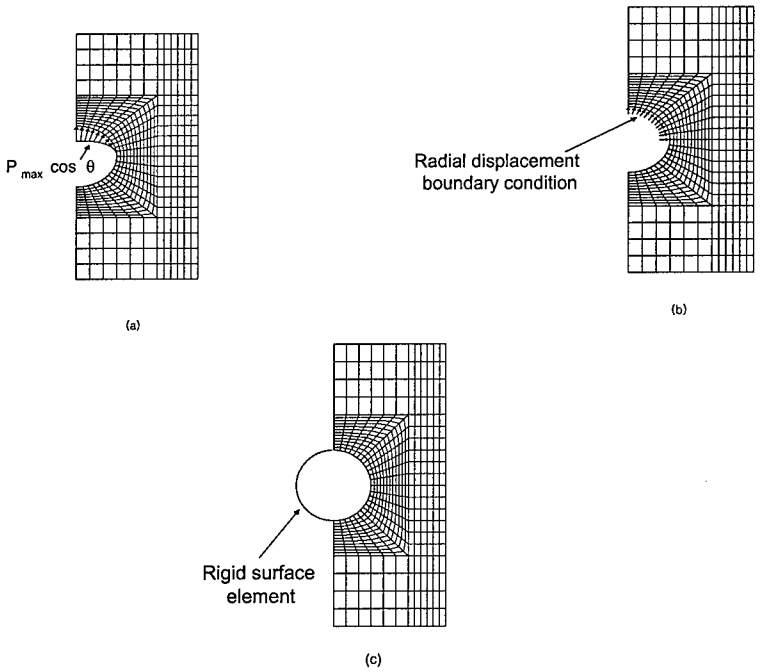


Fig.2. Three methods for modeling the pin and the hole interface
(a) cosine radial load distribution
(b) radial displacement boundary condition
(c) full contact modeling

4. FAILURE CRITERIA

In this study, Hashin's failure criterion, as modified by Chang and Chang [1] and Lessard and Shokrieh [2], has been used. At each displacement increment, the stresses at each Gauss integration points of each element of an individual ply were checked against the failure criterion for failure. The element may fail in one mode only or in several combined modes.

Fiber failure mode

$$\left(\frac{\sigma_1}{X_t}\right) \geq 1 \quad \text{and} \quad \sigma_1 > 0 \quad , \left(\frac{\sigma_1}{X_c}\right) \geq 1 \quad \text{and} \quad \sigma_1 < 0 \tag{1}$$

Matrix failure mode

$$\left(\frac{\sigma_2}{Y_t}\right)^2 + \left(\frac{\sigma_{12}}{S}\right)^2 \geq 1 \quad \text{and} \quad \sigma_2 > 0 \quad , \left(\frac{\sigma_2}{Y_c}\right)^2 + \left(\frac{\sigma_{12}}{S}\right)^2 \geq 1 \quad \text{and} \quad \sigma_2 < 0 \tag{2}$$

Fiber-matrix shearing failure mode

$$\left(\frac{\sigma_1}{X_t}\right)^2+\left(\frac{\sigma_{12}}{S}\right)^2\geq 1 \quad \text{and} \quad \sigma_1>0\ , \qquad \left(\frac{\sigma_1}{X_c}\right)^2+\left(\frac{\sigma_{12}}{S}\right)^2\geq 1 \quad \text{and} \quad \sigma_1<0 \tag{3}$$

where σ_1, σ_2 are ply longitudinal and transverse stresses, respectively.

σ_{12} is a ply shear stress.

X_t , X_c are longitudinal tensile and compressive strength , respectively.

Y_t, Y_c are transverse tensile and compressive strength , respectively.

S is a shear strength.

5. MATERIAL PROPERTY DEGRADATION MODEL

Once failure is occurred, the material properties of the element are degraded according to the type of failure modes.

Fiber tension failure

When fiber tensile failure occurs, it is assumed that the element in the ply is no longer able to carry any load, therefore, the material properties are degraded to zero values as follows.

$$[E_1, E_2, G_{12}, \nu_{12}] \rightarrow [0,0,0,0] \tag{4}$$

Matrix failure or Fiber-matrix shear failure

It is assumed that a matrix or fiber-matrix shear failure do not affect the load carrying capacity in the fiber direction. Therefore, if matrix or fiber-matrix shear failure is reached in the element , the material properties are reduced as to carry only the stress in the fiber direction.

$$[E_1, E_2, G_{12}, \nu_{12}] \rightarrow [E_1,0,0,0] \tag{5}$$

Fiber compression failure

Fiber compression failure occurs in a crush zone area just ahead of the pin and the failed material may even have slightly magnified elastic stiffness, making the failed material stiffer (approaching to be incompressible). It is obvious from the failure criteria that fiber-matrix shear failure occurs prior to fiber compression failure. It is assumed that after fiber compression failure occurs, the damaged element heals and the element recovers its original elastic properties as follows

$$[E_1,0,0,0] \rightarrow [E_1, E_2, G_{12}, \nu_{12}] \tag{6}$$

The failure criteria and material properties degradation rules were implemented in the user subroutine " USFILD" of the ABAQUS/standard code and the progressive failure analysis was carried out. Using this subroutine, it is possible to successively modify the material constitutive law and internal stress and the standard linear elastic material behavior to include damage effect.

6.RESULTS AND DISCUSSIONS

In order to evaluate the effects of friction, the stresses around the hole were computed for laminate made of T300/1034-graphite/epoxy [6]. The two friction coefficients were assumed to be μ=0 or μ=0.2. A value of μ=0.2 is representative of steel on graphite-epoxy. The radial stress,σ_r,and the friction-induced shear stress,$\sigma_{r\theta}$, around the hole were computed. For presentation, stresses were normalized by the nominal average bearing stress. The nominal averaged bearing stress is defined

as S= P/(DT), where P is the load, D is the hole diameter and T is the laminate thickness. Laminate considered was a laminate with a stacking arrangement of $[0_2/\pm45]_S$. This laminate is representative of laminates most commonly used today.

Fig.3. illustrates the stresses around the hole for laminate with frictionless pin(μ=0). Slight difference is observed between the radial stress distribution and the assumed cosinusoidal one in this figure. This is particularly true at the end of the contact region around θ=90. In fact, the cosinusoidal distribution has a 180°contact region(-90°$\leq \theta \leq$90°) . This case has contact regions less than 180° and therefore the cosinusoidal assumption overestimates the contact region.

From Fig.4., it is clear that the friction effect changes the stress distribution around the hole. Aside from producing shear stresses at the hole edge, the bearing stress at θ=0° is reduced. The maximum bearing stress occurs away from the θ=0° direction. It is clear that the cosinusoidal distribution substantially misrepresents the radial stress distribution, especially when the friction exists.

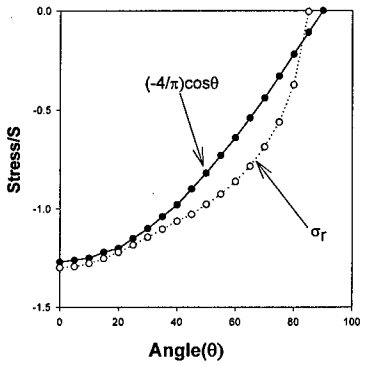


Fig.3. Radial stress distribution of the $[0_2/\pm45]_S$ laminate (W/D=8, E/D=4,μ=0.0)

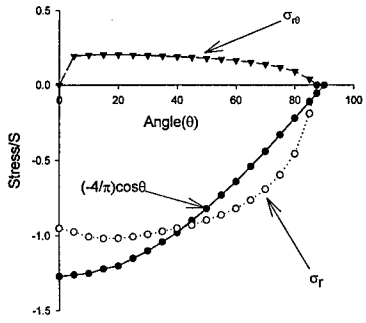


Fig.4. Effect of friction on stress distribution of the $[0_2/\pm45]_S$ laminate(W/D=8,E/D=4,μ=0.2,)

The progressive failure analysis was performed for T300/SP286 graphite/epoxy laminated composites and the results were compared with experimental results [7]. The numerical predictions are presented in Table 1 along with experimental data for the joint in the laminated composites. Good agreement (less then 10% error) was obtained in all cases

Table 1. Comparison of predicted and experimental failure loads [7]

Case No.	Geometry				Predicted ultimate failure load (N)	Averaged experimental ultimate failure load (N)	Percent error (%)
	W / D	E / D	T (mm)	Ply orientation			
1	5.34	2.98	1.07	$(0°/\pm 45°/90°)_S$	4774	4982	4.2
2	5.34	2.04	2.24	$(0°/\pm 45°/90°)_{2S}$	8709	8562	1.7
3	5.34	2.98	1.68	$(0°/\pm 45°/90°/\pm 45°)_S$	6995	7517	6.9
4	5.34	2.98	1.40	$(0_2^o/\pm 45_2^o/90_2^o)_S$	6119	6094	0.4
5	5.34	2.98	1.07	$(0_2^o/\pm 45_2^o)_S$	4262	4363	2.3

REFERENCE

1. Chang, F. K. and Chang, K. Y , Post-Failure Analysis of Bolted Composite Joints in Tension or Shear-Out Failure, J. of Composite Materials , **21** (1987) pp. 809-833
2. Lessard, L. B. and Shokrieh, M. M., Two-Dimensional Modeling of Composites Pinned-Joint Failure, J. of Composite Materials , **29** (1995) pp. 671-697
3. Hung, C. L. and Chang, F. K., Bearing Failure of Bolted Composite Joints. Part Ⅱ: Model and Verification, J. of Composite Materials , **30** (1996) pp. 1359-1400.
4. De Jong, T., Report LR-350, Aerospace Dept, Delft University of Technology, The Netherlands (1982)
5. ABAQUS, Hibbit, Karlsson & Sorenson Inc. 1080 main street, Providence, Rhode Island, USA.
6. Hyer, M. W. And Klang, E. C and Cooper, D. E., The Effects of Pin Elasticity, Clearance, and Friction on the Stresses in a Pin-Loaded Orthotropic Plate, Journal of Composite Materials, **21** (1987) pp. 192-206,
7. Van Siclen, R.C., Evaluation of Bolted Joints in Graphite/Epoxy, Proceedings of the Army Symposium on Solid Mechanics: Role of Mechanics in the Design of Structural Joints (1974) pp.120-138

Key Engineering Materials Vols. 183-187 (2000) pp. 1171-1176
© 2000 Trans Tech Publications, Switzerland

Crystallinity and Mechanical Properties of Glass Fiber Reinforced Thermoplastic Composites by Rapid Press Consolidation Technique

I.J. Shin, D.Y. Kim and D.J. Lee

School of Mechanical Engineering, Yeungnam University
Gyungsan, Gyungbuk 712-749, Korea

Keywords: Crystallinity (X_C), Differential Scanning Calorimetry DSC, PET Matrix Composites, Rapid Press Consolidation Technique RPCT

ABSTRACT

Glass fiber reinforced thermoplastic composites were manufactured by Rapid Press Consolidation Technique (RPCT) as functions of temperature, pressure and time in pre-heating, consolidation and solidification sections during the manufacturing processing. It was found that the material property is greatly affected by pre-heating temperature under vacuum, mold temperature and molding pressure. Among them, the temperature in the mold was the most critical factor in determining the mechanical properties and the molded conditions of specimen. The crystallinity of PET matrix was also investigated by differential scanning calorimetry (DSC) measurements for various processing conditions. The level of crystallinity (X_C) depended strongly on the mold temperature, cooling rate and the type of composite. The difference in X_C is believed to be one important factor in characterizing the mechanical properties.

1. INTRODUCTION

Fiber reinforced polymer composites have been used for a variety of engineering applications and their manufacturing processes have been developed continuously. Recently, as a concern about environment is increased, the consumption of thermoplastics is increased more greatly than that of the thermosetting polymers. The thermopalstic composites have a number of advantages over the thermosetting composites, for example, greater impact resistance, elimination of controlled storage requirements, recyclability and improved working environment. But, the most important difference is the possibility of rapid and cost-effective manufacturing processing.

The manufacturing process of the thermoplastic composites is designed and developed to satisfy the need of reliable and simple processing technique in this paper. Continuous fiber reinforced thermoplastic composites are manufactured by advanced process called Rapid Press Consolidation Technique (RPCT) [1]. The quality of the thermoplastic composites can be determined by several factors, for example, bonding strength between fiber and matrix, fiber deformation, porosity,

molecular arrangement. Among these factors, the level of molecular arrangement is closely related to crystallinity. The objective of this study is to assess crystallinity and tensile strength of composites by RPCT depending on temperature, pressure and time in pre-heating, consolidation and solidification sections during the manufacturing processing. Also, two types of composites from the combination of film, fiber and fabric are tested to investigate the reliability of RPCT.

2. RAPID PRESS CONSOLIDATION TECHNIQUE (RPCT)

2.1. Facility of RPCT

The main equipments of RPCT consist of pre-heating unit, conveyor system and press. Pre-heating unit has low capacity of press, mold and vacuum pump.

Pre-heating unit: This unit is an automatic pre-heating system. The press has a maximum pressing force of 7 kN, such a low pressure applied to the material at final step of the pre-heating section. The maximum molding temperature is 350℃ and vacuum pump is working during pre-heating section in order to prevent the creation of the porosity.

Conveyor system: After pre-heating, conveyor carries the material to the press in order to consolidate and this unit has a speed controller.

Press: The press is a hydraulic press with a maximum pressing force of 300 kN. The maximum press stroke is 100 mm. The maximum mold temperature is 500℃ and the type of mold is 2D-plate. The pressing time is controlled with an adjustable timer starting when the force or the piston reaches the material.

2.2. Process of RPCT

The processes of RPCT divide into three sections: pre-heating, consolidation and solidification. In this process, it is very important to optimize the correlation among temperature, pressure and time.

Pre-heating section: In this section, the material is heated over the melting temperature under vacuum to remove the porosity of raw material. And, low pressure is applied to let the matrix infiltrate into the fiber, which renders a good mechanical property of the composite.

Consolidation section: Consolidation is performed after temperature is raised over the melting temperature of material. When constant pressing force is applied, this specimen is molded and the matrix and fiber are bonded together. The material property is related to a great extent to the crystallinity of material, which is affected by the degree of consolidation. Consolidation terminates when full compaction and adhesion between the plies are achieved

Solidification section: This section is in the step of cooling the consolidated composite. In order to prevent the creation of porosity resulted from shrinkage during solidification, a sufficient residual pressure in the matrix must be maintained during the final stages of the process.

3. EXPERIMENTS

The matrix material is thermoplastic polyethyleneterephthalate(PET) and reinforcing fiber is continuous E-glass. Two types of composites are used. One is the combination of PET film and glass woven fabric and the other is the combination of PET yarn and glass yarn. The volume fraction of glass is 40% and the thickness of specimen is approximately 1.7mm. The specimen was placed between PTFE(teflon) coated fabrics in a clamping frame. The processing parameters e.g. temperature, pressure and time in pre-heating unit and press have been investigated as shown in

Table 1. The pressing force in the pre-heating section is fixed at 3 kN and the vacuum pressure is about 10^5 Pa.

Tensile specimen was made according to ASTM D 3037-76. The crystallinity of PET matrix was also investigated by differential scanning calorimetry (DSC).

Table 1. The processing parameters of RPCT. Specimen No. 1 is the basic parameters

Unit	Pre-heating			Press		
No.	Pre-heating Temperature (℃)	Pre-heating time (min)	Pressing time (sec)	Mold temperature (℃)	Pressing time (sec)	Pressing force (kN)
1	**290**	**12**	**10**	**140**	**15**	**125**
2	**280**	12	10	140	15	125
3	**300**	12	10	140	15	125
4	290	**9**	10	140	15	125
5	290	**15**	10	140	15	125
6	290	12	**5**	140	15	125
7	290	12	**15**	140	15	125
8	290	12	10	**80**	15	125
9	290	12	10	**200**	15	125
10	290	12	10	140	**10**	125
11	290	12	10	140	**20**	125
12	290	12	10	140	15	**75**
13	290	12	10	140	15	**175**

4. RESULTS AND DISCUSSION

4.1. Optimum conditions for RPCT

All the processing parameters in pre-heating and consolidation sections are investigated by tensile test and visual inspection. The specimens are made according to Table 1. In the solidification section, all the specimens are cooled at room temperature.

Fig. 1 represents the tensile strength as a function of pre-heating temperature. The best condition is 290℃ and the next is 300℃. Since the tensile strengths are almost same in both cases, either 300℃ or 290℃ may be adopted as pre-heating temperature. Fig. 2 shows the conditions of pre-heating time. The tensile strength for the case of 12min is stronger than the others. Fig. 3 shows the effect of pressing time in pre-heating section. The material has the maximum tensile strength at 10sec. In this step, the glass fiber is immerged in PET matrix by low pressing force, which provides a good bonding condition between fiber and matrix. Fig. 4 represents the tensile strength as a function of mold temperature. 140℃ is the most moderate temperature for crystallization. Fig. 5 shows the effect of pressing time in consolidation section. The optimum condition is 15sec. Fig. 6 represents the tensile strength with the pressing force in consolidation section. The material has the maximum tensile strength at 125 kN. In this study, the specimen was made in simple plates. However, in the case of 3-D specimen with curvature, a bigger pressing force is needed. Also, if the fiber volume fraction is increased, the applied pressing force should be increased.

From the results of the tensile test, the optimum condition is No. 1 in Table 1. The corresponding tensile strength is about 252 MPa.

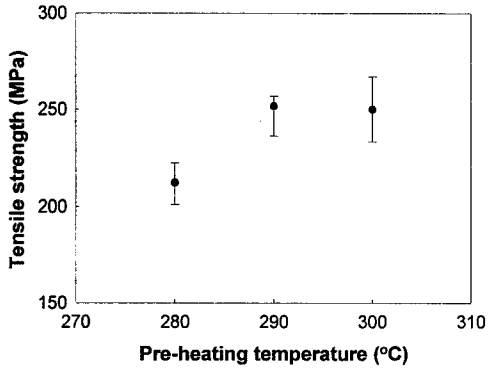


Fig. 1. Tensile strength vs. pre-heating temp.

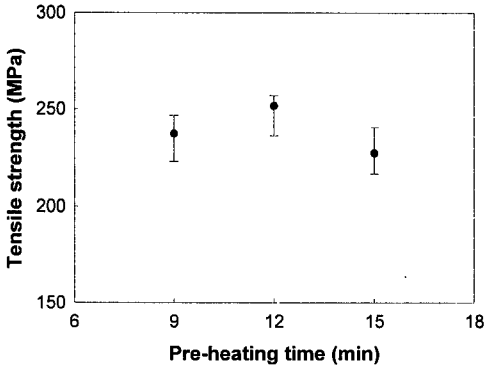


Fig. 2. Tensile strength vs. pre-heating time.

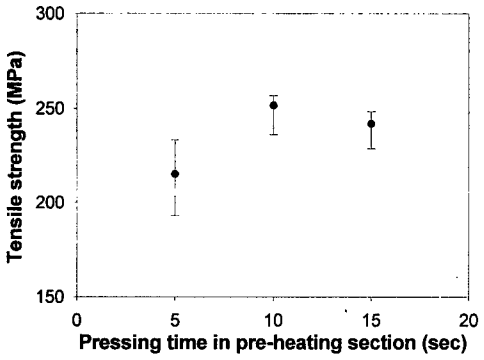


Fig. 3. Tensile strength vs. pressing time in pre-heating section.

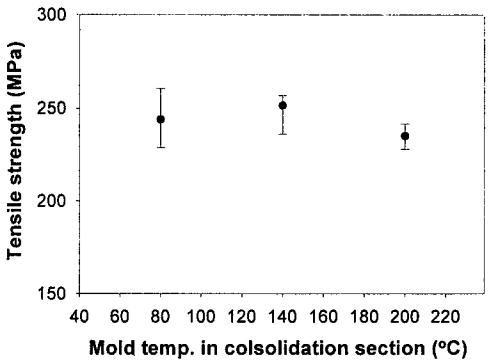


Fig. 4. Tensile strength vs. mold temperature in colsolidation section.

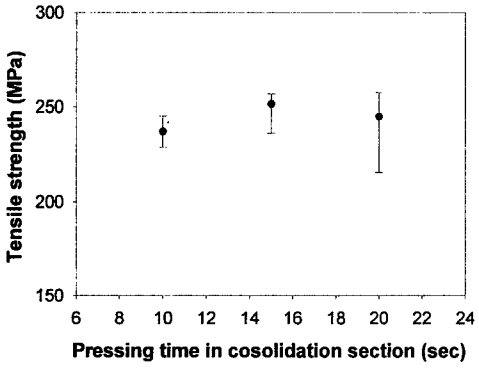


Fig. 5. Tensile strength vs. pressing time in consolidation section.

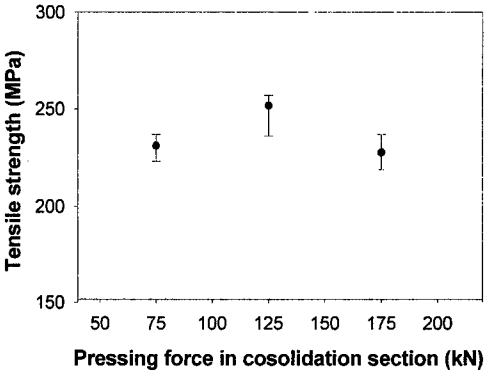


Fig. 6. Tensile strength vs. pressing force in consolidation section.

Four different cooling conditions were adopted. And, they are fast, normal A, normal B and slow cooling. The specimens were made by four cooling conditions, respectively. The conditions of pre-heating and consolidation sections were No. 1 in Table 1.

Slow cooling: the specimens were hold in the mold after the applied pressing force was removed. The cooling rate is about 1℃/min.

Normal A cooling: the specimens removed from the mold of press were cooling at room temperature. The cooling rate is about 8℃/min.

Normal B cooling: the specimens were hold in the mold after the applied pressing force was removed. The cooling rate is about 15℃/min.

Fast cooling: the specimens had been immerged in cold water for 3 minutes as soon as the plates were consolidated. The cooling rate is about 70℃/min

The tensile strength is investigated in a variety of cooling conditions as shown in Fig. 7. Four specimens are manufactured according to No. 1 in Table.1. The different cooling conditions are adopted in the final step of solidification. The tensile test is performed to assess the cooling rate effect as shown in Fig 7. The slow cooling rate is the best condition, which has enough time to crystallize the material and increase the material strength.

The tensile strength for all the processing parameters is investigated for the rapid press consolidation technique. The optimum manufacturing conditions for the case of PET film and glass woven fabric are summarized in Table 2 and the corresponding tensile strength in the optimum conditions is 258 MPa.

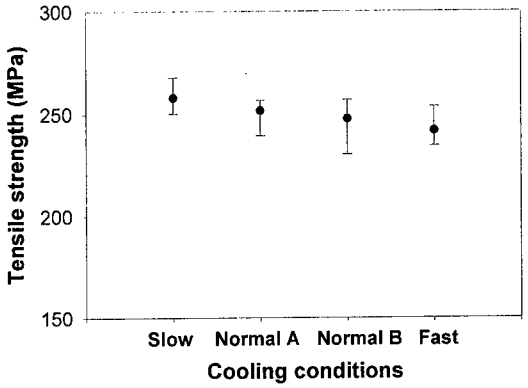


Fig. 7. Tensile strength with different cooling conditions.

Table 2. The optimum conditions for the case of PET film and glass woven fabric

Section	Pre-heating			Consolidation			Solidification
Optimum conditions	Pre-heating temp. (℃)	Pre-heating Time (min)	Pressing time (sec)	Mold temp. (℃)	Pressing time (sec)	Pressing force (kN)	
	290	**12**	**10**	**140**	**15**	**125**	**Slow cooling**

4.2. Crystallinity

The level of crystallinity depends strongly on the thermal history as well as other processing

parameters. The effect of mold temperature and cooling rate on the crystallinity is investigated by utilizing DSC. In the case of mold temperature, two types of composite are used for comparison. As depicted in Fig. 8, the degree of crystallinity (X_C) is affected by mold temperature. At 140℃, the X_C is the highest. In most cases, PET can be crystallized best at about 190℃. When the material is pressed at 140℃ after removed from pre-heating unit at high temperature, the material seems to keep its temperature of 190℃. In addition to the mold temperature, the used materials of composite affect the X_C. The case of PET yarn and glass yarn shows higher X_C than that of PET film and glass fabric.

Fig. 9 shows a trend of decreasing crystallinity with the cooling rate. When cooled slowly, the material stays longer than the fast cooled material near best crystallization temperature of 190℃, and has enough time for crystallization.

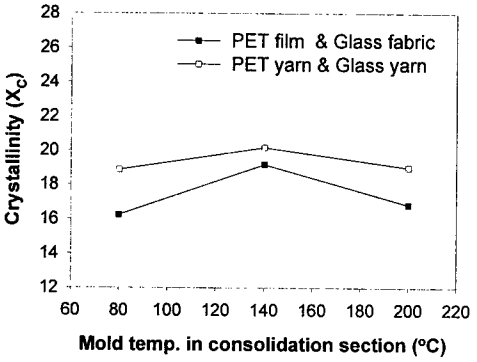


Fig. 8. Crystallinity vs. mold temperature of two different composites.

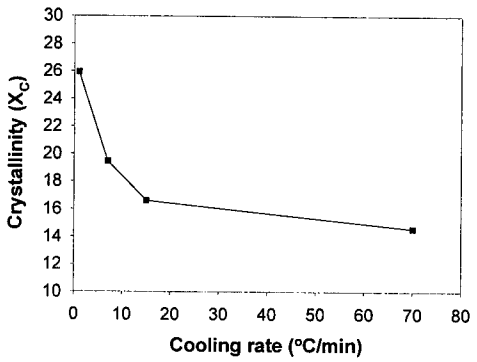


Fig. 9. Crystallinity as a function of cooling rate.

5. CONCLUSIONS

The optimum conditions of RPCT were decided by measuring tensile strength of material as functions of temperature, pressure and time in pre-heating, consolidation and solidification sections. The tensile strength for the optimum conditions is 258 MPa.

Crystallinity (X_C) was assessed by mold temperature and cooling rate in order to find the correlation between crystallinity and tensile strength. As a result, crystallinity as well as tensile strength is the highest when the mold temperature is 140℃, and they are increased when the material is cooled slowly. The difference in X_C is believed to be one important factor in increasing the tensile strength.

Two different types of composites have been compared to find out their effect on the crystallinity. When PET and glass yarns are used, the material shows higher crystallinity than the case of PET film and glass fabric. The material with PET and glass fibers can have better wetting and closer molecular contact distance than that with PET film and glass fabric.

REFERENCES

1. T. L. Andersent, Proceeding of 18th International Symposium on Materials Science, (1997) p.237
2. C. M. Pistor and S. I. Guceri, J. Composite Materials, **33**, (1999) p.306

Key Engineering Materials Vols. 183-187 (2000) pp. 1177-1182
© 2000 Trans Tech Publications, Switzerland

Fractography of Damaged Carbon Fiber/Epoxy Composites after Low-Velocity Impact

M.S. Sohn[1], X.Z. Hu[1] and J.K. Kim[2]

[1] Department of Mechanical & Materials Engineering, The University of Western Australia, Nedlands WA 6907, Australia

[2] Department of Mechanical Engineering, Hong Kong University of Science and Technology, Clear Water Bay, Pokfulam Road, Kowloon, Hong Kong, China P.R.

Keywords: Carbon Fiber Composites, Impact Damage Modes, Low-Velocity Impact, Short Fiber Reinforcement

ABSTRACT

The sub-surface damage modes in carbon fiber/epoxy composite laminates after low-velocity impact were investigated. The effects of interlayers inserted between continuous fiber layers were evaluated on impact damage resistance of composites. These interlayers were made of short fibers and a tough polymer film, such as Kevlar fibers, Zylon fibers and poly(ethylene-co-acrylic acid) (PEEA) film. Optical and scanning electron microscopy was employed to study the impact damage mechanisms and their correlations with the interlayer reinforcements.

1. INTRODUCTION

Fiber reinforced plastic (FRP) composite laminates have many inherent drawbacks due to layered structures. Among them, delamination is one of the major concerns, which becomes particularly important under low energy impact loading as impact damage can hardly be seen from the surface [1]. Besides delamination, other typical impact damage modes, such as matrix cracking and debonding of fibers from the matrix, are generally involved [2,3]. Impact damage resistance and damage tolerance of composites can be quantitatively characterized by measuring the damage initiation energy and the load bearing capacity of laminates given the specified amount of damage [4]. To enhance the damage resistance of composites, a number of techniques have been proposed and a review on this subject was presented [5]. These techniques include the change in fiber layer structure, the use of woven fabrics and the introduction of third phase materials in the composite. As a consequence of these methods, different damage mechanisms are ensued.

The main goal of this paper is to characterize the fractography of low-velocity impact damage in carbon fiber/epoxy composite laminates containing interlayers of short Kevlar, Zylon fibers and PEEA film between continuous fiber layers.

2. MATERIALS

NCT301 carbon fiber/epoxy prepregs (supplied by Newport Adhesives and Composites) were used to prepare composite laminate specimens. The prepreg cloth has the weight per area of 300 g/m2 and consists of 48K yarns. The volume percentage of fiber over the prepreg before curing was

about 65%. Ten-ply composite laminates were prepared by hand-lay up with a stacking sequence of $[0/90]_5$. During the lay-up process, three different interlayer materials were introduced:
Two different types of Kevlar 49 short fibers of 15 mm in length with 0.8 wt % and 5-7 mm in length with 0.4 wt %; The Primacor 3440 PEEA (poly(ethylene-co-acrylic acid)) film (supplied by Dow Chemical) of 0.1 mm in thickness; Toyobo Zylon AS short fibers of 6 mm in length with 0.8 wt %.

The composites were consolidated using the curing cycle recommended by the manufacturer based on the compression molding technique.

3. LOW-VELOCITY IMPACT RESPONSE

An instrumented Dynatup 8250 drop-weight impact machine was employed to perform the non-penetrating impact tests. An impactor equipped with a hemispherical nose of 12.7 mm in diameter was impacted onto the center of a test window of 75 mm in diameter. A series of the test were conducted for each specimen with five different impact energies between 3 and 33 J. Impact load-time (P-t) curves were obtained directly from the computer interfaced to the machine. Typical P-t curves obtained for an impact energy of about 25 J are shown in Figure 1.

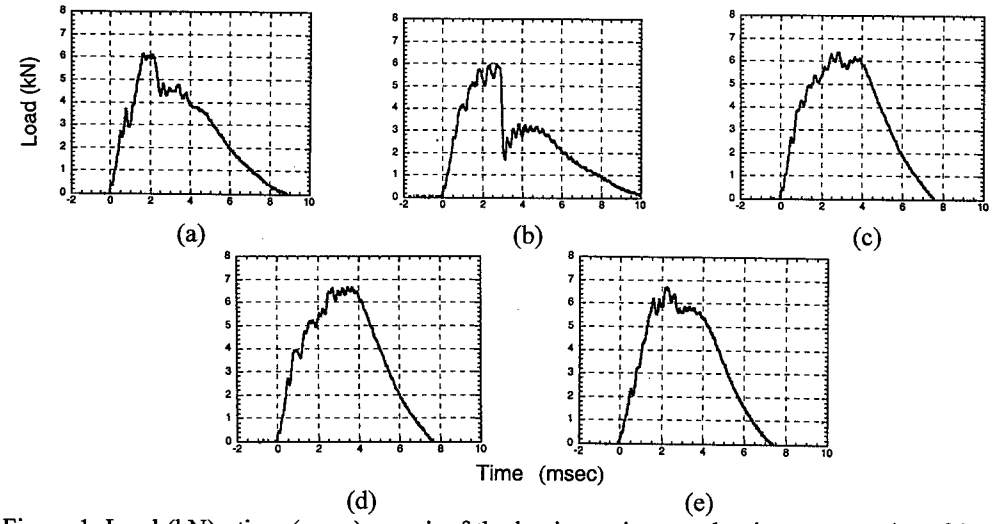


Figure 1. Load (kN) –time (msec) curves of the laminates impacted at impact energies of 25 J; (a) without any reinforcement, (b) Kevlar fibers of 15 mm, 0.8 wt %, (c) Kevlar fibers of 5-7 mm, 0.4 wt %, (d) Zylon fibers and (e) PEEA film.

The impact energy values corresponding to damage initiation, at which the first load drop is displayed in the ascending portion of the curves, were quite similar in the range from 2.3 to 2.6 J for the five different composite laminates. Meanwhile, the peak loads varied from 6 to 6.8 J. The diagrams for the plain composite and the Kevlar (15 mm) reinforced composite (Figure 1(a) and (b)) showed longer impact responding time, namely about 10 msec while the other diagrams (Figure 1(c), (d) and (e)) all had less than 8 msec. This means that the absorbed impact energy values for the first two composites ((a) 80 and (b) 82% of applied impact energy, respectively) were consistently higher than those for the other three composites ((c) 60, (d) 53 and (e) 67%). The absorbed energy estimated from the P-t diagram includes both the elastic and plastic energies. Hence, the proportion of both energy components cannot be directly obtained from the machine.

It, however, can be seen that the reinforcements used for the interlayers in Fig. 1(c), (d) and (e) result in less damage.

4. RESIDUAL STRENGTHS OF LAMINATES

The compression after impact (CAI) strength can be used to indicate the composite's damage tolerance. Damage tolerance refers to the capability of composites given the damage existing in the composite structure. Compressive test using Boeing compressive test fixture was performed on the impacted composite laminate specimens. During the test, some laminates impacted under low impact loads experienced failures at the edges rather than at the impact center. Therefore, the specimens failed at the edges were ignored. Table 1 shows the CAI strengths of the laminates impacted at 25 J. The composite with PEEA films showed the lowest value. This composite was most penalized in total composite weight increase due to the introduction of the interlayers. The total volume of the composite with PEEA was about 20% higher than that of the other composites. The CAI values of composites with Kevlar of 15 mm and Zylon fibers were similar to each other.

Table 1. Residual compressive strengths of the laminates after impact at 25 J.

	plain	Kevlar 15 mm	Kevlar 5-7 mm	Zylon 6 mm	PEEA film
CAI (MPa)	112	110	94	105	72

5. FRACTOGRAPHY

Surface Damage Assessment

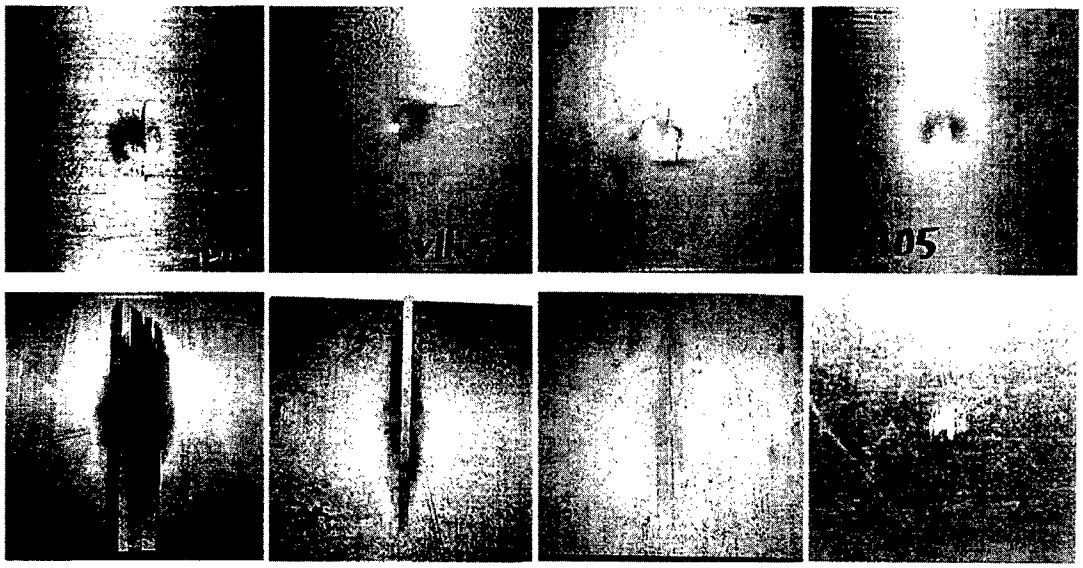
The photographs of damage produced on the front and back surfaces of the impacted composite specimens are shown in Figure 2. The transverse crack on the front surface of the plain composite is shown in Figure 2(a). The crack direction is closely related to the carbon fiber direction of the 10th (bottom) plane (90°). The back surface experiences severe splits in the fiber direction and even separation of the split part of the 10th plane with width of 5 to 15 mm from the edge of the laminate. This is the extension of the delamination in the bottom interlaminar region. As shown in Figure 2(b), the impact damage on the front and back surfaces for the composite containing interlayers made with Kevlar fibers of 5-7 mm in length were less severe than the others. The front surface had small cracks in both 0° and 90° directions. The split in the bottom layer was narrower than the control without interlayers. The damage in the composite with Kevlar fibers of 15 mm in length were very similar to those exhibited in Figure 2(b). The composites with Zylon fibers showed much higher resistance to impact damage (Figure 2(c)) than those in Figure 2(a) and (b). In Figure 2(d), the composite interleaved by PEEA film exhibited totally distinct damage behavior. The front surface hardly exhibited visible cracks. On the back surface, a small area under the impact experienced extensive fiber fracture due to the impact-induced bending. In other words, the PEEA film layers acted differently from those containing short fibers under impact loading. Detailed damage mechanisms are studied using a scanning electron microscope (SEM) in the next section.

Optical Microscopy

Cross-sectional optical photography was performed for the specimen impacted at 25 J. Figure 3(a) and (b) shows the micrographs of composites without interlayers and those with interlayers made of Zylon fibers. Impact loads were applied on the top surface of laminates as shown in the photographs. Neither Kevlar nor Zylon can be observed in this micrograph due to the low magnification.

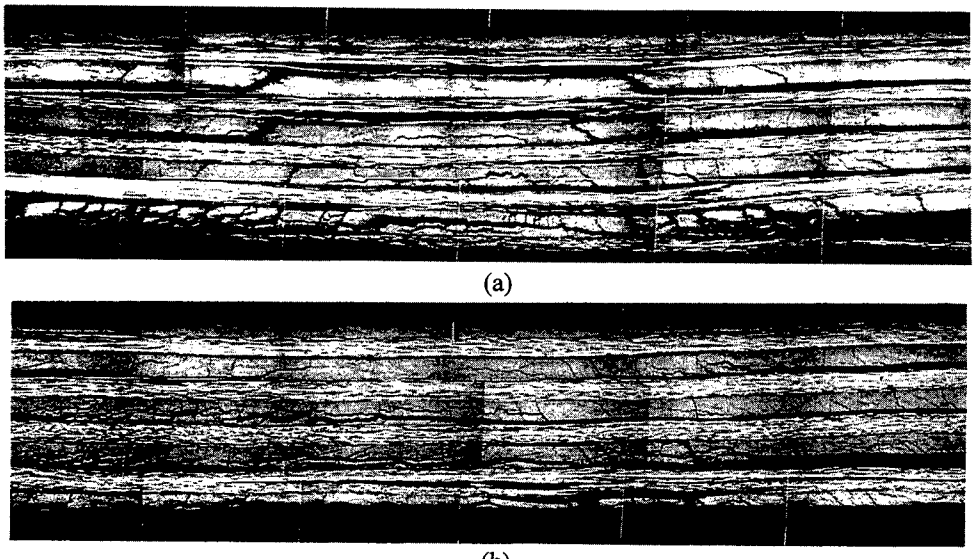
Typical impact-induced fracture occurred in the control laminate. The top-hat shape fracture pattern shown in Figure 3(a) is consistent with the previous observation [6] in that delamination, transverse cracking, intra-ply crackings were the major damage modes. In the control composite,

extensive delaminations were observed. At both ends of delaminations, transverse matrix cracks were developed with 45° to the subsequent fiber planes. At the bottom plane of the laminate, severe fracture was exhibited accompanying separation of the 10^{th} plane from the 9^{th} plane at one end. This is attributed to the largest bending occurring at the outermost surface of specimen.



(a) (b) (c) (d)

Figure 2. Damages produced on front and back surfaces of the impacted laminates at 25J; (a) plain, (b) Kevlar fibers, 5-7 mm, (c) Zylon fibers and (d) PEEA film.



(a)

(b)

Figure 3. Cross-sectional micrographs of the laminates (a) without any reinforcement and (b) with Zylon (AS) fibers.

The damages induced in the laminate with interlayers of Zylon fibers (Figure 3(b)) can be well contrasted with those in the control. No extensive delamination took place in the top four

interlayers. This may be due to the high elastic energy component that may arise from the short Zylon fibers. Delaminations occurred extensively due to the bending stiffness mismatch between the adjacent layers of different fiber orientations [7]. Some fiber fractures were also found in both composites.

Scanning Electron Microscopy

Scanning electron microscopy was performed for the impacted composite specimens. As shown in Figure 2, most composite specimens underwent separation of the bottom plane with longitudinal splits from the 9th plane at an impact energy of about 25 J. After sectioning the composite through the impact center, the interface between the 9th and 10th planes was examined using the SEM without the 10th layer. In this section, the distinct damage mechanisms due to the different interlayer reinforcement are discussed.



Figure 4. Fracture surface of plain composite



Figure 5. Kevlar fibrillation (15 mm in length)



Figure 6. Splits in Kevlar (15 mm)



Figure 7. Fibrillation between split parts in Kevlar (5 mm)

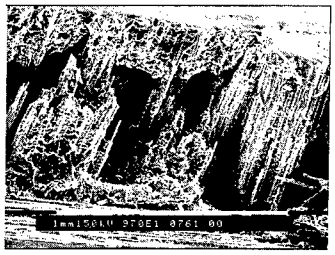


Figure 8. Gap between 9th and 10th in composite with PEEA

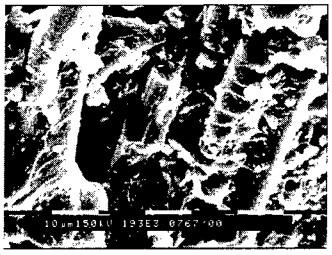


Figure 9. Higher magnification of Figure 8.

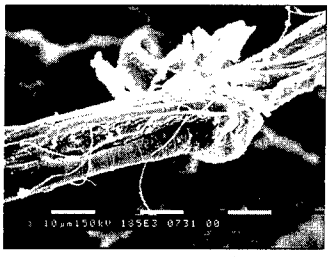


Figure 10. Fracture of Zylon (AS)



Figure 11. Zylon fiber in matrix.

Figure 4 shows the fracture surface induced by the impact at the interface between 9th and 10th planes for the control. Fragmented matrix particles were clearly seen on the fracture surface. Some pull-out marks were shown in the upper part of the micrograph. Figures 5 and 6 show the typical fracture patterns of the composites with interlayers containing Kevlar fibers of 15 mm in length. In Figure 5, a Kevlar fiber was split into two in equal portion in the fiber direction, and fibrillation

occurred from the split gap. These fibrils wrapped the nearby Kevlar fibers. Figure 6 exhibits longitudinal splitting of fiber surface and peel-off as well as fine fibrillation. These types of Kevlar fracture were also often found under quasi-static loading [8]. However, the fracture of Kevlar fiber of 5-7 mm shown in Figure 7 is peculiar. Two split longitudinal parts of a Kevlar fiber were separated but bridged with fine fibrils whose ends come from the two parts. This fracture occurred probably owing to the fact that impact loading was fast enough to fracture the fiber into two parts before the stress transferred to allow surface fibrillation.

Figure 8 shows the fracture pattern between the 9^{th} and 10^{th} planes. The 10^{th} plane was not fully separated in this specimen. The PEEA film was fused into the continuous carbon fiber layers during the processing and formed a very strong bond with the adjacent fiber layers, especially in fiber bundle as shown in the micrograph. Figure 9 is the higher magnification of the micrograph provided in Figure 8. The carbon fibers are shown strongly coated by the resin matrix. Extensive fracture in Zylon was displayed in Figure 10. Half the fiber in fiber direction was severely deformed without sustaining the fiber shape. This type of fiber fracture pattern was not reported previously. Some fibrillation process also took place in conjunction with plastic deformation. Figure 11 is the micrograph exhibiting Zylon adhered to the matrix plane. Some extensive hackles were formed due to the shear process in this specimen [9]. These observations are well contrasted to the behavior of the composites containing interlayers of Kevlar fibers, which exhibited little matrix coating on the fiber surface.

6. SUMMARY

Fractography of damage in carbon fiber/epoxy composites containing interlayers was performed after drop-weight impact. Photographs taken for the front and back surfaces of impact indicate clearly the effectiveness of the interlayers with short fibers. Optical microscopy on the cross-section of the specimens showed that the composite with Zylon was least damaged. The SEM micrographs exhibited various fracture mechanisms of the interlayers. The Kevlar fibers experienced unusual longitudinal splitting along with extensive fibrillation between two split parts. The fracture of Zylon was distinct from that of Kevlar in terms of peculiar fiber deformation. The composite with PEEA showed a very strong bond with the carbon fiber layer by fusing into the continuous carbon prepregs. However, the CAI strength of the composite with PEEA layer was the lowest amongst all composites studied, due probably to the increased composite volume with a lowered fiber volume fraction.

ACKNOWLEDGEMENT

The authors thank the Australian Research Council (ARC) for continuous support of this project through the ARC Postdoctoral Research Fellowship of the first author (MSS).

REFERENCE

1. J.E. Masters, Key Eng. Mat., **37** (1989) p.317
2. S.P. Joshi & C.T. Sun, J. Comp. Mat., **19** (1985) p.51
3. W.J. Cantwell, & J. Morton, Composites **22** (1991) p.347
4. M.N. Ghasemi-Nejhad & A. Parvizi-Majidi, Composites **21** (1990) p.155
5. J.K. Kim, Key Eng. Mat. **141-143** (1989) p.149
6. D.J. Boll, W.D. Bascom, J.C. Weidner & W.J. Murri, J. Mat. Sci., **21** (1986) p.2667
7. S. Hong and D. Liu, Exp. Mech. **29** (1989) p.115
8. M.S. Sohn & X.Z. Hu, Composites, **26** (1995) p.849
9. A.C. Garg, Eng. Frac. Mech., **23** (1986) p.103

Key Engineering Materials Vols. 183-187 (2000) pp. 1183-1188
© 2000 Trans Tech Publications, Switzerland

Anisotropic Mechanical Behavior of Three Dimensional Glass Fabric Reinforced Composites

H.S. Lee[1], S.H. Hong[1], J.R. Lee[2] and Y.K. Kim[3]

[1] Department of Material Science and Engineering, Korea Advanced Institute of Science and Technology, 373-1 Kusung-dong, Yusung-gu, Taejon 305-701, Korea

[2] Polymer Composite Research Laboratory, Korea Research Institute of Chemical Technology, PO Box 9, Daeduk-danji, Taejon 305-600, Korea

[3] Research Center of Kangnam Junggong, 684-9 Sunggok-dong, Ansan, Kyunggi-do 425-110, Korea

Keywords: 3D Glass Fabric Reinforced Composites, Anisotropy, Compressive Test, Flexural Test, Woven Glass Fabrics

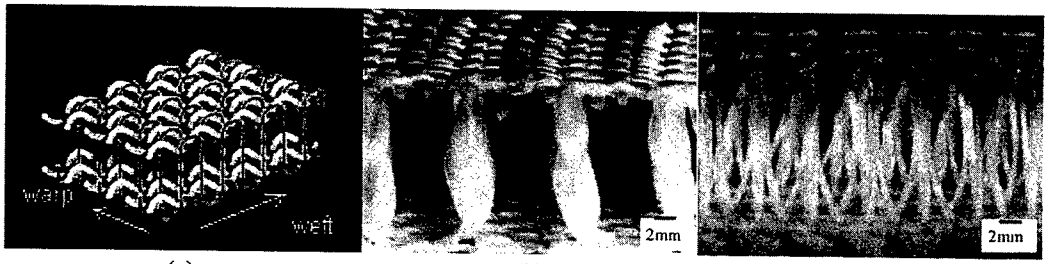
ABSTRACT

The mechanical behavior of three dimensional glass fabric reinforced composites, named Parabeam 3D composites, with two plain woven fabrics and vertical yarns were investigated by compressive and 4-point flexural tests. The main advantage of 3D glass fabric reinforced composites is that the pile threads in the core bind the facesheets together, thus are able to hinder the delamination between layers. Both the compressive strength and flexural strength of 3D glass fabric reinforced composites were inversely proportional to a square of the thickness of 3D glass fabric reinforced composites. The compressive strengths decreased from 12.0MPa to 2.7MPa with increasing the thickness of 3D glass fabric reinforced composites from 3.2mm to 8.2mm. The flexural strengths decreased from 25.2MPa to 3.8MPa in warp direction and decreased from 27.5MPa to 5.0MPa in weft direction with increasing the thicknesses of 3D glass fabric reinforced composites from 3.2mm to 8.2mm. The flexural strength in weft direction was 30% higher than that in warp direction showing anisotropic mechanical behavior due to a larger number of vertical yarns in weft direction.

1. INTRODUCTION

One of the problems to use relatively cheap laminates composite in the commercial aircraft industry is their susceptibility to delamination between the layers[1-2]. The promising solution to this problem is the incorporation of fiber tows normal to the laminate plane by stitching or weaving. The development of three-dimensional (3D) woven composites was required in order to enhance the mechanical properties such as the compressive and flexural strength. The mechanical properties of 3D woven composites are improved mainly due to an interlock of weaver. But the disadvantages have been in 3D woven composites which are the higher cost as well as the discrete load drop due to the microcracking of matrix and the microbuckling of aligned fiber tows[3-8]. Therefore, a few automated systems and new textile processes have been created or are under development to reduce cost and to obtain the critical configurations of fibers preventing the

cost and to obtain the critical configurations of fibers preventing the catastrophic breaks of 3D woven composites. The 3D glass fabric reinforced composites, named Parabeam 3D composites, consisting of three-dimensional E-glass woven fabrics and polyester matrix were investigated by compressive and 4-point flexural test[9]. The 3D glass fabric reinforced composites is a hollow structure as shown in Fig. 1(a), 1(b) and 1(c). The 3D glass fabric reinforced composites are composed of two plain woven fabrics and vertical yarns, which are simultaneously woven. Fig. 1(b) and 1(c) shows a cross-section of the 3D glass fabric reinforced composites in warp and weft directions, respectively. The main advantage of 3D glass fabric reinforced composites is that the pile threads in the core binds the facesheets together, thus are able to hinder the delamination between layers. However, the mechanical properties and the deformation behavior of the hollow structure such as 3D glass fabric reinforced composites were not fully understood. In this study, the mechanical properties and the deformation behavior of 3D glass fabric reinforced composites with varying thicknesses of 3.2~8.2mm were investigated by compressive tests and 4-point flexural tests.



(a) (b) (c)

Fig. 1. Structures of parabeam 3D woven fabric with weft and warp direction[10]. (a) Structure of parabeam 3D woven fabric, (b) cross-sections of parabeam 3D woven fabrics of warp direction, (c) cross-sections of parabeam 3D woven fabrics of weft direction.

2. EXPERIMENTAL PROCEDURES

3D glass fabric reinforced composites were fabricated by infiltrating 20vol% polyester resin matrix into 3D E-glass woven fabric at 25°C by scrubbing the steel. The thicknesses of 3D glass fabric reinforced composites used in this study were 3.2mm, 4.7mm and 8.2mm, respectively. 3D glass fabric reinforced composites infiltrated by polyester were cured at 100°C for 24hrs and post-cured at 100°C for 1hrs. In order to enhance the curing rate, MEKP (methylethyl ketonperoxide) was used as additives. The dimension of compressive test specimens and 4-point flexural test specimens were 50mm×50mm and 50mm×150mm, respectively. The 4-point flexural test specimens were fabricated with the warp direction and the weft direction. The compressive tests were performed according to ASTM C365 and the flexural tests were performed according to ASTM C393.

3. RESULTS AND DISCUSSION

3.1. Structure of 3D Glass Fabric Reinforced Composites

The 3D glass fabric reinforced composites were made by weaving yarns on a loom that interlaces at right angle to each other and by weaving vertical yarns between upper and lower plain fabrics,

simultaneously[10]. There are channels of 4mm wide in warp direction and 1mm wide in weft directions. 3D glass fabric reinforced composites show anisotropy mainly due to a different number of vertical yarns with warp and weft direction. Therefore, the flexural strengths of weft direction were higher than that of warp direction due to a higher number of vertical yarns within upper and lower plain fabrics. The compressive and flexural strengths were sensitively dependent on the buckling of vertical yarns. In order to understand the variation of compressive and flexural strengths with the thickness, the simple equation, which showed the straight bar was buckled in elastic range and under both end fixed, was able to be suggested as following Eq. (1). Although this equation was in the case of straight bar, it would be agreement in the case of rigid vertical yarns coated with cured polyester as long as the elastic deformation and the symmetric buckling of rigid vertical yarns were assumed[11].

$$\sigma = \frac{\pi^2 E}{(l/r)^2} \tag{1}$$

where, σ is stress on specimen when buckling occurs, E is elastic modulus of fiber, l is length of vertical yarns, and r is radius of gyration which is the same as the result by dividing the radius of vertical fiber with $\sqrt{2}$. According to Eq. (1), The stress on 3D glass fabric reinforced composites containing the vertical yarns between upper and lower woven plain fabrics is inversely proportional to a square thickness of 3D glass fabric reinforced composites. Therefore, it will be predicted that the compressive strengths and the flexural strengths of 3D glass fabric reinforced composites are decreased with thickness of vertical yarns.

3.2. Compressive Behavior of 3D Glass Fabric Reinforced Composites

The measured strengths, moduli and specific strengths of 3D glass fabric reinforced composites during compressive test were summarized in Table 1. The compressive strength of 3D glass fabric reinforced composites was decreased to 12.0MPa, 7.0MPa and 2.7MPa and the compressive modulus was decreased to 100MPa, 100MPa and 90MPa with increasing thickness of 3.2mm, 4.7mm and 8.2mm, respectively. This result showed that compressive strengths were proportional inversely with square thickness of 3D glass fabric reinforced composites as show in Fig. 2(a). The 3D glass fabric reinforced composites with thicknesses of 3.2mm, 4.7mm and 8.2mm, respectively, showed a higher specific compressive strength than honeycomb composites because parabeam 3Dcomposites need not to adhere the facesheets[12-14]. Fig. 2(b) shows that the comparison of typical compressive stress-compressive strain curves of 3D glass fabric reinforced composites during compressive test. The conventional 3D woven composites showed the discrete stress drop due to the microcracking of matrix and the microbuckling of aligned tows[14]. However, as shown in Fig. 1(b), the compressive stress-compressive strain curve of 3D glass fabric reinforced composites was developed continuously without a discrete drop of stress-strain curve, then a maximum compressive strength was reached. The reason is that a lot of vertical yarns between two plain woven fabrics were buckled simultaneously with preventing the rapid fracture of 3D glass fabric reinforced composites.

3.3. Flexural Behavior of 3D Glass Fabric Reinforced Composites

The measured flexural strength, flexural modulus and specific flexural strength of 3D glass fabric reinforced composites were presented in Table 2.

Table 1. Compressive properties of 3D glass fabric reinforced composites.

Properties	Unit	Thickness (mm)		
		3.2	4.7	8.2
Compressive Strength	MPa	12.0	7.0	2.7
Compressive Modulus	MPa	100.0	100.2	90.1
Specific Compressive Strength	MPa·m^3/Kg	0.019	0.015	0.009

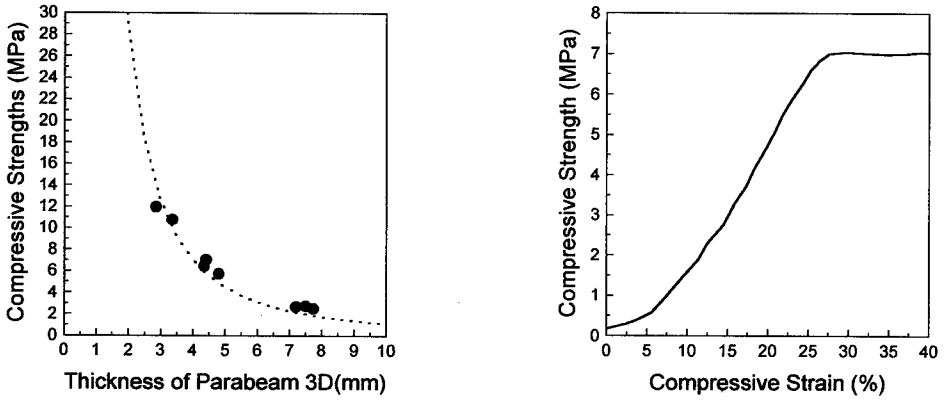


Fig. 2. Compressive strengths and deformation behavior of 3D glass fabric reinforced composites with increasing thickness. (a) Compressive strengths of 3D glass fabric reinforced composites, which showed compressive strength were proportioned to a square of thickness, (b) typical compressive stress-compressive strain curves of 3D glass fabric reinforced composites.

The flexural strength and modulus of 3D glass fabric reinforced composites could be obtained as following Eq. (2) and Eq. (3), respectively,

$$\sigma = \frac{PL}{4t(d+c)b} \tag{2}$$

$$E = \frac{P}{b\Delta} \cdot \frac{11L'^3}{(d^3 - c^3)} \tag{3}$$

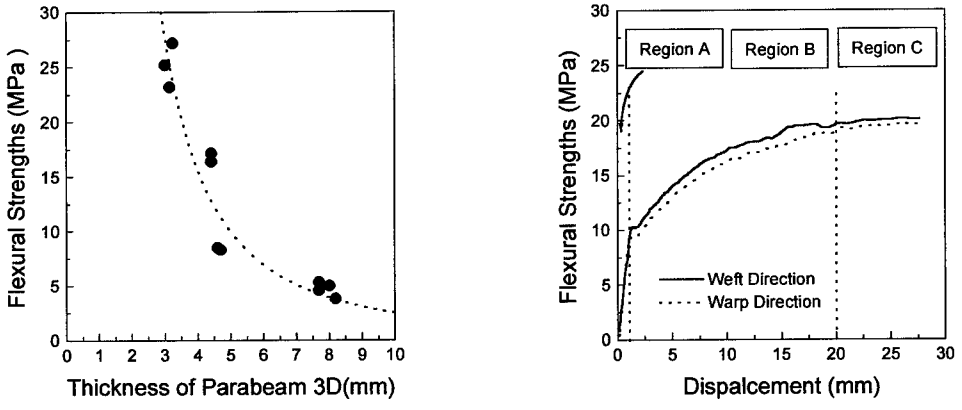
where, P is maximum load, L is span length, t is face thickness, d is specimen thickness, c is length of vertical fiber, b is specimen width, Δ is total beam mid-span deflection, and L' is a half span length. During the flexural test, the shear of vertical yarns in 3D glass fabric reinforced composites occurred and then the core shear strength was calculated as following Eq. (4).

$$\tau = \frac{P}{(d+c)b} \tag{4}$$

The core shear strengths of 3D glass fabric reinforced composites decreased to 2.0MPa, 1.3MPa, 0.9MPa in warp direction and 3.4MPa, 2.9MPa, 1.4MPa in weft direction with increasing thickness. The flexural strengths of 3D glass fabric reinforced composites decreased to 25.2MPa, 8.3MPa, 3.8MPa in warp direction and 27.5MPa, 8.5MPa, 5.0MPa in weft direction, and also the flexural moduli decreased to 3.6GPa, 2.4GPa, 0.6GPa in warp direction and 6.4GPa, 2.4GPa, 0.8GPa in weft direction with increasing thicknesses of 3.2mm, 4.7mm and 8.2mm, respectively. The flexural strengths in weft direction were 2~30% higher than in warp direction. Anisotropy of 3D glass fabric reinforced composites can be explained by the fact that the number of vertical yarns in weft direction is more than that in warp direction. The flexural strengths of 3D glass fabric reinforced composites were proportioned inversely with square thickness of 3D glass fabric reinforced composites as shown in Fig. 3(a). Fig. 3(b) shows typical load-displacement curves of 3D glass fabric reinforced composites during flexural test with warp direction and weft direction, respectively.

Table 2. Flexural properties of 3D glass fabric reinforced composites.

Properties	Unit	Thickness (mm)					
		3.2		4.7		8.2	
		warp	weft	warp	weft	warp	weft
Core Shear Strength	MPa	2.0	3.4	1.3	2.9	0.9	1.4
Flexural Strength	MPa	25.2	27.5	8.3	8.5	3.8	5.0
Flexural Modulus	GPa	3.6	6.4	2.4	2.4	0.6	0.8
Specific Flexural Strength	MPa·m^3/Kg	0.039	0.043	0.018	0.019	0.013	0.017



(a) (b)

Fig. 3. Flexural strengths and deformation behavior of 3D glass fabric reinforced composites with increasing thickness. (a) Flexural strengths of parabeam 3D composites which showed flexural strengths were proportioned to square of thickness, (b) typical load-displacement obtained during flexural deformation of 3D glass fabric reinforced composites.

These curves showed that the elastic deformations were proceeded with increasing load and, after sharp drop peak, plastic deformation with relative constant load was progressed without regard to the woven direction of specimens. Therefore, the flexural deformation behavior of 3D glass fabric reinforced composites was categorized into region A, B and C based on typical flexural strengths-displacement curves. In region A, flexural deformation occurred elastically with increasing the flexural strengths. In region B, the flexural strength decreased rapidly due to the fracture of plain woven fabrics and then the buckling of vertical yarns occurred slowly with increasing the flexural strenngth. In region C, plastic deformation of 3D glass fabric reinforced composites became extreme with nearly constant strength.

4. CONCLUSIONS

The compressive strengths of 3D glass fabric reinforced composites decreased from 12.0MPa to 2.7MPa, and the flexural strengths of 3D glass fabric reinforced composites decreased from 25.2MPa to 3.8MPa in warp direction and decreased from 27.5MPa to 5.0MPa in weft direction with increasing the thickness of 3D glass fabric reinforced composites from 3.2mm to 8.2mm. The compressive and flexural strengths of 3D glass fabric reinforced composites were proportioned inversely with a square of thickness of 3D glass fabric reinforced composites, which indicates that the mechanical strengths are sensitively dependent on the buckling of vertical yarns. The flexural strengths in weft direction were 30% higher than those in warp direction showing strong anisotropic mechanical behavior due to a larger number of vertical yarns in weft direction.

REFERENCES

1. R. E. Horton, and J. E. McCarty, Engineered Materials Handbook, ASM International, **1** (1987)
2. B. N. Cox, J. Comp. Mater. **28**, 12 (1994) p. 1114.
3. B. N. Cox, W. C. Carter and N. A. Fleck, Acta Metall. Mater. **42**, 10 (1994) p. 3463.
4. Gajanan S. Bhat, Materials and Manufacturing Processes, **10**, 4 (1995) p. 667.
5. A. J. Klein, Advanced Composites, **3**, 3 (1988) p. 32.
6. I. Verpoest, F. Ko, B. Wulfhorst and A. Beukers, Seminar on New Textile for Composites, Leuven, Belgium, (1991).
7. K. Swinkels, Proc. ICCM-9, Madrid 1993, Univ. Zaragoza, (1993).
8. T. Chou, F. Ko, Textile Structural Composites, Elsevier, Amsterdam, (1989).
9. G. V. Dijk, data-sheet from Parabeam Helmond, Nederland, (1993).
10. http://www.tokyoweb.or.jp/PDS/index.html.
11. F. P. Beer and E. R. Johnston, Jr., McGraw-Hill Book Company, (1992).
12. J. W. Weeton, D. M. Peters and K. L. Thomas, American Society for Metals, (1986).
13. J. J. Alba and A. Miravete, Adv. Mater. 7, 2 (1995).
14. B. N. Cox, M. S. Dadkhah, R. V. Inman and W. L. Morris, Acta Metall. Mater. **40** (1992) p. 3285.

Key Engineering Materials Vols. 183-187 (2000) pp. 1189-1194
© 2000 Trans Tech Publications, Switzerland

Prediction of Compressive Strength of Stiffened Composite Plate after Impact

C.S. Hong[1], C.W. Kong[2] and C.G. Kim[1]

[1] Department of Aerospace Engineering, Korea Advanced Institute of Science and Technology, 373-1 Kusong-dong, Yusung-gu, Taejon 305-701, Korea

[2] Rocket Structures/Materials Department Space Technology R&D Division, Korea Aerospace Research Institute, PO Box 113, Taejon 305-600, Korea

Keywords: Buckling, Compressive Strength, Delamination, Impact, Postbuckling, Stiffened Composite Plate

ABSTRACT

It is important to develop numerical methods for the prediction of the residual strength of damaged structures in damage tolerance design. The buckling and postbuckling strength of stiffened composite plates with impact damage are studied numerically and experimentally. The delamination distributions through the thickness due to low velocity impact are predicted by finite element analysis. The delamination failure criterion under impact loading is modified for stiffened composite plates. The predicted delamination distributions are compared with experimental ones those are detected by an improved ultrasonic technique. To predict residual strength, a progressive failure model with degradation of elastic moduli in damaged region is adopted in a nonlinear finite element method. The degradation ratio in each sublaminate is determined by delamination distributions through the thickness of laminates. The predicted buckling and postbuckling residual strength show good agreements with experimental results. The impact damage and the postbuckling residual strength of blade stiffened composite plate are discussed.

1. Introduction

Impact damage is one of the major factors degrading the compressive strength of composite structures. A limited number of papers on the prediction of CAI strength and the effect of impact damage on stiffened composite plates have been reported. It was difficult to predict the impact characteristics or the CAI strength of stiffened plates from the data of unstiffened plates. Madan *et al.*[1] showed that the skin bay impact produced great strength reductions and no damage growth occurred before the ultimate failure. Greenhalgh *et al.*[2] recommended that the impact damages of

unstiffened plates did not represent stiffened plates. The effects of impact locations on the compressive strength of stiffened composite plates were studied by experiments. In this study, the impact damage of stiffened composite plates was predicted by the finite element analysis implemented by modified failure criterion. To predict residual strengths, a progressive failure model with the degradation of elastic moduli in the damaged region was adopted in a nonlinear finite element analysis.

2. Impact Damage and Postbuckling Strength Analysis

2.1. Failure Criterion for Low Velocity Impact Damage Analysis

To predict the ply-by-ply delamination due to low velocity impact, the stress obtained from ABAQUS was analyzed. The finite element is S8R, shell element. Choi and Chang [3] proposed the failure criterion due to impact as follows;

$$D_a\left[\left(\frac{\sigma_2}{Y}\right)_n^2+\left(\frac{\tau_{13}}{R}\right)_n^2+\left(\frac{\tau_{23}}{Q}\right)_{n+1}^2\right]=e_D^2 \tag{1}$$

where D_a is an experimental constant. Y, Q, R are strengths for each stress component. n and $n+1$ correspond to the upper and lower plies of the nth interface, respectively. If e_D is larger than unity, the delamiantion failure occurs. Choi and Hong[4] modified Eq.(1) and then predicted the impact damage of composite plates as follows.

$$\left(\frac{\sigma_2}{Y_T}\right)_n^2+\left(\frac{\tau_{13}}{R}\right)_n^2+\left(\frac{\tau_{23}}{Q}\right)_{n+1}^2\geq 1 \tag{2}$$

where σ_2 is the summation of the residual thermal stress and the mechanical stress. The physical meaning of this criterion is shown in Fig. 1.

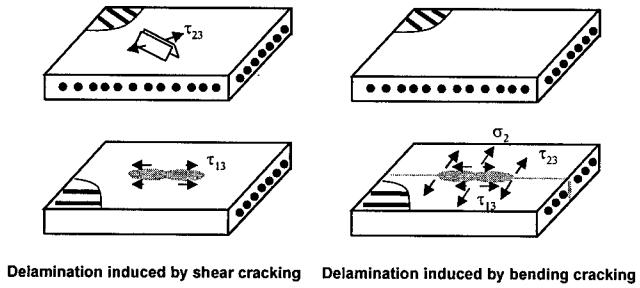


Fig. 1. Schematic description of delamination growth under impact loading.

If shear crack induced delamination, the interlaminar transverse shear stress τ_{13} in the layer just below the interface governs the delamination growth. If bending crack induced delamination, τ_{13} in the right below the interface governs the major growth of delamination and the in-plane bending stress σ_2 in the layer right below the interface advances the delamiantion growth in the secondary direction. However, τ_{23} in the layer right below the interface can also contribute to the delamiantion growth. If composite structures have complex shapes, τ_{23} may be an important component. We propose a modified failure criterion as follows;

$$\left(\frac{\sigma_2}{Y_T}\right)_n^2 + \left(\frac{\tau_{13}}{R}\right)_n^2 + \left(\frac{\tau_{23}}{Q}\right)_n^2 + \left(\frac{\tau_{23}}{Q}\right)_{n+1}^2 \geq 1 \tag{3}$$

where σ_2 is given by

$$\{\sigma_2\} = \{\sigma_2\}^{me} + \{\sigma_2\}^{th} \tag{4}$$

2.2. Prediction of Residual Compressive Strength

The ratio of the stiffness reduction is determined by using delamination distributions through the thickness, as shown in Fig. 2. Each delamination size through the thickness was obtained from C-SCAN. It is assumed that the delaminated plies, which may contain matrix cracking, did not carry the compressive load. Therefore, the modulus retention ratio in each sublaminate is expressed as

$$\begin{aligned} R_i &= 1-(A_i + A_{i-1})/(2A_{ref}) \\ A_0 &= A_1, A_n = A_{n-1}, i = 1,2,\ldots,n \end{aligned} \tag{5}$$

where A_{ref} is the 2D projected delamination area, A_i is the area of the i-th delamination, and R_i is the modulus retention ratio of the i-th sublaminate. The axial, transverse and shear moduli of the i-th sublaminate in the degradation region are multiplied by the same retention ratio

$$\begin{aligned} E_1^{i*} &= R_i E_1^i \\ E_2^{i*} &= R_i E_2^i \\ G_{12}^{i*} &= R_i G_{12}^i \end{aligned} \tag{6}$$

The nonlinear finite element analysis [5] is used to predict the residual strength. To estimate the failure load, the maximum stress criterion is applied to the average stresses in the principal material directions of each layer of each element. The complete unloading model was applied to all areas including delaminated regions. In the present analysis, the effects of local impact damages on the global buckling are considered in finite element model by introducing the stiffness reduction region instead of a local buckling analysis.

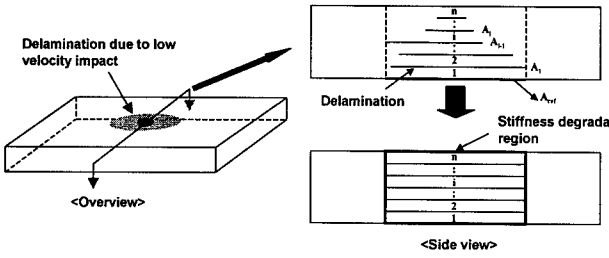


Fig. 2. Stiffness degradation region .

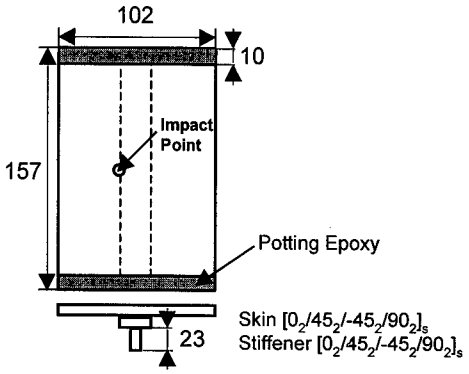


Fig. 3. Blade stiffened composite plate.

2.3. Experiments

A drop-weight impact test machine is used for the low speed impact test. The total mass of the whole drop-weight is 1.0 *kg*. The local diameter of the impactor tup is 12.7 *mm*. After impact tests, each specimen is inspected by using C-SCAN gating technique. After ultrasonic detections of the impact damage, specimens are tested under the compression. The loaded ends are potted in the casting resin and they are machined flat and normal to the loading direction uniformly. The loading rate is 0.5 *mm/min*.

3. Results and Discussion

The Graphite/Epoxy used. The ply thickness is 0.125 *mm*. The material properties are E_1 = 130.0 *GPa*, E_2 =E_3=10.0 *GPa*, G_{12} = G_{13}= 4.85 *GPa*, G_{23} = 3.62 *GPa*, ν_{12} = ν_{13}= 0.31, ν_{23} = 0.52, X_T=1933 *MPa*, X_C=1051 *MPa*, Y_T=51 *MPa*, Y_C=141 *MPa*, S=61 *MPa* where X is the strength in the fiber direction, Y is the strength in transverse direction, subscripts T and C represent tension and compression, respectively. The shape and the dimension of the blade stiffened plate are shown in Fig. 3. The impact location is over the stiffener foot. The comparison of the analysis with the experiment about the ply-by-ply delamination is shown in Fig. 4. Impact energies is 5 *J* and 9 *J*. The peak force of 5 *J* is 3300 *N*. The additional stress component, τ_{23} in the layer right below the interface, gave the failure prediction close to the experiment. The delamination shapes in the upper skin are similar to those of the unstiffened plate. However, the shapes show a little difference in the bottom skin due to the stiffener. The 2D projected delamination shape is a rectangular and the major axis is parallel to the stiffener. Fig. 5 shows the comparison of delamination distributions. The area in the bottom layer of the skin is the largest. Analytical results show good agreements with

experiments.

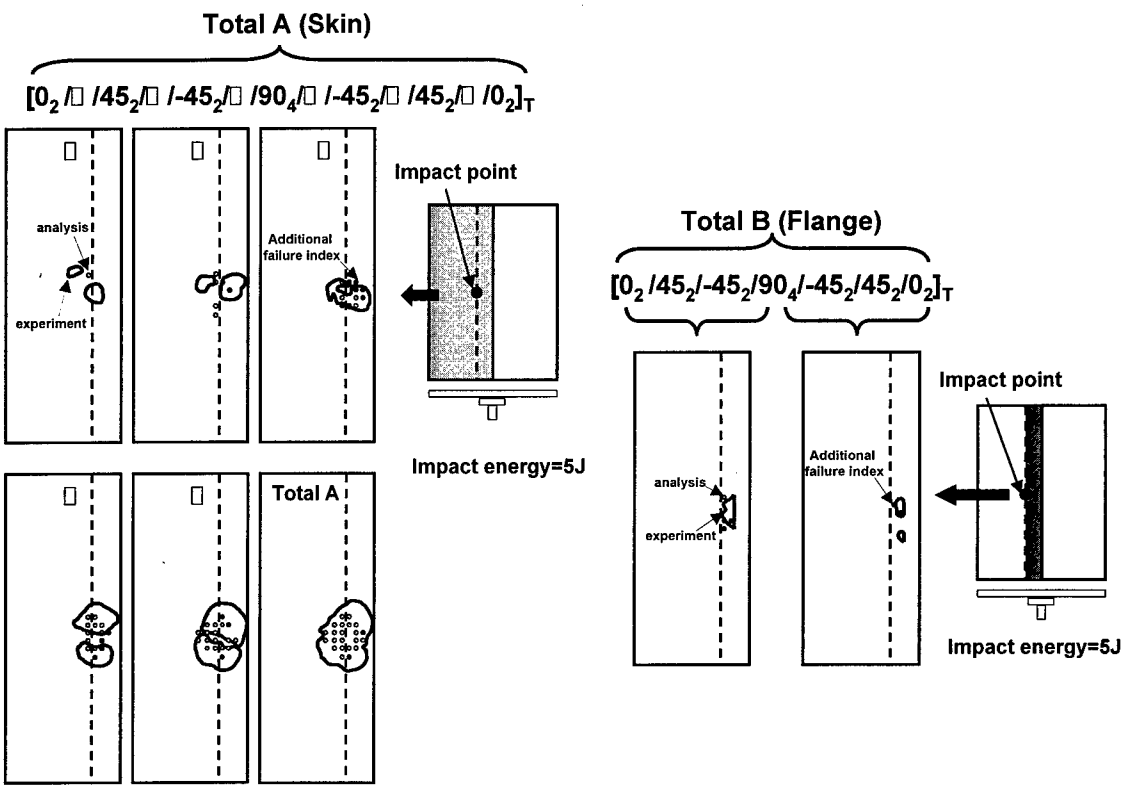


Fig. 4. Comparison of analysis with experiment about delamination distribution.

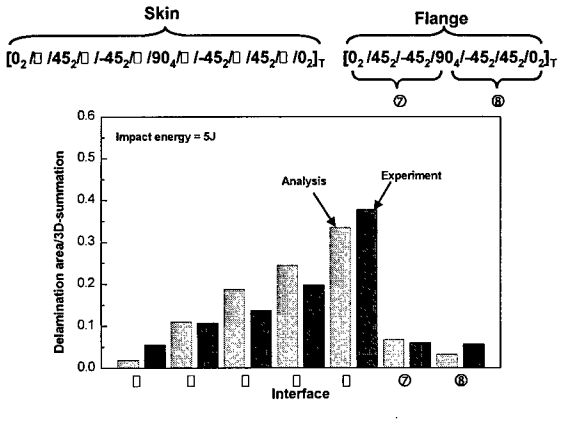


Fig. 5. Comparison of delamination size.

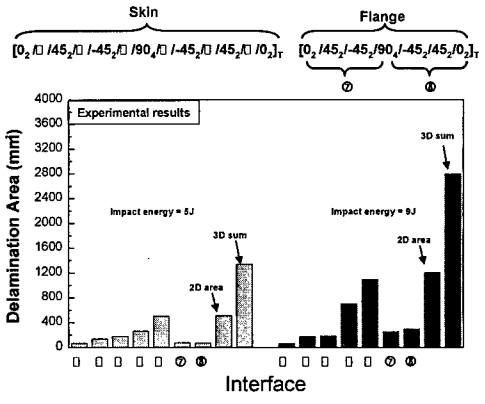


Fig. 6. Delamination distributions.

Therefore, the area obtained from the analysis can be applied to the prediction of residual strength. The delamination sizes according to the impact energy levels are summarized in Fig. 6. The 2D projected area of 9 *J* is twice as large as that of 5 *J* and the 3D summation area of 9 *J* is also twice as large as that of 5 *J*. Therefore, the increase rate of the 2D projected area is proportional to that of the 3D summation area.

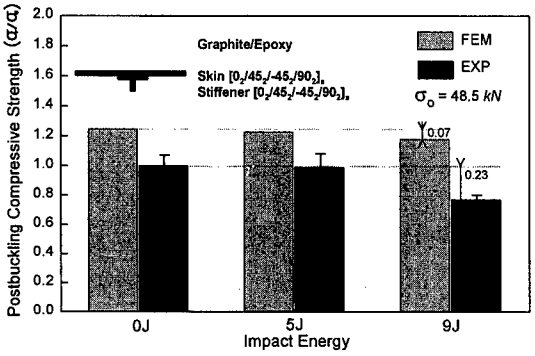


Fig. 7. Postbuckling residual strength.

In postbuckling analysis, the damaged region in the analysis was assumed as a rectangle. The postbuckling residual strengths are shown in Fig. 7. The reductions of the postbuckling compressive strength are dominant for 9 *J*, both the analysis and the experiment.

4. Conclusions

The impact damage of stiffened composite plates was predicted by the finite element analysis implemented by the modified failure criterion. The postbuckling strengths for stiffened composite plates with various impact energies were studied numerically and experimentally. The predicted postbuckling residual strengths showed good agreements with experiments.

REFERENCE

1. R.C.Madan, and M.J.Shuart, Composite Materials: Testing and Design(Ninth Volume), ASTM STP 1059, Philadelphia (1990) p.64
2. E.Greenhalgh, and D.Roberts, 11th Int. Conf. On Composite Materials, Gold Coast, Australia (1997) p.2-573.
3. H.Y.Choi, and F.K.Chang, J. Composite Materials, **26(14)** (1992) p.2134
4. I.H.Choi, and C.S.Hong, J. the Korean Society for Composite Materials, **22(4)** (1994) p.78
5. J.H.Kweon, C.S.Hong, and I.C.Lee, AIAA J., **33(2)** (1995) p.217

Key Engineering Materials Vols. 183-187 (2000) pp. 1195-1200
© 2000 Trans Tech Publications, Switzerland

Void Nucleation Models and Their Implications for the Material Behavior of Rubber-Modified Epoxies

H.-Y. Jeong

Department of Mechanical Engineering, Sogang University,
1 Shinsoo-dong, Mapo-gu, Seoul 121-742, Korea

Keywords: Porous Solid, Pressure-Sensitivity, Rubber-Modified Epoxy, Void Nucleation Model

ABSTRACT

A macroscopic yield criterion for porous solids with pressure-sensitive matrices modeled by Coulomb's yield criterion was obtained by generalizing Gurson's yield criterion with consideration of the hydrostatic yield stresses for a spherical thick-walled shell and by fitting the finite element results of a voided cube. The macroscopic yield criterion is valid for negative hydrostatic stresses as well as for positive hydrostatic stresses. From the yield criterion, a plastic potential function for the porous solids was derived either for plastic normality flow or for plastic non-normality flow of pressure-sensitive matrices. In addition, elastic relations, an evolution rule for the plastic behavior of the matrices, a consistency equation and a void volume evolution equation were derived to complete a set of constitutive relations. The set of constitutive relations was implemented into a finite element code ABAQUS to analyze the material behavior of rubber-modified epoxies. The cavitation and the deformation behavior were analyzed around a crack tip under Mode I plane strain conditions. In the analyses, the cavitation of rubber particles was considered via three different void nucleation models. The numerical results indicate that a circular cavitation zone can be obtained with void nucleation controlled by the macroscopic hydrostatic stress. The results also imply that the mean value and the standard deviation for the macroscopic hydrostatic stress-controlled void nucleation model can be determined by comparing the sizes of a plastic zone and a cavitation zone with those observed in experiments.

1. INTRODUCTION

In contrast to the classical plasticity theories, experiments showed that yielding of metals or polymers is dependent on the hydrostatic stress [1-6]. The dependency of yielding on the hydrostatic stress, so called the pressure-sensitivity of yielding, has been modeled by Coulomb's yield criterion. However, if there exist microvoids or soft inclusions even in a solid which does not show any pressure-sensitivity of yielding, the macroscopic yielding of the solid becomes pressure-sensitive. Taking into account the macroscopic pressure-sensitivity of yielding, Gurson [7,8] developed a yield function for porous solids.

It has been well known that some brittle polymers can be toughened by adding rubber particles. For example, some rubber-modified epoxies are ten times or more tougher than epoxy resins [9-11]. Experiments showed that as the rubber-modified epoxies deform, rubber particles cavitate and shear yielding occurs subsequently [9-11]. Therefore, in order to analyze the plastic deformation of the

rubber-modified epoxies, both the pressure-sensitivity of the matrices and the macroscopic pressure-sensitivity due to cavitated rubber particles should be taken into account. In addition, the cavitation can be considered as void nucleation occurring in the composite materials.

The author [12,13] and Lazzeri and Bucknall [14] developed two different yield functions for porous solids with pressure-sensitive matrices, but these functions are not valid for negative hydrostatic stresses. However, the new yield function presented in this paper is applicable to negative hydrostatic stresses as well as positive hydrostatic stresses. From the yield function, a plastic potential function for the porous solids was derived either for plastic normality flow or for plastic non-normality flow of pressure-sensitive matrices. In addition, elastic relations, an evolution rule for the plastic behavior of the matrices, a consistency equation and a void volume evolution equation were derived to complete a set of constitutive relations. The set of constitutive relations was implemented into a finite element code ABAQUS as a user material subroutine to analyze the material behavior of rubber-modified epoxies. The cavitation and the deformation behavior were analyzed around a crack tip under Mode I plane strain small-scale yielding conditions. In the analyses, the cavitation of rubber particles was considered via three different void nucleation models: maximum stress-controlled void nucleation model, hydrostatic stress-controlled void nucleation model and plastic strain-controlled void nucleation model. These models are expressed in the form of the normal distribution function [15]. The maximum stress-controlled void nucleation model resulted in a cavitation zone elongated perpendicular to the crack line, but the hydrostatic stress-controlled void nucleation model resulted in an almost circular cavitation zone. The plastic strain-controlled void nucleation model resulted in an unreasonably small cavitation zone formed along the crack line. All three void nucleation models resulted in a plastic zone along the crack line. It is noteworthy that the circular cavitation zone obtained only by the hydrostatic stress-controlled void nucleation model looks similar to that obtained by experiments. In addition, the mean value and the standard deviation required for the hydrostatic stress-controlled void nucleation model could be determined by using the contour plots of the hydrostatic stress around a crack and by comparing the sizes of the cavitation zone and the plastic zone obtained by numerical analyses with those obtained by experiments.

2. CONSTITUTIVE LAW

2.1. Yield Function and Plastic Potential Function

In order to develop a yield function for porous solids with pressure-sensitive matrices, the upper bound approach Gurson [7,8] relied on can not be used because it is difficult to find a kinematically admissible velocity field for the pressure-sensitive matrix modeled by Coulomb's yield criterion. Instead, the hydrostatic yield stress $(\Sigma_m)_y$ can be found, using the equilibrium equation and Coulomb's yield criterion, i.e. the lower bound approach, and it is expressed as follows.

$$(\Sigma_m)_y = \frac{\sigma_o}{\mu'}\{1 - f^{\left(\frac{\pm 2\mu'}{3\pm 2\mu'}\right)}\} \tag{1}$$

Here, σ_o is $\sqrt{3}\tau_o$, τ_o is the shear flow stress, μ' is $\sqrt{3}\mu$, μ is the pressure-sensitivity factor, and f is the void volume fraction. It can be proven from Eq.1 that $(\Sigma_m)_y$ becomes equal to $\pm\frac{2}{3}\sigma_o \log f$ as μ approaches 0. That is, $2f\cosh\left(\frac{3\Sigma_m}{2\sigma_o}\right)$ becomes equal to $1+f^2$, and Gurson's yield function is satisfied. However, when μ is not equal to 0, $2f\cosh\left\{\frac{3+\mathrm{sign}(\Sigma_m)2\mu'}{2\mu'}\log\left(1-\mu'\frac{\Sigma_m}{\sigma_o}\right)\right\}$ becomes equal to $1+f^2$.

In addition, a yield function for porous solids with pressure-sensitive matrices should reduce to

Gurson's yield function when μ is equal to 0, and it should reduce to Coulomb's yield criterion when f is equal to 0. Based on these requirements, a new yield function was proposed. Taking into account the interaction between voids, three parameters ($q_1 = 1.35,\ q_2 = 0.95, q_3 = 1.35$) were incorporated in the yield function. The three parameters were obtained by fitting the yield function to finite element results of macroscopic hydrostatic stresses and macroscopic effective stresses causing massive plastic deformation in a voided model.

$$\Phi_y(\Sigma,\sigma_o,f,\mu') = \left(\frac{\Sigma_e}{\sigma_o}\right)^2 + \left(1-\mu'\frac{\Sigma_m}{\sigma_o}\right)^2\left[2q_1 f\cosh\left\{q_2\frac{3+\mathrm{sign}(\Sigma_m)2\mu'}{2\mu'}\log\left(1-\mu'\frac{\Sigma_m}{\sigma_o}\right)\right\} - 1 - q_3 f^2\right] = 0 \quad (2)$$

Here, Σ is the macroscopic Cauchy stress exerting on the porous solid, Σ_e is the macroscopic effective stress, and Σ_m is the macroscopic hydrostatic stress.

Experiments showed that during plastic deformation steels or polymers modeled by Coulomb's yield criterion dilate less than is predicted by the normality plastic flow rule [4-6]. This means that the plastic potential function is not the same as the yield function. The plastic potential function $\Phi_p(\Sigma,\sigma_p,f,\beta')$ for porous solids with pressure-sensitive matrices can be obtained by replacing μ' with β' ($=\sqrt{3}\beta, \beta$ is the plastic dilatancy factor) in the yield function $\Phi_y(\Sigma,\sigma_o,f,\mu')$ and by finding a fictitious stress σ_p [12,13].

2.2. Void Nucleation Models and Void Volume Evolution Equation

The increase of void volume arises both from the growth of existing voids and from the nucleation of voids. For the nucleation of voids, two models have been used; one is the stress-controlled void nucleation model and the other is the plastic strain-controlled void nucleation model. For the stress-controlled void nucleation model the sum of the tensile flow stress and the macroscopic hydrostatic stress was used as the controlling stress in many researches [16-18]. The sum was suggested to be an approximation to the maximum stress transmitted across the particle-matrix interface, and void nucleation was believed to depend on the sum [19]. However, the cavitation zones created in rubber-modified epoxies were almost circular [11,20], and they look similar to the contour plots of the macroscopic hydrostatic stress. Therefore, in this paper the macroscopic hydrostatic stress was also evaluated as the controlling stress.

The void volume evolution equation can be expressed as follows.

$$\dot{f} = (1-f)[tr(D^p) - \beta'\dot{\varepsilon}_e^p] + A\dot{\sigma}_o + B\dot{\Sigma}_m + C\dot{\varepsilon}_e^p \quad (3)$$

Here, $\dot{\varepsilon}_e^p$ is the effective plastic strain rate, and $tr(D^p)$ is the trace of the rate-of-deformation tensor. For the maximum stress-controlled void nucleation model,

$$A = B = \frac{f_B}{s\sigma_y\sqrt{2\pi}}\exp\left[-\frac{1}{2}\left(\frac{\sigma_o+\Sigma_m-\sigma_N}{s\sigma_y}\right)^2\right],\ C = 0 \quad (4)$$

For the macroscopic hydrostatic stress-controlled void nucleation model,

$$A = 0,\ B = \frac{f_B}{s\sigma_y\sqrt{2\pi}}\exp\left[-\frac{1}{2}\left(\frac{\Sigma_m-\sigma_N}{s\sigma_y}\right)^2\right],\ C = 0 \quad (5)$$

For the plastic strain-controlled void nucleation model,

$$A = B = 0, C = \frac{f_B}{s\sqrt{2\pi}} \exp\left[-\frac{1}{2}\left(\frac{\varepsilon_e^p - \varepsilon_N}{s}\right)^2\right] \tag{6}$$

Here, f_B is the volume fraction of void nucleating particles, s and σ_N (or ε_N) are the standard deviation and the mean value of the normal distribution function, respectively.

2.3. Material Properties of Rubber-Modified Epoxies

Some polymers including epoxy show initial strain softening and subsequent hardening as well as strain-rate sensitivity. A simple power law was adopted to account for the strain-rate sensitivity, and a combination of a power law and a logarithmic function was used to account for the strain-softening-and-hardening. In addition, the Young's modulus and Poisson's ratio for porous solids become different from those for the matrices especially when the void volume fraction is large, and they were calculated by adopting the self-consistent scheme combined with the average stress scheme [21]. Detailed explanations on these material properties can be found in author's previous paper [22].

3. MATERIAL BEHAVIOR OF RUBBER-MODIFIED EPOXIES

3.1. Cavitation Zone in a Rubber-Modified Epoxy and Hydrostatic Stress Contours

Pearson and Yee [11] conducted four-point bending tests on double-notched specimens of the rubber-modified epoxy (DGEBA/PIP/CTBN-8(10)) which contained 12% of volume fraction of CTBN rubber particles, and they obtained an optical microscopy at the midplane near the crack tip. The optical microscopy showed a shear yielding zone formed along the crack line and a circular cavitation zone surrounding the shear yielding zone. The length of the shear yielding zone was about 600 μm, and the diameter of the cavitation zone was about 1600 μm. They also reported the fracture toughness K_{IC} to be 2.10 $MPa\, m^{1/2}$.

Based on the asymptotic solutions of stress fields around a crack tip under Mode I plane strain conditions, the contour of the hydrostatic stress can be expressed in polar coordinates as follows.

$$r = d\,(1 + \cos\,\theta) \qquad \text{where} \quad d = \frac{(1+\nu)^2 K_I^2}{9\pi\Sigma_m^2} \quad \text{and } \nu \text{ is Poisson's ratio} \tag{7}$$

A contour plot (the bigger solid line) of hydrostatic stress and a circle passing through the same intersection points on the x- and y-axes are shown in Fig. 1. It is easy to prove that the diameter of the circle is equal to $2.5d$. Since in the early stage of ductile fracture a crack grows in a stable manner, the contour plot of a hydrostatic stress grows and advances as shown in Fig. 1. Therefore,

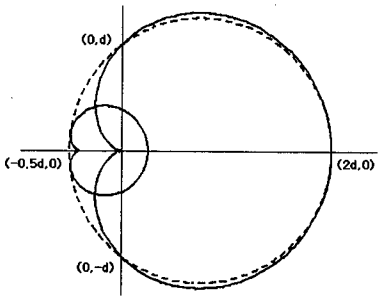


Fig. 1. Contour plots of the hydrostatic stress in front of a crack tip

it can be said that in the experiments [11] the circular cavitation zone was created with the crack growing in a stable manner for some distance, and the hydrostatic stress can be attributed to the rubber cavitation. Thus, $2.5d = 1600\,\mu m$, from which the hydrostatic stress causing cavitation in the rubber-modified epoxies can be approximated to be 22.3 *MPa*.

Assume that the void volume fraction at the boundary of the cavitation zone is about 0.005 which is 4.17% of the total volume fraction of rubber particles. Then, the mean value and the standard deviation for the hydrostatic stress-controlled void nucleation model can be determined in such a way that the probability of the normal distribution function is equal to about 4.17% as the hydrostatic stress increases from 0 *MPa* to 22.3 *MPa*.

3.2. Material Behavior around a Crack-Tip in a Rubber-Modified Epoxy

In order to evaluate the validity of void nucleation models for modeling the rubber cavitation and subsequent material behavior of rubber-modified epoxies, the constitutive law along with the void nucleation models were implemented as a user material subroutine in ABAQUS. For the hydrostatic stress-controlled void nucleation model, two sets of the mean value and the standard deviation were selected; $\sigma_N = 0.750\sigma_y, s = 0.260$; $\sigma_N = 1.333\sigma_y, s = 0.712$. For the maximum stress-controlled nucleation model, $\sigma_N = \sigma_y, s = 0.25$ were used. Finally, for the plastic strain-controlled

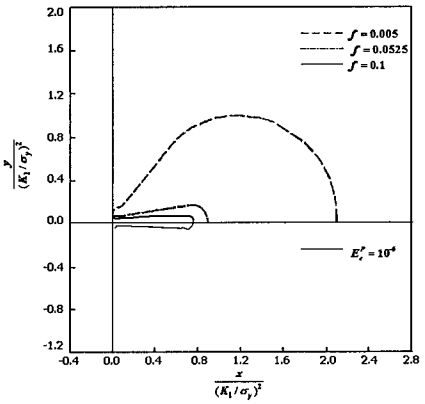


Fig. 2. Contour plots of the void volume fraction and the plastic strain with $\sigma_N = 0.750\sigma_y$ and $s = 0.260$

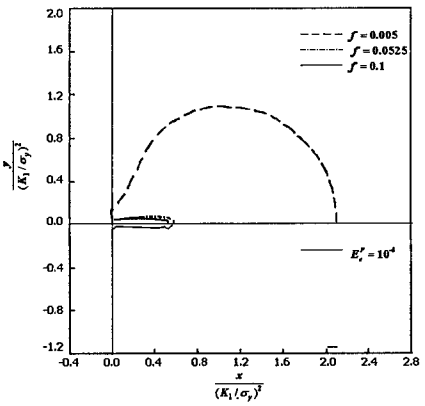


Fig. 3. Contour plots of the void volume fraction and the plastic strain with $\sigma_N = 1.333\sigma_y$ and $s = 0.712$

void nucleation model, $\varepsilon_N = 10^{-6}, s = 2.5\times10^{-7}$ were used. Since the maximum stress-controlled void nucleation model resulted in a cavitation zone elongated perpendicular to the crack line, and the plastic strain-controlled void nucleation model resulted in very small cavitation zone, these two void nucleation models do not seem to be appropriate for modeling the rubber cavitation. However, the two sets of the standard deviation and the mean value for the hydrostatic stress resulted in almost circular cavitation zones as shown in Figs. 2 and 3.

The dimensionless length of the shear yielding zone and the dimensionless diameter of the cavitation zone observed in the experiment are $x/(K_I/\sigma_y)^2 = 0.77$ and 2.04, respectively. Therefore, the sizes of the cavitation zones the hydrostatic stress-controlled void nucleation model resulted in are comparable to that of the cavitation zone observed in the experiment. However, the length of the shear yielding zone is comparable when $\sigma_N = 0.750\sigma_y$.

4. CONCLUSIONS

The constitutive law along with the hydrostatic stress-controlled void nucleation model resulted in the cavitation zone and the shear yielding zone which are in a good agreement with those observed in the experiment. The mean value and the standard deviation required for the void nucleation model could be determined by using the contour plots of the hydrostatic stress around a crack and by comparing the sizes of the cavitation zone and the plastic zone obtained by numerical analyses with those obtained by experiments. The constitutive law along with the void nucleation model can be utilized for the material behavior analysis of porous solids with pressure-sensitive matrices such as rubber-modified epoxies.

REFERENCES

1. S. S. Sternstein and L. Ongchin, Am. Chem. Soc. Polym. Prep., **10** (1969) p.1117
2. S. Rabinowitz, I. M. Ward and J. S. C. Perry, Journal of Materials Science, **5** (1970) p.29
3. J. A. Sauer, K. D. Pae and S. K. Bhateja, J. of Macrom. Science-Physics, **B8** (1973) p. 631
4. W. A. Spitzig, R. J. Sober and O. Richmond, Acta Metallurgica, **19** (1975) p.1129
5. W. A. Spitzig, R. J. Sober and O. Richmond, Metallurgical Transactions, **7A** (1976) p.1703
6. W. A. Spitzig and O. Richmond, Polymer Engineering and Science, **19** (1979) p.1129
7. A. L. Gurson, Ph.D. Thesis, Brown University (1975)
8. A. L. Gurson, Journal of Engineering Materials Technology, **99** (1977) p.2
9. A. F. Yee and R. A. Pearson, Journal of Materials Science, **21** (1986) p.2462
10. R. A. Pearson and A. F. Yee, Journal of Materials Science, **21** (1986) p.2475
11. R. A. Pearson and A. F. Yee, Journal of Materials Science, **26** (1991) p.3828
12. H.-Y. Jeong, Ph.D. Thesis, University of Michigan (1992)
13. H.-Y. Jeong and P. Jwo, International Journal of Solids and Structures, **32** (1995) p.3669
14. A. Lazzeri and C. B. Bucknall, Journal of Materials Science, **28** (1993) p.6799
15. C.-C. Chu and A. Needleman, Transactions of the ASME, **102** (1980) p.249
16. V. Tvergaard, Journal of the Mechanics and Physics of Solids, **30** (1982) p.399
17. J. Pan, M. Saje and A. Needleman, International Journal of Fracture, **21** (1983) p.261
18. A. Needleman and V. Tvergaard, J. of the Mechanics and Physics of Solids, **35** (1987) p.151
19. A. S. Argon and J. Im, Metallurgical Transactions, **6A** (1975) p.839
20. A. F. Yee, D. Li and X. Li, Journal of Materials Science, **28** (1993) p.6392
21. G. P. Tandon and G. J. Weng, Journal of the Applied Mechanics, **55** (1988) p.126
22. H.-Y. Jeong and J. Pan, Polymer Engineering and Science, **36** (1996) p.2306

Key Engineering Materials Vols. 183-187 (2000) pp. 1201-1206
© 2000 Trans Tech Publications, Switzerland

On-line Frequency Estimation and Adaptive Vibration Control of Composite Structures with Delaminations

Keun-Ho Rew, Jae-Hung Han and In Lee

Department of Aerospace Engineering, Korea Advanced Institute of Science and Technology, 373-1 Kusong-dong, Yusong-gu, Taejon 305-701, Korea

Keywords: Adaptive Vibration Control, Composite Structures, Delamination, On-Line Frequency Estimation, Piezoelectric Actuator

ABSTRACT

An on-line natural frequency estimation method and an adaptive vibration control of composite beams are investigated. Once delaminations occur in the composite structures, dynamic characteristics of the structures are changed including the decreases of natural frequencies due to the defected stiffness. In this paper, a real-time frequency estimation method is proposed to detect frequency shifts of the specimen. In addition, an on-line adaptive controller, named Adaptive Positive Position Feedback (APPF), is suggested. Glass/Epoxy composite beams with delaminations at different locations are manufactured and surface bonded piezoceramic actuator is used as an actuator. It is found that the estimated frequencies converge to real ones, and successful multi-mode vibration suppression is achieved using the proposed on-line adaptive controller.

1. INTRODUCTION

The active vibration control has been an interesting research topic, since more and more lightweight materials are adopted in the structural members. Generally, the controllers are designed under the assumption that the system is time-invariant. Local structural failures such as delaminations in composite structures yield the variations of dynamic characteristics. Structures with minor failures can still support static loadings. However, the changes of dynamic characteristics can cause the inefficiency of the time-invariant controllers, or sometimes induce unstable behaviors of the system.

One of the possible approaches to overcome this problem is the application of adaptive controls. The early research motive of the adaptive vibration control was the vibration suppression of the changeable space structures such as deployable structures and robot manipulators. Many algorithms on the adaptive controls can be found in reference [1] including adaptive filtering, adaptive pole placement, and artificial neural networks. Filtered-x-LMS feedforward control was successfully applied to adaptive noise control [2].

However, adaptive multi-modal vibration control in real-time is not well explored yet. One reason is the spillover phenomenon, where the control energy for the target modes flows into

undesired vibration modes. Another obstacle is heavy computational burden of the algorithm, since the adjustment of the controller should be carried out at every time step. Therefore, it is required to develop a fast algorithm for system identification and vibration controller with less spillover.

In this paper, a multi-modal frequency estimation method is proposed to detect the frequency shifts of the specimen in real-time. In addition, an efficient adaptive multi-modal control algorithm, named Adaptive Positive Position Feedback (APPF), is suggested and applied to experimental vibration suppressions of composite beams with delaminations.

2. ADAPTIVE POSITIVE POSITION FEEDBACK

The proposed APPF controller is composed of a frequency estimation block and a variable Positive Position Feedback (PPF) block.

2.1. Estimation of Multi-modal Frequencies

Since 1970's, many algorithms have been developed for the on-line multi-modal frequency estimation in the fields of radar, sonar, communication, and so on [3-4].

The Recursive Least Squares (RLS) method and the Bairstow method comprise the present frequency estimation algorithm. RLS method recursively estimates the coefficients of characteristic equation of a linear system with relatively light computational load, and gives good converged results from arbitrary initial parameters.

The measured signal, y, can be modeled in a characteristic equation as follows:

$$y(N) = -\sum_{k=1}^{n} a_k y(N-k) + \varepsilon(N) \qquad (1)$$

where ε is the error between measured and estimated signals. The square of the error is minimized with respect to the following objective function using RLS method,

$$V = \sum_{i=1}^{n} \lambda^{n-i} \varepsilon^2(i) \qquad (2)$$

where λ is a forgetting factor, which weighs the relative importance between the past and present errors. The smaller λ is, the more adaptable to the changes of system dynamics RLS method becomes, but the more sensitive to noise it becomes. The forgetting factor is selected to be 0.998, in this paper.

The even order characteristic equation is factorized into couples of 2nd order characteristic equations by using iterative algorithms in order to obtain natural frequencies in real-time. The Bairstow method, which is devised by Hitchcock and Bairstow, is used for the decomposition of the characteristic equation in this study. Since only arithmetic operations (plus, minus, multiplication, and division) are used, it is very concise and fast to give good convergence. In addition, only real variables are needed to implement the algorithm so that computer memory can be used more efficiently. It can be stated from our various simulation studies that the computational load of the Bairstow method is, in general, much less than the half of that of the subspace iteration method.

After the natural frequencies are identified with the Bairstow method, those frequencies are sorted in magnitude using a simple straight insertion algorithm [4].

2.2. Variable PPF Controller

Fanson and Caughey proposed a simple feedback control algorithm for the vibration suppression, named the PPF controller, in 1987 [5]. The PPF controller has been applied to diverse vibration control problems since it is practical and inherently prevents spillover phenomena. However, it has disadvantages such that it will add flexibility at low frequency and can be applied only to vibration or noise suppression.

Here is the transfer function of a PPF controller for a single mode vibration,

$$H_{PPF}(s)_i = \frac{\omega_f^2}{s^2 + 2\varsigma_f \omega_f s + \omega_f^2} \cdot Kc_i \qquad (3)$$

where $H_{PPF}(s)_i$ is the PPF controller for a specific mode; $(\ )_i$ is the index for the mode to be controlled; ω_f is the filter frequency of the PPF controller, which is generally set to the same value as ω_n, the natural frequency of the structure; ζ_f is the damping ratio of the PPF controller. When it increases, the robustness to natural frequency variations increases, but the performance is degraded. The value of ζ_f was chosen as 0.2 in this study. Kc_i's are pre-adjusted gains. Since the lowest two modes are to be controlled, two PPF controllers are connected in parallel, in this paper.

3. DESCRIPTION OF VIBRATION CONTROL EXPERIMENTS

Four types of cantilevered Glass/Epoxy composite beams with delamination in various locations are manufactured as shown in Table 1 and Fig. 1. The delaminations are artificially made through inserting Teflon films into midplane of the specimens. A piezoceramic actuator and a laser displacement sensor are used. Since piezoelectric actuators exert control forces through induced strains on the base composite structures, actuators are bonded near the root of the specimen.

Table 1. The specification of delaminated beams (dimension : *mm* from root).

Specimen No.	1st natural freq. [*Hz*]	2nd natural freq. [*Hz*]	Delamination [*mm*]	1. Base beam : Glass/Epoxy [0/+45/-45/90]$_s$ 0.85x20x240
dbX	11.25	66.50	None	2. Detection point: 150 from the root
dbA	11.25	66.25	0 ~ 25	
dbB	11.25	62.00	25 ~ 50	3. Piezo-ceramic : Fuji C82 0.4 x 20 x 25
dbC	10.75	58.00	50 ~ 75	

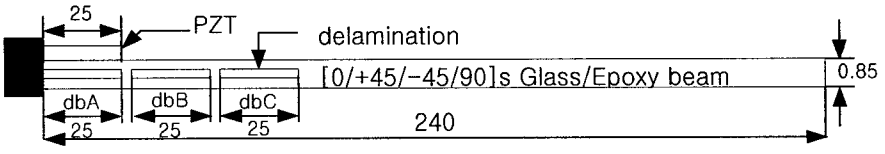


Fig. 1. Composite beams with delaminations (dimension : *mm*).

The experimental setup for the real-time frequency estimation and adaptive control has been prepared as shown in Fig. 2. The measured signal from the laser displacement sensor is fed into the DSP board and the control signal is calculated in DSP controller. External random disturbance generated by the source module of the FFT analyzer is mixed with the control output via the summing circuit, and is applied to the piezoelectric actuator after 500 times voltage amplification. The frequency estimation block is performed at every 6 *msec*, i.e., 167 *Hz*, and the control signal is calculated at 1 kHz. After the estimated frequencies are converged, the gains, Kc_i's are fixed to $0.3\times[1, -6]$, and the closed loop frequency responses between the random external disturbance and the sensor signal are monitored using a FFT analyzer.

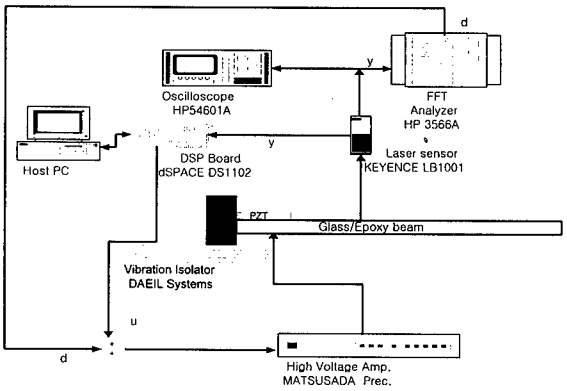


Fig. 2. Configuration of experimental setup.

4. EXPERIMENTAL RESULTS AND DISCUSSIONS

The measured signal from the laser displacement sensor and estimated signals by Eq. (1) are in coincident in moderate precision as shown in Fig. 3.

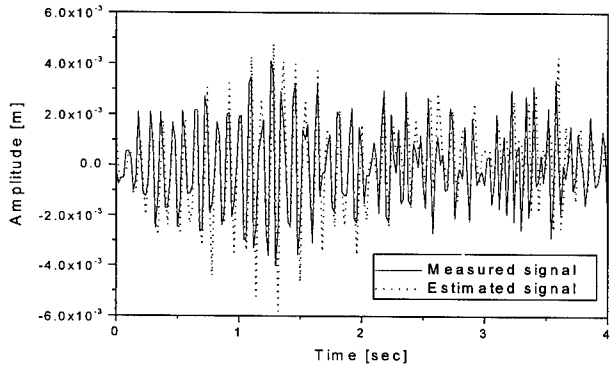


Fig. 3. Measured and estimated signals for specimen dbX.

One example of the natural frequency estimation process is presented in Fig. 4. From arbitrary initial values, the estimated natural frequencies are converged to real ones, which are measured from off-line modal testing. The first and second natural frequencies of the specimen dbC are reduced as much as 4.44% and 12.8%, respectively, with respect to the specimen dbX. The overall variations in frequency response functions according to delamination locations are shown in Fig. 5.

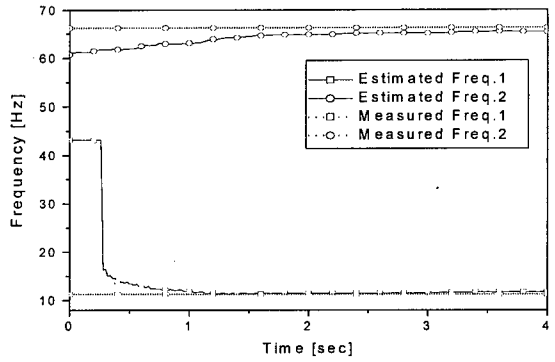


Fig. 4. Natural frequency estimation results for specimen dbX.

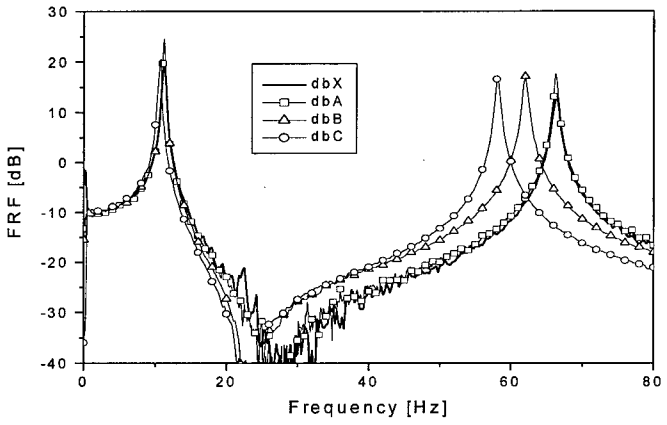
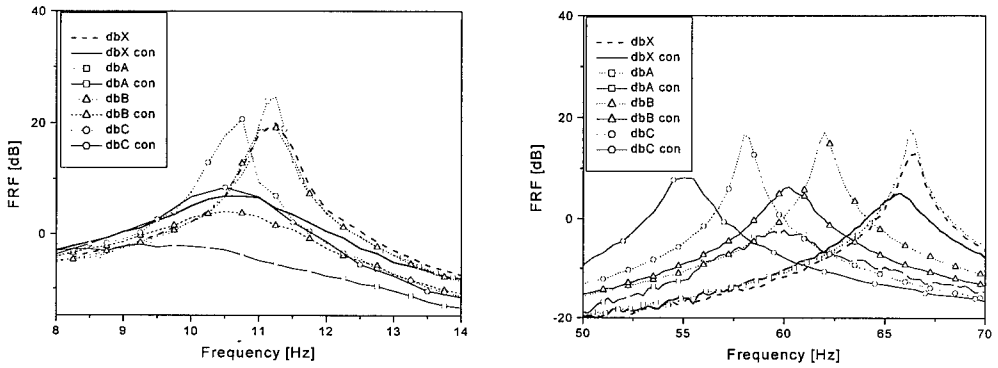


Fig. 5. Overall frequency responses without control.

It is also observed that frequency variations do not deteriorate the estimation performance. Experimental vibration control results in frequency domain are presented in Fig. 6, where "con" indicates the controlled responses. Significant vibration reduction is achieved for the lowest two modes, around 15 and 10 dB, respectively. Note that we did not redesign the controllers for each specimen. The controller is automatically adapted to each specimen.



(a) 1st mode frequency responses (b) 2nd mode frequency responses

Fig. 6. Adaptive vibration control results in frequency domain.

5. CONCLUSION

An on-line natural frequency estimation method and an adaptive vibration controller, APPF, are proposed for the suppression of multi-mode vibrations of the delaminated composite beams with piezoelectric actuators. The experimental results show that the proposed frequency estimation algorithm effectively estimates the real natural frequencies in real-time and that the APPF controller can reduce the multi-mode vibrations of structures.

It is expected that the proposed frequency estimation method can be applied to the failure detection of the structures. In addition, the present APPF controller can be applied in diverse vibration control problems including lightweight structures with varying natural frequencies.

REFERENCE

1. G.C.Goodwin, and K.S.Sin, Adaptive Filtering Prediction and Control, 2nd ed., Prentice-Hall Inc., (1984).
2. S.M.Kim, Active Noise Control Algorithm Based on Noise Frequency Estimation, MS thesis of department of mechanical engineering of KAIST, (1998).
3. P.A.Regalia, Adaptive IIR Filtering in Signal Processing and Control, Marcel Denkker Inc., (1995), Ch.10.
4. W.H.Press, et al, Numerical recipes in C, 2nd ed., The Cambridge Press, (1988), Ch.9.
5. J.L.Fanson, and T.K.Caughey, AIAA SDM Conference, Paper No. 87-0902, (1987).

Key Engineering Materials Vols. 183-187 (2000) pp. 1207-1212
© 2000 Trans Tech Publications, Switzerland

Strength and Fracture of Cu-based Filamentary Nanocomposites

S.I. Hong, J.H. Chung and H.S. Kim

Department of Metallurgical Engineering, Chungnam National University,
Taedok Science Town, Taejon 305-764, Korea

Keywords: Barrier Strengthening, Cu-Nb, Filament, Grain Boundary, Nanocomposite, Strength, Substructure Strengthening

ABSTRACT

The strength of Cu-Nb nanocomposite was predicted as a function of drawing strain by assuming that the contribution of the partial grain boundaries (connecting the edge of Nb filaments) to the strength decreases as the interfilamentary spacing decreases at high drawing strains. The good agreement between the predicted yield stress and the experimental data at drawing strains between 6 and 9.5 supports that the effectiveness of substructure strengthening of Cu and Nb in heavily deformed Cu-Nb nanocomposites decreases with increasing drawing strain. At drawing strains above 10, Nb filaments reached a thickness of approximately 10 nm and thereafter further working resulted in random rupture of the filaments rather than continued plastic deformation and thinning, which may result in the slower increase of the strength than the predicted values with drawing strain. The insensitivity of the ductility of Cu-Nb nanocomposites to Nb content is associated with the crack initiation from Nb filaments. Since the fracture strain of Nb filaments would remain the same in various Cu-Nb microcomposites at a given drawing strain, the ductility is insensitive to Nb content.

1. INTRODUCTION

It has been well documented that heavily-drawn, copper-niobium nanocomposites possess high strength and high conductivity [1, 2]. Since niobium has little solubility in copper, the conductivity of the copper is not strongly affected by the addition of niobium. Following extensive mechanical deformation of Cu-Nb, niobium dendrites transform into fine niobium ribbons as a result of the <110> niobium texture upon drawing [1]. This nanostructure contributes to the ultrahigh strength of Cu-Nb nanocomposites. The strength of heavily deformed Cu-Nb exceeds that predicted by the rule-of-mixtures (ROM), and a fundamental understanding of the strengthening mechanisms involved has been the subject of much discussion [1-3]. Spitzig and his coworkers [1, 2] suggests a barrier strengthening model while Funkenbusch and Courtney [3] believe that stored dislocations have a role in substructural hardening. Hangen and Raabe [5] recently proposed an analytical model for the calculation of the yield strength of Cu-Nb nanocomposite. The model of Hangen and Raabe [4] and that of Spitzig and his coworkers [1, 2] have a great deal of resemblance since both models attribute the strength to the difficulty of propagating plastic flow through the interface. The purpose of this

study was to enhance our understanding of the strengthening mechanisms associated with Cu-Nb nanocomposites by examiningthe previous studies on mechanical and microstructural stability of Cu-based nanocomposites [1-8].

2. ANALYSIS

2.1. Strength of Heavily Cold Drawn Cu-Nb Nanocomposite

.Verhoeven et al.[2] and Spitzig et al. [1] developed a strengthening model based on the critical stress to move dislocations in the matrix between the interphase barriers. Considering that both phases contribute to the flow stress, the rule of mixtures was proposed to predict the composite strength. The yield strength of Cu-Nb nanocomposites can be described as follows:

$$\sigma_{Cu\text{-}Nb} = f_{Cu}\{ \sigma_0 + [MAGb/2\pi\lambda] \ln(\lambda/b) \}_{Cu} + f_{Nb}\{ \sigma_0 + [MAGb/2\pi t] \ln(t/b) \}_{Nb} \quad (1)$$

where $\sigma_{Cu\text{-}Nb}$ is the yield strength of the Cu-Nb nanocomposite, σ_0(Cu) and σ_0(Nb) are friction stresses in the each phases, f_{Cu} and f_{Nb} are the volume fractions of the copper and niobium, M is the Taylor factor (M equal to 3 in F.C.C. metals and 2 in B.C.C. metals), A is a constant depending on the character of the dislocation (1.21 for mixed dislocations) G(Cu) and G(Nb) are shear moduli (48.3 GPa for Cu and 37.5 GPa for Nb), b(Cu) and b(Nb) are Burgers vectors (0.26 nm for Cu and 0.29 for Nb), λ(Cu) is the interfilamentary Cu thickness and t(Nb) are the thicknesses of Nb filament. The values of λ(Cu) and t(Nb) can be given by the following equations [2]:

$$\lambda(Cu) = C \exp(-d\,\eta), \qquad t(Nb) = C' \exp(-d'\,\eta) \quad (2)$$

where C, C', d and d' are constants. The values of these constants were determined to be 14204, 1353, 0.53 and 0.49 respectively (see Fig. 3 of Ref. 2). Actually Verhoeven et al. [2] used the equation (1) to predict the ultimate tensile strength of Cu-Nb nanocomposite, which is not exactly correct since equation (1) relates yield behavior as noted by Verhoeven et al. [2]. It has been suggested that the model of Verhoeven et al. [2] overestimates the yield strength of Cu-based nanocomposites [9] especially at high drawing strains ($\eta > 4$). The overestimation of the yield stress in the model of Verhoeven et al. was attributed to the significant exponential dependence of the predicted strength on the drawing ratio [9] or the stress concetration due to dislocation pile-ups [4] which was not considered in the model of Verhoeven et al. [2].

Equation (1) can be rearranged to separate the total yield strength into two components, the substructural strengthening component, σ_{sub}(Cu-Nb), and the filament boundary strengthening term, $\sigma_{filament}$(Cu-Nb), as follows:

$$\sigma_{Cu\text{-}Nb} = \sigma_{sub}(Cu\text{-}Nb) + \sigma_{filament}(Cu\text{-}Nb) = f_{Cu}\sigma_0(Cu) + f_{Nb}\sigma_0(Nb) + f_{Cu}\{[MAGb/2\pi t] \ln(t/b) \}_{Cu} + f_{Nb}\{[MAGb/2\pi t] \ln(t/b) \}_{Nb} \quad (3)$$

where σ_{sub}(Cu-Nb)) is the strengthening component which result from dislocation structure, subgrain boundaries, grain boundaries, precipitates, alloying elements etc. in each phase and $\sigma_{filament}$ (Cu-Nb) is the strengthening component associated with the Hall-Petch type interaction between the dislocations and the phase boundaries. Verhoeven et al. [2] used the ultimate tensile strengths of comparably deformation processed pure Cu and pure Nb wires for friction stresses, σ_o(Cu) and σ_o(Nb). It is well known that the microstructure of heavily deformed Cu-Nb nanocomposites is much finer than pure Cu processed in a similar manner because the recovery, recrystallization, and grain growth cycle is effectively blocked by Nb filaments [1].

In Fig. 1(a)-1(d), the schematic microstructures of Cu-Nb nanocomposites at a low (1(a) and 1(b)) and a high (1(c) and 1(d)) drawing ratio are shown. Fig. 1(a) and 1(c) show the longitudinal sections and Fig. 1(b) and 1(d) show the transverse sections. At low drawing strains, the microstructural scale of the Cu matrix is finer than the spacing between the Nb phases. Therefore, it may be reasonable to assume that the substructural strengthening in pure Cu and Nb phase fully contribute to the yield strength of Cu-Nb nanocomposite, $\sigma_{Cu\text{-}Nb}$, at low drawing strains. The substructure strengthening term σ_{sub}(Cu-Nb) can be determined as the volumetric weighted average of the yield strengths of the individual phases. Since no reliable yield strengths of pure Cu and Nb as a function of the drawing strain are available, they were calculated from the UTS [1, 4]. It is well known that the work hardenability (i.e. the difference between the UTS and the YS) decreases with deformation strain. Therefore the substructure strengthening term σ_{sub}(Cu-Nb) at low draw strains was assumed to be given by the following equation:

$$\sigma_{sub}(\text{Cu-Nb}) = (0.5 + 0.04\,\eta)\,[f_{Cu}\,\sigma_{UTS}(\text{Cu}) + f_{Nb}\,\sigma_{UTS}(\text{Nb})] \quad (4)$$

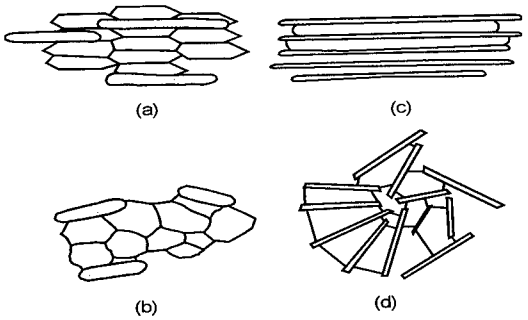


Fig. 1. Schematic microstructures of Cu-Nb nanocomposites at a low (1(a) and 1(b)) and a high (1(c) and 1(d)) drawing ratio. The longitudinal (1(a) and 1(c)) and transverse sections (1(b) and 1(d))

At high drawing strains where the microstructural scale of the Cu matrix is limited by Nb filaments [1], no substantial elongated cells and/or grains, which were known to strengthen the heavily deformed pure Cu were observed (Fig. 1(c) and 1(d)). The effectiveness of the substructure

strengthening due to elongated grains and cells in the Cu matrix of the Cu-Nb nanocomposite at high drawing strains would be much lower than that expected from the UTS or the YS of the heavily deformed pure Cu. The substructure strengthening in metals can also be described by an equation of the Hall-Petch type. Since the total grain boundary area of the array of the cylinderical elongated subgrains and/or grains is inversely proportional to the diameter of the cylinder, the Hall-Petch type equation can be modified as follows:

$$\sigma = \sigma_0 + k\,\mathbf{d}^{-1/2} = \sigma_0 + k'\,\mathbf{S}^{1/2} \qquad (5)$$

where **d** is the separation of the boundaries of elongated cells, subgrains or grains, **S** is the total boundary area of elongated cells, subgrains or grains and k and k' are constants. As shown in Fig. 2, in heavily drawn Cu-Nb, only partial grain boundaries connecting the edge of Nb filaments were observed [7, 8]. Fig. 2(a), 2(b) and 2(c) show schematically how the partial grain boundaries connecting the edge of Nb filaments were formed progressively with decreasing interfilamentary Cu thickness, λ. The cylindrical grain cannot be squeezed out because the symmetric deformation around the drawing axis [1] cannot be restrained outside the volume protected by Nb filaments. The total boundary area of subgrains and/or grains decreases with drawing strain (Fig. 2) since the boundaries of elongated cells, subgrains and/or grains existed at lower drawing strains (Fig. 1(a) and 1(b)) may become unstable and a great deal of them may be absorbed at the interfaces of Nb filaments as the interfilamentary Cu thickness, λ, become smaller than the equlibrium size, d_{eq}, of elongated subgrains and/or grains with increasing drawing strain (Fig.1(c) and 1(d)).

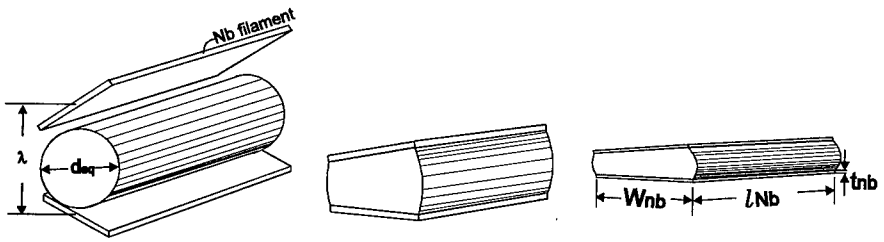


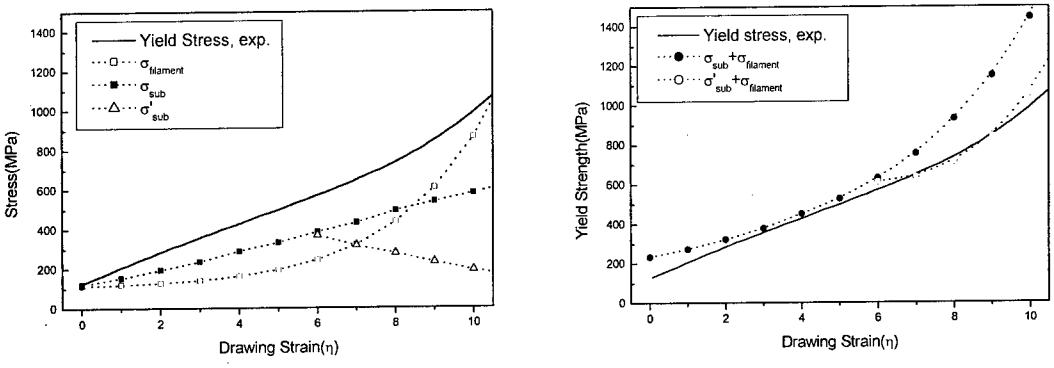
Fig. 2. A schematic illustration on the formation of the partial grain boundaries (connecting the edge of Nb filaments) with decreasing interfilamentary Cu thickness, λ.

The total boundary area of elongated subgrains and grains at high drawig strains may be proportional to the ratio (λ/W_{Nb}) of the interfilamentary Cu thickness, λ, to the width, W_{Nb}, of Nb filament as shown in Fig. 2(b) and 2(c). Therefore, the substructure strengthening due to elongated subgrains and grains in the Cu matrix of the Cu-Nb nanocomposite may be proportional to $(\lambda/W_{Nb})^{1/2}$ as shown in equation (5). Therefore the substructure strengthening term σ_{sub}'(Cu-Nb) at high drawing strains can be expressed as follows:

$$\sigma_{sub}'(\text{Cu-Nb}) = (\lambda/W_{Nb})^{1/2}\{(0.5 + 0.04\,\eta)\,[f_{Cu}\,\sigma_{UTS}(\text{Cu}) + f_{Nb}\,\sigma_{UTS}(\text{Nb})]\} \qquad (6)$$

The yield strength of Cu-Nb nanocomposites at high drawing strains can be described as the sum of σ_{sub}'(Cu-Nb) and $\sigma_{filament}$ (Cu-Nb).

In Fig. 3(a), the contribution of σ_{sub}(Cu-Nb), σ_{sub}'(Cu-Nb) and $\sigma_{filament}$ (Cu-Nb) to the total yield strength are shown separately. to the total yield strength are shown separately. It should be noted that σ_{sub}'(Cu-Nb) gradually decreases at high drawing strains. As shown in Fig. 3(a), σ_{sub}'(Cu-Nb) decreases with increasing drawing strain. The decrease of σ_{sub}'(Cu-Nb) was attributed to the decrease of the effectiveness of the substructure strengthening due to elongated subgrains and grains. In Fig. 3(b), the observed yield stress [1, 5] is plotted along with the yield stress predicted from equations (3) and (4) for low drawing strains (η<5.5, represented by closed circles) and that predicted from equations (3) and (6) for high drawing strains (η>5.5, represented by open circles). As shown in this figure, the yield stress predicted from equations (3) and (4) deviates from the experimental data at drawing strains higher than 5.5. The good agreement between the predicted yield stress and the experimental data at drawing strains between 6 and 9.5 supports that the effectiveness of substructure strengthening of Cu and Nb in heavily deformed Cu-Nb nanocomposites decreases at high drawing strains. At draw strains above 10, Nb filaments reached a thickness of approximately 10 nm (Fig. 1 of Ref. 2) and thereafter further working resulted in random rupture of the filaments rather than continued plastic deformation and thinning [9], which may result in the slower increase of the strength than the predicted values with drawing strain.



(a) (b)

Fig. 3. (a) Contributions of σ_{sub}(Cu-Nb), σ_{sub}'(Cu-Nb) and $\sigma_{filament}$ (Cu-Nb) to the total yield strength. (b) The predicted yield stress plotted along with the experimental data [1, 4].

2.2. Ductility of Cu-Nb Nanocomposites.

One of the most interesting observation in Cu-Nb nanocomposites is that the ductility remained relatively constant irrespective of volume percentage of Nb filaments whereas the strength increased rapidly with Nb content [10]. The fractographs showed ductile fractures irrespective of

Nb contents. The dimple size in Cu rich area was observed to be larger. Spitzig et al. [1] reported that the dimple size in Cu-Nb decreased with increasing draw ratio in agreement with decreasing average spacing between Nb filaments. They [1] also reported that Nb filaments were evidently observed within the dimples. The observation of Spitzig et al. [1] suggests that cracks were likely to originate from Nb filaments. The insensitivity of the ductility of Cu-Nb nanocomposites to Nb content as observed by Hong and Hill [10] can be explained if the crack initiates from Nb filaments and the ductility of Cu-Nb wires is determined by the fracture strain of Nb filaments. Since the fracture strain of Nb filaments would remain the same in various Cu-Nb nanocomposites at a given drawing strain, the ductility is insensitive to Nb content.

3. CONCLUSIONS

Based upon a study of the microstructural and mechanical stability of Cu-Nb microcomposite wires fabricated by the bundling and drawing process, the following conclusions can be drawn.

(1) The strength of Cu-Nb nanocomposite was predicted as a function of drawing strain by assuming that the contribution of the partial grain boundaries to the strength decreases as the interfilamentary spacing decreases at high drawing strains. The good agreement between the predicted yield stress and the experimental data at drawing strains that the effectiveness of substructure strengthening in heavily deformed Cu-Nb nanocomposites decreases with increasing drawing strain.

(2) The insensitivity of the ductility of Cu-Nb nanocomposites to Nb content is associated with the crack initiation from Nb filaments. Since the fracture strain of Nb filaments would remain the same in various Cu-Nb microcomposites at a given drawing strain, the ductility is insensitive to Nb content.

ACKNOWLEDGEMENTS

This work has been supported by the Korea Science and Engineering Foundation (971-0803-034-2).

REFERENCES

1. W. A. Spitzig, A. R. Pelton, and F. C. Laabs, *Acta metall.*, **35**, 2427 (1987).
2. J. D. Verhoeven, L. S. Chumbley, F. C. Laabs, and W. A. Spitzig, *Acta metall. mater.*, **39**, 2825 (1991).
3. P. D. Funkenbusch and T. H. Courtney, *Acta metall.*, **33**, 913 (1985).
4. U. Hangen and D. Raabe, *Acta metall. mater.*, **43**, 4075 (1995).
5. S. I. Hong, M. A. Hill, Y. Sakai, J. T. Wood, and J. D. Embury, *Acta metall. mater.*, **43**, 3313 (1995).
6. S. I. Hong and M. A. Hill, *Acta metall. mater.*, **46**, 4111 (1998).
7. S. I. Hong and M. A. Hill, *Mater. Sci. Eng.*, in press (2000).
8. S. I. Hong and M. A. Hill, *Scripta Mater.*, in press (2000).
9. C. Biselli and D. G. Morris, *Acta metall. mater.*, **42**, 163 (1994).
10. S. I. Hong and M. A. Hill, unpublished work. (1999).

Key Engineering Materials Vols. 183-187 (2000) pp. 1213-1218
© 2000 Trans Tech Publications, Switzerland

Modeling of Thermal Shock Spalling Crack in a Ceramic Slab

Pengfei He[1] and W.J. Clegg[2]

[1] Key Laboratory of Solid Mechanics of Department of Education of China, Tongji University, Shanghai 200092, China P.R.

[2] Department of Materials Science and Metallurgy, University of Cambridge, Pembroke Street, Cambridge CB2 3QZ, UK

Keywords: Ceramics, Fracture Mechanics, Spalling Cracks, Thermal Shock

ABSTRACT

The transient thermal stress problem for a ceramic slab with a single spalling crack is investigated by numerical method. The ceramic slab is assumed to be insulated on one face and cooled by surface convection on other faces. In the paper, inertia effects are assumed negligible and possible temperature dependence of material properties is not considered. The crack surface, which is parallel to the cooled faces, is considered as insulated face. But, for the crack surface normal to the cooled face, two kinds of limitation thermal boundary conditions, insulated case and cooled case, have been considered. Cooling time – dependent energy release rates have been calculated using finite element method package, ABAQUS. Influence of the crack length, the crack depth, heat transfer coefficient between the slab surface and the coolant, and the materials properties on the maximum energy release rates has been discussed. It is found the spalling crack initiation is unstable, and for given thermal shock condition, energy release rate for spalling crack can exceed that for vertical crack if spalling crack depth is deep enough.

1. INTRODUCTION

Cracking of ceramics, duo to thermal shock, has been recognized as crucial failure phenomenon. There are many works concerning with the subject [1-3]. But, these works just paid attentions to vertical cracks normal to cooled faces. Recently, the water quench experiments on dense alumna ceramics under various temperature difference have been finished by authors. The experimental results show that, when the temperature difference is equal to or slighter above the critical temperature difference, spalling cracks parallel to the cooled face are dominated failure mechanism, but at high severity of thermal shock, only vertical cracks normal to cooled face can be seen, and multi-cracking is dominate cracking mechanism [4]. The cooled face may be replaced by the spalling cracking, so it is more danger compared with the vertical cracking.

In the paper, a ceramic slab with a single spalling crack under thermal shock is analyzed by numerical method.

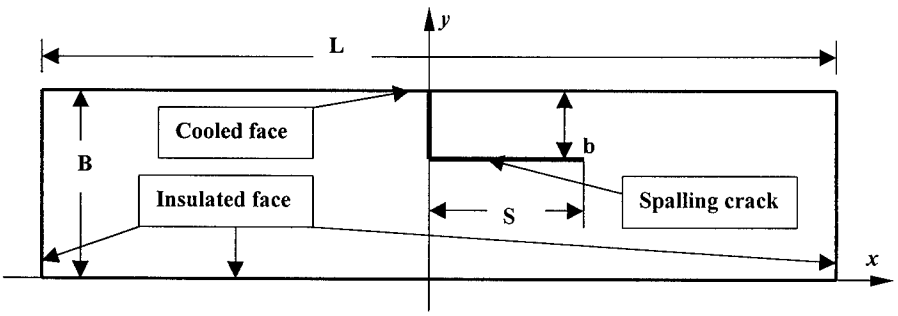


Fig.1. Schematic of slab with a single spalling crack cooled at Y = B and insulated along Y = 0 and X = ±0.5L.

For simplicity and complying with our experimental procedure, basically problem is depicted in Fig. 1. A ceramic slab 10 mm in width (B =10mm) and 35 mm in length (L = 35mm), at an initial uniform temperature T_0, is assumed to be insulated along y = 0. At time t = 0, the faces y = B, x = ±0.5L are suddenly subjected to Newtonian convection cooling, the coolant temperature is T_r. A single spalling crack of b depth and s length is initiated on the cooled face x = B. The inertia and dynamic effects are assumed negligible. In addition, all thermo-elastic coupling effects and temperature dependence of the materials properties are neglected, and the slabs are assumed to be isotropic, homogeneous and linear elastic continuum.

ABAQUS, a commercial finite element method package [5], was used to determine the temperature and thermal stress distribution in the slab and the energy release rate G for the crack.

2. TEMPERATURE AND STRESS FIELDS

Referring to Fig. 1, assuming the temperature field is independent on the thermal stresses field, governing equations for the temperature field in the slab can be written as a two – dimensional differential equation as following:

$$\frac{\partial T}{\partial t} = \kappa\left(\frac{\partial^2 T}{\partial x^2} + \frac{\partial^2 T}{\partial y^2}\right) \tag{1}$$

Where T is the temperature in the slab at cooling time t, κ is the thermal diffusivity. The initial condition is $T(0,x,y) = T_0$, while the boundary condition are given by

$$\begin{aligned} \kappa\frac{\partial T}{\partial x}\Big|_{x=0} &= \kappa\frac{\partial T}{\partial y}\Big|_{y=0} = 0 \\ \kappa\frac{\partial T}{\partial x}\Big|_{x=B} &== h[T(B,y,t) - T_r] \\ \kappa\frac{\partial T}{\partial y}\Big|_{y=\pm 0.5L} &== h[T(x,0.5L,t) - T_r] \end{aligned} \tag{2}$$

where h refers to the heat coefficient between the cooled faces and the coolant. The surface of the spalling crack can be divided two parts, first parts, the surfaces parallel to x-axis, second part, the surfaces parallel to y-axis. Because the heat problem can be assumed approximately to be symmetry to y-axis, first part of the surfaces can be considered as insulated faces, for second part, two limitation cases, insulated and cooled, will be considered.

With the temperature field, cooling time dependent thermal stresses field can be obtained. It is found that normal stress component σ_{xx} is a dominated stress component in the slab, and the stress is compressive in middle zone of the slab, but tensile in zones adjacent the cooled face, reaches maximum on the cooled face. Compared with the stress, other stress components are small, and can be omitted. The stress profile suggests strongly that thermal shock cracks will be initiated on the cooled face and the crack direction is parallel to y-axis. But, propagation of the crack may be arrested by the compressive stress in the middle zone of the slab. In addition, the normal stress σ_{xx} is changes dramatically with variant y, according to paper [6], such stress gradient may support the driving force for spalling crack.

3. ENERGY RELEASE RATE FOR SPALLING CRACK

Quarter singularity element is used to simulate the singularity stress field at crack tip. Based on the thermal stress distribution around the tip, energy release rate, G may be determined by J-integral [6]. The parameters, as given in Table 1, have been used to obtain following numerical results unless new specifications were given.

First, energy release rates, G as a function of cooling time t is plotted in Fig. 2 for two kinds of thermal boundary conditions of the crack surfaces. It is found that the rates, for both cases, increase rapidly as the cooling time t increases, reaching maximum when t $\approx$ 0.33 s, after which decrease. Actually, we found also that the time corresponding to maximum energy release rate increases as the crack depth b increase, but not sensitive to other parameters. In addition, the rate is large for cooled crack surface case than that for insulated crack surface case.

Table 1. Thermal and mechanical properties used in the calculation

Thermal conductivity (k)	30 *W/(mK)*	Specific heat (C)	800 *J/(kg.K)*
Density (ρ)	3000 kg/m^3	Young's Modulus (E)	396 *GPa*
Poisson's Ratio (ν)	0.2	Temperature Difference (T_0-T_r)	230 ^0C
Crack depth (b)	2.5 *mm*	Crack length (s)	0.5 *mm*
Coefficient of thermal expansion (α)		$8.5\times10^{-6}(1/K)$	
Heat Transfer coefficient (h)		30000 (W/m^3K)	

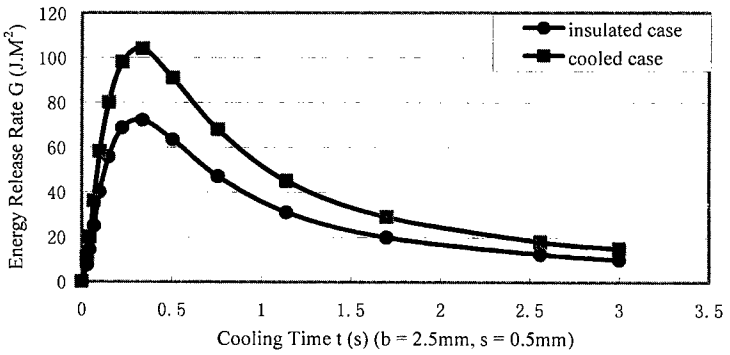


Fig.2. The energy release rates G as a function of the cooling time t

Effects of crack depth b on the maximum energy release rate for vertical crack (s = 0) and spalling crack (s = 0.5 mm), are shown in Fig. 3. The rate for vertical crack increases quickly with increasing of crack depth b, (implies the initiation of the vertical crack is in unstable), reaching maximum when b $\approx$ **0.5** mm, and then descends. The result is agreement with the thermal stress profile mentioned above. The rate for the crack increases as the crack depth b increases, but not quickly compared with that for vertical crack, when b $\approx$ B/3, it takes maximum, and then decreases. The result may be explained energetically. First, crack is initiated unstable as a vertical crack, after propagating rapidly to a certain depth, blocked by the compressive stress in middle zone where the T-stress at the crack tip becomes positive, so the crack path parallel to cooled face becomes more favorable than vertical path. In addition, according to [7], at any given cooling time, a mode I crack path parallel to cooled face is available, for small b, however the strain energy stored in such a thin spalling layer is insufficient to driving spalling. It is also found that when b $\leqslant$ B/3, the energy release rates are large for vertical crack than that for the spalling crack, but when b > B/3, the opposite situation is true. These numerical results can be used to explain reasonable the experimental results given by [4].

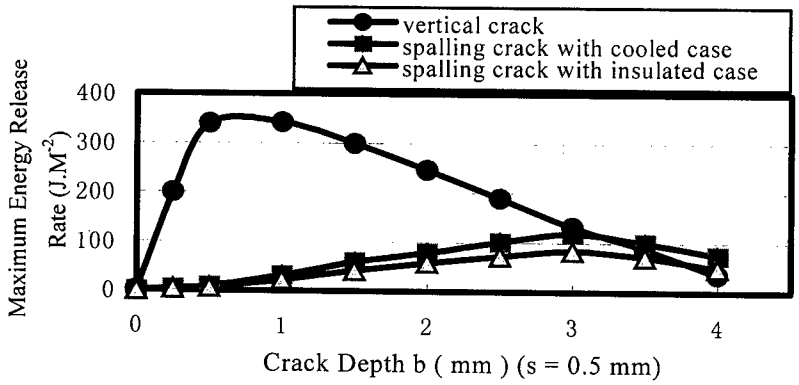


Fig. 3. Comparison of the maximum energy release rate for the spalling crack with that for the vertical crack

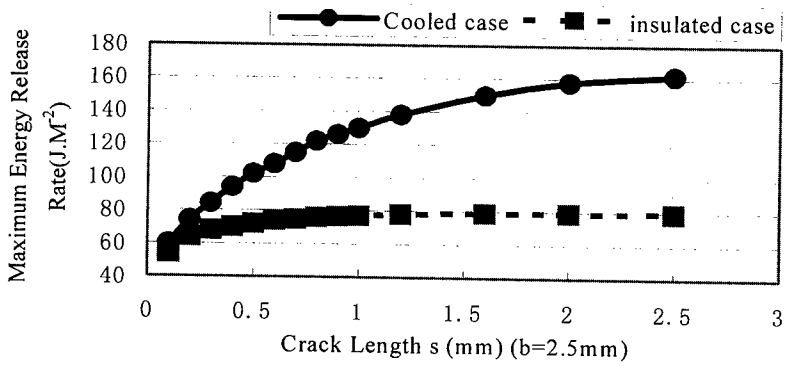


Fig.4. The maximum energy release rate G as a function of the length s of the spalling crack for the two cases of the thermal boundary conditions

Effects of the crack length s on maximum energy release rates, for two cases of crack surface thermal boundary conditions, are plotted in Fig.4. Maximum energy rates for both cases increase as crack length s increase, and the rate for cooled case is large than that for insulated case. When crack length s is very small, it is naturally that the effect of thermal boundary condition of the crack surface on the energy release rates can be expected to be very small. Actually, the spalling crack can be considered as putative crack kicking out the plane of the parent crack, which was studied by Nemat-Nasser [8] and He [9]. Energy release rate for putative crack with very small length can be determined by stress intensity factors for parent crack. Our result is agreement with results given by He [9]. Maximum energy release rates for both the spalling crack and the vertical crack increase with increasing of h and α , which is expected.

4. CONCLUDING REMARKS

Based on the stresses profile, it can be concluded that the crack induced by the thermal shock will be initiated on the cooled face, and for a single crack case, propagation of the crack firstly inwards in a direction normal to the cooled face, when enters compressive zone, the propagating path will be changed from normal to cooled face into parallel to cooled face. This was explained further by investigating the effect of crack depth b on energy release rates for both vertical cracks and spalling cracks.

The energy release rates for the spalling crack increase as crack depth b, reaching maximum when $b \approx B/3$, and then decreases, and with increasing of the crack length s, the energy release rate increases. The results imply initiation of the spalling crack is unstable, and after initiating it will propagates quickly. This is complying with experimental observation [4].

ACKNOWLEDGEMENT

European Community Under Brita/Euram Programme (Contract No. BRPR, CT96. 0287), and China Natural Science Foundation (Contract No. 19972048) are gratefully acknowledged for their support.

REFERENCES

1. H.F.Nied, J. Thermal Stress, 6 (1983) p.217
2. H.A.Bahr, Theoretical and Applied Fracture Mechanics, 8 (1987) p. 33
3. H.A.Hahr, Theoretical and Applied Fracture Mechanics, 10 (1988) p. 219
4. C.Yuan, P.He, R.Stern, and W.J.Clegg, Thermal Shock of Porous Materials I: Properties and Experimental Observation, to be subjected
5. ABAQUA version 5.4, Hibbitt and Sorensen (1994)
6. B.Lawn, Fracture of Brittle Solid, Second Edition, Cambridge University Press (1993)
7. J.W.Hutchinson, and Z.Suo, Advanced in Applied Mechanics, McGraw-Hill Ltd. New York (1980) p. 63
8. K.Hayashihn and Nemat-Nasser, J. Applied Mechanics, 48 (1981) p. 520
9. M.Y.He, amd J.W.Hutchinson, J. Applied Mechanics, 56 (1989) p. 2p70

Key Engineering Materials Vols. 183-187 (2000) pp. 1219-1224
© 2000 Trans Tech Publications, Switzerland

Analytical Study of Prestrain Effects on Elastic Properties in Shape Memory Alloys

H.G. Kim[1], H.K. Noh[1], Y.T. Cho[1], J.Y. Kim[2], S.K. Park[3] and D.J. Lee[4]

[1] Division of Mechanical and Industrial Engineering, Jeonju University,
1200 Hyojadong 3Ga, Wansanku Jeonju, 560-759, Korea

[2] Division of Mechanical Engineering, Chosun University,
375 Seosukdong, Dongku, Kwangju 501-759, Korea

[3] Division of Mechanical and Automotive Engineering, Yosu National University,
San 96-1, Dunduckdong, Yosu, Chonnam 550-749, Korea

[4] Division of Mechanical Engineering, Youngnam University,
214 Daedong, Kyungsan, Kyungbuk 712-749, Korea

Keywords: Eshelby's Method, FEM, Metal Matrix Composite, Micromechanics, Particle Dispersed, Residual Stress, Shape Memory Effect, TiNi Alloy

ABSTRACT

Tensile elastic behavior of a metal matrix composite (MMC) by the shape memory effect (SME) of dispersed TiNi particles was theoretically and numerically studied. An analytical model was constructed for the prediction of the average residual stress and Young's modulus in the basis of the Eshelby's equivalent inclusion method. The analysis was performed on the TiNi particle/Al metal matrix composites with varying volume fractions and prestrains of the particle. It was found that the residual stress is substantially influenced by the prestrained SME in predeformed particles whereas Young's modulus is independent of prestrain. The internal stress fields using FEM analysis are presented and discussed in detail.

1. INTRODUCTION

When MMCs are fabricated at high temperature or annealed and consecutively cooled down to room temperature, the MMCs show undesirable properties, such as the low tensile yield strength as well as the low ultimate strength. These results are mainly due to residual stresses that are caused by the mismatch of the CTE between the matrix and particle or fiber. Residual stresses generated from either thermal or mechanical treatment play an important role in the load-bearing process in composites [1-7].

The residual stresses induced in a short fiber MMC by a number of researchers have been observed in W fiber/Cu composites [8] and in SiC whisker/6061 Al composites. In the case of SiC whisker/6061 Al composite materials [9,10], a study conducted by Arsenault and Taya [11] indicated that the yield stress of the composite uniaxial compression is different from that under uniaxial tension. It was further indicated that this

asymmetric response is a direct consequence of the average tensile thermal residual stresses in the matrix. The residual stress in the matrix and fillers of composite influences the composite's mechanical properties such as the yield stress and fracture toughness. The effect of the thermally induced residual stress on the yield stress was discussed by Wakashima *et al* [12]. who predicted that the yield stress in compression exceeds that in tension for continuous B fiber/Al composite.

Compressive stress in the matrix is a kind of a beneficial factor that enhances the tensile properties of a metal matrix composite (MMC). Pursuing this idea further, one can use a special filler that shrinks in the matrix at use temperature, thereby introducing compressive stress along the direction of the shrinkage. SMAs such as TiNi exhibit such shrinkage at the austenitic stage if they are subjected to pretensile strain at the martensitic stage [6]. Recently, it is developed two types of smart composite utilizing TiNi fiber as a reinforcement, TiNi/Al and TiNi/epoxy by Hamada *et. al* [13,14]. They succeeded in improving both the yield stress of TiNi/Al and the fracture toughness of TiNi/epoxy at high temperature.

In this paper, an analytical method by which the increase in the elastic tensile properties of SMA particulate/metal matrix composite has been studied for the TiNi particle/Al matrix composite. The present model is based on Eshelby's equivalent inclusion method [15]. The problem of residual stress field by the SME and Young's modulus in the metal matrix composite with varying volume fractions and prestrains of the particle was solved to predict the elastic tensile properties. The advantages of the Eshelby's model are that it can solve a three dimensional composite system such as particulate reinforced composite and also can take into account the effect of volume fraction of particulate with ease. The present model system was also calculated by FEM to investigate the internal stress field in the matrix.

2. BASIC PROCEDURE OF ESHELBY'S EQUIVALENT INCLUSION METHOD

An infinitely extended material (D-Ω) with the elastic moduli C^m_{ijkl}, containing an ellipsoidal domain (Ω) with the elastic moduli C^f_{ijkl} (Fig. 1(a)) is considered here. Ω is called an ellipsoidal inhomogeneity [16]. We investigate the disturbance in an applied stress caused by presence of this inhomogeneity. Let us denote the applied stress at infinity by σ^o_{ij} and the corresponding strain by $\frac{1}{2}(\mu^o_{i,j} + \mu^o_{j,i})$. The stress disturbance and the displacement disturbance are denoted by σ_{ij} and, μ_j respectively. Then the total stress (actual stress) is $\sigma^o_{ij} + \sigma_{ij}$, and the total displacement is $\mu^o_i + \mu_i$. Stress components σ_{ij} are in self-equilibrium; that is, $\sigma_{ij,j}=0$ and $\sigma_{ij}=0$ at infinity. When a finite body is considered, $\sigma_{ij}\, n_j=0$ on the boundary, where n_j is the normal unity vector on the boundary. Hooke's law is written as

$$\sigma^o_{ij} + \sigma_{ij} = C^f_{ijkl}(\mu^o_{k,l} + \mu_{k,l}) \quad \text{in } \Omega \tag{1}$$

$$\sigma^o_{ij} + \sigma_{ij} = C^m_{ijkl}(\mu^o_{k,l} + \mu_{k,l}) \quad \text{in D-}\Omega \tag{2}$$

The equivalent inclusion method is used to simulate the stress disturbance using the eigenstress resulting from an inclusion which occupies the space Ω. In the case of homogeneous material, the applied strain ε^o_{ij} is $(\mu^o_{i,j} + \mu^o_{j,i})/2$ at infinity, the resulting total stress is $\sigma^o_{ij} + \sigma_{ij}$ in Ω. Then the Hooke's law yields

$$\sigma^{o}_{ij} + \sigma_{ij} = C^{m}_{ijkl} (\mu^{o}_{k,l} + \mu_{k,l} - \varepsilon^{*}_{ij}) \quad \text{in } \Omega \tag{3}$$

$$\sigma^{o}_{ij} + \sigma_{ij} = C^{m}_{ijkl} (\mu^{o}_{k,l} + \mu_{k,l}) \quad \text{in D-}\Omega \tag{4}$$

where $\sigma^{o}_{ij} = C^{m}_{ijkl} \mu^{o}_{k,l}$ and ε^{*}_{ij} is an eigenstrain in Ω. The neccessary and sufficient condition for the equivalency of the stresses and strains in the above two problems of inhomogeneity and inclusion is

$$C^{f}_{ijkl}(\mu^{o}_{k,l} + \mu_{k,l}) = C^{m}_{ijkl}(\mu^{o}_{k,l} + \mu_{k,l} - \varepsilon^{*}_{ij}) \quad \text{in } \Omega \text{ or} \tag{5}$$

$$C^{f}_{ijkl}(\varepsilon^{o}_{kl} + \varepsilon_{kl}) = C^{m}_{ijkl}(\varepsilon^{o}_{kl} + \varepsilon_{kl} - \varepsilon^{*}_{kl}) \quad \text{in } \Omega \tag{6}$$

If σ^{o}_{ij} is a uniform stress, ε^{*}_{ij} is also uniform in Ω

$$\varepsilon_{kl} = \frac{1}{2}(\mu^{o}_{i,j} + \mu^{o}_{j,i}) = S_{klmn} \varepsilon^{*}_{mn} \tag{7}$$

where S_{klmn} is called Eshelby's tensor [17] for isotropic materials. Substitution of Eq. (7) into Eq. (6) leads to

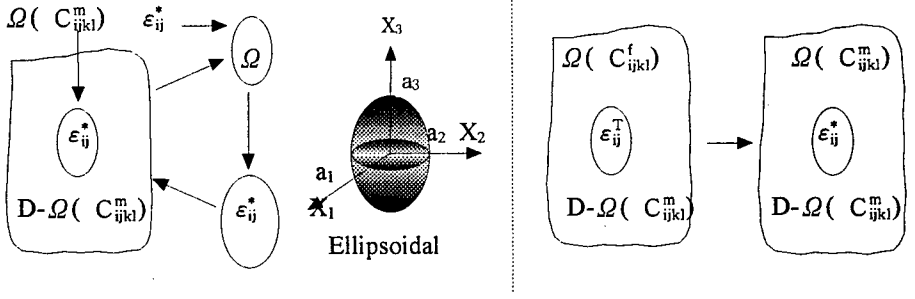
$$C^{f}_{ijkl}(\varepsilon^{o}_{kl} + S_{klmn} \varepsilon^{*}_{mn}) = C^{m}_{ijkl}(\varepsilon^{o}_{kl} + S_{klmn} \varepsilon^{*}_{mn} - \varepsilon^{*}_{kl}) \tag{8}$$

from which the six unknowns, ε^{*}_{ij}, are determined. We assume that the matrix and fillers are isotropic in stiffness so that the stiffness tensor of matrix (D-Ω) and fillers (Ω) (Fig. 1(b)), which are denoted by C^{m}_{ijkl} and C^{f}_{ijkl}, is given by

$$C^{m}_{ijkl} = \lambda^{m} \delta_{ij} \delta_{kl} + \mu^{m}(\delta_{ik} \delta_{jl} + \delta_{il} \delta_{kj})$$

$$C^{f}_{ijkl} = \lambda^{f} \delta_{ij} \delta_{kl} + \mu^{f}(\delta_{ik} \delta_{jl} + \delta_{il} \delta_{kj}) \tag{9}$$

where δ is Kronecker's delta, λ^{m} (λ^{f}) and μ^{m} (μ^{f}) are Lame's constants of the matrix (filler).



(a) (b)

Fig. 1 (a) Eshelby's inclusion model and (b) Applied equivalent inclusion method.

The transformation strain ε^{T}_{ij} which is caused by the shape recovery of the particles by their SME exists only in the particles. Eshelby [15] first pointed out that the stress disturbance in an applied stress due to the presence of an inhomogeneity can be simulated by an eigenstress caused by an inclusion when the eigenstress is chosen properly. this equivalency is called the equivalent inclusion method.

3. COMPOSITE STRENGTHENING PROCEDURE FOR THE SME

The procedure of strengthening mechanism in a composite by use of the SME for TiNi is as can be seen in the Fig 2(a) through (d) [6]. The shape recovery process induces

compressive stress in the matrix along the prestrain direction, which in turn enhances the tensile properties direction and the tensile properties of the composite at the austenitic stage.

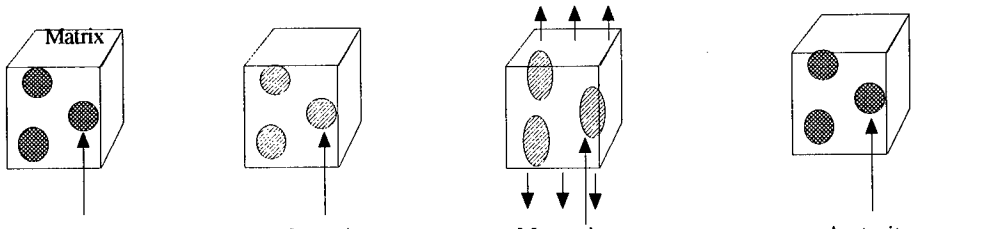


Fig. 2 Schematic of strengthening mechanism in TiNi/Al composite by SME.

4. ANALYTICAL ELASTIC MODEL FOR SMA

After the shape memory treatment, uniaxial prestrain ε_{ij}^{s} is applied to a composite along the x_3-axis (Fig. 3). There are two methods of prestraining TiNi particles: (1) tensile prestrain and (2) compressive prestrain. The TiNi particles so prestrained attempt to return to the initial spherical shape as shown in Fig. 3, upon heating above the (A_s) point. Due to the constraint by the surrounding matrix, a complete recovery of TiNi particles to a spherical shape cannot be achieved.

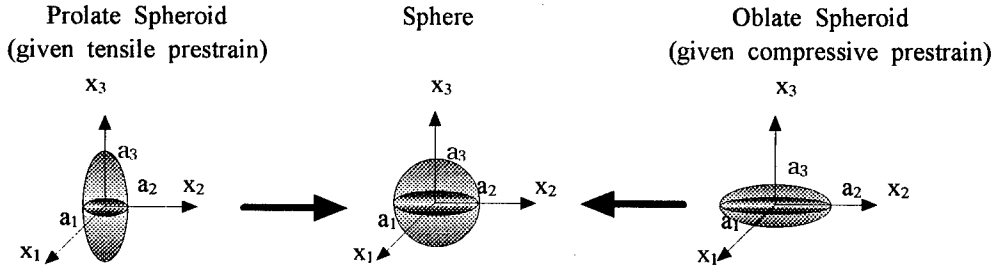


Fig. 3 The model of the shape deformation and calculation of strain by SME.

The aspect ratio α of deformed particles is given by Eq. (10)

$$\alpha = \frac{a_3}{a_1} \tag{10}$$

where a_1 is the length of deformed particles in the transverse direction (along x_1-axis) and a_3 is along x_3-axis. If the volume of each particle is assumed to be constant before and after the deformation, the prestrain ε_{ij}^{s} for the spherical TiNi particle are related to the aspect ratio of the deformed particles α. Then the analytical model for the calculation of residual stresses in a MMC is calculated as below [6].

$$\langle \sigma_{11} \rangle_m = \langle \sigma_{22} \rangle_m = -2V_f \mu^m (U_{11} \varepsilon_{11}^{s} + U_{13} \varepsilon_{33}^{s}), \quad \langle \sigma_{33} \rangle_m = -2V_f \mu^m (U_{31} \varepsilon_{11}^{s} + U_{33} \varepsilon_{33}^{s}) \tag{11}$$

where $\langle \sigma_{11} \rangle_m$, $\langle \sigma_{22} \rangle_m$ and $\langle \sigma_{33} \rangle_m$ are the average residual stresses in the matrix along the x_1, x_2 and x_3-axis, respectively. U_{ij} is given in the previous study [6] and they are the function of Poisson's ratio and Young's moduli of the matrix and filler, and volume fraction of fillers. Likewise, The analytical model for the Young's modulus in a MMC is calculated as below [6].

$$E_c = \frac{E_m}{1 + \frac{E_m}{\sigma_o} V_f \varepsilon_{33}^*} \tag{12}$$

where E_m and E_c are Young's moduli of the matrix and composite, respectively and $\varepsilon_{33}^* = M\frac{\sigma_o}{E_m}$ (M is a constant) is computed as follows.

5. RESULTS AND DISCUSSION

The material properties of Al matrix and TiNi filler used in the present analysis are as follows. Al matrix [11]: E_m=69GPa, ν_m=0.33, σ_{ym}=32MPa and TiNi particles [13]: E_f=82GPa (austenite), ν_f=0.43 where E_m and E_f are the Young's moduli of the matrix and filler, and ν_m and ν_f are the Poisson's ratios of the matrix and filler, respectively. The average residual stress in the matrix along the longitudinal direction (the x_3-axis) and the transverse direction (the x_1 or-x_2 axis), when the particles are deformed from prolate spheroid to sphere, are shown as the solid and dashed lines in Fig. 4(a) and (b), respectively.

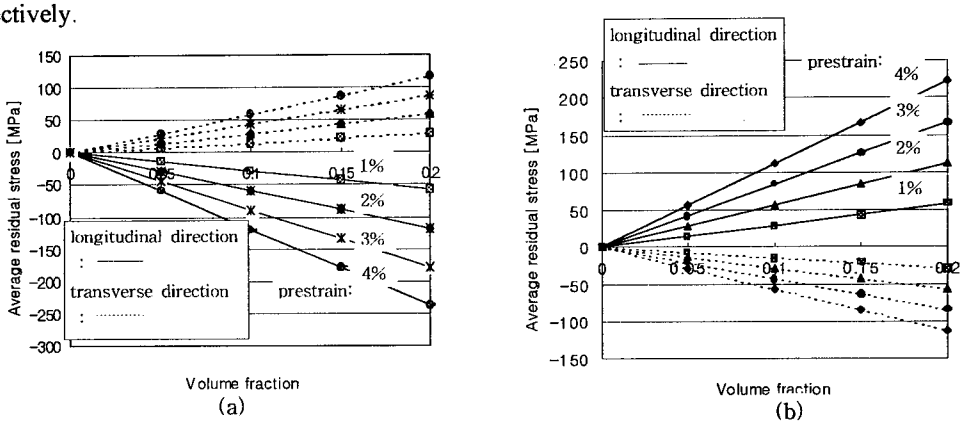


Fig. 4 Average residual stresses of Al matrix as a function of volume fraction in TiNi particle. Prestrain is given to the composite from 1% to 4%. (a) Longitudinal direction, (b) Transverse direction.

On the other hand, the internal stress field in the matrix is shown in Fig. 5 (V_f=0.1, prestrain=1%). Fig. 5(a) indicates the stresses in the case of prolate inclusion and Fig. 5(b) indicates those of oblate inclusion. It should be noted that the residual stress along the longitudinal direction is compressive and that along the transverse direction is tensile. Fig. 6 shows Young's modulus as a function of volume fraction and prestrains.



Fig. 5 Residual stress contours in the matrix. (a) prolate inclusion, (b) oblate inclusion.

6. CONCLUSIONS

The strengthening behavior of MMC by the SME for dispersed TiNi particles was analytically studied. Compared to the unreinforced Al matrix, the residual stress of a TiNi particle MMC increases along the longitudinal direction of TiNi particles when a particle MMC is given tensile prestrain. Young's modulus of the composite increases as the volume fraction of the particles increases. Prestrain has no effect on Young's modulus of the the composite but volume fraction has effect on it.

ACKNOWLEDGEMENT

This work was supported by the Jeonju University research fund.

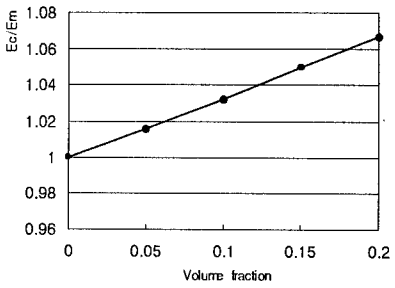


Fig. 6 Young's modulus in the composite as a function of volume fraction in TiNi particle.

REFERENCES

1. H. Li, J.B. Li, Z.G. Wang, C.R. Chen and D.Z. Wang, Met and Mat. Trans. A, **29A** (1998).
2. M. Taya and R.J. Arsenault, Metal Matrix Comp., Perg. Press, Elmsford, NY (1989), p. 101
3. T.H. Jeong, D.J. Lee and H.G. Kim, J. Kor. Soc. of Mech. Eng. (A), **21**, No. 10 (1997).
4. N. Shi, R.J. Arsenault, A.D. Krawitz, and L.F. Smith, Metallurgical Transactions A, **24A** (1993).
5. C.B. Demakos, P.S. Theocaris, J. Composite Materials, **33**, No. 6 (1999), p. 498
6. Y.T. Cho, H.G. Kim, H.K. Noh, D.J. Lee, J. the Korean Soc. Machine Tool Engineers, **8**, (1999), p. 42
7. T.H. Jeong, D.J. Lee, H.G. Kim, J. Korean Soc. Auto. Eng., **6**, No. 6 (1998), p. 53
8. K.K. Chawla and M. Metzger, J. Mater. Sci., **7** (1983), p. 34
9. R.J. Arsenault and R.M. Fisher, Scripta Metall. **17** (1983), P. 57
10. M. Vogelsang, R.J. Arsenault and R.M. Fisher, Metall. Trans. **17A** (1986), p. 379
11. R.J. Arsenault and M. Taya, Acta Metallurgica et Materialia, **35**, No. 3 (1987), p. 651
12. K. Wakashima, Y. Suzuki, and S. Umekawa, J. Comp. Mat., **13** (1979), p. 288
13. K. Hamada, J.H. Lee, K. Mizuuchi, M. Taya, and K. Inoue, Met. Mat. Trans. A, **29A** (1998).
14. H.G. Kim, D.J. Lee, T.H. Nam, S.G. Lim, J. IER, Jeonju University, **1** (1995), p. 61
15. J.D. Eshelby, Proc. Roy. Soc. London, **A241** (1957), p. 376
16. M. Taya and R.J. Arsenault, Met. Metrix Comp. Pergamon Press, Oxford (1989), p. 35

Key Engineering Materials Vols. 183-187 (2000) pp. 1225-1230
© 2000 Trans Tech Publications, Switzerland

A Study on the Friction and Wear Characteristics of Brake Pads for Al MMC Brake Disc

S.J. Kwon and B.C. Goo

Rolling Stock Division, Korea Railroad Research Institute,
374-1, Wolam-dong, Uiwang-city, Kyonggi-do, Korea

Keywords: Aluminum Matrix Composite Brake Disc, Friction Temperature, Mean Friction Coefficient, Organic Brake Pad, Wear Rate

ABSTRACT

Brake disc materials for rolling stock in Korea have been mainly cast-iron. Recently, speed-up of conventional trains needs a lighter brake disk to reduce the unsprung mass of bogie. In the light of weight reduction of the brake disc, ferrous materials are not very effective. One of alternative materials is a ceramic particle dispersed aluminum alloy composite, which is much lighter than ferrous materials and has good friction and wear resistance under service conditions. Along with disks, brake pads of good quality suitable to the new disk should be developed. In this study, three kinds of full size organic pads are tested for 20% ceramic particle dispersed aluminum alloy composite brake disc that is also full size. The developed disk and pads show good friction and wear characteristics and no thermal cracks are produced.

1. INTRODUCTION

Brake systems play an important role for the safety of railway vehicles. One main item of the brake system is disc brake. Brake discs and pads should be light, resist to high temperature, and absorb enough friction energy. For the purpose of satisfying these requirements, recently new materials such as forged steel with high resistance to thermal cracking, aluminum alloys, carbon-carbon composites and etc. are being developed. In the light of weight reduction, ferrous materials are not effective. In Japan and Germany, ceramic particle dispersed aluminum alloy composites are under development.[1,2]. They are much lighter than ferrous materials and have good wear resistance under common test conditions. Aluminum is one of the representative materials for weight reduction. The density of aluminum is 2.7. So weight is about 40 % of the cast-iron of the same size. But the fusion temperature of pure aluminum is 660℃ which is lower than the obtained

temperature of discs under severe friction heat of braking. So aluminum itself has not been considered friction material in railway. In the case of aluminum composite with dispersed ceramic particles, frictional characteristics, resistance to wear, resistance to heat and etc. are much improved. [2]. A few weight percent of ceramic particles dispersed in aluminum matrix ameliorate strength, resistance to wear, and resistance to friction heat.

In this paper, we tested friction and wear characteristics of an aluminum composite disc and three kinds of organic brake pads developed by Korean companies.

2. FRICTION MECHANISM AND EQUATIONS

The disc brake of railway vehicles is schematically shown in Fig. 1.

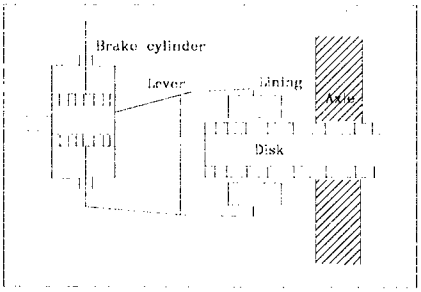


Fig.1. Mechanism of disc brake for rolling stock

The movement of the brake cylinder pressures the brake linings(or pads) to the rotating disc fixed on the axle. Friction force is produced between the brake disc and the brake pads. Frictional work by the friction force is transformed into friction heat, which is absorbed by the brake disc and the brake pads. The braking force, F, is given by the product of the normal force, P, and the friction coefficient, f, between the brake disc and the brake pads.

$$F = f_m P \tag{1}$$

The mean friction coefficient in brake dynamometer test is defined by the following equation.

$$f_m = k\frac{W \times R_m \times \Delta V}{P \times B' \times R_b \times g \times T} \tag{2}$$

where W(kgm s^2) is mass of inertia, R_m (m) is wheel radius, ΔV (m/s) is the velocity change, k is constant, B' is braking lever ratio, R_b (m) is effective braking radius, g(m/s^2) is acceleration of gravity, T is torque produced by the braking force, F.

Wear of the lining, S, is defined by Eq. (3).

$$S = \frac{10 \times \Delta W}{\rho \times A} \tag{3}$$

where ΔW (g/cm^2) is the weight difference of the lining before and after the test, ρ is the density of the lining, A (cm^2) is the contact area between the lining and the disc. According to Eq. (3), S can be considered the average depth worn away of the brake pad.

3. FRICTION AND WEAR TEST

The functional diagram of the brake dynamometer is shown in Fig. 2. The test of disc brake and block brake can be carried out. The moment of inertia is adjusted by four flywheels.

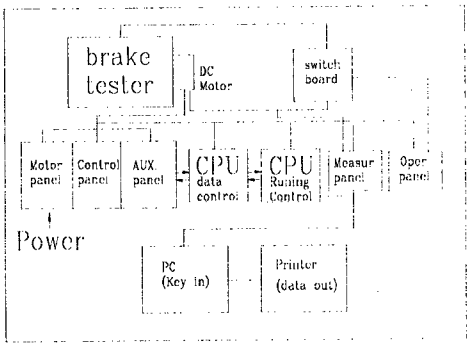


Fig.2. Functional diagram of the brake dynamometer



Fig.3. Brake pad

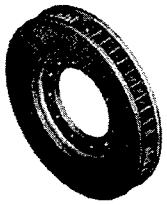


Fig.4. Brake disc

Full size test specimens of brake pads and brake disc are shown in Fig. 3 and Fig. 4. The outer diameter of the disc is 660 mm. One disc and three kinds of brake pads were tested. The chemical compositions of the brake disc are shown in Table 1. And the mechanical and physical properties of the brake disc are shown in Table 2.

Table 1. Chemical compositions of the Al MMC brake disc (%)

Si	Fe	Cu	Mg	Ti	Al	Others
8.5	0.2	0.2	0.45~0.65	0.2	-	0.1~0.3

Table 2. Mechanical and physical properties of the Al MMC and cast-iron brake disc

	Tensile strength (kg/mm^2)	Elongation rate (%)	Hardness (HB)	Young's modulus (kg/mm^2)	Density (g/mm^3)
Al MMC	23.3	5	90	8,500	2.7
Cast-iron	25.0	-	190	11,000	7.1

The chemical compositions of the brake pads are shown in Table 3. And the mechanical and physical properties of the brake pads are shown in Table 4.

Table 3. Chemical compositions of the brake pads

	Resin	Rubber	Steel Fiber	Graphite	Others
A	10-15%	25-35%	5-10%	5-10%	30-50%
B	10-20%	5-10%	15-20%	10-20%	30-60%
C	5-15%	5-10%	5-15%	10-15%	40-60%
D	7-15%	1-5%	2-10%	2-5%	50-60%

Table 4. Mechanical and physical properties of the brake pads

	Compressive strength (kg/㎟)	Gogan Hardness	Density (g/㎟)
A	6.9	35	2.30
B	5.9	180	2.26
C	6.7	36	2.37
D	5.9	34	2.18

The applied moment of inertia is 1200 (kg m^2). Brake caliper force is 1600(kg) x 2. Initial temperature of each test is below 60℃. The temperature of the pads and the disc are measured at the depth of 10 mm and 20 mm respectively by thermocouples.

4. EXPERIMENTAL RESULTS

Fig. 5 and Fig. 6 show respectively the instantaneous and mean friction coefficients up to the braking speed 150 km/h.

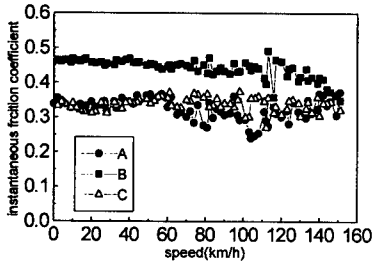


Fig.5. Instantaneous friction coefficient

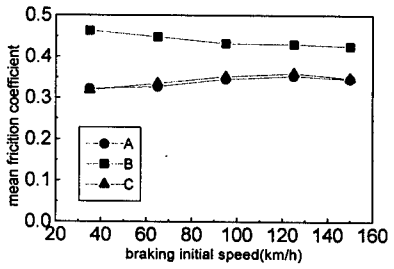


Fig.6. Mean friction coefficient

The range of the instantaneous friction coefficient is 0.25~0.5. The variation of instantaneous friction coefficient of pad A is greater than those of pads B and C. In case of pad B, the instantaneous friction coefficient is the greatest, but the variation of instantaneous friction coefficient is rather smooth. The range of mean friction coefficient is 0.31~0.47. In case of pad A and C, the mean friction coefficient increases with the braking start speed. In case of pad B, the mean friction coefficient decreases with the braking start speed. The variation of mean friction coefficient is rather smooth.

Fig. 7 and Fig. 8 show the temperature of the linings and discs up to the braking speed 150 km/h. The temperature of pad B with the highest friction coefficient is the lowest. The temperature difference of pads B and C at 150km/h is about 80℃. The temperature difference of disc for pads B and C at 150km/h is about 20℃.

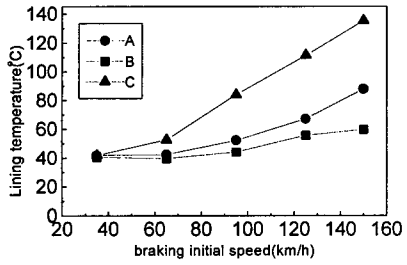


Fig.7. Temperature of brake pad

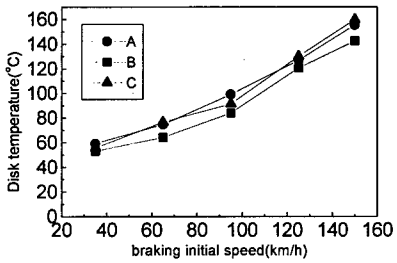


Fig.8. Temperature of brake disc

Fig. 9 shows the wear amount of the pads A, B, and C after a cycle of 20 stops at programmed braking speeds ; 65,35,95,150,65,125,95,95,35,125,65,65,150,95,125,125,35,35,150,65 km/h. Each clamping force is 1,600 kg. The wear amount of pad A is the lowest. The wear amount of pad C is the highest.

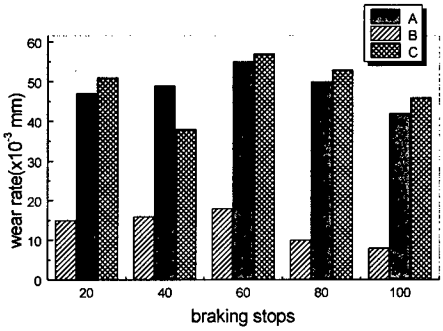


Fig.9. Wear rate of brake pad

Fig. 10 and Fig. 11 show the mean friction coefficient and maximum temperature of the pad D and cast-iron disk. These results are presented for the comparison with the previous results (Fig.6,7).

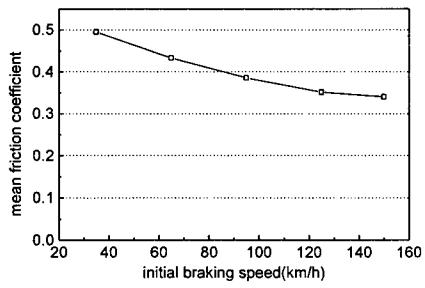


Fig.10. Mean friction coefficient of the pad D

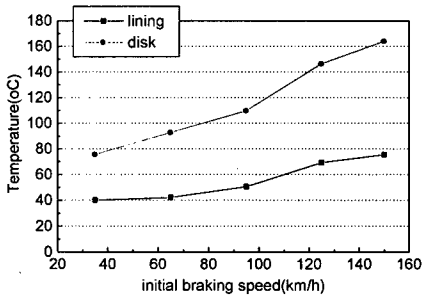


Fig.11. Temperature of the pad D and cast-iron disc

The mean friction coefficient of the pad D decreases as the braking start speed increases. The variation of the mean friction coefficient is severe.

5. DISCUSSION AND CONCLUSIONS

The aluminum alloy disc and three kinds of organic brake pads show interesting friction and wear characteristics. The obtained instantaneous friction coefficient range is 0.25~0.5. And the obtained mean friction coefficient range is 0.31~0.47. The variation of the friction coefficient is rather smooth. The friction coefficient of the brake pad B is the highest, which seems to result from the more quantity of the steel fiber. Thanks to the good heat conduction of aluminum alloy, the temperature of the brake disc is below 160℃. The temperature of the pads is below 140℃. The temperature rise of the pad B is the lowest. No heat cracks were occurred during the braking tests. The pad A shows the best friction and wear characteristics.

REFERENCES

1. I. Wolf, DB Studies Higher Levels of Braking Power, IRJ (1996).
2. T. Tsujimura, K. Takao, A. Watanabe, E. Nishii, "*Development of Aluminum Alloy Composite Brake Disk for Rolling Stocks*," QR of RTRI, Vol. 36, No. 3 (1995) p.149~154.

Key Engineering Materials Vols. 183-187 (2000) pp. 1231-1236
© 2000 Trans Tech Publications, Switzerland

On Targets Strength of Ceramic Materials for Impacting Penetration

Yi Sun[1], Jun Ma[1], Yu Zhou[2] and Tao Li[1]

[1] Department of Astronautics and Mechanics, Harbin Institute of Technology, Harbin 150001, China P.R.

[2] School of Material Science, Harbin Institute of Technology, Harbin 150001, China P.R.

Keywords: Ceramic Materials, Dilatational Phase Transformation, Penetration, Pressure-Sensitivity, Target Strength

ABSTRACT

The influences of stress-induced dilatational phase transformation and pressure-sensitive property on the target strength of ceramic materials are investigated based on Tate's model. A theoretical solution for the dynamic expansion model of a spherical cavity is developed to consider the effect of dilatational phase transformation toughening. The results of detailed calculations show that dilatational phase transformation could effectively inhibit the cavity-expansion for idealized cases. This work would be of importance in penetration-resistance design.

1. INTRODUCTION

Armor material is one of the important applications of structural ceramics because of its merits of extreme hardness and low density. It will become one of high-performance armor materials if its toughness is improved properly. The study of ceramics toughening is a focus that has been concerned by material scientists and mechanics scientists all the time. The phase transformation toughening is considered to be the best understood toughening mechanism of structural ceramics. However, it is still restricted to the static cases.

In analyzing the process of penetration, Tate [1,2] proposed an one-dimensional jet theory model in which he introduced a parameter R_t to represent the strength of target materials. Bishop *et al.* [3] developed a theory for quasistatic cavity expansion in ductile materials which was applied with considerable success to the experimental results found in deep punching of metals. Sternberg [4] and Forrestal *et al.* [5,6] applied this model to evaluate the parameter R_t for ceramic materials. In the present study, the target strength of ceramic materials with stress-induced phase transformation are investigated. The inertial effects and the influence of shear stress components in cracked region are taken into account. The influence of pressure-sensitive behavior of ceramic materials in plastic deformation is also investigated.

2. BASIC EQUATIONS

From Forrestal *et al.* [5,6], the target strength of ceramic materials can be evaluated by the expansion of a spherically symmetric cavity from zero initial radius at constant velocity V (as shown in Fig. 1). For small and moderate values of V, there exist three deformation regions: an elastic region, a region with radial cracks (including a phase transforming region), and a plastic region. The plastic region is bounded by $r=Vt$ and $r=ct$, the cracked region is bounded by $r=ct$ and $r=c_1t$. In the cracked region, the phase transforming region is bounded by ξ_1 and ξ_2, the elastic region is bounded by $r=c_1t$ and $r=c_dt$, where r is the radial Eulerian coordinates, t is time, c and c_1 are interface velocities, and c_d is the elastic dilatation velocity. Take r, θ and φ as spherical coordinates. Let σ_α, ε_α and v_α $(\alpha=r,\theta,\varphi)$ be the stress (positive in compression), strain and velocity components in spherical coordinates, then we have

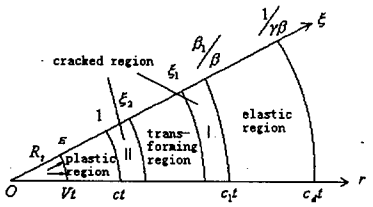


Fig.1. Cavity expansion model

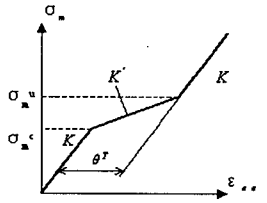


Fig.2. Stress-strain relation in phase transforming region

2.1. Mass Conservation Equation

$$\rho\left(\frac{\partial v}{\partial r}+\frac{2v}{r}\right)=-\left(\frac{\partial \rho}{\partial t}+v\frac{\partial \rho}{\partial r}\right) \tag{1}$$

2.2. Linear Momentum Equation

$$\frac{\partial \sigma_r}{\partial r}+\frac{2}{r}(\sigma_r-\sigma_\theta)=-\rho\left(\frac{\partial v}{\partial t}+v\frac{\partial v}{\partial r}\right) \tag{2}$$

2.3. Constitutive Equations

(1) Plastic region

The yield function is

$$f=\sigma_e+\lambda\sigma_m-\tau=0 \tag{3}$$

where $\sigma_e=|\sigma_\theta-\sigma_r|$ is the equivalent stress, $\sigma_m=(\sigma_r+2\sigma_\theta)/3$ is the mean stress, λ and τ define the pressure-dependent shear strength. For pressure-sensitive materials, we assume

$$\dot{\varepsilon}_{kk}^{p}=\chi\,\dot{\varepsilon}_{eq}^{p} \tag{4}$$

(2) Cracked region

$$\sigma_\theta = \sigma_\varphi = 0, \quad \varepsilon_r = \frac{\sigma_r}{E}, \quad \varepsilon_\theta = -\frac{\nu\sigma_r}{E} \tag{5}$$

(3) Elastic region

$$\varepsilon_r = \frac{1}{E}(\sigma_r - 2\nu\sigma_\theta), \quad \varepsilon_\theta = \frac{1}{E}[(1-\nu)\sigma_\theta - \nu\sigma_r] \tag{6}$$

(4) Phase transforming region

The critical condition for phase transforming [7] is

$$\sigma_m + \kappa\tau_{\max} = \sigma^c, \quad \kappa = \gamma^T / \varepsilon_{ii}^T \tag{7}$$

in which σ^c is the critical transformation stress, γ^T is the shear transformation strain and ε_{ii}^T is the volumetric transformation strain. The stress-strain relation can be written as [8] (see Fig.2)

$$\sigma_m = \begin{cases} K\varepsilon_{\alpha\alpha}, & \sigma_m \le \sigma_m^c \\ \sigma_m^c(1-K'/K) + K'\varepsilon_{\alpha\alpha}, & \sigma_m^c \le \sigma_m \le \sigma_m^u \\ (\sigma_m^u - \sigma_m^c)(1-K'/K) + K\varepsilon_{\alpha\alpha}, & \sigma_m \ge \sigma_m^u \end{cases} \tag{8}$$

where K' and K are the volumetric moduli within and outside the phase transforming region. Let θ_p^T be the rate of volume expansion of transformed particles, f_p be their volume fraction. Thus

$$\sigma_m^u = \sigma_m^c + f_p\theta_p^T K'\left(1-\frac{K'}{K}\right)^{-1} \tag{9}$$

3. STRESS AND VELOCITY FIELDS

We define the dimensionless variables and introduce the similarity transformation

$$S = \frac{\sigma_r}{\tau}, \quad U = \frac{v}{c}, \quad \varepsilon = \frac{V}{c}, \quad P = \frac{\rho c^2}{K}, \quad \xi = \frac{r}{ct} \tag{10}$$

From Eq.1, Eq.2 and the relation $\dot{\varepsilon}_{kk} = \dot{\varepsilon}_{kk}^e + \dot{\varepsilon}_{kk}^p$, we get the coupled equations in standard forms suitable for numerical evaluation with the Runge-Kutta method.

(1) Plastic region

$$\frac{dU}{d\xi} = \frac{-1}{1+(K/\tau)(U-\xi)^2\phi P}\left[\frac{2(3-\chi)}{3+2\chi}\frac{U}{\xi} + \alpha\phi(U-\xi)\left(\frac{\lambda S}{\xi}+\frac{1}{\xi}\right)\right] \tag{11}$$

$$\frac{dS}{d\xi}=\frac{1}{(U-\xi)\phi}\left(\frac{dU}{d\xi}+\frac{2(3-\chi)}{3+2\chi}\frac{U}{\xi}\right) \tag{12}$$

$$\frac{dP}{d\xi}=\frac{P}{\xi-U}\left(\frac{dU}{d\xi}+2\frac{U}{\xi}\right) \tag{13}$$

where

$$\alpha=\frac{6}{3+2\lambda}\quad,\quad \phi=\frac{-\alpha\tau}{2(3+2\chi)E}[9(1-2\nu)+2\lambda(1+\nu)\chi] \tag{14}$$

(2) Cracked region

$$\frac{dU}{d\xi}=\frac{1}{1+\dfrac{3(K'/\tau)\beta^2\xi^2}{[3(K'-\sigma_m^c)/\tau+S]^2}}\left[-\frac{2U}{\xi}+\frac{2S}{3(K'-\sigma_m^c)/\tau+S}\right] \tag{15}$$

$$\frac{dS}{d\xi}=-\frac{1}{1+\dfrac{3(K'/\tau)\beta^2\xi^2}{[3(K'-\sigma_m^c)/\tau+S]^2}}\left[\frac{2S}{\xi}+\frac{6(K'/\tau)\beta^2U}{3(K'-\sigma_m^c)/\tau+S}\right] \tag{16}$$

in which

$$\beta^2=\rho_0c^2/\tau \tag{17}$$

The solutions for cracked region and elastic region for both incompressible and compressible materials have been given by Forrestal *et al.* [6]. Let $\beta_1^2=\rho_0c_1^2/\tau$. From the transformation condition $S(\xi=\xi_1)=3\sigma_m^c/\tau$ and $S(\xi=\xi_2)=3\sigma_m^u/\tau$, we can determine the boundaries of transforming region

$$\xi_2=\frac{\sqrt{4\beta^4\varepsilon^6+12(\sigma_m^c/\tau+f_p\theta_p^TK'/\tau)(Y/\tau+2\beta^2\varepsilon^3)}-2\beta^2\varepsilon^3}{6(\sigma_m^c/\tau+V_p\theta_p^TK'/\tau)} \tag{18}$$

$$\xi_1=\frac{1}{6\sigma_m^c/\tau}\left\{\left[\left(\frac{3F(\beta_1/\beta)^3\beta^2}{E/3\tau-3\beta_1^2}\right)^2+\frac{24F(\sigma_m^c/\tau)(E/3\tau+3\beta_1^2)(\beta_1/\beta)^2}{E/3\tau-3\beta_1^2}\right]^{\frac{1}{2}}-\frac{3F(\beta_1/\beta)^3\beta^2}{E/3\tau-3\beta_1^2}\right\} \tag{19}$$

From the condition of velocity continuity at the plastic-cracked interface $\xi=1$, we have

$$\varepsilon^3=\frac{3\xi_2^{\,2}(\sigma_m^c+f_p\theta_p^TK')/\tau-Y/\tau}{2\beta^2(1-\xi_2)} \tag{20}$$

The target strength R_t is the radial stress at the cavity surface, thus it can be given as

$$R_t = \left[\frac{3+2\lambda}{\lambda(3-\lambda)}\right]\varepsilon^{-\alpha\lambda} - \frac{1}{\lambda} + \frac{6}{(\alpha\lambda-1)(\alpha\lambda-4)}\left(\frac{\rho_0 V^2}{\tau}\right) + 2\left(\frac{\rho_0 V^2}{\tau}\right)\left(\frac{\varepsilon}{\alpha\lambda-1} - \frac{\varepsilon^4}{\alpha\lambda-4}\right)\varepsilon^{-\alpha\lambda} \quad (21)$$

3. RESULTS AND DISCUSSION

Based on above analysis, we made a detailed calculation for the value of R_t over a wide range of possible parameters. In the calculation, we take Y=1930Mpa, E=221GPa, T/Y=0.08, ν=0.5, θ_p^T=0.04, ρ=3420Kg/m^3.

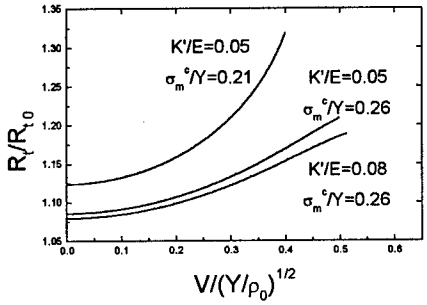


Fig.3. Influence of cavity-expansion velocity V on target strength R_t

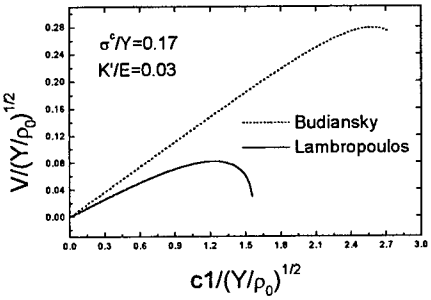


Fig.4. Inhibition of cavity expansion by dilatational phase transformation

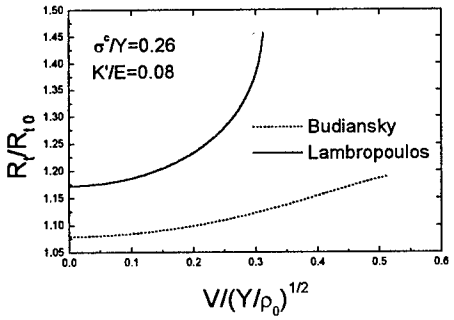


Fig.5. Influence of shear stress components on target strength R_t

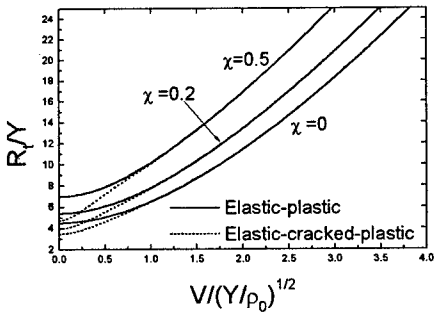


Fig.6. Influence of pressure-sensitivity on target strength R_t

Fig.3 shows the influence of critical stress σ_m^c, bulk module K' and material inertia on the target strength R_t. Here K' represents the distribution of the critical stress of phase transformation of the particles in specimen. If such critical stresses are mainly determined by the size, shape and distribution of the particles, then it can be deduced that the more uniform the size and distribution of the particles, the smaller the value of K' and the stronger the enhancement of phase transformation on R_t. It can be seen from Fig.4 that the dilatational transformation effect can

effectively inhibit the cavity-expansion for idealized cases.

In present model, the maximum shear stress component is commensurate with the mean stress in cracked region. Therefore the effect of shear stress components on transformation toughening should be considered. In order to find the range of values of the parameter κ, it is recalled that the magnitude of the shear transformation strain γ^T considerably exceeds the volumetric strain ε_{ii}^T. Typical values are $\gamma^T = 16\%$ and $\varepsilon_{ii}^T = 4\%$. From Fig.5, it can be seen that the influence is significant.

The plastic (smashed) deformation of ceramic materials is quite different from that of the normal concept. The pressure-sensitive constitutive equations are more reasonable and realistic in describing such a process. For plastically compressible materials, the results of calculation are shown in Fig.6. For slow enough V, there are three regions of response: an elastic region, a radially cracked region and a plastic region. As V increases, the cracked region diminishes and is eliminated eventually. It can be seen that the smash property of ceramic materials contributes to increasing target strength R_t to a certain extent.

4. SUMMARY

From the above analysis, it is shown that:

(1) The dilatational phase transformation can increase the target strength of ceramic materials. With a proper choice of the material parameters, the increase may be significant.

(2) For the model including cracked region, the influence of shear stress components on transformation yielding function is important in analyzing the phase-transformation effect on target strength of ceramic materials.

(3) The pressure-sensitive constitutive equations are more reasonable in describing the plastic (smashed) deformation process of ceramic materials, and the smash property of ceramic materials contributes to increasing target strength R_t to a certain extent.

AKNOWLEDGEMENT

This work is supported by the Start-up Foundation for Post-doctorate of Heilongjiang Province and the Excellent Youth Foundation of Harbin Institute of Technology.

REFERENCES

1. A. Tate, J. Mech. Phys. Solids, (15) 1967 p. 387
2. A. Tate, J. Mech. Phys. Solids, (17) 1967 p. 141
3. R. F. Bishop, Proc. Phys. Society, (57) 1945 p. 147
4. J. Sternberg, J. Appl. Phys., 65 (1989) p. 3417
5. M. J. Forrestal and D. B. Longcope, J. Appl. Phys., 67 (1990) p. 3669
6. M. J. Forrestal and D. Y. Tzou, Int. J. Impact Engng., 19 (1997) p. 4127
7. J. C. Lambropoulos, Int. J. Solids Struct., 22 (1986) p. 1083
8. B. Budiansky, J. W. Hutchinson and J. C. Lambropoulos, Int. J. Solids Struct., 19 (1983) p. 337

Key Engineering Materials Vols. 183-187 (2000) pp. 1237-1242
© 2000 Trans Tech Publications, Switzerland

Effects of Heat Treatment on Bending Strength of Aluminum Alloy Matrix Composites Reinforced Aluminum Borate Whisker

S.C. Huh[1], H.K. Yoon[2], K.H. Park[3] and S.P. Lee[4]

[1] School of Transport Vehicle Engineering, Gyeong Sang National University, Korea

[2] School of Mechanical & Industrial System Engineering, Dong-eui University, 24 Gaya dong, Pusan jin-ku, Pusan 614-714, Japan

[3] Department of Mechanical Engineering, Graduate School of Dong-eui University, 24 Gaya dong, Pusan jin-ku, Pusan 614-714, Korea

[4] Institute of Advanced Energy, Kyoto University, Goksho, Uji, Kyoto 611-0011, Japan

Keywords: Aging Treatment, Metal Matrix Composites, Solution Treatment, Squeeze Casting, Whisker

ABSTRACT

The ABO_w/AC4CH composite was fabricated by a squeeze casting method. The volume fraction of the whisker was 20%. The composition of matrix alloy was Si : 7.1wt%, Mg : 0.39wt%, Cu : 0.01wt%, Fe : 0.11, Al : 92.3wt%. The composites were solutionized at various temperatures and times : 480°C, 520°C and 560°C, 5minutes, 30minutes, 60minutes and 90minutes, then quenched into water and maintained at 25°C, to investigate the effect of precipitation on the properties of the composite. The bending strength was tested by an MTS 810 material test system, and micro-Vicker's hardness was investigated by aging time. Microstructure and interfacial reaction were studied by scanning electron microscope and X-ray diffraction (XRD).

1. INTRODUCTION

Whisker reinforced metal matrix composites (MMC) have significant potential for demanding mechanical applications within the defense, aerospace, and automotive industries. In this paper, aluminum alloy-based metal matrix composites with whisker reinforcements have been produced by squeeze casting, to obtain the higher specific mechanical properties necessary to achieve better performance[1]. Recently, a low cost aluminum matrix composite reinforced by aluminum borate whiskers ($Al_{18}B_4O_{33w}$, ABO_w) has been studied by many researchers[2].

In this study, aluminum-solution alloy squeezed into the preform, which made by the aluminum borate whisker.

The aim of the present work was to analyze how interface products play a highly significant role in the fracture behaviour and the mechanical property of composites. Previous work[3] on Al/ABO_w composites indicated that interfacial reaction obviously exists between the whisker and the matrix alloy(AC4CH). And so, in this paper, the effect of interfacial reaction by heat solution treatment was observed by SEM image and XRD analysis.

2. PREPARATION

2.1. Preparation of Preform

The aluminum borate whisker(9Al2O3·2B203w) was used for preparing the preform. The whisker(150g) was dispersed in water(1000cc) with binder(0.1g) and mixed. Then the whisker-water-pulp was compressed to make the preform without water as follow.

The no-water preform was sintered for 4 hours, at 1200°C and heated 5°C /min.

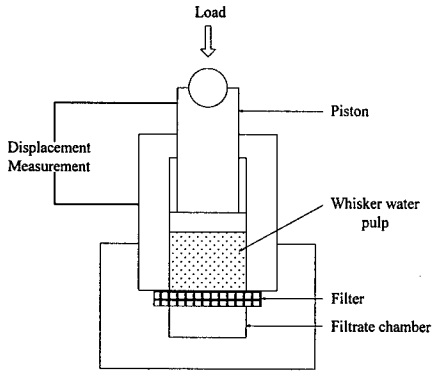


Fig. 1 Fabrication of aluminum borate whisker preform

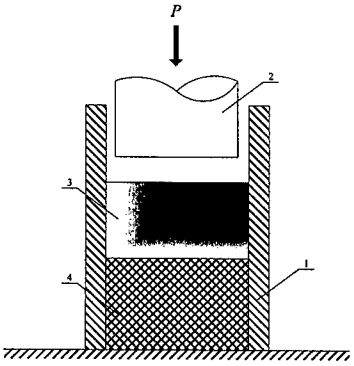


Fig. 2 Diagram of squeeze casting : (1) mould; (2) plunger; (3) melt; (4) preform of aluminum borate whisker

2.2. Squeeze Casting Process

The sintered preform was preheated at 700°C, and was placed in mould. As a mould was uniform 250°C temperature, 750°C aluminum-solution alloy(AC4CH, JIS standard) was squeezed into the preform. At squeeze casting, the pressure was 100MPa, pressing speed 50mm/s, and press-holding time 30 seconds.

The schematic of squeeze casting process is illustrated as Fig. 2.

3. EXPERIMENTAL PROCEDURES

3.1. Heat Treatment

Metal matrix composites(aluminum borate whisker and AC4CH) by squeeze casting method took a heat treatment T6, which is one of the typical aluminum heat treatment. Generally, T6 treatment consist of two steps, that is, the aging was treated about 200°C after solution treatment was executed about 520°C. And bending strength was investigated after solution treatment and micro-Vicker's hardness was evaluated by aging treatment. The various heat treatments were executed by condition of temperature and time.

Table 1 Heat treatment conditions of metal matrix composite and AC4CH

Symbol	Solution treatment		Aging treatment	
Specimen I. D.	Temperature(°C)	Time(minute)	Temperature(°C)	Time(hour)
MMC&AC4CH480-5	480	5	220	0, 1, 2, 3, 4, 5
MMC&AC4CH 520-5	520	5	220	0, 1, 2, 3, 4, 5
MMC&AC4CH 560-5	560	5	220	0, 1, 2, 3, 4, 5
MMC&AC4CH 480-30	480	30	220	0, 1, 2, 3, 4, 5
MMC&AC4CH 480-60	480	60	220	0, 1, 2, 3, 4, 5
MMC&AC4CH 480-90	480	90	220	0, 1, 2, 3, 4, 5

3.2. Mechanical Test

The effect of solution treatment was evaluated by bending test(MTS model 810, 10tonf). The bending specimen was machined by 37.5mm(length) and 4mm(thickness). The span length, gap between two support-points, is 30mm and test speed is 0.1mm/min. Solutionized specimen was treated aging at 220°C and Vicker's hardness was measured each time for 5 hours[4].

4. RESULTS

4.1. Effect of Solution Treatment

The results of solution treatment of AC4CH roughly showed a tendency that the strength and the ductility increase with increasing solution treatment temperature and time. In case of MMC, only strength were increased with increasing solution treatment temperature and time, and the fracture process was a very fracture mechanism.

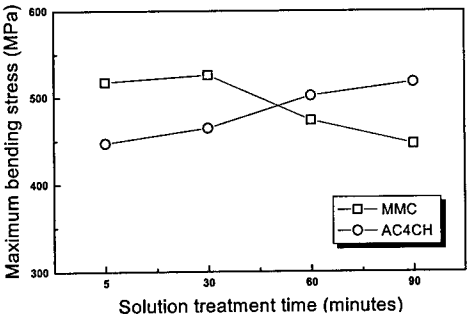


Fig. 3 Results of maximum bending stress at various solution-treatment times.

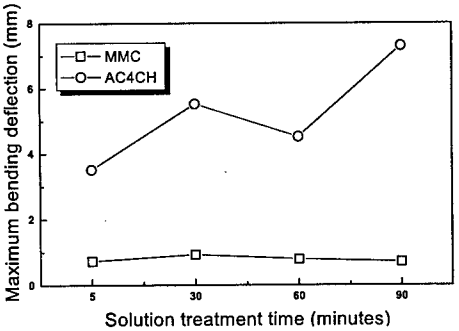


Fig. 4 Results of maximum bending deflection at various solution-treatment times.

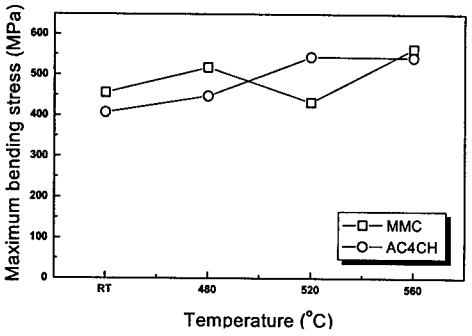


Fig.5 Results of maximum bending stress at various solution-treatment temperatures.

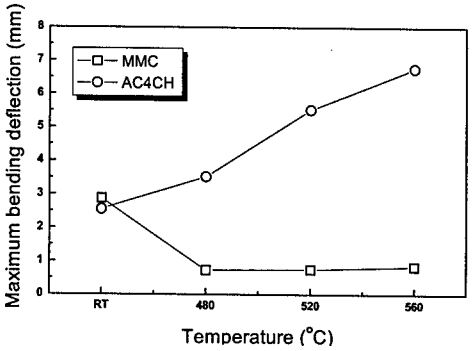


Fig. 6 Results of maximum bending deflection at various solution-treatment temperatures.

4.2. Effect of Aging Treatment

After solution-treatment, the aging was treated at 220°C, for 5 hours. The Vicker's hardness was measured each one times. The Vicker's hardness by various solution-treatment temperatures were decreased with increasing aging time. Because solution-treatment time was so short that reaction products between whisker and AC4CH cannot grow, and matrix(AC4CH) is higher influential than the whisker

By various solution-treatment times, the Vicker's hardness was decreased with decreasing solution-treatment time

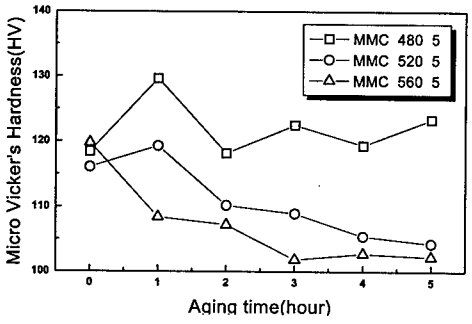


Fig. 7 Results of micro-Vicker's hardness by solution-treatment temperature

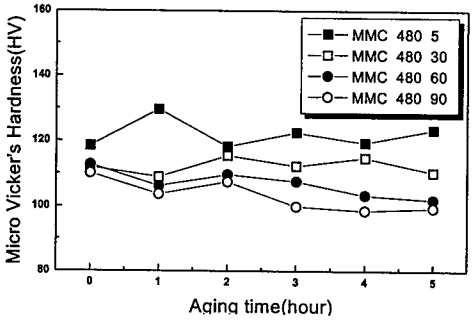


Fig. 8 Results of micro-Vicker's hardness by solution-treatment time

4.3. Fracture Surface and X-Ray Analysis

Fig. 9 shows SEM images that are variously solution-treated fracture surface. We can confirm smaller grain size as heat-treatment goes on. The X-ray shows that $MgAl_2O_3$ peaks after heat treatment were higher than none-heat treatment[5][6].

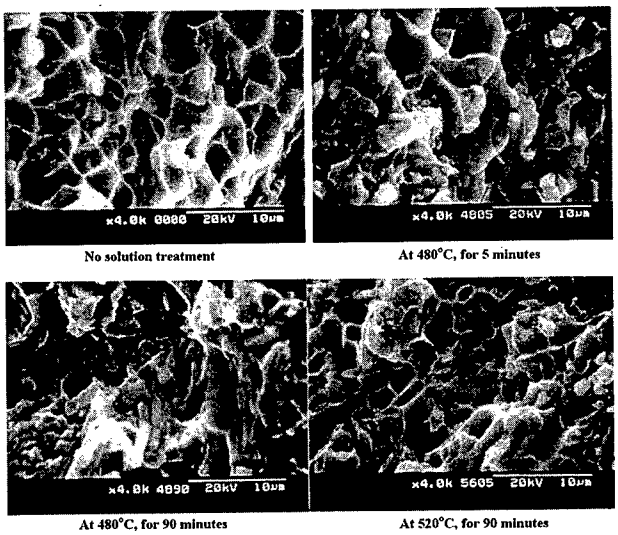


Fig. 9 SEM image of fracture surface treated by various temperature and time

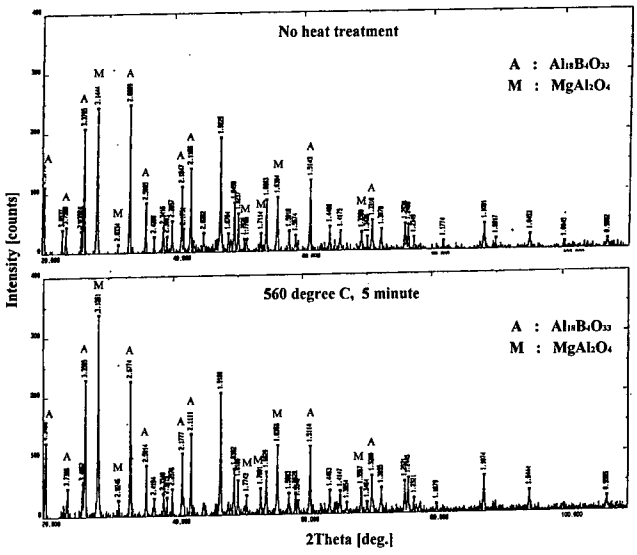


Fig. 10 Result of x-ray diffraction analysis

5. CONCLUSIONS

In this paper, aluminum alloys-based metal matrix composites with whisker reinforcements have been produced by squeeze casting, then to investigate the heat treatment effect, MMC and AC4CH(matrix) were solutionized at various temperatures and times. The results are summarized as follows

The AC4CH(matrix) showed a tendency that the strength and toughness increases with increasing solution treatment temperature and time. The strength of MMC was increased with increasing solution treatment temperature and time, but the fracture mechanism was very brittle.

The micro-Vicker's hardness of MMC was decreased with increasing solution temperature and aging time.

The more solution treatment was executed, the smaller grain size of MMC observed. And the more solution treatment was executed, the more $MgAl_2O_4$ observed to the interface between whisker and AC4CH by x-ray diffraction.

REFERENCE

1. S. Y. Chang, T. Hiroyasu, and K. Akihiko, "Mechanical Properties and Fracture Process of SiCw/Mg Composites Produced by Squeeze Casting and Extrusion", Materials Transaction, JIM, Vol. 38, No. 1, (1997), pp. 18～27.
2. W. S. Gibbs, J. J. Petrovic and R. E. Honnell, "SiC whisker $MoSi_2$--matrix composites", Ceram. Eng. Sci. Proc., Vol. 8, (1987), pp. 645～648.
3. W. D. Fei, X. D. Jiang, C. Li and C. K. Yao, "Effect of interfacial reaction on the Young's modulus of aluminium borate whisker reinforced aluminium composite", Journal of Materials Science letters, Vol 15, (1996), pp. 1966～1968.
4. S. Takeuchi, M. Yoshida, J. Pan, G. Sasaki and H. Fukunaga, "Mechanical properties of aluminum-borate whisker reinforced magnesium alloy composites by semi-solid process", First Asian-Australasian Conference on Composite Materials(ACCM-1), October 7-9, (1998), pp. 5331～5334.
5. Y. C. Ko and C. F. Chan, "Effect of spinel Content on hot strength of alumina-spinel castables in the temperature range 1000-1500℃", Journal of the European Ceramic Society, Vol. 19, (1999), pp. 2633～2639.
6. P. LU, R. E. Loehman, K. G. Ewsuk and W. G. Fahrenholtz, "Transmission electron microscopy study of interfacial microstructure formed by reacting Al-Mg alloy with mullite at high temperature", Acta Materialia, Vol. 47, 1999, pp. 3099～3104.

Key Engineering Materials Vols. 183-187 (2000) pp. 1243-1248
© 2000 Trans Tech Publications, Switzerland

Mechanical Properties of Tungsten Fiber Reinforced Ti-6Al-4V Alloy

S. Nishida[1], K. Hayashi[2], N. Hattori[1], K. Nakano[3],
Y. Yanagida[4] and H. Tamasaki[5]

[1] Faculty of Science and Engineering, Saga University, Honjyo 1, Saga-shi 840-8502, Japan

[2] Graudate School, Faculty of Science and Engineering, Saga University, Honjo-machi 1, Saga-shi 840-8502, Japan

[3] Takada Industry Co. Ltd., Yahata-Nishi-Ku, Kitakyusyu 806-8567, Japan

[4] Kuroki Engineering Co. Ltd., Yahata-Nishi-Ku, Kitakyusyu 806-0012, Japan

[5] Nittetsu Bolten Co. Ltd., Yukihashii, Fukuoka 824-0038, Japan

Keywords: HIP Treatment, MMC, Tensile Strength, Ti-6Al-4V Alloy, Tungsten Fiber

ABSTRACT

The purpose of this study is to investigate the static mechanical properties of Ti-alloy matrix composite fabricated by HIP treatment. Ti-6Al-4V alloy and W short fiber were used for matrix and reinforcement, respectively. Ti-6Al-4V alloy is known as one of representative Ti-alloys and W short fiber possesses excellent mechanical properties, such as high tensile strength, hardness number and high melting temperature. According to this experimental results, it is found that hardness and tensile strength of this material increase with the increase in volume fraction of W short fiber. In addition, the highest value of tensile strength achieved among the metal matrix composites for this material becomes 1,520MPa under the condition of W fiber volume fraction of V_f=9% (corresponding to the diameter of W short fiber by 20μm).

1. INTRODUCTION

Composite material has been expected for high-performance one, which has excellent properties such as high heat-resistance, low thermal expansion and abrasion resistance, etc... Metal matrix composite (MMC) e.g. could be applied to various fields of industries in the future [1]. The mechanical properties of MMC are dependent on the strength of matrix/reinforcement interface and fabricating process affected by the material combination [2]. Therefore, the reliability and reproducibility of the parts are very low, and the performance meeting a demand of various structural materials has not been achieved yet.

High specific strength defined as the ratio of tensile strength per density is necessary for a matrix of MMC. Ti-alloy is considered as an attractive matrix because it possesses excellent specific strength and corrosion resistance [3]. For the fabricating process, HIP (Hot Isostatic Pressing) treatment is known as one of most advanced powder-metallurgical methods for reducing the manufacturing cost of Ti [4,5]. It is possible to produce a part with near net shape using HIP process.

In this study, fiber reinforced composite material in which using Ti-alloy for matrix and W short fiber for reinforcement was produced by HIP treatment. In addition, rotary swaging process was employed to improve the arrangement of fiber orientation in the Ti-alloy matrix. The evaluation of the mechanical properties of this MMC is reported and discussed in this paper.

Table1 Chemical composition mass%

Al	V	Fe	O	C	N	H
6.14	3.93	0.17	0.19	0.011	0.014	0.009

Table 2 Tensile strength and aspect ratio of W fiber

	Fiber diameter d μm	Tensile strength σ_B MPa	Aspect ratio l*/d		
			Max.	Min.	Ave.
W20	20	3430	135	7.0	47.9
W30	30	3270	147	7.3	48.2

*l; Fiber length

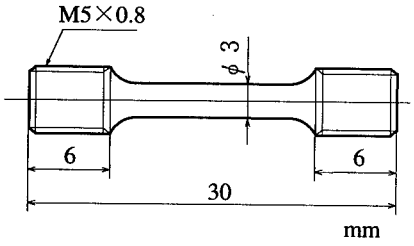


Fig.1 Shape and dimensions of specimen

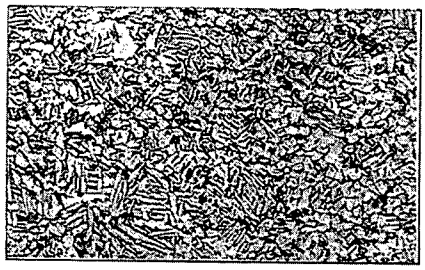


Fig.2 Surface observation result of transverse section for TW0

2. EXPERIMENTAL PROCEDURE

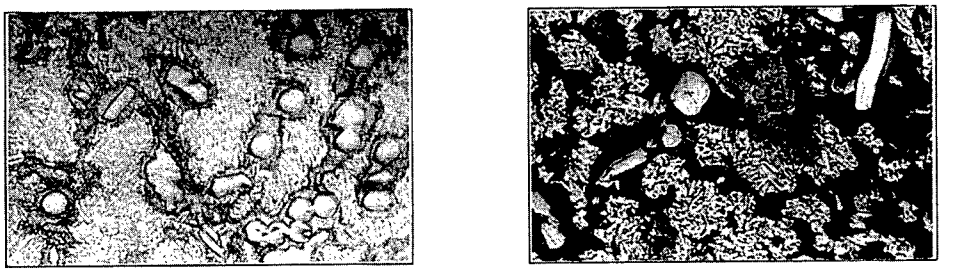
Table 1 lists chemical compositions of Ti-alloy powder. The Ti-alloy powder was produced by the atomization method. Average particle size is about 100 μm.

Table 2 lists the tensile strength, density and aspect ratio of W fiber, respectively. The nominal diameter of the W fiber are 20 and 30 μm (W20 and W30), respectively. Tensile strength of W20 is higher than that of W30. As shown in table 2, there is no apparent difference recognized between the smallest and largest aspect ratio of each W short fiber. After mixing Ti-alloy powder and W short fiber at a specified volume with a V mil mixer, then HIP process was carried out. Condition of HIP treatment was 100MPa pressure at 950℃ for 1hr in Argon gas. This temperature was controlled to be under the transformation temperature of Ti-alloy matrix and hence the mechanical property or microstructure of Ti-alloy matrix would be neither greatly affected nor damaged.

Rotary-swaging processing was conducted in order to improve the arrangement of W short fiber in the Ti-alloy matrix and furthermore to improve the strength in the specified orientation, after heated at 950℃ in an electric furnace. The MMC specimen using W20 and W30 reinforcement hereafter are referred to as TW20 and TW30, respectively, and TW0 represents the Ti-alloy matrix material (without any reinforcement) that was fabricated by the same process. In addition, a sub-number may be attached to indicate the volume fraction of W fiber (e.g. TW20-9 represents TW20 with 9% W fiber reinforcement.)

For observing the microstructure, specimen surface was polished with emery paper then lapped with Al_2O_3 polishing powder and later etched with Kroll's reagent (HF; 2ml, HNO_3 ; 4ml, H_2O; 1000ml).

Figure 1 shows the shape and dimensions of the tensile test specimen. Tensile tests were carried out using an hydraulic universal testing machine (with capacity of 98kN) in room environment.



(a) TW20-9 (b) TW30-9 200 μ m

Fig.3 Surface observation result of transverse section for TW20-9 and TW30-9

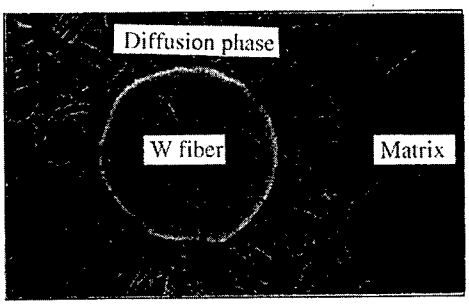
3. EXPERIMENTAL RESULTS

3.1 Surface Observation Result

Figure 2 shows the micrograph of TW0, this figure shows quite uniformly fine equiaxial α phase that particularly achieved by HIP treatment [6] .

Figure 3 (a) and (b) show the micrographs of the transverse section of TW20-9 and TW30-9. These figures show that the microstructure contains no severe defect such as large pores, debonding interfaces or clusters of W short fiber. From these results, it is considered that both the dispersing and mixing process of Ti-alloy powder with W short fiber and HIP treatment condition were quite adequate that resulted in the uniform distribution of W short fiber in the Ti-alloy matrix. As a result of the EPMA analysis, the interface of Ti-alloy matrix/ W short fiber is a diffusion phase in which the W atom diffuses into the Ti-alloy matrix.

Figure 4 shows the SEM micrograph of TW20-9's cross-section. The hardness of Ti-alloy matrix, W short fiber and interface's diffusion phase according to the position indicated in this micrograph is listed in the Table 3, respectively. The average hardness of the diffusion phase is about 10% higher than that of the Ti-alloy matrix.



10 μ m

Fig.4 Diffusion phase for TW20-9

Table 3 Hardness test result

No	Hardness number HV		
	Composite*	Ti-alloy matrix**	Diffusion phase*
TW0	358	358	—
TW20-1	325		
TW20-9	356		
TW30-1.5	345		
TW30-2	396		
TW30-3	370	383	435
TW30-4	340		
TW30-5	392		
TW30-7	409		
TW30-9	410		

* ; HV(1.96N) ** ; HV(0.049N)

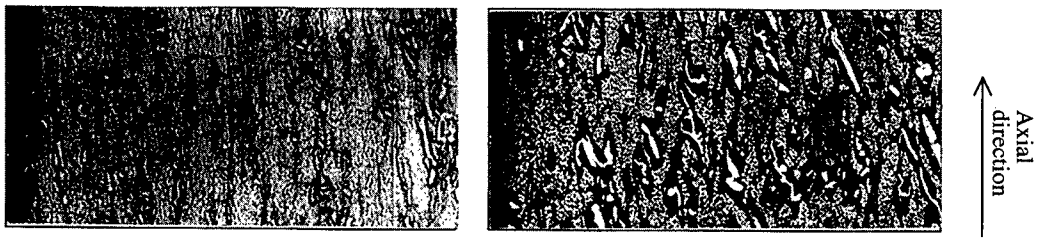


Fig.5 Surface observation result of longitudinal section forTW20-9 and TW30-9

Table 4 Hellman's orientation coefficient

No	Max.	Min.	Ave
TW20-1	0.998	-0.500	0.863
TW20-9	1.000	0.469	0.925
TW30-1.5	1.000	-0.061	0.803
TW30-2	0.997	-0.328	0.745
TW30-3	1.000	-0.404	0.391
TW30-4	1.000	-0.051	0.807
TW30-5	1.000	0.417	0.859
TW30-7	0.998	0.230	0.797
TW30-9	0.999	-0.059	0.775

Table 5 Tensile test result

No	Tensile strength σ_B MPa
TW0	1088
TW20-1	1335
TW20-9	1520
TW30-1.5	1145
TW30-2	1173
TW30-3	1135
TW30-4	1150
TW30-5	1276
TW30-7	1303
TW30-9	1303

Figure 5(a) and (b) show the micrographs of TW20-9 and TW30-9 for the longitudinal section. From this figure, it is recognized that W short fibers are well orientated to the axial direction of the specimen. Though it is not covered in the figure, similar orientation of W short fiber is obtained in the whole specimen. It is reasonable to consider the rotary swaging conducted as a secondary working after HIP treatment is effective for unifying the orientation of W short fiber in the MMC. It was found that, the degree of co-orientation of W short fibers to the extruded direction increases with the volume fraction of W short fibers. It is generally known that the strength of the fiber-reinforced composite is dependent to the orientation of the fiber [7]. Therefore, it is necessary to evaluate quantitatively the orientation of W short fiber in the specimen. This evaluation was reformed using the Hellman's orientation coefficient and as listed in Table 4. The axially facing fiber orientation angle was measured for the fibers near the center of the longitudinal section of each specimen. Hellman's orientation coefficient F is expressed in the following equation.

$$F=\{3\ (\cos 2\theta)\ -1\}/2 \quad \cdots \quad (1)$$

where, θ is fiber orientation angle for the extruding direction. F=1, F=0 and F=-1/2 indicate the state of a complete parallel orientation, a random orientation, and a complete vertical orientation,

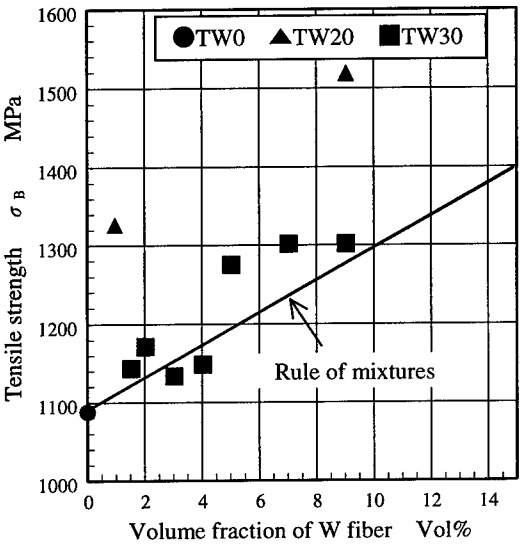


Fig.6 Relation between tensile strength and volume fraction of W fiber



Fig.7 The characteristic part of the fracture surface for TW20-9

respectively. The results in the circumstance of this work show a tendency of improvement with the increase in W short fiber volume fraction and with the decrease of the cross section of W short fiber. Consequently, fiber orientation in TW20 is better than that in TW30 and TW20-9 possesses the best result among all of the specimens.

3.2 Tensile Test Results

Table 5 lists the tensile test results. The tensile strength of TW0 shows a higher value with respect to the tensile strength of Ti-alloy fabricated by a conventional thick plate. Therefore, the condition for HIP applied in this work is considerably suitable.

Figure 6 illustrates the relation between tensile strength and the volume fraction of W short fiber. The curve in the figure shows simple rule of mixtures calculated from the volume ratio of reinforcement and matrix. A linear rule of mixtures is shown in the following equation [8].

$$\sigma_c = \sigma_f V_f + \sigma_m (1-V_f) \quad \cdots \quad (2)$$

Where, σ_f and σ_m are tensile strength of W fiber and Ti-alloy matrix, respectively. And, V_f is volume fraction of W fiber. From this figure, the tensile strength of TW20 and TW30 tends to improve with the increase in volume fraction of W short fiber. Tensile strength of TW20 shows about 13% higher value than that of TW30, and it is interesting to know that this value is even higher than the tensile strength calculated by the equation (2).

4. DISCUSSION

From the tensile test result, it is concluded that the W short fiber is effective for improving the tensile strength of the Ti-alloy matrix composite and there is a correlation between the improvement of tensile strength and the W fiber volume fraction. Therefore, mechanism of the improvement in tensile strength of this MMC will be thoroughly discussed in the following. Generally, Ti-alloy has high deformation resistance for sintering, Therefore, the sintering of Ti-alloy has been often carried out at high temperature about 1100~1200℃. The strength of the reinforcement may decrease by the recrystallization in this circumstance. In the meantime, the recrystallization temperature for the W fiber is definitely high enough to prevent recrystallization even at the maximum temperature required for HIP process of Ti-alloy matrix. It is considered that the use of W fiber for Ti-alloy

matrix provides no specified restriction of HIP treatment temperature due to its especially high transformation temperature.

Figure 7 shows the fracture surface of the tensile specimen. From this figure, as the pull-out-fiber from the Ti-alloy matrix is hardly observed, the interface strength between W short fiber and Ti-alloy matrix is significantly strong. It is significant to know that the use of nonmetal fiber which does not lose fiber strength at sintering temperature of the Ti-alloy such as SiC whisker or carbon fiber [9,10] has been normally experienced the problem of weak interface. The tensile strength estimated from the hardness of diffusion phase is higher than that of the Ti-alloy matrix. Therefore, it is considered that the existence of the diffusion phase improves considerably the strength of the composite material. It is concluded that W fiber would be suitable for the reinforcement of Ti-alloy matrix MMC.

5. CONCLUSIONS

The W short fiber reinforced Ti-alloy matrix MMC was successfully fabricated by HIP process then its static mechanical property was investigated. Main results obtained in this study is as follows:

(1) The tensile strength of the W fiber reinforced Ti-alloy matrix MMC tends to improve with the increase in volume fraction of the W fiber and the best value of tensile strength achieved in this work is 1520MPa corresponding to the MMC reinforced with diameter of W fiber by 20 μ m at the volume fraction of V_f=9%.

(2) As a result of the surface observation, the existence of defects such as cluster and porosity is not observed. That is to say, dispersion and mixing between W short fiber and Ti-alloy matrix are good and the current HIP condition is suitable.

(3) Swaging process unifies the orientation of W short fiber to the axial direction that greatly affects the unidirectional tensile strength of this composite material.

(4) The existence of the diffusion phase at the interface of the W short fiber and the Ti-alloy matrix improves the strength of this type of composite material.

ACKNOWLEDGEMENT

This study had been performed under the sponsorship of Fukuoka Industry Science & Technology Foundation.

REFERENCES

1) T.Hayashi , The composite material engineering,(1980).p1173-1181
2) H,Ochiai et al.: Journal of the Japan Society for Composite Materials,21-2,(1995),p37-46.
3) H.Kusamichi et al.: Titanium and its applications,(1983),p90.
4) T.Kimura et al.: Journal of the Japan Society of Mechanical Engineers,28-11,(1998),p897-901.
5) Titanium material researchers, Present aspect of Titanium materials research in Japan,(1989),p81.
6) R.Watanabe et al.: Journal of the Japan Institute of Metals,28-11,(1989),p893-896.
7) Y.Imai et al.: Journal of the Japan Society for Composite Materials,18-3,(1993),p129-133.
8) Y.Minoda.: Journal of The Iron and Steel Institute of Japan,75-9,(1989),p363-368.
9) K.Honda et al.: Journal of Japan Institute of Metals,58-1(1994),p91-97.
10) T.Yamamura et al.: Journal of the Japan Society for Composite Materials,17-1,(1991),p24-31.

Key Engineering Materials Vols. 183-187 (2000) pp. 1249-1254
© 2000 Trans Tech Publications, Switzerland

Behavior of Cyclic Fatigue Crack Growth for SiC Ceramics

Yong-Hak Huh[1], Kyung-Jin Yoon[1], Seong-Jae Cho[1] and Jiho Song[2]

[1] Material Evaluation Center, Korea Research Institute of Science and Standards, Science Town, Taejon 305-600, Korea

[2] Department of Mechanical Engineering, Korea Advanced Institute of Science and Technology, Seoul, Korea

Keywords: Crack Closure, Cyclic Fatigue Crack Growth, Hysteresis Loop, Load-Differential Strain Curve, Silicon Carbide Ceramic, Silicon Carbide Composite Ceramic, Stress Ratio

ABSTRACT

Behavior of cyclic fatigue crack growth and crack closure in silicon carbide ceramics has been investigated. Hot-pressed monolithic SiC and SiC composite reinforced with TiB_2 particulate were used in this study. Cyclic fatigue tests for stress ratios of 0.1, 0.3 and 0.6 were carried out using four-point bend specimens. The load-strain and load-differential strain curves were monitored with crack growth. They show non-linearities due to crack closure and hysteresis loop. The crack opening level is determined from the load-differential strain curve. The crack opening ratio is nearly constant with the crack propagation at a given stress ratio and is dependent on the stress ratio. Crack in theses ceramics shows a susceptibility to cyclic fatigue loading. Crack growth rates obtained during cyclic loading are relatively well described by the cyclic parameter, $\Delta K_{eff}/(1-K_{max}/K_{IC})$, which can account for the effects of crack closure and the maximum stress intensity factor. The growth rate curve based on this relationship shows a transition.

1. INTRODUCTION

Behavior of subcritical crack growth under cyclic loading in several structural ceramics, such as Al_2O_3, Si_3N_4 and ABC-SiC, has been reported[1-7]. Cyclic fatigue crack growth in these materials was explained by various mechanisms of crack tip shielding[8]. Frictional degradation of grain bridging along cracked ligament of the specimen[9] has been accepted as the most dominant mechanism. Therefore, the actual crack driving force, K_{tip}, is defined as K_{app}-K_s, where K_{app} and K_s represent the far-field loading and the shielding capacity of the bridging zone, respectively[10]. It is considered that K_{tip} may control the crack growth in ceramic materials. Some methods[7,10,11] have been suggested to determine K_{tip}, but they are not sufficient in explaining cyclic crack growth behavior quantitatively.

Experimental results by several researchers showed that the cyclic fatigue crack growth rate in ceramic materials greatly depends on the maximum stress intensity factor, K_{max}, and relatively weakly on the stress intensity factor range, ΔK (or ΔK_{eff})[1-5]. Thus, the cyclic fatigue crack growth

rate can be expressed as a function of two parameters, i.e.

$$\frac{da}{dN} = f(K_{\max}, \Delta K \text{ or } \Delta K_{eff}) \quad (1)$$

On the other hand, Huh and Song[4] proposed a new expression for cyclic fatigue crack growth rate in aluminas. The relation was presented as a function of K_{max}, ΔK_{eff} and fracture toughness, K_{IC}, with considering that the fracture toughness influences more or less the cyclic fatigue crack growth rates. They showed that the relationship can be used to evaluate the effect of microstructure and stress ratio relatively systematically.

Therefore, in this study, behavior of cyclic fatigue crack growth for monolithic silicon carbide and silicon carbide composite reinforced with TiB_2 particulate is investigated, using the new expression for evaluation of crack growth rate. Meanwhile, behavior of crack closure is also examined with stress ratio.

2. EXPERIMENTAL PROCEDURES

Two kinds of SiC ceramics, monolithic SiC and SiC composite reinforced with TiB_2 particulate, were fabricated by a conventional hot-pressing technique. Powder mixtures of 95wt%SiC-5wt%Al_2O_3 and 95wt%(85vol.%SiC-15vol.%TiB_2)-5wt%Al_2O_3 were hot-pressed at 2050°C and 30MPa under vacuum, and plates of 40x40x10mm were obtained. Bending strength and fracture toughness are 610MPa and 3.55MPa $m^{1/2}$ for monotonic SiC, respectively, and 570MPa and 4.98MPa $m^{1/2}$ for SiC-TiB_2 composite, respectively.

Four-point bend specimens of 6x3x40mm were machined from the plate. A chevron notch was introduced into the specimens. A side surface of the specimen was lapping-polished to a mirror-like surface finish with 1 μm diamond paste to facilitate easy measurement of fatigue crack length. Pre-cracking prior to cyclic fatigue test was carried out by cyclic fatigue loading at stress ratio R of 0.1 and at a frequency of 10Hz, using load-decreasing technique.

Cyclic fatigue tests were carried out under constant amplitude, four-point bending loads, using servo-hydraulic fatigue testing machine. The pre-cracked specimens were cyclically loaded at stress ratio of R=0.1, 0.3, and 0.6 and at a frequency of 10Hz. Crack length was measured by a travelling microscope with a resolution 1μm equipped with a CCD camera. Variations of back-face strain compliance of the specimen with cyclic fatigue crack growth were continuously monitored through PC-based measurement system. Crack closure was measured by the unloading compliance technique[13] from the load-differential strain curve.

3. RESULTS AND DISCUSSION

3.1. Cyclic fatigue crack growth

The monolithic SiC and SiC-TiB_2 composite ceramics used in this study were susceptible to the cyclic fatigue crack growth[5]. The results obtained under cyclic fatigue loading at R=0.1, 0.3 and 0.6 are presented in Fig. 1. The crack growth rate, *da/dN*, is plotted as a function of the maximum stress intensity factor K_{max} and the stress intensity factor range ΔK, respectively. Growth rates, as a function of K_{max}, increase with decreasing the stress ratio, R, at a given K_{max}, but effect of stress ratio on the growth rates is not so strong. On the other hand, growth rates, based on ΔK, are affected very strongly by the stress ratio and increase with increasing R. The cyclic fatigue crack growth rates in SiC ceramics greatly depend on K_{max} and relatively weak on ΔK, as has been well reported by other researchers[1-5].

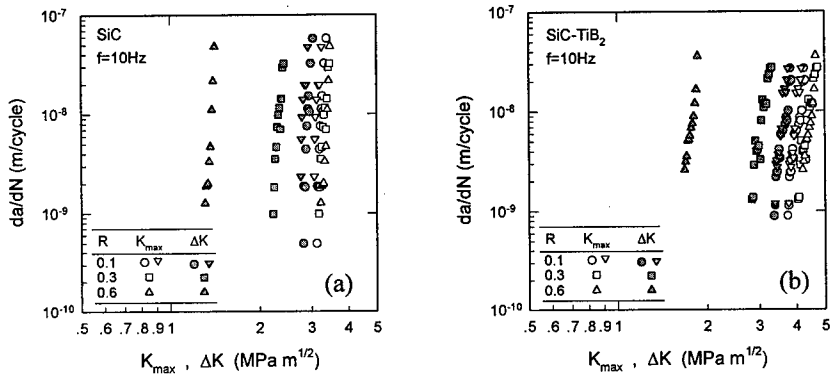


Fig. 1. Cyclic fatigue crack growth rate as a function of K_{max} and ΔK.
(a) for monolithic SiC. (b) for SiC-TiB_2 composite.

3.2. Behavior of crack opening

Figure 2 shows a typical example of variations of load-differential strain curves with crack growth for SiC ceramics. The non-linearities and hysteresis loop appear at the early stage of precracking and this shape of the curve remains unchanged during the test. A typical shape of the curve can be represented as in Fig. 3(a). The shape of the curve like Fig. 3(a) has been reported in aluminas[5,7,12]and silicon nitride[2]. As reported by several researchers [2,5,7,12], the hysteretic behavior of the curve may be related to the frictional sliding of the bridging grains in bridging region along cracked ligament. The non-linearities of the curve can result from the hysteretic behavior and crack closure[4,5]. The crack closure in ceramics can be induced by fracture surface roughness and debris generated by frictional wear at bridging grains[9].

It is not easy to define the crack closure from the curve, including non-linearities and hysteresis loop, like Fig. 3(a). However, Huh and Song[4] suggested a new definition in aluminas, assuming that the hysteretic behavior and crack closure occur independently. Figure 3 represents the procedure to define the crack closure in SiC ceramics according to their concept. The resultant load-differential strain curve, as shown in Fig. 3(c), is obtained by subtracting Fig. 3(b) from Fig. 3(a). Figure 3(b), which is a symmetrical load-differential strain curve, can be obtained by generating lower portion of the curve artificially with mapping the upper portion of the curve of Fig. 3(a) with respect to the center point of O of the curve. The curve of Fig. 3(c) is expected to display the

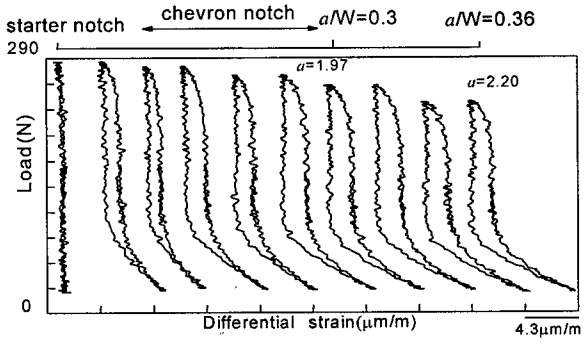


Fig. 2. Variations of load-differential strain curves with crack growth for SiC-TiB_2 composite.

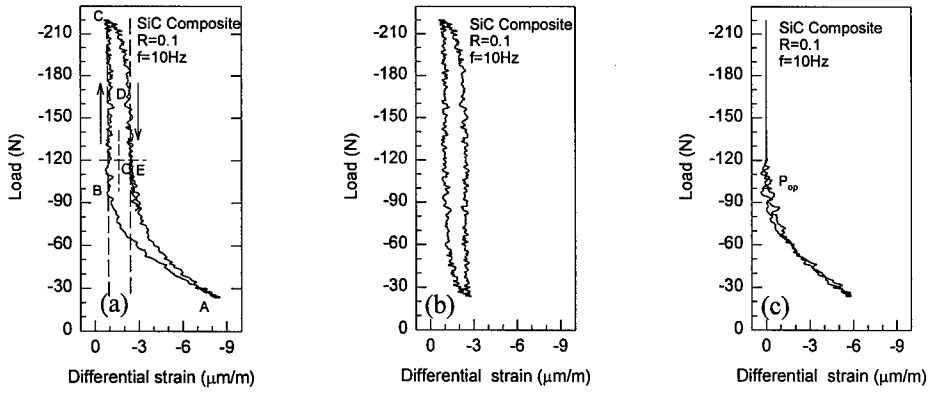


Fig. 3. Definition of crack opening level in SiC ceramics.

compliance variation due to crack closure alone.

Crack opening ratio U* corresponding to the crack opening point (K_{op}^*) newly obtained from the resultant load-differential strain curve is plotted in Fig. 4. Here, crack opening ratio U* is defined by

$$U^* = \frac{K_{max} - K_{op}^*}{K_{max} - K_{min}} \quad (2)$$

Furthermore, the crack opening ratio U_Q determined by using the original definition proposed by Elber[13] is plotted in Fig. 4. For SiC ceramics, the value of U* is nearly the same as U_Q for R=0.1 and 0.3, whereas the value of U* is higher than U_Q for a higher R value. The discrepancy between the values of U* and U_Q for high R values was also shown in aluminas[4]. The value of U* is nearly constant for a given R. For SiC, the values of U* is about 0.5, 0.6 and 0.8 for R=0.1, 0.3 and 0.6, respectively, indicating that the crack opening ratio U* increases consistently with increasing stress ratio. The value of U* for SiC-TiB_2 composite is also dependent on the stress ratio. For low R values, the values of U* for SiC are lower than those for SiC-TiB_2 composite.

3.3. Evaluation of cyclic fatigue crack growth

It was reported that the conventionally measured crack opening data U_Q were not useful for evaluating the crack growth rates in aluminas where the compliance curve showed hysteresis[4]. Therefore, for the SiC ceramics used in this study, it may be reasonable to use the data of U* instead of U_Q because the load-strain curve includes the hysteretic component as shown in Fig. 3. Figure 5 shows the crack growth rates replotted as a function of effective stress intensity factor range ΔK_{eff}* based on U*. In comparison with the results based on ΔK shown in Fig. 1, those based

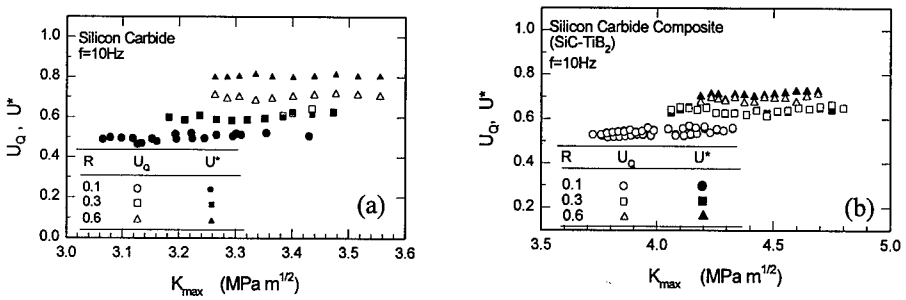


Fig. 4. Crack opening ratio as a function of K_{max}.

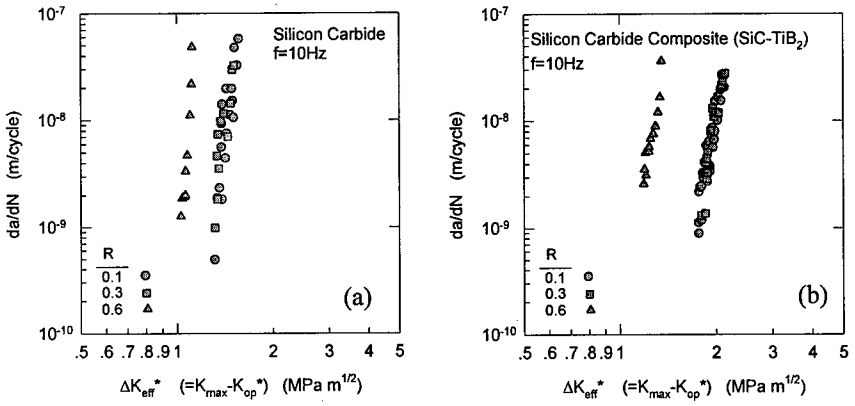


Fig. 5.Cyclic fatigue crack growth rates as a function of ΔK_{eff}*.

on ΔK_{eff}* reveal that the effect of stress ratio is considerably diminished. However, it can be seen that the crack growth rates are not evaluated sufficiently by ΔK_{eff}* alone, as shown in the results for aluminas[4].

To explain the above-mentioned behavior more systematically, the following expression was proposed:

$$\frac{da}{dN} = C\left(\frac{\Delta K_{eff}}{1 - K_{max}/K_{IC}}\right)^{m} \tag{3}$$

Figure 6 shows the crack growth rates evaluated by the Eq. 3. It can be seen that the growth rates are relatively well represented by Eq. 3, although the data are a little scattered. For SiC ceramics used in this study, the crack growth rate curve shows a transition. The growth rate curve may be divided into two regions, I and II, as shown in Fig. 6. The exponent m of Eq. 3 for Region II is 2.4 and 2.1 for monolithic SiC and for SiC-TiB_2 composite, respectively. These values are similar to those obtained for aluminas[4]. The transition of the curve, as shown in Fig. 6, is compared to the results in aluminas[4], where the curve was divided into three regions, I, II and III. There are few results of the crack growth rate evaluated by ΔK_{eff} using SiC ceramics, but Gilbert *et al*[1] reported some results obtained for ABC-SiC. In Fig. 7, the results are replotted by using Eq. 3. Although the crack opening may be defined in a different manner from that shown in Fig. 3, the results are well

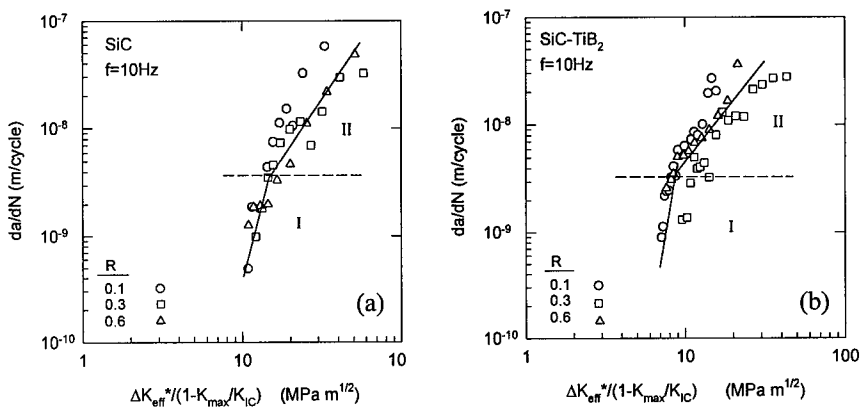


Fig. 6. Cyclic fatigue crack growth rates as a function of ΔK_{eff}*/(1-K_{max}/K_{IC}).

expressed by Eq. 3. And, the curve of the growth rates has a transition. So, it can be said that the cyclic fatigue crack growth rates in SiC ceramics is well represented by Eq. 3.

In this study, the method outlined in Fig. 3 for definition of crack opening and Eq. 3 for evaluation of crack growth rates show useful interpretation of the experimental data in SiC ceramics. However, as commented by Huh and Song[4], it may be necessary to further examine the validity of these methods for other ceramics.

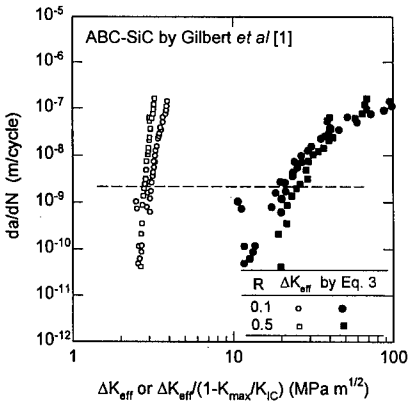


Fig. 7. Cyclic fatigue crack growth rates for ABC-SiC.

4. CONCLUSIONS

The cyclic fatigue crack growth behavior for monolithic SiC and SiC-TiB_2 composite has been investigated. The conclusions are summarized as follows.

(1) The crack for SiC ceramics shows to be susceptible to the cyclic loading. Fatigue crack growth rates under cyclic loading are greatly dependent on K_{max} and relatively weakly on ΔK.

(2) The load-differential strain curves show non-linearities and hysteresis loop. The crack opening ratio, which is obtained from the curve, is nearly constant with the crack propagation at a given stress ratio and is dependent on the stress ratio.

(3) Crack growth rates obtained during cyclic loading are relatively well described by the cyclic parameter, $\Delta K_{eff}/(1-K_{max}/K_{IC})$. The growth rate curve based on this relationship shows a transition.

REFERENCE

1. C.J. Gilbert, J.J. Cao, W.J. Moberlychan, L.C. Dejonghe and R.O. Ritchie, *Acta metall. mater.* **44**, (1996) p.3199.
2. C.J. Gilbert, R.H. Dauskardt and R.O. Ritchie, *J. Am. Ceram. Soc.* **78**, (1995) p.2291.
3. R.H. Dauskardt, B.J. Dalgeish, D. Yao, R.O. Ritchie and P.F. Becher, *J. Mater. Sci.* **28**, (1993) p.3258.
4. Y.H. Huh and J. Song, Fatigue Fract. Engng. Mater. Struct. 21 (1998) p. 1575
5. Y.H. Huh, S.J. Cho, K.J. Yoon and J. Song, Fatigue'96(ICF), Germany, Berlin, (1996) p.1675
6. F. Tamai and K. Hirano, *JSME*, **60**, (1994) p.1150 (in Japanese).
7. M, Li and F. Guiu, *Acta metall. mater.*, **43**, (1995) p.1871
8. R. O. Ritchie, *Mater. Sci. Engng. A*, **103**, (1988) p.15.
9. S. Lathabai, J. Rodel and B. R. Lawn, *J. Am. Ceram. Soc.* **74**, (1991) p.1340.
10. J. Rodel, J.F. Kelly and B.R. Lawn, *J. Am. Ceram. Soc.* **73**, (1990) p.3313.
11. X. Hu and Y-W Mai, *J. Am. Ceram. Soc.* **75**, (1992) p.848.
12. F. Guiu, M. Li and M.J. Reece, *J. Am. Ceram. Soc.*, **75**, (1992) p.2976.
13. W. Elber, *Engng. Fract. Mech.* 2, (1970) p.37

Key Engineering Materials Vols. 183-187 (2000) pp. 1255-1260
© 2000 Trans Tech Publications, Switzerland

A Model on the Strengthening and Embrittlement of Devitrified Nanocomposites

Hyoung Seop Kim[1], Sun Ig Hong[1] and Min-Seok Sohn[2]

[1] Department of Metallurgical Engineering, Chungnam National University, Yusong, Taejon 305-764, Korea

[2] Department of Mechanical and Materials Engineering, The University of Western Australia, Nedlands WA 6907, Australia

Keywords: Amorphous Alloys, Devitrification, Embrittlement, Hardening, Mixture Model, Partial Crystallization

ABSTRACT

A mixture model in which partially crystallized (devitrified) amorphous alloys are regarded as a nanocomposite of precipitates and a remaining amorphous matrix is presented. The model aims at describing the strengthening and ductile-brittle transition behaviour of devitrified nanocomposites. The nano-sized particles are treated as perfect materials because there are hardly any imperfections within the particles. The matrix is treated as amorphous materials, in which the solute concentration increases with the volume fraction of particles. A simple rule of the mixtures was used for calculating the strength of the nanocomposites. By assuming the perfectly mixed solution, the embrittlement of the matrix with the volume fraction of particles is considered. As an example, the model was applied to Al-Ni-Y alloys. The strength and the embrittlement of the devitrified Al-Ni-Y were investigated using the proposed model and compared with the published data available.

1. INTRODUCTION

Nanocrystals embedded in amorphous matrix through partial crystallization or controlling cooling speeds during rapid solidification, termed as nanometer-scale composites or nanocomposites [1], can obviously improve mechanical properties of metallic glasses. For example, it has been reported [2] that Al-based amorphous alloys exhibit high tensile strength above 100 MPa and a nanocomposite composed of a homogeneous dispersion of nanoscale Al particles within the remaining amorphous matrix can significantly increase the tensile strength up to about 1.5 times as high as that of the corresponding amorphous single phase alloys. Following the discovery of Zr-based bulk metallic glasses with wide supercooled regions, recently, it was found [3] that through partial crystallization, nanocrystal phases can be formed in some Zr-based bulk metallic glasses and the strength of the nanocomposites can be significantly improved.

Although several different explanations for the strengthening mechanisms in these

nanocomposite materials have been proposed, it is still unclear how the presence of nanocrystal phases improves the strength of the metallic glasses. Inoue's group [2] suggested that the increase of the strength is due to an enhancement of the resistance to shear deformation caused by the nanoparticles which have higher strength than the amorphous phase with the same composition, and the solute strengthening effect is not significant [4]. On the other hand, Greer's group [5] attributed the hardening of the nanocomposites to the solute enrichment of the remaining amorphous matrix, but they appear not to have taken into consideration the presence of nanoparticles and the decrease of the volume fraction of the remaining amorphous phase. Recently, Kim *et al.* [6] proposed a mixture model to describe quantitatively the strengthening behaviour, considering the composition change in the remaining matrix.

Another important issue for engineering applications is an embrittlement problem. As the volume fraction of the nanoparticles increases during the heat treatment, the hardness of the specimen increases at early stage and exhibits brittle fracture behaviour later. An interesting observation is that the ductile-brittle transition of partially crystallized amorphous alloys occurred even before the brittle intermetallic precipitated in the matrix. Kim *et al.* [7] attributed the decrease of ductility to the decrease increase of the volume fraction of nanoparticles. Yoon *et al.* [8] suggested that nanoparticles act as crack initiation sites because shear deformation of the amorphous matrix is registered by strong nanoparticles. Kim and Hong [9] suggested a model of the ductile-brittle transition of devitrified amorphous alloys on the assumption that the diffusivity of one element is so low that the rejected atoms are limited near the interface region.

In this paper, we present a simplified model of the previous study [9] using a full mixture model regarding the material as a nanophase composite with homogeneous solute concentration.

2. MODEL

Fig. 1 shows a schematic of the mixture model in the partially crystallized amorphous alloy by heat treating the fully amorphous alloy. The solute elements rejected from the nanoparticles during the heat treating are distributed in the remaining amorphous matrix. The concentration profiles of the solute elements varies with the diffusion rate of each element. As heat treatment proceeds, the solute element diffuse each other and homogeneous mixing can be obtained. It was shown [10] that the results of the finite element calculations for the analysis of plastic deformation in nanocrystalline materials are almost the same as those obtained using the rule of mixtures.

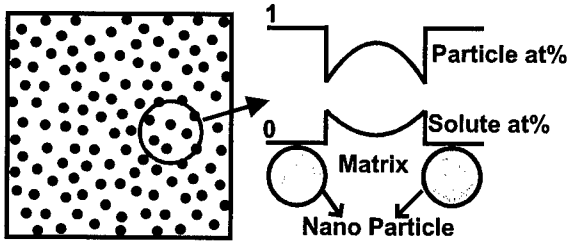


Fig. 1. A schematic model of precipitate particles embedded in amorphous matrix and schematic concentration profiles of solute atoms.

Therefore, in this study the following simple rule of mixtures based on the volume fraction of each phase is used for the overall strength of the nanocomposites.

$$\sigma_{eff} = f_p \sigma_p + f_m \sigma_m \tag{1}$$

where σ and f refer to the strength and volume fraction of each phase, and subscripts p and m refer to precipitate particle and amorphous matrix, respectively. The necessary parameters for the analysis are the mechanical properties and volume fraction of each phase. The volume fraction of each phase can be measured directly from DSC curves [11] or directly from image analysis of TEM images [12].

The nanoparticles can be usually assumed to have the theoretical maximum strength, since they are so fine that that contains no dislocations or other imperfections [2]. However if the nanoparticles grow, the effect of the grain size on the strength of particles should be considered, e.g. the Hall-Petch relation. The deformation behaviour of remaining amorphous matrix is flow-like, therefore dislocations do not contribute to the deformation of this material. The main factor determining the mechanical properties of the amorphous matrix is the chemical composition. The strength of the amorphous material with various chemical compositions can be measured from fully amorphous ribbon specimens. The strength of the remaining amorphous matrix is used from the fully amorphous ribbon's experimental results.

The most important parameter which determines the embrittlement of the fully amorphous alloy was suggested to be the chemical composition [2]. As the solute contents of the alloys, e.g. Al-Ni-Y alloys, increases from pure metal, the microstructure of melt spun ribbon was observed to change from crystalline phase through a mixture structure of amorphous plus crystalline phase and then ductile amorphous phase to brittle amorphous phase [2,13]. During primary crystallization, the composition of the amorphous matrix changes since there is total rejection of solute atoms from the crystallite into the matrix as the volume fraction of the particles increases. A partially crystallized amorphous alloy was assumed to become brittle if the concentration of solute atoms in the remaining amorphous matrix exceed the critical solute concentration above which the fully amorphous alloys are brittle based on the experimental results.

3. APPLICATION ON THE MODEL

The full mixture model described above was applied to the Al-Ni-Y alloys. The computation results were compared with the experimental data available in the literature. The composition change of the matrix during the devitrification can be obtained using the following equation on the assumption that there is no volume change during the reaction:

$$\begin{aligned} Al_{1-C_{Ni,0}-C_{Y,0}} Ni_{C_{Ni,0}} Y_{C_{Y,0}} &= f_{Al} Al + (1-f_{Al}) Al_{C_{Al}} Ni_{C_{Ni}} Y_{C_Y} \\ &= f_{Al} Al + (1-f_{Al}) Al_{\frac{1-f_{Al}-C_{Ni,0}-C_{Y,0}}{1-f_{Al}}} Ni_{\frac{C_{Ni,0}}{1-f_{Al}}} Y_{\frac{C_{Y,0}}{1-f_{Al}}} \end{aligned} \tag{2}$$

where $C_{Ni,0}$ and $C_{Y,0}$ are the initial concentration of Ni and Y and C_{Al}, C_{Ni} and C_Y are the average concentration of Al, Ni and Y in the remaining amorphous matrix after heat treatment, respectively.

The theoretical shear strength of Al particle is 1.53 GPa [14] and a theoretical hardness value is 7.96 GPa. As the solute concentration of the Al-Ni-Y amorphous alloys increases, the hardness increases. The composition dependency of the hardness of fully amorphous Al-Ni-Y alloys measured fits a linear relation, Eq. (3), [6] within the amorphous formation range (solute

concentration between 0.1 and 0.2).

$$H_{am} = -883 + 28900(C_{Ni} + C_Y) \ . \tag{3}$$

Inoue *et al.* [13] found that the amorphous Al-Ni-Y alloys containing over 80 at% Al atoms can be bent by 180 ° without fracture. Therefore, it can be assumed that the critical solute (Ni+Y) composition for the ductile-brittle transition of amorphous alloys was approximately 20at%.

4. RESULT AND DISCUSSION

Using the proposed full mixture model, the strengthening behaviour and the ductile-brittle transition behaviour of Al-Ni-Y alloys with various alloy composition have been investigated. In the model as the volume fraction of Al nanoparticles f_{Al} increases, the average concentration of solute in the remaining amorphous matrix, $(C_{Ni} + C_Y)/(1 - f_{Al})$, increases slowly at first due to the large matrix volume which can accommodate the ejected solute elements, and faster during the later stage due to the decreased volume of the remaining matrix, see Fig. 2. $Al_{50}(Ni+Y)_{50}$ represents the maximum amorphous solute concentration, $Al_{90}(Ni+Y)_{10}$ represents the minimum initial amorphous solute concentration, and $Al_{80}(Ni+Y)_{20}$ represents the initial maximum solute concentration for ductile behavior. The dotted 20 % solute concentration line divides the solute range into two parts. The phase compositions above the dotted line are brittle. This line will be called the ductile-brittle transition line hereafter. Therefore, even if the initial ribbon, for example $Al_{85}(Ni+Y)_{15}$, is ductile, the solute content of the amorphous matrix increases during heat treatment as the volume fraction of fcc-Al increases, and the amorphous phase becomes brittle. Alloys with greater than 20 % solute are always brittle.

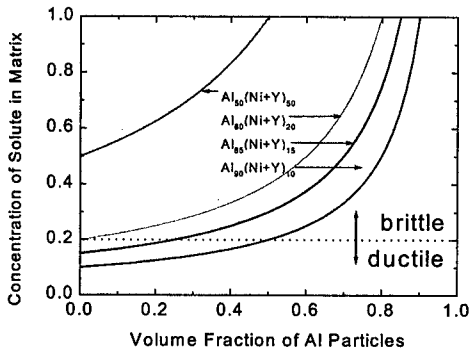


Fig. 2 Solute concentration changes of the remaining matrix after primary crystallization.

Fig. 3 compares the calculated hardness values and experimental ones from the literature [2,5] as a function of the volume fraction of Al particles for various alloy compositions. Considering the inaccuracy of the experimental measurements of the volume fraction and the hardness, the uncertainty of the hardness of Al particle and the inhomogeneity of solute in the matrix, the agreement between the experimental and predicted results is satisfactory.

In Fig. 4 the critical volume fraction of Al particles for the ductile-brittle transition predicted from the mixture model is plotted along with the experimental data from the literature as a function of the initial solute concentration. Considering the scatter of the experimental data described above,

the agreement between the experimental data and the prediction is not bad except one datum.

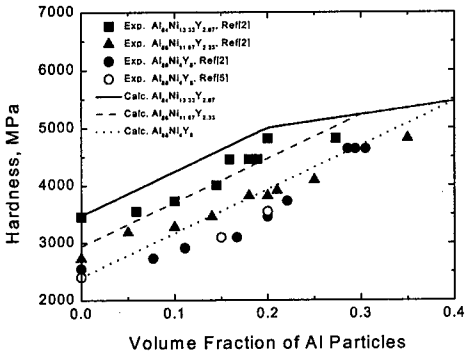


Fig. 3. Comparison between the mixture model calculation and published experimental hardness data [2,5] as a function of the volume fraction of Al particles for various alloy compositions.

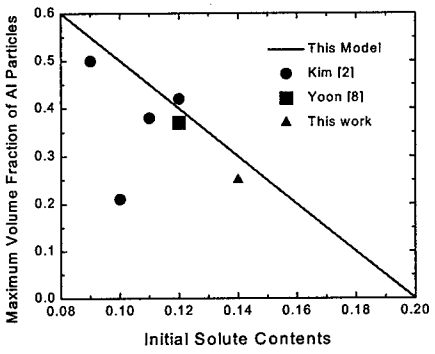


Fig. 4. The critical volume fraction of Al particles for the ductile-brittle transition predicted from the mixture model is plotted along with the experimental data from the literature as a function of the initial solute concentration.

5. CONCLUSIONS

In this study, the strengthening behaviour and the embrittlement behaviour of partially crystallized amorphous alloys (devitrified nanocomposites) have been analyzed using a full mixture model which uses the rule of mixtures based on the volume fraction of each phase. The nanoscale particles are treated as a perfect material with a theoretical shear strength. The strength of the amorphous matrix is used from the fully amorphous ribbon's experimental results assuming that the solute composition is constant as an average value throughout the matrix. Comparison between the calculated hardness values and the experimental results in the literature shows good agreement. A partially crystallized amorphous alloy was assumed to become brittle if the concentration of solute atoms in the remaining amorphous matrix exceeds the critical solute concentration above which the

fully amorphous alloys are brittle based on the experimental results. Considering the scatter of the experimental data described above, the agreement between the experimental data and the prediction is not bad. This model not only explains the experimental results but can also be used to select alloy compositions and heat treatment schedules for the desired properties.

REFERENCES

1. A.L.Greer, Nature, **368** (1994) p. 688
2. Y.H.Kim, A. Inoue and T. Matsumoto, Mater. Trans. JIM, **31** (1990) p. 747
3. P.S.Frankwicz, S.Ram and H.-J.Fecht, Appl. Phys. Lett., **68** (1996) p. 2825
4. M.W.Chen, A.Inoue, C.Fan, A.Sakai and T.Sakurai, Appl. Phys. Lett., **74** (1999) p. 2131
5. Z.C.Zhong, X.Y.Jiang and A.L.Greer, Phils. Mag., B **76** (1997) p. 505
6. H.S.Kim, P.J.Warren, B.Cantor and H.R.Lee, Nanostructured Mater., **11** (1999) p. 241
7. Y.H.Kim, A.Inoue and T.Matsumoto, Mater. Trans. JIM, **32** (1991) p. 331
8. G.M.Yoon, Y.H.Kim, B.H.Jung and J.B.Kim, J. Korean Inst. Met. Mater., **34** (1996) p. 696
9. H.S.Kim and S.I.Hong, Acta Metall., **47** (1999) p. 2059
10. H.S.Kim, C.Suryanarayana, S-J.Kim and B.S.Chun, Powder Metall., **41** (1998) p. 217
11. A.Inoue, H.Tomika and T.Matsumoto, J. Mater. Sci., **18** (1983) p. 153
12. A.Inoue, H.M.Kimura, S.Sasamori and T.Matsumoto, Nanostructured Mater., **3** (1996) p. 363
13. A.Inoue, K.Ohtera, A.P.Tsai and T.Matsumoto, J. Appl. Phys., **27** (1988) p. L479
14. N.Wang, Z.Wang, K.T.Aust and U.Erb, Acta Mater., **43** (1985) p. 519

Key Engineering Materials Vols. 183-187 (2000) pp. 1261-1266
© 2000 Trans Tech Publications, Switzerland

Contact Damage Analysis of Ceramic/Metal Bilayer Composites with Various Modulus Mismatches

Hong Zhao, Xiaozhi Hu and Mark B. Bush

Department of Mechanical and Materials Engineering
The University of Western Australia
Nedlands WA 6907, Australia

Keywords: Ceramic/Metal Bilayer Composites, Contact Damage, Cracking, Modulus Mismatch, Yielding

ABSTRACT

Two ceramic/metal bilayer composites with metal substrates having modulus higher than and similar to the coating modulus are prepared and tested. At large coating thicknesses, the critical loads for Hertzian cone crack initiation are independent of thickness for bilayers with compatible moduli, but decrease with diminishing coating thickness for bilayers with substrates having higher modulus than the coating modulus. At small coating thicknesses, the Hertzian cone crack initiation could be suppressed due to substrate yielding, and initial fracture shifts away the contact area, resulting in a peak in the critical load for cone crack initiation. Careful selection of component properties and layer geometry may therefore be used to maximise the surface crack resistance of the bilayer composites.

1. INTRODUCTION

Ceramic/metal bilayer composites are frequently encountered in various engineering applications and in restorative dentistry. It is understood that cracking in the ceramic coating or along the ceramic/metal interface and yielding in the metal substrate can lead to failure of the layered composites [1-5]. To efficiently prevent the contact damage in the ceramic/metal bilayer system, it is crucial to understand where and how the initial damage occurs in the bilayer structure.

Initial contact damage in ceramic/metal bilayer composites from surface contact may manifest as surface cracking in the ceramic coating due to Hertzian contact stress, cracking in the ceramic coating at the ceramic/metal interface due to bending stress, or yielding in the metal substrate. Previous studies [4,5] showed that, in porcelain/Pd-alloy bilayer composites subject to surface indentation, the first damage takes the form of surface-initiated cone cracks outside the contact area at large coating thickness (> 300 μm), while the damage firstly occurs as yield in the substrate at small coating thickness (< 300 μm). In the latter case, attendant subsurface transverse median

cracks are also observed in the coating as a result of the substrate yielding. In this ceramic/metal system, where the Pd-alloy substrate has a higher Young's modulus (120 - 140 GPa) than that of the porcelain coating (65 - 70 GPa), the coating/substrate modulus mismatch could play an important role in determining which failure mode starts first. However, our understanding of the influence of modulus mismatch on critical loads leading to cracking and yielding in the layered composites is still limited.

The objective of the present work is to conduct a comparative study of the failure modes and the corresponding influence of modulus mismatch and coating thickness. The ceramic/metal systems utilised in the study are porcelain/Au-alloy bilayer composites, having comparable Young's moduli in both layers (1:1.3), and porcelain/Co-alloy bilayer composites, with the metal substrate having much higher modulus than that of the coating (1:3.1).

2. LAYER PREPARATION AND TESTING PROCEDURE

Porcelain/Au-alloy bilayers and porcelain/Co-alloy bilayers, which are commonly used in dentistry, were chosen in this comparative study. The characteristics of the porcelain and Au-alloy and Co-alloy are shown in Table 1.

Table 1. Characteristics of porcelain coating and metal substrates

	Brand name	Composition	Young's modulus (GPa)
Porcelain	Vita Omega 900	–	70
Au-alloy	Argendent 88	88.0% Au – 9.0% Pt balanced by: In, Ta, Sn, Rh and Ir	88
Co-alloy	Novarex	55% Co – 25% Cr – 10% W balanced by: Ru, Nb. Al, Y and Zr	220

Following manufacturers' recommendations, Au-alloy pellets and Co-alloy pellets were melted at 1200 - 1300°C and 1400 – 1500°C, respectively, and cast into blocks of 20 × 15 × 3 mm. These blocks were ground, oxidised at 960°C, and finally sandblasted to provide a good bonding surface for the ensuing coating. Dental porcelain was then applied in sequential layers (each of thickness 300 μm) onto the prepared metal blocks. Each layer was treated as followed: (a) heat rapidly to 600°C in air; (b) heat to 900°C in vacuum in 6 minutes and hold for 2 minutes; (c) cool in air (more slowly for Co-alloy bilayers due to the relatively high thermal expansion mismatch between the two layers). After firing, the top surfaces of the porcelain coatings were ground to specified thicknesses and polished to 1 μm finish.

Indentations (shown in Fig. 1) were made using tungsten carbide (WC) spheres of radii 2.38 and 3.98 mm. The indenters were mounted in the crosshead of an Instron 4300 universal testing machine and driven at a crosshead speed of 0.2 mm/min [7,8]. The cone crack on the coating surface first appears as an arc, then grows to complete the ring crack as the load is further increased.

The loads corresponding to both initiation and completion of the ring crack were recorded. The average and load span of the two loads are seen as the critical load and its error, respectively. The indented surfaces were observed using an optical microscope with Nomarski interference.

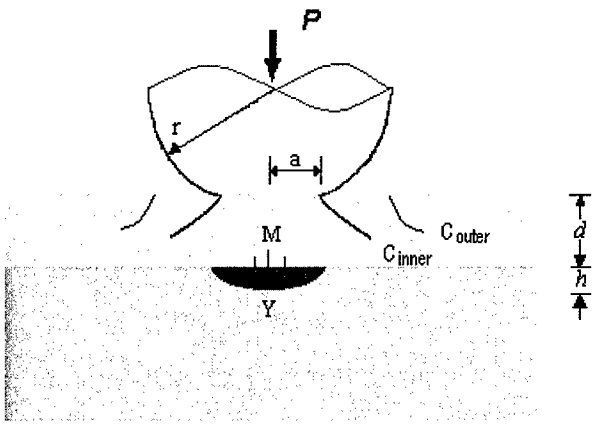


Fig.1. Schematic of the contact between a spherical indenter of radius r under a load P and a ceramic/metal bilayer with coating thickness d. The contact may produce inner Hertzian cone cracks (C_{inner}), outer circumferential cracks (C_{outer}) and median cracks (M) in the coating, and a yield zone of depth h in the substrate.

3. RESULTS AND DISCUSSION

Fig. 2 shows the dependent of critical loads P_C for cone crack initiation in the porcelain/Au-alloy and porcelain/Co-alloy systems on the coating thickness d, for indenter radii r = 2.38 and 3.98 mm, respectively. At large coating thicknesses, the critical load P_C for the porcelain/Au-alloy system is independent of coating thickness d, while P_C for the porcelain/Co-alloy system diminishes as the coating thickness reduces. At small coating thicknesses, critical load peaks are observed in the porcelain/Au-alloy system, at a coating thickness of about 300μm, and the peak slightly shifts with different indenter size.

The data in Fig. 2 have been normalised to eliminate the effect of indenter radius r, by plotting normalised critical load P_C/r against normalised coating thickness d/r, as shown in Fig. 3. It is more clearly shown that the porcelain/Au-alloy system has a stable critical load curve, except for a peak appearing at small coating thickness, but the porcelain/Co-alloy system has a declining curve as the coating thickness decreases. This is in good agreement with the results of previous studies, such as porcelain/alumina [4] and porcelain/Pd-alloy systems [5,9].

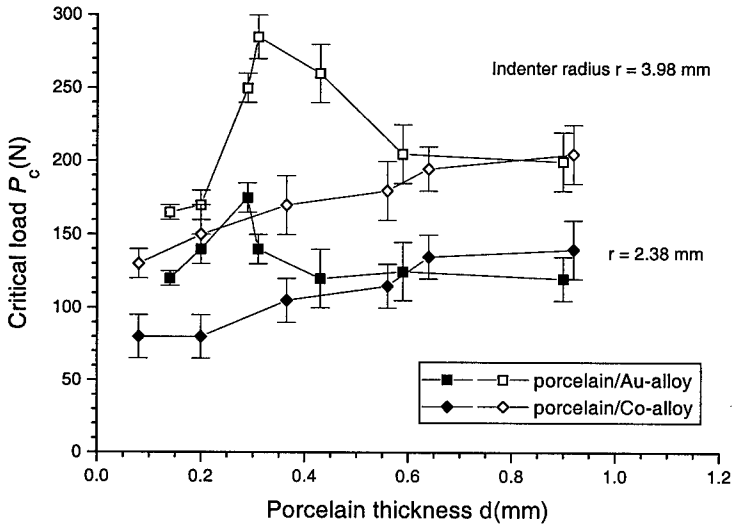


Fig. 2. Critical loads P_C for ring cracking on the top surface of the coating as a function of coating thickness d for porcelain/Au-alloy bilayers and porcelain/Co-alloy bilayers, showing data for specific sphere radii r. Error bars denote the load range over which cone cracks first appear as short arcs, and finally complete themselves as full circles.

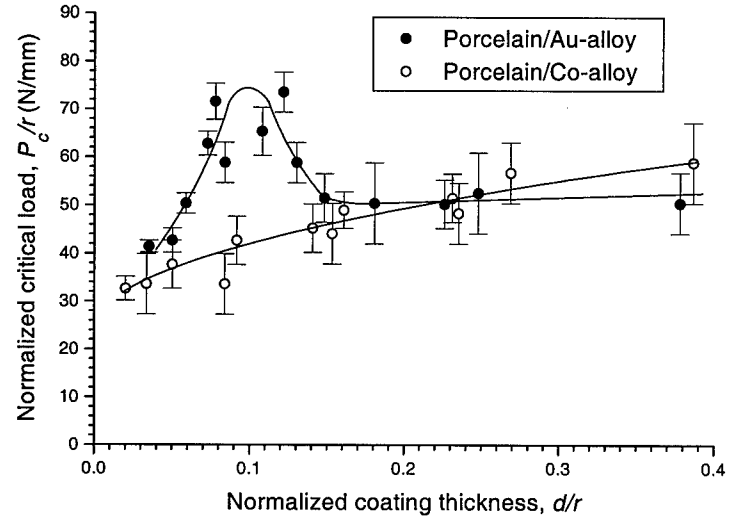


Fig. 3. Data of Fig. 2 normalised by the sphere radius r.

The insensitivity of the porcelain/Au-alloy system to the coating thickness is expected, as the elastic properties of the composite are very similar to the porcelain monolithic. The change of coating thickness therefore has little effect on the critical load, as long as the substrate yield does not occur. However, in the porcelain/Co-alloy system, where the substrate has a much higher modulus than that of the coating, the stiff substrate limits the coating deflection, resulting in a higher maximum Hertzian tensile stress immediately outside the contact area. As a result, the cone crack forms at a relative low load.

Once the substrate yields, the damage mode becomes more complicated. It is observed that, at the critical thicknesses of the peak critical loads (about 300 μm for the porcelain/Au-alloy system), the fracture mode switched from inner cone cracks at large thicknesses to outer cone cracks at small thicknesses. This behaviour is very similar to the results observed in glass/polymer system [10]. It has been demonstrated that, in a ceramic/metal system, the substrate yielding may appear as initial damage in the bilayer structure [4,5]. We postulate that the observed critical load peaks are related to substrate yield. At the beginning of yielding, the substrate modulus is effectively decreasing, leading to increasing the critical load, as in the glass/polymer system. As the substrate yield progresses, the coating beneath the contact is pushed further into the substrate, producing an effective bending of the coating and thereby shifting the location of maximum surface tensile stress away from the contact area. The outer circumferential crack then becomes favoured.

The peak values in the critical load curves shed some light on the critical load optimisation in the porcelain/Au-alloy system, provided that limited yielding in the substrate can be tolerated. More experiments to investigate the yielding in the substrates and interface-initiated median cracking in the coatings are under way. A numerical study is also being carried out to explain the underlying phenomena.

4. SUMMARY

The modulus mismatch plays an important role in determining the initial damage in the ceramic/metal bilayer composites. At large coating thicknesses, the critical loads for cone crack initiation remain constant for bilayers with compatible elastic moduli, but decrease with diminishing the coating thickness for bilayers with substrates having much higher modulus than the coating modulus. At small coating thicknesses, the critical load for ring crack initiation may substantially increased as a result of the substrates yielding. It may be feasible to exploit this behaviour to maximise the critical load for surface damage, provided substrate damage can be tolerated.

ACKNOWLEDGMENT

The authors would like to thank D. Castaldini at Perth Dental Hospital and P. Chantler at the School of Oral Health Science, The University of Western Australia, for assistance in preparing the specimens. This work was supported by grants from the Australian Research Council.

REFERENCE

1. Y. G. Jung, S. Wuttiphan, I. M. Peterson, and B. R. Lawn, J. Dent. Res., **78** (1999) p.887.
2. A. Pajares, L. Wei, and B. R. Lawn, *J. Am. Ceram. Soc*, **79** (1996) p.1907.
3. A. Pajares, L. Wei, B. R. Lawn, N. P. Padture, and C. C. Berndt, Mater. Sci. Eng., **A208** (1996) p.158.
4. H. Zhao, X. Z. Hu, M. Bush, and B. Lawn, International Workshop on Fracture Mechanics and Advanced Engineering Materials, Sydney, Australia (1999) p. 427.
5. H. Zhao, X. Z. Hu, M. Bush, and B. Lawn, J. Mater. Res., (2000), in press.
6. K. J. Anusavice, Phillips' Science of Dental Materials (10th ed.), W. B. Saunders Company (1996).
7. B. R. Lawn and T. R. Wilshaw, J. Mater. Sci., **10** (1975) p.1049.
8. B. R. Lawn, J. Am. Ceram. Soc., **81** (1998) p.1977.
9. S. Wuttiphan, B. R. Lawn, and N. P. Padure, J. Am. Ceram. Soc., **79** (1996) p.634.
10. H. Chai, B. Lawn, and S. Wuttiphan, J. Mater. Res., **14** (1999) p.3805.

Key Engineering Materials Vols. 183-187 (2000) pp. 1267-1272
© 2000 Trans Tech Publications, Switzerland

Abrasive Wear Behavior of Hybrid Metal Matrix Composites

J.I. Song[1], S.I. Bae[1], K.C. Ham[2] and K.S. Han[3]

[1] Department of Mechanical Engineering, Changwon National University
9 Sarim-dong, Changwon, Kyongnam 641-773, Korea

[2] Department of Machine Design, Inha Technical Junior College
4 Yonghyun-dong, Nam-gu, Inchon 402-752, Korea

[3] Department of Mechanical Engineering, Pohang University of Science and Technology
San 31 Hyoja-dong, Nam-gu, Pohang 790-784, Korea

Keywords: Abrasive Wear, Carbon Fiber, Fractographic Study, Hybrid Metal Matrix Composite, Solid Lubricant Wear, Squeeze Casting Method

ABSTRACT

Wear behavior of $Al/Al_2O_3/C$ hybrid metal matrix composites fabricated by squeeze casting method was characterized. The effects of volume fraction of carbon fiber on wear behavior of hybrid composites was investigated. Wear behavior of $Al/Al_2O_3/C$ composites was characterized by the dry spindle wear test under various sliding speeds.

The wear resistance of $Al/Al_2O_3/C$ composites was remarkably improved over Al/Al_2O_3 composites by adding carbon fibers to $Al/Al_2O_3/C$ composites. Specifically, at the intermediate sliding speed the wear resistance of $Al/Al_2O_3/C$ composites containing 8 vol.% carbon fiber was found to be better than that of the rest of the carbon hybrid composites. From fractographic studies, damaged sections in wear surfaces of hybrid composites at intermediate sliding speed were not observed due to the formation of solid lubrication film. The solid lubrication film which was formed as a result of adding carbon fibers improved the wear resistance of carbon hybrid composites because this film reduced the high friction force between MMCs and counter material.

1. INTRODUCTION

Recently, there has been an effort to use discontinuously reinforced metal matrix composites for primary structural applications. These composites can offer distinct technological advantages over continuously reinforced MMCs including fabricability using squeeze infiltration method[1, 2], as well as cost advantages due to lower fiber costs. Particularly, carbon fiber reinforced aluminum alloys are expected to be used in an internal combustion engine comprised of a cylindrical fiber reinforced portion which is formed of a mixture of an alumina based fiber and a carbon fiber with a light alloy matrix. Carbon fibers serve as solid lubrication in order to achieve good wear resistance at high temperature. In recent years there has been considerable success in synthesizing various

aluminum alloys with carbon chopped and particle dispersions using inexpensive foundry techniques.

Up to now, most investigations have studied the fabrication process and mechanical properties of carbon fiber reinforced metal matrix composites, but very few studies on the wear resistance have been available in the literature[3-7]. Moreover, the reinforcements with one kind of fiber have been the major subject of research and development, while reinforcement with the hybrid fibers, especially, alumina based carbon hybrid metal matrix composites, has not been widely investigated.

The purpose of this study is to characterize the wear behavior of $Al/Al_2O_3/C$ hybrid metal matrix composites fabricated by squeeze infiltration method. Wear tests were carried out under various sliding speed conditions to identify wear behavior clearly. Wear mechanism of hybrid MMCs is suggested by the examinations of worn surfaces. The effect of volume fraction of carbon chopped fibers on wear resistance of $Al/Al_2O_3/C$ hybrid metal matrix composites is discussed in detail.

2. EXPERIMENTAL PROCEDURE

2.1 Materials and Fabrication

For the fabrication of $Al/Al_2O_3/C$ hybrid composites, an AC2B aluminum alloy (JIS Type AC2B) was used as a matrix. Alumina fibers, SAFFIL RF Grade, from ICI Co. and carbon fibers, Kreca, from Kureha Chemical Industry Co. were used. Specifications of alumina fibers and pitch based carbon fibers are shown in Table 1 [8].

Prepared preforms with 20 volume percents were as follows : Al_2O_3-20vol.%, Al_2O_3-16vol.%/C-4vol.%, Al_2O_3-12vol.%/C-8vol.%, and Al_2O_3-10vol.%/C-10vol.%, respectively. By the direct squeeze infiltration method, Al/Al_2O_3 and $Al/Al_2O_3/C$ composites are obtained. After squeeze casting, cast ingots were treated by T6 heat treatment.

Table 1. Specification of short alumina and chopped carbon fibers

Material	Density (g/cm^3)	Diameter (mm)	Length (mm)	Aspect ratio(l/d)	T. S (GPa)	E (GPa)
Al_2O_3	3.3	4	150	38	2.0	310
Carbon	1.9	16	144	9.0	1.8	276

2.2 Dry Wear Tests

Dry wear tests were carried out using the spindle type wear tester from Riken - Ogoshi Co., at room temperature. Fig.1 shows a schematic diagram of the spindle type wear tester. Oil quenched SCM 4 was used as counter material of disc type. Here, SCM 4 is equivalent to AISI 4140. An electronic balance able to weigh up to 10^{-5} g was used to measure weight loss of composites. Wear tests were performed under the followings conditions; final load ; 12.6 kg_f, sliding distance ; 400 m, various sliding speeds ; 0.51 m/sec, 1.97 m/sec and 3.62 m/sec, respectively. After wear tests, wear surfaces were also examined by scanning electron microscope(SEM).

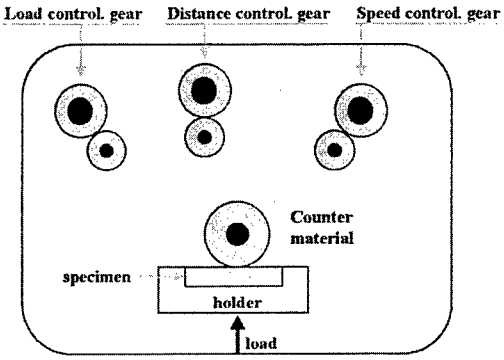


Fig.1 Schematic diagram of abrasive wear tester

3. RESULTS AND DISCUSSION

3.1 Fabrication and Mechanical Property

The optimum temperature in this study can be obtained as follows. The actual preheating temperature of the mold and preform is 500 °C and that of the lower cap is 500 °C because the mold is assembled in air before setting the preform into the mold. For minimum fiber damage, the applied pressure has to be as low as possible. 25 MPa for Al/Al_2O_3 composite and $Al/Al_2O_3/C$ composites is the minimum for perfect infiltration up to 20% volume fraction of discontinuous MMCs.

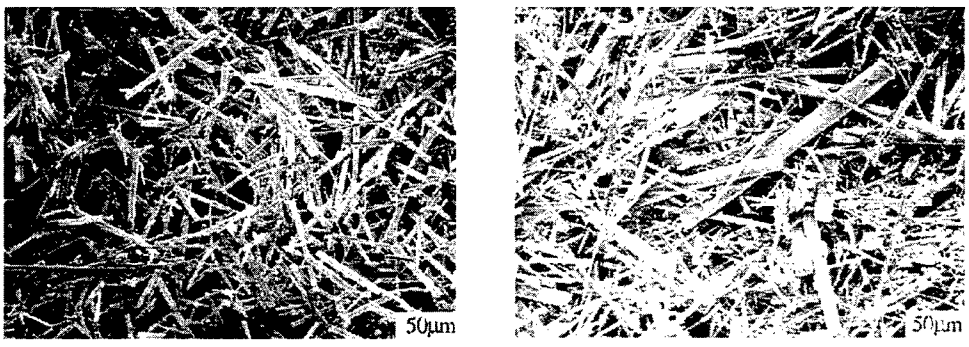


Fig. 2 SEM photographs of (a) Al_2O_3 and (b) carbon hybrid preform

Fig. 2 illustrates SEM photographs of various preforms of (a) 20 vol.%-Al_2O_3 and (b) 20vol.%-Al_2O_3/8vol.%-C, respectively. The reinforcements show uniform distributions and good bindings between fibers by silica binder. As shown in SEM photographs, carbon fibers are thicker than alumina fibers. Alumina and hybrid preforms in Fig. 2 have not shown agglomeration of silica colloid(SiO_2) between the interface of reinforced fibers due to using the microwave drying system. Fig.3 shows ultimate tensile strength (U.T.S) for various composites. As indicated in this figure, in the case of Al/Al_2O_3composite, UTS are improved up to 20% compared with unreinforced matrix

alloy. However, carbon hybrid systems are linearly decreased by increasing the addition of carbon fiber. As compared with the unreinforced matrix alloy, UTS of carbon hybrid compsites is deteriorated in the volume fraction range of 4% to 10% carbon. There is little effect on the increase of the tensile properties with increasing volume fraction of carbon fiber.

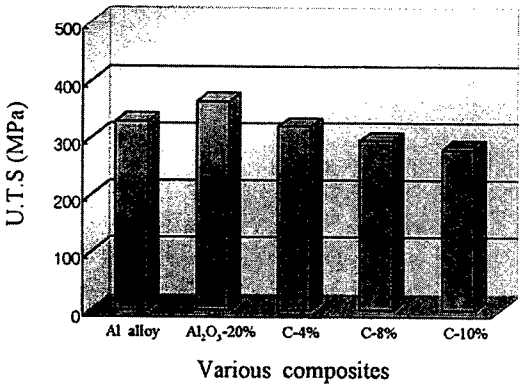


Fig. 3 UTS of various composites

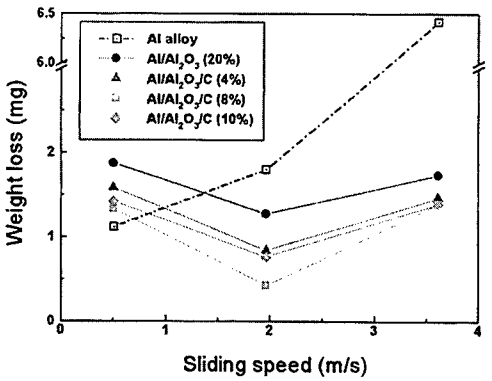


Fig. 4 Wear behavior of various composites

3.2 Wear Behavior

Fig. 4 shows the effects of sliding speeds on weight losses (volume) of AC2B Al alloy, Al/Al_2O_3 and hybrid composites at various sliding speeds, 0.51, 1.97 and 3.62 m/sec. On the whole, above the sliding speed of 1.97 m/sec, the wear resistance of MMCs is improved remarkably. This is due to reinforcements which can endure the friction force generated on the wear surface.

In Al matrix alloy, weight losses of AC2B Al alloy increased continuously up to 1.97m/sec. But, above the sliding speed of 1.97 m/sec, the wear loss of AC2B Al alloy increased abruptly . That is, wear behavior of AC2B Al alloy changed along with the sliding speed. It means that wear mechanisms are strongly dependent upon the sliding speed. Major wear mechanisms of AC2B Al alloy are abrasive and adhesive wear at sliding speeds up to 1.14 m/sec, therefore, an AC2B Al alloy is worn by the force of friction generated on the wear surface. Consequently, an AC2B Al alloy starts to be worn out abruptly.

In discontinuous MMCs, however, in all speed ranges the wear resistance of $Al/Al_2O_3/C$ composites is better than that of AC2B Al alloy, except at the sliding speed of 0.51 m/sec. Weight losses of MMCs are greater than that of the unreinforced matrix alloy at the low sliding speed, 0.51 m/sec, because reinforcements abrade the matrix by the high friction force and this abrasion deteriorates the wear resistance of Al/Al_2O_3 and $Al/Al_2O_3/C$ composites. In other words, at low sliding speed the frictional forces are large enough to fracture and pull out the reinforcements from the matrix, and these particles abrade the wear surface of composite materials. As the sliding speed increases, the friction force becomes weakened due to the reduction of the friction coefficient, and reinforcements can resist the weak friction force. In consequence, weight loss decreases until the melt wear becomes the major mechanism for wear due to the rise of temperature on the specimen. At the high sliding speeds, 3.62 m/sec, the wear resistance gets worse and weight loss starts to increase, due to the melt wear of the matrix alloy by the ascent of temperature.

3.3 Wear Surface Analysis

The above wear behavior can be explained based on microstructure analysis as follows. Wear surfaces of both AC2B Al alloy and $Al/Al_2O_3/C$ composites containing 8 vol.% carbon fiber were examined by SEM. At low sliding speed, 0.51 m/sec, we found evidence of abrasive wear in ploughing or grooving. That is, at the low sliding speed, the AC2B Al alloy formed grooves by the shearing action of the friction force generated on the wear surface. However, the wear surface of $Al/Al_2O_3/C$ composites exhibited a number of deep wear grooves. At low sliding speed, the frictional forces of MMCs are large enough to fracture and pull out the reinforcements from the matrix, and these particles abrade the wear surface of composite materials.

Fig. 5 represents overall wear surfaces of AC2B Al alloy and Al/ Al_2O_3-12vol.%/C-8vol.% composite at intermidiate sliding speeds, 1.97 m/. The damaged section on the wear surface of AC2B Al alloy is shown in Fig. 5 (a). Wear debris and distorted surfaces in AC2B Al alloy are more distinguished than in Al/ Al_2O_3/C composites. The distorted section and debris are formed at the locally fractured area of the matrix alloy. This localized fracture is caused by highly localized friction forces which come from the non-uniform surface of the counter material and defected areas of the wear surface. The growth of the damaged section is advanced by the fracture of the wear surface. Wear surfaces of AC2B Al alloy show that abrasive and adhesive wear is the dominant wear mechanism at intermediate sliding speeds. By contrast, the wear surface of $Al/Al_2O_3/C$ composites is completely different from that of AC2B Al alloy. That is, the wear surface of $Al/Al_2O_3/C$ composites shows virtually no damaged region. In $Al/Al_2O_3/C$ composites, abrasion of reinforcements and the matrix is seldom observed due to the remarkable reduction of friction forces applied to the wear surface. Fig.5(b) illustrates an alumina fiber being pulled-out (see arrow) and being struck on the wear surface. Visible lack of damage is due to the presence of lubrication film formed by the addition of carbon fibers on the wear surface of hybrid composites. Consequently, this result gives rise to the improvement of wear resistance.

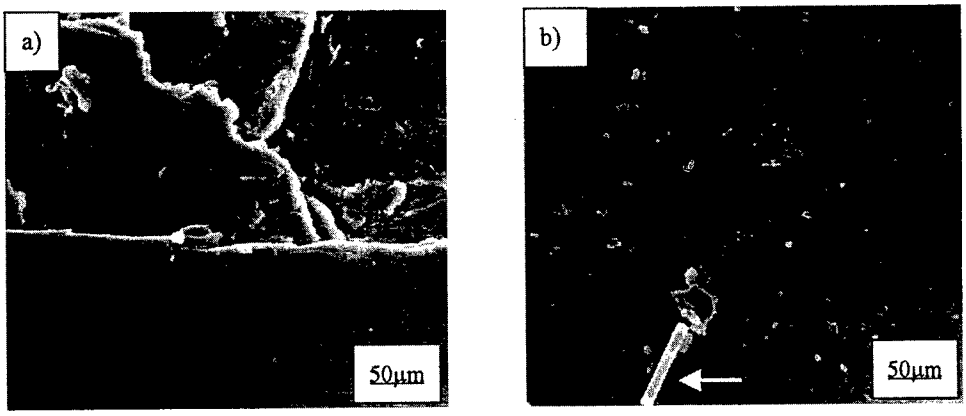


Fig. 5 Wear surfaces of (a) Al matrix and (b) $Al/Al_2O_3/C$ composites

As the sliding speed increases, adhesive and slip phenomena also appear at the high sliding speed, 3.96 m/sec. Here, adhesive wear can be detected by removed materials and slip phenomenon can also be found in the wave patterns of materials. The removal of the material seems to be accelerated by fractures of short alumina fibers and the matrix which might be due to the high friction force applied on the wear surface. Localized melted areas owing to the ascent of

temperature are observed in both AC2B Al alloy and $Al/Al_2O_3/C$ composites. Wear of AC2B Al alloy seems to start by localized melting of the surface and to proceed by delaminations from the large plastic deformation of the matrix. In carbon hybrid composites, some wear patterns like wave shape which might be related to melt and slip, indicated by an arrow, are often seen.

4. CONCLUSIONS

The wear resistance of $Al/Al_2O_3/C$ composites was remarkably improved over Al/Al_2O_3 composites by adding carbon fibers to $Al/Al_2O_3/C$ composites. The effects of amounts of carbon fibers having volume fraction of 2% can be ignored until the sliding speed is 0.51 m/sec. Specifically, at the intermediate sliding speed of 1.97m/sec, the wear resistance of $Al/Al_2O_3/C$ composites containing 8 vol.% carbon fiber was found to be better than that of the rest of carbon hybrid composite, but amounts of carbon volume fraction were of little effect on wear resistance at high sliding speed of 3.62m/sec.

Wear surfaces of $Al/Al_2O_3/C$ composites at low sliding speed showed more severe groove formations than those of matrix alloy. This abrasive wear seen in the fractographic analysis was due to the frictional forces which were large enough to fracture and pull out the reinforcements from the matrix. At intermediate sliding speeds, however, damaged sections in wear surfaces of hybrid composites were seldom observed. The solid lubrication film formed as a result of adding carbon fibers improved the wear resistance of carbon hybrid composites because this film reduced the high friction force between MMCs and counter material. At high sliding speed, localized melt and slip and large plastic deformations due to the high frictional heat are the dominant factors contributing to the removal of MMCs.

REFERENCE

1. Mortensen, A., Masur, L.J., Cornie, J.A. and Flemings, M.C., Metallurgical Transaction A, **20A** (1989) p.2535
2. Bengtson, S., Li, C.H. and Warren R., Proceeding ICCM - VIII, **3**(1989) p.607
3. Amateau, M.F., J. Comp. Mat., **10** (1976) p.279
4. Das, S. and Prasad, S. V. ,Wear, **133** (1989) p.173
5. Towata, S., Yamada, S., and Ohwaki, S., Transactions of the Japan Institute of Methods, **26**(8) (1985) p. 563
6. Das, S., Prasad, S. V. and Rohatgi, P.K. , Proceeding of International Symposium on Advances Cast Reinforced Metal Composites, ASM International (1988) p. 243
7. Long,T.T., Nishimura,T., Aisaka,T. and Morita, M., Transactions of the Japan Institute of Methods, **29**(11) (1988) p. 920
8. Data Sheet from ICI Co and Kureha Co

Key Engineering Materials Vols. 183-187 (2000) pp. 1273-1278
© 2000 Trans Tech Publications, Switzerland

Evaluation of Formability Properties of P/M Copper Preforms at Elevated Temperatures

T. Senthilvelan[1], A. Venkatraman[1] and K. Raghukandan[2]

[1] Department of Mechanical Engineering, Pondicherry Engineering College, Pondicherry 605 014, India

[2] Department of Production Engineering, Annamalai University, Annamalai Nagar 608 002, India

Keywords: Apparent Strain Hardening Exponent, Apparent Strength Coefficient, Coefficient of Friction, Elevated Temperature, Formability, Powder Metallurgy

ABSTRACT

Powder metallurgical manufacturing route claims a host of techno-economic advantages. However defect free and superior products can be obtained only if the process parameters are controlled optimally during forming. This paper envisages the identification of optimal conditions of stress, strain, forming temperature and interfacial friction while deforming P/M copper preforms at elevated temperatures.

1. INTRODUCTION

Sintered P/M route provides attractive gains over other methods of manufacture of net shaped components. Compared to conventional forging or casting processes, this process has number of techno-economic advantages like recycling of swarf, no need for flash in forging, products with uniform grain structure etc. However in Powder Metallurgy route, components with desired properties can be obtained, only if the formability parameters viz., stress, strain and temperature are controlled properly [1].

Rao et.al [2,3] have investigated the deformation behaviour of aluminium alloys at different temperatures and strain rates, in order to develop processing maps. In the research work [4] a modeling technique has been proposed to determine the workability of a given workpiece. By extending the analysis to P/M materials, Khun and Downey [5] have investigated the deformation characteristics and proposed a plasticity theory to determine the yield criterion for sintered iron powder materials. Elwakil [6,7] has predicted the values of flow parameters for sintered iron P/M billets at room temperatures. In the research work [8] the flow properties of aluminium powder preforms were determined by performing compression tests at different temperatures. Investigations on the flow properties of P/M copper at elevated temperatures appear to be scarce. Hence in this present investigation, compression tests were performed on the P/M copper specimens at elevated temperatures and also at different compression speeds in order to analyse the effects of strain rate on the formability of P/M copper preforms.

2. EXPERIMENTAL DETAILS

Electrolytic pure copper powder was compacted to three different density levels viz., 7.00 g/cc, 7.35 g/cc and 7.70 g/cc. All of them were sintered in endo-gas atmosphere at 1173 K for 60 minutes. Rings with the dimensions (Outer Diameter : Inner Diameter : Height) in the ratio of 6:3:2 were cut from the sintered samples to perform the standard ring compression tests as outlined by Male and Cockroft [9]. In the present investigation, the rings' dimensions were kept as 30:15:10 mm as Outer Diameter : Inner Diameter : Height. The ring compression tests were performed at temperatures ranging from room temperature to 1073 K in steps of 473 K. The above compression tests were performed at two different speeds viz., 5 seconds and 50 seconds to analyse the effects of strain rate. From the ring compression tests data, punch force vs stroke plots were prepared.

2.1 Determination of True stress – True strain Relationship

Since the volume constancy principle cannot be extended to P/M compression (due to persistent void closure and subsequent change in the density), the weight constancy principle has been widely adopted as a basis for computing the instantaneous area [6]. In this regard, stage wise upsetting tests were carried out on all the rings to generate densification versus strain diagram. From these two diagrams, the true stress (σ) and true strain (ϵ) values at different temperatures were computed. These true stress and strain values were plotted in a log – log graph for various densities and temperatures. The relationship obtained between σ and ϵ, at various temperatures, in a log – log plot is a straight line suggesting that the flow data could be represented by an exponential relation such as,

$$\sigma = K_a \epsilon^{n_a} \qquad [1]$$

where n_a is the strain hardening exponent ($d\sigma/d\epsilon$) and K_a is the strength co-efficient. K_a is equal to σ when ϵ takes a value of unity.

2.2 Effect of Co-efficient of Friction in Metal Forming

In metal forming processes, the co-efficient of friction plays a significant role in determining the life of the tool, the formability of the work material and the quality of the finished product. In forming processes two types of friction, namely slipping and sticking friction can occur. If the co-efficient of friction is less than 0.5, it is called slipping friction, otherwise it is called sticking friction.

Male and Cockroft [9] have developed a nomogram which facilitates the determination of the co-efficient of friction from the ring compression test itself. In the present investigation, with the help of the above nomogram, different values of co-efficient of friction were determined for various test conditions.

3 RESULTS AND DISCUSSION

3.1 Densification Plots

The force vs stroke plots, developed for the extreme temperatures during compression of P/M copper rings are shown in Fig. 1. The force requirement for hot working is less by 50 - 60% than the force required at room temperature for the same amount of deformation. Stage wise

upsetting tests were carried out at all the temperatures to study the effect of densification with magnitude of strain. One such variation is shown in Fig.2. From the densification plots, it is observed that densification rate is an inverse function of the initial density of the preform. Similar trend was observed by Elwakil [6] also. Generally the rate of densification increases with the temperature. The true stress and true strain values were computed using the aforesaid graphs.

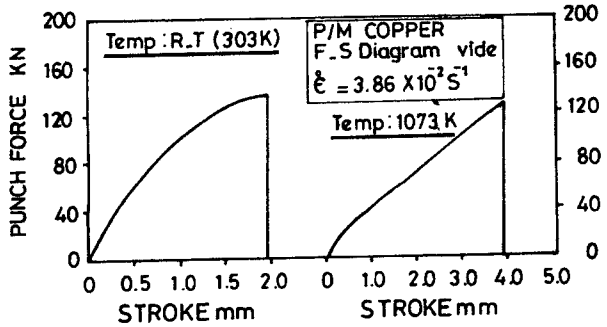


Fig.1 F – S diagram for P/M Copper

3.2 Influence of Temperature on Plastic Properties

True stress vs True strain values were transferred to log – log plots. For all the different temperatures and density conditions these plots were prepared. One such log – log plot is shown in Fig.3. The true stress values at $\in = 1$ gives the value of strength coefficient ($\mathbf{K_a}$). The slope of the line is strain-hardening exponent ($\mathbf{n_a}$). These two parameters are fitted into Hollomon – Ludwick equation [6] from which the stress requirement for any forming process can be determined.

Fig.4 shows the influence of forming temperature and strain rate on the strength co-efficient for different densities. For higher initial preform density, higher is the $\mathbf{K_a}$ value and it decreases as temperature increases. This effect is due to the loss in hot hardness and subsequent softening of material at high temperatures. It can be seen that at higher strain rates, $\mathbf{K_a}$ value is also higher. This is because at higher strain rates, strain hardening is more, which demands more flow stress and consequently higher is the $\mathbf{K_a}$ value. However beyond 700 K the strain rate effect is not so significant as at low temperatures and the window tends to become closer.

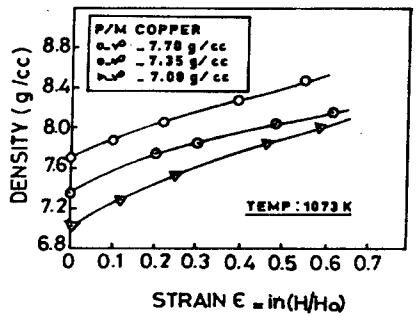


Fig.2 Variation of Densification with strain

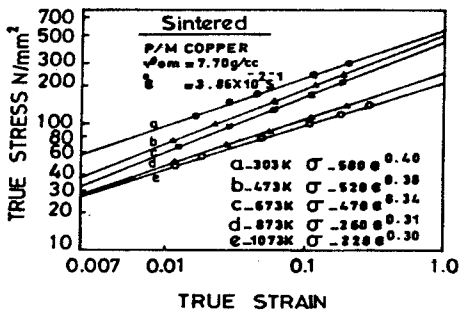


Fig.3 Log – Log Plot of σ - ϵ

Generally when deforming wrought materials at hot working range, the material would not experience strain hardening and as a result the value of **n** approaches zero. But in the case of P/M materials, $\mathbf{n_a}$ does not approach zero at high temperatures because unlike wrought materials, strain hardening occurs in porous materials due to the following two factors [1]:

(i) Porous preforms harden during deformation because the metallic matrix strain hardens, and

(ii) Porous preforms harden during deformation because the density is increasing (due to reduction of pore volume) and the effective load carrying cross section increases.

The first factor is sensitive to temperature but the second factor is not sensitive to temperature. Therefore there is an effective deformation hardening of porous preforms even at elevated temperatures. The effects of temperature and strain rate on the strain-hardening exponent for different initial densities are shown in Fig.5. From this figure, the following inferences can be made:

- As temperature increases $\mathbf{n_a}$ value gradually decreases.
- However even at 1073 K for P/M materials the $\mathbf{n_a}$ value is 0.30, whereas in the case of wrought copper the value of **n** at this temperature is 0.05. Drop in $\mathbf{n_a}$ value is not appreciable beyond 700 K, because the densification is more at higher temperatures.
- Generally $\mathbf{n_a}$ value is more at higher strain rates. Because at high strain rates due to rapid loading, surface hardness increases which increases $\mathbf{n_a}$ value.

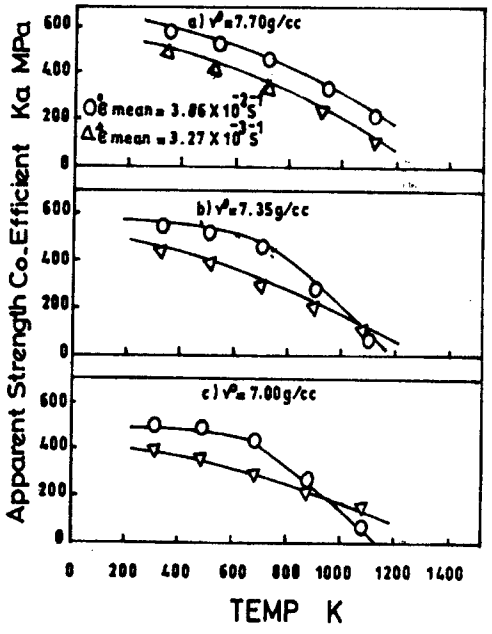


Fig.4 Variation of K_a with Temperature

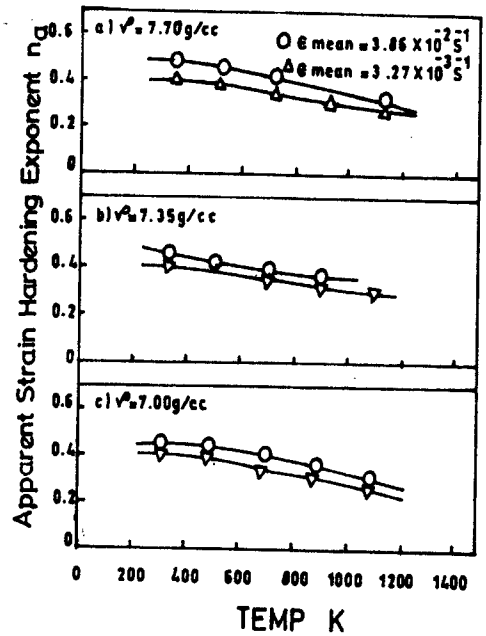


Fig.5 Variation of n_a with Temperature

3.3 Determination of Co-efficient of Friction (μ)

All the specimens were lubricated with MoS_2 before compression. To determine the co-efficient of friction, the upset ring specimens were measured to determine the changes in internal diameter and reduction in height. The calibration chart was referred to, in order to determine the value of co-efficient of friction [9]. The main advantage of Male and Cockroft method is that it involves only the physical measurements of the shape change of upset ring unlike other tests, which require the mechanical properties of the material and the forming loads. The variation of co-efficient of friction with forming temperatures for different initial preform densities is shown in the Fig.6. It is observed that with the increase in forming temperature, the co-efficient of friction value increases because at elevated temperatures flow stress and hardness values of the material drop. Subsequently softening of material takes place, which causes more asperity contact between the tool and work piece. Similar observation was made for wrought copper and its alloys [10].

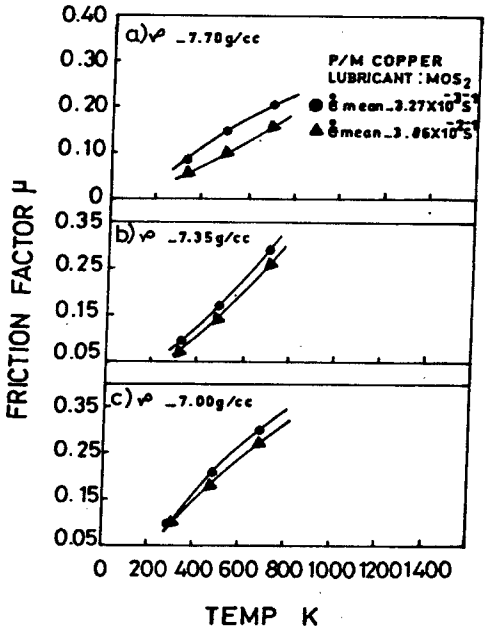


Fig.6 Variation of μ with Temperature

Amongst the different strain rates, the value of co-efficient of friction is more at low strain rates than at higher strain rates. Because in slow rate of pressing, much time is available for the asperity contact between the metal and work piece which is responsible for higher co-efficient of friction values. It is also observed that co-efficient of friction value is higher for lower initial preform density. Because lower density preforms will give more yields during deformation and spread in the lateral direction, causing more contact of the material between tool and work piece; hence more frictional effect exists between tool and work piece.

4. CONCLUSIONS

The following conclusions are drawn from this research work:

(1) In the compression of P/M copper preforms, the flow stress (σ) vs. true strain ($\in$) relationship at elevated temperatures can be expressed in the form of an equation shown below:

$$\sigma = K_a \in^{n_a}$$

(2) The constant K_a and n_a are found to be temperature and strain rate dependent.

(3) Both strength coefficient (K_a) and strain hardening exponent (n_a) decrease as temperature increases. Beyond 700K the drop is not appreciable.

(4) Even at elevated temperatures, n_a assumes some significant value unlike the wrought material which approaches zero. This is due to the densification taking place throughout the deformation.

(5) Boundary friction co-efficient increases up to 673 K. Beyond this value, determination of the co-efficient of friction becomes difficult since sticking friction occurs. Similar trend was observed for wrought copper in the work of reference [10]. At lower strain rates, much time is available for asperity contact and hence boundary friction co-efficient values are higher.

REFERENCES

1. H.W. Antes, Progress in Powder Metallurgy, 28 (1973) p.5

2. K.P. Rao, Tran. Indian Institute of Metals, 37 (1984) p.477

3. K.P. Rao, 9th AIMTDR Conference, IIT Madras, India (1984) p.349

4. H.L. Gegel, Int. Conf., on the Technology of Plasticity, Stuttgart, Germany (1987)

5. H.A. Khun, and C.L. Downey, Int. J. Powder Metallurgy, 7 (1971) p.15

6. S.D. Elwakil, 15th MTDR Conference, Birmingham, U.K. (1974) p.443

7. S.D. Elwakil, 15th MTDR Conference, Birmingham, U.K. (1974) p.645

8. A. Kumar et. al., Tran. Indian Institute of Metals, 37 (1984) p.569

9. A.T. Male and M. G. Cockroft, J. Institute of Metals, 93 (1964) p.489

10. C.P. Ravichandran, M.Tech., Thesis, IIT, Madras, (1981)

Key Engineering Materials Vols. 183-187 (2000) pp. 1279-1284
© 2000 Trans Tech Publications, Switzerland

Effects of Interface and Residual Stress on Mechanical Properties of Ceramic/Metal System

T.W. Kim[1] and S.W. Park[2]

[1] School of Mechanical Engineering, Kook-Min University, Seoul, Korea

[2] Multi-functional Ceramic Research Center, Korea Institute of Science and Technology, Korea

Keywords: Brazed, Ceramic/Metal System, Interface, Residual Stress

ABSTRACT

Effects of interface, especially microstructural change, and residual stress on the mechanical properties of ceramic/metal system were investigated for a selected brazed silicon nitride/stainless steel system. In order to reduce the residual stress by thermal mismatch, thereby to enhance the joint fracture strength, pure Cu was used as an interlayer. The observed microstructural changes within interlayer as well as within brazing alloy were taken into account for finite element analysis(FEA) of residual stress developed in the joint. The 4-point flexural strengths were measured for Si_3N_4/Cu/stainless steel 316 joints with a thickness change of Cu interlayer. It was found that FEA calculations for residual stress, developed in Si_3N_4/stainless-steel joints with a Cu interlayer, could explain the location shift in fractured initiation as well as the variation of fracture strength with Cu-interlayer's thickness change.

1. INTRODUCTION

The recently developed structural ceramics have been applied to advanced industrial components, due to excellent thermal, mechanical properties, and good chemical stabilities[1]. The problems of low fracture toughness and high manufacturing cost for structural ceramics have been alleviated via ceramic to metal joining technology[2,3]. The method compensates the brittle nature of ceramics while maintaining their attractive structural properties. The active metal brazing[3] technique has been preferred for non-oxide ceramic/metal joints, since active metal brazing method is practical for mass production of the ceramic/metal joint with variable joint geometry.

Upon cooling of the ceramic/metal joint from the brazing temperature, the thermal-mismatched residual stress can be inevitably induced. Such residual stress is known to affect the strength characteristics of ceramic/metal joint system[3,4]. The residual stress needs to be reduced for enhancing mechanical strength of ceramic/metal joints. The maximum residual stress developed in ceramic can be reduced with the use of an interlayer material having either closer thermal expansion coefficient to the ceramic, or having low yield strength[5].

Most FEA(Finite Element Analysis) research works for ceramic/metal joints have dealt with simple relations between maximum residual stress and fracture strength without any appreciable microstructural features taken into account. The analysis without counting microstructural change in the joint interface, often, cause disagreement between the measured and predicted joint properties[6]. The deficiencies, therefore, need to be addressed by incorporating the microstructural effect into the procedures for residual stress analysis.

The objective of present study is to examine the role of microstructural change near the joint interface for brazed Si_3N_4/stainless-steel joint with Cu interlayer on the residual stress developed, which in turn affects the fracture strength of the joint. The computed residual stresses by FEA, together with bending strengths results, were analyzed to examine the fracture behavior of a brazed Si_3N_4/stainless-steel joint with Cu interlayer.

2. EXPERIMENTAL PROCEDURES

Hipped silicon nitride (Si_3N_4) with 6wt% of Y_2O_3 as sintering aid and stainless steel 316 were used for base materials to be joined. Pure copper (purity>99%), with thickness ranging between 0.1 and 1.0 mm, were used as an interlayer. Cu-interlayers were heat-treated prior to brazing in order to release any existing residual stress within the interlayer. The filler metal for brazing was Ag-35 wt.% Cu-2 wt.% Ti alloy (Wesgo, Cusil-ABA), and its thickness was about 0.05 mm as-received. The relevant thermo-mechanical properties of materials used for the joint are shown in Table 1[7]. The mating surfaces for Si_3N_4 and stainless steel were polished down to 2μm diamond paste before brazing. All materials were washed in ultrasonic cleaner using trichloroethylene, aceton, and iso-propanol solution sequentially. The brazing was performed at a temperature of 850^{0}C for 10 minutes under vacuum of about 1.3mPa. The Si_3N_4 of 3x4x15mm in size was bonded to the stainless steel of an identical dimension. The joint strength was evaluated by 4-point bending tests with a crosshead speed of 0.5 mm/min. The inner and outer span were 10 and 20 mm, respectively.

Table 1. Mechanical properties for materials used in ceramic/metal system

	Young's modulus (GPa)	Poisson's ratio	Thermal expansion coefficient (10^{-6}/°C)	Yield strength (Mpa)
Si_3N_4	300	0.22	3.2	870*
Cu	120	0.37	17.7	70
Stainless Steel 316	150	0.25	14.0	240
Cusil ABA (Ag-Cu-Ti)	83	0.36	18.5	271

* fracture strength

A commercial finite element program, ABAQUS[8], was used to compute the maximum as well as the distribution of thermal-mismatch residual stress developed within the joint during cooling from the brazing temperature. In order to compare the computed residual stresses directly

with the fracture strength results for joints, a 3-dimensional finite element model was established based on the actual joint geometry. The thickness of interlayer ranged between 0.1 and 0.8 mm. In order to consider the effect of plastic deformation of materials, elasto-plastic analysis was conducted for residual stress calculations.

The SEM(scanning electron microscopy) microstructure and composition near the interfacial region were taken into account in the FEA computation for residual stress developed in brazed Si_3N_4/stainless steel joint with Cu-interlayer.

3. RESULTS AND DISCUSSION

Examining the SEM microstructures of the joint interface for Si_3N_4/stainless steel joint with Cu-interlayer revealed that the Cu-interlayer of 0.1mm thickness in joint interface completely dissolved into Cusil-ABA brazing alloy[9]. Similar amounts of Cu-interlayer seemed to be dissolved into brazing alloy for Si_3N_4/stainless steel joint with 0.2 mm Cu-interlayer. As a consequence, the original thickness for the Cu-interlayer of 0.2 mm in Si_3N_4/stainless steel joint was reduced, which in turn increased the thickness for brazing alloy. The change of composition in brazing alloy is expected to induce change in microstructure and thus mechanical properties of brazing alloy, especially increase in yield strength[7] due to dissolution of large amount of Cu.

Maximum tensile residual stress developed in the joint could be considered as one of the major factors determining the joint strength. The maximum residual stress developed in the joint was calculated with the relative distance from the interface as shown in Fig. 1. It shows steep residual stress changes with a distance starting from Si_3N_4/brazing alloy interface along the edge of Si_3N_4. For the joints investigated with Cu-interlayer ranging from 0.1 to 1.0 mm, the maximum residual stress was determined to be the largest for the joint with Cu-interlayer of 0.1mm. As compared with the joint with Cu-interlayer of 0.1mm, substantial amount of residual stress was reduced for the joint with Cu-interlayer of 0.2 mm in thickness.

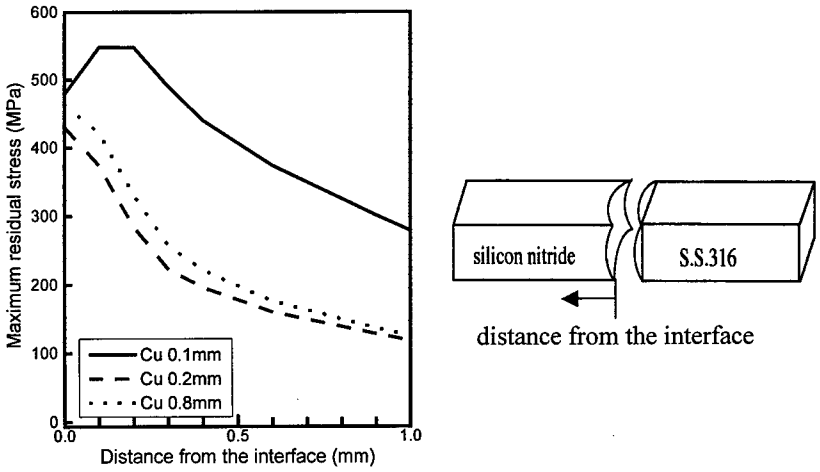


Fig. 1. Change of maximum residual stress with the distance from the interface

It is also important to note that there was a location shift for maximum residual stress depending on the thickness of Cu-interlayer. For Si_3N_4/stainless steel joint with 0.1 mm-thick Cu-

interlayer, the maximum tensile residual stress was found to be developed within Si_3N_4 slightly away from the interface as was the case with the joint without any interlayer. Therefore, the fracture for Si_3N_4/stainless steel joint with 0.1 mm-thick Cu-interlayer is expected to occur away from the Si_3N_4-stainless steel interface region within the bulk of the Si_3N_4 . However, the maximum residual stress for the joint with Cu-interlayer with thicker than 0.2 mm occurred at the Si_3N_4/braze interface.

Fig. 2 shows the maximum residual stress calculated for Si_3N_4/stainless steel joints depending on the thickness of Cu-interlayer..

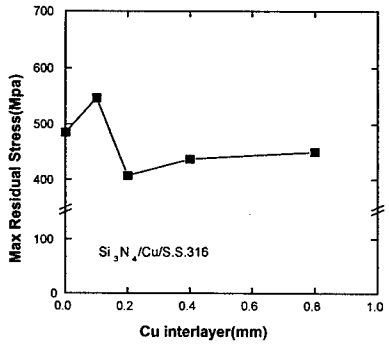


Fig. 2. Change of maximum residual stress with Cu interlayer thickness

The change in fracture strength appears to represent the inverse variation of residual stress reasonably well as shown in Fig. 3. The bending fracture strength was improved for the joint from with 0.1mm to with 0.2mm of Cu-interlayer's thickness, followed by gradual fracture strength reduction with further increases of Cu interlayer's thickness. The largest bending strength was obtained to be 310 MPa for the joint with 0.2 mm-thick Cu-interlayer. But the bending strength was found to be reduced for further thickness increases of Cu-interlayer, indicating that the maximum bending strength for Si_3N_4/Cu/stainless steel joint can be as high as 310 MPa with minimal residual stress within the joint.

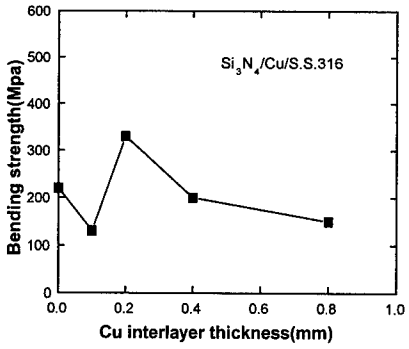


Fig. 3. Change of fracture strength with Cu interlayer thickness

The maximum residual stress for the joint with 0.1 mm-thick Cu interlayer was calculated to be increased than that for the joint without any Cu-interlayer. This was expected because the entire Cu-interlayer of 0.1 mm completely had dissolved in brazing alloy. The elimination of low-yield strength Cu interlayer not only prevented the efficient reduction of residual stress develeloped within Si_3N_4 by the plastic deformation of Cu, but also resulted in an increase of the virtual thickness in the brazing alloy. The increase of brazing alloy has been known to reduce the joint strength. Consequently, the inefficient reduction of residual stress within the joint with Cu-interlayer of 0.1mm has resulted in a low joint strength.

Without considering the dissolution of Cu-interlayer into the brazing alloy during the FEA modeling, the onset of decrease in residual stress would have been for the joint with Cu interlayer of 0.1 mm in thickness instead of Cu-interlayer of 0.2 mm as exhibited in Fig. 1. It is regarded, therefore, that the dissolution of Cu-interlayer into brazing alloy[9] needs to be considered for the proper calculation of the residual stress developed within the joint. As the thickness of Cu interlayer increased from 0.1 to 0.2 mm, the residual stress developed within the Si_3N_4 was computed to be decreased due to the plastic deformation of the retained Cu-interlayer. A further thickness increase of the Cu interlayer did not effectively induces the plastic deformation of the cu-interlayer owing to strain-hardening, and resulted in a increase of residual stress.

The consistent variations of the maximum tensile residual stress and the measured fracture strength indicate that the microstructural effects near the joint interface should not be overlooked in the residual stress computation for brazed Si_3N_4/stainless steel joints with a cu-interlayer where appreciable microstructure changes take place during a brazing process. Therefore, the consideration of the microstructural change is required to assess the validity of the FEA for residual stress. Indeed, consistent data between the maximum tensile residual stress and fracture strength data for the joint depending on the Cu-interlayer of variable thickness can only be obtained by taking the microstructural change into account.

4. CONCLUSIONS

The following conclusions were drawn based on the ceramic/metal system with interlayer. The bending strengths for brazed Si_3N_4/stainless steel joints with Cu interlayer were found to be closely related to the thickness of Cu-interlayer. The dissolution of Cu interlayer into Cusil ABA brazing alloy changes the microstructure of the joint interface including Cu-interlayer. The joint with Cu-interlayer of 0.1mm in thickness, exhibiting complete dissolution of Cu-interlayer into the brazing alloy, showed a lower bending strength than that for the joint without Cu-interlayer. The higher bending strength for the joint with 0.2mm-thick Cu-interlayer than that for 0.1mm thick Cu-interlayer was caused by the remained Cu-interlayer during brazing process. The finite element analysis of residual stress, with microstructural changes counted, directly reflected the variation in the measured fracture strength as a function of Cu-interlayer's thickness. Present results demonstrate that microstructural change near the joint interface for brazed Si_3N_4/stainless steel joint with Cu interlayer should be included in the FEA procedure in order to estimate the change in the bending strength of the joint properly.

REFERENCE

1. J. B. Wachtman, Mechanical Properties of Ceramics, John Wiley & Sons Inc (1996)
2. J. M. Howe, Mater. Res. Soc. Symp. Proc. 314 (1993) p.27

3. M. Schwartz, Brazing:For the Engineering Technologists, Chapman & Hall (1995)
4. . K. Suganuma, J. Mater. Sci., 22,8 (1987) p.2702
5. S. P. Kovalev, P. Miranzo, and M. I. Osendi, J. Am. Ceram. Soc. 81,9 (1998) p.2342
6. S. Peteves, G. Ceccone, M. Paulasto, V. Stamos, P. Yvon, J. Met. (1996) p.48
7. W. D. Callister, Mat. Sci. and Eng., Wiley (1994)
8. ABAQUS User's manual, HKS (1997)
9. T.Kim,N.Yang,H. Jang, and S.Park, 6th International Symposium on Ceramic Materials and Components for Engines,Japan Fine Ceramic Association (1997) p.321

Key Engineering Materials Vols. 183-187 (2000) pp. 1285-1290
© 2000 Trans Tech Publications, Switzerland

Design and Fabrication of Tooling for P/M Ferrous Gears

A. Venkatraman and T. Senthilvelan

Department of Mechanical Engineering, Pondicherry Engineering College,
Pondicherry 605 014, India

Keywords: Corrosion, Gears, Hardness, Powder Metallurgy, Tooling

ABSTRACT

This paper discusses the design and fabricational aspects of a tooling set consisting of a die, top punch, bottom punch, core rod and coil springs to make powder metallurgical gears. With this tooling arrangement P/M gears were compacted and then sintered. Hardness, radial crushing strength and corrosion resistance properties of these sintered gears were determined.

1. INTRODUCTION

The use of P/M gears is gaining (commercial) momentum because of the following techno-economic advantages:

(a) Close dimensional tolerances are obtainable
(b) Can combine a gear with other mechanical elements such as cam etc. into one piece
(c) Reduction of metal scrap by 80%
(d) Provides true involute tooth profile and full fillet radius
(e) Readily incorporates residual porosity thereby reducing weight
(f) Because of the porosity, less running noise occurs (porosity dampens sound) and also self-lubrication is possible by oil impregnation.

The above merits attracted many researchers in the past to investigate the performance of P/M gears. Smith [1] has investigated the fabrication and performance of P/M gears. Kalander et.al [2,3] have presented an over view of the P/M gear fabrication and its applications.. The surface durability and wear characteristics have been investigated in the research works [4,5]. In this present investigation, P/M gears were subjected to steam treatment and the properties of steam treated gears were compared with the sintered gears.

2. DESIGN AND FABRICATION

2.1 Materials

The tooling set designed and fabricated was a floating die set to provide the effect of double-action compaction because this will minimize the density gradient within the component and other consequent problems during service. The die, punches and the core rod were fabricated with high-carbon high-chromium steel which is otherwise called die steel. The guide rods were fabricated with mild steel. The accessories like helical springs, nuts and washers conforming to the required specifications were purchased from the market.

2.2 Fabrication of Tooling

The fabrication methods and sequence of tooling are shown Fig.1 in the form of a flow chart.

2.3 Hardening

Die, top punch, bottom punch and core rod were heat-treated. The main aim of the heat treatment is to increase the hardness of the material of the components so as to withstand any surface indentations that may be caused during powder compaction. Hardening was carried out at 1273 K temperature for 60 minutes. Then the gears were oil quenched. Subsequently tempering operation was carried out at 573 K for 45 minutes to relieve the locked up internal stresses. The tooling set was finally hardened to Rockwell C-55. The final match between the die and punches was obtained by finishing the punches by lapping. The tooling components are shown in Fig.2 as photograph.

Fig.1 Stages in Tooling Fabrication

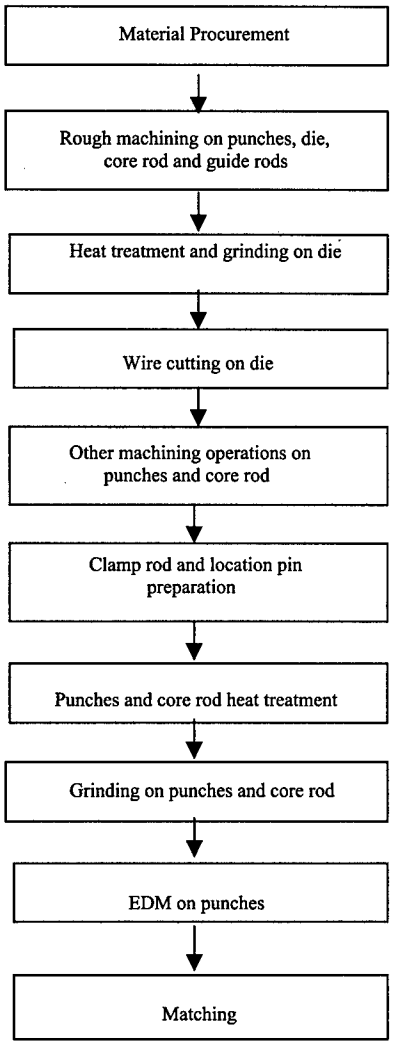
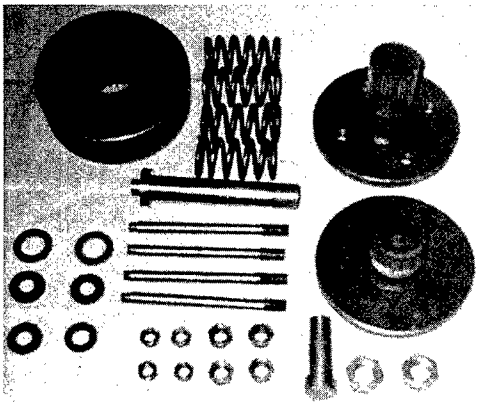


Fig.2 Fabricated Toolings



3. EXPERIMENTAL DETAILS

Powder selection

Pure ferrous powder conforming to ASI 100.29 specification, manufactured by Hoganas company was procured. The other details of the ferrous powder are:
Apparent Density (g/cc) : 2.92
Flow rate (sec/50 gm) : 29.6
Compressibility (g/cc)at 4.2 t / Sq.cm : 6.8
Percentage Carbon : 0.01

Binding Material

2% Electrolytic copper (Trade Mark : ECI) was added as the binding material to improve the ductitlity.

Lubricant

1% Zinc Stearate was used as admixed lubricant. The same lubricant was applied to all the sliding parts which include die walls, periphery of the punches and core rods.

3.1 Compaction and Sintering

Compaction was done in a 100 Tonne UTM to obtain four different green density levels viz., 5.5 g/cc, 5.75 g/cc, 6.00 g/cc and 6.24 g/cc whose theoretical densities are 70%, 74%, 77% and 80% respectively.

The details of compaction particulars are shown in Table 1.

Table 1.

S.No.	Density g/cc	Compaction load in tonnes	Total weight of the powder in grams	Iron powder weight in grams (97.3% by weight)	Copper powder weight in grams (2.7% by weight)	Zinc Stearate weight in grams (1% by weight)
1	5.50	66	188.36	183.27	5.09	1.88
2	5.75	71	196.92	191.60	5.32	1.97
3	6.00	79	205.48	199.94	5.54	2.06
4	6.24	87	213.70	207.93	5.77	2.14

The green P/M ferrous gears were sintered in a continuous furnace of chain conveyor type and the sintering parameters are as furnished below:

Sintering temperature : 1393 K
Rapid burn off zone temperature : 673 K
Conveyor chain speed : 70 mm/min
Protective atmosphere : Endo gas
Sintering time : 60 minutes

3.2 Testing

The sintered ferrous P/M gears were subjected to steam treatment. Steam treatment is a frequently applied secondary operation in the P/M industry whose main objective is to increase the surface hardness of the components, which experience wear and tear [6]. This treatment is of paramount importance for gears since gear pair experiences wear and tear during meshing. Also from the economic point of view, this desirable property is achieved at fairly low production costs. In this process of steam heat treatment, super heated steam is generated and the gears are placed in this steam bath for a duration of 90 minutes at about 803 K. A hard magnetite-oxide (Fe_3O_4) layer is formed which gives an effect similar to that of case hardening.

4. RESULTS AND DISCUSSION

4.1 Radial Crushing Test

The green strength of a compact may be determined in number of ways depending on the geometry and the type of damage the part is likely to be exposed. The radial crushing test (according to British Standards 1131 : part 5) had been chosen for the present investigation since the geometry of the gears is cylindrical. In accordance with the above standard, the compacts were loaded in an UTM in such a way that the loading axis was perpendicular to the bore of the product and the load for the appearance of first crack was observed. The radial crushing strength was calculated from the following expression:

$$\sigma_s = W(D - T) / (L T^2) \qquad [1]$$

where σ_s = Minimum acceptable strength, MPa
W = Minimum acceptable breaking load, N
D = Outside diameter of the gear, mm
T = Wall thickness of the gear, mm
L = Face width of the gear, mm

It is observed that as the initial density of the component is higher, the radial crushing strength increases for both as sintered and steam treated gears. Radial crushing strength value increases from 5 to 10% for steam treated gears over the as sintered gears. This variation is shown in Fig.3.

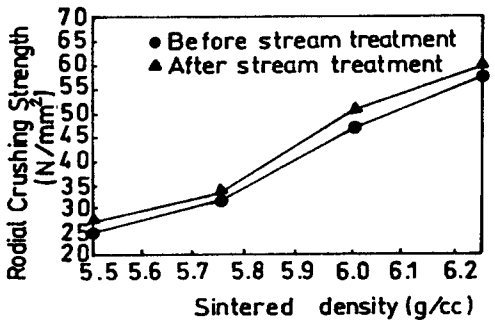


Fig.3 Variation of Radial Crushing Strength Vs Density

4.2 Hardness Measurement

Hardness measurement was done on the as sintered and steam treated gears. Hardness is an essential quality required to impart wear resistance for gears while sliding during meshing. The hardness of the gears was measured in the Rockwell F- scale on the as sintered and steam treated gears. The variation of hardness on surface and on teeth with density of the gears is shown in figures 4 and 5.

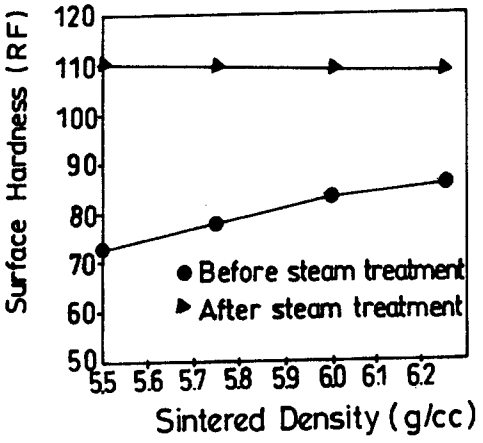


Fig.4 Surface hardness Vs Density

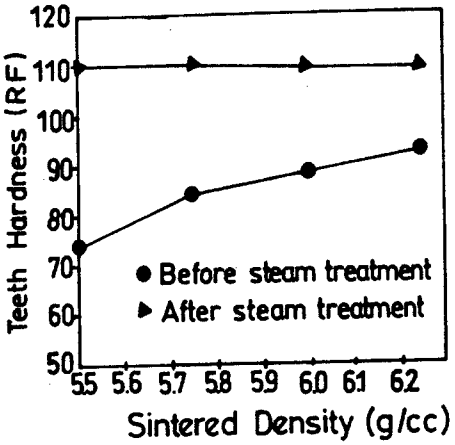


Fig.5 Teeth hardness Vs Density

It is observed that after the steam treatment, the hardness of the gears increases by 30%. This is due to the filling of the pores and surface with ferrous oxide coating. It is also observed that the hardness on the teeth is more than that of the surface. This is because the punch load was directly acting upon the teeth and thereby strain hardened the teeth.

4.3 Corrosion Test

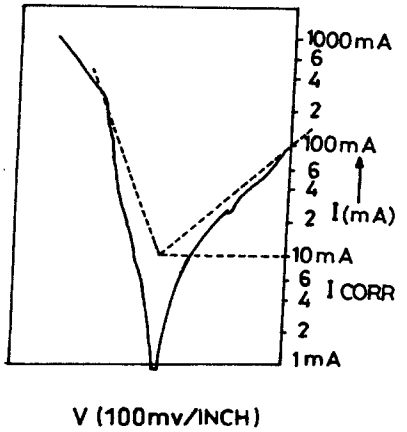


Fig.6 As sintered sample (Corrosion Test)

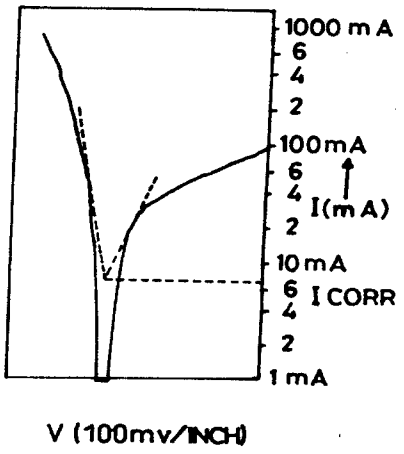


Fig.7 Steam treated sample (Corrosion Test)

A representative sample was cut from each of the as sintered and steam treated gears. These samples were subjected to accelerated corrosion tests.

The values taken during the corrosion tests are shown in the Figures 6 and 7. These figures show that corrosion rate for as sintered gears is 0.025 mm/year (981.95 micro inches/year) and the corrosion rate for steam treated gears is 0.0175 mm/year (687.36 micro inches/year). Hence it is concluded that the steam treatment has enhanced the corrosion resistance of as sintered gears by over 30%. This is so because during steam treatment a black layer of ferrous oxide is formed on the surface of the component which protects further oxidation.

5. CONCLUSIONS

The following conclusions are arrived at from the present research work:

1. Tooling set of die, top and bottom punches, core rod and other connecting fasteners were designed and fabricated in order to make P/M gears.

2. Ferrous powder with 2% copper powder addition was compacted to four different densities (70%, 74%, 77% and 80% of theoretical density) to obtain P/M gears. These green gears were sintered in endogas atmosphere at 1393 K.

3. The sintered gears were subjected to steam treatment and this treatment had enhanced the hardness at teeth and surface, radial crushing strength and corrosion resistance.

REFERENCES

1. Smith, Walter .E, Gear Manufacture and Performance, ASM (1974) p.257

2. S.D. Kalandar Sahib, and K. Gopinath, 15th National P/M Conference, Srinagar, India (1989)

3. S.D. Kalandar Sahib, and K. Gopinath, Pow. Met. Science and Technology, 2 (1991) p.25

4. C. Madhavan, and K. Gopinath, Pow. Met. Science and Technology, 4 (1991) p.30

5. C. Madhavan, and K. Gopinath, Pow. Met. Science and Technology, 5 (1994) p.29

6. A.J. Khan et. al., Pow. Met., 29 (1986) p.207

Key Engineering Materials Vols. 183-187 (2000) pp. 1291-1296
© 2000 Trans Tech Publications, Switzerland

Effects of Sintering Conditions on Mechanical Properties of Mechanically Alloyed Tungsten Heavy Alloys

Ho J. Ryu and Soon H. Hong

[1] Department of Materials Science and Engineering, Korea Advanced Institute of Science and Technology, 373-1 Kusong-dong, Yusung-gu, Taejon 305-701, Japan

Keywords: Mechanical Alloying, Mechanical Properties, Solid State Sintering, Tungsten Heavy Alloy, Two-Step Sintering

ABSTRACT

The effects of sintering conditions on microstructural evolution and mechanical properties of mechanical alloyed tungsten heavy alloy were investigated. W, Ni and Fe powders were mechanically alloyed in a tumbler ball mill with milling speed of 75 rpm, ball-to-powder ratio of 20:1 and ball filling ratio of 15%. Mechanically alloyed powders were compacted and solid state sintered at 1300°C for 1 hour in hydrogen atmosphere. The solid state sintered tungsten heavy alloy was subsequently liquid phase sintered at 1470°C with varying the sintering time from 4 min to 90 min. The solid state sintered tungsten heavy alloy showed fine tungsten particles of 3μm in diameter and high relative density above 99%. The volume fraction of matrix phase was measured as 11% and tungsten/tungsten contiguity was 0.74 in solid state sintered tungsten heavy alloys. Two-step sintered tungsten heavy alloys showed finer tungsten particles of about 6-15 μm and volume fraction of matrix phase of 16% and tungsten/tungsten contiguity of 0.40. The solid state sintered tungsten heavy alloy exhibited yield strength about 1100 MPa due to a finer tungsten particles, while showed low elongation and impact energy due to a large tungsten/tungsten contiguity. The yield strength of two-step sintered tungsten heavy alloys increased with decreasing the tungsten particle size and volume fraction of matrix.

1. INTRODUCTION

Tungsten heavy alloys consist of spherical tungsten particles with average size of 30-40 μm in W-Ni-Fe solid solution matrix. Tungsten heavy alloys have been fabricated by liquid phase sintering process of blended powders of tungsten, nickel and iron at temperatures above 1460°C in a hydrogen atmosphere[1]. Tungsten heavy alloys are used as kinetic energy penetrators, counterweight, radiation shields, vibration damping devices and electrical contacts due to their combination of high density, strength and ductility[2]. Recently, a number of investigations have been carried out to improve the mechanical properties and penetration capabilities of kinetic energy penetrators made of tungsten heavy alloys[3,4]. The mechanical properties of tungsten heavy alloys were known to be improved by refining the microstructures of tungsten heavy alloys[5]. Mechanical alloying process is known as a fabrication process that can produce ultra-fine homogeneous powders[6]. Therefore, mechanical alloying process has been suggested as a process to develop advanced tungsten heavy alloys with improved mechanical properties[5]. Various tungsten heavy

alloys were mechanically alloyed using attritors, Spex mills and tumbler ball mills and were followed by the solid state sintering at temperatures from 1200°C to 1425°C[7,8].

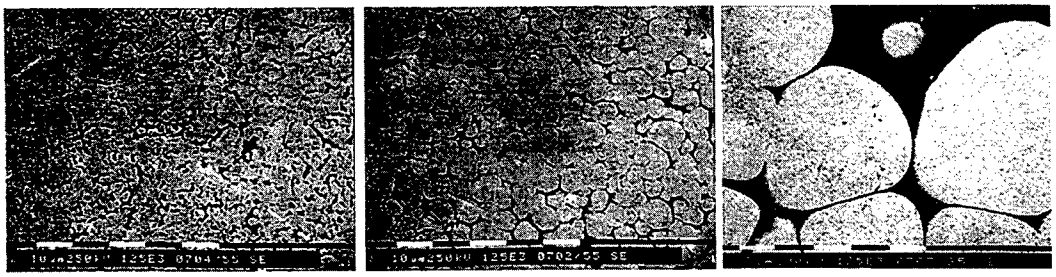
In this study, solid state sintering was carried out at 1300°C for 1 hour to achieve full densification of mechanically alloyed tungsten heavy alloys. Liquid phase sintering of solid state sintered tungsten heavy alloys was subsequently performed to control the microstructural factors such as tungsten particle size, tungsten/tungsten contiguity and the matrix volume fraction to avoid abrupt coarsening of tungsten particles in liquid phase matrix. Effects of the microstructural factors on mechanical properties of tungsten heavy alloys were investigated.

2. EXPERIMENTAL PROCEDURES

The tungsten powders of 2.5 μm, nickel powders of 2.5 μm and iron powders of 3.5 μm were mechanically alloyed in a tumbler ball mill to produce tungsten heavy alloys with the composition of 93W-5.6Ni-1.4Fe. Milling speed was 75 rpm, milling time was varied up to 72 hours, ball-to-powder ratio was 20:1 by weight and ball filling ratio was 15% in volume fraction. The mechanically alloyed powders were compacted into green compacts and were sintered at temperature of 1300°C for 1 hour in a hydrogen atmosphere. Solid state sintered tungsten heavy alloy was sintered at temperatures from 1445°C to 1485°C with varying sintering time from 4 min. to 90 min in a hydrogen atmosphere. The two-step sintered specimens were annealed at 1150°C for 1 hour in nitrogen atmosphere and then water-quenched to prevent hydrogen embrittlement and impurity segregation during the cooling stage. Densities of the sintered specimens were measured by the Archimedes water immersion method. The sizes of tungsten particles, matrix volume fraction and tungsten/tungsten contiguity of sintered tungsten heavy alloy were measured by using scanning electron microscopy. The heat treated specimens were tensile tested at a strain rate of 1.33×10^{-3}/s and the failure mechanisms of tungsten heavy alloys were analyzed from observation of fractographies of tensile tested specimens.

3. RESULTS AND DISCUSSION

Fig. 1(a) shows microstructures of a solid state sintered tungsten heavy alloy using mechanically alloyed powders. The solid state sintered tungsten heavy alloy using mechanically alloyed powders



(a) (b) (c)

Fig. 1. The scanning electron micrographs showing the microstructures of (a) solid state sintered 93W-5.6Ni-1.4Fe tungsten heavy alloys sintered at 1300°C for 1 hour, (b) two-step sintered 93W-5.6Ni-1.4Fe tungsten heavy alloys sintered at 1470°C for 4 min, and (c) liquid phase sintered 93W-5.6Ni-1.4Fe tungsten heavy alloys sintered at 1485°C for 1 hour.

showed much finer tungsten particles about 3 μm compared to the tungsten particles of 30-40 μm in liquid phase sintered tungsten heavy alloy. The liquid phase sintered tungsten heavy alloy showed spherical tungsten particles distributed in continuous matrix phase, while the solid state sintered tungsten heavy alloy showed interconnected tungsten particles. Volume fraction of matrix phase and area fraction of contiguous tungsten-tungsten boundary, so called tungsten/tungsten contiguity[9], of solid state sintered tungsten heavy alloys using mechanically alloyed powders was measured as 11% and 0.74. Comparing the matrix volume fraction of 17% and tungsten/tungsten contiguity of 0.35 for liquid phase sintered tungsten heavy alloys using blended powders with same composition, the matrix volume fraction decreased and tungsten/tungsten contiguity increased for solid state sintered tungsten heavy alloy using mechanically alloyed powders.

Fig. 2 shows scanning electron micrographs of tungsten heavy alloys sintered at temperatures of 1445°C, 1460°C, 1470°C and 1485°C for 4 min after solid state sintering at 1300°C for 1 hour. When sintered at temperature below 1460°C, tungsten particles remain interconnected each other, however, when sintered at temperature above 1470°C, tungsten particles were spherodized and matrix phase was penetrated into tungsten-tungsten boundaries. The secondary sintering time increased up to 90 min at 1470°C to investigate the effect of liquid phase sintering time on the microstructural evolution of two-step sintered tungsten heavy alloy. The sizes of tungsten particles increased from 6 μm to 15 μm with increasing secondary sintering time from 4 min to 90 min. The relationship between tungsten particle size and liquid phase sintering time was found to satisfy the LSW theory[10,11] as follows,

$$\bar{r}_t^3 - \bar{r}_0^3 = k(t - t_0) \qquad (1)$$

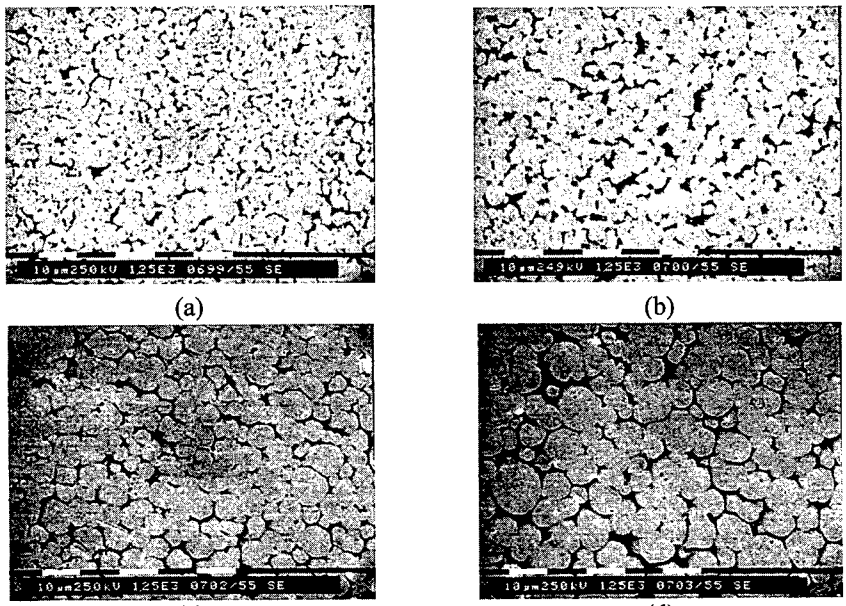


Fig. 2. The scanning electron micrographs of two-step sintered tungsten heavy alloys sintered at (a)1445°C, (b) 1460°C, (c) 1470°C and (d) 1485°C for 4 min after solid state sintering at 1300°C for 1 hour.

where $\bar{r}_t$ is average radius of particle at time, t, $\bar{r}_0$ is average radius of particle at time, t_0, and k is coarsening rate. The coarsening rate of mechanically alloyed tungsten heavy alloy was measured as 25.5 μm^3/min. at temperature of 1470°C as shown in Fig. 3.

The tungsten/tungsten contiguity was reduced from 0.74 to 0.40 after subsequent secondary sintering of solid state sintered tungsten heavy alloys due to high matrix volume fraction and low dihedral angle between tungsten and matrix phase. The tungsten particle size of 6-15 μm in two-step sintered tungsten heavy alloys using mechanically alloyed powders was finer than that of 30-40μm in conventional liquid phase sintered tungsten heavy alloys.

Tensile tests were performed to characterize the mechanical properties of tungsten heavy alloys using mechanically alloyed powders. Solid state sintered tungsten heavy alloys using mechanically alloyed powders exhibited high yield strength about 1100 MPa but showed low elongation of 0.5%. Comparing to liquid phase sintered tungsten heavy alloys using mixed powders with same composition, yield strength increased from 620 MPa to 1100 MPa and elongation decreased from 25% to 0.5%. Yield strength of tungsten heavy alloy can be formulated using Hall-Petch type equation as follows[12,13],

$$\sigma_y = \sigma_0 + k_1 G b \rho^{1/2} \tag{2}$$

where σ_y is yield strength, σ_0 is intrinsic strength, k_1 is a constant, G is shear modulus, b is Burgers vector and ρ is dislocation density in matrix phase. Dislocation density, ρ, is inversely proportional to the matrix thickness, λ,

$$\sigma_y = \sigma_0 + k_2 G b \lambda^{-1/2} \tag{3}$$

where k_2 is a constant. Matrix thickness can be formulated in terms of tungsten particle size and matrix volume fraction using geometrical relationship as follows,

$$\lambda = \frac{2}{3} D \left(\frac{V_M}{1 - V_M} \right) \tag{4}$$

where D is diameter of tungsten particles and V_M is the matrix volume fraction. The relationship between yield strength and microstructural parameters, i.e. tungsten particle size and matrix volume fraction, is expressed in Eq.(5),

$$\sigma_y = \sigma_0 + k_3 G b \left(\frac{1 - V_M}{D V_M} \right)^{1/2} \tag{5}$$

where k_3 is a constant. According to Eq.(5), yield strength of tungsten heavy alloy increased with decreasing the tungsten particle size and matrix volume fraction. The higher yield strength of solid state sintered tungsten heavy alloy using mechanically alloyed powders is due to smaller tungsten particle size of 3 μm and lower matrix volume fraction of 11%. Fig. 3 shows a relationship between yield strength of tungsten heavy alloys and the microstructural parameter, $[(1-V_M)/DV_M)]^{1/2}$, defined in Eq. (5). Yield strengths of various tungsten heavy alloys such as liquid phase sintered, two-step sintered and solid state sintered tungsten heavy alloys satisfied the relationship proposed by Eq. (5).

Fig. 4 shows the fractographies of tensile tested specimens of solid state sintered tungsten heavy alloys, two-step sintered tungsten heavy alloy using mechanically alloyed powders and liquid phase sintered tungsten heavy alloy using blended powders. Tungsten heavy alloys shows four different fracture modes such as tungsten cleavage, matrix rupture, tungsten-tungsten interfacial debonding, and tungsten-matrix interfacial debonding[14]. Churn and Yoon[14] reported that the cracks are formed preferentially at the tungsten-tungsten interfaces and linked each other to give catastrophic failure, because the tungsten-tungsten interfacial boundaries are the weakest. Most of fractured interfaces are composed of tungsten-tungsten interface boundaries in solid state sintered tungsten heavy alloys

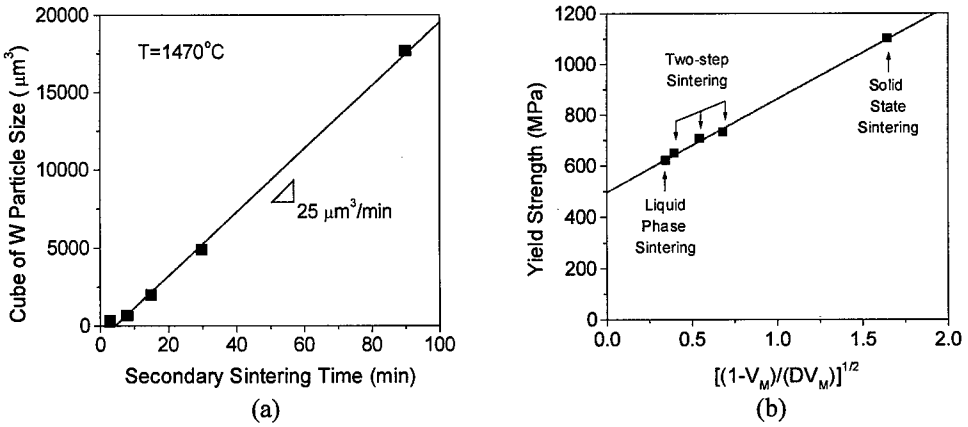


Fig. 3. (a) The linear relationship of cube of tungsten particle size with increasing secondary sintering time from 4 min. to 90 min. at 1470°C in two-step sintered tungsten heavy alloys. (b) The variation of yield strength as a function of microstructural parameters of tungsten heavy alloys sintered with different conditions.

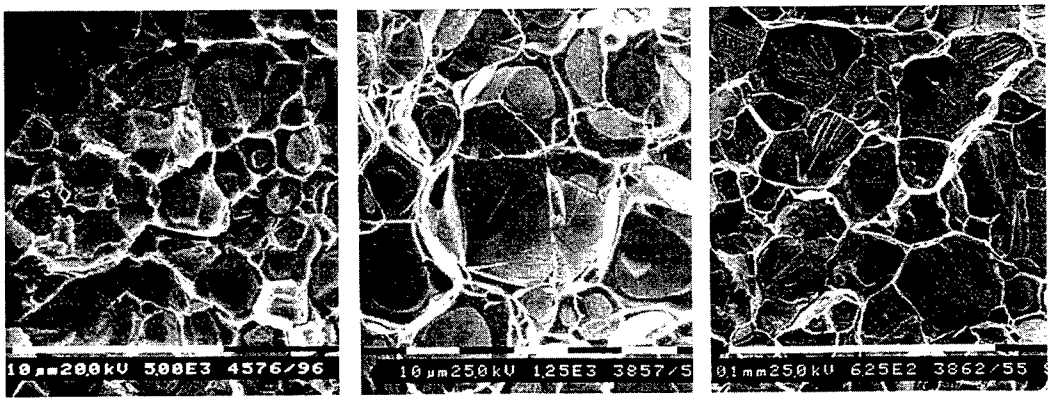


Fig. 4. The fractographies of (a) predominant tungsten/tungsten debonding mode in solid state sintered tungsten heavy, (b) mixed fracture modes in two-step sintered tungsten heavy alloy and (c) predominant tungsten cleavage mode in liquid phase sintered tungsten heavy alloy.

using mechanically alloyed powders, while tungsten cleavage and matrix rupture are mainly shown in liquid phase sintered tungsten heavy alloy using mixed powders. The brittle fracture behavior of solid state sintered tungsten heavy alloy using mechanically alloyed powders is attributed to the large tungsten/tungsten contiguity and low matrix volume fraction. Larger tungsten/tungsten contiguity gives more preferential sites for microcrack nucleation and lower matrix volume fraction makes the microcracks link up easily each other without blunting of crack tip[15].

4. CONCLUSIONS

When solid state sintered at 1300°C, tungsten heavy alloys showed ultra-fine tungsten particles of about 3 μm with high density above 99%. The solid state sintered tungsten heavy alloys using mechanically alloyed powders exhibited high yield strength of about 1100 MPa due to a high volume fraction of fine grained tungsten particles, but showed reduced elongation and impact energy due to a large area fraction of tungsten/tungsten interfaces. The solid state sintered tungsten heavy alloy was subsequently liquid phase sintered at 1470°C with varying the sintering time from 4 min to 90 min. Two-step sintered tungsten heavy alloy using mechanically alloyed powders showed finer tungsten particles of about 6-15 μm than that of 30-40μm in conventional liquid phase sintered tungsten heavy alloy. Mechanical properties of tungsten heavy alloy were found to be related to microstructural parameters such as tungsten particle size and tungsten-tungsten contiguity, which can be controlled by the two-step sintering process.

REFERENCES

1. R.M. German, Sintering Theory and Practice, John Wiley & Sons, Inc. New York, NY (1996) p.230
2. R.M. German, Proc. Inter. Conf. on Tungsten and Tungsten Alloys, (Eds.) A. Bose and R.J. Dowding, MPIF, New Jersey (1992) p.3
3. W.D. Cai, Y.Li, R.J. Dowding, F.A. Mohamed and E.J. Lavernia, Rev. Particulate Mater., **3** (1995) p.71
4. A. Bose, H.R.A. Couque and J. Lankford, Jr., Inter. J. Powder Metall., **28** (1992) p.383
5. S. Cytron, Proc. Inter.Conf. on Adv. Composite Mater., (Eds.) T. Chandra and A.K. Dhingra, TMS, Pennsylvania (1993) p.973
6. L. Lu and M.O. Lai, Mechanical Alloying, Kluwer Academic Publishers, Massachusetts (1998) p.5
7. M.L. Ovecoglu, B. Ozkal and C. Suryanarayana, J. Mater. Res. **11** (1996) p.1673
8. H.J. Ryu, S.H. Hong and W.H. Baek, J. Mater. Processing. Technol. **63** (1997) p.292
9. J. Gurland, Trans. AIME, **236** (1966) p.642
10. I.M. Lifshitz and V.V. Slyozov, J. Phys. Chem. Solids, **19** (1961) p.35
11. C. Wagner, Z. Electrochem., **65** (1961) p.581
12. M.F. Ashby, Phil. Mag. **14** (1966) p.1157
13. M.F. Ashby, Phil. Mag. **18** (1970) p.399
14. K.S. Churn and D.N. Yoon, Powder Metall., **22** (1979) p.175
15. B.H. Rabin and R.M. German, Metall. Trans. A, **19** (1988) p.1523

Key Engineering Materials Vols. 183-187 (2000) pp. 1297-1302
© 2000 Trans Tech Publications, Switzerland

Analysis of Strengthening Mechanism in Hybrid Short Fiber/Particle Reinforced Metal Matrix Composites

S.W. Jung[1], J.H. Lee[2], J.B. Nam[3], H.W. Nam[1] and K.S. Han[1]

[1] Department of Mechanical Engineering, Pohang University of Science and Technology
San 31 Hyoja-dong, Nam-gu, Pohang 790-784, Korea

[2] R&D team 2, Defense Division, Daewoo Heavy Industries Ltd.,
Sungjoo-dong, Changwon, Kyongnam 641-120, Korea

[3] Sheet Products and Process Research Group, Technical Research Laboratories,
Pohang Iron and Steel Co., Koe-dong, Nam-gu, Pohang 790-785, Korea

Keywords: Cluster Structure, Fiber, Hybrid Composite, Particle, Strengthening Mechanisms

ABSTRACT

This paper presents an analytical method considering tensile strength enhancement in hybrid fiber/particle/aluminum composites(MMCs). The tensile strength and elastic modulus of the hybrid MMCs are even 20% higher than those of the fiber reinforced MMCs with same volume fraction of reinforcements. This phenomenon is explained with the cluster model which is newly proposed in this research, and the strengthening mechanisms by a cluster is analyzed using modified rule of mixtures. The present theory is then compared with experimental results which is performed using squeeze infiltrated hybrid MMCs made of hybrid Al_2O_3 short fiber/particle preform and AC8A alloy as base metal and the agreement is found to be satisfactory.

1. INTRODUCTION

Short fiber reinforced composites are used increasingly as a structural material because they not only provide superior mechanical properties, but they can also be easily produced by the rapid, low-cost molding process. However, fiber processing is more expensive than particle and as result many research have been done to fabricate hybrid composite using particles in addition to fibers. The use of high percentage of cheap particles may reduce the cost of composites and improve some properties such as stiffness[1,2], hardness, creep and heat distortion[3,4]. But most of particles used in the hybrid composites do not increase the tensile strength due to 'hybrid effect' which is equivalent to a decrease of a fiber efficiency factor for the strength of hybrid composites[5].

The decrease of the strength is a common phenomenon for hybrid composites fabricated by injection molding process and has been explained by a number of researchers. The strength increase found in hybrid metal matrix composites fabricated by metal infiltration to hybrid preform is a special phenomenon and the cause is still unclear.

The main objective of the present work is to investigate the combined effect of fiber and particles on the tensile strength and the stiffness and to explain the cause of the increase in the properties. Analytic theory is derived by applying modified rule of mixture [5-7] and the cluster model which is newly proposed in this analysis, and experiments performed for the verifications of the theory.

2. THEORY

The strength increase in hybrid Al_2O_3 fiber/particle reinforcements MMCs are assumed to be caused by the cluster structure which is formed during the fabrication of hybrid fiber/particle preform. In a hybrid preform, all particles gather around the crossing of fibers and form clusters as shown in Fig.1. The cluster bind each of fibers and the binding lead to additional strengthen effects. The cluster model present in this paper is to analyze the strengthening mechanism on the assumption of all particles form same size of spherical clusters. The theory consisted of the probability analysis for a fiber to be included in a cluster and the fiber length factor analysis using modified rule of mixture.

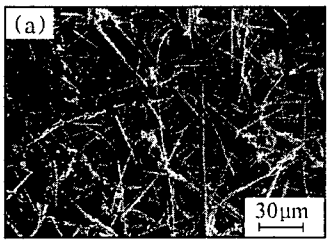


Fig.1. SEM photography of hybrid Al_2O_3 particle/fiber preform

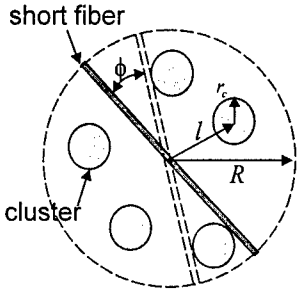


Fig.2. Schematic diagram of short fiber and clusters distribution modes

2.1. Probability analysis

To calculate the probability of a short fiber to be included in a cluster, let's consider a spherical domain of radius R which is a half of a fiber length as in Fig.2 . Then the probability becomes:

$$p(c) = \frac{V_p}{2}\left[\frac{R^3}{r_c^3} + 1 - \left(\sqrt{\frac{R^2}{r_c^2} - 1}\right)^3\right] \tag{1}$$

Since the probability of the position of the cluster in a fiber is uniform, the probability for a fiber to be included in a cluster which located within the distance of x from the center of the fiber is given by;

$$P(x) = \frac{x}{L}p(c) \tag{2}$$

2.2. Cluster Effect on The Elastic Modulus

The elastic modulus of hybrid composite can be expressed using modified rule of mixture by :

$$E_c = \chi_1\chi_2 V_f E_f + \chi_p V_p E_p + (1 - V_f - V_p)E_m \tag{3}$$

where subscript f means fiber, p particle and χ_1 and χ_2 are, respectively, the fiber orientation and fiber length factors for modulus. The cluster structure increases the fiber efficiency factor $\chi_1\chi_2$, To analyze the cluster effect on elastic modulus, the effects of fibers E_{cf}, particles E_{cp} and matrix E_{cm} respectively, should be estimated because the replacement of a part of fiber by brittle particles can reduce or increase the modulus. Each of components of the modulus is represented as followings:

$$E_{cf} = \chi_1\chi_2 V_f E_f = E_{ccw} - (1 - V_f)E_m \tag{4}$$

$$E_{cp} = \chi_p V_p E_p = E_{cu} - (1 - V_p)E_p \tag{5}$$

$$E_{cm} = (1 - V_f - V_p)E_m \tag{6}$$

where E_{ccw} represent the modulus from Christen and Waals' analysis[8] and E_{ca} is that from ashelby method[9]. E_{ccw} is estimated by the Christen and Waals' method for the composites with 3-D random fiber orientation. The method uses the averaging approach based on the properties of unidirectional composites. In unidirectional composites, clusters increase the effective fiber length by joining each of the fibers as shown in Fig.3 and increase the longitudinal modulus E_l which is given by:

$$E_1 = \chi_2 V_f E_f + (1 - V_f) E_m \tag{7}$$

where χ_2 is given by:

$$\chi_2 = 1 - \frac{\tanh(\beta L/2)}{\beta L/2} \tag{8}$$

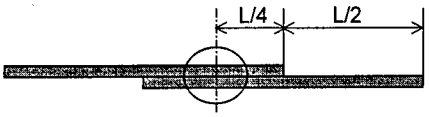


Fig.3. Shematic diagram of the increase of the fiber length factor by clusters structure.

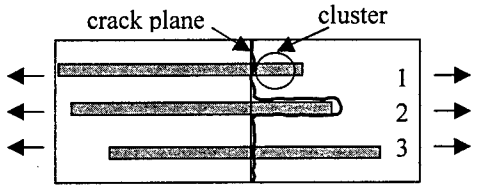


Fig.4. Schematic diagram of a crack which has developed across and around fibers

The effective length of fiber L_e in Eq.(8) is derived from the Eq.(6) for x=1/4L and given by Eq.(9). The average position of x=1/4L from the end of fiber as in Fig.3. is determined from the fact that the probability of the location of a cluster in the fiber is uniform.

$$L_e = L + \frac{L}{2} p(c) \tag{9}$$

Inserting the modulus E_l to Christensen and Waals analysis which is given by:

$$E_{ccw} = \frac{[E_1 + (4\nu_{12}^2 + 8\nu_{12} + 4)K_{23}][E_1 + (4\nu_{12}^2 - 4\nu_{12} + 1)K_{23} + 6(G_{12} + G_{23})]}{3[2E_1 + (8\nu_{12}^2 + 12\nu_{12} + 14)K_{23} + 4(G_{12} + G_{23})]} \tag{10}$$

Then, the modulus of E_{ccw} is calculated. The E_{ca} is estimated by applying simplied ashelby method [9] given by:

$$8E_{ca}^2 + [(7 - 15V_p)E_p + (7 - 15V_m)E_m]E_{ca} - 7E_pE_m = 0 \tag{11}$$

2.3. Cluster Effect on Tensile Strength

The tensile strength of hybrid composite can also be expressed by modified rule of mixture as:

$$\sigma_c = \chi_3 \chi_4 V_f \sigma_f + \chi_p V_p \sigma_p + (1 - V_f - V_p)\sigma_m \tag{12}$$

where σ_p is the ultimate strength of particle and $\chi_p V_p \sigma_p$ is particle efficiency factor. It is assumed that particle reinforcement on the tensile strength is negligible, i.e., $\chi_p V_p \sigma_p = \sigma_m$. Then, the Eq.(12) becomes ;

$$\sigma_{cu} = \chi_3 \chi_4 V_f \sigma_{fu} + (1 - V_f)\sigma_m \tag{13}$$

Fiber efficiency factor is related not only to the fiber length and the fiber orientation factor but also to the interfacial adhesion strength between fibers/matrix and particle/matrix[5]. However, we limit quantitative analysis to the fiber length factor in this study. For unidirectional short fiber composites $\chi_3 = 1$ and $\chi_4 < 1$. If the fiber length is uniform and equals to L, the length factors is given by ;

$$\chi_4 = L/(2L_c) \text{ for } L < L_c \tag{14}$$

$$\chi_4 = 1 - L_c/(2L) \text{ for } L > L_c \tag{15}$$

where L_c, the critical fiber length, is given by ;

$$L_c = r_f \sigma_{cu} / \tau_i, \tag{16}$$

where τ_i and r_f are the interfacial shear stress between matrix and the fiber radius, respectively. If the composites included in clusters, the length factor of fibers will be changed. The change of the length factor can be estimated from the average bridging force required to break the composite at some random cross section[6] and there are three kinds of strengthening mechanism according to the length of shorter fiber section.

CASE 1 : $l < L_c/4$

If fibers without cluster will fully debond and shorter segment will pull out. However, if the short segment of a fiber included in a cluster as the fiber number 1 in Fig.4., then the longer segment will pull out and the length factor is given by ;

$$\chi_4 = \frac{L}{2L_c}(1 + \frac{7}{6}p(c)) \tag{17}$$

CASE 2 : $L_c/4 < l < L_c/2$

If the short segment length of the fiber with a cluster is less than $L - L_c/2$, the fibers will break at the failure of composites, and if the segment length is between $L - L_c/2$ and L, the fiber will be pulled out;

$$\chi_4 = \frac{L}{2L_c}\{1 + (\frac{2}{3} + \frac{1}{2}(3 - \frac{L_c}{L})(1 - \frac{L_c}{L})^2)p(c)\} \tag{18}$$

CASE 3: $l > L_c/2$

Fibers of which shorter segment is short than $L_c/2$ and not included in a cluster will be pulled out and those included in a cluster will be broken. The fraction of corresponding fibers is L_c/L. If the shorter segment is larger than $L_c/2$, fibers will be broken regardless of clusters and the fraction of corresponding fibers is $1 - L_c/L$:

$$\chi_4 = 1 - \frac{L_c}{2L} + \frac{1}{3}\frac{L_c}{L}p(c) \tag{19}$$

From the Eq.(17), (18) and (19) the fiber length factors are evaluated. For the fiber composites which is not contain particles, the probability p(c) is zero and the factor of Eq.(17), (18) and (19) become equivalent to the Eq.(14) and (15). This indicate that the derivation process in this research is reasonable ;

3. EXPERIMENT

Hybrid metal matrix composites were fabricated with Al_2O_3 fiber and Al_2O_3 particles of ICI Co. as reinforcements and AC8A aluminum as matrix. Mechanical properties of the material used are listed in Table 1 and composition of all the specimens are listed in Table 2. The MMCs were fabricated with squeeze casting method using hybrid preforms sintered at 1000 °C. Tensile tests were performed by MTS with a displacement control of 1 mm/min rate at room-temperature.

Table 1. Specifications of reinforcements and matrix of MMCs

Materials	Diameter (μm)	Length (μm)	Tensile Strength (MPa)	Young's Modulus (GPa)
Al_2O_3 fiber	3.0	150	2010	310
Al_2O_3 Particle	1.0	1.0	-	380
AC8A	-	-	275	73

Table 2. Composition of MMCs specimens

No.	Material type	Matrix (%)	V_f(%)	V_p(%)
F15	Fiber MMCs	85	15	-
F10P5	Hybrid MMCs	85	10	5
F20	Fiber MMCs	80	20	-
F10P10	Hybrid MMCs	80	10	10

4. RESULTS AND DISCUSSIONS

The probability for a fiber to be included in a cluster depends on the size of cluster r_c/R and the volume fraction of particles V_p. The probability increases as the (r_c/R) decreases and approaches to V_p as r_c/R closer to 1. The radius of a cluster observed to be about 10 μm to 20 μm from SEM photographs such as Fig.1, thus 15 μm was used as an average in the analysis.

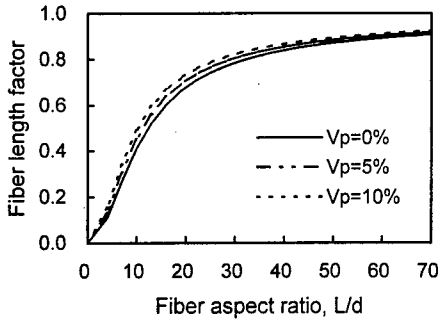


Fig.5. Fiber length factor for elastic modulus χ_2 as function of L/d and V_p

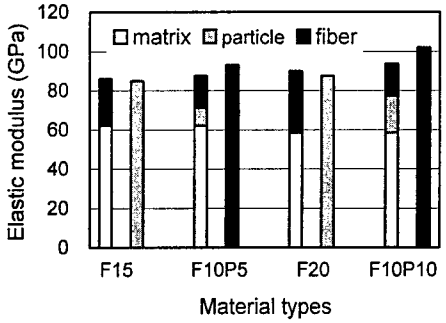


Fig.6. Elastic modulus of MMCs from theoretical prediction and tensile test

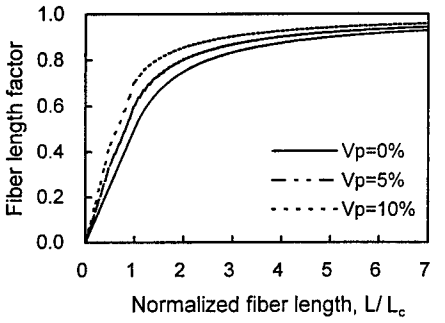


Fig.7. Fiber length factor for tensile strength χ_4 tensile test

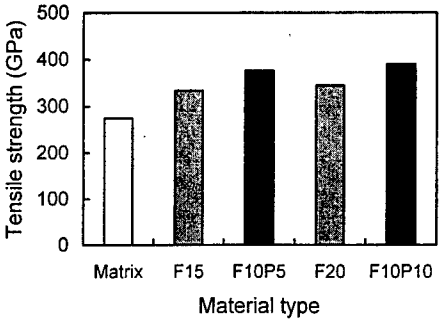


Fig.8. Tensile strength of MMCs from as a function of L/ L_c and V_p

Fig.5 shows the length factor for elastic modulus according to fiber aspect ratio and particle volume fraction. The length of fibers used in this study is L/d=50 and the increase of the length factor is 1.4% for V_p=5% and 2.6% for V_p=10% compared with the fiber composites. The increase of the length factor increases the modulus of hybrid composite less than 0.1%. Therefore the effect is negligible.

Fig.6 shows the elastic modulus from the experiment (right) and theory (left). The theoretical values are represented as a sum of each component from the Eq.(4), (5) and (6). The theory estimates the elastic modulus of hybrid composite smaller than experimental value while it

estimates the fiber composites almost accurately. The difference between the theoretical prediction and experiment is the evidence of the existence of coupling effects between fiber and particles.

The length factor, χ_4, for tensile strength of hybrid composites with L_c=22 μm is represented in Fig.7. The graph consists of three type of curve according to the fiber length, L/L_c, 0 to 0.5, 0.5 to 1 and more than 1 and it is continuous at the interface of 0.5 and 1. The L/L_c of MMCs in this study is evaluated to be 6.8 on the assumption of perfect bonding between fiber and matrix. For the L/L_c, the increase in length factor is 1.6% for V_p=5% and 3.3% for V_p=10%. Though the increase of the factor for tensile strength is larger than that for elastic modulus, it is small and insufficient to explain the tensile strength increase in hybrid composite.

Fig.8 shows the tensile strength from tensile test. The strength of hybrid composite is much larger than fiber composite with same volume fraction of reinforcements. Therefore, we deduce that the hybrid composite also have positive coupling effect on the tensile strength in addition to on the elastic modulus.

As shown in Fig.5 and Fig.7, the coupling effect induced by cluster structure is not sufficiently analyzed with length factor increase. However qualitative explanation is possible. The cluster structure induces additional bending rigidity by joining each of independent fibers and thus increase the elastic modulus. It also increases tensile strength by changing fracture mechanism which is related not only fiber length but also fiber orientation. The effective fiber length crossing the crack plane is proportional to fiber angle given by $L_e=L\cos\theta$ and as the effective length decreases the increase in fiber length factor for tensile strength is larger as shown in Fig.7.

5. CONCLUSIONS

The increase of tensile strength in hybrid fiber/particle MMCs have been studied using cluster model and following conclusions have been drawn.

1. The hybrid MMCs have additional strengthening effect on tensile strength and elastic modulus caused by the cluster structure which is formed during the fabrication of fiber preform.
2. The strengthening mechanism by cluster structure can be explained with factors of modified rule of mixture. The increase of the elastic modulus is due to bending rigidity increase and the strength is due to the change of fracture mechanism.
3. The strengthening mechanics of hybrid composite with cluster structure related with particle volume fraction, cluster size and fiber length. As the particle fraction increases and fiber length, cluster size decreases, the strengthening effect by a cluster increases.

ACKNOWLEDGEMENT

The authors wish to acknowledge the financial supports of the Korea Research Foundation made in the program year of 1998 (No:1998-017-E00002).

REFERENCE

[1] D.M.Bigg, Poly. Compos., 8 (1987) p.115
[2] B.Pukanszky, A.Rockenbauer and F.H.J. Maurer, Composites, 15 (1994) p.205
[3] S.J. Feltham and B.Yates, J. Mater. Sci., 17 (1982) p.2309
[4] M.O.W. Richardson, Polymer Engineering Composites., Applied Science, London (1977)
[5] S.Y. Fu and B.Lauke, Composites Part A, 29A (1998) p.575
[6] S.Y. Fu and B. Lauke, Compos. Sci. Tech., 56 (1996) p.1179
[7] M.R.Piggott, J. Compos. Mater, 28 (7) (1994) p.588
[8] R.M. Christensen and F.M. Waals, J. Compos. Mater. 3 (1968) p. 352
[9] S.F. Corbin and D.S. Wilkinson, Acta Metall. Mater., 42 (1994) p.1211

Key Engineering Materials Vols. 183-187 (2000) pp. 1303-1308
© 2000 Trans Tech Publications, Switzerland

Effects of Welding Process and Crack Orientation on da/dN of Titanium Alloys

Qingfen Li[1], Huocai Ni[2], Sanglin Yang[1], Zhaoxia Cui[1], Xianhai Peng[1] and Liquan Wang[1]

[1] College of Mechanical & Electrical Engineering, Harbin Engineering University, Harbin 150001, China P.R.

[2] Zhengzhou Mechanical & Electrical Engineering Research Institute, Zhengzhou 450052, China P.R.

Keywords: Crack Orientation, Fatigue Crack Growth Rate (da/dN), HAZ, Ti-Alloy, Welding Process

ABSTRACT

The effects of welding process and crack orientation on da/dN were experimentally studied with SENB specimens of a Chinese Ti-alloy plate and rolled ring. Results show that the fatigue crack growth rate da/dN of C-R direction specimens is higher than those of L-R ones. And the da/dN values of welded joint is much higher than those of base metal and HAZ. It means that the welding process may lead to a great reduction in the fatigue property of the Ti-alloy, and that the effect of crack orientation on da/dN is not negligible. Further analysis is discussed.

1 INTRODUCTION

Conventional fatigue crack data is derived from smooth specimens and is given in the form of an S-N curve and an endurance limit. Fracture mechanics, however, can treat the case of a known or postulate flaw in terms of stress intensity range $\Delta K = Y\Delta\sigma\sqrt{\pi a}$ at the tip of the crack.

A large proportion of service failures can be traced to the development of fatigue crack growth. When the applied stress range is small, fatigue crack growth can occupy a substantial part of the structure total life. Fig 1 shows a schematic representation of the three distinct regions of fatigue crack growth under constant amplitude load fluctuations[1].

In region II, the fatigue crack growth is represented by a Paris law equation of the following form

$$\frac{da}{dN} = c(\Delta K)^n \tag{1}$$

Where c and n are numerical constants.

The measurement of crack growth and studying the factors influencing da/dN of Ti-alloy are

very important in Fracture Mechanics and engineering applications. An experimental investigation of effects on da/dN of Ti-alloy is therefore carried out on this paper.

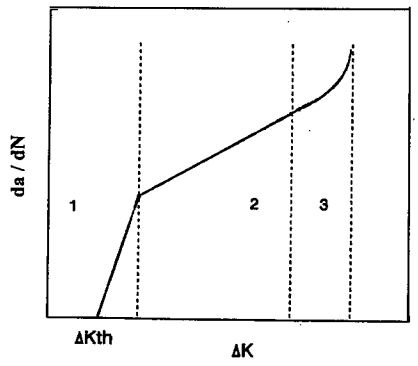


Fig. 1. The three distinct regions of fatigue crack growth

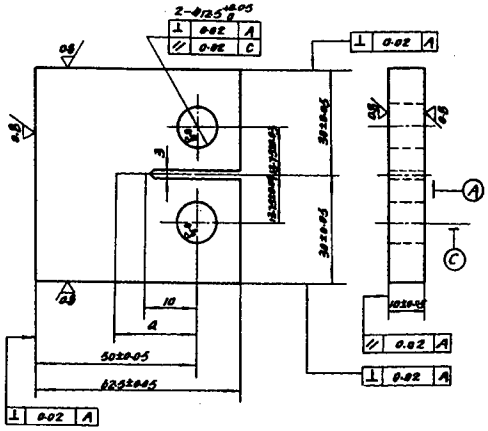


Fig. 2. CT specimen

2 EXPERIMENTAL PROCEDURE

2.1 Material and Specimens

A Ti-alloy plate and its rolled ring were used. The chemical composition is given in table 1 and the mechanical properties in table 2. CT specimens were used for the testing of da/dN, and the size is given in Fig 2. Specimens made from the plate were cut along L-T direction, and those from the rolled ring were along L-R and C-R direction respectively (see Figs. 3 and 4).

2.2 Experimental Procedure

The tests for fatigue crack growth rate of base metal were performed in accordance with GB 6398-86[2], and those of welded joint and HAZ were with GB 9447-88[3]. A Mayes-50E test machine was used for specimens from rolled ring and an Instron-1343 machine for specimens from plate. All specimens were subjected to constant amplitude load-control. The frequency was 15Hz for rolled ring specimens and 10Hz for plate ones. The load range is ΔP=4.95KN with the load ratio R being 0.05 for rolled ring specimens and 0.1 for plate ones.

All test were made at room temperature, 22-26℃.

Table 1 Chemical Composition of Test Materials

	Ti	Al	B	Fe	Si	C	N	H	O	
Plate	95.57	4.0	0.005	0.23	0.05	0.025	0.024	0.005	0.084	
Rolled ring	95.64	3.975	0.005	0.215	<0.005	0.016	0.023		0.073	

Table 2 Mechanical Properties of Ti-alloy Plate

	σ_b(MPa)	$\sigma_{0.2}$ (MPa)	δ %	E(MPa)	v	a_{KU}(J/cm^2)
Plate	682	605	18.5	1.106×10^5	0.34	74.9
Rolled ring	712	615	16.3	1.310×10^5		71.4

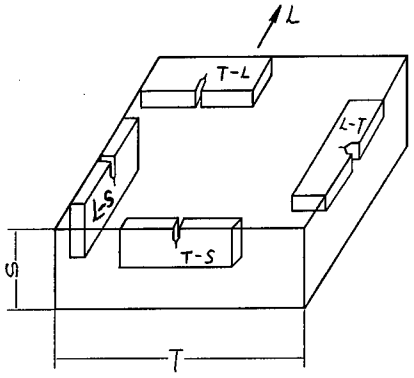


Fig.3 Specimen Orientation for a plate

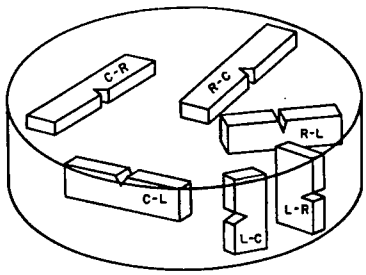


Fig. 4. Crack Plane Orientation Identification Code for Drawn Bars

3 RESULTS AND DISCUSSION

The experimental results of da/dN of five groups are shown in Figs. 5-9. Figure 10 gives the comparison of the results for base metal, welded joint and HAX.

In Figs. 5 and 6, it follows that

for L-R direction:

$$(da/dN)_{\text{I}} = 1.120\times10^{-16}(\Delta K)^{6.693}$$
$$(da/dN)_{\text{II}} = 1.565\times10^{-11}(\Delta K)^{3.0048}$$

for C-R direction:

$$(da/dN)_{\text{I}} = 3.813\times10^{-15}(\Delta K)^{5.55}$$
$$(da/dN)_{\text{II}} = 7.853\times10^{-11}(\Delta K)^{2.55}$$

The above results show that the fatigue crack growth rate da/dN of C-R direction is higher than that of L-R direction. It means that in Ti-alloy material, crack orientation has an effect on fatigue property. It is therefore very important to select a proper crack orientation in engineering practice.

From Figs. 7、8 and 9, we have

for base metal plate:

$$(da/dN)_{\text{I}} = 1.5206\times10^{-19}(\Delta K)^{10.5003}$$
$$(da/dN)_{\text{II}} = 2.0000\times10^{-9}(\Delta K)^{3.3504}$$

for HAZ:

$$(da/dN)_{\text{I}} = 9.6474\times10^{-7}(\Delta K)^{8.3401}$$
$$(da/dN)_{\text{II}} = 1.0000\times10^{-9}(\Delta K)^{3.5978}$$

for welded joint:

$$(da/dN)_{\text{I}} = 2.0410\times10^{-12}(\Delta K)^{6.4388}$$
$$(da/dN)_{\text{II}} = 4.6000\times10^{-8}(\Delta K)^{2.8029}$$

It may be clearly seen that the da / dN value of the welded joint is much higher than that of the base metal and HAX. This means that the welding process may lead to a great reduction in the fatigue property of the Ti-alloy.

A further analysis will be conducted in a follow up paper because of the space limitation.

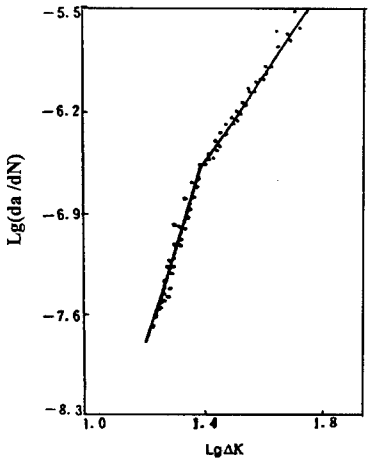


Fig. 5. da/dN vs ΔK of rolled ring(L—R)

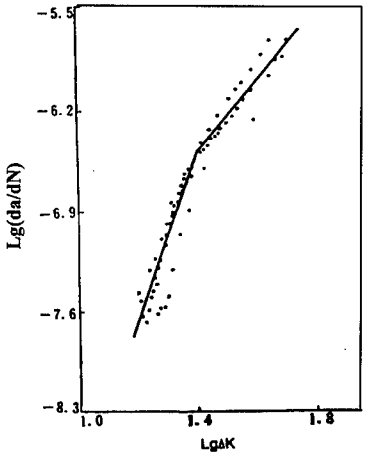


Fig. 6. da/dN vs ΔK of rolled ring(C—R)

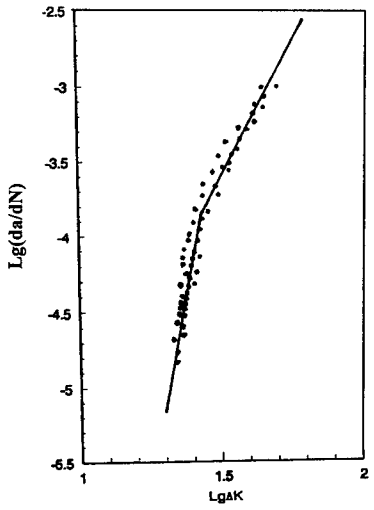


Fig. 7. da/dN vs ΔK of base metal plate (L—T)

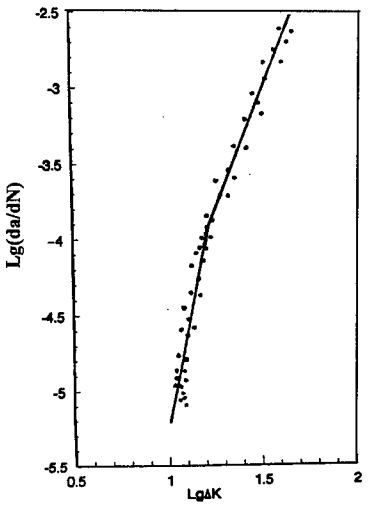


Fig. 8. da/dN vs ΔK of welded joint

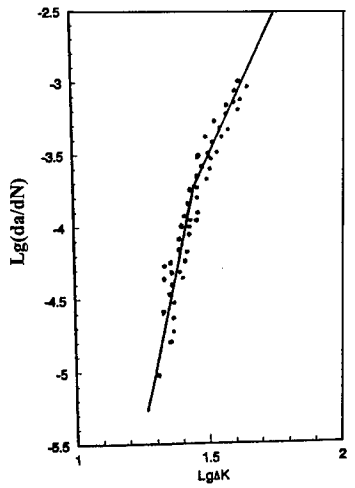


Fig. 9 . da /dN vs ΔK of HAZ

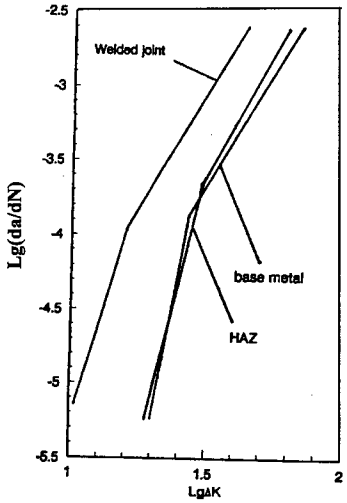


Fig. 10. Comparison of base metal plate, welded joint and HAZ

4 CONCLUSIONS

(1) The fatigue crack growth rate da/dN of C-R direction is higher than that of L-R direction. It means that the crack orientation has an effect on fatigue property.
(2) The da/dN values of welded joint are much higher than those of the base metal and HAZ.
(3) The welding process can result in a great reduction of fatigue property of the Ti-alloys.

REFERENCES

1. Y.W.Mai, Application of fracture mechanics in power generation, 《Mechanical Engineering Transactions》 (1982).
2. Standard Method of Test for Fatigue Crack Growth Rate of Metallic Materials, GB6398-86, The Chinese Standard Institution (1986).
3. Standard Method of Test for Fatigue Crack Growth Rate of Welded Joint, GB9447-88, The Chinese Standard Institution (1988).

Key Engineering Materials Vols. 183-187 (2000) pp. 1309-1314
© 2000 Trans Tech Publications, Switzerland

Laser Welding of Ti-Ni Shape Memory Alloy Wire and its Fatigue Properties

Y.S. Kim[1] and J.D. Kim[2]

[1] Department of Mechanical and Materials Engineering, Korea Maritime University, Dongsam-dong, Youngdo-ku, Pusan 606-791, Korea

[2] Division of Marine System Engineering, Korea Maritime University, Dongsam-dong, Yeongdo-gu, Pusan 606-791, Korea

Keywords: Fatigue Properties, Laser Welding, Shape Memory Alloy, Shape Memory Effect

ABSTRACT

Ti-50.9at%Ni wires were welded using pulsed YAG laser. The laser welded wires were tested for investigating the shape memory effect and the ability of super elasticity. The fatigue properties of the welded wires were investigated using the rotary bending fatigue tester specially designed for wires. Moreover, the effect of defocusing distance during laser welding on the static and fatigue properties was investigated.

The shape memory effect and super elasticity of the laser welded wires were approximately identical with that of base metal at the test temperature below 353K. However, the welded wires were broken within elastic limit at the test temperature above 353k. Under the cyclic bending loading conditions, the welded wires could be useful only below the elastic limit, while the base metal had sufficient fatigue life even the stress induced M-phase region. The fatigue strength of the welded wires was about half of that of the base metal. The deterioration of the static and fatigue properties in the welded wires was proven to be from the large difference of the transformation behavior between the base metal and welded part that is caused by vaporization of Ni-content at the welded part during the welding process. The defocusing distance below 3mm acted more largely on lowering the strength of the welded wires than that of 6mm or 8mm.

1. INTRODUCTION

The Ti-Ni shape memory alloy wires are expected as a very useful material in the fields of actuator, sensor, or medical appliance. For the promotion of practical use of that wire, it is very important to establish its welding method. Several papers have been reported about the welding method of the shape memory alloy. The gas tungsten arc welding, friction welding, resistance welding, electron beam welding, and laser welding have so far been tried to apply to the joining of a shape memory alloy[1-5]. In order to obtain the successful welded part of the shape memory alloy, it is necessary to make the heat affected zone as narrow as possible[4]. The laser welding is considered to be the superior joining method of the shape memory alloy in respect of obtaining the very narrow heat affected zone due to its high energy, high power density, and small heat input.

For making the reliable welded assembly of the shape memory alloy, the fatigue properties of the welded part must be understood. However, the welding methods of the alloy have so far been discussed based on the tensile breaking load; no work with regard to the fatigue properties has yet been conducted.

The present work was intended to apply the pulsed YAG laser welding to the joining of the Ti-Ni shape memory alloy wire. The strength of the welded wire was discussed on the basis of tensile breaking load and cyclic bending fatigue tests.

2. EXPERIMENTAL PROCEDURE

The composition of the alloy used were Ti-50.9at%Ni. The ingots of the alloy were hot drawn, and then cold drawn by 30% to wire of 1.0 mm diameter. The wire was cut to 100mm length for base metal specimen and to 50mm length for welded specimen. The cut wires were annealed at 673K for 3.6 ks followed by water quenching. After the heat-treatment, the specimens were polished lightly by emery papers to remove the lightly oxidized surface layer. The transformation temperatures of the prepared specimens appeared to as follows by DSC test : R*= 310K, Ms= 223K, A*= 288K, AR*= 313K. ARf=323K. The welded specimens were made by butt welding of the 2 wires of 50mm length using the pulsed YAG laser. The welding conditions are as follows; focal length = 150mm, defocusing distance = 3mm, 6mm, 8mm, lamp voltages = 320V, pulse length = 5ms, pulse energy = 7.8J, shield gas = Ar, 30l/min. The schematic diagram of the welding process is shown in Fig. 1. The welding was performed by 4 shots of the beam in the circumference of the butt joint. For avoiding the welding distortions, both base metal wires were fixed in the jig during welding process.

The shape memory effect and super elasticity for the base metal and welded specimens were evaluated using a Shimadzu Autograph AG10kND Instron type tester with a heating chamber.

Fatigue tests were carried out using a rotary bending tester which is specially designed for wires in the previous work[6]. The schematic diagram of the cyclic bending fatigue test for the welded wire is shown in Fig. 2. In this test, the cyclic strain amplitude is changeable by changing the arc radius of the specimen. The tests were conducted under constant temperature, 293K and constant cyclic speed, 6.7Hz.

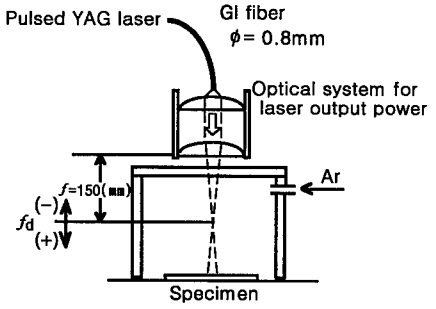


Fig.1. Schematic diagram of the laser welding process(*fd*:defocusing distance).

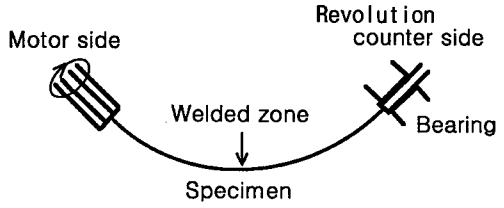


Fig.2. Schematic diagram of the cyclic bending fatigue test welded wire.

The transformation behaviours of the base metal and welded part were inspected by the DSC test. The functional and fatigue properties were discussed in conjunction with the change of the defocusing distance in welding process. For clarifying the reason for the difference in fatigue life between the base metal and welded wire occurs, the transformation temperature as a function of Ni-content was investigated. Moreover, the effect of the heat treatment at 673K for 3.6 ks followed by water quenching for the welded specimens was inspected by the fatigue tests.

3. RESULTS AND DISCUSSION

3.1 Functional Properties of the Welded Wire

From the appearance of the welded part, the welding zones appeared to have a little different width with the change in the defocusing distance during the welding process. The width of the zones appeared as 1mm at the defocusing distances of the 6mm and 8mm, however, it appeared as

1.3mm at 3mm. The beam diameter increases with increasing the defocusing distance, while the energy density decreases. The appearing of the wider width at 3mm defocusing distance is considered to be from the higher energy density nevertheless smaller beam diameter.

Fig. 3, 4 shows the strain- stress curves for the base metal, welded specimens with 6mm and 3mm defocusing distance, respectively. The recovery strains by the heating are indicated by arrows in each diagrams. The base metal shows full shape memory effect at 263K, and it shows super elasticity at 323K and 353K. The welded specimens with 6mm defocusing distance shows nearly same behavior as base metal except somewhat lower martensite inducing stress at the temperature below 353K. Above 353K, the specimen breaks within the elastic limit. However, the welded specimen with 3mm defocusing distance shows only shape memory effect at 263K. The welded zone acts as a strain concentration part in the loading due to the change of its Ni-content during the welding process. The reason for the change of the Ni-content at welded zone will be discussed in Section 3.3. Therefore, the wider welded zone at 3mm defocusing distance leads to large strain concentrations and brings the lower strength.

The breaking within elastic limit at high temperature in the welded specimens is considered to be due to the large difference in the yield strength between the base metal and welded zone at high temperature region. The critical stress for inducing the martensite, namely yield strength in Ti-Ni

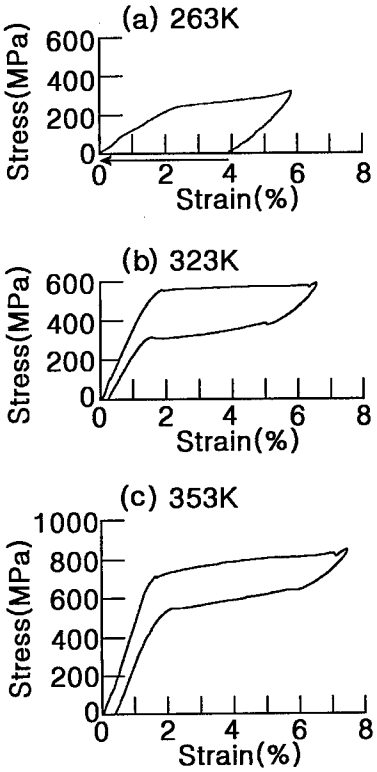


Fig.3. Strain-stress curve for base metal.

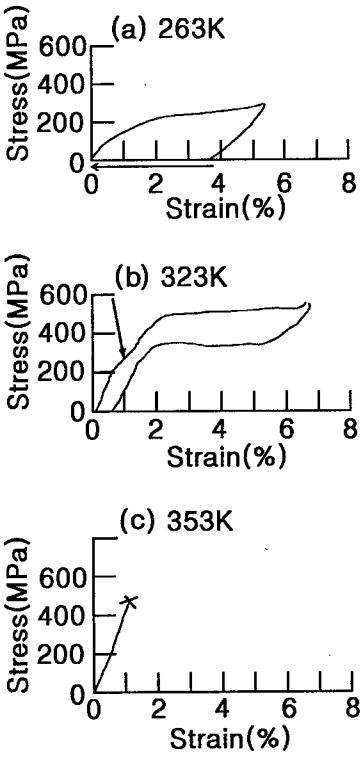


Fig.4. Strain-stress curve of welded specimen with 6mm defocusing distance. Arrows in (b) indicates 1-step martensitic transformation.

alloy becomes higher with the rise in the temperature of Ti-50.9at%Ni alloy[6]. The yield strength of base metal will increase with increasing the temperature; however, that of welded zone will not increase in same rate because of its change of Ni content during welding process as above mentioned. Thus, large difference in strength occurs at higher temperature, and leads to large stress concentration at welded zone. As the result, the welded specimen breaks within elastic limit at high temperature region.

Moreover, from the above s-s curves, it is known that the welded specimen shows the 2 step transformation behaviours even at temperatures above 323K as shown by arrow in Fig. 4, while the base metal shows only 1 step transformation above 323K. The 2 step transformation below 323K indicates the R-phase transformation and martensitic transformation. This 2 step transformation behaviour is shown in both of base metal and welded specimen as shown in Fig. 3 and 4. In general, R-phase transformation does not appear in Ti-Ni alloy above 323K[7]. The 2 step transformation behavior in welded specimen above 323K is considered to be caused by the separate martensitic transformation at welding zone and base metal.

3.2 Fatigue Properties of the Welded Wire

Fig. 5 shows the strain amplitude(ε_a)- number of cycles to failure(Nf) curves in the cyclic bending fatigue tests for the base metal and laser welded specimens at 293K. The welded specimens were investigated for the change of defocusing distance during welding process and the effect of the post weld heat treatment. The ε_a-Nf curve of the base metal is composed of 3 straight lines divided by 2 turning points. In the previous work[6], the authors clarified that these turning points are coincident with the elastic limit strain and proportional limit strain, respectively. This figure shows that the fatigue life of base metal is over $5x10^3$ cycles even under strain amplitude of 3.5 % which is M-phase region [see figure 3]. However, the welded specimens show 1 straight line and its fatigue life is not recognized over 1.5% strain amplitude. Moreover, the welded specimens show somewhat different fatigue life according to the defocusing distance; the 3mm defocusing distance shows a little shorter fatigue life than 6mm and 8mm. This difference comes probably from the degree of strain concentration caused by the difference of the width of welding zone as mentioned in Section 3.1. Moreover, in this figure, the post weld heat treatment at 673K for 3.6 ks followed by water quenching is shown to have no effect on the fatigue life. From Fig 5,

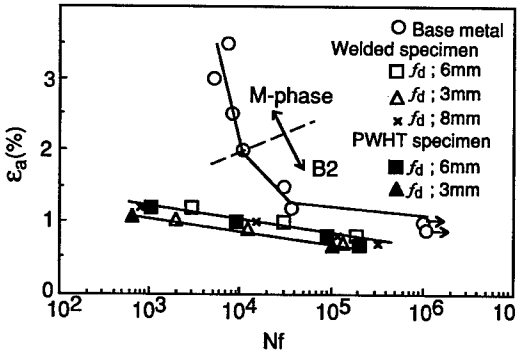


Fig.5. Strain amplitude(ε_a)-number of cycle to failure (Nf) curves for base metal and welded specimen. (PWHT : Post Weld Heat Treatment;673K 1hr, WQ)

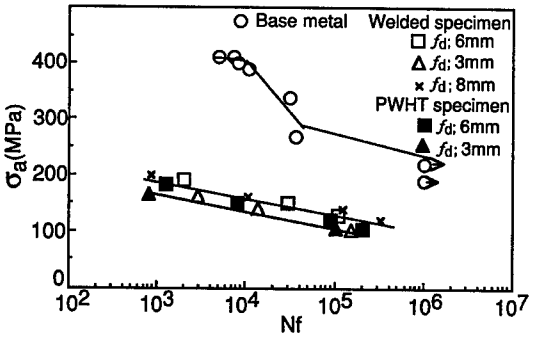


Fig.6. Stress amplitude (σ_a)-Nf curves for base metal and welded specimen.

it is known that the fracture strain amplitude at $2x10^5$cycles for the welded specimens is about the half of that for base metal. Fig. 6 shows the stress amplitude(σ_a)- Nf curves for the base metal and welded specimens.The curves were obtained from ε_a - Nf data by the conversion of ε_a into σ_a using the strain- stress curve. The σ_a- Nf curve of base metal shows to be composed of 3 straight lines divided by 2 turning points, while that of welded specimens 1 straight line. The curves show that the fracture stress amplitude at 2x 10^5cycles for welded specimens is about half of that for base metal. The reason why the difference in fatigue life between the base metal and welded specimens occurs, will be discussed in Section 3.3.

3.3 The Difference in Transformation Behaviour Between the Base Metal and Welded Specimen

In order to understand the reason why the difference in static and fatigue properties between the base metal and welded specimens occur, the transformation behaviour of the base metal and welded zone must be understood. Fig. 7 shows the results of the DSC test for the base metal and weld metal. The top and bottom curves were measured during cooling and heating, respectively. The DSC curves of the base metal show two separate peaks upon cooling and heating. The peaks upon cooling correspond to the R-phase and martensitic transformation whose peak temperatures are denoted by R* and M*, respectively. The reverse transformation temperatures upon heating are denoted by A* and AR*. The corresponding Ms, As, Af, ARs and ARf points are shown in this figure. On the other hand, the weld metal shows only one peak upon cooling and heating whose temperatures are denoted by M* and A*. In the weld metal, R- phase transformation does not occur because of solution-treated effect due to the heating cycle during welding process. From Fig. 7, it is known that the M* and A* point of weld metal are markedly higher than those of base metal. The M* point of weld metal is found to be 315K.

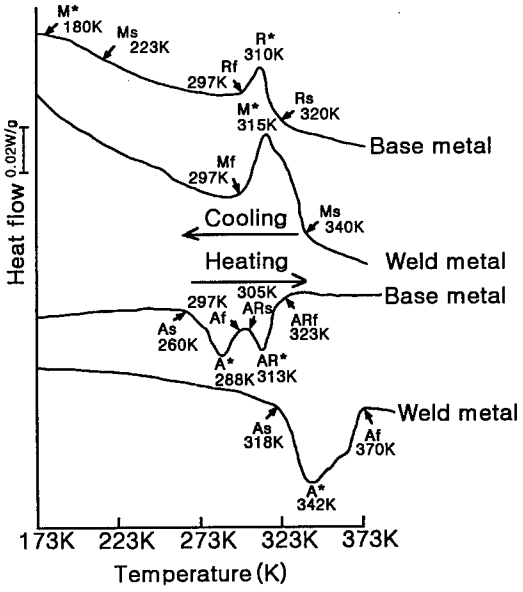


Fig.7. DSC curves for base metal and weld metal.

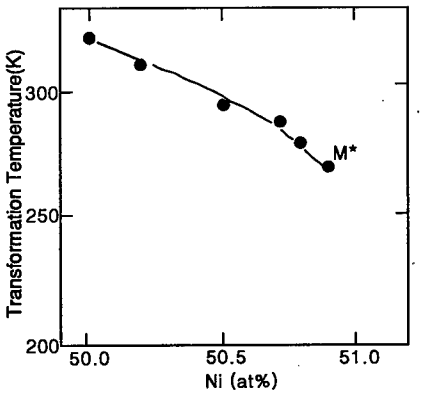


Fig.8. M*points as a function of the Ni-content.

In order to clarify the reason why the M* point rises in the weld metal, the relation between the compositions and M* point were investigated for the solution treated Ti-Ni alloy. Fig. 8 shows the M* points as a function of the Ni content in the solution treated Ti-Ni binary alloy. This figure shows that the M* point rises with decreasing the Ni content. From this figure, Ni-content of M* point at 315K appears to be about 50at%. The original Ni content of the specimen was 50.9at%, and accordingly about 0.9at% of Ni has disappeared; the excess Ni content evaporates during welding process. By this way, the change of the compositions occurs in the welded zone and the transformation points of welded zone become higher than that of the base metal. Besides, the weld metal softens and leads to strain concentration in the static and cyclic bending load.

From the above discussions, it is concluded that the difference in the static and fatigue properties between the base metal and welded specimens has resulted from the change of the compositions at the weld zone during the welding process. For the purpose of improving the fatigue properties of the welded wire, the solid state welding method which does not accompanying the fusion of the joining metal is recommended.

4. CONCLUSIONS

The Ti- 50.9at%Ni alloy wires were welded using the pulsed YAG laser, and the functional and fatigue properties of the welded wire were investigated for the purpose of clarifying the application of the laser welding to the joining of the shape memory alloy wire. Main results obtained are summarized as follows.

1) The laser welded wires show nearly same shape memory effect and super elasticity as the base metal at the temperature below 353K, and it shows 2 step transformation behaviours at welding zone and base metal.

2) The welded wires are broken within the elastic limit at the temperature above 353K, while the base metal shows the super elasticity.

3) Under the cyclic bending loading conditions, the welded wires are useful only within the elastic limit, while the base metal has sufficient fatigue life even in the stress induced M-phase region.

4) The deterioration of the static and fatigue properties in the welded wires comes from the large difference in the transformation behaviour between the base metal and welded part which is caused by vaporization of Ni-content at the welded part during the welding process.

5) The defocusing distance below 3mm in the laser welding process acts more largely on lowering the strength of the welded wires than that of 6mm or 8mm.

6) The post weld heat treatment at 673K for 3.6 ks followed by water quenching does not improve the fatigue properties of the welded wires.

REFERENCES

1. W.J.Buehler and R.C.Wiley, United State Naval Ordnance Laboratory, NOLTR61-75 (1961) August, 68.
2. K.Kimura, S.Shirai, H.Tobusi and H. Iwanaga, collected papers of JSME, **58** (1992) p.2465.
3. M.Makita, K.Kimura, H.Tobusi and P.H.Lin, collected papers of JSME, **60** (1994) p.2603.
4. A.Hirose, M.Uchihara, T.Araki, K.Honda and M.Kondoh, J.JIM. **54** (1990) p.262.
5. H.Matsuda, Master thesis,Welding Research Institute, Osaka University (1992).
6. Y.S.Kim, T.Matsunaga and S.Miyazaki, Abstracts of JIM, No.119,170 (1996) p.168
7. S.Miyazaki and K.Otsuka, Metall. Trans. A, **17A** (1986) p.53.

Key Engineering Materials Vols. 183-187 (2000) pp. 1315-1320
© 2000 Trans Tech Publications, Switzerland

Investigation on Improving Fatigue Properties of Welded Joints by Ultrasonic Peening Method

Lixing Huo, Dongpo Wang, Yufeng Zhang and Junmei Chen

Department of Mechanical Engineering, Tianjin University, Tianjin 300072, China P.R.

Keywords: Fatigue Strength, Low Carbon Steel, Ultrasonic Peening, Welded Joint

ABSTRACT

Fatigue strength of welded joints in welded structures are much lower than that of base metals. Many experiments show that the fatigue crack normally initiates at welded toe, so that the fatigue strength can be increased dramatically by peening weld toe.[1,2,3]

Ultrasonic peening made by Tianjin University in China under the financial support of Natural Science Foundation of China is one of the most useful methods to improve fatigue behavior of weld toe due to improving toe geometry, removing defects and modifying the residual stresses distribution in this region.

For evaluating the ultrasonic peening performance carried out by our equipment, the fatigue tests were performed on butt and cruciform joints of Q235B steel both in the as-welded and peened condition. Test results are as follows:

1.Both butt and cruciform peened joints show a significant increase in fatigue life under different stress levels (high cycle fatigue). The results show that the fatigue life of the peened weld toe was 20~30 times as long as the as-welded joints, and in many cases the fatigue cracking initiation was transferred to the base metal instead of the weld toe.

2.The increase in fatigue strength (at 2×10^6 cycles)of the peened Q235B butt welded joints compared to the as-welded joints was 57%,and for the cruciform joints, the increase was 64~71%. The fatigue strength of both the butt and cruciform welded joints were no lower than that of the base metal. In such cases, weld joints is not the degense location any longer.

1. INTRODUCTION

Fatigue is one of the main forms of the failures of the welded structure. Many experiments show that the fatigue crack mainly initiates at the weld toe, so that the fatigue strength can be increased by treatment the welded toe.[1.2]

Ultrasonic peening made by Tianjin University in China under financial support of Natural Science Foundation of China is one of the most useful methods to improve fatigue life due to improving toe geometry, removing defects and introducing benefit compressive residual stress, as well as 1) It can be used not only for plate butt joints, but also for the tube joints, to which it is difficult by using other methods, such as TIG dressing. 2) It can be applied not only to the process of structure manufacturing in the working shop, but also to the field welding condition such as to bridges, oil platforms, ships and so on. 3) High treatment velocity (at the velocity of half meter per

minute). 4) Other advantages: it don't produce noise; the whole device is not heavy. (the peening unit weight is only several kilograms.)

Fig.1 is the picture of the ultrasonic peening device. One of the most important part in peening device is energy transform part, which based on piezoelectric ceramic transducer, is convenient to use for its small size, light weight, lower power to supply and easy to apply. The equipment is matched with the special ultrasonic power generator which used IGBT as the higher power component, matched with delicate frequency tracing system and the constant vibrating velocity control system, controls the quality of the ultrasonic peening results. The peening unit, named ultrasonic peening gun, consists of the sound system, shell and holder, and was designed to give high treatment velocity (at the velocity of half meter per minute) and strong peening force.

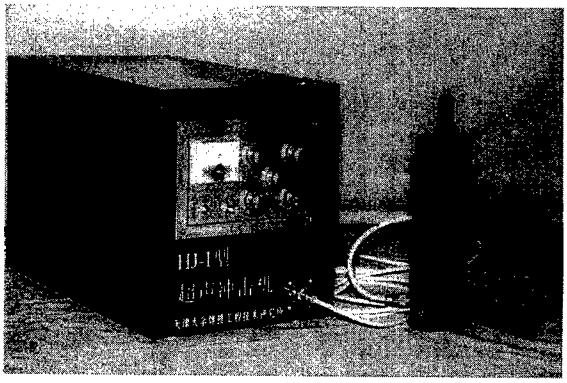


Fig.1.Ultrasonic peening device

2. MATERIAL, SPECIMENS AND TESTING CONDITION

Table 1.Mechanical properties of Q235B steel

material	σ_s /MPa	σ_b /MPa	δ
Q235B	267.4	435.5	26%

The material used in this research program is Q235B steel. Table 1 gives the mechanical properties of this steel. Both as-welded and peening conditions of the cruciform (under tensile) and the butt (under four-point bending) joints were considered in this study. The welding parameters are given in table 2.

2.1.Preparation of butt Welded Joints

On the surfaces of each piece of the specimen, a X groove was cutting and a thickness equity to 1mm was left in the middle of the specimen in order to prevent or reduce distortion. The welds were

Table 2. Welding process parameters

Joints	(1 pass) welding current (A)	(2 pass) welding current (A)	Welding Voltage (V)
Butt joints	110	120	24~30
Cruciform joints	130	150	25~30

produced in two passes by manual arc welding with J422 electrode.

2.2.Preparation of Cruciform welded joint:

A X groove with 60° angle was cutting for the load-carrying piece of the specimen. The welds were produced in two passes by same manual arc welding with J422 electrode. In order to prevent or reduce distortion, spot-fixing weld was accepted and opposite distortion was taken before welding.

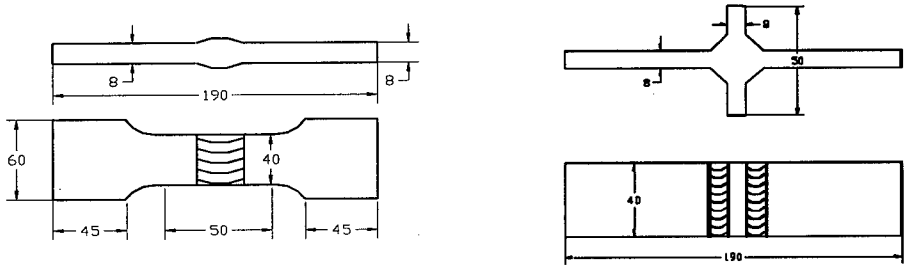


Fig.2.Shapes and dimensions of specimens (unit: mm)

2.3.Fatigue Tests:

The fatigue tests were performed on a high-frequency fatigue testing machine with a capacity of 100KN. For the butt joints subjected to tensile loads, a stress ratio R=0.1 was selected. For the cruciform joints subjected to four point bending, the stress ratio R=0.25 and R= - 0.5 were selected.

2.4.Ultrasonic Peening Operation

The peening gun was held approximately normal to the weld face and inclined at 45° to the base metal surface. The gun was move along the weld at an approximate speed of 0.5m/min and two times peening were used to obtain smooth weld toe geometry. The current of the device used is 0.5 ampere.

3.EXPERIMENTAL RESULTS AND DISCUSSIONS

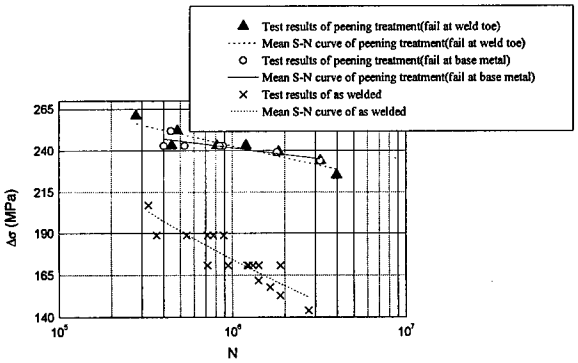


Fig.3.S-N curves of butt joints (R=0.1)

The fatigue tests results of the butt and cruciform joints of as-welded and peened condition were

plotted in S-N curves (see Fig.3, 4, 5). In table 3 the fatigue strength (at 2×10^6 cycles) of the butt and cruciform joints with and without peening treatment are given. The fatigue limits were derived from the method shown in the Fig.4. The fatigue limit is the mean value between the fatigue

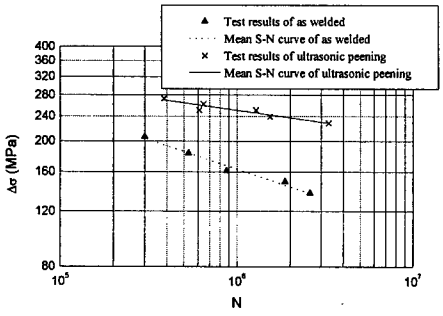


Fig.4.S-N curves of cruciform joints (R=0.25)

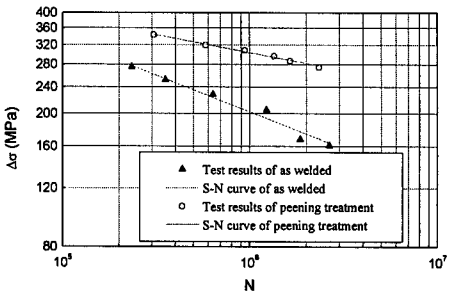


Fig.5.S-N curves of cruciform joints (R= - 0.5)

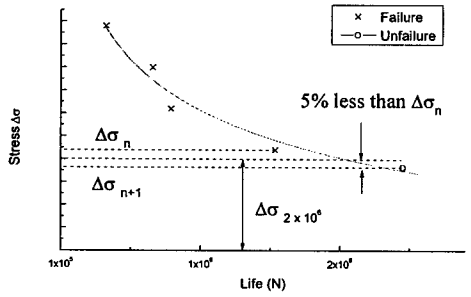


Fig.6.Determination of fatigue strength (2×10^6)

strength corresponding to the specimen, whose life is just higher than 2×10^6 and the fatigue strength corresponding to the specimen ,whose life is just lower than 2×10^6.

The results from S-N curves are as follows:

Compared with welded joints, the peened joints show significant increase in the fatigue life under different stress levels and the fatigue strength at a cycles 2×10^6.

On the butt peened joints, fatigue crack initiated at the weld toe under cycles much more than that on the as welded joints for some specimens, however for more specimens, fatigue crack initiation occurred in the base metal. The S-N curves of both crack initiation conditions are similar in the slope and fatigue stress levels, so that the fatigue strength of the peened joints can be considered as same as the base metal. Compared to the as-welded joints, the increase in fatigue strength (at 2×10^6 cycles) of the peened Q235B butt joints was 57%. For the cruciform peened joints, most cracks occurred in the base metal. The increase in fatigue strength of the peened cruciform joints tested with R=0.25 was 64%.

Table 3. The fatigue limit of welded joints and with peening treatment joints

Type	Fatigue strengths (Δσ/Mpa)		
	As welded	Treatment	Improving degree/%
Butt joints	148.5	234	57
Cruciform joints (R=0.25)	142.5	234	64
Cruciform joints (R=-0.5)	165	282	71

For the specimen tested with R= - 0.5, the increase was 71%.

Table 4 gives the fatigue life (under the same stress level) of the two series joints. According to the S-N curves (see from fig.3, 4, 5), the fatigue life of welded joints corresponding to the stress which comes from the peened joints corresponding to 2×10^7 cycles can be obtained. The results shows in Table 4.

Table 4 . The fatigue life of welded joints and with peening treatment joints

Joints	Condition	Stress	life
Butt joints	As welded	228	1.65×10^5
(R=0.1)	Treatment	228	1.0×10^7
Cruciform joints	As welded	211	2.4×10^5
(R=0.25)	Treatment	211	1.0×10^7
Cruciform joints	As welded	235	5.12×10^5
(R= - 0.5)	Treatment	235	1.0×10^7

Analysis of the results shows that the fatigue life of the peened joints was 40~60 times as long as the as-welded joints. Provided that the deviation of the test results were taking into consideration, the improvement was 20~30 times.

Test results reveal that the ultrasonic peening was an effective technique for improving the fatigue properties of the welded joints. The fatigue strength of the peened joints was nearly equal to the base metal. In such cases, welded joints is not the degense location any longer.

4.CONCLUSIONS

1) Both the butt and cruciform peened Q235B joints show a significant increase in fatigue life under different stress levels (high cycle fatigue), and also increase in fatigue strength under the same cycles. The difference in stress level was increasing with the increase of cycles.

2) The relative improvement in fatigue limit (at 2×10^6 cycles) caused by ultrasonic peening of the butt and cruciform joints were respectively 57%and 64%~71% compared with the as-welded condition.

3) The fatigue strengths of both the butt and cruciform welded joints were no lower than that of the base metal, when ultrasonic peening of the joints were carried out. Compares with the peened butt welded joint, the fatigue of cruciform welded joints after peened are increased more significantly.

4) The fatigue life of peened joints at least was 20~30 times as long as the as-welded joints.

ACKNOWLEGEMENTS

This project is supported by the National Natural Science Foundation of China, Project No. 59575061.

REFERENCES

1.J.Janosch, H.Koneczny, S.Debiez (France), E.C.Statnikov (Russia).V.J.Troufiakov and P.P.Mikhee (Ukraine), Welding in the world , 37(1996)p.72
2.T.R.Gurney, Fatigue of welded Structure, Cambridge University Press, England(1979)
3.P.P.Mikheev, A Ya Nedoseka, Automatic welding, march, 32(1984) p.37

Key Engineering Materials Vols. 183-187 (2000) pp. 1321-1326
© 2000 Trans Tech Publications, Switzerland

The Characteristics of Fatigue Strength in Laser Tailored Welded Blanking Sheet Metal

T.Y. Oh[1], Y.K. Kwon[2], C.J. Lee[3] and D.S. Kwak[3]

[1] School of Mechanical and Industrial System Engineering, KyungHee University, 1 Seocheon-Ri, Kihung-Eup, Youngin-Diry, Kyunggi-Do 449-701, Korea

[2] Department of Computer Aided Design, Doowon Technical College, 678 Jangwon-Ri, Juksan-Myon, Ansung-City, Kyunggi-Do 456-890, Korea

[3] Department of Mechanical Engineering, Graduate School, KyungHee University, 1 Seocheon-Ri, Kihung-Eup, Youngin-City, Kyunggi-Do 449-701, Korea

Keywords: Fatigue Behavior, Laser Weld, Prestrain, Strain Constrain, Tailored Welded Blank

ABSTRACT

For the Tailor Welded Blank sheet used for automobile body panel, the characteristics of fatigue strength and crack propagation behavior were studied. As a base test, mechanical properties around welding zone were examined. The results indicated that there were no significant decreases in mechanical properties, but hardness around welding bead was 2.3 times greater than base material. The fatigue strength was the highest when the loading direction was parallel to the welding direction, which was about 85% of tensile strength of base material. It was decreased by 8.5% when the thickness of specimen and base material was different, and it is increased by 25% when pre-strain was applied. The crack propagation rate was noticeably decreased around welding line and rapidly increased as it passed by welding line. Reviewing the shape of the crack propagation, crack width around welding line was wide around the welding zone due to retardation of crack growth, but it became narrow passing welding line due to decreased toughness.

1. Introduction

The laser tailored blank welding is widely used in pressing down automobile body panels, since it is proven to be very effective in improving reliability and productivity [(1)]. Some benefits using tailored blank welding is its high welding speed, deep welding depth, small deformation due to heat input, and its highly flexible productivity under any circumstances. [(2)-(5)] But, there are still several problems to be solved besides benefits, such as formability and structural stability. In recent years, the research on formability [(6)-(8)] has attracted considerable interest, and an increasing effort is being

devoted to propose best welding conditions to improve formability. Comparing to active research activities on formability, so little research on structural stability was under way. [9]-[11] Also, the research related to laser welding was only limited to the level of evaluating mechanical properties.[12]-[13] But, to extend the use of tailored welded blanking in production, structural stability taking into account its used environment should be examined carefully. In the research, the characteristics of fatigue strength due to external loading were studied for the tailor welded blank sheet.

2. Experiments

2-1 Specimen and welding condition

As a specimen, cold-rolled SPCEN(KS D 3512) plates at 0.9mm and 2.0mm were selected. The detailed mechanical properties for the base metal before and after welding are reported in Table 1. The result shows 10% increase in tensile strength after welding compare to base material.

Table 1. Mechanical properties of testing material

Mechanical Properties				Welding Condition			
Specimen	Yield Stress (MPa)	Tensile Strength (MPa)	Elongation (%)	Material	Power (kW)	Speed (m/min)	Thickness (mm)
Base Metal	215.7	339.3	39	SPCEN	4	6	0.9+0.9
Laser Weld	261.3	374.2	25	SPCEN	4	5	0.9+2.0

The shapes of the specimen used in these experiments are shown in the following two figures: one for the estimation of fatigue strength (Fig. 1) and the other for the study of crack propagation behavior (Fig. 2). The welding line was chosen to be parallel and perpendicular to the loading direction in strength test case and paraller to the loading direction in propagation test case. For the fatigue crack propagation test, 13mm pre-crack was applied beforehand.

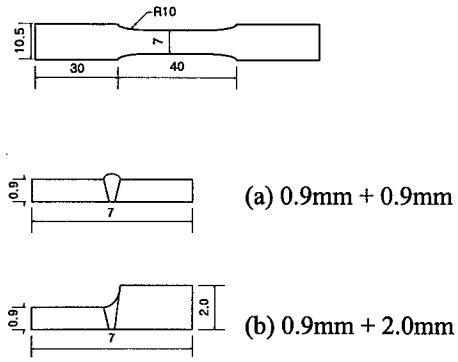


Fig. 1 Dimension of specimens for fatigue strength test

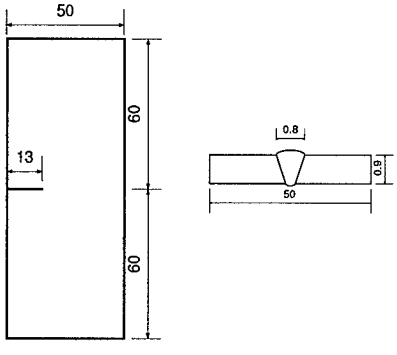


Fig. 2 Dimension of specimen for fatigue crack propagation test

2-2 Fatigue test

The Fatigue strength test was performed at room temperature at zero stress ratio(R=0) using Instron 8501 (servo-hydraulic fatigue tester). The moment when specimen was completely separated from each other was regarded as fracture, and the test was repeated until 10^6 cycle in case specimen was not broken down. For the fatigue crack propagation test, zero stress ratio(R=0) was applied at 10Hz. After the tests, the crack length was measured according to ASTM E647 using movable microscope, and the fatigue behavior around the welding area was examined using metal microscope and scanning electrode microscope (SEM).

3. Test results and considerations

3-1 Change in hardness and structure around welding area

The following figure (Fig. 3) shows how hardness number (H_V) changed around welding area. The hardness number for the base material was 85. But, It was 192 for the welding bead, which was 2.3 times greater than base material's H_V. The distribution of hardness number was uniform around base material but increased rapidly at welding area, because heat affected zone was rarely appeared. This was due to the characteristics of laser welding where thermal energy was applied only to local area rather than through conduction.

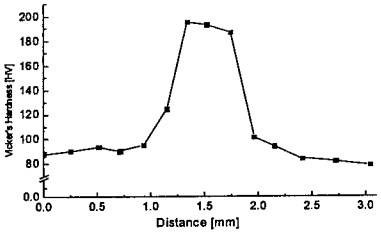


Fig. 3 Micro Vicker's Hardness.

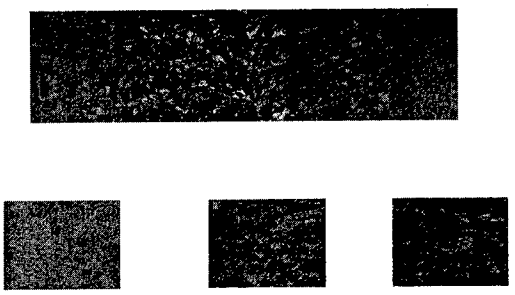


Fig. 4 The Shape of Welding Surface

This phenomenon could also be seen in metal structure. The shape of welding surface was shown in the above figure (Fig. 4), where welding bead is visible in the middle. While the base material has typical SPCEN structure as shown in Fig.4a, the shape of grain and its boundary was collapsed (Fig. 4c). Also, borderline between metal and welding bead structure was clear without any intermediate area. This indicates that heat affected zone could be minimized since most of the energy was concentrated to local area.

3-2 Fatigue strength result

After butt laser welding, the fatigue test result for plates with same thickness was compared with the case with different thickness (Fig. 5). The relation between life and stress was extrapolated by secant method for each specimen. The fatigue limit was 290MPa for the specimen with same thickness (0.9+0.9mm), which was 85% of tensile strength for the base material (339MPa). For the plates with different thickness (0.9mm+2.0mm), its limit resulted in 265MPa. The strength was lower in plates with different thickness due to notch effect caused by discontinuous face. As a result,

this effect induced stress concentration and decreased fatigue limit.

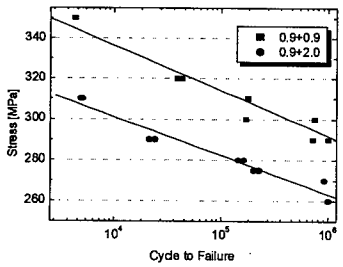


Fig. 5 Fatigue test results.

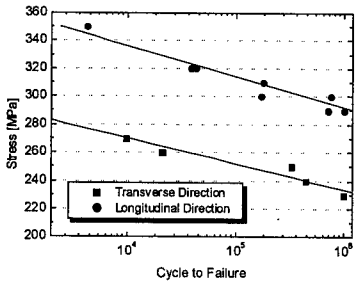
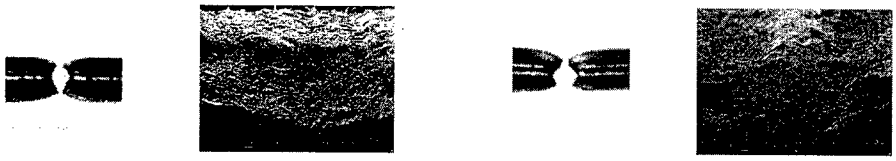


Fig. 6 Fatigue test results

In figure 6, the fatigue limit with respect to welding direction is shown. The fatigue limit for the specimen welded in longitudinal direction resulted in 230MPa. This was slightly above the general ferrous metal case where fatigue limit is about 55% of tensile strength. In this case, fatigue crack usually does not initiate neither from welding area nor from heat affected zone, but from base material. When loading was applied perpendicular to the welding direction, fatigue fracture problem at welding area could be ignored since strength is higher than base material. To summarize, fatigue crack initiates from the welding area when welding direction is parallel to the loading direction. But, it initiates from the base material when two directions are perpendicular to each other. This results could be explained by the fact that strain constraint was caused by strength discontinuity due to increase in hardness number. The strain constraint phenomenon was also visible in of fracture surface by fractography(Fig. 7). Crack initiated from the flat area in the middle, which could be identified as welding bead by macroscopically. As seen in fracture surface for 0.9+0.9mm specimen (Fig. 7a), crack initiated in the middle welding area and propagated to both side of base material. But, for 0.9+2.0mm case, crack unequally grew more toward 2.0mm side due to large constraint effect (Fig. 7b).



(a) 0.9+0.9mm (b) 0.9+2.0mm

Fig. 7 Fracture surfaces (S.E.M 500x)

In general, crack started from the welding bead and propagated until it finally became brittle fracture at base material.

3-3 Crack growth behavior

The fatigue stability and characteristics of fatigue crack growth was examined carefully. In stress intensity factor calculation, residual stress around welding area was disregarded. Also, the finite element analysis was utilized for 0.9+2.0mm case to compare results by varying thickness. As shown in fatigue crack growth results (Fig. 8), growth rate decreased around welding bead but

increased greatly resulting similar behavior of base material. Specially, for the case of 0.9+2.0mm, its growth rate decreased right after crack initiation due to notch effect. Though its rate was faster than 0.9+0.9 case, its growth behavior was similar to base material as it passes by welding area. This was also visible in the fatigue crack shape around welding zone (Fig. 9). As crack size grew till reaches welding bead, its growth rate decreased rapidly resulting wider width than base material. As it later passed by welding bead, its rate decreased rapidly and the shape changed to very narrow. But, its shape changed back to as before when it passed by welding bead.

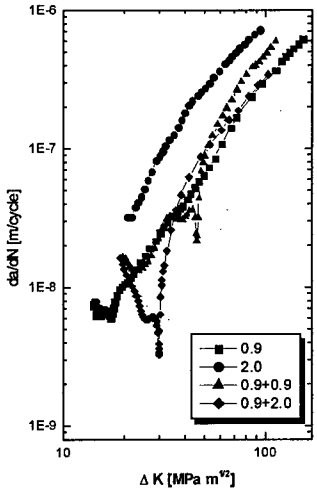


Fig. 8 Fatigue crack propagation.

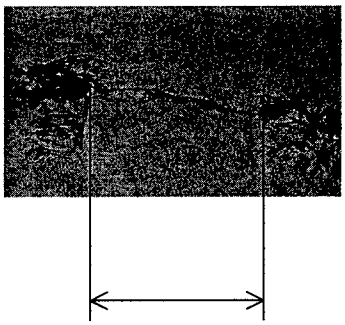


Fig. 9 Shape of fatigue crack around welding zone.

4. Conclusion

1. When loading was applied parallel to the welding line, tensile strength at welding area was increased by 10% compare to base material. And, its hardness was 2.3 times greater than base material.

2. Fatigue strength was the highest (85% of tensile strength) when loading and welding direction was parallel and thickness is same for specimens. The fatigue strength was 8.5% less when plates with different thickness are welded together.

3. In base material, fatigue crack propagated generally. But, around welding bead, there were signs of crack growth retardation due to increased strength. Later, as crack grows, propagation speed got faster and crack shape became narrower around welding bead due to fracture toughness.

5. References

1. Andy P.Lee, Erick Feltham and Jon Van Deventer, Tailor Welded Blank Technology for Automotive Applications, SAE 960817
2. Wllfried Prange, Christoph Schnelder and Albrecht J. Sellge, Application of Laser-Beam-Welded

Sheet Metal, SAE 890853
3. Albrecht J. Selige and Wilfried Prange, Production and Usage of Laser Beam Welded Sheet Metal, SAE 970413
4. Lutz Hanicke and Osten Strandberg, Roof Laser Welding in Series Productions, SAE 930021
5. Suh, J. Han, Y. H. Kim, J. O. and Lee, Y. S. laser beam welding and formability of steel plates with different thicknesses, Journal of the Korean Welding Society, Vol.14, N.1, (1996) pp.82-91
6. Jiun-Ren Hwang, Ji-Liang Doong and Chee-Chang Chen, Fatigue Crack Growth in Laser Weldments of Cold Rolled Steel, Materials Transactions, JIM, Vol. 37, No. 8, (1996) pp. 1443-1446
7. M.F.Shi, Effects of Strain Gradient and Curvatures on Forming Limits Diagram for Anisotropic Sheets, J. Mat. Shaping Technol., (1991) Vol. 9, pp.45-52
8. M.F.Shi, Formability Issues in the Application of Tailor Welded Blank Sheets, SAE 930278
9. R.B. Wilson and T.E. Fine, Fatigue Behavior of Spot Welded High Strength Steel Joints, SAE 810354
10. D.H. Orts, Fatigue Strength of Spot Welded Joints in a HSLA Steel, SAE 810355
11. J.A Davidson and E.J. Imhof, The Effect of Tensile Strength on the Fatigue Life of Spot-Welded Sheet Steels, SAE 840110
12. P.C Wang and K.M Ewing, A Comparison of Fatigue Strengths : Laser Beam vs. Resistence Spot Welds, Welding Journal, October, (1991) pp.43-47
13. Charles S.Lin, Fracture Mechanics Characteristics of Laser-Welded Aluminum-Lithium Sheet Joints, SAE 881405

Key Engineering Materials Vols. 183-187 (2000) pp. 1327-1332
© 2000 Trans Tech Publications, Switzerland

Effect of the Mismatching of *J*-Integral for Pipe Welded Joint with Circumferential Surface Crack

L.X. Huo, Y.I. Liu, Y.F. Zhang and H.Y. Jing

College of Material Science and Engineering, Tianjin University, Tianjin 300072, China P.R.

Keywords: Cracked Pipe Welds, Elastic-Plastic Fracture Mechanics, Finite Element Method, *J*-Integral, Mismatching, Surface Crack

ABSTRACT

A three-dimensional finite element model was developed for elastic-plastic fracture analysis of welded joint with circumferential surface crack in the pipe; the distribution of *J*-integral along surface crack front was studied. Finally, the effects of the mismatching on *J*-integral are discussed in detail based on the mechanical properties between weld metal and base metal. The analyses include both yield strength over-mismatching and under-mismatching and strain-hardening parameters mismatching.

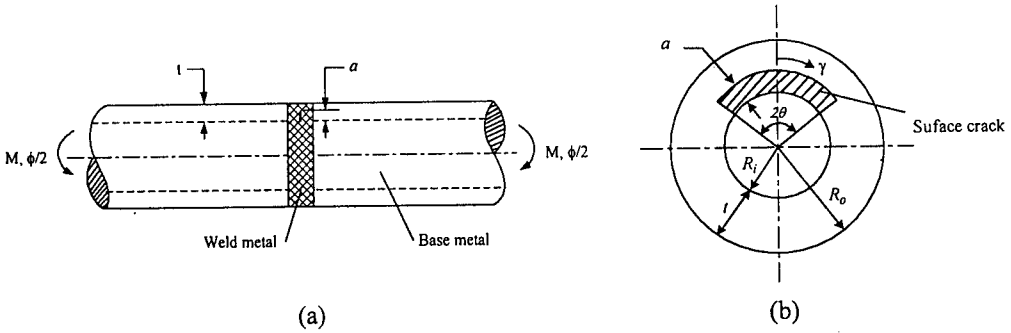
1. INTRODUCTION

The assessment of surface flaws is of great importance in structural integrity analyses. *J*-integral based on the elastic-plastic fracture mechanics has become a useful analytical technique for dealing with ductile material fracture. The fracture analysis of surface crack is a complicated three-dimensional problem, especially for the welded joints because of material heterogeneity. At present, most of analyses for the welded joints are based on homogeneous materials, which merely consider material properties of either base or weld metals [1]. This will lead to over-conservative or under-conservative predictions depending on the strength mismatching of the base versus weld material. This paper presents a three-dimensional finite element model for the pipe welded joint with circumferential surface crack, and then elastic-plastic fracture analyses were carried out to examine the distribution laws of *J*-integral and the effects of the mismatching on *J*-integral.

2. FINITE ELEMENT MODEL

The object of the finite element analysis is a typical carbon steel girth welded joint with a circumferential surface crack subjected to pure bending moment M, as shown in Figure 1(a). The rotation of one pipe end relative to the other is denoted by ϕ. The cross-section and dimension of pipe joint containing the internal surface crack is shown in Figure 1(b). The outer

radius R_0 and wall thickness t of the pipe are 54mm and 12mm, respectively. It is assumed that the pipe has a constant-depth circumferential surface crack. The total crack angle 2θ is 90 degree and the crack depth is a=3mm. Reference angle measured form center of the surface crack is defined by γ. The material property data for base and weld metal are shown in Table 1.



(a) (b)

Fig. 1 Circumferential surface-cracked pipe welded joint under pure bending moment

Table 1 Material property for base metal and weld metal

Material type		Yield stress σ_y (MPa)	Elastic modulus E (GPa)	Poisson ratio ν	Hardening exponent n	Hardening constant α
Over-matching	Base metal	261.2	202.0	0.3	3.97	7.44
	Weld metal	365.7	210.0	0.3	3.00	10.34
Under-matching	Base metal	327.6	202.0	0.3	4.245	8.77
	Weld metal	262.08	200.0	0.3	7.0	1.0

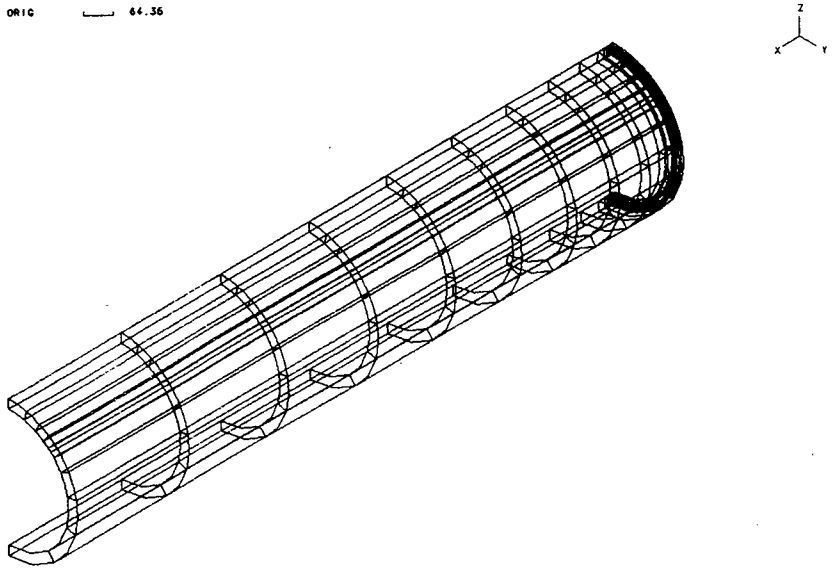


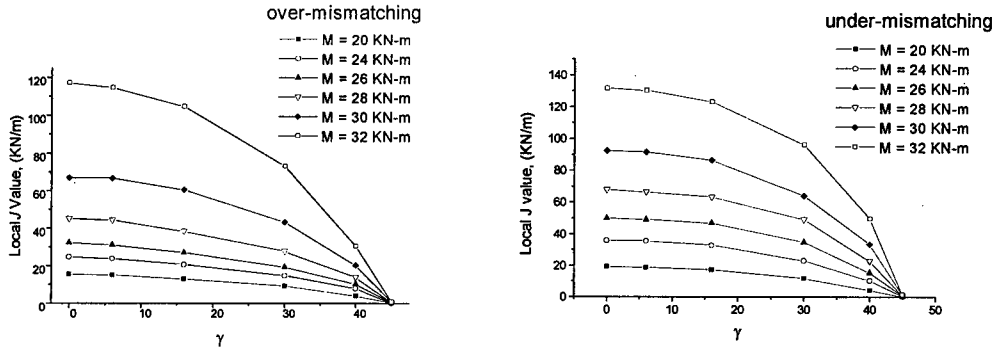
Fig. 2 Finite element model and Mesh subdivision near the surface crack

Consider geometrical and load symmetry, only one-fourth of the pipe was modeled in the

computation. The finite element analyses have been performed with the software ADINA [2] and a *J*-integral post-processing program developed by the authors. The multi-linearized stress-strain relation is used for the FEM analyses with 20-noded three-dimension isoparametric element and a 2×2×2 Gaussian integration scheme. *J*-integral is determined by virtual crack extension (VCE) method [3]. In order to compute accurately the crack tip fields and *J*-integral for surface-cracked pipe weld joint, it is important to select a suitable and adequate refined finite element mesh. As shown in Figure 2, the typical finite element mash consists of 660 elements and 3683 nodes. Singular degenerate elements were used in the vicinity of the crack front.

3. DISTRIBUTION OF *J*-INTEGRAL ALONG SURFACE CRACK FRONT

The distribution of *J*-integral along the surface crack front has been obtained from the energy release rate due to a local virtual crack extension for two kinds of mismatching welded joint. As shown in Figure 3, it can be seen that the distribution of *J*-integral is not uniform along the surface crack, and *J*-integral at the center of the crack has a maximum value. When γ moves along the crack front from the center to the end, the *J*-integral values fall down gradually. The decreasing speed is not obvious at low γ values; with the raising of γ, the decreasing speeds increase conspicuously especially at high load level.



(a) (b)

Fig. 3 The distribution of *J*-integral along the surface crack front

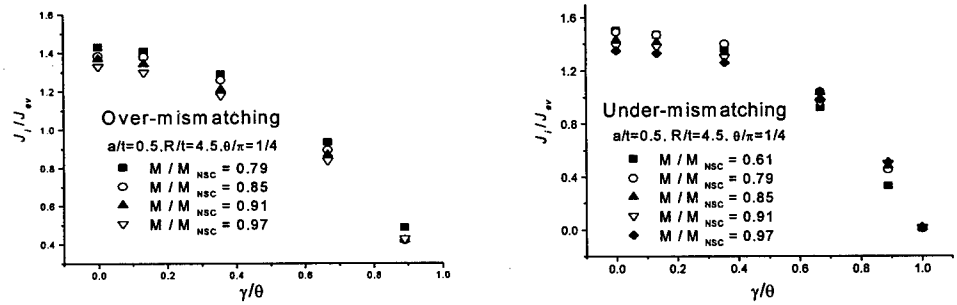
As shown in Figure 4, local *J*-integral value J_i of all cases have been normalized by the average value of *J*-integral J_{ev}, at the same time, the angle γ have been normalized by the crack half angle θ. It shows that the influence of bending moment level on J_i/J_{ev} is slight, J_i/J_{ev} value at the center of crack is about 1.4 times more than that of crack end for variable load level and different matching joint. M_{NSC} is the Net-Section-Collapse or limit moment for surface crack [4]. It is given by the following equation:

$$M_{NSC} = 2\sigma_f R_m^2 t\left[2\sin\beta - \frac{a}{t}\sin\theta\right] \tag{1}$$

Where
$$\beta = \frac{\pi - \theta(a/t)}{2} - \frac{\pi R_i^2 P}{4 R_m \sigma_f t} \tag{2}$$

Where the value of flow stress, σ_f is assumed to be the average of the yield stress σ_y and the ultimate stress σ_u of base metal. R_m is the mean radius; P is internal pressure of pipe.

From Figure 3 and Figure 4, it indicates that crack-driving force at the center of surface crack is maximum, and it will decrease along the crack front from the center to the end [5]. So the crack propagation along the thickness direction is not at the same time, even though for the constant-depth surface crack. J-integral at the center of crack will achieve critical value J_{IC} firstly and start to propagate; then with the increasing of moment, J-integral near the crack center will achieve critical value J_{IC} and propagate subsequently. so the configuration of surface crack will change into elliptical shape.



(a) (b)

Fig. 4 The distribution of J_i /J_{ev} along the surface crack front

4. EFFECT OF THE MISMATCHING ON *J*-INTEGRAL FOR SURFACE CRACK

In this study, the pipe-welded joint is idealized by bi-material structure, i.e. by base metal and weld metal. The weld mismatching included the strength mismatching and the strain hardening parameters mismatching. Consider a pipe welded joints with R_0=54mm, t =6mm, θ =45° and the surface crack depth a =3mm. The material parameters of base metal keep constant i.e. σ_{yb} = 327.6MPa, n_b=4.25, α_b=8.77 and E_b=202GPa; the material parameters of weld metal give several cases respectively according to different mismatching ratio.

4. 1 Effect of strength mismatching

For the strength mismatching, the material parameters of weld metal are given as P_M = 0.7, 0.8 0.9 1.0 1.1 1.2 1.3, n_w=7.0, α_w=1.0 and E_w=200GPa. P_M is the strength-matching factor; the yielding strength of weld metal is given as $\sigma_{yw} = P_M \sigma_{yb}$. In these cases, No .1, 2 and 3 (P_M = 0.7, 0.8 0.9) are under-mismatching; No.4 (P_M = 1.0) is equal mismatching; No.5, 6 and 7 (P_M = 1.1 1.2 1.3) are over-mismatching. Load level λ is given as $\lambda = M / M_{NSC}$.

As shown in Figure 5, it reveals that the influence of the strength mismatching on J integral value is remarkable. With the increasing of strength mismatching factor and yielding strength of

weld metal, J–integral values decrease conspicuously for prescribed load level, especially at high load level. By compared all of cases, weld joints with constant base metal have a general law for a given load level λ: $J_{\text{under-mismatching}} > J_{\text{equal mismatching}} > J_{\text{over-mismatching}}$.

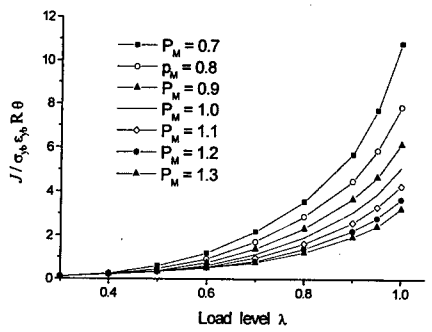
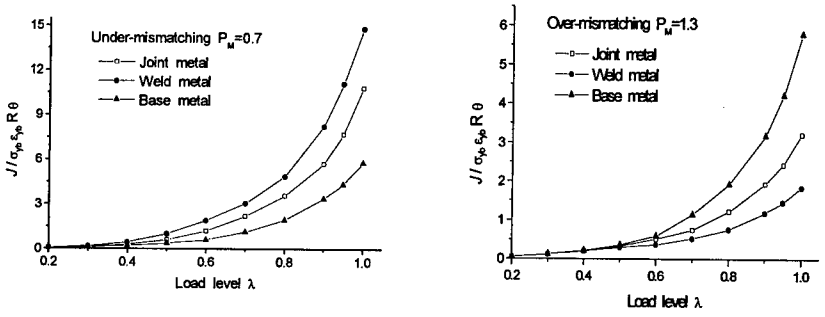


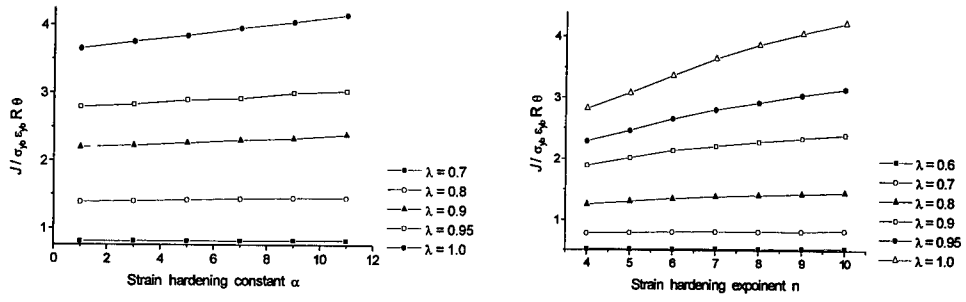
Fig. 5 Effect of strength mismatching on J-integral

In order to compare J-integral of welded joint with base metal and weld metal, J-integral value of all base metal or all weld metal has also been determined by finite element method. As shown in Figure 7, for prescribed load level λ, over-mismatching welded joints have $J_{\text{weld metal}} < J_{\text{joint metal}} < J_{\text{base metal}}$; under-mismatching welded joints have $J_{\text{base metal}} < J_{\text{joint metal}} < J_{\text{weld metal}}$. Therefore, if the estimation methods for homogeneous material are used for welded joints, this may lead to over-conservative or under-conservative predictions depending on the strength-mismatching ratio. Generally, for over-mismatching welded joints, it is more conservative to obtain crack driving force J by using base-metal parameters; and it is more conservative by using weld metal parameters for under-mismatching welded joints.



(a) (b)

Fig. 6 Comparison of J-integral of joint metal and base metal and weld metal



(a) (b)

Fig. 7 Effect of the strain hardening parameters on J-integral

4.2 Effect of Strain-hardening parameters mismatching

For the hardening exponent matching, the material parameters of weld metal are given as σ_{yw}=393.1MPa, E_w=200GPa, n_w= 4.0, 5.0, 6.0, 7.0, 8.0, 9.0, 10.0, α_w = 1.0. For the hardening constant mismatching, the material parameters of weld metal are respectively given as σ_{yw} =393.1MPa, E_w=200GPa, n_w=7.0, α_w= 1.0, 3.0, 5.0, 7.0, 9.0, 11.0. As shown in Figure 7, the influence of the strain-hardening parameters mismatching on J-integral is not obvious, especially for strain hardening constant. Only at high load level λ, with the increment of hardening parameters, J values increase slightly.

5. CONCLUSIONS

(1) The distribution of J-integral is not uniform along the surface crack, and J-integral at the center of the crack has a maximum value. When γ moves along the crack front from the center to the end, J-integral values fall down gradually.

(2) The crack-driving force at the center of surface crack is maximum, then will decrease along the crack front from the center to the end. So J-integral at the center of crack will achieve critical value and start to propagate firstly.

(3) The influence of bending moment level on J/J_{ev} is slight. J_i /J_{ev} value at the center of crack is about 1.4 times more than that of crack end for variable load level and different mismatching joint.

(4) The influence of the strength mismatching on J integral value is remarkable. Weld joints with constant base material have a general law for a given load level λ: $J_{\text{under-matching}} > J_{\text{equal matching}} > J_{\text{over-matching}}$.

(5) For prescribed load level λ, over-mismatching weld joints have $J_{\text{weld metal}} < J_{\text{joint metal}} < J_{\text{base metal}}$; under-mismatching weld joints have $J_{\text{base metal}} < J_{\text{joint metal}} < J_{\text{weld metal}}$.

(6) The influence of the strain-hardening parameters mismatching on J-integral is not obvious, especially for strain hardening constant.

ACKNOWLEGEMENTS

This project is supported by the National Natural Science Foundation of China, Project No. 59675046.

REFERENCES

1. Y. Lei, and R. A. Ainsworth, Int. J. Pres. Ves. & Piping, **74** (1997), p.237
2. W. Brocks, W. Muller and J. Olschewski, Comp. & Struct. **21** (1985), p.137
3. H. G. DeLorenzi, Engrg. Fract. Mechanics, **21** (1985), p.129
4. P. Krishnaswamy, P. M. Scott, et al, Short Cracks in Piping and Piping Welds, NUREG/CR-6298, BMI-2183, Sep, (1995). P.4-55
5. K. K. Yoon and D. E. Killian, J. of Pressure Vessel Technology, **117** (1995), p.66

Key Engineering Materials Vols. 183-187 (2000) pp. 1333-1338
© 2000 Trans Tech Publications, Switzerland

Validation of Defect Assessment Method for Structures with Weldments

Yun-Jae Kim

School of Mechanical Engineering, SungKyunKwan University,
300 Ch'onch'on-dong, Changan-gu, Suwon 440-746, Korea

Keywords: Defect Assessment Method, Strength Mismatch, Weldment

ABSTRACT

The defect assessment procedure for structures with significant strength mismatch, resulting from the Brute-Euram SINTAP protect, is validated against testing data of mismatched specimens with idealised weldments. It provides confidence in the use of the proposed method for assessing defective weld strength mismatched structures.

1. INTRODUCTION

Defects in structural components are likely to occur within or near weldments across which tensile properties vary significantly. In particular, recent advanced welding techniques produce tensile properties of the weld metal which may be quite different from those of the base material [1]. Such significant mismatch can affect the crack driving force such as the J integral and crack opening displacement significantly. Although a significant progress has been made on assessing defects in structural components for the last three decades, the resulting defect assessment methods [2-4] are restricted to the homogeneous structure. Recently, defect assessment methods specific to strength mismatched structures have been developed by incorporating the strength mismatch effect into the methods for homogeneous structures [5,6].

Within the European Brite-Euram project, SINTAP (Structural Integrity Assessment Procedure for European Industry) [7], the Task 1 dealt with the strength mismatch effect, of which the main aim is to provide an unified procedure for defect assessment method specific to structures with weldments, in the presence of significant strength mismatch. The resulting SINTAP method for strength mismatched structures is based on two existing defect assessment methods for welded structures [5,6]. Detailed equations of the method have been set out by blending the essence of these two methods. Further modifications were made to cope with the quality of input information, such as that of the tensile properties of materials.

This paper provides experimental validation of the proposed SINTAP method using data generated within the SINTAP project.

2. SUMMARY OF WELDMENT TESTING

Within the SINTAP project, experiments were performed at AEA Technology, involving testing of mis-matched specimens with idealised weldments. Detailed information can be found in the AEA report [8], and only relevant information will be given below.

2.1 Material Properties

In the experimental programme, two different materials, having different yield and ultimate strength values, were produced by heat-treating an A533B-1 steel. Mean tensile strength data for the resulting two materials are given in **Table 1**. The yield strength of the higher strength material (designated as M1 material) is about 50% higher than that of the lower strength material (designated as M3 material). It should be noted that the M3 material exhibits Lüders strain of a length about 0.8%. In the M1 material, however, a Lüders plateau is not visible, due to its high yield strength and low hardening capacity at low strains. Note that Young's modulus, E, and Poisson's ratio, ν, are same for both materials.

2.2 Toughness Properties

Fracture toughness testing was carried out using deeply cracked (a/W=0.65) compact tension (CT) specimens with total 20% side grooves. **Figure 1** shows the resulting J-resistance curves. The off-set power law fits to the data, together with $J_{0.2}$ initiation values:

$$J(\Delta a) = c_1 + c_2(\Delta a)^m \tag{1}$$

are listed in **Table 2**. It should be noted that for validation purposes, the best fit to two data sets is used, instead of the lower one. The resulting $J(\Delta a)$ data are converted to $K_{mat}(\Delta a)$ using

$$K_{mat}(\Delta a) = \sqrt{E \cdot J(\Delta a)/(1-\nu^2)} \tag{2}$$

Table 1. Mean tensile data for two base materials and HAZ.

Material	σ_Y (MPa)	σ_U (MPa)
M1	738	849
M3	497	647

Table 2. Information on toughness data. No crack growth correction was applied in the test.

	$J(\Delta a)$ (MJ/m^2)			$J_{0.2}$
	c_1	c_2	M	(MJ/m^2)
M1	0.094	0.095	0.779	0.122
M3	-0.027	0.311	0.401	0.136

2.3 Testing of Mismatch Specimens

Strength mis-matched specimens with idealised weldments were produced by electron-beam (EB) welding, resulting in two different strength mis-matched specimens: highly over-matched (strength mismatch ratio at the yield stress, $M=\sigma_{YW}/\sigma_{YB}\approx 1.48$) and highly under-matched ($M\approx 0.68$) specimens, see **Fig. 2**. Single edge notched specimens in three point bend (SE(B)) with total 20% side grooves were produced, having the crack in the centre of the weldment. Two different crack lengths were chosen, a/W=0.45 and 0.65, and three identical specimens were tested for each case. All specimens failed by extensive ductile tearing, and the maximum loads were obtained from experimental records.

3. DUCTILE TEARING ANALYSIS

Using the test data described in the previous section, ductile tearing analysis is performed to predict the maximum load, which are then compared with the measured values from the experiment.

3.1 Construction of FAD

There are two different levels in the SINTAP mismatch method, depending on the quality of tensile properties [7]. When only limited tensile data are available for both weld and base materials, such as the yield and ultimate tensile strengths, the level 2 FAD can be used, whereas the higher level, level 3 FAD, is used when full stress strain data for both materials are available. For the sake of space, only relevant equations are provided here, but detailed equations, together with full descriptions, can be found from Section I.4 in [7].

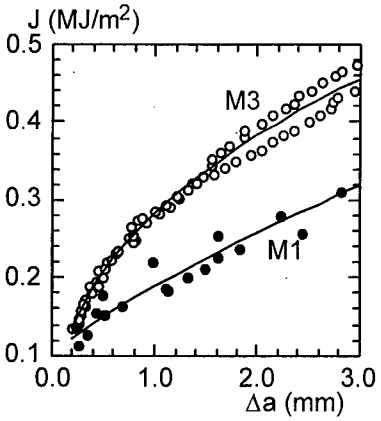


Fig. 1. J-R curves for base materials. Circles show experimental data and lines the corresponding off-set power law fit.

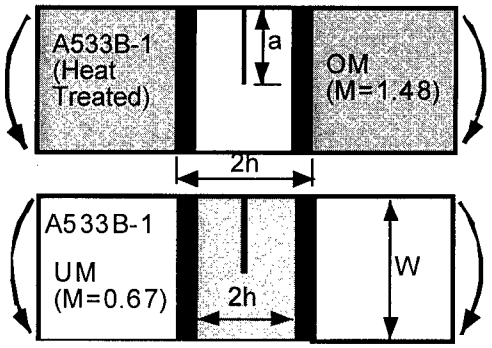


Fig. 2. Mismatch testing specimens and their dimensions.

Level 2

As both material in this experiment exhibit a yield plateau, the following sets of equations should be sued to construct the FAD:

$$f(L_r)=\begin{cases}\left(1+L_r^2/2\right)^{-1/2} & \text{for} \quad 0\le L_r<1\\ \left(\lambda_M+1/(2\lambda_M)\right)^{-1/2} & \text{for} \quad L_r=1\\ f(1)\cdot(L_r)^{(N_M-1)/2N_M} & \text{for} \quad 1<L_r<L_r^{\max}=0.5\left(1+0.3/(0.3-N_M)\right)\end{cases} \tag{3}$$

$$\lambda_M=\frac{(F_{YM}/F_{YB}-1)\lambda_W+(M-F_{YM}/F_{YB})\lambda_B}{(M-1)} \tag{4}$$

$$\lambda_W=1+0.0375(E_W/\sigma_{YW})(1-\sigma_{YW}/1000)$$
$$\lambda_B=1+0.0375(E_B/\sigma_{YB})(1-\sigma_{YB}/1000) \tag{5}$$

$$N_M=\frac{(M-1)}{(F_{YM}/F_{YB}-1)/N_W+(M-F_{YM}/F_{YB})/N_B} \tag{6}$$

$$N_W=0.3(1-\sigma_{YW}/\sigma_{UW})$$
$$N_B=0.3(1-\sigma_{YB}/\sigma_{UB}) \tag{7}$$

In eqns. (3)-(7), M is defined at the yield stress, $M=\sigma_{YW}/\sigma_{YB}$, and the value of F_{YM}/F_{YB} should be found for that value of M. Note that F_{YM} is the mismatch limit load of the defective mismatched

component of interest, and F_{YB} is the plastic yield load assuming the component is wholly made of the base material. For mismatched SE(B) specimens, the F_{YM} solutions are given in the SINTAP limit load compendium (Section III.2 in [7]).

Level 3

$$f(L_r)=\left(\frac{E\varepsilon_e}{\sigma_e}+\frac{L_r^2\sigma_e}{2E\varepsilon_e}\right)^{-1/2} \quad \text{for } 0\le L_r\le L_r^{\max}=\bar{\sigma}_e/\sigma_{Ye} \tag{8}$$

$$\sigma_e(\varepsilon^p)=\frac{(F_{YM}/F_{YB}-1)\cdot\sigma_W(\varepsilon^p)+(M-F_{YM}/F_{YB})\cdot\sigma_B(\varepsilon^p)}{(M-1)}$$
$$\sigma_{Ye}=\frac{F_{YM}}{F_{YB}}\sigma_{YB};\bar{\sigma}_e=\frac{F_{YM}(\bar{\varepsilon}^p)}{F_{YB}}\sigma_B\left(\bar{\varepsilon}^p\right) \tag{9}$$

Note M in eqn. (9) is defined not only at the yield stress (0.2% plastic strain) but also at a number of different plastic strain values ε^p:

$$M(\varepsilon^p)=\sigma_W(\varepsilon^p)/\sigma_B(\varepsilon^p) \tag{10}$$

and F_{YM}/F_{YB} should be found for those values of M, from Section III.2 in [7].

The resulting failure assessment curves are shown in **Fig. 3** for over-matched specimens, and in **Fig. 4** for undermatched specimens.

3.2 Ductile Tearing Analysis

Construction of the tearing locus for a given load requires two parameters, L_r and K_r. The parameter L_r for a given load F at some discrete values of crack length, a_j, and the second parameter, K_r, can be calculated from

$$L_r(a_j)=F/F_{YM}(a_j)$$
$$K_r(a_j)=K(a_j)/K_{mat}(\Delta a_j) \tag{11}$$

where $K_{mat}(\Delta a_j)$ from eqn. (2). The SIF, K, was calculated according to the SIF handbook [9]. The resulting tearing loci are shown in **Figs. 3** and **4** for various load levels. In the assessment, the maximum load can be determined when the locus satisfies the tangency condition to the FAC.

3.3 Results

For overmatched specimens, the predicted maximum loads, F_m^p, are shown in **Fig. 3**, together with the measured maximum loads, F_m^e, in the test. The prediction using the level 3 FAD is conservative but only by 10%. The level 2 FAD gives slightly more conservative results. Such conservatism is likely to result from the conservatism embedded in the assessment of bending configurations for materials with Lüders strain. For undermatched specimens, however, the tangency condition occurs beyond $L_r=L_r^{max}$ for the level 3 FAD, **Fig. 4**, implying that failure is dominated by complete plastic collapse. Such behaviour can happen in typical laboratory test specimens. In the present work, F_m^p is obtained when the locus touches the $L_r=L_r^{max}$ line, as shown in **Fig. 4**. The conservatism in the

level 3 curve increases up to 20%. However, as shown in **Fig. 4**, if the FAD would be extended beyond L_r^{max}, similar level of conservatism to that for overmatching could be expected. Again, the level 2 FAD gives more conservative results than the level 3 FAD. The conservatism in the level 2 FAD increases up to 30%. As a conclusion, the results from this experimental validation strongly support the methodology of the SINTAP method for weld strength mis-match.

4. CONCLUSIONS

This paper provides experimental validation of the defect assessment method, proposed within the European Brite-Euram project, SINTAP (Structural Integrity Assessment Procedure for European Industries). The present validation provides confidence in the use of the newly developed SINTAP method for assessing defective strength mismatched structures.

In this experiment, failure was dominated by plastic collapse. More experimental data covering fracture-dominated failure cases, such as wide plate test or full-scale pipe tests, are needed for further validations.

ACKNOWLEDGEMENTS

Financial support from the CEC for the SINTAP project is gratefully acknowledged. This work was performed when the author was working at GKSS Research Centre (Germany) and British Energy Generation Ltd (UK). He wishes to acknowledge Prof. Schwalbe and Dr. R A Ainsworth for valuable comments. The author also acknowledges the SAFE Research Centre at the Sungkyunkwan University for support.

REFERENCES

1. Proc. European Symp. on Assessment of Power Beam Welds, GKSS Research Centre, Geesthacht, Germany (1999)
2. A Zahoor, Ductile Fracture Handbook, Novotech. Corp. (1991)
3. R6: Assessment of the Integrity of Structures Containing Defects, Nuclear Electric Procedure R/H/R6, Revision 3 (1998)
4. K-H Schwalbe, et al., EFAM ETM 97, GKSS 98/E/6, GKSS Research Centre, Germany (1998)
5. R6: Appendix 16: Allowance for Strength Mismatch Effects, Nuclear Electric Procedure R/H/R6, Revision 3 (1998)
6. K-H Schwalbe, et al., EFAM ETM-MM 96, GKSS 97/E/9, GKSS Research Centre, Germany (1997)
7. SINTAP Procedure Final Version (1999), Brite-Euram Project BE95-1426
8. G Wardle and S Jacques, AEA Technology Report AEAT-0894 (1997)
9. H. Tada et al., The Stress Analysis of Cracks Handbook, Paris Production Inc., St. Louis, Missouri (1985)

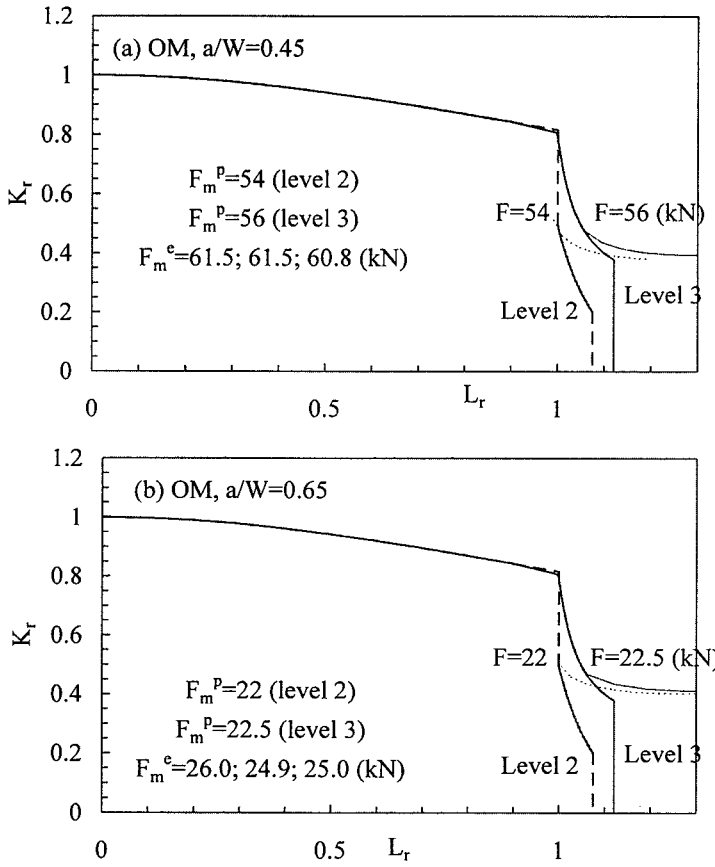


Fig. 3. Ductile tearing analysis for overmatched (OM) specimens.

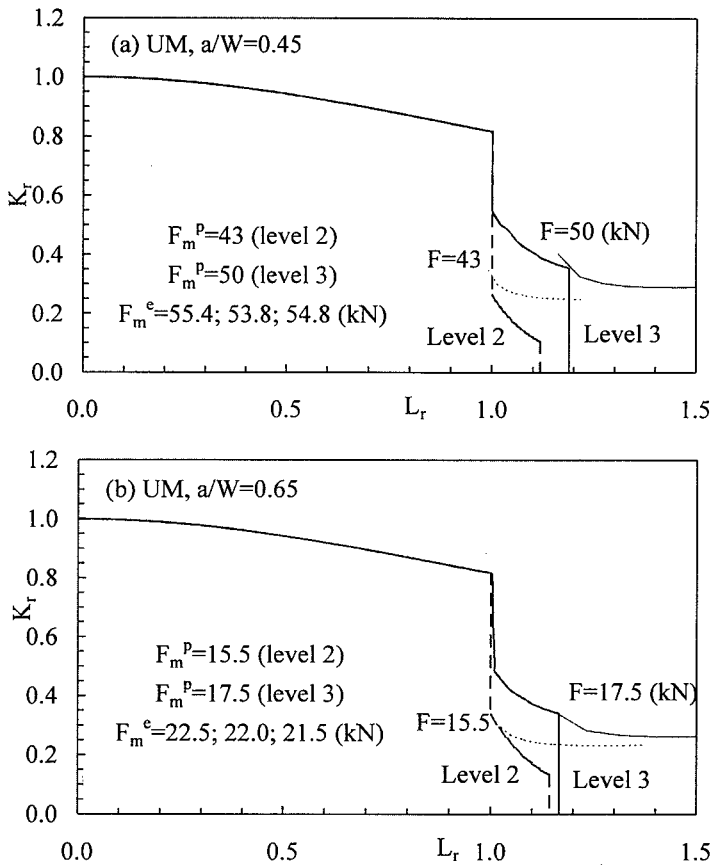


Fig. 4. Ductile tearing analysis for undermatched (UM) specimens.

Key Engineering Materials Vols. 183-187 (2000) pp. 1339-1344
© 2000 Trans Tech Publications, Switzerland

The Use of Temper Bead Welding for the Repair of Thick Walled Pressure Vessels

R.N. Ibrahim and T. Shehata

Department of Mechanical Engineering, Monash University,
900 Dandenong Road, Caulfield East, Victoria 3145, Australia

Keywords: Flux Cored Arc Welding, Penetration, Post Welding Heat Treatment, Residual Stresses, Solid Wires, Temper Bead Welding

ABSTRACT

This paper investigates the Temper Bead welding (TBW) technique using the Flux Cored Arc Welding (FCAW) process. The FCAW process increases productivity, improves welding efficiency and provides a more cost-effective method of Temper Bead Welding (TBW) repairs compared with the other commonly used TBW techniques such as manual metal arc welding (MMAW) and gas metal arc welding (GMAW) which use solid wire. An automatic welding rig was created so that the TBW process could be tested using flux cored wire under different conditions. An experimental investigation was conducted to find the optimal welding parameters of the TBW using FCAW. This experimental investigation was done in order to provide the desired mechanical properties and microstructures without Post-Welding Heat Treatment (PWHT).

Due to the difficulties encountered in the determination of residual stresses, the weld penetration depth into the base material was used as a guide to control residual stresses. In this study, analytical solution was used to support the use of TBW to repair damaged structures. This solution was based on statistical and experimental data. These data were used to establish the relationships between the technological parameters of TBW and the factors responsible for the quality of the required structure.

1. INTRODUCTION

According to the ASME standard, the conventional repair welding for wall steel constructions, which have a thickness of more than 40 mm requires PWHT to achieve the desired microstructure properties. The microstructure of the welding surrounded area is affected by the heat of the welding process. This affected area is known as the heat-affected zone (HAZ). The desired microstructure properties of HAZ are these properties which are as close as possible to the parent material properties. For some structures, however, PWHT is very expensive or difficult. Publications to date [1,2], have shown that the temper bead welding (TBW) can provide the desired microstructure properties of the welding without PWHT. The TBW provides that satisfactorily and solid wire welding processes such as MMAW or GMAW are applied to TBW successfully.

TBW is used to heat-treat the welded part or parts during the welding process instead of PWHT. TBW employs a multiple-pass deposition of the welding metal. Each layer of beads provides heat for the thermal treatment of the microstructure of the previous weld bead or the layer, as shown in

figure 1. TBW techniques have been used successfully for a number of repairs in USA and Canada, by using manual metal arc welding (MMAW) process or gas metal arc welding (GMAW) process, and its use is accepted and specified by the ASME Boiler and Pressure Vessel codes [3].

The quality of the temper bead-welding repair is very sensitive to some welding parameters [2] specific to the welding process employed. These parameters are the welding position and its effect on the bead shape, the bead deposition sequence, the welding current, the traverse speed, the arc length, the wire feeding speed, the torch angle, the preheat and inter-run temperatures and the heat inputs.

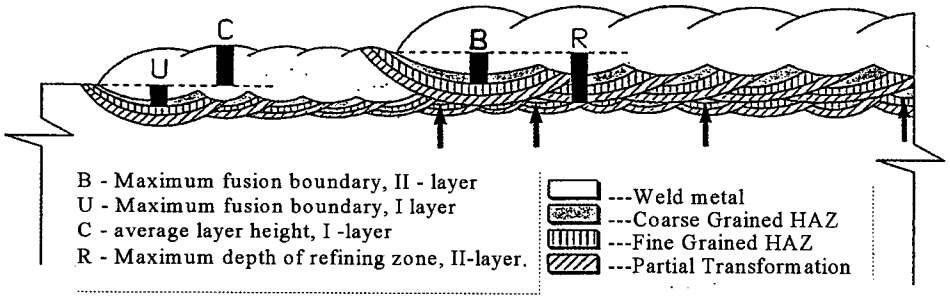


Fig. 1. Two-layer section shown schematically exhibiting approximately 85% refinement of the first layer coarse grained HAZ by the second layer [3].

There are several industry-attractive aspects of TBW that need further investigation. One of these is the application of the flux-cored arc welding (FCAW) process that uses hollow welding wire filled with flux. There has been limited research into the effectiveness of this process [2,3] but a preliminary study [4,5] indicates that FCAW might have a number of advantages over the commonly used solid wires such as MMAW or GMAW process. The welding parameters that can provide the required microstructure and minimum residual stresses in thick walled weldments need to be established to validate the application of flux cored arc welding (FCAW).

2. THE RELATIONSHIP BETWEEN THE WELDING PARAMETERS AND THE DEPTH OF PENETRATION

The depth of penetration is a direct result of the welding heat input. It is necessary to have a desirable depth of penetration to gain sufficient bonding between the parent material and the welding material. Normally, the process of quickly heating and cooling the welding region is associated with residual stresses and different grain sizes across the HAZ. The welding heat source is the applied electrical power (E) and the amount of the welding heat input (H) depends on the welding traverse speed (v) along the parent material beside the applied electrical power.

$$E = I * V * \eta \qquad \text{Watt} \qquad (1)$$

Where

I is the welding electrical current in Amp,
V is the welding voltage in volt and
η is the electrical power transmission efficiency.

(η) can be considered equal one in case of measuring I and V as close as possible to the welding spot. Welding heat input can be calculated by applying equation (2)

$H = (0.06 * I * V) / v$ kJ/mm (2)

Where

v is traverse speed in mm/min

In the FCAW process, the welding electrical current (I) is adjusted automatically according to the wire feeding speed. The welding voltage adjusted for the welding electrode size. It is clear, therefore, that the effects of (I) and (V) are limited and controlled, which means that the traverse speed (v) has the main effect on the welding heat input (H). Another parameter that should be considered is the arc length (A). The (A) represents the intensity of the welding heat source.

3. EPERIMENTAL WORK

The investigation was conducted by using the automatic welding rig shown in figure 2. The traveling mechanism (A) was operated with constant speeds varying from 120 mm/min to 700 mm/min. The wire feeding system (15) was operated at 820 to 5600 mm/min. The welding machine (B) was worked at up to 400A.

Experimental data was collected to study the relationship between the depth of penetration and the welding main parameters as presented in Table 1. The welds were divided into three groups, Group 1, Group 2 and Group 3. In each group only one parameter was changed. For Groups 1 and 2 the arc length was changed, for Group 3 the traverse speed was changed. Two different gases were used in the manufacturing of the welds, for Groups 1 and 3, Argon Shield 100 gas was used, but for Group 2 CO2 gas was used. Commercially manufactured C-Mn steel plates of 10 and 12 mm thickness were used for all welds in this investigation. A steel plate of 12 mm thickness was used for Groups 1 and 2, but a plate of 10 mm thickness was used for Group 3. The voltage for Groups 1; 2 and 3 were 30, 29 and 29 volts respectively. The electrical current for welds of Groups 1; 2 and 3 were 350, 380 and 380 respectively. The weldments (see Table 1) were manufactured using the basic flux-cored wire (AWS A5.20:E70T-4).

Table 1. The temper bead welding carried out using different Shield gases and Traverse speeds.

Group No.	Pass No.	Traverse Speed mm/min.	Arc length (A) Mm.	Penetration (P) Mm.
1	1	620	25	5
	2	620	29	4.5
	3	620	23	6
2	4	620	23	4.5
	5	620	28	4
	6	620	25	5
3	7	1000	25	4
	8	253.5	25	8
	9	600	25	6

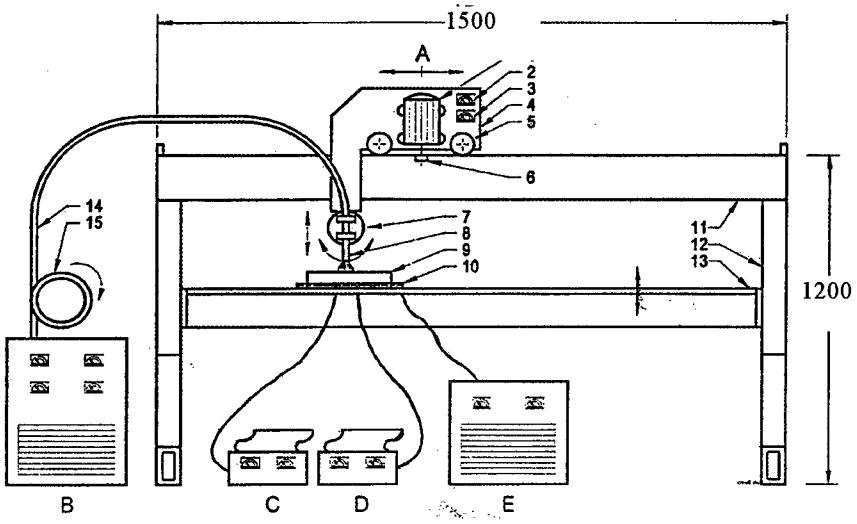


Fig. 2. Experimental Installation

A) Traveling mechanism B) Welding machine C) 12-channel chart recorder.
D) Real time-temperature chart recorder. E) Preheating elements controller.
1. 240V low speed motor. 2. Fine current control for motor. 3. Travel speed gauge.
4. Frame carriage. 5. Steel wheels. 6. Gear.
7. Variable head. 8. Welding torch. 9. Work piece.
10.Electrical heating elements. 11. Main frame. (horizontal beam)
12. Main frame. (Supporting legs) 13. Table 14.Welding lead.
15.Welding wire feeding system.

4. RESULTS AND DISCUSSION

By applying Merit Function " χ^2 " on Groups 1 and 3, a mathematical relationship between the depth of penetration (P) as output and the traverse speed (v) and the arc length (A) as inputs can be presented as following:

$$P = -0.0054\,v + 0.93\,A - 0.023\,A^2 \qquad (3)$$

From equation (3), the relationship between the depth of penetration (P) and either the traverse speed (v) at different arc lengths or the arc length (A) at different traverse speeds can be plotted as shown in Figures (3) and (4) respectively.

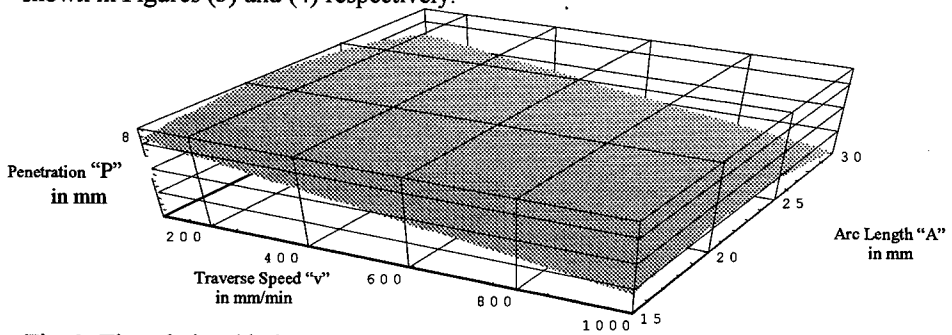


Fig. 3. The relationship between Traverse Speed "v", Arc Length "A" and Penetration "P" of welds (groups "1" and "3", Argon Shield 100 gas).

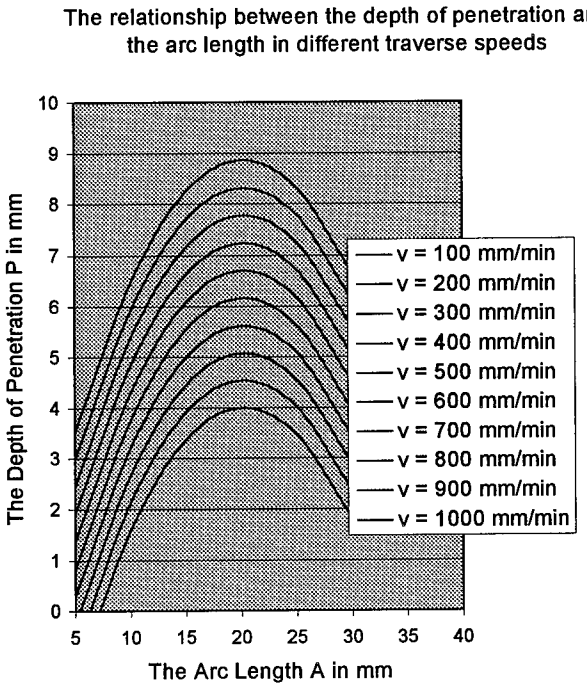


Fig. 4. The relationship between the depth of penetration (P) and the arc length (A) in different traverse speeds.

The relationship between the depth of penetration (P) and the arc length (A) at different traverse speeds (as shown in Figures 3 and 4) demonstrates that a decrease in the traverse speed at the same arc length is associated with an increase in the depth of penetration. Between arc length 5and 20.22 mm, any increase in the arc length at the same traverse speed is associated with an increase in the depth of penetration. Therefore, with increasing heat, the spark heat, more heat transfers through the parent material. In the case of the small arc length, the welding torch absorbed a fraction of the heat. The heat conductivity of the torch material is higher than that of the low carbon steel, so less heat transfers to the parent material. Also at this stage, the same penetration was achieved when an increase in the arc length was associated with an increase in the traverse speed. Furthermore, any increase in the arc length between 20.22 and 30 mm was associated with a decrease in the depth of penetration as the surrounding ambient absorbs more heat.

A comparison of the results from [4,5] for FC wires and the results from [6,7] for solid wires, reveals that FC wires achieved deeper penetration for the same welding conditions (heat input, arc length and traverse speed). Therefor if the same welding conditions, to achieve the same depth of penetration, then FC wires should be operated in faster speed than the solid wire. Therefore, the FCAW process can provide higher productivity than solid wire processes.

5. CONCLUSION

Using FCAW process with TBW technique will increase the productivity, improve welding operation and efficiency and provide a more cost-effective method of weld repairs to the industry in comparison with the other commonly processes known with TBW technique such as MMWA and GMAW.

REFERENCES

1. C. D. Lundin, WRC Bulletin 412, (1996) p. 16 - 26.
2. T. W. Lau, M. L. Lau, et al. WRC Bulletin 412, (1996) p. 35 - 42.
3. J. S. Edgley, M. Pitrun, Pressure Vessels and Pipwork Conference, Australia, Sydney (1993).
4. R. N. Ibrahim, T.Shehata, ICM8, 8th International Conference on the Mechanical Behavior of Materials, Canada, British Colombia, (1999) p. 771
5. R. N. Ibrahim, T. Shehata, 9th International Conference on Pressure Vessels Technology, Australia, Sydney, April 9 - 14, 2000.
6. M. Sato, K. Suda, et al, Journal of Japan Welding Society, 65 (1996) p. 13
7. N. U. Ahmed, B. L. Jarvis, Australian welding journal, V43, 3rd. Quarter (1998) P.40

Key Engineering Materials Vols. 183-187 (2000) pp. 1345-1350
© 2000 Trans Tech Publications, Switzerland

Welding Residual Stress Analysis and Fatigue Crack Growth Characteristics of Multi-Pass Welded Pipe Weldment

C.H. Kim[1], D.H. Bae[1], S.Y. Cho[1] and B.K. Kim[2]

[1] Sschool of Mechanical Engineering, Sungkyunkwan University,
300 Chonchon-dong, Changan-Gu, Suwon, Kyonggi-do 440-746, Korea

[2] Department of Mechanical Design, Myongji College,
50-3 Namgajyua-dong, Seodaemoon-gu, Seoul 120-728, Korea

Keywords: Crack Closure, Effective Stress Intensity Factor Range (ΔK_{eff}), Fatigue Crack Growth Characteristic, Stress Intensity Factor, Welding Residual Stress

ABSTRACT

Welding residual stresses are generated as a result of the large nonlinear thermal loading by a moving heat source. Moreover, multi-pass welding of thick section subjects to multiple thermal cycles and inelastic strain patterns. Thus, more complex residual stress distribution is generated through the plate thickness. When these residual stresses are tensile, it makes increase the crack driving force and reduce the resistance of brittle fracture. Therefore, accurate prediction of residual stresses is very important. In this study, welding residual stresses of the multi-pass welded A106 Gr B steel pipe weldment were analyzed by finite element analysis (FEA) using the element rebirth technique, and compared with experimental results. And then, in order to estimate fatigue crack growth characteristics considered the effect of residual stresses, concept of crack closure effect was introduced. From the results, the trend of welding residual stress distribution that was calculated by using the element rebirth technique of FEA was well agreed with the experimental result. And crack closure phenomena was not observed above R=0.5. And also, K_{op}/K_{max} was independent of K_{max}. Considering crack closure phenomenon in A106 Gr B Steel weldment, fatigue crack growth characteristic curves can be effectively estimated.

1. INTRODUCTION

Welding is a widespread method in constructing structure. However, generation of welding residual stress is inevitable. These residual stresses add to the primary load stresses to increase the crack driving force and strain at the crack tip front that promotes premature brittle fracture of the welded joint. And also, they affect to fatigue crack growth behaviors. Therefore, accurate calculation of welding-induced residual stresses and estimation of their effects on fatigue crack behaviors are very important. To date, many investigators have attempted to estimate residual stress distribution and to evaluate fatigue crack growth characteristics in the residual stress field [1,2,3]. In this study, welding residual stress distribution of multi pass welded A106 Gr B steel pipe weldment was calculated by the recent FEA method. And then, representative fatigue crack growth characteristic curve was obtained by introducing crack closure concept.

2. WELDING RESIDUAL STRESS ANALYSIS

2.1 FEA Modeling

A twenty four-pass welded A106 Gr B steel pipe was considered in this study. Its chemical compositions and mechanical properties are illustrated in Table 1. and Table 2., respectively.

Table 1. Chemical compositions of A106 Gr B steel

	C	Mn	Si	P	S	Ni	Cr+Mo	Ni+Cu
A106 Gr B	0.10	0.86	0.21	0.010	0.004	0.10	0.06	0.39

Table 2. Mechanical properties of A106 Gr B steel

	Tensile	
A 106 Gr B	Y.S.	T.S
	367MPa	486MPa

The only first pass was welded by GTAW (gas tungsten arc welding), the other passes were by FCAW (flux cored arc welding). The thickness was 30 mm and the outer diameter was 254 mm. Two-dimensional finite element analysis model was used in both thermal and mechanical analyses. The FEA model is as shown in Fig. 1.

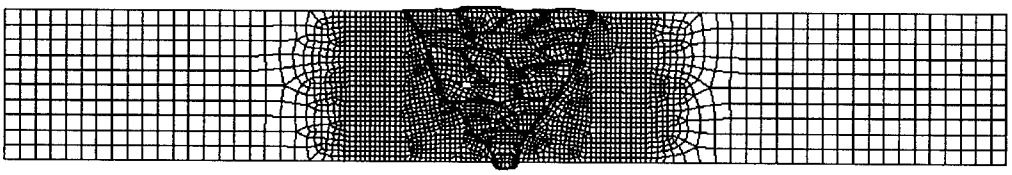


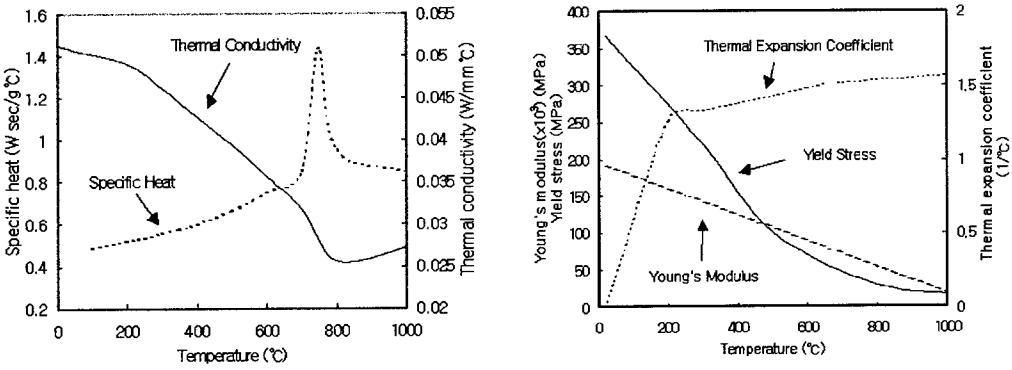
Fig.1. FEA model for welding residual stress analysis.

Four-node heat transfer elements and 4-node generalized plane strain elements were used. The area with oblique lines represents the layers of the weld bead determined by the actual weld coupon. Finer meshes were generated in the weld metal regions to handle the greater nonlinearity and to obtain accurate results. I-DEAS, a commercial pre- and post-processor was used for the mesh generation. ABAQUS was employed for the transient temperature and subsequent residual stress analyses. The total number of elements is 3064 and the total number of nodes is 3370.

2.2 Assumptions and Simulation Procedures

The uncoupled thermal-mechanical analysis was conducted, which means that the temperature

fields and histories were calculated from the thermal analysis and then used as an input database for the subsequent stress analysis. Identical time steps were used for both thermal and mechanical analyses. In performing the temperature analysis, it was assumed that the initial temperatures of base and weld metals were assumed at a pre-heat temperature (100 °C). The temperature dependent material properties of Fig.2 were used in the analysis. However, the conductivity and specific heat in the molten pool were assumed to be constant. The effect of latent heat of fusion, which is the internal energy change during melting or solidification, was also considered in the thermal analysis. The heat loss coefficient applied to all exposed surfaces was 0.0817 W/m²°C. Other thermal boundary conditions such as radiation and forced convection due to the shielding gas flow were neglected. These terms only become significant when the behavior of a molten pool flow is of interest. Because of the high temperatures in the molten pool, it is trivial in the residual stress simulations. Similarly, radiation and convection influences on the microstructures and cooling rates in weld metal, as well as heat losses or gains from phase transformation were neglected.



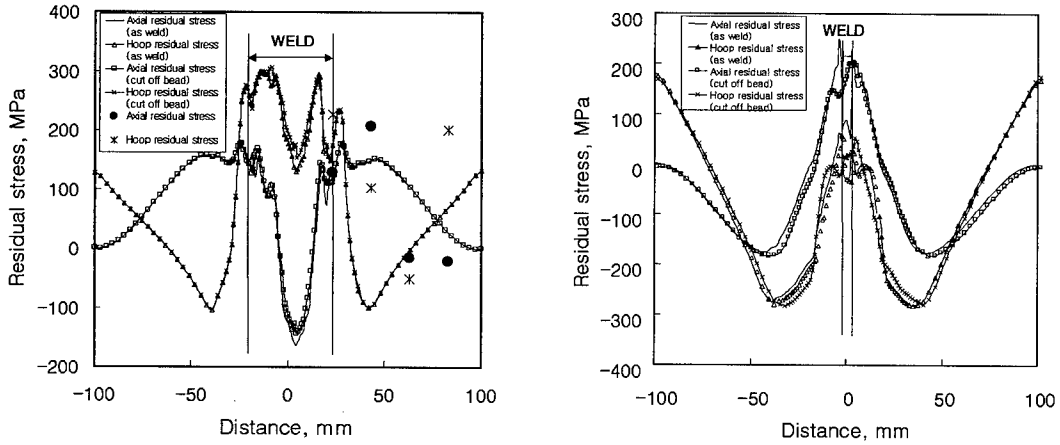
(a) Thermal properties (b) Mechanical properties

Fig. 2. Temperature dependent material properties of A106 Gr B steel

In performing the stress analysis, the mechanical and physical properties of Fig.2, which are yield stress, elastic and plastic modulus and thermal expansion coefficient, were considered temperature dependent. Mechanical properties were however assumed constant above the melting point. The temperature dependency of Poisson's ratio was neglected. A constant value of 0.3 was used in the analysis. The element rebirth technique was employed to include the multi-pass weld metal deposition effects. With this technique, the elements simulating each weld pass were grouped at the model generation stage. During analysis, these element groups which presented weld passes were first removed and then reactivated at a specified moment to simulate a given deposition sequence of weld passes. When a group of weld elements were activated, specific initial temperatures were imposed at all nodes associated with the weld elements. The heat input was imposed onto the specific newly activated element groups representing a depositing pass at a given time. In this study, ramp heat input model was used. The heat-input model used the ramp function was developed by Tsai *et al.* [4].

2.3 FEA Results and Discussion

The predicted welding residual stress distributions on the top surface and the experimental results were compared in Fig. 3. Experimental values were well agreed with the results of FEA. So, it was certified that analysis method used in this study was reasonable. The peak residual stresses of the outer and the inner surface were located around the HAZ (heat affected zone). The trend of the predicted residual stress distribution is much different from that of single pass welding. In case of single pass welding, high compressive stresses are generated in the outer surface, and tensile stresses are generated in the inner surface. However, in multi-pass welding, contraction of subsequent pass is always constrained by previous passes. Thus, the residual stresses generated from the earlier passes dominate the residual stresses of the final pass. And, when the weld bead of the top surface was cut off for post weld treatment after welding, residual stresses of the weld bead on the surface were slightly released due to the variation of its shape and constraint condition.



(a) outer surface (b) inner surface

Fig.3. Welding residual stress distributions

3. FATIGUE CRACK GROWTH CHARACTERISTICS

3.1. Specimen and Test Procedure

Test specimen was prepared with SEN (single edge notched) type. Material and welding condition were same with those of FEA model. Notch was located in the root of weldment where high tensile residual stress was generated in. Generally, owing to residual stresses are influenced by stress ratio, ΔP-constant fatigue crack growth tests were carried out under various stress ratios (R=0.1, 0.3, 0.5). And, in order to systematically estimate fatigue crack growth characteristic curves in regardless of stress ratios, the concept of crack closure was induced. To detect accurate crack opening point, precision COD gage was used. And, all procedures were computerized

3.2. Test Results and Discussion

Crack closure behaviors of A106 Gr B steel weldment were shown in Fig.4. K_{op} was increased with $K_{\max}$ increased. $K_{op}/K_{\max}$ was however independent of $K_{\max}$. These tendencies

can be explained by plasticity induced crack closure mechanism. And this result has been already certified in the earlier research[5]. However, crack closure phenomena was not observed in R=0.5, where K_{min} is higher than K_{op}.

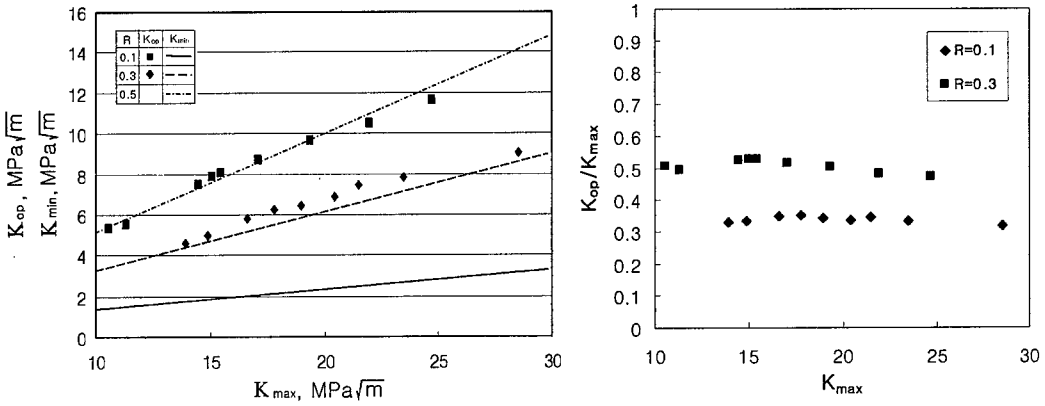


Fig.4. Crack closure behaviors in A106 Gr B steel weldment

Crack closure effects according to stress ratio variation can be expressed by the ratio of stress intensity factor range (U).

$$U = \frac{K_{max} - K_{op}}{K_{max} - K_{min}} = a + b \cdot R \tag{1}$$

a and b are experimental constants. Elber was suggested that a was 0.5 and b was 0.4 for aluminum alloy [6]. In this study, the values of a and b were applied 5.55 and 5.04 respectively.

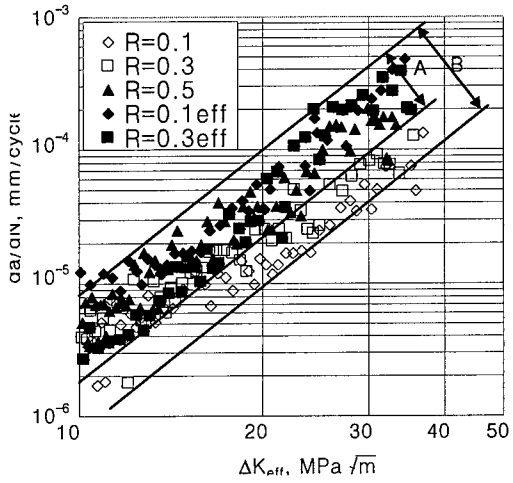


Fig.5. Fatigue crack growth characteristics of A106 Gr B steel weldment.

Many researchers were shown that fatigue crack growth characteristic curves could be represented by ΔK_{eff} in regardless of the stress ratios [7]. From this view point, crack closure concept can effectively estimate fatigue crack growth characteristics in residual stress field. ΔK_{eff} in the residual stress field is given by

$$\Delta K_{eff} = (K_{\max} + K_{res}) - (K_{op} + K_{res}) = K_{\max} - K_{op} \quad (2)$$

Fatigue crack growth characteristic curves were shown in Fig.5. B is scatter band of the characteristic curves that has not considered the crack closure effect. A is scatter band of curves represented by ΔK_{eff}. All data were included in the same scatter band. Thus, reasonable fatigue crack growth characteristic curve of A106 Gr B steel weldment could be obtained.

4. CONCLUSION

From the above, obtained results are as follows,

1) Welding residual stress distribution that was calculated by using the element rebirth technique of FEA was qualitatively well agreed with the experimental result.
2) Crack closure phenomena was not observed above R=0.5. and, $K_{op} / K_{\max}$ was independent of $K_{\max}$
3) Considering crack closure phenomenon in A106 Gr B Steel weldment, fatigue crack growth characteristics curve can be effectively estimated.

ACKNOWLEDGMENT

The authors are grateful for the support provided by a grant from the Korea and Engineering Foundation (KOSEF) and Safety and Structural Integrity Research Center (SAFE) at the Sungkyunkwan University.

REFERENCE

1. V. Ramamurti, etal, Residual Stress Analysis in Weldments : Engineering Fracture Mechanics Vol. 38, No. 6, (1991) pp. 385-391.
2. T. Nitschke-Pagel. and H. Wohlfahrt, Influence of Residual Stress on the Fatigue Strength of High Strength structural Steel : European Conference on Residual Stresses. IIW-Nr XIII (1992) pp. 1514-1593
3. Y. W. Shi, etal, Effect of Welding Residual Stresses on Fatigue Crack Growth Behaviour in Butt Welds of a Pipeline Steel : Engineering Fracture Mechanics Vol. 36, No. 6, (1990) pp. 893-902.
4. Y. L. Shim, Z. Feng, S. G. Lee, D. S. Kim, J. J. Jaeger, J. C. Papritan and C. L. Tsai, Determination of Residual Stresses in Thick-Section Weldment. Welding Journal **71 (9)** (1992) p.305 - 312.
5. M. Katcher and M. Kaplan, Effect of R-Factor Crack Closure on Fatigue Crack Growth for Aluminum and Titanium Alloy, ASTM STP 559, (1974)p. 264-282,.
6. W. Elber, The Significance of Fatigue Crack Closure, ASTM STP 486, (1971) p.230-242
7. J.A. Todd, L. Chen, E.Y. Yankov and S, Mostovoy, Crack Closure Effects of Fatigue Crack Growth Thresholds and Remaining Life in an HSLA Steel, JPVT, (1997) p. 37-44

Author Index

A

Adachi, T. 731
Ahn, Heung Gu 391
Akama, M. 1035
An, C.W. 349, 481
An, J.Y. 987
An, W.K. 1087
Ando, Kotoji 803, 833, 921, 1047
Aoki, Yoshio 1093
Aoyama, E. 643
Arakawa, K. 265, 409

B

Bae, D.H. 415, 957, 993, 1345
Bae, S.I. 1029, 1267
Bahk, Saemahn 529
Bai, C.H. 277
Bai, Shiwei 433
Bai, Shu-Lin 761, 839, 987, 1075
Bai, Yong 1023
Baik, Y.M. 31
Bush, Mark B. 1261
Byon(Goichi Ben), O.I. 1093
Byun, T.S. 607

C

Cha, H.J. 655
Chae, S.H. 1135
Chang, T. 181
Chang, Yoon-Suk 505
Chau, K.T. 109, 809, 857
Chen, J.K. 761, 1075
Chen, Jian 487
Chen, Junmei 1315
Chen, Z. 187
Cheong, YongMoo 845
Cho, D.W. 559
Cho, J.R. 373, 403
Cho, M.H. 355
Cho, M.R. 43, 493
Cho, S.K. 517
Cho, S.Y. 993, 1345
Cho, Seong-Jae 1249
Cho, Y.T. 1219
Choi, J.B. 655, 869
Choi, J.H. 481
Choi, N.S. 247, 1081
Choi, S.J. 827
Choi, Sang-Woo 619
Choi, W.C. 559
Choi, Younho 1099
Choo, KeeNam 845
Chu, M.C. 833, 1047
Chun, H.-J. 427, 1069
Chung, J.H. 1207
Chung, K.H. 43
Clegg, W.J. 1213
Cotterell, B. 187
Cui, Zhaoxia 589, 1303

D

Dai, F.L. 737
Ding, C.F. 127
Du, S.H. 91
Du, Shanyi 487
Duan, Zhuping 343

E

Earmme, Y.Y. 1123
Ebara, R. 939

F

Fang, D.N. 821
Fang, F. 175
Fang, Q.Z. 951
Feng, W.J. 241
Feng, X.Q. 667
Feng, Xia-Ting 385, 713
Fu, Guoru 969
Fu, Ran 695
Fu, Y.F. 785
Fujimoto, T. 313, 445
Fujinami, A. 583
Fujisaki, T. 565
Fukuda, T. 583
Fukui, Y. 565
Fukuyama, K. 553

G

Gao, C.Y. 277
Gao, J.G. 67
Gao, S.L. 1063

Geni, M. 625
Gladkovsky, S.V. 863
Gladkovsky, V.A. 863
Goo, B.C. 1225
Goto, H. 999
Gross, D. 331
Guo, W. 181, 193
Guo, Yongjin 1111

H
Ha, D.Y. 373, 403
Ha, J.K. 283
Ham, K.C. 1029, 1267
Han, Jae-Hung 1201
Han, Kyung Seop 547, 661, 945, 1011, 1117, 1267, 1297
Han, S.Y. 361, 379, 439
Hattori, N. 169, 963, 1243
Hawong, J.S. 283
Hayashi, K. 1243
He, Buolin 613
He, L. 457
He, Pengfei 1213
Herrmann, K.P. 1141
Higashi, K. 851
Hirata, T. 851
Hirogaki, T. 643
Homma, Hiroomi 893
Hong, C.S. 535, 1189
Hong, J.H. 607
Hong, K.S. 463
Hong, S.I. 1207
Hong, Soon H. 1153, 1183, 1291
Hong, Sun Ig 1255
Hong, Youshi 157
Hou, Yunfeng 319
Hu, X.Z. 1177
Hu, Xiaozhi 1261
Hua, Y. 571, 881
Huang, Jianlong 37
Huang, M.L. 785
Huang, S.Z. 571, 881
Huang, Y. 9
Huang, Z.P. 761, 1075
Huh, N.S. 655
Huh, S.C. 1237
Huh, Yong-Hak 1249
Huo, Lixing 613, 1315, 1327
Hurtado, Juan A. 1
Hwang, B.S. 791
Hwang, J.S. 307
Hwang, K.C. 9, 821
Hwang, S.S. 707
Hwang, W. 661, 673, 945, 1117
Hyakutake, Hiizu 601

I
Ibrahim, R.N. 1339
Igawa, H. 25
Ikeda, T. 73
Im, J.W. 1041
Imanaka, M. 583
Inoue, H. 643
Ishigami, H. 921
Ishii, H. 827

J
Jang, P.-S. 1069
Jang, Y.K. 869
Jarng, Soon Suck 391
Jeong, H.-Y. 1195
Jeong, S.K. 1135
Jiang, H.Y. 79
Jiang, J.G. 67
Jiang, Z.Q. 571, 881
Jin, F. 725, 755
Jin, Tae-Eun 505, 797
Jing, H.Y. 1327
Jo, C.H. 349, 481
Joo, S.G. 535
Joung, K.K. 1029
Ju, Dong-Ying 97
Jung, C.K. 1011
Jung, J.H. 517
Jung, S.G. 797
Jung, S.W. 1117, 1297

K
Kanemitsu, M. 1159
Kanemitsu, Tsuyoshi 337
Kang, Heung-Seok 743
Kang, K.W. 271
Kang, Tae Jin 1165
Katayama, T. 643
Kikuchi, M. 625
Kikuchi, Masanori 875
Kim, B.H. 791
Kim, B.K. 1345
Kim, C. 295, 469
Kim, C.G. 1189

Kim, C.H. 993, 1345
Kim, D.S. 415
Kim, D.Y. 1171
Kim, E. 349
Kim, G.H. 307
Kim, H.G. 1219
Kim, H.P. 595, 707
Kim, H.S. 815, 1207
Kim, Hyoung Seop 1255
Kim, Hyung-Kyu 743
Kim, Hyun-Su 505
Kim, I.S. 607
Kim, J. 631
Kim, J.B. 767
Kim, J.D. 1309
Kim, J.H. 103, 933, 1029
Kim, J.K. 85, 271, 1063, 1177
Kim, J.S. 595, 707, 1123
Kim, J.Y. 1219
Kim, K.H. 1029, 1147
Kim, K.S. 31, 349, 463, 481
Kim, Kyung-Suk 1
Kim, M.G. 933
Kim, M.H. 415, 1105
Kim, Moon-Saeng 915
Kim, P.W. 1153
Kim, S.H. 403
Kim, S.J. 19
Kim, SungSoo 845
Kim, T.W. 295, 1279
Kim, Y.C. 1153
Kim, Y.H. 1017
Kim, Y.J. 655, 869
Kim, Y.K. 1183
Kim, Y.S. 355, 1309
Kim, YoungSuk 845
Kim, Yun-Jae 133, 1333
Kishimoto, Kikuo 121, 541, 779, 1053
Kobayashi, Albert S. 97, 325
Kobayashi, Y. 999
Kodama, K. 145
Kohzu, M. 851
Komohara, Y. 73
Kong, C.W. 1189
Kook, J.S. 731
Kuboki, T. 289
Kuk, I.H. 707
Kumazawa, N. 565
Kwak, D.S. 1321
Kwon, H.S. 595
Kwon, J.D. 577, 827, 975
Kwon, S.J. 1225
Kwon, SangChul 845
Kwon, Y.D. 355, 469
Kwon, Y.K. 1321

L

Lang, Fuyuan 55
Lee, C.J. 1321
Lee, C.S. 945
Lee, D.J. 1171, 1219
Lee, Dong Nyung 679
Lee, H.J. 283, 673
Lee, H.S. 1183
Lee, H.Y 559
Lee, In 1201
Lee, J.H. 61, 295, 1297
Lee, J.J. 259, 1147
Lee, J.K. 791
Lee, J.R. 1105, 1183
Lee, J.Y. 307
Lee, Je Hyeng 391
Lee, Joon-Hyun 619, 887
Lee, K.R. 767
Lee, K.W 103
Lee, Kyung Woo 1165
Lee, Min-Rae 887
Lee, O.S. 283, 349, 481
Lee, Ouk Sub 307, 325
Lee, S.B. 103
Lee, S.C. 463
Lee, S.G. 903
Lee, S.H. 1087
Lee, S.P. 1237
Lee, S.W. 427
Lee, T.H. 379, 439
Lee, W.H. 577
Lee, W.I. 631
Lee, Y.S. 451, 577, 975
Li, C.Y. 511
Li, Ch. 211
Li, Dahong 253
Li, H.B. 67
Li, J.C. 217
Li, Qingfen 589, 1303
Li, T.J. 67
Li, Tao 1231
Li, Tingjie 433, 713
Li, Youtang 37, 319
Li, Z. 181

Li, Z.L. 79, 91
Li, Zheng 301
Liang, Wei 199
Liang, Z.Z. 637
Liao, Guo-Hong 1023
Lim, B.S. 1041
Lim, J.H. 1123
Lim, J.K. 379, 439
Lim, Y.S. 595, 707
Lin, P. 637, 809, 857
Lin, Xiaoying 423
Liu, B. 821
Liu, C.L. 277
Liu, Chuntu 151, 163
Liu, H.Y. 637
Liu, J.X. 139
Liu, J.Z. 127
Liu, Li 423
Liu, X.F. 139
Liu, X.L. 139
Liu, Y.I. 1327
Liu, Y.J. 951
Liu, Z.D. 987, 1075
Liu, Zongde 839
Long, Ping 589
Lyu, M.Y. 259

M

Ma, Jun 1231
Ma, Maoyuan 589
Machida, Kenji 49
Mada, T. 265, 289
Maeng, J.S. 361
Mai, Y.-W. 217
Mao, X.P. 987
Matsui, K. 921
Matsuo, T. 499, 523
Miyazaki, N. 73
Mizumoto, M. 719
Morino, K. 749, 981, 1017

N

Nagawa, M. 475
Nakamura, A. 73
Nakano, K. 963, 1243
Nakayasu, H. 1159
Nakazato, Kohji 893
Nam, H.W. 1117, 1297
Nam, J.B. 1297
Nam, J.H. 115
Nam, Jaebok 547
Ni, Huocai 589, 1303
Nie, G.H. 1005
Nishida, S. 169, 963, 1243
Nishimura, F. 749, 981, 1017
Nishioka, T. 313, 445
Nisitani, H. 553, 749, 981, 1017
Noda, N.-A. 475, 499, 523
Noh, H.K. 1219
Notomi, M. 121
Notomi, Mitsuo 779

O

Oguchi, T. 97
Oh, T.Y. 1321
Okada, H. 565
Omiya, M. 541
Osaka, K. 583

P

Pae, S.M. 673
Paik, K.W. 1123
Park, D.G. 607
Park, H. 295
Park, H.C. 661, 673, 945
Park, Hoon Cheol 1099
Park, I.S. 791
Park, J.B. 1129
Park, J.C. 577, 975
Park, J.G. 469
Park, Jae Chull 391
Park, K.H. 1237
Park, M.K. 529
Park, S.B. 791
Park, S.J. 1105
Park, S.K. 1219
Park, S.W. 1279
Park, Y.W. 577, 975
Peng, Xianhai 1303
Putra, I.S. 649
Pyo, C.R. 655

Q

Qi, H.B. 571, 881
Qu, Shaoxing 1111

R

Raghukandan, K. 205, 1273
Rew, Keun-Ho 1201
Rui, Zhiyuan 37

Ryu, Ho J. 1291

S
Saimoto, A. 553
Sakakura, K. 313
Sakamoto, Hidetoshi 719
Sato, Shigemi 803, 833, 1047
Sawa, Yoshiaki 337
Senthilvelan, T. 205, 1273, 1285
Seo, D.C. 103
Seto, M. 713
Shehata, T. 1339
Shen, Yapeng 199
Shi, H.J. 277
Shi, R. 1005
Shi, Y.P. 397
Shibuya, T. 541
Shibuya, Toshikazu 779
Shih, Shaochiu 253
Shim, D.J. 869
Shim, D.S. 85
Shimamoto, A. 97, 115, 145
Shimomura, T. 115
Shin, D.C. 283
Shin, D.K. 259
Shin, Hyung-Seop 915
Shin, I.J. 1171
Shin, K.C. 1147
Sohn, I. 957
Sohn, M.S. 1177
Sohn, Min-Seok 1255
Son, S.Y. 963
Song, D.Y. 1129
Song, H.S. 791
Song, J.I. 1029, 1267
Song, Jiho 1249
Song, K.N. 451
Song, Y.Y. 607
Sonoya, Keiji 909
Su, B. 211
Su, Wei 969
Su, Xianji 301
Suh, M.W. 61, 415
Sun, Chengwei 343
Sun, Hai-Hong 1023
Sun, Yi 1231
Sung, K.D. 493
Susuki, I. 1035
Syam, Bustami 893

T
Takahashi, Akiyuki 875
Takahashi, K. 229, 265, 289, 409, 1017, 1081
Takao, Y. 815
Takase, Y. 475
Takeda, N. 1129
Takeuchi, K.-I. 475
Tamasaki, H. 1243
Tan, Xianxiang 343
Tanabe, S. 851
Tanaka, M. 367
Tanaka, Y. 999
Tang, C.A. 637, 785, 809, 857
Tang, G.H. 457
Teranishi, T. 553
Tobe, Shogo 909
Todo, M. 409
Tong, Pin 695
Tsuji, Kiichi 803

U
Umezaki, E. 115, 145

V
Venkatraman, A. 205, 1273, 1285

W
Wang, Bintuan 899, 927
Wang, C.H. 217
Wang, Dongpo 1315
Wang, Lili 253
Wang, Liquan 1303
Wang, T.J. 725, 755
Wang, Tiejun 121, 779
Wang, W.X. 815
Wang, Y.S. 331
Wang, Z.K. 725, 755
Wei, Yaobing 55, 319
Wen, Sanggang 343
Won, Y.G. 1153
Wong, R.C.K. 109
Wong, Robina H.C. 109, 809, 857
Woo, S.W. 975
Wu, Linzhi 487
Wu, S.X. 511
Wu, X.R. 127

X
Xing, Y.M. 737

Xu, Ping 385
Xu, Yongjun 151, 163

Y
Yamada, Y. 939
Yamaguchi, T. 719
Yamamoto, H. 169
Yamamoto, Toshihiro 601
Yamamura, H. 939
Yanagida, Y. 1243
Yang, I.Y. 731
Yang, Kun 839, 987
Yang, Qingxiong 899, 927
Yang, Sanglin 1303
Yang, Shanglin 589
Yang, W. 175, 737
Yang, W.H. 43, 493
Yang, Y.C. 661
Yao, F. 833, 1047
Yao, Z.H. 277
Ye, L. 217
Yeh, B.H. 1153
Yin, H.L. 349
Yoon, H.K. 1087, 1237
Yoon, K.H. 451
Yoon, Kwang Joon 1099
Yoon, Kyung-Jin 1249
Yoon, S.J. 517, 1135
You, D.X. 127
Yu, Hualong 157
Yu, J.M. 61
Yu, X.B. 223
Yun, T.H. 355, 469

Z
Zeng, P. 397, 457
Zeng, Xiangguo 1141
Zhan, F.L. 79, 91
Zhang, Guang 433
Zhang, Junqian 1141
Zhang, R.J. 1005
Zhang, S.B. 571, 881
Zhang, S.S. 951
Zhang, Tong-Yi 695, 773
Zhang, X.P. 217
Zhang, Yufeng 613, 1315, 1327
Zhao, Feng 343
Zhao, Hong 1261
Zhao, J. 67
Zhao, Jianheng 343
Zhao, M.H. 951
Zhao, Minghao 199, 695
Zheng, J. 139
Zhong, Z. 223
Zhou, Aixi 55
Zhou, Yu 1231
Zhu, T. 175
Zhuang, Zhuo 1111
Zong, Z. 725
Zou, Z.Z. 241, 511

Keyword Index

2

2-Phase 933

3

30Cr2MoV Steel 987
3D Glass Fabric Reinforced Composites 1183

8

8 Harness Woven Fabric 1153

A

A Beam Structure 61
Ablative Composites 1153
Abrasive Wear 1267
Acoustic Emission 713, 887, 903
Across-Laminar 1153
Actuator 673
Adaptive Vibration Control 1201
Adhesive 43
Adhesive Shear Stress 43
Adhesively Bonded Butt Joints 583
AE Count 903
AE Energy 903
AE Hit 903
Aero-Engine 969
AFM 827
Aging Treatment 1237
Alloy 600 ..... 595, 707
Alloy 690 707
Aluminum Matrix Composite Brake Disc 1225
Aluminum/GFRP Hybrid Tube 1147
Amorphous Alloys 1255
Anisotropy 679, 1183
Anodic Oxidation 1105
Apparent Strain Hardening Exponent 1273
Apparent Strength Coefficient 1273
APS 909
Artificial Neural Network 957
Atmosphere Corrosion 899, 927
Attenuation-Based Method 887
Austenite 863
Autocorrelation Function 19
Automobile Hood Design 439
Axial Crush 1147

B

Ball Indentation Test 607
Barkhausen Noise 607
Barrier Strengthening 1207
Basal Pole Component (F) 845
Bending Fatigue 571
Bending Strength 803, 833, 1081
BFM 553
Biaxial Load 115
Biaxiality Ratios 115
Blind Hole 749
Body Force Method 499, 523
Boundary Conditions of Displacement 37
Boundary Conditions of Stress 37
Boundary Element Method 91
Boundary-Layer Effect 43
Brazed 1279
Brittle Failure 637
Brittle Polymers 265
B-Spline 415
Buckling 187, 451, 1189
Buckling Mode Shape 451

C

Calendar Fatigue Life 927
Cantilever Beam (CB) Specimen 845
Carbon Fiber 571, 881, 1105, 1129, 1267
Carbon Fiber Composites 1177
Carbon/Epoxy Laminates 945
Carbon/PEEK Composite 1063
Caustic Curve 349
Caustics Method 115, 265
Cavitation 851
Cavity 139, 821
CBA 1123
CCD Camera 601
Cement Block 301
Cement Mortar 253
Center of Dilatation 109
Ceramic Composite 833
Ceramic Materials 1231
Ceramic/Metal Bilayer Composites 1261
Ceramic/Metal System 1279

Ceramics 1213
CF8M 577, 975
CFGFRP 1129
CFRP 1093, 1129
CFRP Laminates 915
Chemical Erosion 713
Chimes 457
Cluster Structure 1297
Coat 839
Coating Crack 211
Co-Curing Method 1087
COD-Decrease-Parameter 589
Coefficient of Friction 1273
Cohesive Force Model 541
Collective Evolution 157
Collinear Cracks 199
Combined Mechanical and Electrical Loading 695, 773
Combined Stress 97
Compliance Method 993
Compliant Substrate 187
Composite Element Method 397
Composite Laminates 535
Composite Materials 307, 1111
Composite Plate 355, 469
Composite Structures 1201
Compressive Residual Stress 921
Compressive Strength 1189
Compressive Test 1183
Condition 463
Configuration of Lamina 1159
Constant ΔK Fatigue Crack Growth Test 19
Constitutive Relation 667
Constraint Effects 193, 869, 875
Contact Area 939
Contact Damage 1261
Contact Failure 743
Contact Problems 475
Contact Stress Distribution 493
Contour Induction Heating 921
Controllable Fracture 55
Convergence Rate 379
Cooling Rate 1063
CORPUS Model 649
Corrosion 1285
Corrosion Cell 993
Corrosion Fatigue 993, 999, 1023
Coupled Electromechanical Field 725
Coupled Field 139
Coupling 475
Cr Depletion 707
Crack 25, 139, 175, 181, 331, 385, 511, 613, 821
Crack Bridging Model 103
Crack Closure 217, 649, 743, 1249, 1345
Crack Coalescence 809, 981
Crack Depth/Specimen Width (a/W) 589
Crack Extension 779
Crack Growth Life Prediction 649
Crack Growth Rate 31, 367, 993
Crack Healing 803, 833, 1047
Crack Identification 61
Crack Initiation 169, 999
Crack Kinking 73, 97
Crack Opening Period 743
Crack Orientation 1303
Crack Propagating Velocity 283
Crack Propagation 169, 565, 981, 1017, 1035
Crack Surface Displacement 103
Crack System 55
Crack Technique 55
Crack Tip 9, 157, 737
Crack Velocity 247, 265
Cracked Pipe Welds 1327
Cracked Piping System 505
Crack-Healed Zone 1047
Cracking 187, 1261
Crantz-Schardin Type Stroboscopic Camera 337
Creep Fracture 367
Creep Life 903
Creep Rupture Strength 903
Creep-Fatigue 1041
Critical Impact Energy 271
Crush Energy Absorption 1099
Crystallinity 1063, 1171
Cumulative Damage 927, 945
Cu-Nb 1207
Curing Method 1087
Cutting Forces 643
Cyclic Fatigue Crack Growth 1249
Cyclic Fatigue Strength 803, 1047
Cyclic Hardening 975
Cyclic Loading 1075
Cyclic Stress-Strain Curve 975
Cylindrical Interface Crack 241
Cylindrical Specimen 749

D
Damage 253, 295, 583, 601, 1075
Damage Detection 1093
Damage Mechanism 731
Damage Parameter 583
Damage Zone 893
Damage-Tolerance Analysis 649
Debonding 43
Defect Assessment Method 1333
Deformation 121, 679
Deformation Energy 205
Defric Coating 939
Degraded Material 577
Delamination 187, 731, 1153, 1189, 1201
Delamination Fracture 247
Delaunay Automatic Triangulation 445
Delayed Hydride Cracking DHC 845
Design of Reinforcement 439
Detonation 343
Devitrification 1255
Die Entrance Angle 547
Differential Scanning Calorimetry DSC 1171
Dilatational Phase Transformation 1231
Dilute Sulfuric Acid 999
Dimple Fracture 875
Direct Current Potential Drop DCPD 655
Directional Stability 55
Discrete Micromechanical Model 373
Dislocation 607
Distributed Parameter 361
DL-EPR Test 595
Domain Walls 607
Double Cracks 37
Double Shot Peening 921
Drill's Life 643
Ductile Polymer 289
Ductile Fracture 121
Ductile Iron 933
Dynamic Crack Bifurcation 313
Dynamic Crack Curving 313
Dynamic Crack Kinking 313
Dynamic Crack Propagation 265, 313, 325, 445
Dynamic Fracture 259, 313, 331, 445
Dynamic Fracture Mechanics 445, 1111
Dynamic Fracture Toughness ... 229, 301, 893
Dynamic Impact 451
Dynamic Interface Crack Stress Field 325
Dynamic Interfacial Fracture 313
Dynamic Isochromatics 283
Dynamic J Integral 445
Dynamic Loading Device 283
Dynamic Maximum Compressive Stresses 307
Dynamic Modeling 457
Dynamic Photoelastic Experimental Method 283
Dynamic Photoelastic Hybride Method 283
Dynamic Photoelasticity 337
Dynamic Photoelasticity Method 349, 481
Dynamic Recrystallization 851
Dynamic Response 423
Dynamic Stress Component 283
Dynamic Stress Intensity Factor 241, 301, 325, 349
Dynamic Stress-Strain Behavior 307
Dynamic Triaxial Compressive Loads 67
Dynamical Loading 253

E
Edge Cracks 79, 523, 743
Effective Flexural Modulus 247
Effective Stress Intensity Factor Range (ΔK_{eff}) 1345
Eigenfunction 163
Eigenvalue 163
Elastic Half Plane 109
Elastic Plastic Crack Propagation 565
Elastic Restraint 1135
Elastic Shear Buckling 517
Elastic Wave Scattering 241
Elasticity 499, 523
Elastic-Plastic Behavior 451
Elastic-Plastic Fracture Mechanics 1327
Elastic-Plastic SFEM 613
Electrical Resistance 1129
Electrodeposition 679
Electromagnetic Thermoelasticity 139
Electronic Speckle Pattern Interferometry ESPI 391
Element Modeling 397
Element Removal Method 379
Element-Free Galerkin Method EFGM 487
Elevated Temperature 1273
Elliptical Holes 25
Embrittlement 577, 1255
Energy Absorption Characteristics 1147

Energy Release Rate 259, 695, 773
Engineering Analysis 505
Epoxy Fraction 1081
Equilibrium Equation 157
Equivalent Engineering Modulus 1159
Equivalent Stress 999
Errors of the Reduced Integration 355, 469
Eshelby's Method 1219
Eulerian Finite Element Method 565
Eutectic Silicon Particle 1017
Evolutionary Structural Optimization 379
Expansion Fracture 277
Experimental Measurement 277
Experimental Study 1075
Explosion Experiment 319
Explosive Loading 277, 319
Extrapolation Method 553

F
Face Milling 559
Failure 785, 969
Failure Analysis 1099
Failure Behavior 1129
Failure Criterion 1165
Failure Index 1117
Failure Mode 535
Failure Pattern 809
Failure Probability 797
Failure Wave 343
Fatigue 719, 749, 933, 951, 969, 981, 1321
Fatigue Calendar Life 899
Fatigue Crack Growth 85, 127, 1303, 1345
Fatigue Crack Growth Resistance 19
Fatigue Design Criterion 957
Fatigue Life 909, 999
Fatigue Life Prediction 945, 957, 1011
Fatigue Limit 921, 933, 963
Fatigue Modulus 945, 1011
Fatigue Properties 1309
Fatigue Reliability 927
Fatigue Strength 415, 899, 915, 1315
Fatigue Test 951, 1029
FEM 553, 625, 1093, 1219
FEM Analysis 875
Ferroelectrics 175
Fiber 1297
Fiber Bridging 247, 1111
Fiber Orientation 815
Fiber Pull-Out 1153
Fiber Waviness 427, 1069
Fiber-Metal Laminates 1117
Filament 1207
Finite Element 1111
Finite Element Analysis 133, 373, 403, 505, 529, 547, 869, 1099
Finite Element Method 61, 97, 391, 475, 511, 541, 767, 1327
Finite Element Method of Lines 151
Finite Element Modelling 409
First and Second Crack Coalesence 857
Fixed Boundary 463
Fixing Element 475
Flexural Properties 631
Flexural Strength 1159
Flexural Test 1183
Fluid-Structure Interaction 349, 481
Flux Cored Arc Welding 1339
Forced Motion 469
Formability 1273
Fractal Dimension 367
Fractographic Study 1267
Fractography 169, 719, 731
Fracture 169, 319, 679, 695, 773, 969
Fracture Boundary Curve 1053
Fracture Mechanics 91, 97, 115, 145, 193, 409, 541, 565, 1005, 1213
Fracture Origin 749
Fracture Path Prediction 445
Fracture Ratio 505
Fracture Strength of Notch 791
Fracture Toughness 49, 73, 779, 863
Fracture Transformation 55
Framed Plate 319
Free Fall Shock 451
Frequency Effects 31
Fretting 743
Fretting Fatigue 915, 939
Fretting Pad Material 915
Friction Coefficient 547, 915
Friction Temperature 1225
FRP 601, 1135
FT-IR 1105
Full-Scale Pipe 655
Functionally Graded Materials 331, 373, 487, 511
Fuzzy Method 433

G
Gas Turbine 1029
Gauss Sampling Point 355, 469

Gears 921, 1285
Generalized Energy Function 55
Genetic Algorithm 1117
Glass Fiber 295
Global Displacement Fitting Procedure 79
Grain Boundary 1207
Grain Boundary Characteristic 851
Grain Boundary Sliding 367
Grain Boundary Triple Junction 851
Grain Size 707
Graphite/Epoxy Laminates 731
Graphite/Epoxy Square Tubes 1099
Grating Lobe 619
Grid 451, 463
Grillages 463
Growth-Strain Method 361
Gurson' s Constitutive Function 875
Gurson's Model 625

H

Hardening 1255
Hardness 987, 1285
Hardware-in-the-Loop 655
HAZ 1303
Healing Condition 803, 833
Heat Treatment 933
Heterogeneity 637, 785
Heterogeneous Materials 667
Hierarchical Models 403
High Density Polyethylene 229
High Impact Polystyrene 229, 289
High Strain Rate 97, 277, 307
High Temperature Fatigue Crack Growth 1041
High Temperature Strength 803, 1047
Higher Mode Deformation 673
High-Speed Loading 289
High-Speed Photography 289, 313
High-Speed Shadowgraph Technique 343
High-Strain-Rate-Superplasticity 851
Hill's Nonquadratic Yield Function 547
HIP Treatment 1243
Hold Time 31, 1041
Horizontal Crack 109
Horizontal Fatigue Tester 993
HREM-Moiré 737
Hybrid Composite 1297
Hybrid Fiber Reinforced Concrete 571, 881
Hybrid Metal Matrix Composite 1267
Hysteresis Loop 1249

I

Image Processing 145
Impact 731, 1189
Impact Damage 271, 1177
Impact Fracture 229, 313, 445
Impact Location Detection 661
Impact Test 577
Imperfect Interface 223
Inconel 718, 1029
Infinite Plate 199
Ingot Material 205
Initial Stress 755
Initial Velocity 451
Injection Moulding 1081
In-Plane Shear Forces 517
Insulating and Conducting Cracks 695, 773
Intensity Factor 139
Interaction Effect 523
Interaction Energy Method 259
Interface 1279
Interface Adhesion 1063
Interface Crack 49, 73, 541
Interface Fracture Toughness 541
Interface Layer 331
Interface of Bi-Material 211
Interfacial Compliance 223
Intergranular Carbide 707
Intergranular Corrosion 595
Interlaminar Fracture Toughness 229, 815, 1063
Interlaminar Shear Strength 1105
Internal Damaged of Drilled Hole 643
Inverse Fracture Problem 37
Inverse Problem 61, 1093
Irwin Method 145
ISM Method 903
Isochromatics 145
Isotropic/Orthotropic Bimaterials 283

J

J-Integral 31, 133, 505, 541, 869, 1327
Joint Strength 1165
J-Q Analysis 869
J-Q-Tz Theory 193

K

K-Type Tubular Joints 1005

L
Laminate 1141
Laminated Composites 403, 1165
Lamination 1123
Lamination Theory 1159
Large Strain 277, 289
Laser Profilometry 1123
Laser Surface Melting 595
Laser Weld 1321
Laser Welding 1309
Leak Detection 887
Leak-Before-Break LBB 655
Life of Propagation 1005
Life Prediction 1029
Limit Analysis 133
Limit Ironing Reduction 547
LMP Method 903
Load Interaction 127
Load-Differential Strain Curve 1249
Local Buckling Strength 1135
Local Fracture Criterion 1053
Localization 637, 785
Localized Flexibility 1093
Longitudinal Stiffener 517
Love Waves 725, 755
Low Carbon Steel 1315
Low Cycle Fatigue .. 749, 975, 981, 987, 1017
Lower Edge Crack 283
Low-Velocity Impact 295, 1177
Luminance 601

M
Machine Element 475
Magnetoelasticity 199
Martensitic Transformation 863
Mathematical Modelling 631
Matrix Cracking 1141
Matrix Ductility 1063
Maximum Hoop Stress Criterion 1053
MCM-D 1123
Mean Friction Coefficient 1225
Mechanical Alloying 1291
Mechanical Loading 863
Mechanical Parameter 433
Mechanical Properties 1291
Mechanical Property Degradation 631
Mechanically Fastened Joints 1011
Mechanism Method 463
Mechanistic Model 217
Median Filtering 391
Mesoscopic 785
Metal Matrix Composites 1219, 1237
Metal/Ceramic Joint 529
Metastable Phases 863
Method of Caustics 313
Micro Defects 767
Micro Vickers Hardness Test 577
Microcrack Interaction 667
Microcracks 667
Microcrystalline Grain 839
Micromechanics 1, 121, 1219
Microscopic Deformation 175
Microscopic Mechanism 127
Microshrinkage 749, 981
Microstructure 863, 881, 933
Mismatching 1327
Mixed Mode 49, 73, 541
Mixed Mode Fracture 1053
Mixed Mode Loading 325, 1035
Mixed-Mode 1141
Mixture Model 1255
MMC 625, 1243
Modal Design Sensitivity Analysis 439
Mode Analysis 355
Mode I 169, 815
Mode II 169
Model Accuracy 403
Modeling Error 403
Modified 16-Node Solid Element 355, 469
Modulus Mismatch 1261
Moiré Interferometry 409
Molded and Machined Notch 791
Monte Carlo Method 391
Monte Carlo Simulation 367, 1129
Morphology 779
$MoSi_2$ 909
Moving Element Method 445
Moving Least-Squares MLS Method 487
Mullite/SiC Ceramics 803
Multi-Axial Loading 945
Multi-Crack 809
Multicrack Growth Model 367
Multidirectional Composites 247
Multilayer 1123
Multi-Layered Structure 1081
Multiple Cracks 97
Multiple Layers CFRP 1159

N
Nanocomposite 1207

Nano-Deformation 737
Nano-Fractography 827
Nanomechanics 1
NaOH 707
Neural Network 559
Neural Network Modeling 713
Neutron Dose 607
Nondestructive Evaluation 619, 887, 1069
Nonlinear Behavior 637
Nonlinear Displacement Field 409
Nonlinear Evolution 713
Nonlinear Flexural Behavior 427
Normal Distribution 85
Notch 181, 601, 999
Notch Sensitivity Factor 1029
Nucleation Time 761
Numerical Analysis 457, 499, 523
Numerical Approximation Error 403
Numerical Minimization 631
Numerical Simulation 385, 637, 785

O

On-Line Frequency Estimation 1201
On-Line Monitoring 887
Optical Extensometer 229
Optical Fiber Vibration Sensor 661
Optical Micrograph 577
Optical-Fiber Extensometer 289
Optimization 415
Optimization Technique 61
Optimum Design 493, 1117
Organic Brake Pad 1225
Orientation Angle 1159
Orthotropic Plate 517
Orthotropic Structural Shapes 1135
Overall and Local Responses 373
Overall Elastic Properties 667
Overload 423
Oxidation 833

P

P/M Copper 205
Partial Crystallization 1255
Partial Interfacial Debonding 761
Partial Slip 743
Particle 1297
Particle Dispersed 1219
Particulate-Reinforced Composite Materials 761
Patched Crack 103
Path Independent Integral 445
PC/ABS 779, 1053
Peak Strength 809, 857
Penetration 1231, 1339
Percolation 367
Perturbation Method 613
PET Matrix Composites 1171
Phase Shifting 391
Phase Unwrapping 391
Phase Velocity 725, 755
Phased Array 619
Phenol Resin 1105
Photoelastic Experiment 115
Photoelasticity 145
PID Control 361
Piezoelectric Actuator 1201
Piezoelectric Ceramics 673, 821
Piezoelectric Element 619
Piezoelectric Layered Structures 725, 755
Piezoelectric Materials 695, 773
Pinned Joint 1165
Pipe Flange 475
Pit 939
Plain-Woven Glass/Epoxy Composites 271
Plane Compressional Wave 223
Plane Problem 199
Plastic Deformation 541
Plastic Hinge 463
Plasticity 217
Plate 397
PMMA 265
Polarization Curve 707
Polyamide 6 1081
Polycarbonate 121, 229, 601
Polymer 121, 1075
Polymer Alloy 779, 1053
Polymer Matrix Composites PMC 229, 295
Polynomial Approximation 49
Polypropylene Fiber 571, 881
Porosity 963
Porous Solid 1195
Post Welding Heat Treatment 1339
Postbuckling 1189
Powder Metallurgy 1273, 1285
Pressure-Sensitivity 1195, 1231
Pressurized Thermal Shock 797
Prestrain 1321
Printing Wiring Board 643
Probabilistic Fatigue 927

Probabilistic Fracture Mechanics 797
Progressive Collapse 1023
Progressive Failure Analysis 535, 1165
Pseudo Dynamic Elastic Moduli 307
P-S-N Curve 951
PTS Screening Criteria 797
Punch Shape 743

Q

Quasi-Cleavage Fracture 737

R

Random Fatigue 1005
Random Variable 85
Rapid Press Consolidation Technique RPCT 1171
Rapid Solidification 839
Rate of Test 247
Rayleigh Wave Velocity 325
Rayleigh-Ritz Method 517
Recovery of Strength 803, 1047
Recrystallization 679
Reduction of Stress Intensity Factor 43
Reduction Ratio 379
Regular Fracture 55
Reinforcement 385
Reissner Plate 151, 163
Reissner Shell 151
Relative Thickness Ratio 373
Reliability 613, 957
Remaining Life 987
Remanent Polarization 821
Residual Strength 271
Residual Strength Analysis 649
Residual Stress 73, 529, 1219, 1279, 1339
Resonances 969
Response Surface Method 1023
Retardation Coefficient 85
Rigid Particle 1075
Rock Mass 385, 433
Rock Material 67
Rock Microfracturing Process 713
Rolling Contact Fatigue 1035
Rolling Stock 493
Roughness 217
Rubber Contents 583
Rubber Modified Adhesive 583
Rubber Toughened PMMA 409
Rubber-Modified Epoxy 1195
Rule of Mixtures 373

S

SA508-3 607
Scale Effect 1
Scattering 223
Sealing Performance 475
Secondary Curing Method 1087
Selected Load Sequence 127
SEM 625, 749, 981
SEM Observation 779
Semi-Elliptical Notch 523
SENB Specimen 869
Sensitivity Analysis 1023
Sensitization 595
SENT Specimen 869
Separated Dynamic J Integral 445
Separation of Solid 319
Shadow Spot Method 301
Shape Control 673
Shape Memory Alloy 673, 1309
Shape Memory Effect 1219, 1309
Shape Optimization 361
Shear 37
Shear Fracture 1053
Ship Hull Girders 1023
Shock Adiabatics 253
Short Crack 217
Short Fiber Reinforcement 1177
Si_3N_4/SiC Ceramics 1047
SiC Particle 625
Silica Particulate Filled Epoxide Resin 1053
Silicon Carbide Ceramic 1249
Silicon Carbide Composite Ceramic 1249
Silicon Nitride 833
Simulation 391
Single-Asperity-Contact Friction 1
Single-Node Quadratic Element 91
Singular Integral Equation 241, 499
Singular Line Mapping 151
SiO_2 909
Sliding Crack Model 67
Slip 767
Small Diameter Drilling 643
Smart Structure 661
S-N Curve 1029
SN-DCB Specimen 815
Sobel Edge Enhancement 391
Soft ferromagnetic Materials 199
Softening 987
Solid Lubricant Wear 1267
Solid State Sintering 1291

Solid Wires 1339
Solution Treatment 1237
Source Location 887
Spalling Cracks 1213
Spatial Random Process 19
Specific Damping Capacity 469
Spherical Inhomogeneity 223
Spheroidal Graphite Cast Iron 749, 981
Split Hopkinson Pressure Bar SHPB 307
Spot-Welded 415
Spot-Welded Joint 957
Spraying 839
Squeeze Cast Aluminium Alloy 1017
Squeeze Casting 1237
Squeeze Casting Method 1267
Stacking Sequence 1141
Stainless Steel 304 31
Staircase 951
Static Analysis 355
Static Fatigue Strength 803, 1047
Statistics 951
Steel D&I Can 547
Stiffened Composite Plate 1189
Stiffened Cylinder 481
Stiffness Reduction Method 535
Stoney's Formula 1123
Strain Constrain 1321
Strain Control 975
Strain Energy 517
Strain Energy Density Factor 957
Strain Gauges 289
Strain Gradient Plasticity 9
Strain Hardening Exponent 205
Strength 67, 637, 679, 839, 1207
Strength Mismatch 1333
Strength Recovery 833
Strengthening Mechanisms 1297
Stress 969
Stress Analysis 475, 547
Stress Concentration . 25, 601, 767, 969, 1011
Stress Concentration Factor 499, 523, 999
Stress Control 361
Stress Corrosion Cracking (SCC) 707
Stress Cutting 55
Stress Double Shot Peening 921
Stress Intensity Factor 25, 31, 37, 49, 79, 109, 115, 145, 151, 163, 211, 259, 265, 319, 331, 487, 511, 523, 553, 743, 993, 1345
Stress Intensity Factor Range 999
Stress Interaction Effect 767
Stress Ratio 827, 1249
Stress Relaxation 1123
Stress Shot Peening 921
Stress Triaxiality 121, 625, 875
Stress Wave 337
Stress Wave Propagation 349, 481
Stress-Strain Fields 193
Striation Height 827
Striation Width 827
Striation-like Marking 719
Structural Steels 939
Structure Analysis 61, 423
STS 316L 1041
Substructure Strengthening 1207
Surface Acoustic Wave Devices 725, 755
Surface Crack 505, 1005, 1327
Surface Roughness 915
Surface-Roughness Evolution 1
SUS304 1011

T

Taguchi Method 1087
Tailored Welded Blank 1321
Target Strength 1231
Tearing Modulus 505
TEM Observation 779
Temper Bead Welding 1339
Temperature 583, 815
Temporal Fractal 713
Tensile Properties 779
Tensile Stiffness 25
Tensile Strength 1243
Tensile Tests 577
Tension 25, 601
Texture 679, 845
The Fourth Compressor Pan 969
Thermal Aging 631, 975
Thermal Barrier Coating 909
Thermal Cycle 529
Thermal Shock 1213
Thermomechanical Bow 1123
Thermoplastic Polymer 631
Thermoplastics 121
Thermotropic Liquid Crystalline Polymers 1081
Thick Composites 427, 791, 1069
Thickness Effect 127, 193, 271
Thickness Polynomials 403
Thin Film 187

Thin-Walled Plate 451
Three Flaws 857
Three Gorge Project 385
Three-Dimensional Cracks 193
Three-Dimensional Fields 181
Threshold 999
Threshold Impact Energy 271
Threshold Stress Intensity Factor (K_{IH}) 845
Ti-6Al-4V Alloy 1243
Ti-Alloy 1303
Time-of-Flight Base of Method 887
Time-Variation Reliability Assessment 1023
TiNi Alloy 1219
Tool Wear 559, 643
Tooling 1285
Topology Optimization 379, 439
Toroidal Hole 499
Toughness Testing Standards 133
Trigger Mechanism 1147
TTP Method 903
Tungsten Fiber 1243
Tungsten Fiber Content Ratio 963
Tungsten Fiber Reinforced Ti-6Al-4V (W/Ti-6Al-4V) Alloy 963
Tungsten Heavy Alloy 1291
Two-Dimensional Elasticity 25
Two-Step Sintering 1291

U

Ultrasonic Peening 1315
Ultrasonic Testing 619
Ultrasonics 1069
Underwater Explosion 481
Undulation 1153
Unidirectional Carbon Prepreg 1087
Unified Description 181
Unloading Behavior 265
Unloading Rate 265
Upper Edge Crack 283

V

Vane Components 1029
Vapor Deposition 679
Variability 85
Variable Amplitude Loading 85
VCFEM 373
Vibration 391
Vibration Analysis 397
Virgin Material 577
Virtual Crack Extension Method 49
Virtual Work 463
Viscoelastic Material 761, 893
Void 875
Void Configuration 625
Void Growth 761
Void Nucleation Model 1195
Void Volume Fraction 625
Voids 157
Volume Control 361
Volume Fraction 373
VPS 909

W

Wakashima-Tsukamoto Estimate 373
Wall Ironing 547
Wear Rate 1225
Weibull Distribution 19
Weight Function Method 103
Welded Joint 1315
Welded Pipe 613
Welding Process 1303
Welding Residual Stress 1345
Weldment 1333
Wheel-Rail Contact 493
Whisker 1237
White Light Photoelastic Experiment 145
Wide-Plate 655
Winch 719
Window Pillar Member 415
Wire Rope 719
With-Laminar 1153
Workpiece Material 559
Woven Glass Fabrics 1183

X

XPS 1105

Y

Y4 Steel 301
Yield Strength 589
Yielding 1261

Z

Zr-2.5%Nb 845

Key Engineering Materials

Specializing in Advanced Ceramics and Composites

Recent Volumes:
for complete tables of contents please visit http://www.ttp.net

Electroceramics in Japan III, *Eds. N. Murata, K. Shinozaki and T. Kimura*

Advances in Engineering Plasticity, *Eds. T.X. Yu, Q.P. Sun and J.K. Kim*

Engineering Ceramics: Multifunctional Properties, *Eds. P. Sajgalík and Z. Lencés*

Creep and Fracture of Engineering Materials and Structures , *Eds. T. Sakuma, K. Yagi*

Electroceramics in Japan II, *Eds. N. Mizutani, K. Shinozaki, N. Kamehara, T. Kimura*

Damage Assessment of Structures, *Eds. M.D. Gilchrist, J.M. Dulieu-Barton, K. Worden*

Time Dependent Mechanical Response of Engineering Ceramics, *Eds. E. Yasuda, F. Wakai, L.M. Manocha, Y. Tanabe*

High Temperature Ceramic Matrix Composites III, *Eds. K. Niihara, K. Nakano, T. Sekino, E. Yasuda*

The Science of Engineering Ceramics II, *Eds. K. Niihara, T. Sekino, E. Yasuda, T. Sasa*

Novel Synthesis and Processing of Ceramics, *Eds. H. Suzuki, K. Komeya and K. Uematsu*

Electroceramics in Japan I, *Eds. N. Mizutani, K. Shinozaki, N. Kamehara and T. Kimura*

Oxides: Phase Transitions, Non Stoichiometry, Superconductors, *Ed. C. Boulesteix*

Zirconia Engineering Ceramics: Old Challenges - New Ideas, *Ed. E. Kisi*

Solidification Processing of Reinforced Metals, *by R. Asthana*

Sol-Gel Production, *Ed. H. Schmidt*

Fracture and Strength of Solids, *Eds. P. Tong, T.Y. Zhang and J.K. Kim*

Experimental Techniques and Design in Composite Materials, *Ed. Pierluigi Priolo*

Impact Response and Dynamic Failure of Composites and Laminate Materials, *Eds. J.K. Kim and T.X. Yu*

Advanced Ceramic Tools for Machining Application - III, ***Ed. I.M. Low***

Polymer Blends and Polymer Composites, *L. Ye and Y.-W. Mai*

Euro Ceramics V, *Eds. P. Abelard, J. Baxter, D. Bortzmeyer et al.*

Ceramic and Metal Matrix Composites, *Eds. M. Fuentes, J.M. Martínez-Esnaola, A.M. Daniel*

Electrical Properties of Oxide Materials, *J. Nowotny and C.C. Sorrell*

Advanced Ceramic Materials, *Hamid Mostaghaci*

Fracture of Composites, *Ed. E.A. Armanios*

Metal Matrix Composites, *Ed. G.M. Newaz*

***Key Engineering Materials** presents 18 volumes per year, each centering on a special topic of current interest in the fields of advanced ceramics and composites. The yearly subscription rate is 1404.00 CHF.*

Please place your trial subscription with complete return rights:

Trans Tech Publications Ltd • Brandrain 6 • CH-8707 Zuerich-Uetikon • Switzerland
Fax: (++41) 1 922 10 33 • E-Mail: ttp@ttp.net • Web Site: http://www.ttp.net